

# THE JOURNAL of the Acoustical Society of America

Vol. 102, No. 6

December 1997

<b>ACOUSTICAL NEWS—USA</b>	3235
USA Meetings Calendar	3238
<b>ACOUSTICAL NEWS—INTERNATIONAL</b>	3240
International Meetings Calendar	3240
<b>OBITUARIES</b>	3242
<b>REVIEWS OF ACOUSTICAL PATENTS</b>	3243
<b>SELECTED RESEARCH ARTICLE [10]</b>	
Active control of finite amplitude acoustic waves in a confined geometry	Pai-Tsung Huang, J. G. Brisson 3256
Surface wave formation at an impedance discontinuity	Michael R. Stinson, Gilles A. Daigle 3269
<b>GENERAL LINEAR ACOUSTICS [20]</b>	
Tube waves and mandrel modes: Experiment and theory	Chaur-Jian Hsu, Sergio Kostek, David Linton Johnson 3277
Oblique coherent waves inside and outside a randomly cracked elastic solid	Y. C. Angel, A. Bolshakov 3290
On Green's functions for a cylindrical cavity	Earl G. Williams 3300
Acoustic bullets: Transient Bessel beams generated by planar apertures	Peter R. Stepanishen, Jie Sun 3308
Sound transmission through elastic porous wedges and foam layers having spatially graded properties	Yeon June Kang, J. Stuart Bolton 3319
Group velocity formulas for the symmetry planes of a stressed anisotropic elastic solid	Kwang Yul Kim, Tsung-Tsong Wu, Wolfgang Sachse 3333
On the low-frequency oscillation of a fluid layer between two elastic plates	Waled Hassan, Peter B. Nagy 3343
<b>NONLINEAR ACOUSTICS, MACROSONICS [25]</b>	
Nonlinear elastic constants of solids with cracks	Veniamin E. Nazarov, Alexander M. Sutin 3349
Temperature discontinuities between elements of thermoacoustic devices	James R. Brewster, Richard Raspet, Henry E. Bass 3355
Diagnosis of periodic and chaotic responses in vibratory systems	L. Dai, M. C. Singh 3361
The effects of a soluble surfactant on quadrupole shape oscillations and dissolution of air bubbles in water	Thomas J. Asaki, Philip L. Marston 3372
<b>AEROACOUSTICS, ATMOSPHERIC SOUND [28]</b>	
Comparisons of exact and approximate convection of plane waves in a simple shear flow	Laurine Leep-Apolloni, David R. Dowling 3378

(Continued)

## CONTENTS—Continued from preceding page

**UNDERWATER SOUND [30]**

<b>Coupled-mode modeling of acoustic scattering from three-dimensional, axisymmetric objects</b>	John A. Fawcett	3387
<b>A finite-difference time-domain solution to scattering from a rough pressure-release surface</b>	Frank D. Hastings, John B. Schneider, Shira L. Broschat	3394
<b>Novel acoustic wave resonance scattering formalism</b>	Huinam Rhee, Youngjin Park	3401
<b>Vertical coherence of ambient noise in shallow water overlying a fluid seabed</b>	Grant B. Deane, Michael J. Buckingham, Christopher T. Tindle	3413
<b>Nonlinear tomographic inversion by using Wentzel–Kramers–Brillouin modal condition</b>	E. C. Shang, Y. Y. Wang, A. G. Voronovich	3425
<b>Adaptive beamforming against reverberation for a three-sensor array</b>	Joseph N. Maksym, Michael Sandys-Wunsch	3433
<b>Multipath compensation in shallow water environments using a virtual receiver</b>	Martin Siderius, Darrell R. Jackson, Daniel Rouseff, Robert Porter	3439

**ULTRASONICS, QUANTUM ACOUSTICS, AND PHYSICAL EFFECTS OF SOUND [35]**

<b>Comparison between prediction and measurement of viscoelastic moduli in composite materials versus temperature using ultrasonic immersion technique with oil</b>	Sandrine Baudouin, Bernard Hosten	3450
<b>Comparison of elastic constant determination in anisotropic materials from ultrasonic group and phase velocity data</b>	A. D. Degtyar, S. I. Rokhlin	3458
<b>Determination of elastic moduli, density, attenuation, and thickness of a layer using ultrasonic spectroscopy at two angles</b>	Anton I. Lavrentyev, Stanislav I. Rokhlin	3467
<b>Why fluid loading has an opposite effect on the velocity of dilatational waves in thin plates and rods</b>	Waled Hassan, Peter B. Nagy	3478
<b>A simplified model for linear and nonlinear processes in thermoacoustic prime movers. Part I. Model and linear theory</b>	M. Watanabe, A. Prosperetti, H. Yuan	3484
<b>A simplified model for linear and nonlinear processes in thermoacoustic prime movers. Part II. Nonlinear oscillations</b>	H. Yuan, S. Karpov, A. Prosperetti	3497

**TRANSDUCTION [38]**

<b>Characterization of porous piezoelectric ceramics: The length expander case</b>	Tomás E. Gómez Alvarez-Arenas, Francisco Montero de Espinosa	3507
--	--	------

**STRUCTURAL ACOUSTICS AND VIBRATION [40]**

<b>Vibration and dynamic response control of cantilevers carrying externally mounted stores</b>	L. Librescu, S. S. Na	3516
<b>Frequency derivative approach for identification of the wave resonances on immersed elastic bodies</b>	Bertrand Dubus, Antoine Lavie, Naum D. Veksler	3523
<b>An analytical investigation of the active attenuation of the plate flexural wave transmission through a reinforcing beam</b>	Nicole J. Kessissoglou, Jie Pan	3530
<b>Analysis of ceramic thickness shear piezoelectric gyroscopes</b>	J. S. Yang	3542

**ACOUSTICAL MEASUREMENTS AND INSTRUMENTATION [58]**

<b>An experimental-numerical technique for evaluating the bulk and shear dynamic moduli of viscoelastic materials</b>	R. Lance Willis, T. Shane Stone, Yves H. Berthelot, Walter M. Madigosky	3549
---	---	------

**ACOUSTIC SIGNAL PROCESSING [60]**

<b>An experimental evaluation of split-beam processing as a broadband bearing estimator for line array sonar systems</b>	Stergios Stergiopoulos, Anthony T. Ashley	3556
--	---	------

**PHYSIOLOGICAL ACOUSTICS [64]**

<b>Growth rate of simultaneous masking in cat auditory-nerve fibers: Relationship to the growth of basilar-membrane motion and the origin of two-tone suppression</b>	Xiao Dong Pang, John J. Guinan, Jr.	3564
---	-------------------------------------	------

(Continued)

## CONTENTS—Continued from preceding page

<b>Effects of stapedius-muscle contractions on the masking of auditory-nerve responses</b>	Xiao Dong Pang, John J. Guinan, Jr.	3576
<b>Frequency-dependent enhancement of basilar membrane velocity during olivocochlear bundle stimulation</b>	David F. Dolan, Meng He Guo, Alfred L. Nuttall	3587
<b>Frequency specificity of the human auditory brainstem and middle latency responses to brief tones. I. High-pass noise masking</b>	Peggy Oates, David R. Stapells	3597
<b>Frequency specificity of the human auditory brainstem and middle latency responses to brief tones. II. Derived response analyses</b>	Peggy Oates, David R. Stapells	3609
<b>The effects of click level, click rate, and level of background masking noise on the inferior colliculus potential (ICP) in the normal and carboplatin-treated chinchilla</b>	Robert Burkard, Patricia Trautwein, Richard Salvi	3620
<b>PSYCHOLOGICAL ACOUSTICS [66]</b>		
<b>Modeling the relation between the intensity just-noticeable difference and loudness for pure tones and wideband noise</b>	Jont B. Allen, Stephen T. Neely	3628
<b>Auditory discrimination of material changes in a struck-clamped bar</b>	Robert A. Lutfi, Eunmi L. Oh	3647
<b>Effect of the relative phase of amplitude modulation on the detection of modulation on two carriers</b>	Shigeto Furukawa, Brian C. J. Moore	3657
<b>Infants' pitch perception: Masking by low- and high-frequency noises</b>	Christine Rogers Montgomery, Marsha G. Clarkson	3665
<b>Electrode discrimination and speech recognition in postlingually deafened adult cochlear implant subjects</b>	Terry A. Zwolan, Leslie M. Collins, Gregory H. Wakefield	3673
<b>Information from time-varying vibrotactile stimuli</b>	Ian R. Summers, Philip G. Cooper, Paul Wright, Denise A. Gratton, Peter Milnes, Brian H. Brown	3686
<b>Estimating parameters for psychometric functions using the four-point sampling method</b>	Chan F. Lam, Judy R. Dubno, Jayne B. Ahlstrom, Ning-Ji He, John H. Mills	3697
<b>SPEECH PERCEPTION [71]</b>		
<b>Speechreading and the structure of the lexicon: Computationally modeling the effects of reduced phonetic distinctiveness on lexical uniqueness</b>	Edward T. Auer, Jr. and Lynne E. Bernstein	3704
<b>Stop-consonant and vowel perception in 3- and 4-year-old children</b>	Ralph N. Ohde, Katarina L. Haley	3711
<b>Perceptual differences in infant cries revealed by modifications of acoustic features</b>	Athanassios Protopapas, Peter D. Eimas	3723
<b>Do weak syllables count for newborns?</b>	Brit van Ooijen, Josiane Bertoncini, Alessandra Sansavini, Jacques Mehler	3735
<b>Adult and infant perception of two English phones</b>	Judith E. Pegg, Janet F. Werker	3742
<b>Estimating articulation scores</b>	Christine M. Rankovic, Robin M. Levy	3754
<b>Central auditory system plasticity: Generalization to novel stimuli following listening training</b>	Kelly Tremblay, Nina Kraus, Thomas D. Carrell, Therese McGee	3762
<b>BIOACOUSTICS [80]</b>		
<b>Acoustic properties of egg yolk and albumen in the frequency range 20–400 MHz</b>	N. Akashi, J. Kushibiki, F. Dunn	3774
<b>Ultrasonic relaxation associated with proton transfer reaction in aqueous solutions of heterocyclic amines</b>	Sadakatsu Nishikawa, Masumi Satoh	3779
<b>Decorrelation of intravascular echo signals: Potentials for blood velocity estimation</b>	Wenguang Li, Charles T. Lancée, E. Ignacio Céspedes, Antonius F. W. van der Steen, Nicolaas Bom	3785
<b>Frequency tuning of the dolphin's hearing as revealed by auditory brain-stem response with notch-noise masking</b>	Vladimir V. Popov, Alexander Ya. Supin, Vladimir O. Klishin	3795

(Continued)

## CONTENTS—Continued from preceding page

## LETTERS TO THE EDITOR

Surface-controlled drop oscillations in space [25]	R. Glynn Holt, Yuren Tian, Joseph Jankovsky, Robert E. Apfel	3802
Collective and localized modes of mono-coupled multi-span beams with large deterministic disorders [40]	A. S. Bansal	3806
Cochlear models and minimum phase [64]	Egbert de Boer	3810

## ERRATA

Erratum: "Elasto-acoustics of a two-dimensional strip by a hybrid method" [J. Acoust. Soc. Am. 102, 955–967 (1997)]	Michael El-Raheb	3814
---	------------------	------

## TECHNICAL NOTES AND RESEARCH BRIEFS

Tuning process of xylophone and marimba bars analyzed by finite element modeling and experimental measurements	J. Bretos, C. Santamaria, J. Alonso Moral	3815
--	---	------

INDEX TO VOLUME 102		3820
---------------------	--	------

SUBJECT INDEX TO VOLUME 102		3825
-----------------------------	--	------

AUTHOR INDEX TO VOLUME 102		3858
----------------------------	--	------

## NOTES CONCERNING ARTICLE ABSTRACTS

1. The number following the abstract copyright notice is a Publisher Item Identifier (PII) code that provides a unique and concise identification of each individual published document. This PII number should be included in all document delivery requests for copies of the article.
2. PACS numbers are for subject classification and indexing. See June and December issues for detailed listing of acoustical classes and subclasses.
3. The initials in brackets following the PACS numbers are the initials of the JASA Associate Editor who accepted the paper for publication.

**Document Delivery:** Copies of articles can be ordered for \$15 per copy from the AIP/Member Society document delivery service "Articles in Physics," 75 Varick Street, New York, NY 10013; Fax: 212-301-4060; Telephone: 800-480-PHYS (800-480-7497) (in U.S. and Canada), or 212-301-4000; E-mail: [articles@aip.org](mailto:articles@aip.org); URL: <http://www.aip.org/articles.html>

# ACOUSTICAL NEWS—INTERNATIONAL

Walter G. Mayer

Physics Department, Georgetown University, Washington, DC 20057

## ISMA'97: International Symposium on Musical Acoustics

An international symposium on musical acoustics (ISMA'97) took place at The University of Edinburgh, Edinburgh, Scotland, 19–22 August 1997. The symposium, which included a joint session on the History of Musical Acoustics with the Galpin Society Colloquium on Historical Musical Instrument Acoustics and Technology, was held during the famous Edinburgh Festival, to the delight of attendees. Over 100 invited and contributed papers were presented, covering all areas of musical acoustics. D. Murray Campbell, Department of Physics and Astronomy, chaired ISMA'97, while Arnold Myers, Faculty of Music, organized the Colloquium on Historical Musical Instruments.

In addition to the technical program, participants were treated to a rich menu of concerts and social events, including a recital on historical keyboard instruments in the Russell Collection, a "Ceilidh" (informal concert) by the participants (see Fig. 1), a concert of electronic music, a concert of music for the New Violin Octet, and a memorable banquet at the country manor home of the Earl and Countess of Wymess with Renaissance music on period instruments.



FIG. 1. Informal music at the Ceilidh. Murray Campbell is at the left.

Edinburgh is an exciting place to be at Festival time. In addition to many impromptu street performances, most of the ISMA'97 attendees took in the Military Tattoo (with over 150 bagpipes as well as several military bands!) as well as a rich menu of orchestral and organ concerts, not to mention the numerous events in the "Edinburgh fringe."

THOMAS D. ROSSING

Physics Department  
Northern Illinois University  
DeKalb, Illinois 60115

## EUROMECH announces 1998 and 1999 meetings

The Council of the European Mechanics Society (EUROMECH) has released the list of EUROMECH Colloquia and Conferences which will take place in 1998 and 1999. The number of Colloquium participants is limited and those interested in attending, by invitation only, should contact the local organizer. The list of colloquia which might be of interest to acousticians follows.

1998:

**Modeling and control of adaptive mechanical structures**, 11–13 March, Magdeburg, Germany. ulrich.gabbert@mb.uni-magdeburg.de

**Surface slicks and remote sensing of air-sea interactions**, 6–8 April, Warwick, UK. nhtfred@aol.com

**Nonlocal aspects in solid mechanics**, 20–22 April, Mulhouse, France. jf.ganghoffer@univ-mulhouse.fr

**Recent computational developments in steady and unsteady naval hydrodynamics**, 27–29 April, Poitiers, France. guillbaud@univ-poitiers.fr

**Waves in two-phase flows**, 27–30 April, Istanbul, Turkey. gokcol@sariyer.cc.itu.edu.tr

**Stability and control of shear flows with strong temperature or density gradients**, 20–22 May, Prague, Czech Republic. marsik@bivoj.it.cas.cz

**Aerodynamics and aeroacoustics of tracked high-speed ground transportation**, 8–10 June, Göttingen, Germany. g.e.a.meier@dlr.de

**Fatigue life in the gigacycle regime**, 29 June–3 July, Paris, France. bathias@cnam.fr

**Steady and unsteady separated flows**, 6–9 July, Manchester, UK. euro384@ma.man.ac.uk

**Continuation methods in fluid dynamics**, 6–9 September, Aussois, France. henry@mecaflu.ec-lyon.fr

**Inelastic analysis of structures under variable loads: theory and engineering applications**, 8–11 September, Aachen, Germany. weichert@uranus.iam.rwth-aachen.de

**Laminar-turbulent transition mechanisms and prediction**, 14–17 September, Göttingen, Germany. uwe.dallmann@dlr.de

**Dynamics and vibro-impact systems**, 15–18 September, Loughborough, UK. v.i.babitsky@lboro.ac.uk

1999:

**Physiological flows and flow-structure interactions**, April, Graz, Austria. perktold@fmatdds01.tu-graz.ac.at

**Instability, bifurcation and localization in fracture of materials**, 10–12 May, Paris, France. gilles.rousselier@der.edfgdf.fr

**Wind tunnel modeling of dispersion in environmental flows**, 13–15 September, Prague, Czech Republic. janour@bivoj.it.cas.cz

The EUROMECH Conferences are open to all those interested, with attendance of about 150 to 600. The three conferences scheduled for 1998 are:

**2nd EUROMECH Mechanics of Materials Conference**, 23–26 February, Magdeburg, Germany. mecamat@mb.uni-magdeburg.de

**7th EUROMECH Turbulence Conference**, 30 June–3 July, St.-Jean Cap Ferrat, France. <http://www.obs-nice.fr/etc7>

**3rd EUROMECH Mechanics of Materials Conference**, November/December, UK. e.busso@ic.ac.uk

The current President of EUROMECH is David G. Crighton, FRS and Fellow of this Society; The Secretary-General is Bengt Lundberg of Uppsala University, Sweden. Additional information is available from the Secretary-General, [bengt.lundberg@teknikum.uu.se](mailto:bengt.lundberg@teknikum.uu.se) or via Fax +46 18 183 122.

## International Meetings Calendar

Below are announcements of meetings to be held abroad. Entries preceded by an \* are new or updated listings with contact addresses given in parentheses. Month/year listings following other entries refer to issues of the *Journal* which contain full calendar listings or meeting announcements.

December 1997

9–11 \***29th Annual Scientific Meeting—British Medical Ultrasound Society**, Bournemouth, UK. (Secretary, BMUS, 36 Portland Place, London W1N 3DG, UK; Fax: +44 171 323 2175)

16–17 **Underwater Acoustics Conference**, Loughborough. 10/97

15–18 **5th International Congress on Sound and Vibration**, Adelaide. 10/96

**February 1998**

2–6

**Ultrasonic Technological Processes—98**, Moscow. 6/97**March 1998**

4–5

**4th Annual Conference of the Society of Acoustics of Singapore**, Singapore. 10/97

23–27

**DAGA 98** (German Acoustical Society Meeting), Zürich. 8/96

31–2

**Acoustics 98**, Cranfield University, UK. 10/97**April 1998**

27–30

**\*Waves in Two-phase Flows** (EUROMECH Colloquium), Istanbul, Turkey. (C. Delale, Mechanical Engineering Department, Istanbul University, Avcilar Kampusu, 34850 Avcilar, Istanbul, Turkey; e-mail: gokcol@sariyer.cc.itu.edu.tr)**May 1998**

10–14

**6th Meeting of the European Society of Sonochemistry**, Rostock-Warnemünde. 10/97

18–22

**7th Spring School on Acousto-optics and Applications**, Gdańsk. 8/97

25–27

**Noise and Planning 98**, Naples. 2/97**June 1998**

8–10

**EAA/EEAA Symposium “Transport Noise and Vibration,”** Tallinn. 10/96

9–12

**8th International Conference on Hand-Arm Vibration**, Umea. 6/97

20–28

**Joint Meeting of the 16th International Congress on Acoustics and 135th Meeting of the Acoustical Society of America**, Seattle. 6/97**July 1998**

1–12

**\*NATO ASI “Computational Hearing,”** Il Ciocco (Tuscany), Italy. (S. Greenberg, International Computer

Science Institute, 1947 Center St., Berkeley, CA 94704, USA; Fax: +1 510 643 7684; e-mail: comhear@icsi.berkeley.edu; Web: www.icsi.berkeley.edu/real/comhear98)

**September 1998**

7–9

**Nordic Acoustical Meeting 98**, Stockholm. 10/97

14–16

**Biot Conference on Poromechanics**, Louvain-la-Neuve. 10/97

14–16

**ACUSTICA 98**, Lisbon. 10/97

14–18

**35th International Conference on Ultrasonics and Acoustic Emission**, Chateau of Trešć. 10/97**November 1998**

16–18

**Inter-Noise 98**, Christchurch. 4/96

20

**Recreational Noise**, Queenstown. 10/97

23–27

**ICBEN 98: Biological Effects of Noise**, Sydney. 12/96

30–4

**5th International Conference on Spoken Language Processing**, Sydney. 6/97**March 1999**

15–19

**Joint Meeting of DAGA, EAA Forum Acusticum, and 137th Meeting of the Acoustical Society of America**, Berlin. 6/97**June 1999**

28–30

**1st International Congress of the East European Acoustical Association**, St. Petersburg. 10/97**July 1999**

4–9

**10th British Academic Conference in Otolaryngology**, London. 10/97**September 1999**

1–4

**15th International Symposium on Nonlinear Acoustics (ISNA-15)**, Göttingen. 10/97

# OBITUARIES

*This section of the Journal publishes obituaries concerning the death of Fellows of the Society and other acousticians eminent in the world of acoustics. When notified, the Editor-in-Chief solicits a summary of the person's life and contributions from an ASA member thoroughly familiar with the details, if possible. If a promised obituary is never received, a brief obituary notice may be published later.*

---

## George J. Thiessen • 1913–1997

George J. Thiessen, a Fellow Emeritus of the Acoustical Society, died suddenly at his home on 17 January 1997. He became a member of the Society in 1953 and a Fellow in 1963.

George Thiessen was born in May 1913 in the Ukraine, the ninth of twelve children. His father was a minister of the Mennonite Church. The family had recently moved from Germany to escape turmoil in Central Europe, but between 1916 and 1923 they survived the devastation of six armies fighting across their land. George's father eventually arranged for many people, including his whole family, to leave. By great good fortune the parents and eleven surviving children were able to come together to Canada, settling in Saskatchewan where they again survived, this time the "dust bowl" era of the 1930s. These childhood experiences shaped George's character as a man who was hardworking and self-reliant, and of great integrity and humility.

George obtained a B.Sc. from the University of Saskatchewan in 1935 and a M.Sc. in 1937. He obtained a Ph.D. in nuclear physics under Enrico Fermi from Columbia University in New York in early 1941. Canada was already into World War II, and George felt that duty required him to return to the war effort at the National Research Council in Ottawa. At that time Great Britain was the only unoccupied country in Western Europe still opposing Nazi Germany, and Canada was its main source of overseas supplies. Since German U-boats were a major threat, the Physics Division at NRC was almost totally devoted to sonar, acoustic mines, and torpedoes. At its peak, the Acoustics Section numbered between 40 and 50 people. After the war NRC returned to a peacetime, more balanced, scientific effort. Soon the Acoustics Section shrank to only four people with George as the only scientist, working with three technicians.

George's self-reliance, ingenuity with mechanical devices, and frugality enabled the acoustics group to survive, strengthen, and gradually grow. During the next few years numerous young postdoctoral scientists from half a dozen foreign countries each worked for a year in the acoustics laboratory.

George was like a father figure to the mostly young bachelors, and often invited them to his home at Christmas and other occasions. Edgar Shaw joined the section in 1950. Tony Embleton arrived in 1952. Joe Piercy joined about 1955. All three stayed for their whole professional careers. There was steady sustainable growth over many years at the rate of one person every three or four years, which served us well. In good economic times the Acoustics Section at NRC never grew as fast as some others, but in difficult times it never shrank. George was trusted by management, and his section always provided good return. The Acoustics Section chose to do most of its basic science on topics that could clearly be applied for the social or economic benefit of society. Thus we developed liquid-filled ear defenders, now used worldwide to protect people's hearing, and redesigned major noisemaking parts of paper-making and nail-making machinery so that they were quieter. Much later, the efforts at George's laboratory helped a fledgling loudspeaker industry in Canada improve its products and become a major global player.

George served the Acoustical Society of America with distinction. Among other activities, he arranged the technical program for the first Society meeting held outside the United States—in Ottawa in 1959. Bringing that meeting to Ottawa was due in part to the stature that his laboratory had then earned. In 1959 George was elected a Fellow of the Royal Society of Canada, Canada's most prestigious academic society covering all disciplines. He was its Treasurer from 1968 to 1973.

George Thiessen's total integrity, honesty, and humility, as well as his work ethic, have influenced a great number of professional colleagues that have followed him. I consider myself immensely privileged to have been among these people. For me and my family, George was a superb mentor and friend.

TONY F. W. EMBLETON

# REVIEWS OF ACOUSTICAL PATENTS

**Daniel W. Martin**

7349 Clough Pike, Cincinnati, Ohio 45244

The purpose of these acoustical patent reviews is to provide enough information for a Journal reader to decide whether to seek more information from the patent itself. Any opinions expressed here are those of reviewers as individuals and are not legal opinions. Printed copies of United States Patents may be ordered at \$3.00 each from the Commissioner of Patents and Trademarks, Washington, DC 20231.

## Reviewers for this issue:

GEORGE L. AUGSPURGER, Perception Incorporated, Box 39536, Los Angeles, California 90039

MAHLON D. BURKHARD, 31 Cloverdale Heights, Charles Town, West Virginia 25414

RONALD B. COLEMAN, BBN Acoustic Technologies, 70 Fawcett Street, Cambridge, Massachusetts 02138

HARVEY H. HUBBARD, 325 Charleston Way, Newport News, Virginia 23606

SAMUEL F. LYBARGER, 101 Oakwood Road, McMurray, Pennsylvania 15317

D. LLOYD RICE, 11222 Flatiron Drive, Lafayette, Colorado 80026

CARL J. ROSENBERG, Acentech Incorporated, 33 Moulton Street, Cambridge, Massachusetts 02138

ERIC E. UNGAR, Acentech Incorporated, 33 Moulton Street, Cambridge, Massachusetts 02138

ROBERT C. WAAG, University of Rochester Medical Center, 601 Elmwood Avenue, Rochester, New York 14642

**5,591,945**

## 43.20.Fn ACOUSTIC TOUCH POSITION SENSOR USING HIGHER ORDER HORIZONTALLY POLARIZED SHEAR WAVE PROPAGATION

Joel Kent, assignor to Elo TouchSystems, Incorporated  
7 January 1997 (Class 178/19); filed 19 April 1995

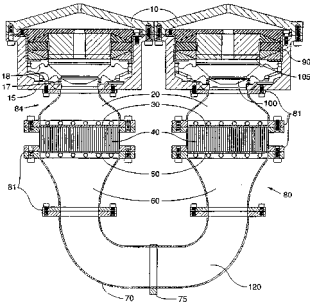
An interesting example of applied acoustics is the video touch screen. Acoustic touch sensors typically employ arrays of transmitters and receivers along their edges. Waves traveling through the substrate are perturbed by an object touching the panel, and the location of the object can then be calculated by analyzing the receiver signals. The patent provides a good review and describes a design that is said to provide improved operation, along with easier fabrication.—GLA

**5,647,216**

## 43.35.Ud HIGH-POWER THERMOACOUSTIC REFRIGERATOR

Steven L. Garrett, assignor to the United States of America  
15 July 1997 (Class 62/6); filed 31 July 1995

This thermoacoustic refrigerator uses two loudspeakers **10** connected electrically to drive cones **100** 180° out of phase to sustain a half-wavelength standing wave within gas mixture **120** in resonator **80**. The resonator contains hot-side reducers **20**, hot-side heat exchangers **30**, stacks



**40**, cold-side heat exchangers **50**, and cold-side reducers **60**. An alternative design uses a single loudspeaker with a double-acting piston to produce

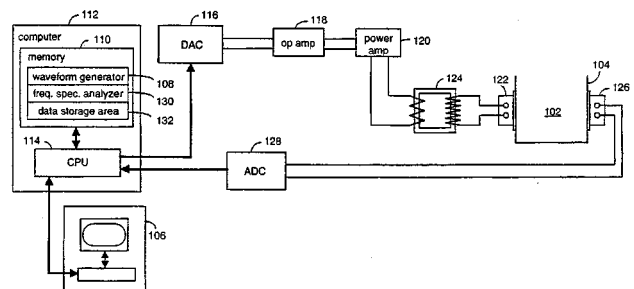
resonant excitation of the gas within a resonator tube having a looped shape to provide a more compact unit.—DWM

**5,636,179**

## 43.35.Zc SONIC SPECTROMETER AND TREATMENT SYSTEM

Bogdan J. Slomka, assignor to Iowa State University Research Foundation  
3 June 1997 (Class 367/95); filed 9 February 1996

This system for sonic treatment of various objects first generates a wide range of sound frequencies for radiation, then analyzes sound reflected from the object for detection of resonance frequencies, and finally radiates



toward the object a spectrum of sound concentrated at the detected frequencies of resonance.—DWM

**5,586,195**

## 43.38.Ja BODY-ACOUSTIC DEVICE

Hitomi Ishigaki and Masako Tamura, assignors to Capcom Company  
17 December 1996 (Class 381/188); filed in Japan 18 November 1992

A loudspeaker is mounted on a flexible diaphragm that divides a drum-shaped enclosure into two chambers. The diaphragm is also provided with a small port opening. "As a result, sufficient and clear body-felt sound, especially heavy bass sound, can be obtained through vibration of the housing outer walls."—GLA

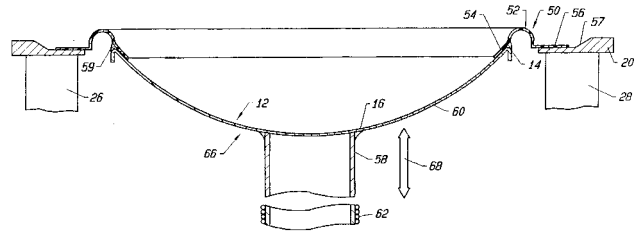


5,590,212

**43.38.Ja DIAPHRAGM FOR A CAPACITANCE TYPE LOUDSPEAKER**

Masaru Uryu *et al.*, assignors to Sony Corporation  
31 December 1996 (Class 381/191); filed in Japan 30 July 1993

An improved diaphragm for electrostatic loudspeakers is described which has optimum surface resistivity and is relatively unaffected by humidity. A stable, high polymer conductive layer is formed on a high molecular film base using straightforward production techniques.—GLA



assembly 62 and 58 is attached to the cone and centered by a conventional spider (not shown). Voila!—a loudspeaker structure said to greatly reduce distortion.—GLA

5,594,805

**43.38.Ja LOUDSPEAKER**

Yoshio Sakamoto *et al.*, assignors to Kabushiki Kaisha Kenwood  
14 January 1997 (Class 381/199); filed in Japan 31 March 1992

A lightweight “gapless” electrodynamic loudspeaker uses special voice coil wire having a conductive core clad with magnetic material, or vice versa. The patent document includes many helpful diagrams.—GLA

5,629,503

**43.38.Ja VIBRATION DAMPING DEVICE**

Leonard Thomasen, assignor to Tekna Sonic, Incorporated  
13 May 1997 (Class 181/199); filed 8 February 1994

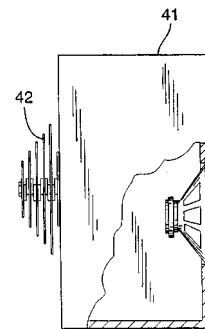
Stagger-tuned, frictional-loss damping plates 42 are attached to one or more panels of loudspeaker box 41. This seemed to be more gimmick than

5,606,626

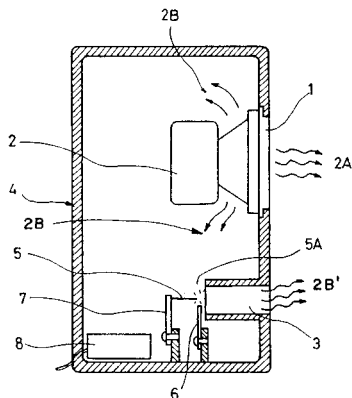
**43.38.Ja SPEAKER SYSTEM WITH AN ANION GENERATOR AND TELEVISION USING THE SPEAKER SYSTEM**

Chan H. Kim *et al.*, assignors to Goldstar Company  
25 February 1997 (Class 381/159); filed in Republic of Korea 21 December 1993

Ionized air generators supposedly promote health and suppress odors. In a television loudspeaker enclosure, there is plenty of room for anion generator 5A and its power supply 8. Moreover, ionized air 2B is distributed



substance, but reviews of the commercial version report that it is practical and effective in minimizing panel resonance.—GLA



throughout the viewing area by the action of vent 3. With a little more research they may rediscover the corona wind loudspeaker and simply use the audio signal to modulate the anion generator.—GLA

5,483,197

**43.38.Lc POWER AMPLIFIER CIRCUIT FOR AUDIO SIGNAL AND AUDIO DEVICE USING THE SAME**

Kei Nishioka *et al.*, assignors to Rohm Company  
9 January 1996 (Class 330/273); filed in Japan 28 September 1993

This power amplifier is intended for use in battery-operated devices such as cassette tape players. A loudspeaker is connected across two pairs of output transistors in a bridge configuration. In this case, however, pulse width modulation is used for maximum efficiency. Circuitry and operation are clearly described in the patent.—GLA

5,608,810

**43.38.Ja LOUDSPEAKER STRUCTURE**

David Hall, assignor to Velodyne Acoustics, Incorporated  
4 March 1997 (Class 381/193); filed 29 February 1996

The claims of this short patent do not allow one to get a grip on what is supposedly being described. The illustrations are much easier to understand. Loudspeaker cone 16 is shaped like a wok. A conventional voice coil

5,543,753

**43.38.Lc AUDIO FREQUENCY POWER AMPLIFIERS WITH ACTIVELY DAMPED FILTER**

Robert C. Williamson, assignor to Carver Corporation  
6 August 1996 (Class 330/297); filed 22 June 1994

Audio power amplifiers employing tracking power supplies offer significant advantages in terms of cost and operating efficiency. In practice, it

is difficult to accurately track the signal being amplified, especially at high frequencies. This patent describes a fairly elaborate circuit employing forward compensation plus an actively damped current feedback loop. "The resulting inverter generates an output voltage that tracks an input voltage thereof with improved frequency response within the frequency range of interest."—GLA

5,592,559

**43.38.Lc SPEAKER DRIVING CIRCUIT**

Ryutaro Takahashi and Toru Hayase, assignors to Sharp Kabushiki Kaisha  
7 January 1997 (Class 381/111); filed in Japan 2 August 1991

Why bother with D/A converters and power amplifiers? Why worry about negative feedback and stability? Simply send your digital audio signal through a delta-sigma converter and switch the power supply voltage directly to a loudspeaker voice coil.—GLA

5,596,395

**43.38.Lc METHOD AND APPARATUS FOR DRIVING A SELF-RESONANT ACOUSTIC TRANSDUCER**

Emery L. Bess and Harry S. Erskine, assignors to Preco, Incorporated  
21 January 1997 (Class 340/384.7); filed 23 May 1995

For some kind of warning signal, say, an auto alarm, one might use an underdamped moving-coil loudspeaker driven at its resonance frequency. An easy way to accomplish this is to use voice coil impedance as the tuning element of a simple oscillator circuit. The circuit is a somewhat more complicated variation that drives the loudspeaker with a series of pulses. The timing of the pulses is controlled by back EMF generated by the voice coil.—GLA

5,544,228

**43.38.Md METHOD AND APPARATUS FOR TRANSMISSION OF FULL FREQUENCY DIGITAL AUDIO**

Byron D. Wagner *et al.*, assignors to The Walt Disney Company  
6 August 1996 (Class 379/67); filed 27 September 1993

A general method is described which facilitates interactive transmittal and retrieval of full-range audio signals plus data information over the public switched telephone network. The patent is written so broadly that it is difficult to pin down exactly how the method differs from accepted practice. However, in 1993, when the patent was filed, its novelty was probably more evident.—GLA

5,485,514

**43.38.Si TELEPHONE INSTRUMENT AND METHOD FOR ALTERING AUDIBLE CHARACTERISTICS**

Michael E. Knappe and Brian R. Shelton, assignors to Northern Telecom Limited  
16 January 1996 (Class 379/387); filed 31 March 1994

"It is an object of the present invention to provide a telephone instrument and method for altering a voice signal received from a telephone line to simulate a characteristic of spatial presence." Signals received from a telephone line are directed to left and right channels. "In each channel, the signals are processed via a direct path, an early reflection path...and a reverberant decay path... In each channel, the outputs from the three paths are summed with different weights."—MDB

5,632,048

**43.38.Si PROTECTOR HEARING HELMET**

David Mortell *et al.*, assignors to Protector Development  
27 May 1997 (Class 2/423); filed 20 September 1995

A helmet for use by riders of motorcycles or bicycles is described. The helmet covers the head but has a clear portion in front of the eyes. Ear-phones in the helmet fit snugly against the ears. Hearing conduits from the earcups to the outside of the helmet allow the entrance of important sounds and also provide ventilation.—SFL

5,647,011

**43.38.Si HEADPHONE SOUND SYSTEM**

Andrew W. Garvis, Longwood, FL  
8 July 1997 (Class 381/123); filed 24 March 1995

The object of the patent is to alert a person listening to music from a portable CD system, for example, that other sounds of importance may be present. A unit that can be worn on the belt contains a microphone and electronic circuitry that switches the output of the music source off to allow the listener to determine the nature of the local direct sounds. The switching occurs when the level of the direct sounds exceeds an adjustable amount. Once turned off, the music source must be turned back on by the listener.—SFL

5,615,380

**43.38.Tj INTEGRATED CIRCUIT COMPUTER SYSTEM HAVING A KEYBOARD INPUT AND A SOUND OUTPUT**

Gilbert P. Hyatt, Las Vegas, NV  
25 March 1997 (Class 396/800); filed 9 April 1991

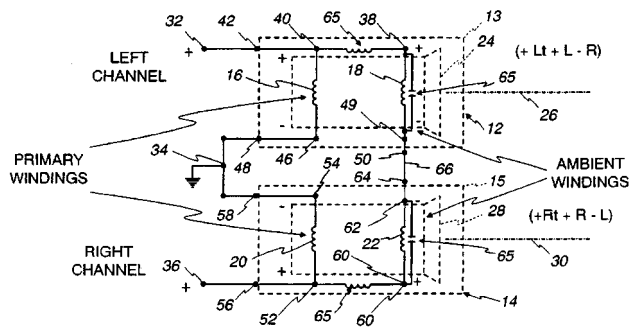
The broad title of this patent about computer systems having a keyboard input and a sound output is probably a good indicator of its scope. Originally filed in 1977, almost twenty years before issuance, the patented system provides a dynamic memory with a memory refresh feature synchronized with computer control signals. The system is "particularly suitable for operator interaction, integrated circuit data processors, and dynamic memories." An article concerning application of this system to television games is the first of 85 referenced publications listed.—DWM

5,594,801

**43.38.Vk AMBIENT EXPANSION LOUDSPEAKER SYSTEM**

Charles L. McShane, Mount Prospect, IL  
14 January 1997 (Class 381/24); filed 26 May 1994

Prior systems, including the inventor's two earlier patents, have employed spaced-apart loudspeakers for each stereophonic channel to widen the stereo stage and attenuate interaural crosstalk. Here dual-coil loudspeakers do the job. Voice coils 16 and 20 are connected conventionally to left



and right channels. Coils 18 and 22 respond to the difference signal. Low-pass filters 65 limit the difference signal to frequencies below 800 Hz or so. Since only two sound sources are involved, the effect essentially duplicates that of the "spread" control found on some stereo amplifiers.—GLA

5,596,644

#### 43.38.Vk METHOD AND APPARATUS FOR EFFICIENT PRESENTATION OF HIGH-QUALITY THREE-DIMENSIONAL AUDIO

Jonathon S. Abel and Scott H. Foster, assignors to Aureal Semiconductor, Incorporated  
21 January 1997 (Class 381/17); filed 27 October 1994

With a little signal processing trickery the listener can be fooled into thinking that a sound originates from a location well above or outside the sound stage defined by two loudspeakers. Synthetic acoustic ambience can be included as well. Really convincing spatial effects are not easy to achieve, and to some extent must be tailored to the ears of a particular listener. The popularity of computer games makes this a fertile field for inventors and patent attorneys. This patent includes a good overview of the state of the art. It then describes a method for spatializing multiple sources that can be used for binaural or monaural presentation to one or more listeners.—GLA

5,615,270

#### 43.38.Vk METHOD AND APPARATUS FOR DYNAMIC SOUND OPTIMIZATION

Thomas E. Miller *et al.*, assignors to International Jensen, Incorporated  
25 March 1997 (Class 381/57); filed 6 June 1995

To compensate for the masking effect of noise in automobiles one would like to control not only the gain but also the frequency response of the audio system. Patents already exist for such "anti masking" systems. In this case the processing is done in the digital domain using adaptive filters.—GLA

5,635,643

#### 43.40.Le IDENTIFYING SOURCE OF ACOUSTIC EMISSIONS IN STRUCTURES USING LAMB WAVES AND VIBRATION MODES

Arup K. Maji, assignor to The University of New Mexico  
3 June 1997 (Class 73/587); filed 15 March 1995

This patent pertains to the global monitoring of a structure in relation to locating the source of acoustic emissions that may be caused by such disturbances as the growth of fatigue cracks. The approach delineated in the patent makes use of two phenomena. (1) In view of the fact that an acoustic emission pulse activates different modes of Lamb waves, whose modes have different propagation velocities, the approach determines the distance between the source of the pulse and a transducer by measuring the differences between the arrival times of different Lamb wave modes. (2) Since it was observed during tests of a bridge that acoustic emissions occurred at regular repetition intervals which are related to the natural frequencies of individual structural members, the approach seeks to identify the member that is the source of the observed acoustic emission by measuring the repetition rates and relating these to known (previously measured) member natural frequencies.—EEU

5,630,485

#### 43.40.Tm TELESCOPING VIBRATION DAMPER WITH A TWO DISK BASE VALVE

Hubert Beck, assignor to Fichtel & Sachs AG  
20 May 1997 (Class 188/322.14); filed in Germany 26 February 1994

This patent discloses a damper such as may be used in an automotive shock absorber. The damper consists of a work cylinder into which there fits a piston (attached to a piston-rod) that divides the cylinder into two chambers. A jacket tube that surrounds the work cylinder constitutes an equalization chamber. A valve, located at the base of the work cylinder, creates a flow connection between the lower portion of the work cylinder and the equalization chamber. The essence of this patent is the design of the base valve, which is constructed of two or more notched disks that can be manufactured simply and economically.—EEU

5,636,826

#### 43.40.Tm VIBRATION CONTROL DEVICE

Osamu Nakagaki *et al.*, assignors to Toyota Gosei Company  
10 January 1997 (Class 248/562); filed in Japan 10 March 1994

The device described in this patent is an automotive engine mount or similar vibration isolator that includes a snubbing device to prevent excessive excursions. The specific designs discussed in the patent are said to consist of relatively few parts that are easy to assemble and adequately strong.—EEU

5,637,938

#### 43.40.Tm TUNED DYNAMIC VIBRATION ABSORBER

Victor M. Vukorpa *et al.*, assignors to Whirlpool Corporation  
10 June 1997 (Class 310/51); filed 16 August 1994

In order to reduce the noise and vibration of an electric motor, such as that in a dishwasher, a dynamic absorber is attached to the motor housing. The absorber described in this patent consists of a mass at the end of a cantilever beam that is attached to the motor housing. The absorber is tuned to suppress torsional vibrations of the motor at about 100 or 120 Hz. Also included in the patent are low-vibration motors that incorporate this absorber, and appliances that incorporate such motors.—EEU

5,558,477

#### 43.40.Vn VIBRATION DAMPING SYSTEMS USING ACTIVE NEGATIVE CAPACITANCE SHUNT CIRCUIT WITH PIEZOELECTRIC REACTION MASS ACTUATOR

Douglas R. Browning *et al.*, assignors to Lucent Technologies, Incorporated  
24 September 1996 (Class 408/143); filed 2 December 1994

A method for providing broadband active damping for a boring bar machine tool using piezoelectric actuator material is presented. The capacitive impedance of the piezoelectric material bonded to the tool is compensated over a broad frequency range by using a negative capacitance shunt circuit provided by a voltage-controlled voltage source. The resulting electrical load impedance of the actuator and shunt impedance network is completely resistive, thereby enhancing the mechanical damping. Analog electrical circuitry for the shunt network is discussed which provides not only the negative capacitance but also the shunt resistance for enhancing the mechanical damping.—RBC

### 43.40.Vn ACTIVE VIBRATION DAMPING ARRANGEMENT FOR TRANSPORTATION VEHICLES

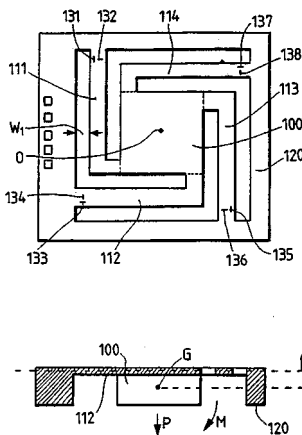
Richard Gran *et al.*, assignors to Northrop Grumman Corporation  
1 October 1996 (Class 181/206); filed 12 July 1995

This patent describes a multi-axis active mount device for augmenting the isolation of the passenger compartment of transport vehicles provided by passive mounts. The active portion of this mount system is positioned in parallel (mechanically) with a passive mount located between the suspension and passenger compartment. The system is said to provide active damping, but the prescribed goal is to minimize the response of bi-directional accelerometers located on the underside of the passenger compartment by reacting the force against the suspension system components (i.e., enhance vibration isolation). The actuators are hydraulic cylinder pistons oriented in X or Y configurations to reduce both sway and heave motions of the passenger compartment.—RBC

### 43.40.Yq SEMI-CONDUCTOR ACCELERATION SENSOR HAVING THIN BEAM SUPPORTED WEIGHT

Katsumichi Ueyanagi, assignor to Fuji Electric Company  
13 February 1996 (Class 73/514.33); filed in Japan 25 March 1992

In the version illustrated, the accelerometer is fabricated by micro machining silicon semiconductor material. Piezo resistance elements 131–



138 are components of a Wheatstone bridge. Mass 100 comprises the inertial mass which is supported by beams 111–114.—MDB

### 43.40.Yq NON-LINEAR VIBRATION DEVICE

Jeffrey Richards, Las Vegas, NV  
4 March 1997 (Class 368/10); filed 7 May 1993

The device described in this patent is intended primarily for winding self-winding mechanical wrist watches when they are not being used. The device, which simulates some of the motions that a watch would experience as it is being worn, consists of a platform on which one or more watches can be placed and which is supported on soft springs. The platform is set into motion by a motor-driven cam arrangement that is designed so that it alternates between pulling and pushing on the platform, releasing it after each pull or push so that it can vibrate freely for a short time.—EEU

### 43.40.Yq VEHICLE VIBRATION SIMULATOR

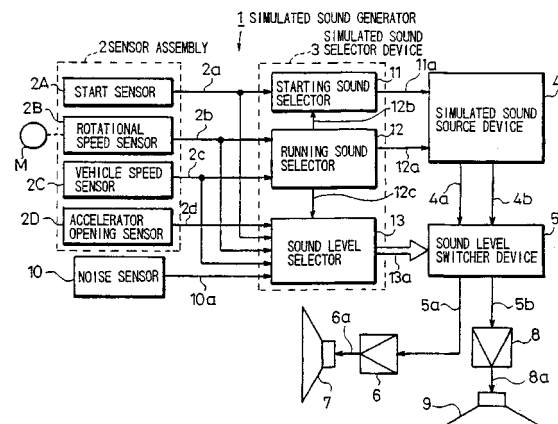
Norman C. Otto, William J. Pielemeier, and Raymond C. Meier, Jr., assignors to Ford Motor Company  
8 April 1997 (Class 73/669); filed 5 July 1995

This simulator, which is intended to simulate the exposure of an occupant to vibration in a motor vehicle, includes separate modules for the seat, the floor pan, and the steering column, with each module capable of being vibrated independently of the others.—EEU

### 43.50.Ed SIMULATED SOUND GENERATOR FOR ELECTRIC VEHICLES

Makoto Koike *et al.*, assignors to Honda Giken Kogyo Kabushiki Kaisha  
3 June 1997 (Class 340/441); filed in Japan 21 December 1993

Electric automobiles generate considerably less sound than conventional gasoline-powered vehicles. This patent describes a system intended to make the electric-powered vehicle sound conventional. Sensors 2A–D are responsive to the start, rotor speed, vehicle speed, and accelerator of the



electric automobile. The sensors control simulated sound generators 11 for starting sound, 12 for running sound, and 13 for adjusting the sound level. Mixing and controlled amplification produce amplified sound from automobile loudspeakers 7 and 9.—DWM

### 43.50.Gf ARRANGEMENT FOR LOWERING THE NOISE LEVEL OF A COOLING LAYER IN A PULP DRYER

Bertel Karlstedt and Henrik Pettersson, assignors to Valmet Corporation, Helsinki, Finland  
11 March 1997 (Class 34/60); filed in Finland 29 June 1994

This patent relates to the control of noise during the processes of cooling and drying wood pulp used in the paper making industry. Baffles consisting of perforated sheets, backed up by sound-absorbing materials such as foam, plastic, or mineral wool, are arranged perpendicular to the flow or inclined in relation to it in order to limit the radiation of noise due to aerodynamic origin out into the surrounding work areas.—HHH

5,610,360

**43.50.Gf LARGE CALIBER GUN MUFFLER**

Raymond P. Kazyaka and Raymond J. Kazyaka, assignors to Wright Malta Corporation  
11 March 1997 (Class 89/14.4); filed 14 March 1995

This patent relates to a muffler for noise control during the test firing of large caliber artillery weapons. It consists of a large volume pressure vessel having massive walls and which can be buried in sand. Muzzle blast gases are contained as well as the blast noise.—HHH

5,613,253

**43.50.Gf APPARATUS FOR PREVENTING BED FRAME SQUEAKING**

Jean M. Rose, Mt. Morris, MI  
25 March 1997 (Class 5/309); filed 5 April 1996

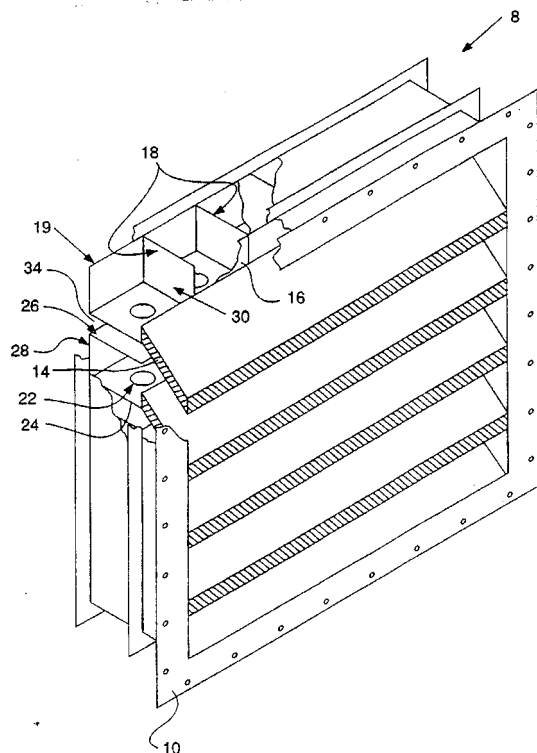
This patent relates to the control of noise and scratching due to relative motions between the headboard, footboard, and side rail elements of the main bed frame. Shims of about 3/16-in. thickness, comprised of a central plate of aluminum, and outside surfaces of resilient materials such as Neoprene, are placed in the bolted joints.—HHH

5,625,172

**43.50.Gf ENGINE ENCLOSURE AIR INLET/ DISCHARGE SOUND ATTENUATOR**

John R. Blichmann and Brian S. Johnson, assignors to Caterpillar, Incorporated  
29 April 1997 (Class 181/204); filed 18 April 1995

This patent relates to the noise attenuation of an internal combustion engine enclosure with minimal pressure loss. Sound absorptive louvers for



high-frequency noise control are placed in series with an array of Helmholtz resonators tuned to attenuate low-frequency components.—HHH

5,553,514

**43.50.Ki ACTIVE TORSIONAL VIBRATION DAMPER**

Janusz Walkowc, assignor to Stahl International, Incorporated  
10 September 1996 (Class 74/574); filed 6 June 1994

A method for damping resonant torsional vibrations in a member such as a pulse-driven shaft is described. The semi-active damping system damps resonant torsional vibrations by imparting periodic torsional impulses in the opposite direction to the twisting motion. In one version a high-speed damper flywheel and an eddy current brake are attached to the shaft, with the ability to apply torsional impulses to the damper flywheel. The eddy current brake is controlled by a computer that calculates the appropriate torsional impulse magnitude and timing to apply. The approach appears to be semi-active as the torsional impulses are applied only in a signal angular direction.—RBC

5,558,298

**43.50.Ki ACTIVE NOISE CONTROL OF AIRCRAFT ENGINE DISCRETE TONAL NOISE**

Frederic G. Pla, assignor to General Electric Company  
24 September 1996 (Class 244/1 N); filed 5 December 1994

This patent relates to control of tonal noise in aircraft engines. Piezoceramic actuator patches are mounted to either side of a noise-radiating panel in the engine. The patches are bonded to the panel in such a way as to provide a compressive prestress in the piezoceramic patch. This compressive prestressing is said to increase the amplitude of the canceling noise that can be generated to control engine tonal noise. As is commonly done, a dc electric bias voltage is also applied to the piezoceramic to increase the allowable ac voltage signal that can be applied so as not to exceed the depolarizing voltage for the actuator material.—RBC

5,559,893

**43.50.Ki METHOD AND DEVICE FOR ACTIVE NOISE REDUCTION IN A LOCAL AREA**

Asbjørn Krokstad *et al.*, assignors to Sinvent A/S  
24 September 1996 (Class 381/71); filed in Norway 22 July 1992

This patent relates to a system for providing local noise reduction in a three-dimensional sound field using active control. The system includes a loudspeaker with two microphones mounted to the headrest of a passenger seat in an automobile. According to the patent, the open loudspeaker, radiating as a dipole, will reduce the acoustic feedback between the loudspeaker and the microphones, as well as reduce amplification of sound at neighboring seat locations.—RBC

5,568,558

**43.50.Ki ADAPTIVE NOISE CANCELLATION DEVICE**

Dov Ramm *et al.*, assignors to International Business Machines Corporation  
22 October 1996 (Class 381/94); filed 3 December 1993

This patent describes an in-wire noise cancellation algorithm for howl cancellation in full duplex speakerphones. In contrast to the stochastic-gradient least-mean-squares (LMS) algorithm, which requires  $O(N)$  operations per sample to update all  $N$  coefficients of an adaptive finite-impulse-response (FIR) filter, the proposed algorithm requires  $O(N \log N)$  operations per  $N$  samples to update the  $N$  coefficients. The algorithm expresses the adaptive filter as a combination of basis functions spanning narrow bands in frequency. In each of these subbands, there is only one filter coefficient to be determined. These coefficients are solved using a LMS formulation.—RBC

5,619,020

### 43.50.Ki MUFFLER

Owen Jones and Michael C. J. Trinder, assignors to Noise Cancellation Technologies, Incorporated  
8 April 1997 (Class 181/206); originally filed 28 August 1992

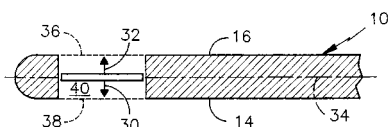
This patent uses active noise control technology for muffling the noise from the exhaust of an internal combustion engine. A unique feature of the design is the internal physical arrangement which results in an essentially benign environment for the loudspeakers.—HHH

5,613,649

### 43.50.Nm AIRFOIL NOISE CONTROL

Robert H. Schlinker and Edward J. Kerschen, assignors to United Technologies Corporation  
25 March 1997 (Class 244/IN); filed 21 July 1994

This patent relates to the reduction of noise from airfoils, particularly those arranged in rows or cascades, such as are found in the compressor or turbine sections of gas turbine engines. An airfoil 10 encountering periodic pressure and velocity fluctuations at its leading edge is equipped with a means 30 for generating antisymmetric pressure waves having a phase and



amplitude to cancel the acoustic pressure waves resulting from the above leading edge encounters. Various generating devices such as pistons and leading edge flaps would be located about one acoustic wavelength downstream of the leading edge.—HHH

5,644,872

### 43.55.Ev SOUND ABSORBING PANEL

Jay Perdue, Amarillo, TX  
8 July 1997 (Class 52/144); filed 6 March 1995

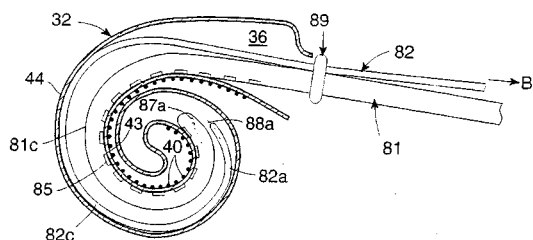
This self-supporting sound-absorbing panel can be attached to walls and ceilings. It has a core assembly made from a mat of rockwool, and a front and back layer of glass fiber cloth, and a rigid perimeter (rectangular) frame. A cloth facing can be stretched across the unit.—CJR

5,645,585

### 43.64.Me COCHLEAR ELECTRODE IMPLANT ASSEMBLY WITH POSITIONING SYSTEM THEREFOR

Janusz A. Kuzma, assignor to Cochlear Ltd.  
8 July 1997 (Class 623/10); filed 15 March 1996

An implantable cochlear electrode assembly includes a flexible rodlike electrode carrier 81 and a flexible positioning member 82 to facilitate insertion of the electrode carrier into the cochlea. The member is removed when



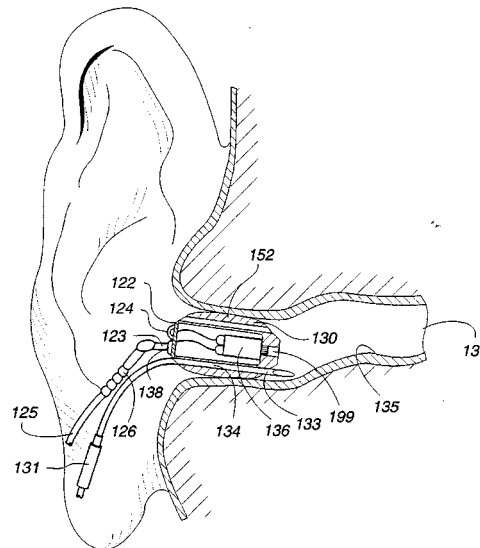
the electrode carrier is in place. Conductors to each of the electrodes are contained in the electrode carrier.—SFL

5,645,074

### 43.66.Sr INTRACANAL PROSTHESIS FOR HEARING EVALUATION

Adnan Shennib and Richard Urso, assignors to Decibel Instruments, Incorporated  
8 July 1997 (Class 128/746); filed 17 August 1994

This patent relates to an intracanal prosthesis consisting of a hearing-aid-type receiver small enough to fit into the ear canal, in combination with a probe microphone that can measure sound pressure level in the ear canal, preferably near the tympanic membrane. Monaural and binaural tests are described. In combination with the intracanal prosthesis, relatively complex



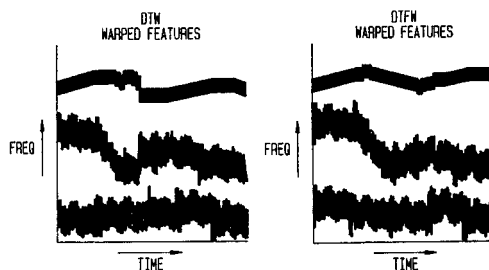
electronic units are described that are stated to be capable of doing audiometric evaluation, hearing-aid prescription, hearing-aid simulation and hearing-aid fitting. The patent extensively describes measurements that it is possible to make, utilizing 37 figures to supplement the text.—SFL

5,625,747

### 43.72.Ar SPEAKER VERIFICATION, SPEECH RECOGNITION AND CHANNEL NORMALIZATION THROUGH DYNAMIC TIME/FREQUENCY WARPING

Randy G. Goldberg et al., assignors to Lucent Technologies, Incorporated  
29 April 1997 (Class 395/2.52); filed 21 September 1994

This speech processing system uses dynamic time/frequency warping to perform speaker verification, speech recognition, and certain channel optimizations. A three-dimensional time/frequency space consists of the sum



of squares of the spectral differences between test and reference utterances. Dynamic programming techniques are then used to find the minimal distance pathway representing the time and frequency axis warpings.—DLR

5,630,013

#### 43.72.Ew METHOD OF AND APPARATUS FOR PERFORMING TIME-SCALE MODIFICATION OF SPEECH SIGNALS

Ryoji Suzuki and Masayuki Misaki, assignors to Matsushita Electric Industrial Company  
13 May 1997 (Class 395/2.25); filed in Japan 25 January 1993

This speech rate modifier uses a fade-in/fade-out method of blending overlapping speech segments to change the duration of portions of the signal having similar spectral characteristics. Speech segments suitable for time scale alteration are located by a continuous autocorrelation function.—DLR

5,615,297

#### 43.72.Gy TRANSMISSION SYSTEM FOR CODED SPEECH SIGNALS AND/OR VOICEBAND DATA

Andrew G. Davis, assignor to British Telecommunications public limited company  
25 March 1997 (Class 395/2.1); filed in European Patent Office 15 November 1991

This speech and digital data coding system automatically detects whether the incoming signal is speech or data, and switches to the appropriate encoding system. The speech or data coding mode is transmitted along with each packet using a curious interaction with a packet parity bit. If a packet arrives at the receiver with unexpected parity, the receiver first tries to interpret the data using the mode not currently in effect. If this fails, the packet is then reinterpreted in the current mode, assuming transmission errors have occurred.—DLR

5,615,298

#### 43.72.Gy EXCITATION SIGNAL SYNTHESIS DURING FRAME ERASURE OR PACKET LOSS

Juin-Hwey Chen, assignor to Lucent Technologies, Incorporated  
25 March 1997 (Class 395/2.37); filed 14 March 1994

This speech coding system includes a frame generator to create a speech signal from previously transmitted parameters in the event that a packet is lost in transmission. Depending on whether the ongoing speech was voiced or unvoiced during the last received packet, a different reconstruction strategy is used. In either case, an excitation signal is extrapolated from the available data. For voiced speech, linear prediction filter coefficients are modified to increase the formant bandwidths. Some of the normal packet processing tasks are not required, making up for the extra time needed to generate the missing signals.—DLR

5,621,852

#### 43.72.Gy EFFICIENT CODEBOOK STRUCTURE FOR CODE EXCITED LINEAR PREDICTION CODING

Daniel Lin, assignor to Interdigital Technology Corporation  
15 April 1997 (Class 395/2.28); filed 14 December 1993

This code excited linear prediction speech coder forms a three-valued excitation sequence  $(-1, 0, 1)$  by combining pairs of codebook entries from two binary codebooks. Each of the binary-valued excitation codebooks is amenable to various efficient search procedures. One of the binary codebooks is assigned values of  $(0, 1)$  and the other  $(-1, 0)$ . Chosen entries from the two codebooks can then be summed to produce the ternary excitation sequences.—DLR

5,621,853

#### 43.72.Gy BURST EXCITED LINEAR PREDICTION

William R. Gardner, San Diego, CA  
15 April 1997 (Class 395/2.28); filed 1 February 1994

This linear prediction speech coder uses a variety of strategies to encode the excitation signal based on characteristics of the LPC residual. Since the residual typically fits a pattern of being a sequence of individual shaped bursts of energy, the primary approach is to locate matching shapes in a burst shape codebook in which each shape is stored as a sequence of 40 samples. Additional parameters consist of the burst gain and location within the frame. Both closed and open loop search methods are described.—DLR

5,625,687

#### 43.72.Gy ARRANGEMENT FOR ENHANCING THE PROCESSING OF SPEECH SIGNALS IN DIGITAL SPEECH INTERPOLATION EQUIPMENT

Clifford L. Sayre III, assignor to Lucent Technologies, Incorporated  
29 April 1997 (Class 379/416); filed 31 August 1995

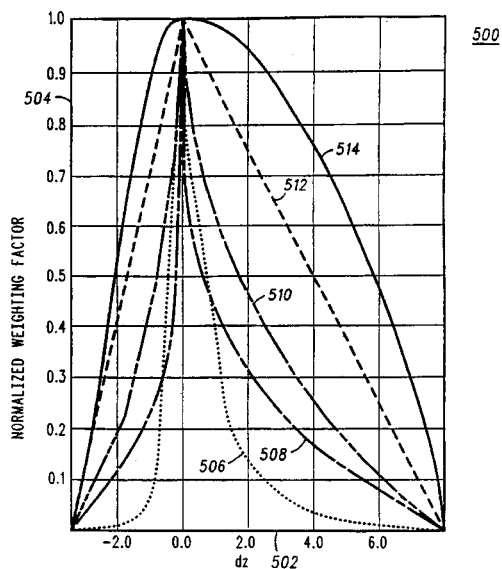
According to this patent, the assignee's method for transmission of speech signals by optical fiber includes a preprocessor known as Digital Speech Interpolation (DSI). A part of the DSI compression system is the deletion of all sounds when no speech signal is present. At the receiver, a white noise filler is reinserted during such periods. This patent improves the result by transmitting a compressed interval of the noise to be used for such reinsertions when the background noise level exceeds a preset threshold.—DLR

5,625,743

#### 43.72.Gy DETERMINING A MASKING LEVEL FOR A SUBBAND IN A SUBBAND AUDIO ENCODER

James L. Fiocca, assignor to Motorola, Incorporated  
29 April 1997 (Class 395/2.14); filed 7 October 1994

The Moving Picture Experts Group (MPEG) has defined a standard for speech compression based on subband coding. In the MPEG system, bits are assigned to each band according to the relationship between the signal level in the band and the band masking level. Calculating the masking level



involves a complex sequence of psychoacoustic computations. This patent presents a simplified method of computing signal-to-mask ratios for the subbands.—DLR

5,625,744

### 43.72.Gy SPEECH PARAMETER ENCODING DEVICE WHICH INCLUDES A DIVIDING CIRCUIT FOR DIVIDING A FRAME SIGNAL OF AN INPUT SPEECH SIGNAL INTO SUBFRAME SIGNALS AND FOR OUTPUTTING A LOW RATE OUTPUT CODE SIGNAL

Kazunori Ozawa, assignor to NEC Corporation  
29 April 1997 (Class 395/2.31); filed in Japan 9 February 1993

This speech coder divides a speech frame into four to eight subframes and performs linear prediction analysis of the signal in each subframe. Line spectral pair parameters are computed and divided into several parameter regions. Each parameter region is then encoded using a vector quantization system.—DLR

5,630,011

### 43.72.Gy QUANTIZATION OF HARMONIC AMPLITUDES REPRESENTING SPEECH

Jae S. Lim and John C. Hardwick, assignors to Digital Voice Systems, Incorporated  
13 May 1997 (Class 395/2.14); filed 5 December 1990

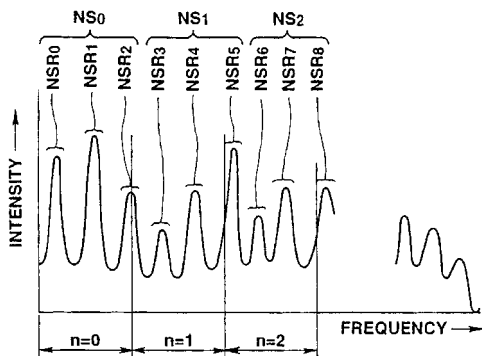
This speech coder analyzes each speech frame into a pitch signal and a set of harmonic amplitudes. A harmonic predictor is then constructed, based on the amplitudes and the number of harmonics in the current and previous frames. Error correction coding is applied to the frame-by-frame differential predictor values, which are then transmitted.—DLR

5,630,012

### 43.72.Gy SPEECH EFFICIENT CODING METHOD

Masayuki Nishiguchi *et al.*, assignors to Sony Corporation  
13 May 1997 (Class 395/2.17); filed in Japan 27 July 1993

This speech coding system uses a two-step procedure to make the voiced/unvoiced decision. Frames of the incoming speech signal are transformed to FFT amplitude spectra. A cutoff of 500–700 Hz first isolates the low-frequency spectrum as the input to a preliminary pitch-period analysis.



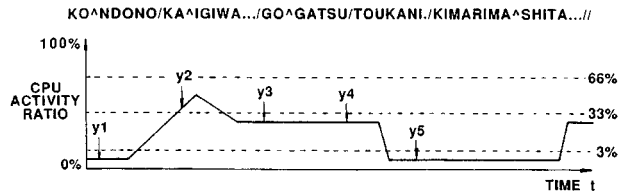
If the initial low-frequency region appears to be voiced, a subsequent pitch analysis is performed with a higher cutoff frequency, making use of results from the first analysis.—DLR

5,615,300

### 43.72.Ja TEXT-TO-SPEECH SYNTHESIS WITH CONTROLLABLE PROCESSING TIME AND SPEECH QUALITY

Yoshiyuki Hara and Tsuneo Nitta, assignors to Toshiba Corporation  
25 March 1997 (Class 395/2.69); filed in Japan 28 May 1992

This phonetic parameter-based text-to-speech synthesis system includes a mode control allowing the operator to trade off speech quality for improved processing speed. Synthesis parameters are stored in the form of



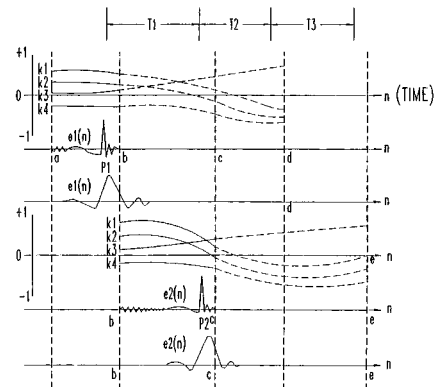
cepstral coefficients with up to 20 values stored for each frame. By selecting the number of coefficients to be used for resynthesis, frames using 6, 10, or 20 coefficients can be constructed with corresponding computational cost.—DLR

5,617,507

### 43.72.Ja SPEECH SEGMENT CODING AND PITCH CONTROL METHODS FOR SPEECH SYNTHESIS SYSTEMS

Chong R. Lee and Yong K. Park, assignors to Korea Telecommunication Authority  
1 April 1997 (Class 395/2.09); filed in Republic of Korea 6 November 1991

This speech synthesizer constructs the speech signal by combining waveform segments having the duration of a fundamental period. To construct a wavelet database, training speech data are resolved into excitation and spectral components. The spectral vectors are then processed to con-



struct a database of wavelet transform segments. During synthesis, an excitation signal is produced by zero-extending a stored excitation waveform. The spectral contribution is added by placing chosen wavelets at selected points in time and smoothing between neighboring wavelet patterns.—DLR



5,615,256

### 43.72.Kb DEVICE AND METHOD FOR AUTOMATICALLY CONTROLLING SOUND VOLUME IN A COMMUNICATION APPARATUS

Osamu Yamashita, assignor to NEC Corporation  
25 March 1997 (Class 379/390); filed in Japan 13 May 1994

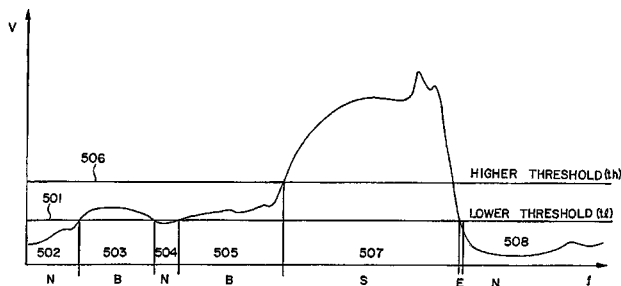
This communication system circuit monitors the sound level from a microphone and changes a volume control during silent intervals. The system continuously computes the difference between the present signal level and a long-term average signal level. When this difference exceeds a preset threshold, a speech event is detected and any AGC action is inhibited.—DLR

5,617,508

### 43.72.Kb SPEECH DETECTION DEVICE FOR THE DETECTION OF SPEECH END POINTS BASED ON VARIANCE OF FREQUENCY BAND LIMITED ENERGY

Benjamin K. Reaves, assignor to Panasonic Technologies, Incorporated and Matsushita Electric Industrial Company  
1 April 1997 (Class 395/2.42); filed 5 October 1992

This speech presence detector is based on a measurement of the variance of the energy within a band of 250–3500 Hz. The band-limited signal energy is measured in each 25-ms frame of the input signal. At each frame time, the energy variance is computed over a sliding span of 50 frames, or 0.64 s. When the variance exceeds a low threshold, a tentative speech begin



event is registered. Speech is confirmed if the variance exceeds a high threshold for at least 0.3 s, and ends when the variance again falls below the low threshold. Use of the signal variance allows speech detection in a variety of noise conditions, such as music, motor noise, or other speakers.—DLR

5,615,296

### 43.72.Ne CONTINUOUS SPEECH RECOGNITION AND VOICE RESPONSE SYSTEM AND METHOD TO ENABLE CONVERSATIONAL DIALOGUES WITH MICROPROCESSORS

Vincent M. Stanford *et al.*, assignors to International Business Machines Corporation  
25 March 1997 (Class 395/2.1); filed 12 November 1993

This combination speech recognizer and voice response system is designed for automated information access. It includes a data processing system to generate phrases for a text-to-speech synthesizer, and uses a speaker-independent continuous speech recognition technology suitable for the telephone system or other applications in which the speaker is not experienced in the use of the system. At each state of progress of the conversation, the computer displays a selection of prompts or "topic phrases." The user may read one of the prompts or speak a related phrase. Spoken inputs are

grouped into phrases of four words or less for a simplified form of word spotting.—DLR

5,615,299

### 43.72.Ne SPEECH RECOGNITION USING DYNAMIC FEATURES

Lalit R. Bahl *et al.*, assignors to International Business Machines Corporation  
25 March 1997 (Class 395/2.63); filed 20 June 1994

This speech recognition technique uses a set of discriminant matrices based on the sequences detected by a continuous hidden Markov model (HMM). Each matrix corresponds to a particular relationship between neighboring phonemes. Acoustic feature vectors are computed from frames of the incoming speech signal. Adjacent feature vectors are grouped and then multiplied by each of a set of discriminant matrices. The resulting vectors can be processed by a simpler discrete HMM recognizer.—DLR

5,617,509

### 43.72.Ne METHOD, APPARATUS, AND RADIO OPTIMIZING HIDDEN MARKOV MODEL SPEECH RECOGNITION

William M. Kushner *et al.*, assignors to Motorola, Incorporated  
1 April 1997 (Class 395/2.65); filed 29 March 1995

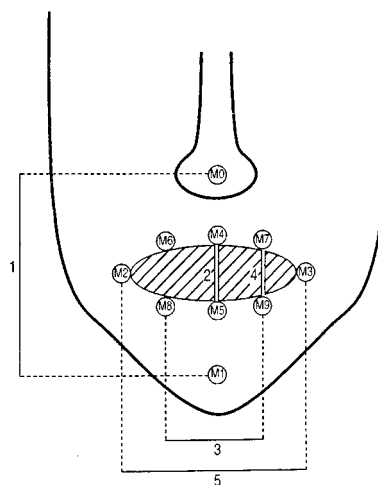
In a typical hidden Markov model (HMM) based speech recognizer, a potential decoding path is scored by the likelihood that the HMM sequence making up that path best fits the given sequence of speech vectors. This system improves the scoring performance by monitoring the dynamic pattern of the likelihood scores as potential paths are evaluated. The rationale is that the dynamic pattern will distinguish a path having local regions of better or worse fit from one with a preferred pattern of board, generally similar matches.—DLR

5,621,858

### 43.72.Ne NEURAL NETWORK ACOUSTIC AND VISUAL SPEECH RECOGNITION SYSTEM TRAINING METHOD AND APPARATUS

David G. Stork and Gregory J. Wolff, assignors to Ricoh Corporation  
15 April 1997 (Class 395/2.41); filed 26 May 1992

This speech recognizer uses features from a video image of the speaker's face as well as a more traditional acoustic feature set. The acoustic analyzer uses a bank of fourteen mel-scale filter bands with short-term energy level detectors. The video image is processed to compensate for head size and position and then elements of lip and mouth movements are



assessed and reduced to five speech-related facial features. Every 10 ms, combined feature sets are fed to the input layer of a time-delay neural network, which is trained to generate specific output signals for each of ten different utterances.—DLR

5,621,859

**43.72.Ne SINGLE TREE METHOD FOR GRAMMAR DIRECTED, VERY LARGE VOCABULARY SPEECH RECOGNIZER**

**Richard M. Schwartz and Long Nguyen, assignors to BBN Corporation**  
15 April 1997 (Class 395/2.65); filed 19 January 1994

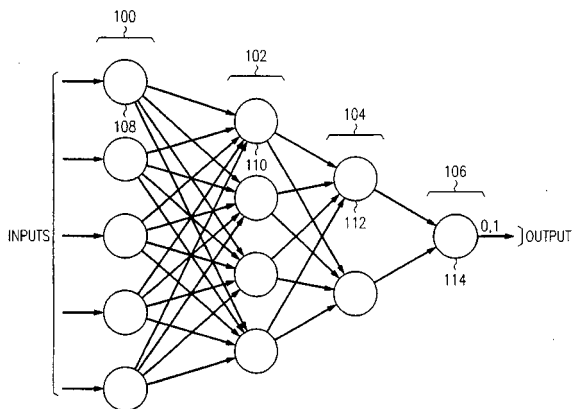
This large-vocabulary speech recognizer navigates a single tree-structured phonetic hidden Markov model (HMM) for each frame of input speech features. Thus, even at this early stage of the recognition process, grammatical context probabilities are brought into play. The grammar probabilities combine with the accumulating phonetic evidence to determine the likelihood that a state of the HMM will result in assigning the correct identification of the spoken input.—DLR

5,623,578

**43.72.Ne SPEECH RECOGNITION SYSTEM ALLOWS NEW VOCABULARY WORDS TO BE ADDED WITHOUT REQUIRING SPOKEN SAMPLES OF THE WORDS**

**Rajendra P. Mikkilineni, assignor to Lucent Technologies, Incorporated**  
22 April 1997 (Class 395/2.64); filed 28 October 1993

The speech recognition system described here seems to lie somewhere on the borderline between a word-oriented template matching system and a phonetic sequence recognizer. New words may be added to the vocabulary



based on a phonetic transcription. Once the new word is spoken into the recognizer, the detected phonetic sequence is used to improve the stored word model.—DLR

5,625,749

**43.72.Ne SEGMENT-BASED APPARATUS AND METHOD FOR SPEECH RECOGNITION BY ANALYZING MULTIPLE SPEECH UNIT FRAMES AND MODELING BOTH TEMPORAL AND SPATIAL CORRELATION**

**William D. Goldenthal and James R. Glass, assignors to Massachusetts Institute of Technology**  
29 April 1997 (Class 395/2.63); filed 22 August 1994

Phonetic recognition systems have most recently relied on the hidden Markov model (HMM) approach to the recognition of phonetic sequences. However, the traditional HMM system does not take any explicit account of the dynamic or temporal structure of speech. The system presented here performs a dynamic analysis of the spectral feature information, constructing time patterns referred to as "tracks." A track represents the temporal structure of an acoustic parameter of the target phonetic set. An error measure is computed of the fit of incoming acoustic vectors against the target tracks.—DLR

5,627,939

**43.72.Ne SPEECH RECOGNITION SYSTEM AND METHOD EMPLOYING DATA COMPRESSION**

**Xuedong Huang and Shenzi Zhang, assignors to Microsoft Corporation**  
6 May 1997 (Class 395/2.65); filed 3 September 1993

The system disclosed in this patent consists of a method for reducing the memory storage requirement for the probability tables of a hidden Markov model (HMM) speech recognizer. The acoustic feature space of human speech is compressed to a vector quantization codebook. For each word in the speech input, an output probability is computed for each codebook entry. A table of probabilities of codebook entries by vocabulary words is compressed by rows such that, once a codebook entry has been selected, only the corresponding table row need be decompressed.—DLR

5,623,539

**43.72.Pf USING VOICE SIGNAL ANALYSIS TO IDENTIFY AUTHORIZED USERS OF A TELEPHONE SYSTEM**

**Charles S. Bassenyemukasa and Randolph J. Pilc, assignors to Lucent Technologies, Incorporated**  
22 April 1997 (Class 379/88); filed 27 January 1994

This patent presents an application of a speaker verification system to determine whether a telephone conversation includes one or more speakers who are not authorized to use the telephone line. No specific verification technology is described. When the system detects an unauthorized user, it may take optional actions including call termination, recording the call, disabling the line, playing noise, or otherwise intruding into the conversation or requesting identification from the line users.—DLR

5,644,095

**43.75.Fg BRASS INSTRUMENT IMPROVEMENT**

**John R. Davidson, Garden City, MI**  
1 July 1997 (Class 84/453); filed 3 April 1995

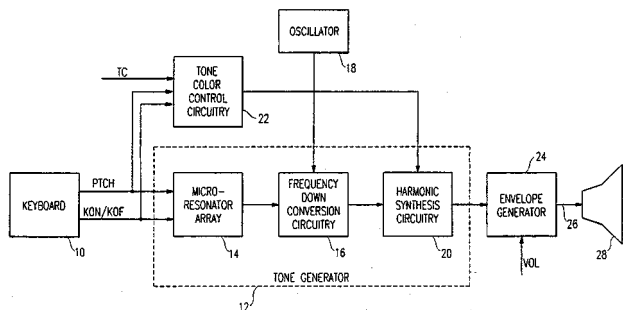
This patent discloses several types of preshaped pieces of damping material which a brass instrument player may press against surfaces of the instrument tubing or valves to suppress sympathetic vibrations of the instrument structure that add undesirable sounds to the instrument tone.—DWM

5,569,871

### 43.75.Tv MUSICAL TONE GENERATING APPARATUS EMPLOYING MICRORESONATOR ARRAY

James A. Wheaton *et al.*, assignors to Yamaha Corporation  
29 October 1996 (Class 84/625); filed 14 June 1994

“A musical tone generating apparatus employs an array of microresonant structures to generate the harmonic component signals of a musical tone to be generated. The microresonant structures produce high frequency signals which are down converted to audio frequency range by mixing them with a high frequency reference signal. The desired tone color is achieved



by modifying the relative amplitudes of the harmonic component signals to produce a desired tone color. A large number of microresonators are preferably integrated on a single integrated circuit substrate to provide a variable tone generating system in a relatively compact environment.”—DWM

5,633,473

### 43.75.Tv ELECTRONIC MUSICAL INSTRUMENT

Yasuhiko Mori *et al.*, assignors to Korg, Incorporated  
27 May 1997 (Class 84/625); filed in Japan 26 June 1992

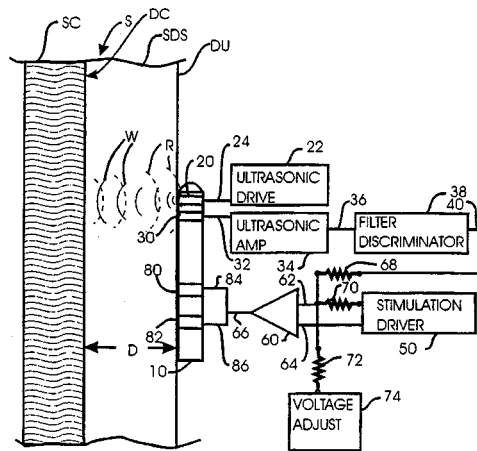
“The vibration of a vibratory element, caused by applying thereto a shock, is detected by a vibration sensor and provided as an electric shock signal to a resonance circuit. The resonance frequencies and resonance decay time of the resonance circuit can freely be adjusted. By setting the resonance frequencies and resonance decay time of the resonance circuit to arbitrary values, desired frequency components are extracted from the electric shock signal and output as a sound signal of an electronic musical instrument.”—DWM

5,628,317

### 43.80.Sh ULTRASONIC TECHNIQUES FOR NEUROSTIMULATOR CONTROL

Warren Starkebaum and Mark T. Rise, assignors to Medtronic, Incorporated  
13 May 1997 (Class 128/660.03); filed 4 April 1996

This patent describes ultrasonic techniques for stimulating nerve tissue adjacent to or within the spine. Ultrasonic transducer 20 adjacent to spinal column S radiates waves W through dura DU. Reflected echo waves R are received by transducer 30 to generate a distance signal corresponding to distance D. “The distance signal is used to adjust the amplitude of an



electrical stimulation signal that stimulates the spinal cord or adjacent tissue so that the value of the stimulation signal tends to remain uniform in spite of changes in the relative distance between the transducer/receiver and the predetermined portion of the spinal cord.”—DWM

5,611,344

### 43.80.Vj MICROENCAPSULATED FLUORINATED GASES FOR USE AS IMAGING AGENTS

Howard Bernstein *et al.*, assignors to Acusphere, Incorporated  
18 March 1997 (Class 128/662.02); filed 5 March 1996

These gases such as octafluoropropane that are stronger reflectors than microparticles containing air are encapsulated with a capsule diameter suitable for the tissue to be imaged, and the capsules may be bioadhesive for enhanced imaging of mucosal surfaces.—RCW

5,611,345

### 43.80.Vj MEDICAL INSTRUMENT WITH IMPROVED ULTRASONIC VISIBILITY

John F. Hibbeln, Downers Grove, IL  
18 March 1997 (Class 128/662.05); filed 24 April 1995

This instrument has a noncircular portion that is adapted for insertion into a patient. The noncircular part contains an exterior planar surface from which an ultrasonic beam is reflected specularly.—RCW

5,615,678

### 43.80.Vj INTEGRAL AUTO-SELECTING YOKE/ TRANSDUCER CONNECTOR FOR ULTRASOUND TRANSDUCER PROBE

Thomas R. Kirkham *et al.*, assignors to General Electric Company  
1 April 1997 (Class 128/660.01); filed 25 November 1994

This connector contains built-in switches that detect when a transducer has been removed from its yoke. Based on the status of the probe switch and other feedback information, a system controller activates the out-of-holder transducer if it has priority. This eliminates the need to trace the cable of a desired probe to the cable connector.—RCW

5,625,137

**43.80.Vj VERY LOW SCATTER LIQUID AND SOLID  
TISSUE MIMICKING MATERIAL FOR  
ULTRASOUND PHANTOMS AND METHOD OF  
MAKING THE SAME**

**Ernest L. Madsen and Gary R. Frank, assignors to Wisconsin  
Alumni Research Foundation  
29 April 1997 (Class 73/1.84); filed 25 May 1995**

This material has a backscatter coefficient about 40 dB below that of human liver. The ultrasonic sound speed and attenuation in the material mimick those in human tissue. A hydroxy compound, such as *n*-propanol, is included to control the ultrasonic speed of propagation. A preservative, such as thimerosal, is included to suppress bacterial invasion. The use of scattering particles in the material allows a broad range of relative backscatter levels to be achieved in ultrasonic test objects.—RCW

5,628,320

**43.80.Vj ULTRASOUND IMAGE RECONSTRUCTION  
USING BACK-PROPAGATION**

**Tat-Jin Teo, assignor to Siemens Medical Systems, Incorporated  
13 May 1997 (Class 128/660.07); filed 29 March 1996**

Image reconstruction is accomplished first by a temporal Fourier transformation of measured time-domain signals, and then by spatial Fourier transformation of the result in order to produce an angular spectrum decomposition of the signals. The angular spectrum is then propagated to image planes or lines at depths other than the measurement depth throughout the region to be imaged. The backpropagated signals are then inversely transformed twice to obtain the corresponding time-domain signals. An entire image may be reconstructed from a single transmitted pulse, or several pulses can be transmitted and an image can be reconstructed from each and then registered. An increase in speed of image generation relative to conventional *b*-scanning is possible since an entire volumetric image may be produced using the signals from only one round-trip propagation time.—RCW

# Active control of finite amplitude acoustic waves in a confined geometry<sup>a)</sup>

Pai-Tsung Huang and J. G. Brisson

*Cryogenic Engineering Laboratory, Department of Mechanical Engineering, Massachusetts Institute of Technology, Cambridge, Massachusetts 02139*

(Received 21 November 1996; accepted for publication 1 June 1997)

An active control approach was developed to observe and control nonlinear effects for high-amplitude acoustic waves in a cavity. The acoustic medium was air at ambient pressure and temperature. A harmonic cavity was driven using a multi-frequency drive to selectively drive the fundamental mode and suppress nonlinear interactions between the fundamental and other modes. A semi-empirical model was developed using effective quadratic and cubic nonlinear coupling coefficients to predict resonator response. The cavity was also shown to act as an acoustic mixer. Typical acoustic pressure amplitudes were 1000 Pa (SPL 154 dB *re*: 20  $\mu$ Pa). © 1997 Acoustical Society of America. [S0001-4966(97)00211-7]

PACS numbers: 43.10.Ln, 43.25.Gf, 43.20.Ks [MAB]

## INTRODUCTION

Renewed interest in finite-amplitude acoustic waves in confined geometries has been stimulated by developments in acoustic compressors, thermoacoustic engines, and thermoacoustic refrigerators. These devices store energy in the form of an acoustic standing wave in a resonant cavity. When a standing wave is driven to high amplitude in an acoustic resonator, nonlinear effects couple energy from low- to high-frequency modes, ultimately resulting in shock wave formation and heightened dissipation. Studies by Coppens and Sanders<sup>1,2</sup> and Gaitan and Atchley<sup>3</sup> have shown that these nonlinear effects can be suppressed with the use of a detuned or an anharmonic cavity. Both thermoacoustic devices and acoustic compressors currently rely on this passive technique to suppress shock wave formation. Anharmonic cavities suppress mode-to-mode coupling when driven with a single-frequency drive primarily because the resonant frequencies of the cavity are nonintegral multiples of the fundamental. We will show here that mode-to-mode coupling can be suppressed using a multi-frequency drive. Although this concept is applicable to both harmonic and anharmonic cavities, our investigation uses a harmonic cavity.

Section I is an overview of the theory for this work, followed by a formal development of the theory similar to that of Coppens and Sanders<sup>2</sup> for finite-amplitude standing waves. In Sec. II we discuss the experimental apparatus and procedure, followed by a discussion of our computational model. We finish with a discussion of the results and our conclusions.

## I. THEORY

Figure 1(a) depicts a piston resonantly driving the fundamental mode of a harmonic resonator. The pressure response, as measured by the pressure gauge on the end of the resonator, can be written as a Fourier series of sinusoidal

terms where the first term has the frequency of the drive,  $\omega_1$ , and the frequency of each subsequent term is an integral multiple of  $\omega_1$ . The amplitudes and relative phases of these terms depend on the geometry of the cavity.

The pressure response for the case shown in Fig. 1(a) can also be written as a perturbation series for the nonlinear interactions present in the resonator, as shown in Fig. 1(b). The advantage of this series over that of the Fourier series mentioned above is that only the first few terms of the series are necessary to describe the response. Unfortunately, the perturbation series and the Fourier series do not directly correspond. In general, each term in the perturbation series will contain several frequency components. We will show that for a quadratically nonlinear cavity driven in the manner described above, the nonzero frequency components present in each perturbation term are as shown in Fig. 1(b). The first term  $p^{(1)}$  corresponds to the linear response of the cavity to the drive at frequency  $\omega_1$ . In turn, the second term  $p^{(2)}$  arises from the quadratic nonlinear interaction of the first-order response  $p^{(1)}$  with itself which generates a response at  $2\omega_1$ . The third-order term  $p^{(3)}$  comes from  $p^{(1)}$  quadratically interacting with  $p^{(2)}$  resulting in a response at  $2\omega_1 + \omega_1 = 3\omega_1$  and  $2\omega_1 - \omega_1 = \omega_1$ . The fourth-order term comes from  $p^{(1)}$  interacting with  $p^{(3)}$  and from  $p^{(2)}$  interacting with itself, and so the response is at  $2\omega_1$  and  $4\omega_1$ , and so on.

We can diagram the process of generating the first four terms of the perturbation series as shown in Fig. 1(c) for a quadratic nonlinearity. The resonant response of the cavity,  $p^{(1)}$ , interacts with itself to generate  $p^{(2)}$ . In turn,  $p^{(2)}$  interacts with  $p^{(1)}$  to generate  $p^{(3)}$ . Then, both  $p^{(2)}$  interacting with itself and  $p^{(1)}$  interacting with  $p^{(3)}$  generates  $p^{(4)}$ . This diagram reveals that if the  $p^{(2)}$  term is suppressed (set to zero), then all the subsequent perturbation terms are identically zero and the resonator response would be that of the direct linear response to the  $\omega_1$  drive. The effect is shown schematically by dotted lines in Fig. 1(d). We see that the suppression of the second-order perturbation term results in the suppression of all higher-order perturbation terms and

<sup>a)</sup>“Selected research articles” are ones chosen occasionally by the Editor-in-Chief, that are judged (a) to have a subject of wide acoustical interest, and (b) to be written for understanding by broad acoustical readership.

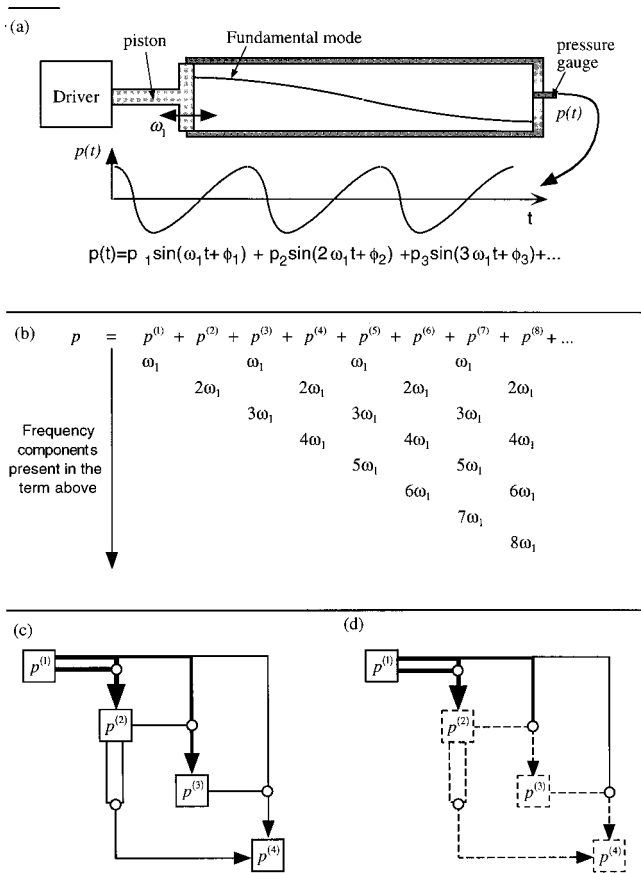


FIG. 1. (a) A heuristic drawing of the experimental apparatus. The cavity is driven by the piston at its fundamental resonant frequency  $\omega_1$ . At large enough drive amplitudes, the pressure response measured by the pressure gauge is periodic but nonsinusoidal and can be expressed in a Fourier series of the form shown. (b) The perturbation expansion for the quadratically nonlinear cavity and the frequency components each term contains. (c) A schematic diagram of the interactions (mathematical operations) used to generate the first four terms in the perturbation solution of the quadratically nonlinear cavity. The interaction (shown by the symbol  $\circ$ ) of the linear response,  $p^{(1)}$ , with itself results in the second-order perturbation solution  $p^{(2)}$ . Interaction between  $p^{(1)}$  and  $p^{(2)}$  then results in  $p^{(3)}$ , and so on. (d) The same interaction diagram as in (c), but with an emphasis on the interactions that involve the amplitude of  $p^{(2)}$  (dashed lines). If the amplitude of  $p^{(2)}$  is set equal to zero, then all subsequent perturbation responses are zero.

thus suppresses the excitation of the high-frequency modes of the cavity.

In the analysis that follows, we will show that the cancellation of the  $p^{(2)}$  term above can be achieved by moving the drive piston with a waveform that contains two sinusoidal terms. The first term is the original drive signal at frequency  $\omega_1$  and the second term has frequency  $2\omega_1$ . We will also show that if both quadratic and cubic nonlinearities are important, then two additional drive frequencies (in addition to the original drive signal) are needed to suppress the nonlinear response of the cavity. We start now with the solution of the linear wave equation for an arbitrary driving function to establish our notation.

## A. Linear response

The low-amplitude response of the resonator can be modeled using the linear wave equation with dissipation,

$$\left( c_0^2 \nabla^2 - \frac{\partial^2}{\partial t^2} + \frac{\partial}{\partial t} \mathcal{S} \right) \frac{p}{c_0^2} = -F(\mathbf{r}, t), \quad (1)$$

where  $t$  is time,  $p$  is the acoustic pressure,  $c_0$  is the sound speed under ambient conditions and  $\mathcal{S}$  is a linear operator that leads to absorption and dispersion. Here,  $F(\mathbf{r}, t)$  is the driving term that is a function of space ( $\mathbf{r}$ ), and time. For the moment, we will assume  $F(\mathbf{r}, t)$  is the forcing function due to externally imposed motions and forces. The Fourier transform of Eq. (1) is

$$(c_0^2 \nabla^2 + \omega^2 - i\omega \eta(\omega)) \frac{\tilde{p}(\mathbf{r}, \omega)}{c_0^2} = -\tilde{F}(\mathbf{r}, \omega), \quad (2)$$

where  $\eta(\omega)$  is the Fourier transform of the operator  $\mathcal{S}$ ,  $i = \sqrt{-1}$ ,  $\omega$  is an angular frequency, and the  $\sim$  symbol delineates the time Fourier transform of the quantity underneath it. A solution for Eq. (2) is easily found by expanding  $\tilde{p}(\mathbf{r}, \omega)$  in terms of real orthonormal eigenfunctions,  $|m\rangle$ , and eigenvalues,  $-k_m^2$ , of  $\nabla^2$  operator (solutions to  $\nabla^2 |m\rangle = -k_m^2 |m\rangle$  that satisfy the resonator boundary conditions). The spatial components of  $\tilde{p}(\mathbf{r}, \omega)$  can be expanded in terms of these spatial eigenfunctions

$$\tilde{p}(\mathbf{r}, \omega) = \sum_{m=1}^{\infty} a_m(\omega) |m\rangle, \quad (3)$$

where  $a_m(\omega)$  are frequency-dependent coefficients that need to be determined.

Substituting Eq. (3) into Eq. (2), multiplying the equation by the  $n$ th eigenfunction, integrating over the volume of the resonator, solving for  $a_m(\omega)$ , and substituting into Eq. (3) we find

$$\tilde{p}(\mathbf{r}, \omega) = \sum_{m=1}^{\infty} |m\rangle \left\{ \frac{\langle m | \tilde{F} \rangle - i\omega \sum_{n \neq m} a_n(\omega) \langle m | \eta | n \rangle}{(\omega^2/c_0^2 - k_m^2 - i\omega \langle m | \eta | m \rangle)} \right\}, \quad (4)$$

where we have used Dirac-like notation for the integrals over the volume of the resonator:  $\langle m | \tilde{F} \rangle \equiv \int d^3r \{ |m\rangle \tilde{F}(\mathbf{r}, \omega) \}$  and  $\langle m | \eta | n \rangle \equiv \int d^3r \{ |m\rangle \eta | n \rangle \}$ . The orthonormality condition is described by  $\langle m | n \rangle = \delta_{mn}$ , where  $\delta_{mn}$  is the Kronecker delta function ( $\delta_{mn} = 1$  when  $m$  equals  $n$  and  $\delta_{mn} = 0$  when  $m$  is not equal to  $n$ ). In our analysis, we neglect the second term in the numerator since it is a sum of the small spatial cross coupling due to the linear operator  $\eta$ . We cannot neglect the small  $\langle m | \eta | m \rangle$  term in the denominator since there are frequencies where the  $\omega^2/c_0^2 - k_m^2$  term will vanish.

Equation (4) simplifies considerably for a single-frequency drive. If the resonator is sinusoidally driven at a frequency  $\omega_{\text{dr}}$  near the  $n$ th cavity resonance ( $\omega_n = k_n c_0$ ), then  $\tilde{F}(\mathbf{r}, \omega) = \tilde{F}(\mathbf{r}) (\delta(\omega - \omega_{\text{dr}}) + \delta(\omega + \omega_{\text{dr}}))$ . The  $n$ th term dominates the response of the resonator since the denominator is small only for that term and so

$$\tilde{p}(\mathbf{r}, \omega) = |n\rangle \left\{ \frac{\langle n | \tilde{F}(\mathbf{r}) \rangle}{\omega^2/c_0^2 - k_n^2 - i\omega \langle n | \eta | n \rangle} \right\} \times (\delta(\omega - \omega_{\text{dr}}) + \delta(\omega + \omega_{\text{dr}})). \quad (5)$$

The integral  $\langle n|\eta|n\rangle$  is small and a slowly varying function of frequency. With this in mind, we replace  $\langle n|\eta|n\rangle$  by its value evaluated at the resonant frequency,  $\omega_n = k_n c_0$ . If we define

$$c_n^2 \equiv c_0^2 \left( 1 - \frac{c_0^2}{\omega_n} \frac{\text{Im} \langle n|\eta|n\rangle|_{\omega=\omega_n}}{i} \right),$$

$$Q_n \equiv \frac{\omega_n}{\text{Re} \langle n|\eta|n\rangle|_{\omega=\omega_n}},$$

where Re means ‘‘the real part of’’ and Im means ‘‘the imaginary part of,’’ Eq. (5) can then be simplified to

$$\tilde{p}(\mathbf{r}, \omega) = |n\rangle \left\{ \frac{\langle n|\tilde{F}(\mathbf{r}, \omega)\rangle}{\omega^2/c_n^2 - k_n^2 - i(\omega\omega_n/Q_n)} \right\}. \quad (6)$$

Equation (6) is a description of the simple harmonic response of the resonator driven at its  $n$ th mode. It is characterized by the modes quality factor  $Q_n$  and phase velocity  $c_n$ . In this work, these properties are experimentally determined from the harmonic response of the resonator for each mode:  $c_n^2$ 's are determined by measuring the frequencies of the response peaks for the resonator and  $Q_n$ 's are determined from the widths of the response peaks. Although these numbers could have been determined from a knowledge of the geometry, they are experimentally determined and used in our computational model.

Incorporating the observations made in the last several paragraphs, the linear response of the resonator [Eq. (4)] to an arbitrary forcing function of frequency  $\omega$  is

$$\tilde{p}(\mathbf{r}, \omega) = \sum_{m=1}^{\infty} |m\rangle \left\{ \frac{\langle m|\tilde{F}(\mathbf{r}, \omega)\rangle}{\omega^2/c_m^2 - k_m^2 - i(\omega\omega_m/Q_m)} \right\}. \quad (7)$$

Equation (7) shows that given any forcing function of frequency  $\omega$ , the linear response is the sum of spatial terms with the same frequency (time) dependence. This equation is valid only for infinitesimal-amplitude response; for finite amplitudes, the original wave equation must be modified with nonlinear terms to better describe the response. Next we discuss the finite-amplitude response for the *quadratic* nonlinear wave equation. Using an effective nonlinear coupling coefficient, we will demonstrate how nonlinear harmonics are excited and how they may be actively suppressed.

## B. Quadratic nonlinearities

In their analysis, Coppens and Sanders<sup>2</sup> used the quadratic nonlinear equation

$$\begin{aligned} & \left( c_0^2 \nabla^2 - \frac{\partial^2}{\partial t^2} + \frac{\partial}{\partial t} \mathcal{F} \right) \frac{p}{\rho_0 c_0^2} \\ &= - \frac{\partial^2}{\partial t^2} \left[ \left( \frac{u}{c_0} \right)^2 + \frac{\gamma-1}{2} \left( \frac{p}{\rho_0 c_0^2} \right)^2 \right], \end{aligned} \quad (8)$$

where  $u$  is the acoustic velocity. The form is identical to Eq. (1) provided  $-F(\mathbf{r}, t)$  is set equal to the right-hand side of

Eq. (8). For our analysis, we have chosen a simpler nonlinear equation of the form

$$\left( c_0^2 \nabla^2 - \frac{\partial^2}{\partial t^2} + \frac{\partial}{\partial t} \mathcal{F} \right) \frac{p}{c_0^2} = -F_{\text{dr1}}(\mathbf{r}, t) - F_{\text{dr2}}(\mathbf{r}, t) - \varepsilon_q p^2, \quad (9)$$

where  $\varepsilon_q$  is an effective quadratic coupling coefficient and is assumed constant. We have inserted two drive terms  $F_{\text{dr1}}$  and  $F_{\text{dr2}}$  that correspond to externally imposed drive forces on the resonator.

Our intent is not to present an exhaustive treatment of the nonlinearities found in our cavity, but to present a new technique for controlling and measuring acoustic disturbances in a confined geometry. There is a loss of some physics in adopting Eq. (9) in lieu of Eq. (8); however, the basic coupling from mode to mode can be modeled using the simpler form.

The Fourier transform in time of Eq. (9) results in

$$\begin{aligned} & (c_0^2 \nabla^2 - \omega^2 - i\omega\eta(\omega)) \frac{\tilde{p}(\mathbf{r}, \omega)}{c_0^2} \\ &= -\tilde{F}_{\text{dr1}}(\mathbf{r}, \omega) - \lambda \tilde{F}_{\text{dr2}}(\mathbf{r}, \omega) - \lambda \varepsilon_q \tilde{p}(\mathbf{r}, \omega) * \tilde{p}(\mathbf{r}, \omega), \end{aligned} \quad (10)$$

where the \* symbol denotes the convolution integral,

$$f(\omega) * g(\omega) = \frac{1}{\sqrt{2\pi}} \int_{-\infty}^{+\infty} f(s)g(\omega-s)ds.$$

The terms on the right-hand side of Eq. (10) tagged with the expansion parameter  $\lambda$  are assumed much smaller than the  $F_{\text{dr1}}$  term. The value of the expansion parameter  $\lambda$  will ultimately be set to 1 when computing the solution. It is included here to facilitate in the perturbation expansion that follows.

Expanding  $\tilde{p}$  in a perturbation series in powers of  $\lambda$

$$\tilde{p} = \tilde{p}^{(1)} + \lambda \tilde{p}^{(2)} + \lambda^2 \tilde{p}^{(3)} + \dots = \sum_{n=1}^{\infty} \lambda^{n-1} \tilde{p}^{(n)}, \quad (11)$$

and substituting into Eq. (10) and equating the first four like powers of  $\lambda$ , we find

$$\lambda^0: \quad (c_0^2 \nabla^2 - \omega^2 - i\omega\eta(\omega)) \frac{\tilde{p}^{(1)}(\mathbf{r}, \omega)}{c_0^2} = -\tilde{F}_{\text{dr1}}(\mathbf{r}, \omega), \quad (12)$$

$$\begin{aligned} \lambda^1: \quad & (c_0^2 \nabla^2 - \omega^2 - i\omega\eta(\omega)) \frac{\tilde{p}^{(2)}(\mathbf{r}, \omega)}{c_0^2} \\ &= -\tilde{F}_{\text{dr2}}(\mathbf{r}, \omega) - \varepsilon_q \tilde{p}^{(1)}(\mathbf{r}, \omega) * \tilde{p}^{(1)}(\mathbf{r}, \omega), \end{aligned} \quad (13)$$

$$\begin{aligned} \lambda^2: \quad & (c_0^2 \nabla^2 - \omega^2 - i\omega\eta(\omega)) \frac{\tilde{p}^{(3)}(\mathbf{r}, \omega)}{c_0^2} \\ &= -2\varepsilon_q \tilde{p}^{(1)}(\mathbf{r}, \omega) * \tilde{p}^{(2)}(\mathbf{r}, \omega), \end{aligned} \quad (14)$$

$$\lambda^3: (c_0^2 \nabla^2 - \omega^2 - i\omega\eta(\omega)) \frac{\tilde{p}^{(4)}(\mathbf{r}, \omega)}{c_0^2}$$

$$= -\varepsilon_q [\tilde{p}^{(1)}(\mathbf{r}, \omega) * \tilde{p}^{(3)}(\mathbf{r}, \omega) + \tilde{p}^{(2)}(\mathbf{r}, \omega) * \tilde{p}^{(2)}(\mathbf{r}, \omega)]. \quad (15)$$

The first-order response of the cavity,  $\tilde{p}^{(1)}(\mathbf{r}, \omega)$ , is just the linear response to  $F_{dr1}$ , an external single-tone driving force, and is easily calculated using Eq. (7). The perturbation series equations above suggest that the coupling between the modes can be thought of as a cascade of interactions from one mode to the next. The  $F_{dr1}$  drives the cavity, resulting in a linear response to that drive  $\tilde{p}^{(1)}(\mathbf{r}, \omega)$ . The convolution  $\tilde{p}^{(1)}(\mathbf{r}, \omega)$  with itself then acts as the driving term for the second-order response  $\tilde{p}^{(2)}(\mathbf{r}, \omega)$  (assume for the moment the additional external forcing tone drive  $F_{dr2}=0$ ). The third-order response of the cavity is dependent on the convolution of  $\tilde{p}^{(1)}(\mathbf{r}, \omega)$  with  $\tilde{p}^{(2)}(\mathbf{r}, \omega)$ . In turn, the fourth-order response of the cavity is dependent on convolution integrals that involve  $\tilde{p}^{(2)}(\mathbf{r}, \omega)$  and  $\tilde{p}^{(3)}(\mathbf{r}, \omega)$ . Every drive term beyond the second-order equation is either dependent directly on the second-order response,  $\tilde{p}^{(2)}(\mathbf{r}, \omega)$ , or on a quantity that directly depends on  $\tilde{p}^{(2)}(\mathbf{r}, \omega)$ ; therefore, *if the response  $\tilde{p}^{(2)}(\mathbf{r}, \omega)$  can be suppressed to zero, the response of the quadratically nonlinear cavity will only be the linear response to  $F_{dr1}$ .*

To determine how we can suppress the second-order response of the resonator, we solve Eq. (13) with the same method used to obtain Eq. (7) and find

$$\tilde{p}^{(2)}(\mathbf{r}, \omega) = \sum_{m=1}^{\infty} |m\rangle \times \left\{ \frac{\langle m | \tilde{F}_{dr2}(\mathbf{r}, \omega) + \varepsilon_q \tilde{p}^{(1)}(\mathbf{r}, \omega) * \tilde{p}^{(1)}(\mathbf{r}, \omega) \rangle}{\omega^2/c_m^2 - k_m^2 - i(\omega\omega_m/Q_m)} \right\}. \quad (16)$$

For the suppression of nonlinear effects in the cavity,  $F_{dr2}$  must be chosen so that the above sum is zero. A sufficient but not very practical condition is  $\tilde{F}_{dr2}(\mathbf{r}, \omega) + \varepsilon_q \tilde{p}^{(1)}(\mathbf{r}, \omega) * \tilde{p}^{(1)}(\mathbf{r}, \omega) \equiv 0$  for all  $\omega$  and  $\mathbf{r}$ .

---


$$\tilde{p}^{(2)}(\mathbf{r}, \omega) = \sum_{m=1}^{\infty} |m\rangle \left\{ \frac{\langle m | \tilde{F}_{dr2}(\mathbf{r}, \omega) + \varepsilon_q (\tilde{p}^{(1)}(\mathbf{r}))^2 \{ \delta(\omega - 2\omega_{dr1}) + \delta(\omega + 2\omega_{dr1}) \} \rangle}{\omega^2/c_m^2 - k_m^2 - i(\omega\omega_m/Q_m)} \right\}. \quad (20)$$


---

The passive approach to mode coupling suppression is to design the cavity so that the (undesired) modes with high resonant frequencies are not integral multiples of the driven mode's resonant frequency. This insures that there is no mode with a resonant frequency close to  $2\omega_{dr1}$  and the second-order response is small (nonresonant). This is equivalent to designing the cavity so that all the denominators in Eq. (20) are large.

If there is a mode (call it the  $j$ th mode) that is nearly

A less stringent condition can be realized by considering that the response of the cavity is large only when  $\omega = \pm k_m c_m$ . The response  $\tilde{p}^{(2)}(\mathbf{r}, \omega)$  will be small if, for all  $m$ , the mode average  $\langle m | \tilde{F}_{dr2}(\mathbf{r}, \omega) + \varepsilon_q \tilde{p}^{(1)}(\mathbf{r}, \omega) * \tilde{p}^{(1)}(\mathbf{r}, \omega) \rangle = 0$  for all frequencies near  $k_m c_m$ . This condition is what we use to actively suppress the nonlinear effects in our resonant cavity.

We illustrate the concept with a simple example. Here, we assume a large resonator driving force is of the form  $F_{dr1}(\mathbf{r}, t) = F_{dr1}(\mathbf{r}) \cos(\omega_{dr1} t)$ , where  $F_{dr1}(\mathbf{r})$  is dependent on the geometry of the cavity and  $\cos(\omega_{dr1} t)$  is the time-dependent component of  $F_{dr1}(\mathbf{r}, t)$ . The drive frequency  $\omega_{dr1}$  is assumed nearly resonant with  $n$ th resonant mode of the cavity (i.e.,  $\omega_{dr1} \approx k_n c_n$ ). The Fourier transform of the driving term is  $\tilde{F}_{dr1}(\mathbf{r}, \omega) = \pi \tilde{F}_{dr1}(\mathbf{r}) (\delta(\omega - \omega_{dr1}) + \delta(\omega + \omega_{dr1}))$ . The first-order response of the resonator, by Eq. (5), is

$$\tilde{p}^{(1)}(\mathbf{r}, \omega) = \tilde{p}^{(1)}(\mathbf{r}) (\delta(\omega - \omega_{dr1}) + \delta(\omega + \omega_{dr1})), \quad (17)$$

where

$$\tilde{p}^{(1)}(\mathbf{r}) = |n\rangle \left\{ \frac{\langle n | \tilde{F}_{dr1}(\mathbf{r}) \rangle}{\omega^2/c_n^2 - k_n^2 - i(\omega\omega_n/Q_n)} \right\} \pi. \quad (18)$$

The drive term due to nonlinearities is calculated by convoluting  $\tilde{p}^{(1)}(\mathbf{r}, \omega)$  with itself:

$$\varepsilon_q \tilde{p}^{(1)}(\mathbf{r}, \omega) * \tilde{p}^{(1)}(\mathbf{r}, \omega)$$

$$= \varepsilon_q \int_{-\infty}^{+\infty} \tilde{p}^{(1)}(\mathbf{r}, s) \tilde{p}^{(1)}(\mathbf{r}, \omega - s) ds$$

$$= \varepsilon_q (\tilde{p}^{(1)}(\mathbf{r}))^2 \{ 2\delta(\omega) + \delta(\omega - 2\omega_{dr1}) + \delta(\omega + 2\omega_{dr1}) \}. \quad (19)$$

We can neglect the  $\delta(\omega)$  term since we do not expect an acoustic response at zero frequency. (The Coppens and Sanders expression for the nonlinear operator has a second derivative in time which does not allow a zero frequency driving term.) The second-order response of the cavity to the nonlinearity is

---

resonant at  $2\omega_{dr1}$ , then the second-order mode can be quenched by driving the cavity with  $\tilde{F}_{dr2}(\mathbf{r}, \omega)$  such that

$$\langle j | \tilde{F}_{dr2}(\mathbf{r}, \omega) \rangle = -\varepsilon_q \{ \delta(\omega - 2\omega_{dr1}) + \delta(\omega + 2\omega_{dr1}) \} \times \langle j | (\tilde{p}^{(1)}(\mathbf{r}))^2 \rangle. \quad (21)$$

Equation (18) provides the values of  $(\tilde{p}^{(1)}(\mathbf{r}))^2$ , the compensating drive  $\tilde{F}_{dr2}(\mathbf{r}, \omega)$  is a single-frequency drive at  $2\omega_{dr1}$ , and  $\varepsilon_q$  is the effective quadratic coupling coefficient.



Notice that the spatial variation of  $\tilde{F}_{\text{dr2}}(\mathbf{r}, \omega)$  does not have to match the spatial variation of  $\varepsilon_q(\tilde{p}^{(1)}(\mathbf{r}, \omega))^2$ . The only requirement is that the ‘‘mode average’’ of these quantities must be equal and opposite for the modes that are resonant with the frequencies present in  $(\tilde{p}^{(1)}(\mathbf{r}, \omega))^2$ . The mode-averaged function  $\langle j|\tilde{F}_{\text{dr2}}(\mathbf{r}, \omega)\rangle$  can thus be determined given  $\varepsilon_q$  and  $\tilde{p}^{(1)}(\mathbf{r}, \omega)$ .

### C. Cubic nonlinearities

If the pressure amplitudes present in the resonator are large enough, then there will be significant cubic nonlinearities. We should be able to directly observe the cubic nonlinear response of the cavity if we experimentally quench the quadratic nonlinearities. We model this by adding a cubic term to Eq. (9):

$$\begin{aligned} & \left( c_0^2 \nabla^2 - \frac{\partial^2}{\partial t^2} + \frac{\partial}{\partial t} \cdot \mathcal{F} \right) \frac{p}{c_0^2} \\ &= -F_{\text{dr1}}(\mathbf{r}, t) - \lambda F_{\text{dr2}}(\mathbf{r}, t) \\ & \quad - \lambda^2 F_{\text{dr3}}(\mathbf{r}, t) - \lambda \varepsilon_q p^2 - \lambda^2 \varepsilon_c p^3, \end{aligned} \quad (22)$$

where  $\varepsilon_c$  is the effective cubic coupling coefficient. Here  $F_{\text{dr3}}(\mathbf{r}, t)$  is a forcing function that will be used to cancel the cubic response of the cavity. Once again,  $\lambda$  is an expansion parameter used to obtain the perturbation expansion. Following the same procedure used to obtain Eqs. (12)–(15), we obtain

$$\lambda^0: \quad (c_0^2 \nabla^2 - \omega^2 - i\omega\eta(\omega)) \frac{\tilde{p}^{(1)}(\mathbf{r}, \omega)}{c_0^2} = -\tilde{F}_{\text{dr1}}(\mathbf{r}, \omega), \quad (23)$$

$$\begin{aligned} \lambda^1: \quad & (c_0^2 \nabla^2 - \omega^2 - i\omega\eta(\omega)) \frac{\tilde{p}^{(2)}(\mathbf{r}, \omega)}{c_0^2} \\ &= -\tilde{F}_{\text{dr2}}(\mathbf{r}, \omega) - \varepsilon_q \tilde{p}^{(1)}(\mathbf{r}, \omega) * \tilde{p}^{(1)}(\mathbf{r}, \omega), \end{aligned} \quad (24)$$

$$\begin{aligned} \lambda^2: \quad & (c_0^2 \nabla^2 - \omega^2 - i\omega\eta(\omega)) \frac{\tilde{p}^{(3)}(\mathbf{r}, \omega)}{c_0^2} \\ &= -\tilde{F}_{\text{dr3}}(\mathbf{r}, \omega) - 2\varepsilon_q \tilde{p}^{(1)}(\mathbf{r}, \omega) * \tilde{p}^{(2)}(\mathbf{r}, \omega) \\ & \quad - \varepsilon_c \tilde{p}^{(1)}(\mathbf{r}, \omega) * \tilde{p}^{(1)}(\mathbf{r}, \omega) * \tilde{p}^{(1)}(\mathbf{r}, \omega), \end{aligned} \quad (25)$$

$$\begin{aligned} \lambda^3: \quad & (c_0^2 \nabla^2 - \omega^2 - i\omega\eta(\omega)) \frac{\tilde{p}^{(4)}(\mathbf{r}, \omega)}{c_0^2} \\ &= -\varepsilon_q \tilde{p}^{(1)}(\mathbf{r}, \omega) * \tilde{p}^{(3)}(\mathbf{r}, \omega) - \varepsilon_q \tilde{p}^{(2)}(\mathbf{r}, \omega) * \tilde{p}^{(2)}(\mathbf{r}, \omega) \\ & \quad - 3\varepsilon_c \tilde{p}^{(1)}(\mathbf{r}, \omega) * \tilde{p}^{(1)}(\mathbf{r}, \omega) * \tilde{p}^{(2)}(\mathbf{r}, \omega). \end{aligned} \quad (26)$$

Since Eqs. (23) and (24) are identical to Eqs. (12) and (13), we see that  $\tilde{F}_{\text{dr2}}(\mathbf{r}, \omega)$  can be used to suppress  $\tilde{p}^{(2)}(\mathbf{r}, \omega)$  in the exactly the same manner as before. Unfortunately, this does not completely suppress the coupling of energy from the fundamental to higher modes. Equation (25) shows that if  $\tilde{p}^{(2)}(\mathbf{r}, \omega)$  is actively suppressed, there still will be a nonlinear cubic response  $[\tilde{p}^{(3)}(\mathbf{r}, \omega)]$  in the cavity due

to cubic coupling term  $-\varepsilon_c \tilde{p}^{(1)}(\mathbf{r}, \omega) * \tilde{p}^{(1)}(\mathbf{r}, \omega) * \tilde{p}^{(1)}(\mathbf{r}, \omega)$ . The energy then cascades to the other modes of the resonator through terms like  $-\varepsilon_q \tilde{p}^{(1)}(\mathbf{r}, \omega) * \tilde{p}^{(3)}(\mathbf{r}, \omega)$  in Eq. (26).

The cubic nonlinearities can be suppressed by choosing  $\tilde{F}_{\text{dr3}}(\mathbf{r}, \omega)$  to suppress the  $-\varepsilon_c \tilde{p}^{(1)}(\mathbf{r}, \omega) * \tilde{p}^{(1)}(\mathbf{r}, \omega) * \tilde{p}^{(1)}(\mathbf{r}, \omega)$  contribution to  $\tilde{p}^{(3)}(\mathbf{r}, \omega)$  in Eq. (25) [the  $-2\varepsilon_q \tilde{p}^{(1)}(\mathbf{r}, \omega) * \tilde{p}^{(2)}(\mathbf{r}, \omega)$  term is already zero since  $\tilde{p}^{(2)}(\mathbf{r}, \omega)$  has been actively set to zero with the appropriate  $\tilde{F}_{\text{dr2}}(\mathbf{r}, \omega)$ ]. With both  $\tilde{p}^{(2)}(\mathbf{r}, \omega)$  and  $\tilde{p}^{(3)}(\mathbf{r}, \omega)$  equal to zero, Eq. (26) shows that the fourth-order response  $\tilde{p}^{(4)}(\mathbf{r}, \omega)$  is zero. In fact, all the drive terms in the higher-order perturbation equations are zero.

The procedure to choose the cubic suppression term,  $\tilde{F}_{\text{dr3}}(\mathbf{r}, \omega)$ , is entirely analogous to the procedure used in selecting  $\tilde{F}_{\text{dr2}}(\mathbf{r}, \omega)$  in the quadratic case. The response  $\tilde{p}^{(3)}(\mathbf{r}, \omega)$  will be small if, for all  $m$ , the mode average  $\langle m|\tilde{F}_{\text{dr3}}(\mathbf{r}, \omega) + \varepsilon_c \tilde{p}^{(1)*}(\mathbf{r}, \omega) * \tilde{p}^{(1)*}(\mathbf{r}, \omega) * \tilde{p}^{(1)}(\mathbf{r}, \omega)\rangle = 0$  for all frequencies near  $k_m c_m$  [again, we have assumed that  $\tilde{p}^{(2)}$  has been actively set to zero by  $\tilde{F}_{\text{dr2}}(\mathbf{r}, \omega)$ ].

For the single-frequency drive,  $F_{\text{dr1}}(\mathbf{r}, t) = F_{\text{dr1}}(\mathbf{r}) \cos(\omega_{\text{dr1}} t)$ , which was the example used for the quadratic nonlinear equation, the cubic response term to the cubic nonlinear equation is

$$\begin{aligned} \varepsilon_c \tilde{p}^{(1)*}(\mathbf{r}, \omega) * \tilde{p}^{(1)*}(\mathbf{r}, \omega) * \tilde{p}^{(1)}(\mathbf{r}, \omega) &= \varepsilon_c \int_{-\infty}^{+\infty} ds \int_{-\infty}^{+\infty} dz [\tilde{p}^{(1)}(\mathbf{r}, s) \\ & \quad \times \tilde{p}^{(1)}(\mathbf{r}, z) \tilde{p}^{(1)}(\mathbf{r}, \omega - s - z)] \\ &= \frac{\varepsilon_c}{8} (\tilde{p}^{(1)}(\mathbf{r}))^3 \\ & \quad \times [3\delta(\omega - \omega_{\text{dr1}}) + 3\delta(\omega + \omega_{\text{dr1}}) \\ & \quad + \delta(\omega - 3\omega_{\text{dr1}}) + \delta(\omega + 3\omega_{\text{dr1}})], \end{aligned} \quad (27)$$

where  $\tilde{p}^{(1)}(\mathbf{r})$  is determined by Eq. (18). The cubic nonlinearity has two contributions in this case. The first two terms in Eq. (27) are at the original drive frequency  $\omega_{\text{dr1}}$  and alter the fundamental mode’s response from the pure linear response described by Eq. (5). The other two terms are driving the resonator at three times  $\omega_{\text{dr1}}$ . These terms will couple energy from the fundamental to higher-frequency modes. If we have a resonance near  $3\omega_{\text{dr1}}$ , then the cubic response can be suppressed by requiring

$$\begin{aligned} \langle m|\tilde{F}_{\text{dr3}}(\mathbf{r}, \omega)\rangle &= -\varepsilon_c \langle m|\tilde{p}^{(1)}(\mathbf{r}) \tilde{p}^{(1)}(\mathbf{r}) \tilde{p}^{(1)}(\mathbf{r})\rangle \\ & \quad \times [\delta(\omega - 3\omega_{\text{dr1}}) + \delta(\omega + 3\omega_{\text{dr1}})], \end{aligned} \quad (28)$$

where the eigenfunction  $|m\rangle$  is understood to correspond to the mode that is nearly resonant at  $3\omega_{\text{dr1}}$  ( $k_m c_m \approx 3\omega_{\text{dr1}}$ ).

Active suppression of only the quadratic response of the resonator allows the direct determination of the effective cubic coupling coefficient,  $\varepsilon_c$ . If  $\tilde{F}_{\text{dr2}}(\mathbf{r}, \omega)$  is chosen to suppress the quadratic response of the cavity and  $\tilde{F}_{\text{dr3}}(\mathbf{r}, \omega) \equiv 0$ , then the third-order response of the cavity (to order  $\lambda^2$ ) is

$$\begin{aligned} \tilde{p}^{(3)}(\mathbf{r}, \omega) = & \tilde{p}_f^{(3)}(\mathbf{r})[\delta(\omega - \omega_{\text{dr1}}) + \delta(\omega + \omega_{\text{dr1}})] + \tilde{p}_h^{(3)}(\mathbf{r}) \\ & \times [\delta(\omega - 3\omega_{\text{dr1}}) + \delta(\omega + 3\omega_{\text{dr1}})], \end{aligned} \quad (29)$$

where

$$\tilde{p}_f^{(3)}(\mathbf{r}) = \frac{3\varepsilon_c}{8} |1\rangle \left\{ \frac{\langle 1 | (\tilde{p}^{(1)}(\mathbf{r}))^3 \rangle}{(\omega_{\text{dr1}})^2/c_1^2 - k_1^2 - i((\omega_{\text{dr1}})\omega_1/Q_1)} \right\} \pi \quad (30)$$

and

$$\begin{aligned} \tilde{p}_h^{(3)}(\mathbf{r}) = & \frac{\varepsilon_c}{8} |3\rangle \\ & \times \left\{ \frac{\langle 3 | (\tilde{p}^{(1)}(\mathbf{r}))^3 \rangle}{(3\omega_{\text{dr1}})^2/c_3^2 - k_3^2 - i((3\omega_{\text{dr1}})\omega_3/Q_3)} \right\} \pi. \end{aligned} \quad (31)$$

Using Eq. (31), the effective cubic coupling coefficient can be determined from measurements of the amplitude of the response of the cavity at  $3\omega_{\text{dr1}}$  and at  $\omega_{\text{dr1}}$ . The amplitude of the total response of the cavity at  $\omega_{\text{dr1}}$  is really the sum of  $\tilde{p}^{(1)}(\mathbf{r})$  and  $\tilde{p}_f^{(3)}(\mathbf{r})$ . We can neglect the  $\tilde{p}_f^{(3)}(\mathbf{r})$ , since it is of higher order, and attribute the measured response at  $\omega_{\text{dr1}}$  to  $\tilde{p}^{(1)}(\mathbf{r})$ . The cavity's response at  $3\omega_{\text{dr1}}$  is used to determine  $\tilde{p}_h^{(3)}(\mathbf{r})$ . Equation (31) can then be solved to determine  $\varepsilon_c$ .

#### D. Mode coupling

In addition to suppression of nonlinear effects, the multi-frequency drive technique allows us to directly measure the nonlinear coupling coefficient between any two modes. Suppose a harmonic cavity (a cavity whose modes are integral multiples of the fundamental) is strongly driven at frequency  $\omega_f$  near the cavity's fundamental frequency  $\omega_1$ , and driven weakly at frequency  $\omega_h$  near a higher cavity resonant frequency,  $\omega_j$ . In addition, we will suppose that the second-order response to the fundamental drive is actively suppressed. Assume for the moment that only quadratic nonlinear effects are present. Then the principal response of the cavity will be at  $\omega_f$ ,  $\omega_h$ ,  $\omega_f - \omega_h$ , and  $\omega_f + \omega_h$ .

To see this, let  $F_{\text{dr1}}(\mathbf{r}, t) = F_{\text{dr1}}(\mathbf{r})[\cos(\omega_f t) + \xi \cos(\omega_h t)]$ , where  $\xi$  is a number much smaller than 1. The first-order response of the cavity is

$$\tilde{p}^{(1)}(\mathbf{r}, \omega) = \tilde{p}_f^{(1)}(\mathbf{r})[\delta(\omega - \omega_f) + \delta(\omega + \omega_f)] + \tilde{p}_h^{(1)}(\mathbf{r})$$

where

$$\tilde{p}_f^{(1)}(\mathbf{r}) = |1\rangle \left\{ \frac{\langle 1 | \tilde{F}_{\text{dr}}(\mathbf{r}) \rangle}{\omega_f^2/c_1^2 - k_1^2 - i(\omega_f\omega_1/Q_1)} \right\} \pi \quad (33)$$

and

$$\tilde{p}_h^{(1)}(\mathbf{r}) = |j\rangle \left\{ \frac{\langle j | \tilde{F}_{\text{dr}}(\mathbf{r}) \rangle}{\omega_h^2/c_j^2 - k_j^2 - i(\omega_h\omega_j/Q_j)} \right\} \pi \cdot \xi. \quad (34)$$

In this case, the convolution integral in the quadratic driving term in Eq. (13) is

$$\begin{aligned} \tilde{p}^{(1)*} \tilde{p}^{(1)} = & 2[(\tilde{p}_f^{(1)}(\mathbf{r}))^2 + (\tilde{p}_h^{(1)}(\mathbf{r}))^2] \delta(\omega) + (\tilde{p}_f^{(1)}(\mathbf{r}))^2 \\ & \times [\delta(\omega - 2\omega_f) + \delta(\omega + 2\omega_f)] + (\tilde{p}_h^{(1)}(\mathbf{r}))^2 \\ & \times [\delta(\omega - 2\omega_h) + \delta(\omega + 2\omega_h)] + 2\tilde{p}_i^{(1)}(\mathbf{r}) \\ & \times \tilde{p}_h^{(1)}(\mathbf{r})[\delta(\omega - (\omega_h - \omega_f)) + \delta(\omega + (\omega_h - \omega_f))] \\ & + 2\tilde{p}_i^{(1)}(\mathbf{r})\tilde{p}_h^{(1)}(\mathbf{r})[\delta(\omega - (\omega_h + \omega_f)) \\ & + \delta(\omega + (\omega_h + \omega_f))]. \end{aligned} \quad (35)$$

The first term is a zero-frequency drive term which does not contribute. The second term is the nonlinear response due to the fundamental mode. We will assume that this nonlinear drive term is actively suppressed. The third term is the nonlinear response due to the (small)  $\omega_h$  drive. Since this term is of order  $\xi^2$ , we will neglect it. The last two terms are of order  $\xi$ . They correspond to nonlinear interactions between the two modes of the cavity. The total response of the cavity (to leading order in  $\lambda$ ) is

$$\begin{aligned} \tilde{p}(\mathbf{r}, \omega) = & \tilde{p}_f^{(1)}(\mathbf{r})[\delta(\omega - \omega_f) + \delta(\omega + \omega_f)] + \tilde{p}_h^{(1)}(\mathbf{r}) \\ & \times [\delta(\omega - \omega_h) + \delta(\omega + \omega_h)] + \tilde{p}_-^{(2)}(\mathbf{r}) \\ & \times [\delta(\omega - (\omega_h - \omega_f)) + \delta(\omega + (\omega_h - \omega_f))] \\ & + \tilde{p}_+^{(2)}(\mathbf{r})[\delta(\omega - (\omega_h + \omega_f)) + \delta(\omega + (\omega_h + \omega_f))], \end{aligned} \quad (36)$$

where

$$\tilde{p}_-^{(2)}(\mathbf{r}) = 2\varepsilon_q |j-1\rangle \left\{ \frac{\langle j-1 | \tilde{p}_f^{(1)}(\mathbf{r})\tilde{p}_h^{(1)}(\mathbf{r}) \rangle}{(\omega_h - \omega_f)^2/c_{j-1}^2 - k_{j-1}^2 - i((\omega_h - \omega_f)\omega_{j-1}/Q_{j-1})} \right\} \pi, \quad (37)$$

and

$$\tilde{p}_+^{(2)}(\mathbf{r}) = 2\varepsilon_q |j+1\rangle \left\{ \frac{\langle j+1 | \tilde{p}_f^{(1)}(\mathbf{r})\tilde{p}_h^{(1)}(\mathbf{r}) \rangle}{(\omega_h + \omega_f)^2/c_{j+1}^2 - k_{j+1}^2 - i((\omega_h + \omega_f)\omega_{j+1}/Q_{j+1})} \right\} \pi. \quad (38)$$

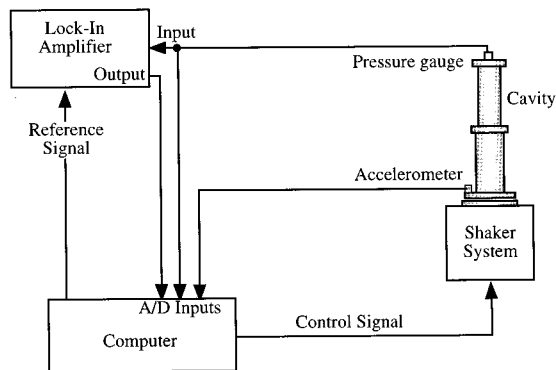


FIG. 2. A schematic diagram for the control loop used in this investigation. The computer generates two signals. One is a single-frequency reference signal for the lock-in amplifier and the other is a multi-frequency signal used to drive the shaker table. The output of the accelerometer, which is mounted at the base of the cavity, is input to the computer. The pressure gauge signal is input to both the computer and the lock-in amplifier. The lock-in amplifier acts as a filter and phase comparator between the reference signal and the fundamental pressure response signal from the cavity. The lock-in amplifier's output is fed back to the computer.

The indices  $j-1$  and  $j+1$  refer to the modes that are nearly resonant with the frequencies  $\omega_h - \omega_f$  and  $\omega_h + \omega_f$ , respectively. Equations (37) and (38) allow a direct means of determining  $\varepsilon_q$  from the experimental cavity response data. Equation (36) shows that the amplitudes of  $\tilde{p}_-^{(2)}(\mathbf{r})$ ,  $\tilde{p}_+^{(2)}(\mathbf{r})$ ,  $\tilde{p}_f^{(1)}(\mathbf{r})$ , and  $\tilde{p}_h^{(1)}(\mathbf{r})$  are easily measured by taking a fast Fourier transform in time of the pressure response signal in the cavity. From this and the measured values of the  $Q_n$ 's and  $c_n$ 's, the value of  $\varepsilon_q$  can be determined using Eq. (37) or Eq. (38).

In the above example, the fundamental mode's nonlinearities were suppressed to allow a large-amplitude single-frequency oscillation to exist in the cavity. If a small excitation at some higher resonant frequency is introduced in the cavity, the cavity will respond at that frequency and at the sum and difference frequencies of the fundamental and the higher frequency excitation. If the amplitude of the fundamental mode is large enough, the nonlinear response to the high-frequency excitation can be larger than the direct linear response to that excitation, since the nonlinear term is proportional to the very large amplitude of the fundamental mode.

## II. EXPERIMENT

### A. Apparatus

Our apparatus is shown schematically in Fig. 2. The computer generates a control signal that is input into the shaker system. Based on this input, the shaker physically shakes the air-filled cavity to induce acoustic oscillations. A pressure gauge,<sup>4</sup> mounted on the top of the acoustic cavity, measures the acoustic pressure oscillations inside the cavity. The output of this gauge is, in turn, fed to a lock-in amplifier and back to the computer. An accelerometer<sup>5</sup> is used to directly measure the accelerations imposed on the cavity by the shaker.

The acoustic cavity, shown in Fig. 3, consists of two aluminum cylinders of different diameters welded end to end

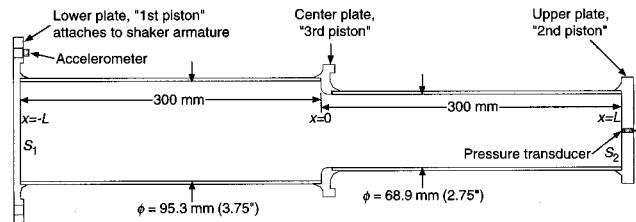


FIG. 3. A cross-sectional drawing of the cylindrical resonator used in this work. The inner diameters of the resonator are 95.3 and 68.9 mm. The dimension  $L$  is 0.3 m. The mass of the cavity is 2.7 kg. The cavity modes are driven by bodily shaking the cavity. In this case each of the cavity's "plates" act as drive pistons.

with a transitional flange. The large diameter cylinder is welded to a flanged aluminum plate to allow the securing of the cavity to the shaker table. The cavity is closed by an aluminum "upper" plate welded to the small diameter tube. Holes for both a pressure transducer and an air inlet are machined in the upper plate. In these experiments, the cavity is filled with air at ambient temperature and pressure.

The cavity design was dominated by the requirement that the first five axial modes of the cavity can be directly driven by the motion of the shaker system and by the ease of construction. We chose a cavity that was harmonic (the resonant frequencies of the higher modes are integral multiples of the fundamental) to insure large nonlinear effects in the cavity.

We considered using a right circular cylinder as a resonator since the resonant frequencies are harmonically related in this type of cavity. Unfortunately, the even modes in such a cylinder cannot be driven by the shaker. The pressure at each of the end plates of the right circular cavity are in phase with each other for the even modes. In the shaker-driven cavity, the motions of the end plates are constrained to move in "180° out of phase" with each other. (If we visualize the end plates as two drive pistons, one piston "compresses" the gas while the other "expands" the gas.) In the even modes, the end plate pressure is in phase while the end plate volume displacements are out of phase, the " $p dv$ " work done by one piston is identically canceled out by the work done on the other piston for the even modes. The net result is that there is very weak coupling of the shaker drive to the even modes of the cavity. This is not true for the odd modes since the end plate pressures are 180° out of phase.

We settled on the two-diameter resonator geometry to allow our drive to couple to both the "even" and "odd" modes of the resonator. In order to insure that the modes of the two-diameter resonator were harmonically related, we chose the length of each half of the resonator to be the same.

The axial modes of the cavity are driven by displacing the cavity in its axial direction with an LDS<sup>6</sup> type 722 shaker. The system is capable of developing 2.9-kN force and has a well-characterized response to 3000 Hz. The analog drive signal for the shaker system is generated by a 60-MHz Pentium-based computer running Labview<sup>7</sup> software and a National Instruments<sup>7</sup> type ATM-MIO-16E-2 digital-to-analog board.

In these measurements we drive the fundamental mode at high amplitude; consequently, there is significant dissipa-

tion in the cavity and the gas temperature changes over the duration of the experiment. Since the acoustic velocity is temperature dependent, the resonant frequencies of the cavity shift with time. In order to ensure that the fundamental mode is continuously driven at resonance we use a control loop, consisting of the lock-in amplifier, the computer, and the shaker/resonator, to lock the drive frequency to the fundamental mode's resonant frequency. The computer outputs a three-frequency component waveform to drive the shaker. The lowest drive frequency is near the cavity's fundamental resonance and the others are at two and three times the lowest drive frequency. A reference signal in phase with the lowest frequency drive component is input to the reference port of the lock-in amplifier. The output of the pressure gauge is connected to the input port of the lock-in amplifier. The phase of the lock-in amplifier is set so that the output of the amplifier is zero when the cavity is driven at resonance. Since the phase of the pressure response of the cavity is a strong function of frequency around the resonance, the dc voltage output of the lock-in amplifier is proportional to the drive frequency deviation from the resonant frequency of the cavity (for drive frequencies sufficiently close to the resonant frequency). The "error" voltage output from the lock-in amplifier is input back into the computer which adjusts the drive frequencies so that the lowest drive frequency is resonant with the cavity. The computer software uses a proportional control algorithm in determining the output frequencies.

The major effort in developing the experimental system was in developing computer software that tracks the fundamental resonance, generates the multifrequency waveform input for the shaker, records the cavity pressure waveforms, and records and displays the Fourier transform of the cavity pressure waveform in real time. The software also allows the user to specify or sweep the amplitudes, frequencies, and relative phases of the three frequency components of the drive waveform while the system is in operation. The most general computer output waveform used for cancellation is of the form

$$F_{dr}(t) = F_{dr1} \cos(\omega_1 t) + F_{dr2} \cos(2\omega_1 t + \phi_2) + F_{dr3} \cos(3\omega_1 t + \phi_3), \quad (39)$$

where  $F_{dr1}$ ,  $F_{dr2}$ , and  $F_{dr3}$  are amplitudes,  $\omega_1$  is the lowest angular frequency present in the drive, and  $\phi_2$  and  $\phi_3$  are phase angles.

Experimentally, the most convenient unit for expressing the amplitudes of oscillation with the shaker is acceleration. The voltage input to the shaker amplifier from the computer is proportional to the force put on the armature of the shaker. Since the combined mass of the shaker armature and the resonator shell dominates the physical response of the armature/resonator system, the acceleration of the cavity is directly proportional to the voltage output by the computer. It is for this reason that we will refer to all the drive amplitudes [ $F_{dr1}$ ,  $F_{dr2}$ ,  $F_{dr3}$  in Eq. (39)] in units of  $g$  ( $9.806 \text{ m/s}^2$ ).

## B. Procedure

The procedure is divided into four separate sections. First, the cavity is driven at low amplitude and the linear response of the cavity is characterized. Second, the drive amplitude is increased to where the quadratic nonlinearities are dominant in the response of the resonator. These nonlinearities are then suppressed using a two-tone driving function. Third, the cubic nonlinearities are investigated by increasing the drive amplitude still further and using a three-tone drive to suppress both the quadratic and cubic responses. Finally, we show the cavity can be used as an acoustic mixer.

### 1. Linear response

The linear resonator response is determined by driving the resonator with low-amplitude single-frequency drive signal [ $F_{dr2}$  and  $F_{dr3}$  are set to zero in Eq. (39)]. The drive frequency ( $\omega_1$ ) is swept over each of first four resonances of the cavity and the pressure response of the cavity is recorded. The resulting amplitude versus frequency curves are fit to determine the resonant frequency and the quality factor for each of the first four resonant modes.

### 2. Quadratic nonlinear response

The fundamental mode is driven with a low-amplitude single-tone drive [ $F_{dr2}$  and  $F_{dr3}$  are set to zero in Eq. (39)]. The drive frequency is locked to the fundamental resonance using the control loop described above. The amplitude of the single-tone drive is now increased to a level where the pressure response waveform begins to steepen from that of the pure sinusoid observed in the linear response studies. The Fourier transform of the pressure waveform shows a clear increase in the nonlinear response of the cavity at twice the fundamental frequency.

To suppress the nonlinear response at twice the fundamental frequency, a second tone, at twice the fundamental frequency ( $2\omega_1$ ), is imposed with a small amplitude  $F_{dr2}$  and phase  $\phi_2$  [see Eq. (39)]. The phase of the second drive tone is swept until there is a minimum in the  $2\omega_1$  cavity pressure response. This is easily seen in the Fourier transform of the pressure response by following the magnitude of the peak at  $2\omega_1$ . In turn, the amplitude  $F_{dr2}$  is then adjusted to further minimize the  $2\omega_1$  pressure response. The procedure is repeated by alternating between the phase and the amplitude adjustments until the second-order response of the cavity is suppressed.

### 3. Quadratic and cubic nonlinear response

The system is once again driven by a low-amplitude single tone locked to the fundamental resonance of the cavity. The amplitude of the drive is then increased above that of the quadratic case. The quadratic nonlinearities are suppressed in the fashion described above. If the amplitude of the fundamental drive is large enough, then the suppression of the  $2\omega_1$  pressure response will not result in the quenching of the response at  $3\omega_1$  (due to direct cubic coupling from the fundamental). The  $3\omega_1$  cavity response is suppressed using a procedure analogous to the one used to cancel the quadratic

response. A third tone, at three times the fundamental frequency ( $3\omega_1$ ), is imposed with small amplitude  $F_{dr3}$  and phase  $\phi_3$  [see Eq. (39)]. The phase and the amplitude of this drive component are alternately adjusted so as to cancel the cavity response at  $3\omega_1$ .

#### 4. Nonlinear interactions between modes

Nonlinear coupling between the fundamental mode and other modes can be measured using a three-tone driving function similar to that of Eq. (39):

$$F_{dr}(t) = F_{dr1} \cos(\omega_1 t) + F_{dr2} \cos(2\omega_1 t + \phi_2) + F_{drn} \cos(n\omega_1 t + \phi_n), \quad (40)$$

where  $F_{dr1}$ ,  $F_{dr2}$ , and  $F_{drn}$  are amplitudes,  $\omega_1$  is the fundamental drive angular frequency,  $n$  is an integer, and,  $\phi_2$  and  $\phi_n$  are phase angles. The system is driven at an amplitude,  $F_{dr1}$ , where quadratic nonlinearities dominate the response. Here  $F_{dr2}$  and  $\phi_2$  are chosen (using the methods outlined above) to quench the nonlinear response of the resonator. At this point, the Fourier transform of the resonator response is

$$|m\rangle = \begin{cases} \left\{ \begin{array}{l} \sqrt{\frac{2}{S_1 L(1+S_r)}} \sin(k_m x), \quad -L \leq x \leq 0 \\ S_r \sqrt{\frac{2}{S_1 L(1+S_r)}} \sin(k_m x), \quad 0 < x < L \end{array} \right\}, & \text{for } m=1,3,5,\dots, \\ \left\{ \begin{array}{l} \sqrt{\frac{2}{L(S_1+S_2)}} \cos(k_m x), \quad -L \leq x \leq L, \end{array} \right\}, & \text{for } m=2,4,6,\dots, \end{cases}$$

where  $x$  is the longitudinal position in the resonator (see Fig. 3),  $S_1$  and  $S_2$  are the surface areas of the lower and upper plates,  $S_r$  is the area ratio  $S_r = S_2/S_1$ ,  $L$  is the length of each half of the resonator (see Fig. 3), and  $k_m$  is the wave number of the  $m$ th mode,  $k_m = m\pi/L$ . A more in-depth discussion of the computational model is available in the thesis by Huang.<sup>9</sup>

### IV. RESULTS AND DISCUSSION

#### A. Linear response

The resonant frequencies of the resonator do vary over time due to the inherent temperature dependence of the speed of sound in air. However, the fundamental resonant frequency for our resonator was typically 284.5 Hz. The other resonances for this cavity design are nearly harmonic with the fundamental mode. The ratios of the second, third, and fourth resonant frequencies to those of the first are 2.02, 3.00, and 4.04, respectively. The quality factors for the first, second, third, and fourth resonances are 173, 220, 300, and 320, respectively.

#### B. Quadratic nonlinear response

Figure 4(a) shows the pressure trace when the cavity's fundamental mode is driven with a single-frequency drive.

a pure monotone at  $\omega_1$ . A third tone is now introduced into the resonator at  $n\omega_1$  by adding a third signal, with small amplitude  $F_{drn}$ , to the drive. The amplitudes of the Fourier transform of the resonator response are recorded.

### III. COMPUTATIONAL MODEL

A semi-empirical computational model was written using Maple V<sup>8</sup> to compare the resonator response to our theory. The program calculates the response of the resonator using the perturbation solutions described in Sec. I. We restrict our model to a manifold that includes only the first four resonant modes to limit the model's computational complexity. The model requires as inputs the quality factors and the resonant frequencies for the first four resonances. These values are experimentally determined from the linear response measurements outlined above. The two adjustable coupling parameters  $\epsilon_q$  and  $\epsilon_c$  characterize the nonlinear coupling between modes.

The normalized pressure eigenfunctions for our resonator geometry are of the form

The peak acceleration of the cavity is 2.1 g's. The pressure gauge is positioned at a pressure antinode and registers a peak pressure amplitude of 576 Pa. The ambient pressure inside the resonator is  $10^5$  Pa. There is a slight steepening in the pressure-time trace due to nonlinear effects in the resonator. These effects are more apparent in the Fourier transform of the pressure shown in Fig. 4(b). Not surprisingly, the fundamental mode is strongly excited by the resonant drive. However, the Fourier transform of the pressure signal also shows that both the second and the third mode are nonlinearly driven.

Figure 4(c) shows the response of the resonator when a second tone is introduced to suppress the second mode's response. Here the drive is of the form of Eq. (39) with  $F_{dr1} = 2.1$  g,  $F_{dr2} = 2.2$  g,  $\phi_2 = 310^\circ$ , and  $F_{dr3} = 0$  g. The second mode is directly suppressed by introducing a second tone and the pressure amplitude of the fundamental increases to 582 Pa. The third mode is not excited because, at this amplitude, there is only quadratic coupling between the modes. Once the second mode is suppressed there is no path for the energy to be coupled from the fundamental to the third mode.

The phasing of the second drive tone is critical to canceling the nonlinear response of the resonator. Figure 5(a) is

a plot of the measured pressure amplitude of both the second (dark curve) and third (light curve) modes versus  $\phi_2$  [see Eq. (39)]. We see that the second mode exhibits both constructive interference, at  $\phi_2$  equal to  $135^\circ$ , and destructive interference, at  $\phi_2$  equal to  $305^\circ$ . If the amplitude of the second drive tone was not appropriate for complete cancellation, the minimum at  $305^\circ$  would be nonzero.

There is no direct suppression of the third mode for the data shown in Fig. 5(a) ( $F_{dr3}=0$ ). We see that the nonlinear response of the third mode is directly tied to the amplitude of the second mode. The computational model results, shown in Fig 5(b), qualitatively confirm this behavior.

We are interested in seeing whether our simple quadratic model for the nonlinear resonator captures the overall coupling between the first two modes. To check this, we plot the forcing amplitude of the second mode necessary to achieve cancellation ( $F_{dr2}$ ) versus the forcing amplitude of the fundamental mode ( $F_{dr1}$ ) in Fig. 6. The two plots are that of experimental measurements (individual points) and the response ‘‘predicted’’ by the nonlinear quadratic model (continuous curve). The quadratic coupling coefficient ( $\epsilon_q$ ) used in the computational model is determined from low-amplitude measurements and Eq. (16). The cubic coupling coefficient ( $\epsilon_c$ ) is assumed here to be zero. The overall trend of the data is mimicked by the model; however, the model overpredicts by about 35% the second mode’s drive amplitude at high fundamental drive amplitudes. In both the experimental data and the computational model, the drive force necessary for cancellation of the second mode response goes as the square of the fundamental drive force.

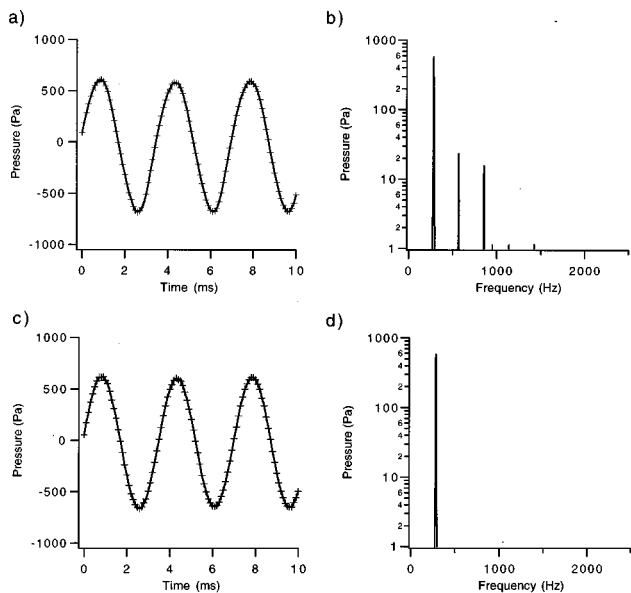


FIG. 4. Experimental pressure versus time plots and pressure amplitude spectra before and after the quenching of second harmonic. (a) Pressure profile and (b) pressure amplitude spectrum at resonance with  $F_{dr1}=2.1$  g and  $F_{dr2}=0$  g. (c) Pressure profile and (d) amplitude spectrum at resonance with second harmonic suppressed with  $F_{dr1}=2.1$  g,  $F_{dr2}=2.2$  g, and  $\phi_2=310^\circ$ . Hatch marks on the pressure versus time graphs indicate data points.

### C. Quadratic and cubic nonlinear response

If the cavity is driven at amplitudes still higher than those discussed above, then the cubic nonlinearities will make themselves felt. Figure 7 shows the cavity response when driven at a higher amplitude ( $F_{dr1}=4.6$  g). The overall pressure response to a single tone drive, shown in Fig. 7(a), is clearly distorted. The Fourier transform of this pressure trace, Fig. 7(b), shows a significant response in all of the first eight modes of the cavity. If a second tone is introduced to suppress the second mode response of the resonator (here  $F_{dr2}=10$  g), then the response of the resonator looks much more harmonic [Fig. 7(c)]. The Fourier transform of the signal [Fig. 7(d)] shows that the responses of all but the third, fourth, and fifth modes of the resonator have been eliminated. The remaining third mode is the result of cubic nonlinear coupling and can be used to determine the coupling coefficient  $\epsilon_c$ . We then add a third tone to suppress the third mode response ( $F_{dr3}=0.33$  g). The overall pressure response is shown in Fig. 7(e) and the Fourier transform of this signal is shown in Fig. 7(f). We see that in this case the introduction of only two additional drive tones is sufficient to

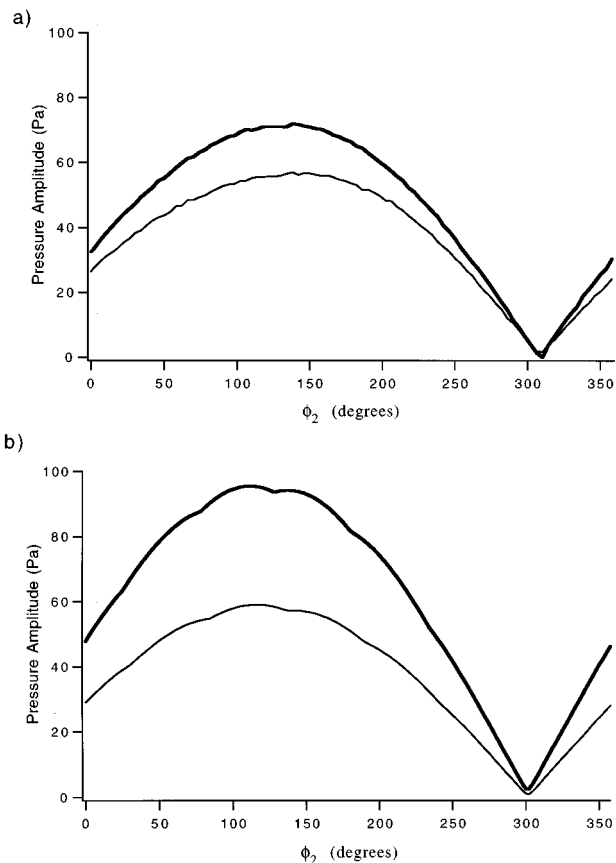


FIG. 5. (a) Experimental amplitudes of the second (dark line) and third harmonics (light line) as a function of relative phase  $\phi_2$  between the forcing tones. Notice that the third harmonic response follows the second’s response, although only the second is being actively controlled. Suppression of both harmonics occurs when  $\phi_2$  is  $305^\circ$ . (b) The corresponding plot for computational amplitudes of the second and third harmonics as a function of relative phase  $\phi_2$  between the first two forcing tones. The amplitudes of the two forcing tones are  $F_{dr1}=2.7$  g and  $(F_{dr2})_{comp}=4.9$  g. The scallops in the computed curves are computational artifacts.

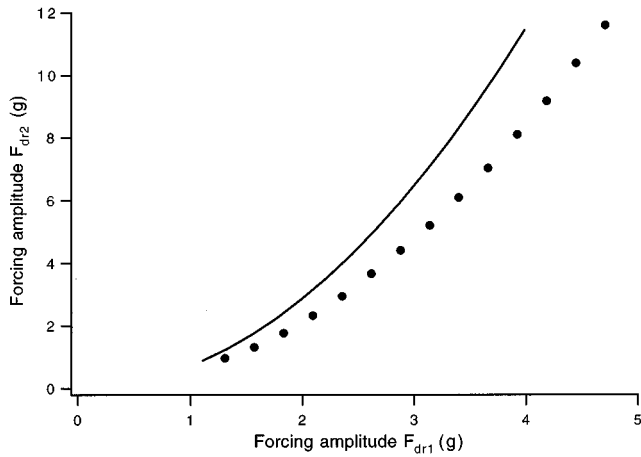


FIG. 6. Experimental (●) and computational (curve) amplitudes of the second forcing tone,  $F_{dr2}$ , required to suppress the second harmonic as a function of the amplitude of the first forcing tone,  $F_{dr1}$ .

suppress the energy transfer from the fundamental mode to the fourth and higher modes of the resonator.

The pressure amplitude of the fundamental mode increases with the presence of the canceling drive tones. In Fig.

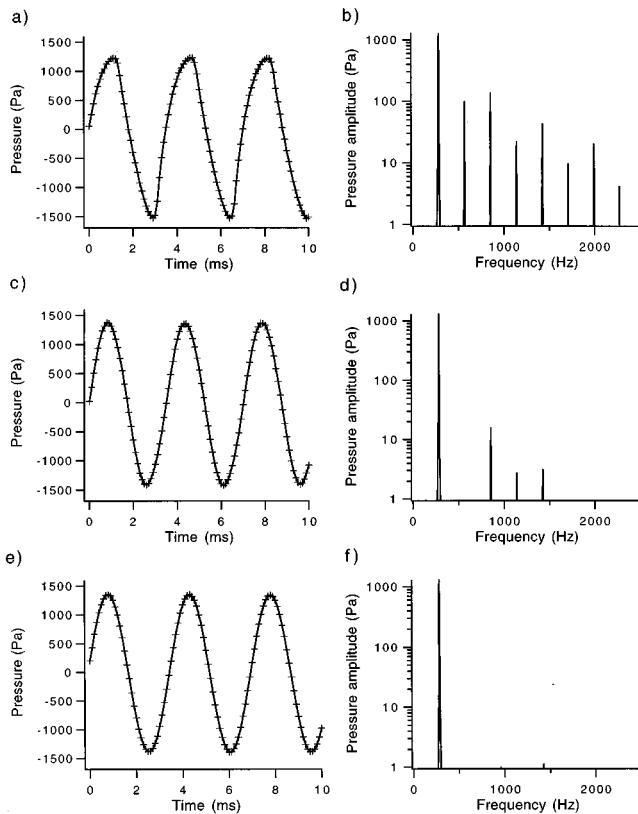


FIG. 7. The first two plots are (a) the experimental pressure versus time and (b) the amplitude spectrum at resonance with a single-frequency drive ( $F_{dr1}=4.6$  g). The following two plots are (c) the experimental pressure versus time and (d) amplitude spectrum at resonance with second harmonic suppressed;  $F_{dr1}=4.6$  g,  $F_{dr2}=10$  g, and  $\phi_2=320^\circ$ . The final two plots are (e) the experimental pressure versus time and (f) the amplitude spectrum at resonance with both the second and third harmonics suppressed;  $F_{dr1}=4.6$  g,  $F_{dr2}=10$  g,  $F_{dr3}=0.33$  g,  $\phi_2=320^\circ$ , and  $\phi_3=322^\circ$ . Hatch marks on the pressure versus time graphs indicate data points.

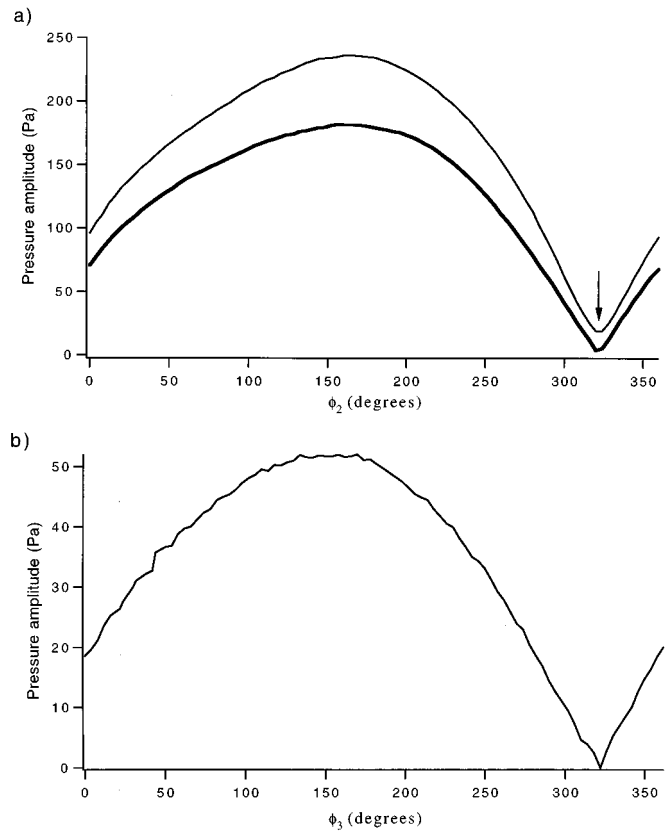


FIG. 8. (a) Experimental amplitudes of the second (dark line) and third harmonics (light line) as a function of relative phase  $\phi_2$  between the first two forcing tones. Note that the amplitude of the third harmonic is always larger than the second harmonic and is nonzero when the second harmonic is suppressed at  $\phi_2=320^\circ$  (see arrow). (b) A plot of the third harmonic's pressure amplitude versus  $\phi_3$  while  $\phi_2$  is held constant at  $320^\circ$ . A third forcing tone is added and the relative phase between the third and first forcing tones,  $\phi_3$ , is swept while the third harmonic pressure amplitude is recorded. The third harmonic is suppressed when  $\phi_3$  is  $320^\circ$ .

7(b), (d), and (f), the fundamental mode's pressure response is 1242 Pa (one tone drive, no cancellation), 1319 Pa (two-tone drive), and 1326 Pa (three tone drive), respectively.

Figure 8(a) shows the experimentally determined dependence of the second and third mode amplitudes as a function of the drive phase  $\phi_2$ . The second mode response is quenched when  $\phi_2$  is  $320^\circ$ ; however, the third mode response is nonzero due to cubic interactions (see arrow).

Figure 8(b) shows the third mode response versus the drive phase angle  $\phi_3$ . The amplitude  $F_{dr2}$  and phase angle  $\phi_2$  are set so that the cavity's second mode response is zero throughout the measurement. The same constructive and destructive interference present in Fig. 5 is seen here. The third mode's response is completely suppressed when  $\phi_3$  is  $322^\circ$ .

We have observed that the third forcing tone amplitude  $F_{dr3}$  needed to suppress the third mode response grows as the cube of  $F_{dr}$ . The computational amplitudes needed to suppress the third mode response ( $F_{dr3}$ ) were also found to be about 35% higher than the actual experimental values. This disparity might be attributed to our assumption that the cavity itself is rigid. We have seen a mechanical resonance in our system at 795 Hz. Since the first and second gas reso-

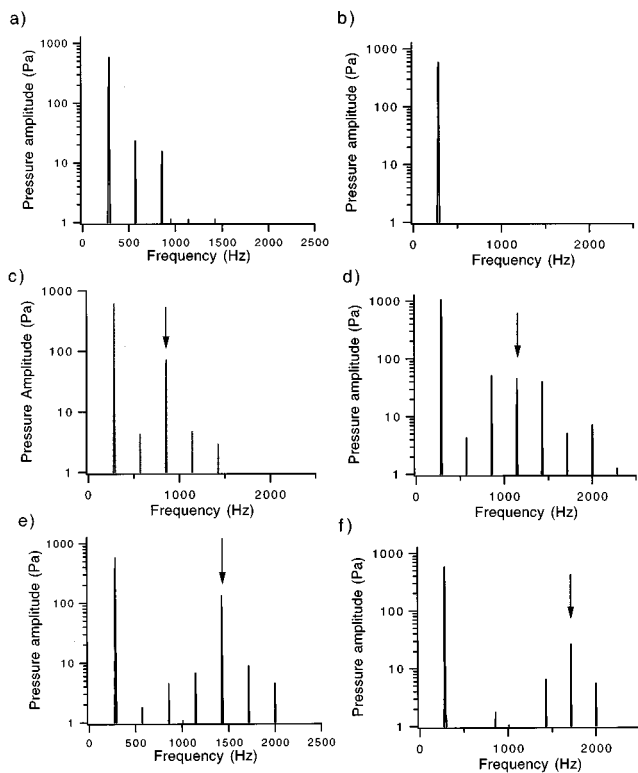


FIG. 9. Pressure amplitude spectra showing two mode nonlinear interactions. (a) The response when driven with a single-frequency forcing function at the fundamental resonance. (b) The second harmonic is suppressed by adding an appropriate second forcing tone, resulting in a clean linear response. (c) A third forcing tone at three times the fundamental resonant frequency is added, as indicated by the arrow, resulting in nonlinearly excited second, fourth, and fifth harmonics. The drive amplitudes  $F_1$ ,  $F_2$ , and  $F_3$  are 2.7, 3.5, and 1.3 g, respectively. (d) The third forcing tone is at four times the fundamental resonant frequency, resulting in nonlinearly excited third and fifth harmonics. The drive amplitudes  $F_1$ ,  $F_2$ , and  $F_4$  are 4.0, 7.5, and 7.5 g, respectively. (e) The third forcing tone is at five times the fundamental resonant frequency, resulting in nonlinearly excited fourth and sixth harmonics. The drive amplitudes  $F_1$ ,  $F_2$ , and  $F_5$  are 2.7, 3.5, and 1.1 g, respectively. (f) The third forcing tone is at six times the fundamental resonant frequency, resulting in nonlinearly excited fifth and seventh harmonics. The drive amplitudes  $F_1$ ,  $F_2$ , and  $F_6$  are 2.7, 3.5, and 4.4 g, respectively.

nance frequencies are below this mechanical resonance frequency, the cavity should behave as a rigid cylinder when driving these modes. However, this may not be true for the third gas resonance. Our model for the third forcing tone does not account for any phase difference between the driving surfaces of the resonator.

#### D. Nonlinear interactions between modes

The active control approach is not limited to mode suppression but can be used to directly probe the nonlinear coupling between modes. To illustrate this, we have included the sequence of graphs in Fig. 9. In Fig. 9(a) the Fourier transform of the response of the cavity is shown when the cavity's fundamental resonance is driven by a single tone. Since (in this case) the fundamental drive amplitude is not too large, a single drive tone at twice the fundamental drive frequency is sufficient to suppress the nonlinearities [see Fig 9(b)].

In Fig. 9(c), we impose a third drive tone with a frequency three times the fundamental frequency, as indicated by the arrow. [The form of the drive signal is that of Eq. (40) for all the plots presented in Fig. 9.] The dominant cavity response is the first and third mode's linear response to the drive. However, the quadratic nonlinear coupling between these two modes has generated two other dominant modes, the second and the fourth. We also see the existence of the fifth mode, which is the result of two sets of quadratic interactions, one between the fundamental and the fourth mode, and the other between the third and the second mode.

In Fig. 9(d), the third drive tone is now at a frequency four times the fundamental frequency. The dominant nonlinearly excited modes are the third and fifth modes, corresponding to the sum and difference of the two driving frequencies. Note that the amplitudes of these nonlinearly excited modes are of the same order as the directly driven fourth mode. This is not surprising since the amplitudes of the quadratically excited modes are proportional to both the large fundamental mode amplitude and the fourth mode amplitude. The lesser peaks are, once again, primarily due to quadratic coupling between the more dominant peaks. Figure 9(e) and (f) are the corresponding responses of the resonator when the third drive frequency is at five and six times the fundamental frequency.

From these figures, it becomes apparent that the nonlinear quadratic intermodal coupling coefficients for a specific resonator can be directly probed using this multi-tone drive approach. In the cases outlined above, the fundamental mode is driven to an amplitude where the quadratic nonlinearities are significant. The nonlinear response of the cavity due to the fundamental mode interacting with itself is suppressed by the canceling drive at twice the fundamental frequency. By directly driving the  $m$ th mode at small amplitude, the quadratic nonlinear interactions between the fundamental mode and the  $m$ th mode manifest themselves unambiguously as the response at the sum and difference of the fundamental and the  $m$ th-mode drive frequencies. The effective quadratic coupling coefficient between the specific modes can be determined from the response amplitudes and Eqs. (37) and (38).

We have demonstrated here that the cavity can be used as an acoustic mixer. If the cavity is driven to an acoustic amplitude where the quadratic interactions are important and suppressed, then the introduction of low-amplitude tone into the cavity can result in a frequency-shifted response that is greater in amplitude than the introduced tone [as in Fig. 9(d)]. This method could be used, for example, to directly heterodyne two acoustic signals.

Our computational model successfully predicts the overall trends in the response of the cavity. Quantitatively, however, disparities of 35% and larger are common. We believe that this is primarily due to the sensitivity of the nonlinear response to the relative frequency spacing of the modes. The quality factor for each of the resonances has a typical value of 200. If the relative positions of the mode frequencies are not known to better than 0.5%, then the predicted nonlinear response will be suspect. For example, suppose that the fundamental mode is driven resonantly *exactly* at 285 Hz. If the second mode of the resonator has a resonance at *exactly* 570



Hz ( $=2 \times 285$  Hz), then the nonlinear drive term (which is at twice the drive frequency) is resonant with the second mode. The response of the second mode will be large. Suppose now the second mode has a resonant frequency of 575 Hz and a quality factor of 287.5 (we choose this value for convenience). The second mode will not respond resonantly for drive frequencies that are outside the “resonance band” of the mode, in this case  $575 \pm (575/287.5)$  Hz or between 573 and 577 Hz. If the fundamental mode is driven again at 285 Hz, then the nonlinear quadratic drive term results in an excitation in the cavity at 570 Hz. Unfortunately, this is not within the resonance band of the mode and there is only a small quadratic nonlinear response. The 5-Hz shift (a relative shift of less than 1%) has substantially altered the nonlinear response of the cavity. The effect is compounded when the modes that are excited by nonlinear interactions of the (now diminished) second mode are considered. This susceptibility to error due to the relative position of the modes is reduced in the anharmonic cavity case where the mode frequencies are generally not integral multiples of each other.

## V. CONCLUSIONS

The use of a multi-frequency drive dramatically increases the flexibility in interrogating the nonlinearities inherent in a resonator. We are able to observe and directly measure the second- and third-order responses of the cavity. In addition, we can suppress the coupling from the fundamental mode to higher-order modes by actively canceling the quadratic and cubic nonlinear response of the cavity.

Passive suppression techniques have shown significant increases in the achievable pressure amplitudes in a resonator. By combining both the active and passive<sup>1-3</sup> approaches for the suppression of mode-mode coupling still higher amplitude waves with minimal distortion can be generated.

Using a perturbative solution of a simplified nonlinear wave equation, we have developed a semi-empirical model for the resonator response to a multifrequency drive. The qualitative behavior of the model agrees with experiment; quantitatively the model overestimates the measured responses by about 35%.

## ACKNOWLEDGMENT

This work was supported by the MIT Sloan Basic Fund.

<sup>1</sup>A. B. Coppens and J. V. Sanders, “Finite-amplitude standing waves in rigid-walled tubes,” *J. Acoust. Soc. Am.* **43**, 516–529 (1968).

<sup>2</sup>A. B. Coppens and J. V. Sanders, “Finite-amplitude standing waves within real cavities,” *J. Acoust. Soc. Am.* **58**, 1133–1140 (1975).

<sup>3</sup>D. F. Gaitan and A. A. Atchley, “Finite-amplitude standing waves in harmonic and anharmonic tubes,” *J. Acoust. Soc. Am.* **93**, 2489–2495 (1993).

<sup>4</sup>Model 8510C, Endevco, 30800 Rancho Viejo Road, San Juan Capistrano, CA 92675.

<sup>5</sup>Model J357B01, Piezotronics, Inc., 3425 Walden Avenue, Depew, NY 14043-2495.

<sup>6</sup>Ling Dynamic Systems, 60 Church Street, Yalesville, CT 06492.

<sup>7</sup>National Instruments, 6504 Bridge Point Parkway, Austin, TX 78730-5039.

<sup>8</sup>Maple V, Waterloo Maple, Inc., 450 Phillip Street, Waterloo, Ontario N2L 5J2, Canada.

<sup>9</sup>P. T. Huang, Master’s thesis, Department of Mechanical Engineering, Massachusetts Institute of Technology, 1996.

# Surface wave formation at an impedance discontinuity<sup>a)</sup>

Michael R. Stinson and Gilles A. Daigle

*Institute for Microstructural Sciences, National Research Council, Ottawa, Ontario K1A 0R6, Canada*

(Received 25 January 1997; revised 10 July 1997; accepted 25 July 1997)

The formation of air-coupled acoustic surface waves over an impedance plane has been studied in a series of model experiments. Surface waves were generated at an impedance discontinuity on a flat surface, one section of the surface being acoustically hard, and the other composed of an array of small cavities with an effective impedance suitable for surface wave propagation. A point source of sound (800 Hz–2 kHz) was located on the hard surface and the vertical sound pressure distribution measured over the impedance plane, at various distances. The formation, propagation, and decay of the surface waves were clearly observed. The measured pressure distributions are consistent with the theoretical formulation of Rasmussen [J. Sound Vib. **84**, 598–602 (1982)] for propagation of sound over an impedance jump. An alternative formulation for the case of plane waves incident at grazing angles to a surface has been described by McAninch and Myers [AIAA 26th Aerospace Sciences Meeting, paper AIAA-88-0179 (1988)]. This simpler formulation has been found to be consistent with our measurements, and with the Rasmussen theory, when the distance between source and impedance discontinuity is sufficiently large. [S0001-4966(97)03011-7]

PACS numbers: 43.10.Ln, 43.28.Fp, 43.20.Fn [LCS]

## INTRODUCTION

The study of surface waves is useful in understanding the propagation of sound over ground surfaces. Surface waves over an impedance plane are expected when the imaginary component of the surface impedance is a *springlike* reactance and is greater than the resistive component (Brekhovskikh, 1959). This often occurs for natural ground surfaces and is most pronounced in special circumstances, e.g., thin layers of snow-covered ground (Albert, 1992). The effect on the propagation of sound from a point source is to produce sound pressure levels in excess of those that would be obtained over an acoustically rigid boundary at low frequencies.

By constructing special model surfaces with controlled acoustical characteristics, the formation of surface waves can be achieved relatively easily. Their properties, and the applicability of theoretical models that describe them, can be studied experimentally. In a recent paper, Daigle *et al.* (1996) examined the propagation of surface waves over such a model surface using acoustical pulses. In this paper, the *formation* of surface waves at an edge of the model surface is studied in more detail. An initial presentation of results was given by Stinson *et al.* (1992). Subsequently, the impedance of the model surface has been determined more carefully. Revised calculations of the sound fields above the model surface, using the improved impedance model, have been performed and are reported here.

## I. THEORY

There are a variety of different types of acoustical surface waves that can arise at the interface between two media (Tolstoy, 1973; Brekhovskikh, 1980). We are considering here an air-coupled surface wave in which there is a coupled

oscillation of the air within a porous solid and the air above the surface (Brekhovskikh, 1959; Donato, 1978; Raspet and Baird, 1989; Daigle, 1991; Stinson *et al.*, 1993). The collective oscillation is localized near the interface and propagates along the interface with a phase speed less than the free-field speed of sound. For propagation above an impedance plane under certain geometrical conditions, there are simple analytical solutions of the Helmholtz equation that exhibit these surface wave properties (Daigle *et al.*, 1996).

The work to be described in this paper focuses on the geometry shown in Fig. 1. A flat surface is separated into two half-planes by a discontinuity in surface impedance. Sound from a point source located above one half-plane (specific impedance  $Z_1$ ) propagates toward a receiver that is located above the other half-plane (our model surface, having specific impedance  $Z_2$ ). The receiver is moved vertically (coordinate  $y$ ) giving a pressure profile  $p(y)$ . The formation and properties of surface waves are observed by examining the shape of these profiles.

### A. Conditions for observation of surface waves

The air-coupled surface wave being investigated here does not arise for all impedance surfaces and, when it does occur, its presence may not be easily identified. The conditions under which surface waves can propagate and be observed are established by considering first the case of an impedance plane characterized by a single acoustic impedance  $Z$  (i.e., take  $Z_1 = Z_2 \equiv Z$ ). We look for plane-wavelike solutions,

$$p \propto e^{i\alpha x} e^{i\beta y}, \quad (1)$$

of the Helmholtz equation  $\nabla^2 p + k^2 p = 0$  above a surface at  $y = 0$ , subject to the boundary condition

$$\left( \frac{dp}{dy} + \frac{i\rho\omega}{Z} p \right)_{y=0} = 0, \quad (2)$$

<sup>a)</sup>“Selected research articles” are ones chosen occasionally by the Editor-in-Chief, that are judged (a) to have a subject of wide acoustical interest, and (b) to be written for understanding by broad acoustical readership.

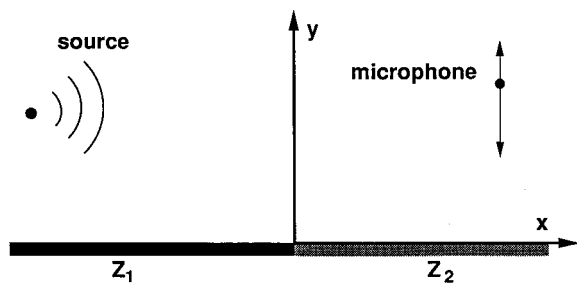


FIG. 1. Sketch of the geometry being considered. An acoustical source is located above an impedance half-plane having an impedance  $Z_1$ . The receiver is located over the other half-plane which has impedance  $Z_2$ . The  $x, y$  coordinate system has its origin at the impedance discontinuity. For the experiments, pressure is measured along a vertical line giving a profile  $p(y)$ . We are considering the case of acoustically hard first surface, i.e.,  $Z_1$  effectively infinite, and source located on the ground.

where  $k = \omega/c$  is the wave number,  $\omega$  is the angular frequency,  $c$  is the free-space sound speed,  $\rho$  is the air density, and  $Z$  is the specific acoustic impedance of the porous surface. An  $\exp(-i\omega t)$  time convention is being assumed. For propagation in the  $+x$  direction, we find

$$\beta/k = -\rho c/Z \quad (3)$$

and

$$\alpha/k = \sqrt{1 - (\rho c/Z)^2}. \quad (4)$$

These expressions can be used to generate criteria for the observation of surface waves. First, for a bounded solution, the imaginary part of  $\beta$  must be positive, or else the pressure in Eq. (1) would increase without limit with height  $y$ . It is thus required that  $\text{Im}(Z) > 0$ . That is, the surface must have a “springlike” reactance. Given that this condition is satisfied, then from Eq. (1) the sound pressure decreases exponentially with height, so the surface wave is localized near the surface. Going further, we can insist that the pressure amplitude decay sufficiently rapidly with height that a surface wave can be conveniently observed. A reasonable (although arbitrary) criterion is that the pressure amplitude should drop to its  $1/e$  point within a free-space wavelength  $\lambda$ , giving  $\text{Im}(\beta)\lambda > 1$ . On the other hand, the attenuation in the propagation direction  $x$  should *not* be too rapid and we take  $\text{Im}(\alpha)\lambda \ll 1$ . With these restrictions, it is found that observation of surface waves is anticipated provided that, roughly, both  $\text{Re}(Z) < \text{Im}(Z)$  and that the reactance lies in the range  $2 < \text{Im}(Z)/\rho c < 6$ .

The solution of Eq. (1) has implicitly assumed a source far removed from the region of observation. We make the assumption that, even when the source of the surface waves (e.g., an impedance discontinuity) is not distant, the conditions for the propagation and observation of surface waves is essentially the same as determined above.

## B. Generation of surface waves

Surface waves can be generated at a discontinuity of surface impedance. Their presence will be noted in measured vertical sound pressure distributions. An indication of what features should be looked for in the measured profiles that follow is given in the sequence of panels of Fig. 2. The

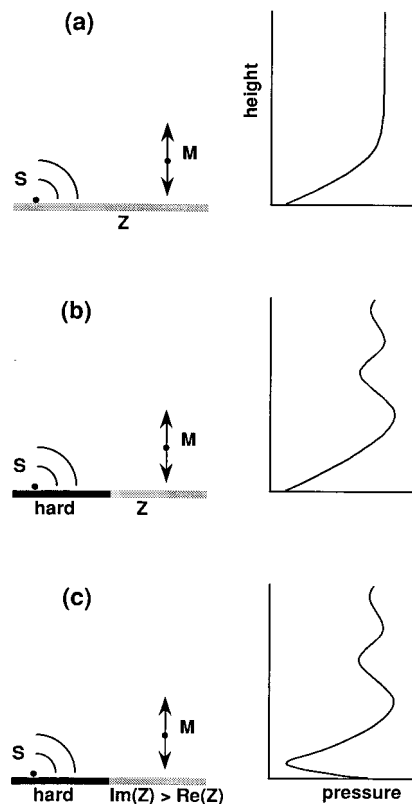


FIG. 2. Sketch to explain the shape of the measured vertical sound pressure profiles (through point  $M$ ). In (a), over a surface whose impedance is not appropriate for the formation of surface waves, we anticipate a sound pressure (relative to free field) that is approximately independent of height except for a “Lloyd’s mirror” interference close to the surface. With an impedance discontinuity, in (b), interference with an edge-diffracted component adds ripples to the profile. Finally, (c) if the impedance is actually appropriate for surface wave propagation, an additional component, localized near the surface, is found.

following discussion is applicable for any frequency, subject to satisfaction of the stated impedance conditions.

Consider first in panel (a) the case of a source located directly on an impedance plane and suppose that the impedance  $Z$  is such that no surface waves would be anticipated (e.g., a masslike reactive component). Then, the profile that would be measured some distance away is as sketched on the right-hand side of this panel. The sound pressure (normalized by the free-field sound pressure) would be roughly constant, except near the surface where it is reduced due to a “Lloyd’s mirror” effect (i.e., the reflection coefficient  $R_p$  is  $-1$  at grazing incidence). This result may be confirmed through application of the theory of Thomasson (1976) or Chien and Soroka (1975). For example, using a normalized surface impedance of  $(0.1, -1.3)$  at 1500 Hz, the profile at a horizontal range of 100 cm would look nearly as shown in Fig. 2(a), taking a maximum vertical height of 300 cm. Next, if the incident sound travels initially over an acoustically hard surface, as sketched in panel (b), oscillations in the profile are expected due to interference between direct and edge-diffracted (at the impedance jump) paths (McAninch and Myers, 1988). Finally, we suppose that the surface impedance actually satisfies the conditions appropriate for the formation of surface waves, as discussed in the previous sec-

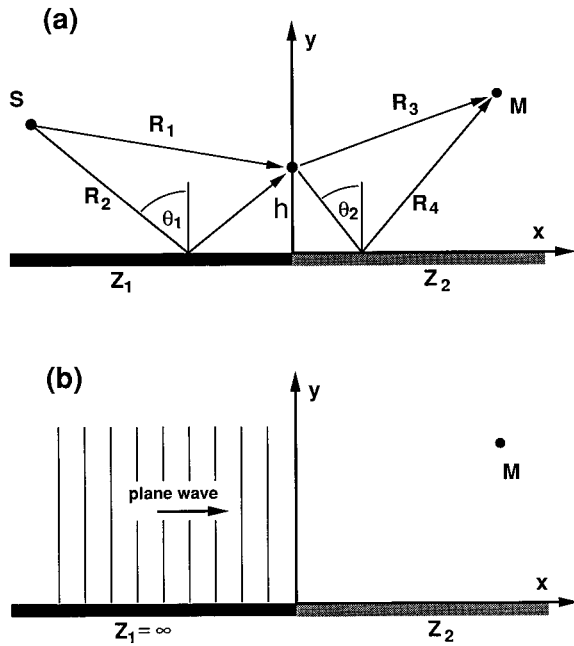


FIG. 3. Two approaches for modeling the effect of an impedance discontinuity. (a) The approach developed by Rasmussen (1982) introduces an intermediate plane at  $x=0$  and integrates contributions over height  $h$ . (b) The McAninch and Myers approach (1988) assumes a plane-wave front at  $x=0$  and develops an exact solution of the parabolic equation for  $x>0$ , so is appropriate when the source is located a large distance from the discontinuity and the impedance  $Z_1$  is effectively infinite.

tion. The profile sketched in panel (c) is obtained. There will be an additional component to the profile (i.e., the surface wave), localized near the surface.

### C. Point source

The first of two theoretical models to describe the pressure profiles is discussed here. Whether the source is close to the impedance discontinuity or some distance away, the approximate theoretical formulation of Rasmussen (1982) may be applied. As indicated in Fig. 3(a), an intermediate vertical plane is introduced at the discontinuity and for each position  $h$  on this plane the four paths  $R_m$  are constructed ( $m=1-4$ ). The pressure profile  $p(x,y)$  is then obtained from the velocity potential

$$\begin{aligned} \Phi(x,y) = & x(8\pi k)^{1/2} \frac{e^{-i\pi/4}}{16\pi^2} \int_0^\infty \left[ \frac{e^{ik(R_1+R_3)}}{(R_3^3 R_1 (R_1+R_3))^{1/2}} \right. \\ & + Q_2 \frac{e^{ik(R_1+R_4)}}{(R_4^3 R_1 (R_1+R_4))^{1/2}} \\ & + Q_1 \frac{e^{ik(R_2+R_3)}}{(R_3^3 R_2 (R_2+R_3))^{1/2}} \\ & \left. + Q_1 Q_2 \frac{e^{ik(R_2+R_4)}}{(R_4^3 R_2 (R_2+R_4))^{1/2}} \right] dh \end{aligned} \quad (5)$$

through  $p=i\rho\omega\Phi$ .  $Q_1$  and  $Q_2$  are the spherical reflection coefficients appropriate to the two half-plane impedance conditions. They are calculated using standard approximations (e.g., Chien and Soroka, 1975, 1980) given the surface im-

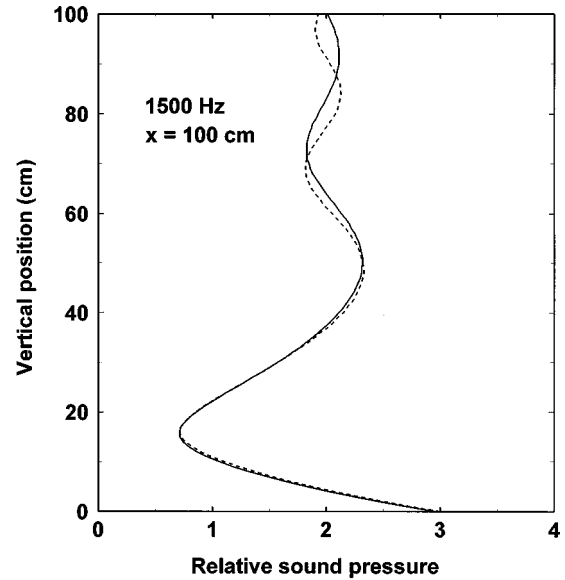


FIG. 4. Comparison of the McAninch and Myers theory (dashed curve) to that of Rasmussen (solid curve). The calculations assume a sound frequency of 1500 Hz, a receiver position of  $x=100$  cm, and a surface impedance  $Z_2=(0.5+3i)\rho c$ . For the Rasmussen approach, the source was located on the ground at  $x=-10\,000$  cm.

pedances and angles of incidence ( $\theta_1$  and  $\theta_2$ ). For both surfaces, we use

$$Q = R_p + (1 - R_p)F(w), \quad (6)$$

where

$$R_p = (\cos \theta - \rho c/Z) / (\cos \theta + \rho c/Z) \quad (7)$$

and the numerical distance is

$$w = (ikR/2)^{1/2} (\cos \theta + \rho c/Z), \quad (8)$$

with the complex root being chosen so that  $-\pi/4 < \arg w < 3\pi/4$  (Stinson, 1995). For the acoustically hard surface, we set  $Z=Z_1=\infty$ ,  $\theta=\theta_1=\pi/2$ , and  $R=R_2$ , and obtain  $Q=Q_1=1$ . For the other surface, we set  $Z=Z_2$ ,  $\theta=\theta_2$ , and  $R=R_4$ , giving  $Q=Q_2$ . The function  $F(w)$  is given by

$$F(w) = 1 + i\pi^{1/2} w \exp(-w^2) \operatorname{erfc}(-iw). \quad (9)$$

In the calculations, we normalize the velocity potential by the corresponding free-field velocity potential (i.e., the field that would be obtained if source and receiver only were present) which is simply  $\Phi_{ff} = \exp(ikR_T)/(4\pi R_T)$ , where  $R_T$  is the source-receiver distance.

As will be discussed in Sec. II, the model surface is not strictly locally reacting and the impedance  $Z_2$  depends somewhat on the angle of incidence  $\theta_2$  of the sound. In the integration over the variable  $h$ , the use of angle-dependent values for  $Z_2$  (and, hence, for  $Q_2$ ) was necessary to achieve a good fit with experimental data.

### D. Quasi-plane waves

An alternative theory to apply when the sound source is located far from the impedance discontinuity is the exact theoretical formulation (for the parabolic approximation to the wave equation) given by McAninch and Myers (1988). It

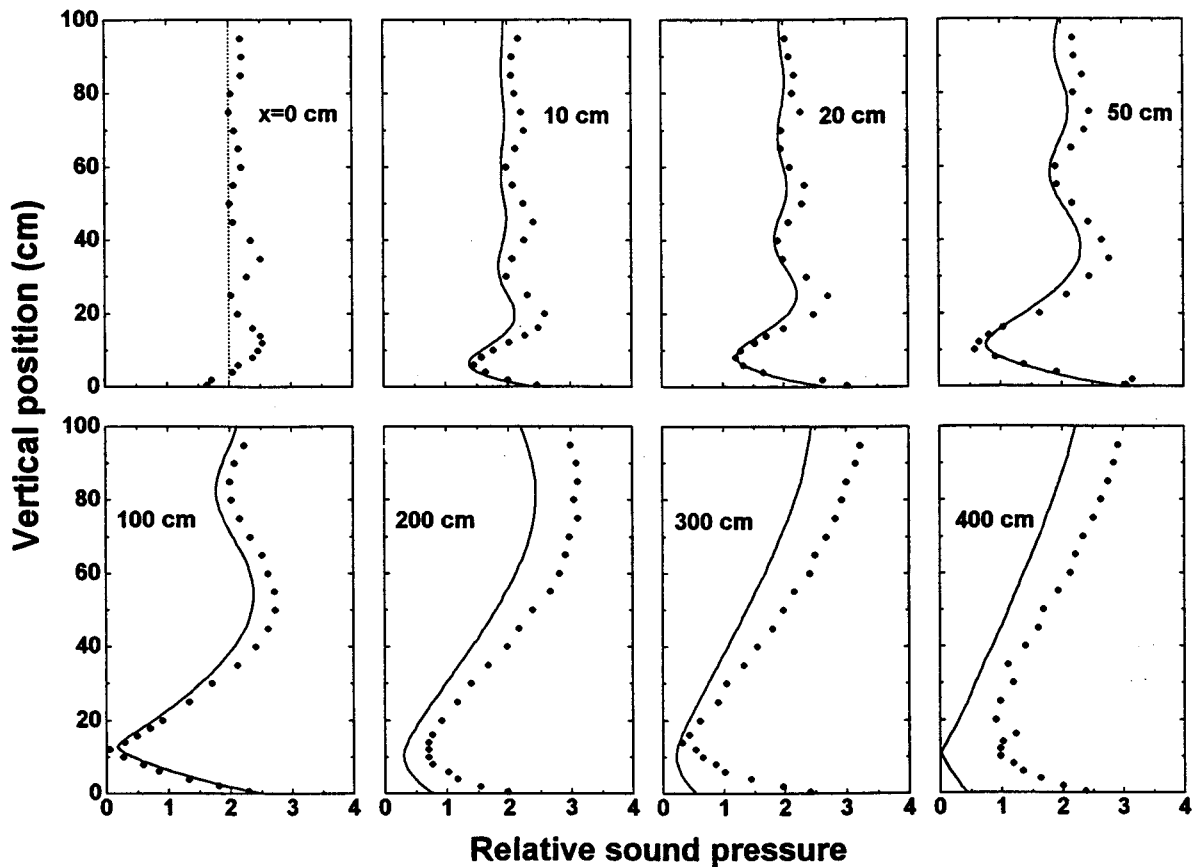


FIG. 5. Vertical sound pressure profiles for 1500 Hz at various receiver positions. The source is fixed at a position  $x = -400$  cm. The solid dots correspond to measured data. The solid curves are predictions using the Rasmussen theory. The surface wave is apparent within the first 15 cm of the surface.

is assumed that, for the incident sound, plane-wave fronts exist right up to the impedance discontinuity, as indicated in Fig. 3(b). The sound pressure above the impedance half-plane, relative to the incident pressure (pressure doubling not accounted for), is given by

$$p = A(x, y) \exp(ikx), \quad (10)$$

where

$$A(x, y) = 1 - \operatorname{erfc}[-(i\pi/2)^{1/2}\eta] + \exp[-i\pi(\eta\xi + \xi^2/2)] \times \operatorname{erfc}[-(i\pi/2)^{1/2}(\eta + \xi)] \quad (11)$$

with

$$\eta = (k/\pi x)^{1/2}y, \quad \xi = (kx/\pi)^{1/2}/\zeta, \quad (12)$$

where  $\zeta = Z_2/\rho c$  is the normalized specific surface impedance.

We can compare the theory of Rasmussen in the far source regime to the theory of McAninch and Myers. As an example, results are shown in Fig. 4 for a receiver position 100 cm from the discontinuity at 1500 Hz with an assumed normalized specific surface impedance of (0.5, 3.0). The dashed curve was obtained using the expressions of McAninch and Myers. The solid curve was calculated from the theory of Rasmussen, taking a source position  $x = -10\,000$  cm (note that increasing the source-discontinuity distance further makes little difference in the calculated profile). The agreement is good, suggesting that the McAninch

and Myers procedure (computationally much quicker) is appropriate for describing the formation of surface waves under long-range propagation conditions.

The presence of the surface wave is evident within the first 15 cm above the surface, in both formulations. Its form is qualitatively similar to the profile predicted in Fig. 2(c). Additional calculations, not shown here, have been done using a normalized impedance of (0.5, -3.0) which does not support surface waves: The vertical sound pressure profiles for this impedance condition look like the profile shown in Fig. 2(b).

## II. EXPERIMENTAL PROCEDURE

The model surface has been described previously by Daigle *et al.* (1996). It is composed of a lattice of square cavities (sides of 1.315 cm, depth of  $l = 2.56$  cm). Two layers of commercial overhead lighting panels were used to construct the lattice, with screws to align the layers and secure them to a rigid wooden base. A thin layer of cork lies between the lattice and base to prevent air leakage. The surface has a maximum size of approximately 4.5 by 8.5 m. In most experiments, though, the surface is partially covered by thin metal sheets to provide the acoustically rigid impedance condition.

It had originally been expected that the model surface would be locally reacting, with adjacent cells communicating

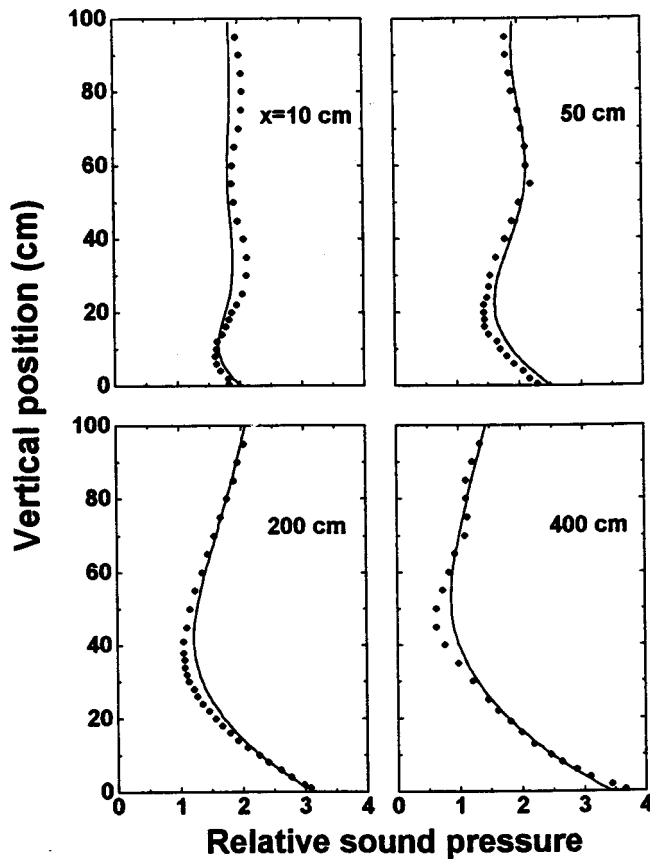


FIG. 6. Same as for Fig. 5, except for a frequency of 800 Hz.

acoustically only by way of the air above the structure. It was discovered later that there was some acoustical leakage between the cells by way of small gaps between the two layers that comprise the lattice structure. As a result, the surface impedance is not independent of the angle of incidence of sound. Acoustical modeling of the structure and subsidiary measurements (Daigle *et al.*, 1996) show that the effective surface impedance is given by

$$Z_2 = i\rho c \cot\left(\frac{kl}{2}\right) \frac{1 - q \tan^2(kl/2) - \epsilon \tan(kl/2) \sin^2 \theta_2}{1 + q + \epsilon \cot(kl/2) \sin^2 \theta_2} \times (1 + \delta)^2. \quad (13)$$

The term  $\epsilon$  accounts for the acoustical leak impedance between adjacent cells of the lattice;  $q$  is related to the finite impedance of the underlying cork surface. Both  $\epsilon$  and  $q$  are complex quantities. The expressions for these parameters and more detailed discussion can be found in the paper noted above. The term  $\delta$  accounts for the wall thickness of the plastic making up the lattice structure and has a value of 0.141.

For an “ideal” surface, we would have  $\epsilon=0$ ,  $q=1$  and  $\delta=0$ , giving an effective surface impedance of  $Z_2 = i\rho c \cot(kl)$ . This simple form provides a rough approximation to the actual impedance. The measured impedances (Daigle *et al.*, 1996) are not too different in magnitude but are notable in the addition of a nonzero resistive component to  $Z_2$  and a dependence on angle of incidence, because of the  $\epsilon$  term.

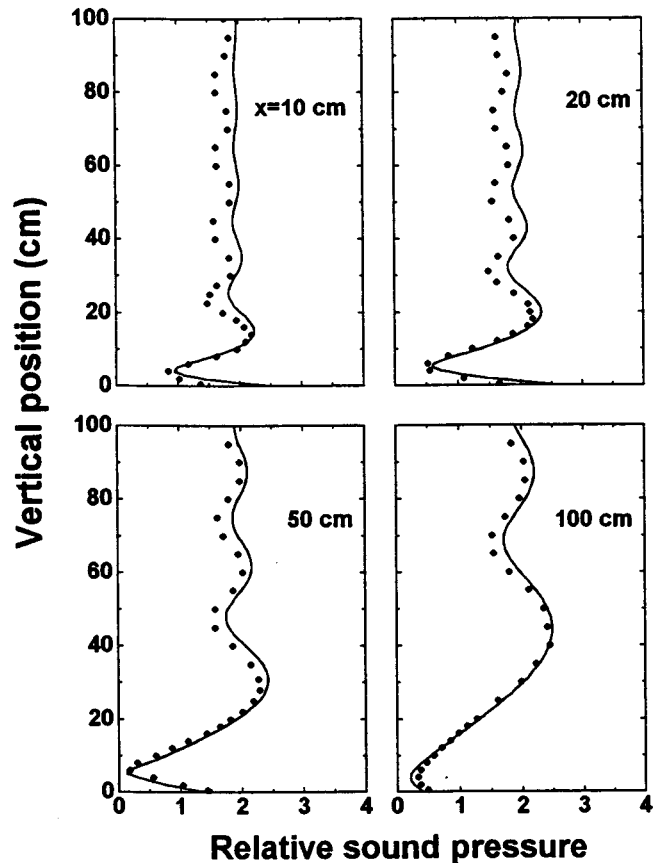


FIG. 7. Same as for Fig. 5, except for a frequency of 2000 Hz. The surface wave experiences greater attenuation at this frequency.

The receiver was a  $\frac{1}{2}$ -in. microphone suspended above the surface; its height was varied between 0 and 100 cm. A second reference microphone on the hard surface was used to calculate equivalent free-field levels to which all pressure measurements were referred. Because the experiments were performed indoors, it was necessary to utilize pulsed pure-tone signals and use appropriate gating of signals to avoid extraneous reflections. Measurements were made at frequencies between 800 and 2000 Hz. At frequencies below 800 Hz, longer pulses are required and it becomes difficult to gate out reflections; at frequencies above 2000 Hz, the surface wave attenuates too rapidly with range, for the impedance surface in use here.

### III. RESULTS

The formation and propagation of surface waves has been observed in two series of measurements. For the first series, the source was fixed in position and the vertical pressure profile  $p(y)$  measured at several different receiver positions  $x$ . For the second series, the horizontal distance between impedance discontinuity and receiver was fixed and profiles determined for different source positions.

First, the source was located on the acoustically hard surface a distance 400 cm away from the impedance discontinuity. The sound frequency was 1500 Hz. Figure 5 shows the vertical profiles (as solid dots) measured at eight receiver positions over the model surface between  $x=0$  and  $x$

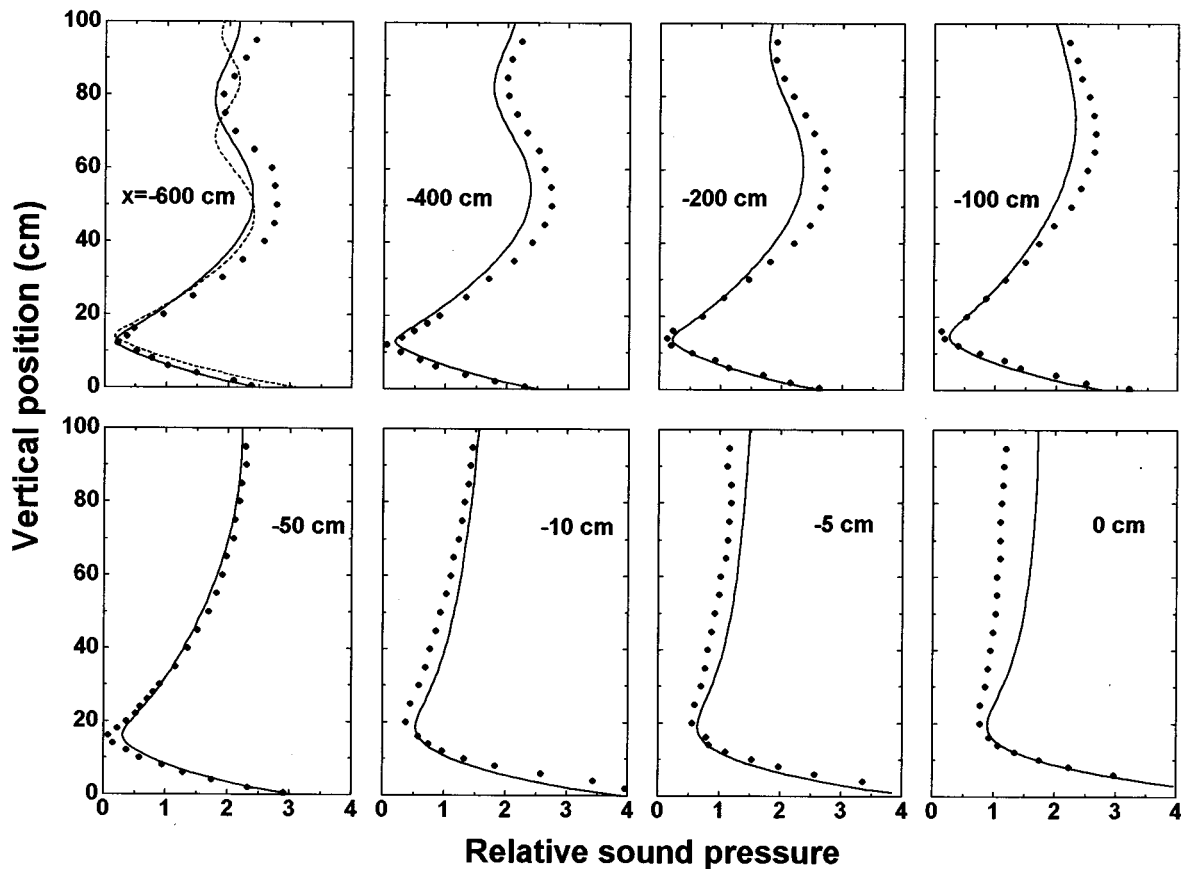


FIG. 8. Vertical sound pressure profiles, at a fixed receiver position of  $x=100$  cm, for various source positions. The sound frequency is 1500 Hz. The solid dots correspond to measured data. The smooth curves are predictions obtained from the Rasmussen theory. The dashed curve shown on the first panel ( $x = -600$  cm) has been obtained using the theory of McAninch and Myers.

$=400$  cm. At the first of these ( $x=0$  cm), the pressure, relative to free field, shows the least variation with height, being within 25% of a value of 2 at all vertical positions. Over a hard surface, allowing for pressure doubling, the relative pressure would be exactly 2. At the impedance discontinuity, though, ripples in the profile are evident. As the receiver range is increased, the ripples expand vertically. These ripples are the result of an interference between the direct path (source to receiver) and an edge-diffracted path (source to discontinuity to receiver). The location of the ripples, the periodicity with vertical position, and the expansion with range can be predicted reasonably well with this interpretation.

Of primary interest, though, is the occurrence of the surface wave within the first 15 cm or so above the impedance surface. It forms rapidly, being evident at a distance of 10 cm from the impedance discontinuity, and continues to grow as the range increases. The wave reaches its maximum strength at a range of 20–50 cm and decays with range beyond this.

Also shown in Fig. 5 are the theoretical predictions (smooth curves) obtained using the Rasmussen formulation (except that a prediction for  $x=0$  was not possible). The calculated profiles show the same qualitative features as the measured results. In particular, the existence of the surface wave and the interference ripples are predicted. Quite good quantitative agreement between theory and experiment is

found, except for the larger ranges. Some of the differences can be attributed to (1) uncertainty in the surface impedance  $Z_2$  (Daigle *et al.*, 1996), (2) backscattering of acoustic energy from the end of the model surface, and (3) to drift in source strength over the course of the experiment due, perhaps, to heating within the compression driver/exponential horn source.

Results are shown in Figs. 6 and 7 for sound frequencies of 800 and 2000 Hz, respectively. Quite good agreement is obtained between theory and experiment. The surface wave is quite strong for 800 Hz. At 2000 Hz, though, the surface wave is seen to attenuate relatively rapidly with range so that it is nearly gone after propagating 100 cm from the impedance discontinuity.

For application to long-range propagation, sources will be at distances much greater than 400 cm from the impedance discontinuity. An indication of what might be expected can be obtained by performing these indoor measurements with different source positions. In the second series of measurements, shown in Fig. 8, the pressure profile was always measured at a position  $x = 100$  cm. The source was located at various positions between  $x = -600$  and  $x = 0$  cm. The measurements (solid dots) are compared to the corresponding predictions using Rasmussen's theory (smooth curves). The sound frequency was 1500 Hz. The characteristic oscillations of pressure with receiver height are again observed. They are

seen to compress downward as the source moves back from the discontinuity (consistent with the explanation of interference between direct and edge-diffracted paths as their origin). The surface wave is evident at all times; its shape is essentially independent of the source location. The theory of Rasmussen is found to work well for this experimental configuration. It is clear that the overall profile is approaching a limiting profile with the source at a distance of just 600 cm from the discontinuity. With the source more distant than this, the theory of McAninch and Myers would be appropriate. On the first panel of Fig. 8, the dashed curve shows the prediction obtained using the McAninch and Myers theory (the impedance corresponding to grazing incidence has been assumed). This prediction is very similar to the Rasmussen calculation below a height of 50 cm, giving a surface wave of nearly the same amplitude. Differences between the two approaches are apparent at heights greater than this.

#### IV. CONCLUSIONS

The formation of air-coupled surface waves at the interface between an acoustically hard surface and a porous impedance surface has been observed. A specially constructed structure was used for the impedance surface, to optimize this formation and subsequent propagation of the surface waves over the surface. The surface wave component was clearly evident in the vertical pressure profile and reached significant amplitudes. For the impedance surface used, the surface waves were localized within 15 cm or so of the surface. The theoretical formulation of Rasmussen (1982) was found to give predictions in close agreement with the measured results.

When the source is sufficiently far from the impedance discontinuity, as would be the case in many outdoor applications, the wavefronts at the interface become essentially plane. A simpler formulation due to McAninch and Myers (1988) can then be used. It was found that the Rasmussen theory, in the limit where the source is a long distance from the impedance discontinuity, and the McAninch and Myers theory gave comparable predictions.

#### ACKNOWLEDGMENTS

We would like to thank René St. Denis for his efforts collecting data and preparing some of the figures. Discus-

sions with Dr. Karsten Bo Rasmussen (Danish Technical University) and Dr. Michael K. Myers (George Washington University) are appreciated. The work was supported in part by the Defence Research Establishment Valcartier, Department of National Defence, Canada.

- Albert, D. G. (1992). "Observations of acoustic surface waves propagating above a snow cover," in *Proceedings of the 5th International Symposium on Long Range Sound Propagation* (Milton Keynes, U.K.), pp. 10–16.
- Brekhovskikh, L. M. (1959). "Surface waves in acoustics," *Sov. Phys. Acoust.* **5**, 3–12.
- Brekhovskikh, L. M. (1980). *Waves in Layered Media* (Academic, New York).
- Chien, C. F., and Soroka, W. W. (1975). "Sound propagation along an impedance plane," *J. Sound Vib.* **43**, 9–20.
- Chien, C. F., and Soroka, W. W. (1980). "A note on the calculation of sound propagation along an impedance surface," *J. Sound Vib.* **69**, 340–343.
- Daigle, G. A., Stinson, M. R., and Havelock, D. I. (1996). "Experiments on surface waves over a model impedance plane using acoustical pulses," *J. Acoust. Soc. Am.* **99**, 1993–2005.
- Daigle, G. A. (1991). "Role of surface waves in outdoor noise propagation," in *Proceedings of Inter-Noise '91* (Sydney, Australia), pp. 455–458.
- Donato, R. J. (1978). "Model experiments on surface waves," *J. Acoust. Soc. Am.* **63**, 700–703.
- McAninch, G. L., and Myers, M. K. (1988). "Propagation of quasiplane waves along an impedance boundary," *AIAA 26th Aerospace Sciences Meeting*, paper AIAA-88-0179.
- Rasmussen, K. B. (1982). "A note on the calculation of sound propagation over impedance jumps and screens," *J. Sound Vib.* **84**, 598–602.
- Raspet, R., and Baird, G. E. (1989). "The acoustic surface wave above a complex impedance ground surface," *J. Acoust. Soc. Am.* **85**, 638–640.
- Stinson, M. R. (1995). "A note on the use of an approximate formula to predict sound fields above an impedance plane due to a point source," *J. Acoust. Soc. Am.* **98**, 1810–1812.
- Stinson, M. R., Daigle, G. A., and Havelock, D. I. (1992). "The formation of surface waves over a model surface," in *Proceeding of the 5th International Symposium on Long Range Sound Propagation* (Milton Keynes, U.K.), pp. 17–28.
- Stinson, M. R., Daigle, G. A., and Havelock, D. I. (1993). "The measurement of air-coupled surface waves over a porous surface," in *Proceedings of Inter-Noise '93* (Leuven, Belgium), pp. 1683–1686.
- Thomasson, S.-I. (1976). "Reflection of waves from a point source by an impedance boundary," *J. Acoust. Soc. Am.* **59**, 780–785.
- Tolstoy, I. (1973). *Wave Propagation* (McGraw-Hill, New York).



# Tube waves and mandrel modes: Experiment and theory

Chaur-Jian Hsu, Sergio Kostek, and David Linton Johnson

*Schlumberger-Doll Research, Old Quarry Road, Ridgefield, Connecticut 06877-4108*

(Received 16 June 1997; accepted for publication 2 September 1997)

The characteristics of tube waves in a borehole, with and without a solid cylindrical mandrel, which may be either elastic or poro-elastic, are compared. With an elastic mandrel, the tube waves are slower, more dispersive, and more sensitive to the formation shear modulus than without. Similarly extensional mode characteristics are compared in the presence of a formation. In the presence of an elastic formation the extensional mode is faster, more dispersive than without, and it is only slightly sensitive to the formation shear properties. These calculated characteristics are in excellent agreement with our measured data. Additionally, the characteristics of tube waves and extensional modes are studied in a borehole in the presence of a concentric liquid-saturated porous mandrel whose acoustic properties are calculated using the Biot theory. The coupling of the tube wave propagating in the annulus with the slow wave propagating in the porous mandrel introduces attenuation and additional dispersion to the tube waves; the effect on the extensional mode is slight. Theoretically calculated and experimentally measured dispersion and attenuation are in excellent agreement with each other, with no adjustable parameters. Whether the mandrel is porous or not, there are two modes which are weakly dispersive in the quasistatic limit. Very roughly, the two modes consist of an extensional mode in the rod and a fluid-based mode in the annulus which are coupled together. © 1997 Acoustical Society of America. [S0001-4966(97)06412-6]

PACS numbers: 43.20.Mv, 43.20.Jr [ANN]

## INTRODUCTION

The acoustic properties of a fluid-filled cylindrical cavity in an elastic solid have received a great deal of attention, not the least because of its technical importance in the search for oil reserves. The classic papers by Tsang and Rader<sup>1</sup> as well as those by Kurkjian and Chang<sup>2</sup> have established that, depending on the spatial dependence of the sourcing transducer, the acoustic signal is composed of many different components. Some of these are normal modes of the system, corresponding to poles in the appropriate Green's function, and others, "head waves," corresponding to branch points. If the source has an axially symmetric component, it is known that at low frequencies the dominant contribution to the acoustic signal is due to the lowest lying mode in the problem, the "tube wave." Here, low frequency means that the wavelengths of all bulk modes are large compared to the borehole radius. In this limit the tube wave becomes nondispersive with a speed which is simply expressed in terms of the properties of the fluid and the solid. This article is devoted to an experimental and theoretical investigation of the effects of a mandrel, a solid circular cylinder, on the properties of the tube wave, considered as a function of frequency. As part and parcel of this understanding we also investigate the effects of the formation on the extensional mode of the mandrel, as well as the behavior of the other modes in the system.

In wireline sonic logging, the tool itself is usually not considered in the models for data processing and interpretation. This practice is based on the fact that the receiver sections of wireline sonic tools are designed to be acoustically transparent, typically accomplished with slotted housings and bellows. Moreover, compressional and shear head waves result from the critical refraction of bulk waves propagating

in the formation; therefore, their slownesses should be independent of the presence of mandrels. On the other hand, for certain other applications, such as imaging reflectors located away from the borehole, it is desirable to attenuate the tube wave in order to enhance these formation arrivals. Furthermore, a rigid tool housing may be necessary or desirable for cost and operation reasons. For these reasons we consider the effects of a mandrel which is either an elastic solid (no attenuation) or a porous medium (attenuation due to the Biot slow wave) and we focus only on the normal modes, such as the tube wave. Our work is a logical extension of the work of Tang and Cheng<sup>3</sup> who specialized in the case of a rigid and nonporous mandrel.

The organization of this article is as follows: We describe our experimental technique in Sec. I. We outline our theoretical treatment in Sec. II although most details are actually presented in the Appendix. We treat the mandrel either as an isotropic elastic medium or as an isotropic poro-elastic medium for which it is well known that the Biot theory provides an excellent description. Section III is devoted to an analysis of our results, both experimental and theoretical. We present our conclusions in Sec. IV. In this article we consider only the properties, dispersion, and attenuation of the normal modes. We do not consider actual waveform calculations which could, of course, be done using more involved techniques, such as real-axis integration.<sup>9</sup> We note that modal characteristics are independent of sourcing properties whereas waveforms are not.

## I. EXPERIMENTAL PROCEDURE

A schematic of the experiment, which is immersed in a water tank, is shown in Fig. 1. A transmitter positioned near the bottom of the borehole emits a pulsed acoustic signal. A

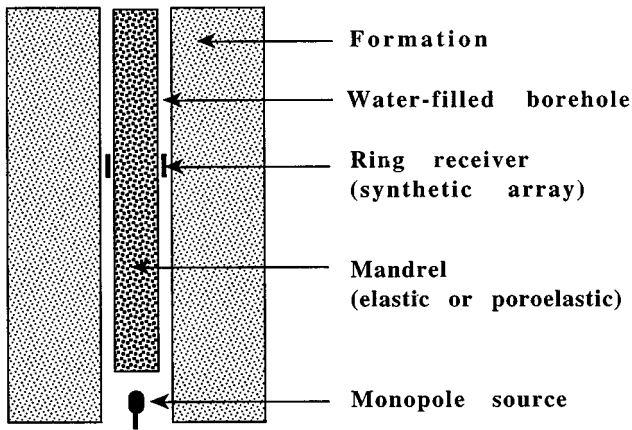


FIG. 1. Schematic diagram for measuring modal characteristics of an axially symmetric mode in an elastic formation with a fluid-filled borehole and a mandrel which may be either an elastic medium or a porous solid. The ring receiver is positioned along the axis at intervals with constant spacing to form a synthetic array.

ring receiver is positioned in the water annulus concentrically with the mandrel and the borehole; its axial position is controlled via a stepping motor to form a constant interval synthetic array. The acoustic pressure is recorded as a function of time and receiver location. Recorded waveforms are processed with Prony's method<sup>4</sup> to estimate the slowness and the attenuation of the various modes as functions of frequency. A normal mode varies axially and temporally as  $e^{i(k_z z - \omega t)}$ ; we write  $k_z = \omega s(\omega) + i\gamma(\omega)$ , where  $s(\omega)$  is the phase slowness and  $\gamma(\omega)$  is the attenuation.

Our experiments are done using two formations, stainless steel (a *hard* formation) and polyethylene (a *soft* formation). The acoustic properties of these two materials bracket those of the vast majority of actual rock formations. We have used two different elastic mandrels, stainless steel and polymethylmethacrylate (PMMA). The relevant properties of these materials are listed in Table I. The boreholes are 1.25 in. (3.175 cm) in diameter. The mandrel rods are 0.75 in. (1.905 cm) in diameter. Thus the mandrel to borehole size ratio is 0.6. The outer radius of the polyethylene formation is 6.0 in. (15.240 cm) which is sufficiently large to be considered infinite in the calculations. The outer diameter of the steel formation, however, is only 2.25 in. (5.715 cm). Nonetheless, as we shall see, this is sufficiently large to allow quantitative comparison against the theory developed for an unbounded formation.

We have used two different porous media as mandrels also. The relevant Biot parameters are listed in Table II

TABLE I. Material parameters for elastic mandrel/borehole experiments. For convenience, both the phase speeds and the phase slownesses are listed. All parameters were determined independently.

Material	$\rho$ (kg/m <sup>3</sup> )	Compressional		Shear	
		$V_p$ (km/s)	$S_p$ ( $\mu$ s/m)	$V_s$ (km/s)	$S_s$ ( $\mu$ s/m)
Stainless steel	7900	5.80	172	3.10	323
Polyethylene	960	2.38	420	0.912	1096
Polymethylmethacrylate (PMMA)	1180	2.64	379	1.27	787
Water	1000	1.48	676	...	...

TABLE II. Material parameters for the poro-elastic mandrels. All quantities were measured separately, except  $\Lambda$  and  $f_c$ , which are calculated from the others as indicated.

	Parameter	QF-20	QF-50
Pore space	$\phi$	0.42	0.41
	$\alpha_\infty$	1.9	1.7
	$\kappa_0$ ( $\mu$ m) <sup>2</sup>	31.5	47.2
	$\Lambda$ ( $\mu$ m) = $\sqrt{8\alpha_\infty\kappa_0/\phi}$	33.8	39.6
Fluid phase	$\rho_f$ (kg/m <sup>3</sup> )	1000	1000
	$K_f$ (GPa)	2.19	2.19
	$\eta$ (kg/m s)	0.0010	0.0010
	$f_c$ (kHz) = $\frac{1}{2\pi} \frac{\eta\phi}{\rho_f\kappa_0\alpha_\infty}$	1.12	0.81
Solid phase	$\rho_s$ (kg/m <sup>3</sup> )	2730	2700
	$K_s$ (GPa)	33.4	33.4
Frame moduli	$K_b$ (GPa)	8.5	8.5
	$N$ (GPa)	6.5	5.8

where we use the notation of Refs. 5 and 7. These parameters were determined by direct measurement on the samples as described by Ref. 7 except that the  $\Lambda$  parameter was assumed to be related to the other parameters, as indicated in Table II.

We demonstrate our technique with a simple example. Figure 2 shows waveforms as functions of time and receiver location acquired in the borehole in the steel formation without a mandrel. The dominant signal is a primarily fluid-based, nearly nondispersive tube wave which is easily visible. The very early arrivals are due to modes primarily in the steel formation. There is also a cut-off mode which is not easily visible but whose properties can be deduced from our processing. Figure 3(a) shows the results in which phase slowness is plotted as a function of frequency. There are two modes shown in Fig. 3(a), neither of which had any measurable attenuation, over and above background scatter. Our background attenuation seems to be randomly scattered over a range of values  $3 \pm 8$  dB/m. The tube wave has a slowness nearly equal to that of water (676  $\mu$ s/m) and has little dispersion. The other higher-order mode in the borehole has less phase slowness and has steep dispersion near a cutoff frequency of about 60 kHz. The symbols denote experimental data and the solid lines denote results of the numerical mode search which we describe in the next section; they agree very well. This higher-order mode has a simple dispersion relation in the limit that the formation is rigid:<sup>8</sup>

$$k_z = \sqrt{(\omega/V_f)^2 - (j_{1,1}/b)^2}, \quad (1)$$

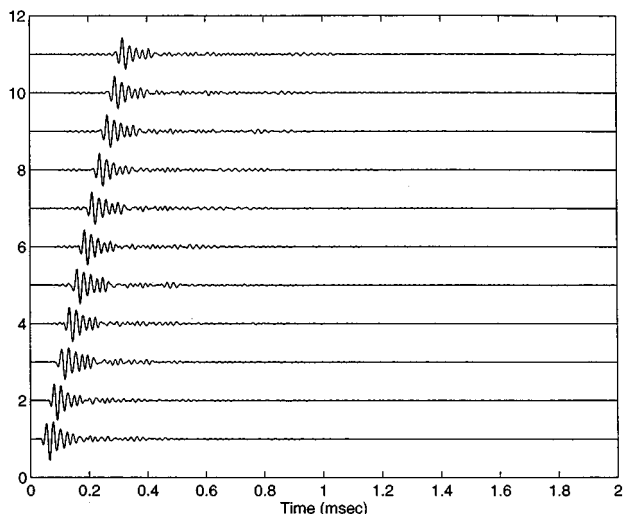


FIG. 2. Received signals in a borehole in a steel formation with no mandrel. The source transducer was driven with a single cycle sine wave at 40 kHz. Waveforms were recorded every 6.35 mm. We show waveforms every 38.1 mm.

where  $j_{1,1} \approx 3.832$  is the first nontrivial zero of the Bessel function  $J_1(x)$ ,  $V_f$  is the speed of sound in the fluid, and  $b$  is the borehole radius. This approximate theory gives a cutoff frequency of 57 kHz, which is close to that which is observed. We return to a discussion of this figure in Sec. III.

## II. THEORY

We idealize the experimental geometry as a cylindrically symmetric one of infinite extent in which the mandrel occupies the region  $0 < r < a$ , the fluid occupies the region  $a < r < b$ , and the elastic formation extends to infinity,  $b < r < \infty$ . Aside from introducing obvious errors of approximation, this last assumption precludes the possibility of describing a mode which is primarily an extensional mode in the (finite thickness) formation, a mode which is possible to detect experimentally.

In this article we consider axially symmetric normal modes in which all relevant quantities vary axially and temporally as  $e^{i(k_z z - \omega t)}$ . We wish to determine the dispersion relation  $k_z = k_z(\omega)$ . The displacements are written as linear combinations of cylindrical solutions to the wave equations in the three media. The relative amplitudes of these individual solutions are determined by the requirement that certain boundary conditions be satisfied. In the elastic outer medium there is an outgoing cylindrical shear wave and an outgoing cylindrical compressional wave. In the fluid-filled annular region there are both incoming and outgoing cylindrical compressional waves; there are no shear waves. In the case that the mandrel is an elastic medium, there is a cylindrical compressional wave and a cylindrical shear wave, each of which is regular at the center,  $r=0$ . The amplitudes of these six waves are determined by the boundary conditions at the two interfaces: continuity of radial displacement  $u_r$ , continuity of radial stress  $\tau_{rr}$ , and vanishing of tangential stress  $\tau_{zr}$ . This homogeneous system of equations can have a nontrivial solution if and only if the determinant of the  $6 \times 6$  matrix of coefficients vanishes. At each frequency

the correct axial wave number  $k_z$  is that which satisfies said equation. Its value is determined by a numerical search algorithm. As there is no attenuation mechanism,  $k_z$  is real-valued for all truly propagating modes.

However, there are experimentally relevant “pseudo-modes” which can occur when the phase speed of a mode becomes greater than the phase speed of one or both of the bulk modes in the formation. In these cases, the mode loses energy by radiating into the formation. The normal-mode wave vector  $k_z$  is complex valued; it may be near the real axis but is on a different Riemann sheet, as we explain below. In general, then, we write  $k_z(\omega) = \omega s(\omega) [1 + i/(2Q(\omega))]$  where  $s(\omega)$  is the phase “slowness” of the mode and  $1/Q(\omega)$  is the specific attenuation of the mode. [Occasionally we write  $k_z(\omega) = \omega \tilde{s}(\omega)$ , where  $\tilde{s} = s_1 + i s_2$  is complex valued. Note that  $1/Q = 2s_2/s_1$ .] A more complete discussion is provided in the Appendix.

When a porous medium is used as the mandrel we describe its properties in terms of the Biot theory of poro-elasticity, as has been done previously in related problems.<sup>3-6,9-13</sup> Here, the displacement of the fluid and of the solid are treated separately and on an equal footing, although they are coupled to each other. The significant difference between the case of an elastic mandrel and that of a poro-elastic mandrel is that in the latter there are fast and slow compressional waves, as well as a shear wave within the mandrel. It is the coupling into the slow compressional mode in the mandrel which, we shall see, is the mechanism for increased attenuation of the tube wave when there is a poro-elastic mandrel. The four boundary conditions at the mandrel/fluid interface are continuity of total stress ( $\tau_{rr}$  and  $\tau_{rz}$ ), continuity of fluid, and continuity of pore pressure. The determinant of the resulting  $7 \times 7$  matrix of coefficients is set equal to zero and we search, numerically, for  $k_z$  as before. Here, however,  $k_z$  is always complex valued because of the attenuation mechanism. It is convenient to write  $k_z(\omega) = \omega s(\omega) + i \gamma(\omega)$  in which the slowness  $s$  and the attenuation  $\gamma$  are real-valued functions of frequency. A more complete description is also presented in the Appendix.

## III. RESULTS

### A. Elastic mandrel

In this section we consider the modal properties of a fast and a slow formation with and without an elastic mandrel. The distinction between fast and slow is whether the formation shear speed is larger or smaller, respectively, than the fluid speed.

First, in Fig. 3(a) we compare our experimental results against our theoretical calculations for an open borehole (no mandrel) in a steel formation, filled with water. This is a “fast” formation. Because of the huge acoustic contrast between the two media, the modal structure we observe is essentially that for a fluid in a rigid formation. The tube wave (red curve) has a slowness nearly equal to that of a compressional wave in water ( $676 \mu\text{s/m}$ ). Similarly, the dispersive mode (black curve) is essentially that of a cut-off mode, as discussed in Sec. I. For slownesses larger than the shear slowness in steel ( $323 \mu\text{s/m}$ ) the modes are true guided

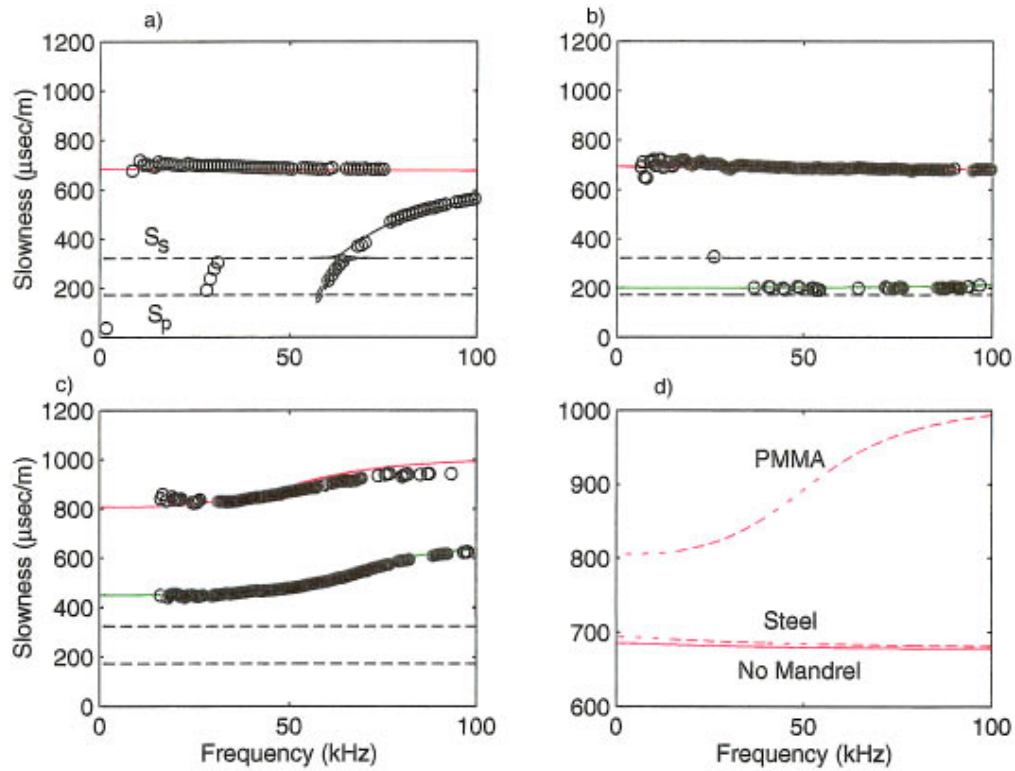


FIG. 3. Modal slownesses from the processing of the recorded waveforms as in Fig. 2 for three configurations consisting of a borehole in a steel formation. The symbols represent data and the solid lines are the results of the theoretical mode search algorithm. Red curves are tube waves, green curves are the (pseudo-) extensional modes. The dashed horizontal lines are the formation shear and compressional slownesses. (a) Open, water-filled borehole in a steel formation. (b) Steel mandrel/water annulus/steel formation. (c) PPMA mandrel/water annulus/steel formation. (d) Calculated dispersion of the tube waves in (a)–(c).

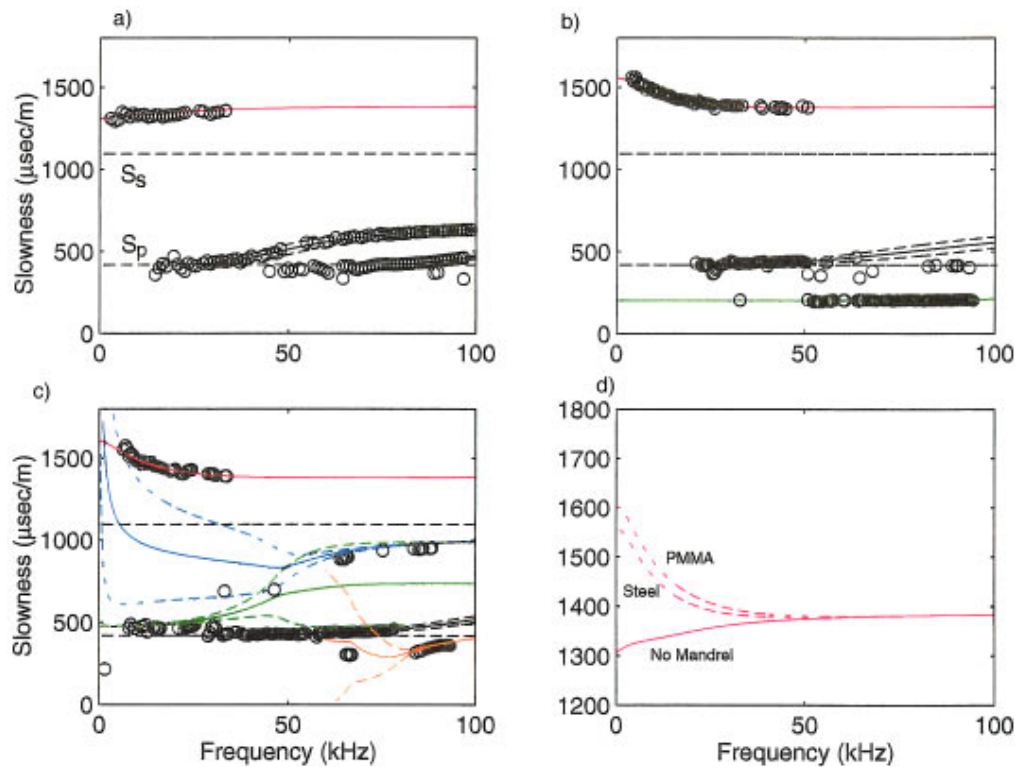


FIG. 4. Modal slownesses for three configurations consisting of a water-filled borehole in a polyethylene formation. Same conventions as in Fig. 3. For all pseudo-modes the quantities  $s_1(\omega) \pm s_2(\omega)$  are plotted as dashed lines, whereas  $s_1(\omega)$  is plotted as a solid curve. (a) No mandrel. (b) Steel mandrel/water annulus/polyethylene formation. (c) PPMA mandrel/water annulus/polyethylene formation. The two different parts of the pseudo-extensional mode are shown in blue and in green. Also, there is a pseudo-mode shown in orange. (d) Calculated dispersion of the tube waves in (a)–(c).

modes with no attenuation ( $1/Q \equiv 0$ ). However, a cut-off pseudo-mode persists for slownesses below this value. In order to describe this mode we consider the following choice of Riemann sheet in Eqs. (A5):  $\text{Im}[\kappa(\text{shear}, \text{compressional})] < 0$ . This choice guarantees that energy radiates into the relevant bulk modes. The resulting mode has finite attenuation due to this radiation condition. In Fig. 3(a) we plot  $s_1(\omega)$  (solid black lines) as well as  $s_1(\omega) \pm s_2(\omega)$  (dashed lines) where  $s_{1,2}$  are, respectively, the real and the imaginary parts of the complex-valued slowness. This device gives us a simple picture of how well defined the pseudo-mode may be. When the dashed lines nearly converge onto the solid line, the pseudo-mode is nearly lossless, as is the case for the pseudo-modes shown in Fig. 3. Its further relevance is demonstrated in Fig. 4 and in a subsequent article.<sup>14</sup>

As the frequency is lowered, the slowness of the upper part of the cut-off mode decreases until it equals the shear slowness of the steel. At this point  $\kappa(\text{shear}) \equiv 0$  and this is a branch point of the calculation. Computationally, as the frequency is lowered further, the root finding algorithm does find a solution but as the attenuation is negative,  $1/Q < 0$ , we do not attach any physical importance to it. Such behavior, where a mode disappears into the shear branch point, has been observed before.<sup>15</sup>

Similarly, as the frequency is raised, the complex-valued slowness of the lower part of the cut-off mode becomes equal to the shear slowness of the steel and this part of the dispersion curve disappears into a branch point, too. As a point of information, if we choose a slightly different condition  $\text{Im}[\kappa(\text{shear})] < 0$ , but  $\text{Im}[\kappa(\text{compressional})] > 0$ , we find a lower part of the curve which is similar to that of Fig. 3(a) but which exists only between the compressional and the shear slownesses of steel.

The slight amount of tube wave dispersion seen in the data at low frequencies and not predicted by the theory may be due to the fact that the finite outer radius of the steel can not safely be taken to be infinite as we have done. Similarly, there is a hint of another mode between 20 and 30 kHz. See Ref. 16 for an analysis of the modal structure of fluid-loaded cylindrical shells.

We now consider the effect of an elastic mandrel introduced into this borehole. In Fig. 3(b), we show the effect of a steel mandrel. (Our notation in this and subsequent figures is that the materials are listed as mandrel/annulus/formation.) There are two qualitative differences from the open borehole case. First, because the annular width of fluid has been reduced, the cut-off mode has been pushed to higher frequencies, outside of our experimental bandwidth. Second, there is another weakly dispersive mode (green curve), which is essentially an extensional mode in the steel mandrel. Strictly speaking, this is a pseudo-mode because it is faster than the formation shear. Because the impedance contrast between the mandrel and the water is so large, however, the speed of this mode is nearly equal to that of an extensional mode in the rod. Also, the attenuation is so small (i.e.,  $s_2 \ll s_1$ ) that the width of this mode [the difference between the two dashed curves,  $s_1(\omega) \pm s_2(\omega)$ ] does not show on the scale of the plot. Similarly, the tube wave (red curve) is nearly nondis-

persive with a slowness nearly equal to that of the fluid.

Figure 3(b) demonstrates a general characteristic: There are two modes, a quasiextensional mode and a quasitube wave, each of which tends to a finite slowness in the limit of zero frequency. We derive an analytic expression for the low-frequency limit of these two modal speeds later in this subsection.

If the mandrel is a relatively compliant material, such as PMMA, there is a much more significant effect on the modal characteristics, as shown in Fig. 3(c). Both the tube wave (red curve) and the extensional mode (green curve) are slower than the formation shear and so each is a well-defined mode ( $1/Q \equiv 0$ ). The tube wave has been significantly slowed, relative to those in Fig. 3(a) and (b). To illustrate this last point, we show all three tube wave dispersion curves in Fig. 3(d). In the high-frequency limit, two of them tend to the slowness of a Scholte wave at a water/steel interface; the other tends to that of a water/PMMA interface.

If the formation is a slow one, the effects of introducing a mandrel can be extremely complex, as we show with a polyethylene formation. Figure 4(a) is the open borehole case. There is a tube wave (red curve) which is slower (by a factor of 2) than the compressional wave in water. There are two pseudo-modes in the region between the formation shear and the formation compressional slownesses. They are “leakier” than their counterparts in Fig. 3, as can be seen by the splitting between  $s_1(\omega) + s_2(\omega)$  and  $s_1(\omega) - s_2(\omega)$ . We use the conditions  $\text{Im}[\kappa(\text{shear})] < 0$ , and  $\text{Im}[\kappa(\text{compressional})] > 0$  to describe these modes. Both modes terminate at the compressional branch point.

The modifications of this open borehole case due to the presence of a steel mandrel are fairly straightforward as shown in Fig. 4(b). Again, the extensional mode (green curve), although faster than the formation bulk modes, is nearly nonattenuative as it was for steel/water/steel in Fig. 3(b). The tube wave (red curve) is noticeably slower and more dispersive than that of the open borehole case, Fig. 4(a).

The modal structure of the system consisting of a PMMA mandrel, water, and a polyethylene formation is profoundly complex as shown in Fig. 4(c). For each mode, we plot the real part of the theoretically calculated slowness,  $s_1(\omega)$ , as a solid curve and we plot  $s_1 \pm s_2$  as dashed curves of the same colour. This device gives a visual indication of how “leaky” each mode is predicted to be; when all three curves come together the mode is predicted to be relatively lossless. There is a single, well-defined, completely lossless mode, the tube wave (red curve), which is similar to that for steel/water/polyethylene. Also, there is a pseudo-mode (black curves) which starts at the formation  $P$  slowness at 17 kHz and is mildly dispersive and moderately lossy, as for steel/water/polyethylene. There is an additional high- $Q$  mode (orange curve) in the range 82–95 kHz with a slowness about 325  $\mu\text{s}/\text{m}$  which is not apparent in the steel/water/polyethylene system. This mode is predicted to be very lossy below 80 kHz and, indeed, we were not able to track it experimentally below that frequency.

The biggest differences, however, are to be found within the complex of two dispersive and lossy branches (the blue

curves and the green curves) with slownesses in the region between the formation shear and formation compressional slownesses. These two branches, which seem to “want” to cross but are mutually repelled, represent the equivalent of the extensional mode in steel/water/polyethylene. In the limit of low frequencies the one branch (green) tends to a well-defined limit with no loss ( $1/Q \equiv 0$ ; the dashed green curves converge on the solid.) This branch, however, becomes very lossy at high frequencies. The other branch (blue), lossy at low frequencies, becomes essentially lossless at high frequencies. We note that in the two limits where these modes become relatively lossless, our experimental technique is able to detect and quantify them. The acoustic properties of this system will be considered at length in a future article.<sup>14</sup>

The conclusions that can be drawn so far are that even though the geometries considered are quite simple, the acoustic properties can be quite complex. In all six cases considered, there is excellent agreement between the theory and the experimental results, in elaborate detail in many cases.

Since a purpose of our investigations is to consider the effect that a mandrel has on tube wave characteristics, let us compare and contrast the theoretical tube wave characteristics for the different geometries. We do so in Fig. 3(d) for the fast (steel) formation and in Fig. 4(d) for the slow (polyethylene) formation; note the change in scales. In the former case, we see that the presence of a steel mandrel does not appreciably change the tube wave speed, which is essentially that of the fluid; steel is nearly incompressible as compared to water and the mode is nearly pistonlike motion of the water with little radial motion. The PMMA mandrel, by contrast, significantly slows this mode. This is to be expected because PMMA is much more compliant than steel. In the polyethylene formation, the tube wave is already much slower than the water speed because polyethylene is relatively compliant. For this reason, a steel mandrel and a PMMA mandrel have a similar effect on the tube wave in this formation. In all cases, in the limit of high frequencies the tube wave evolves into a Scholte wave<sup>17</sup> which is a surface wave confined to the interface between the water and either the mandrel or the formation, whichever is slower. This is why the tube waves of Fig. 4(d) all tend to the same high-frequency limit (water/polyethylene interface) but those of Fig. 3(d) do not; the water/PMMA interface has a much slower Scholte wave than that of water/steel. Similarly, the quasiextensional mode evolves into a Scholte wave confined to the remaining interface.

We note that when there is a solid mandrel there are two distinct modes which become nondispersive and lossless in the low-frequency limit,  $\omega \rightarrow 0$ , even for the PMMA mandrel/water annulus/polyethylene formation. We now present an analytical derivation of the properties of these two modes in this limit. Intuitively, there is a mode which is more or less an extensional mode in the rod and there is a mode which is more or less a fluid mode, although the two couple and renormalize their speeds. (The situation is similar to that of a fluid-filled borehole with a casing which is not bonded to the formation.<sup>18</sup>) White<sup>19</sup> has derived a simple expression for the (single) phase speed in the case where

there is no mandrel. We extend his derivation to the present case. In the quasistatic limit the axial and the radial deformations in the mandrel are independent of the radial coordinate. We write the axial and the radial displacements in the mandrel as

$$u_z = f(z, t), \quad u_r = rg(z, t). \quad (2)$$

[In fact, it will turn out that  $g = \beta(\partial f / \partial z)$  for some constant  $\beta$  which is an effective Poisson's ratio for the problem.] The displacement in the formation is purely radial, in this limit. The radial displacement  $u_r$  at the borehole wall ( $r = b$ ) is simply<sup>19</sup>

$$u_r(b^+) = bP/2\mu_F, \quad (3)$$

where  $P(z, t)$  is the (radially independent) pressure in the fluid and  $\mu_F$  is the shear modulus of the formation. Similarly, in this quasistatic limit we need to deal only with the axial component of the displacement in the fluid  $u(z, t)$ . This is because the pressure in the annulus is spatially constant and the relevant radial components are expressible in terms of the other unknowns.

We have four unknown functions,  $u$ ,  $f$ ,  $g$ , and  $P$  and we need four equations which relate them to each other. First, under a deformation the change in the fluid volume  $\Delta V$  must be related to the fluid pressure  $P$  by the bulk modulus of the fluid,  $K_f$ :  $\Delta V = -(P/K_f)V$ . We consider the net influx of fluid into a region of the borehole annulus between  $z$  and  $z + \Delta z$ . The initial volume of the fluid is  $V = \pi(b^2 - a^2)\Delta z$ :

$$\Delta V = -\frac{P}{K_f} \pi(b^2 - a^2)\Delta z. \quad (4)$$

The net influx of fluid into this region is

$$\Delta V = \left[ \frac{\partial u}{\partial z} \pi(b^2 - a^2) + \frac{\pi b^2}{\mu_F} P - 2\pi a^2 g \right] \Delta z. \quad (5)$$

These last two equations can be combined:

$$(1-x) \frac{\partial u}{\partial z} + \left[ \frac{1}{\mu_F} + \frac{1-x}{K_f} \right] P - 2xg = 0, \quad (6)$$

where  $x = (a/b)^2$  is the area fraction of borehole occupied by the mandrel. Equation (6) explicitly makes use of the assumption that the fluid pressure  $P$  has no radial variation in the annulus. Second, the equation of motion in the fluid is simply

$$\rho_f \frac{\partial^2 u}{\partial t^2} = -\frac{\partial P}{\partial z}. \quad (7)$$

Third, continuity of radial stress at the mandrel/fluid boundary is given by (A11),  $\tau_{rr}(a^-) = -P$ , which we rewrite using (A2) and (2)

$$2(\lambda + \mu)g + \lambda \frac{\partial f}{\partial z} = -P, \quad (8)$$

where  $\lambda$  and  $\mu$  are the Lamè coefficients of the mandrel. Finally, the axial motion  $u_z$  in the mandrel is given by (A1), (A2), and (2):

$$\rho_s \frac{\partial^2 f}{\partial t^2} = 2\lambda \frac{\partial g}{\partial z} + (\lambda + 2\mu) \frac{\partial^2 f}{\partial z^2}, \quad (9)$$

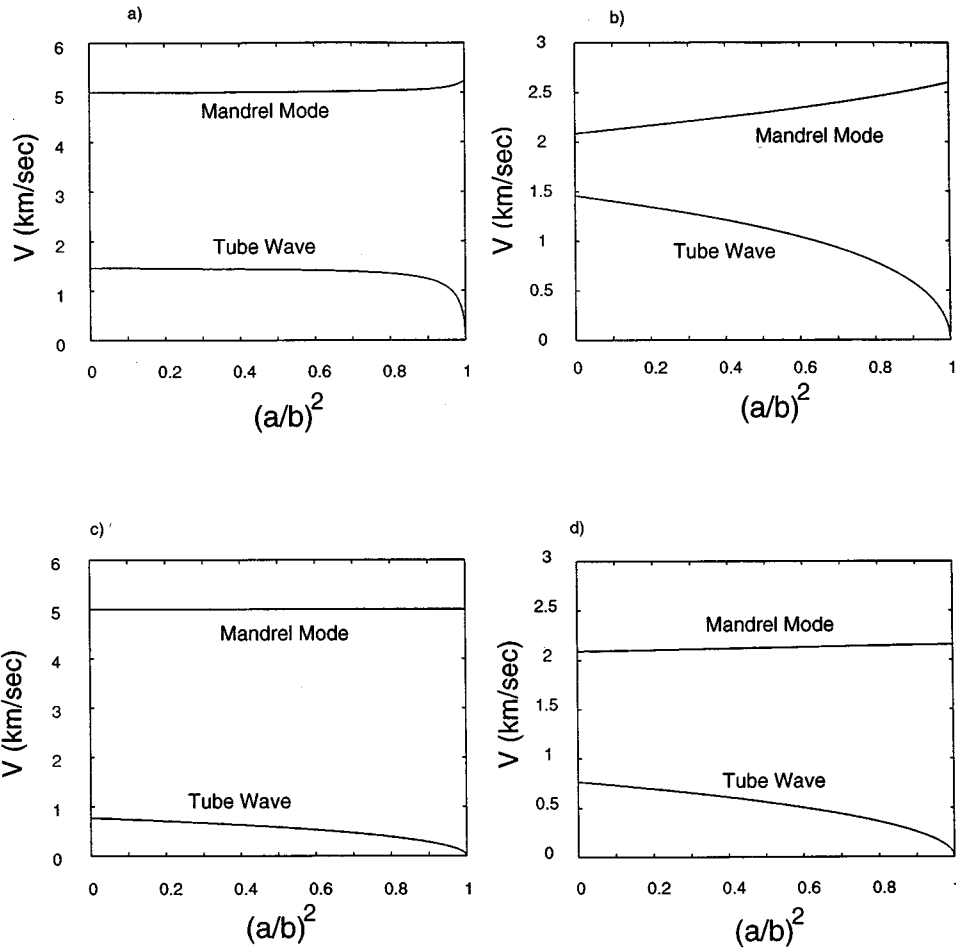


FIG. 5. Theoretical mode speeds in the quasistatic limit,  $\omega \rightarrow 0$ , for an elastic mandrel as a function of the filling fraction of the mandrel in the borehole. (a) Steel mandrel/water/steel formation. (b) PMMA mandrel/water/steel formation. (c) Steel mandrel/water/polyethylene formation. (d) PMMA mandrel/water/polyethylene formation. The theory and the data of Figs. 3 and 4 correspond either to the open borehole case  $(a/b)^2=0$ , or to the value  $(a/b)^2=0.36$  in the presence of the mandrel.

where  $\rho_s$  is the mandrel density. [We note in passing that the boundary condition  $\tau_{zr}(a^-)=0$  is satisfied only if one keeps the next term in the expansion (2)  $u_z=f-(1/2)r^2(\partial g/\partial z)$  but this next term does not affect the speeds in the quasistatic limit.] These four equations [(6), (7), (8), and (9)], admit two nondispersive solutions whose phase speeds  $v_{\pm}$  are the roots of the following quadratic equation:

$$[(1-x)\rho_s(\lambda+\mu)S_T^2+x\rho_f\rho_s]v^4 - \{(1-x)(\lambda+\mu)[YS_T^2+\rho_s] + x\rho_f(\lambda+2\mu)\}v^2 + (1-x)(\lambda+\mu)Y=0, \quad (10)$$

where  $Y=\mu(3\lambda+2\mu)/(\lambda+\mu)$  is the Young's modulus of the free mandrel and

$$S_T^2(x)=\rho_f\left[\frac{1}{K_f}+\frac{1}{\mu_F(1-x)}\right]. \quad (11)$$

$S_T$  is the phase slowness of the tube wave in the limit the mandrel is rigid,  $(\lambda,\mu)\gg K_f, \mu_F$ , as may easily be checked. Our result for the two modes differs from the result of Norris<sup>20</sup> who considered only the fluid-based mode and apparently made the assumption that the mandrel undergoes plane stress. Our analysis shows that, for either mode, the mandrel deformation is neither plane strain nor plane stress.

The value of  $x=(a/b)^2$  corresponding to the data and calculations of Figs. 3 and 4 is either  $x=0$  or  $x=0.36$ ; we have checked that our low-frequency result agrees with the numerical modal search result to at least five significant digits in all ten cases, at a frequency of 100 Hz.

We plot the solutions to Eq. (10) in Fig. 5(a)–(d). (We plot modal speeds, rather than slownesses, in order to see that one of the speeds has a limiting value of zero, as we discuss below.) Several features emerge from a consideration of Fig. 5: (1) In the limit that the mandrel occupies a small fraction of the borehole, the speeds tend to finite values, namely

$$\lim_{x \rightarrow 0} v_{\pm} = \begin{cases} \sqrt{Y/\rho_s} \\ 1/S_T(x=0). \end{cases} \quad (12)$$

That is, the one speed is equal to the speed in a rod, as if there was no formation, the other is equal to the speed of a tube wave, as if there was no rod; (2) Departures from these limiting values are modest, especially for small values of  $x=(a/b)^2$ . There is somewhat more of a variation when the mandrel is PMMA than when it is steel. From Eq. (10) it is possible to prove that if the open-borehole tube wave speed

is slower than the free mandrel speed then the presence of a mandrel acts to slow down the tube wave even if the mandrel is rigid; the more compliant the mandrel, the slower is the tube wave. Similarly, the presence of the formation acts to speed up the extensional mode when the extensional speed in the rod is faster than the tube wave. This behavior is clearly seen in Fig. 5; (3) In the limit the mandrel fills the borehole, the speed of the fluid-based mode tends to zero, and the other speed tends to a finite limit:

$$\lim_{x \rightarrow 1} v_{\pm} = \begin{cases} \sqrt{\frac{(3\lambda + 2\mu)\mu + (\lambda + 2\mu)\mu_F}{\rho_s[\lambda + \mu + \mu_F]}} \\ 0. \end{cases} \quad (13)$$

This first expression tends to the value appropriate to an extensional mode in a free rod,  $\sqrt{Y/\rho_s}$  when  $\mu_F \ll (\lambda, \mu)$ , which makes physical sense, and to the value appropriate to a longitudinal wave,  $\sqrt{(\lambda + 2\mu)/\rho_s}$  when  $\mu_F \gg (\lambda, \mu)$ , which also makes sense. (Within the context of the formalism we employ, there is perfect axial slip between the two solids even as  $x \rightarrow 1$ .) For any value of  $\mu_F$ , the value of this speed,  $v_{+}(x=1)$ , lies between these two limits; (4) With a rigid mandrel the sensitivity of the tube wave slowness to formation shear modulus  $\mu_F$  is amplified by the factor of  $1/(1-x)$ , as shown in Eq. (11). With a mandrel of finite rigidity, the tube wave is even slower, depending on the mandrel moduli.

## B. Porous and permeable mandrel

In this section we consider the modal structure of the steel formation in the presence of two different porous mandrels, whose properties are listed in Table II. Our notation follows that of Ref. 7 where it was explicitly demonstrated how to measure all the input parameters needed to calculate all the measurable properties of the fast, slow, and shear waves. Excellent agreement between theory and experiment was found for materials similar to the two considered here and we therefore consider the use of the Biot theory appropriate to our problem. See also Ref. 5 for a comparison of theory with experiment for a borehole acoustics problem in which the formations are described by the Biot theory.

These two materials are not very different from each other except for their permeabilities. In both cases the Biot crossover frequency  $f_c$  is well below our experimental bandwidth. Thus all our data are in the high-frequency limit where the slow wave is propagatory (high  $Q$ ). In Figs. 6 and 7 we plot the real part of the slowness as well as the attenuation as a function of frequency. There are no adjustable parameters in the theory and the agreement between the measured and the calculated results is excellent, especially for the (real) slowness. Note that the real part of the slownesses cross near  $350 \mu\text{s/m}$  in QF-20 (Fig. 6) but that there is a small gap between the two branches in QF-50 (Fig. 7); in the former case, the attenuations do not cross whereas in the latter they do. Note also from these figures that the crossover region from Biot low frequency to Biot high frequency is around 1 kHz, as per Table II.

As discussed in Ref. 7, the attenuation in the high-frequency limit of the Biot theory is governed by the  $\Lambda$  pa-

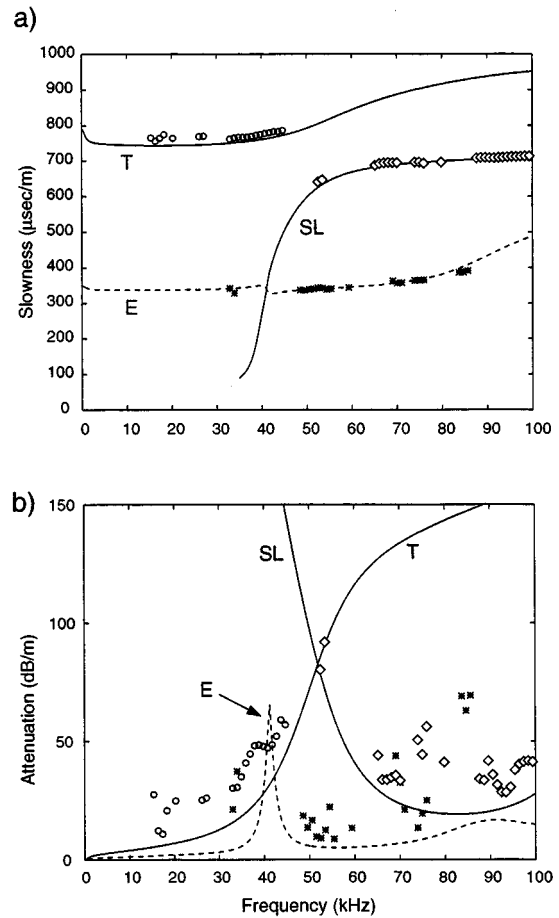


FIG. 6. Experimental and theoretical results for the modal characteristics in a QF-20 mandrel/water annulus/steel formation. (a) The real part of the slowness. (b) The attenuation. The dashed theory curves labeled “E” and the experimental (\*) characters refer to the extensional mode. The open symbols (○) and the solid curves labeled “T” refer to one branch of the tube-wave/slow-wave mode; the open symbols (◇) and the solid curves labeled “SL” refer to the other. Mandrel parameters from Table II.

rameter, and not by the permeability  $\kappa_0$ . We have made the assumption that the two are related to each other, at least approximately, by

$$\Lambda = \sqrt{8\alpha_{\infty}\kappa_0/\phi}, \quad (14)$$

for reasons expanded upon in Ref. 7 and references therein. [Basically,  $\Lambda$  is a specific measure of dynamically connected pore sizes. Qualitatively, and even quantitatively, it satisfies the definition of an approximate hydraulic radius, as per Eq. (14).] For the purposes of this article, therefore, we do not consider  $\Lambda$  to be an independent parameter. This is not an exact relationship, however, and the systematic way in which the measured attenuation is larger than the calculated may be due to the fact that the true value of  $\Lambda$  is smaller than we have assumed. We could have measured  $\Lambda$  using superfluid  $^4\text{He}$  acoustics.<sup>21</sup>

There is a simple way to understand the apparently complicated modal structure of Figs. 6 and 7. We see that there still are two more or less nondispersive modes but there seems to be a cut-off mode, similar in appearance to that of Fig. 3(a), which cuts across and couples with both the tube wave and the extensional mode. This mode is plainly not the



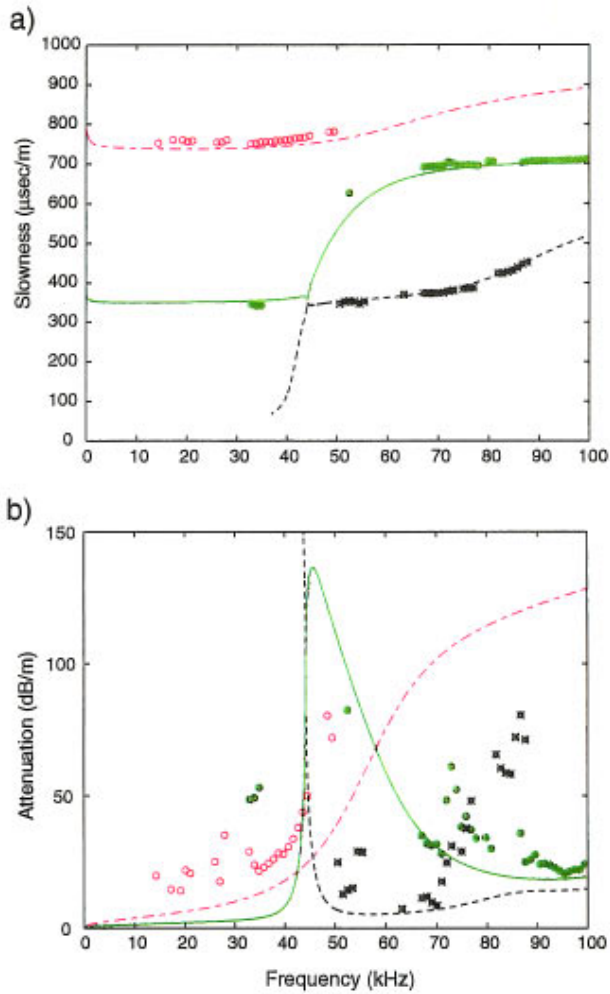


FIG. 7. As in Fig. 6, for QF-50 material. The green curve and symbols refer to a mode which is more or less an extensional mode at low frequencies, a cut-off slow wave at intermediate frequencies, and a tube wave at high frequencies. The red curve and symbols refer to the mode which is a tube wave at low frequencies and a cut-off slow wave at high frequencies. The black curve and symbols refer to the remaining mode.

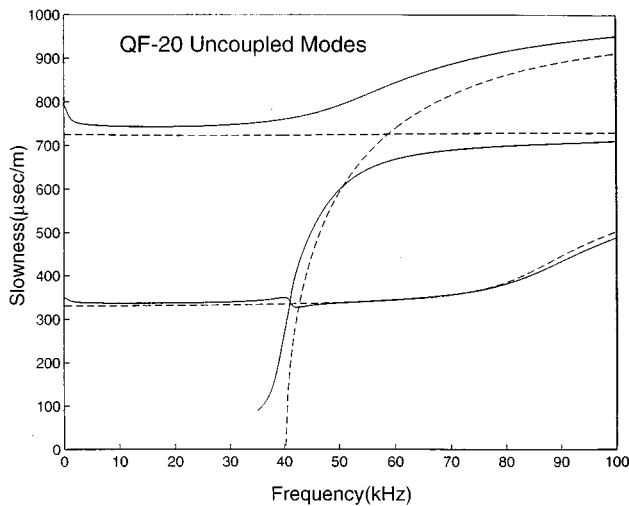


FIG. 8. Comparison of the decoupled modes theory (dashed lines) against the full theory of Fig. 6. QF-20 mandrel/water annulus/steel formation. The decoupled modes were calculated from a simple theory, as described in the text.

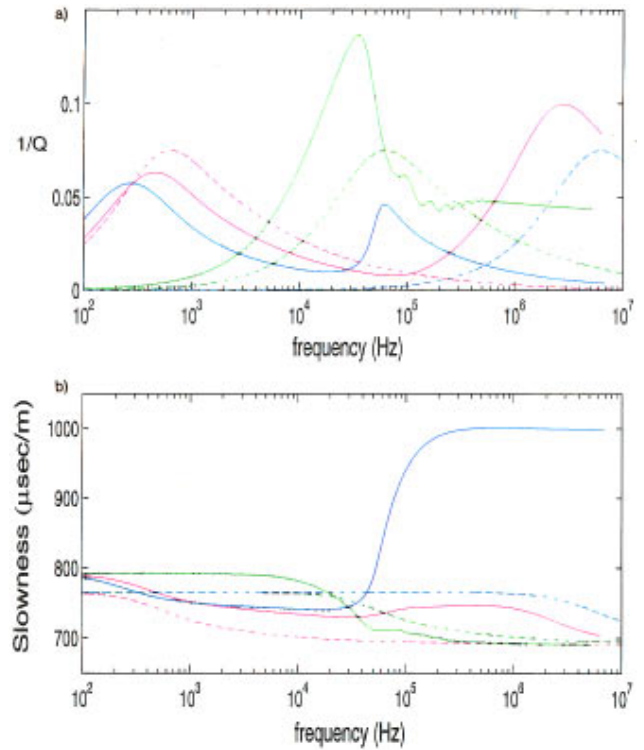


FIG. 9. Comparison of tube wave properties over a wide frequency range using different values of the permeability. All other parameters are the same as for QF-20/water/steel. (a) Specific attenuation and (b) dispersion. The solid curves represent the results of the full modal search theory and the dashed curves represent the results of the approximate theory, (25): red ( $\kappa_0 = 0.01 \mu\text{m}^2$ ), green ( $\kappa_0 = 1.0 \mu\text{m}^2$ ), and blue ( $\kappa_0 = 100 \mu\text{m}^2$ ).

same as that described by Eq. (1) for the simple reason that the slowness tends at high frequencies to a value which is greater than that of the fluid. In fact, this mode is essentially a slow wave confined to the porous mandrel, with some coupling to the two other modes. The simplest way to see this is from the following calculations which make our claims more explicit. First, since the calculations of Figs. 6 and 7 are all well into the high-frequency limit of the Biot theory, we calculate the bulk speeds of the fast, slow, and shear waves in this limit, completely neglecting the effects of viscosity. For the QF-20 sample, the parameters of Table II give these slownesses as  $S_{\text{fast}} = 309 \mu\text{s/m}$ ,  $S_{\text{shear}} = 524 \mu\text{s/m}$ , and  $S_{\text{slow}} = 996 \mu\text{s/m}$ . (Because the frame moduli for QF-20 are fairly stiff, the slow wave slowness is approximately given by  $S_{\text{slow}} \approx S_f \sqrt{\alpha_\infty}$ ; in any event, the slow wave is always at least as slow as this limiting expression and therefore it is always slower than the pore fluid.<sup>22</sup>) Next, we ask: What are the properties of a nonporous, elastic medium whose compressional and shear speeds match the calculated values of the fast and shear waves? Since the total density of the fluid saturated sample is  $\rho_{\text{total}} = 2003 \text{ kg/m}^3$ , we find the effective elastic constants to be  $K_{\text{eff}} = 11.2 \text{ GPa}$  and  $\mu_{\text{eff}} = 7.31 \text{ GPa}$ . With these values for the effective elastic constants of a nonporous mandrel it is straightforward to calculate the normal modes as described in the previous subsection. Since the formation is fast (steel) the slownesses of both modes are greater than that of the formation shear and therefore they are real-valued; they are plotted as dashed lines in Fig. 8 along with the results of the full theory of Fig. 6, which are plotted

as solid lines. Finally, we idealize the cut-off mode as purely a slow wave in the porous mandrel for which the pore pressure may be written as

$$P = J_0(\kappa r) e^{i(k_z z - \omega t)}, \quad (15)$$

where

$$\kappa^2 + k_z^2 = \omega^2 S_{\text{slow}}^2. \quad (16)$$

For this mode only we idealize the boundary condition on the surface of the mandrel as purely one of pressure release, neglecting completely the interaction with the fluid annulus, i.e.,  $P(r=a^-) = 0$ . Equation (15) can satisfy this boundary condition provided  $\kappa = j_{0,1}/a$  where  $j_{0,1} \approx 2.405$  is the first zero of  $J_0$ . Therefore the slowness of this cut-off slow wave mode is

$$S(\omega) = \sqrt{S_{\text{slow}}^2 - \left(\frac{j_{0,1}}{\omega a}\right)^2}. \quad (17)$$

Equation (17) is also plotted as a dashed line in Fig. 8. It is clear that the modal structure of the full theory may be thought of as a mutual coupling of these simpler uncoupled modes.

Several features emerge from the comparison of the full theory against that of the decoupled modes: (1) Our identification of the nature of these modes is made more precise because the decoupled modes give a reasonably accurate quantitative description of the dispersion of all three branches, except in the crossing regions where they mix; (2) in the full theory, the cut-off slow wave couples more strongly to the tube wave than it does to the rod extensional mode. This is more or less obvious since the slow wave is basically a pore-fluid-based mode and the tube wave is an annular-fluid-based mode. In general the fluid will want to flow freely in and out of the pores thus coupling the two. Indeed, it is this very coupling which predicts the attenuation, when the viscous effects are taken into account; (3) the experimental geometry of Fig. 1 does not facilitate detecting a mode which is primarily based upon motion of the pore fluid in the mandrel. For this reason we are able to obtain data only on those modes with appreciable energy in the fluid annulus, as shown in Figs. 6 and 7; (4) notwithstanding, the system is aware that there is this cut-off slow wave: How else might one account for the precipitous drop in the measured tube wave slownesses (Figs. 6 and 7) as one crosses the mixing region?

We note in passing that the weak structure in the quasiextensional mode as it is crossed by the cut-off mode is analogous to that seen by Berryman<sup>23</sup> who considered the modal structure of an isolated porous rod (no fluid annulus, no formation) with open pore boundary conditions.

Is it possible to derive an analytic expression which accurately describes the quasistatic properties of these two modes, the extensional mode and the tube wave, analogous to that which we derived for the elastic mandrel, Eq. (10)? This is a subtle question to which the simple answer (yes) is misleading.

For the analogous problem of extensional modes in an isolated porous rod, Gardner<sup>24</sup> has developed a well-known

low-frequency approximation which involves three assumptions: (1) The frequency is well below the Biot critical frequency:

$$\omega^B = \frac{\eta \phi}{\rho_f \kappa_0 \alpha_\infty}. \quad (18)$$

In this limit the fast wave and the shear wave are propagatory and nondispersive,  $k_+ = \omega/V_P$  and  $k_{sh} = \omega/V_S$ . The slow wave is diffusive

$$k_- = \sqrt{i\omega/C}, \quad (19)$$

where the diffusivity of the slow wave is proportional to the permeability,  $C \propto \kappa_0/\eta$ , with a proportionality constant which depends upon the elastic parameters in the problem<sup>5,10</sup> [see also Eq. (23), below]; (2) the wavelengths of the fast wave and of the shear wave are large compared to the rod radius:  $k_+ a \ll 1$ ,  $k_{sh} a \ll 1$ ; (3) because the extensional mode has the property  $k_z \propto \omega$ , and because of assumption 1, the radial component of the wave vector for the slow wave, Eq. (A15) becomes  $\kappa_- = k_- = \sqrt{i\omega/C}$  independent of  $k_z$ . With these three reasonable assumptions, Gardner was able to derive a simple expression for the dispersion and the attenuation of the extensional mode. This expression has been used extensively to analyze experimental data on porous rods.<sup>12</sup>

As shown by Johnson and Kostek,<sup>6</sup> the subtle problem with the Gardner theory is that unless the permeability is small compared with a certain crossover value of permeability, approximation 3 is not a good one; the neglected terms are of the same order of importance, and have the same frequency dependence, as those which are retained. Let us consider this issue in the present instance. It is straightforward, if tedious, to implement the above mentioned approximations in the  $7 \times 7$  determinant described in the Appendix, as did Gardner for the problem of an isolated porous rod. The resulting expression is a quadratic equation in  $[k_z]^2$ , which is both messy and uninformative. If, however, we specialize to the case of a rigid porous mandrel, it is a simple matter to deduce the low-frequency characteristics of the slower, fluid-based mode. Equation (3) is unchanged. Instead of (6) we have

$$(1-x) \frac{\partial u}{\partial z} + \left[ \frac{1}{\mu_F} + \frac{1-x}{K_f} \right] P - 2\phi u_r(a^-) a/b^2 = 0, \quad (20)$$

where the displacement of the pore fluid is related to the pore pressure by Darcy's law

$$\phi \frac{\partial \mathbf{u}}{\partial t} = - \frac{\kappa_0}{\eta} \nabla P_f. \quad (21)$$

The pore pressure is governed by the slow wave in the low-frequency, stiff-frame limit:

$$P_f = P \frac{J_0(\kappa_- r)}{J_0(\kappa_- a)} e^{i(k_z z - \omega t)}, \quad (22)$$

where the normalization has been chosen to ensure continuity of pore pressure at  $r=a$ . To this point  $\kappa_-$  still has an implicit dependence on  $k_z$ , viz.,  $\kappa_- = \sqrt{i\omega/C - k_z^2}$ . The diffusivity of the slow wave, in the stiff frame limit, is,

$$C = \frac{\kappa_0 K_f}{\eta \phi}. \quad (23)$$

Self-consistency within Eqs. (20)–(22) requires

$$k_z^2 = \omega^2 \rho_f \left[ \frac{1}{K_f} + \frac{1}{(1-x)\mu_F} - \frac{2i\kappa_0 \kappa_- a J_1(\kappa_- a)}{\omega \eta (b^2 - a^2) J_0(\kappa_- a)} \right]. \quad (24)$$

Equation (24) is an implicit equation for  $k_z(\omega)$ . At this point, if we employ assumption 3, as did Gardner, we have an explicit solution:

$$k_z^2 = \omega^2 \rho_f \left[ \frac{1}{K_f} + \frac{1}{(1-x)\mu_F} + \frac{x}{1-x} \frac{\phi}{K_{fp}} \Theta(\sqrt{i\omega/Ca}) \right], \quad (25)$$

where

$$\Theta(y) = \frac{2J_1(y)}{yJ_0(y)}. \quad (26)$$

The essential physics of this result is that the frequency dependence is a reflection of whether the diffusion length of the slow wave  $\sqrt{C/\omega}$  is large or small compared to the mandrel size  $a$ .

As was discussed in Ref. 6 in the context of an isolated mandrel, Eq. (25) is an accurate approximation to (24) only if the permeability is small compared to a crossover permeability  $\kappa_{xc}$ . If the reverse is true,  $\kappa_0 \gg \kappa_{xc}$ , then the approximate theory is never a good approximation to the full theory, not even in the limit as the frequency tends to zero as we shall demonstrate. Employing, in the present instance, the same analysis as in Ref. 6 we find

$$\kappa_{xc} = \frac{\eta \phi V_T a}{\sqrt{8} K_f}, \quad (27)$$

where  $V_T$  is the (real-valued) tube wave phase speed in the zero frequency limit. Using the values of the parameters of Table II we have  $\kappa_{xc} = 1.0 \mu\text{m}^2$  which is small compared against the actual values. Therefore this Gardner-like theory is inapplicable to our experimental data, or even to the low-frequency extrapolation thereof.

Notwithstanding, it is informative to compare/contrast the modal characteristics implied by (25) against those of the full theory. We consider hypothetical cases for which the formation is steel and the mandrel is QF-20, as in Fig. 6, but with different values of the permeability, namely  $\kappa_0 = 0.01, 1.0, \text{ and } 100 \mu\text{m}^2$ . The results for the specific attenuation and the dispersion are plotted in Fig. 9(a) and (b), respectively. The solid curves represent the results of the full modal search theory while the dashed curves represent the results of the approximate theory, Eq. (25).

First, when  $\kappa_0 = 0.01 \mu\text{m}^2$  (the red curves) we see that there is very good agreement between the full theory and the approximate, (25), at low frequencies but not at high. [The relatively small difference between the two, in the vicinity of the low-frequency peak around 500 Hz, is due to the fact that QF-20 is not exactly rigid. We have verified that if the frame moduli are increased by a factor of 10, say, the full theory is virtually indistinguishable from (25).] By inspection of (25)

we see that it predicts that the dispersion and the specific attenuation are each a scaled function of frequency divided by permeability,  $1/Q = f(\omega/\kappa_0)$ , so that the peak position simply scales with  $\kappa_0$ ; as with the Gardner theory for a free rod,<sup>24</sup> the peak frequency is given by  $a\sqrt{\omega/C} = 2.5$ . Therefore this crossover frequency is given by

$$\omega^G = \frac{\kappa_0 K_f}{\eta \phi} \left( \frac{2.5}{a} \right)^2, \quad (28)$$

and it has a value  $\omega^G/2\pi = 5.7 \times 10^2$  Hz when the permeability is  $\kappa_0 = 0.01 \mu\text{m}^2$ , as is plainly seen in Fig. 9. As the frequency is increased the validity of the approximations that led to (25) breaks down. Eventually, the Biot theory itself crosses over into the high-frequency limit wherein the slow wave is propagatory, not diffusive. This crossover frequency is given by Eq. (18) and it has a value  $\omega^B/2\pi = 3.5$  MHz when the permeability is  $\kappa_0 = 0.01 \mu\text{m}^2$ , as is also plainly seen in Fig. 9, full theory. Obviously, (25) is not able to describe the modal properties in this frequency range.

As the permeability is increased, the lower-frequency peak, (28), increases whereas the high-frequency peak, (18), decreases. These peak frequencies coincide,  $\omega^G = \omega^B$ , when the permeability has a value given by (27), to within factors of order unity. It has the value, as we mentioned earlier, of  $1.0 \mu\text{m}^2$ . In Fig. 9(a) and (b) we show in green a comparison of the full theory and of the approximate theory; we see that the latter has only qualitative validity for this value of the permeability.

As the permeability is further increased, the Biot crossover frequency  $\omega^B$  continues to decrease. The Gardner crossover frequency  $\omega^G$  now has no meaning; for frequencies near this value the slow wave is no longer diffusive but it is propagatory. We demonstrate the situation in the blue curves of Fig. 9(a) and (b) with  $\kappa_0 = 100 \mu\text{m}^2$  for which  $\omega^B/2\pi = 3.5 \times 10^2$  Hz. Equation (28) is replaced by the condition that the wavelength of the slow wave is comparable to the radius of the mandrel, i.e., that the frequency be near the cutoff frequency implied by (17):

$$\omega_{co} = \frac{j_{0,1}}{S_{\text{slow}} a}. \quad (29)$$

The value of this frequency, 40 kHz, is independent of the permeability. It is abundantly clear that the approximate solution, (25), has no real validity in any frequency range because  $\kappa_0 \gg \kappa_{xc}$ . The attenuations predicted by the full theory and by the approximate theory have the same frequency dependence at low enough frequency,  $1/Q \propto \omega$ , but the former increases with increasing permeability while the latter decreases.

## IV. CONCLUSIONS

(1) Laboratory experiments, numerical modeling, and analytical low-frequency approximations have been conducted to investigate mandrel effects on tube waves. They are all in substantial agreement with each other for elastic as well as for poro-elastic mandrels. In all cases the requisite parameters were determined by independent measurements on the materials in question.

(2) The presence of a mandrel in a borehole results in slower tube waves than those propagating in the same borehole without the mandrel. On the other hand, the presence of a formation results in faster extensional modes in the mandrel than those propagating in the same mandrel without the formation

(3) These effects are greater with slower formation shear, larger mandrel, and more compliant mandrel. However, even when the ratio of radii is  $a/b=0.6$  there is only a modest effect on mode speeds in the quasistatic limit.

(4) The mandrel effect on the mode which is primarily fluid based is not equivalent to a reduced borehole size. This is because there are two coupled modes, each of which has a speed which depends intimately on the parameters of all components as well as the size ratios. There are two coupled modes which are (nearly) nondispersive, whether the mandrel is elastic or poro-elastic.

(5) The presence of a mandrel can create a more appreciable dispersion in the tube wave than without.

(6) A poro-elastic mandrel can cause all modes to have very enhanced attenuation. In the case of the tube wave it is essentially due to the coupling of the tube wave with the slow wave in the mandrel. The attenuation of the slow wave, in turn, is due to viscous dissipation within the pore fluid. Due to the attenuation mechanism inherent in the Biot theory, all modes have complicated dispersion and attenuation considered as functions of frequency. The picture is different depending upon whether the permeability is large or small compared to the crossover permeability,  $\kappa_{xc}$ .

## APPENDIX

We consider an azimuthally symmetric solution to the wave equation for which the radial and axial displacements,  $u_r$  and  $u_z$ , are functions of  $(r, z)$  only. In cylindrical coordinates the equations of motion are

$$\rho u_{r,tt} = \tau_{rr,r} + \tau_{rz,z} + \frac{1}{r} [\tau_{rr} - \tau_{\theta\theta}], \quad (A4)$$

$$\rho u_{z,tt} = \tau_{zr,r} + \tau_{zz,z} + \frac{1}{r} \tau_{zr},$$

where a comma denotes differentiation with respect to the variable that follows it. The elements of the stress tensor are

$$\begin{aligned} \tau_{rr} &= \lambda(u_{r,r} + u_r/r + u_{z,z}) + 2\mu u_{r,r}, \\ \tau_{zz} &= \lambda(u_{r,r} + u_r/r + u_{z,z}) + 2\mu u_{z,z}, \\ \tau_{\theta\theta} &= \lambda(u_{r,r} + u_r/r + u_{z,z}) + 2\mu u_r/r, \\ \tau_{rz} &= \mu(u_{r,z} + u_{z,r}), \\ \tau_{zr} &= \tau_{rz}, \end{aligned} \quad (A2)$$

and  $\lambda$  and  $\mu$  are the Lamè coefficients of the material in question.

In an elastic solid we write the displacement in terms of scalar and vector potentials:

$$\mathbf{u} = A \nabla \Phi + B \nabla \times (\Psi \hat{\theta}), \quad (A3)$$

where  $A$  and  $B$  are arbitrary constants, to be determined by the boundary conditions. In the elastic formation, which we suppose to extend to infinity,  $b < r < \infty$ , the waves correspond to outgoing cylindrical waves. Thus the potentials are given in terms of Hankel functions:

$$\Phi = H_0^{(1)}(\kappa_p r), \quad \Psi = H_1^{(1)}(\kappa_s r). \quad (A4)$$

(Henceforth, we presume a factor  $e^{i(k_z z - \omega t)}$  in all quantities.) The compressional and shear radial wave vectors are simply

$$\begin{aligned} \kappa_p &= \sqrt{(\omega/V_p)^2 - k_z^2}, \\ \kappa_s &= \sqrt{(\omega/V_s)^2 - k_z^2}, \end{aligned} \quad (A5)$$

where  $V_p$  and  $V_s$  are the compressional and shear speeds, respectively, in the elastic medium. A true normal mode of the system, one that is confined exponentially to the region of the borehole, must have  $\text{Im}[\kappa_p], \text{Im}[\kappa_s] > 0$ . This can happen only if the mode is slower than the formation shear. There are, however, physically relevant ‘‘pseudo-modes’’ which lose energy by radiating into either the shear or the shear and the compressional formation bulk modes. For these leaky waves we take  $\text{Im}[\kappa_{p,s}] > 0$ , as the case may be.

In the fluid-filled annular region  $a < r < b$  there is no shear component to the motion ( $\mu \equiv 0$ ) but there is an incoming as well as an outgoing wave:

$$\Phi = CH_0^{(1)}(\kappa_f r) + DH_0^{(2)}(\kappa_f r), \quad (A6)$$

where

$$\kappa_f = \sqrt{(\omega/V_f)^2 - k_z^2}. \quad (A7)$$

When the mandrel is an elastic solid the displacement in the region  $0 < r < a$  is given by an equation analogous to (A3):

$$\mathbf{u} = E \nabla \Phi + F \nabla \times (\Psi \hat{\theta}), \quad (A8)$$

but here the requirement is that the solution be regular at  $r = 0$ . Thus the potentials are written in terms of Bessel functions:

$$\Phi = J_0(\kappa_p r), \quad \Psi = J_1(\kappa_s r). \quad (A9)$$

Of course, the elastic constants in the mandrel are, generally, different from those of the outer formation. Thus  $\kappa_{p,s}$  are different in the two regions.

The coefficients  $A, B, C, D, E$ , and  $F$  are determined by the requirement that the boundary conditions be satisfied. At the outer radius these are continuity of radial displacement and continuity of radial and tangential stresses:

$$\begin{aligned} u_r(b^+) &= u_r(b^-), \\ \tau_{rr}(b^+) &= \tau_{rr}(b^-), \\ \tau_{rz}(b^+) &= 0. \end{aligned} \quad (A10)$$

Similarly at the inner radius we have

$$\begin{aligned} u_r(a^-) &= u_r(a^+), \\ \tau_{rr}(a^-) &= \tau_{rr}(a^+), \\ \tau_{rz}(a^-) &= 0. \end{aligned} \quad (A11)$$

It is straightforward, if tedious, to express these boundary conditions in terms of the to-be-determined constants  $A$ – $F$  by means of (A2)–(A9). The coefficients depend on  $\omega$  and  $k_z$  through the appropriate Bessel and Hankel functions. The resulting six homogeneous equations in six unknown amplitudes can have a nontrivial solution if and only if the determinant of the matrix of coefficients vanishes. We employ a numerical search routine to find the lowest-order solutions  $k_z(\omega)$ . In the case of an elastic mandrel,  $k_z$  is real-valued for propagating modes. In the case of the pseudo-modes,  $k_z$  can have a small, positive imaginary part, as discussed in the text.

When the mandrel is a porous fluid-saturated solid, the displacements in the region  $0 < r < a$  are treated in an analogous manner except that the Biot theory is employed so that the displacement of the solid and the fluid components are followed separately and on an equal footing. Our formalism is quite similar to that of Ref. 10. The displacement of the solid component is expressed as

$$\mathbf{u} = H\nabla\Phi_+ + K\nabla\Phi_- + L\nabla\times(\Psi\hat{\theta}), \quad (\text{A12})$$

while that of the fluid is

$$\mathbf{U} = HG_+\nabla\Phi_+ + KG_-\nabla\Phi_- + LG_{sh}\nabla\times(\Psi\hat{\theta}). \quad (\text{A13})$$

$\Phi_+$  is the contribution due to the fast compressional wave,  $\Phi_-$  is that due to the slow compressional wave, and  $\Psi$  is that due to the shear wave. The factors  $G_{\pm}$  and  $G_{sh}$  are known functions of frequency, as given in Ref. 10.  $H$ ,  $K$ , and  $L$  are constants to be determined through the boundary conditions. Since the solution must be regular at the origin, we have

$$\Phi_{\pm} = J_0(\kappa_{\pm}r), \quad \Psi = J_1(\kappa_{sh}r), \quad (\text{A14})$$

where

$$\kappa_{\pm} = \sqrt{k_{\pm}^2 - k_z^2}, \quad \kappa_{sh} = \sqrt{k_{sh}^2 - k_z^2}. \quad (\text{A15})$$

The wave numbers of the fast, slow, and shear waves,  $k_{\pm}$  and  $k_{sh}$  are determined by solving the Biot equations, as described by Ref. 10. In terms of these displacements, the stress tensor due to the fluid component  $\tau^f$  and that due to the solid  $\tau^s$  are readily calculated. [Equations (C-5a) and (C-5b) of Ref. 10.] Boundary conditions (A10) are still relevant but instead of (A11) we now have continuity of fluid

$$\phi U_r(a^-) + (1 - \phi)u_r(a^-) = u_r(a^+), \quad (\text{A16})$$

continuity of total stress

$$\begin{aligned} \tau_{rr}^s(a^-) + \tau_{rr}^f(a^-) &= \tau_{rr}(a^+), \\ \tau_{rz}^s(a^-) + \tau_{rz}^f(a^-) &= 0, \end{aligned} \quad (\text{A17})$$

and continuity of pore pressure

$$\tau_{rr}^f(a^-)/\phi = \tau_{rr}(a^+). \quad (\text{A18})$$

This last follows from our assumption of the open pore boundary condition as discussed in Ref. 10 and others. We now have seven homogeneous equations (A10) and (A16)–(A18), in seven unknowns  $A$ ,  $B$ ,  $C$ ,  $D$ ,  $H$ ,  $K$ ,  $L$ . The requisite wave number  $k_z(\omega)$  is determined numerically, as before. Because the Biot equations admit of a dissipative

mechanism due to the flow of a viscous fluid,  $k_z$  is complex valued. We express the solutions as  $k_z = \omega s(\omega) + i\gamma(\omega)$  wherein  $s$  is the phase slowness and  $\gamma$  is the attenuation.

<sup>1</sup>L. Tsang and D. Rader, "Numerical evaluation of the transient acoustic waveform due to a point source in a fluid-filled borehole," *Geophysics* **44**, 1706–1720 (1979).

<sup>2</sup>A. L. Kurkjian and S. K. Chang, "Acoustic multipole sources in fluid-filled boreholes," *Geophysics* **51**, 148–163 (1986).

<sup>3</sup>X. M. Tang and C. H. Cheng, "Effects of a logging tool on the Stoneley waves in elastic and porous boreholes," *Log Analyst* **34**, 46–56 (1993).

<sup>4</sup>L. L. Scharf, *Signal Processing: Detection, Estimation, and Time Series Analysis* (Addison-Wesley, New York, 1991), p. 407.

<sup>5</sup>K. W. Winkler, H.-L. Liu, and D. L. Johnson, "Permeability and borehole Stoneley waves: Comparison between experiment and theory," *Geophysics* **54**, 66–75 (1989).

<sup>6</sup>D. L. Johnson and S. Kostek, "A limitation of the Biot–Gardner theory of extensional waves in fluid-saturated cylinders," *J. Acoust. Soc. Am.* **97**, 741–744 (1995).

<sup>7</sup>D. L. Johnson, T. J. Plona, and H. Kojima, "Probing porous media with first and second sound. II. Acoustic properties of water-saturated porous media," *J. Appl. Phys.* **76**, 115–125 (1994).

<sup>8</sup>P. M. Morse and K. U. Ingard, *Theoretical Acoustics* (McGraw-Hill, New York, 1968), p. 509 ff.

<sup>9</sup>D. P. Schmitt, M. Bouchon, and G. Bonnet, "Full-wave synthetic acoustic logs in radially semiinfinite saturated porous media," *Geophysics* **53**, 807–823 (1988).

<sup>10</sup>S. K. Chang, H.-L. Liu, and D. L. Johnson, "Low-frequency tube waves in permeable rocks," *Geophysics* **53**, 519–527 (1988).

<sup>11</sup>H.-L. Liu, "Borehole modes in a cylindrical fluid-saturated permeable medium," *J. Acoust. Soc. Am.* **84**, 424–431 (1988).

<sup>12</sup>R. Mörig and H. Burkhardt, "Experimental evidence for the Biot–Gardner theory," *Geophysics* **54**, 524–527 (1989).

<sup>13</sup>A. N. Norris, "Stoneley-wave attenuation and dispersion in permeable formations," *Geophysics* **54**, 330–341 (1989).

<sup>14</sup>D. L. Johnson and C.-J. Hsu (unpublished).

<sup>15</sup>E. W. Peterson, "Acoustic wave propagation along a fluid-filled cylinder," *J. Appl. Phys.* **45**, 3340–3350 (1973); L. J. Baker, "The effect of the invaded zone on full wavetrain acoustic logging," *Geophysics* **49**, 796–809 (1984); S. W. Lang, A. L. Kurkjian, J. H. McClellan, C. F. Morris, and T. W. Parks, "Estimating slowness dispersion from arrays of sonic logging waveforms," *ibid.* **52**, 530–544 (1987).

<sup>16</sup>B. K. Sinha, T. J. Plona, S. Kostek, and S.-K. Chang, "Axisymmetric wave propagation in fluid-loaded cylindrical shell I: Theory," *J. Acoust. Soc. Am.* **92**, 1132–1143 (1992); T. J. Plona, B. K. Sinha, S. Kostek, and S.-K. Chang, "Axisymmetric wave propagation in fluid-loaded cylindrical shell II: Theory versus experiment," *ibid.* **92**, 1144–1155 (1992).

<sup>17</sup>J. G. Scholte, "On the large displacements commonly regarded as caused by Love-waves and similar dispersive surface-waves," *Proc. K. Ned. Akad. Wet.* **51**, 533–543 (1948); *ibid.* **51**, 624–649 (1948); *ibid.* **51**, 828–835 (1948); *ibid.* **51**, 969–976 (1948); E. Strick and A. S. Ginzburg, "Stoneley-wave velocities for a fluid-solid interface," *Bull. Seismol. Soc. Am.* **46**, 281–292 (1956); J. H. Ansell, "The roots of the Stoneley wave equation for solid-liquid interfaces," *PAGEOPH* **94**, 172–188 (1972).

<sup>18</sup>M. Schoenberg and T. L. Marzetta, "Tube and casing waves in unbonded cased boreholes," *Proceedings of the 1st International Congress (Brazilian Geophysical Society, Rio de Janeiro, 1989)*.

<sup>19</sup>J. E. White, *Underground Sound* (Elsevier, Amsterdam, 1983).

<sup>20</sup>A. N. Norris, "The speed of a tube wave," *J. Acoust. Soc. Am.* **87**, 414–417 (1990).

<sup>21</sup>D. L. Johnson, D. L. Hemmick, and H. Kojima, "Probing porous media with first and second sound. I. Dynamic permeability," *J. Appl. Phys.* **76**, 104–114 (1994).

<sup>22</sup>D. L. Johnson and T. J. Plona, "Acoustic slow waves and the consolidation transition," *J. Acoust. Soc. Am.* **72**, 556–565 (1982).

<sup>23</sup>J. G. Berryman, "Dispersion of extensional waves in fluid-saturated porous cylinders at ultrasonic frequencies," *J. Acoust. Soc. Am.* **74**, 1805–1812 (1983).

<sup>24</sup>G. H. F. Gardner, "Extensional waves in fluid-saturated porous cylinders," *J. Acoust. Soc. Am.* **34**, 36–40 (1962).

# Oblique coherent waves inside and outside a randomly cracked elastic solid

Y. C. Angel and A. Bolshakov<sup>a)</sup>

Department of Mechanical Engineering and Materials Science, Rice University, MS 321, 6100 Main Street, Houston, Texas 77005-1892

(Received 17 February 1997; accepted for publication 15 August 1997)

Propagation of antiplane waves in an elastic solid that contains a cracked slab region is investigated. The cracks have a uniform probability density in the slab region, are parallel to the boundaries of the slab, and the solid is uncracked on either side of the slab. When an antiplane wave is obliquely incident on the cracks, it is shown that the average (coherent) motion in the solid is governed by a pair of integral equations. This result is obtained by taking an average of the exact system of equations for  $N$  nonintersecting cracks and by letting  $N$  tend to infinity keeping the crack density constant. Then, it is assumed that the average exciting stress near a fixed crack is equal to the average coherent stress, and it is shown that the pair of integral equations yields simple analytical formulas for the complex-valued wave number and the refracted waves inside the slab as well as for the wave amplitudes outside the slab. These quantities depend on incident angle, crack density, frequency, and slab thickness. Numerical results, which are valid for small values of the crack density, are presented as functions of frequency and incident angle. © 1997 Acoustical Society of America. [S0001-4966(97)00712-1]

PACS numbers: 43.20.Bi, 43.20.Fn, 43.20.Jr, 43.35.Cg [ANN]

## INTRODUCTION

Sound waves are a powerful tool to evaluate material properties, to detect and characterize flaws in solids, and to explore geophysical formations. These applications have motivated many analytical investigations in the area of elastic wave propagation through solids containing randomly distributed inhomogeneities.

Analytical predictions for multiple scattering by inclusions of various types have been obtained by McCarthy and Carroll,<sup>1</sup> Varadan *et al.*,<sup>2</sup> Kerr,<sup>3</sup> and Bose.<sup>4</sup> In the case of cracks, one can refer to Kikuchi,<sup>5,6</sup> Mikata and Achenbach,<sup>7</sup> Angel and Achenbach,<sup>8</sup> Zhang and Achenbach,<sup>9</sup> Zhang and Gross,<sup>10,11</sup> Angel and Koba,<sup>12</sup> Kawahara and Yamashita,<sup>13</sup> Smyshlyaev *et al.*,<sup>14</sup> Eriksson *et al.*,<sup>15</sup> Mikata,<sup>16</sup> Smyshlyaev and Willis,<sup>17</sup> Angel and Koba,<sup>18</sup> and other authors therein.

The problem of evaluating the average (coherent) motion in a solid containing randomly distributed inhomogeneities is very complex. In the references cited above, physically related assumptions, which limit the range of validity of the predictions and which are not always fully understood, have been necessary to obtain numerical results. It is often assumed that: (i) the average forward motion can be represented by a complex-valued wave number, (ii) the average backward motion is negligible, and (iii) the distribution of inhomogeneities is dilute.

In a recent work, Angel and Koba<sup>18</sup> derived governing equations of general validity for the multiple scattering of normally incident antiplane waves on a cracked slab. These equations show that, once the average exciting field near a fixed crack is chosen, then the average total motion is com-

pletely determined everywhere in the solid. In particular, the exciting field determines whether or not the average forward motion can be represented by a complex-valued wave number. Further, the exciting field determines the average backward motion and places bounds on the concentration of inhomogeneities. Thus, a single assumption on the form of the exciting field yields many important results.

As a special case, Angel and Koba<sup>18</sup> assume as in Foldy<sup>19</sup> that the average total and exciting fields near a fixed crack are equal. Then, the governing equations yield simple explicit expressions for the complex-valued wave number and the backward and forward motions everywhere in the cracked solid.

In this paper, we show that the method developed by Angel and Koba<sup>18</sup> can be generalized to the case of oblique incidence. In particular, we obtain simple formulas for the complex-valued wave number, the reflection coefficient, and the transmission coefficient in terms of the incident angle.

In Section I, we consider an unbounded elastic solid with a slab region containing a random distribution of cracks. The cracks are identical and parallel to the boundaries of the slab, and an oblique antiplane wave is incident on the cracks. We obtain equations for the average total displacement in the solid in terms of the average scattered displacement corresponding to a fixed crack. In Sec. II, we invoke the translational symmetry along the infinite length of the cracked slab, which allows us to simplify the equations of Sec. I. The average total displacement in the solid is now governed by Eqs. (34)–(36).

In Section III, we examine Eqs. (34)–(36) in the special case where the average exciting stress near a fixed crack is equal to the average total stress. Then, we find that there is a forward and a backward motion that propagate in the cracked region with complex-valued wave numbers  $\pm K$ , where  $K$

<sup>a)</sup>Currently at Baker Hughes INTEQ, P.O. Box 670968, Houston, TX 77267-0968.

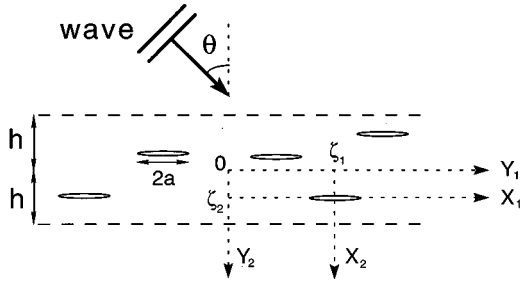


FIG. 1. Obliquely incident antiplane wave on a cracked slab of thickness  $2h$ .

depends on frequency, crack density, and incident angle. We also obtain formulas for the velocity, attenuation, and refraction angle in the slab. Outside the slab, we find that the transmission and reflection coefficients are given by Eqs. (56) and (57), respectively. The limits of these quantities are examined. It is shown, in particular, that our numerical results are valid only for small values of the crack density not greater than  $1/\pi$ .

Section IV contains a discussion of the numerical method of solution and of the results. Plots for the velocity, attenuation, and refraction angle inside the slab, as well as for the reflection and transmission coefficients, are presented as functions of frequency and incident angle.

## I. FORMULATION AND PRELIMINARIES

We consider a linearly elastic, homogeneous, and isotropic solid that contains a uniform distribution of parallel cracks, as shown in Fig. 1. The cracks have width  $2a$ , lie in planes orthogonal to the  $(y_1, y_2)$  plane, extend to infinity in the  $\pm y_3$  directions, and their centers are uniformly distributed in the open slab  $V_\infty^h$  of width  $2h$  defined by

$$V_\infty^h = \{(y_1, y_2) \in \mathbb{R}^2: |y_1| < \infty, |y_2| < h\}. \quad (1)$$

We define  $\zeta$  to be the position vector of a crack center and we attach a system of orthogonal axes  $(x_1, x_2)$  at  $\zeta$ . The transformation of coordinates from the  $(y_1, y_2)$  system to the  $(x_1, x_2)$  system is given by

$$x_1 = y_1 - \zeta_1, \quad (2)$$

$$x_2 = y_2 - \zeta_2, \quad (3)$$

where  $\zeta_1$  and  $\zeta_2$  are the coordinates of  $\zeta$  in the  $(y_1, y_2)$  system, and  $|\zeta_2| < h$ . The speed  $c_T$  and the slowness  $s_T$  of transverse waves in the uncracked solid are given by

$$c_T^2 = \mu/\rho, \quad s_T = 1/c_T, \quad (4)$$

where  $\rho$  and  $\mu$  are the mass density and the shear modulus of the solid. An incident antiplane wave propagates toward the cracks at an angle  $\theta$  relative to the  $y_2$  axis. The displacement  $u^{\text{inc}}$ , which is in the  $y_3$  direction, is given by

$$u^{\text{inc}}(y_1, y_2) = u_0 \exp[ik(y_1 \sin \theta + y_2 \cos \theta)], \quad (5)$$

$$k = \omega s_T,$$

where the time-harmonic factor,  $\exp(-i\omega t)$ , is omitted. In (5),  $u_0$  is the amplitude,  $\omega$  is the frequency, and  $\theta$  varies in the range  $0 \leq \theta < \pi/2$ .

The incident wave (5) is subjected to multiple reflections between the cracks. We omit throughout this work the factor  $\exp(-i\omega t)$ , which is common to all field variables in a steady-state regime.

Since the distribution of cracks is uniform, the number  $n$  of cracks per unit area in  $V_\infty^h$  is constant on average. Next, we define the open rectangle  $V_N^h$  by

$$V_N^h = \left\{ (y_1, y_2) \in \mathbb{R}^2: |y_1| < \frac{N}{4hn}, |y_2| < h \right\}, \quad (6)$$

where  $N$  is an integer. The rectangle  $V_N^h$  has area  $N/n$  and contains  $N$  cracks on average. Also,  $V_N^h$  is contained in  $V_\infty^h$  and approaches  $V_\infty^h$  as  $N$  approaches infinity.

We first consider the case in which the wave (5) is incident on  $N$  cracks that occupy distinct deterministic positions in the rectangle  $V_N^h$ . In this case, the total displacement  $u^T$  in the solid is represented in terms of the incident displacement  $u^{\text{inc}}$  and of the displacements  $\bar{u}^{\text{sc}}$  scattered by the  $N$  cracks in the form

$$u^T(y_1, y_2 | \Lambda^N) = u^{\text{inc}}(y_1, y_2) + \sum_{i=1}^N \bar{u}^{\text{sc}}(y_1, y_2; \zeta^i | \Lambda^N), \quad (7)$$

where  $\Lambda^N = (\zeta^1, \dots, \zeta^N)$  denotes the configuration of cracks in the rectangle  $V_N^h$ , and the center position  $\zeta^i$  after the semicolon is used to label the displacement scattered by the  $i$ th crack. We define the exciting displacement  $\bar{u}^E$  on the  $i$ th crack as the total displacement minus the  $i$ th scattered displacement. Thus, one has

$$\bar{u}^E(y_1, y_2; \zeta^i | \Lambda^N) = u^T(y_1, y_2 | \Lambda^N) - \bar{u}^{\text{sc}}(y_1, y_2; \zeta^i | \Lambda^N). \quad (8)$$

On the  $i$ th crack we attach a system of coordinates  $(x_1^i, x_2^i)$  such that the transformation of coordinates from the  $(y_1, y_2)$  system to the  $(x_1^i, x_2^i)$  system is given by (2) and (3), with a superscript  $i$  attached to the  $x$  and  $\zeta$  variables. Then, to each quantity  $\bar{\mathcal{U}}$  (where  $\bar{\mathcal{U}}$  represents any displacement or stress component) we associate a quantity  $\mathcal{U}$  such that

$$\mathcal{U}(x_1^i, x_2^i; \zeta^i | \Lambda^N) = \bar{\mathcal{U}}(y_1, y_2; \zeta^i | \Lambda^N). \quad (9)$$

Next, we assume that the  $N$  cracks are randomly and uniformly distributed with constant number density  $n$  in the rectangle  $V_N^h$  of (6). In addition, we assume that the  $N$  parallel cracks have no points of contact and that they are exchangeable. Then, we can define a probability density function  $p: \Omega^{2N} \rightarrow \mathbb{R}$ , where  $\Omega^{2N}$  is the  $N$ -fold Cartesian product of  $V_N^h$ , such that the partial integral of  $p$  over the  $(N-1)$ -fold Cartesian product  $\Omega^{2N-2}$  is equal to  $n/N$ . Further, the integral of  $p$  over  $\Omega^{2N}$  is equal to unity. Under these conditions, the average  $\langle \bar{\mathcal{U}} \rangle_N$  of the quantity  $\bar{\mathcal{U}}$  for the  $i$ th crack is independent of the index  $i$  of the crack and is given in terms of the partial average  $\langle \bar{\mathcal{U}} \rangle_{N-1}$  by

$$\langle \bar{\mathcal{U}} \rangle_N(y_1, y_2) = \frac{n}{N} \int_{V_N^h} \langle \bar{\mathcal{U}} \rangle_{N-1}(y_1, y_2; \zeta) d\zeta. \quad (10)$$

In Eq. (10), the partial average  $\langle \bar{\mathcal{U}} \rangle_{N-1}$  is defined as the integral over the region  $\Omega^{2N-2}$  of  $\bar{\mathcal{U}}$  times  $(N/n)p$ .

The average total displacement  $\langle u^T \rangle_N$  in the solid is obtained by multiplying (7) by  $p$ , integrating over  $\Omega^{2N}$ , and using (10). The result is

$$\langle u^T \rangle_N(y_1, y_2) = u^{\text{inc}}(y_1, y_2) + n \int_{V_N^h} \langle \bar{u}^{\text{sc}} \rangle_{N-1}(y_1, y_2; \boldsymbol{\zeta}) d\boldsymbol{\zeta}. \quad (11)$$

In the following, we take the limit of (11) as the number  $N$  of cracks tends to infinity. In the limit, there is an infinite number of cracks that are randomly and uniformly distributed with constant number density  $n$  in the rectangle  $V_\infty^h$  of (1). We assume that  $\langle u^T \rangle_N$  and  $\langle \bar{\mathcal{U}} \rangle_{N-1}$  have limits as  $N$  tends to infinity for fixed values of the coordinates  $(y_1, y_2)$  and of the crack center position  $\boldsymbol{\zeta}$ , and we define these limits by

$$\langle u^T \rangle_\infty(y_1, y_2) = \lim_{N \rightarrow \infty} \langle u^T \rangle_N(y_1, y_2), \quad (12)$$

$$\langle \bar{\mathcal{U}} \rangle_\infty(y_1, y_2; \boldsymbol{\zeta}) = \lim_{N \rightarrow \infty} \langle \bar{\mathcal{U}} \rangle_{N-1}(y_1, y_2; \boldsymbol{\zeta}). \quad (13)$$

We also assume that the limit  $\langle \bar{u}^{\text{sc}} \rangle_\infty$  is reached uniformly with respect to the position  $\boldsymbol{\zeta}$  in each finite rectangle contained in  $V_\infty^h$ . It follows that the limit and integration operations can be interchanged in the integral of (11). Thus, using (12) and (13), one finds that the limit of (11) is given by

$$\langle u^T \rangle_\infty(y_1, y_2) = u^{\text{inc}}(y_1, y_2) + n \int_{V_\infty^h} \langle \bar{u}^{\text{sc}} \rangle_\infty(y_1, y_2; \boldsymbol{\zeta}) d\boldsymbol{\zeta}. \quad (14)$$

We recall that, for  $N$  cracks occupying deterministic positions in  $V_N^h$ , one can write  $N$  Helmholtz differential equations for the  $N$  scattered displacements  $u^{\text{sc}}$ . There are also  $N$  boundary conditions, which impose the vanishing of the total stress  $\sigma_{23}$  on the  $N$  crack faces and the vanishing of the scattered displacement of order  $i$  ( $i = 1, \dots, N$ ) in the plane  $x_2^i = 0$  for  $|x_1^i| \geq a$ . If for each  $i$  we multiply these equations by  $(N/n)p$  and integrate over the region  $\Omega^{2N-2}$ , keeping the  $i$ th crack position fixed, and assuming that the integration and the differentiations can be interchanged, we obtain  $N$  identical differential equations and  $N$  identical boundary conditions. Thus, eliminating the unnecessary superscript  $i$ , we can denote by  $\boldsymbol{\zeta}$  the position of a fixed crack and by  $(x_1, x_2)$  the axes attached to the fixed crack. In the limit as  $N \rightarrow \infty$ , assuming that the limit operation and the differentiations can be interchanged, we find that the Helmholtz differential equation is

$$\langle u^{\text{sc}} \rangle_{\infty, \alpha\alpha}(x_1, x_2; \boldsymbol{\zeta}) + k^2 \langle u^{\text{sc}} \rangle_\infty(x_1, x_2; \boldsymbol{\zeta}) = 0, \quad x_2 > 0, \quad (15)$$

where the derivatives are taken with respect to  $x_1$  and  $x_2$  and a summation is implied over the repeated index  $\alpha$ . In (15), the average scattered displacement  $\langle u^{\text{sc}} \rangle_\infty$  is defined by using (13) and the coordinate transformation (2) and (3). The general formula is

$$\begin{aligned} \langle \mathcal{U} \rangle_\infty(x_1, x_2; \boldsymbol{\zeta}) &= \langle \mathcal{U} \rangle_\infty(y_1 - \zeta_1, y_2 - \zeta_2; \boldsymbol{\zeta}) \\ &= \langle \bar{\mathcal{U}} \rangle_\infty(y_1, y_2; \boldsymbol{\zeta}). \end{aligned} \quad (16)$$

The boundary conditions for the average scattered displacement are given in terms of the average exciting displacement  $\langle u^E \rangle_\infty$  by

$$\begin{aligned} \frac{\partial}{\partial x_2} \langle u^{\text{sc}} \rangle_\infty(x_1, x_2; \boldsymbol{\zeta}) \Big|_{x_2=0^+} \\ = - \frac{\partial}{\partial x_2} \langle u^E \rangle_\infty(x_1, x_2; \boldsymbol{\zeta}) \Big|_{x_2=0}, \quad |x_1| < a, \end{aligned} \quad (17)$$

$$\langle u^{\text{sc}} \rangle_\infty(x_1, 0; \boldsymbol{\zeta}) = 0, \quad |x_1| \geq a. \quad (18)$$

In (17), the average exciting displacement is obtained by using (8), (13), and (16).

## II. PROBABILISTIC SLAB PROBLEM

Since the slab extends to infinity in the  $\pm y_1$  directions with boundaries parallel to the  $y_1$  axis, and has a uniform distribution of cracks, it follows that the total displacement  $\langle u^T \rangle_\infty(y_1, y_2)$  has the same dependence on  $y_1$  as the incident displacement  $u^{\text{inc}}(y_1, y_2)$ . Thus, we write

$$\langle u^T \rangle_\infty(y_1, y_2) = \langle u^T \rangle_\infty(y_2) \exp(iky_1 \sin \theta). \quad (19)$$

The translational invariance (19) is similar to that used by Angel and Achenbach<sup>20</sup> in the case of obliquely incident Rayleigh waves on a surface-breaking crack. Because of the translational invariance, the values taken by any average quantity at  $(x_1, x_2)$  for a crack fixed at  $(\zeta_1 + q, \zeta_2)$  and for a crack fixed at  $(\zeta_1, \zeta_2)$  differ only by a factor  $\exp(ikq \sin \theta)$ , for all real numbers  $q$ . Thus, we write

$$\langle \mathcal{U} \rangle_\infty(x_1, x_2; \zeta_1, \zeta_2) = \langle \mathcal{U} \rangle_\infty(x_1, x_2; \zeta_2) \exp(ik\zeta_1 \sin \theta). \quad (20)$$

Likewise, the values taken by any average quantity at  $(y_1 + q, y_2)$  for a crack fixed at  $\boldsymbol{\zeta} + q\mathbf{e}_1$  and at  $(y_1, y_2)$  for a crack fixed at  $\boldsymbol{\zeta}$  differ only by a factor  $\exp(ikq \sin \theta)$ , for all real numbers  $q$ . Thus, one has

$$\langle \bar{\mathcal{U}} \rangle_\infty(y_1, y_2; \boldsymbol{\zeta}) = \langle \bar{\mathcal{U}} \rangle_\infty(0, y_2; \boldsymbol{\zeta} - y_1\mathbf{e}_1) \exp(iky_1 \sin \theta), \quad (21)$$

where  $\mathbf{e}_1$  is a unit vector attached to the  $y_1$  axis. Substituting (19) and (21) into (14) and changing the  $\zeta_1$  integration variable that runs along the entire real axis, one finds that

$$\langle u^T \rangle_\infty(y_2) = u^{\text{inc}}(y_2) + n \int_{V_\infty^h} \langle \bar{u}^{\text{sc}} \rangle_\infty(0, y_2; \boldsymbol{\zeta}) d\boldsymbol{\zeta}, \quad (22)$$

where  $u^{\text{inc}}(y_2)$  is given by

$$u^{\text{inc}}(y_2) = u_0 \exp(iky_2 \cos \theta). \quad (23)$$

We now use the correspondence (16) and the translational property (20) to infer that

$$\begin{aligned} \langle \bar{u}^{\text{sc}} \rangle_\infty(y_1, y_2; \zeta_1, \zeta_2) &= \langle u^{\text{sc}} \rangle_\infty(y_1 - \zeta_1, y_2 - \zeta_2; \zeta_2) \\ &\quad \times \exp(ik\zeta_1 \sin \theta). \end{aligned} \quad (24)$$



Substituting (24) into (22) with  $y_1=0$ , we find that the average total displacement has the form

$$\langle u^T \rangle_\infty(y_2) = u^{\text{inc}}(y_2) + n \int_{V_\infty^h} \langle u^{\text{sc}} \rangle_\infty(-\zeta_1, y_2 - \zeta_2; \zeta_2) \exp(ik\zeta_1 \sin \theta) d\zeta. \quad (25)$$

Substituting (20) into the differential equation (15) and the boundary conditions (17) and (18), one has

$$\langle u^{\text{sc}} \rangle_{\infty, \alpha\alpha}(x_1, x_2; \zeta_2) + k^2 \langle u^{\text{sc}} \rangle_\infty(x_1, x_2; \zeta_2) = 0, \quad x_2 > 0, \quad (26)$$

$$\left. \frac{\partial}{\partial x_2} \langle u^{\text{sc}} \rangle_\infty(x_1, x_2; \zeta_2) \right|_{x_2=0^+} = - \left. \frac{\partial}{\partial x_2} \langle u^{\text{E}} \rangle_\infty(x_1, x_2; \zeta_2) \right|_{x_2=0}, \quad |x_1| < a. \quad (27)$$

$$\langle u^{\text{sc}} \rangle_\infty(x_1, 0; \zeta_2) = 0, \quad |x_1| \geq a. \quad (28)$$

Notice that Eqs. (26)–(28) are identical to those obtained by Angel and Koba<sup>18</sup> for the case of normal incidence, but here they are valid only when the crack is fixed at  $\zeta_1=0$ ; in the case of normal incidence, they are valid for any value of  $\zeta_1$ .

By taking the Fourier transform of (26) with respect to the  $x_1$  variable, solving the resulting ordinary differential equation, and using the boundary condition (28), one can obtain as in Angel<sup>21</sup> an integral representation for the displacement  $\langle u^{\text{sc}} \rangle_\infty$ . The result, which corresponds to a wave motion that propagates away from the crack, can be written as

$$\langle u^{\text{sc}} \rangle_\infty(x_1, x_2; \zeta_2) = \frac{\text{sgn}(x_2)}{2\pi} \int_{-\infty}^{\infty} \left\{ \int_{-a}^a \langle u^{\text{sc}} \rangle_\infty(\nu, 0^+; \zeta_2) \times L(x_1 - \nu, x_2, \xi) d\nu \right\} d\xi. \quad (29)$$

In (29), the sign function shows the antisymmetry of  $\langle u^{\text{sc}} \rangle_\infty$  with respect to the  $x_1$  axis and the integrand  $L$  is given by

$$L(x_1, x_2, \xi) = \exp(-i\xi x_1) \exp(-\beta|x_2|), \quad (30)$$

where  $\beta$  is defined by

$$\beta^2 = \xi^2 - k^2, \quad \text{Im}(\beta) \leq 0, \quad \text{Re}(\beta) \geq 0. \quad (31)$$

Now, substituting (29) into (25), performing the  $\zeta_1$  integration from  $-X$  to  $X$ , where  $X$  is a large number, and using the localization lemma (Sneddon<sup>22</sup>) to obtain the limit as  $X \rightarrow \infty$ , we find that  $\langle u^T \rangle_\infty$  is given by

$$\langle u^T \rangle_\infty(y_2) = u^{\text{inc}}(y_2) + n \int_{-h}^h \left\{ \int_{-a}^a \langle u^{\text{sc}} \rangle_\infty(\nu, 0^+; \zeta_2) \times \exp(-ik\nu \sin \theta) d\nu \right\} \text{sgn}(y_2 - \zeta_2) \times \exp(ik|y_2 - \zeta_2| \cos \theta) d\zeta_2. \quad (32)$$

We can now define a function  $b$  in the interval  $(-a, a) \times (-h, h)$  such that

$$\langle u^{\text{sc}} \rangle_\infty(x_1, 0^+; \zeta_2) = \begin{cases} \int_{-a}^{x_1} b(\nu; \zeta_2) d\nu, & |x_1| < a, \\ 0, & |x_1| \geq a, \end{cases} \quad (33)$$

together with

$$\int_{-a}^a b(\nu; \zeta_2) d\nu = 0. \quad (34)$$

In Eqs. (33) and (34), the parameter  $\zeta_2$  is such that  $|\zeta_2| < h$ . Substituting (33) inside the integral (32), interchanging the integration order, and using (34), we obtain

$$\langle u^T \rangle_\infty(y_2) = u^{\text{inc}}(y_2) - \frac{in}{k \sin \theta} \int_{-h}^h \left\{ \int_{-a}^a b(\nu; \zeta_2) \times \exp(-ik\nu \sin \theta) d\nu \right\} \text{sgn}(y_2 - \zeta_2) \times \exp(ik|y_2 - \zeta_2| \cos \theta) d\zeta_2. \quad (35)$$

In the limit as  $\theta \rightarrow 0$ , it can be shown by using (34) that (35) yields the same expression as that obtained by Angel and Koba<sup>18</sup> for the case of normal incidence.

Using the boundary condition (27) and the representations (29) and (33), we can show, as in Angel,<sup>21</sup> that the function  $b$  satisfies the singular integral equation

$$\int_{-a}^a b(\nu; \zeta_2) \left[ \frac{1}{\nu - x_1} + S(\nu - x_1) \right] d\nu = -\pi \left. \frac{\partial}{\partial x_2} \langle u^{\text{E}} \rangle_\infty(x_1, x_2; \zeta_2) \right|_{x_2=0}, \quad |x_1| < a, \quad (36)$$

where the function  $S$  is given by

$$S(x) = \int_0^\infty \left( \frac{\beta}{\xi} - 1 \right) \sin(\xi x) d\xi. \quad (37)$$

If the average exciting displacement  $\langle u^{\text{E}} \rangle_\infty$  were known near a fixed crack, (35) and (36) could be viewed as a pair of coupled integrodifferential equations for  $\langle u^T \rangle_\infty$  and  $b$ . The solution of these equations would be valid for all frequencies and all densities of non-intersecting cracks.

### III. COMPLEX-VALUED WAVE NUMBER

We now assume that, in a small neighborhood of a fixed crack, the average exciting displacement is equal to the average total displacement. Thus, using (16), (19), (20), and the coordinate transformation (2) and (3), one has

$$\begin{aligned} \langle u^{\text{E}} \rangle_\infty(x_1, x_2; \zeta_2) &= \langle \bar{u}^{\text{E}} \rangle_\infty(y_1, y_2; 0, \zeta_2) \\ &= \langle \bar{u}^{\text{E}} \rangle_\infty(x_1, x_2 + \zeta_2; 0, \zeta_2) \\ &= \langle u^T \rangle_\infty(x_1, x_2 + \zeta_2) \\ &= \langle u^T \rangle_\infty(x_2 + \zeta_2) \exp(ikx_1 \sin \theta). \end{aligned} \quad (38)$$

In Eq. (38), the third equality follows from the assumption that the exciting and total displacements are equal. It follows from Eqs. (36) and (38) that the ratio of  $b(\nu; \zeta_2)$  to  $\langle u^T \rangle'_\infty(\zeta_2)$ , where the prime superscript denotes the deriva-

tive, does not depend on  $\zeta_2$ . Thus we define a function  $b$  that depends only on  $\nu$  such that

$$b(\nu; \zeta_2) = b(\nu) \langle u^T \rangle'_\infty(\zeta_2), \quad (|\zeta_2| < h). \quad (39)$$

The function  $b$  satisfies equations that follow from (34), (36), (38), and (39). These equations are

$$\int_{-a}^a b(\nu) \left[ \frac{1}{\nu - x_1} + S(\nu - x_1) \right] d\nu = -\pi \exp(ikx_1 \sin \theta), \quad |x_1| < a, \quad (40)$$

$$\int_{-a}^a b(\nu) d\nu = 0. \quad (41)$$

Substituting (39) into (35) and using (23), we find that the average total displacement has the form

$$\begin{aligned} \langle u^T \rangle_\infty(y_2) &= u_0 \exp(iky_2 \cos \theta) \\ &\quad - nBa^2 \int_{-h}^h \langle u^T \rangle'_\infty(\zeta_2) \operatorname{sgn}(y_2 - \zeta_2) \\ &\quad \times \exp(ik|y_2 - \zeta_2| \cos \theta) d\zeta_2, \end{aligned} \quad (42)$$

where  $B$  is a complex-valued number that is defined by

$$Ba^2 = \frac{i}{k \sin \theta} \int_{-a}^a b(\nu) \exp(-ik\nu \sin \theta) d\nu. \quad (43)$$

Differentiating (42) twice in the range  $|y_2| < h$ , we find that

$$(1 + 2na^2B) \langle u^T \rangle''_\infty(y_2) + k^2 \cos^2 \theta \langle u^T \rangle_\infty(y_2) = 0, \quad (|y_2| < h). \quad (44)$$

The general solution of this equation is

$$\langle u^T \rangle_\infty(y_2) = C \exp(iKy_2) + D \exp(-iKy_2), \quad (45)$$

where  $C$  and  $D$  are complex-valued constants and  $K$  is a complex-valued wave number. The number  $K$  is given by

$$K^2 = \bar{K}^2 k^2 \cos^2 \theta, \quad \bar{K}^2 = 1/(1 + 2na^2B). \quad (46)$$

Since  $\operatorname{Im}(B)$  is negative for all frequencies, as will be seen in the next section, it follows that  $\bar{K}^2$  lies in the upper complex plane. We define  $\bar{K}$  to be the complex root of  $\bar{K}^2$  that lies in the first quadrant. Thus, we write  $K$  in the form

$$\begin{aligned} K &= k \cos \theta \operatorname{Re}(\bar{K}) + i\alpha, \\ \alpha &= k \cos \theta \operatorname{Im}(\bar{K}), \quad (\operatorname{Re}(\bar{K}) > 0, \operatorname{Im}(\bar{K}) > 0), \end{aligned} \quad (47)$$

where  $\alpha$  is an attenuation coefficient.

Combining (19), (45), and (47), one finds that the average total displacement in the slab has the form

$$\begin{aligned} \langle u^T \rangle_\infty(y_1, y_2) &= C \exp(-\alpha y_2) \exp \left[ i \frac{\omega}{c} (y_2 \cos \theta_S \right. \\ &\quad \left. + y_1 \sin \theta_S) \right] + D \exp(\alpha y_2) \\ &\quad \times \exp \left[ i \frac{\omega}{c} (-y_2 \cos \theta_S + y_1 \sin \theta_S) \right]. \end{aligned} \quad (48)$$

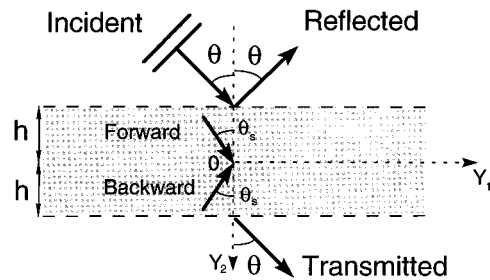


FIG. 2. Average waves inside and outside the cracked slab.

In Eq. (48), the velocity  $c$  and the refraction angle  $\theta_S$  are defined by

$$c = \frac{c_T}{V(\theta)}, \quad \cos \theta_S = \frac{\cos \theta \operatorname{Re}(\bar{K})}{V(\theta)}, \quad \sin \theta_S = \frac{\sin \theta}{V(\theta)}, \quad (49)$$

where

$$V(\theta) = [\sin^2 \theta + \cos^2 \theta (\operatorname{Re} \bar{K})^2]^{1/2}. \quad (50)$$

The first term in (48) represents a forward wave propagating with velocity  $c$  at an angle  $\theta_S$  relative to the positive  $y_2$  direction, and its amplitude decays as  $\exp(-\alpha y_2)$  as  $y_2$  increases. The second term in (48) represents a backward wave propagating with velocity  $c$  at an angle  $\theta_S$  relative to the negative  $y_2$  direction, and its amplitude decays as  $\exp(\alpha y_2)$  as  $y_2$  decreases.

To determine the constants  $C$  and  $D$ , we substitute (45) into (42). This yields a linear system of two equations for  $C$  and  $D$ . The solution is

$$C = 2u_0K(K + k \cos \theta) \exp[-i(K - k \cos \theta)h]/\Delta, \quad (51)$$

$$D = -2u_0K(K - k \cos \theta) \exp[i(K + k \cos \theta)h]/\Delta, \quad (52)$$

$$\begin{aligned} \Delta &= (K + k \cos \theta)^2 \exp[-2i(K - k \cos \theta)h] \\ &\quad - (K - k \cos \theta)^2 \exp[2i(K + k \cos \theta)h]. \end{aligned} \quad (53)$$

Outside the slab,  $|y_2| > h$ , Eq. (42) can be written in the form

$$\langle u^T \rangle_\infty(y_2) = u_0T \exp(iky_2 \cos \theta), \quad y_2 > h, \quad (54)$$

$$\begin{aligned} \langle u^T \rangle_\infty(y_2) &= u_0 \exp(iky_2 \cos \theta) + u_0R \\ &\quad \times \exp(-iky_2 \cos \theta), \quad y_2 < -h. \end{aligned} \quad (55)$$

In (54) and (55), the transmission coefficient  $T$  and the reflection coefficient  $R$  are given by

$$T = 4kK \cos \theta / \Delta, \quad (56)$$

$$R = (K^2 - k^2 \cos^2 \theta) [\exp(-2iKh) - \exp(2iKh)] / \Delta. \quad (57)$$

Figure 2 illustrates the results obtained in formulas (48), (54), and (55) for the average wave motion inside and outside the slab.

We now write the basic equations of the problem in dimensionless form. For this purpose, we introduce the following notations

$$\tilde{\omega} = \omega s_T a, \quad \tilde{c} = c/c_T, \quad \tilde{\alpha} = \alpha a, \quad \tilde{K} = K a, \quad (58)$$

$$\epsilon = n a^2, \quad \tilde{h} = h/a, \quad \tilde{y}_2 = y_2/a, \quad x = x_1/a, \quad (59)$$

$$\tilde{b}(\nu) = b(a\nu), \quad \tilde{S}(x) = aS(ax), \quad \tilde{\beta}^2(u) = u^2 - 1, \\ \text{Im}(\tilde{\beta}) \leq 0, \quad \text{Re}(\tilde{\beta}) \geq 0. \quad (60)$$

Then, the integral equations (40) and (41) yield

$$\int_{-1}^1 \tilde{b}(\nu) \left[ \frac{1}{\nu-x} + \tilde{S}(\nu-x) \right] d\nu \\ = -\pi \exp(i\tilde{\omega}x \sin \theta), \quad |x| < 1, \quad (61)$$

$$\int_{-1}^1 \tilde{b}(\nu) d\nu = 0. \quad (62)$$

In (61), the function  $\tilde{S}$  is obtained from (37) and (60) and is given by

$$\tilde{S}(x) = \tilde{\omega} \int_0^\infty \left[ \frac{\tilde{\beta}(u)}{u} - 1 \right] \sin(\tilde{\omega}ux) du. \quad (63)$$

From (46), (47), (49), (58), and (59), we infer that the dimensionless complex-valued wave number  $\tilde{K}$  has the form

$$\tilde{K} = \frac{\tilde{\omega} \cos \theta_s}{\tilde{c}} + i\tilde{\alpha}, \quad \tilde{K}^2 = \tilde{K}^2 \tilde{\omega}^2 \cos^2 \theta, \quad (64)$$

$$\tilde{K}^2 = 1/(1 + 2\epsilon B).$$

In (64),  $B$ , the velocity  $\tilde{c}$ , and the attenuation  $\tilde{\alpha}$  are given by

$$B = \frac{i}{\tilde{\omega} \sin \theta} \int_{-1}^1 \tilde{b}(\nu) \exp(-i\tilde{\omega}\nu \sin \theta) d\nu, \quad (65)$$

$$\tilde{c} = 1/V(\theta), \quad \tilde{\alpha} = \tilde{\omega} \cos \theta \text{Im}(\tilde{K}). \quad (66)$$

Using Eqs. (58) and (59), we find that the constants  $C$  and  $D$  of (51) and (52) can be written in the form

$$C/u_0 = 2\tilde{K}(\tilde{K} + \tilde{\omega} \cos \theta) \exp[-i(\tilde{K} - \tilde{\omega} \cos \theta)\tilde{h}]/\tilde{\Delta}, \quad (67)$$

$$D/u_0 = -2\tilde{K}(\tilde{K} - \tilde{\omega} \cos \theta) \exp[i(\tilde{K} + \tilde{\omega} \cos \theta)\tilde{h}]/\tilde{\Delta}, \quad (68)$$

$$\tilde{\Delta} = (\tilde{K} + \tilde{\omega} \cos \theta)^2 \exp[-2i(\tilde{K} - \tilde{\omega} \cos \theta)\tilde{h}] \\ - (\tilde{K} - \tilde{\omega} \cos \theta)^2 \exp[2i(\tilde{K} + \tilde{\omega} \cos \theta)\tilde{h}]. \quad (69)$$

Finally, the transmission and reflection coefficients  $T$  and  $R$  of (56) and (57) take the form

$$T = 4\tilde{\omega}\tilde{K} \cos \theta / \tilde{\Delta}, \quad (70)$$

$$R = (\tilde{K}^2 - \tilde{\omega}^2 \cos^2 \theta) [\exp(-2i\tilde{K}\tilde{h}) - \exp(2i\tilde{K}\tilde{h})] / \tilde{\Delta}. \quad (71)$$

As  $\epsilon$  approaches zero, the complex-valued wave number  $\tilde{K}$ , the velocity  $\tilde{c}$ , and the attenuation  $\tilde{\alpha}$  of (64) and (66) are given by

$$\tilde{K} = \tilde{\omega} \cos \theta (1 - \epsilon B) = \tilde{\omega} \cos \theta [1 - \epsilon \text{Re}(B)] \\ - i\epsilon \tilde{\omega} \cos \theta \text{Im}(B), \quad (72)$$

$$\tilde{c} = 1 + \epsilon \cos^2 \theta \text{Re}(B), \quad (73)$$

$$\tilde{\alpha} = -\epsilon \tilde{\omega} \cos \theta \text{Im}(B), \quad \text{as } \epsilon \rightarrow 0.$$

Since the real and imaginary parts of  $B$  are negative, as will be seen in the next section, we infer from (73) that  $\tilde{c} < 1$  and  $\tilde{\alpha} > 0$  as  $\epsilon$  approaches zero. Further, the attenuation  $\tilde{\alpha}$  is proportional to the crack density  $\epsilon$  and the cosine of the angle  $\theta$  for small values of  $\epsilon$ .

In the general case, when  $\epsilon$  is not necessarily approaching zero, we can solve (64) for  $\text{Re}(\tilde{K})$  and  $\text{Im}(\tilde{K})$ , and we find that

$$\text{Re}(\tilde{K}) = Q/(\sqrt{2}|1 + 2\epsilon B|), \\ \text{Im}(\tilde{K}) = -2\epsilon \text{Im}(B)/(\sqrt{2}Q|1 + 2\epsilon B|), \quad (74) \\ Q = [\text{Re}(1 + 2\epsilon B) + |1 + 2\epsilon B|]^{1/2}.$$

Then, substitution of (74) into (66) and (50) yields formulas for the velocity  $\tilde{c}$  and the attenuation  $\tilde{\alpha}$ .

For small values of the frequency  $\tilde{\omega}$  and values of the incident angle  $\theta$  in the range  $0 < \theta < \pi/2$ , we can approximate the singular integral equation (61) by neglecting real terms of  $O(\tilde{\omega}^2)$  and imaginary terms of  $O(\tilde{\omega}^3)$ . Then, we can solve the approximated equation, by using the method of Muskhelishvili,<sup>23</sup> and evaluate the expression  $B$  of (65). The result is

$$B = -\frac{\pi}{2} + \frac{\pi}{8} \tilde{\omega}^2 \log \tilde{\omega} - i \left( \frac{\pi \tilde{\omega}}{4} \right)^2, \quad \text{as } \tilde{\omega} \rightarrow 0, \quad (75)$$

where terms of  $O(\tilde{\omega}^2)$  and  $O(\tilde{\omega}^3)$  are neglected in the real and imaginary parts, respectively. Observe that (75) does not contain the angle  $\theta$ . Next, we obtain limiting expressions for the velocity  $\tilde{c}$  and the attenuation  $\tilde{\alpha}$  as the frequency  $\tilde{\omega}$  approaches zero by substituting (75) into (74), (50), and (66). The limits are

case 1:  $\epsilon < 1/\pi$

$$\tilde{c} = \frac{(1 - \epsilon\pi)^{1/2}}{[\cos^2 \theta + \sin^2 \theta (1 - \epsilon\pi)]^{1/2}} + O(\tilde{\omega}^2 \log \tilde{\omega}), \quad (76)$$

$$\tilde{\alpha} = \frac{\epsilon \pi^2 \tilde{\omega}^3 \cos \theta}{16 (1 - \epsilon\pi)^{3/2}} + O(\tilde{\omega}^4);$$

case 2:  $\epsilon > 1/\pi$

$$\tilde{c} = \frac{1}{\sin \theta} + O(\tilde{\omega}^4), \quad \tilde{\alpha} = \frac{\tilde{\omega} \cos \theta}{(\epsilon\pi - 1)^{1/2}} + O(\tilde{\omega}^2). \quad (77)$$

From (76) and (77), we see that the attenuation vanishes in the limit as  $\tilde{\omega}$  approaches zero. The velocity at  $\tilde{\omega} = 0$  decreases from 1 at  $\epsilon = 0$  to 0 at  $\epsilon = 1/\pi$ , and then jumps to the value  $1/\sin \theta$  as  $\epsilon$  becomes greater than  $1/\pi$ . Since this jump at  $\epsilon = 1/\pi$  from a zero value to a value greater than unity does not appear to be physically acceptable, we conclude that the numerical results in this paper are valid for small values of  $\epsilon$  that cannot exceed  $1/\pi$ .

According to the numerical results presented in the next section, the high-frequency limit of  $B$  when  $0 \leq \theta < \pi/2$  is such that

$$\lim_{\tilde{\omega} \rightarrow \infty} B = 0, \quad \lim_{\tilde{\omega} \rightarrow \infty} \tilde{\omega} B \cos \theta = -2i. \quad (78)$$

Therefore, we infer from (66), (49), (50), (74), and (78) that

$$\lim_{\tilde{\omega} \rightarrow \infty} \tilde{c} = 1, \quad \lim_{\tilde{\omega} \rightarrow \infty} \tilde{\alpha} = 2\epsilon, \quad \lim_{\tilde{\omega} \rightarrow \infty} \theta_S = \theta \quad (\text{for all } \epsilon). \quad (79)$$

The limits of the transmission coefficient  $T$ , reflection coefficient  $R$ , and constants  $C$  and  $D$  can be found from (67)–(71), (64), (74), and (78). One finds that

$$\lim_{\tilde{\omega} \rightarrow \infty} |T| = \exp(-4\epsilon\tilde{h}), \quad \lim_{\tilde{\omega} \rightarrow \infty} |R| = 0, \quad (80)$$

$$\lim_{\tilde{\omega} \rightarrow \infty} |C| = u_0 \exp(-2\epsilon\tilde{h}), \quad \lim_{\tilde{\omega} \rightarrow \infty} |D| = 0.$$

Observe that the results (80) do not depend on the angle  $\theta$ . In view of (48) and (80), one can see that only the forward wave is significant in the high-frequency limit. The limits of the transmission and reflection coefficients as  $\tilde{h} \rightarrow \infty$  can be obtained from (69)–(71). For  $0 \leq \theta < \pi/2$ , since  $\text{Im}(\bar{K}) > 0$ , one has

$$\lim_{\tilde{h} \rightarrow \infty} |T| = 0, \quad \lim_{\tilde{h} \rightarrow \infty} |R| = |\bar{K} - 1| / |\bar{K} + 1|. \quad (81)$$

In the case where  $\tilde{\omega}\tilde{h}$  approaches zero, since  $\bar{K}$  is bounded for all frequencies, one infers from (69)–(71) that  $T$  and  $R$  are given to within terms of  $O(\tilde{\omega}^2\tilde{h}^2)$  by

$$T = 1 - q\tilde{\omega}\tilde{h}, \quad R = q\tilde{\omega}\tilde{h}, \quad q = i(1 - \bar{K}^2)\cos \theta. \quad (82)$$

We now observe that Kawahara and Yamashita<sup>13</sup> have considered the scattering of elastic waves by a fracture zone containing randomly distributed cracks. Their formulation is similar to ours, but they obtain analytical formulas only for the special case of small crack densities. In the case where  $\epsilon$  approaches zero, and  $\tilde{\omega}\tilde{h}$  is bounded, we find from (70) and (71) that the moduli of  $T$  and  $R$  are given to within terms of  $O(\epsilon^2)$  by

$$|T| = 1 + 2\epsilon\tilde{\omega}\tilde{h} \cos \theta \text{Im}(B), \quad (83)$$

$$|R| = \epsilon|B| \sin(2\tilde{\omega}\tilde{h} \cos \theta).$$

The results (83) show that there is an error in (41.1) and (41.2) of Kawahara and Yamashita.<sup>13</sup> The quantity  $\Phi$  that they define in (14) is equal to  $-2Ba^2$ . Their results (16.1) and (38.2) for the complex-valued wave number and the velocity agree with (72) and (73).

#### IV. NUMERICAL RESULTS

The numerical results presented in this section are obtained by solving the singular integral equation (61) together with the auxiliary equation (62) for the case where the unknown function  $\tilde{b}$  has square-root singularities at the crack tips. Using the approximation method of Erdogan and Gupta,<sup>24</sup> we have obtained from (61) and (62) a linear sys-

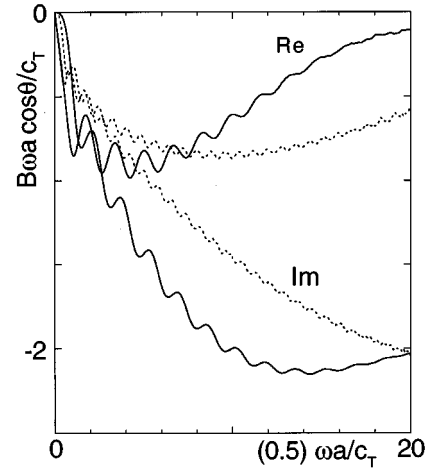


FIG. 3. Real and imaginary parts of  $B\omega a \cos \theta / c_T$  versus the frequency for  $\theta = 60$  degrees (—) and versus  $0.5 \times$  frequency for  $\theta = 75$  degrees (---).

tem of equations. We have solved this system numerically for 1000 values of the dimensionless frequency  $\tilde{\omega}$  in the range  $[0, 10]$  and for angles of incidence in the range  $[0, \pi/2]$ . For each frequency and angle of incidence, the system of equations consists of 100 complex-valued equations for 100 complex-valued unknowns.

Figure 3 shows the real and imaginary parts of  $\tilde{\omega}B \cos \theta$  versus the dimensionless frequency  $\tilde{\omega}$  for incident angles  $\theta = 60^\circ$  and  $75^\circ$ . At high frequency, the real parts approach the value zero and the imaginary parts the value  $-2$ , as stated in Eq. (78). Observe that the frequency scale for the curves corresponding to  $75^\circ$  extends to  $\tilde{\omega} = 40$ , and the convergence toward the limits is slow for these curves.

Figures 4 and 5 show the modulus of the reflection coefficient versus the dimensionless frequency for incident angle  $\theta = 60^\circ$   $\{\theta = 75^\circ\}$ , crack densities  $\epsilon = 0.01, 0.03, 0.05$  and thickness  $\tilde{h} = 5$ . The curves are obtained using Eqs. (71), (64), and (65). The corresponding curves for normal incidence ( $\theta = 0^\circ$ ) can be found in Angel and Koba.<sup>18</sup>

The reflection is small (less than 0.1) in the two figures.

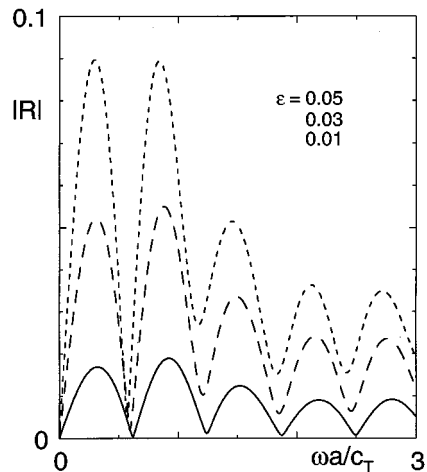


FIG. 4. Modulus of the reflection coefficient versus the frequency for  $h/a = 5$ ,  $\epsilon = 0.01, 0.03, 0.05$ , and incident angle  $\theta = 60$  degrees.

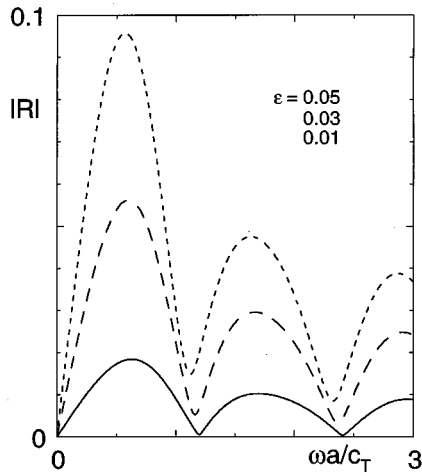


FIG. 5. Modulus of the reflection coefficient versus the frequency for  $h/a = 5$ ,  $\epsilon = 0.01, 0.03, 0.05$ , and incident angle  $\theta = 75$  degrees.

At  $\tilde{\omega} = 0$ , the value of  $|R|$  is zero. As  $\tilde{\omega}$  increases, the values of  $|R|$  have cyclic variations caused by interference phenomena inside the cracked region. The first minimum on each of the curves occurs at a frequency of approximately  $\tilde{\omega} = \pi/(2\tilde{h} \cos \theta)$ , which corresponds to an incident wave of wavelength  $4h \cos \theta$ . The following minima occur approximately at wavelengths that are integer multiples of  $4h \cos \theta$ , which is consistent with (83).

Notice that the angles of incidence in Figs. 4–5 are such that  $4 \cos(75^\circ) \approx 2 \cos(60^\circ) = \cos(0^\circ)$ . Thus, there are twice as many cycles in Fig. 4 as in Fig. 5, and twice as many cycles in Fig. 6 of Angel and Koba<sup>18</sup> as in Fig. 4. For high frequencies the reflection approaches the limit  $|R| = 0$  of (80).

Figures 6 and 7 show the modulus of the transmission coefficient versus the dimensionless frequency for incident angle  $\theta = 60^\circ$  ( $\theta = 75^\circ$ ), crack densities  $\epsilon = 0.01, 0.03, 0.05$  and thicknesses  $\tilde{h} = 3, 30$ . The curves are obtained using Eqs. (70), (64), and (65). The corresponding curves for normal

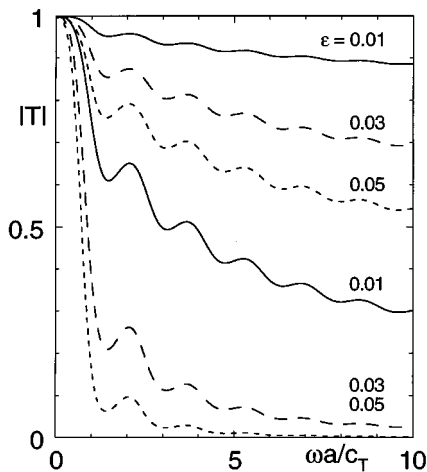


FIG. 6. Modulus of the transmission coefficient versus the frequency for  $h/a = 3$  (3 upper curves) and  $h/a = 30$  (3 lower curves),  $\epsilon = 0.01, 0.03, 0.05$ , and incident angle  $\theta = 60$  degrees.

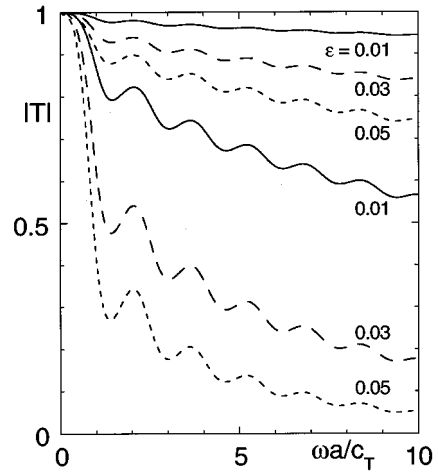


FIG. 7. Modulus of the transmission coefficient versus the frequency for  $h/a = 3$  (3 upper curves) and  $h/a = 30$  (3 lower curves),  $\epsilon = 0.01, 0.03, 0.05$ , and incident angle  $\theta = 75$  degrees.

incidence ( $\theta = 0^\circ$ ) can be found in Angel and Koba.<sup>18</sup> At  $\tilde{\omega} = 0$ , the value of  $|T|$  is 1. As  $\tilde{\omega}$  increases, the values of  $|T|$  decrease. The decrease is steeper when the crack density  $\epsilon$  is larger, when the thickness  $\tilde{h}$  is larger and when the incident angle  $\theta$  is closer to  $0^\circ$  (normal incidence). As the frequency  $\tilde{\omega}$  becomes large, the values of  $|T|$  approach the limit  $\exp(-4\epsilon\tilde{h})$  of (80) independently of the angle of incidence  $\theta$ . In the case of normal incidence (Figs. 7 and 8 in Angel and Koba<sup>18</sup>) the curves are nearly horizontal for frequencies  $\tilde{\omega}$  greater than 3. For incident angles of  $60^\circ$  and  $75^\circ$  (Figs. 6 and 7, respectively), the limits of the curves are not entirely apparent even at frequencies as high as  $\tilde{\omega} = 10$ , and calculations for higher frequencies are needed to see convergence to the limit of (80).

Figures 8–13 have been generated by increasing the incident angle in steps of 0.5-degree starting at 0 degree. Figures 8 and 9 show the modulus of the reflection coefficient versus the incident angle for  $\epsilon = 0.03$ , frequencies  $\tilde{\omega} = 1.0$ ,

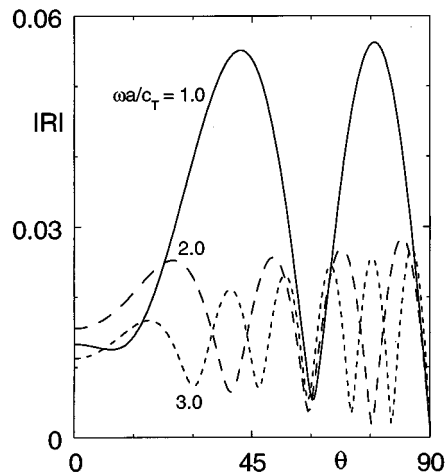


FIG. 8. Modulus of the reflection coefficient versus the incident angle (degrees) for  $h/a = 3$ ,  $\epsilon = 0.03$ , and  $\omega a/c_T = 1.0, 2.0$ , and  $3.0$ .

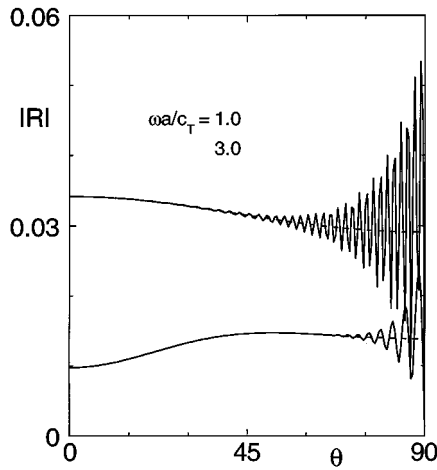


FIG. 9. Modulus of the reflection coefficient versus the incident angle (degrees) for  $h/a=50$  (—),  $h/a=\infty$  (---),  $\epsilon=0.03$ , and  $\omega a/c_T=1.0$  and 3.0.

2.0, 3.0 {1.0, 3.0} and thickness  $\bar{h}=3$  {50}. The reflection is zero at  $\theta=90^\circ$  (when the cracks are parallel to the direction of wave propagation). According to Figs. 8 and 9, the reflection coefficient is an oscillating function of the incident angle. In Fig. 8, the number of oscillations increases as  $\bar{\omega}$  increases, and the period of the oscillations decreases as the incident angle  $\theta$  increases. The limiting expression of  $|R|$  given in (81) is represented in Fig. 9 by dashed lines for  $\bar{\omega}=1.0$  and 3.0, respectively. It can be seen that the dashed lines are good mean-value representations of the reflection coefficient.

Figure 10 shows the modulus of the transmission coefficient versus the incident angle for  $\epsilon=0.03$ , frequencies  $\bar{\omega}=1.0, 3.0, 10.0$  and thicknesses  $\bar{h}=3, 30$ . The transmission decreases significantly as the slab thickness increases, is equal to 1 at  $\theta=90^\circ$ , and increases as the angle  $\theta$  increases from  $0^\circ$  to  $90^\circ$ . This shows that the incident wave is less and less affected by the cracks as the angle increases.

Figures 11–13 show the refraction angle, the velocity

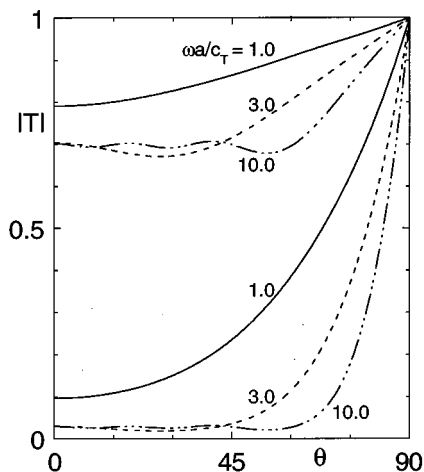


FIG. 10. Modulus of the transmission coefficient versus the incident angle (degrees) for  $h/a=3$  (3 upper curves) and  $h/a=30$  (3 lower curves),  $\epsilon=0.03$ , and  $\omega a/c_T=1.0, 3.0$ , and 10.0.

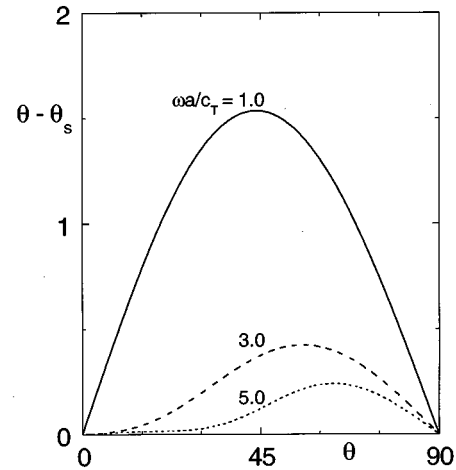


FIG. 11. Difference between the incident and refraction angles (degrees) versus the incident angle (degrees) for  $\epsilon=0.03$ , and  $\omega a/c_T=1.0, 3.0$ , and 5.0.

and the attenuation in the slab versus the incident angle for  $\epsilon=0.03$  and frequencies  $\bar{\omega}=1.0, 3.0, 5.0$ . For these frequencies and this crack density, the refraction angle {velocity in the slab} is close to the incident angle {velocity in an uncracked solid}, and the attenuation is less than 0.07. The angles  $\theta$  and  $\theta_S$  are equal at  $\theta=0^\circ$  and  $\theta=90^\circ$ . Notice from (49) that

$$c/c_T = \sin \theta_S / \sin \theta. \quad (84)$$

It follows from (84) and from the result  $\theta_S=0^\circ$  when  $\theta=0^\circ$  that the ratio  $\theta_S/\theta$  is equal to  $c/c_T$  in the limit as  $\theta \rightarrow 0$ . The value of  $c/c_T$  in the limit as  $\theta \rightarrow 0$  is shown in Fig. 12.

## V. CONCLUSIONS

We have investigated the propagation of obliquely incident antiplane waves in an elastic solid containing a random distribution of slit parallel cracks. The cracks occupy a slab region of the solid and are parallel to the boundaries of the slab. Using the exact coupled equations of the multiple crack

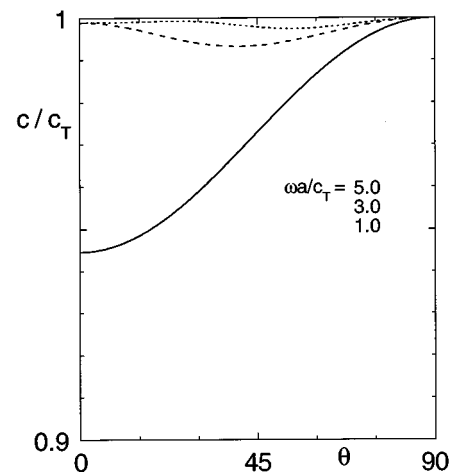


FIG. 12. Velocity versus the incident angle (degrees) for  $\epsilon=0.03$ , and  $\omega a/c_T=1.0, 3.0$ , and 5.0.

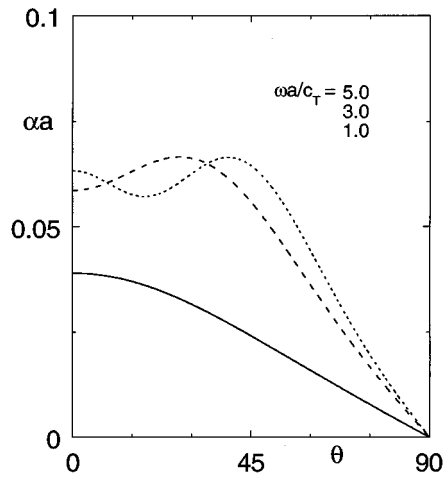


FIG. 13. Attenuation versus the incident angle (degrees) for  $\epsilon=0.03$ , and  $\omega a/c_T=1.0, 3.0$ , and  $5.0$ .

problem, we have derived integrodifferential equations of general validity for the average (coherent) wave motion in the solid.

To obtain analytical and numerical results, we have assumed that the average exciting field near a fixed crack is equal to the average total field. This assumption, which limits the range of validity of the numerical results, allows us to show that the wave motion in the slab can be represented by a complex-valued wave number that depends on frequency, crack density, and incident angle. Further, we have determined the reflection amplitude and the transmission amplitude outside the slab in terms of the complex-valued wave number, frequency, incident angle, and slab thickness, and we have studied in detail the implications of the formulas.

Numerical results have been obtained at a low cpu-time cost by solving an integral equation for each frequency and each incident angle. Curves for the reflection coefficient show interference effects that are of interest for ultrasonic non-destructive evaluation and seismic wave exploration.

## ACKNOWLEDGMENTS

This material is based in part upon work supported by the Texas Advanced Technology Program under Grant No. 003604-004.

<sup>1</sup>M. F. McCarthy and M. M. Carroll, "Multiple scattering of SH waves by randomly distributed dissimilar scatterers," in *Wave Phenomena: Modern Theory and Applications*, edited by C. Rogers and T. B. Moodie (Elsevier, North-Holland, 1984), pp. 433–451.

- <sup>2</sup>V. K. Varadan, Y. Ma, and V. V. Varadan, "Scattering and attenuation of elastic waves in random media," *Pure Appl. Geophys.* **131**, 577–603 (1989).
- <sup>3</sup>F. H. Kerr, "The scattering of a plane elastic wave by spherical elastic inclusions," *Int. J. Eng. Sci.* **30**, 169–186 (1992).
- <sup>4</sup>S. K. Bose, "Ultrasonic plane SH wave reflection from a uni-directional fibrous composite slab," *J. Sound Vib.* **193**, 1069–1078 (1996).
- <sup>5</sup>M. Kikuchi, "Dispersion and attenuation of elastic waves due to multiple scattering from inclusions," *Phys. Earth Planet. Interiors* **25**, 159–162 (1981).
- <sup>6</sup>M. Kikuchi, "Dispersion and attenuation of elastic waves due to multiple scattering from cracks," *Phys. Earth Planet. Interiors* **27**, 100–105 (1981).
- <sup>7</sup>Y. Mikata and J. D. Achenbach, "Reflection and transmission by an infinite array of randomly oriented cracks," *J. Acoust. Soc. Am.* **83**, 38–45 (1988).
- <sup>8</sup>Y. C. Angel and J. D. Achenbach, "Attenuation and speed of antiplane waves in a cracked solid using the Kramers–Kronig relations," *J. Acoust. Soc. Am.* **90**, 2757–2762 (1991).
- <sup>9</sup>Ch. Zhang and J. D. Achenbach, "Effective wave velocity and attenuation in a material with distributed penny-shaped cracks," *Int. J. Solids Struct.* **27**, 751–767 (1991).
- <sup>10</sup>Ch. Zhang and D. Gross, "Wave attenuation and dispersion in randomly cracked solids—I. Slit cracks," *Int. J. Eng. Sci.* **31**, 841–858 (1993).
- <sup>11</sup>Ch. Zhang and D. Gross, "Wave attenuation and dispersion in randomly cracked solids—II. Penny-shaped cracks," *Int. J. Eng. Sci.* **31**, 859–872 (1993).
- <sup>12</sup>Y. C. Angel and Y. K. Koba, "Propagation of antiplane waves in a multi-cracked solid," in *Anisotropy and Inhomogeneity in Elasticity and Plasticity*, edited by Y. C. Angel (ASME, New York, 1993), AMD-Vol. 158, pp. 51–57.
- <sup>13</sup>J. Kawahara and T. Yamashita, "Scattering of elastic waves by a fracture zone containing randomly distributed cracks," *Pure Appl. Geophys.* **139**, 121–144 (1992).
- <sup>14</sup>V. P. Smyshlyaev, J. R. Willis, and F. J. Sabina, "Self-consistent analysis of waves in a matrix-inclusion composite—III. A matrix containing cracks," *J. Mech. Phys. Solids* **41**, 1809–1824 (1993).
- <sup>15</sup>A. S. Eriksson, A. Boström, and S. K. Datta, "Ultrasonic wave propagation through a cracked solid," *Wave Motion* **22**, 297–310 (1995).
- <sup>16</sup>Y. Mikata, "SH-waves in a medium containing a disordered periodic array of cracks," *J. Appl. Mech.* **62**, 312–319 (1995).
- <sup>17</sup>V. P. Smyshlyaev and J. R. Willis, "Effective relations for nonlinear dynamics of cracked solids," *J. Mech. Phys. Solids* **44**, 49–75 (1996).
- <sup>18</sup>Y. C. Angel and Y. K. Koba, "Complex-valued wave number, reflection, and transmission in an elastic solid containing a cracked slab region," *Int. J. Solids Struct.* **35**, 573–592 (1997).
- <sup>19</sup>L. L. Foldy, "The multiple scattering of waves I. General theory of isotropic scattering by randomly distributed scatterers," *Phys. Rev.* **67**, 107–119 (1945).
- <sup>20</sup>Y. C. Angel and J. D. Achenbach, "Reflection and transmission of obliquely incident Rayleigh waves by a surface-breaking crack," *J. Acoust. Soc. Am.* **75**, 313–319 (1984).
- <sup>21</sup>Y. C. Angel, "On the reduction of elastodynamic crack problems to singular integral equations," *Int. J. Eng. Sci.* **26**, 757–764 (1988).
- <sup>22</sup>I. N. Sneddon, *The Use of Integral Transforms* (McGraw-Hill, New York, 1972), pp. 32–33.
- <sup>23</sup>N. I. Muskhelishvili, *Singular Integral Equations* (Noordhoff, Groningen, The Netherlands, 1953).
- <sup>24</sup>F. Erdogan and G. D. Gupta, "On the numerical solution of singular integral equations," *Q. Appl. Math.* **30**, 525–534 (1972).

# On Green's functions for a cylindrical cavity

Earl G. Williams

*Physical Acoustics, Code 7137, Naval Research Laboratory, Washington, DC 20375*

(Received 26 November 1996; accepted for publication 1 September 1997)

This paper presents a set of Green's functions for Neumann and Dirichlet boundary conditions for the Helmholtz equation applied to the interior of a cylindrical cavity which are based on evanescent wave expansions instead of the usual normal mode expansions. The evanescent expansion capitalizes on the known physics of the shell–fluid interaction, given a cavity with flexible walls, providing a pressure field which decays exponentially (in the limit of small wavelength) into the interior of the cavity when the wall vibration is subsonic. Due to this decay the evanescent Green's functions converge much faster than the conventional Green's functions which are built up out of the interior eigenmodes of a rigid (or pressure release) cavity. Furthermore, these evanescent Green's functions can be inverted in a fairly straightforward way to provide the foundations for solving the inverse holography problem, that is, the reconstruction of the normal surface velocity from a measurement of the pressure in the interior. [S0001-4966(97)05012-1]

PACS numbers: 43.20.Bi, 43.20.Mv, 43.20.Tb [JEG]

## INTRODUCTION

Green's functions provide a concise mathematical formulation to solve problems in the radiation and scattering of sound from bodies.<sup>1</sup> The free space Green's function appears in the Helmholtz integral equation (HIE) which provides an integral method of predicting the pressure field from a knowledge of the normal velocity and pressure fields on the HIE surface,  $S$ , for both exterior problems (actual sources within  $S$ ) or interior problems (sources outside  $S$ ). It is well known that knowledge of both the pressure and velocity fields overspecifies the boundary conditions needed to provide a unique solution. Only one of these fields is needed to solve the problem. Thus it is possible to construct a modification of the free space Green's function which satisfies Neumann boundary conditions (the normal derivative vanishes) or Dirichlet boundary conditions (the function vanishes) on  $S$ . We call these constructed functions Neumann and Dirichlet Green's functions, respectively, to reflect the boundary conditions they satisfy. When these are used in the HIE one of the terms drops out and a simpler integral equation is obtained.

The motivation behind the development of these simplified integral equations is their application to near-field acoustical holography, which deals with the inversion of these equations, that is, solving for the unknown in the integrand from a knowledge of the value of the integral at many points.<sup>2</sup> In particular, application of NAH to noise control problems inside of aircraft is simplified if the Neumann or Dirichlet Green's functions are known for the geometry of interest.<sup>3</sup>

The construction of the Neumann and Dirichlet Green's functions for the interior (cavity) problem generally is carried out by a classical treatment, using interior resonance modes for the corresponding boundary condition. For example, the Neumann Green's function is determined from the rigid body modes (eigenfunctions) of the prescribed cavity. Applications to a cylindrical cavity to model radiation of

sound into the interior of an aircraft fuselage are found in the literature.<sup>4–7</sup>

In the study of panel radiation and room acoustics the rectangular cavity Green's function built up out of normal modes is used.<sup>8,9</sup> This Green's function has also been used to deal with point reacting walls,<sup>10–12</sup> and wave field extrapolation in semi-infinite waveguides with point reacting walls.<sup>13</sup>

A close look at the Green's functions based on normal modes reveals a problem when dealing with flexible walls, however. In general, cavity walls may support subsonic as well as supersonic waves or modes on their surfaces. Subsonic vibration implies wavelengths which are shorter than the acoustic wavelength. This leads to radiation from the wall which is short circuited, and inefficient. This inefficiency is exhibited by a pressure field which decays into the cavity, that is, a field which is evanescent. The slower the wave, the stronger the decay. It is desirable that the Green's function also exhibit this same dependency for subsonic vibration. However, since the classic Green's function is constructed from normal modes, it does not easily demonstrate this behavior, and one is forced to sum over many modes to approximate the decay of a single evanescent wave.

Fortunately, one can derive a Green's function which explicitly matches this decay for evanescent waves, without resorting to summation of eigenfunctions. We find derivations of this form in the electromagnetic literature for the Neumann and Dirichlet Green's functions for those special cases of the electric and magnetic fields which lead to the Helmholtz equation. We choose to call this form of the Green's function the evanescent Green's function. Tyras<sup>14</sup> develops both the normal mode and evanescent Dirichlet and Neumann Green's functions for a variety of two-dimensional geometries including angular sectors and circular regions. The electrostatic ( $k=0$ ) form of the evanescent Green's function for rectangular and cylindrical cavities appears in Jackson,<sup>15</sup> which provided the inspiration for the develop-



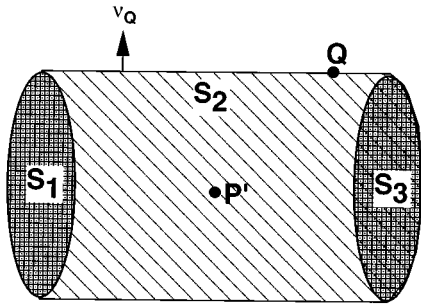


FIG. 1. Cylindrical cavity with surface  $S$  and interior volume  $V$ , bounded by end caps  $S_1$  and  $S_3$  and by the cylindrical surface  $S_2$ . The point  $P'$  associated with the cylindrical coordinates  $(\rho', \phi', z')$  lies inside (or on the surface), and the point  $Q$  with coordinates  $(\rho, \phi, z)$  is on  $S$ .

ment presented here. Some details of the development for the evanescent Neumann<sup>16,17</sup> and Dirichlet<sup>18</sup> Green's functions for the cylindrical cavity have already been presented by the author. This paper presents the full details. Apparently also inspired by Jackson, a similar development for the Neumann Green's function for a finite rectangular waveguide has been presented by Nelisse *et al.*<sup>19</sup>

A general formula for the construction of evanescent Green's functions is given by Morse and Feshbach<sup>20</sup> which is used by Hanish<sup>21</sup> to derive specific formulas for various acoustic waveguides. However, it does not appear that the specific formula for the three-dimensional cylindrical cavity has appeared concisely in a single place, pieces of the Green's function being scattered throughout the cited publications. Thus we hope that this paper serves to bring all the details of the evanescent Green's function for the cylindrical cavity, including the basic derivation, into one paper.

## I. EVANESCENT NEUMANN GREEN'S FUNCTION FOR A CYLINDRICAL CAVITY

Let  $S = S_1 \cup S_2 \cup S_3$  define the surface of a cylindrical cavity of length  $L$  and radius  $a$ , as shown in Fig. 1. Here,  $S_1$  and  $S_3$  are the flat endcaps of the cavity, and  $S_2$ , with  $0 \leq z \leq L$ , is the cylindrical section. Let  $V$  be the volume of the cavity bounded by  $S$ , and  $P'$  be a point with cylindrical coordinates  $(\rho', \phi', z')$  in  $V$  or on  $S$ , and  $Q$  a point with cylindrical coordinates  $(\rho, \phi, z)$  on  $S$ . The Helmholtz integral equation provides, for the pressure  $p$ ,

$$\alpha(P')p(P') = \int \int \left[ \frac{\partial p(Q)}{\partial v_Q} G(P'|Q) - p(Q) \frac{\partial G(P'|Q)}{\partial v_Q} \right] dS, \quad (1)$$

where  $G$  is the free space Green's function (time dependence  $e^{-i\omega t}$ ) given by

$$G(P'|Q) = \frac{e^{ik|P'-Q|}}{4\pi|P'-Q|},$$

and  $v_Q$  is the outward normal to  $S$ , and

$$\alpha(P') = \begin{cases} 1: & P' \in V \\ \frac{1}{2}: & P' \in S \\ \frac{1}{4}: & P' \in S_2 \cap (S_1, S_3) \end{cases}.$$

We seek to modify  $G$  by addition of a homogeneous solution in order to create the evanescent Neumann Green's function,  $G_N$ , which satisfies the boundary condition,

$$\frac{\partial G_N}{\partial v_Q} = 0, \quad (2)$$

everywhere on  $S$ , and is a solution of

$$\nabla^2 G_N + k^2 G_N = -\delta(P' - Q). \quad (3)$$

With this modification the second term in Eq. (1) disappears, resulting in the following surface integral:

$$\alpha(P')p(P') = \int \int \frac{\partial p(Q)}{\partial v_Q} G_N(P'|Q) dS. \quad (4)$$

The pressure,  $p$ , is a solution of

$$\nabla^2 p + k^2 p = 0 \quad (5)$$

in  $V$ , and there is no restriction on  $\partial p(Q)/\partial v_Q$  on  $S$ . The latter is related to the normal velocity,  $v_n$ , on the walls of the cavity by Newton's law,

$$v_n(Q) = \frac{1}{i\omega\rho_0} \frac{\partial p(Q)}{\partial v_Q}, \quad (6)$$

where  $\rho_0$  is the density of the fluid in the cavity.

The mathematical details of the derivation are presented in Appendix A. The evanescent Green's functions presented there are valid when both  $P'$  and  $Q$  are in  $V$  (or on  $S$ ), even though Eq. (4) restricts  $Q$  to the boundary. Three separate cases are considered in the Appendix,  $Q \in S_1$ ,  $Q \in S_2$ , and  $Q \in S_3$ , deriving different forms of the Green's function for each case. This is necessitated by the desire for direct evanescent decay of  $G_N(P'|Q)$  as  $P'$  moves away from  $S$  into the cavity, for subsonic vibration on  $S$ .

### A. Radial evanescent decay from the cylindrical surface

Consider first the surface  $S_2$ , the cylindrical surface ( $0 \leq z \leq L$ ). Referring to Eq. (A9) of Appendix A we let  $Q \in S_2$  ( $\rho_Q = a$ ) and use the Wronskian relation  $J_n(x)Y'_n(x) - Y_n(x)J'_n(x) = 2/\pi x$  to obtain

$$G_N(P'|Q \in S_2) = \frac{1}{2\pi a L} \sum_{n=-\infty}^{\infty} e^{in(\phi - \phi')} \times \sum_{m=0}^{\infty} \epsilon_m \cos\left(\frac{m\pi z}{L}\right) \cos\left(\frac{m\pi z'}{L}\right) \frac{J_n(k_m \rho')}{k_m J'_n(k_m a)}, \quad (7)$$

where

$$k_m = \sqrt{k^2 - (m\pi/L)^2} \quad (8)$$

and

$$\epsilon_m = \begin{cases} 1: & m = 0 \\ 2: & m \neq 0 \end{cases}.$$

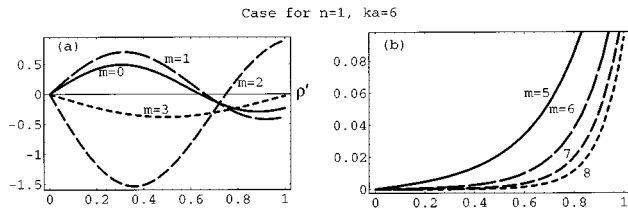


FIG. 2. Plot of  $J_n(k_m \rho') / k_m J'_n(k_m a)$  vs  $\rho'$  for  $ka=6$ ,  $L=2$ , and  $a=1$  for eight values of  $m$ . In (a)  $m=0-3$  and  $k_m$  is real corresponding to a standing wave field. In (b)  $m=5-8$  and  $k_m$  is imaginary corresponding to an evanescent decay from the surface of the shell at  $a=1$ , as can be seen.

The interpretation of Eq. (7) is made clearer by considering the result of a single helical standing wave with indices  $(m', n')$  on the surface  $S_2$  given by

$$\frac{\partial p(Q)}{\partial \nu_Q} = \begin{cases} \cos\left(\frac{m' \pi z}{L}\right) e^{in' \phi}: & Q \in S_2 \\ 0: & Q \in S_1 \\ 0: & Q \in S_3 \end{cases}$$

Inserting this into Eq. (4) and noting the orthogonality in  $z$  and  $\phi$ , we find that the radiated pressure field trace matches to the helical wave vibration,

$$p(P') \propto e^{in' \phi'} \cos\left(\frac{m \pi z'}{L}\right) \frac{J_n(k_m \rho')}{k_m J'_n(k_m a)},$$

where  $n = -n'$  and  $m = m'$ . The radial variation of the resulting pressure is thus given by the ratio of Bessel functions in Eq. (7). It is here where the desired evanescent behavior is to be found, as we will now show.

Rewriting Eq. (8) in terms of the structural,  $\lambda_m \equiv 2L/m$ , and acoustic,  $\lambda = 2\pi/k$ , wavelengths yields

$$k_m = \frac{2\pi}{\lambda_m \lambda} \sqrt{\lambda_m^2 - \lambda^2}.$$

Thus it is clear that when  $\lambda_m < \lambda$ ,  $k_m$  is pure imaginary, leading to modified Bessel functions for the radial dependence in Eq. (7). In the limit as  $\lambda_m \rightarrow 0$  ( $m \rightarrow \infty$ ), the asymptotic form of the modified Bessel function leads to

$$\frac{J_n(k_m \rho')}{k_m J'_n(k_m a)} \rightarrow \frac{e^{-2\pi(a-\rho')/\lambda_m}}{2\pi/\lambda_m}.$$

This is an important result as it shows that the pressure field decays exponentially from the cylindrical surface, a decay that increases as the wavelength of the structural vibration,  $\lambda_m$ , decreases. It is not surprising that this result is identical to the decay found in the exterior problem dealing with the radiation from the surface of a vibrating cylinder.<sup>22</sup>

To illustrate with an example, we consider a case in which  $ka=6$ ,  $L=2$ , and  $a=1$ . In Fig. 2 we plot  $J_n(k_m \rho') / k_m J'_n(k_m a)$  vs  $\rho'$  for eight values of  $m$ . The standing wave nature of the Green's function is clear in Fig. 2(a) for small values of  $m$ . However, when  $m > 4$ , Fig. 2(b) clearly shows that the radial part of the Green's function is evanescent and decays away from the surface at  $\rho' = 1$ . Note that  $kL = 12$  corresponds to a little less than four half acoustic wavelengths in the axial direction. Since  $m$  corresponds

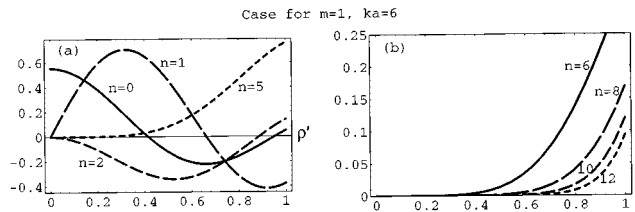


FIG. 3. Same as Fig. 2 except that  $n$  is varied with  $m=1$  constant. Although the argument of the Bessel functions remain real, it can be seen that the field becomes evanescent when  $n > ka$ .

to the number of half structural wavelengths we are clearly in the acoustic short circuit condition, leading to a decaying pressure field.

One would expect an evanescent condition to arise due to subsonic waves in the  $\phi$  direction. Since  $n$  measures the number of structural full wavelengths in one circumference and  $ka$  the number of acoustic wavelengths in that same distance, we expect that evanescent waves will arise when  $n > ka$ . This is illustrated in Fig. 3, where again  $J_n(k_m \rho') / k_m J'_n(k_m a)$  vs  $\rho'$  from Eq. (7) is plotted, but now as a function of  $n$  for  $m=1$ . We see that for low values of  $n$  the field reaches the axis of the cylinder indicating standing waves. However, for large values ( $n > ka$ ), the field decays from the boundary and is evanescent.

## B. Axial evanescent decay from the endcaps

Now we turn to the case in which  $Q \in S_1$  and present the corresponding  $G_N$ . Of course we could merely return to Eq. (A9) of Appendix A and set  $z=0$ . However, the resulting axial dependence of an individual term is clearly never evanescent. To remedy this we turn to the second form of  $G_N$  given in Eq. (A15). On  $S_1$  this equation yields, given  $z_< = 0$  and  $z_> = z'$ ,

$$G_N(P'|Q \in S_1) = -\frac{1}{\pi a^2} \sum_n e^{in(\phi - \phi')} \times \sum_{s=1}^{\infty} \frac{\kappa_{ns}^2 J_n(\kappa_{ns} \rho/a) J_n(\kappa_{ns} \rho'/a)}{(\kappa_{ns}^2 - n^2) J_n^2(\kappa_{ns})} \times \frac{\cos(\gamma_{ns}(L - z'))}{\gamma_{ns} \sin(\gamma_{ns} L)}, \quad (9)$$

where

$$\gamma_{ns} \equiv \sqrt{k^2 - (\kappa_{ns}/a)^2} \quad (10)$$

and  $\kappa_{ns}$  are roots of the derivative of  $J_n$ ,

$$J'_n(\kappa_{ns}) = 0. \quad (11)$$

Similarly, for the right endcap,  $Q \in S_3$ , we again use Eq. (A15) with  $z_> = L$  and  $z_< = z'$  to yield

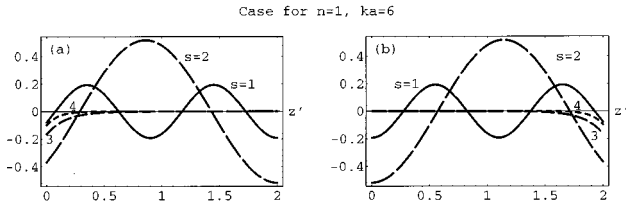


FIG. 4. Plots of the axial dependence of the Green's function in Eqs. (9) and (12) as a function of  $s$  for  $n=1$ . (a) Plot of  $\cos(\gamma_{ns}(L-z'))/\gamma_{ns} \sin(\gamma_{ns}L)$  vs  $z'$  for the case when  $Q \in S_1$  and (b)  $\cos(\gamma_{ns}z')/\gamma_{ns} \sin(\gamma_{ns}L)$  vs  $z'$  when  $Q \in S_3$ . When  $s=1$  or  $2$  we can see that the field extends over the whole cavity. This field becomes strongly evanescent when  $s>2$  decaying from the left endcap in (a) and from the right endcap in (b). Note because  $\kappa_{12} = 5.331$  and  $\kappa_{11} = 1.841$ , the cos function oscillates more rapidly for  $s=1$  than for  $s=2$  since  $\kappa_{12}$  is closer to  $ka=6$  [see Eq. (10)].

$$G_N(P'|Q \in S_3) = -\frac{1}{\pi a^2} \sum_n e^{in(\phi-\phi')} \times \sum_{s=1}^{\infty} \frac{\kappa_{ns}^2 J_n(\kappa_{ns}\rho/a) J_n(\kappa_{ns}\rho'/a)}{(\kappa_{ns}^2 - n^2) J_n^2(\kappa_{ns})} \times \frac{\cos(\gamma_{ns}z')}{\gamma_{ns} \sin(\gamma_{ns}L)}. \quad (12)$$

In both cases, Eq. (9) and Eq. (12), evanescent decay arises when  $\gamma_{ns}$  in Eq. (10) becomes imaginary since the cos function becomes a hyperbolic cosine. Again in the limit as  $s \rightarrow \infty$  or  $n \rightarrow \infty$  ( $\kappa_{ns} \rightarrow s + n/2 - \pi/4$ ), this dependence for  $Q \in S_1$  is

$$\frac{\cos(\gamma_{ns}(L-z'))}{\gamma_{ns} \sin(\gamma_{ns}L)} \rightarrow \frac{e^{-z'|\gamma_{ns}|}}{|\gamma_{ns}|},$$

and for  $Q \in S_3$ ,

$$\frac{\cos(\gamma_{ns}z')}{\gamma_{ns} \sin(\gamma_{ns}L)} \rightarrow \frac{e^{-(L-z')|\gamma_{ns}|}}{|\gamma_{ns}|},$$

and we can see that the pressure field decays exponentially from either endcap.

We illustrate the axial case in Fig. 4, which shows the axial dependence of the Green's function,  $[\cos(\gamma_{ns}(L-z'))]/[\gamma_{ns} \sin(\gamma_{ns}L)]$  vs  $z'$  for the same physical parameters as the previous figures. Figure 4(a) corresponds to  $Q$  on the left endcap and Fig. 4(b) to  $Q$  on the right endcap. In these cases  $s$  varies, with  $s=1,2$  corresponding to real  $\gamma_{ns}$  and  $s=3,4$  corresponding to imaginary  $\gamma_{ns}$ , the latter leading to evanescent decay from the endcaps as indicated in the figure.

### C. Summary of the Neumann case

Equations (7), (9), and (12) specify the evanescent Neumann Green's function when  $Q \in S$  for use in the integral equation, Eq. (4), and correctly model the physics of the fluid/structure interaction at the boundaries of the flexible walls of the cylindrical cavity. The computational importance of these equations rests in the fact that there exists a threshold index in the summations in  $m$ ,  $n$ , and  $s$ , above which one of the functions in the summation becomes evanescent, that is, decaying with respect to index in an expo-

ponential fashion, as we have illustrated in Figs. 2–4. The sums converge rapidly under these conditions. In fact, as  $P'$  moves away from the boundary into the interior, the rate of convergence increases as can be seen in Figs. 2(b), 3(b), and 4.

### 1. Case when $P'$ is on $S$

This case was excluded in Appendix A, since Eq. (A3) and Eq. (A5) are valid on the open interval [not including the endpoints,  $z = z' = (0, L)$ , or  $\rho = \rho' = a$ ]. Due to the definition of the delta function, when  $P' \in S_2$  then the jump condition of Eq. (A7) is only half as much ( $= -1/2\rho'$ ) and the right-hand side of Eq. (A8) as well as Eq. (A9) are reduced by half. This factor exactly cancels the contribution of  $\alpha = \frac{1}{2}$  in Eq. (4). Furthermore, when  $P'$  is also on one of the ends of the surface  $S_2$ , the right-hand side of Eq. (A3) must also be reduced by half, again due to the definition of the delta function, leading to an additional multiplicative factor of  $\frac{1}{2}$  in Eq. (A9). The resulting factor of  $\frac{1}{4}$  again exactly cancels  $\alpha = \frac{1}{4}$  in Eq. (4).

The same result occurs for the other two cases, Eq. (9) and Eq. (12), when  $P' \in S$ . The  $\alpha$  in Eq. (4) is again canceled out by the additional factor in the Green's functions.

### D. Classic Neumann Green's function

For sake of comparison we present here the classic cavity Green's function which is presented in many textbooks as well as work by Pope<sup>4,5</sup> and Cheng:<sup>7</sup>

$$G_N(P'|Q) = \sum_{n=0}^{\infty} \sum_{m=0}^{\infty} \sum_{s=1}^{\infty} \frac{\Psi_{nms}(Q)\Psi_{nms}^*(P')}{(\beta_{nms}^2 - k^2) \iiint \Psi_{nms}^2 dV}, \quad (13)$$

where

$$\Psi_{nms}(Q) \equiv J_n(\kappa_{ns}\rho/a) e^{in\phi} \cos(m\pi z/L), \quad (14)$$

and similarly for  $\Psi_{nms}(P')$ . The eigenfrequencies are given by

$$\beta_{nms}^2 = (\kappa_{ns}/a)^2 + (m\pi/L)^2,$$

and the normalization is

$$\iiint \Psi_{nms}^2 dV = \pi a^2 (1 - n^2/\kappa_{ns}^2) J_n^2(\kappa_{ns}) \frac{L}{\epsilon_m}. \quad (15)$$

The frequency dependence appears only in the denominator, and the arguments of the functions are always real. Here  $\beta_{nms}$  provides the resonance frequencies of the modes of a rigid cavity.

### 1. Comparison of classic and evanescent Green's functions

In the case of the normal mode expansion of the Green's function, Eq. (13), the modes never become evanescent and the sum decays only as  $1/\beta_{nms}^2$ . Furthermore, only two summations are needed for the evanescent Green's function in Eqs. (7), (9), and (12), whereas three are necessary for Eq. (13). Also the summations in  $m$ ,  $n$ , and  $s$  for the evanescent Green's function truncate very quickly when evanescent conditions arise. Since both Green's functions must give identi-

cal results, comparison shows that the summation in Eq. (13) over  $s$  (with  $Q \in S_2$ ) must result in a single term of Eq. (7), that is,  $J_n/(k_m J'_n)$ . Similarly, the summations in Eq. (13) over  $m$  (with  $Q \in S_1$ ) must result in a single term of Eq. (9), i.e.,  $\cos/(\gamma_{ns} \sin)$ .

Note that both Green's functions become infinite at the interior eigenfrequencies of a rigid cavity given by the zeros of the denominator in Eq. (13). For the evanescent Green's function the zeros of the denominator of Eq. (7) are found when  $J'_n(k_m a) = 0$ . This occurs when

$$k_m a = \kappa_{ns},$$

or, using Eq. (8), when

$$k^2 = (\kappa_{ns}/a)^2 + (m\pi/L)^2 = \beta_{nms}^2,$$

the latter equality corresponding to the definition of  $\beta_{nms}$  for the classic Green's function.

## II. EVANESCENT DIRICHLET GREEN'S FUNCTIONS FOR A CYLINDRICAL CAVITY

Returning to Eq. (1) we seek a Green's function,  $G_D$ , which vanishes on the surface  $S$ ,

$$G_D = 0, \quad (16)$$

and is a solution of

$$\nabla^2 G_D + k^2 G_D = -\delta(P' - Q). \quad (17)$$

Due to Eq. (16) the first term of Eq. (1) is removed, yielding

$$\alpha(P')p(P') = - \int \int p(Q) \frac{\partial G_D(P'|Q)}{\partial \nu_Q} dS. \quad (18)$$

Equation (5) applies and there is no restriction on  $p(Q)$  on the boundary.

Again the derivation, which follows that of the Neumann Green's function, is sketched out in Appendix B. Two forms of the Green's function are relevant for the problem, when  $Q \in S_1$  or  $S_3$  and when  $Q \in S_2$ . In the first case we use Eq. (B4), yielding for  $Q \in S_1$

$$\begin{aligned} \frac{\partial G_D}{\partial \nu_Q} &= - \left. \frac{\partial G_D}{\partial z} \right|_{z < 0} \\ &= \frac{-1}{\pi a^2} \sum_{n=-\infty}^{\infty} e^{in(\phi - \phi')} \\ &\quad \times \sum_{s=1}^{\infty} \frac{J_n(\bar{\kappa}_{ns} \rho/a) J_n(\bar{\kappa}_{ns} \rho'/a) \sin(\bar{k}_{ns}(L - z'))}{J_{n+1}^2(\bar{\kappa}_{ns}) \sin(\bar{k}_{ns} L)}, \end{aligned} \quad (19)$$

and for  $Q \in S_3$

$$\begin{aligned} \frac{\partial G_D}{\partial \nu_Q} &= \left. \frac{\partial G_D}{\partial z} \right|_{z > L} \\ &= \frac{-1}{\pi a^2} \sum_{n=-\infty}^{\infty} e^{in(\phi - \phi')} \\ &\quad \times \sum_{s=1}^{\infty} \frac{J_n(\bar{\kappa}_{ns} \rho/a) J_n(\bar{\kappa}_{ns} \rho'/a) \sin(\bar{k}_{ns}(z'))}{J_{n+1}^2(\bar{\kappa}_{ns}) \sin(\bar{k}_{ns} L)}, \end{aligned} \quad (20)$$

where

$$\bar{k}_{ns} \equiv \sqrt{k^2 - \bar{\kappa}_{ns}^2/a^2}, \quad (21)$$

and  $\bar{\kappa}_{ns}$  is determined from [compare to Eq. (11)]

$$J_n(\bar{\kappa}_{ns}) = 0. \quad (22)$$

When  $Q$  lies on the cylindrical section,  $Q \in S_2$ , then (using the Wronskian relationship for the Bessel functions) Eq. (B3) yields

$$\begin{aligned} \frac{\partial G_D}{\partial \nu_Q} &= \frac{\partial G_D}{\partial \rho} = \frac{-1}{\pi L a} \sum_{n=-\infty}^{\infty} e^{in(\phi - \phi')} \\ &\quad \times \sum_{m=1}^{\infty} \sin\left(\frac{m\pi z}{L}\right) \sin\left(\frac{m\pi z'}{L}\right) \frac{J_n(k_m \rho')}{J_n(k_m a)}, \end{aligned} \quad (23)$$

where  $k_m$  is given by Eq. (8).

## III. SUMMARY

The evanescent Neumann and Dirichlet Green's functions, which have been derived here for the pressure in a flexible, cylindrical cavity, provide an efficient and physical means for numerical calculations. In particular, the motivation behind this work was the application of near-field acoustical holography to study the coupling between the interior pressure and the fuselage vibration for an aircraft cabin. The NAH proceeds to solve for the inverse of Eq. (4) and Eq. (18) when the acoustic pressure is measured at many points over a imaginary cylindrical box in the interior.<sup>3</sup> This inversion provides the normal velocity on the fuselage, and thus can be used to predict the pressure, via Eq. (4), anywhere inside the cavity. The details of the inversion and of actual experiments carried out on a Cessna fuselage will be discussed in an upcoming paper.

## ACKNOWLEDGMENTS

This work was supported by NASA and ONR.

## APPENDIX A: THE NEUMANN GREEN'S FUNCTIONS

The derivation here was inspired by a similar derivation for the electrostatic Green's function in cylindrical coordinates given in Jackson.<sup>15</sup> Equation (4) arises from the Helmholtz integral equation [Green's second identity, Eq. (1)], in which the free space Green's function has been modified so that

$$\frac{\partial G_N(P'|Q)}{\partial \nu_Q} = 0$$

on the surface in Eq. (4). Also resulting from Green's theorem is the fact that  $G_N(P'|Q)$  must satisfy

$$\nabla^2 G_N + k^2 G_N = -\frac{\delta(\rho - \rho')}{\rho} \delta(\phi - \phi') \delta(z - z'), \quad (\text{A1})$$

where  $P' \in V$  is a point with cylindrical coordinates  $(\rho', \phi', z')$ , and  $Q \in V$  a point with cylindrical coordinates  $(\rho, \phi, z)$ .  $V$  is the volume bounded and includes the surface  $S$  of the cylindrical cavity. We now proceed to derive two different forms for  $G_N$ , one which is evanescent in the axial direction and another which is evanescent in the radial direction.

### 1. First form of $G_N$ , evanescent radially

We expand the delta functions on the right-hand side of Eq. (A1) into complete sets of orthogonal functions, given continuity in  $\phi$  and  $\phi'$ ,

$$\delta(\phi - \phi') = \frac{1}{2\pi} \sum_{n=-\infty}^{\infty} e^{in(\phi - \phi')}, \quad (\text{A2})$$

and Neumann boundary conditions in  $z$ ,

$$\delta(z - z') = \frac{1}{L} \sum_{m=0}^{\infty} \epsilon_m \cos(m\pi z/L) \cos(m\pi z'/L). \quad (\text{A3})$$

The latter is valid for  $z'$  on the open interval  $(0, L)$ . Similarly we expand  $G_N(P'|Q)$  in  $z$  and  $\phi$ , leaving the function  $g_{nm}$  in  $\rho$  and  $\rho'$  unknown:

$$\begin{aligned} G_N(P'|Q) &= \frac{1}{2\pi L} \sum_{n=-\infty}^{\infty} e^{in(\phi - \phi')} \\ &\times \sum_{m=0}^{\infty} \epsilon_m \cos(m\pi z/L) \\ &\times \cos(m\pi z'/L) g_{nm}(\rho, \rho'), \end{aligned} \quad (\text{A4})$$

with the boundary conditions

$$\left. \frac{\partial G_N}{\partial z} \right|_{z=0} = \left. \frac{\partial G_N}{\partial z} \right|_{z=L} = 0.$$

Inserting Eq. (A4) into (A1) yields a differential equation for the unknown radial function,  $g_{nm}$ :

$$\begin{aligned} \left[ \frac{1}{\rho} \frac{d}{d\rho} \left( \rho \frac{d}{d\rho} \right) + k^2 - \left( \frac{n}{\rho} \right)^2 - \left( \frac{m\pi}{L} \right)^2 \right] g_{nm}(\rho, \rho') \\ = -\frac{\delta(\rho - \rho')}{\rho}. \end{aligned} \quad (\text{A5})$$

The boundary condition on  $G_N$  requires

$$\left. \frac{\partial}{\partial \rho} g_{nm}(\rho, \rho') \right|_{\rho=a} = 0. \quad (\text{A6})$$

The function which satisfies Eq. (A5) and the necessary jump condition ( $\rho' < a$ ),

$$\left. \frac{dg_{nm}}{d\rho} \right|_{\rho=\rho'+\epsilon} - \left. \frac{dg_{nm}}{d\rho} \right|_{\rho=\rho'-\epsilon} = -\frac{1}{\rho'}, \quad (\text{A7})$$

associated with it, along with the boundary condition, Eq. (A6), is

$$g_{nm} = \frac{\pi}{2} J_n(k_m \rho_{<}) \left[ J_n(k_m \rho_{>}) \frac{Y'_n(k_m a)}{J'_n(k_m a)} - Y_n(k_m \rho_{>}) \right]. \quad (\text{A8})$$

We use the convention that  $\rho_{>}$  represents the larger of  $\rho$  and  $\rho'$ , and  $\rho_{<}$  the smaller. Substitution of Eq. (A8) back into Eq. (A4) yields the desired Green's function,

$$\begin{aligned} G_N(P'|Q) &= \frac{1}{4L} \sum_{n=-\infty}^{\infty} e^{in(\phi - \phi')} \\ &\times \sum_{m=0}^{\infty} \epsilon_m \cos\left(\frac{m\pi z}{L}\right) \cos\left(\frac{m\pi z'}{L}\right) \\ &\times J_n(k_m \rho_{<}) \left[ J_n(k_m \rho_{>}) \frac{Y'_n(k_m a)}{J'_n(k_m a)} \right. \\ &\left. - Y_n(k_m \rho_{>}) \right]. \end{aligned} \quad (\text{A9})$$

### 2. Second form of $G_N$ , evanescent axially

Returning to Eq. (A1), another form of the Neumann Green's function can be obtained by expanding the delta functions in  $\rho$  and  $\phi$  using complete sets of the corresponding orthogonal functions, leaving the delta function in  $z$ . Noting that

$$\begin{aligned} \int_0^a J_n(\kappa_{ns} \rho/a) J_n(\kappa_{ns} \rho'/a) \rho \, d\rho \\ = \frac{a^2}{2} \left( 1 - \frac{n^2}{\kappa_{ns}^2} \right) J_n^2(\kappa_{ns}) \delta_{ss'}, \end{aligned} \quad (\text{A10})$$

and that  $J'_n(\kappa_{ns}) = 0$ , the delta function in  $\rho$  is then

$$\begin{aligned} \frac{\delta(\rho - \rho')}{\rho} &= \frac{2}{a^2} \sum_{s=1}^{\infty} J_n(\kappa_{ns} \rho'/a) J_n(\kappa_{ns} \rho/a) \\ &\times \frac{\kappa_{ns}^2}{(\kappa_{ns}^2 - n^2) J_n^2(\kappa_{ns})}. \end{aligned} \quad (\text{A11})$$

Thus, expanding  $G_N$  into eigenfunctions in  $\rho$  and  $\phi$  leads to

$$\begin{aligned} G_N(P'|Q) &= \frac{1}{\pi a^2} \sum_{n=-\infty}^{\infty} e^{in(\phi - \phi')} \\ &\times \sum_{s=1}^{\infty} \frac{\kappa_{ns}^2 J_n(\kappa_{ns} \rho/a) J_n(\kappa_{ns} \rho'/a)}{(\kappa_{ns}^2 - n^2) J_n^2(\kappa_{ns})} g_{ns}(z, z'). \end{aligned} \quad (\text{A12})$$

Inserting this result into Eq. (A1) yields

$$\frac{d^2 g_{ns}}{dz^2} + (k^2 - (\kappa_{ns}/a)^2)g_{ns} = -\delta(z - z'),$$

whose solution satisfying the Neumann boundary conditions and the jump condition on  $(0, L)$ ,

$$\left. \frac{dg_{ns}}{dz} \right|_{z=z'+\epsilon} - \left. \frac{dg_{ns}}{dz} \right|_{z=z'-\epsilon} = -1, \quad (\text{A13})$$

is

$$g_{ns}(z, z') = -\frac{\cos(\gamma_{ns}z_{<})\cos(\gamma_{ns}(L - z_{>}))}{\gamma_{ns} \sin(\gamma_{ns}L)}, \quad (\text{A14})$$

where

$$\gamma_{ns} \equiv \sqrt{k^2 - (\kappa_{ns}/a)^2}.$$

Inserting Eq. (A14) into Eq. (A12) yields the alternate form of the Green's function,

$$G_N(P'|Q) = -\frac{1}{\pi a^2} \sum_{n=-\infty}^{\infty} e^{in(\phi - \phi')} \times \sum_{s=1}^{\infty} \frac{\kappa_{ns}^2 J_n(\kappa_{ns}\rho/a) J_n(\kappa_{ns}\rho'/a)}{(\kappa_{ns}^2 - n^2) J_n^2(\kappa_{ns})} \times \frac{\cos(\gamma_{ns}z_{<})\cos(\gamma_{ns}(L - z_{>}))}{\gamma_{ns} \sin(\gamma_{ns}L)}. \quad (\text{A15})$$

It is informative to realize that the derived Green's functions are solutions to a different problem.  $G_N(P'|Q)$  provides the pressure at a point  $P'$  in  $V$  due to a point source located at  $Q$  in  $V$  in a cylindrical box with rigid walls.

## APPENDIX B: THE DIRICHLET GREEN'S FUNCTIONS

In this case we seek the Green's function,  $G_D(P'|Q)$ , which vanishes for  $Q \in S$ , again satisfying Eq. (A1). Equation (A2) remains the same, but Eqs. (A3) and (A11) are replaced with the orthonormal eigenfunctions for the pressure release cavity,  $\sqrt{2/L} \sin(m\pi z/L)$  for the axial direction and  $\sqrt{2} J_n(\bar{\kappa}_{ns}\rho/a) / (a J_{n+1}(\bar{\kappa}_{ns}))$  for the radial direction. In this case  $\bar{\kappa}_{ns}$  are the roots of  $J_n(\bar{\kappa}_{ns}) = 0$ .

The derivation proceeds identically to that given for the Neumann Green's functions using the two completeness relations for Dirichlet boundary conditions,

$$\delta(z - z') = \frac{2}{L} \sum_{m=1}^{\infty} \sin\left(\frac{m\pi z}{L}\right) \sin\left(\frac{m\pi z'}{L}\right) \quad (\text{B1})$$

and

$$\frac{\delta(\rho - \rho')}{\rho} = \frac{2}{a^2} \sum_{s=1}^{\infty} J_n(\bar{\kappa}_{ns}\rho/a) J_n(\bar{\kappa}_{ns}\rho'/a) \frac{1}{J_{n+1}^2(\bar{\kappa}_{ns})}. \quad (\text{B2})$$

The final two forms of the Dirichlet Green's function are (1) evanescent radially,

$$G_D(P'|Q) = \frac{1}{2L} \sum_{n=-\infty}^{\infty} e^{in(\phi - \phi')} \times \sum_{m=1}^{\infty} \sin\left(\frac{m\pi z}{L}\right) \sin\left(\frac{m\pi z'}{L}\right) \times \left[ J_n(k_m \rho_{>}) \frac{Y_n(k_m a)}{J_n(k_m a)} - Y_n(k_m \rho_{>}) \right] J_n(k_m \rho_{<}), \quad (\text{B3})$$

and (2) evanescent axially,

$$G_D(P'|Q) = \frac{1}{\pi a^2} \sum_{n=-\infty}^{\infty} e^{in(\phi - \phi')} \times \sum_{s=1}^{\infty} \frac{J_n(\bar{\kappa}_{ns}\rho/a) J_n(\bar{\kappa}_{ns}\rho'/a)}{J_{n+1}^2(\bar{\kappa}_{ns})} \times \frac{\sin(\bar{k}_{ns}z_{<})\sin(\bar{k}_{ns}(L - z_{>}))}{\bar{k}_{ns} \sin(\bar{k}_{ns}L)}, \quad (\text{B4})$$

where

$$\bar{k}_{ns} \equiv \sqrt{k^2 - \bar{\kappa}_{ns}^2/a^2}. \quad (\text{B5})$$

These Green's functions also provide two solutions to another problem, that is, the pressure field (at  $P'$ ) generated by a point source (at  $Q$ ) in a cylindrical cavity with pressure release walls.

- <sup>1</sup>P. Morse and H. Feshbach, *Methods of Theoretical Physics* (McGraw-Hill, New York, 1953), Chap. 7.
- <sup>2</sup>E. G. Williams and J. D. Maynard, "Holographic Imaging without the wavelength resolution limit," *Phys. Rev. Lett.* **45**, 554–557 (1980).
- <sup>3</sup>E. G. Williams, B. Houston, and P. Herdic, "Using NAH to reconstruct the surface velocity and interior acoustic intensity from interior pressure measurements," *Proceedings Inter-Noise96*, Liverpool UK (1996), pp. 2553–2558.
- <sup>4</sup>L. D. Pope and J. F. Wilby, "Band-limited power flow into enclosures," *J. Acoust. Soc. Am.* **62**, 906–911 (1977).
- <sup>5</sup>L. D. Pope, D. C. Rennison, C. M. Willis, and W. H. Mayes, "Development and validation of preliminary analytical models for aircraft interior noise prediction," *J. Sound Vib.* **82**, 541–575 (1982).
- <sup>6</sup>L. Cheng and J. Nicolas, "Radiation of sound into a cylindrical enclosure from a pont-driven endplate with general boundary conditions," *J. Acoust. Soc. Am.* **91**, 1504–1513 (1992).
- <sup>7</sup>L. Cheng, "Fluid-structural coupling of a plate-ended cylindrical shell: Vibration and internal sound field," *J. Sound Vib.* **174**, 641–654 (1994).
- <sup>8</sup>J. Pan and D. A. Bies, "The effect of fluid-structural coupling on sound waves in an enclosure-Theoretical part," *J. Acoust. Soc. Am.* **87**, 691–707 (1990).
- <sup>9</sup>D. Ouellet, J. L. Guyader, and J. Nicolas, "Sound field in a rectangular cavity in the presence of a thin, flexible obstacle by the integral equation method," *J. Acoust. Soc. Am.* **89**, 2131–2139 (1991).
- <sup>10</sup>P. Morse and K. Ingard, *Theoretical Acoustics* (McGraw-Hill, New York, 1968), Sec. 9.4.
- <sup>11</sup>Y. W. Lam and D. C. Hodgson, "The prediction of the sound field due to an arbitrary vibrating body in a rectangular enclosure," *J. Acoust. Soc. Am.* **88**, 1993–2000 (1990).
- <sup>12</sup>D. L. Hallman, "NAH for Interior Spaces," Ph.D. thesis, Purdue University, 1995.
- <sup>13</sup>N. J. Doelman, "A general theory for wave field extrapolation in bounded and unbounded homogeneous media," *J. Acoust. Soc. Am.* **88**, 1964–1974 (1990).

- <sup>14</sup>G. Tyras, *Radiation and Propagation of Electromagnetic Waves* (Academic, New York, 1969), Chap. 8.
- <sup>15</sup>J. D. Jackson, *Classical Electrodynamics* (Wiley, New York, 1975), 2nd ed., p. 116. (In particular, see problem 3.21.)
- <sup>16</sup>E. G. Williams, "NAH for the Aircraft Interior Noise Problem," presented at the NASA Interior Noise Workshop, Langley VA, April 1995.
- <sup>17</sup>E. G. Williams and B. H. Houston, "New Green Functions for Nearfield Acoustical Holography in Aircraft Fuselages," 2nd AIAA/CEAS Aeroacoustics Conference, Paper 96-1703, State College, PA, May 1996.
- <sup>18</sup>E. G. Williams, "The NAH Experimental Method Applied to Vibration and Radiation in Light and Heavy Fluids," *Int. J. Comput. Struct.* (in press).
- <sup>19</sup>H. Nelisse, O. Beslin, and J. Nicolas, "Panel Dynamic Response to a Reverberant Acoustic Field," *AIAA J.* **33**, 1590–1596 (1995).
- <sup>20</sup>P. M. Morse and H. Feshbach, *Methods of Theoretical Physics* (McGraw-Hill, New York, 1953), p. 892.
- <sup>21</sup>S. Hanish, *A Treatise on Acoustic Radiation* (Naval Research Laboratory, Washington, DC, 1989), 3rd ed., pp. 103–113.
- <sup>22</sup>E. G. Williams, H. D. Dardy, and K. B. Washburn, "Generalized nearfield acoustical holography for cylindrical geometry: Theory and experiment," *J. Acoust. Soc. Am.* **81**, 389–407 (1987).

# Acoustic bullets: Transient Bessel beams generated by planar apertures

Peter R. Stepanishen and Jie Sun

*Department of Ocean Engineering, University of Rhode Island, Kingston, Rhode Island 02881*

(Received 29 April 1997; accepted for publication 5 September 1997)

Acoustic bullets are defined to be waves which maintain their peak amplitude and/or general shape as they propagate in free space. A general theoretical approach is presented to investigate the space-time properties of a new class of acoustic bullets which are defined here as acoustic transient Bessel beams. The approach encompasses both baseband and modulated carrier signal wave fields. Closed form space-time expressions are developed using Fourier and Hilbert transform methods for several special cases of transient Bessel beams. The space-time source distributions for generating such wave fields from planar apertures are developed from the free space wave fields via the use of the Rayleigh surface integral solution for time-dependent fields. Finally, numerical results are presented to illustrate the general space-time characteristics of the acoustic transient Bessel beams. © 1997 Acoustical Society of America. [S0001-4966(97)05812-8]

PACS numbers: 43.20.Fn, 43.20.Px [ANN]

## INTRODUCTION

Acoustic bullets are defined here to be waves which maintain their peak amplitude and/or general shape as they propagate in free space. Several types of such wave fields have been recently uncovered. In 1983, Brittingham discovered the first localized wave (LW) solution to the homogeneous Maxwell's equation which he termed the Focus Wave Mode (FWM).<sup>1</sup> This solution corresponds to a Gaussian beam which propagates through space with local variations. A free parameter in the solution determines the overall characteristics of the field corresponding to a quasi-transverse plane wave at one extreme and a narrow spatially transverse pulse at the other extreme.

Shortly afterwards, Ziolkowski introduced a procedure to construct new localized wave (LW) solutions.<sup>2</sup> The procedure was based on an integration over the free parameter in the FWM with a specific weight function. He further developed these localized wave solutions to Electromagnetic Directed-Energy Pulse Trains (EDEPT), which are solutions to the homogeneous Maxwell's equation, and Acoustic Directed-Energy Pulse Trains (ADEPT) which are solutions to the free space scalar wave equation.<sup>3</sup> These localized wave solutions have received enormous attention in the literature.<sup>4-12</sup>

In 1987, Durnin presented a new family of nonsingular solutions to the reduced or Helmholtz equation, which are called the Bessel beams.<sup>13,14</sup> He showed the harmonic field in a transverse plane was unaltered as the wave propagated in free space and transverse spatial widths much less than a wavelength were achieved with an infinite depth of field for an infinite aperture. Considerable interest within the optics community resulted in a number of studies of such fields. In particular, the generation and properties of Bessel beams were further studied by numerous researchers.<sup>15-21</sup>

As result of its obvious crossover to the acoustics community, Bessel beams have received considerable attention amongst ultrasonic researchers. Shortly after the publication of Durnin's work, Hsu *et al.*<sup>22</sup> described the fabrication and

associated experimental results for a harmonic Bessel beam ultrasonic transducer. Lu and Greenleaf<sup>23</sup> subsequently developed a harmonic Bessel beam ultrasonic transducer using a ceramic/polymer composite. More recently, Lu and Greenleaf developed a nondiffracting solution<sup>24,25</sup> to the free space scalar wave equation which was termed an X wave because of the X shape appearance of the field in a plane through the axis of the beam. Numerical studies for the finite source aperture realization of X waves were also presented by Lu and Greenleaf.<sup>24,25</sup>

The present paper focuses on the development of a generalized approach to investigate the space-time properties of a new class of acoustic bullets, designated here as acoustic transient Bessel beams, which include X waves as a special case. In Sec. I, the general theory of acoustic transient Bessel beams is developed for baseband and modulated carrier wave fields using time-domain, Fourier and Hilbert transform techniques. Closed form expressions for several special cases of acoustic transient Bessel beams are then developed in Sec. II. Surface integral equations and the space-time planar aperture distributions which are required to generate acoustic transient Bessel beams from planar apertures are then discussed in Sec. III. In particular, the well known Rayleigh surface integral for time-dependent fields, when combined with the results from Secs. II and I, provides a relatively simple approach to determine the general space-time properties of the acoustic transient Bessel beams which are generated from planar apertures. Finally, numerical results are presented in Sec. IV to illustrate some general characteristics of acoustic transient Bessel beams.

## I. GENERAL THEORY

Consider acoustic wave propagation in an unbounded ideal medium where  $(r, \varphi, x, t)$  are cylindrical space-time coordinates,  $c$  is the constant sound speed of the media, and  $a$  is a characteristic length of interest. Normalized cylindrical space-time coordinates  $(\rho, \varphi, z, \tau)$  as shown in Fig. 1 are introduced where  $\rho = r/a$ ,  $z = x/a$  and the normalized time is



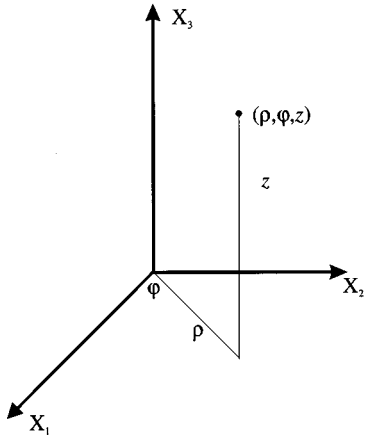


FIG. 1. Normalized coordinates: Cartesian and cylindrical coordinates.

$\tau = ct/a$ . The normalized acoustic wave equation for the pressure field  $p(\rho, z, \tau)$  can then be expressed in the normalized cylindrical coordinate system as

$$\left[ \frac{1}{\rho} \frac{\partial}{\partial \rho} \left( \rho \frac{\partial}{\partial \rho} \right) + \frac{1}{\rho^2} \frac{\partial^2}{\partial \varphi^2} + \frac{\partial^2}{\partial z^2} - \frac{\partial^2}{\partial \tau^2} \right] p(\rho, \varphi, z, \tau) = 0. \quad (1)$$

Using separation of variables it is easily shown that a solution to the free space scalar wave equation in Eq. (1) can be written in the form

$$p_{k_1, k_2}(\rho, \varphi, z, \tau) = J_n(k_1 \rho) e^{i(k_3 \tau - k_2 z + n \varphi)}, \quad (2)$$

where  $k_1^2 + k_2^2 = k_3^2$ . It is noted that  $p_{k_1, k_2}$  is an  $n$ th order nondiffracting Bessel beam and

- (1) For  $n=0$ ,  $p_{k_1, k_2}(\rho, \varphi, z, \tau) = J_0(k_1 \rho) e^{i(k_3 \tau - k_2 z)}$ , which is an axisymmetric solution to the free space scalar wave equation in Eq. (1); this is the zeroth order nondiffracting Bessel beam used by Durin.<sup>13,14</sup>
- (2) If  $n=0$  and  $k_1=0$ , then  $p_{k_2}(\rho, \varphi, z, \tau) = e^{ik_2(\tau - z)}$ , which is a plane wave solution.
- (3) If  $k_1 = \Omega \sin \zeta$  and  $k_2 = \Omega \cos \zeta$ , then  $p_{k_1, k_2}(\rho, \varphi, z, \tau) = J_n(\Omega \sin \zeta \rho) e^{i\Omega(\tau - z \cos \zeta) + in\varphi}$ , which is the  $n$ th-order nondiffracting portion of the Axicon beams.<sup>26,24</sup>

Consider now the  $n=0$  or axisymmetric nondiffracting portion of the Axicon beams. A new family of solutions to the free space scalar wave equation can be constructed, by integrating over the free parameter  $\Omega$  with an arbitrary weight function  $W(\Omega)$ ,

$$p(\rho, z, \tau) = \frac{1}{2\pi} \int_{-\infty}^{\infty} W(\Omega) J_0(\Omega \sin \zeta \rho) e^{i\Omega(\tau - z \cos \zeta)} d\Omega, \quad (3)$$

which is in the form of a Fourier integral. For the case of  $\rho=0$  it is obvious that

$$p(0, z, \tau) = w(\tau - z \cos \zeta), \quad (4)$$

where  $w(\tau)$  and  $W(\Omega)$  are a Fourier transform pair, i.e.,  $w(\tau) \Leftrightarrow W(\Omega)$  where

$$w(\tau) = \frac{1}{2\pi} \int_{-\infty}^{\infty} W(\Omega) e^{i\Omega\tau} d\Omega, \quad (5)$$

$$W(\Omega) = \int_{-\infty}^{\infty} w(\tau) e^{-i\Omega\tau} d\tau. \quad (6)$$

More generally it is observed that  $p(\rho, z, \tau)$  can be expressed as follows:

$$p(\rho, z, \tau) = w(\tau) \otimes j(\rho, z, \tau), \quad (7)$$

where  $\otimes$  denotes the convolution operation and

$$j(\rho, z, \tau) = \frac{1}{2\pi} \int_{-\infty}^{\infty} J_0(\Omega \sin \zeta \rho) e^{i\Omega(\tau - z \cos \zeta)} d\Omega. \quad (8)$$

The integral in Eq. (8) can, however, be readily evaluated to obtain the following closed form expression for  $j(\rho, z, \tau)$ ,

$$j(\rho, z, \tau) = \frac{1}{\pi [(\rho \sin \zeta)^2 - (\tau - z \cos \zeta)^2]^{1/2}},$$

$$0 < |\tau - z \cos \zeta| < \rho \sin \zeta,$$

$$= 0, \quad |\tau - z \cos \zeta| > \rho \sin \zeta, \quad (9)$$

which for  $\rho=0$  can be expressed as

$$j(0, z, \tau) = \delta(\tau - z \cos \zeta), \quad (10)$$

where  $\delta()$  denotes the Dirac delta function. It is thus obvious that  $j(\rho, z, \tau)$  is nonzero only over the domain  $-\rho \sin \zeta + z \cos \zeta < \tau < \rho \sin \zeta + z \cos \zeta$ ; hence,  $j(\rho, z, \tau)$  at any spatial point is a time-limited function, i.e., a function with a finite time duration. In light of Eq. (7) it is also obvious that  $j(\rho, z, \tau)$  is an impulse response function relating  $w(\tau)$  to  $p(\rho, z, \tau)$  for all  $w(\tau)$  of interest.

In contrast to the preceding development,  $w(\tau)$  is now considered to be the real part of an analytic signal which may be represented as follows:

$$w_a(\tau) = w(\tau) + i\hat{w}(\tau), \quad (11)$$

where  $w(\tau)$  and  $\hat{w}(\tau)$  are a Hilbert transform pair,<sup>27</sup> i.e.,

$$\hat{w}(\tau) = \int_{-\infty}^{\infty} \frac{w(\tau')}{\pi(\tau - \tau')} d\tau' \quad (12)$$

and

$$w(\tau) = - \int_{-\infty}^{\infty} \frac{\hat{w}(\tau')}{\pi(\tau - \tau')} d\tau', \quad (13)$$

where the Cauchy principal values of the integrals are assumed. The following Fourier transform relationships are of course well known:

$$w_a(\tau) \Leftrightarrow W_a(\Omega), \quad (14)$$

where

$$W_a(\Omega) = 2W(\Omega)u(\Omega) \quad (15)$$

and  $u(\Omega)$  is the familiar Heaviside step function, i.e.,

$$u(\Omega) = 1, \quad \Omega > 0,$$

$$= 0, \quad \Omega < 0. \quad (16)$$

The analytic signal  $j_a(\rho, z, \tau)$  associated with  $j(\rho, z, \tau)$  may now be introduced as follows:

$$j_a(\rho, z, \tau) = j(\rho, z, \tau) + i\hat{j}(\rho, z, \tau), \quad (17)$$

where  $j(\rho, z, \tau)$  was defined in Eq. (8). Since  $j_a(\rho, z, \tau)$  can also be expressed as the following inverse Fourier transform,

$$j_a(\rho, z, \tau) = \frac{1}{\pi} \int_0^\infty J_0(\Omega \sin \zeta \rho) e^{i\Omega(\tau - z \cos \zeta)} d\Omega, \quad (18)$$

it then follows from Eqs. (17) and (18) that

$$\hat{j}(\rho, z, \tau) = \frac{1}{\pi} \int_0^\infty J_0(\Omega \sin \zeta \rho) \sin[\Omega(\tau - z \cos \zeta)] d\Omega. \quad (19)$$

The integral in Eq. (19) is, however, readily evaluated from standard integral tables<sup>28</sup> to obtain the following expression:

$$\begin{aligned} \hat{j}(\rho, z, \tau) &= 0, \quad 0 < \tau - z \cos \zeta < \rho \sin \zeta \\ &= \frac{1}{\pi[(\tau - z \cos \zeta)^2 - (\rho \sin \zeta)^2]^{1/2}}, \\ &0 < \rho \sin \zeta < \tau - z \cos \zeta. \end{aligned} \quad (20)$$

Since the integrand in Eq. (19) is an odd function of  $\tau - z \cos \zeta$ , it then follows that  $\hat{j}(\rho, z, \tau)$  can be expressed as

$$\begin{aligned} \hat{j}(\rho, z, \tau) &= \frac{1}{\pi[(\tau - z \cos \zeta)^2 - (\rho \sin \zeta)^2]^{1/2}}, \\ &\rho \sin \zeta + z \cos \zeta < \tau, \\ &= 0, \quad -\rho \sin \zeta < \tau - z \cos \zeta < \rho \sin \zeta, \\ &= \frac{-1}{\pi[(\tau - z \cos \zeta)^2 - (\rho \sin \zeta)^2]^{1/2}}, \\ &\tau < -\rho \sin \zeta + z \cos \zeta. \end{aligned} \quad (21)$$

Since  $j(\rho, z, \tau)$  and  $\hat{j}(\rho, z, \tau)$  are nonzero over nonoverlapping regions of the  $\tau$  axis it is obvious they satisfy the orthogonal property of a Hilbert transform pair;<sup>27</sup> however, the energy associated with each signal is not finite.

In a similar manner, the analytic signal  $p_a(\rho, z, \tau)$  associated with  $p(\rho, z, \tau)$  may now be introduced as follows:

$$p_a(\rho, z, \tau) = p(\rho, z, \tau) + i\hat{p}(\rho, z, \tau). \quad (22)$$

In light of Eq. (7) it is then easily shown that  $p_a(\rho, z, \tau)$  can be expressed in several forms as follows:

$$\begin{aligned} p_a(\rho, z, \tau) &= j(\rho, z, \tau) \otimes w_a(\tau) \\ &= j_a(\rho, z, \tau) \otimes w(\tau) \\ &= \frac{1}{2} j_a(\rho, z, \tau) \otimes w_a(\tau). \end{aligned} \quad (23)$$

It is noted the above relationships are valid for all signals of interest, independent of their bandwidth.

An important class of  $w(\tau)$  consists of amplitude and phase modulated carrier signals which can be represented as follows:

$$w(\tau) = a_w(\tau) \cos(2\pi f_0 \tau + \theta_w(\tau)), \quad (24)$$

where  $a_w(\tau)$  is the amplitude modulation,  $\theta_w(\tau)$  is the phase modulation and  $f_0$  is the carrier frequency. For those signals where the bandwidth of the modulation is small relative to the carrier frequency,  $w_a(\tau)$  can then be approximated as follows:

$$w_a(\tau) = \mu_w(\tau) e^{i2\pi f_0 \tau}, \quad (25)$$

where  $\mu_w(\tau)$  is the complex envelope which can be represented as

$$\mu_w(\tau) = a_w(\tau) e^{j\theta_w(\tau)}. \quad (26)$$

In a similar manner  $p_a(\rho, z, \tau)$  can be represented for this class of bandwidth restricted signals as follows:

$$p_a(\rho, z, \tau) = \mu_p(\rho, z, \tau) e^{i2\pi f_0 \tau}, \quad (27)$$

where

$$\mu_p(\rho, z, \tau) = a_p(\rho, z, \tau) e^{i\theta_p(\rho, z, \tau)} \quad (28)$$

and the real pressure signals of interest are thus represented as

$$p(\rho, z, \tau) = a_p(\rho, z, \tau) \cos(2\pi f_0 \tau + \theta_p(\rho, z, \tau)) \quad (29)$$

For this case it is noted that

$$\mu_p(\rho, z, \tau) = \frac{1}{2} \mu_j(\rho, z, \tau) \otimes \mu_w(\tau), \quad (30)$$

where

$$\mu_j(\rho, z, \tau) = j_a(\rho, z, \tau) e^{-i2\pi f_0 \tau}. \quad (31)$$

Since  $\mu_j(\rho, z, \tau)$  is a function of  $f_0$  it is noted that  $\mu_p(\rho, z, \tau)$  will in general also be a function of  $f_0$ .

## II. SPECIAL CASES

Several special cases of acoustic transient Bessel beams are now addressed. Consider first the following representation for  $w(\tau)$  as a baseband signal:

$$w(\tau) = \frac{B}{T} \text{rect}(\tau/T), \quad (32)$$

where

$$\begin{aligned} \text{rect}(\tau/T) &= 1, \quad |\tau| < T/2, \\ &= 0, \quad |\tau| > T/2. \end{aligned} \quad (33)$$

It is obvious that  $w(\tau)$  can also be expressed as

$$w(\tau) = \frac{B}{T} \left[ u\left(\tau + \frac{T}{2}\right) - u\left(\tau - \frac{T}{2}\right) \right], \quad (34)$$

where  $B$  is a constant.

After defining the integral of  $j(\rho, z, \tau)$  as follows,

$$i(\rho, z, \tau) = \int_{-\infty}^{\tau} j(\rho, z, \tau') d\tau', \quad (35)$$

it is easily shown by direct integration that

$$\begin{aligned}
i(\rho, z, \tau) &= 0, \quad \tau < -\rho \sin \zeta + z \cos \zeta, \\
&= \left[ 1 - \frac{1}{\pi} \cos^{-1} \left( \frac{\tau - z \cos \zeta}{\rho \sin \zeta} \right) \right], \\
&\quad -\rho \sin \zeta + z \cos \zeta < \tau < \rho \sin \zeta + z \cos \zeta, \\
&= 1, \quad \rho \sin \zeta + z \cos \zeta < \tau.
\end{aligned} \tag{36}$$

It then follows from Eq. (7) that  $p(\rho, z, \tau)$  can be expressed as

$$p(\rho, z, \tau) = \frac{B}{T} \left[ i \left( \rho, z, \tau + \frac{T}{2} \right) - i \left( \rho, z, \tau - \frac{T}{2} \right) \right]. \tag{37}$$

In the limit as  $T \rightarrow 0$  it is noted that

$$\lim_{T \rightarrow 0} p(\rho, z, \tau) = B j(\rho, z, \tau). \tag{38}$$

As a second representation for  $w(\tau)$  consider the following baseband signal,

$$w(\tau) = \frac{1}{\pi} \frac{BA}{A^2 + \tau^2}, \tag{39}$$

which, in contrast to the first case in Eq. (32), is not time-limited. It is easily shown from Eq. (5) using residue theory that

$$W(\Omega) = B e^{-|\Lambda \Omega|}. \tag{40}$$

Since  $W(\Omega)$  is an even function of  $\Omega$ , the associated time-dependent pressure  $p(\rho, z, \tau)$  for this case can then be expressed using Eq. (3) as

$$\begin{aligned}
p(\rho, z, \tau) &= \frac{B}{\pi} \int_0^\infty J_0(\Omega \sin \zeta \rho) \\
&\quad \times \cos(\Omega(\tau - z \cos \zeta)) e^{-\Omega A} d\Omega.
\end{aligned} \tag{41}$$

The integral can, however, be readily integrated to obtain the following closed form expression for  $p(\rho, z, \tau)$  for  $\rho \sin \zeta > 0$ :

$$p(\rho, z, \tau) = \frac{B}{\pi} \frac{[\sqrt{(A^2 + (\rho \sin \zeta)^2 - (\tau - z \cos \zeta)^2) + 4A^2(\tau - z \cos \zeta)^2 + A^2 + (\rho \sin \zeta)^2 - (\tau - z \cos \zeta)^2}]^{1/2}}{\sqrt{2} \sqrt{(A^2 + (\rho \sin \zeta)^2 - (\tau - z \cos \zeta)^2) + 4A^2(\tau - z \cos \zeta)^2}}. \tag{42}$$

The following expression for the on-axis pressure for this case is also simply obtained from Eq. (41):

$$p(0, z, \tau) = \frac{BA}{\pi [A^2 + (\tau - z \cos \zeta)^2]}. \tag{43}$$

At a time  $\tau'$  it is obvious from Eq. (43) that the center of the wave field, i.e., the pulse center, occurs at a spatial location  $z'$  where  $\tau' = z' \cos \zeta$  with an associated peak value for the field of  $B/\pi A$ . The radial dependence about the pulse center is simply obtained from Eq. (42) and can be expressed as

$$p(\rho, z', \tau') = \frac{B}{\pi \sqrt{A^2 + (\rho \sin \zeta)^2}}. \tag{44}$$

If the axial and radial pulse widths about the pulse center are defined by the locations where the field is equal to  $B/(n\pi A)$ , it is simply shown that

$$\Delta z_n = 2\sqrt{n-1}A/\cos \zeta, \tag{45}$$

$$\Delta \rho_n = 2\rho_n = 2(n^2 - 1)A/\sin \zeta.$$

It is now noted that the spatial widths of the on-axis pulse about the pulse center is independent of  $z'$  and is a constant, i.e., the pulse travels as an acoustic bullet without a change of shape.

Consider now the analytic signal corresponding to the baseband signal in Eq. (39). The Hilbert transform of the baseband signal is readily obtained and the analytic signal can then be represented as follows:

$$w_a(\tau) = \frac{1}{\pi} \left[ \frac{BA}{A^2 + \tau^2} + i \frac{B\tau}{A^2 + \tau^2} \right]. \tag{46}$$

Since  $w_a(\tau)$  can also be represented as

$$w_a(\tau) = \frac{B}{\pi \sqrt{A^2 + \tau^2}} e^{i(\tau/A)}, \tag{47}$$

it is thus apparent from Eq. (26) that

$$a_w(\tau) = \frac{B}{\pi \sqrt{A^2 + \tau^2}} \tag{48}$$

and

$$\theta_w(\tau) = \frac{\tau}{A}. \tag{49}$$

Since the Fourier transform of  $w_a(\tau)$  is simply expressed as follows,

$$W_a(\Omega) = 2B e^{-A\Omega} u(\Omega), \tag{50}$$

it is easily shown that  $p_a(\rho, z, \tau)$  for this case can be expressed in a closed form as follows:

$$p_a(\rho, z, \tau) = \frac{B}{\pi} \frac{1}{[(\rho \sin \zeta)^2 + (A - i(\tau - z \cos \zeta))^2]^{1/2}}. \tag{51}$$

The above solution was previously developed by Lu and Greenleaf<sup>24,25</sup> who defined the resultant field as an X-wave field. In light of the present development it is clear that the real part of  $p_a(\rho, z, \tau)$  is equivalent to the baseband pressure  $p(\rho, z, \tau)$  in Eq. (42). It is equally clear from the present development that the imaginary part of  $p_a(\rho, z, \tau)$  is the Hilbert transform of  $p(\rho, z, \tau)$  which can be expressed as

$$\hat{p}(\rho, z, \tau) = \frac{B}{\pi} \frac{[\sqrt{(A^2 + (\rho \sin \zeta)^2 - (\tau - z \cos \zeta)^2) + 4A^2(\tau - z \cos \zeta)^2} - A^2 - (\rho \sin \zeta)^2 + (\tau - z \cos \zeta)^2]^{1/2}}{\sqrt{2} \sqrt{(A^2 + (\rho \sin \zeta)^2 - (\tau - z \cos \zeta)^2) + 4A^2(\tau - z \cos \zeta)^2}}. \quad (52)$$

This latter field thus corresponds to the imaginary part of  $w_a(\tau)$  which is the Hilbert transform of  $w(\tau)$ , i.e.,  $\hat{w}(\tau) \rightarrow \hat{p}(\rho, z, \tau)$  where  $\hat{w}(\tau)$  is known from Eq. (46).

The following expression for the on-axis pressure for the analytic signal  $p_a(\rho, z, \tau)$  is simply obtained from Eq. (51):

$$p_a(0, z, \tau) = \frac{B}{\pi} \frac{1}{A - i(\tau - z \cos \zeta)}. \quad (53)$$

At the pulse center the peak value for the field is again  $B/\pi A$ , which is to be expected since  $\hat{p}(0, z, \tau)$  is zero at the pulse center. The radial dependence about the pulse center is also simply obtained from Eq. (51) and can be expressed as

$$p_a(\rho, z', \tau') = \frac{B}{\pi \sqrt{A^2 + (\rho \sin \zeta)^2}}. \quad (54)$$

If the axial and radial pulse widths about the pulse center are now defined by the locations where the field is equal to  $B/(n\pi A)$ , it is simply shown that:

$$\Delta z_n = 2\sqrt{n^2 - 1}A/\cos \zeta, \quad (55)$$

$$\Delta \rho_n = 2\rho_n = 2\sqrt{n^2 - 1}A/\sin \zeta.$$

Once again it is observed that the spatial widths of the on-axis pulse about the pulse center are independent of  $z'$  and are constant, i.e., the pulse travels as an acoustic bullet.

As a final case of interest consider now the following amplitude modulated signal,

$$w(\tau) = \frac{1}{\pi} \frac{BA}{A^2 + \tau^2} \cos(2\pi f_0 \tau), \quad (56)$$

where the amplitude modulation is the baseband signal in Eq. (39) and  $f_0 A \gg 1$ . The associated analytic signal for this case can then be approximated as follows:

$$w_a(\tau) = \frac{1}{\pi} \frac{BA}{A^2 + \tau^2} e^{i2\pi f_0 \tau}. \quad (57)$$

It is thus apparent that

$$\mu_w(\tau) = a_w(\tau) = \frac{1}{\pi} \frac{BA}{A^2 + \tau^2}. \quad (58)$$

The pressure field of interest  $p(\rho, z, \tau)$  can then be directly evaluated via the use of Eq. (7) or indirectly by taking the real part of  $p_a(\rho, z, \tau)$  which can be evaluated via the use of Eq. (30).

### III. TRANSIENT BESSEL BEAMS GENERATED BY PLANAR SOURCES

The geometry of interest here is shown in Fig. 2 to consist of a baffled planar source in the plane  $z=0$ . An approach is presented now to determine the space-time properties of transient Bessel beams generated by finite apertures, i.e., pla-

nar circular transducers or arrays, which are excited with an appropriate axisymmetric space-time distribution to generate a transient Bessel beam. The distributions of interest are required to result in the space-time transient Bessel beams of the previous section for the case of an infinite aperture.

It is well known that the space-time acoustic field from a planar source may be represented as the following surface integral, i.e.,

$$p(\rho, z, \tau) = \int_0^{\sigma_0} \rho_s d\rho_s \int_0^{2\pi} d\theta \frac{\cos(R, z)}{2\pi R} \times \left\{ \frac{\partial p(\rho_s, 0, \tau_s)}{\partial \tau_s} + \frac{p(\rho_s, 0, \tau_s)}{R} \right\}_{\tau_s = \tau - R}, \quad (59)$$

where  $\cos(R, z) = \hat{R} \cdot \hat{z}$ . In contrast to the representation of the acoustic field due to the dipole source distribution in Eq. (59) the following retarded potential or classical Rayleigh surface integral solution<sup>29,30</sup> can also be used to evaluate the acoustic pressure field  $p(\rho, z, \tau)$  from a planar source using space-time methods, i.e.,

$$p(\rho, z, \tau) = \int_0^{\sigma_0} \rho_s d\rho_s \int_0^{2\pi} d\theta \frac{1}{2\pi R} \times \left\{ \frac{\partial u(\rho_s, 0, \tau_s)}{\partial \tau_s} \right\}_{\tau_s = \tau - R}, \quad (60)$$

where  $R = \sqrt{\rho^2 + \rho_s^2 - 2\rho\rho_s \cos \theta + z^2}$  and  $\partial u(\rho, 0, \tau)/\partial \tau$  is the space-time normal acceleration distribution of interest.

Since the surface pressure in Eq. (59) may be obtained from the preceding section, Eq. (59) can, in principle, be used to evaluate  $p(\rho, z, \tau)$  where it is noted that the surface pressure beyond the aperture is considered to be zero. As an

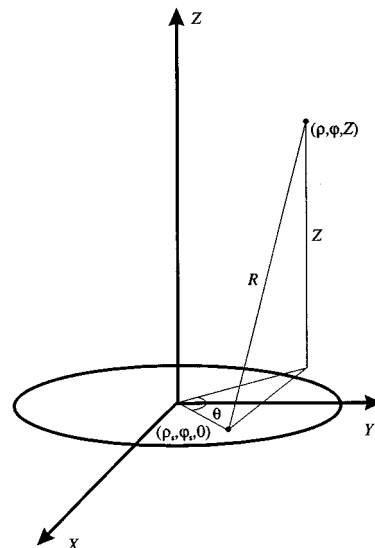


FIG. 2. The geometry of interest.

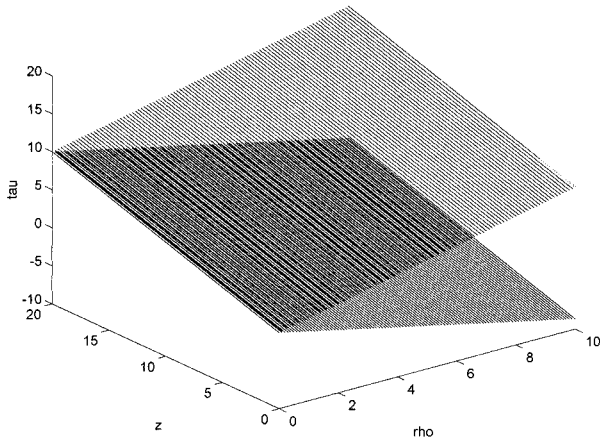


FIG. 3. The boundaries for the nonzero response of the impulse response.

alternative, Eq. (60) may be used, in which case the space-time normal acceleration distribution of interest is presumed known and specified to be zero outside the aperture. Since the surface acceleration can be more directly controlled in a planar array of acoustic projectors, Eq. (60) is the equation of choice here to investigate the space-time characteristics of transient Bessel beams. In light of the linearized momentum equation at the boundary  $z=0$ , it is apparent that

$$\frac{\partial u(\rho_s, 0, \tau_s)}{\partial \tau_s} = - \left. \frac{\partial p(\rho_s, z, \tau_s)}{\partial z} \right|_{z=0} \quad (61)$$

and it then follows that

$$p(\rho, z, \tau) = - \int_0^{\sigma_0} \rho_s d\rho_s \int_0^{2\pi} d\theta \frac{1}{2\pi R} \times \left\{ \left. \frac{\partial p(\rho_s, z, \tau_s)}{\partial z} \right|_{\tau_s = \tau - R} \right\}_{z=0}, \quad (62)$$

where the surface pressure is known from the results in the preceding section.

#### IV. NUMERICAL RESULTS

Numerical results are first presented here for the impulse response  $j(\rho, z, \tau)$  which is of fundamental importance for acoustic transient Bessel beams. It is first noted that the time region of support of the impulse response  $j(\rho, z, \tau)$  is bounded by two planes in  $(\rho, z, \tau)$  space as illustrated in Fig. 3 for the particular case of  $\zeta = \pi/3$ . The spatial region of support in  $(\rho, z)$  space at a fixed  $\tau$  thus consists of a characteristic V-shape, i.e., a conical section as illustrated in Fig. 4, which travels in the  $z$  direction as  $\tau$  increases according to the relationship  $\tau = z \cos \zeta$ . It is thus obvious that the normalized phase velocity along the  $z$  axis is equivalent to  $1/\cos \zeta$  and the time duration of the impulse response is independent of  $z$  and is equivalent to  $2\rho \sin \zeta$ . It is interesting to note that the normalized impulse response  $\rho \sin \zeta j(\rho, z, \tau)$  at each point  $(\rho, z)$  is simply a function of a single parameter  $\alpha = (\tau - z \cos \zeta)/\rho \sin \zeta$  as illustrated in Fig. 5 and is zero for  $|\alpha| > 1$ . The time histories at different spatial locations are

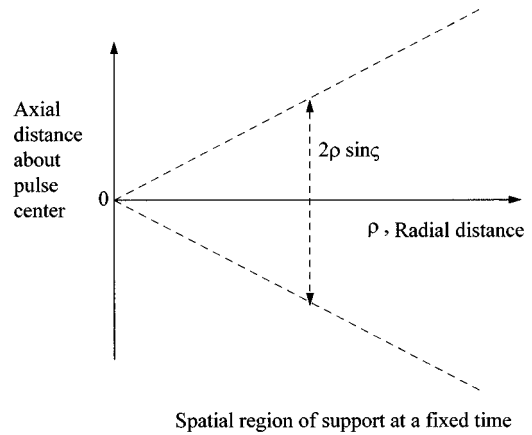


FIG. 4. Spatial region of support at a fixed time.

thus identical, apart from an amplitude and time scaling, and exhibit weak singularities at the start and end of the pulse corresponding to  $|\alpha| = 1$ .

In contrast to the impulse response  $j(\rho, z, \tau)$  which exhibits singularities as noted above, the step or integrated impulse response which is equivalent to  $i(\rho, z, \tau)$  is well behaved due to the weak nature of the endpoint singularities in  $j(\rho, z, \tau)$ . The integrated normalized impulse response can also be expressed as a function of a single parameter  $\alpha$  as illustrated in Fig. 3 where the response is noted to be zero for  $\alpha < -1$  and one for  $\alpha > 1$ . The turn-on transient associated with the case of  $w(\tau) = u(\tau)$  is thus readily visualized from Fig. 6. More specifically, for a fixed  $\tau'$  the spatial field is unity below the lower conical surface where  $\tau' = z \cos \zeta + \rho \sin \zeta$ . The field decreases to zero in the manner illustrated in Fig. 6 in the V-shaped conical region about the pulse center and is zero in the region above the boundary  $\tau' = z \cos \zeta - \rho \sin \zeta$ . As noted in Sec. I the pressure field resulting from a rectangular pulse is easily visualized via a difference of two step responses where the latter response exhibits a time delay which is a simple translation of the conical surfaces in Fig. 3 in the  $-z$  direction.

Consider now the pressure field associated with the baseband signal in Eq. (39). The simple closed form expres-

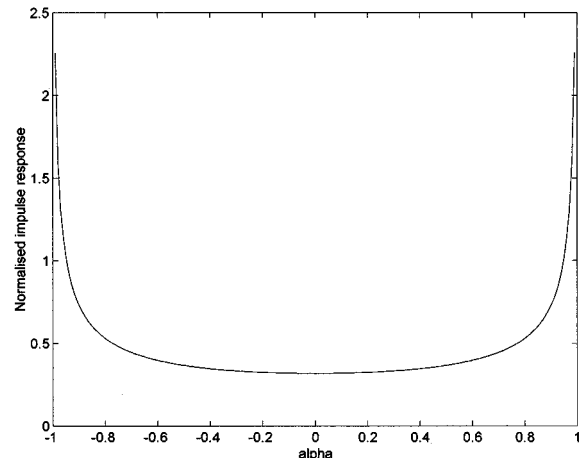


FIG. 5. The normalized impulse response versus alpha where  $\alpha = (\tau - z \cos \zeta)/\rho \sin \zeta$ .

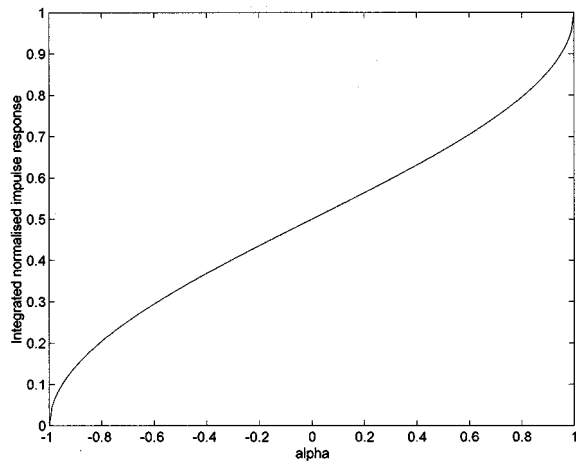


FIG. 6. The integrated normalized impulse response versus alpha where  $\alpha = (\tau - z \cos \xi) / \rho \sin \xi$ .

sion for  $p(\rho, z, \tau)$  in Eq. (42) was used to obtain the numerical results in Fig. 7(a) which illustrate the spatial field about the pulse center for  $A = 0.125$  and  $\zeta = 4^\circ$ . The  $-3$  and  $-6$  dB contours corresponding to this pressure surface are shown in Fig. 7(b). Since  $p(\rho, z, \tau)$  can be interpreted as resulting from the convolution of the baseband signal and the impulse response  $j(\rho, z, \tau)$  — see Eq. (7) — it is not surprising that the general characteristics of the field associated with the impulse response  $j(\rho, z, \tau)$  are readily observed in the numerical results for  $p(\rho, z, 0)$ , e.g., the characteristic V-shape of the field is readily apparent. It is also clear that the spatial

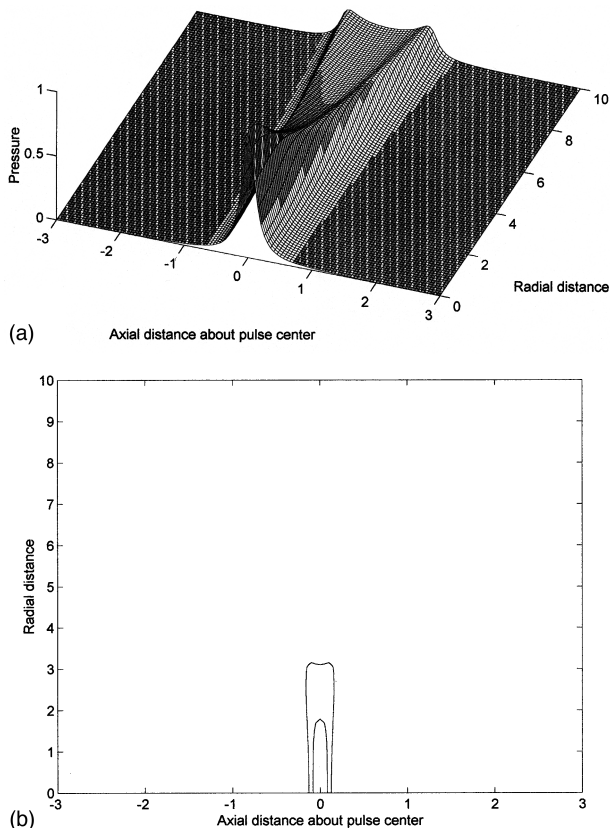


FIG. 7. (a) Baseband wave—pressure map for  $B = \pi i^* A$  and  $A = 0.125$ . (b) Baseband wave—contour plot for  $B = \pi i^* A$  and  $A = 0.125$ .

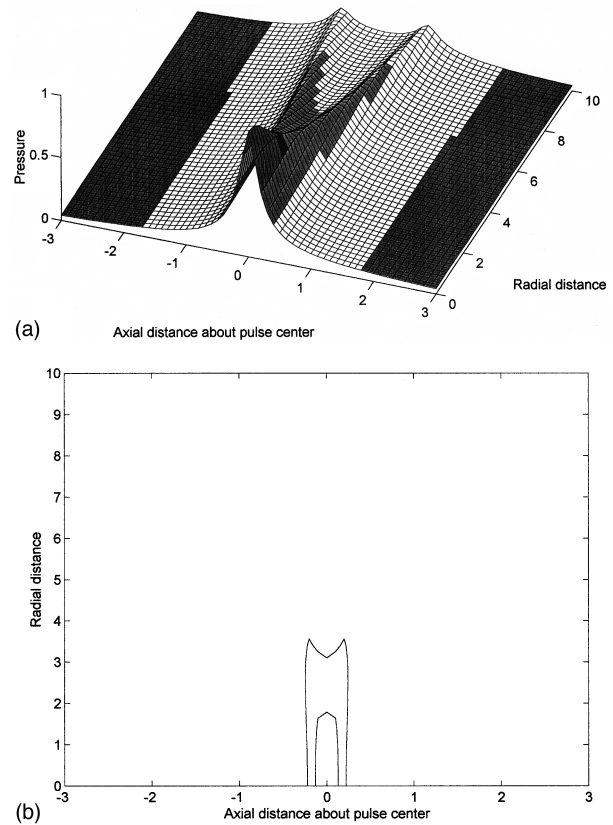


FIG. 8. (a) X-wave—pressure map for  $B = \pi i^* A$  and  $A = 0.125$ . (b) X-wave—contour plot for  $B = \pi i^* A$  and  $A = 0.125$ .

widths on the associated contour plots in Fig. 7(b) corresponding to  $n = \sqrt{2}$  and 2 agree with the general expressions in Eq. (45).

The peak on-axis value of the baseband field is noted from Fig. 7 to be a constant at the pulse center and the on-axis pressure is noted to exhibit the same spatial behavior about the center of the pulse as the baseband temporal signal. Since the pressure field propagates in the  $z$  direction with a normalized phase velocity of  $1/\cos \zeta$  the pressure map in Fig. 7(a) also provides information on the temporal behavior of the field. It is thus evident that the on-axis pressure at any location also exhibits the same temporal behavior as the baseband signal. The time-dependent pressure about the pulse center at off-axis points is also noted to exhibit a linearly increasing pulse duration with radial distance with a symmetric pulse shape about the pulse center and finite maxima associated with the boundaries of the V-shaped region noted above. Once again, the results are to be expected since  $p(\rho, z, \tau)$  can be interpreted as resulting from the convolution of the baseband signal and the impulse response  $j(\rho, z, \tau)$ .

The pressure field associated with the analytic signal in Eq. (46) is now considered where it is again observed that the real part of the signal corresponds to the previously considered baseband signal. The infinite aperture case is first addressed where the simple closed form expression for  $p_a(\rho, z, \tau)$  in Eq. (51) was used to obtain the numerical results in Fig. 8(a) which illustrate the magnitude of the analytic signal for the spatial pressure field about the pulse cen-

ter for  $A=0.125$  and  $\zeta=4^\circ$ . The  $-3$  and  $-6$  dB contours corresponding to this pressure surface are shown in Fig. 8(b). Once again it is not surprising that the general characteristics of the field associated with the impulse response  $j(\rho, z, \tau)$  are observed in the numerical results. It is also clear that the spatial widths on the associated contour plots corresponding to  $n=\sqrt{2}$  and 2 agree with the general expressions in Eq. (55). These results are in general agreement with the earlier work of Lu and Greenleaf.<sup>24,25</sup>

The general spatial-temporal characteristics of the field for this case are readily apparent from inspection of the analytical results in Sec. II and the results in Fig. 8. In particular, it is noted the general characteristics of the field are, not unexpectedly, similar to the baseband case, i.e., the peak on-axis value of the field is noted to be a constant at the pulse center and the on-axis pressure is noted to exhibit the same spatial behavior about the center of the pulse as the baseband temporal signal. Since the pressure field for this case also propagates in the  $z$  direction with a normalized phase velocity of  $1/\cos \zeta$ , the pressure map in Fig. 8(a) also provides information on the temporal behavior of the field, i.e., the on-axis pressure at any location also exhibits the same temporal behavior as the baseband signal and the time-dependent pressure about the pulse center at off-axis points exhibits a linearly increasing pulse duration with radial distance with a symmetric pulse shape about the pulse center and finite maxima associated with the boundaries of the V-shaped region noted above.

Numerical results for the field generated by a finite space-time aperture are now presented for the analytic signal in Eq. (46). In contrast to the approach of Lu and Greenleaf,<sup>24,25</sup> the following results are based on the formulation presented in Sec. III. More specifically, the projection of the field from the finite aperture is formulated as a Neumann boundary value problem which is then solved using space-time integration methods. A planar aperture with a normalized radius of  $\sigma_0=32$  which is excited with the space-time normal acceleration distribution required to launch the amplitude modulated signal of interest is considered with the previously considered parameters  $A=0.125$  and  $\zeta=4^\circ$ . It is noted that the aperture distribution which is required to obtain the analytic pressure is complex; thus, the magnitude, i.e., the envelope, and the real and imaginary parts, of the space-time source distribution are shown in Fig. 9.

The magnitudes of the on-axis time-dependent pressures are shown in Fig. 10(a)–(e) as a function of normalized time about the pulse centers corresponding to  $z=78, 157, 314$  and  $785$ , respectively. It is apparent that the desired uniform maximum response at the pulse center is evident for  $z \lesssim 314$ . Each of the pressure responses can be interpreted as the sum of an infinite aperture contribution and edge generated contribution. For small  $z$  the infinite aperture X wave and a clearly defined edge generated wave are apparent. As the axial distance increases, the interaction of the edge wave and the infinite aperture X wave of interest increases, i.e., the wave components overlap, and the peak amplitude of the on-axis wave decreases. The associated near to far field transition which results from the overlapping of these components in time as the axial distance is increased is clearly

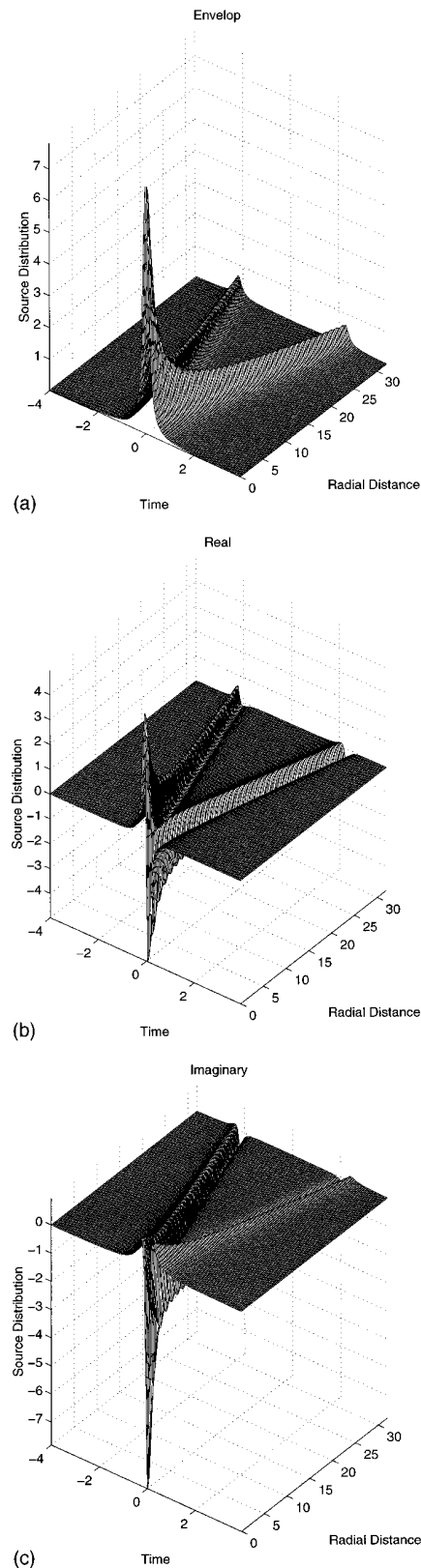


FIG. 9. Space-time source distribution. (a) Envelope. (b) Real part. (c) Imaginary part.

apparent from the sequence in Fig. 10. A similar decomposition of the on-axis field from a uniformly excited aperture was also previously noted using a space-time impulse response approach.<sup>31</sup> An estimate for the axial near to far field

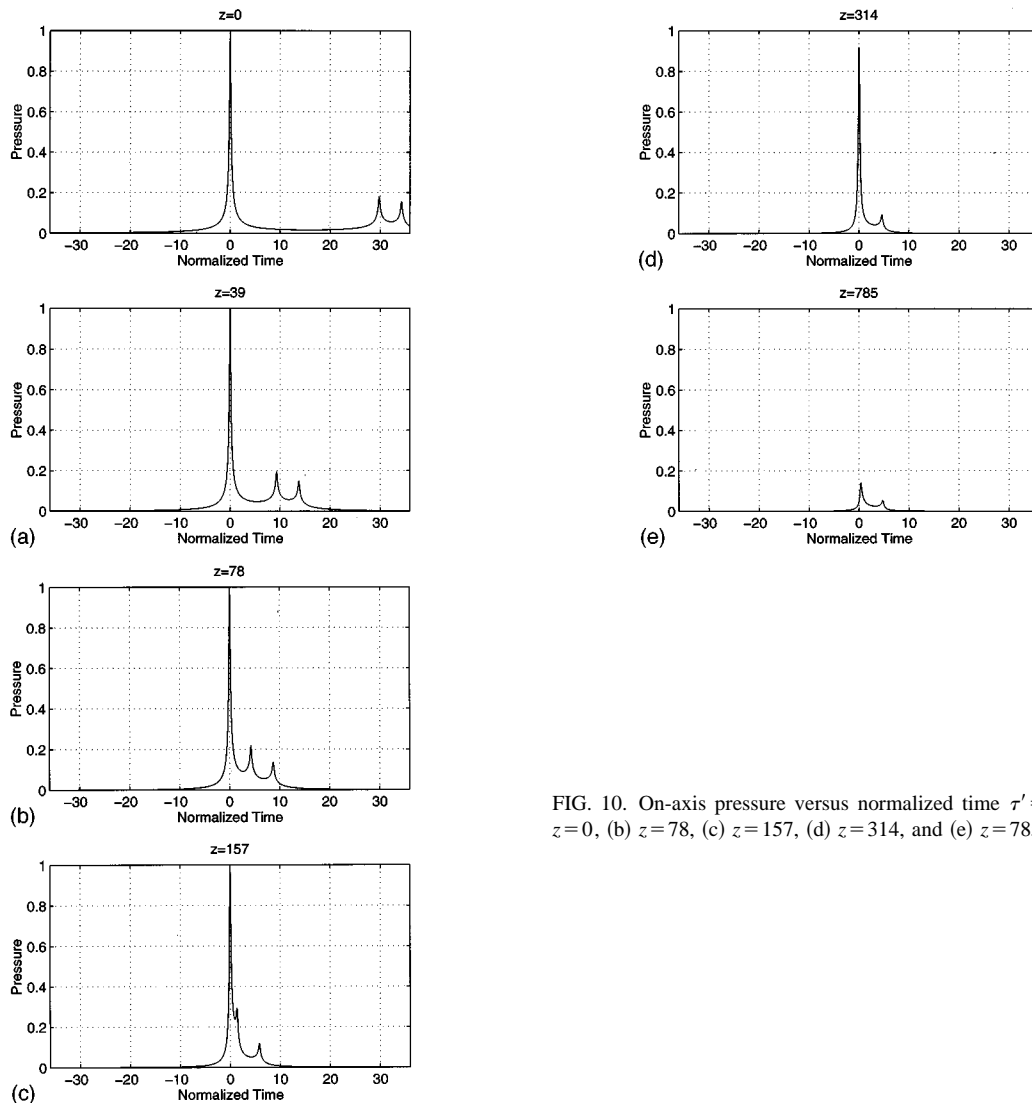


FIG. 10. On-axis pressure versus normalized time  $\tau' = \tau - z \cos \xi$  for (a)  $z=0$ , (b)  $z=78$ , (c)  $z=157$ , (d)  $z=314$ , and (e)  $z=785$ .

transition distance of  $z_t \approx \sigma_0 \cot(\zeta)$  was developed for harmonic Bessel beams<sup>13,14</sup> and leads to a value of approximately 457, which is in reasonable agreement with the present numerical results for the transient Bessel beam.

Since the radial dependence of the pressure field at the pulse center is also of interest and importance in applications, the magnitudes of the pressure for the radial space-time pressure surfaces are presented in Fig. 11(a)–(c) for normalized time about the pulse centers corresponding to  $z = 78, 157$  and  $785$ , respectively. As a result of the edge generated wave the envelopes exhibit a more undulatory behavior relative to the analogous results for an infinite aperture which can be obtained from the results in Fig. 8. In particular, it is noted for the infinite aperture case that the radial width  $\rho_2 \approx 3.1$ , which is approximately 10% of the radius of the finite aperture of present interest. The spatial width of the field for the finite aperture is reasonably well estimated by the field-width relationships in Eq. (55) for axial distances much less than the axial near to far field transition distance. As  $z$  increases the effect of the edge generated wave become progressively more important; however, the aperture width provides a reasonable upper bound for

$z < z_t$ . Clearly, the field exhibits an increasing spatial divergence for axial distances beyond the transition distance.

## V. SUMMARY AND CONCLUSIONS

The development of a generalized approach to investigate the space-time properties of a new class of acoustic bullets, designated here as acoustic transient Bessel beams, has been presented for baseband and analytic signal wave fields using time-domain, Fourier and Hilbert transform techniques. In general, infinite space and time-dependent planar aperture distributions are required to generate such beams; however, the basic approach can be simply used to investigate the generation of such wave fields from both space and time limited aperture distributions. A consistent approach to evaluate such source distributions based on the solution of a Neumann boundary value problem was presented.

Closed form expressions for several special cases of acoustic transient Bessel beams were developed in the paper. A baseband impulse response  $j(\rho, z, \tau)$  was introduced as the key to understanding and evaluating the space-time properties of acoustic transient Bessel beams. Simple convolution



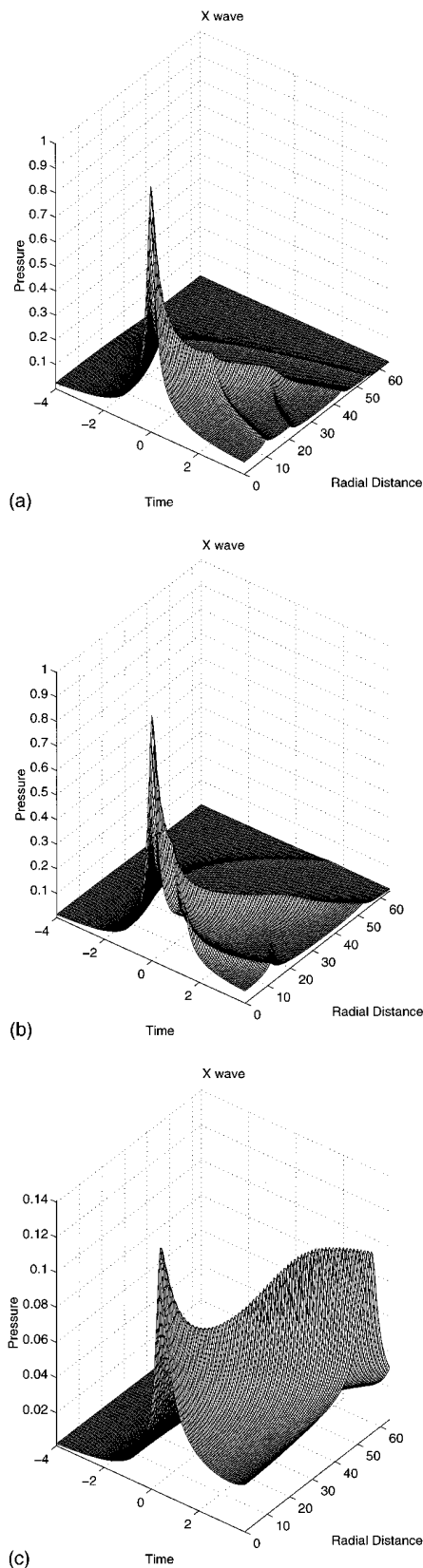


FIG. 11. Radial pressure field versus normalized time  $\tau' = \tau - z \cos \xi$  at pulse center for (a)  $z=78$ , (b)  $z=157$ , and (c)  $z=785$ .

integral relationships were developed for baseband fields. Hilbert transform relationships were then used to develop analogous relationships for analytic signals including amplitude modulated carrier fields. The space-time properties of

the transient Bessel beams can be readily investigated using the convolution integral relationships. In particular, it is noted that the convolution integral relationship in Eq. (7) can be used to investigate the space-time properties of the transient Bessel beams for all real signals of interest.

Numerical results were then presented to illustrate the general characteristics of acoustic transient Bessel beams for several signals. For all cases the general characteristics were simply related back to the characteristics of the impulse response  $j(\rho, z, \tau)$ . The characteristic V-shape of the field was readily apparent for all cases and the normalized phase velocity along the  $z$  axis was equivalent to  $1/\cos \xi$ . Although numerical results were presented for only a single case where  $A=0.125$  and  $\xi=4^\circ$ , it is clear that the lateral and axial widths can be controlled for both the baseband and amplitude modulated case via the selection of the parameters  $A$  and  $\xi$ .

It was noted that transient Bessel beams can be realized with a finite space-time aperture which can generate a beam that is much narrower than the physical source aperture size. The expression for the axial near to far field transition distance of  $z_t \approx \sigma_0 \cot(\xi)$  provides a reasonable first estimate of the transition distance; however, it is noted that  $z_t$  must also depend on the bandwidth parameter  $A$ . The importance of the edge generated wave from the finite aperture was observed and provided a simple interpretation of the near to far field transition process. A lateral resolution less than the aperture size is possible; however, the field exhibits an increasing spatial divergence for axial distances beyond the transition distance to the far field. This area is being addressed in more detail using an impulse response approach based on the present analysis and will be reported shortly.<sup>32</sup> The supersonic speed of transient Bessel beams is also being addressed using a new space-time approach that was recently developed to investigate the self-focusing properties of acoustic bullets.<sup>33</sup>

- <sup>1</sup>J. N. Brittingham, "Focus wave modes in homogeneous maxwell's equations: transverse electric mode," *J. Appl. Phys.* **54**, 1179–1189 (1983).
- <sup>2</sup>R. W. Ziolkowski, "Exact solutions of the wave equation with complex source locations," *J. Math. Phys.* **26**, 861–863 (1985).
- <sup>3</sup>R. W. Ziolkowski, "Localized transmission of wave energy," *Eng. Res.*, 16–23 (1988).
- <sup>4</sup>R. W. Ziolkowski, I. M. Besieris, and A. M. Shaarawi, "Localized wave representations of acoustic and electromagnetic radiation," *Proc. IEEE* **79**, 1371–1378 (1991).
- <sup>5</sup>I. M. Besieris, A. M. Shaarawi, and R. W. Ziolkowski, "A bidirectional traveling plane wave representation of exact solutions of the scalar wave equation," *J. Math. Phys.* **30**, 1254–1269 (1989).
- <sup>6</sup>J. V. Candy, R. W. Ziolkowski, and D. K. Lewis, "Transient waves estimation: a multichannel deconvolution application," *J. Acoust. Soc. Am.* **88**, 2235–2247 (1990).
- <sup>7</sup>J. V. Candy, R. W. Ziolkowski, and D. K. Lewis, "Transient waves: reconstruction and processing," *J. Acoust. Soc. Am.* **88**, 2248–2258 (1990).
- <sup>8</sup>J. E. Hernandez, R. W. Ziolkowski, and S. R. Parker, "Synthesis of the driving functions of an array for propagating localized wave energy," *J. Acoust. Soc. Am.* **92**, 550–562 (1992).
- <sup>9</sup>T. T. Wu, "Electromagnetic missiles," *J. Appl. Phys.* **57**, 2370–2373 (1985).
- <sup>10</sup>T. T. Wu, R. W. P. King, and H. M. Shen, "Spherical lens as a launcher of electromagnetic missiles," *J. Appl. Phys.* **62**, 4036–4040 (1987).
- <sup>11</sup>R. W. Ziolkowski and D. K. Lewis, "Verification of the localized wave transmission effect," *J. Appl. Phys.* **68**, 6083–6086 (1990).

- <sup>12</sup>R. W. Ziolkowski, "Localized wave physics and engineering," *Phys. Rev. A* **44**, 3960–3984 (1991).
- <sup>13</sup>J. Durnin, "Exact solutions for nondiffracting beams. I. The scalar theory," *J. Opt. Soc. Am.* **4**, 651–654 (1987).
- <sup>14</sup>J. Durnin and J. J. J. Miceli, "Diffraction-free beams," *Phys. Rev. Lett.* **58**, 1499–1501 (1987).
- <sup>15</sup>J. Durnin, J. J. J. Miceli, and J. H. Eberly, *Experiments with Nondiffracting Needle Beams* (Optical Society of America, Washington, DC, 1987), p. 208.
- <sup>16</sup>G. Indebetow, "Nondiffracting optical fields: Some remarks on their analysis and synthesis," *J. Opt. Soc. Am. A* **6**, 150–152 (1989).
- <sup>17</sup>F. Gori, G. Guattari, and C. Padovani, "Model expansion for  $j_0$ -correlated schell-model source," *Opt. Commun.* **64**, 311–316 (1987).
- <sup>18</sup>K. Uehara and H. Kikuchi, "Generation of near diffraction-free laser beams," *Appl. Phys. B* **48**, 125–129 (1989).
- <sup>19</sup>L. Vicari, "Truncation of nondiffracting beams," *Opt. Commun.* **70**, 263–266 (1989).
- <sup>20</sup>M. Zahid and M. S. Zubairy, "Directionality of partially coherent bessel-gauss beams," *Opt. Commun.* **70**, 361–364 (1989).
- <sup>21</sup>S. Y. Cai, A. Bhattacharjee, and T. C. Marshall, "'Diffraction-free' optical beams in inverse free electron laser acceleration," *Nucl. Instrum. Methods Phys. Res. A* **272**, 481–484 (1988).
- <sup>22</sup>D. K. Hsu, F. J. Margetan, and D. O. Thompson, "Bessel beam ultrasonic transducer: fabrication method and experiment results," *Appl. Phys. Lett.* **55**, 2066–2068 (1989).
- <sup>23</sup>J. Lu and J. F. Greenleaf, "Ultrasonic nondiffracting transducer for medical imaging," *IEEE Trans. Ultrason. Ferroelectr. Freq. Control* **37**, 438–447 (1990).
- <sup>24</sup>J. Lu and J. F. Greenleaf, "Nondiffracting x waves-exact solutions to free-space scalar wave equation and their finite aperture realization," *IEEE Trans. Ultrason. Ferroelectr. Freq. Control* **39**, 19–31 (1992).
- <sup>25</sup>J. Lu and J. F. Greenleaf, "Experimental verification of nondiffracting x waves," *IEEE Trans. Ultrason. Ferroelectr. Freq. Control* **39**, 441–446 (1992).
- <sup>26</sup>C. B. Burckhardt, H. Hoffmann, and P. A. Grandchamp, "Ultrasound axicon: a device for focusing over large depth," *J. Acoust. Soc. Am.* **54**, 1628–1630 (1973).
- <sup>27</sup>A. Papoulis, *Signal Analysis* (McGraw-Hill, New York, 1980).
- <sup>28</sup>I. S. Gradshteyn and I. M. Ryzhik, *Table of Integrals, Series and Products* (Academic, Orlando, FL, 1980), 2nd ed.
- <sup>29</sup>M. C. Junger and D. Feit, *Sound, Structures, and Their Interaction* (Acoustical Society of America, New York, 1993).
- <sup>30</sup>P. R. Stepanishen, "Acoustic transients from planar axisymmetric vibrators using the impulse response approach," *J. Acoust. Soc. Am.* **70**, 1176–1181 (1981).
- <sup>31</sup>P. R. Stepanishen, "Transient radiation from pistons in an infinite planar baffle," *J. Acoust. Soc. Am.* **49**, 1629–1638 (1971).
- <sup>32</sup>P. R. Stepanishen, "Space-time on-axis and far field properties of acoustic bullets/transient bessel beams via an impulse response approach," *J. Acoust. Soc. Am.* (in preparation).
- <sup>33</sup>J. Sun and P. R. Stepanishen, "Dynamic focusing effects in the generation of acoustic bullets," *J. Acoust. Soc. Am.* (in preparation).

# Sound transmission through elastic porous wedges and foam layers having spatially graded properties

Yeon June Kang

*Department of Mechanical Design and Production Engineering, Seoul National University, San56-1 Shilim-Dong, Kwanak-Ku, Seoul 151-742, Korea*

J. Stuart Bolton

*1077 Ray W. Herrick Laboratories, School of Mechanical Engineering, Purdue University, West Lafayette, Indiana 47907-1077*

(Received 26 March 1996; revised 25 September 1996; accepted 26 September 1996)

Recently a finite element implementation of Biot's elastic porous material theory has been developed for the purpose of modeling and optimizing foam noise control treatments [Y. J. Kang and J. S. Bolton, *J. Acoust. Soc. Am.* **98**, 635–643 (1995)]. That finite element formulation was used in the work reported here to study normal incidence sound transmission through a foam wedge placed in a hard-walled duct. It was found that in some frequency bands the transmission loss of the wedge was significantly higher than that of a plane foam layer of the same volume. That increase in transmission loss was found to result from the conversion, within the foam, of the incident plane wave into a higher-order symmetric mode: that mode was found not to radiate efficiently from the rear surface of the foam wedge. It has also been found that the same increase in transmission loss can be achieved by varying the pore tortuosity across the width (not the depth) of a plane foam layer. Thus it is suggested that lining materials having spatially graded properties may be used to enhance the transmission loss of noise control treatments under some circumstances. © 1997 *Acoustical Society of America*. [S0001-4966(97)02802-6]

PACS numbers: 43.20.Gp, 43.20.Mv, 43.55.Rg [JEG]

## INTRODUCTION

Elastic porous sound-absorbing materials like polyurethane foams differ from fibrous sound-absorbing materials such as glass fiber in the number of wave types that can propagate within them, and thus in their degree of sensitivity to surface boundary conditions. Zwikker and Kosten<sup>1</sup> showed that an elastic porous material such as foam can convey two longitudinal wave types simultaneously, and it is now known that three wave types (two longitudinal and one transverse) can contribute significantly to the observed acoustical behavior of elastic porous materials.<sup>2,3</sup> The acoustical behavior of either isotropic elastic or fibrous porous materials having infinite planar or cylindrical geometries can be modeled by using analytical methods: e.g., plane wave solution techniques.<sup>3,4</sup> Practical noise control treatments having complex shapes and/or nonuniform properties, however, must normally be modeled by using numerical methods such as the finite element method.

Craggs<sup>5-7</sup> developed a finite element model for extended reaction fibrous materials in which the absorbing medium was treated as an effective fluid of complex density and wave number. The latter approach is feasible when the absorbing medium supports only a single longitudinal wave. Recently, a number of displacement-based finite element formulations for elastic porous materials<sup>8-11</sup> have been developed independently, all of them being based on the Biot's theory.<sup>2</sup> Each of these theories fully accounts for the three wave types that can propagate within foams. To demonstrate the accuracy and usefulness of these various foam finite element models, the surface impedance of elastic porous layers and

the sound transmission loss offered by multi-layered foam-lined structures have been calculated and compared with previously established experimental or analytical results.<sup>8,9</sup> However, in all instances, these studies were limited to structures having planar geometries and spatially uniform properties. It is thus of interest to demonstrate the application of foam finite element models to nonplanar structures and/or structures having spatially inhomogeneous properties: that was the initial objective of the work reported here.

Recently Easwaran and Munjal<sup>12</sup> used a fibrous material finite element model to study the absorption characteristics of a fibrous wedge terminating an impedance tube, and they successfully compared their predictions with published experimental results.<sup>13</sup> Subsequently, Kang and Bolton<sup>14</sup> illustrated the application of the foam finite element formulation to the optimal design of foam wedges. In particular, they identified the wedge tip angle that provided the optimal frequency-averaged absorption.

An extension of the latter work is described in this article. In particular, two-dimensional sound transmission through homogeneous foam wedges, and plane foam layers having spatially graded properties are considered. First, however, the two-dimensional boundary conditions that allow a nonplanar foam layer to be coupled to an acoustical system are presented and their incorporation within the previously developed foam finite element formulation is described. Finite element calculations are then presented that show the sound transmission loss of a plane foam layer can be increased significantly at particular frequencies by shaping it into a wedge of the same volume. The increased transmission loss is interpreted as resulting from a mode conversion

process that occurs within the wedge. The results of further calculations are then used to show that the same effect can be induced by spatially grading the tortuosity of a plane foam layer. The latter approach may allow the sound transmission loss offered by a foam layer to be increased without increasing its depth; this finding may be of interest when both high transmission loss and small installation thickness are required in the design of noise control treatments.

## I. THEORY

### A. Finite element formulations

The foam finite element model used in the present work was developed from the differential equations governing wave propagation in elastic porous materials by following procedures described in Refs. 8 and 9. The relationships between the theoretical parameters of that model and the measurable macroscopic parameters that are usually used to describe an elastic porous material (flow resistivity, etc.) are discussed extensively elsewhere.<sup>3,4</sup>

In Ref. 8 it was shown that the global foam system equations can be written in the form:

$$[\mathbf{K}_f] \begin{Bmatrix} \{\mathbf{u}\} \\ \{\mathbf{v}\} \\ \{\mathbf{U}\} \\ \{\mathbf{V}\} \end{Bmatrix} = \begin{Bmatrix} \{\mathbf{F}^1\} \\ \{\mathbf{F}^2\} \\ \{\mathbf{F}^3\} \\ \{\mathbf{F}^4\} \end{Bmatrix}, \quad (1)$$

where

$$F_i^1 = \int_{\Gamma} \phi_i (n_{fx} \sigma_x + n_{fy} \tau_{xy}) d\Gamma, \quad (2a)$$

$$F_i^2 = \int_{\Gamma} \phi_i (n_{fx} \tau_{xy} + n_{fy} \sigma_y) d\Gamma, \quad (2b)$$

$$F_i^3 = \int_{\Gamma} \phi_i n_{fx} s d\Gamma, \quad (2c)$$

$$F_i^4 = \int_{\Gamma} \phi_i n_{fy} s d\Gamma. \quad (2d)$$

In Eq. (1), the vectors  $\{\mathbf{u}\}$ ,  $\{\mathbf{v}\}$ ,  $\{\mathbf{U}\}$ , and  $\{\mathbf{V}\}$  are, respectively, the unknown displacement components of the solid and fluid phases of the foam, i.e.,  $u_x$ ,  $u_y$ ,  $U_x$ , and  $U_y$ , and  $[\mathbf{K}_f]$  is the foam's global dynamic stiffness matrix. In Eqs. (2),  $\sigma_x$ ,  $\sigma_y$ , and  $\tau_{xy}$  are the normal and shear forces per unit material area acting on the solid phase of the foam,  $s$  is the normal force per unit material area acting on the foam's fluid component,  $\phi_i$  is the shape function,  $n_{fx}$  and  $n_{fy}$  are  $x$  and  $y$  components of the outward unit normal vector,  $\mathbf{n}_f$ , of the foam system, and  $d\Gamma$  is the arc length of an infinitesimal line element along the boundary.

The finite element formulation for acoustical domains (i.e., regions in which only a single longitudinal wave propagates) can be derived from the wave equation in a homogeneous acoustic medium, and can be expressed as<sup>6,7</sup>

$$[\mathbf{K}_a]\{\mathbf{p}\} = \{\mathbf{Q}\}, \quad (3)$$

where

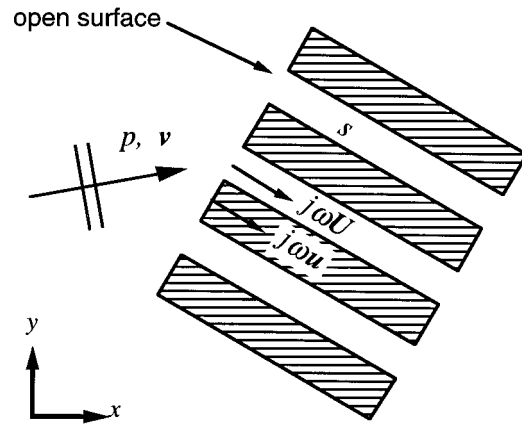


FIG. 1. Exaggerated cross-sectional view of a foam layer having an open surface and arbitrary orientation with respect to the global coordinate axes.

$$Q_i = -j\omega\rho_0 \int_{\Gamma} \phi_i (\mathbf{n}_a \cdot \mathbf{v}_a) d\Gamma. \quad (4)$$

In Eq. (3),  $\{\mathbf{p}\}$  is the vector of unknown nodal pressures,  $\{\mathbf{Q}\}$  is the normal volume velocity flux vector, and the matrix  $[\mathbf{K}_a]$  is defined as  $([\mathbf{T}] - k^2[\mathbf{S}])$ , where  $[\mathbf{T}]$  and  $[\mathbf{S}]$  are the kinetic and strain energy matrices, respectively. In Eq. (4),  $\mathbf{v}_a$  is the acoustic particle velocity in the acoustical domain,  $\mathbf{n}_a$  is the outward unit normal vector at the domain surface, and  $\cdot$  denotes the scalar product.

### B. Boundary conditions at non-normal interfaces

Shown schematically in Fig. 1 is an exaggerated cross-sectional view of a foam surface that is oriented arbitrarily with respect to the global coordinate axes. The forces normal to the surface should be balanced at the nodal points along the interface joining the acoustical and foam systems, and the normal volume velocity should be continuous. Those boundary conditions are

$$hp\mathbf{n}_a = s\mathbf{n}_f, \quad (5a)$$

$$(1-h)p\mathbf{n}_a = (\sigma_x n_{fx} + \tau_{xy} n_{fy})\mathbf{i} + (\tau_{xy} n_{fx} + \sigma_y n_{fy})\mathbf{j}, \quad (5b)$$

$$v_{an} = j\omega(1-h)u_n + j\omega h U_n, \quad (5c)$$

where  $h$  is the surface porosity (and the surface porosity is here assumed to equal the volume porosity),  $p$  is the sound pressure in the acoustical domain,  $v_{an}$  is the particle velocity in the acoustical domain normal to the acoustical system/foam system interface,  $u_n$  and  $U_n$  are the foam's solid and fluid phase displacements normal to the interface, respectively, and  $\mathbf{i}$  and  $\mathbf{j}$  are, respectively, the unit vectors in the  $x$  and  $y$  directions. The first of these conditions requires that the force per unit material area acting on the fluid component of the foam be equal to the porosity times the pressure in the exterior acoustic field. The second equation expresses a similar relation for the force acting on the solid phase. The final condition represents the continuity of normal volume velocity at the interface. These boundary conditions allow the interface of the acoustical and foam systems to be curved, textured, or to be oriented arbitrarily.

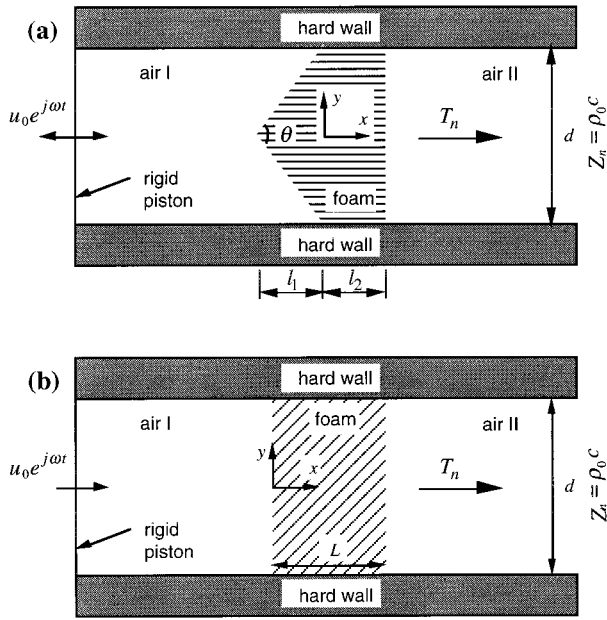


FIG. 2. Configurations for calculation of sound transmission through (a) a wedge having uniform properties, and (b) a plane foam layer ( $L=5.4$  cm,  $d=5.4$  cm) having a spatial variation of tortuosity or flow resistivity.

The configurations studied in the present work are shown in Fig. 2. These arrangements explicitly represent foam layers placed in plane wave tubes. However, owing to the symmetry of the arrangement, they can also be used to represent normal incidence plane wave transmission through an infinite array of identical foam blocks. Note that all calculations presented here are two-dimensional: i.e., the foam is considered to be infinitely deep in the  $z$  direction, and no motion in the  $z$  direction is allowed.

For configurations such as those shown in Fig. 2, the foam finite elements can be coupled with either finite element or modal representations of the acoustical system at the interface of the acoustical and foam systems.<sup>9</sup> In the present work, it was convenient to couple the foam finite elements with acoustical finite elements on the incident side of the foam, and with a modal representation on the transmission side of the foam. By using the latter coupling procedure, the total number of degrees-of-freedom of the problem may be reduced compared to an approach in which the transmission side airspace is also discretized. In addition, the latter approach allows the detailed modal behavior of the transmitted sound field to be studied.

At the incident surface of the foam, the interface conditions (5a)–(5c) should be satisfied. Upon substituting interface conditions (5a)–(5c) into Eqs. (2a)–(2d) and (4), and applying the Galerkin's weighted-residual approximation (i.e.,  $u_x \approx \sum_{j=1}^m u_j \phi_j$ ,  $U_x \approx \sum_{j=1}^m U_j \phi_j$ , and  $p \approx \sum_{j=1}^m p_j \phi_j$ ), one obtains

$$F_i^1 = n_{ax}(1-h) \int_{\Gamma} \phi_i p \, d\Gamma \approx n_{ax}(1-h) \sum_{j=1}^m p_j \int_{\Gamma} \phi_i \phi_j \, d\Gamma, \quad (6a)$$

$$F_i^2 = n_{ay}(1-h) \int_{\Gamma} \phi_i p \, d\Gamma \approx n_{ay}(1-h) \sum_{j=1}^m p_j \int_{\Gamma} \phi_i \phi_j \, d\Gamma, \quad (6b)$$

$$F_i^3 = n_{ax}h \int_{\Gamma} \phi_i p \, d\Gamma \approx n_{ax}h \sum_{j=1}^m p_j \int_{\Gamma} \phi_i \phi_j \, d\Gamma, \quad (6c)$$

$$F_i^4 = n_{ay}h \int_{\Gamma} \phi_i p \, d\Gamma \approx n_{ay}h \sum_{j=1}^m p_j \int_{\Gamma} \phi_i \phi_j \, d\Gamma, \quad (6d)$$

$$Q_i = \omega^2 \rho_0 \int_{\Gamma} \phi_i \mathbf{n}_a \cdot [(1-h)\mathbf{u} + h\mathbf{U}] \, d\Gamma \approx n_{ax} \omega^2 \rho_0 (1-h) \int_{\Gamma} \phi_i u_x \, d\Gamma + n_{ax} \omega^2 \rho_0 h \times \int_{\Gamma} \phi_i U_x \, d\Gamma + n_{ay} \omega^2 \rho_0 (1-h) \times \int_{\Gamma} \phi_i u_y \, d\Gamma + n_{ay} \omega^2 \rho_0 h \int_{\Gamma} \phi_i U_y \, d\Gamma. \quad (6e)$$

The components of the outward unit normal vector of the acoustical system at the nodes of the interface, i.e.,  $n_{ax}$  and  $n_{ay}$ , should be evaluated at the interface.

On the transmission side of the foam, the sound field can be written as

$$p_2 = \sum_{n=0,2,4,\dots}^{\infty} e^{-jk_n x} T_n \cos \frac{n\pi}{d} y, \quad (7)$$

where  $k_n = [(\omega/c_0)^2 - (n\pi/d)^2]^{1/2}$ ,  $c_0$  is the speed of sound in the air,  $T_n$  are the complex amplitudes of the transmitted modes, and  $d$  is the width of the hard-walled duct. Since asymmetric modes have zero forcing under the excitation of a normally incident plane wave, the sound field in the transmitted region as expressed in Eq. (7) represents a superposition of an infinite number of symmetric modes. By following the coupling procedures that were described in Ref. 9, one obtains at the rear surface of the foam system

$$F_i^1 = -(1-h) \sum_{n=0,2,4,\dots}^{\infty} e^{-jk_n L} T_n \int_{\Gamma} \phi_i \cos \frac{n\pi}{d} y \, d\Gamma, \quad (8a)$$

$$F_i^2 = 0, \quad (8b)$$

$$F_i^3 = -h \sum_{n=0,2,4,\dots}^{\infty} e^{-jk_n L} T_n \int_{\Gamma} \phi_i \cos \frac{n\pi}{d} y \, d\Gamma, \quad (8c)$$

$$F_i^4 = 0, \quad (8d)$$

$$j\omega\rho_0^2(1-h)u_j + j\omega\rho_0^2 h U_j - \sum_{n=0,2,4,\dots}^{\infty} k_n e^{-jk_n L} T_n \cos \frac{n\pi}{d} y = 0. \quad (8e)$$

Note that owing to the nature of Eq. (8e), the number of transmitted modes included in the series representation can

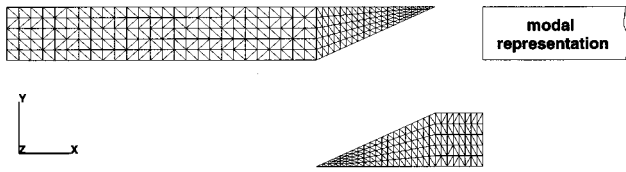


FIG. 3. Typical finite element mesh of the acoustical and foam systems (case W6 is shown in this figure).

be no larger than the number of nodes on the transmission side foam surface.

Complete coupled system equations are obtained by moving the terms on the right-hand sides of Eqs. (6a)–(6e) and (8a)–(8d) into the proper position within the global dynamic stiffness matrix of the system equations in a systematic way, and then by augmenting the system equation with Eq. (8e). When the acoustical and foam systems are coupled, the system equations take the form

$$\begin{bmatrix} [\mathbf{K}_a] & [\mathbf{K}_{af1}] & \vdots \\ [\mathbf{K}_{af2}] & [\mathbf{K}_f] & [\mathbf{K}_{af3}] \\ \vdots & [\mathbf{K}_{af4}] & [\mathbf{K}_{af5}] \end{bmatrix} \begin{Bmatrix} \{\mathbf{P}\} \\ \{\mathbf{u}\} \\ \{\mathbf{v}\} \\ \{\mathbf{U}\} \\ \{\mathbf{V}\} \\ \{\mathbf{T}_n\} \end{Bmatrix} = \begin{Bmatrix} \{\mathbf{Q}\} \\ \{\mathbf{F}^1\} \\ \{\mathbf{F}^2\} \\ \{\mathbf{F}^3\} \\ \{\mathbf{F}^4\} \\ \{\mathbf{0}\} \end{Bmatrix}, \quad (9)$$

where the submatrices  $[\mathbf{K}_{af1}]$  and  $[\mathbf{K}_{af2}]$  result from coupling the foam finite elements with the acoustical finite elements of the incident-side airspace, and the submatrices  $[\mathbf{K}_{af3}]$ ,  $[\mathbf{K}_{af4}]$ , and  $[\mathbf{K}_{af5}]$  result from coupling the foam finite elements with the modal representation of the sound field in the transmission side airspace.

## II. TRANSMISSION LOSS CALCULATIONS

### A. General approach

The normal incidence sound transmission loss was calculated for the configurations shown in Fig. 2(a) and (b), i.e., for a wedge having uniform properties and for a plane foam layer having either spatially varying tortuosity (the motivation for varying the tortuosity in this way will be discussed

TABLE I. Dimensions of the foam wedges.

Case	Dimensions		
	$\theta$ (degree)	$l_1$ (cm)	$l_2$ (cm)
W1	180	0.00	5.40
W2	132	1.20	4.80
W3	97	2.40	4.20
W4	74	3.60	3.60
W5	59	4.80	3.00
W6	48	6.00	2.40
W7	41	7.20	1.80
W8	36	8.40	1.20
W9	28	10.80	0.00

TABLE II. Spatial variation of the tortuosity within a plane foam layer.

y coordinate (cm)	Case No.							
	0	1	2	3	4	5	6	7
2.16~2.70	7.80	7.00	6.00	5.00	4.00	3.00	2.00	1.00
1.62~2.16	7.80	7.20	6.45	5.70	4.95	4.20	3.45	2.70
1.08~1.62	7.80	7.40	6.90	6.40	5.90	5.40	4.90	4.40
0.54~1.08	7.80	7.60	7.35	7.10	6.85	6.60	6.35	6.10
0.00~0.54	7.80	7.80	7.80	7.80	7.80	7.80	7.80	7.80

below in Sec. III B) or spatially varying flow resistivity. In all cases, the foam layers were placed in a 5.4-cm-wide hard-walled duct. In the model, a distance of at least 13.2 cm was maintained between the rigid piston and the wedge tip. In all cases, only the upper half of the model was discretized, since the problems were symmetric with respect to the  $x$  axis. The incident airspace and foam were meshed by using three-noded linear triangular elements which were not larger than 0.3 cm on any of their sides. These elements make it possible to model the acoustical behavior of the foam modeled here at frequencies up to 5 kHz.<sup>9</sup> A typical finite element mesh is shown in Fig. 3, in which case there were 269 nodes and 435 elements in the incident airspace, 159 nodes and 255 elements for the foam, and 6 symmetric modes for the modal representation of transmission side sound field. A plane wave was assumed to be generated by a piston at the left end of the acoustical system, i.e., unit velocities were prescribed at the nodes of the left-hand face of the acoustical system I. In addition, the acoustical system II was assumed to extend to infinity in the  $x$  direction, i.e., waves were only allowed to propagate away from the transmission side face of the foam layer. The origin of the coordinate system was always placed as shown in Fig. 2(a), i.e.,  $y=0$  corresponds to the mid-line of the duct, and  $x=0$  was placed within the foam at the beginning of the plane section. At its lateral edges, the foam was assumed to be either fully constrained (i.e.,  $u_x=0$ ,  $u_y=0$  and  $U_y=0$  at  $y=\pm d/2$ ) or lubricated (i.e.,  $u_y=0$  and  $U_y=0$  at  $y=\pm d/2$ ). The plane wave transmission coefficient, and thus the normal incidence transmission loss, could then be calculated from the complex amplitude of the transmitted plane wave,  $T_0$ , that was obtained by solving Eq. (9). Note that the sound field to the left of the foam layer was decomposed into incident and reflected wave (with amplitudes  $P_{in}$  and  $P_r$ , respectively) by using the complex pressures at two adjacent nodes (separated in the  $x$  direction) in the air space I. The plane wave sound transmission coefficient was then calculated as  $\tau_0=T_0/P_{in}$ . Finally, the normal incidence

TABLE III. Spatial variation of the flow resistivity within a plane foam layer ( $\times 10^3$ ).

y coordinate (cm)	Case No.				
	0	8	9	10	11
2.16~2.70	25.0	20.0	15.0	10.0	5.0
1.62~2.16	25.0	22.5	20.0	17.5	15.0
1.08~1.62	25.0	25.0	25.0	25.0	25.0
0.54~1.08	25.0	27.5	30.0	32.5	35.0
0.00~0.54	25.0	30.0	35.0	40.0	45.0

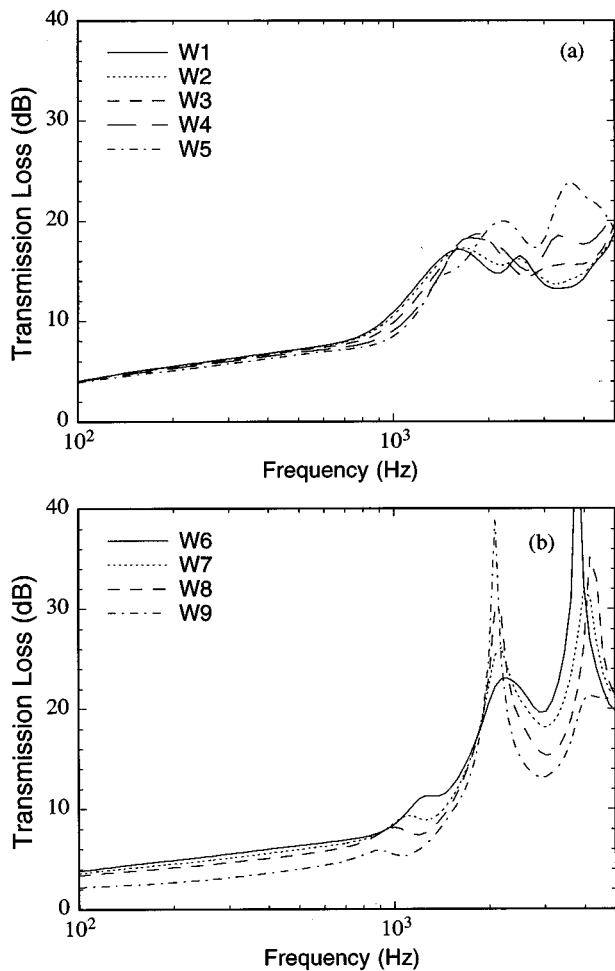


FIG. 4. Normal incidence sound transmission loss of a wedge whose edges are lubricated.

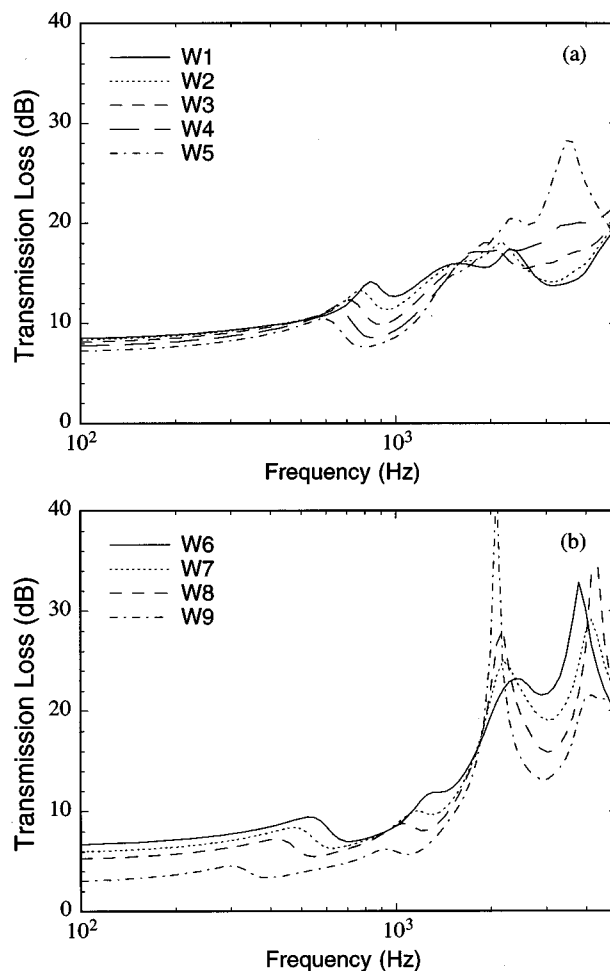


FIG. 5. Normal incidence sound transmission loss of a wedge whose edges are constrained.

transmission loss could be obtained from  $TL = 10 \log(1/|\tau_0|^2)$ . In all cases, calculations were restricted to frequencies below the cut on of the first higher-order symmetric mode in the transmitted-side air space (approximately 6.3 kHz).

The foam parameters used in the present calculations were bulk density of the solid phase,  $\rho_1 = 30 \text{ kg/m}^3$ ; *in vacuo* bulk Young's modulus,  $E_m = 8 \times 10^5 \text{ Pa}$ ; *in vacuo* loss factor,  $\eta = 0.265$ ; bulk Poisson's ratio,  $\nu = 0.4$ ; flow resistivity,  $\sigma = 25 \times 10^3 \text{ mks Rayls/m}$ ; tortuosity,  $\epsilon' = 7.8$ ; and porosity,  $h = 0.9$ . When considering plane foam layers having spatially graded properties, the tortuosity and flow resistivity were varied as described in Secs. II C and II D, respectively.

## B. Wedges

The sound transmission characteristics of a wedge-shaped foam layer having uniform properties were studied in the configuration shown in Fig. 2(a). When the duct width is held constant, while the total volume of foam is itself maintained constant, the wedge dimensions can be defined by a single design parameter: a wedge tip angle,  $\theta$ . The dimensions of all the wedges considered here are summarized in Table I: the wedge tip angle was systematically decreased

from  $180^\circ$  (a plane foam layer) to  $28^\circ$  (the smallest wedge tip angle that did not create a gap between the duct wall and the wedge).

## C. Plane foam layers having spatially graded tortuosity

To demonstrate that sound transmission characteristics similar to those of the wedge can be produced by using a plane foam layer, the tortuosity of a constant depth foam layer was varied across the width of the foam layer. For the configuration shown in Fig. 2(b), the tortuosity was decreased in piecewise-constant steps from 7.8 at the center ( $y=0$ ) to a minimum value in the foam adjacent to the hard walls. The variation was considered to be symmetric with respect to the  $x$  axis. The details of the spatial variation of the tortuosity within the foam layer for the cases considered here are summarized in Table II. Note that the tortuosity variation within the plane foam layer was implemented simply by varying the tortuosity assigned to the foam finite elements forming one sublayer of the material. Thus, although the foam layer as a whole is anisotropic, it is composed of isotropic sublayers. Note also that the plane layers consid-

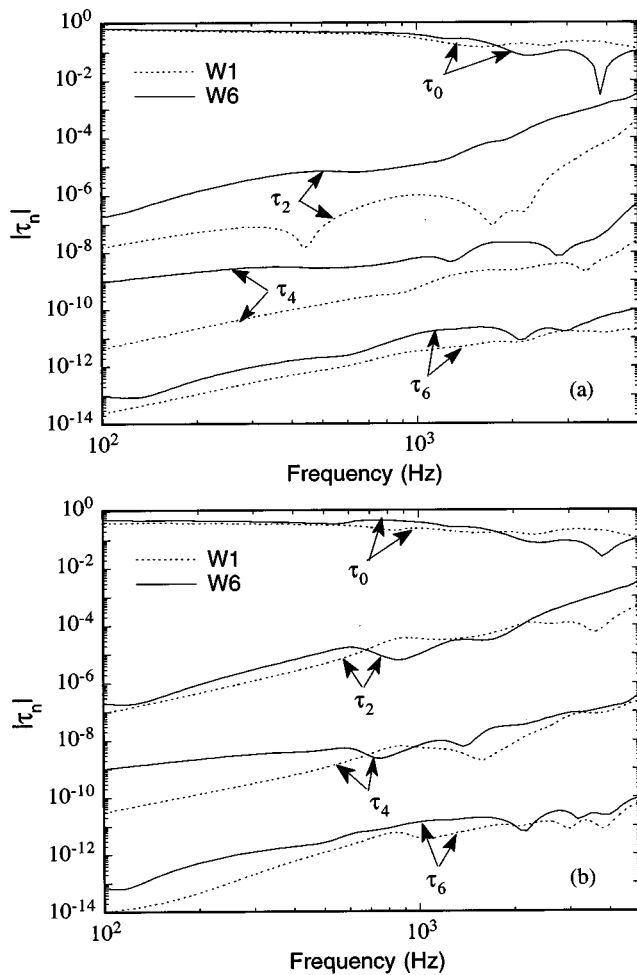


FIG. 6. Magnitude of the plane wave transmission coefficient,  $|\tau_0|$ , and of the transmission coefficients of the higher-order symmetric modes,  $|\tau_n|$  ( $n = 2, 4, 6, \dots$ ), for cases W1 and W6 for (a) lubricated and (b) constrained configurations.

ered here had the same volume as the wedges described the preceding section: i.e., the dimensions of the foam layer were  $5.4 \text{ cm} \times 5.4 \text{ cm}$ .

#### D. Plane foam layers having spatially graded flow resistivity

To demonstrate the effect of the spatial variation of flow resistivity on the sound transmission characteristics of a plane foam layer, the flow resistivity of a constant depth foam layer was varied in the same way as the tortuosity across the width of the foam layer. For the configuration shown in Fig. 2(b), the flow resistivity was decreased in piecewise-constant steps from a maximum at the center to a minimum value in the foam adjacent to the hard walls. In each case, the flow resistivity averaged over the complete foam layer was the same. The variation was considered to be symmetric with respect to the  $x$  axis. The details of the spatial variation of the flow resistivity within the foam layer for the cases studied here are summarized in Table III. The dimensions of the foam layer in this case were also  $5.4 \text{ cm} \times 5.4 \text{ cm}$ .

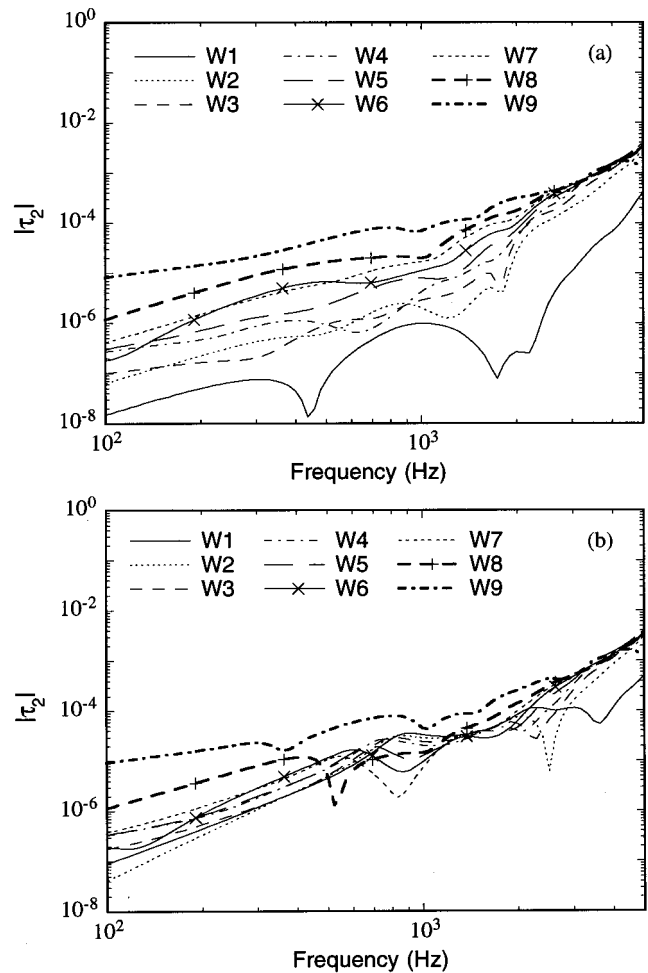


FIG. 7. Magnitude of the transmission coefficient of the first higher-order symmetric mode,  $|\tau_2|$ , for wedges having various tip angles for (a) lubricated and (b) constrained configurations.

### III. RESULTS AND DISCUSSION

#### A. Wedges

First, the transmission losses of foam wedges having various wedge tip angles were calculated using the finite element model described in Sec. III. The results calculated when the edges of the wedge were either lubricated (i.e., unconstrained) or constrained along the hard walls are shown in Figs. 4 and 5, respectively.

For both the lubricated and constrained cases, the transmission loss was found to increase in particular frequency ranges with decreasing tip angle at the expense of reduced transmission loss in the low and mid-frequency ranges. The decreased transmission loss at low frequencies may be attributed to the progressive decrease in layer thickness near the wall (i.e., near  $y = \pm d/2$ ) as the wedge tip angle decreases: that thickness reduces to zero at  $\theta = 28^\circ$ . It may also be seen in Figs. 4 and 5 that the low-frequency transmission loss of the constrained wedges is increased compared to that of the lubricated wedges owing to the stiffening effect of the edge constraint.<sup>9</sup> This effect occurs at frequencies below the resonance associated with the total mass of the foam layer acting against the stiffness afforded by the edge constraints. That resonance occurs at approximately 800 Hz in case W1 (see



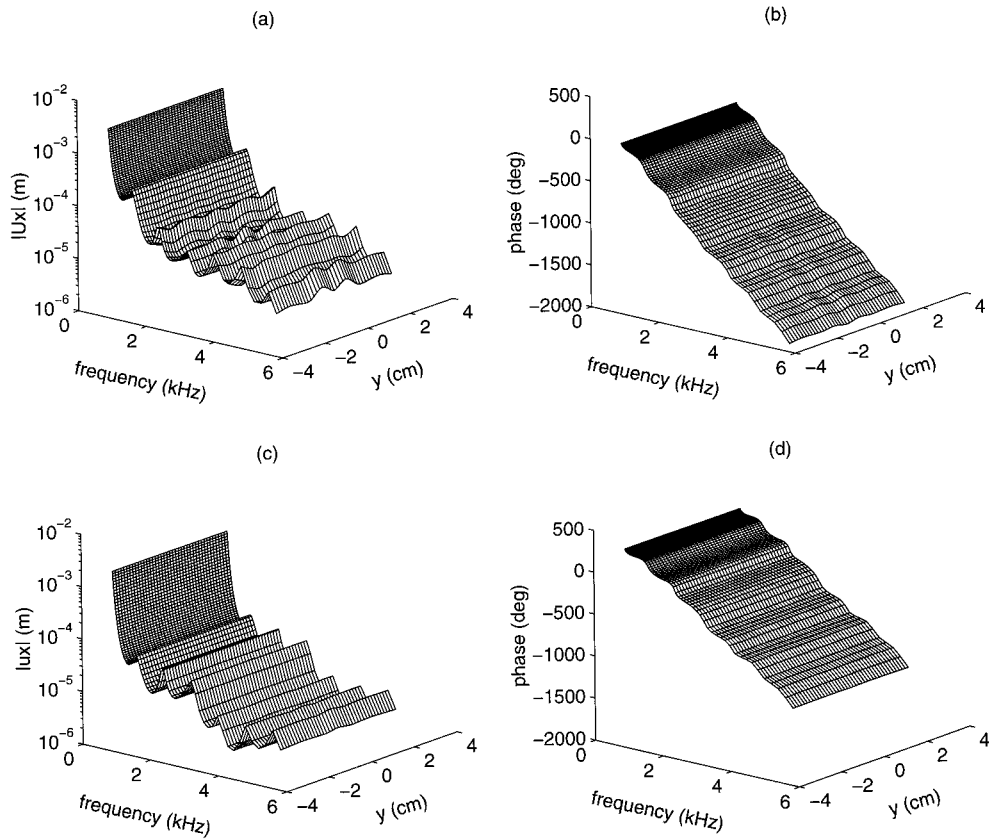


FIG. 8. Lubricated case W1. (a) Amplitude and (b) phase of  $x$  component of fluid phase displacement, and (c) amplitude and (d) phase of  $x$  component of solid phase displacement.

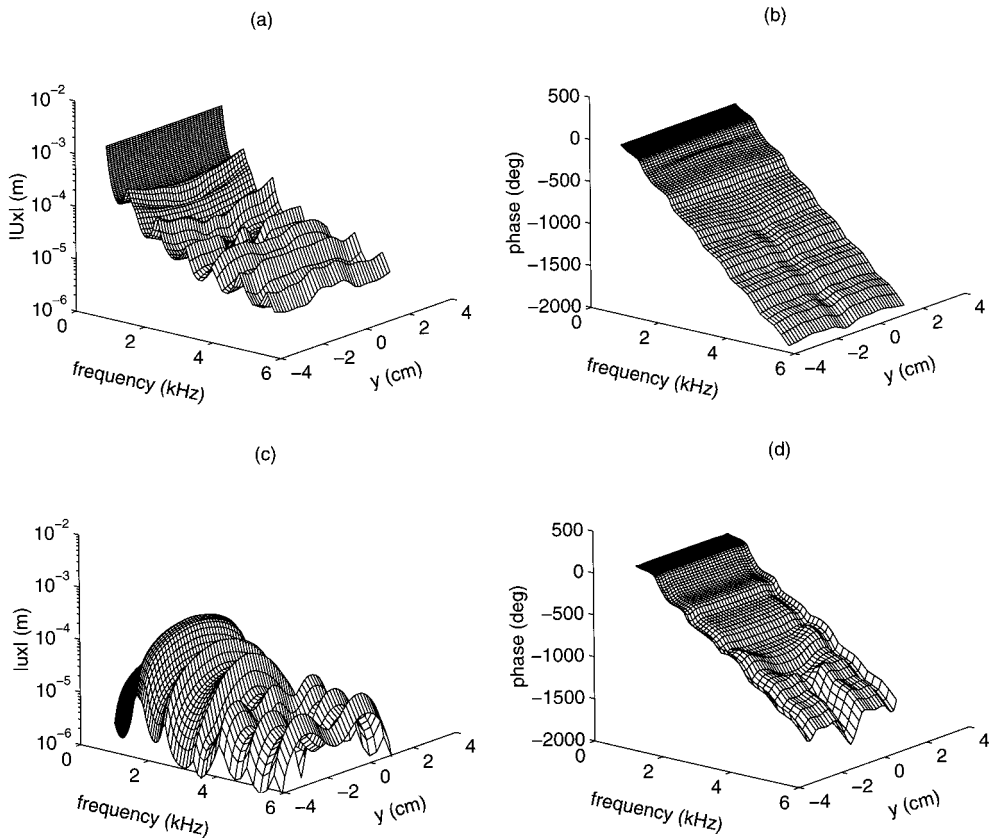


FIG. 9. Constrained case W1. (a) Amplitude and (b) phase of  $x$  component of fluid phase displacement, and (c) amplitude and (d) phase of  $x$  component of solid phase displacement.

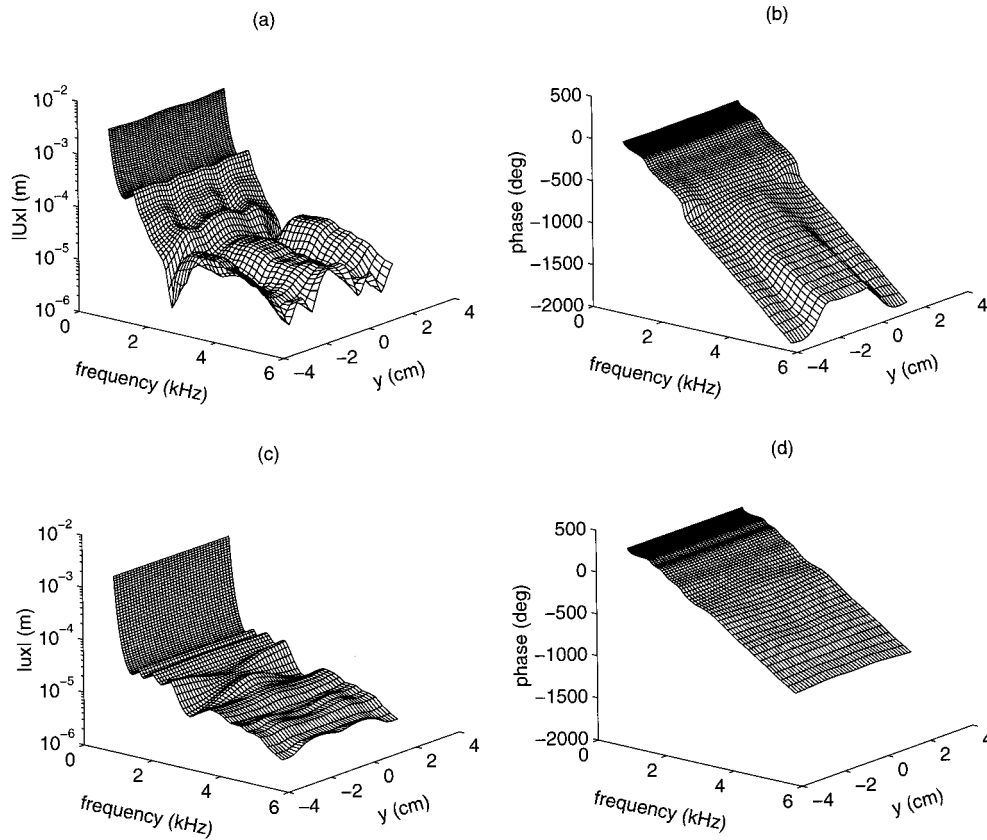


FIG. 10. Lubricated case W6. (a) Amplitude and (b) phase of  $x$  component of fluid phase displacement, and (c) amplitude and (d) phase of  $x$  component of solid phase displacement.

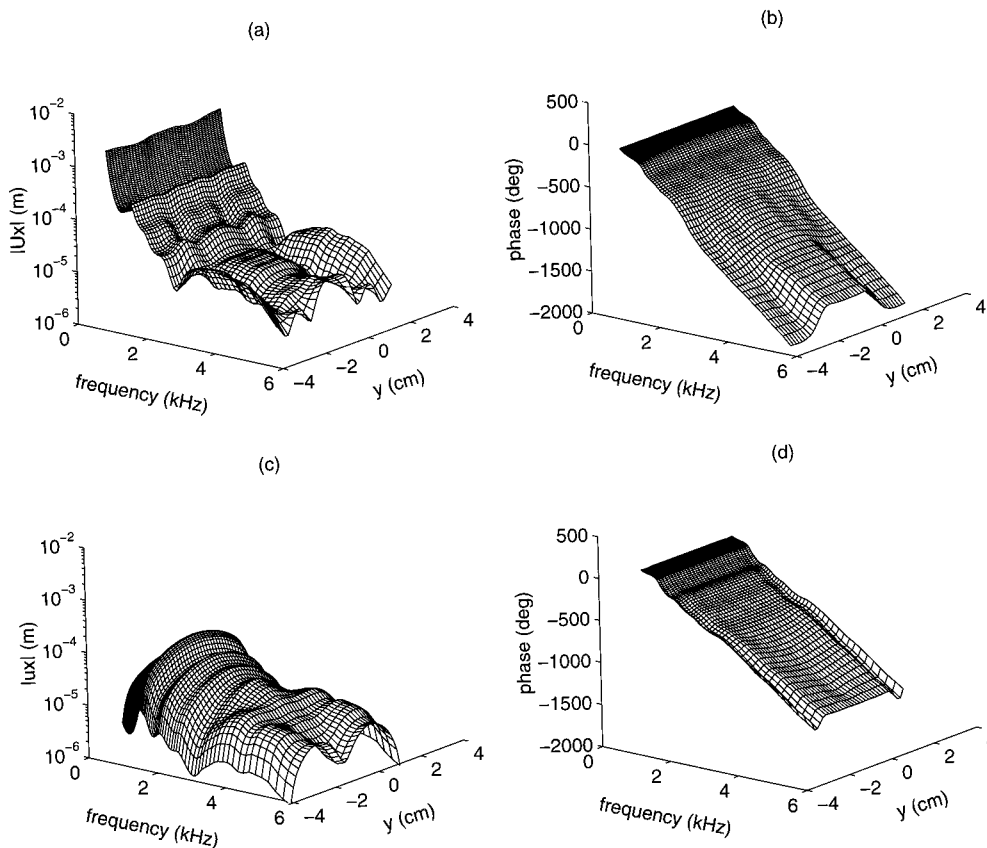


FIG. 11. Constrained case W6. (a) Amplitude and (b) phase angle of  $x$  component of solid phase displacement, and (c) amplitude and (d) phase of  $x$  component of fluid phase displacement.

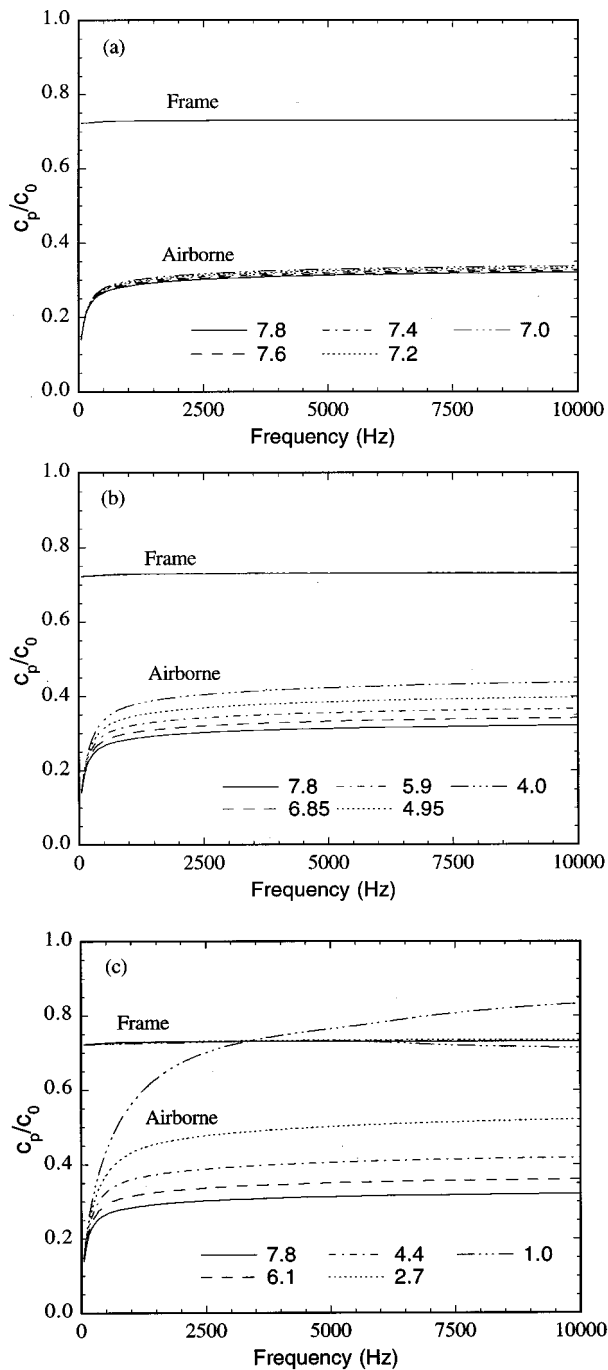


FIG. 12. Normalized phase speeds of frame and airborne waves (with respect to the speed of sound in the air): (a) case 1, (b) case 4, and (c) case 7.

Fig. 5) and shifts to progressively lower frequencies as the wedge tip angle is decreased. The decrease in resonance frequency is consistent with the effect of reducing the length of contact along the walls, which in turn results in a decrease of the stiffness due to edge constraint.

Note, however, that when the wedge tip angle is between approximately  $30^\circ$  and  $60^\circ$  (i.e., cases W5 to W9), the transmission loss is significantly increased compared to that of the plane foam layer (case W1) in frequency bands centered near 2 and 4 kHz. It was of interest to determine the cause of that increased transmission loss. To this end, results for the plane foam layer (case W1) and the wedge having a

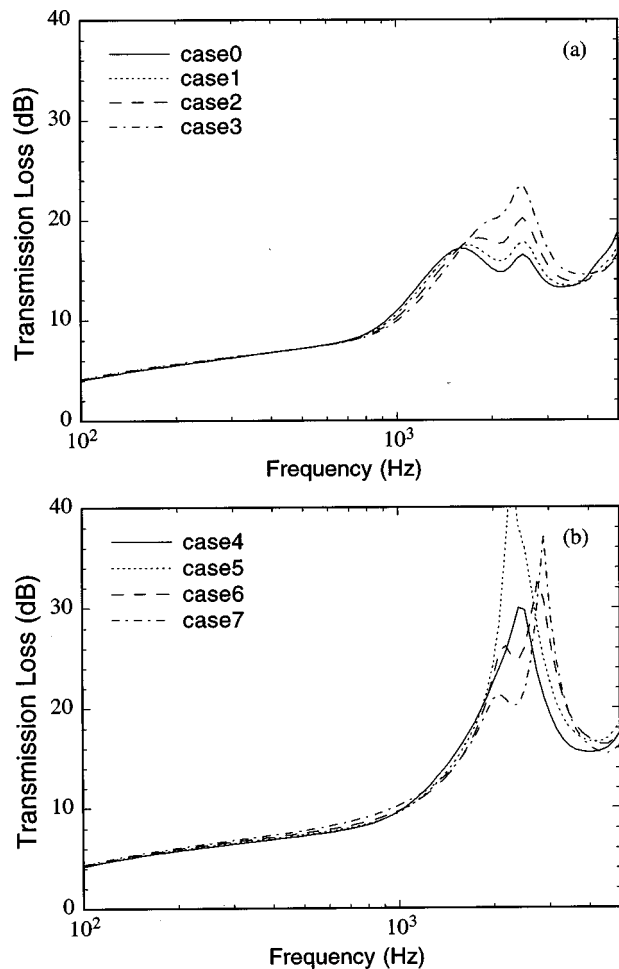


FIG. 13. Normal incidence sound transmission loss of a foam layer having spatial variation of tortuosity and whose edges are lubricated.

tip angle of  $48^\circ$  (case W6) were compared in detail.

The magnitude of the modal transmission coefficients,  $|\tau_n|$ , for both cases W1 and W6 is shown in Fig. 6. Here the modal transmission coefficients for the higher-order modes were defined to be  $\tau_n = T_n/P_{in}$ . From Fig. 6, it may be seen that the transmission coefficients of the higher-order modes for case W6 with lubricated edges were always larger than those for case W1 over the range of frequencies considered here. A similar but weaker trend was observed for the corresponding constrained edge configurations. Note especially that the magnitude of the plane wave transmission coefficient,  $|\tau_0|$ , for case W6 falls below that for case W1 at frequencies above 2 kHz, and that  $|\tau_0|$  drops to approximately the level of  $|\tau_2|$  near 4 kHz. As a result, the ratio of the contribution of the higher-order mode wave components to that of the plane wave component in the transmitted sound field at the rear surface of the foam layer is larger in case W6 than in case W1. Further, to illustrate the tendency for the higher-order transmission coefficients to increase in magnitude with decreasing wedge tip angle, the magnitude of the first higher-order symmetric mode transmission coefficient,  $|\tau_2|$ , was plotted for all wedge angles considered here (see Fig. 7).

Owing to the relatively high porosity of the foam, the

volume velocity boundary condition [Eq. (5c)] at the rear surface of the foam requires that the axial fluid motion within the foam be approximately equal to the axial fluid motion in the airspace immediately outside the foam. Hence, the modal structure of the transmitted sound field may be taken to approximate the modal nature of the fluid borne wave motion within the foam layer. Thus the results of Figs. 6 and 7 indicate that reshaping a plane foam layer into a wedge enhances the excitation of higher-order symmetric modes within the fluid phase of the foam. Note that fluid-borne waves within the foam propagate at a speed slower than that in unconfined air by a ratio of approximately  $\epsilon'^{-1/2}$  at frequencies above 1 kHz for the foam considered here (see Fig. 3 in Ref. 9). Since  $\epsilon'$  here is equal to 7.8, the first two higher-order symmetric modes within the fluid phase of the foam would be expected to cut on at approximately 2.2 and 4.4 kHz, respectively, while in an air-filled channel of the same width, they would begin to propagate at 6.3 and 12.6 kHz, respectively. Note, of course, that in a dissipative medium there is not a clear distinction between propagating and nonpropagating modes. Nevertheless, it appears likely that the enhanced transmission loss of the wedges in the vicinity of 2 and 4 kHz may be associated with the excitation of higher-order symmetric modes within the wedges. The reason that excitation of those modes at the expense of the plane wave mode may enhance the transmission loss of the wedge is considered next.

Figures 8–11 show the magnitudes and phases of the  $x$  component of the fluid and solid phase displacements at the rear surface of the foam for both the lubricated and constrained cases W1 and W6. The finite element results are shown in all cases. Note that since the magnitude of the  $x$  component of the solid phase displacement is always zero at  $y = \pm d/2$  (i.e., at  $y = \pm 2.7$  cm in Figs. 8–11) for the constrained cases, the magnitude and phase values at those locations were omitted from Figs. 9(c) and (d), 11(c) and (d).

By comparing Figs. 8(a) and 9(a), it may be seen that constraining the edges of the foam layer in case W1 does not significantly affect the  $x$  component of the fluid displacement except at relatively low frequencies (i.e., below 1 kHz), when viscous and inertial effects cause the motion of the solid and fluid phases of the foam to be well coupled. The fluid motion at the foam's rear surface is also essentially plane (i.e., there is relatively little  $y$  variation of the axial fluid velocity), although minor modal contributions are visible, more noticeably in the constrained than in the lubricated case. In the lubricated case, the solid phase displacement is also essentially plane [see Fig. 8(c)], while in the constrained case, the modal contribution to the solid motion is clearly evident [see Fig. 9(c)].

It may be seen from both Figs. 10 and 11 that the  $x$  component of the fluid displacement for case W6 shows much larger contributions from higher-order symmetric modes at the rear surface of the foam than was apparent in case W1. The fluid phase motions in both the lubricated and constrained cases [see Figs. 10(a) and 11(a), respectively] were very similar and were essentially plane up to approximately 2 kHz, above which frequency the first symmetric mode appears to be dominant. Above 4 kHz, there is also

evidence of the next symmetric mode contributing to the result. As for case W1, the solid phase response was essentially plane in the lubricated case, and modal in nature in the constrained case [compare Figs. 10(c) and 11(c)].

The difference between the responses of cases W1 and W6 are also evident when the phase of the  $x$ -component of the fluid displacement is considered. The phase of the fluid displacement in case W1 shows very little  $y$  variation, reflecting the nearly plane nature of the wave process in this case [see Figs. 8(b) and 9(b)]. The phase of the fluid displacement in case W6 shows relatively large changes along the  $y$  axis [see Figs. 10(b) and 11(b)]. In particular, it is clear in case W6 that there is a large phase difference between the fluid displacement in the central and edge regions of the foam. This phase difference is consistent with the modal response described above. When the displacement in the central region of the foam's rear surface is  $180^\circ$  out-of-phase with the motion in the edge region, the total volume of fluid displacement is minimized, and hence the coupling with the plane transmitted wave is poor: therefore the transmission loss is increased. Note that owing to their spatial similarity the symmetric modes within the foam can couple directly with the corresponding symmetric modes in the transmitted-side air space; but since the latter modes are not cut on at the frequencies considered here, they cannot carry energy away from the foam's rear surface. Thus the high transmission loss of the wedges at 2 and 4 kHz may be attributed to volume velocity cancellation at the foam's rear surface that results from the excitation of symmetric modes within the foam wedge. Since the higher-order symmetric modes are not strongly excited within the foam layer in case W1, this volume velocity cancellation effect does not operate in the latter case.

Note finally that although the magnitude of the motion of the solid phase of the foam was comparable with that of the fluid phase in all cases, the former motion does not couple well with the transmitted sound field owing to the relatively small surface area of the solid phase.

From an examination of the results presented here, it was concluded that the increased transmission loss of the wedges compared with a plane layer of the same volume in particular high-frequency bands resulted from the fact that at those frequencies the incident plane wave is converted, within the foam wedge, into higher-order symmetric modes that do not couple well with the transmitted plane sound field when the phase distribution over the rear surface of the foam causes the net axial volume velocity to be minimized.

The question remains, however: Why are the higher-order symmetric modes so well excited in the wedge, even when the incident sound field is plane? Recall that in the foam considered here, the speed of the fluid-borne waves is substantially less than the speed of wave propagation in unconfined air. Thus when the incident plane wave encounters the tip of the wedge, the central section of the wavefront falls progressively farther behind the portion of the wavefront propagating through the narrowing air channel formed between the wedge and the hard wall. Thus, the initially plane wave front becomes curved by the time it reaches the rear portion of the foam, the degree of curvature depending on

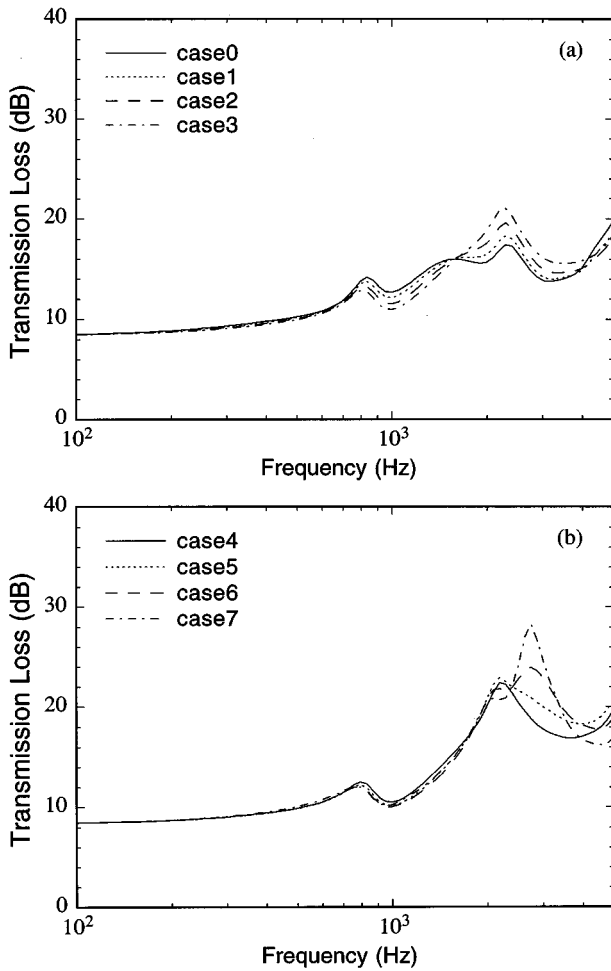


FIG. 14. Normal incidence sound transmission loss of a foam layer having spatial variation of tortuosity and whose edges are constrained.

the extension of the wedge [dimension  $l_1$  in Fig. 2(a)], which in turn depends on the tip angle  $\theta$  (at least when the foam volume is held constant in the transformation). The curved wave front couples relatively well with higher-order symmetric modes within the rear portion of the wedge, and clearly not so well with planar waves propagating within the foam. Thus it is suggested here that the shape of the wedge, acting in combination with a difference in wave propagation speeds in the foam and the adjacent air space, can cause higher-order symmetric modes to be preferentially excited within a foam wedge.

### B. Plane foam layers having spatially graded tortuosity

It may be possible to take advantage of the enhanced transmission loss of the wedge in particular frequency bands in some noise control applications. Unfortunately, a larger installation depth would be required if wedge-shaped foam layers were to be used to replace a plane layer. It was, however, noted in the previous subsection that the enhanced transmission loss of the wedges could be attributed to the wavefront curvature that results from the difference in wave propagation speed within the foam wedge and the adjacent air space. It was hypothesized that the same effect could be

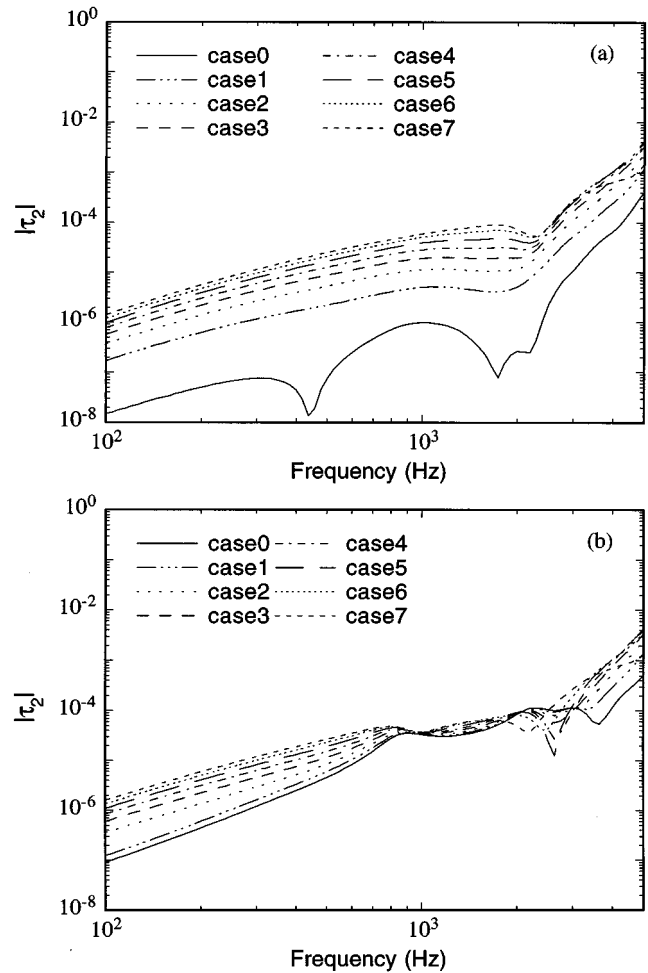


FIG. 15. Magnitude of the transmission coefficient of the first higher-order symmetric mode,  $|\tau_2|$ , for a plane foam layer having spatially graded tortuosity for (a) lubricated and (b) constrained configurations.

produced by appropriately grading the speed of airborne wave propagation across the width of a plane, constant depth layer. Since at high frequencies (above 1 kHz for the foam considered here) the fluid-borne wave propagation speed is proportional to  $\epsilon'^{-1/2}$ , the speed of wave propagation can be controlled by varying the tortuosity from a maximum at the center of the foam layer (i.e.,  $y=0$ ) to a minimum at the edge of the layer (i.e.,  $y=\pm d/2$ ). In the cases considered here, the tortuosity was graded as described in Sec. III C (note that the case referred to as W1 in the previous subsection is denoted here as case 0).

For example, Fig. 12 shows the normalized phase speed,  $c_p/c_0$ , of the longitudinal frame and airborne waves for the various tortuosities of cases 1, 4, and 7. First, it may be seen that the speed of the frame wave is higher than that of airborne wave (except when  $\epsilon'=1.0$ ). It may also be seen that the speed of the airborne wave increases significantly as the tortuosity decreases, while the frame wave speed is not significantly affected by the tortuosity.

Figures 13 and 14 show the transmission losses of plane foam layers having spatially graded tortuosity in the lubricated and constrained configurations, respectively. In both configurations, the high-frequency transmission loss progressively increased as the spatial variation of tortuosity was

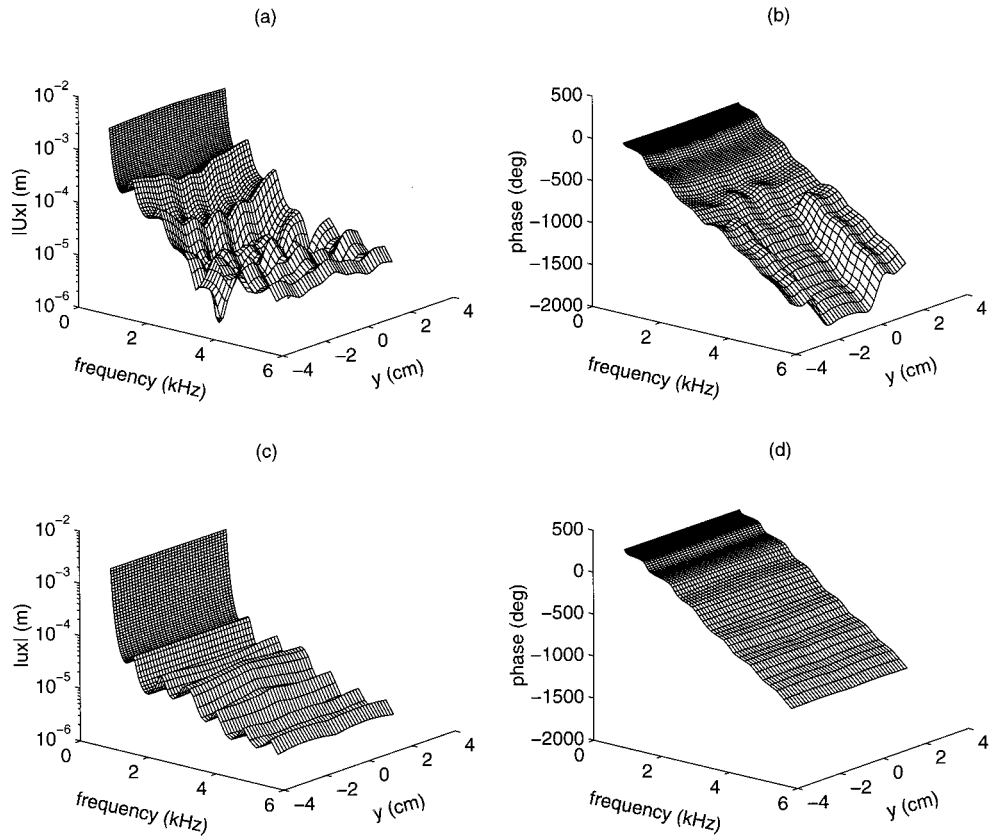


FIG. 16. Lubricated case 7. (a) Amplitude and (b) phase of  $x$  component of solid phase displacement, and (c) amplitude and (d) phase of  $x$  component of fluid phase displacement.

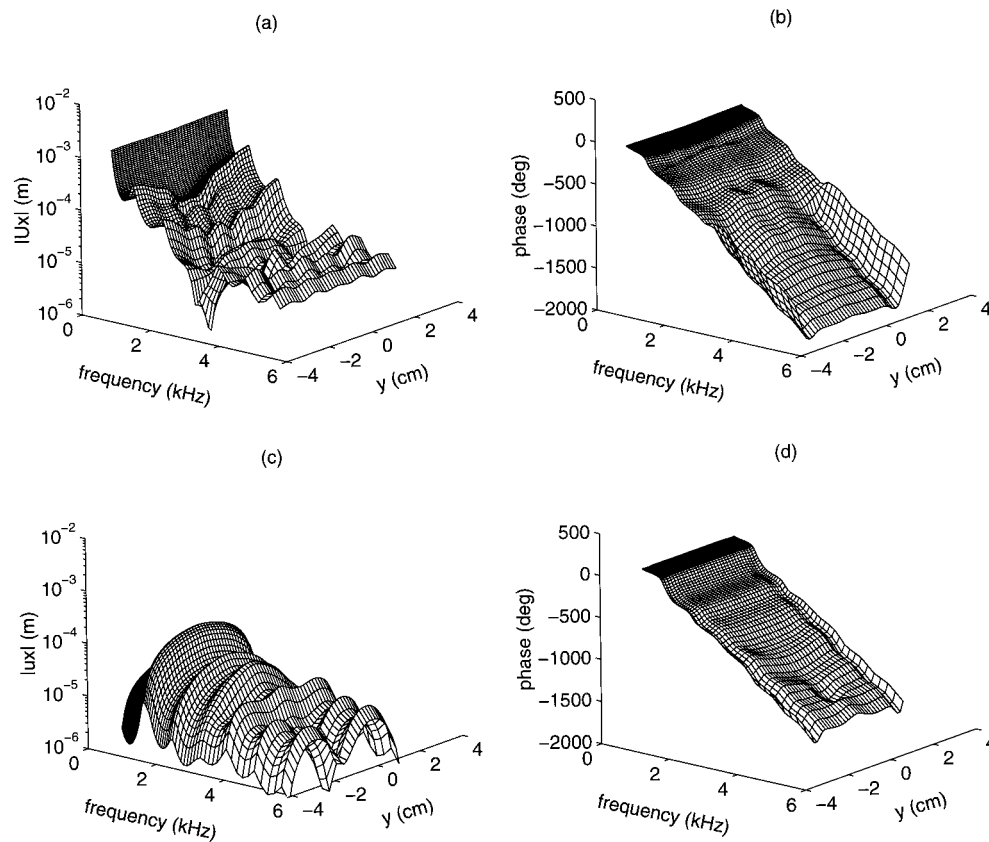


FIG. 17. Constrained case 7. (a) Amplitude and (b) phase of  $x$  component of solid phase displacement, and (c) amplitude and (d) phase of  $x$  component of fluid phase displacement.

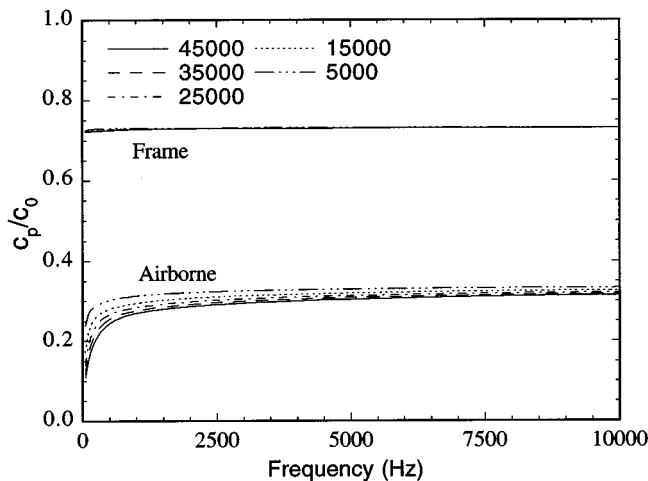


FIG. 18. Normalized phase speeds of frame and airborne waves (with respect to the speed of sound in the air) for case 11.

made larger, with the rate of increase being larger for the lubricated than for the constrained case. It is interesting to note that there is not a significant decrease in transmission loss at low frequencies in these cases, unlike the wedge case. Thus the use of a plane foam layer having spatially graded tortuosity may be preferable to a wedge in noise control applications.

The magnitude of the first higher-order symmetric mode transmission coefficient,  $|\tau_2|$ , is plotted in Fig. 15. As was noted in connection with Fig. 7,  $|\tau_2|$  increases progressively (i.e., the first higher-order symmetric mode is progressively more strongly excited) as the variation of tortuosity increases, except in a midfrequency range for the constrained cases.

Finally, Figs. 16 and 17 illustrate the magnitude and phase of the  $x$  component of the fluid and solid phase displacements at the rear surface of the foam layer for case 7 in the lubricated and constrained configurations, respectively. The modal nature of the fluid phase displacement at the rear surface of the foam is evident from Figs. 16(a) and 17(a). In this case, however, the modal structure of the fluid-borne wave field within the foam is likely to be relatively complicated owing to the inhomogeneity of the wave speed across the width of the foam: i.e., there will no longer be a close spatial match between the fluid-borne modes in the foam and the modes in the transmission-side air space. Nevertheless, as was the case for the wedge, the axial fluid displacement in the central and edge regions was found to be out-of-phase across the width of the foam layer: that effect is more evident for the lubricated case [Fig. 16(b)] than for the constrained case [Fig. 17(b)], thus accounting for the higher transmission loss given by the former configuration. Therefore, it was concluded that the phase variations across the width of the foam layer resulting from the spatial variation of tortuosity can cause the net axial volume velocity at the rear surface of the plane foam layer to be minimized in certain frequency ranges, thus enhancing the layer's transmission loss.

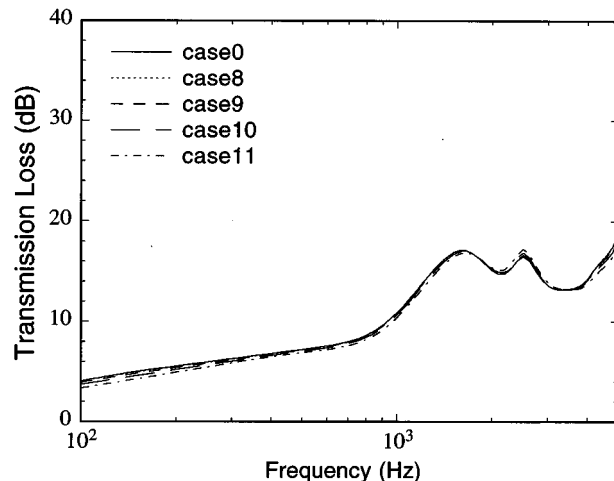


FIG. 19. Normal incidence sound transmission loss of a foam layer having spatial variation of flow resistivity and whose edges are lubricated.

### C. Plane foam layers having spatially graded flow resistivity

The effect of spatial variation of the flow resistivity on the sound transmission loss of a plane foam layer was also investigated. In the cases studied here, the flow resistivity was graded spatially as described in Sec. II D. First, it may be seen from Fig. 18 that for the foam considered here the flow resistivity has a relatively small effect on the speed of the airborne wave even for the case having the largest variation in flow resistivity (case 11). As may then be seen from Fig. 19, varying the flow resistivity across the width of the layer does not appear to be an efficient way of increasing the layer's transmission loss in particular frequency bands, presumably because of the flow resistivity's relatively minor effect on the airborne wave speed. This conclusion may be different for different types of foams and for different frequency ranges of interest.

## IV. CONCLUSIONS

In this paper, non-normal boundary conditions that allow for an arbitrary orientation of a foam interface with respect to the global coordinate axes have been presented and integrated with a previously developed finite element formulation for elastic porous materials. By using these interface conditions, it was shown the sound transmission loss of a foam wedge is significantly higher in some frequency bands than that of a plane foam layer having the same volume. It was concluded that this increase in transmission loss resulted from the conversion within the foam of the incident plane wave into higher-order symmetric modes that could not radiate efficiently from the rear surface of the foam wedge. It has also been shown that the same transmission loss characteristics can be produced by using a plane, constant depth foam layer when the fluid-borne wave propagation speed is varied across the width of the foam layer by grading the tortuosity of the material. Finally, it was found that grading the flow resistivity in the same way did not result in a similar enhancement of the transmission loss.

## ACKNOWLEDGMENTS

The authors are grateful to Automated Analysis Corporation of Ann Arbor, MI, for the financial support of this work that was made possible by a NASA SBIR program.

- <sup>1</sup>C. Zwikker and C. W. Kosten, *Sound Absorbing Materials* (Elsevier, New York, 1949).
- <sup>2</sup>M. A. Biot, "Theory of propagation of elastic waves in a fluid-saturated porous solid I. Low-frequency range. II. Higher frequency range," *J. Acoust. Soc. Am.* **28**, 168–191 (1956).
- <sup>3</sup>J. S. Bolton, N.-M. Shiau, and Y. J. Kang, "Sound transmission through multi-panel structures lined with elastic porous materials," *J. Sound Vib.* **191**, 317–347 (1996).
- <sup>4</sup>J. F. Allard, *Propagation of Sound in Porous Media: Modeling Sound Absorbing Materials* (Elsevier Science, New York, 1993).
- <sup>5</sup>A. Craggs, "A finite element model for rigid porous absorbing materials," *J. Sound Vib.* **61**, 101–111 (1978).
- <sup>6</sup>A. Craggs, "Coupling of finite element acoustic absorption models," *J. Sound Vib.* **66**, 605–613 (1979).
- <sup>7</sup>A. Craggs, "A finite element model for acoustically lined small rooms," *J. Sound Vib.* **108**, 327–337 (1986).
- <sup>8</sup>Y. J. Kang and J. S. Bolton, "Finite element modeling of isotropic elastic porous materials coupled with acoustical finite elements," *J. Acoust. Soc. Am.* **98**, 635–643 (1995).
- <sup>9</sup>Y. J. Kang and J. S. Bolton, "A finite element model for sound transmission through foam-lined double panel structures," *J. Acoust. Soc. Am.* **99**, 2755–2765 (1996).
- <sup>10</sup>J. P. Coyette and H. Wynendaele, "A finite element model for predicting the acoustic transmission characteristics of layered structures," in *Proceedings of Inter-Noise 95* (Noise Control Foundation, Poughkeepsie, NY, 1995), Vol. 2, pp. 1279–1282.
- <sup>11</sup>N. Atalla and R. Panneton, "Numerical prediction of sound transmission through multilayer structures with isotropic elastic porous materials," in *Proceedings of Inter-Noise 95* (Noise Control Foundation, Poughkeepsie, NY, 1995), Vol. 2, pp. 1295–1298.
- <sup>12</sup>V. Easwaran and M. L. Munjal, "Finite element analysis of wedges used in anechoic chambers," *J. Sound Vib.* **160**, 333–350 (1993).
- <sup>13</sup>W. Koidan, G. R. Hruska, and M. A. Pickett, "Wedge design for National Bureau of Standard anechoic chambers," *J. Acoust. Soc. Am.* **52**, 1071–1076 (1972).
- <sup>14</sup>Y. J. Kang and J. S. Bolton, "Optimal design of acoustical foam treatments," *ASME J. Vib. Acoust.* **181**, 498–504 (1996).



# Group velocity formulas for the symmetry planes of a stressed anisotropic elastic solid

Kwang Yul Kim

*Department of Theoretical and Applied Mechanics, Thurston Hall, Cornell University, Ithaca, New York 14853-1503*

Tsung-Tsong Wu

*Institute of Applied Mechanics, National Taiwan University, Taipei, Taiwan*

Wolfgang Sachse

*Department of Theoretical and Applied Mechanics, Thurston Hall, Cornell University, Ithaca, New York 14853-1503*

(Received 9 January 1997; accepted for publication 18 July 1997)

This paper presents analytic formulas for the group velocity of quasilongitudinal, quasitransverse, and shear-horizontally (*SH*) polarized pure-transverse modes propagating in an arbitrary direction on the symmetry planes of a stressed anisotropic elastic medium with orthotropic or higher symmetry. The group velocity equations are expressed in terms of the thermodynamic elastic stiffness coefficients and stresses acting on the medium. An example is provided with a (001) silicon crystal compressed at uniaxial stress. © 1997 Acoustical Society of America.

[S0001-4966(97)00511-0]

PACS numbers: 43.20.Jr [ANN]

## INTRODUCTION

The group velocities of various modes of an elastic wave propagating in an elastic anisotropic medium in the stress-free natural state have been extensively treated by many authors.<sup>1-3</sup> Explicit analytic formulas for phase velocities in the symmetry direction and in an arbitrary direction of symmetry planes are also given in the literature.<sup>1,2,4</sup> Because of the complexity of the group velocity surfaces in an anisotropic medium, no explicit analytic formula for the group velocity in a general direction exists. However, in the symmetry directions, the phase and group velocities coincide and this leads to valuable relations between the group velocity and elastic constants of the medium. Recently, the first author extended the group velocity expressions to an arbitrary direction on the symmetry planes<sup>5</sup> and Kim *et al.*<sup>6-9</sup> gave the detailed treatment on the methods of determining all the elastic constants of an anisotropic medium from group velocity data measured in symmetry directions and planes. Based on the two-dimensional Stroh formalism for the elastodynamic problems, Wang<sup>10</sup> gave an elegant treatment for the cusps of the group velocity surfaces.

Equations of phase velocities at finite deformation of an elastic medium under arbitrary stresses were formulated by Toupin and Bernstein<sup>11</sup> and Thurston.<sup>12,13</sup> In the symmetry directions of a stressed medium that maintains orthotropic or higher symmetry, the group and phase velocities coincide with each other, as in the case of an stress-free medium. This gives relations between the group velocities of the pure mode to the diagonal elements of the elastic constant matrix. However, to the authors' knowledge, there appears no explicit analytic formulation for the group velocity in an arbitrary direction of symmetry planes. In this paper we derive the group velocity expressions for the shear-horizontally (*SH*) polarized pure-transverse (*PT*) modes, quasilongitudinal

(*QL*) and quasitransverse (*QT*) modes propagating on the symmetry planes of the stressed medium. Our approach is basically an extension of the methods used in Ref. 5 to the stressed medium, replacing Christoffel's tensor by the equivalent acoustical tensor in the stressed state, where the group velocity direction is again found to be normal to the equivalent slowness surface in the stressed state.

The elastic waves emanating from their sources propagate at the speed of group velocities which depend on the direction of propagation in an anisotropic medium. Since the group velocity, just like the phase velocity, also depends on the stress on the medium, the measurement of group velocity may yield information about the stresses acting on the medium. This effect, known as acoustoelasticity,<sup>14</sup> is generally small in the moderate stress range below 1 GPa, and still detectable if one measures the wave speed very accurately. However, the change in group or phase velocity will be significant in very high stresses, which can be found in the interior of planets such as the Earth and Jupiter and inside the diamond-anvil high-pressure cell in the laboratory,<sup>15</sup> where the stresses acting on a material may be much higher than its Young's modulus in the natural state. A study of group velocity will contribute to the understanding of the acoustoelastic effect and the behavior of a material under high pressures.

## I. PHASE AND GROUP VELOCITIES, AND SLOWNESS OF A STRESSED MEDIUM: GENERAL FORMULATION

Suppose that a small amplitude wave motion  $\mathbf{u}$  is superposed on the finite deformation caused by static stresses  $\sigma_{ij}(\mathbf{X})$  acting on the medium. We denote the coordinate of a particle of a stressed elastic body at finite deformation state by  $\mathbf{X}$ , which we adopt as a reference coordinate for deforma-

tion. The equation of motion for the deformation  $\mathbf{u}$  of a homogeneous medium is written in the absence of body force as<sup>11,12</sup>

$$\rho_X \ddot{u}_i = [\delta_{ik} \sigma_{jl}(\mathbf{X}) + C_{ijkl}(\mathbf{X})] \frac{\partial^2 u_k}{\partial X_j \partial X_l} = B_{ijkl} \frac{\partial^2 u_k}{\partial X_j \partial X_l}, \quad (1)$$

where  $\rho_X$  is the material density at  $\mathbf{X}$  and  $B_{ijkl} \equiv \delta_{ik} \sigma_{jl}(\mathbf{X}) + C_{ijkl}(\mathbf{X})$ .  $C_{ijkl}(\mathbf{X})$ , the thermodynamic elastic coefficient evaluated at  $\mathbf{X}$ , is defined at constant entropy  $S$  as

$$C_{ijkl}(\mathbf{X}) = \rho_X \left( \frac{\partial^2 U}{\partial \xi_{ij} \partial \xi_{kl}} \right)_{S, \mathbf{X}}. \quad (2)$$

In Eq. (2),  $U$  is the internal energy per unit mass of the material, the strain from the reference state  $\mathbf{X}$  is given by

$$\xi_{ij} = \frac{1}{2} \left( \frac{\partial u_i}{\partial X_j} + \frac{\partial u_j}{\partial X_i} + \frac{\partial u_s}{\partial X_i} \frac{\partial u_s}{\partial X_j} \right), \quad (3)$$

and the thermodynamic coefficients  $C_{ijkl}(\mathbf{X})$  have a familiar symmetry as the elastic stiffness constants defined in the stress-free natural state do.

However, the elastic coefficients  $B_{ijkl}$  lack the full symmetry found in  $C_{ijkl}(\mathbf{X})$  and cannot be expressed using the abbreviated Voigt notation. We rearrange  $B_{ijkl}$  and define a new set of wave propagation coefficients  $\tilde{C}_{ijkl}$ , which can be abbreviated using Voigt's notation. Following Huang<sup>16</sup> and Born and Huang,<sup>17</sup> we write  $\tilde{C}_{ijkl}$  as

$$\tilde{C}_{ijkl} = (B_{ikjl} + B_{iljk})/2 = \delta_{ij} \sigma_{kl} + (C_{ikjl} + C_{iljk})/2. \quad (4)$$

Note that  $\tilde{C}_{ijkl} = \tilde{C}_{jikl}$  and  $\tilde{C}_{ijkl} = \tilde{C}_{ijlk}$ .  $\tilde{C}_{ijkl}$  obeys Huang's condition

$$\tilde{C}_{ijkl} - \tilde{C}_{klij} = \tilde{C}_{\mu\nu} - \tilde{C}_{\nu\mu} = \delta_{ij} \sigma_{kl} - \delta_{kl} \sigma_{ij}, \quad (5)$$

where the subscripts  $\mu$  and  $\nu$  ( $\mu, \nu = 1, 2, \dots, 6$ ) are the Voigt indices. The  $6 \times 6$  array  $\tilde{C}_{\mu\nu}$  is shown in Table III of Ref. 12 and has in general 26 linearly independent elements. Using the  $\tilde{C}_{ijkl}$  coefficients, the equation of motion is expressed as

$$\rho_X \ddot{u}_i = \tilde{C}_{ijkl} \frac{\partial^2 u_j}{\partial X_k \partial X_l}. \quad (6)$$

Writing the acoustical tensor as

$$\Gamma_{ij}(\mathbf{n}) = \tilde{C}_{ijkl} n_k n_l \quad (7)$$

for the plane wave propagating with wave vector  $\mathbf{k} = 2\pi\mathbf{n}/\lambda$ , wave length  $\lambda$ , wave normal  $\mathbf{n}$ , and phase velocity  $\mathbf{V}$ , one obtains the phase velocity equations

$$(\tilde{C}_{ijkl} n_k n_l - \rho_X V^2 \delta_{ij}) u_j = 0, \quad (8)$$

$$\det[\Gamma_{ij} - \rho_X V^2 \delta_{ij}] = 0. \quad (9)$$

$\Gamma_{ij}$  is the symmetrical tensor whose eigenvectors are the possible directions of particle displacement and whose eigenvalues are the corresponding values of  $\rho_X V^2$ .

In terms of slowness,  $\mathbf{s} = \mathbf{n}/V = \mathbf{k}/\omega$  defined as the inverse phase velocity, where  $\omega$  denotes the angular frequency, the slowness surface  $\Lambda$  of the stressed medium is represented by

$$\Lambda = \det[\tilde{C}_{ijkl} s_k s_l - \rho_X \delta_{ij}] = 0. \quad (10)$$

The group velocity  $\mathbf{V}_g$ , commonly defined as

$$\mathbf{V}_g \equiv \nabla_{\mathbf{k}} \omega, \quad (11)$$

satisfies the relations

$$\mathbf{V}_g \cdot \mathbf{n} = V, \quad \mathbf{V}_g \cdot \mathbf{s} = 1. \quad (12)$$

From Eqs. (10) and (12) it can be shown that<sup>1</sup>

$$\mathbf{V}_g = \frac{\nabla_{\mathbf{s}} \Lambda}{\mathbf{s} \cdot \nabla_{\mathbf{s}} \Lambda}, \quad (13)$$

which indicates that the group velocity points in the direction normal to the slowness surface, as in the case of the stress-free natural state. Note that Eq. (13) holds valid for a stressed medium as a result of  $\Gamma_{ij} = \Gamma_{ji}$  in Eq. (7),  $\tilde{C}_{ijkl} \neq \tilde{C}_{klij}$  notwithstanding.

In the following we will restrict ourselves to the wave propagation with wave normal  $\mathbf{n}$  lying in the symmetry plane of a medium possessing orthotropic or higher symmetry, where the three axes of orthotropic symmetry are taken as the coordinate axes,  $X_1$ ,  $X_2$ , and  $X_3$ , whose directions are simply denoted as [100], [010], and [001], respectively. Likewise, we denote the  $X_1 X_2$  plane whose normal points in the  $X_3$  direction by (001), and analogously for the  $X_2 X_3$  and  $X_1 X_3$  planes. The orthotropic medium is characterized by nine thermodynamic, elastic-stiffness coefficients:  $C_{11}$ ,  $C_{22}$ ,  $C_{33}$ ,  $C_{12}$ ,  $C_{23}$ ,  $C_{13}$ ,  $C_{44}$ ,  $C_{55}$ , and  $C_{66}$ , just as an orthorhombic medium in the stress-free natural state is. Here, we deal with only those media which possess three mutually perpendicular symmetry planes, and therefore exclude materials of triclinic, monoclinic, and trigonal symmetries. A medium, which has orthorhombic, tetragonal (422,  $4mm$ ,  $\bar{4}2m$ , and  $4/mmm$  classes), cubic, hexagonal (622,  $6mm$ ,  $\bar{6}2m$ , and  $6/mmm$  classes), transversely isotropic, or isotropic symmetry in the stress-free natural state, can be considered as a medium with orthotropic or higher symmetry, when it is uniaxially, biaxially, or triaxially loaded with the directions of the principal-stress axes coinciding with those of material symmetry. This condition for maintenance of orthotropic or higher symmetry can be stated as

$$\sigma_{12} = \sigma_{13} = \sigma_{23} = 0 \quad \text{or} \quad (14)$$

$$\partial X_i / \partial a_j = \lambda_i \delta_{ij} \quad (i \text{ not summed}),$$

where  $a_j$  represents a coordinate of a particle along the  $j$ -th direction in the stress-free natural state and  $\lambda_i$  is a principal stretch in the  $i$ -th direction. Note that the symmetry relation  $C_{\mu\nu} = C_{\nu\mu}$  holds for the medium in the natural state, while Huang's condition Eq. (5) holds for a stressed medium.

## II. PHASE VELOCITIES OF A STRESSED MEDIUM

Phase velocities in a stressed anisotropic medium are treated in detail in Refs. 12–14. We introduce this section as a reference that is necessary for the derivation of group velocities to be presented in Sec. III. For waves propagating on symmetry planes of an elastic medium, we choose specifically, without loss of generality, a wave normal  $\mathbf{n} = [n_1, 0, n_3] = [\sin \theta, 0, \cos \theta]$  lying on the (010) plane at an

angle  $\theta$  to the [001] direction. Because of the mirror symmetry across the (001) plane, we restrict the angle  $\theta$  to  $-90^\circ \leq \theta \leq 90^\circ$ . Wave propagations in the (100) and (001) symmetry planes can be treated by the proper rotation of indices.

The acoustical tensors  $\Gamma_{ij}$  in the (010) plane can be found in Table III of Ref. 12 by setting  $n_2=0$  and  $\sigma_{13}=0$ .

Equation (9) for the wave propagation in the (010) plane yields

$$(\Gamma_{22} - \rho_X V^2)[(\Gamma_{11} - \rho_X V^2)(\Gamma_{33} - \rho_X V^2) - \Gamma_{13}^2] = 0. \quad (15)$$

For simplicity of notation we introduce the following identities:

$$C_{11\pm} \equiv C_{11} \pm C_{55}, \quad C_{33\pm} \equiv C_{33} \pm C_{55}, \quad (16)$$

$$C_{13\pm} \equiv C_{13} \pm C_{55};$$

for the pure-index, effective elastic coefficients  $C_{\mu\mu}^{(i)}$  ( $\mu$  not summed;  $\mu=1,2,\dots,6$ ),

$$C_{\mu\mu}^{(i)} \equiv C_{\mu\mu} + \sigma_{ii} \quad (i \text{ not summed}; i=1,2,3); \quad (17)$$

for mixed-index, effective elastic coefficients  $C_{\mu\nu}^{(i)}$  ( $\mu \neq \nu$ ;  $\mu, \nu=1,2,3$ ),

$$C_{\mu\nu}^{(i)} \equiv C_{\mu\nu} - \sigma_{ii} \quad (i \text{ not summed}; i=1,2,3); \quad (18)$$

and for the following effective elastic-stiffness constants

$$C_{11\pm}^{(1)} \equiv C_{11}^{(1)} \pm C_{55}^{(1)}, \quad C_{13\pm}^{(1)} \equiv C_{13}^{(1)} \pm C_{55}^{(1)}, \quad (19)$$

$$C_{33\pm}^{(3)} \equiv C_{33}^{(3)} \pm C_{55}^{(3)}, \quad C_{13\pm}^{(3)} \equiv C_{13}^{(3)} \pm C_{55}^{(3)}.$$

The first term in the parenthesis of Eq. (15) represents the pure-transverse (*PT*) mode polarized in the [010] direction and propagating with phase velocity

$$\rho_X V^2 = \Gamma_{22} = C_{66}^{(1)} \sin^2 \theta + C_{44}^{(3)} \cos^2 \theta \quad (PT \text{ mode}). \quad (20)$$

The square bracket term in Eq. (15) yields the phase velocities for the quasilongitudinal (*QL*) and quasitransverse (*QT*) modes propagating on the (010) plane and polarized on the same plane:

$$(\rho_X V^2)^2 - (\Gamma_{11} + \Gamma_{33})(\rho_X V^2) + (\Gamma_{11}\Gamma_{33} - \Gamma_{13}^2) = 0, \quad (21)$$

$$\begin{aligned} 2\rho_X V^2 &= \Gamma_{11} + \Gamma_{33} \pm [(\Gamma_{11} - \Gamma_{33})^2 + 4\Gamma_{13}^2]^{1/2} \\ &= C_{11+}^{(1)} \sin^2 \theta + C_{33+}^{(3)} \cos^2 \theta \\ &\quad \pm [(C_{11-} \sin^2 \theta - C_{33-} \cos^2 \theta)^2 \\ &\quad + 4C_{13+}^2 \sin^2 \theta \cos^2 \theta]^{1/2}, \end{aligned} \quad (22)$$

where + and - signs in front of the square bracket refer to the *QL* and *QT* modes, respectively.

Equations (20) and (22) express the phase velocities of various modes propagating in an arbitrary direction on the (010) symmetry plane of a stressed medium. Similar expressions can be found for the other symmetry planes, (100) and (001), by an appropriate rotation of indices for the elastic constants and stresses. In particular, for the pure-longitudinal and pure-transverse modes propagating in the symmetry directions, one can easily find in matrix form

$$\rho_X [V_{ij}^2] = \begin{bmatrix} C_{11}^{(1)} & C_{66}^{(1)} & C_{55}^{(1)} \\ C_{66}^{(2)} & C_{22}^{(2)} & C_{44}^{(2)} \\ C_{55}^{(3)} & C_{44}^{(3)} & C_{33}^{(3)} \end{bmatrix}, \quad (23)$$

where  $V_{ij}$  denotes the phase velocity propagating in the  $X_i$  direction and polarized in the  $X_j$  direction. Equation (23) indicates that all the pure-index or diagonal-element thermodynamic elastic coefficients can be determined from measurements of the pure-mode phase velocities propagating in three symmetry directions. Note that the elastic constants  $C_{11-}$  and  $C_{33-}$  appearing in Eq. (22) can be similarly determined using Eq. (23), since  $C_{11-} = C_{11-}^{(1)}$  and  $C_{33-} = C_{33-}^{(3)}$ . This means that the elastic coefficient  $C_{13+} = C_{13} + C_{55}$  appearing in Eq. (22) can also be determined from measurements of the *QL*- or *QT*-mode phase velocity together with the pure-mode phase velocities propagating in symmetry directions. Note also that  $C_{13+} = C_{13+}^{(1)} = C_{13+}^{(3)}$  and therefore,  $C_{13}^{(1)}$  and  $C_{13}^{(3)}$  in Eq. (18), which appear in the formulas of the effective Young's modulus and Poisson's ratios of a stressed orthotropic medium,<sup>18,19</sup> can also be similarly obtained from measurements of relevant pure- and *QL*- (or *QT*-) mode phase velocities.

Since the phase and group velocities are identical for waves propagating along the symmetry directions, Eq. (23) also applies for the pure-mode group velocity by simply replacing  $V_{ij}$  by  $(V_g)_{ij}$ . On the other hand, along an off-symmetry direction on the symmetry plane, the direction of the group velocity deviates from that of the wave normal, and in the following section we deal with the derivation of the group velocity formulas and their application to determination of the group velocity surfaces and the mixed-index elastic coefficients.

### III. GROUP VELOCITIES OF A STRESSED MEDIUM

The group velocity corresponding to a wave normal  $\mathbf{n} = [\sin \theta, 0, \cos \theta]$  in the (010) slowness plane can be calculated using Eq. (13). Because of the mirror symmetry across the (010) symmetry plane, all the points in the (010) slowness plane map onto the (010) plane of the group-velocity surface. However, except for isotropic and transversely isotropic media, the converse is not generally true, as is well known in the theory of phonon focusing.<sup>20,21</sup> Because of the nonspherical, concave, or convex shape of the *QT* slowness surface of an anisotropic medium, some points that do not lie in the (010) section of the *QT* slowness surface may map onto the (010) group-velocity section. The group-velocity sections that do not correspond to the (010) slowness plane are not of interest here. Hence, we deal with only those group velocity sections that correspond to the (010) slowness plane. We denote the direction of group velocity by an angle  $\zeta$  measured to the [001] direction. Because of the mirror symmetry across the (001) plane, we confine  $\zeta$  to  $-90^\circ \leq \zeta \leq 90^\circ$ , just as  $\theta$ . For simplicity of notation we write

$$p \equiv \tan \theta, \quad q \equiv \tan \zeta. \quad (24)$$

## A. Pure-transverse mode

Equation (20) yields the equation of the (010) slowness section of the pure-transverse mode

$$\Lambda_{PT} = C_{66}^{(1)} s_1^2 + C_{44}^{(3)} s_3^2 - \rho_X = 0, \quad (25)$$

$$\rho_X s_3^{-2} = C_{66}^{(1)} p^2 + C_{44}^{(3)}. \quad (26)$$

Applying Eq. (13) to Eqs. (25) and (26), one obtains

$$V_{g1} = s_3 C_{66}^{(1)} p / \rho_X, \quad (27a)$$

$$V_{g3} = s_3 C_{44}^{(1)} / \rho_X, \quad (27b)$$

$$q = \tan \zeta = \frac{V_{g1}}{V_{g3}} = \frac{C_{66}^{(1)} p}{C_{44}^{(3)}}, \quad (28a)$$

$$p = \tan \theta = \frac{C_{44}^{(3)} q}{C_{66}^{(1)}}, \quad (28b)$$

$$\begin{aligned} (\rho_X V_g^2)^{-1} &= [\rho_X (V_{g1}^2 + V_{g3}^2)]^{-1} \\ &= (C_{66}^{(1)})^{-1} \sin^2 \zeta + (C_{44}^{(3)})^{-1} \cos^2 \zeta. \end{aligned} \quad (29)$$

Equations (28a) and (28b) give the conversion relations between the directions of phase and group velocities of the *SH*-polarized PT mode. Equation (29) indicates the elliptical section of  $V_g$  with the principal semiaxes given by  $\sqrt{C_{44}^{(3)}/\rho_X}$  and  $\sqrt{C_{66}^{(1)}/\rho_X}$ .

## B. Quasilongitudinal and quasitransverse modes

We again introduce for simplicity of notation

$$A \equiv C_{11}^{(1)} C_{33}^{(3)} + C_{55}^{(1)} C_{55}^{(3)} - C_{13+}^2, \quad (30)$$

$$B \equiv C_{11-} C_{33-} - 2C_{13+}^2 = C_{11-} C_{33-} - 2C_{13+}^{(1)} C_{13+}^{(3)}, \quad (31)$$

$$\begin{aligned} D &\equiv \frac{1}{n_3^2} [(\Gamma_{11} - \Gamma_{33})^2 + 4\Gamma_{13}^2]^{1/2} \\ &= [(C_{11-} p^2 - C_{33-})^2 + 4C_{13+}^2 p^2]^{1/2}, \end{aligned} \quad (32)$$

$$F \equiv C_{11}^{(1)} C_{55}^{(1)} s_1^4 + C_{33}^{(3)} C_{55}^{(3)} s_3^4 + A s_1^2 s_3^2, \quad (33)$$

$$G \equiv \rho_X (C_{11+}^{(1)} s_1^2 + C_{33+}^{(3)} s_3^2), \quad (34)$$

$$U_1 \equiv 2C_{11}^{(1)} C_{55}^{(1)} p^2 + A - \rho_X s_3^{-2} C_{11+}^{(1)}, \quad (35)$$

$$U_3 \equiv 2C_{33}^{(3)} C_{55}^{(3)} + A p^2 - \rho_X s_3^{-2} C_{33+}^{(3)}, \quad (36)$$

$$Q \equiv C_{11+}^{(1)} p^2 + C_{33+}^{(3)} - 2\rho_X s_3^{-2}, \quad (37)$$

where the quantity  $\rho_X s_3^{-2}$  can be obtained from Eq. (22) and expressed as

$$2\rho_X s_3^{-2} = C_{11+}^{(1)} p^2 + C_{33+}^{(3)} \pm D. \quad (38)$$

The positive and negative signs in front of  $D$  in Eq. (38) correspond to the *QL* and *QT* modes, respectively.  $D$  is by definition always greater than zero in an anisotropic medium. Substitution of Eq. (38) into Eq. (37) yields the identity

$$Q = \mp D, \quad (39)$$

where the negative and positive signs correspond to the *QL* and *QT* modes, respectively.  $B$  in Eq. (31) and  $D$  in Eq. (32) are related by

$$B = \frac{1}{2p^2} (C_{11-}^2 p^4 + C_{33-}^2 - D^2). \quad (40)$$

The group velocities of both the *QL* and *QT* modes can be found analytically from the equation of the slowness surface, which can be derived from Eq. (21) as

$$\Lambda = F - G + \rho_X^2 = 0, \quad (41)$$

where  $F$  and  $G$ , specified by Eqs. (33) and (34), are respectively homogeneous functions of degree 4 and 2 in  $s$ . Using Euler's theorem on a homogeneous function, it is easy to show that

$$s \cdot \nabla_s \Lambda = 4F - 2G = 2(G - 2\rho_X^2) = 2\rho_X s_3^2 Q. \quad (42)$$

From Eq. (13) one obtains

$$V_{g1} = \frac{s_1 U_1}{\rho_X Q}, \quad V_{g3} = \frac{s_3 U_3}{\rho_X Q}, \quad (43)$$

$$q \equiv \tan \zeta = \frac{V_{g1}}{V_{g3}} = \frac{s_1 U_1}{s_3 U_3} = \frac{U_1 p}{U_3}, \quad (44)$$

$$\rho_X V_g^2 = \rho_X (V_{g1}^2 + V_{g3}^2) = \frac{(1+q^2) U_3^2}{\rho_X s_3^{-2} Q^2}. \quad (45)$$

To proceed further, we first consider the *QL* mode and then the *QT* mode.

### 1. Quasilongitudinal mode

For the *QL*-mode propagation the upper sign in front of Eqs. (38) and (39) applies to Eqs. (35)–(37), (44), and (45). After some algebra,  $U_1$  and  $U_3$  in Eq. (44) reduce to

$$U_1 = (B - C_{11-}^2 p^2 - C_{11+}^{(1)} D) / 2, \quad (46)$$

$$U_3 = (B p^2 - C_{33-}^2 - C_{33+}^{(3)} D) / 2. \quad (47)$$

Substitution of Eqs. (46) and (47) into Eq. (44) leads to the following relationship

$$q = \frac{p(B - C_{11-}^2 p^2 - C_{11+}^{(1)} D)}{B p^2 - C_{33-}^2 - C_{33+}^{(3)} D}, \quad (48)$$

which can also be expressed in the form of

$$C_{11-}^2 p^3 + q(B p^2 - C_{33-}^2) - B p + (C_{11+}^{(1)} p - C_{33+}^{(3)} q) D = 0. \quad (49)$$

Equation (48) or (49) can be used to find the direction of a wave normal  $p$  corresponding to that of a group velocity lying in the (010) plane and vice versa, when the relevant values of thermodynamic elastic coefficients and stresses exerted in a medium are known. Substituting Eq. (40) into Eq. (49) and rearranging the resulting equation in terms of powers in  $D$ , one obtains

$$\begin{aligned} (1 - pq) D^2 - 2p(C_{33+}^{(3)} q - C_{11+}^{(1)} p) D + (1 + pq) \\ \times (C_{11-}^2 p^4 - C_{33-}^2) = 0, \end{aligned} \quad (50)$$

which yields

$$D = \frac{1}{1-pq} \{p(C_{33+}^{(3)}q - C_{11+}^{(1)}p) \pm [p^2(C_{33+}^{(3)}q - C_{11+}^{(1)}p)^2 - (1-p^2q^2)(C_{11-}^2p^4 - C_{33-}^2)]^{1/2}\}. \quad (51)$$

For a given group direction  $q$  in the above equation, we choose the region of  $p$  which makes  $D$  real and positive. Finally, from Eqs. (38)–(40), (47), and (45), one obtains the expression for the group velocity

$$\rho_x V_g^2 = \frac{(1+q^2)[C_{11-}^2p^4 - C_{33-}^2 - D(D+2C_{33+}^{(3)})]^2}{8D^2(C_{11+}^{(1)}p^2 + C_{33+}^{(3)} + D)}. \quad (52)$$

The above equation can be used in combination with either Eq. (49) or Eq. (51). The former case applies when the relevant  $C_{ij}$  and stresses acting in a medium are known. For a given group-velocity direction  $q = \tan \zeta$ , one uses Eq. (49) to find  $p$ ; Eq. (32) to calculate  $D$ ; and then Eq. (52) to obtain the group velocity. The latter case applies to an inverse approach by which  $C_{13+}$  can be found from the measured values of a group velocity  $V_g$  for the given direction  $q$ ,  $C_{11+}^{(1)}$ ,  $C_{11-}$ ,  $C_{33+}^{(3)}$ , and  $C_{33-}$ . As indicated by Eq. (23),  $C_{11+}^{(1)}$ ,  $C_{11-} = C_{11-}^{(1)}$ ,  $C_{33+}^{(3)}$ , and  $C_{33-} = C_{33-}^{(3)}$  can be obtained from measurements of the pure-mode wave speeds propagating in the symmetry directions. Equation (52), when  $D$  in it is substituted by Eq. (51) with the known values of  $q$ ,  $V_g$ ,  $C_{11+}^{(1)}$ ,  $C_{11-}$ ,  $C_{33+}^{(3)}$ , and  $C_{33-}$ , becomes a function of single variable  $p$ , which can be solved for to find the values of  $D \geq 0$ ,  $B$ , and  $C_{13+}$  via Eqs. (51), (40), and (31), respectively. This in turn yields the value of  $C_{13}$  if the stresses  $\sigma_{11}$  and  $\sigma_{33}$  are known.

## 2. Quasitransverse mode

In the propagation of the  $QT$  mode, Eqs. (38) and (39) are both determined with the lower sign in front of  $D$ . The application of very similar procedures to those taken in the  $QL$  mode yields

$$q = \frac{p(B - C_{11-}^2p^2 + C_{11+}^{(1)}D)}{Bp^2 - C_{33-}^2 + C_{33+}^{(3)}D}, \quad (53)$$

$$C_{11-}^2p^3 + q(Bp^2 - C_{33-}^2) - Bp - (C_{11+}^{(1)}p - C_{33+}^{(3)}q)D = 0, \quad (54)$$

$$D = \frac{1}{1-pq} \{p(C_{11+}^{(1)}p - C_{33+}^{(3)}q) \pm [p^2(C_{11+}^{(1)}p - C_{33+}^{(3)}q)^2 - (1-p^2q^2)(C_{11-}^2p^4 - C_{33-}^2)]^{1/2}\}, \quad (55)$$

$$\rho_x V_g^2 = \frac{(1+q^2)[C_{11-}^2p^4 - C_{33-}^2 - D(D-2C_{33+}^{(3)})]^2}{8D^2(C_{11+}^{(1)}p^2 + C_{33+}^{(3)} - D)}. \quad (56)$$

The calculation of the group velocity for a given direction  $\zeta$  and the determination of  $C_{13+}$  from the relevant measurements can be achieved in a way similar to those achieved in the  $QL$  mode. However, the measurement of the group velocity of the  $QT$  mode is generally much more difficult than that of the  $QL$  mode in the signal generated by a small, pointlike source and detected by a small, pointlike piezoelectric detector, except in the case of the signal detected by the noncontact displacement transducer such as a capacitive

transducer or a laser interferometer. Detailed discussion on the group velocity of the  $QL$  and  $QT$  modes and its application to determination of elastic constants in nonacoustoelastic case ( $\sigma_{ij} = 0$ ) is provided in Refs. 5–8.

## C. Extension to higher-symmetry media

### 1. Stressed tetragonal medium

A material of cubic symmetry of  $432$ ,  $\bar{4}3m$ , and  $m3m$  classes behaves similar to but not exactly as one of tetragonal symmetry, when the material is stressed in three cubic-axes directions with two equal biaxial stresses or when it is uniaxially loaded along a cubic-axis direction. We term here such stressed media as having tetragonal symmetry. The Huang's condition Eq. (5) holds for tetragonal symmetry, while  $\bar{C}_{ijkl} = \bar{C}_{klij}$  for tetragonal symmetry. This means that tetragonal symmetry is maintained only when hydrostatic pressures are applied to a material of tetragonal symmetry. A medium of tetragonal symmetry of  $422$ ,  $4mm$ ,  $\bar{4}2m$ , and  $4/mmm$  classes also behaves tetragonally when it is deformed with three principal stresses,  $\sigma_{11} = \sigma_{22}$  and  $\sigma_{33}$ . It has a total of six thermodynamic elastic coefficients:

$$\begin{aligned} C_{11} &= C_{22}, & C_{33}, & C_{12}, \\ C_{13} &= C_{23}, & C_{44} &= C_{55}, & C_{66}, \end{aligned} \quad (57)$$

where the direction of tetragonal symmetry is taken as the  $X_3$  direction.

In a tetragonal material, the (010) plane is equivalent to the (100) plane and the group velocities of the  $PT$ ,  $QL$ , and  $QT$  modes propagating in these planes and the (001) plane are governed by those equations previously derived for orthotropic material with the use of Eq. (57) and  $\sigma_{11} = \sigma_{22}$ . In the  $\{n_1, \bar{n}_1, 0\}$ -type diagonal symmetry plane, where the wave normal and group velocity propagate in the  $\langle n_1, n_1, n_3 \rangle$  direction at angles  $\theta$  and  $\zeta$  to the  $x_3$  direction, respectively,

$$n_1^2 = n_2^2 = n_d^2/2 = \sin^2 \theta/2, \quad n_d^2 + n_3^2 = 1. \quad (58)$$

Equation (9) is now factored as

$$(\Gamma_{11} - \Gamma_{12} - \rho V^2)[(\Gamma_{33} - \rho V^2)(\Gamma_{11} + \Gamma_{12} - \rho V^2) - 2\Gamma_{13}^2] = 0, \quad (59)$$

where

$$\begin{aligned} \Gamma_{11} &= (C_{11}^{(1)} + C_{66}^{(1)})n_d^2/2 + C_{44}^{(3)}n_3^2, \\ \Gamma_{33} &= C_{44}^{(1)}n_d^2 + C_{33}^{(3)}n_3^2, \\ \Gamma_{12} &= (C_{12} + C_{66})n_1n_2 = (C_{12}^{(1)} + C_{66}^{(1)})n_d^2/2, \\ \Gamma_{13} &= (C_{13} + C_{44})n_1n_3 = C_{13+}n_dn_3/\sqrt{2}. \end{aligned} \quad (60)$$

The first factor in parenthesis of Eq. (59) yields the relation for the  $PT$  mode propagating on the  $\{n_1, \bar{n}_1, 0\}$ -type plane and polarized in the  $\langle n_1, \bar{n}_1, 0 \rangle$  direction. Following the similar procedures as in Sec. III A, one finds exactly the same relations for the  $PT$  mode on the diagonal plane of a tetragonal medium by replacing  $C_{66}^{(1)}$  by  $(C_{11}^{(1)} - C_{12}^{(1)})/2$  in

Eqs. (20), (28a), (28b), and (29). The *PT*-mode group velocity is then given by

$$(\rho_x V_g^2)^{-1} = [(C_{11}^{(1)} - C_{12}^{(1)})/2]^{-1} \sin^2 \zeta + (C_{44}^{(3)})^{-1} \cos^2 \zeta \quad (PT \text{ mode}). \quad (61)$$

The terms in the square bracket of Eq. (59) yield relations for the *QL* and *QT* modes. Following the procedures similar to those in Sec. III B of this paper and Sec. II C of Ref. 5, one finds that exactly the same relations between  $V_g$ ,  $p = \tan \theta$ ,  $q = \tan \zeta$ ,  $C_{ij}$ , and  $\sigma_{ij}$  can be obtained for the *QL* and *QT* modes in the corresponding Eqs. (46)–(56) and the defining Eqs. (31) and (32) by simply replacing:  $C_{55}$  by  $C_{44}$ ;  $C_{55}^{(1)}$  by  $C_{44}^{(1)}$ ;  $C_{55}^{(3)}$  by  $C_{44}^{(3)}$ ;  $C_{11}$  by  $K$ ;  $C_{11\pm}$  by  $K_{\pm}$ ;  $C_{11}^{(1)}$  by  $K^{(1)}$ ; and  $C_{11\pm}^{(1)}$  by  $K_{\pm}^{(1)}$ , where  $K$ ,  $K_{\pm}$ ,  $K^{(1)}$ , and  $K_{\pm}^{(1)}$  are now defined as

$$K \equiv (C_{11} + C_{12} + 2C_{66})/2, \quad (62a)$$

$$K_{\pm} \equiv K \pm C_{44}. \quad (62b)$$

$$K^{(1)} \equiv (C_{11}^{(1)} + C_{12}^{(1)} + 2C_{66}^{(1)})/2, \quad (63a)$$

$$K_{\pm}^{(1)} \equiv K^{(1)} \pm C_{44}^{(1)}, \quad (63b)$$

where  $C_{11}^{(1)}$ ,  $C_{66}^{(1)}$ ,  $C_{12}^{(1)}$ , and  $C_{44}^{(1)}$  have previously been defined in Eqs. (17) and (18). The group-velocity and relevant relations for the *QL* and *QT* modes are

$$K_{\pm}^2 p^3 + q(Bp^2 - C_{33-}^2) - Bp \pm (K_{\pm}^{(1)} p - C_{33+}^{(3)} q)D = 0, \quad (64)$$

$$D = \frac{1}{1 - pq} \{ \pm p(C_{33+}^{(3)} q - K_{\pm}^{(1)} p) \pm [p^2(C_{33+}^{(3)} q - K_{\pm}^{(1)} p)^2 - (1 - p^2 q^2)(K_{\pm}^2 p^4 - C_{33-}^2)]^{1/2} \}, \quad (65)$$

$$\rho_x V_g^2 = \frac{(1 + q^2)[K_{\pm}^2 p^4 - C_{33-}^2 - D(D \pm 2C_{33+}^{(3)})]^2}{8D^2(K_{\pm}^{(1)} p^2 + C_{33+}^{(3)} \pm D)}. \quad (66)$$

In Eqs. (64)–(66) above, the upper and lower signs in both  $\pm$  and  $\mp$  apply to the *QL* and *QT* modes, respectively, except for the  $\pm$  sign in front of the square bracket in Eq. (65), which applies to both *QL* and *QT* modes. Note that  $B$  and  $D$  in Eqs. (64)–(66) are respectively defined by Eqs. (31) and (32), where  $C_{11-} = C_{11-}^{(1)}$  is now replaced by  $K_- = K_-^{(1)}$ .

## 2. Stressed transversely isotropic medium

An isotropic medium at the natural state behaves as a transversely isotropic medium when it is loaded in three arbitrarily chosen, mutually perpendicular directions with two equal biaxial stresses, say  $\sigma_{11} = \sigma_{22}$ . The case of  $\sigma_{11} = \sigma_{22} = 0$  is common in uniaxial tension or compression tests. In a transversely isotropic medium there are five independent thermodynamic elastic coefficients:

$$C_{11} = C_{22}, \quad C_{33}, \quad C_{12}, \quad C_{13} = C_{23}, \quad (67)$$

$$C_{44} = C_{55}, \quad C_{66} = (C_{11} - C_{12})/2.$$

Any plane parallel to the axis of transverse symmetry is called a zonal plane and all the zonal planes are identical. There is no distinction between the {010}- and {110}-type planes, which are all identical to the zonal plane. Any zonal

plane is a principal plane and any direction normal to the zonal plane is also a principal-stress direction.

For the wave propagation in the zonal plane with wave normal  $\mathbf{n}$  and group velocity  $\mathbf{V}_g$  directed at angles  $\theta$  and  $\zeta$  to the  $X_3$  symmetry axis, respectively, there is a one-to-one correspondence between the directions of the wave normal and the group velocity and all the points in the zonal slowness plane map themselves onto the same zonal group-velocity plane. What holds for the (010) plane of the orthotropic medium in Secs. III A and III B also holds for the zonal plane of a transversely isotropic medium with Eq. (67) and  $\sigma_{11} = \sigma_{22}$  substituted in the appropriate relations.

For the wave propagation in the (001) basal plane normal to the axis of transverse symmetry, all the propagation directions are identical and principal symmetry directions. All the phase velocities are of the pure mode and coincide with group velocities of the pure mode. Their relations are indicated by the first-row elements of Eq. (23) with Eq. (67) and  $\sigma_{11} = \sigma_{22}$  and satisfied.

## IV. GROUP-VELOCITY SECTIONS ILLUSTRATED WITH A UNIAXIALLY LOADED SILICON CRYSTAL

In this section we illustrate the effect of stress on the group-velocity sections with a silicon crystal when it is uniaxially compressed in the direction that coincides with a cubic-axis direction of the crystal in the stress-free natural state. We will take, as an example, the (010) and (110) group-velocity sections when the silicon crystal is compressed normal to the (001) plane at  $\sigma_{33} = -1$  GPa with all other stress components being zero. As mentioned in Sec. III C 1, the silicon crystal in this case behaves tetragonally and it has six thermodynamic elastic coefficients  $C_{ijkl}$  as indicated by Eq. (57). They are related to the second- and third-order elastic constants referred to the coordinates of the stress-free natural states by<sup>12,22</sup>

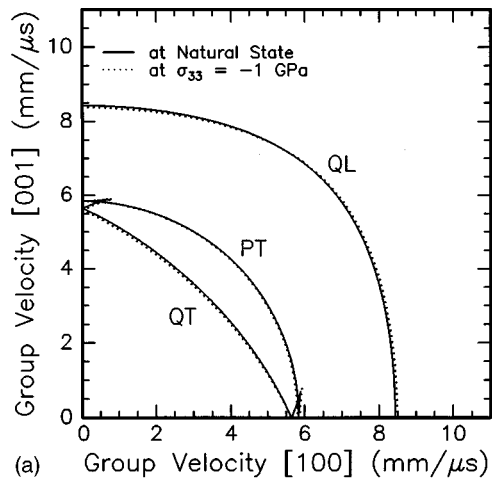
$$C_{ijkl} = \frac{\rho_X}{\rho_a} \frac{\partial X_i}{\partial a_p} \frac{\partial X_j}{\partial a_q} \frac{\partial X_k}{\partial a_r} \frac{\partial X_l}{\partial a_s} c_{pqrs}^N(\mathbf{X}) = \frac{\rho_X}{\rho_a} \frac{\partial X_i}{\partial a_p} \frac{\partial X_j}{\partial a_q} \frac{\partial X_k}{\partial a_r} \frac{\partial X_l}{\partial a_s} [c_{pqrs}(\mathbf{a}) + c_{pqrsmn}(\mathbf{a}) \eta_{mn} + \dots], \quad (68)$$

where  $\mathbf{a}$  denotes a coordinate of a particle in the stress-free natural state,  $c_{pqrs}^N(\mathbf{X})$  is the thermodynamic elastic coefficient that is referred to the natural state and evaluated at the initial state  $\mathbf{X}$ ,  $c_{pqrs}(\mathbf{a})$  and  $c_{pqrsmn}(\mathbf{a})$  are the second-order and third-order elastic constants, which are both referred to and evaluated at the natural state  $\mathbf{a}$ , and

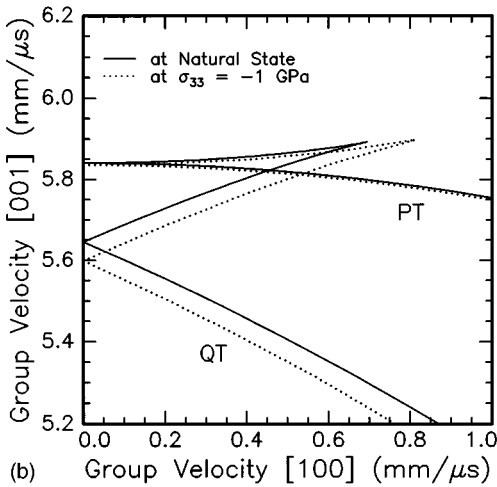
$$\eta_{mn} = \left( \frac{1}{2} \right) \left[ \frac{\partial u_m}{\partial a_n} + \frac{\partial u_n}{\partial a_m} + \frac{\partial u_s}{\partial a_m} \frac{\partial u_s}{\partial a_n} \right] \quad (69)$$

is a finite strain referred to the natural state.

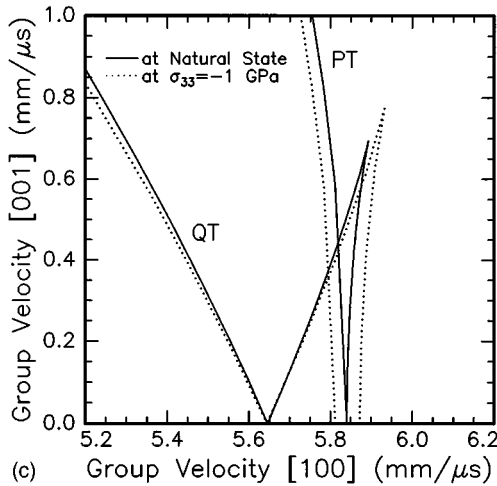
$c_{pqrs}(\mathbf{a})$  for cubic silicon are:<sup>2</sup>  $c_{11} = 165.7$  GPa,  $c_{12} = 63.9$  GPa, and  $c_{44} = 79.56$  GPa. Its density at the natural state is  $\rho_a = 2332$  kg/m<sup>3</sup>. Using these values of the second-order elastic constants and the density evaluated at the natural state, the (010) and (110) group-velocity sections of silicon are plotted with solid lines in Figs. 1 and 2, respectively.



(a) Group Velocity [100] (mm/μs)



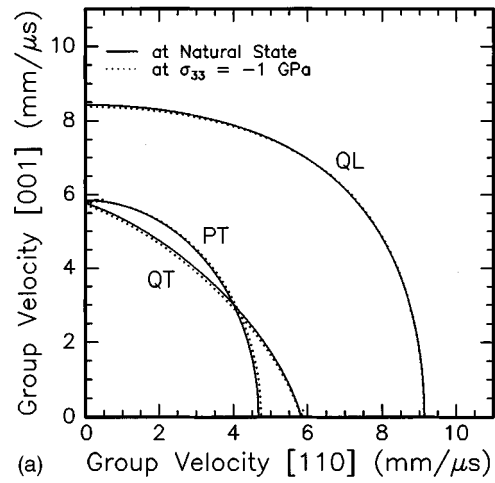
(b) Group Velocity [100] (mm/μs)



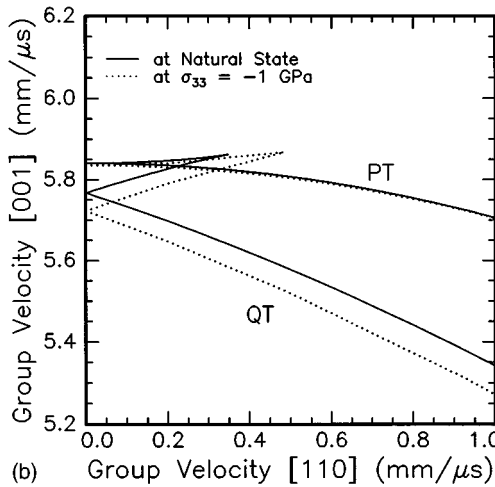
(c) Group Velocity [100] (mm/μs)

FIG. 1. The (010) group-velocity sections of silicon at natural state and at  $\sigma_{33} = -1$  GPa: (a) global view; (b) expanded view of the transverse group-velocity sections near the [001] direction; and (c) expanded view of the transverse group-velocity sections near the [100] direction.

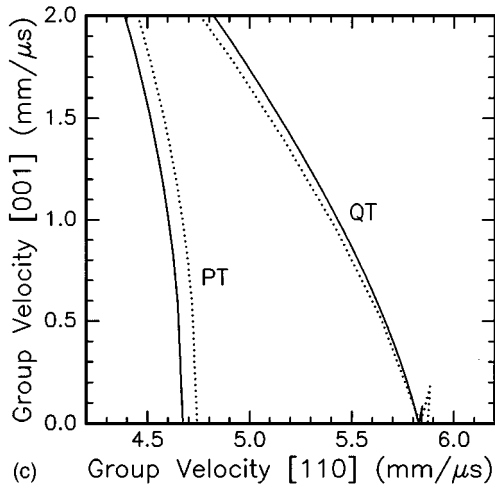
The third-order elastic constants  $c_{pqrs mn}$  (a) of silicon, evaluated in the natural state, are:<sup>23,24</sup>  $c_{111} = -795$  GPa,  $c_{112} = -445$  GPa,  $c_{123} = -75$  GPa,  $c_{144} = 15$  GPa,  $c_{155} = -310$  GPa, and  $c_{456} = -86$  GPa. Using the values of the second-order and third-order elastic constants of silicon and the identity relations between the third-order elastic constants:



(a) Group Velocity [110] (mm/μs)



(b) Group Velocity [110] (mm/μs)



(c) Group Velocity [110] (mm/μs)

FIG. 2. The (110) group-velocity sections of silicon at natural state and at  $\sigma_{33} = -1$  GPa: (a) global view; (b) expanded view of the transverse group-velocity sections near the [001] direction; and (c) expanded view of the transverse group-velocity sections near the [110] direction.

$c_{111} = c_{222} = c_{333}$ ,  $c_{144} = c_{255} = c_{366}$ ,  $c_{112} = c_{223} = c_{133} = c_{113} = c_{122} = c_{233}$ ,  $c_{155} = c_{244} = c_{344} = c_{166} = c_{266} = c_{355}$  for cubic silicon,  $C_{ijkl}$  at  $\sigma_{33} = -1$  GPa are calculated according to Eq. (68) to yield:  $C_{11} = C_{22} = 168.51$  GPa,  $C_{33} = 165.31$  GPa,  $C_{44} = C_{55} = 80.70$  GPa,  $C_{66} = 79.06$  GPa,  $C_{12} = 63.32$  GPa, and  $C_{13} = C_{23} = 65.72$  GPa. The density  $\rho_X = 2340$  kg/m<sup>3</sup> is obtained at  $\sigma_{33} = -1$  GPa. Using these thermodynamic elas-

tic coefficients  $C_{\mu\nu}$  obtained at  $\sigma_{33} = -1$  GPa, the (010) and ( $\bar{1}\bar{1}0$ ) group-velocity sections of silicon are also displayed in Figs. 1 and 2, respectively, with dotted lines. The group-velocity sections near the [001] and [100] axes of these symmetry planes, which correspond to the wave normals lying in nonsymmetry planes, are neither of interest here nor within the scope of this work and therefore not included in the figures. The group velocity of the longitudinal ( $L$ ) mode in the [001] and [100] directions is 8.429 mm/ $\mu$ s in the natural state. Under  $\sigma_{33} = -1$  GPa, the change in group velocity of this mode is about  $-0.59\%$  in the [001] loading direction, while it is about  $0.67\%$  in the [100] transverse to the loading direction. The group velocity of the  $QL$  mode at  $\sigma_{33} = -1$  GPa varies from that in the natural state by  $0.37\%$  in the [101] direction,  $45^\circ$  away from the loading direction, while it changes minimally by  $-0.016\%$  in the [110] perpendicular to the loading direction. The group velocities along both the [101] and the [110] directions in the natural state are 9.129 mm/ $\mu$ s.

Figures 1(b), 1(c), 2(b), and 2(c) display detailed views of the group velocity sections of the transverse mode near the symmetry directions. Figures 1(b) and 2(b) indicate that along the [001] direction are four rays with distinct velocities: pure  $L$  ray shown,  $PT$  ray shown in both figures, intermediate-speed  $QT$  ( $IQT$ ) ray shown in Fig. 2(b), and slow  $QT$  ( $SQT$ ) ray shown in Fig. 1(b). These rays propagate at 8.429 mm/ $\mu$ s, 5.841 mm/ $\mu$ s, 5.767 mm/ $\mu$ s, and 5.646 mm/ $\mu$ s, respectively, in the natural state. Their speeds change respectively by  $-0.59\%$  (already mentioned),  $-0.085\%$ ,  $-0.77\%$ , and  $-0.82\%$  at  $\sigma_{33} = -1$  GPa. The group-velocity sections of the fast  $QT$  ( $FQT$ ) and  $PT$  modes make a tangential contact with each other in the [001] direction, and their speeds are identical along this direction both in the natural state and at  $\sigma_{33} = -1$  GPa. The  $FQT$  mode along the [001] direction becomes a pure mode which is polarized in the [100] direction, while the  $PT$  mode is polarized in the [010] direction as mentioned before. Note that the  $IQT$  and  $SQT$  rays are of the oblique mode, the wave normals of which lie in nonsymmetry directions on the ( $\bar{1}\bar{1}0$ ) and (010) planes, respectively.

The  $IQT$  ray along the [100] direction in the natural state propagates at 5.767 mm/ $\mu$ s with its oblique wave normal lying on the  $\{011\}$ -type planes. However, this ray no longer travels along the [100] direction under the influence of stress  $\sigma_{33}$ , since the presence of the stress  $\sigma_{33}$  causes the  $\{011\}$ -type planes to be no longer symmetry planes. Referring to Fig. 1(c), the group velocity of the  $SQT$  ray with 5.646 mm/ $\mu$ s in the natural state varies very slowly with stress ( $-0.030\%$  at  $\sigma_{33} = -1$  GPa) along the [100] direction. The group velocities of the  $FQT$  and  $PT$  modes, which are degenerate with the speed 5.841 mm/ $\mu$ s along the [100] direction in natural state, split into opposite directions under the stress  $\sigma_{33}$  and the difference between them, 0.0602 mm/ $\mu$ s at  $\sigma_{33} = -1$  GPa, is about  $1.03\%$  of their speed in the natural state. The former mode is polarized in the [001] direction, and the latter in the [010] as aforementioned. The group velocities of these pure modes along the [100] direction are equal to their phase velocities and they are respectively called the  $SV$  (shear vertical) and  $SH$  (shear

horizontal) types. Under a stress  $\sigma_{22}$  acting, these two modes interchange their role. It is well known in acoustoelasticity that the difference between the wave speeds of the  $SV$  and  $SH$  types that propagate in the [100] normal to the loading direction is proportional to the difference between the two principal stresses,  $\sigma_{33} - \sigma_{22}$ .<sup>14</sup>

In the face-diagonal direction [110] [see Fig. 2(c)], the group velocity of the  $FQT$  ray changes by  $0.54\%$  from 5.841 mm/ $\mu$ s in the natural state to 5.873 m when  $\sigma_{33} = -1$  GPa, while that of the  $SQT$  ray hardly changes ( $0.15\%$ ) from 5.828 mm/ $\mu$ s in the natural state to 5.837 m at  $\sigma_{33} = -1$  GPa. However, the change in the group velocity of the  $PT$  mode is quite significant. It varies by  $1.5\%$  from 4.672 mm/ $\mu$ s in the natural state to 4.741 mm/ $\mu$ s at  $\sigma_{33} = -1$  GPa.

A phase velocity of the  $SH$ -polarized  $PT$  mode propagating in an oblique direction of the symmetry planes is difficult to measure, but its group velocity is easy to obtain by employing a point-source/point-detector technique.<sup>7,8</sup> This mode provides certain advantages for estimating residual stresses acting in an elastic body.<sup>25,26</sup> We take an example of the  $SH$ -mode propagating in the  $45^\circ$  direction to the loading direction in the (010) and ( $\bar{1}\bar{1}0$ ) planes. It is easy to obtain from Eqs. (29) and (61) that these  $PT$  modes propagate in the natural state at the group velocities 5.841 mm/ $\mu$ s in the (010) plane and 5.160 mm/ $\mu$ s in the ( $\bar{1}\bar{1}0$ ) plane, while at  $\sigma_{33} = -1$  GPa they travel respectively at 5.824 mm/ $\mu$ s and 5.204 mm/ $\mu$ s. The effect of the uniaxial compressive stress  $\sigma_{33}$  on the  $PT$  mode in silicon is greater in the ( $\bar{1}\bar{1}0$ ) plane than in the (010) plane.

It may be interesting to see the stress sensitivity of the magnitude and direction of group velocities at the cuspidal edges shown in Figs. 1(b), 1(c), 2(b), and 2(c). We follow the method adopted in Ref. 5 for calculation of the polar coordinates of these points, the magnitude of group velocity  $V_g$  and the angular direction  $\zeta$ . In the natural state the coordinates of these cuspidal edges near the [001] direction shown in Figs. 1(b) and 2(b) are calculated to be (5.934 mm/ $\mu$ s,  $6.72^\circ$ ) and (5.873 mm/ $\mu$ s,  $3.40^\circ$ ). They respectively move to (5.953 mm/ $\mu$ s,  $7.83^\circ$ ) and (5.887 mm/ $\mu$ s,  $4.71^\circ$ ) at  $\sigma_{33} = -1$  GPa. We notice that changes in the direction of the cuspidal edges are rather substantial, being more than  $1^\circ$ . The cuspidal edges near the [100] and [110] directions shown in Figs. 1(c) and 2(c) vary respectively from (5.934 mm/ $\mu$ s,  $83.28^\circ$ ) and (5.846 mm/ $\mu$ s,  $89.16^\circ$ ) to (5.983 mm/ $\mu$ s,  $82.57^\circ$ ) and (5.886 mm/ $\mu$ s,  $88.25^\circ$ ), resulting in the directional change of  $0.71^\circ$  and  $0.91^\circ$  and in the appreciable variation of the magnitude of their group velocities by  $0.8\%$  and  $0.7\%$ , respectively. However, because of the effect of *eidolon* associated with the diffraction of sound waves of finite wave length,<sup>27</sup> it is not easy to measure the directional change.

Overall, it is worth mentioning that the effect of stress on the group velocity of the  $PT$  and  $FQT$  modes is larger for waves propagating in the direction normal to loading and minimal along the loading direction, while for the oblique modes, such as  $IQT$  and  $SQT$  modes, the effect is the opposite; that is, much greater along the loading direction and minimal along the direction normal to loading. For the lon-



itudinal mode propagating in the (010) plane, the effect is roughly equal in magnitude in both directions but opposite in sign. In the (110) plane the stress effect on the longitudinal mode is greater along the loading direction and minimal in the direction normal to the loading.

## V. GROUP VELOCITY OF THE OBLIQUE MODE ALONG THE SYMMETRY DIRECTION

One distinct feature found in some anisotropic materials is the presence of an oblique-mode group velocities along the symmetry directions, such as the  $SQT$  and  $IQT$  rays shown in Figs. 1(b), 1(c), 2(b), and 2(c). These oblique-mode rays do not exist in an isotropic material. It may be worthwhile to derive the expressions governing the group velocity of the oblique modes along the symmetry directions. The oblique-mode rays are always associated with the  $QT$  slowness surface and the existence of these rays along the symmetry direction requires the  $QT$  slowness surface to be concave around that symmetry direction. The concavity condition in a stress-free natural state was discussed by Musgrave<sup>1</sup> and Wang<sup>10</sup> and we discuss the concavity condition of the  $QT$  slowness surface in a stressed medium for the case that only the normal stress components  $\sigma_{ii}$  ( $i$  not summed;  $i=1,2,3$ ) are acting and all shear stress components in the medium are zero, i.e.,  $\sigma_{12}=\sigma_{13}=\sigma_{23}=0$ . Following the similar procedures used in Refs. 1 and 10, it is easy to show the concavity conditions both of the (010) slowness section of the  $QT$  mode in an orthotropic material and of the (110) slowness section of the  $QT$  mode in a tetragonal material. For normal solids in which the conditions of  $C_{11}>C_{55}$ ,  $C_{33}>C_{55}$ , and  $K>C_{44}$  hold, the concavity conditions around the [001] direction are

$$C_{13+}^2 > C_{11}^{(1)} C_{33-} \quad (70a)$$

and

$$C_{13+}^2 > K^{(1)} C_{33-}, \quad (70b)$$

for the (010) and (110)  $QT$  slowness sections, respectively. Likewise, the concavity conditions around the [100] direction of the (010)  $QT$  slowness section and around the [110] direction of the (110)  $QT$  slowness section are respectively given by

$$C_{13+}^2 > C_{33}^{(3)} C_{11-} \quad (71a)$$

and

$$C_{13+}^2 > C_{33}^{(3)} K_{-}. \quad (71b)$$

When conditions (70a), (70b), (71a), and (71b) are satisfied, there exist the rays of the oblique mode propagating along the symmetry directions, and they are all satisfied in silicon. The expressions for the group velocity  $V_g$  of the oblique mode along the [001] direction can be derived by similar procedures found in Refs. 6 and 9 and written as

$$C_{11-}^2 (\rho_X V_g^2)^2 + 2(C_{11+}^{(1)} C_{13+}^2 - C_{11-} C_{pr-}) \rho_X V_g^2 + (C_{13+}^4 - 2C_{pr+} C_{13+}^2 + C_{pr-}^2) = 0 \quad (72)$$

for the ray whose oblique wave normal lies on the (010) plane of the orthotropic material, and

$$K_{-}^2 (\rho_X V_g^2)^2 + 2(K_{+}^{(1)} C_{13+}^2 - K_{-} K_{pr-}) \rho_X V_g^2 + (C_{13+}^4 - 2K_{pr+} C_{13+}^2 + K_{pr-}^2) = 0 \quad (73)$$

for the ray whose oblique wave normal lies on the (110) plane of the tetragonal material. In Eqs. (72) and (73)  $C_{pr\pm}$  and  $K_{pr\pm}$  are defined by

$$C_{pr\pm} \equiv C_{11}^{(1)} C_{33}^{(3)} \pm C_{55}^{(1)} C_{55}^{(3)}, \quad (74a)$$

$$K_{pr\pm} \equiv K^{(1)} C_{33}^{(3)} \pm C_{44}^{(1)} C_{44}^{(3)}. \quad (74b)$$

Similar expressions for the group velocity of the oblique mode propagating either in the [100] or in the [110] direction can be found by interchanging the indices 1 and 3 in Eq. (72) for the former direction and by interchanging  $K_{-}$  and  $C_{33-}$  and also interchanging  $K_{+}^{(1)}$  and  $C_{33+}^{(3)}$  in Eq. (73) for the latter direction. Using Eqs. (72) and (73) and equivalent equations, the group velocities of the  $IQT$  and  $SQT$  modes along the symmetry directions of silicon at  $\sigma_{33} = -1$  GPa can be conveniently obtained and are identical with those in Figs. 1 and 2.

## VI. DISCUSSION

We have derived various group-velocity formulas for the symmetry planes of a stressed elastic medium with orthotropic or higher symmetry and shown the effect of uniaxial compressive stress on the (010) and (110) group-velocity sections and the cuspidal features of a tetragonal silicon specimen as an example.

The derived formulas can also be used to determine the effective elastic coefficients and in principle the third-order elastic constants via Eq. (68). Since the determination of the third-order elastic constants are quite a complicated topic, interested readers are referred to Refs. 22 and 24 for detail. It was already mentioned that the pure-index effective elastic coefficients  $C_{\mu\mu}^{(i)}$  ( $\mu$  not summed;  $\mu=1,2,\dots,6$ ;  $i=1,2,3$ ) can be determined via Eq. (23) from measurements of the group or phase velocities of the pure-mode propagating in the symmetry direction. Determination of a mixed-index elastic coefficient, say  $C_{13+}$ , can be calculated from the  $QL$  or  $QT$  group-velocity data measured along an oblique direction in the symmetry plane and using the results developed in Sec. III. For detailed procedures on determination of the mixed-index elastic constants, readers are referred to Sec. III B of Ref. 5. If the  $QT$  slowness surface is concave around the symmetry direction, say the [001] axis,  $C_{13+}$  can be also determined via Eqs. (72) and (73) from measurements of the group velocities of the oblique mode along the [001] direction. Kim *et al.*<sup>6,9</sup> determined  $C_{13}$  of zinc and  $C_{12}$  of silicon in their stress-free, natural state from the measurements of the group velocities of the oblique mode propagating in the [001] direction. Since  $C_{13+} = C_{13+}^{(1)} = C_{13+}^{(3)}$ , one can also determine both  $C_{13}^{(1)} = C_{13} - \sigma_{11}$  and  $C_{13}^{(3)} = C_{13} - \sigma_{33}$ , which appear in the expressions of the effective elastic coefficients  $K_{ijkl}^S \equiv (\partial\sigma_{ij}/\partial\epsilon_{kl})_S$ , the effective Young's modulus and Poisson's ratios.<sup>18</sup>

When isotropic materials, such as steel and aluminum alloy commonly used in engineering structures, are subjected to uniaxial tension or compression, they behave as trans-

versely isotropic materials with the axis of transverse symmetry parallel to the loading direction. In this case Eq. (67) holds and one can calculate the group-velocity sections in a similar way as we did with the (001) silicon crystal. This situation often arises in estimation of residual stresses when it is necessary to measure the acoustoelastic birefringence constant. Since the third-order elastic constants of polycrystalline materials vary significantly from specimen to specimen and reliable, reported data of them are scarce in literature, we have not attempted here to predict the effects of stress on the group-velocity surfaces of structural materials.

When the applied stresses are hydrostatic pressures  $p$  such that  $\sigma_{ij} = -p\delta_{ij}$ , one can apply the superposition principle for the effect of three equal normal stresses acting on a medium to calculate the group velocities in the medium under hydrostatic pressures. The effect of hydrostatic pressures  $p$  on the elastic constants and the density of solids abounds in the literature.<sup>24,28,29</sup> Since the symmetry of a material remains unchanged under hydrostatic pressures, the effect of hydrostatic pressures on the group velocity in symmetry planes can be calculated following the same approaches taken in Ref. 5, whereby the elastic constants at the natural state are simply replaced by the effective elastic constants obtained under the hydrostatic pressures.

The effect of stress on the group velocities in nonsymmetry planes and even the group velocities on the symmetry planes, which correspond to the wave normals lying in a nonsymmetry plane, are very difficult to approach analytically. It may be calculated using the numerical method such as the Monte Carlo method. This is currently under investigation.

## VII. CONCLUSIONS

We have derived closed-form analytic formulas that relate both thermodynamic elastic coefficients and stresses to the group velocities of  $PT$ ,  $QL$ , and  $QT$  modes propagating in an arbitrary direction on the symmetry planes of a stressed medium with orthotropic or higher symmetry. Analytic formulas relating the directions of the group velocity and the corresponding wave normal on the symmetry plane are also presented for all three modes. These relations can be applied to determine the group-velocity sheets of the symmetry planes of the stressed medium and to obtain the mixed-index elastic coefficients. The group-velocity sections of silicon which is loaded in the  $[001]$  direction with a compressive stress of  $\sigma_{33} = -1$  GPa are shown as an example.

## ACKNOWLEDGMENTS

The first and third authors appreciate the financial support from the Office of Naval Research under Grant No. N00014-95-1-0429.

<sup>1</sup>M. J. P. Musgrave, *Crystal Acoustics* (Holden-Day, San Francisco, 1970).

<sup>2</sup>B. A. Auld, *Acoustic Fields and Waves in Solids* (Krieger, Malabar, FL, 1990), 2nd ed., Vol. 1.

<sup>3</sup>J. F. Havlice, W. L. Bond, and L. B. Wigton, "Elastic poynting vector in a piezoelectric medium," *IEEE Trans. Sonics Ultrason.* **SU-17**, 246–249 (1970).

<sup>4</sup>A. G. Every, "General closed-form expressions for acoustic waves in

elastically anisotropic solids," *Phys. Rev. B* **22**, 1746–1760 (1980).

<sup>5</sup>K. Y. Kim, "Analytical relations between the elastic constants and the group velocity in an arbitrary direction of symmetry planes of media with orthorhombic or higher symmetry," *Phys. Rev. B* **49**, 3713–3724 (1994).

<sup>6</sup>K. Y. Kim and W. Sachse, "Determination of all elastic constants of transversely isotropic media with a cusp around the symmetric axis by use of elastic pulses propagating in two principal directions," *Phys. Rev. B* **47**, 10 993–11 000 (1993).

<sup>7</sup>K. Y. Kim, R. Sribar, and W. Sachse, "Analytical and optimization procedures for determination of all elastic constants of anisotropic solids from group velocity data measured in symmetry planes," *J. Appl. Phys.* **77**, 5589–5600 (1995).

<sup>8</sup>K. Y. Kim, T. Ohtani, A. R. Baker, and W. Sachse, "Determination of all elastic constants of orthotropic plate specimens from group velocity data," *Res. Nondestruct. Eval.* **7**, 13–29 (1995).

<sup>9</sup>K. Y. Kim, A. G. Every, and W. Sachse, "Determination of the elastic constants of anisotropic solids from group velocities measured in symmetry directions," *Int. J. Mod. Phys. B* **10**, 235–246 (1996).

<sup>10</sup>L. Wang, "Determination of the ray surface and recovery of elastic constants of anisotropic elastic media: Direct and inverse approach," *J. Phys.: Condens. Matter* **7**, 3863–3880 (1995).

<sup>11</sup>R. A. Toupin and B. Bernstein, "Sound waves in deformed perfectly elastic materials. Acoustoelastic effect," *J. Acoust. Soc. Am.* **33**, 216–225 (1961).

<sup>12</sup>R. N. Thurston, "Effective elastic coefficients for wave propagation in crystals under stress," *J. Acoust. Soc. Am.* **37**, 348–356 (1965).

<sup>13</sup>R. N. Thurston, "Waves in solids," in *Handbuch der Physik* Vol. VIa/4, Chief Editor: S. Flügge, *Mechanics of Solids VI*, Editor: C. Truesdell (Springer-Verlag, New York, 1974), pp. 109–308.

<sup>14</sup>Y. H. Pao, W. Sachse, and H. Fukuoka, "Acoustoelasticity and ultrasonic measurements of residual stresses," in *Physical Acoustics*, Vol. 17, edited by W. P. Mason and R. N. Thurston (Academic, New York, 1984), pp. 62–143.

<sup>15</sup>A. L. Ruoff, H. Xia, and Q. Xia, "The effect of a tapered aperture on x-ray diffraction from a sample with a pressure gradient: Studies on three samples with a maximum pressure of 560 GPa," *Rev. Sci. Instrum.* **63**, 4342–4348 (1992).

<sup>16</sup>K. Huang, "On the atomic theory of elasticity," *Proc. R. Soc. London, Ser. A* **203**, 178–194 (1950).

<sup>17</sup>M. Born and K. Huang, *Dynamical Theory of Crystal Lattices* (Clarendon, Oxford, 1954).

<sup>18</sup>K. Y. Kim, "Thermodynamics at finite deformation of an anisotropic elastic solid," *Phys. Rev. B* **54**, 6245–6254 (1996).

<sup>19</sup>K. Y. Kim and W. Sachse, "The theory of thermodynamic-acoustoelastic stress gauge," *J. Appl. Phys.* **80**, 4934–4943 (1996).

<sup>20</sup>G. A. Northrop and J. P. Wolfe, "Phonon imaging: Theory and applications," in *Nonequilibrium Phonon Dynamics*, edited by W. E. Bron (Plenum, New York, 1985), pp. 165–242.

<sup>21</sup>A. G. Every, "Formation of phonon-focusing caustics in crystals," *Phys. Rev. B* **34**, 2852–2862 (1986).

<sup>22</sup>R. N. Thurston and K. Brugger, "Third-order elastic constants and the velocity of small amplitude elastic waves in homogeneously stressed media," *Phys. Rev. A* **133**, 1604–1610 (1964).

<sup>23</sup>J. J. Hall, "Electronic effects in the elastic constants of  $n$ -type silicon," *Phys. Rev.* **161**, 756–761 (1967).

<sup>24</sup>R. F. S. Hearmon, *Numerical Data and Functional Relationships in Science and Technology*, Ländolt-Bernstein, edited by K.-H. Hellwege and A. M. Hellwege (Springer-Verlag, New York, 1979), New Series, Group III, Vol. 11.

<sup>25</sup>R. B. King and M. Fortunko, "Determination of in-plane residual stress states in plates using horizontally polarized shear waves," *J. Appl. Phys.* **54**, 3027–3035 (1983).

<sup>26</sup>C. S. Man and W. Y. Lu, "Towards an acoustoelastic theory for measurement of residual stresses," *J. Elast.* **17**, 159–182 (1987).

<sup>27</sup>K. Y. Kim, K. C. Bretz, A. G. Every, and W. Sachse, "Ultrasonic imaging of the group velocity surfaces about the cubic axis in silicon," *J. Appl. Phys.* **79**, 1857–1863 (1996).

<sup>28</sup>J. R. Macdonald, "Review of some experimental and analytical equations of state," *Rev. Mod. Phys.* **41**, 316–349 (1969).

<sup>29</sup>G. R. Barsch and Z. P. Chang, "Adiabatic, isothermal, and intermediate pressure derivatives of the elastic constants for cubic symmetry," *Phys. Status Solidi* **19**, 139–151 (1969).

# On the low-frequency oscillation of a fluid layer between two elastic plates

Waled Hassan and Peter B. Nagy

*Department of Aerospace Engineering and Engineering Mechanics, University of Cincinnati, Cincinnati, Ohio 45221*

(Received 4 June 1997; accepted for publication 5 September 1997)

In 1965, Lloyd and Redwood predicted the existence of a new guided mode of wave propagation in solid–fluid–solid trilayers [Acustica **16**, 169–173 (1965)]. In this so-called fluid mode, the two solid plates flex sideways in a symmetric way while the fluid in the thin gap between them is squeezed forward and backward parallel to the direction of wave propagation. This mode is slower than the lowest-order bending mode of the plates and asymptotically approaches the Stoneley–Scholte mode of the solid–fluid interface at high frequencies. While the other modes of the solid–fluid–solid trilayer are very similar to the free vibrations of the free solid plates which are only slightly perturbed by the fluid coupling between the plates, the fluid mode cannot be related to any classical Lamb mode in the plates. It is shown in this paper that at low frequencies the fluid mode is truly a coupled vibration of the solid and the fluid, which contribute the stiffness and the inertia, respectively. The highly dispersive phase velocity of this mode was measured over a frequency range of one decade by using a laser interferometric technique. The experimental results were found to be in good quantitative agreement with the theoretical predictions. To the best of our knowledge, these measurements constitute the first conclusive experimental evidence of the existence of the dispersive fluid mode predicted by Lloyd and Redwood. © 1997 Acoustical Society of America. [S0001-4966(97)05512-4]

PACS numbers: 43.20.Mv [ANN]

## INTRODUCTION

The problem of guided waves in solid–fluid–solid trilayers has been studied in great detail both theoretically and experimentally. Lloyd and Redwood were the first to investigate guided wave propagation in a layered plate composed of two solids with perfect contact, slip, or a fluid layer at their interface.<sup>1</sup> Cherif *et al.* studied the acoustic reflection coefficient of aluminum–water–Plexiglas trilayers at normal incidence.<sup>2</sup> Couchman *et al.*<sup>3</sup> and Guyott and Cawley<sup>4</sup> reported on the phenomenon of resonance splitting, or the formation of doublets in the vicinity of classical Lamb modes, in symmetrical trilayers. Laperre and Thys investigated elastic wave dispersion in both symmetric and asymmetric trilayers composed of two solid plates separated by a fluid layer.<sup>5</sup> The related problem of solid trilayers has been also extensively investigated because of its practical importance in numerous applications. A number of papers have appeared on the use of trilayers as antireflection coating.<sup>6–8</sup> Other works concentrated on the development of a nondestructive ultrasonic test for adhesively bonded plates.<sup>9–15</sup> It was shown that several properties of the adhesive layer, such as its cohesive strength, can be extracted from reflection or transmission experiments and from guided wave dispersion.

Figure 1 shows a symmetric trilayer composed of a thin fluid film between two identical, isotropic, and homogeneous plates. The main goal of this paper is to experimentally investigate the dispersive fluid mode in this structure. This mode was first predicted by Lloyd and Redwood based on numerical analysis of the dispersion equation more than 30 years ago.<sup>1</sup> They presented the phase velocities and particle displacements of various modes of propagation at different

frequencies. Figure 2 shows the normalized phase velocity ( $c_x/c_T$ ) versus normalized frequency ( $2h\omega/c_T$ ) dispersion curves for the seven lowest-order guided modes of the structure, where  $c_x$  is the phase velocity of the guided mode,  $c_T$  is the shear velocity in the plates,  $h$  is the half-width of the plates, and  $\omega$  is the angular frequency. The material properties and dimensions were taken from the original paper of Lloyd and Redwood.<sup>16</sup> We are going to investigate only the lowest-order symmetric mode, which is indicated by the arrow and called the “fluid” mode. Lloyd and Redwood reported the existence of this new and unique mode of wave propagation in the case of two identical plates with a thin fluid layer between them. They also pointed out some of its main features, including the dominantly transverse vibration of the plates combined with the dominantly longitudinal motion of the fluid between them and the resulting very slow and strongly dispersive phase velocity, but did not explore its physical nature in greater depth. A mode with similar characteristics has been predicted by Franklin in the case of a fluid layer between an elastic plate and a solid substrate.<sup>17</sup> Recently, Coulouvrat *et al.* further investigated the existence of global symmetric and antisymmetric guided waves propagating in solid–fluid–solid trilayers.<sup>18</sup> They presented approximate analytical expressions for the case of a thin and compliant fluid layer and confirmed the previously reported phenomena of resonance splitting and formation of doublets for moderately thin liquid films and they also confirmed the existence of the slow “fluid” mode of wave propagation first reported by Lloyd and Redwood.

In order to gain better understanding of the physical behavior of the lowest-order symmetric mode, we will first

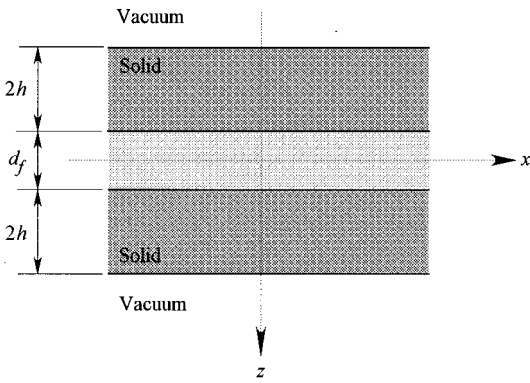


FIG. 1. Geometry of the solid–fluid–solid trilayer and the coordinate system.

examine the low-frequency asymptotic dispersion equation<sup>18</sup> of this intriguing mode and cast it into a form that better separates the contributions of the solid and fluid constituents. Then we will present a simple physical model to derive the same low-frequency asymptotic dispersion equation and to better illuminate the physical nature of the fluid mode in this range. In order to emphasize how the flexing plates squeeze the fluid through the narrow gap between them, we will refer to the highly dispersive low-frequency asymptote of the fluid mode as the “squirting” mode. Finally, the existence of the fluid mode will be confirmed by experimental measurements over a wide frequency range. To the best of our knowledge, this mode has been predicted from theoretical investigations only but has never been experimentally observed before.

### I. LOW-FREQUENCY ASYMPTOTIC BEHAVIOR OF THE FLUID MODE

The schematic diagram of a symmetric trilayer composed of a thin fluid film between two identical, isotropic, and homogeneous plates was previously shown in Fig. 1. The two plates have the same thickness of  $2h$  and are composed of the same material, characterized by density  $\rho_s$ , shear wave velocity  $c_T$ , and longitudinal wave velocity  $c_L$ .

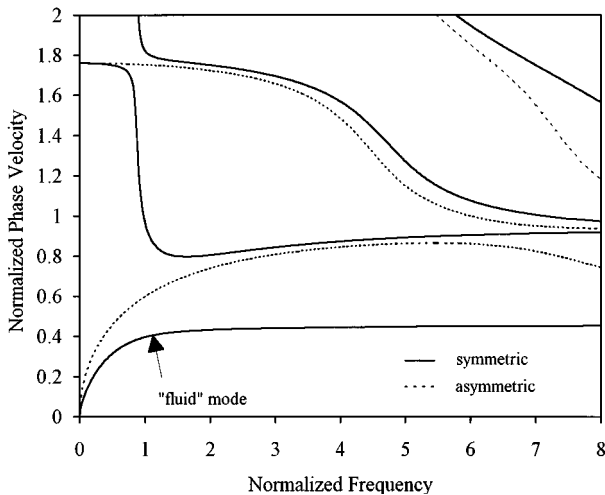


FIG. 2. Normalized phase velocity ( $c_x/c_T$ ) versus normalized frequency ( $2h\omega/c_T$ ) curves for the solid–fluid–solid trilayer.

The density, sound velocity, and thickness of the fluid layer are  $\rho_f$ ,  $c_f$ , and  $d_f$ , respectively. The  $z$  direction is chosen along the thickness of the plates which are infinite in the perpendicular  $x$  and  $y$  directions. For symmetry purposes the origin of the coordinate system is chosen at the center of the fluid layer.

The dispersion equation of such a system can be obtained from the boundary conditions that must be satisfied by the stresses and displacements at each fluid–solid and vacuum–solid interface. For this particular case of interest this would result in a  $10 \times 10$  matrix system. The vanishing determinant of this system gives the desired dispersion equation. However, symmetry can be exploited to reduce the size of this matrix system and to obtain a relatively simple closed-form expression for the dispersion relation. The dispersion equations of the symmetric and antisymmetric modes are, respectively, given by Eqs. (4) and (5) in Ref. 18. It must be emphasized that symmetry or antisymmetry is global with respect to the center of the fluid layer. The displacements inside each plate individually obey no symmetry or antisymmetry relation with respect to the center of the plate. The special mode we are focusing on is the low-frequency asymptote of the lowest-order symmetric mode, i.e., the fluid mode. Coulouvrat *et al.* derived an explicit low-frequency approximation for the phase velocity of this mode by asymptotic expansion of the exact dispersion equation. For convenient comparison to our later results we include their equation here:

$$\frac{k_x}{k_T} \approx \left[ \frac{3\rho_f h}{4(1 - c_T^2/c_L^2)\rho_s d_f} \right]^{1/6} (k_T h)^{-2/3}, \quad (1)$$

where  $k_x = \omega/c_x$  is the wave number in the  $x$  direction and  $k_T = \omega/c_T$  is the wave number of the shear wave in the plate. In its current form, Eq. (1) seems to imply that the density of the plates plays a role in determining the propagation characteristics of this mode. However, this appearance is just an artifact caused by the normalization process based on the shear wave number in the solid,  $k_T = \omega/c_T = \omega\sqrt{\rho_s/\mu}$ , where  $\mu$  is the shear modulus of the solid. Substituting this expression for  $k_T$  along with the ratio between the shear and longitudinal velocities in the solid  $1 - c_T^2/c_L^2 = 1/(2 - 2\nu)$  expressed in terms of Poisson’s ratio  $\nu$ , we arrive at the following expression for the phase velocity:

$$c_x \approx \left[ \frac{Eh^3 d_f \omega^4}{3(1 - \nu^2)\rho_f} \right]^{1/6}, \quad (2)$$

where  $E$  denotes Young’s modulus. Equation (2) is equivalent to Eq. (1), however, it has the advantage of better elucidating the physical nature of the mode it represents. It clearly shows that this mode depends on the stiffness of the plates and the density of the liquid film between them. On the other hand, the mode does not depend on either the density of the solid or the bulk modulus of the fluid. According to Eq. (2), the phase velocity is not simply a function of the fluid mass over a unit area since the fluid density is not multiplied but rather divided by the thickness of the fluid layer. Later, we will demonstrate that this intriguing feature is due to the squirting effect of the thin gap between the plates, which accelerates the fluid more and more as the gap

narrows. In the next section we proceed to further investigate the physical nature of this mode and we derive Eq. (2) from an independent physical approach.

## II. PHYSICAL MODEL FOR THE SQUIRTING MODE

The squirting mode of a thin fluid layer bounded by two thin solid plates corresponds to longitudinal (along the  $x$  direction) vibrations of the fluid caused by the symmetric transverse vibrations of the plates. This interpretation of the mode agrees with the displacement profiles presented by Lloyd and Redwood (see Fig. 4b in Ref. 1). It also implies that as the two plates undergo small symmetric transverse vibrations in opposite directions they force the fluid in the very thin gap between them to experience a much larger displacement in the longitudinal direction, hence the name ‘‘squirting’’ mode. Based on this simple physical model, we present the following derivation that leads to Eq. (2) starting from the basic principles of strength of materials and fluid mechanics.

Let us consider again the solid–fluid–solid trilayer shown in Fig. 1. We will start from the well-known differential equation governing the bending deformation of a plate:

$$\frac{2h^3 E}{3(1-\nu^2)} \frac{\partial^4 w}{\partial x^4} = -p, \quad (3)$$

where  $w$  is the transverse displacement in the  $z$  direction and  $p$  denotes the fluid pressure. The balance of momentum equation for the fluid can be written as

$$\rho_f \frac{\partial^2 u}{\partial t^2} = -\frac{\partial p}{\partial x}, \quad (4)$$

where  $u$  denotes the longitudinal displacement of the fluid. In order to relate the longitudinal motion of the fluid to the transverse motion of the plate we can exploit the continuity equation for incompressible fluid

$$w = \frac{d_f}{2} \frac{\partial u}{\partial x}. \quad (5)$$

Combining Eqs. (3)–(5) yields the following wave equation:

$$\frac{Eh^3 d_f}{3(1-\nu^2)\rho_f} \frac{\partial^6 w}{\partial x^6} = \frac{\partial^2 w}{\partial t^2}. \quad (6)$$

For harmonic vibrations of the form  $w = Ae[i(k_x x - \omega t)]$ , we can obtain the dispersion equation by substituting  $\partial^6 w / \partial x^6 = -k_x^6 w$  and  $\partial^2 w / \partial t^2 = -\omega^2 w$  into Eq. (6), which leads to

$$\frac{Eh^3 d_f}{3(1-\nu^2)\rho_f} k_x^6 = \omega^2. \quad (7)$$

Rearranging this equation to obtain the phase velocity  $c_x = \omega/k_x$  of the squirting mode as a function of frequency leads to Eq. (2).

Figure 3 shows the phase velocity of the fluid mode plotted as a function of frequency for the case of two 5-mm-thick aluminum plates bordering a 1-mm-thick water layer. The shear and longitudinal wave velocities in aluminum were taken as  $c_T = 3100$  m/s and  $c_L = 6380$  m/s, respectively, while the density of aluminum was taken as  $\rho_s = 2800$

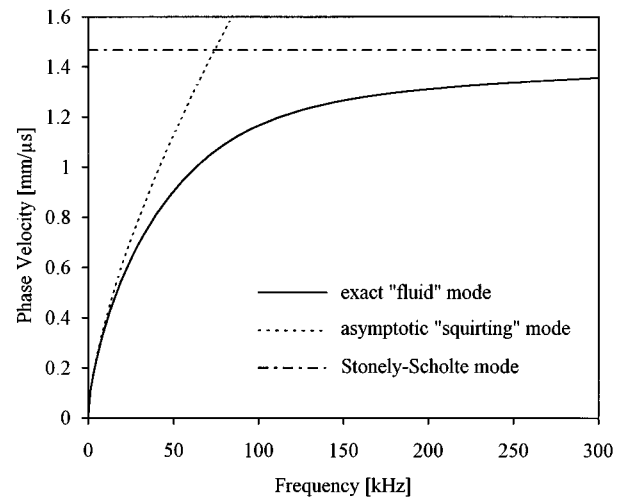


FIG. 3. Phase velocity of the fluid mode plotted as function of frequency along with its low- and high-frequency asymptotes.

kg/m<sup>3</sup>. The sound velocity in water was taken as  $c_f = 1470$  m/s, and its density as  $\rho_f = 1000$  kg/m<sup>3</sup>. The solid line represents the dispersion curve obtained by numerically solving the exact dispersion equation [Eq. (4) in Ref. 18]. The dotted line represents the low-frequency asymptote given by Eq. (2). We notice the improvement in the agreement between the exact dispersion curve of the fluid mode and the asymptotic squirting mode as the frequency gets smaller and smaller. At very high frequencies the fluid mode approaches the Stoneley–Scholte interface wave velocity which is represented by the dash-dot-dash line in Fig. 3.

True Rayleigh and Lamb waves are free vibrations of the solid. In the typical cases of high solid-to-fluid density ratio, the phase velocities of these modes are but slightly affected by fluid loading though they become attenuated by leakage into the fluid. On the other hand, the Stoneley–Scholte mode along a fluid–solid interface is essentially the vibration of the fluid side, which is but slightly perturbed by the existence of the solid. In comparison, the low-frequency squirting mode is a truly coupled vibration of the solid and fluid constituents. It is supported by the stiffness of the solid plates and the inertia of the fluid layer between them and is not just a weak perturbation of the fundamental mode of one of the constituents as is the case for leaky Rayleigh and leaky Lamb waves and the Stoneley–Scholte wave. This feature is also characteristic to the well-known lowest-order bending mode in a submerged plate.<sup>19</sup> The radiation impedance caused by fluid loading of the plate is pure real for leaky (supersonic) modes and pure imaginary for true (subsonic) ones, such as the lower branch of the flexural mode. At low frequencies, the vibrating mass of the fluid represented by this pure imaginary radiation impedance becomes much larger than the plate’s own inertia. A combination of the stiffness of the plate and the radiation inertia of the fluid results in a dispersion behavior rather similar to that of the squirting mode. At very low frequencies both modes have very small phase velocities while at high frequencies both asymptotically approach the Stoneley–Scholte velocity. However, at low frequencies the phase velocity of the

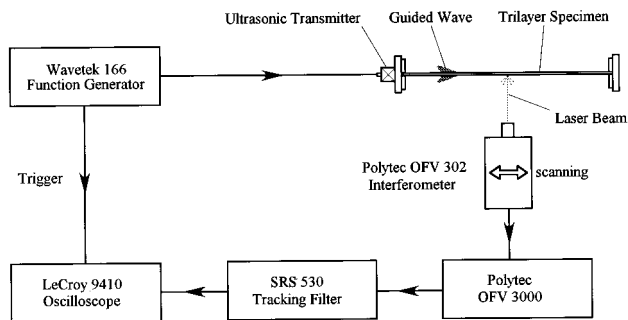


FIG. 4. Schematic diagram of the experimental setup used in measuring the phase velocity of the fluid mode.

lowest-order bending mode in a submerged plate is proportional to  $\omega^{3/5}$  vs  $\omega^{2/3}$  for the squirting mode. It is worth mentioning that Desmet *et al.* recently reported the experimental observation of the lowest-order bending mode of a thin membrane loaded by fluid on one side by using thermoelastic generation and optical detection based on laser beam deflection.<sup>20</sup>

Whenever an acoustic mode propagating in a fluid–solid structure produces large relative motion between the fluid and solid constituents the viscosity of the fluid is expected to assume a crucial role. The primary effect of viscosity is usually to cause significant, sometimes prohibitive, attenuation combined with a less significant effect on the velocity. In order to assess the attenuation of the fluid mode caused by fluid viscosity, we adapted the numerical technique recently developed to study the effects of fluid viscosity on leaky Lamb waves.<sup>21</sup> We found that the fluid mode is much more attenuated by the viscosity of the fluid than the other modes because of the very large relative motion of the fluid with respect to the solid plates. However, the most important conclusion we can draw from these calculations is that, in spite of its relative sensitivity to fluid viscosity, the attenuation of the fluid mode is quite low. For water, the predicted attenuation coefficient is approximately 2 dB/m between 15 and 150 kHz and is not expected to affect our experimental efforts to observe the fluid mode.

### III. EXPERIMENTAL TECHNIQUE AND RESULTS

As we have pointed out before, the low-frequency fluid mode in a solid–fluid–solid trilayer is unlike the well-known modes of wave propagation of fluid–solid layered structures (e.g., leaky Rayleigh, leaky Lamb, and Stoneley–Scholte modes) in the sense that it is not associated dominantly with one of the constituents of the structure while only weakly perturbed by the presence of the other. On the contrary, it is a mode that couples the fluid and the solid in an interesting way. The solid plates contribute their stiffness to this mode while the fluid layer provides the necessary inertia. Consequently, this mode can be effectively generated and detected from either the solid or the fluid component of the trilayer system. We have taken advantage of this fact in designing an experimental setup to measure the phase velocity of the fluid mode. Figure 4 shows the schematic diagram of the experimental arrangement. A damped 200-kHz ultrasonic immer-

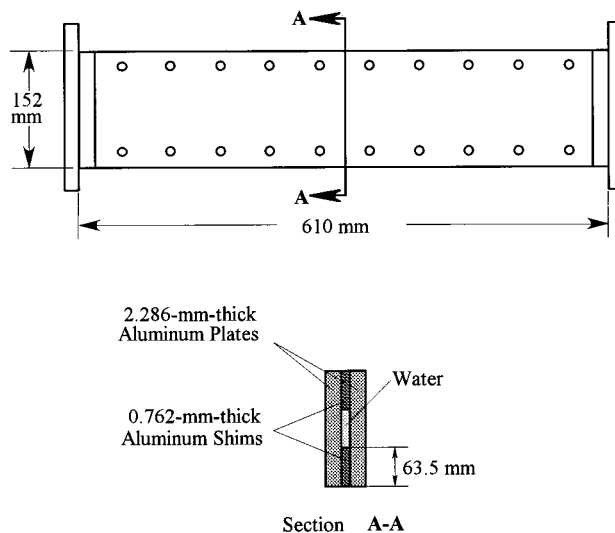


FIG. 5. Geometry and dimensions of the aluminum–water–aluminum trilayer arrangement used in the dispersion experiment.

sion transducer is used as a transmitter to shake the water filling the thin gap between the two aluminum plates. The transducer is excited by a 300- $\mu$ s-long tone-burst signal generated by a function generator that is also used to trigger an oscilloscope which displays the rf signal that can be acquired by a computer for further processing. The vibrations generated in the trilayer structure are detected from the outside using a Polytec OFV 302 Helium-Neon laser interferometer. An SRS 530 tracking filter was used to prefilter the signal acquired by the interferometer before digitizing by a LeCroy 9410 oscilloscope.

The geometry of the aluminum–water–aluminum trilayer arrangement is shown in Fig. 5. It consists of two 610 $\times$ 152 $\times$ 2.286-mm aluminum plates separated by two 610 $\times$ 63.5 $\times$ 0.762-mm aluminum shims. The plates are put together as one unit by a series of screws along the two longer edges of the specimen. The gap between the two plates that can be filled with water is only 25-mm wide and its actual thickness as measured by ultrasonic transmission at 5 MHz was 0.8175 mm on the average, approximately 7% larger than the thickness of the separator shims. The reduction in the width of the water layer was necessary to restrain sideways water motion thereby simulating the infiniteness in the theoretical model in the lateral direction. The whole arrangement was sealed using silicone rubber.

The fluid mode was generated by an immersion transducer on the fluid side and detected after different propagation distances by a laser interferometer on the outside on one of the solid plates. Transmission measurements through the whole length of the specimen were also attempted by means of a second immersion transducer mounted at the other end, but resulted in much less accurate results due to the interference between the fluid mode and faster spurious structural vibrations that coupled the two transducers. With the interferometric technique the propagation length could be continuously changed, which resulted in a better suppression of these interferences and consequently higher experimental accuracy in the frequency range of interest.

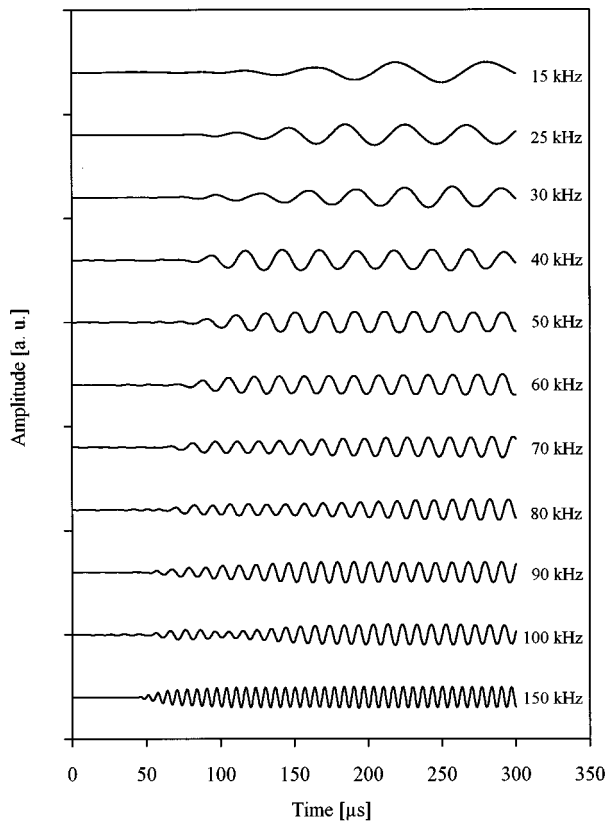


FIG. 6. Typical rf signals detected at a point 83 mm away from the ultrasonic transmitter at 11 different frequencies

Figure 6 shows examples of typical rf signals detected in the dispersion experiment at a point 83 mm away from the transmitter at 11 different frequencies. As the frequency is decreased, the rf signal becomes longer and longer in the time domain, which itself is an obvious indication of dispersion. In order to accurately measure the phase velocity of the fluid mode as a function of frequency, individual measurements were performed by detecting the normal vibration of the plate at different points on the plate above the water layer by the interferometer at specific frequencies. A peak was identified in the detected rf signal and monitored in the time domain as the detection point was moved through a larger distance (50–100 mm) in numerous small (2–5 mm) steps in order to assure that the same peak was followed. The phase velocity of the fluid mode was then determined as the ratio of the total propagation distance to the accumulated propagation time. Figure 7 shows the results of the phase velocity measurements superimposed on the theoretically calculated dispersion curve of the fluid mode. The experimental error of our measurements, which is mainly limited by the previously mentioned spurious interferences, is estimated at  $\pm 7\%$ . This uncertainty is indicated by error bars in Fig. 7. Considering the numerous technical difficulties associated with the measurement, the agreement between the experimental and theoretical results is quite good.

#### IV. CONCLUSIONS

The low-frequency fluid mode in symmetric solid–fluid–solid trilayers is a special mode of wave propagation in

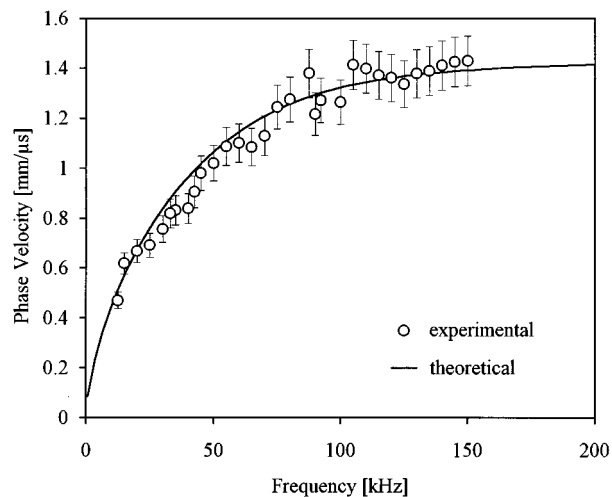


FIG. 7. Experimentally measured phase velocity of the fluid mode in the aluminum–water–aluminum trilayer.

which the two plates flex sideways in opposite phase thereby forcing the fluid in the thin gap between them to undergo large displacements in the longitudinal direction. This is a unique mode which cannot be associated with any of the free Lamb modes in a single plate. A simple physical model that provides a better insight into the physics of this mode was presented. Based on this model, we derived from first principles the low-frequency asymptote of this mode. It was shown that in this range the fluid mode can be described as a squirting motion produced by the flexing plates squeezing the fluid through the thin gap between them. Exploiting the fact that this mode could be excited and detected from both the solid and fluid constituents of the trilayer structure, a dispersion experiment was designed to measure its phase velocity as a function of frequency. An ultrasonic immersion transmitter and a laser interferometric receiver were used to study the fluid mode over a wide frequency range. The experimentally measured phase velocity values turned out to be in good agreement with those predicted by theory. To the best of our knowledge, these measurements constitute the first conclusive experimental evidence of the existence of the dispersive fluid mode originally predicted by Lloyd and Redwood in 1965.

<sup>1</sup>P. P. Lloyd and M. Redwood, "Wave propagation in a layered plate composed of two solids with perfect contact, slip, or a fluid layer at their interface," *Acustica* **16**, 169–173 (1965).

<sup>2</sup>M. Cherif, J. L. Izicki, G. Maze, and J. Riphoche, "Structure multicouche plane immergée dans l'eau. Influence des résonances sur la diffusion acoustique," *Acustica* **64**, 179–187 (1987).

<sup>3</sup>J. C. Couchman, F. H. Chang, B. G. W. Yee, and R. J. Bell, "Resonance splitting in ultrasonic spectroscopy," *IEEE Trans. Sonics Ultrason.* **SU-25**, 293–300 (1978).

<sup>4</sup>C. C. H. Guyott and P. Cawley, "The ultrasonic vibration characteristics of adhesive joints," *J. Acoust. Soc. Am.* **83**, 632–640 (1988).

<sup>5</sup>J. Laperre and W. Thys, "Mode coupling in solid/fluid/solid trilayers," *J. Acoust. Soc. Am.* **96**, 1643–1650 (1994).

<sup>6</sup>B. G. Martin, "Theory of the acoustical properties of symmetric multilayer structures," *J. Appl. Phys.* **66**, 1931–1934 (1989).

<sup>7</sup>B. G. Martin, Z. Y. Cheng, and C. C. Lee, "Theory of symmetric multilayer structures as layer replacement for Chebyshev acoustic antireflection coatings," *J. Acoust. Soc. Am.* **87**, 193–200 (1990).

- <sup>8</sup>B. G. Martin, "Acoustical properties of symmetric multilayers," *J. Acoust. Soc. Am.* **91**, 1469–1473 (1992).
- <sup>9</sup>S. Rokhlin, M. Hefets, and M. Rosen, "An elastic interface wave guided by a thin film between two solids," *J. Appl. Phys.* **51**, 3579–3582 (1980).
- <sup>10</sup>S. Rokhlin, M. Hefets, and M. Rosen, "An ultrasonic interface wave method for predicting the strength of adhesive bonds," *J. Appl. Phys.* **52**, 2847–2851 (1981).
- <sup>11</sup>C. C. H. Guyott and P. Cawley, "The measurement of through-thickness plate vibrations using a pulsed transducer," *J. Acoust. Soc. Am.* **83**, 623–631 (1988).
- <sup>12</sup>P. B. Nagy and L. Adler, "Nondestructive evaluation of adhesive joints by guided waves," *J. Appl. Phys.* **66**, 4658–4663 (1989).
- <sup>13</sup>S. E. Hannenman and V. K. Kinra, "A new technique for ultrasonic nondestructive evaluation of adhesive joints: Part I. theory," *Exp. Mech.* **32**, 323–331 (1992).
- <sup>14</sup>S. E. Hannenman, V. K. Kinra, and C. Zhu, "A new technique for ultrasonic nondestructive evaluation of adhesive joints: Part II. Experiment," *Exp. Mech.* **32**, 332–339 (1992).
- <sup>15</sup>A. Pilarski and J. L. Rose, "Lamb wave mode selection concepts for interfacial weakness analysis," *J. Nondestruct. Eval.* **11**, 237–249 (1992).
- <sup>16</sup>Our Fig. 2 is slightly different from the corresponding Fig. 4a in Ref. 1. We verified that the reason for this is that Lloyd and Redwood's figure shows the results for a solid-to-fluid density ratio of unity rather than the 2.69 value given in the figure caption.
- <sup>17</sup>H. Franklin, "Propagation des ondes d'interface dans les milieux à plusieurs couches. Application à certains modèles de fonds marins," Thèse de l'Université Pierre et Marie Curie (Paris 6), 1991.
- <sup>18</sup>F. Coulouvrat, O. Lenior, J. L. Izbicki, and M. Rousseau, "Lamb-type waves in a symmetric solid-fluid-solid trilayer," *Acustica* (to be published).
- <sup>19</sup>M. C. Junger and D. Feit, *Sound, Structures, and Their Interaction* (MIT, Cambridge, MA, 1986), p. 238.
- <sup>20</sup>C. Desmet, V. Gusev, W. Lauriks, C. Glorieux, and J. Thoen, "Lowest antisymmetric Lamb mode in a thin membrane loaded with a fluid," *J. Acoust. Soc. Am.* (to be published).
- <sup>21</sup>A. H. Nayfeh, and P. B. Nagy "Excess attenuation of leaky Lamb waves due to viscous fluid loading," *J. Acoust. Soc. Am.* **101**, 1–10 (1997).



# Nonlinear elastic constants of solids with cracks

Veniamin E. Nazarov and Alexander M. Sutin

*Institute of Applied Physics, Russian Academy of Sciences, 46 Uljanov Street, 603600, Nizhny Novgorod, Russia*

(Received 24 May 1996; revised 26 February 1997; accepted 26 February 1997)

Experimental data on a cracked medium exhibiting high acoustic nonlinearity is a commonly observed phenomenon. Here a physical model of a medium with cracks is suggested to explain the observed phenomena. The model is based on the assumption of uniform stress that is valid for a low concentration of cracks. The crack behavior is described using the model in which a crack is represented as an elastic contact of two rough surfaces, pressed one to the other under the action of internal stresses in the surrounding solid. Linear and nonlinear acoustic constants of the fractured medium are calculated. It is shown that, in this medium, negative values of the Poisson's ratio and anomalously high values of the nonlinear constants are possible. © 1997 Acoustical Society of America. [S0001-4966(97)05910-9]

PACS numbers: 43.25.Ba, 43.25.Dc [MAB]

## LIST OF SYMBOLS

$x_i$ or $x, y, z$	the Cartesian system coordinate	$C_t, C_l$	the transverse and longitudinal velocities of elastic waves
$\sigma_{xx}, \sigma_{yy}, \sigma_{zz}$	the components of stress tensor	$\rho$	the density of the medium
$E$ and $\nu$	the Young modulus and the Poisson ratio of a solid	$W(h)$	the function of peak distribution over the heights $h$
$E^*$	$= E/2(1 - \nu^2)$	$\delta$	$= h - d$ —the displacement of the peak from the middle line
$U_x, U_y, U_z$	the components of vector displacement	$f$	the force needed for the compression of the peak
$U_{xx}, U_{yy}, U_{zz}$	the components of strain tensor	$a$	the radius of the spherical top
$\sigma_{nn}$	the normal stresses	$b$	the radius of the circle stamp
$\varphi$ and $\theta$	the angles of orientation of the crack	$\psi$	the apex angle of the obtuse cone
$x'_i$ or $x', y', z'$	the new Cartesian coordinate system	$n$	the peaks' amount in the full square of the crack surface
$dU'_{z'z'}$	the additional strain along the $z'$ axis	$h_s$	$= 2^{1/2}h_0$
$\Delta V(\varphi)$	the volume variation of a single crack	$h_0$	the effective height of the roughnesses
$N(\varphi, \theta)$	the function of the crack's distribution in the angles $\varphi$ and $\theta$	$R$	the radius of the crack
$\alpha$	the linear coefficient of elasticity of the crack	$U_0(r)$	the normal displacement of crack surfaces under the normal stress
$\beta$ and $\gamma$	the nonlinear (quadratic and cubic) coefficients of elasticity of the crack	$V_0$	the volume of the crack
$dU_{xx}, dU_{yy}, dU_{zz}$	the additional strain due to the cracks in the system coordinate $x_i$	$d_0$	the distance between the middle lines of the cracks' surfaces
$U'_{xx}, U'_{yy}, U'_{zz}$	the components of the strain tensor in the rod with cracks	$\bar{\sigma}$ and $\bar{d}$	the variations of the stress compressing of the crack and the distance between middle lines of the cracks' surfaces
$E' = EG_1$ and $\nu'$	the Young modulus and the Poisson ratio of a fractured media		
$G_2$ and $G_3$	the quadratic and cubic nonlinearity parameters of a fracture media		

## INTRODUCTION

Great interest in nonlinear acoustics and geophysics has been expressed recently in the investigation of microinhomogeneous media exhibiting high acoustic nonlinearity.<sup>1-3</sup> Among media with high nonlinearity are liquids containing gas bubbles,<sup>4,5</sup> granular,<sup>6-8</sup> porous,<sup>9,10</sup> and polycrystalline media; some metals,<sup>11</sup> and piezoceramics.<sup>12</sup> Experimental observations of high nonlinearity of earth rocks<sup>13-18</sup> has stimulated the development of nonlinear seismology.

The interest in the nonlinear phenomena of such media also is due to the possibility of using nonlinear acoustic effects for nondestructive testing. The conventional methods of nondestructive testing utilize the measurement of linear acoustic parameters of the investigated media (i.e., the excitation and the reception of the waves take place with the same frequencies).<sup>19-22</sup> The influence of cracks on the propagation and scattering of linear acoustic waves has been discussed in many books and articles (see, for example, Refs. 21 and 22).

Recently, nonlinear vibro-acoustic methods have been investigated in which the excited and received frequencies are different. These methods provide new opportunities for detecting various defects in materials with high attenuation and reflection. The basic concept of the proposed methods is simple: materials containing defects have a much larger nonlinear response than materials with no defects.

Nonlinear methods of acoustic diagnostics based on measuring a scattered field at the second harmonic frequency of the radiated signal were first used to detect gas bubbles in a liquid.<sup>4,5</sup> Later, similar methods were suggested for the detection of cracks in layered materials<sup>23</sup> and for crack detection in large carbon electrodes.<sup>24</sup>

A strong increase in the nonlinear acoustic parameter of steel due to the accumulation of defects caused by static loading was observed by a method based on the modulation of sound by vibration.<sup>25</sup> It has been demonstrated that similar methods can be applied for detection of very small cracks in metals.<sup>26</sup> Nonlinear acoustic methods also can be used to determine the strength of concrete.<sup>27</sup>

Theoretical comprehension of the vast experimental material is far from complete. There are models which describe nonlinear acoustic effects in a liquid with gas bubbles,<sup>1,3,5</sup> in porous rubberlike media,<sup>13</sup> and granular media.<sup>11,28</sup> The influence of cracks on the elastic constants of rocks<sup>29-31</sup> was treated for the linear case only.

The present paper deals with the model in which the linear and nonlinear acoustic constants of the cracked medium are calculated. The elastic solid surrounding the crack is assumed to be linear and the medium nonlinearity is connected only with the crack. This assumption is valid when the nonlinear acoustic parameters of the cracked medium are much higher than the nonlinear parameter of the solid.

## I. MODEL ASSUMPTION

A thin rod to which a longitudinal stress is applied has been chosen as an object for obtaining linear and nonlinear constants of a medium with cracks. We make the following approximations.

- (1) Each crack is modeled as the contact of two rough surfaces restricted to a circle of radius  $R$ , the latter being small compared to the radius of the rod.
- (2) The spatial distribution of the cracks in the rod material is uniform and the concentration of cracks is rather small. The result is that they do not interact with one another.
- (3) A crack changes its volume only under the action of a normal stress to the crack surface. We neglect sliding motions of the crack surfaces, and assume that shear stresses do not influence cracks.
- (4) The total strain of a medium with cracks is the summation of the strain for a perfectly homogeneous medium plus the strain associated with cracks. It is assumed that the stress is uniform and its value applied to any crack is equal to that applied to the body as a whole.
- (5) The nonlinear properties of a medium with cracks are mainly determined by the nonlinearity of cracks; the solid may be considered linear and satisfying Hooke's

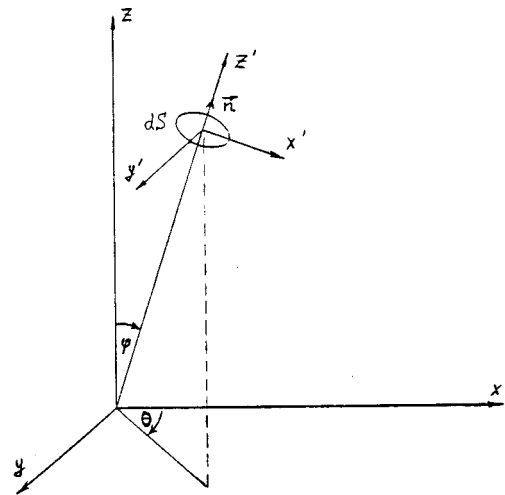


FIG. 1. The coordinate system for calculating the orientation of a single crack.

law. The nonlinear terms are assumed to be small compared to linear terms.

These assumptions are valid at low crack concentrations. They are the usual approximation for calculating the effects of cracks on elastic constants of solids.<sup>29-31</sup>

## II. OBTAINING THE EQUATIONS THAT DETERMINE ACOUSTIC PARAMETERS OF A CRACKED MEDIUM

Let the stress  $\sigma_{zz} = \sigma$  be uniform and act along the rod axis  $z$ . In a rod without cracks this stress produces a longitudinal strain:<sup>32</sup>

$$U_{zz} = \frac{\partial U_z}{\partial z} = \frac{\sigma_{zz}}{E}, \quad (1)$$

where  $E$  is the Young modulus of the solid.

In the transverse directions of the rod there occur the strains

$$U_{xx} = \frac{\partial U_x}{\partial x} = -\nu U_{zz}, \quad U_{yy} = \frac{\partial U_y}{\partial y} = -\nu U_{zz}, \quad (2)$$

while the stresses  $\sigma_{xx}$  and  $\sigma_{yy}$  are absent ( $\nu$  is the Poisson's ratio of the solid). In Eqs. (1) and (2)  $U_x$ ,  $U_y$ ,  $U_z$  are the components of the displacement vector in the Cartesian system coordinates  $x$ ,  $y$ ,  $z$  (Fig. 1).

A small thin element of area  $dS$  in a solid surrounding a single crack with the normal  $\mathbf{n}$  oriented at an angle  $\varphi$  to the  $z$  axis (Fig. 1) undergoes the normal  $\sigma_{nn}$  stresses.<sup>33</sup>

$$\sigma_{nn} = \sigma \cos^2 \varphi. \quad (3)$$

To obtain the elastic constants of a cracked medium, we introduce a new coordinate system  $(x'_i)$  and find the additional strains  $dU_{xx}$ ,  $dU_{yy}$ ,  $dU_{zz}$  produced by those cracks (the normal  $\mathbf{n}$  to their surfaces coincides with the  $z'$  axis), while the projection of this axis on the plane  $z=0$  makes an angle  $\theta$  with the  $x$  axis (the  $y'$  axis is parallel to the  $y$  axis) (Fig. 1). It is evident that in such a medium the additional

strain  $dU'_{z'z'}$ , occurs along the  $z'$  axis. A variation in crack volume  $\Delta V(\varphi)$  leads to the additional strain

$$dU'_{z'z'} = \Delta V(\varphi) N(\varphi, \theta) \sin \varphi \, d\varphi \, d\theta, \quad (4)$$

where  $N(\varphi, \theta)$  is a function of the crack distribution within the angles  $\varphi$  and  $\theta$  [ $N(\varphi, \theta) \sin \varphi \, d\varphi \, d\theta$  is the number of cracks with normals oriented from  $\varphi$  and  $\theta$  to  $\varphi + d\varphi$  and  $\theta + d\theta$  in the unit volume] and  $\Delta V(\varphi)$  is the volume variation of a single crack. All the remaining components of the tensor strain  $dU'_{i'k'}$  are equal to zero.

According to our approximation (3), we shall assume that the crack volume variation is related to the stress normal to the crack by the nonlinear dependence,  $\Delta V = F(\sigma_{nn}/E)$ . This dependence can be expanded in the Taylor series with an accuracy up to the cubic term rather small stresses ( $\sigma \ll E$ ):

$$\Delta V = \alpha(\sigma_{nn}/E) + (\beta/2)(\sigma_{nn}/E)^2 + (\gamma/6)(\sigma_{nn}/E)^3, \quad (5)$$

where  $\alpha$ ,  $\beta$ , and  $\gamma$  are the linear and nonlinear (quadratic and cubic) coefficients of elasticity of the crack. These coefficients will be obtained below for the simplest models of a crack.

According to the law of tensor transformation from the new coordinate system ( $x'_i$ ) to the old one ( $x_i$ ),<sup>34</sup> we have the tensor components  $dU_{ik}$  of the additional strain due to cracks with normals oriented from  $\varphi$  and  $\theta$  to  $\varphi + d\varphi$  and  $\theta + d\theta$ :

$$\begin{aligned} dU_{zz} &= dU'_{z'z'} \cos^2 \varphi, \\ dU_{xx} &= dU'_{z'z'} \sin^2 \varphi \cos^2 \theta, \\ dU_{yy} &= dU'_{z'z'} \sin^2 \varphi \sin^2 \theta. \end{aligned} \quad (6)$$

To find additional strains due to all cracks, we shall integrate Eqs. (4)–(6) with respect to  $\varphi$  and  $\theta$ . By adding the strain components  $U_{zz}$ ,  $U_{xx}$ , and  $U_{yy}$  [Eqs. (1) and (2)] of the rod without cracks, we obtain the components of the tensor strain of the rod with cracks:

$$\begin{aligned} U'_{zz} &= \frac{\sigma}{E} \left( 1 + \int_0^{2\pi} \int_0^{\pi/2} N(\varphi, \theta) \sin \varphi \right. \\ &\quad \left. \times \cos^4 \varphi \left[ \alpha + \frac{\beta\sigma}{2E} \cos^2 \varphi + \frac{\gamma\sigma^2}{6E^2} \cos^4 \varphi \right] d\varphi \, d\theta \right). \end{aligned} \quad (7a)$$

$$\begin{aligned} U'_{zz} &= \frac{\sigma}{E} \left( -\nu + \int_0^{2\pi} \int_0^{\pi/2} N(\varphi, \theta) \sin^3 \varphi \right. \\ &\quad \times \cos^2 \varphi \cos^2 \theta \left[ \alpha + \frac{\beta\sigma}{2E} \cos^2 \varphi \right. \\ &\quad \left. \left. + \frac{\gamma\sigma^2}{6E^2} \cos^4 \varphi \right] d\varphi \, d\theta \right), \end{aligned} \quad (7b)$$

$$\begin{aligned} U'_{yy} &= \frac{\sigma}{E} \left( -\nu + \int_0^{2\pi} \int_0^{\pi/2} N(\varphi, \theta) \sin \varphi \cos^4 \varphi \right. \\ &\quad \left. \times \sin^2 \theta \left[ \alpha + \frac{\beta\sigma}{2E} \cos^2 \varphi + \frac{\gamma\sigma^2}{6E^2} \cos^4 \varphi \right] d\varphi \, d\theta \right). \end{aligned} \quad (7c)$$

Using these equations in the linear approximation ( $\beta = \gamma = 0$ ), one can easily find the Poisson's ratio  $\nu'$  of a medium with isotropically oriented cracks [ $N(\varphi, \theta) = N_0/2\pi$ ]:

$$\nu' = \frac{\nu - \alpha N_0/15}{1 + \alpha N_0/5}. \quad (8)$$

It is seen that the presence of cracks in a solid reduces the Poisson ratio and, at  $\alpha N_0 > 15\nu$ , the ratio becomes negative. The variation range of the Poisson ratio in such media is determined by the inequality

$$-\frac{1}{3} \leq \nu' \leq \nu \leq \frac{1}{2}. \quad (9)$$

It is known that the Poisson ratio of a solid is related to the longitudinal ( $C_l$ ) and transverse ( $C_t$ ) velocities of elastic waves as follows:<sup>32</sup>

$$\nu = \frac{1 - 2(C_t/C_l)^2}{2[1 - (C_t/C_l)^2]}. \quad (10)$$

In some measurements of porous rocks an anomalously large ratio of the velocities  $C_t$  and  $C_l$  ( $C_t/C_l > 2^{-1/2}$ ) was observed. This corresponded to a negative Poisson's ratio.<sup>35</sup>

The equation describing the longitudinal wave propagation in the rod can be found from the Newton equation<sup>32</sup>

$$\rho U_z = \partial \sigma(\varepsilon) / \partial z, \quad \varepsilon = U'_{zz}, \quad (11)$$

where  $\rho$  is the density of the medium.

From Eq. (7a) we can calculate the dependence  $\sigma = \sigma(\varepsilon)$  for the rod (on  $\sigma/E \ll 14/\beta N_0 G_1$ ,  $\sigma/E \ll 27\beta/7\gamma$ ):

$$\sigma(\varepsilon) = EG_1 [\varepsilon - (G_2/2)\varepsilon^2 - (G_3/6)\varepsilon^3], \quad (12)$$

where

$$\begin{aligned} G_1 &= (1 + g_1)^{-1} \leq 1, \quad G_2 = 2g_2/(1 + g_1)^2, \\ G_3 &= 6g_3[1 - 2g_2^2/g_3(1 + g_1)]/(1 + g_1)^3, \end{aligned} \quad (13)$$

$$\begin{aligned} g_1 &= \alpha \int_0^{2\pi} \int_0^{\pi/2} N(\varphi, \theta) \sin \varphi \cos^4 \varphi \, d\varphi \, d\theta, \\ g_2 &= (\beta/2) \int_0^{2\pi} \int_0^{\pi/2} N(\varphi, \theta) \sin \varphi \cos^6 \varphi \, d\varphi \, d\theta, \end{aligned} \quad (14)$$

$$g_3 = (\gamma/6) \int_0^{2\pi} \int_0^{\pi/2} N(\varphi, \theta) \sin \varphi \cos^8 \varphi \, d\varphi \, d\theta.$$

For isotropically oriented cracks Eqs. (13) and (14) become

$$\begin{aligned} G_1 &= (1 + \alpha N_0/5)^{-1}, \quad G_2 = \beta N_0 G_1^2/7, \\ G_3 &= \gamma N_0 G_1^3 [1 - 27G_1 \beta^2 N_0/49\gamma]/9. \end{aligned} \quad (15)$$

It follows from expressions (8) and (13)–(15) that at rather low crack concentration ( $\alpha N_0 \ll 1$ ), the variation of

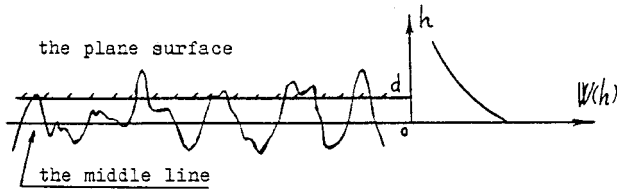


FIG. 2. The crack model. The elastic contact between rough and plane surfaces.

the Poisson ratio and the Young modulus due to the presence of cracks is slight, while the variation of the nonlinear parameters may be rather strong.

### III. CRACK MODEL AND OBTAINING CRACK PARAMETERS

It is possible to calculate the linear and nonlinear acoustic parameters of a cracked medium if one knows the parameters  $\alpha$ ,  $\beta$ , and  $\gamma$  for a single crack and the crack concentration. We can describe a crack as an elastic contact of initially rough surfaces, pressed together by the internal stress from the surrounding material. Such a roughness is the inherent property of real crack surfaces in various solids (rocks, metals, etc.).<sup>36,37</sup>

According to the approximation given in Eq. (1), the contact area has the shape of a circle with radius  $R$ . First, we consider the stress due to deformation of the top of the rough surface. When two elastic surfaces contact without friction, contact stresses depend only on the relative profile of the surfaces. Therefore, when determining the elastic properties, the contact in the crack may be replaced by the contact of a plane rigid surface with an elastic solid having the initial profile of the undeformed surfaces. We can briefly repeat the analysis performed in Ref. 38. The rough surface is characterized by the distribution function  $W(h)$  of the top heights  $h$  counted from the so-called middle line (Fig. 2), so that  $W(h)dh$  is the number of tops having a height from  $h$  to  $h + dh$  per unit of crack surface area.

Let us consider the contact in which the distance from the middle line to the rigid surface becomes equal to value  $d$  under the action of the stress  $\sigma_1$  applied to crack surfaces. In this case the irregularities with the top heights initially exceeding  $d$  become planar. The force  $f$  required for the compression of each irregularity depends on the displacement  $\delta = h - d$  of each top and on the type of the irregularity. For the irregularities of the crack surfaces, we assume that the top of each irregularity has the following possible shapes:

- (i) part of a sphere with radius  $a$ ,
- (ii) obtuse cone with the apex angle  $2\psi \approx \pi$ ,
- (iii) a circle cylinder with radius  $b$ .

The force  $f$  needed for the compression of one top is determined by the following expressions:<sup>38</sup>

- (i) for the part of sphere:  $f = (4/3)E^*(a/2)^{1/2}\delta^{3/2}$ ,
- (ii) for the cone:  $f = \pi E^* \delta^2 \tan \psi$ ,
- (iii) for the circle cylinder:  $f = 4E^* b \delta$ ,

where  $E^* = E/2(1 - \nu^2)$ .

To find the dependence of the total stress  $\sigma_1$  due to irregularities on the displacement  $d$ , one should sum up the forces for all the irregularities of the height  $h \geq d$ :

$$\sigma_1(d) = - \int_d^\infty f(h-d)W(h) dh. \quad (17)$$

This integral can be calculated analytically for only some special functions of top height distribution. In particular, for the exponential distribution of top heights, which is described by the formula

$$W(h) = n(\pi R^2 h_s)^{-1} \exp(-h/h_s), \quad (18)$$

where  $n$  is the number of tops in the full square of the crack surface,  $h_s = 2^{1/2}h_0$  and  $h_0$  is the characteristic height of the rough surface irregularities.

In this case integral (17) has a simple form

$$\sigma_1(d) = -nE_1 \exp(-d/h_s), \quad (19)$$

where

- (i) for the spherical tops  $E_1 = (2\pi)^{-1/2}h_s^{3/2}a^{1/2}R^{-2}E^*$ ,
- (ii) for the conical tops  $E_1 = 2h_s^2R^{-2}E^* \tan \psi$ ,
- (iii) for the circle tops  $E_1 = 4\pi^{-1}h_s b R^{-2}E^*$ .

Equation (19) determines the stress due to the compression of the irregularities. This stress tries to open the crack; however, because the crack is in an equilibrium state, this stress  $\sigma_1$  is compensated by an opposite stress  $\sigma_0$ , due to internal stress in the surrounding solid. We cannot correctly determine this stress; however, it is possible to estimate it.

Assuming that the stress  $\sigma_0$ , which tries to close the rough surface crack, is equal in magnitude but opposite in sign to such external stresses applied normal to the crack on plane surfaces, assuming their volumes are equal. As shown in Ref. 39, the normal displacement,  $U_0(r)$ , of surfaces of an initially plane crack is described by the expression

$$U_0(r) = 4(1 - \nu^2)[R^2 - r^2]^{1/2}\sigma_0/\pi E, \quad (20)$$

and the volume  $V_0$  of this crack is determined by

$$V_0 = 16(1 - \nu^2)R^3\sigma_0/3E, \quad (21)$$

where  $r$  is a radial coordinate in the plane of the crack. Therefore the external stress  $\sigma_0$  applied to the crack with plane surfaces is connected with its volume by the relationship

$$\sigma_0 = 3EV_0/16(1 - \nu^2)R^3. \quad (22)$$

We also assume that the same formula determines the stress due to internal stress into the solid for cracks with rough surfaces and that the volume  $V_0$  is equal to the volume  $V_1 = \pi R^2 d_0$  of the considered real crack, where  $d_0$  is the distance between middle lines of the crack surfaces. Therefore, from Eq. (22) it follows that

$$\sigma_0(d_0) = 3\pi E d_0/16R(1 - \nu^2). \quad (23)$$

In the equilibrium state of the crack, this compressive stress  $\sigma_0(d_0)$  is compensated by the elastic force  $\sigma_1(d_0)$  of the rough surface contacts, determined by Eq. (22), i.e.,

$$3\pi E d_0 / 16R(1 - \nu^2) = n E_1 \exp(-d_0/h_s). \quad (24)$$

Equations (23) and (24) determine a compressing stress  $\sigma_0$  and static distance  $d_0$  between middle lines of the surfaces within the frames of the considered crack model.

Now let us consider the variation of the crack volume under the action of an acoustic wave passing through the crack. If there is additional acoustic small stress  $\tilde{\sigma}$  ( $|\tilde{\sigma}| \ll \sigma_0$ ) leading to the crack surface distance variation  $\tilde{d}$  ( $|\tilde{d}| \ll d_0$ ), then the equilibrium state equation has the form

$$\tilde{\sigma} = \sigma_0(d_0 + \tilde{d}) - \sigma_1(d_0 + \tilde{d}). \quad (25)$$

Substituting Eqs. (19), (23), and (24) into Eq. (25), we obtain a second set of expressions for the variation of distance  $\tilde{d}$  between the crack surfaces and the crack volume  $\Delta V$ :

$$\tilde{\sigma}/\sigma_0 = (1 + h_s/d_0)(\tilde{d}/h_s) - (\tilde{d}/h_s)^2/2 + (\tilde{d}/h_s)^3/6, \quad (26)$$

or, on  $\tilde{d}/h_s \ll 2(1 + h_s/d_0)$ ,

$$\Delta V = \pi R^2 \tilde{d} = \pi R^2 h_s [g_1(\tilde{\sigma}/\sigma_0) + g_2(\sigma/\sigma_0)^2 + g_3(\sigma/\sigma_0)^3], \quad (27)$$

where  $g_1 = (1 + h_s/d_0)^{-1}$ ,  $g_2 = g_1^3/2$ ,  $g_3 = (2 - h_s/d_0)g_1^4/6$ . By comparing Eq. (5) and Eq. (27) we have the expressions for the linear and nonlinear elastic constants  $\alpha$ ,  $\beta$ , and  $\gamma$  of cracks:

$$\alpha = \pi h_s R^2 (E/\sigma_0)(1 + h_s/d_0)^{-1} > 0, \quad (28)$$

$$\beta = \pi h_s R^2 (E/\sigma_0)^2 (1 + h_s/d_0)^{-3} > 0, \quad (29)$$

$$\gamma = \pi h_s R^2 (E/\sigma_0)^3 (2 - h_s/d_0)(1 + h_s/d_0)^{-4}. \quad (30)$$

Knowledge of elastic constants  $\alpha$ ,  $\beta$ , and  $\gamma$  for a single crack allows us to determine the Poisson ratio, the Young modulus, and the parameters of the quadratic and the cubic nonlinearities of the cracked medium according Eqs. (8) and (12)–(15).

From Eqs. (29) and (30) follows that, unlike  $\beta$ , which must satisfy  $\beta > 0$ , the sign of the coefficient  $\gamma$  may be either positive or negative depending on the parameters of the crack  $h_s$  and  $d_0$ . Therefore, unlike the parameter of quadratic nonlinearity  $G_2$  that is always positive, the sign of the cubic nonlinear parameter  $G_3$  may be either positive or negative.

#### IV. SOME ESTIMATIONS

We estimate the elastic characteristics of the medium having isotropically distributed cracks with the following parameters: the irregularities of the crack surfaces have the shape of cones with an apex angle  $2\psi = 176^\circ$ , the radius of which is restricted to  $R = 10^{-1}$  cm; the characteristic height of the tops is  $h_s = 10^{-6}$  cm;  $n = 10^5$ ; the Young modulus is  $E = 3 \times 10^{11}$  g/cm s<sup>2</sup>; and the Poissons ratio is  $\nu = 0.25$  [according to Eqs. (23) and (24) this corresponds to the static stress  $\sigma_0 = 5 \times 10^6$  g/cm s<sup>2</sup> and  $d_0 = 3 \times 10^{-6}$  cm]. In this case, and at a crack concentration  $N_0 = 30$  cm<sup>-3</sup>, the presence of cracks reduces the Young modulus and Poissons ratio of the medium by about 1%, while the quadratic and the

cubic nonlinearity parameters achieve the values of  $G_2 \approx 200$  and  $G_3 \approx 10^8$ ; i.e., the presence of cracks causes the nonlinear parameter to increase by several orders of magnitude higher than the typical nonlinearity parameters of homogeneous solids.<sup>40</sup>

#### V. CONCLUSION

The suggested model of the medium with a crack and the investigation of its elastic characteristics show that the presence of cracks may result in strong variation of the quadratic and the cubic nonlinearity parameters, while the Young modulus and the Poisson ratio are altered only slightly. This circumstance is the main factor stimulating the development of nonlinear methods of detecting cracks and other similar defects in the structure of solids. The nonlinear methods may have much higher sensitivity to the presence of cracks than the conventional linear methods.

#### ACKNOWLEDGMENT

The research was made possible by a grant from the Russian Fund of Fundamental Investigations (Grant No. 96-05-64459).

- <sup>1</sup>K. A. Naugol'nykh and L. A. Ostrovsky, *Nonlinear Wave Processes in Acoustics* (Nauka, Moscow, 1990) (to be published by Cambridge U.P., 1996).
- <sup>2</sup>L. A. Ostrovsky, "Wave processes in media with strong acoustic nonlinearity," *J. Acoust. Soc. Am.* **90**, 3332–3338 (1991).
- <sup>3</sup>V. E. Nazarov, L. A. Ostrovsky, I. A. Soustova, and A. M. Sutin, "Nonlinear acoustics of microinhomogeneous media," *Phys. Earth Planet. Inter.* **50**, 65–73 (1988).
- <sup>4</sup>F. H. Fenlon, in *On the Amplification of Modulated Acoustic Waves in Gas-Liquid Mixtures, Cavitation and Inhomogeneities in Underwater Acoustics*, edited by W. Lauterborn (Springer-Verlag, Heidelberg, 1980), pp. 141–150.
- <sup>5</sup>A. M. Sutin, "Nonlinear acoustic phenomena in sub surface bubble layers and its usage for bubble measurements," in *Breaking Waves: IUTAM Symposium*, Sydney, Australia, 1991, edited by M. L. Banner and R. H. J. Crimshaw (Springer-Verlag, Berlin, 1992), pp. 223–228.
- <sup>6</sup>I. Yu. Belyaeva, L. A. Ostrovsky, and E. M. Timanin, "Experiments on harmonic generation in grainy media," *Acoust. Lett.* **15**, 221–224 (1992).
- <sup>7</sup>I. Yu. Belyaeva, V. Yu. Zaitsev, and L. A. Ostrovsky, "Nonlinear acousto-elastic properties of grainy media," *Sov. Phys. Acoust.* **39**, 25–32 (1993).
- <sup>8</sup>H. A. Deresiewicz, "Review of some recent studies of the mechanical behavior of granular media," *Appl. Mech. Rev.* **11**, 259–261 (1958).
- <sup>9</sup>L. A. Ostrovsky, "Nonlinear acoustics of slightly compressible porous media," *Sov. Phys. Acoust.* **34**, 908–913 (1988).
- <sup>10</sup>I. Yu. Belyaeva and E. M. Timanin, "Experimental investigation of nonlinear properties of porous elastic media," *Sov. Phys. Acoust.* **37**, 1026–1028 (1991).
- <sup>11</sup>V. E. Nazarov, "Influence of the structure of copper on its acoustics nonlinearity," *Fiz. Met. Metalloved.* **3**, 172–178 (1991) (in Russian).
- <sup>12</sup>J. K. Na and M. A. Breazeale, "Ultrasonic nonlinear properties of lead zirconate-titanate ceramics," *J. Acoust. Soc. Am.* **95**, 3213–3221 (1994).
- <sup>13</sup>T. De Fazio, K. Aki, and J. Alba, "Solid Earth tide and observed change in the 'in situ' seismic velocity," *J. Geophys. Res.* **78**, 1319–1322 (1973).
- <sup>14</sup>*Problems of Nonlinear Seismics*, edited by A. V. Nikolaev and I. M. N. Galkin (Nauka, Moscow, 1987) (in Russian).
- <sup>15</sup>V. E. Zimenkov and V. E. Nazarov, "Nonlinear acoustics effects in rock samples," *Fiz. Zemli.* **1**, 13–18 (1993) (in Russian).
- <sup>16</sup>P. A. Johnson and K. R. McCall, "Observation and implications of nonlinear elastic wave response in rock," *Geophys. Res. Lett.* **21**, 165–168 (1994).
- <sup>17</sup>G. D. Meegan, Jr., P. A. Johnson, K. R. McCall, and R. Guyer, "Observations of nonlinear elastic wave behavior in sandstone," *J. Acoust. Soc. Am.* **94**, 3387–3391 (1993).
- <sup>18</sup>P. A. Johnson and T. J. Shankland, "Nonlinear generation of elastic

- waves in crystalline rock and sandstone: continuous wave travel time observations," *J. Geophys. Res.* **94**, 17 729–17 734 (1989).
- <sup>19</sup>R. E. Green, *Ultrasonic Investigation of Mechanical Properties* (Academic, New York, 1973).
- <sup>20</sup>J. Krautkramer and H. Krautkramer, *Ultrasonic Testing of Materials* (Springer-Verlag, Berlin, 1977).
- <sup>21</sup>J. D. Achenbach, W. Lin, and L. M. Keer, "Mathematical modelling of ultrasonic wave scattering by sub-surface cracks," *Ultrasonics* **24**(4), 207–215 (1986).
- <sup>22</sup>Y. C. Angel and J. D. Achenbach, "Reflection and transmission of elastic waves by a periodic array of cracks: oblique incidence," *Wave Motion* **7**(4), 375–397 (1985).
- <sup>23</sup>V. A. Antonets, D. M. Donskoy, and A. M. Sutin, "Nonlinear vibro-diagnostics of splitting and unglueing in multilayered constructions," *Mech. Composit. Mater.* **5**, 934–937 (1986) (in Russian).
- <sup>24</sup>A. Sutin, C. Delclos, and M. Lenclud, "Investigations of the second harmonic generation due to cracks in large carbon electrodes," in *Proceeding of the 2nd International Symposium on Acoustical and Vibratory Surveillance Methods and Diagnostic Techniques*, Senlis, France, 10–12 October 1995, pp. 725–735.
- <sup>25</sup>A. Korotkov, M. Slavinsky, and A. Sutin, "Nonlinear vibro-acoustic methods for diagnostics of metal strength properties," in *Advances in Nonlinear Acoustics*, edited by H. Hobæk (World Scientific, Singapore, 1993), pp. 370–375.
- <sup>26</sup>A. S. Korotkov and A. M. Sutin, "Modulation of ultrasound by vibrations in metal constructions with cracks," *Acoust. Lett.* **18**(4), 59–62 (1994).
- <sup>27</sup>I. Schkolnik, "Nondestructive testing of concretes: New aspects," *Nondestr. Test. Eval.* **10**, 351–358 (1993).
- <sup>28</sup>I. Yu. Belyeva, L. A. Ostrovsky, V. Yu. Zaitsev, V. Stefan, and A. M. Sutin, "Comparison of linear and nonlinear elastic moduli for reservoir rock by use of a granular medium model," *J. Acoust. Soc. Am.* **99**, 1360–1365 (1996).
- <sup>29</sup>J. B. Walsh, "The effect of cracks in the compressibility of rock," *J. Geophys. Res.* **70**, 381–389 (1965).
- <sup>30</sup>J. B. Walsh, "The effect of cracks in rocks on Poisson's ratio," *J. Geophys. Res.* **70**, 5249–5257 (1965).
- <sup>31</sup>R. L. Salganik, "Mechanics of media with high amount of cracks," *Izv. Akad. Nauk SSSR. Ser. Mekh. Tverd. Tela* **3**, 149–158 (1973) (in Russian).
- <sup>32</sup>L. D. Landau and E. M. Lifshitz, *Theoria of Elasticity* (Pergamon, New York, 1986).
- <sup>33</sup>S. P. Timoshenko and J. N. Goodier, *Theory of Elasticity* (McGraw-Hill, New York, 1970).
- <sup>34</sup>G. Arfken, *Mathematical Methods for Physicists* (Academic, New York, 1968).
- <sup>35</sup>A. R. Gregory, "Fluid saturation effect on dynamic elastic properties of sedimentary rocks," *Geophysics* **41**, 895–921 (1976).
- <sup>36</sup>B. B. Mandelbrot, D. E. Passoja, and A. J. Paulay, "Fractal character of fracture surfaces of metals," *Nature (London)* **308**, 721–722 (1984).
- <sup>37</sup>B. B. Mandelbrot, *The Fractal Geometry of Nature* (Freeman, San Francisco, 1982).
- <sup>38</sup>K. L. Johnson, *Contact Mechanics* (Cambridge U.P., Cambridge, 1985).
- <sup>39</sup>I. Sneddon, *Fourier Series* (Routledge & Kegan, New York, 1951).
- <sup>40</sup>L. K. Zarembo and V. A. Krasilnikov, *Introduction to Nonlinear Acoustics* (Nauka, Moscow, 1966).

# Temperature discontinuities between elements of thermoacoustic devices

James R. Brewster, Richard Raspet, and Henry E. Bass

*Department of Physics and Astronomy and the National Center for Physical Acoustics,  
University of Mississippi, University, Mississippi 38677*

(Received 9 August 1997; accepted for publication 14 August 1997)

Significant differences in temperatures have been observed between adjoining elements of thermoacoustic prime movers [G. W. Swift, *J. Acoust. Soc. Am.* **92**, 1551–1563 (1992)]. A simple description of the interelement heat transfer process based on the existence of this temperature difference is given. The central assumption of this approach is that the heat transfer process is sufficiently rapid that it is completed in less than the dwell time that the fluid spends in either element. Experimental measurements of the heat transfer coefficient between elements is shown to yield results close to the prediction of this complete heat exchange theory. Predictions are also compared to those based on the heat transfer description put forward by Swift [*J. Acoust. Soc. Am.* **92**, 1551–1563 (1992)]. © 1997 Acoustical Society of America. [S0001-4966(97)02812-9]

PACS numbers: 43.25.Nm, 43.35.Ud [MAB]

## INTRODUCTION

Current thermoacoustic devices typically consist of three elements placed in a resonance tube; a stack and two heat exchangers. These elements are usually arrays of ducts aligned in the direction of acoustic oscillation. The stack supports a longitudinal temperature gradient and is the element in which the desired interchange between thermal and acoustic energies takes place. It is sandwiched between heat exchangers which either supply or remove heat from the stack.

For thermoacoustic engines and refrigerators to operate heat must flow between their component elements. It has been noted<sup>1</sup> that for this heat transfer to be driven by the acoustic wave there must be a discontinuity in temperature between the elements. We will show that this step in temperature between elements is required even in the limit of perfect thermal contact between fluid and solid.

The linear theory for thermoacoustic systems is well established.<sup>2–4</sup> In these papers the energy flow within each element is considered but not the mechanism for heat flow between them. We assert that the transfer of heat between thermoacoustic elements depends on the displacement of the working fluid being finite and therefore is beyond the scope of previous, linear treatments. Consider a prime mover. The temperature gradient imposed on the stack is sufficiently large that the acoustic wave pumps heat from hot to cold while coupling some of this energy into the acoustic wave. In the adjoining heat exchangers there is no temperature gradient; the acoustic wave pumps heat in the opposite direction. Linear theory predicts a discontinuity in the heat flux at the boundary between these elements. As illustrated in Fig. 1, if there is no thermoacoustically driven wave, the heat flux required to maintain the temperature gradient in the stack is sufficiently small to be maintained by longitudinal conduction. The temperature distribution is continuous. After the onset of oscillations, heat is pumped down the stack at an enhanced rate. This will cause the hot end of the stack to cool down and the cold end to heat up until the heat transfer

process at the element interfaces balances this heat flow.

The magnitude of the required interelement temperature difference is quantified via a heat transfer coefficient,  $h$ , the ratio between the rate of heat flow and the size of the temperature step. In the following, the complete heat exchange description is used to derive an expression for  $h$  in terms of the acoustic velocity. Then the experimental measurement of  $h$  is described and the results compared to theory.

## I. THEORY: THE COMPLETE HEAT EXCHANGE LIMIT

In order to gain an understanding of the physics of the interelement heat transfer we treat an idealized case. Consider a stack adjoining a heat exchanger in which the thermal contact between the solid and gas is ideal. Any gas that enters the heat exchanger is assumed to leave at a temperature equal to that of its walls no matter how short the time spent there. This “complete” heat exchange is expected to be realized in the limit of narrow plate spacing.

We assume that the stack is sufficiently insulating that the thermoacoustic contribution to the heat flow down the stack is much larger than that due to longitudinal conduction. For an ideal gas, the hydrodynamic component of the longitudinal enthalpy flow is given by<sup>3</sup>

$$\dot{H}_2 = A \cdot c_p \rho_0 \overline{\langle T(t, \mathbf{r}) \cdot u(t, \mathbf{r}) \rangle}, \quad (1)$$

where  $A$  is the cross-sectional area open to the working fluid,  $c_p$  the heat capacity at constant pressure,  $\rho_0$  the average density,  $T$  the temperature, and  $u$  the longitudinal component of the velocity. The two-dimensional vector  $\mathbf{r}$  is the transverse coordinate. The overbar denotes temporal averaging and  $\langle \rangle$  indicates a spatial average over the cross section. If the stack is thermally isolated and nonconducting, a steady state can only exist if  $\dot{H}_2$  is a constant along its length. Energy must also cross the boundaries between the stack and its heat exchangers at this same rate.

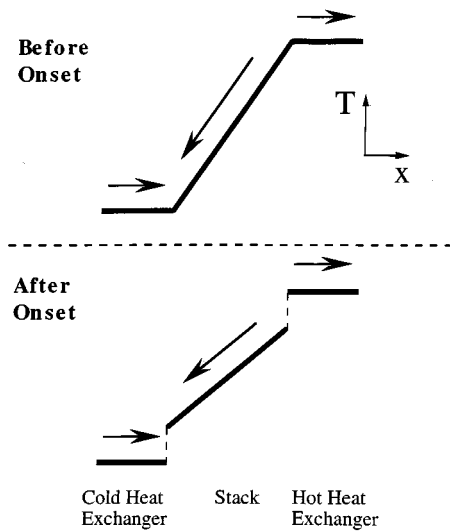


FIG. 1. A schematic diagram illustrating the temperature distribution in a thermoacoustic engine before and after the onset of oscillations. Prior to onset very little heat flows between the elements and the temperature can be assumed to be continuous. After onset a large quantity of heat must flow between the elements. This can only be achieved if there is a discontinuity in their temperatures.

We assume that the velocity fluctuates sinusoidally and that  $\langle u(t, \mathbf{r}) \rangle$  is a continuous function of the longitudinal position. Let the phase be defined such that

$$\langle u(t, \mathbf{r}) \rangle = |u_1| \cdot \sin(\omega t). \quad (2)$$

During the first half of the cycle, gas is leaving the stack and entering the heat exchanger. The exact form of temperature and velocity fluctuation during this phase of the cycle depends on the nature of the interaction between the stack and the fluid. We make the simplifying assumption that the temperature oscillation of the gas leaving the stack is equal to that which would occur in the absence of the heat exchanger. Fluid entering the heat exchanger carries with it no “memory” of its previous visit there. This assumption is a logical partner to that of an ideal heat exchanger in that it is also expected to yield an exact solution in the limit of narrow pore spacings.

In the second phase of the cycle, gas is flowing from the heat exchanger to the stack. The assumption of an ideal heat exchanger implies that the temperature of this gas is fixed at  $T_H$ , the wall temperature of the heat exchanger. The temperature at the interface between the elements thus is given by

$$T(t, \mathbf{r}) = T_0^S + \text{Re}\{T_1^S(\mathbf{r})e^{-i\omega t}\} \quad \text{for } 0 < t < \pi/\omega, \quad (3)$$

$$T(t, \mathbf{r}) = T_H \quad \text{for } \pi/\omega < t < 2\pi/\omega, \quad (4)$$

where  $T_0^S$  is the temperature of the end of the stack wall, and  $T_1^S$  is the oscillating part of the temperature of the fluid within the stack expressed as a complex number. Substituting into Eq. (1),

$$\begin{aligned} \dot{H}_2 = & A \cdot c_p \rho_0 \cdot \frac{\omega}{2\pi} \left[ T_0^S \cdot |u_1| \int_0^{\pi/\omega} \sin(\omega t) dt \right. \\ & + \int_0^{\pi/\omega} \langle T_1^S(\mathbf{r}) \cdot u(\mathbf{r}) \rangle \cdot dt + T_H \\ & \left. \cdot |u_1| \int_{\pi/\omega}^{2\pi/\omega} \sin(\omega t) dt \right]. \quad (5) \end{aligned}$$

The product of two quantities oscillating at frequency  $\omega$  is a periodic function oscillating with a frequency of  $2\omega$ . Therefore

$$\begin{aligned} \frac{\omega}{2\pi} \int_0^{\pi/\omega} \langle T_1^S(\mathbf{r}) \cdot u(\mathbf{r}) \rangle dt = & \frac{1}{2} \cdot \frac{\omega}{2\pi} \int_0^{2\pi/\omega} \langle T_1^S(\mathbf{r}) \cdot u(\mathbf{r}) \rangle dt \\ = & \frac{1}{2} \dot{H}_2, \quad (6) \end{aligned}$$

and Eq. (5) becomes

$$\frac{1}{2} \dot{H}_2 = \frac{1}{\pi} \cdot A \cdot c_p \rho_0 \cdot |u_1| \cdot (T_H - T_0^S). \quad (7)$$

In our experiment an acoustic standing wave is being used to pump heat and the enthalpy flow,  $\dot{H}_2$ , can be assumed equal to the heat flow,  $\dot{Q}_2$ . That is, in a standing wave, the contribution of the work flow to the enthalpy flow is small relative to that of the heat flow. This is not true of thermoacoustic devices in general. The heat transfer coefficient,  $h_c$ , is the rate of heat transfer per unit temperature difference,

$$h_c = \frac{\dot{Q}_2}{T_H - T_0^S} = \frac{2}{\pi} \cdot A \cdot c_p \rho_0 \cdot |u_1|. \quad (8)$$

Note that  $h_c$  is predicted to be linearly dependent on the amplitude of oscillation.

## II. EXPERIMENT: AN EXTERNALLY DRIVEN PRIME MOVER

A controlled experiment was designed to measure the heat transfer coefficient between the stack and heat exchanger inside a longitudinal resonator. Although configured as an engine, the temperature gradient imposed on the stack was below that required for onset of self-sustaining oscillations. Instead, a standing wave was generated by an oscillating piston that forms one end of the tube. The heat flow was determined by measurement of the rate at which electrical power must be supplied to the hot end in order to maintain it at a constant temperature.

The resonator was 3.8 m in overall length and consisted of two sections of aluminum pipe with an inner diameter of 5 cm and a wall thickness of 13 mm. A commercial shaker unit (model VS 100-6, Vibration Test Systems, Aurora, Ohio) drives a piston that reciprocates inside an aluminum sleeve that forms one end of the resonator. The other end of the tube is rigidly sealed. Piston rings made from Rulon, a low-friction polymeric material, ensure that the motion of the driver is smooth and that the seal is gas tight. The tube was always operated in a vertical position with the driver at the bottom. The shaker was powered by the output of a power amplifier that receives a sine-wave input from a signal gen-



erator. The amplitude of the pressure fluctuation was measured using an Endevco pressure transducer rated to be linear for peak signals of up to 1 atm. The transducer was mounted flush with the end of the top end-plate of the tube. The tube was filled with either air, argon, or carbon oxide. All experiments were performed at ambient pressure.

A ceramic lattice of parallel square ducts, manufactured for use as an automotive catalyst support material, was employed as the stack. A section of this stack was cut to a length of 5 cm after being machined so as to fit tightly into the cylindrical resonator. The ducts run parallel to the length of the cylinder. The sides of each opening were 0.79 mm in length and the open fraction of the cross section was 73%.

The heat exchangers were copper parallel plates mounted onto a copper block.<sup>5</sup> The plates extend across a circular hole in the block of equal diameter to that of the rest of the tube. The plates were 10 mm long, 0.5 mm thick, and spaced by 1.00 mm which results in a porosity of 67%. The assembly of stack and heat exchangers was located 1/4 of the length of the tube away from the driver with the hot end below the cold end.

The hot heat exchanger was heated by applying electrical power to two resistive heaters embedded in the copper block. Both the voltage across and the current flowing through the heater were measured and therefore the electrical energy supplied to the heat exchanger was known. A recirculating chiller unit was used to pump water, maintained at a constant temperature of 20 °C, through the other heat exchanger. Thermocouples were placed at four locations; in both heat exchangers and at each end of the stack. The heat exchanger thermocouples were imbedded into the supporting copper block and fixed in place with thermally conducting paste. The stack thermocouples were placed at either end of a pore that was sealed at each end with epoxy. Both thermocouples were imbedded into the sealing bead of epoxy, as near as possible to the end of the stack and close to the center of the circular cross section. Mounting the thermocouples in this manner ensures that the temperature recorded is truly the average temperature of the solid and is not unduly influenced by the temperature of the gas.

After leaving the heater on for ample time to allow the system to reach thermal equilibrium, the temperatures at each of the thermocouples and the electrical power supplied to the heaters were recorded. The driver was then turned on and the tube driven at its 44-Hz resonant frequency. Thermoacoustic action causes heat to be pumped down the temperature gradient of the stack thus cooling the hot heat exchanger. The electrical power supplied to the heaters was increased to approximately balance this extra demand and maintain the heat exchanger near its original temperature.

It is not necessary to achieve an exact heat balance. If the initial rate of change of heat exchanger temperature is known and is sufficiently small, it is possible to accurately correct the heat flow measurement. The energy balance equation at the hot end heat exchanger is

$$E_{\text{in}} = Q_S + Q_L + C \cdot \frac{d}{dt} T_{\text{HH}}, \quad (9)$$

where  $E_{\text{in}}$  is the electrical power supplied to the heater,  $Q_S$  is

the rate at which heat is being drawn down the stack by the acoustic wave,  $Q_L$  is the rate at which heat is leaving the heat exchanger for destinations other than the stack, and  $C$  is the heat capacity of the system.  $T_{\text{HH}}$  is the temperature of the hot heat exchanger.

The value of  $Q_L$  was assumed to be equal to the value of  $E_{\text{electrical}}$  required to maintain a steady-state value of  $T_{\text{HH}}$  in the absence of a sound wave. It is important to the aim of this experiment that  $Q_L$  is not a function of the acoustic amplitude. Experimental evidence that this is indeed the case will be presented below. The value of  $C$  was determined experimentally. From a state of equilibrium and in the absence of a sound wave, a small change in the heater power was made and the rate of change of block temperature recorded. We now apply Eq. (9).  $Q_S$  is zero and because the relative change in temperature is small,  $Q_L$  can be assumed constant.  $C$  can be found by dividing the change in  $E_{\text{in}}$  by the rate of change of temperature.

The heat transfer coefficient between the stack and the hot heat exchanger is defined as

$$h = \frac{Q_S}{T_{\text{HH}} - T_{\text{HS}}}, \quad (10)$$

where  $T_{\text{HS}}$  is the temperature of the hot end of the stack.

A difference in temperature is required between the fins of the heat exchanger and the copper block that surrounds them. Its magnitude was calculated using the heat conduction equation under the assumption that the block is at a uniform temperature and that the rate at which heat is drawn away from a fin is constant at each point on each fin. The formula that results from this analysis is

$$h_s = \frac{Q}{\Delta T} = 2 \frac{w\kappa}{\Omega}, \quad (11)$$

where  $h_s$  is the heat transfer coefficient between the block and the fins of the heat exchanger,  $\kappa$  is the thermal conductivity of the metal,  $w$  is the longitudinal length of the fins, and  $\Omega$  is the fraction of the heat exchanger cross-sectional area open to the oscillating gas.  $\Delta T$  is the difference between the fin temperature at the center of the resonator and that of the surrounding block. Substitution of the values for our geometry gives  $h_s = 12$  W/K. To combine the heat transfer coefficients for a series of heat paths one must add their reciprocals,

$$\frac{1}{h_t} = \frac{1}{h_c} + \frac{1}{h_s}, \quad (12)$$

where  $h_t$  is the total interelement heat transfer coefficient.

### III. RESULTS

With the tube containing air at ambient pressure, the hot heat exchanger was held at a temperature close to 100 °C while sound waves of various amplitudes were driven in the tube. Figure 2 shows  $\Delta T (= T_{\text{HH}} - T_{\text{HS}})$  and  $Q_S$  as a function of the amplitude of the acoustic wave. A similar temperature discontinuity is observed at the cold end of the stack. The step in temperature that opens up at either end of the sack dramatically decreases the temperature gradient down the

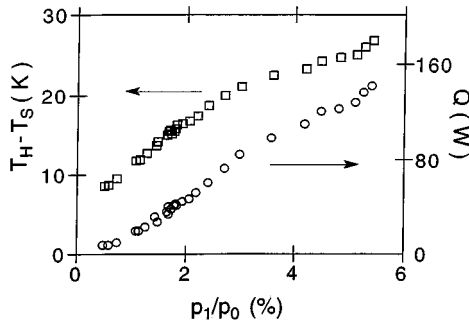


FIG. 2. The temperature difference between hot heat exchanger and the stack (□) and the rate of heat flow from the hot heat exchanger (○), plotted as a function of the acoustic amplitude.

stack. Because of this,  $Q_S$  increases more slowly than the amplitude-squared dependence predicted by the linear theory.

Figure 3 shows the measured heat transfer coefficient over a wide range of amplitudes with air as the working fluid. The graph presents data taken from three different experimental runs. Each yields the same result. The first set of data corresponds to temperature and heat flow measurements given in Fig. 1. The second data set differs in that the hot-end temperature is reduced to 60 °C. In the third set, the walls of the hot section of the tube have been heated such that the temperature of the gas at that end is comparable to that of the hot heat exchanger. The precision of the measurements can be estimated from their spread.

The straight, dashed line in Fig. 3 is the prediction of the complete heat-exchange approximation. The solid line represents the result of taking into account the finite heat capacity of the heat exchanger fines using Eq. (12). At moderate amplitudes the data fall on a straight line that passes through the origin. The data fall 20% below the prediction of the theory.

The experiment was repeated using argon and carbon dioxide as the working fluid. The pressure was again equal to ambient. The measured heat transfer coefficient (Fig. 4) was again less than that predicted by the complete heat-exchange

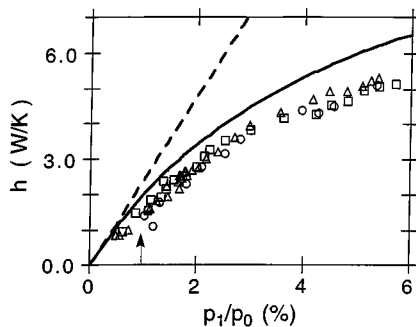


FIG. 3. The measured heat transfer coefficient between the hot heat exchanger and the stack plotted as a function of the acoustic amplitude for air. Three data sets corresponding to different conditions are shown: (Δ)  $T_{HH}=100$  °C, (□)  $T_{HH}=60$  °C, (○)  $T_{HH}=100$  °C with the tube walls heated. The dashed, straight line indicates the prediction of the complete heat-exchange model. The solid curve represents the combination of this result with the model of the heat-exchanger performance given by Eq. (11). The vertical arrow indicates the amplitude at which the predicted total displacement of the gas is equal to the length of the heat exchanger.

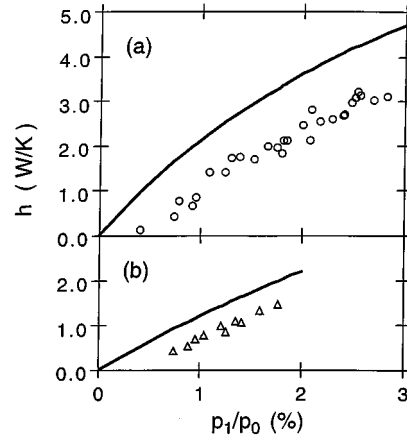


FIG. 4. The measured heat transfer coefficient between the hot heat exchanger and the stack plotted as a function of the acoustic amplitude for CO<sub>2</sub> (a) and argon (b). The curves show the prediction of the complete heat-exchange model using Eq. (12).

theory. The magnitude of this shortfall, approximately 30% in both cases, is somewhat larger than that observed for air. The experimental data appears offset from the theoretical curve and an extrapolation will not pass through the origin.

#### IV. DISCUSSION

It was earlier stated that the analysis described here requires that the quantity  $Q_L$  should be independent of amplitude. The mechanism that would most likely violate this condition is for hot gas, leaving the open end of the heat exchanger to mix the cooler gas before returning.<sup>6</sup> This will cause the acoustic wave to pump heat away from the stack and into the hot duct. For a given degree of mixing, the rate of heat removal should depend on the temperature difference between the heat exchanger and the gas in the hot duct. The magnitude of this temperature difference varied widely during the three experimental runs graphed in Fig. 3. The fact that the same value of the heat transfer coefficient was measured each time shows that little heat was removed by mixing. The assumption of complete heat exchange can be justified by application of a simple approximation similar to a heuristic argument put forward by Hoffer.<sup>7</sup> Consider a slice of inviscid gas at a temperature  $T_C$  entering a heat exchanger whose walls are held at  $T_H$ . The time-dependent temperature distribution can be approximated by the solution of the one-dimensional heat conduction equation for a rod that undergoes an instantaneous change in the temperature of its end. This solution can be found in elementary texts on heat transfer.<sup>8</sup> The average temperature of the slice is given by

$$T(\tau) = T_C + (T_H - T_C) \cdot \theta(\tau), \quad (13)$$

where

$$\theta(\tau) = 1 - \frac{4}{\pi^2} \sum_{n=1}^{\infty} \frac{1}{n^2} (1 - (-1)^n) e^{-(n\pi/2y_0)^2 \alpha \tau}, \quad (14)$$

$\tau$  is the time expired since the slice entered the heat exchanger,  $2y_0$  is the gap between the plates, and  $\alpha$  is the thermal diffusivity of the gas. Equation (13) can be used to

TABLE I. Thermal relaxation times.

Gas	Time for 90% thermal equilibration (relative to % cycle)	
	Heat exchanger	Stack
Air	0.572	0.350
Argon	0.556	0.340
CO <sub>2</sub>	0.898	0.550

calculate a thermal relaxation time. We have chosen a conservative definition of the relaxation time, that is, the time for the average temperature of the gas to rise 90% of the way to that of the heat exchanger. The relaxation times for each of the three gases used here in both the stack and the heat exchanger are given in Table I. It can be seen that in each case the relaxation time is less than half the period of oscillation.

The small vertical line in Fig. 3 indicates the acoustic pressure level at which the amplitude of particle motion at the hot heat exchanger is equal to the length of its plates. At higher amplitudes the displacement is as much as seven times the heat exchanger length. If the displacement is larger than the length of the heat exchanger, the time gas spends in the exchanger will decrease as the amplitude increases. Once this dwell time becomes less than the thermal relaxation time, the complete heat-exchange theory is not expected to hold.

It is informative to compare the complete heat-exchange theory with a description of the heat transfer process put forward by Swift.<sup>1</sup> The rate of heat flow in the transverse direction across the thermal boundary layer is considered. Swift's treatment has been incorporated into the computer code "DELTA E"<sup>9</sup> widely used in the design of thermoacoustic devices. In Ref. 1, the equations are derived for the case of wide plate spacings but in the computer code the resulting formula is applied for all values of plate spacing. For this reason, the comparison is taken beyond the limit of validity stated in Ref. 1.

The rate of heat transport is assumed to be uniform across the heat exchanger and constant in time. It is assumed that the temperature gradient is uniform and transverse inside the thermal boundary and zero elsewhere. This gradient is derived by writing the heat flow as

$$Q = -\kappa \cdot A_t \cdot \frac{\partial T}{\partial y}, \quad (15)$$

where  $\kappa$  is the thermal conductivity and  $A_t$  is the area available for heat conduction. If the total displacement is sufficiently small that no gas completely traverses the heat exchanger during an oscillation, then, for rectangular geometries

$$A_t = \frac{x_1 \cdot A}{y_0}, \quad (16)$$

substituting into Eq. (15) and rearranging:

$$\Delta T_{\text{boundary}} = \frac{Q \cdot y_0}{\kappa \cdot x_1 \cdot A} \cdot \Delta y, \quad (17)$$

where  $x_1$  is one half the total displacement and  $\Delta T$  is the temperature difference between the central gas and the wall and  $\Delta y$  is the width of the thermal boundary layer.  $\kappa$  can be written in terms of the thermal penetration depth  $\delta_k = (2\kappa/c_p\rho\omega)^{1/2}$ ,

$$\Delta T_{\text{boundary}} = \frac{Q}{x_1 \cdot A} \cdot \frac{1}{\omega} \cdot \frac{1}{c_p \rho} \cdot \frac{\beta^2}{2} \cdot \frac{\Delta y}{y_0}, \quad (18)$$

where  $\beta = 2y_0/\delta_k$ . At large plate spacings, it is a reasonable approximation to set the width of the thermal boundary layer equal to  $\delta_k$ . At narrow spacings the thermal boundary layer must occupy the entire gap. For  $y_0 > \delta_k$ ,

$$\Delta y = \delta_k \rightarrow \Delta y/y_0 = 2/\beta \quad (19)$$

and for  $y_0 < \delta_k$ ,

$$\Delta y = y_0 \rightarrow \Delta y/y_0 = 1. \quad (20)$$

By comparing Eq. (17) with Eq. (8) we can write

$$\frac{\Delta T_{\text{boundary}}}{\Delta T_{\text{complete}}} = \begin{cases} \frac{1}{\pi} \cdot \frac{\beta^2}{2}, & y_0 < \delta_k, \\ \frac{1}{\pi} \cdot \beta, & y_0 > \delta_k. \end{cases} \quad (21)$$

The temperature difference predicted by Swift's approach is less than that for complete heat exchange until  $\beta$  reaches the value of  $\pi/2$ . The prediction of a vanishing  $\Delta T$  as the plate spacing becomes small is incorrect. The finite heat capacity of the gas oscillating between the elements has not been taken into account. Application of this model, beyond the limit of applicability state in Ref. 1, may lead to an overemphasis of the merit of narrow and restrictive heat exchangers.

## V. CONCLUSIONS

The chief mechanism of heat exchange between elements of a thermoacoustic device is convection, forced by the action of the acoustic oscillation. For narrow heat exchanger ducts, the heat-exchange process can be modeled by assuming that each particle of gas that enters an element leaves in thermal equilibrium. This complete heat-exchange theory predicts that the interelement heat transfer coefficient will be proportional to the amplitude of the acoustic wave. The experimentally measured heat transfer coefficient was found to be within 20% of the prediction at low to moderate amplitudes. At high amplitudes the heat transfer coefficient is less than that predicted by theory.

## ACKNOWLEDGMENTS

The authors wish to thank Greg Swift for his useful review of a preliminary draft of this manuscript. The research was supported by the Office of Naval Research.

<sup>1</sup>G. W. Swift, "Analysis and performance of a large thermoacoustic engine," *J. Acoust. Soc. Am.* **92**, 1551–1563 (1992).

<sup>2</sup>N. Rott, "Thermoacoustics," *Adv. Appl. Mech.* **20**, 135–175 (1980).

<sup>3</sup>G. W. Swift, "Thermoacoustic engines," *J. Acoust. Soc. Am.* **84**, 1145–1180 (1988).

<sup>4</sup>W. P. Arnott, H. E. Bass, and R. Raspet, "General formulation of thermoacoustics for stacks having arbitrarily shaped pore cross sections," *J. Acoust. Soc. Am.* **90**, 3228–3237 (1991).

- <sup>5</sup>W. P. Arnott, H. E. Bass, and R. Raspet, "Specific acoustic impedance measurements of an air-filled prime mover," *J. Acoust. Soc. Am.* **92**, 3432–3434 (1992).
- <sup>6</sup>G. Mozurkewich, "Heat transfer from a cylinder in an acoustic standing wave," *J. Acoust. Soc. Am.* **98**, 2209–2216 (1995).
- <sup>7</sup>T. J. Hoffer, "Improved efficiency and power density for thermoacoustic coolers," U. S. Navy Annual Research Summary, 15 Oct. '93.
- <sup>8</sup>J. P. Holman, *Heat Transfer* (McGraw-Hill, New York, 1990).
- <sup>9</sup>W. C. Ward and G. W. Swift, "Design environment for low-amplitude thermoacoustic engines," software available through the Energy Science and Technology Software Center, U. S. Department of Energy, Oak Ridge, TN 37831.

# Diagnosis of periodic and chaotic responses in vibratory systems

L. Dai

*Department of Applied Sciences, Red Deer College, Red Deer, Alberta, T4N 5H5 Canada*

M. C. Singh

*Department of Mechanical Engineering, The University of Calgary, Calgary, Alberta T2N 1N4, Canada*

(Received 8 November 1996; accepted for publication 15 July 1997)

This paper is devoted to the development of a new approach to distinguish between a chaotic and a periodic motion of a dynamical system. A criterion namely periodicity ratio is introduced to distinguish a periodic motion from a nonperiodic motion and differentiate chaos from a regular motion by a numerical procedure without plotting any figures. A Duffing's equation and a nonlinear driven pendulum are analyzed by the periodicity ratio. Periodic-chaotic region diagrams are presented which allow a simultaneous comparison of periodic and chaotic behavior of a system with varying system parameters and a variety of initial conditions. © 1997 Acoustical Society of America. [S0001-4966(97)02912-3]

PACS numbers: 43.25.Ts, 43.25.Rq [MAB]

## INTRODUCTION

In analyzing the motion of a nonlinear oscillatory system, it is extremely important to set a criterion for chaos so that a chaotic motion can be distinguished from a regular motion. There are several methods available in the literature<sup>1</sup> for determining the onset of chaotic oscillations and some predictive and diagnostic criteria for chaos are also reported.<sup>2,3</sup> Among these, some are empirical methods that rely upon physical experiments<sup>2</sup> or data based on approximate mathematical models of the corresponding dynamical systems.<sup>1,3</sup> The forced vibration of a buckled beam was studied by Moon.<sup>1,3</sup> He found that chaotic motion would occur when the amplitude of the load acting on the beam becomes sufficiently high. A curve representing the threshold of forcing amplitudes was obtained on the basis of his experiments for different values of forcing frequency. The curve was then employed as an experimental criterion for chaotic vibrations.<sup>3</sup> In 1985, Ciliberto and Gollub<sup>2</sup> reported experimental results of their study on the harmonically driven surface waves in a fluid cylinder. An experimentally determined chaos diagram was presented in their paper. By the diagram, they distinguished chaos from periodic motions of the waves. There are also some criteria for chaos developed on the bases of the Lyapunov exponent and fractal dimension.<sup>4,5</sup> The sensitivity of a dynamical system to a change in its initial conditions is a characteristic of chaotic behavior. The Lyapunov exponent is a measure of the sensitive dependence of a system upon its initial conditions.<sup>4</sup> The fractal dimension measures an extent to which the orbits in a phase space fill a certain subspace.<sup>5</sup> A fractal structure with noninteger dimensionality is considered as a hallmark of chaos. However, when the fractal dimension is close to an integer, some other technique has to be employed to determine whether the system is chaotic. In practical applications, the Lyapunov exponent and fractal dimension are usually found by experiments or computer simulations.

In this paper a new approach for diagnosing a dynamical

system for its chaotic or periodic behavior is developed. With the introduction of a new concept namely periodicity ratio, periodic and nonperiodic motions may be conveniently distinguished, and consequently, chaotic motion can be distinguished from all of the other motions. The periodicity ratio for given parameters in the equation of motion of a dynamical system is determined in a computer simulation over a sufficiently long period of time. The concept of periodicity ratio and its applications to the study of a Duffing's equation and a nonlinear driven pendulum are presented. The periodic-chaotic region diagrams and chaotic region diagrams for the nonlinear systems are provided so that the periodic and chaotic behavior of each system can be analyzed under varying parameters and various initial conditions of the system.

## I. PERIODICITY RATIO FOR DYNAMICAL SYSTEMS

The complex appearance of various graphical representations of periodic and nonperiodic oscillations naturally leads to a search for a relationship between regular and chaotic motions. It is well known<sup>6</sup> that the Poincaré map for periodic oscillations in a steady state consists of a finite number of visible points in the phase plane. Since the motion is periodic, in a large enough time range, each visible point in the Poincaré map represents a large number of points overlapping each other. If, on the other hand a motion is chaotic, the points in a Poincaré map must be spread randomly over the phase plane. In this extreme case there may be a few or even no points overlapping the other points in the corresponding Poincaré map, no matter how large the time range is. In view of this, a criterion for periodic and chaotic motions can be found on the basis of examining the overlapping points with respect to the total number of points in a Poincaré map.

Consider an oscillatory system subjected to a periodic loading of period  $T$ . If the system has a periodic solution  $x(t)$ , the following equation must be satisfied.

$$x(t_0 + jT) = x(t_0), \quad (1)$$

where  $t_0$  is a given time, and  $j$  is the number of periodic points visible in the Poincaré map. No matter how large the time range is, there may only be a finite number of  $j$  points visible in the Poincaré map in this periodic case and all the other points in the Poincaré map overlap the  $j$  visible points. To determine whether a point is an overlapping point or not, we introduce the following expressions:

$$X_{ki} = |x(t_0 + kT) - x(t_0 + iT)|, \quad (2a)$$

$$\dot{X}_{ki} = |\dot{x}(t_0 + kT) - \dot{x}(t_0 + iT)|, \quad (2b)$$

where  $k$  is an integer in the range of  $1 \leq k \leq j$ . Designating  $n$  as the total number of points generated for the Poincaré map regardless whether they are overlapping points or not,  $i$  in the above equation is than an integer satisfying  $1 \leq i \leq n$ .

A point  $(x_i, \dot{x}_i)$  in a Poincaré map is said to be an overlapping point of the  $k$ th point  $(x_k, \dot{x}_k)$  only if the  $i$ th point has the same displacement and velocity as the  $k$ th point. On this basis, the two points  $(x_i, \dot{x}_i)$  and  $(x_k, \dot{x}_k)$  in the phase plane are considered to be overlapping points if the expressions (2a) and (2b) satisfy the following conditions simultaneously.

$$X_{ki} = \dot{X}_{ki} = 0. \quad (3)$$

On the other hand, points under consideration will not be overlapping points if

$$X_{ki} \neq 0 \quad \text{and/or} \quad \dot{X}_{ki} \neq 0. \quad (4)$$

Making use of the conditions in Eqs. (3) and (4), the following formula is developed to calculate the total number of points which have the same coordinates as the  $k$ th point in the Poincaré map.

$$\zeta(k) = \left\{ \sum_{i=k}^n Q(X_{ki}) \cdot Q(\dot{X}_{ki}) \right\} \cdot P \left( \sum_{i=k}^n [Q(X_{ki}) \cdot Q(\dot{X}_{ki})] - 1 \right), \quad (5)$$

where in Eq. (5),  $Q(y)$  and  $P(z)$  are two step functions defined as

$$Q(y) = \begin{cases} 1, & \text{if } y = 0, \\ 0, & \text{if } y \neq 0, \end{cases} \quad (6a)$$

$$P(z) = \begin{cases} 0, & \text{if } z = 0, \\ 1, & \text{if } z \neq 0, \end{cases} \quad (6b)$$

where  $y$  and  $z$  are the arguments of the functions  $Q$  and  $P$ , respectively, in Eq. (5).  $\zeta(k)$  calculated by employing Eq. (5) gives the total number of points coincident with the  $k$ th point including the  $k$ th point itself in the Poincaré map. Therefore there are  $\zeta(k)$  points in the Poincaré map having the same values of displacement and velocity as that of the  $k$ th point. In the case that a pair of points are superposed, a visible point and a point overlapped by the visible point are calculated by Eq. (5) as two overlapping points. For a single visible point without any point overlapping it, Eq. (5) guar-

antees that this single point does not count as an overlapping point. The sum  $\zeta(k)$  thus represents a set of points with the identical coordinates in the phase plane. The first summation in Eq. (5) calculates the number of overlapping points of the  $k$ th point and the function  $P$  assures  $\zeta(k) = 0$  in the case that there is not point overlapping the  $k$ th point among the total number of  $n$  points.

When the number of points overlapping the  $k$ th point is obtained, all the overlapping points corresponding to the  $j$  visible points in the Poincaré map may be consequently obtained by the formula shown below.

$$\text{NOP} = \zeta(1) + \sum_{k=2}^n \zeta(k) \cdot P \left( \prod_{l=1}^{k-1} \{X_{kl} + \dot{X}_{kl}\} \right), \quad (7)$$

where NOP stands for the total number of overlapping points and  $\Pi$  is the symbol for multiplication. Once a point is counted as an overlapping point, it should not be counted again. The  $P$  function in Eq. (7) is used to prevent this duplicate counting in the calculation for NOP.

In Eq. (7) only the overlapping points are counted. The number of overlapping points calculated by using Eq. (7) is in general less than  $n$ , the total number of points generated for a Poincaré map. If the response of a system is periodic, all the points in the Poincaré map are overlapping points and the corresponding NOP can be simply expressed in the form

$$\text{NOP} = \sum_{k=1}^j \zeta(k), \quad (8)$$

where  $j$  is the number of visible points in the Poincaré map. Equation (8) implies that there are  $j$  sets of points involved in the Poincaré map for a periodic case, and the points in the same set are all identical in terms of displacement and velocity.

To describe the number of overlapping points with respect to the total number of points generated for a Poincaré map, a ratio between NOP and  $n$  can be very useful. In fact, the ratio of NOP to  $n$  plays an important role in the establishment of a criterion for chaotic motion. We define the ratio in the following form and call it periodicity ratio.

$$\gamma = \lim_{n \rightarrow \infty} \frac{\text{NOP}}{n}. \quad (9)$$

For a perfect measurement of  $\gamma$ , the time range considered must be  $t \in [0, \infty)$ . However, in practice,  $t$  should be large enough to generate a sufficiently large  $n$ .

If motion of a system in a steady state is periodic, the points in the Poincaré map must all be overlapping points, accordingly,  $\gamma$  in Eq. (9) is unity. If on the other hand the number of overlapping points is zero or very small such that  $\gamma \rightarrow 0$ , the corresponding motion is quasiperiodic or chaotic. The quasiperiodic motions considered in this paper are the cases in which the points of the Poincaré map form a continuous smooth curve in the phase plane. When  $\gamma$  takes a value such that  $0 < \gamma < 1$ , it implies that some points in the Poincaré map are overlapping points while the others are not. Therefore the corresponding motion is a combination of periodic and nonperiodic motions. Obviously,  $\gamma$  can be introduced here as a criterion to distinguish a periodic motion

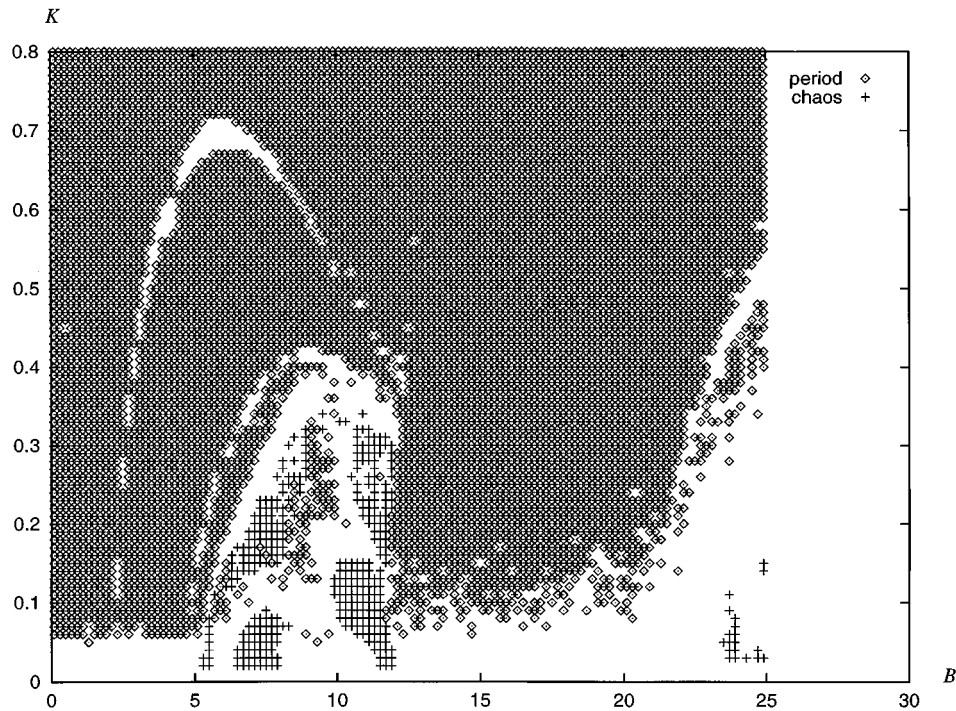


FIG. 1. Periodic-chaotic region diagram for  $\ddot{x} + k\dot{x} + x^3 = B \cos t$ .

from a nonperiodic motion and to differentiate regular motions from chaos.  $\gamma$  describes the nature of periodicity of an oscillatory motion and is a measure of a degree of periodicity for a nonlinear dynamical system. As the value of  $\gamma$  tends to unity the closer its behavior becomes to a periodic oscillatory motion. It is because of this that  $\gamma$  is called the periodicity ratio.

The periodicity ratio  $\gamma$  can be precisely calculated only in the cases for which the analytical solutions corresponding to the dynamical systems are available. For most nonlinear oscillatory systems, however, analytical solutions are impossible or difficult to obtain, the calculation for the periodicity ratio then has to be done on a numerical basis with the aid of a computer. Since  $Q(y)$  and  $P(z)$  in Eqs. (6a) and (6b) are step functions, the numerical calculation for  $\gamma$  can be conveniently carried out by a computer program. In order to calculate  $\gamma$  accurately, the time range considered must be sufficiently wide so that the data representing the total number of points in the corresponding Poincaré map may be large enough for acceptable results.

In diagnosing whether an oscillatory motion is chaotic or not, clearly, one may employ periodicity ratio and simply concentrate on the states of motion with  $\gamma$  close or equal to zero.

## II. APPLICATION OF PERIODICITY RATIO

For a nonlinear dynamical system, it is important to find out as to under what initial conditions and for what values of the system parameters chaotic motion may occur. Ueda studied Duffing's equation in the following form.<sup>7</sup>

$$\ddot{x} + k\dot{x} + x^3 = B \cos t. \quad (10)$$

He found that a wide variety of periodic and chaotic behavior can be obtained by varying the parameters  $k$  and  $B$ . His diagram illustrating the regions of chaotic and periodic motions is widely cited.<sup>1,8</sup> The same system can be examined by an application of the periodicity ratio. A periodic-chaotic region diagram similar to that provided by Ueda can be constructed since periodic and chaotic motions can be diagnosed by the criterion of periodicity ratio  $\gamma$ . In constructing the periodic-chaotic region diagram, the piecewise-constant method<sup>9,10</sup> is used to solve Duffing's equation (10) numerically and to calculate the points for the Poincaré map. The data for generating a Poincaré map may also be calculated by other numerical techniques. For verification purposes, the authors employed the Runge-Kutta method for the numerical calculation. The results obtained by using the two numerical methods are almost identical. A comparison of the two numerical methods is to be reported separately. With the data for the Poincaré map, the periodicity ratio corresponding to different values of  $k$  and  $B$  in the Duffing's equation can be determined by employing Eqs. (5) and (7). Consequently, the nonperiodic cases with  $\gamma$  equal or very close to zero may be differentiated from all of the other cases.

Taking  $k$  and  $B$  as two varying parameters of the system, Fig. 1 is developed to show the periodic and chaotic regions determined by the periodicity ratio. This periodic-chaotic region diagram presents a global aspect of motion for the system. Each point in the diagram represents a state of motion. Therefore the diagram allows a simultaneous comparison of the periodic and chaotic behavior of the system with varying system parameters and variety of initial conditions. It would be appropriate to mention here that a diagram identical to Fig. 1 can also be obtained by using the Runge-Kutta method with assistance of periodicity ratio.

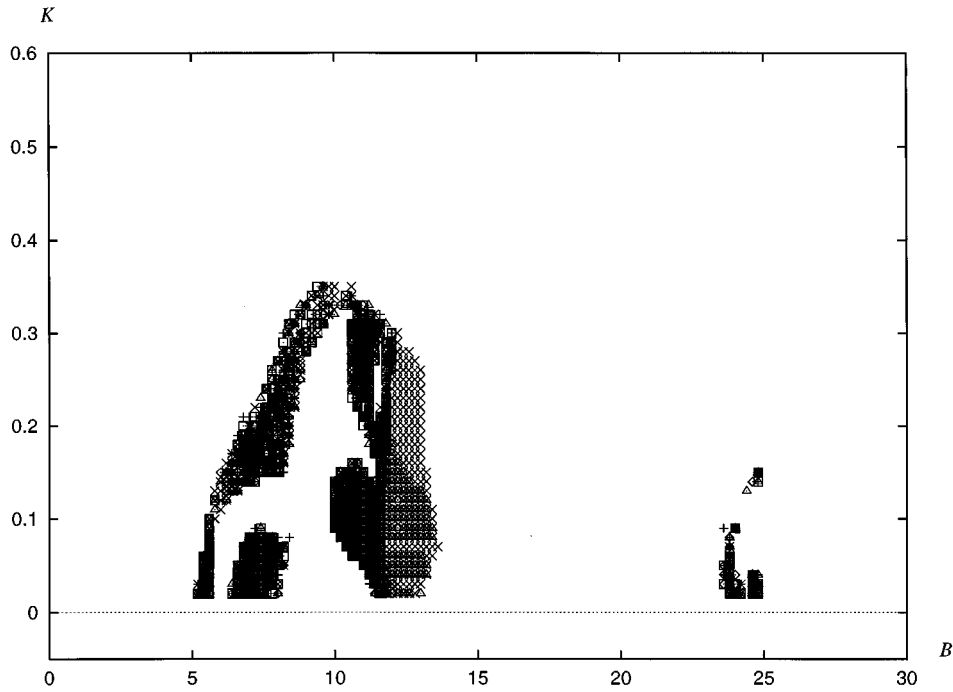


FIG. 2. Chaotic region diagram of the system governed by  $\ddot{x} + k\dot{x} + x^3 = B \cos t$  under various initial conditions.

To emphasize chaotic behavior and dependence of chaos on initial conditions, a chaotic region diagram under various initial conditions is plotted in Fig. 2 for Duffing's equation. The initial condition-dependent regions shown in the figure are almost identical to those presented by Ueda. The unique chaotic regions in Fig. 2 also compare well with the results by Ueda except in two areas. The first area is a window around the point of  $k=0.26$  and  $B=11.4$  as shown in the

figure. According to Ueda's diagram, the motion in this area is uniquely chaotic. However, based on the periodicity ratios calculated for Fig. 2, the motions in this area are found to be period or nonchaotic no matter what initial conditions are taken. As illustrated by a phase trajectory in Fig. 3 for the above point, the motion is indeed periodic. Besides, the shape of the trajectory shown in Fig. 3 is different from all of the trajectories collected by Ueda.<sup>7</sup> Another area is the re-

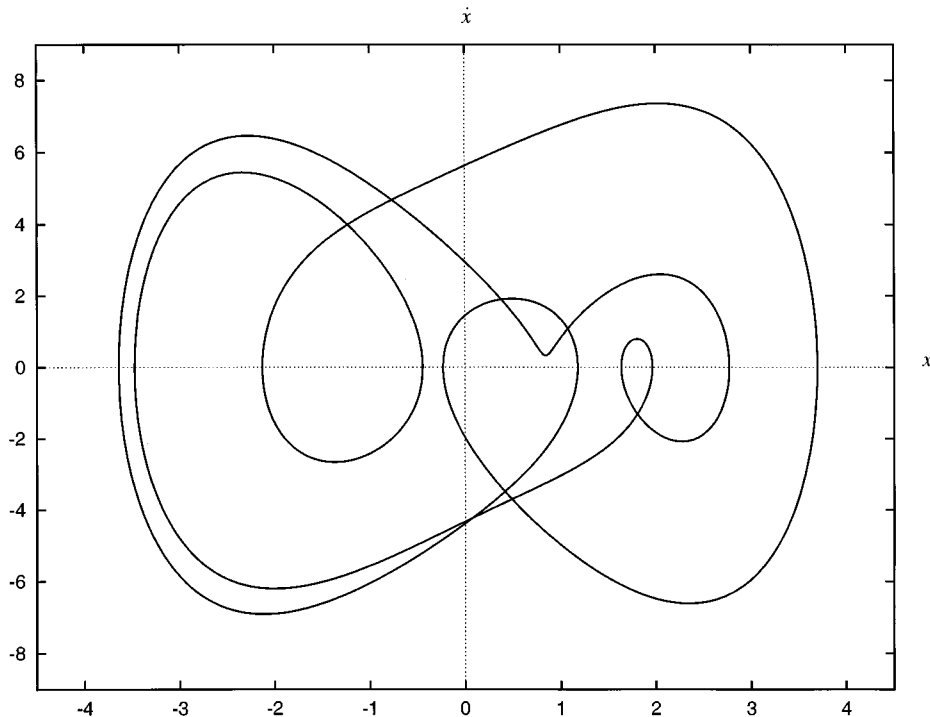


FIG. 3. Phase trajectory of a periodic case governed by  $\ddot{x} + k\dot{x} + x^3 = B \cos t$ ,  $k=0.26$  and  $B=11.4$ .



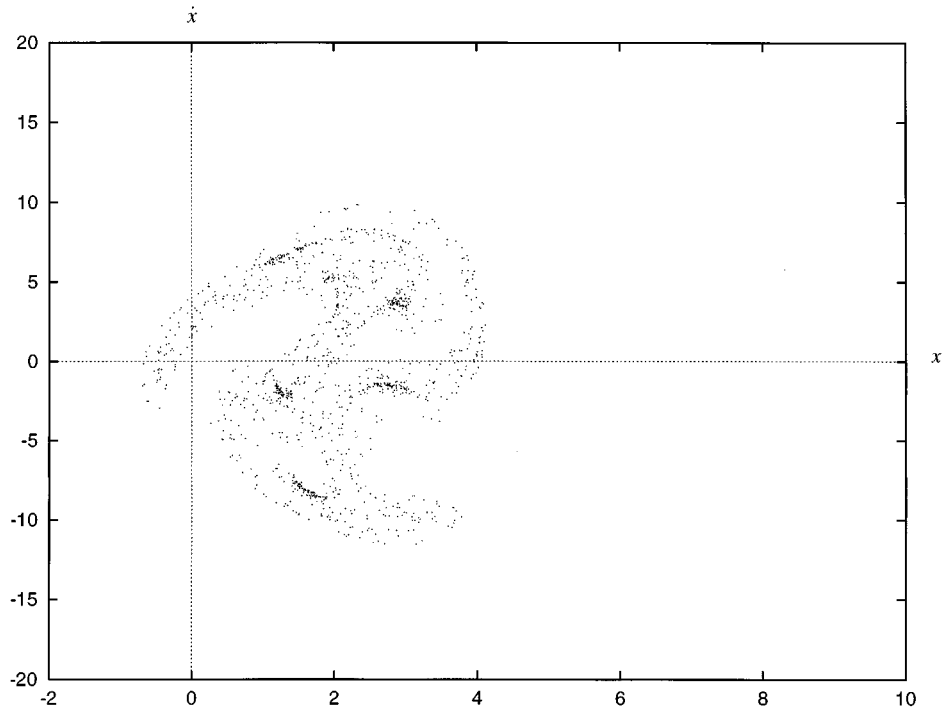


FIG. 4. Poincaré map for  $\ddot{x} + k\dot{x} + x^3 = B \cos t$  at  $k=0.05$  and  $B=23.9$ .

gion around  $k=0.07$  and  $B=23.9$  where Ueda's results imply periodic vibration. The behavior of motion in this area is found to be chaotic since the periodicity ratio obtained for this area is equal to or very close to zero. The motion corresponding to  $k=0.05$  and  $B=23.9$  in this area is studied. The corresponding Poincaré map and phase trajectory are pre-

sented in Figs. 4 and 5, respectively. It is evident that the motion of this case is chaotic.

In addition to the periodic and chaotic regions, some quasiperiodic regions and regions of the nonperiodic motions in between chaos and periodic motions are found in constructing the periodic-chaotic region diagrams. The quasi-

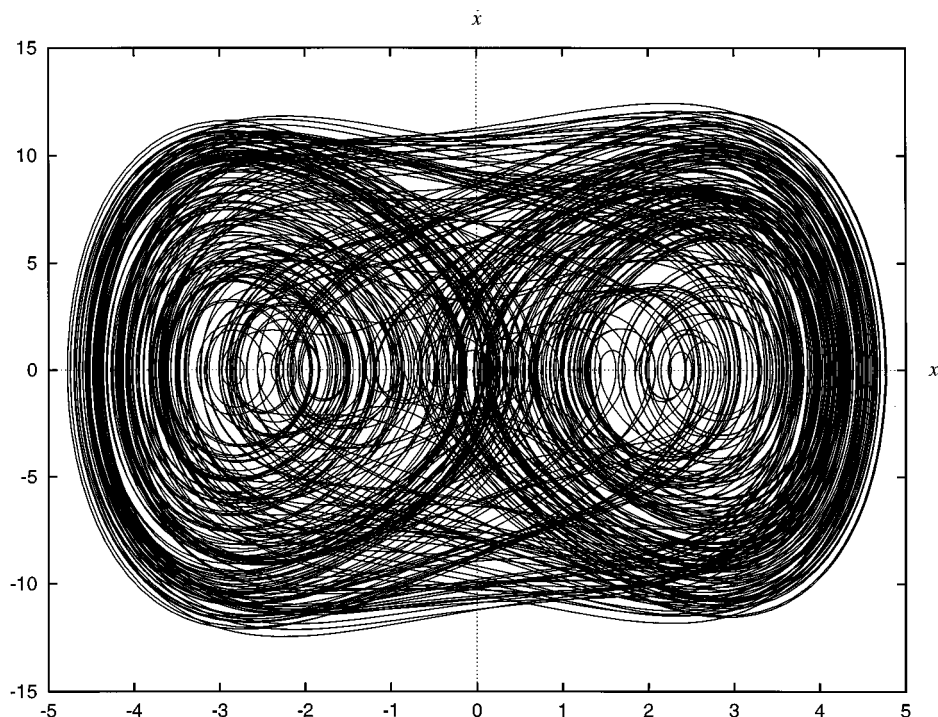


FIG. 5. Phase trajectory for  $\ddot{x} + k\dot{x} + x^3 = B \cos t$  at  $k=0.05$  and  $B=23.9$ .

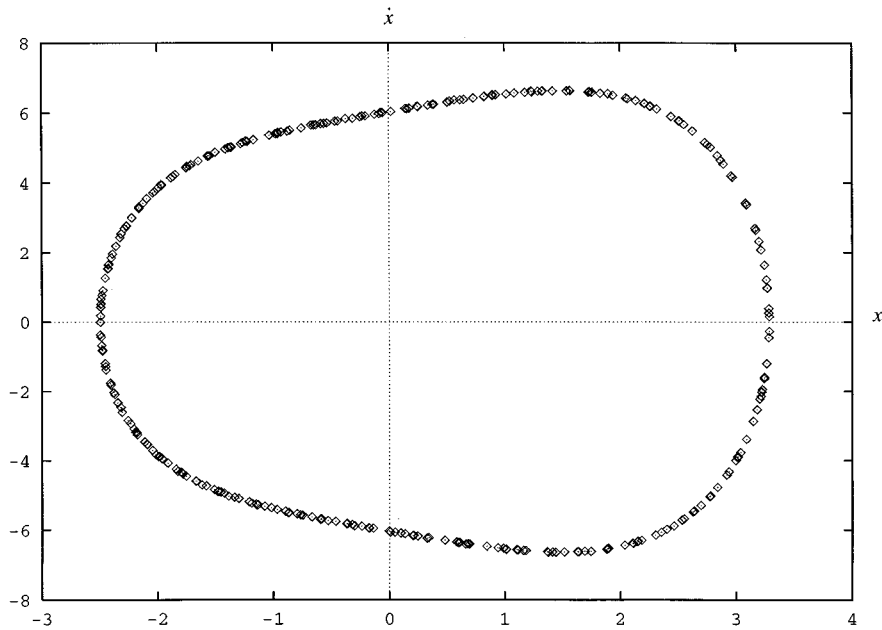


FIG. 6. Poincaré map of a quasiperiodic motion governed by  $\ddot{x} + k\dot{x} + x^3 = B \cos t$ ,  $k=0.0$  and  $B=2.8$ .

periodic regions and the regions of the other motions which are neither periodic nor chaotic are represented by the blank, unmarked regions in Fig. 1. A Poincaré map for a quasiperiodic case is illustrated in Fig. 6. Among the nonperiodic cases with  $\gamma \rightarrow 0$ , quasiperiodic cases have been differentiated from the chaotic cases discussed above. The curve joining all the points in a Poincaré map for a quasiperiodic motion is a continuous smooth curve. Figure 6 shows the Poincaré map of a quasiperiodic motion. From Fig. 6 it can be seen that the points in the Poincaré map indeed form a continuous smooth curve. It is also found that the number of overlapping points

is negligibly small as compared to the total number of points in the Poincaré map such that the corresponding periodicity ratio tends to zero. Since both a quasiperiodic case and a chaotic case have zero periodicity ratio, it is necessary to distinguish the quasiperiodic cases from chaos.

In distinguishing a quasiperiodic motion from chaos, the authors employed the least-squares method with the combination of periodicity ratio. The least-squares method is a well-known technique in fitting a curve to a set of data.<sup>11</sup> Noting the curve joining all the points in a Poincaré map of a quasiperiodic motion must be continuous and smooth, a

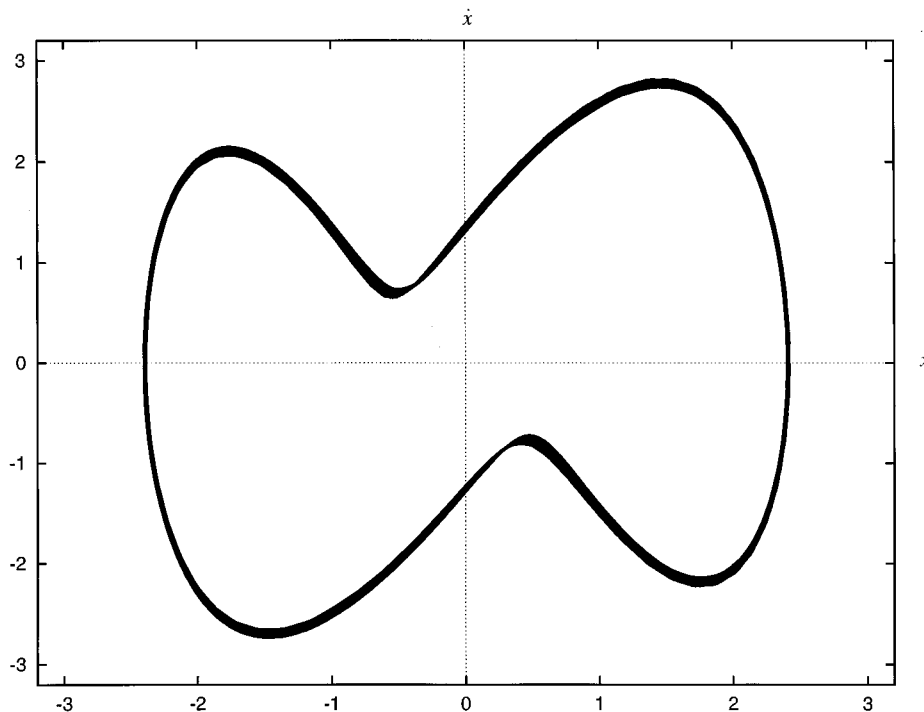


FIG. 7. Phase trajectory of a nonperiodic motion governed by  $\ddot{x} + k\dot{x} + x^3 = B \cos t$ .  $k=0.67$ ,  $B=5.2$ , and  $\gamma=0.8$ .

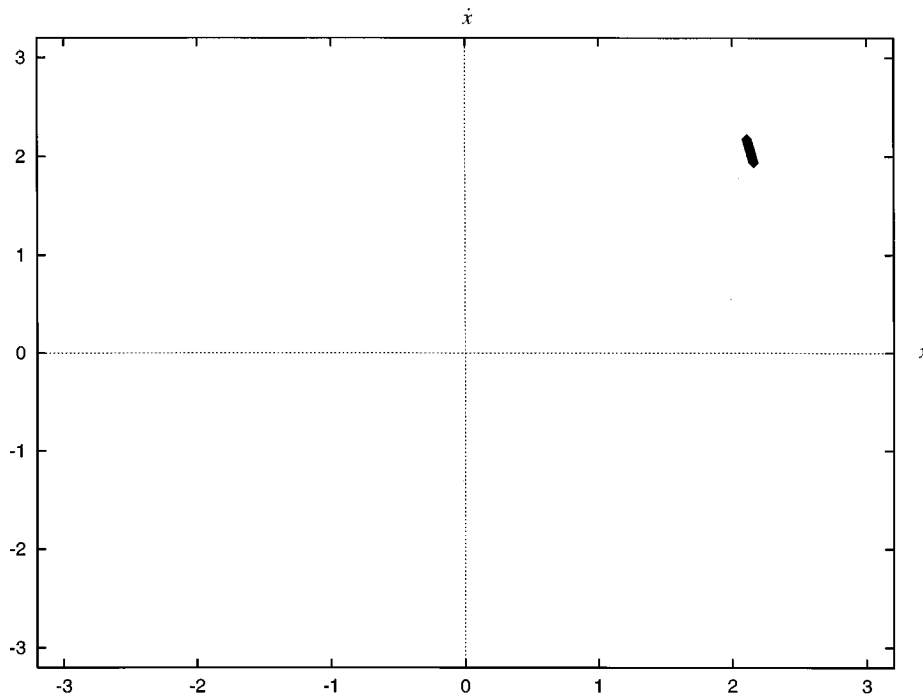


FIG. 8. Poincaré map of a nonperiodic case governed by  $\ddot{x} + k\dot{x} + x^3 = B \cos t$ .  $k=0.67$ ,  $B=5.2$ , and  $\gamma=0.8$ .

curve can always be found to fit with the curve in the Poincaré map by the least-squares method. If all the points of a Poincaré map lie on a curve generated by the least-squares method, the corresponding motion must be quasiperiodic. In fact, with the data of the points on the smooth curve of the Poincaré map, a function of the fitting curve can always be constructed such that all the points generated for the corresponding Poincaré map satisfy the function. With the func-

tion for the fitting curve constructed by the data of a Poincaré map, there is no need to plot curves to distinguish a quasiperiodic motion from a chaotic motion. In distinguishing a quasiperiodic motion from chaos, one may now completely rely on a computer program for numerical calculation.

In the regions of the nonperiodic motions in between chaotic and periodic motions, the behavior of motion tends to be periodic as  $\gamma$  becomes close to a unity, and the behav-

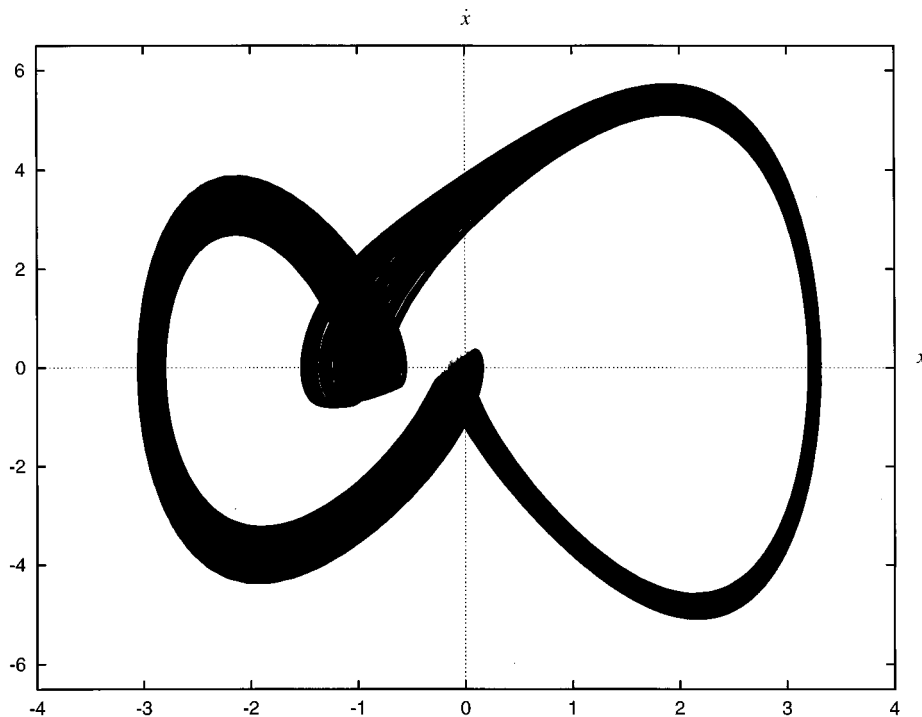


FIG. 9. Phase trajectory of a nonperiodic motion governed by  $\ddot{x} + k\dot{x} + x^3 = B \cos t$ .  $k=0.35$ ,  $B=9.2$ , and  $\gamma=0.17$ .

ior of motion may be chaotic or closer to a quasiperiodic motion when  $\gamma$  approaches zero. From the unmarked region at about  $k=0.67$  and  $B=5.2$  in Fig. 1, a typical nonperiodic case with  $\gamma=0.8$  is examined and its phase trajectory and Poincaré map are illustrated in Figs. 7 and 8, respectively. The corresponding motion in this case is obviously not periodic since the shape of the phase trajectory changes with time and the points in the Poincaré map are not all overlapped. However, the variation of the phase trajectory is very slight and the behavior of motion in this case is therefore almost periodic. Another case with small periodicity ratio ( $\gamma=0.17$ ) is taken from an unmarked region around  $k=0.35$  and  $B=9.2$ . Figure 9 is the phase trajectory corresponding to this case. It can be seen from the figure that the motion in this case is far from periodic. Nevertheless, the motion is not chaotic either since it is not completely random. By the corresponding Poincaré map shown in Fig. 10, the overlapping points at the two ends of the curve can be observed. Therefore the behavior of the corresponding motion is nonperiodic and nonchaotic but rather close to chaotic. However, the interest of this paper is in diagnosing period and chaotic motions in oscillatory systems, the stress is therefore laid on the motions with  $\gamma$  very close or equal to unity for periodic cases and equal or very close to zero for chaotic cases.

The damped pendulum under a sinusoidal external force has been extensively used for the study of chaotic motions.<sup>6,12,13</sup> The damped driven pendulum is physically simple, yet its behavior is very rich in the nonlinear properties of its solutions. With the application of periodicity ratio, periodic and chaotic behavior of a damped pendulum system can be conveniently diagnosed. Periodic–chaotic region diagrams may also be generated for the system by taking into account variations of the system parameters and initial con-

ditions. The damped, sinusoidally driven pendulum of mass  $m$  and length  $l$  can be expressed by the following equation of motion:

$$ml\ddot{\phi} + c\dot{\phi} + mg \sin \phi = A \cos \Omega t, \quad (11)$$

where  $c$  is the viscous coefficient,  $A$  is the amplitude of the external force, and  $\Omega$  is the frequency of the external force acting on the pendulum. For the purpose of minimizing the number of system parameters, the equation of motion may be rewritten in a dimensionless form as

$$\ddot{\phi} + \alpha\dot{\phi} + \sin \phi = F \cos \Omega t, \quad (12)$$

where  $\alpha$  is a parameter related to damping and weight of the system,  $F$  is the forcing amplitude and  $g/l$  is taken to be unity. Although the driving frequency  $\Omega$  can be further eliminated, we keep  $\Omega$  in the equation for convenience in comparing the results with those available in the current literature.

A periodic–chaotic region diagram corresponding to the driven pendulum system governed by Eq. (12) is presented in Fig. 11. In evaluating the nature of motion at different points in the diagram, the piecewise-constant numerical method was used,<sup>9,10</sup> Backer<sup>6</sup> and Gwinn and Westervelt<sup>12</sup> studied the same system governed by Eq. (11) and provided analyses on the periodic and chaotic behavior of the system. Their results were based on the varying system parameter  $F$  and a fixed  $\alpha$  value ( $\alpha=0.5$ ). By the bifurcation diagrams presented in their works, the periodic and nonperiodic cases can be differentiated for different forcing amplitudes. The results corresponding to a different amplitude of the driven force along the line  $\alpha=0.5$  in Fig. 11 match very well with the bifurcation diagrams provided by Backer and Gwinn and

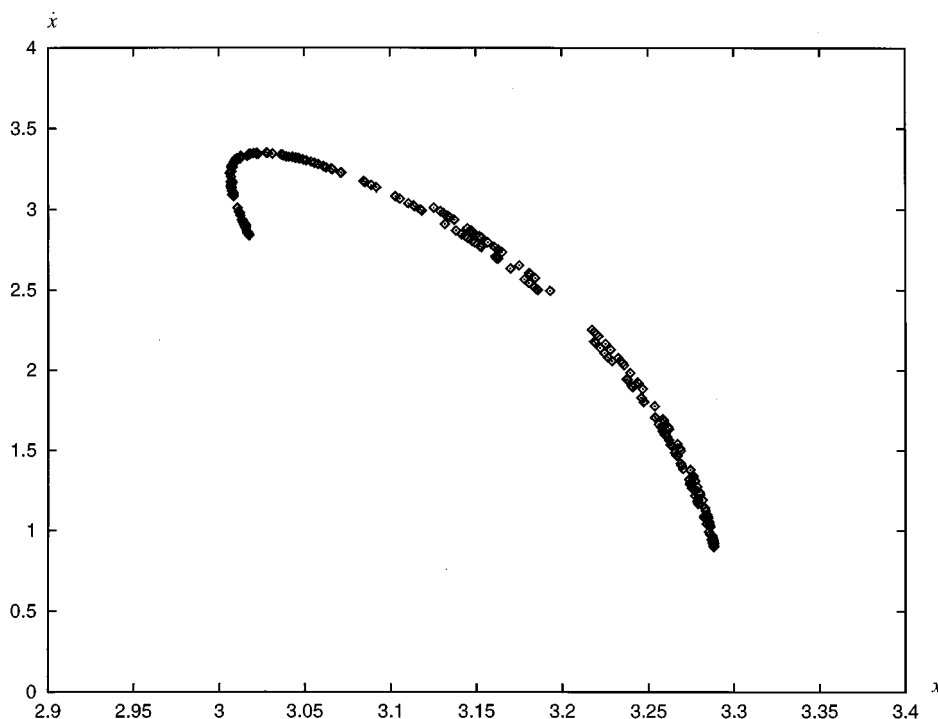


FIG. 10. Poincaré map of a nonperiodic motion for  $\ddot{x} + k\dot{x} + x^3 = B \cos t$ .  $k=0.35$ ,  $B=9.2$ , and  $\gamma=0.17$ .

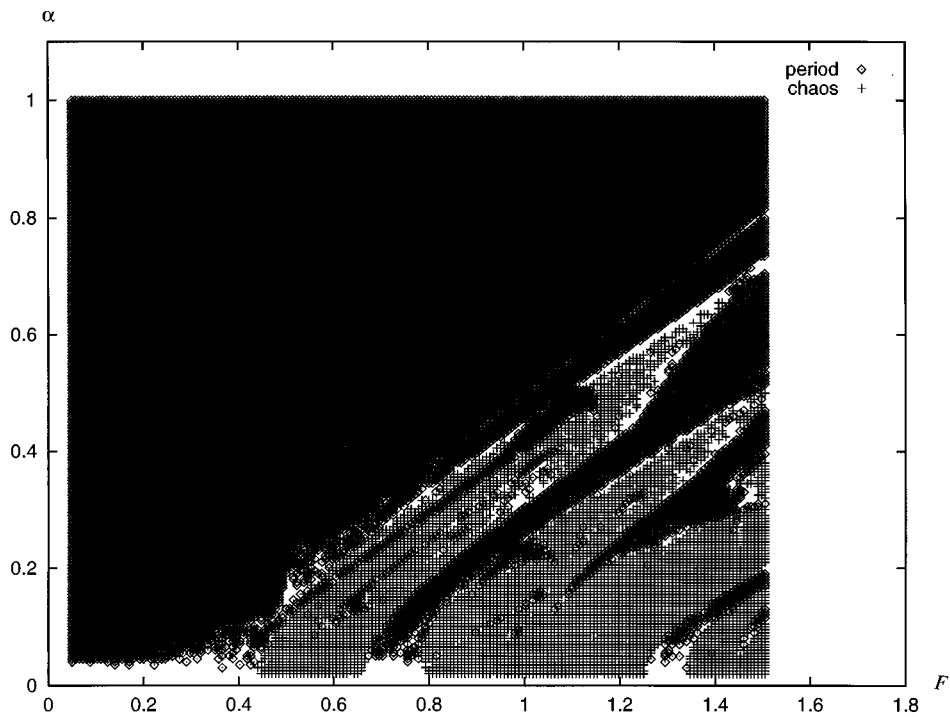


FIG. 11. Periodic-chaotic region diagram for  $\ddot{\phi} + \alpha\dot{\phi} + \sin \phi = F \cos \Omega t$ .  $\Omega = 2/3$ .

Westervelt except that the quasiperiodic motions and the other nonperiodic motions in between periodic motion and chaos are identified and eliminated from the diagram in Fig. 11. It is clear that the periodic-chaotic region diagram provides a global picture of the properties of motion for the pendulum system since the diagram describes the states of motion for the system with varying values of both the system parameters  $\alpha$  and  $F$ .

The diagram in Fig. 11 is apparently divided into two parts by a straight boundary line approximately making an angle of  $31.5^\circ$  with the  $F$  axis and intersecting it at  $F = 0.2$ . On the left-hand side of the boundary, the motions are uniquely periodic. In fact, the motions in this part of the diagram are all simple harmonic oscillations without rotation. The amplitude of the oscillations increases with the increase of the amplitude of the driven force  $F$  and decreases

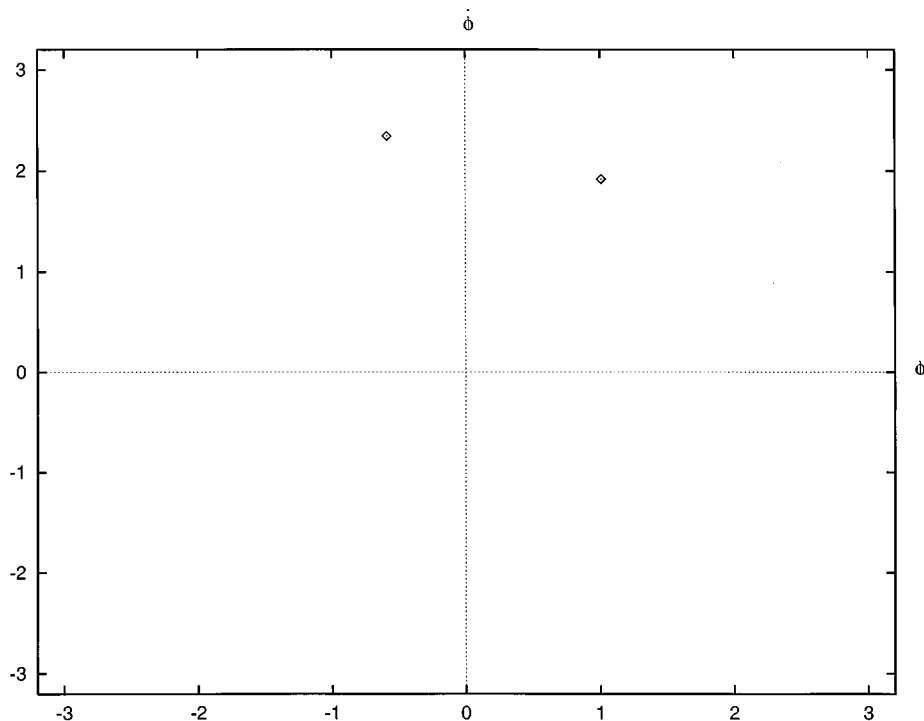


FIG. 12. Poincaré map of a periodic motion for  $\ddot{\phi} + \alpha\dot{\phi} + \sin \phi = F \cos \Omega t$ .  $\Omega = 2/3$ ,  $\alpha = 0.45$ , and  $F = 1.36$ .

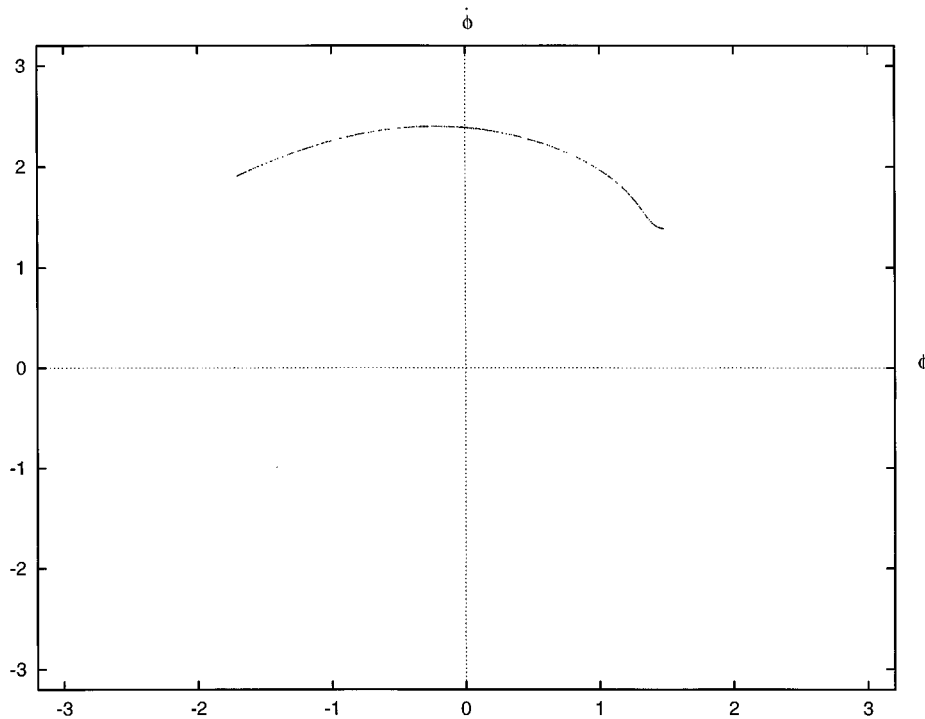


FIG. 13. Poincaré map of a quasiperiodic motion for  $\ddot{\phi} + \alpha\dot{\phi} + \sin\phi = F \cos \Omega t$ .  $\Omega=2/3$ ,  $\alpha=0.45$ , and  $F=1.393$ .

with the increase of the viscous damping. Across the boundary, on the right-hand side of the diagram, the pendulum may rotate about its point of support and the motion may become periodic or chaotic as shown in the figure. According to the periodic-chaotic region diagram and the phase trajectories of the pendulum system, the motions are simple harmonic oscillations if the ratio of  $\alpha$  to  $F$  is greater than 0.61 for  $F$

$\geq 0.4$ . When the ratio of  $\alpha$  to  $F$  is less than 0.61, the corresponding motion of the pendulum may be a combination of rotation and oscillation, and nonperiodic, quasiperiodic, and chaotic motions may then occur.

Since the boundaries of periodic and chaotic regions are distinct in the periodic-chaotic region diagram, routes to chaos can also be traced with the help of the diagram. A

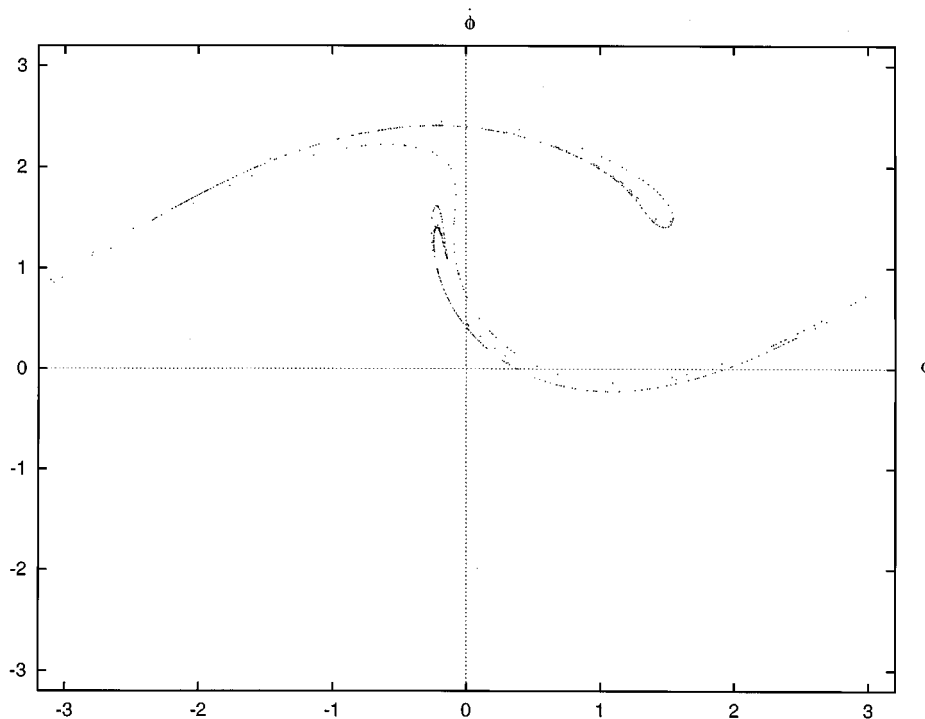


FIG. 14. Poincaré map of a chaotic case for  $\ddot{\phi} + \alpha\dot{\phi} + \sin\phi = F \cos \Omega t$ .  $\Omega=2/3$ ,  $\alpha=0.45$ , and  $F=1.4$ .

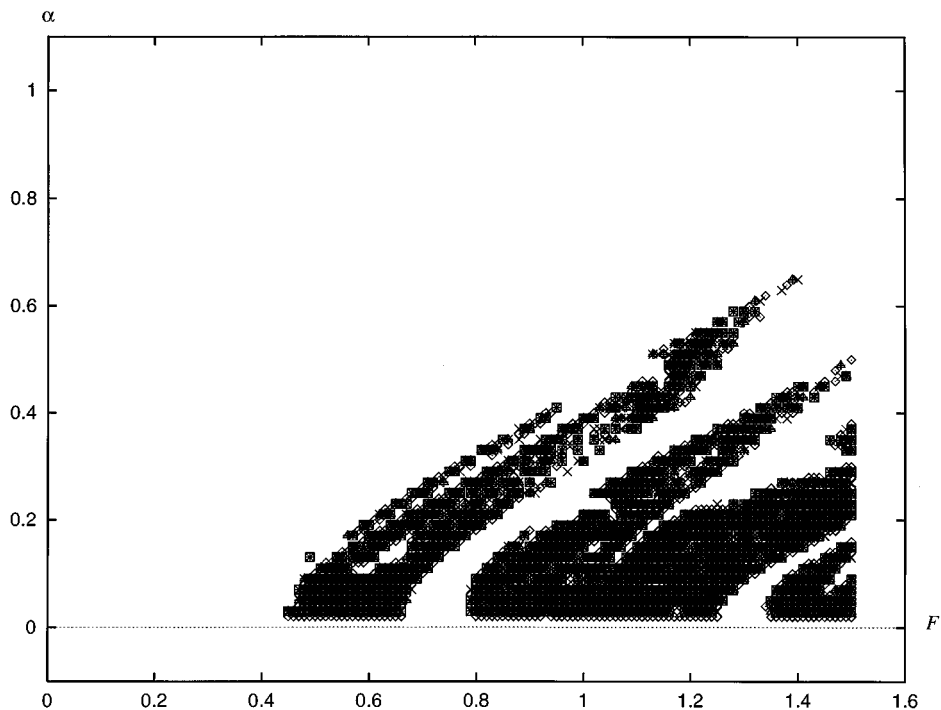


FIG. 15. Chaotic region diagram of the system governed by  $\ddot{\phi} + \alpha \dot{\phi} + \sin \phi = F \cos \Omega t$  under various initial conditions.  $\Omega = 2/3$ .

route from periodic motion to quasiperiodic motion, and then from quasiperiodic to a chaotic motion is illustrated by the Poincaré map shown in Figs. 12–14. As can be seen from these figures, with the same  $\alpha$  value, a slight variation in  $F$  may lead the behavior of motion of the system from periodic motion to quasiperiodic motion and then to chaos.

Chaotic regions under various initial conditions are exhibited in Fig. 15. Based on the initial conditions used for the plotting, it is found that the chaotic regions are independent of the initial conditions within the  $\alpha$  and  $F$  ranges shown in the figure.

As can be seen from the above discussion, the periodicity ratio reveals the behavior of motion of nonlinear oscillatory systems and can be used as an effective criterion for periodic and chaotic motions. With the periodicity ratio, chaotic motion can be conveniently diagnosed for a nonlinear dynamical system and periodic–chaotic region diagrams may be obtained such that a simultaneous comparison of the chaotic and periodic behavior with varying system parameters and various initial conditions becomes available. Making use of the periodicity ratio, the diagnostic procedure for chaotic, quasiperiodic, and periodic motions can be completed by a single computer program without plotting any of the phase trajectories and Poincaré map.

- <sup>1</sup>F. C. Moon, *Chaotic Vibrations* (Wiley, New York, 1987).
- <sup>2</sup>S. Ciliberto and J. P. Gollub, "Chaotic mode competition in parametrically forced surface waves," *J. Fluid Mech.* **158**, 381–398 (1985).
- <sup>3</sup>F. C. Moon, "Experiments on chaotic motions of a forced nonlinear oscillator: Strange attractors," *ASME J. Appl. Mech.* **47**, 638–644 (1980).
- <sup>4</sup>A. Wolf, J. B. Swift, H. L. Swinney, and J. A. Vastano, "Determining Lyapunov exponents from a fine series," *Physica D* **16**, 285–317 (1985).
- <sup>5</sup>J. D. Farmer, E. Ott, and J. A. Yorke, "The dimension of chaotic attractors," *Physica D* **7**, 153–170 (1983).
- <sup>6</sup>G. L. Backer and J. P. Gollub, *Chaotic Dynamics* (Cambridge U. P., Cambridge, England, 1990).
- <sup>7</sup>Y. Ueda, "Steady motions exhibited by Duffing's equations: A picture book of regular and chaotic motions," in *New Approaches to Nonlinear Problems in Dynamics*, edited by P. J. Holmes (SIAM, Philadelphia, 1980), pp. 311–322.
- <sup>8</sup>J. M. T. Thompson and H. B. Stewart, *Nonlinear Dynamics and Chaos* (Wiley, New York, 1986).
- <sup>9</sup>L. Dai and M. C. Singh, "On oscillatory motion of spring-mass systems subjected to piecewise constant forces," *J. Sound Vib.* **173**, 217–231 (1994).
- <sup>10</sup>L. Dai and M. C. Singh, "An analytical and numerical method for solving linear and nonlinear vibration problems," *Int. J. Solids Struct.* **34**, 2709–2731 (1997).
- <sup>11</sup>N. R. Draper and H. Smith, *Applied Regression Analysis* (Wiley, New York, 1981), 2nd ed.
- <sup>12</sup>E. G. Gwinn and R. M. Westervelt, "Fractal basin boundaries and intermittency in the driven damped pendulum," *Phys. Rev. A* **33**, 4143–4155 (1986).
- <sup>13</sup>J. A. Blackburn, S. Vik, B. Wu, and H. J. T. Smith, "Driven pendulum for studying chaos," *Rev. Sci. Instrum.* **60**, 422–426 (1989).

# The effects of a soluble surfactant on quadrupole shape oscillations and dissolution of air bubbles in water

Thomas J. Asaki<sup>a)</sup> and Philip L. Marston

*Department of Physics, Washington State University, Pullman, Washington 99164-2814*

(Received 28 January 1997; accepted for publication 18 August 1997)

Single air bubbles were ultrasonically trapped in aqueous solutions of the soluble surfactant Triton X-100. Quadrupole shape oscillations were induced by modulation of the radiation pressure and the free decay was recorded using an optical extinction technique. The frequency and damping were found to be maximal at a bulk surfactant concentration which only weakly affects the surface tension. At higher concentrations the frequency is reduced due to surface tension depression and the damping approaches a value several times that expected for a clean interface. These results are in qualitative agreement with theoretical predictions based on interfacial viscoelastic considerations. Bubble size and dissolution curves were obtained through the use of digitized bubble images. Dissolution rates are shown to be significantly enhanced by the presence of the surfactant. © 1997 Acoustical Society of America. [S0001-4966(97)02712-4]

PACS numbers: 43.25.Yw [MAB]

## INTRODUCTION

The study of surfactants and their behavior at the interfacial region of an air bubble is important for a variety of applications. The surfactant mediated lifetime and materials transport capabilities of sea bubbles affect the far-ranging phenomena of undersea noise, global climate, and health of coastal populations.<sup>1-3</sup> Industrial applications include liquid cleaning, purification of melts, foam behavior, catalysis, and noncontact materials manipulation. Surfactants may also prove useful in understanding other important phenomena such as cavitation, bubble coalescence, and sonoluminescence.<sup>1,4,5</sup>

Dynamic surface behaviors, such as capillary ripples, are sensitive to the presence of surfactants. Distribution and effects of surfactants can be modeled by surface viscoelasticity, and surface and bulk diffusion. Most notably, a significant enhancement in capillary wave damping is predicted to occur at relatively low surfactant concentrations for both flat and spherical surfaces. A number of studies have measured this phenomenon for flat surfaces using a variety of insoluble surfactants (e.g., see Refs. 6 and 7). Unfortunately, the measured damping enhancement is typically small and detection schemes are prone to noise. Noncontact studies of levitated drops and bubbles are ideally suited for surfactant-related shape oscillation and diffusion experiments, yet only a few studies have been carried out. Lu and Apfel<sup>8</sup> examined the quadrupole oscillations of hexane drops levitated in aqueous solutions of sodium dodecyl sulfate. Air bubbles have been studied in the presence of an insoluble surfactant<sup>9</sup> and in both clean water and seawater.<sup>10</sup>

The present work describes the effects of the water-soluble surfactant Triton X-100 (hereafter denoted TX) on the free quadrupole oscillations and dissolution of air bubbles in water.

## I. SURFACE VISCOELASTICITY

Surface waves on a fluid and oscillations of a fluid droplet can be significantly affected by surfactants. Viscoelastic effects alter the boundary conditions for fluid flow near the interface and give rise to a higher rate of energy dissipation within a boundary layer.<sup>11</sup> The stress relations applicable to the interface and the implications for the boundary layer flow can be understood in terms of a hydrodynamic theory.<sup>7,11</sup> As an introduction to more complicated geometries, consider first the small deformations of a clean interface which has a flat equilibrium shape. The normal component of the stress tensor is given in magnitude by the Laplace pressure that relates the local surface curvature to the surface tension. The tangential surface stress vanishes identically. For monolayer-covered surfaces subject to surface motion the local surface coverage will deviate from the equilibrium value. Since the surface tension is a function of surface coverage it also will vary according to the surface motion. This time-dependent surface tension gives rise to a finite tangential surface stress. The two-dimensional stress tensor  $\sigma_{ij}$  depends both upon the normalized strain  $u_{ij}$  and the rate of strain  $\dot{u}_{ij}$ ,<sup>12</sup>

$$\sigma_{ij} = \gamma \delta_{ij} + \left( \varepsilon_d + \eta_d \frac{\partial}{\partial t} \right) u_{ll} \delta_{ij} + \left( \varepsilon_s + \eta_s \frac{\partial}{\partial t} \right) \times (2u_{ij} - u_{ll} \delta_{ij}), \quad (1)$$

where  $\gamma$  is the equilibrium surface tension,  $\varepsilon_d$  and  $\eta_d$  are the surface dilational elasticity and viscosity, respectively, and  $\varepsilon_s$  and  $\eta_s$  are the surface shear elasticity and viscosity, respectively. Summation notation is used for repeated indices. Dilational moduli describe resistance to changes in area; shear moduli describe resistance to changes in shape. Plastic effects have been ignored. The form of Eq. (1) is sufficiently complicated that several simplifying assumptions are usually made when considering experimental results. The shear parameters are usually considered to be small compared to the dilational parameters. Assuming an isotropic surface and sinusoidal straight-crested surface deformations (say index

<sup>a)</sup>Present address: Los Alamos National Laboratory, MS K764, Los Alamos, NM 87545.



$i=j=1$ ) with harmonic time dependence  $e^{i\omega t}$ ,

$$\sigma_{11} = \gamma + (\varepsilon_d + i\omega\eta_d)u_{11} = \gamma + \varepsilon u_{11}, \quad (2)$$

where a single (possibly complex) surface dilational modulus  $\varepsilon$  suffices to describe the deformation-induced surface stress. Diffusion of soluble surfactants between the interface and the bulk fluid means that the actual surface coverage (and thus  $\varepsilon$ ) depends upon the time scale of the surface deformation. This is true even when local thermodynamic equilibrium is assumed at the surface. If the frequency of the disturbance is fast enough so that little surface adsorption or desorption takes place or if the monolayer is insoluble, then  $\varepsilon$  may be considered to be time independent. This type of surface behaves elastically and can be described fully through the functional dependence of the equilibrium surface tension  $\gamma$  on the surface concentration  $\Gamma$ ,

$$\varepsilon = E \equiv - \frac{\partial \gamma}{\partial \ln \Gamma}, \quad (3)$$

where  $E$  is called the Gibbs elasticity.

The simplest case of a purely elastic surface has been studied extensively. For the damped propagation of capillary ripples on a water surface the boundary layer flow is predominantly potential in both the limits of zero and infinite elasticity  $E$ .<sup>11</sup> The damping is greater, however, in the limit [ $E \rightarrow \infty$ ] which is descriptive of a surface which is inextensible. The damping does not increase monotonically from the clean interface value to the inextensible interface value. Rather, there is a characteristic maximum value at a low value of elasticity,  $E \ll \gamma$ . The damping here is exactly twice the value of the infinite elasticity value.<sup>7</sup>

The situation is somewhat more complicated for the case of oscillations about a spherical shape. The framework for a general soluble surfactant at the interface of a spherical fluid within a host fluid has been worked out by Lu and Apfel.<sup>8,13</sup> Their results reduce to that of Miller and Scriven<sup>14</sup> in the case of an insoluble surfactant. Typically, the characteristic sizes of the fluid flow and diffusion boundary layers are small relative to the characteristic sizes of the disturbance (i.e., wavelength of capillary ripple or bubble radius). Thus, the overall geometry will dictate the quantitative details yet leave the basic free decay features unchanged. A complete description, however, requires knowledge of the interfacial concentration  $\Gamma$  and how the surface tension and viscoelastic parameters depend on that coverage and on time.

A general description of the expected behavior of quadrupole oscillations of a bubble in water in the presence of an insoluble surfactant is discussed by Asaki *et al.*<sup>9</sup> in light of the theoretical work of Miller and Scriven.<sup>14</sup> The essential result is that for constant surface tension and typical values of the interfacial viscosities the free quadrupole oscillation frequency and damping exhibit complicated structure as functions of the interfacial elasticity. Local maxima in the frequency and damping occur at elasticity values much less than the equilibrium surface tension (the surfactant concentration is low enough that the surface tension is not significantly affected). The frequency maximum can be several percent larger than the clean interface result while the damping maximum can be several *times* the clean interface result.

In the limit of large elasticity, the free decay approaches the limiting values of low frequency and large damping relative to the clean interface result. Similar results can be expected for solutions of soluble surfactants.<sup>8</sup>

Interfacial properties associated with soluble surfactants are typically made through surface tension measurements which can be carried out in any convenient geometry. Equilibrium measurements are sufficient for determining the dependence of the interfacial surfactant concentration on the bulk concentration.<sup>15</sup> If the surface can be considered primarily elastic, then one can also determine a Gibbs elasticity by Eq. (3).

## II. BUBBLE DISSOLUTION

The dissolution or growth of a stationary air bubble in a surfactant free fluid is well understood.<sup>16</sup> The governing equation,

$$\frac{\partial R}{\partial t} = \frac{-\kappa(c_s - c_i)}{\rho + 2\phi/3R} \left[ \frac{1}{R} + \frac{1}{(\pi\kappa t)^{1/2}} \right], \quad (4)$$

assumes that the host fluid is stationary and includes the pressure effects due to a curved interface. In Eq. (4)  $R$  is the instantaneous bubble radius,  $\kappa$  is the diffusivity of air in the host fluid, and  $c_i$  and  $c_s$  are the initial and saturation dissolved gas concentrations in the fluid, respectively. The air density  $\rho$  is that of air under the ambient external conditions of pressure and temperature. The parameter  $\phi$  contains pressure-density effects due to a curved interface under tension:

$$\phi = \frac{2m\gamma}{BT}, \quad (5)$$

where  $m$  is the molecular weight of the gas,  $\gamma$  is the interfacial tension,  $T$  is the temperature, and  $B$  is the gas constant. Surface tension effects will be important when  $R \ll \bar{R} \equiv 2\phi/3\rho$ . For clean water  $\bar{R} \approx 100 \mu\text{m}$ . The  $(\pi\kappa t)^{1/2}$  term represents enhanced dissolution in the early stage of an experiment during which the dissolved gas distribution is approaching a steady state. This term will be important as long as  $t \lesssim R^2/\pi\kappa$ . For a bubble in clean water with an initial radius of  $100 \mu\text{m}$ , this stage lasts about 2 or 3 min. For an initial radius of  $750 \mu\text{m}$ , however, this stage may last 1 h or more.

Liebermann<sup>17</sup> performed an experiment on the dissolution of an air bubble in water. The initial bubble radius was about  $700 \mu\text{m}$  and the experiment duration was about 5.5 h. In the analysis, the last term in Eq. (4) was neglected even though this term can have significant effects for the size of bubble observed. Discrepancy in the data from the expected result was explained in terms of "unavoidable surface contamination." An adequate representation of the data can also be obtained by application of the full equation (4).

Berge<sup>18</sup> examined air bubble dissolution in aqueous sucrose and NaCl solutions both in the presence and in the absence of an introduced dissolved protein. While the initial bubble radii were all less than  $11 \mu\text{m}$ , the  $(\pi\kappa t)^{1/2}$  term remained important due to the reduced diffusivity of the solution. Equation (4) was found to adequately describe the

dissolution in the absence of introduced protein. It is shown that the dissolution rates are reduced in the presence of the protein and that bubbles can become stabilized at  $R < 5 \mu\text{m}$ . This stabilization effect has also been observed with other surfactants and in seawater (e.g., see Refs. 19 and 20). On the other hand, Liebermann<sup>17</sup> reports that bubble dissolution rates were not significantly altered by the presence of a variety of surfactants.

The preceding discussion and experiments consider a bubble in a stationary fluid. A bubble trapped near a velocity antinode within an acoustic standing wave is subject to an oscillatory flow which may modify the diffusion of gas into the interfacial region. In addition, oscillating bubbles are subject to steady flow patterns in the presence of adsorbed surfactants.<sup>21</sup> These modifications can, in principle, be included in the theory as convective contributions, and limiting cases for laminar and turbulent flow are considered by Roesler.<sup>22</sup> Finite amplitude oscillations have also been shown to enhance dissolution rates of bubbles in clean water.<sup>23</sup>

The presence of surfactants can have significant effects on gas transfer during the process of rectified diffusion. The growth of small bubbles can be greatly enhanced by the presence of surfactants and thresholds for rectified diffusion are reduced.<sup>24,25</sup> Fyrrillas and Szeri<sup>26</sup> provide a theoretical basis for these observations and further show that in some cases bubble growth can be inhibited in the presence of surfactants. While the large bubbles studied here do not reach the threshold for rectified diffusion, it is possible that the small amplitude radial oscillations (driven by the acoustic radiation pressure used for levitation) alter the gas transfer across a contaminated interface in a similar manner.

### III. EXPERIMENT

Surface tension measurements of various solutions of TX were performed by a filter paper Wilhelmy plate technique.<sup>15</sup> A concentrated stock solution was prepared and various dilute concentrations were obtained by mixing known small quantities of this stock to distilled water samples. The surface tension  $\gamma$  plotted against the logarithm of the molar concentration  $M$  of TX is shown in Fig. 1. The two different symbols represent data obtained from two separate stock solutions on two different days. The temperature for all measurements was  $24.0 \pm 0.5^\circ\text{C}$ . There is very good agreement among the two data sets, suggesting that the ability to reproduce a given concentration is very good. The solid line is a ten-node spline fit to the data obtained from stock solution 2. It was found that about 2 h was necessary for a given solution to come to equilibrium. Also, the extrapolated value of the critical micelle concentration (0.21 mM) compared favorably with values obtained by other researchers.<sup>27-29</sup> Stock solution 2 was used in the experiments described below.

The experimental apparatus is shown in Fig. 2. A full description of the apparatus, experimental technique, and data analysis generally applicable to the study of acoustically levitated bubbles is given in the literature.<sup>10,30</sup> A brief description is given here. Single air bubbles were trapped in the host fluid by means of an ultrasonic levitator. The bubble

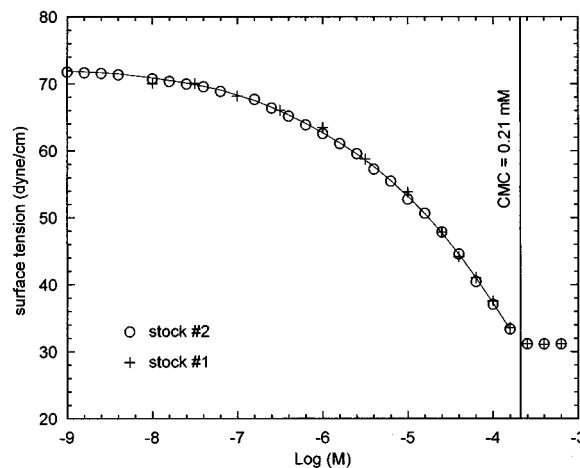


FIG. 1. Measured surface tension versus molar concentration of aqueous Triton X-100. Circles and crosses represent data taken on two separate days and from solutions mixed from two different stock solutions. The solid line is a ten-node spline fit to the data obtained from stock solution #2. The extrapolated critical micelle concentration (CMC) is 0.21 mM.

position is near the center of a  $9 \text{ cm} \times 9 \text{ cm} \times 7 \text{ cm}$  volume of fluid surrounded by plexiglas walls. Quadrupole shape oscillations were induced by modulation of the acoustic radiation pressure and detected by an optical extinction method. This detection scheme relies on the fact that small amplitude quadrupole oscillations produce a sinusoidal variation in the light power at the photodetector. Free decay of oscillations follows termination of the radiation pressure modulation. The time record of the oscillation decay was recorded on a digital oscilloscope. The complex frequency was obtained by fitting the decay record to an exponentially damped sinusoid. Bubble size and aspect ratio were determined from a digi-

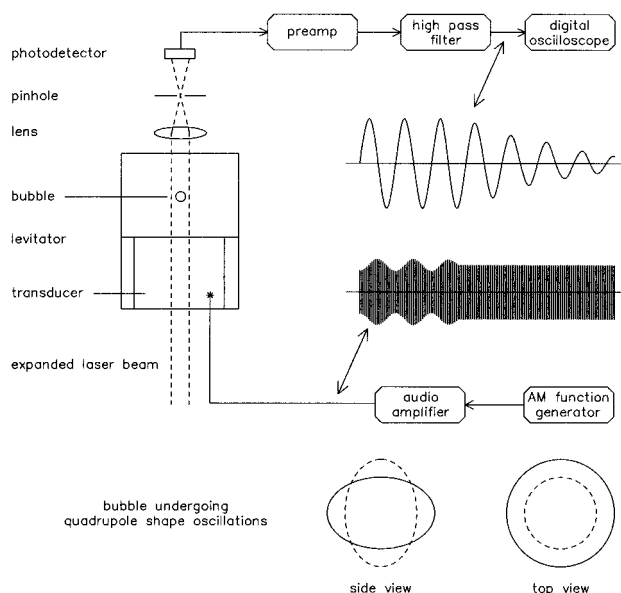


FIG. 2. Experimental setup. A levitated bubble is driven into small amplitude shape oscillations by means of modulated ultrasonic radiation pressure. The free decay of oscillations, subsequent to termination of the modulation, is recorded through an optical extinction method that utilizes the oscillation of the spherical horizontal cross section of the bubble as seen in top view.

tized image of the bubble profile taken immediately following the oscillation decay.

The variables used in the presentation of the data are as follows. The radius of a bubble  $R$  is the radius of a sphere that has the same volume as the given bubble. The aspect ratio  $A$  of a bubble is the ratio of the horizontal to vertical equilibrium diameters. The volume and aspect ratio are determined by a Legendre polynomial fit of the bubble image edge recorded by the CCD camera. The normalized frequency  $F$  and damping  $S$  are the ratio of the measured quantities (given by a fit to the digital oscilloscope record) to the theoretical expectations for a spherical bubble of radius  $R$  with a clean interface.<sup>10,14,31,32</sup> Frequency and damping shifts due to the slightly oblate equilibrium shape of the bubble are on the order of the deviation of the aspect ratio from unity.

Single air bubbles were studied in four separate solutions of TX. A fifth experiment was a control run of distilled water. The TX solutions were characterized by concentrations of  $\log(M) = -8.5, -8.0, -7.5,$  and  $-7.0$ . Each solution was prepared from water that was distilled and stored according to a well-defined repeatable procedure. While the initial dissolved gas concentration was not determined by any analytical means, there is no reason to suspect that it should vary significantly among solutions at the time of introduction into the levitation chamber. It was then allowed 2 h to come to equilibrium within the levitation chamber before a bubble was introduced. During this 2 h, the total solution volume of approximately 0.6 L was in contact with 0.15 L of air also within the levitation chamber. This equilibrium time was not imposed on the distilled water experiment. In each case a bubble was trapped and subsequently allowed to slowly dissolve into the liquid. Data were taken at intervals of 1.5–3 min beginning immediately after bubble injection. Quadrupole oscillation amplitudes were typically only a few percent of the bubble radius. Each bubble in TX solution had an initial radius of approximately  $750 \mu\text{m}$  and data were taken until the bubble size was reduced to about  $400 \mu\text{m}$  (rough limit of detection capability for highly damped shape oscillations). The bubble in clean water had an initial radius of  $650 \mu\text{m}$  and data were taken for 3 h.

## IV. RESULTS AND DISCUSSION

### A. Bubble dissolution

Radius versus time curves for the five bubbles are shown in Fig. 3. The open circles show the distilled water data while the other symbols represent the aqueous TX solution data as indicated. Each of the solid curves was obtained by numerical integration of Eq. (4) using the following parameter values:  $\kappa = 2 \times 10^{-5} \text{ cm}^2/\text{s}$ ;  $c_s = 2.7 \times 10^{-5} \text{ g/cm}^3$ ;  $\rho = 0.00114 \text{ g/cm}^3$ ;  $m = 28.9 \text{ g/mol}$ ;  $\gamma = 72.1 \text{ dyn/cm}$ ;  $B = 8.314 \times 10^7 \text{ erg/mol K}$ ;  $T = 297 \text{ K}$ . Curve A', which closely matches the clean water data, shows the predicted dissolution of a bubble with initial radius  $650 \mu\text{m}$  and  $c_i/c_s = 0.79$ . This curve does not represent a statistical best fit to the clean water data. The value, however, is quite reasonable for the employed water preparation procedure and should closely approximate the initial dissolved gas concentrations in each solution at the time of introduction into the levitation cham-

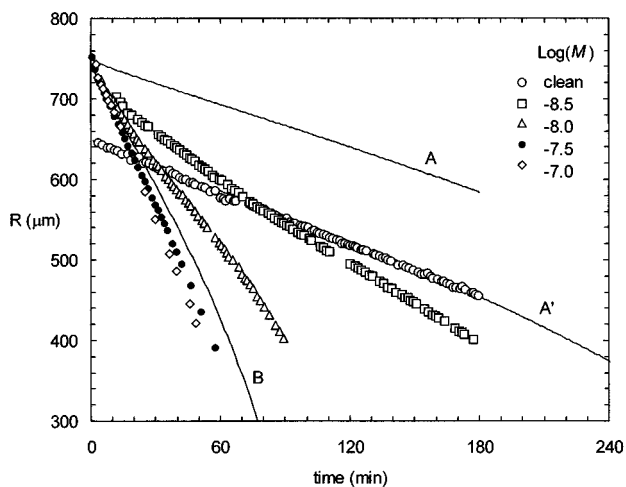


FIG. 3. Radius versus time curves for individual bubbles trapped in aqueous solutions of Triton X-100. Different symbol types indicate various surfactant solution concentrations. Curve A', which closely matches the clean water data, shows the predicted dissolution of a bubble for initial radius  $650 \mu\text{m}$  and  $c_i/c_s = 0.79$ . Curves A and B show the predicted dissolution of a bubble in clean water for initial radius  $750 \mu\text{m}$  and  $c_i/c_s = 0.79$  and  $0.00$ , respectively. Increased surfactant concentration appears to enhance the bubble dissolution rate.

ber. Since the TX solution experiments were allowed an additional 2 h of equilibration time it is inferred that  $c_i/c_s > 0.79$  at the time of bubble injection. The solid curves A and B show the predicted dissolution for a bubble of initial radius of  $750 \mu\text{m}$  and  $c_i/c_s = 0.79$  and  $0.00$ , respectively. Two significant results are noted. First, the presence of TX enhances the rate of gas transfer from the bubble to the water. This effect is clearly seen even for very dilute TX concentration. The corresponding surface concentration is also quite small as is indicated by the very small surface tension depression (Fig. 1). At the higher concentrations the dissolution rate exceeds that expected for water which is completely degassed. This is indicated by the data which lies below curve B. The second result is that the rate of gas transfer is an increasing function of the bulk TX concentration over the range studied.

These results are in marked contrast to previous studies both in terms of surfactant ability to alter dissolution<sup>17</sup> and in the nature of the dissolution enhancement.<sup>18</sup> Clearly, not all surfactants can be expected to affect gas transfer rates in the same manner. The effects seen in the presence of TX may be due to a number of different factors. Some enhancement may be due to steady flows present for oscillating bubbles. This seems an unlikely cause in the present work since this implies that all surfactants should show qualitatively similar results. Stearic acid on a bubble surface appears to show neutrality toward gas transfer.<sup>30</sup> In addition, the typical duty cycle of frequency modulation (and the resulting bubble shape oscillations) is less than 10%. A complete data record acquisition may take anywhere from 1.5–3 min, during which the bubble undergoes driven shape oscillations for 10–15 sec. The subsequent free decay of shape oscillations takes up only 10–300 ms. A more likely explanation is that gas transfer may be affected by surfactant mo-

lecular composition. For example, there is evidence that the hydrophilic polyoxyethylene TX backbone promotes the structural arrangement of local water molecules.<sup>33,34</sup> This may have the effects of altering  $c_s$  in the bulk as well as affecting gas diffusion rates at the bubble interface. These effects would not be present in the case of stearic acid.

### B. Free decay of quadrupole oscillations

Since the resonance frequency and damping constant associated with a given bubble continue to evolve over the course of an experiment, it is assumed that the interfacial concentration of TX is increasing with time and that true equilibrium with the bulk may not be achieved. It is assumed that this approach to equilibrium is slow enough that any single free decay takes place under quasi-static equilibrium conditions with respect to surfactant distribution. For any given record the actual surface concentration of surfactant is not recoverable. However, a long enough experiment would show that for a given bulk concentration the free decay properties would approach an asymptotic value in time. This result was not achieved in these experiments for two reasons. First, the rapid bubble dissolution quickly rendered the bubble too small for obtaining meaningful data, especially at the higher TX concentrations. Second, the eventual collection of additional contaminants on the bubble surface begins to affect the data after about two hours. These contaminants are presumably airborne in origin and travel to the bubble from the free surface of the host water by means of steady fluid flows in the levitator. Significantly improved clean water results were obtained by placing a piece of flat glass over the top of the levitator.<sup>10</sup> The largest bubbles which can be used for these sensitive measurements have radii of approximately  $750\ \mu\text{m}$ . Bubbles larger than this size exhibit unusually large damping of shape oscillations even in the absence of contaminants.<sup>30</sup> While the exact cause of this anomalous damping is not known, it is plausible that it originates from nonlinear coupling with the acoustic field. In this case it may be possible to utilize larger bubbles for these types of surfactant studies in acoustic levitators of modified geometry.

The normalized free decay frequency  $F$  and damping  $S$  of quadrupole shape oscillations are shown in Figs. 4 and 5, respectively. These studies exhibit all of the theoretical properties predicted for a bubble with an elastic or viscoelastic surface. At the lower TX concentrations ( $M$ ) both the frequency and damping are increasing functions of the surface TX coverage  $\Gamma$  (or time). For the larger  $M$ ,  $\Gamma$  becomes large enough to pass through the expected maxima in both the frequency and damping. The maximum frequency enhancement ( $F=1.22$ ) and high- $\Gamma$  limit ( $F=0.83$ ) are more pronounced than those of the insoluble surfactant stearic acid<sup>9</sup> ( $F=1.05$  and  $0.9$ , respectively) but are comparable to those observed for bubbles in seawater.<sup>10</sup> The observed frequency shifts cannot be explained in terms of surface tension changes alone; when  $\Gamma$  is very dilute, increased elasticity, predicted qualitatively by Eq. (3), is more important. The maximum damping enhancement ( $S=9$ ) is similar to studies of both stearic acid and seawater.

The continuing evolution of the free decay properties suggests that the bubble surface and the host fluid never

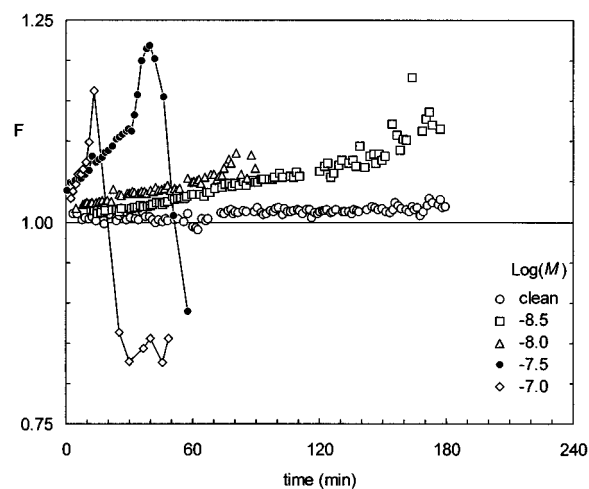


FIG. 4. Frequency associated with the free decay of quadrupole shape oscillations of bubbles trapped in aqueous solutions of Triton X-100. Each symbol type represents a single bubble observed in a solution of the indicated concentration. The lines connecting the high concentration data are drawn as guides to the eye. The symbols correspond to the same data set shown in Fig. 3.

reach equilibrium with respect to the TX distribution. The possible exception is the study carried out in the solution of highest  $M$ . It is not immediately clear why the shortest duration experiment should have the best chance to come to equilibrium. It is possible that the rapid reduction in bubble surface area associated with the high dissolution rate aids in the concentration of surface TX, leading to a quicker approach to equilibrium.

### V. CONCLUSION

Nearly spherical single air bubbles acoustically trapped in solutions of Triton X-100 have been studied for periods of up to 3 h. Dissolution measurements were made by examining digitized images of the bubble profile. The presence of the surfactant was shown to significantly enhance the rate of

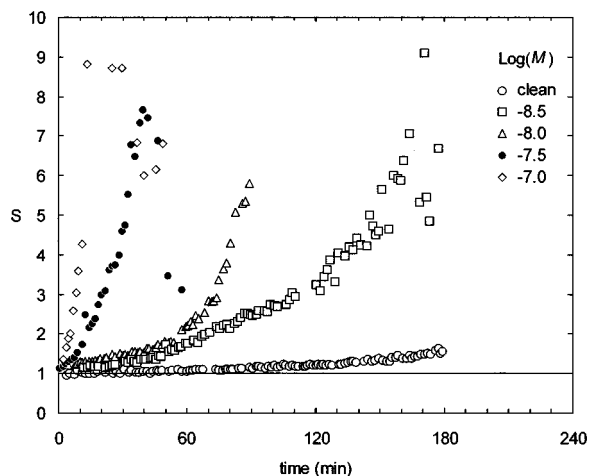


FIG. 5. Damping constant associated with the free decay of quadrupole shape oscillations of bubbles trapped in aqueous solutions of Triton X-100. Each symbol type represents a single bubble observed in a solution of the indicated concentration. The symbols correspond to the same data sets shown in Figs. 3 and 4.

gas transfer into the liquid even at very dilute concentrations. Free decay of quadrupole shape oscillations were induced by temporary modulation of the acoustic radiation pressure. The decay record was obtained by an optical extinction technique. The frequency and damping of these oscillations were recorded as functions of time and surfactant concentration. All of the features expected for a system with a (visco)elastic interface were shown to be present: (1) at very dilute surfactant concentrations (early times) the frequency and damping approach the expected values for a clean interface; (2) both frequency and damping exhibit maxima at characteristic low concentrations; and (3) at high concentrations the frequency is reduced due to surface tension depression and the damping approaches a value several times the clean interface value. Maximal damping values were found to be approximately nine times the clean interface value. Observed frequency enhancements of several percent were due to increased surface elasticity.

This study extended previous work on acoustically levitated samples which demonstrate the utility of these methods for studying interfacial properties of materials. Small isolated samples can be examined over long periods of time under noncontact conditions. The use of a spherical geometry can provide enhanced viscoelastic features (relative to analogous flat surface capillary ripple studies) which are readily observable. Disadvantages of these methods include sample size limitations, a shortened observation time window associated with rapid bubble dissolution, temporal overhead associated with data acquisition, and the (usually) necessary partial degassing of host liquids. The extraction of viscoelastic constants from data is complicated by their non-trivial dependence on surfactant distribution. Nevertheless, the techniques may prove useful in understanding any number of processes in which a liquid interface plays a role.

## ACKNOWLEDGMENT

This work was supported by the United States Office of Naval Research.

<sup>1</sup>T. G. Leighton, *The Acoustic Bubble* (Academic, New York, 1994).

<sup>2</sup>*The Climate and Health Implications of Bubble-Mediated Sea-Air Exchange*, edited by E. C. Monahan and M. A. Van Patten (Connecticut Sea Grant, Groton, CT, 1989).

<sup>3</sup>D. A. Edwards, H. Brenner, and D. T. Wasan, *Interfacial Transport Processes and Rheology* (Butterworth-Heinemann, Woburn, MA, 1991).

<sup>4</sup>L. A. Crum, "Sonoluminescence, sonochemistry, and sonophysics," *J. Acoust. Soc. Am.* **95**, 559–562 (1994).

<sup>5</sup>T. R. Stottlemyer and R. E. Apfel, "The effects of surfactant additives on the acoustic and light emissions from a single stable sonoluminescing bubble," *J. Acoust. Soc. Am.* **102**, 1418–1423 (1997).

<sup>6</sup>B. A. Noskov, "Influence of a monolayer of stearic acid on damping of capillary waves," *Kolloidin. Zh.* **50**, 1035–1039 (1988).

<sup>7</sup>E. H. Lucassen-Reynders and J. Lucassen, "Properties of capillary waves," *Adv. Colloid Interface Sci.* **2**, 347–395 (1969).

<sup>8</sup>H. Lu and R. E. Apfel, "Shape oscillations of drops in the presence of surfactants," *J. Fluid Mech.* **222**, 351–368 (1991).

<sup>9</sup>T. J. Asaki, D. B. Thiessen, and P. L. Marston, "Effect of an insoluble

surfactant on capillary oscillations of bubbles in water: observations of a maximum in the damping," *Phys. Rev. Lett.* **75**, 2686–2689 (1995); **75**, 4336(E) (1995).

<sup>10</sup>T. J. Asaki and P. L. Marston, "Free decay of shape oscillations of bubbles acoustically trapped in water and sea water," *J. Fluid Mech.* **300**, 149–167 (1995).

<sup>11</sup>V. G. Levich, *Physicochemical Hydrodynamics* (Prentice-Hall, Englewood Cliffs, NJ, 1962).

<sup>12</sup>J. A. Mann, "Dynamic surface tension and capillary waves," *Surf. Colloid Sci.* **13**, 145–212 (1984).

<sup>13</sup>H. Lu and R. E. Apfel, "Quadrupole oscillations of drops for studying interfacial properties," *J. Colloid Interface Sci.* **134**, 245–255 (1990).

<sup>14</sup>C. A. Miller and L. E. Scriven, "The oscillations of a fluid droplet immersed in another fluid," *J. Fluid Mech.* **32**, 417–435 (1968).

<sup>15</sup>G. L. Gaines, *Insoluble Monolayers at Liquid-gas Interfaces* (Wiley, New York, 1966).

<sup>16</sup>P. S. Epstein and M. S. Plesset, "On the stability of gas bubbles in liquid-gas solutions," *J. Chem. Phys.* **18**, 1505–1509 (1950).

<sup>17</sup>L. Liebermann, "Air bubbles in water," *J. Appl. Phys.* **28**, 205–211 (1957).

<sup>18</sup>L. I. Berge, "Dissolution of air bubbles by the resistive pulse and the pressure reversal technique," *J. Colloid Interface Sci.* **134**, 548–562 (1990).

<sup>19</sup>B. D. Johnson and R. C. Cooke, "Generation of stabilized microbubbles in seawater," *Science* **213**, 209–211 (1981).

<sup>20</sup>J. S. D'Arrigo, "Biological surfactants stabilizing natural microbubbles in aqueous media," *Adv. Colloid Interface Sci.* **19**, 253–307 (1983).

<sup>21</sup>V. A. Murtsovkin and V. M. Muller, "Steady-state flows induced by oscillations of a drop with an adsorption layer," *J. Colloid Interface Sci.* **151**, 150–156 (1992).

<sup>22</sup>F. C. Roesler, "Comment on 'Gas bubbles in solutions,'" *J. Chem. Phys.* **19**, 512–513 (1951).

<sup>23</sup>T. J. Asaki, P. L. Marston, and E. H. Trinh, "Shape oscillations of bubbles in water driven by modulated ultrasonic radiation pressure: observations and detection with scattered laser light," *J. Acoust. Soc. Am.* **93**, 706–713 (1993).

<sup>24</sup>L. A. Crum, "Measurements of the growth of air bubbles by rectified diffusion," *J. Acoust. Soc. Am.* **68**, 203–211 (1980).

<sup>25</sup>L. A. Crum, "Acoustic cavitation series part five—rectified diffusion," *Ultrasonics* **22**, 215–223 (1984).

<sup>26</sup>M. M. Fyrillas and A. J. Szeri, "Dissolution or growth of soluble spherical oscillating bubbles. The effects of surfactants," *J. Fluid Mech.* **277**, 381–407 (1994).

<sup>27</sup>A. Chattopadhyay and E. London, "Fluorometric determination of critical micelle concentration avoiding interference from detergent charge," *Anal. Biochem.* **139**, 408–412 (1984).

<sup>28</sup>C. Samsonoff, J. Daily, R. Almog, and D. S. Berns, "The use of Coomassie brilliant blue for critical micelle concentration determination of detergents," *J. Colloid Interface Sci.* **109**, 325–329 (1986).

<sup>29</sup>N. Kawashima, N. Fujimoto, and K. Meguro, "Determination of critical micelle concentration of several nonionic surfactants by azo-hydrazone tautomerism of anionic dye," *J. Colloid Interface Sci.* **103**, 459–465 (1985).

<sup>30</sup>T. J. Asaki, "Shape oscillations of bubbles in water driven by modulated ultrasonic radiation pressure and applications to interfacial dynamics," Ph.D. thesis, Washington State University, 1995.

<sup>31</sup>P. L. Marston, "Shape oscillations and static deformation of drops and bubbles driven by modulated radiation stresses—theory," *J. Acoust. Soc. Am.* **67**, 15–26 (1980).

<sup>32</sup>A. Prosperetti, "Free oscillations of drops and bubbles: the initial value problem," *J. Fluid Mech.* **100**, 333–347 (1980).

<sup>33</sup>Y. C. Kong, D. Nicholson, N. G. Parsonage, and L. Thompson, "Monte-Carlo simulations of a single polyoxyethylene C<sub>12</sub>E<sub>3</sub> chain headgroup fixed on a bilayer surface in water," *J. Chem. Soc. Faraday Trans.* **91**, 4261–4268 (1995).

<sup>34</sup>K. Tasaki, "Polyoxyethylene-water interactions: A molecular-dynamics study," *J. Am. Chem. Soc.* **118**, 8459–8469 (1996).

# Comparisons of exact and approximate convection of plane waves in a simple shear flow

Laurine Leep-Apolloni

*Computer Aided Engineering Department, Ford Research Laboratory, Dearborn, Michigan 48121*

David R. Dowling

*Department of Mechanical Engineering and Applied Mechanics, University of Michigan, Ann Arbor, Michigan 48109*

(Received 30 September 1996; revised 24 May 1997; accepted 12 August 1997)

In aero- and environmental-acoustic problems, propagation of sound waves through a medium with a nonuniform mean flow has commonly been treated by several different approximate techniques typically involving integral transforms, geometrical acoustics, or other approximate methods. An effectively exact solution technique that properly incorporates the vector character of mean-flow convection has been found [L. Nijs and C. P. A. Wapenaar, *J. Acoust. Soc. Am.* **87**, 1987–1998 (1990)]. However, the formal and numerical complexity of these techniques, typically coupled with nontrivial impedance boundary conditions, has prevented detailed comparisons of acoustic field variables with and without exact treatment of convection. This paper presents results and comparisons between exact and approximate treatments of acoustic plane waves propagating in a simple shear flow. The solution of the linearized time- and space-dependent equations of inviscid fluid motion, as nondimensionalized herein, depends on two-dimensionless parameters,  $m/f$  and  $ft$ , where  $m$  is the convecting flow's shear rate,  $f$  is the acoustic frequency, and  $t$  is the length of time that the plane waves interact with the shear flow. The exact treatment involves numerical solution of the governing equations. The approximate treatment is handled with a WKB solution valid for  $m/f \ll 1$ . A comparison of results shows that the approximate treatment of convection produces only single digit percentage errors when  $(m/f)(ft) = mt \lesssim 0.5$ . However, pressure amplitude differences increase rapidly beyond  $mt \approx 0.5$  and are found to grow approximately as  $\exp\{+0.4(mt)^2\}$ . In addition, the computed results display phenomena that are completely absent from the WKB solution such as: (i) dynamic misalignment of the acoustic-velocity vector and the wave front normal; and (ii) the existence of significant acoustic perturbation vorticity. © 1997 Acoustical Society of America. [S0001-4966(97)06011-6]

PACS numbers: 43.28.Py, 43.20.Hq [LCS]

## INTRODUCTION

The convection of sound waves by inhomogeneous flow is ubiquitous in atmospheric, automotive, and aeronautical acoustics, and is of concern for noise prediction, noise control, and remote sensing applications. In many cases, the effects of convection on acoustic propagation dominate influences from medium nonuniformity in density, temperature, static pressure, or fluid composition. Unfortunately, turbulent fluctuations in the background flow preclude exact solutions (or even computations) of acoustic convection at the flow Reynolds numbers of interest. In fact, acoustic medium nonuniformity poses inherently difficult problems and has only yielded exact analytical solutions for acoustic propagation under nonflowing circumstances with linear variation in acoustic properties (Li *et al.*, 1990). When background flow is present, exact analytical treatments of acoustic propagation exist only for regions of uniform flow with thin planar boundaries (Morse and Ingard, 1968; Goldstein, 1976; Pierce, 1989). This paper presents a scientific study that focuses on the simplest case of nonuniform acoustic convection: plane wave propagation in an infinite uniformly sheared medium that is otherwise quiescent and homogeneous. While damping, scattering, and generation of sound

by shear-flow turbulence (i.e., Howe, 1995) is beyond the scope of this paper, the findings of this study may provide some insight into these more complex phenomena.

Acoustic convection by nonuniform flow has been treated by several successful approximate techniques that involve at least two simplifications of the full nonlinear conservation equations for inviscid compressible fluid flow (Thompson, 1972). The first approximation, common to all techniques and to this study, is the standard linearization of the fluid-dynamic field equations for acoustic wave fluctuation amplitude approaching zero. The second acoustic convection approximation has been varied to meet application-specific geometric and technical requirements, but it typically amounts to a high-frequency and/or low Mach number formulation of the linearized governing equations. In its simplest version, called the standard approximation in this paper, the speed of sound,  $c$ , is locally modified to account for the fluid convection speed,  $U$ , via  $c(\mathbf{x}) = c_0 + U(\mathbf{x})$ , where  $c_0$  is a constant reference speed of sound. The resulting Helmholtz equation can be solved exactly (if possible), or approximately by a variety of geometric- or ray-acoustic techniques (Lamancusa and Daroux, 1993; Salomons, 1994a, b; Li *et al.*, 1994), or higher-order asymptotic expansions (Sec. III). A more rigorous term-by-term analysis of the lin-

earized fluid dynamic equations by Pierce (1990) showed how a single wave equation can be obtained for a time-and-space varying medium when terms involving temporal and spatial gradients of the medium are neglected compared to equivalent terms involving acoustic field variables. This equation, and others like it but less formally derived, have been the starting point for recent studies of acoustic propagation in nonuniform media (Norton, 1991; Wilson, 1993). The parabolic approximation to the wave equation has also been applied to acoustic propagation in a flowing media with cross-stream flow speed variations (Robertson *et al.*, 1995). A fourth approach, summarized in Pierce (1989), involves assuming that the acoustic velocity is everywhere perpendicular to the acoustic wavefronts and leads to a modified conservation statement for acoustic energy. The current computational effort differs from these studies in that no additional approximation beyond linearization of the governing equations has been made. This linearization-only approach has allowed a previously undocumented wave strengthening mechanism that ultimately limits the accuracy of the other approaches to be identified.

Previous computations of linear-acoustic propagation in a nonuniform flowing atmosphere incorporating the vector nature of true convection (Nijs and Wapenaar, 1990) have been performed through transforming the acoustic equations into Fourier space and then assembling numerical solutions within layers oriented perpendicular to the gradient in the nonuniformity, i.e., horizontal layers with a vertical variation in convection speed. The solution technique is effectively exact for layers much thinner than an acoustic wavelength. However, the authors' neglect of variation in static pressure with height and use of an approximate one-dimensional radial spectrum, while including an exact formulation of acoustic convection, has been a source of technical discussion (Raspet *et al.*, 1992; Nijs and Wapenaar, 1992). Unfortunately, the formal complexity of this technique and the differing emphases of the various approximate formulations has prevented a detailed comparison of acoustic field quantities with and without convection approximations. Such comparisons are presented here and serve to define the proper envelope of application for the standard convection approximation.

This paper addresses only the fundamental aspects of acoustic wave interaction with nonuniform flow by presenting results that would naturally follow a textbook discussion of acoustic propagation in uniform flow. To achieve this goal, the starting point of Nijs and Wapenaar was adopted, but a plane-wave source was chosen instead of a point source to eliminate the complication of wavefront curvature. The nondimensional linearized equations are solved numerically for a harmonic plane [frequency= $f$ (Hz)] launched horizontally in an infinite homogenous medium with a uniform-cross stream convection velocity gradient [ $dU/dy=m$  = constant( $s^{-1}$ )], where  $y$  is the cross-stream coordinate). These computations are compared to a WKB solution of the equivalent Helmholtz equation generated using the standard approximation,  $c(y)=c_0+U(y)$ . To reduce formal complexity, all the computations were performed directly for the nondimensional acoustic field variables,  $p^*$ =pressure fluctuation,

$u^*$ =downstream velocity fluctuation, and  $v^*$ =cross-stream velocity fluctuation, without integral transforms in space or time. With these simplifications, the problem is governed by two dimensionless parameters. The first,  $m/f$ , arises naturally from dimensionless scaling of the field equations and represents the change of the convection-flow Mach number,  $d(U/c_0)$ , per unit change in the  $y$  direction on a per-wavelength basis,  $d(yf/c_0)$ . The second dimensionless ratio,  $ft$  ( $t$ =the length of time that the waves interact with the shear), is determined by the size of the computational domain. These two parameters were varied to determine quantitatively how the differences between exact and approximate treatments evolve as the acoustic wave travels downstream (i.e., as  $t$  increases). The standard approximation was chosen for the comparisons because of its analytic simplicity, and because it represents the greatest meaningful simplification of the full equations that still embodies convective effects. The comparisons include examination of differences in wavefront location, wave amplitude, acoustic perturbation vorticity, and rotation angles of the wavefronts and acoustic-velocity vectors. Here, the acoustic perturbation vorticity is  $\omega_z = \partial v/\partial x - \partial u/\partial y$ , where  $u$  and  $v$  are the acoustic perturbation velocities, and  $x$  and  $y$  are the downstream (horizontal) and cross-stream (vertical) coordinates, respectively. The existence of significant acoustic perturbation vorticity in the simple flow field studied here suggests extensive nontrivial coupling between acoustic and turbulent fluctuations in flows of engineering interest. For comparison,  $\omega_z$  is either approximately or identically zero for most acoustic waves.

While the current problem formulation is too simplistic for direct application to many practical aero- and environmental-acoustic engineering situations, the current results should properly predict parametric trends, and indicate the accuracy of the standard convection approximation and related WKB techniques in more complicated situations when appropriate average shear rates, frequencies, and interaction times are used. In fact, the chosen simplifications render the comparisons independent of both the shear-flow Mach number and the speed of sound, thus making these results applicable to shear flows in either gases or liquids.

The two dimensionless parameters,  $m/f$  and  $ft$ , provide a complete description of plane-wave shear-flow interaction. The parameter  $m/f$  sets the relative strength of the background shear with  $m/f=0$  naturally corresponding to a static medium. The parameter  $ft$  is a counter for the number of acoustic cycles of wave shear-flow interaction. Their product,  $(m/f)(ft)=mt$ , scales the amount of rotation of the acoustic wave fronts. In a typical atmospheric propagation situation ( $f=100$  Hz,  $m=0.3 s^{-1}$ , and a path length of 1 km yielding  $t\approx 3$  s),  $m/f=0.003$ ,  $ft=300$ , and  $mt=0.9$ . Similar values of  $mt$  are found in the turbulent wake flow of a moving automobile. Near a moving vehicle, shear zones develop between the flow passing over the vehicle (typically at 30 m per  $s\approx 65$  mph) and the recirculating flow trapped directly behind the vehicle (average flow velocity near zero with respect to the vehicle). For a typical automobile, the wake extends for approximately two vehicle lengths (about 10 m) behind the vehicle with a half-width of approximately 1 m.

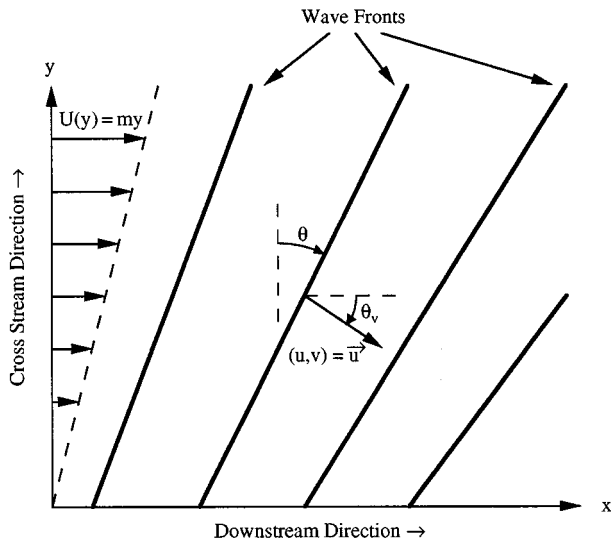


FIG. 1. Schematic of the problem geometry. Here,  $U(y) = my$  is the convection velocity. The  $x$  axis lies in the (horizontal) downstream direction and the  $y$  axis lies in the (vertical) cross-stream direction. An acoustic plane wave is launched from  $x=0$  with a uniform amplitude of unity, and rotates through angle  $\theta$  as it propagates downstream as a result of its interaction with the convection velocity. The angle that the acoustic-velocity vector makes with downstream direction is  $\theta_v = \tan^{-1}\{-v/u\}$ . When  $m=0$ ,  $\theta = \theta_v$ .

In this case ( $f = 100$  Hz,  $m = 30 \text{ s}^{-1}$ , and  $t = 30$  ms), the dimensionless numbers are  $m/f = 0.3$ ,  $ft = 3$ , and  $mt = 0.9$ . The findings presented in the following sections suggest that the standard convection approximation accumulates a 10% deficit in wave strength for  $mt \approx 0.5$ , which grows rapidly as  $mt$  increases beyond 0.5. Hence, acoustic propagation predictions for both of these examples should benefit from an exact treatment of convection.

The remainder of this paper is broken into five sections. The next section specifies the formulation of the problem. The numerical technique used for the exact convection computations is presented in Sec. II. The analytic solution valid for  $m/f \rightarrow 0$  based on the standard convection approximation is described in Sec. III. Comparisons between the numerically exact results and those from the standard convection approximation are given in Sec. IV. The final section contains the conclusions drawn from this research.

## I. PROBLEM FORMULATION AND GEOMETRY

The geometric formulation of the problem is shown schematically in Fig. 1. A plane acoustic wave with frequency  $f$  is launched at  $x=0$  with an initial propagation direction parallel to the  $x$  axis (the downstream or streamwise direction). Except for a nonuniform background flow convection velocity, the acoustic medium is uniform with density  $\rho_0$  and speed of sound  $c_0$ . The convection velocity,  $U$ , is also parallel to the  $x$  axis and depends only on the (vertical) cross-stream coordinate,  $y$ , in a linear fashion,  $U(y) = my$  with  $m = \text{constant}(\text{s}^{-1})$ . The wave propagation domain is two dimensional and semi-infinite. The wavecrest turning angle,  $\theta$ , is measured from the cross-stream direction. The acoustic-velocity turning angle,  $\theta_v = \tan^{-1}\{-v/u\}$ , is

measured from the (horizontal) downstream direction. For plane waves in the absence of flow convection,  $\theta$  and  $\theta_v$  are equal. The two main reasons for studying this geometry and these parameters are to: (i) determine the parametric range of applicability of the standard convection approximation; and (ii) elucidate the wave physics that are neglected when the standard convection approximation is used.

In  $x$ - $y$  Cartesian coordinates, the governing fluid dynamic and constitutive equations, linearized for small acoustic amplitude are

$$\frac{\partial \rho}{\partial t} + U \frac{\partial \rho}{\partial x} + \rho_0 \left( \frac{\partial u}{\partial x} + \frac{\partial v}{\partial y} \right) = 0, \quad (1)$$

$$\frac{\partial u}{\partial t} + U \frac{\partial u}{\partial x} + \frac{1}{\rho_0} \frac{\partial p}{\partial x} = -v \frac{dU}{dy}, \quad (2)$$

$$\frac{\partial v}{\partial t} + U \frac{\partial v}{\partial x} + \frac{1}{\rho_0} \frac{\partial p}{\partial y} = 0, \quad (3)$$

$$p = c_0^2 \rho, \quad (4)$$

where  $\rho$ ,  $u$ ,  $v$ , and  $p$  are the field variables for acoustic density, downstream velocity, cross-stream velocity, and pressure, respectively. These four equations represent conservation of mass (1), conservation of downstream momentum (2), conservation of cross-stream momentum (3), and the linearized isentropic equation of state for the acoustic medium (4). Four terms in Eqs. (1)–(3) involve the convection velocity,  $U$ . The three that appear on the left-hand sides represent convection of the acoustic field variables by  $U$ . The lone  $U$  term on the right side of Eq. (2) represents acoustic convection of the background flow and is effectively a source term for the downstream acoustic velocity that allows the acoustic wave to be strengthened by the background flow once the wave has turned appreciably. There is no equivalent source term in the standard convection-approximation formulation.

The actual wave strengthening mechanism is not hard to understand, and is based on the acoustic wave acquiring energy from the nonuniformity in the background flow. For an ordinary plane wave traveling downstream at angle  $\theta \neq 0$  with respect to the cross-stream axis (Fig. 1), negative  $v$  velocity and positive  $u$  velocities are in phase, i.e.,  $-v$  and  $+u$  are both maximal (minimal) at an acoustic pressure crest (trough). When the shear rate,  $m = dU/dy$ , is positive, negative  $v$  velocity transports higher-convection speed fluid to lower-convection speed regions (and vice versa). When  $-v$  and  $+u$  are in phase, the higher-speed fluid transported by the negative  $v$  velocity makes an in-phase contribution to the positive  $u$  velocity. This augmentation to the  $u$  velocity strengthens the acoustic wave at the expense of the background flow. As will be seen in the following sections, the plane waves of this study are modified by the shear flow but remain planar, and the necessary phase relationship between  $u$  and  $v$  is maintained for the wave strengthening mechanism described here to be effective.

To simplify the later comparisons and reduce the number of independent parameters, the governing equations were cast into dimensionless form by scaling both dependent and independent variables:  $\rho^* = \rho/\rho_0$ ,  $u^* = u/c$ ,  $v^* = v/c$ ,  $p^*$



$=p/(\rho_0 c_0^2)$ ,  $t^* = ft$ ,  $x^* = fx/c_0$ , and  $y^* = fy/c_0$ . With this scaling,  $U = mc_0 y^*/f$  and Eq. (4) becomes  $\rho^* = p^*$ , so Eqs. (1)–(3) are reduced to

$$\frac{\partial p^*}{\partial t^*} + \frac{m}{f} y^* \frac{\partial p^*}{\partial x^*} + \frac{\partial u^*}{\partial x^*} + \frac{\partial v^*}{\partial y^*} = 0, \quad (5)$$

$$\frac{\partial u^*}{\partial t^*} + \frac{m}{f} y^* \frac{\partial u^*}{\partial x^*} + \frac{\partial p^*}{\partial x^*} = -\frac{m}{f} v^*, \quad (6)$$

$$\frac{\partial v^*}{\partial t^*} + \frac{m}{f} y^* \frac{\partial v^*}{\partial x^*} + \frac{\partial p^*}{\partial y^*} = 0. \quad (7)$$

In Eqs. (5), (6), and (7), the dimensionless parameter  $m/f$  appears four times as part of the convection and source terms, and the scaled zero-convection acoustic wave speed is unity. Note that  $c_0$  does not appear in Eqs. (5), (6), or (7).

The boundary conditions on the acoustic variables at  $x^* = 0$  were straightforward. For the exact-convection computations (Sec. II), a plane-wave source with scaled acoustic pressure amplitude of unity was imposed, and the cross-stream acoustic velocity was set to zero,

$$p^*(0, y^*, t^*) = u^*(0, y^*, t^*) \quad (8a)$$

$$= \sin(2\pi t^*), \quad (8b)$$

$$v^*(0, y^*, t^*) = 0, \quad (8c)$$

to launch acoustic waves into the domain. For the WKB solution of the approximate-convection Helmholtz equation (Sec. III), two boundary conditions on the acoustic pressure were required to launch a plane-wave equivalent to that in the exact-convection computations. The first boundary condition, applied at  $x^* = 0$ , was

$$p^*(0, y^*, t^*) = \sin(2\pi t^*). \quad (9)$$

The second was a causality or radiation condition that ensured only downstream propagating acoustic waves.

## II. EXACT-CONVECTION COMPUTATIONAL TECHNIQUE

The exact-convection computations were based on an explicit numerical time marching of Eqs. (5), (6), and (7) using the MacCormack predictor–corrector method (Anderson, 1984) with first-order differencing in time and space with the time step  $\delta t^*$  equal to one-third to one-tenth of the spatial step sizes in both directions,  $\delta x^* = \delta y^* = 0.01$ . This resolution corresponds to more than 333–1000 time steps per acoustic period and 100 grid points per zero-convection acoustic wavelength. Single precision arithmetic was used for all the computations.

The plane wave is launched from the left boundary ( $x^* = 0$ ) by imposing Eqs. (8a)–(8c). The top and bottom boundaries ( $y^* = 0$  and  $y^* = y_{\max}^*$ , with  $y_{\max}^*$  typically near or above 10) employ one-sided differencing of the governing equations (i.e., the predictor and corrector steps use the same first differences) while the exit boundary uses an outflow (no streamwise gradient) condition. Unfortunately, the boundary conditions on the free sides of the computational domain were not perfectly nonreflecting. Other nonreflecting boundary conditions were tested, including the Orlandi boundary

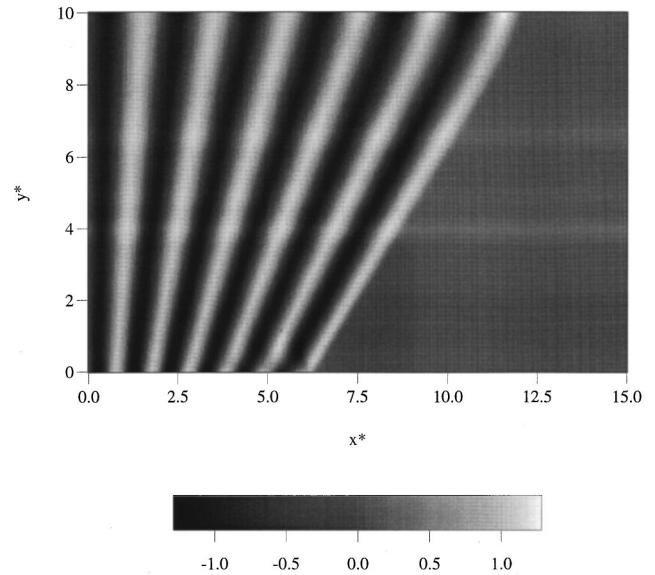


FIG. 2. Computed acoustic pressure field for  $m/f = 0.1$  and  $t^* = 6$ . The computational grid has 1501 points in the downstream direction and 1001 in the cross-stream direction. The acoustic waves strengthen slightly as they propagate. Wavefront distortion near the upper and lower portion of the domain is caused by the imperfect boundary conditions on these domain boundaries. To eliminate spurious results from these regions, results are only drawn from a band  $2c_0/f$  wide, centered between the upper and lower boundaries;  $4 < y^* < 6$ .

condition (Orlandi, 1976) which is based on estimating a local wave celerity from the computed solution, but one-sided differencing was found to be the most robust. The influence of the exit boundary was effectively eliminated by terminating the computation before the leading wavecrest reached the downstream domain edge. The influence of the top and bottom of the domain was mitigated by only drawing results from 200 grid points (a dimensional distance of two zero-shear wavelengths,  $2c_0/f$ ) centered within the cross-stream extent of the computational domain. The final results shown herein were confirmed to be independent of domain size. In all computed cases, results from the leading wavecrest are discarded since they were slightly contaminated by numerical diffusion and dispersion.

A typical wave field, for  $m/f = 0.1$  and  $t^* = 6$ , is shown on Fig. 2. Note that during the elapsed time of  $t^* = 6$ , six waves are generated and that the wave speed at  $y = 0$  is nearly unity in the scaled coordinates. The wave field near  $y^* = y_{\max}^*$  shows some wave front curvature because the boundary condition is unable to produce the appropriate extension of the computed acoustic waves which would be entering the domain through this boundary. Likewise, the wave field near the lower boundary shows some influence of reflections from  $y^* = 0$ . However, the central section of this wave field,  $4 < y^* < 6$ , is relatively uninfluenced by these boundary condition imperfections. The main features investigated in this type of wave field are (i) the location of the pressure extrema, (ii) the angle of rotation of the locus of the pressure extrema, (iii) the acoustic pressure amplitude, (iv) the relative rotation angle of the acoustic velocity, and (v) the existence and persistence of acoustic perturbation vorticity.

### III. WKB SOLUTION FOR APPROXIMATE CONVECTION

To provide both verification and comparison results for the computations, an asymptotic solution to the equivalent approximate-convection problem was sought. For the chosen problem and geometry, the standard convection approximation can be made in Eqs. (1)–(4) by setting  $U=0$  and replacing  $c_0$  with  $c(y)=c_0+my$  to yield

$$\frac{\partial \rho}{\partial t} + \rho_0 \left( \frac{\partial u}{\partial x} + \frac{\partial v}{\partial y} \right) = 0, \quad (10)$$

$$\frac{\partial u}{\partial t} + \frac{1}{\rho_0} \frac{\partial p}{\partial x} = 0, \quad (11)$$

$$\frac{\partial v}{\partial t} + \frac{1}{\rho_0} \frac{\partial p}{\partial y} = 0, \quad (12)$$

$$p = (c_0 + my)^2 \rho. \quad (13)$$

The usual cross differentiation to eliminate the acoustic velocities and density fluctuation, along with the assumption of a time harmonic pressure field, yields a Helmholtz equation with nonuniform speed of sound:

$$\frac{\partial^2 \tilde{p}}{\partial x^2} + \frac{\partial^2 \tilde{p}}{\partial y^2} + \frac{\omega^2}{(c_0 + my)^2} \tilde{p} = 0, \quad (14)$$

where  $p(x, y, t) = \tilde{p}(x, y) e^{-i\omega t}$ ,  $\omega = 2\pi f$ , and the boundary condition at  $x=0$  is  $\text{Re}\{\tilde{p}(0, y) e^{-i\omega t}\} = \sin(\omega t)$ . Under these approximations, the wave- and velocity-turning angles,  $\theta$  and  $\theta_v$  (geometrically defined in Fig. 1), are always equal. A change of coordinates involving the wave-turning angle  $\theta$  and the distance,  $r$ , from the point  $x=0$ ,  $y = -c_0/m$ :

$$x = r \sin \theta, \quad (15a)$$

$$y = r \cos \theta - c_0/m, \quad (15b)$$

converts Eq. (14) to

$$\frac{\partial^2 \tilde{p}}{\partial r^2} + \frac{1}{r} \frac{\partial \tilde{p}}{\partial r} + \frac{1}{r^2} \frac{\partial^2 \tilde{p}}{\partial \theta^2} + \frac{\omega^2}{m^2 r^2 \cos^2 \theta} \tilde{p} = 0. \quad (16)$$

By attempting a separation of variables solution:  $\tilde{p}(r, \theta) = R(r)\Theta(\theta)$ , Eq. (16) can be broken down into two equations valid when  $r \neq 0$ :

$$r^2 \frac{\partial^2 R}{\partial r^2} + r \frac{\partial R}{\partial r} - \gamma^2 R = 0, \quad (17a)$$

$$\frac{\partial^2 \Theta}{\partial \theta^2} + \frac{\omega^2}{m^2 \cos^2 \theta} \Theta + \gamma^2 \Theta = 0, \quad (17b)$$

where  $\gamma^2$  is the separation constant. The solutions to Eq. (17a) are proportional to  $r^{\pm\gamma}$ . For the chosen plane-wave acoustic source [see Eq. (9)],  $\tilde{p}$  must be independent of  $r$  along the  $y$  axis ( $\theta=0$ ). This requires setting  $\gamma=0$ , which makes  $R(r)$  a mere constant. Hence, Eq. (17a) is satisfied trivially,  $\tilde{p}(r, \theta) = \Theta(\theta)$ , and Eq. (17b) reduces to

$$\frac{\partial^2 \tilde{p}}{\partial \theta^2} + \frac{\omega^2}{m^2 \cos^2 \theta} \tilde{p} = 0. \quad (18)$$

Applying the standard exponential WKB expansion (Bender and Orzag, 1978) and solving for the first four exponentiated functions, yields the following solution for  $\tilde{p}(\theta)$ , which is asymptotically valid as  $m/\omega = m/(2\pi f) \rightarrow 0$ :

$$\begin{aligned} \tilde{p}(\theta) \sim & A \sqrt{\cos \theta} \exp \left[ \frac{m^2}{16\omega^2} (\cos^2 \theta - 1) \right] \\ & \times \exp \left\{ \pm i \left( \frac{\omega}{m} - \frac{m}{8\omega} \right) \ln [\sec \theta + \tan \theta] \right. \\ & \left. - \frac{\pm im \sin \theta}{8\omega} \right\}. \end{aligned} \quad (19)$$

In the limit  $m/\omega \rightarrow 0$ , the amplitude factor goes to unity, and the argument of the exponential factor reduces to  $\pm i(\omega/m) \ln [\sec \theta + \tan \theta]$ . Inverting the transformation (15a), (15b) for any finite values of  $x$  and  $y$  leads to:  $\cos(\theta) = (y + c_0/m) / \sqrt{(y + c_0/m)^2 + x^2} \rightarrow 1$ , and  $\ln [\sec \theta + \tan \theta] = \ln \left[ \frac{x + \sqrt{(y + c_0/m)^2 + x^2}}{y + c_0/m} \right] \rightarrow mx/c_0$  as  $m \rightarrow 0$ . With these limiting values, it is found that  $\tilde{p}(x, y) \rightarrow A \exp\{\pm i\omega x/c_0\}$  as  $m \rightarrow 0$  which demonstrates that the asymptotic solution (19) properly reduces to the expected plane-wave form in the limit of zero shear ( $m=0$ ).

The complex amplitude  $A$  in Eq. (19) was determined by the boundary condition at  $x=0$  ( $\theta=0$ ), and the plus signs in the imaginary part of the exponent were chosen to ensure downstream wave propagation. Equation (19) satisfies Eq. (18) down to terms of order  $(m/\omega)^2 = (m/f)^2 / (4\pi^2)$ . Since the largest value of  $m/f$  considered here is 0.3 and the coefficient of the unbalanced  $(m/\omega)^2$  term is at most  $\frac{1}{4}$ , any error associated with Eq. (19) should be less than 0.1%, an uncertainty comparable to that of the numerical results. Hence, for the present purposes, any differences found between numerical solution of Eqs. (5), (6), and (7) and the WKB solution given here were attributed to the standard convection approximation, and not to the approximate character of the asymptotic WKB solution.

The final form for the acoustic pressure,  $p_{\text{WKB}}(\theta, t^*)$ , used for the comparisons in Sec. IV was:

$$\begin{aligned} p_{\text{WKB}}(\theta, t^*) = & \sqrt{\cos \theta} \exp \left[ \frac{m^2}{16\omega^2} (\cos^2 \theta - 1) \right] \\ & \times \sin \left\{ 2\pi t^* - \frac{\omega}{m} \left[ \left( 1 - \frac{m^2}{8\omega^2} \right) \right. \right. \\ & \left. \left. \times \ln [\sec \theta + \tan \theta] - \frac{m^2 \sin \theta}{8\omega^2} \right] \right\}, \end{aligned} \quad (20)$$

where  $\tan \theta = x^*/(y^* + f/m)$ . As expected,  $p_{\text{WKB}}(\theta, t^*) \rightarrow \sin(2\pi t^* - 2\pi x^*)$  in the limit as  $m/\omega \rightarrow 0$ . To match the initial condition of the computed results,  $p_{\text{WKB}}(\theta, t^*)$  was set to zero when the argument of the sine function in Eq. (20), was less than zero.

A sample pressure wave field produced by Eq. (20) for  $m/f=0.1$  is shown in Fig. 3. A visual comparison with Fig. 2 shows little difference in the central wave field except for the lower wave amplitude in Fig. 3 at the larger downstream distances, and slightly greater propagation distance for the WKB waves for  $y^*$  near  $y_{\text{max}}^*$ . As expected from the coordinate transformation, the wavefronts in Fig. 3 appear to rotate about the point  $x^*=0$ ,  $y^* = -f/m$ .

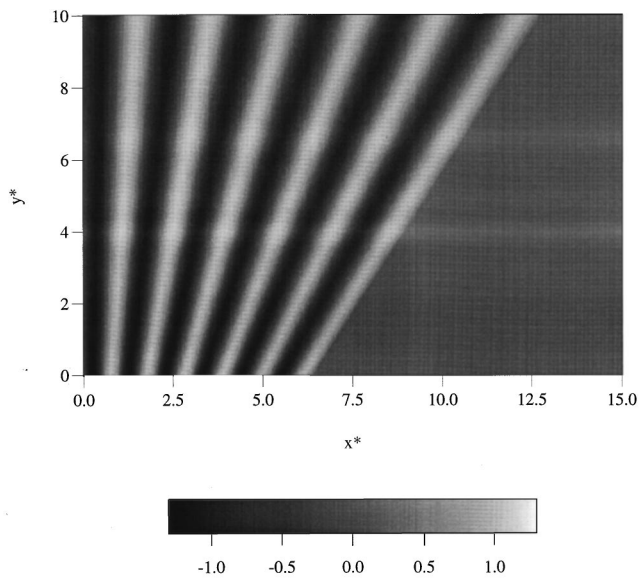


FIG. 3. WKB acoustic-pressure field for  $m/f=0.1$  and  $t^*=6$ . This field plot was generated by evaluation of Eq. (20). In contrast to exact-convection results shown in Fig. 2, these waves propagate slightly faster, and weaken as they propagate.

#### IV. RESULTS AND COMPARISONS

The field output from the computations was post-processed to find the acoustic variables at the positions of the pressure extrema (wave fronts) and at a few locations between extrema in a streamwise band two zero-shear wavelengths wide through the center of the domain. The locus and values at the pressure extrema were determined by local parabolic fitting through the discretized output. Least squares fitting along the wavefronts was used to determine overall wavefront position, and acoustic-pressure amplitude gradient. These data extraction methods were tested by applying them to synthetic computational wave fields generated from the WKB solution to ensure that information was properly extracted from the computed wave fields. When compared to direct evaluations of the WKB solution, the synthetic processed results showed agreement to five or six significant figures, the expected performance limit for single-precision arithmetic. The uncertainty of the reduced results from the exact-convection computations is about one part in a thousand for the field variables, and is predominantly produced by the imperfect boundary conditions on  $y^*=0$ , and  $y^*=y_{\max}^*$ .

The comparisons between the exact-convection computational results (with subscript ‘ecc’), and the approximate-convection WKB results (with subscript ‘WKB’) are provided in Figs. 4–8 for  $m/f=0.01, 0.03, 0.10$ , and  $0.30$ . Smaller values of  $m/f$  did not generate any significant departure between the exact-convection computations and the approximate-convection techniques for the accessible range of  $t^*(0 \leq t^* < 8)$ . Larger values of  $m/f$  were not investigated in this study primarily because they lack physical significance, leading to hypersonic convection speeds for any reasonable computational-domain cross-stream extent. In Figs. 4–6, all the variables refer to positions, times, or conditions at or along the pressure extrema (or wavefronts). Figures 7

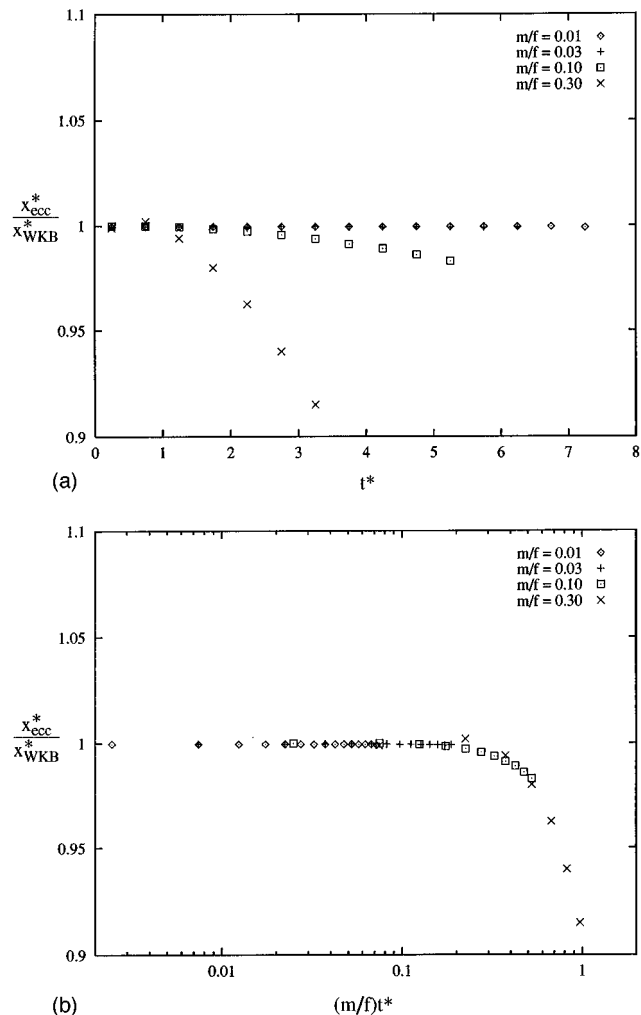


FIG. 4. Wavefront location ratio,  $x_{\text{ecc}}^*/x_{\text{WKB}}^*$ , as a function of  $t^*$  (a), and as function of  $(m/f)t^*$  (b). The simulation results are 2% short of the WKB results when  $(m/f)t^* \approx 0.5$ .

and 8 incorporate information between pressure extrema obtained along lines of  $t^* = \text{constant}$ , oriented and located appropriately via interpolation between nearest neighbor wavefronts.

Figure 4 summarizes the wavefront location results for the centerline of the computational domain. Figure 4(a) and (b) presents the same information using different abscissa scaling. Figure 4(a) shows that the ratio  $x_{\text{ecc}}^*/x_{\text{WKB}}^*$  does not noticeably fall below unity until the wave-shear interaction time exceeds a limit that depends on  $m/f$ . This dependence can be quantified from Fig. 4(b) where the results collapse to a single curve, allowing the identification of  $(m/f)t^* \approx 0.5$  as the approximate wave-shear interaction time for a 2% error in wavefront location.

The observation that the approximate-convection waves travel too fast is consistent with a simple kinematic picture of acoustic propagation with nonzero convection. Consider the motion of an acoustic plane wave that lies at angle  $\theta$  with respect to the vertical. In the exact convection case, the wave’s expected downstream propagation speed is  $c_0/\cos \theta + U(y)$ . In the equivalent approximate convection case, the wave’s expected downstream speed is  $c(y)/\cos \theta = (c_0$

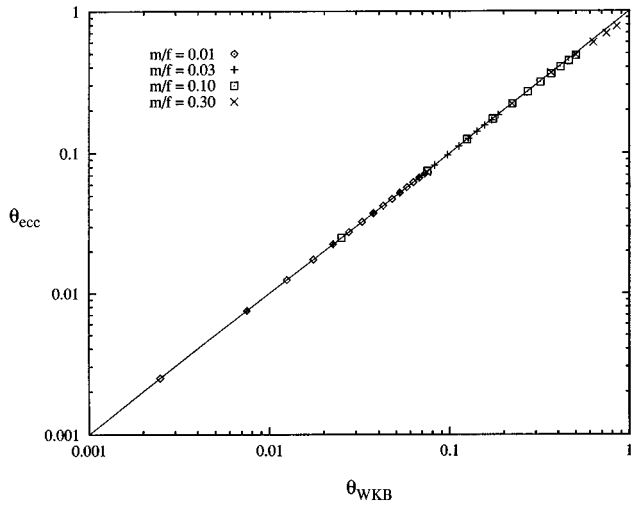


FIG. 5. Exact-convection wavefront turning angle,  $\theta_{ecc}$ , versus WKB approximate-convection turning angle,  $\theta_{WKB}$ . The solid line is given by  $\theta_{ecc} = \theta_{WKB}$ . The two angles differ by about 3% when  $(m/f)t^* \approx 0.5$ .

$+U(y))/\cos \theta$ , which is clearly larger when  $\theta$  and  $U(y)$  are nonzero.

The wavefront turning angle results are shown in Fig. 5 where  $\theta_{ecc}$  is plotted against  $\theta_{WKB}$ . The solid line lies where  $\theta_{ecc} = \theta_{WKB}$ . Figure 5 shows the wavefront rotation angles for the exact- and approximate-convection results,  $\theta_{ecc}$  and  $\theta_{WKB}$ , differ by less than 3% up to  $(m/f)t^* \approx 0.5$  where the turning angle is approximately half a radian ( $\approx 30^\circ$ ). Beyond this angle,  $\theta_{ecc}$  falls further below  $\theta_{WKB}$ . This result is also consistent with the simple kinematic picture mentioned above.

The pressure-amplitude ratio,  $p_{ecc}^*/p_{WKB}^*$ , is plotted versus  $(m/f)t^*$  in Fig. 6. Here,  $p_{ecc}^*$  stays within 10% of  $p_{WKB}^*$  until  $(m/f)t^* \approx 0.5$ . Beyond this point, the exact-convection computations demonstrate marked wave strengthening relative to the WKB results. The smooth curve on Fig. 6 is given by  $\exp\{+0.4(mt)^2\}$ , and is simply a heuristic functional

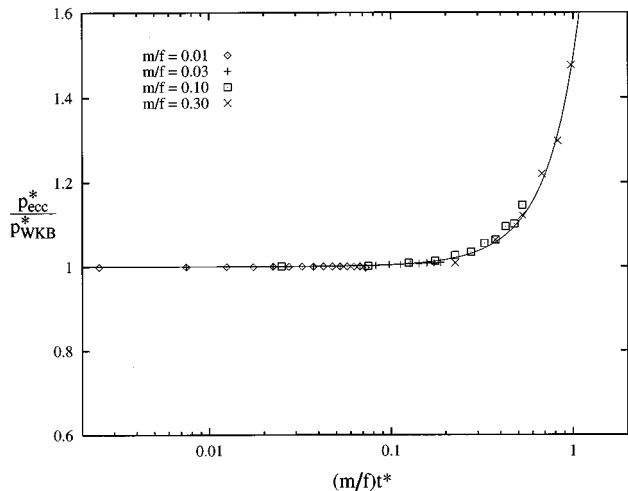


FIG. 6. Pressure wave amplitude ratio,  $p_{ecc}^*/p_{WKB}^*$ , as a function of  $(m/f)t^*$ . The ratio has increased to 1.1 when  $(m/f)t^* \approx 0.5$ . The solid line is given by a heuristic functional form,  $\exp\{+0.4(mt)^2\}$ , and is merely meant to highlight the rapid growth of the pressure ratio for  $mt > 0.5$ .

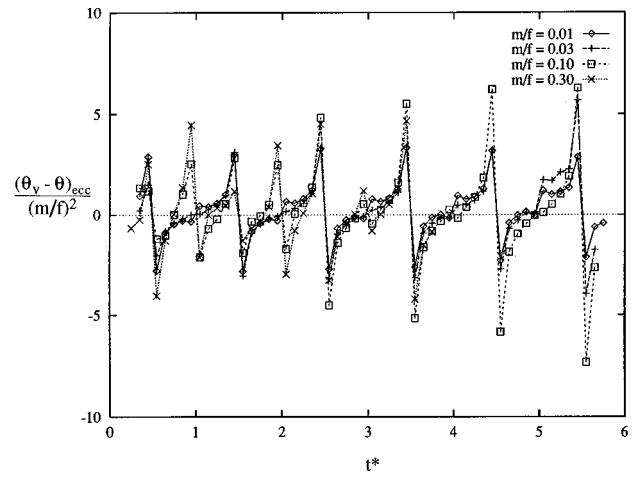


FIG. 7. Difference between the acoustic-velocity vector turning angle  $\theta_v = \arctan(-v/u)$ , and the wavefront turning angle  $\theta$ , divided by the square of the ratio of the convecting flow shear rate to the acoustic frequency,  $(\theta_v - \theta)/(m/f)^2$ , vs  $t^*$ . The difference,  $\theta_v - \theta$ , is zero with the standard convection approximation. Here, the angles are measured in radians and the oscillations generally correspond to the acoustic-velocity vector turning angle leading the wavefront turning angle during acoustic expansion, and lagging it during acoustic compression. The sharp peaks in the computed results occur because  $v$  is nonzero when  $u$  passes through zero. The scatter in the peaks is likely caused by numerical imprecision  $u$  is near zero.

form meant to emphasize this rapid growth in the pressure amplitude ratio. The wave strengthening in the exact-convection results is consistent with the formal difference in the two methods since the standard approximation lacks the acoustic source term of the exact-convection formulation. The pressure gradient along the wavefronts divided by the pressure on the wavefront was typically very small, less than  $10^{-3}$  per zero-shear wavelength,  $c_0/f$ . The lack of such a gradient is consistent with the vertically uniform source-side boundary condition. In addition, the smooth overlap of the computational results for the entire range of  $m/f$  suggests these results are universal for all combinations of  $m/f$  and  $t^*$

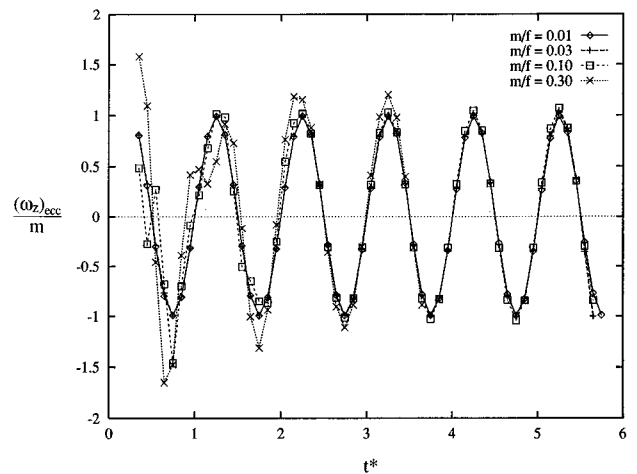


FIG. 8. Acoustic perturbation vorticity,  $\omega_z$ , divided the convection flow vorticity magnitude,  $m$ , vs  $t^*$ . Here, the perturbation vorticity amplitude is shown to be proportional to  $m$ . For comparison,  $\omega_z = 0$  for the standard convection-approximation WKB solution.

with the same product. Hence, the observed wave strengthening appears to be independent of the acoustic frequency, having been found to depend only on  $(m/f)t^* = mt$ .

The acoustic-velocity vector turning angle,  $\theta_v = \tan^{-1}\{-v^*/u^*\}$ , was computed at and in between the wavefronts from the exact-convection wave fields. Results for the difference,  $\theta_v - \theta$ , divided by  $(m/f)^2$  are plotted versus  $t^*$  in Fig. 7 for the four values of  $m/f$ . This difference in turning angles is zero for the standard approximation, a value achieved on average by the exact-convection computational results. The oscillations shown in Fig. 7 generally correspond to the acoustic-velocity vector leading the wavefront turning angle during acoustic expansion, and lagging the wavefront turning angle during acoustic compression. The sharp transitions and jaggedness of the various curves at  $t^* = 0.5, 1.0, 1.5, 2.0$ , etc. are primarily caused by a nonzero phase shift between the  $u$  and  $v$  velocities which leaves  $v \neq 0$  when  $u$  passes through zero, and by numerical imprecision when  $u$  and  $v$  are both small. However, the rough collapse of results shown in Fig. 7 suggests that the acoustic-velocity vector turning angle fluctuations are proportional to  $(m/f)^2$  with a root-mean-square deviation near  $1.5(m/f)^2$  radians ( $\approx 90(m/f)^2$  degrees). The authors believe the strongest imperfections in the collapse at small  $t^*$  are caused by the source boundary condition which enforces  $v = 0$  at  $x = 0$  and therefore does not launch the plane wave with the correct phase angle between the cross-stream and downstream acoustic velocities. However, because these velocity-angle oscillations develop in a self-similar manner after one or two acoustic cycles for all four values of  $m/f$  investigated, they were assumed to be a genuine part of the acoustic wave field.

The acoustic perturbation vorticity,  $\omega_z = \partial v / \partial x - \partial u / \partial y$ , was computed via central differencing of the numerical wave fields, and then scaled by the vorticity magnitude of the convecting flow,  $m$ . Figure 8 shows these results as function of  $t^*$  for the four values of  $m/f$ . Here,  $\omega_z$  is nonzero and oscillatory, with positive vorticity during acoustic expansion and negative vorticity during acoustic compression. The collapse of results for  $t^* > 2$  indicates that  $\omega_z$  is essentially proportional to  $m$ . As required by the linearity of the problem formulation, separate computations with twice the initial source strength showed the perturbation vorticity amplitude to be proportional to the acoustic wave amplitude. These findings are entirely at odds with those from the standard approximation since the appropriate differentiation of Eq. (20) yields  $\omega_z = 0$  throughout the entire domain for any initial  $p^*$  for all  $t^*$ . The lack of perturbation vorticity in the approximate convection solutions stems from replacing the spatially varying convection flow with a spatially varying speed of sound. Like the collapse of the acoustic-velocity vector angle data shown in Fig. 7, a minor inconsistency in the source boundary condition is the likely cause of the apparently oversized perturbation vorticity fluctuations seen for  $m/f = 0.10$  &  $0.30$  for  $t^* < 2$  in Fig. 8.

## V. CONCLUSIONS

The comparisons presented here between plane-wave propagation in a shear flow from exact-convection computa-

tions and an approximate-convection WKB solution provide a calibration for the accuracy of the standard convection approximation, and should provide a means for assessing whether or not exact convection is required for engineering models of aero- and environmental-acoustic propagation. Four major conclusions can be drawn from this investigation.

Results from the standard convection approximation,  $c(y) = c_0 + U(y)$ , should be acceptable for nearly all engineering purposes at high acoustic frequency,  $m/f \rightarrow 0$ , or when the local variation in convection-flow Mach number is small,  $m\lambda/c \rightarrow 0$  ( $\lambda =$  acoustic wavelength), as long as the amount of wavefront rotation caused by shear-flow convection is less than approximately  $30^\circ$ , i.e.,  $(m/f)t^* = mt \leq 0.5$ . At this value of  $mt$ , acoustic pressure amplitudes predicted by the standard convection approximation are found to be low by approximately 10% or 1 dB (the nominal amplitude sensitivity of human hearing), so  $mt \approx 0.5$  is a conservative parametric limit for the applicability of the standard convection approximation. In addition, the standard convection approximation overestimates wavefront location and rotation angle, with errors of 2%–3% for  $mt$  greater than approximately 0.5. This result is consistent with a simple kinematic picture of wave propagation in the presence of convection. For most engineering purposes such deviations at  $mt \approx 0.5$  are probably not significant. However, the accumulated errors could prove critical for precision time-of-flight measurements at values of  $(m/f)t^* \geq 1$ . In particular, amplitude discrepancies grow rapidly beyond  $mt \approx 0.5$  with a nearly 4-dB difference occurring at  $mt \approx 1$ .

Acoustic plane waves propagating in a shear flow are strengthened by an acoustic/shear-flow interaction that is commonly neglected in approximate treatments of acoustic propagation with nonzero convection. This wave strengthening mechanism is driven by the cross-stream acoustic velocity acting with the mean shear to form a source term for the downstream acoustic velocity. Independent of its likely importance in strongly sheared vehicle flows or long range atmospheric sound propagation, this wave strengthening mechanism may also play a fundamental role in sound production in turbulent flows.

The acoustic-velocity vector oscillates about the wave front normal direction with an amplitude proportional to the  $(m/f)^2$ . While these oscillations are small, typically less than a  $1^\circ$  for  $m/f < 0.1$ , they are unaccounted for by the standard convection approximation.

Acoustic plane waves propagating in a shear flow have significant acoustic perturbation vorticity that is proportional to the wave amplitude and to the convecting shear flow's vorticity. By comparison, the acoustic perturbation vorticity is identically zero for the solution generated from the standard approximation.

## ACKNOWLEDGMENTS

The authors wish to thank Dr. Gary Strumolo of the Research Laboratory of Ford Motor Company for encouragement and support, and Professor William Schultz of the University of Michigan for his insightful comments on the manuscript. This research was supported in part by the Ford Motor Company.

- Anderson, D. A., Tennehill, J. C., and Pletcher, R. H. (1984). *Computational Fluid Mechanics and Heat Transfer* (Hemisphere, New York), Chap. 4.
- Bender, C. M., and Orzag, S. A. (1978). *Advanced Mathematical Methods for Scientists and Engineers* (McGraw-Hill, New York), Chap. 10.
- Goldstein, M. E. (1976). *Aeroacoustics* (McGraw-Hill, New York), Chap. 1.
- Howe, M. S. (1995). "The damping of sound by wall turbulent shear layers," *J. Acoust. Soc. Am.* **98**, 1723–1730.
- Lamancusa, J. S., and Daroux, P. A. (1993). "Ray tracing in a moving medium with two dimensional sound speed variation and application to sound propagation over terrain discontinuities," *J. Acoust. Soc. Am.* **93**, 1716–1726.
- Li, Y. L., Liu, C. H., and Franke, S. J. (1990). "Three-dimensional Green's function for wave propagation in a linearly inhomogenous medium—The exact analytic solution," *J. Acoust. Soc. Am.* **87**, 2285–2291.
- Li, Y. L., White, M. J., and Franke, S. J. (1994). "New fast-field programs for anisotropic sound propagation through an atmosphere with a wind velocity profile," *J. Acoust. Soc. Am.* **95**, 718–726.
- Morse, P. M., and Ingard, K. U. (1968). *Theoretical Acoustics* (Princeton U.P., Princeton, NJ), pp. 698–716.
- Nijs, L., and Wapenaar, C. P. A. (1990). "The influence of wind and temperature gradients on sound propagation, calculated with the two way wave equation," *J. Acoust. Soc. Am.* **87**, 1987–1998.
- Nijs, L., and Wapenaar, C. P. A. (1992). "Reply to: 'Comments on the influence of wind and temperature gradients on sound propagation, calculated with the two way wave equation,'" *J. Acoust. Soc. Am.* **91**, 501–504.
- Norton, S. J. (1991). "Reconstructing stratified fluid flow from reciprocal scattering measurements," *J. Acoust. Soc. Am.* **89**, 2567–2572.
- Orlanski, I. (1976). "A simple boundary condition for unbounded hyperbolic flows," *J. Comput. Phys.* **21**, 251–269.
- Pierce, A. D. (1989). *Acoustics* (Acoustical Society of America, New York, 1991), pp. 52, 400–403.
- Pierce, A. D. (1990). "Wave equation for sound in fluids with unsteady inhomogenous flow," *J. Acoust. Soc. Am.* **87**, 2292–2299.
- Raspet, R., Yao, L., Franke, S. J., and White, M. J. (1992). "Comments on 'The influence of wind and temperature gradients on sound propagation, calculated with the two way wave equation,'" *J. Acoust. Soc. Am.* **91**, 498–500.
- Robertson, J. S., Siegmann, W. L., and Jacobson, M. J. (1995). "Low frequency sound propagation modeling over a locally reacting boundary with the parabolic approximation," *J. Acoust. Soc. Am.* **98**, 1130–1137.
- Salomons, E. M. (1994a). "Downwind propagation of sound in an atmosphere with a realistic sound-speed profile: A semianalytical ray model," *J. Acoust. Soc. Am.* **95**, 2425–2436.
- Salomons, E. M. (1994b). "Diffraction by a screen in downwind sound propagation: A parabolic-equation approach," *J. Acoust. Soc. Am.* **95**, 3109–3117.
- Thompson, P. A. (1972). *Compressible-Fluid Dynamics* (McGraw-Hill, New York).
- Wilson, D. K. (1993). "Sound field computations in a stratified, moving medium," *J. Acoust. Soc. Am.* **94**, 400–407.

# Coupled-mode modeling of acoustic scattering from three-dimensional, axisymmetric objects

John A. Fawcett

SACLANT Undersea Research Centre, Viale San Bartolomeo 400, 19138 La Spezia (SP), Italy

(Received 10 February 1997; revised 12 August 1997; accepted 25 August 1997)

In this paper a coupled-mode method for computing the wave field scattered by three-dimensional, axisymmetric fluid objects is presented. The method provides a unified approach to solving three-dimensional scattering problems for axisymmetric objects in free space, in a waveguide, or partially or fully buried in a basement. Numerical computations of scattering from finite cylinders in free space and embedded between two half-spaces are presented. Also, the method is used to compute the scattering from an infinitely long cylinder for which analytical results are available. [S0001-4966(97)03412-7]

PACS numbers: 43.30.Bp, 43.20.Fn [SAC-B]

## INTRODUCTION

A variety of methods<sup>1-7</sup> have been used by authors for the computation of the acoustic or elastic wave field (including backscatter) in range-dependent waveguides. Reference 1 considers as one of its examples, scattering by a buried elastic inclusion in an oceanic waveguide. In the case that the scattering problem has some coordinate of invariance, these types of methods may be used to construct a three-dimensional solution by solving a sequence of two-dimensional problems (for invariance with respect to a horizontal coordinate see, for example, Ref. 8).

The theory of coupled modes has been applied to acoustic and elastic scattering from three-dimensional, azimuthally symmetric features.<sup>9-14</sup> In this type of three-dimensional geometry, the full three-dimensional scattering problem is broken down into a sequence of two-dimensional problems for each angular Fourier component. Each of these two-dimensional problems can then be solved using the coupled-mode approach. Reference 10 considers scattering from a cylindrical elastic inclusion in a bounded elastic waveguide. Reference 11 uses Fourier decomposition in conjunction with a boundary integral equation method (BIEM), but uses the results from coupled-mode computations for comparison with the BIEM results. The coupled-mode solution for scattering in an oceanic waveguide with azimuthally symmetric bathymetry is considered in Refs. 9 and 12 and Refs. 13 and 14 consider a cylindrical island in the oceanic waveguide.

In this paper we use the azimuthally symmetric coupled-mode approach to compute the scattering from three-dimensional objects; in particular, a finite-length acoustic cylinder. We will consider two cases; when the object is surrounded by a homogeneous acoustic free space and when the object is embedded between two half-spaces (i.e., partially buried) (see Fig. 1). When we describe the technique used to solve these two types of problems, it will be apparent that the same methodology can be used to solve scattering problems for an object totally buried, above an interface, and within a water column bounded above by a pressure release surface. Thus this approach provides a unified approach to a variety of object scattering problems.

The medium is divided into two main range sections,

that occupied by the cylinder and the cylinder's exterior. Within the interior domain, the medium is taken to be vertically symmetric about the line  $z=0$  (see Fig. 2) and consists of three layers, an upper homogeneous space, a layer with the cylinder's compressional velocity and density, and a lower homogeneous space. The exterior medium consists of two half-spaces with the same parameters as the upper and lower media in the interior domain; however, the interface between the two spaces,  $z_i$ , in the exterior domain may not necessarily be at  $z=0$ . If, in fact, the upper and lower spaces have the same parameters, a free-space environment is modeled. Although we consider cylinders in this paper, more general azimuthally symmetric objects can be approximated by a sequence of cylindrical rings. In this case, instead of having a single coupling matrix at a particular radius, there are a set of coupling equations at each radial interface. This is analogous to the bathymetric staircase approximation which is used in, for example, Ref. 6.

In order to make the computational domain finite, we impose boundary conditions on large but finite values of  $z$ ,  $z = \pm L$ . Then, in order to nullify the effects of these artificial boundaries we artificially add an attenuation profile to the medium near these boundaries. In order to compute the modal quantities for the resultant velocity profile we use Galerkin's method with the modes for the media without attenuation serving as the trial functions. This is the approach which was used by Evans and Gilbert.<sup>7</sup>

There are closed-form solutions for the acoustic scattering from infinitely long cylinders and we compare the results computed from our method with these solutions. We present the results of some three-dimensional full-field computations for penetrable finite cylinders in free space and for cylinders partially buried in an underlying half-space.

## I. THEORY

In this section we first describe, in general, the coupled-mode approach to azimuthally symmetric scattering problems. We then discuss how we determine the modes and eigenvalues for the problem using Galerkin's method and finally we discuss how we compute the intermodal integrals.

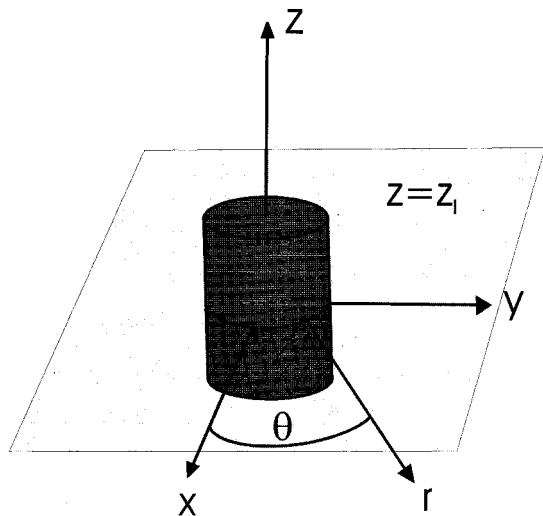


FIG. 1. Schematic of three-dimensional geometry for a partially buried cylinder.

### A. Azimuthally symmetric coupled-mode approach

Let us consider a three-dimensional coordinate system  $(r, \theta, z)$  with the origin of the coordinate system being at the center of a finite length cylinder with radius  $a$ . We consider space divided into two radial sections; the interior section  $0 < r < a$  and the exterior section  $r > a$ . The velocity and density profiles within the interior region are denoted as  $c^{\text{in}}(z)$  and  $\rho^{\text{in}}(z)$  and those for the exterior region as  $c^{\text{ex}}(z)$  and  $\rho^{\text{ex}}(z)$ . In general, we will use the notation “ex” to refer to quantities exterior to the radial extent of the cylinder and “in” for the interior quantities. The profiles for the interior region contain a vertical section corresponding to the cylinder’s velocity and density values. The Helmholtz equation for a point source at  $(r_s, \theta_s, z_s)$  can be written

$$\frac{1}{r} \frac{g!}{\partial r} \left( r \frac{\partial P}{\partial r} \right) + \frac{1}{r^2} \frac{\partial^2 P}{\partial \theta^2} + \frac{\partial^2 P}{\partial z^2} + \frac{\omega^2}{c^2(r, \theta, z)} P = \frac{\delta(r-r_s) \delta(z-z_s) \delta(\theta-\theta_s)}{2\pi r_s}, \quad (1)$$

where at  $r=a$ , the field must satisfy the continuity conditions

$$P^{\text{in}} = P^{\text{ex}}, \quad P_r^{\text{in}} / \rho^{\text{in}}(z) = P_r^{\text{ex}} / \rho^{\text{ex}}(z). \quad (2)$$

The cylinder also has continuity conditions at its top and bottom edges, but these conditions will be satisfied by the modal functions we use for the interior region.

Due to the azimuthal symmetry of the cylinder we can write the solution of Eq. (1) in the form

$$P(r, \theta, z) = \sum_{\nu=0}^{\infty} \Theta_{\nu}(r, z) \epsilon_{\nu} \cos \nu(\theta - \theta_s), \quad (3)$$

where  $\epsilon_{\nu} = 1$  for  $\nu=0$  and  $\epsilon_{\nu} = 2$  otherwise. The partial differential equation for  $\Theta_{\nu}(r, \theta)$  is

$$\frac{1}{r} \frac{\partial}{\partial r} \left( r \frac{\partial \Theta_{\nu}}{\partial r} \right) + \frac{\partial^2 \Theta_{\nu}}{\partial z^2} + \left( \frac{\omega^2}{c^2(r, z)} - \frac{\nu^2}{r^2} \right) \Theta_{\nu} = \frac{\delta(r-r_s) \delta(z-z_s)}{2\pi r_s} \quad (4)$$

and the boundary conditions for  $\Theta_{\nu}(r, z)$ ,  $\nu=0, \dots, \infty$  are those of Eq. (2). Equation (4) now defines a two-dimensional range-dependent scattering problem with the angular order entering through the term  $-\nu^2/r^2$ . This equation can be solved in a variety of ways; in this paper we utilize the coupled-mode approach

First we truncate the infinite medium by imposing the boundary conditions

$$\Theta_{\nu}(r, z=L) = 0, \quad \frac{\partial \Theta_{\nu}(r, z=-L)}{\partial z} = 0. \quad (5)$$

We then minimize the effect of these boundary conditions by introducing artificial attenuation profiles near these boundaries. However, if we wish to model a pressure release surface at the top of a waveguide we would not add an attenuating profile near the top boundary. We seek a solution for  $\Theta_{\nu}(r, z)$  in terms of the vertical modes for the two media;  $\phi_n(z)$  will denote a member of the set of modes for the exterior of the cylinder and  $\psi_n$  a member of the set of modes for the interior. We can write

$$\Theta_{\nu}^{\text{ex}}(r, z) = \sum_{n=1}^N [a_n \phi_n(z) H_{\nu}(k_n^{\text{ex}} r) + \Gamma_n \phi_n(z) J_{\nu}(k_n^{\text{ex}} r)], \quad (6a)$$

where the coefficients  $a_n$  are to be determined and

$$\Gamma_n = \frac{i}{4} H_{\nu}(k_n^{\text{ex}} r_s) \phi_n(z_s) \quad (6b)$$

in the case of a point source, i.e.,  $\Gamma_n$  are the modal expansion coefficients of the known incident field. For  $r < a$  we write

$$\Theta_{\nu}^{\text{in}}(r, z) = \sum_{n=1}^N b_n \psi_n(z) J_{\nu}(k_n^{\text{in}} r). \quad (6c)$$

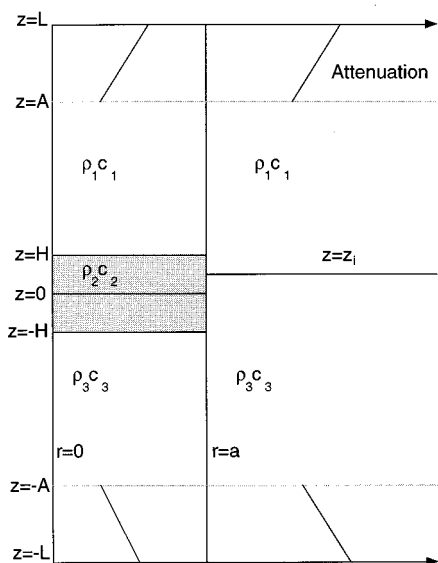


FIG. 2. Schematic of the medium in the  $r$ - $z$  plane used for the coupled-mode problem.



The modes  $\phi_n(z)$  satisfy the vertical eigenvalue equation

$$\frac{d^2 \phi_n(z)}{dz^2} + \left[ \frac{\omega^2}{(c^{\text{ex}})^2(z)} + iQ(z) \right] \phi_n(z) = (k_n^{\text{ex}})^2 \phi_n(z) \quad (7)$$

with the appropriate continuity conditions at medium discontinuities and the boundary conditions of Eq. (5). In Eq. (7) we have explicitly indicated the presence of an attenuation profile  $Q(z)$ . There is a similar eigenvalue/eigenfunction problem for the interior eigenfunctions  $\psi_n(z)$ .

Using the mode set from Eq. (7), the system of coupled-mode equations is formulated. First we write for the continuity of pressure at  $r=a$ ,

$$\begin{aligned} \sum_{n=1}^N b_n \psi_n(z) J_{\nu}(k_n^{\text{in}} a) - a_n \phi_n(z) H_{\nu}(k_n^{\text{ex}} a) \\ = \sum_{n=1}^N \Gamma_n \phi_n(z) J_{\nu}(k_n^{\text{ex}} a) \end{aligned} \quad (8a)$$

and for the continuity of the density-normalized radial derivative of pressure,

$$\begin{aligned} \sum_{n=1}^N b_n \frac{\psi_n(z)}{\rho^{\text{in}}(z)} J_{\nu,r}(k_n^{\text{in}} a) - a_n \frac{\phi_n(z)}{\rho^{\text{ex}}(z)} H_{\nu,r}(k_n^{\text{ex}} a) \\ = \sum_{n=1}^N \Gamma_n \frac{\phi_n(z)}{\rho^{\text{ex}}(z)} J_{\nu,r}(k_n^{\text{ex}} a). \end{aligned} \quad (8b)$$

Multiplying Eq. (8a) by  $\psi_m(z)/\rho^{\text{in}}(z)$  for  $m=1, \dots, N$  and integrating from  $z=-L$  to  $z=L$  we obtain

$$b_m J_{\nu}(k_m^{\text{in}} a) - \sum_{n=1}^N C_{nm} a_n H_{\nu}(k_n^{\text{ex}} a) = \gamma_m, \quad (9a)$$

where

$$C_{nm} \equiv \int_{-L}^L \frac{1}{\rho^{\text{in}}(z)} \phi_n(z) \psi_m(z) dz \quad (9b)$$

and

$$\gamma_m \equiv \sum_{n=1}^N J_{\nu}(k_n^{\text{ex}} a) \Gamma_n \int_{-L}^L \frac{1}{\rho^{\text{in}}(z)} \phi_n(z) \psi_m(z) dz. \quad (9c)$$

Similarly, we multiply Eq. (8b) by  $\psi_m(z)$  for  $m=1, \dots, N$  and integrate from  $z=-L$  to  $z=L$  to obtain

$$b_m J_{\nu,r}(k_m^{\text{in}} a) - \sum_{n=1}^N D_{nm} a_n H_{\nu,r}(k_n^{\text{ex}} a) = \Sigma_m, \quad (10a)$$

where

$$D_{nm} \equiv \int_{-L}^L \frac{1}{\rho^{\text{ex}}(z)} \phi_n(z) \psi_m(z) dz \quad (10b)$$

and

$$\Sigma_m \equiv \sum_{n=1}^N J_{n,r}(k_n^{\text{ex}} a) \Gamma_n \int_{-L}^L \frac{1}{\rho^{\text{ex}}(z)} \phi_n(z) \psi_m(z) dz. \quad (10c)$$

Thus we have a  $2N \times 2N$  system of equations for the coefficient vector  $(b_n; a_n)$  of the form

$$\begin{pmatrix} J_{\nu}(k_n^{\text{in}} a) \delta_{n,m} & C_{nm} H_{\nu}(k_n^{\text{ex}} a) \\ J_{\nu,r}(k_n^{\text{in}} a) \delta_{n,m} & D_{nm} H_{\nu,r}(k_n^{\text{ex}} a) \end{pmatrix} \begin{pmatrix} b_n \\ a_n \end{pmatrix} = \begin{pmatrix} \gamma_m \\ \Sigma_m \end{pmatrix}, \quad (11)$$

where  $\delta_{n,m}$  denotes the Kronecker delta function. The solution of this system yields the modal coefficients for both the interior and exterior modal sets for the  $\nu$ th angular order.

## B. Computation of modes and eigenvalues

We first consider the computation of the modes and eigenvalues for the case that there is no added attenuation profile,  $Q(z)=0$  in Eq. (7), these modes serve as the basis set for the modes when there is an attenuation profile. The medium in the interior cylindrical region consists of the layer corresponding to the object, and upper and lower bounding half-spaces. In the upper portion of the medium we take the solution to be proportional to

$$\sin(\sqrt{(\omega^2/c_1^2 - k_n^2)}[z-L]), \quad (12a)$$

in the lower part of the medium we take the solution to be proportional to

$$\cos(\sqrt{(\omega^2/c_3^2 - k_n^2)}[z+L]). \quad (12b)$$

Within the vertical layer corresponding to the cylinder  $-H \leq z \leq H$ , we consider the solution to have the form

$$a \sin \sqrt{(\omega^2/c_2^2 - k_n^2)}z + b \cos \sqrt{(\omega^2/c_2^2 - k_n^2)}z. \quad (12c)$$

Thus there are four unknown coefficients and there are four equations derived from the continuity of  $p$  and  $p_z/\rho$  at  $z = \pm H$ . This system of homogeneous equations for the coefficients has only the zero solution except at the values of  $k_n$  for which the determinant of the system is zero. Numerically, we search along the real line to locate these values of  $k_n$ .

The eigenvalue/mode problem for the exterior medium is similar. The modes have the form of Eq. (12a) in the upper medium and that of Eq. (12b) in the lower medium. The eigenvalue problem is reduced to satisfying the standard continuity conditions at the interface  $z=z_i$ .

## C. The Galerkin method

Thus far in the discussion, we have assumed that we can determine the modes and eigenvalues for Eq. (7). This is not a trivial problem when there is attenuation in the problem, as in this case the eigenvalues are complex and it is no longer possible to simply search for the eigenvalues along the real line. Instead of searching for complex-valued eigenvalues we will use Galerkin's method to approximate the eigenvalues and eigenfunctions of the problem.

We wish to find modal solutions to Eq. (7),

$$\frac{d^2 \phi_n(z)}{dz^2} + \left[ \frac{\omega^2}{c^2(z)} + iQ(z) \right] \phi_n(z) = k_n^2 \phi_n(z). \quad (13)$$

In Sec. I B we discussed finding the solutions to

$$\frac{d^2 \tau_n(z)}{dz^2} + \frac{\omega^2}{c^2(z)} \tau_n(z) = \hat{k}_n^2 \tau_n(z) \quad (14)$$

with the appropriate boundary conditions and interface continuity conditions. We use these solutions to construct the solution to Eq. (13); we take

$$\phi_n(z) = \sum_{k=1}^N a_k^n \tau_k(z). \quad (15)$$

Substituting the expression of Eq. (15) into Eq. (13) we obtain

$$\sum_{k=1}^N a_k^n \frac{d^2 \tau_k(z)}{dz^2} + \left[ \frac{\omega^2}{c^2(z)} + iQ(z) \right] a_k^n \tau_k(z) = k_n^2 a_k^n \tau_k(z). \quad (16)$$

Multiplying Eq. (16) by  $\tau_m(z)/\rho(z)$  and integrating with respect to  $z$  from  $z=L$  to  $z=L$  and using Eq. (14) we obtain the eigenvalue/eigenvector problem

$$A_{m,k} a_k^n = \lambda_n a_m^n, \quad (17)$$

where the  $(m,k)$  element of  $A$  is given by

$$A_{m,k} = \int_{-L}^L \frac{1}{\rho(z)} \tau_m(z) \tau_k(z) iQ(z) dz + \delta_{m,k} \hat{k}_m^2. \quad (18)$$

A standard eigenvalue/eigenvector decomposition of the matrix  $A$  yields the vectors of coefficients  $a_k^n$ ,  $k=1, \dots, N$  of the trial functions for the mode  $\phi_n(z)$  and the corresponding eigenvalues. In Eq. (18) we choose  $Q(z)$  to be zero everywhere, except for the two intervals  $z=[A, L]$  and  $z=[-L, -A]$ . Within these intervals we take  $Q(z)$  to be linearly increasing from 0 to a user-input value for  $z=\pm L$ . However, as mentioned previously, we can retain either of the boundary conditions of Eq. (5) by using  $Q(z)=0$  near the appropriate boundary.

## D. Computation of intermodal projections

In Sec. I A above, it can be seen that it is necessary to compute integrals of the form

$$\int_{-L}^L \frac{1}{\rho} \phi_n(z) \psi_m(z) dz. \quad (19)$$

We have shown how to compute the modes  $\phi_n$  and  $\psi_m$  in terms of simpler modal functions using Galerkin's method. We now describe an efficient analytic procedure for computing the integrals of the form of Eq. (19). Let

$$\phi_n(z) = \sum_{k=1}^N q_k^n \tau_k(z) \quad (20a)$$

and

$$\psi_n(z) = \sum_{k=1}^N r_k^n \Omega_k(z). \quad (20b)$$

Then Eq. (19) can be expressed as

$$\begin{aligned} & \int_{-L}^L \frac{1}{\rho} \phi_n(z) \psi_m(z) dz \\ &= \sum_{i=1}^N \sum_{j=1}^N q_i^n r_j^m \int_{-L}^L \frac{1}{\rho(z)} \tau_i(z) \Omega_j(z) dz. \end{aligned} \quad (21)$$

The integrals of Eq. (21) are straightforward to evaluate analytically as the functions  $\tau_i(z)$  and  $\Omega_j(z)$  are composed of simple sine and cosine functions. We can express Eq. (21) in terms of matrices

$$\int_{-L}^L \frac{1}{\rho} \phi_n(z) \psi_m(z) dz = A C B^T, \quad (22)$$

where

$$A_{i,j} \equiv q_j^i, \quad B_{i,j} \equiv r_j^i, \quad C_{i,j} \equiv \int_{-L}^L \frac{1}{\rho(z)} \tau_i(z) \Omega_j(z) dz. \quad (23)$$

The profile  $\rho(z)$  in Eq. (23) may be either  $\rho^{\text{in}}(z)$  or  $\rho^{\text{ex}}(z)$  depending on whether one requires the projections of Eqs. (9c) or (10c).

In summary, we construct the modes for the two environments, which have an artificial attenuation profile, by Galerkin's method. This method allows us to express the modes of these environments in terms of simpler modal functions. We compute the intermodal integrals in terms of these simpler modes. Having computed the matrix elements for Eq. (11) we can compute the interior and exterior modal coefficients for the  $\nu$ th angular order for the cylindrical system. Repeating this for several values of  $\nu$  we can construct the three-dimensional solution by Fourier synthesis. It is important to note that the modal computations and projections, etc., do not depend upon the value of  $\nu$  and these computations are only done once.

## E. Computation of the acoustic field

The solution of Eq. (11) yields the  $\nu$ th angular modal coefficients ( $b_j^\nu$ ,  $j=1, \dots, N$ ) for the interior pressure field and the coefficients  $a_j^\nu$  for the scattered field in the exterior region. The total pressure field within the interior region can be computed by

$$p^{\text{in}} = \sum_{\nu=0}^{N_B} \epsilon_\nu \sum_{j=1}^N b_j^\nu J_\nu(k_j^{\text{in}} r) \psi_j(z) \cos[\nu(\theta - \theta_s)] \quad (24)$$

and in the exterior

$$p^{\text{ex}} = \sum_{\nu=0}^{N_B} \epsilon_\nu \sum_{j=1}^N a_j^\nu H_\nu(k_j^{\text{ex}} r) \phi_j(z) \cos[\nu(\theta - \theta_s)] + p^{\text{src}}, \quad (25)$$

where  $p^{\text{src}}$  is the incident field upon the cylinder due to the source and would, in fact, be the total pressure field in the absence of the cylinder. We require a computational expression for this incident field. It is possible to add in the angular/modal expansion for the incident field at each point of computation. However, we instead use simpler representations of the incident field. For example, for a surrounding homogeneous space we use

$$p^{\text{src}} = \frac{\exp(i\omega/c|\mathbf{x}_r - \mathbf{x}_s|)}{4\pi|\mathbf{x}_r - \mathbf{x}_s|}, \quad (26a)$$

where  $\mathbf{x}_r$  and  $\mathbf{x}_s$  are the three-dimensional position vectors of the receiver and source, respectively. In the case of a two-half-space medium, it is more difficult to compute the inci-

dent field; however, in terms of our approximate mode set we can write that

$$p^{\text{src}} \approx \sum_{j=1}^N \frac{i}{4} \phi_j(z) H_0(k_j |\mathbf{r}_r - \mathbf{r}_s|), \quad (26b)$$

where  $\mathbf{r}_r$  and  $\mathbf{r}_s$  are the two-dimensional position vectors in the  $(r, \theta)$  plane of the receiver and source, respectively. The computational advantages of using a source representation of the form of Eq. (26b) have been discussed in Ref. 14.

## II. NUMERICAL EXAMPLES

### A. An infinite cylinder

As a test case for the coupled-mode method we consider an infinitely long cylinder with acoustic parameters  $c_c = 5950$  m/s and  $\rho = 7700$  kg/m<sup>3</sup> with a radius of 0.5 m. These correspond to the compressional parameters of steel. The surrounding homogeneous medium has parameters  $c_0 = 1500$  m/s and  $\rho = 1000$  kg/m<sup>3</sup>. In order to obtain an analytical solution to this problem, we perform a Fourier transform with respect to  $z$  to obtain the two-dimensional problem

$$\begin{aligned} \frac{1}{r} \frac{\partial}{\partial r} \left( r \frac{\partial P}{\partial r} \right) + \frac{1}{r^2} \frac{\partial^2 P}{\partial \theta^2} + \left( \frac{\omega^2}{c^2(r, \theta, z)} - k_z^2 \right) P \\ = \frac{\delta(r - r_s) \delta(\theta - \theta_s)}{2\pi r_s} e^{ik_z z_s}. \end{aligned} \quad (27)$$

For each value of  $k_z$  we can write the exterior scattered pressure field,  $\tilde{p}^{\text{sc}}$  in the form

$$\tilde{p}^{\text{sc}}(r, \theta; k_z) = \sum_{n=0}^N H_n^1(\gamma r) \alpha_n \cos[n(\theta - \theta_s)], \quad (28a)$$

where

$$\gamma \equiv \sqrt{\omega^2/c_0^2 - k_z^2} \quad (28b)$$

and  $\alpha_n$  are determined by the continuity conditions of Eqs. (2). Similarly, the interior solution has the form

$$\tilde{P}(r, \theta; k_z) = \sum_{n=0}^N J_n(\gamma^{\text{in}} r) \beta_n \cos n(\theta - \theta_s). \quad (29)$$

The three-dimensional field is then constructed by performing the numerical quadrature of the wave-number integral,

$$P(r, \theta, z) = 2 \int_{\zeta} \tilde{P}(r, \theta, k_z) \cos(k_z(z - z_s)) dk_z, \quad (30a)$$

where  $\zeta$  represents an integration contour in the complex plane [for  $\text{Re}(k_z) > 0$ ]. In our computations we used

$$\zeta(t) = t - i \tanh(4t/k_{\text{max}})/10, \quad (30b)$$

where we consider  $0 \leq t \leq k_{\text{max}} = 2\omega/1500$ .

In Fig. 3(a), we show the coupled-mode solution in the plane  $z = -1$  m for a 1500-Hz source located at a range of 10 m from the cylinder at  $z = 1$  m. Thus the source is off the right-hand side of the plot and we are considering a horizontal slice of the field. The circular cross section of the cylinder is indicated in the figure and the axis of symmetry (the cylinder's axis) is perpendicular to the plane of the page. In Fig.

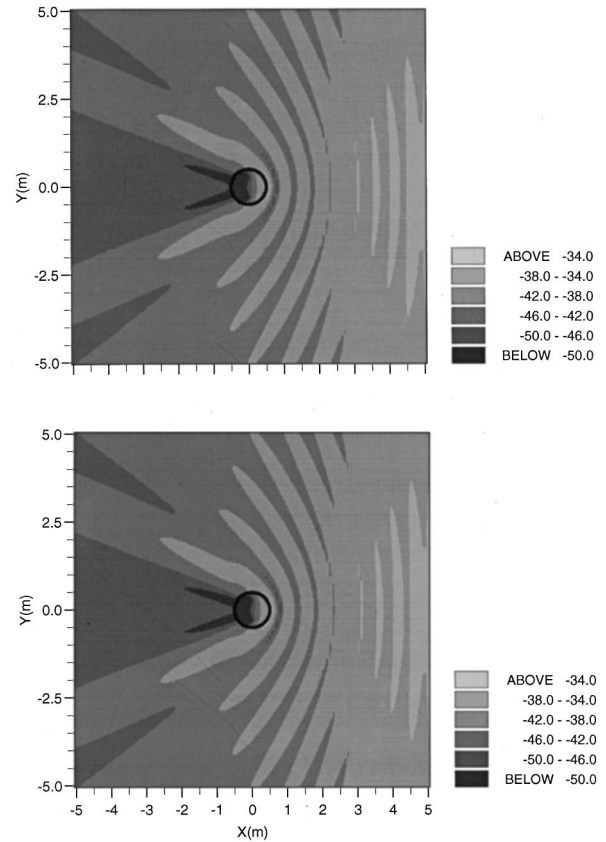


FIG. 3. Two-dimensional slice ( $z = -1$  m) of total field for an infinite cylinder as computed by (a) coupled-mode method and (b) analytic method.

3(b) the corresponding analytic solution is shown. As can be seen, the agreement between the coupled-mode and analytic solutions is excellent. For the coupled-mode solution, we used two homogeneous media; one for the exterior fluid and one with the cylinder's parameters as the interior medium. The minimum and maximum values of  $z$  for the computational domain are  $z = \pm 22$  m. The attenuation profiles start at  $z = \pm 12$  m and the attenuation increases linearly from 0.0 to 5.47 dB/ $\lambda$  at the boundaries. We used 11 azimuthal functions and 141 vertical modes.

### B. A cylindrical disk in free space

We now consider a finite cylinder with the same acoustic parameters as above. The radius is 0.5 m and the total length is also 0.5 m. The point source is located 10.0 m in range from the cylinder and at  $z = 0.25$  m ( $\theta = 0$ ) (i.e., the vertical location of the source is level with the top of the cylinder and is off to the right of the cylinder). We compute the total pressure field in a  $4 \times 4$ -m grid in a vertical slice, the  $x$ - $z$  plane (i.e.,  $\theta = 0, \pi$ ) around and in the cylinder and display the results in Fig. 4 for frequencies 750, 1500, and 3000 Hz. Since we are now considering a vertical slice of the field, the cylinder now appears as a rectangle in Fig. 4 and the axis of symmetry of the cylinder is the  $z$  axis. There is significant scattering from the cylinder in all three cases. There is an interference pattern on the incident side of the cylinder, resulting from the interference of the backscattered and incident energy. As would be expected this pattern is

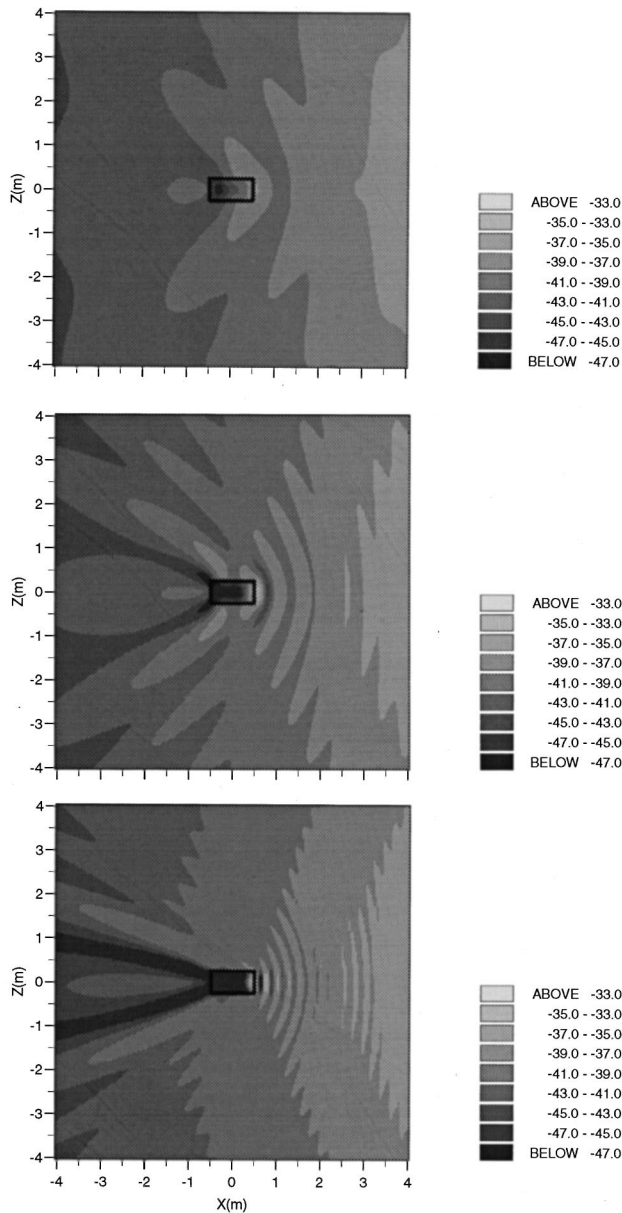


FIG. 4. Two-dimensional slice ( $y=0$ ) of total field for a finite cylinder in free space for a frequency of (a) 750 Hz, (b) 1500 Hz, and (c) 3000 Hz.

more rapidly oscillating in the case of the higher frequencies. Also, there is a shadow zone behind the cylinder. This zone is more sharply defined in the case of the higher frequencies although some energy is still evident behind the cylinder. For the 750-Hz computation we used 100 modes and seven azimuthal terms, for 1500 Hz, 140 modes and 11 azimuthal terms, and for the 3000 Hz example 210 modes and 17 azimuthal terms.

### C. A cylindrical disk embedded in a half-space

We now consider the cylinder of the above example buried 90% in a lower half-space. Instead of a point source, a vertical array of phased sources (17 sources at 0.25-m spacing or four wavelengths for 1500 Hz) is used. In the first example we consider the center of the source at a height of 6 m above the center of the cylinder and 1 m to the right;

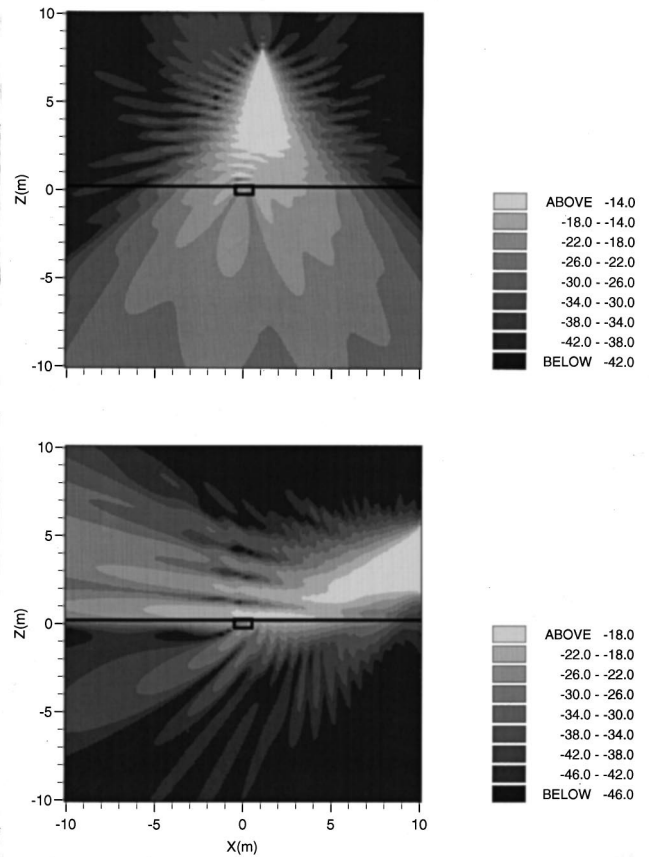


FIG. 5. Two-dimensional slice ( $y=0$ ) of total field for a finite cylinder fractionally buried in lower half-space with (a)  $c=1550$  m/s,  $\rho=1100$  kg/m<sup>3</sup>, and near-normal incidence and (b)  $c=1800$  m/s,  $\rho=1500$  kg/m<sup>3</sup>, and a subcritical grazing angle of incidence.

hence the source beam is almost normally incident upon the cylinder. The bottom half-space has a sound speed of 1550 m/s and a density of 1100 kg/m<sup>3</sup>. The two-dimensional plot of the total pressure field in the  $x-z$  plane is shown in Fig. 5. Because the energy is almost normally incident, there is much penetration into the bottom. A beamlike structure is evident in the shadow area of the cylinder. In the backscattered direction there is a complicated interference pattern caused by the interaction of the incident beam, the reflection of the beam from the interface, and the field scattered by the cylinder.

In the second example, the center point of the source array is located at a horizontal angle of 20° with respect to the cylinder center. The sources are then phased to produce an incident beam of 20°, directly incident upon the cylinder. The sediment sound speed is 1800 m/s for this example and the density is 1500 kg/m<sup>3</sup> and hence the incident angle is subcritical. The interference between the incident and the energy scattered from the cylinder is evident in the backscatter direction and a shadow zone behind the cylinder can be seen in the sediment. The field in the water column, in the forward-scatter direction, is dominated by the reflection of the incident beam off the interface.

For this example we now consider the scattered field. To compute the scattered field in the region  $r > a$  we use Eq. (25) without the source term; in the interior region we sub-

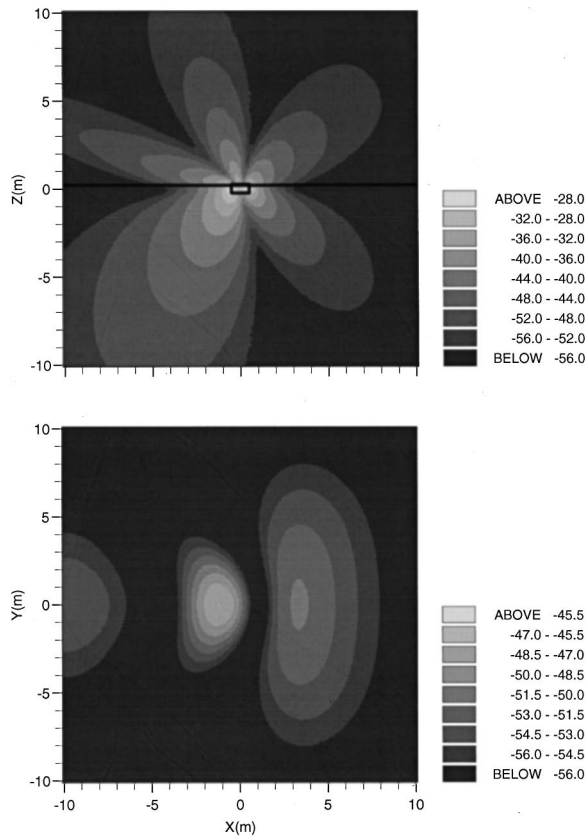


FIG. 6. Two-dimensional slices of scattered field from partially buried cylinder for sediment  $c=1800$  m/s,  $\rho=1500$  kg/m<sup>3</sup>, and a subcritical grazing angle of incidence: (a) vertical slice ( $y=0$  m) and (b) horizontal slice ( $z=4$  m) [please note scale change between (a) and (b)].

tract the source term, Eq. (26b), from the expression for the interior field, Eq. (24). In Fig. 6(a) we show a vertical slice of this field. There is a five-lobed appearance to this field (recall that the scattered field satisfies the appropriate continuity conditions at the water/sediment interface). In Fig. 6(b) we show a horizontal slice of the same field in the water column at  $z=4$  m. This plot shows the horizontal extent of the three lobes in the water column of Fig. 6(a).

### III. SUMMARY

We have shown that coupled modes can be effectively used to solve three-dimensional object scattering problems in the case that the object and the surrounding environment are azimuthally symmetric. We used Galerkin's method to compute eigenfunctions and eigenvalues for vertical velocity profiles with added attenuation profiles. In this paper, the scattering objects considered were finite cylinders; however, more complicated structures including shelled cylinders can be considered by coupling together additional cylindrical domains.

The approach of this paper can be used to model the object scattering in a variety of background environments; free space, half-space, buried and partially buried, and waveguides. It should be possible to use coupled elastic modes<sup>10</sup> to solve analogous scattering problems for elastic objects. In this paper, we considered scattering problems for frequencies up to 3000 Hz, the frequency could be increased at the expense of computing more modes and having larger coupling matrices. Alternatively, for free-space or half-space scattering problems, it might be possible in some cases to reduce the vertical extent of the surrounding space about the object, thereby reducing the number of required modes.

- <sup>1</sup>P. Gerstoft and H. Schmidt, "A boundary element approach to seismo-acoustic facet reverberation," *J. Acoust. Soc. Am.* **89**, 1629–1642 (1991).
- <sup>2</sup>J. T. Goh, H. Schmidt, P. Gerstoft, and W. Seong, "Benchmarks for validating range-dependent seismo-acoustic propagation codes," *IEEE J. Ocean Eng.* **22**, 226–236 (1997).
- <sup>3</sup>M. Dougherty and R. Stephen, "Geoacoustic scattering from seafloor features in the ROSE area," *J. Acoust. Soc. Am.* **82**, 239–256 (1987).
- <sup>4</sup>J. E. Murphy and S. A. Chin-Bing, "A seismo-acoustic finite element model for underwater acoustic propagation," in *Shear Waves in Marine Sediments*, edited by J. M. Hovem, M. D. Richardson, and R. D. Stoll (Kluwer Academic, The Netherlands, 1991), pp. 463–470.
- <sup>5</sup>G. H. Brooke, "An accurate numerical solution for the scattering properties of abrupt discontinuities in acoustic waveguides," *J. Acoust. Soc. Am. Suppl. 1* **68**, S53 (1980).
- <sup>6</sup>R. B. Evans, "A coupled mode solution for acoustic propagation in a waveguide with stepwise depth variations of a penetrable bottom," *J. Acoust. Soc. Am.* **74**, 188–195 (1983).
- <sup>7</sup>R. B. Evans and K. E. Gilbert, "Acoustic propagation in a waveguide with an irregular interface," *Comput. Math. Appl.* **11**, 795–805 (1985).
- <sup>8</sup>J. A. Fawcett and T. W. Dawson, "Fourier synthesis of three-dimensional scattering in a two-dimensional oceanic waveguide using Boundary Integral Equation Methods," *J. Acoust. Soc. Am.* **88**, 1913–1920 (1990).
- <sup>9</sup>R. B. Evans, "Three dimensional acoustic scattering from a cylindrical inclusion in a waveguide," in *Computational Acoustics, Vol. 2, Scattering, Gaussian Beams, and Aeroacoustics, Proceedings of the 2nd IMACS Symposium on Computational Acoustics, 1989*, edited by D. Lee, A. Cakmak, and R. Vichnevetsky (North-Holland, Amsterdam, 1990), pp. 123–132.
- <sup>10</sup>S. Strange and W. Friederich, "Guided wave propagation across sharp lateral heterogeneities: the complete wavefield at a cylindrical inclusion," *Geophys. J. Int.* **111**, 470–482 (1992).
- <sup>11</sup>J. A. Fawcett, "An efficient three-dimensional boundary integral equation method for solving azimuthally symmetric scattering problems in the oceanic waveguide," *J. Acoust. Soc. Am.* **94**, 2307–2314 (1993).
- <sup>12</sup>M. I. Taroudakis, "A coupled-mode formulation for the solution of the Helmholtz equation in water in the presence of a conical sea-mount," *J. Comp. Acoust.* **4**, 101–121 (1996).
- <sup>13</sup>G. A. Athanassoulis and A. M. Propathopoulos, "Three-dimensional acoustic scattering of a source-generated field from a cylindrical island," *J. Acoust. Soc. Am.* **100**, 206–218 (1996).
- <sup>14</sup>G. A. Athanassoulis and K. A. Belibassakis, "All-frequency normal-mode solution of the three-dimensional acoustic scattering from a vertical cylinder in a plane-horizontal waveguide," *J. Acoust. Soc. Am.* **101**, 3371–3384 (1997).

# A finite-difference time-domain solution to scattering from a rough pressure-release surface

Frank D. Hastings,<sup>a)</sup> John B. Schneider,<sup>b)</sup> and Shira L. Broschat<sup>c)</sup>

*School of Electrical Engineering and Computer Science, Washington State University, Pullman, Washington 99164-2752*

(Received 4 April 1997; accepted for publication 21 August 1997)

The finite-difference time-domain (FDTD) method is a numerical technique that makes no explicit physical approximations to the underlying problem. The quality of a FDTD-based solution typically is determined by the discretization of the computational domain—the smaller the spacing, the more accurate the solution. Unfortunately, for large computational domains, i.e., ones spanning many wavelengths, the small spatial step size needed to obtain a high-fidelity solution may lead to a prohibitively large number of unknowns. Here it is shown how the FDTD method can be used to model accurately scattering from pressure-release surfaces above a homogeneous water column. To keep the computational cost manageable, a number of enhancements to the standard FDTD algorithm are employed. These enhancements include correcting for numerical dispersion along the specular direction of the incident insonification, using locally conformal cells at the pressure-release boundary, and propagating the field through the homogeneous water column via an analytic method. The accuracy of the FDTD approach is demonstrated by comparison with an integral equation-based reference solution to the same rough surface scattering problem [Thorsos, *Proceedings of the Reverberation and Scattering Workshop*, pp. 3.2–3.20 (1994) Naval Research Laboratory Book Contribution NRL/BE/7181-96-001]. © 1997 Acoustical Society of America. [S0001-4966(97)03912-X]

PACS numbers: 43.30.Gv, 43.30.Hw, 43.20.Fn [DLB]

## INTRODUCTION

The finite-difference time-domain (FDTD) method is a numerical technique that has been used to solve a wide range of problems for electromagnetic, acoustic, and elastic wave propagation (see, for example, Refs. 1–3). While the FDTD method does not use any explicit physical approximations to the underlying problem, implicit approximations are inherent to any numerical method. For the FDTD method, these approximations include homogeneity of the material over individual cells and a “staircase” approximation to the interface between materials. One strength of a numerical method is that errors introduced by these implicit approximations can, in theory, be made vanishingly small. However, there is a trade-off between accuracy and computational cost. To obtain an accurate solution to a large problem using standard FDTD techniques, the number of unknowns required may be prohibitively large.

In this paper, it is shown that the FDTD method can be used to predict accurately the fields scattered from one-dimensional rough pressure-release surfaces spanning 200, or more, wavelengths of the insonification. This problem naturally lends itself to the use of several algorithm enhancements that permit an accurate solution at a reasonable cost and hence that make the solving of large problems feasible.

In a previous paper, the FDTD method was used in a Monte Carlo technique to obtain scattering cross sections for randomly rough surfaces satisfying the Dirichlet boundary

condition.<sup>4</sup> Both single-scale Gaussian and multiscale Pierson–Moskowitz surface roughness spectra were considered. The FDTD results agreed with those obtained by Thorsos using an integral equation (IE) technique.<sup>5</sup> However, the calculation of a scattering cross section, or scattering strength, requires the determination of fields far from the scatterer. Also, Monte Carlo studies, such as the ones used in Refs. 4 and 5, require averaging of results over many surface realizations. Since near fields are typically more complicated than far fields, and since averaging may mask small errors, it is possible that the FDTD method might not provide accurate results in the near-field for any single surface realization. To address this concern, this paper examines FDTD-based results for a reference problem for which an accurate IE-based solution exists.<sup>6</sup> For this problem, near-field pressures are obtained for a single surface realization. Excellent agreement between the two solutions is obtained. Stephen has published a FDTD solution to the same problem, and his results agree well with the reference solution.<sup>7</sup> The work presented here differs from Stephen’s in that the number of unknowns and the computational time are reduced by more than an order of magnitude. In addition, greater accuracy is obtained.

The FDTD method can be used to yield a full wave, time-domain solution to the surface scattering problem without placing restrictions on the underlying physical geometry. This allows the direct study of the scattering physics, but also permits benchmarking of approximate methods such as the small slope<sup>8</sup> and parabolic equation approximations.<sup>9</sup> Additionally, exact methods can be used to benchmark other less computationally expensive numerical methods. The reference problem considered here is a rigorous test of numeri-

<sup>a)</sup>Electronic mail: fhasting@eecs.wsu.edu

<sup>b)</sup>Electronic mail: schneidj@eecs.wsu.edu

<sup>c)</sup>Electronic mail: shira@eecs.wsu.edu

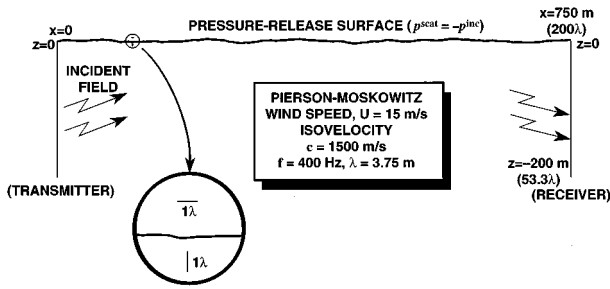


FIG. 1. Reference problem geometry. The surface is drawn to scale. The expanded view shows a segment of the surface and lines with lengths equal to one wavelength of the insonification. The incident field is specified at a range of zero (identified as the transmitter). The goal is to determine the scattered pressure at a range of 750 m over a depth of 200 m (identified as the receiver). The terms transmitter and receiver are used logically and are not meant to imply the existence of a physical device at these locations.

cal accuracy; by comparing results in the near field, it is possible to detect small discrepancies that might not be evident in a far-field comparison. The results presented in this paper, in conjunction with those presented in Ref. 4 verify the accuracy of the FDTD method for the Dirichlet rough surface scattering problem.

The FDTD method is a time-domain method that can provide results over a broad frequency spectrum by means of a single simulation. However, since the reference problem and the corresponding IE reference solution were posed in the frequency domain, the FDTD solution presented here is restricted to a single frequency. Thus, we demonstrate the accuracy of the FDTD method, but do not concentrate on exploiting its full power.

In the next section, we describe the reference problem and present a comparison of the FDTD and IE results. In Sec. II we discuss the details of implementing the FDTD method and the enhancements employed.

## I. REFERENCE PROBLEM AND SOLUTION

The reference problem considered (Fig. 1) consists of a one-dimensional, rough pressure-release sea surface, an isovelocity water column, and harmonic tapered-beam insonification.<sup>6</sup> The rough surface is a single realization from a set of surfaces generated using a Pierson–Moscowitz wave number spectrum for a wind speed of 15 m/s.<sup>10</sup> The surface height is specified over a range of 750 m. The incident harmonic pressure is given at zero range,  $x=0$ , by

$$p_{\text{inc}}(x=0, z) = \exp\left(-\frac{(z-z_0)^2}{g^2}\right) \exp(ikz \sin \theta_i), \quad (1)$$

where  $\theta_i = 10^\circ$  is the mean grazing angle,  $g = 27.55$  m is the half-power width,  $z_0 = -66.12$  m is the location of the pressure maximum, and  $k = 2\pi f/c$   $\text{m}^{-1}$  is the wave number. The frequency  $f$  is 400 Hz and the sound speed in water  $c$  is 1500 m/s. Depth increases in the negative  $z$  direction. The FDTD simulation requires that the incident field be specified on the surface and also at the receiver. Using Green's second theorem, one can express the incident field at any point in the water column in terms of the field at zero range,

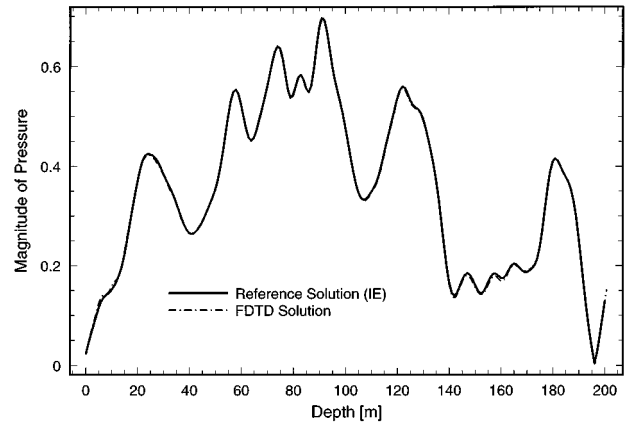


FIG. 2. Pressure magnitude over a depth of 200 m at a range of 750 m. Reference solution and FDTD solution.

$$p_{\text{inc}}(x, z) = 2 \int_{-\infty}^{\infty} p_{\text{inc}}(x'=0, z') \times \frac{\partial G_0(x, z; x', z')}{\partial x'} \Big|_{x'=0} dz', \quad (2)$$

where  $G_0(x, z; x', z')$  is the two-dimensional free-space Green's function given by

$$G_0(x, z; x', z') = \frac{i}{4} H_0^{(1)}(k\sqrt{(x-x')^2 + (z-z')^2}). \quad (3)$$

The maximum value of  $p_{\text{inc}}(x=0, z)$  is unity and occurs at a depth of  $z=z_0$ . As written, (2), with the upper limit of integration at infinity, is for an infinite water column and is not directly applicable to the problem at hand. However,  $p_{\text{inc}}(x=0, z)$  is small for  $z \geq 0$  m, so the integration can be truncated at an upper limit of zero without introducing significant error.

The goal of the reference problem is to find the total pressure at a range of 750 m over a 200-m depth starting at the surface (i.e.,  $x=750$  m and  $-200 \leq z \leq 0$  m). The reference solution was obtained using an IE technique.<sup>6</sup> Careful analysis was done to ensure that numerical errors were small.

Figure 2 shows a plot of the magnitude of the pressure over the 200-m depth for the reference solution and the FDTD solution. The two curves are nearly identical except near depths of 10 and 160 m, where there are slight differences. Adjusting the location of the absorbing boundary condition relative to the surface affected the error at 10 m. Hence, the discrepancy at this location is attributed to artifacts introduced by the absorbing boundary condition. This is discussed further in Sec. II F. No obvious explanation was found for the discrepancy in the data at 160 m; it is most likely due to the differences between the FDTD and IE implementations. (For example, for the FDTD solution the elevation of the pressure-release surface was sampled every  $\frac{1}{16}$  of a wavelength, whereas for the IE solution the surface was sampled every  $\frac{1}{10}$  of a wavelength.) It should be noted that these differences and the resulting discrepancies in the data are well within practical limits.

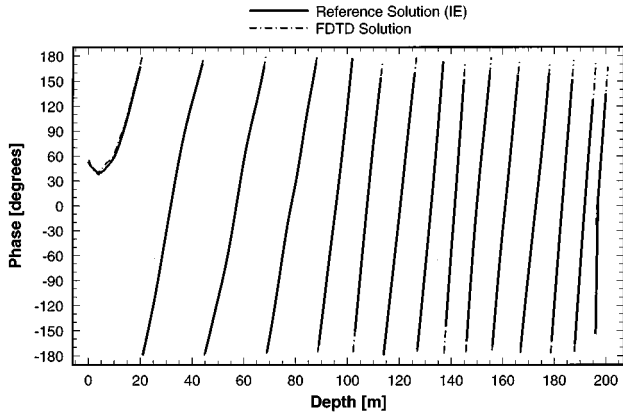


FIG. 3. Pressure phase over a depth of 200 m at a range of 750 m. Reference solution and FDTD solution.

Figure 3 shows the phase of the pressure for the reference solution and the FDTD solution. (The branch cut was taken at  $180^\circ$  and, for the sake of clarity, the segments are not connected across the cut.) Again, the reference solution and FDTD solution exhibit excellent agreement except near a depth of 10 m. The difference seen in the magnitude at 160 m is not present in the phase.

## II. FDTD IMPLEMENTATION

### A. Basic equations

The governing acoustic equations in two dimensions are

$$\frac{\partial p}{\partial t} = -\rho c^2 \left( \frac{\partial v_x}{\partial x} + \frac{\partial v_z}{\partial z} \right), \quad (4)$$

$$\frac{\partial v_x}{\partial t} = -\frac{1}{\rho} \frac{\partial p}{\partial x}, \quad (5)$$

$$\frac{\partial v_z}{\partial t} = -\frac{1}{\rho} \frac{\partial p}{\partial z}, \quad (6)$$

where  $p$  is pressure,  $\vec{v} = v_x \hat{a}_x + v_z \hat{a}_z$  is velocity, and  $\rho$  is density. For the reference problem the isovelocity water column has a density of  $1000 \text{ kg/m}^3$ . The updated equations for the FDTD method are obtained by replacing the derivatives in (4)–(6) by finite differences and solving for “future” fields in terms of present and past fields. To obtain a fully explicit scheme the points at which the fields are evaluated must be offset spatially and temporally. Second-order accurate central differences can be used to approximate all the derivatives if the fields are discretized so they are defined at the following evaluation points:

$$p(x, z, t) = p(i\Delta x, j\Delta z, n\Delta t) = p^n(i, j), \quad (7)$$

$$\begin{aligned} v_x(x, z, t) &= v_x((i+1/2)\Delta x, j\Delta z, (n+1/2)\Delta t) \\ &= v_x^{n+1/2}(i, j), \end{aligned} \quad (8)$$

$$\begin{aligned} v_z(x, z, t) &= v_z(i\Delta x, (j+1/2)\Delta z, (n+1/2)\Delta t) \\ &= v_z^{n+1/2}(i, j), \end{aligned} \quad (9)$$

where  $\Delta x$  and  $\Delta z$  are the range and depth spatial step sizes, respectively, and  $\Delta t$  is the temporal step size. A portion of

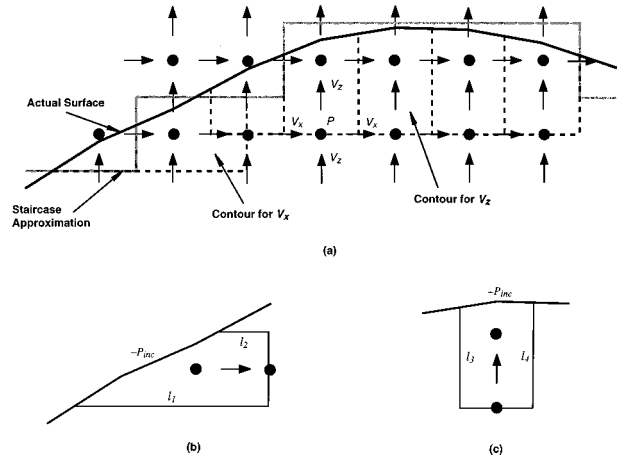


FIG. 4. Staircase and contour path models of the surface are shown. Part (a) shows the actual surface (black solid line) with staircase approximation (gray solid line) and conformal cells (dashed lines). The conformal cells are bounded on the top by the actual surface. Conformal cells are shown for  $v_x$  and  $v_z$  in parts (b) and (c), respectively.

the FDTD grid is shown in Fig. 4. In this work  $\Delta x = \Delta z = \delta$ . On the right-hand side of (7)–(9), the fields are specified by their spatial and temporal indices, i.e., the arguments and the superscripts, respectively. For the  $v_x$  and  $v_z$  components of velocity, the spatial offsets are implied by the field component [i.e.,  $v_x(i, j)$  is not collocated with  $v_z(i, j)$ ]. The temporal offset between the fields is explicitly retained in the temporal index. Replacing the derivatives in (4)–(6) with finite differences and using the discretization of (7)–(9) yields the following update equations:

$$\begin{aligned} p^n(i, j) &= p^{n-1}(i, j) - \rho c \frac{c\Delta t}{\delta} [v_x^{n-1/2}(i, j) \\ &\quad - v_x^{n-1/2}(i-1, j) + v_z^{n-1/2}(i, j) \\ &\quad - v_z^{n-1/2}(i, j-1)], \end{aligned} \quad (10)$$

$$\begin{aligned} v_x^{n+1/2}(i, j) &= v_x^{n-1/2}(i, j) - \frac{1}{\rho c} \frac{c\Delta t}{\delta} \\ &\quad \times [p^n(i+1, j) - p^n(i, j)], \end{aligned} \quad (11)$$

$$\begin{aligned} v_z^{n+1/2}(i, j) &= v_z^{n-1/2}(i, j) - \frac{1}{\rho c} \frac{c\Delta t}{\delta} \\ &\quad \times [p^n(i, j+1) - p^n(i, j)]. \end{aligned} \quad (12)$$

These equations are used in a leap-frog scheme to obtain the unknown future fields in terms of the known past and current fields. This explicit scheme, unlike many implicit schemes, is not unconditionally stable. To obtain a stable solution in two dimensions, the factor  $c\Delta t/\delta$ , known as the Courant number, must be less than or equal to  $1/\sqrt{2}$ . (For more information on the Courant number and stability of the FDTD method the reader is referred to Ref. 1.)

In the remainder of this paper we discuss the application of these equations to solving the reference problem. Several enhancements that are not found in “traditional” FDTD-based solutions are presented. Collectively, these enhancements enable the FDTD method to produce accurate results at a reasonable computational cost.



## B. Incident field and scattered-field formulation

Insonification of the FDTD grid was accomplished using a scattered-field approach for which the field at the pressure-release surface is set to the negative of the incident field. Hence, it was necessary to calculate the incident field at the surface. Incident field data were available from Thorsos in a format suitable for the IE method.<sup>6</sup> However, since the elevations of the pressure-release surface were sampled at different ranges for the FDTD solution, it was necessary to use an independent calculation of the incident field. For the IE solution, (2) was integrated using a single-precision Riemann sum over the limits  $-150 \leq z \leq 0$  m. For the FDTD solution, a semi-infinite, double-precision integral was used. Integration was performed with an adaptive quadrature routine from the QUADPACK integration package.<sup>11</sup>

To exploit fully the power of the FDTD technique, the incident insonification should be transient, allowing information to be obtained over a band of frequencies. However, when results are needed for only a single frequency, as for the case here, one can either use transient insonification and extract the information at the desired frequency or, alternatively, use “quasi-harmonic” illumination and wait for the transients to die out. By “quasi-harmonic” we mean the excitation is zero at the start of the simulation but then, after a gradual ramp in magnitude as described below, varies harmonically. Each approach requires approximately the same number of time steps. With the first approach, the simulation must be run until all energy has propagated out of the computational domain to prevent frequency aliasing. With the second approach, the simulation must be run until all transients dissipate and steady state is obtained. Since the reference problem specified the insonification at a single frequency and a suitable analytic expression for transient illumination was not readily available, we used a quasi-harmonic incident field.

For a point  $(x_s, z_s)$  on the surface, (2) can be used to obtain the scattered field phasor  $A_s \exp(-i\alpha_s)$  (the scattered field is the negative of the incident field as reflected in the phase of  $\alpha_s$ ). In the time domain this becomes  $A_s \cos(\omega t + \alpha_s)$ . Use of this time-domain representation for all surface points throughout the computational domain would cause an exceedingly large transient since all the surface fields would switch on simultaneously. An excessive number of time steps would then be required to dissipate this transient. The transient associated with the introduction of the incident field can be reduced significantly by gradually turning on the field. This can be accomplished by weighting the amplitude of the surface fields in accordance with a temporally ramped plane wave. Specifically, for points on the surface the scattered pressure is

$$p_s(x_s, z_s, t) = A_s \cos(\omega t + \alpha_s) u(\xi) [1 - \exp(-\xi^2/\tau^2)], \quad (13)$$

where  $\xi = ct - x_s \cos \theta_i - z_s \sin \theta_i$ ,  $u$  is the unit step function, and  $\theta_i$  is the incident angle. The time constant  $\tau$  controls the rate at which the surface fields ramp up to their final values; for this work, it was set to approximately ten periods of the harmonic insonification. This modified form of the incident

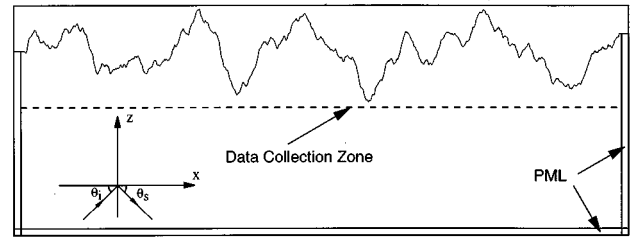


FIG. 5. Computational domain for the FDTD simulation. The PML ABC bounds the lower edge and part of the sides of the domain. The measurement boundary is the line over which the pressures and velocities are measured for transformation to the “receiver.” In this figure the vertical scale has been expanded by a factor of approximately 15.

field affects only the transient and not the steady-state behavior.

## C. Near-field to near-field transformation

As shown in Fig. 1, the reference problem requires calculation of the scattered field over a 200-m depth at a range of 750 m, i.e., over the line labeled “receiver.” A FDTD grid can be constructed to span the entire receiver. After steady state has been obtained, the scattered field at the receiver is then recorded directly from the grid. However, this is not the most efficient approach. Since the water column is homogeneous, it is possible to calculate analytically the scattered field at any point in the water column using a near-field to near-field (NFNF) transformation. This approach has two important advantages over a direct FDTD solution: (i) the computational domain is much smaller and (ii) the effects of numerical dispersion are reduced. As a result, the computational cost is reduced while, at the same time, the accuracy is improved.

Implementation of the NFNF transformation is straightforward. Once steady state is reached, the scattered fields are recorded over an imaginary boundary three cells below the lowest point of the surface. This boundary is referred to as the data collection zone and is shown in Fig. 5. Again employing an analytic expression, similar to (2), the scattered fields at the “receiver” are calculated from the measured fields.

Steady state was defined to exist when the magnitudes and phases no longer changed significantly from one period of the incident field to the next. The simulation was terminated when the average relative change in magnitudes was less than 0.001 and the average change in phase was less than  $0.05^\circ$ . To obtain the values of the magnitudes and phases, the required fields were sampled twice each period along the data collection zone. With harmonic oscillation assumed, the two samples were sufficient to determine the magnitude and phase of the signal.

In the NFNF approach, the computational domain is made large enough to accommodate the surface, the data collection zone, and the absorbing boundary condition. In comparison with the standard FDTD approach, for which the computational domain encloses the entire receiver, the vertical dimension of the domain is reduced by approximately 91%. In addition, for the NFNF approach the fields propa-

gate only from the surface to the data collection zone before they are measured, in contrast to the standard FDTD approach for which the fields propagate from the “transmitter” to the “receiver.” The error introduced by numerical dispersion increases with the distance the fields propagate. Hence, this error is significantly smaller for the NFNF approach as discussed further in the next section

#### D. Dispersion correction

Equations (10)–(12) are inherently dispersive. For a plane wave propagating in the FDTD grid at an angle  $\phi$  with respect to the  $x$  axis, the numeric dispersion relation

$$\left(\frac{\delta}{c\Delta t}\right)^2 \sin^2\left(\frac{\omega\Delta t}{2}\right) = \sin^2\left(\frac{\delta\tilde{k}\cos\phi}{2}\right) + \sin^2\left(\frac{\delta\tilde{k}\sin\phi}{2}\right), \quad (14)$$

where  $\tilde{k}$  is the wave number for the fields propagated by the FDTD simulation and  $\omega$  is the frequency.<sup>1</sup> This reduces to the usual continuous-space dispersion relation, i.e.,  $k^2 = \omega^2/c^2$ , in the limit as  $\delta$  and  $\Delta t$  approach zero. (Note that the FDTD scheme used here discretizes the coupled first-order governing differential equations. However, the dispersion relation is the same for the discretized form of the wave equation.<sup>12</sup>)

To minimize the memory required for a simulation, the coarsest possible grid should be used. However, in practice, certain errors increase as the spatial step size increases, thus imposing limits on the coarseness of the grid. These errors are associated with (i) assuming homogeneity for a material over discrete “cells,” (ii) approximating material boundaries as “staircased,” and (iii) numeric dispersion. In the problem under consideration, the water column is homogeneous so the first source of error is not relevant. The second source of error is considered in the next section. The error associated with numeric dispersion, i.e., the amount that  $\tilde{k}$  differs from the true wave number, is a function of the spatial step size, the angle of propagation, and the Courant number. For a given spatial step size and propagation angle, the error is at a minimum at the Courant limit (which is  $1/\sqrt{D}$  where  $D$  is the number of spatial dimensions in the problem).<sup>13,14</sup> Thus, the Courant limit was used for the FDTD solution to the reference problem. A spatial step size of  $\frac{1}{16}$  of a wavelength is not uncommon in FDTD simulations involving objects (scatterers) less than 10 wavelengths in size. This discretization, though considered large, was found to be acceptable for the reference problem, provided corrections were made for numeric dispersion as described below.

At 16 points per wavelength (PPW) and the Courant limit and assuming plane wave propagation at an angle of  $10^\circ$  [i.e.,  $\phi = 10^\circ$  in (14)], the phase velocity in the FDTD grid is 0.287% slower than the true phase velocity. This difference in velocity seemingly is small, but the error associated with it is cumulative. After a wave propagates through a large computational domain, such as the one considered here, the total phase error can be quite large. Here the difference between  $k$  and  $\tilde{k}$  produces approximately one degree

of phase error per wavelength of propagation. Thus, propagation across the entire 200-wavelength computational domain would result in 200 degrees of phase error.

As discussed in Sec. II C, a NFNF transformation was used to obtain the fields at the receiver. By analytically “propagating” fields whenever possible, a much smaller computational domain was used than would otherwise have been required. However, this scheme mixes analytic and numeric wave numbers over a large computational domain, requiring that the two wave numbers agree more closely than they do when using a discretization of 16 PPW in the standard FDTD method. Fortunately, this problem can be solved in one of two ways: (i) the analytic wave number can be increased to agree with the numeric one or (ii) the material parameters in the simulation can be adjusted to make the numeric wave number agree with the analytic one. In this work, the former approach was used. Thus, in analytic expressions,  $k$  was replaced by  $1.00288k$ . Since the wavelength in the FDTD simulation was contracted, the height and length of the pressure-release surface were scaled correspondingly (divided by a factor of 1.00288). Finally, when transforming back into physical space from numeric space (points in the FDTD grid), the spatial coordinates were rescaled by multiplying by a factor of 1.00288.

The reference problem is well suited to such a simple dispersion correction since the incident field propagates primarily in a single direction (i.e., although the incident insonification is not a plane wave, most of the incident energy propagates at an angle  $\phi$  close to  $10^\circ$  grazing). If the incident field were not approximately planar (e.g., the field due to a line source near the surface), it would be difficult to define a meaningful dispersion correction factor, and dispersion errors would have to be controlled by a suitable selection of the PPW.

It should be noted that for the problem considered here, the benefits of using a dispersion correction are not restricted to results near the specular direction ( $10^\circ$  grazing). The fields coupled into the grid are dictated by an analytic expression for the incident field. It is important that the phase velocity (or wave number) of the analytic expression and the phase velocity of the fields in the grid are matched. Without proper matching, the fields coupled into the grid will behave as if the incident field arrived at an angle other than the true incident angle. By correcting for numerical dispersion, the incident angle is true. However, the scattered fields do leave the surface at all angles. Thus, energy that is propagating in directions other than specular (or backscatter) will suffer some numerical dispersion since the dispersion correction is only exact for a single angle. However, these scattered fields are recorded (at the data collection zone) after traveling only a short distance and, hence, at that point, have not accumulated any significant phase error. Since the fields are analytically propagated after being recorded, no additional phase error is ever introduced.

The type of dispersion correction described above is not restricted to the Dirchlet problem. It can be applied equally well to fluid–fluid and fluid–elastic interface problems.

## E. Surface realization and conformal cell

The reference problem specified heights to a high degree of accuracy, but only at discrete range samples separated by  $\frac{1}{10}$  of a wavelength. Since the FDTD simulation requires a finer discretization in range, it was necessary to interpolate between the surface heights provided. Hence, the resulting surface was slightly different than that used for the IE method.

A standard FDTD implementation uses a Cartesian grid that allows specification of media only to within a grid space. As a result, curved boundaries are modeled using a staircase approximation as shown in Fig. 4(a). Such an approximation can produce significant artifacts due to nonphysical scattering. This is remedied either by using a very finely discretized grid or by using a conformal technique for which the grid structure is altered to conform to the scatterer. In this work, a locally conformal technique was used based on the integral form of (5) and (6). Rewriting these equations as a single vector equation and taking the volume integral of both sides yields

$$\int_V \frac{\partial \vec{v}}{\partial t} dv = - \int_V \frac{1}{\rho} \nabla p dv. \quad (15)$$

Using the identity  $\int_V \nabla \phi dv = \int_S \phi \hat{n} ds$  and reducing to the 2-D case yields

$$\int_S \frac{\partial v_x}{\partial t} ds = - \oint_l \frac{1}{\rho} p n_x dl, \quad (16)$$

$$\int_S \frac{\partial v_z}{\partial t} ds = - \oint_l \frac{1}{\rho} p n_z dl, \quad (17)$$

where surface  $S$  and contour  $l$  are shown in Fig. 4(b) and (c) for field components  $v_x$  and  $v_z$ , respectively. The quantities  $n_x$  and  $n_z$  are the  $x$  and  $z$  components, respectively, of the outward unit normal vector along the contour. This method is analogous to that introduced by Jurgens *et al.*<sup>15</sup> It is assumed that  $v_x$  and  $v_z$  are constant over  $S$  and  $p$  is constant over each segment of the contour. To satisfy the Dirichlet boundary condition, the pressure on the surface is set to the negative of the incident field. The incident field is computed at the center of the contour segment adjoining the surface. Under these assumptions, (16) and (17) reduce to the time-stepping relations

$$v_x^{n+1/2}(i,j) = v_x^{n-1/2}(i,j) - \frac{\Delta t}{\frac{1}{2}(l_1+l_2)\delta\rho} (p^n(i,j) - \sqrt{1+(l_2-l_1)^2} n_x p_{\text{inc}}) \quad (18)$$

$$v_z^{n+1/2}(i,j) = v_z^{n-1/2}(i,j) - \frac{\Delta t}{\frac{1}{2}(l_3+l_4)\delta\rho} (p^n(i,j+1) - \sqrt{1+(l_3-l_4)^2} n_z p_{\text{inc}}), \quad (19)$$

where lengths  $l_1$ ,  $l_2$ ,  $l_3$ , and  $l_4$  are shown in Fig. 4(b) and (c).

Pressure nodes that have one or more neighboring velocities above the pressure-release surface are not used. Instead, the velocities that would normally depend on them for

update are computed using extended cells. Hence, no special update equation is needed for pressure nodes that occur near the surface. To obtain (18) and (19) the conformal cells are approximated as trapezoids. This introduces a slight change in the surface geometry; however, the difference is small compared to the staircase approximation. Conformal-cell updates only occur near the interface; in fact (16) and (17) reduce to (11) and (12) for square cells.

Many of the locally conformal schemes developed for electromagnetics problems can be adapted for acoustics problems. The method used here is adapted from one developed for electromagnetic scattering from perfect electric conductors.<sup>15</sup> Fluid-fluid boundaries are analogous (in 2-D) to dielectric-dielectric boundaries and hence the locally conformal schemes which have been developed for dielectric interfaces can be used to solve fluid-fluid problems. These methods are not restricted to surface scattering problems such as the one considered here—they can also be applied to discrete scatterers with complicated geometries including wedges, slots, and curved surfaces.<sup>1</sup>

## F. Absorbing boundary conditions

For unbounded problems, a FDTD simulation requires the use of absorbing boundary conditions (ABCs). Here, the perfectly matched layer (PML)<sup>16</sup> ABC was used. As shown in Fig. 5, the ABC bounds the computational domain below the surface and terminates on the edges at the water-air interface. The surface was extended with flat buffer zones on either end to accommodate the PML. The PML thickness used was 16 grid spaces.

A minimum vertical grid dimension of 78 cells was used to accommodate the surface and the PML. Increasing this value caused a change in the results at a depth of 10 m; however, the magnitude of the difference between the FDTD and reference solutions remained relatively constant. Hence, it is likely that reflections from the ABC were the cause of the discrepancy at the 10-m depth. To eliminate completely spurious energy from the ABC, it would be necessary to increase the size of the computational domain to such an extent that the problem would become numerically intractable. However, given the published literature documenting the excellent overall performance of the PML ABC and the weak dependence of the observed results on the size of the computational domain, one can be confident that the error introduced by the PML is small.

## G. Comparison with another FDTD solution

A FDTD-based solution to the reference problem has been published by Stephen.<sup>7</sup> His solution is based on the full-grid implementation—that is, the computational domain fully encompasses the surface, “transmitter,” and “receiver.” The incident field is propagated directly from the “transmitter” via the FDTD grid, and no NFNF transformations are used. Table I lists some of the differences between the full-grid solution and the solution presented here. The full-grid solution agreed well with the reference solution. However, with the exception of the field near a depth of 10 m, the results presented in this paper agree better with the

TABLE I. Resource comparison for full-grid and the near-field to near-field (NFNF) transformation implementations.

	Full grid	NFNF
Points/ $\lambda$	20	16
Field	Total	Scattered
Code type	Elastic	Acoustic
Grid	Stairstep	Conformal
Unknowns	$\approx 27 \times 10^6$	$\approx 0.8 \times 10^6$
Time steps	7205	5400
Run time	9 h 22 min	38 min
Machine	DEC Alpha 3000/400	HP 9000/735

reference solution than do the full-grid results. The full-grid solution was obtained using 20 PPW instead of 16. The amount of phase error due to dispersion is reduced 36% when the PPW are increased from 16 to 20. However the NFNF approach with the dispersion correction had better overall accuracy. From Table I, it is apparent that the NFNF approach is computationally more efficient than the full-grid approach. However, the implementation used in Ref. 7 was a general elastic/acoustic scheme. The use of strictly acoustic update equations would reduce the number of unknowns and run time shown for the full-grid approach by a factor of approximately  $\frac{3}{5}$ . The run times shown in Table I provide an estimate of the speed-up that can be realized using the approach presented here (which is more than an order of magnitude faster). However, although the machines on which these codes were run are roughly comparable in computational power factors such as clock speed, cache size, and compiler optimization will also influence run times.

### III. SUMMARY

A FDTD method for simulating scattering from rough, pressure-release surfaces has been presented. The approach relies on a near-field to near-field transformation to reduce computational cost and utilizes a correction for the inherent numerical dispersion of the FDTD method. A conformal grid technique was used to model more accurately the surface geometry at a modest number of points per wavelength (16 PPW). An alternate full-grid FDTD implementation was compared with the NFNF implementation presented here. The comparison shows that the NFNF approach has better overall accuracy and is far more computationally efficient

than the full-grid scheme. Finally, the FDTD solution was compared with the IE reference solution and results for both the magnitude and phase are virtually the same.

### ACKNOWLEDGMENT

This work was supported by the Office of Naval Research, Code 3210A.

- <sup>1</sup>A. Taflove, *Computational Electrodynamics: The Finite-Difference Time-Domain Method* (Artech House, Boston, 1995).
- <sup>2</sup>J. Virieux, "P-SV wave propagation in heterogeneous media: Velocity-stress finite difference method," *Geophysics* **51**(4), 889–901 (1986).
- <sup>3</sup>D. Botteldooren, "Acoustical finite-difference time-domain simulation in a quasi-Cartesian grid," *J. Acoust. Soc. Am.* **95**, 2313–2319 (1994).
- <sup>4</sup>F. D. Hastings, J. B. Schneider, and S. L. Broschat, "A Monte-Carlo FDTD technique for rough surface scattering," *IEEE Trans. Antennas Propag.* **43**(11), 1183–1191 (1995).
- <sup>5</sup>E. I. Thorsos, "The validity of the Kirchhoff approximation for rough surface scattering using a Gaussian roughness spectrum," *J. Acoust. Soc. Am.* **83**, 78–92 (1988).
- <sup>6</sup>E. I. Thorsos, "Test Case 1: Sea surface forward scattering," in *Proceedings of the Reverberation and Scattering Workshop*, edited by D. B. King, S. A. Chin-Bing, J. A. Davis, and R. B. Evans, May 1994, Gulfport, MS, pp. 3.2–3.20. Naval Research Laboratory Book Contribution NRL/BE/7181-96-001.
- <sup>7</sup>R. A. Stephen, "Modeling sea surface scattering by the time-domain finite-difference method," *J. Acoust. Soc. Am.* **100**, 2070–2078 (1996).
- <sup>8</sup>A. Voronovich, *Wave Scattering from Rough Surfaces* (Springer-Verlag, Berlin, 1994).
- <sup>9</sup>F. B. Jensen, W. A. Kuperman, M. B. Porter, and H. Schmidt, eds., *Computational Ocean Acoustics* (American Institute of Physics, New York, 1994).
- <sup>10</sup>E. I. Thorsos, "Acoustic scattering from a Pierson-Moskowitz sea surface," *J. Acoust. Soc. Am.* **88**, 335–349 (1990).
- <sup>11</sup>R. Piessens, E. de Doncker, C. Uberhuber, and D. Kahaner, *QUADPACK, A Subroutine Package for Automatic Integration* (Springer-Verlag, Berlin, 1983).
- <sup>12</sup>R. M. Alford, K. R. Kelly, and D. M. Boore, "Accuracy of finite difference modeling of the acoustic wave equation," *Geophysics* **39**(6), 834–842 (1974).
- <sup>13</sup>A. C. Cangellaris and R. Lee, "On the accuracy of numerical wave simulations based on finite methods," *J. Electromagn. Waves Appl.* **6**(12), 1635–1653 (1992).
- <sup>14</sup>K. L. Shlager, J. G. Maloney, S. L. Ray, and A. F. Peterson, "Relative accuracy of several finite-difference time-domain methods in two and three dimensions," *IEEE Trans. Antennas Propag.* **41**(12), 1732–1737 (1993).
- <sup>15</sup>T. G. Jurgens, A. Taflove, K. Umashankar, and T. G. Moore, "Finite-difference time-domain modeling of curved surfaces," *IEEE Trans. Antennas Propag.* **40**(4), 357–366 (1992).
- <sup>16</sup>J.-P. Berenger, "A perfectly matched layer for the absorption of electromagnetic waves," *J. Comput. Phys.* **114**(1), 185–200 (1994).

# Novel acoustic wave resonance scattering formalism

Huinam Rhee<sup>a)</sup>

Reactor Mechanical Engineering, Korea Power Engineering Company, Yusung-Ku, Taejon 305-353, Korea  
and Department of Mechanical Engineering, Graduate School, Korea Advanced Institute of Science  
and Technology, Taejon, 305-701, Korea

Youngjin Park

Center for Noise and Vibration Control, Department of Mechanical Engineering, Korea Advanced Institute  
of Science and Technology, Yusung-Ku, Taejon, 305-701, Korea

(Received 15 October 1996; revised 28 April 1997; accepted 19 August 1997)

A novel formalism for the exact isolation of resonances from Rayleigh normal modes (or partial waves) for acoustic wave scattering from submerged fluid or elastic bodies is proposed. The resonance scattering function consisting purely of resonance information is proposed. Both the magnitude and phase of isolated resonances can be correctly obtained by using the proposed formalism while previous works based on classical resonance scattering theory can give only magnitude correctly. The reason previous works could produce correct magnitude information for acoustic wave scattering (no mode conversion) is explained. Plane compressive wave scattering from a variety of submerged bodies is analyzed by utilizing the proposed resonance scattering function and the isolated resonances are compared with previously published studies. The exact  $\pi$ -phase shifts through the resonance and at the anti-resonance caused by the interaction between adjacent resonances, which have never been reported before, show that the proposed formalism properly extracts the resonances from each partial wave. © 1997 Acoustical Society of America. [S0001-4966(97)01912-7]

PACS numbers: 43.30.Gv, 43.30.Jx, 43.40.Ey [JHM]

## INTRODUCTION

Since the formalism of classical resonance theory of nuclear reactions was applied to the problem of acoustic wave scattering from submerged elastic circular cylinders and spheres, resonance scattering theory<sup>1,2</sup> has been the foundation of various studies on acoustic and elastic wave scattering. Resonance scattering theory demonstrates in a direct fashion that the strongly fluctuating behavior of the cross section for sound scattering from elastic bodies is caused by a superposition of the scatterer's eigenvibration and a smoothly varying geometric background. The resonance scattering formalism employs the method of linear approximation in the frequency domain as used in nuclear resonance reaction theory. It shows the total scattering is obtained as a sum of resonance terms and a background term. Although other theories have been applied to acoustic and elastic wave scattering problems, resonance scattering theory has uniquely allowed not only a clearer understanding of the *resonance region* of the scattering cross section of any penetrable body, but has also provided the basis for important applications such as a target identification technique by remote sensing.<sup>3,4</sup> Utilizing resonance scattering theory, the resonance terms have been obtained by subtraction of a proper background (rigid, soft or intermediate) from the individual partial waves in the Rayleigh normal mode series in numerous papers<sup>1-8</sup> during the last two decades. The magnitudes of the isolated resonances could be obtained with confidence by this procedure. However, the phase information

has remained unclear and therefore has not usually been discussed clearly in the open literature although the phase information is as important as the magnitude information. In this study, we investigate how the exact resonance information for both magnitude and phase (real and imaginary parts) can be obtained from the Rayleigh normal modes.

Section I briefly reviews classical resonance scattering theory. Section II proposes a novel resonance formalism for acoustic wave scattering from elastic or liquid bodies. The resultant resonance formalism is compared with classical resonance scattering theory. Section III discusses the consistency of the proposed formalism with resonance scattering theory. In Sec. IV, numerical analyses are performed using both the proposed method and the previous method for a variety of typical examples in acoustic wave scattering, and the results are discussed. Finally, Sec. V concludes this paper.

## I. RESONANCE SCATTERING THEORY

Let us consider an infinite plane acoustic wave  $p_0 \exp i(kX - \omega t)$  with a propagation constant  $k = \omega/c$ , incident along the  $X$  axis on a solid elastic cylinder of radius  $a$  and density  $\rho_c$  whose axis coincides with the  $Z$  axis (Fig. 1).

We follow closely the derivation contained in Flax.<sup>1</sup> At a point  $P(r, \phi)$  located in the fluid of density  $\rho_w$  surrounding the cylinder, it produces the following scattered field  $P_{sc}$ :

$$P_{sc}(r, \phi) = p_0 \sum_{n=0}^{\infty} \varepsilon_n i^n A_n(x) H_n^{(1)}(kr) \cos n\phi, \quad (1a)$$

where

<sup>a)</sup>Electronic mail: hnrhee@ns.kopec.co.kr

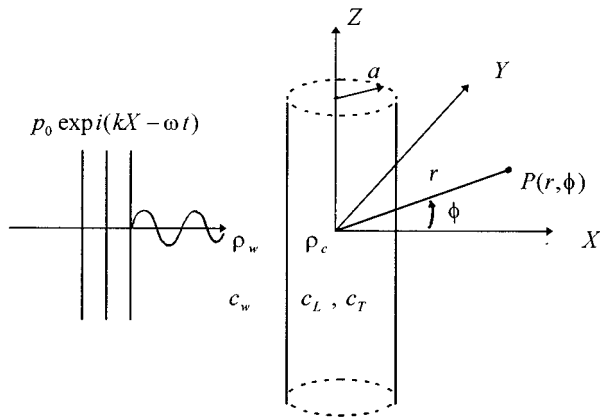


FIG. 1. Geometry for acoustic wave scattering from an infinite circular cylinder.

$$A_n = - \frac{J_n(x)F_n - xJ_n'(x)}{H_n^{(1)}(x)F_n - xH_n^{(1)'}(x)} \quad (1b)$$

The time dependence  $\exp(-i\omega t)$  disappears because steady state is being studied.  $p_0$  is the incident pressure magnitude,  $\varepsilon_n$  is the Neumann factor ( $\varepsilon_n = 1$  for  $n = 0$ , and  $\varepsilon_n$

$= 2$  for  $n > 0$ ),  $J_n$  and  $H_n^{(1)}$  are the Bessel function and the Hankel function of the first kind, respectively, and the quantity  $F_n$ , related to the modal mechanical impedance of the cylinder (Junger and Feit<sup>9</sup>), is the quotient of two  $2 \times 2$  determinants

$$F_n = - \frac{\rho_w x_T^2 D_n^{(1)}(x_L, x_T)}{\rho_c x_T^2 D_n^{(2)}(x_L, x_T)}, \quad (2a)$$

where

$$D_n^{(1)}(x_L, x_T) = \begin{vmatrix} a_{22} & a_{23} \\ a_{32} & a_{33} \end{vmatrix}, \quad D_n^{(2)}(x_L, x_T) = \begin{vmatrix} a_{12} & a_{13} \\ a_{32} & a_{33} \end{vmatrix}. \quad (2b)$$

The elements  $a_{lm}$  are given in standard texts.<sup>5</sup> The argument  $x$  of the Bessel and Hankel functions in Eq. (1b) is  $x = ka = \omega a / c_w$ , where  $c_w$  is the speed of sound in the ambient fluid. The prime denotes differentiation with respect to the argument. The matrix elements  $a_{lm}$  of Eq. (2b) contain Bessel functions with arguments  $x_L = k_L a = \omega a / c_L$  and  $x_T = k_T a = \omega a / c_T$ , where  $c_L$  and  $c_T$  are, respectively, the speeds of longitudinal and transversal waves in the cylinder material. In the far field where  $r \gg a$ , the asymptotic form of Hankel function may be written as

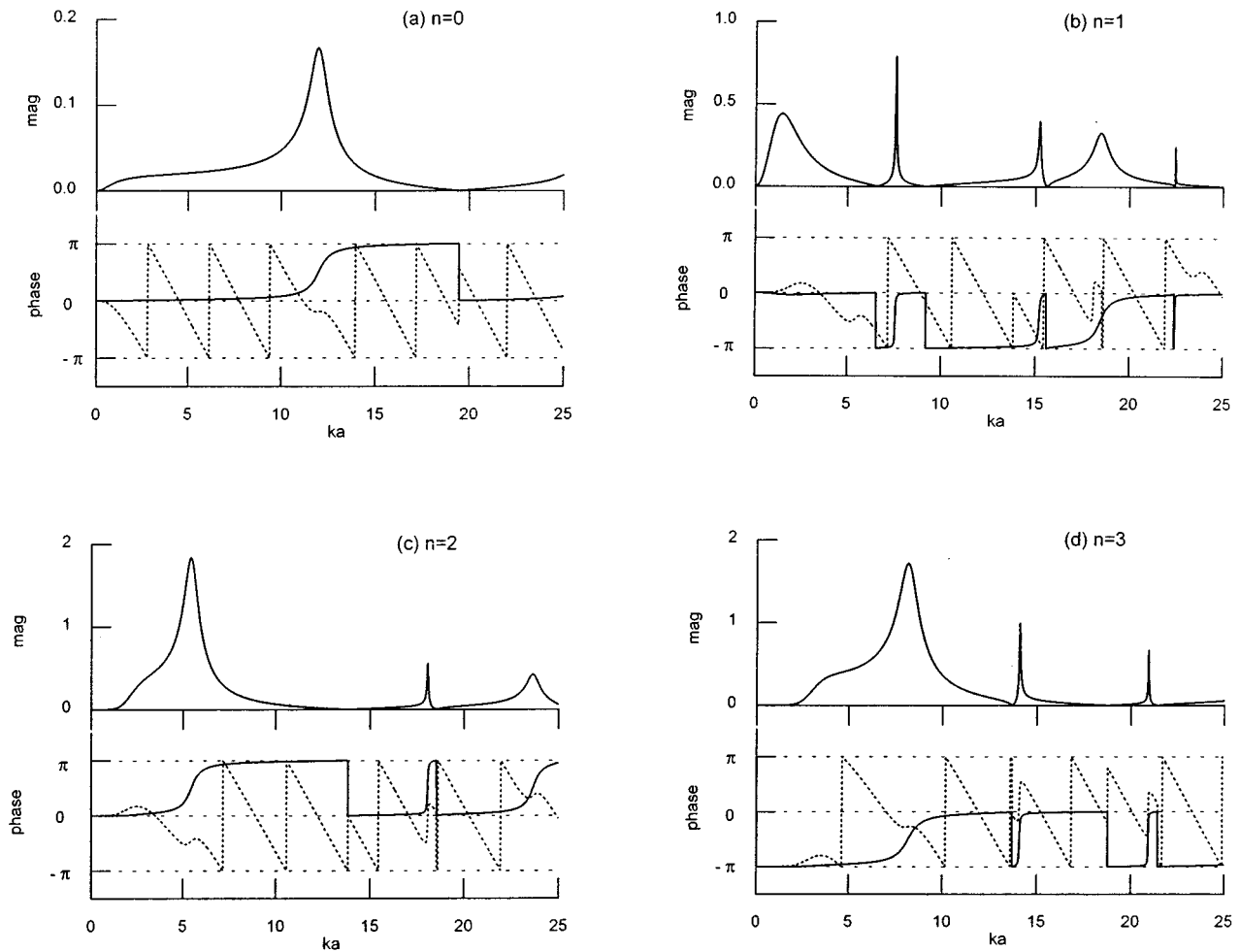


FIG. 2. Comparison of magnitudes and phases of isolated resonances by new method (solid curve) and previous method (dotted curve) for  $n$ th scattered partial waves for a submerged aluminum sphere with (a)  $n=0$ , (b)  $n=1$ , (c)  $n=2$ , (d)  $n=3$ .

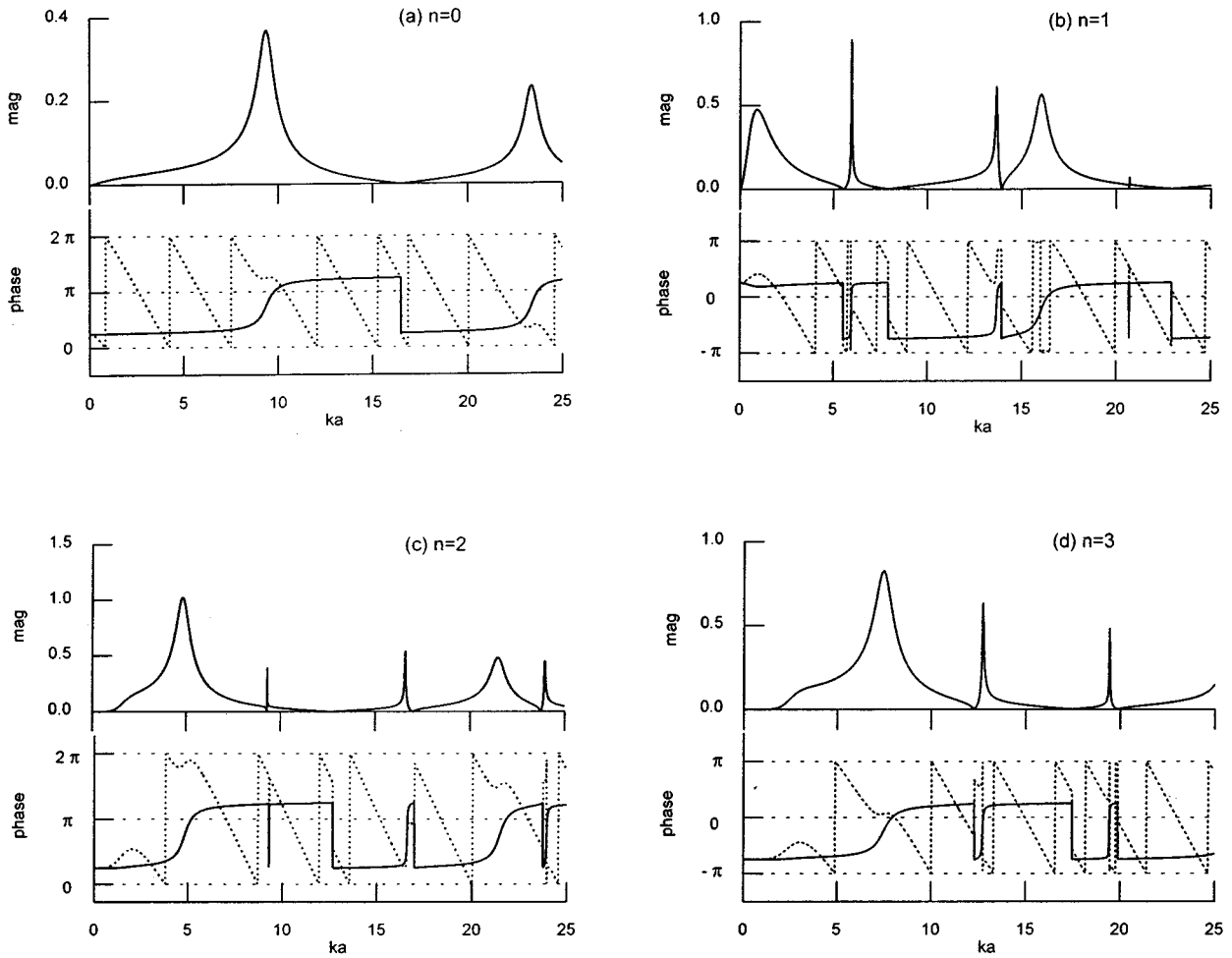


FIG. 3. Comparison of magnitudes and phases of isolated resonances by new method (solid curve) and previous method (dotted curve) for  $n$ th scattered partial waves for a submerged aluminum cylinder with (a)  $n=0$ , (b)  $n=1$ , (c)  $n=2$ , (d)  $n=3$ .

$$H_n^{(1)}(kr) \sqrt{\frac{2}{\pi i k r}} i^{-n} e^{i k r}, \quad (3)$$

$$f_\infty(\phi) = \sum_{n=0}^{\infty} f_n(\phi). \quad (8)$$

Then, the far field scattered pressure becomes

$$P_{sc}(\phi) = p_0 e^{i k r} \sqrt{\frac{2}{\pi i k r}} \sum_{n=0}^{\infty} \varepsilon_n A_n(x) \cos n \phi. \quad (4)$$

The far field form function  $f_\infty$  is defined to give a non-dimensional representation of the scattered pressure

$$f_\infty(\phi) = \sqrt{\frac{2r}{a}} \frac{P_{sc}}{p_0} e^{-i k r}. \quad (5)$$

It can be given as in another form by using Eq. (4),

$$f_\infty(\phi) = \frac{2}{\sqrt{\pi i x}} \sum_{n=0}^{\infty} \varepsilon_n A_n(x) \cos n \phi. \quad (6)$$

The individual normal modes or partial waves which make up the form functions are defined as

$$f_n(\phi) = \frac{2}{\sqrt{\pi i x}} \varepsilon_n A_n(x) \cos n \phi \quad (7)$$

so that

[Some of the individual normal modes in Eq. (7) were plotted by Flax.<sup>1</sup> However, we note that, in Fig. 2 of Flax,<sup>1</sup> the graphical plots for  $f_n(\phi)$ 's were reversed for the cylinder and sphere cases. Flax,<sup>2</sup> Veksler,<sup>5</sup> and Überall<sup>6</sup> also provided plots for  $f_n(\phi)$ 's labeled for a cylinder but were actually  $f_n(\phi)$ 's for a sphere.]

There are two limiting cases of these results. If  $\rho_c \rightarrow \infty$ , the solution applies to scattering by a rigid cylinder:

$$A_n(x)^r = - \frac{J_n'(x)}{H_n^{(1)'}(x)}. \quad (9)$$

If  $\rho_c \rightarrow 0$ , the solution applies to scattering by a soft cylinder:

$$A_n(x)^s = - \frac{J_n(x)}{H_n^{(1)}(x)}. \quad (10)$$

The scattered pressure of Eq. (1a) may be rewritten as the normal mode series (setting  $p_0=1$ )

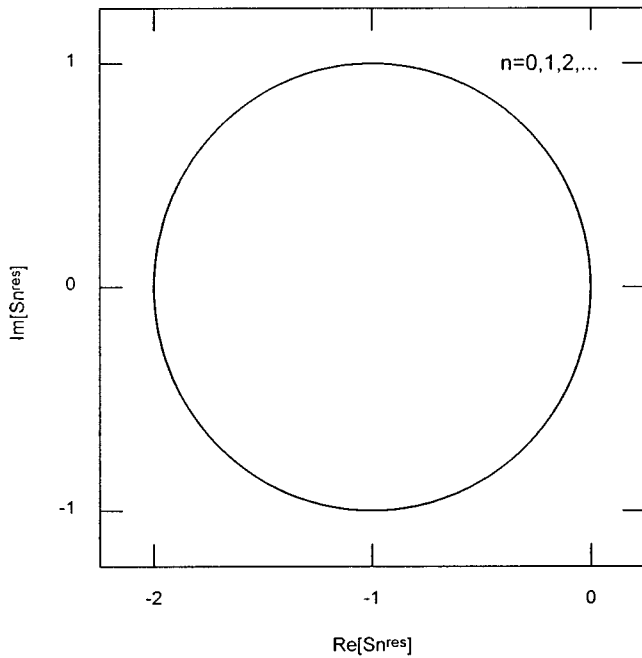


FIG. 4. Nyquist plot for the resonance scattering function for any partial wave number for all frequency range for any type of scatterer immersed in water.

$$P_{sc}(r, \phi) = \frac{1}{2} \sum_{n=0}^{\infty} \varepsilon_n i^n (S_n - 1) H_n^{(1)}(kr) \cos n\phi, \quad (11)$$

where the scattering function of the  $n$ th mode with a constant unit magnitude, containing the scattering phase shifts  $\delta_n$  is introduced as follows:

$$S_n = e^{2i\delta_n}. \quad (12)$$

In the present case,

$$S_n - 1 = 2A_n(x). \quad (13)$$

For rigid and soft cylinders, the scattering functions are, respectively,

$$S_n^r = -\frac{H_n^{(2)'}}{H_n^{(1)'}} = e^{2i\delta_n^r} \quad (14a)$$

and

$$S_n^s = -\frac{H_n^{(2)}}{H_n^{(1)}} = e^{2i\delta_n^s}. \quad (14b)$$

The corresponding phase shifts can be shown to be the real quantities

$$\tan \delta_n^r = \frac{J_n'(x)}{Y_n'(x)}, \quad \tan \delta_n^s = \frac{J_n(x)}{Y_n(x)}. \quad (15)$$

A rigid or soft scattering function may be factored out from the elastic scattering function as follows:

$$S_n = S_n^r (F_n^{-1} - z_n^{(2)-1}) / (F_n^{-1} - z_n^{(1)-1}) \quad (16a)$$

or

$$S_n = S_n^s (F_n - z_n^{(2)}) / (F_n - z_n^{(1)}), \quad (16b)$$

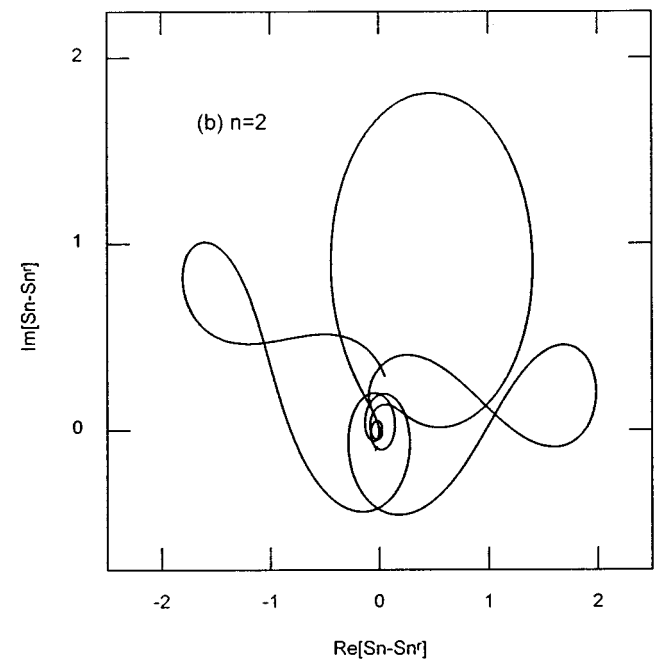
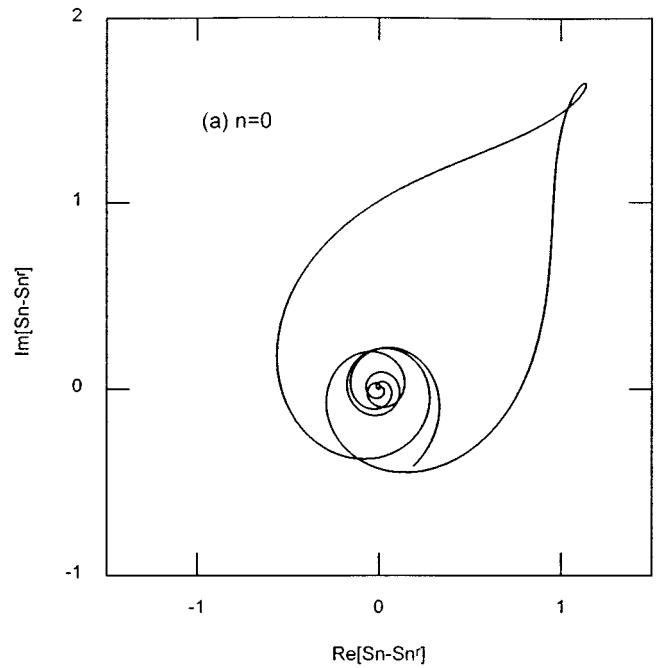


FIG. 5. Nyquist plot for  $S_n - S_n^r$  for  $n$ th scattered partial waves for a submerged aluminum sphere with (a)  $n=0$ , (b)  $n=2$ , up to  $ka=25$ .

where the quantities

$$z_n^{(i)} = x H_n^{(i)'}(x) / H_n^{(i)}(x), \quad i = 1, 2 \quad (16c)$$

are related to the modal specific acoustic impedances (Junger and Feit<sup>9</sup>).

Employing some mathematical manipulations,<sup>1,2</sup> which are omitted here for the sake of brevity, resonance scattering theory shows that the quantity that appears in Eq. (11) can be approximated as



TABLE I. Acoustic properties of materials.<sup>11</sup>

	Mass density (kg m <sup>-3</sup> )	Longitudinal wave velocity (m s <sup>-1</sup> )	Shear wave velocity (m s <sup>-1</sup> )
Air	1.12	340	...
Water	1000	1480	...
Aluminum	2800	6370	3070

$$S_n - 1 = 2ie^{2i\delta_n^r} \left[ \sum_{l=1}^{\infty} \frac{\frac{1}{2}\Gamma_{nl}^r}{x_{nl}^r - x - \frac{1}{2}i\Gamma_{nl}^r} + e^{-i\delta_n^r} \sin \delta_n^r \right], \quad (17a)$$

or

$$S_n - 1 = 2ie^{2i\delta_n^s} \left[ \sum_{l=1}^{\infty} \frac{\frac{1}{2}\Gamma_{nl}^s}{x_{nl}^s - x - \frac{1}{2}i\Gamma_{nl}^s} + e^{-i\delta_n^s} \sin \delta_n^s \right], \quad (17b)$$

where  $x_{nl}^r$  or  $x_{nl}^s$  is the  $l$ th resonance frequency of the  $n$ th mode, and  $\Gamma_{nl}^r$  or  $\Gamma_{nl}^s$  is the resonance width which is related to radiation damping. Based on expressions (17a) and (17b), resonance scattering theory argues that the scattered field is a summation of two components, i.e., the resonance component which is the first term of Eqs. (17a) and (17b), and the smooth background component which is the second term of the same equations. Utilizing this resonance scattering theory, numerous books and papers<sup>1-8</sup> have obtained the resonance information of the scatterer by just subtracting the proper background term (rigid, soft or intermediate) from the total scattered pressure field:

$$f_n^{\text{res}}(\phi) = \frac{2}{\sqrt{\pi ix}} \varepsilon_n (A_n - A_n^r) \cos n\phi = f_n - f_n^r \quad (18a)$$

or

$$f_n^{\text{res}}(\phi) = \frac{2}{\sqrt{\pi ix}} \varepsilon_n (A_n - A_n^s) \cos n\phi = f_n - f_n^s. \quad (18b)$$

The case of plane acoustic wave scattering from an elastic sphere can be treated quite analogously to that of a cylinder. The detailed procedures will be omitted here and the final expressions corresponding to Eqs. (18a) and (18b) are, respectively,

$$f_n^{\text{res}}(\phi) = -\frac{2}{x} i(2n+1)(A_n - A_n^r) P_n(\cos n\phi) = f_n - f_n^r \quad (19a)$$

or

$$f_n^{\text{res}}(\phi) = -\frac{2}{x} i(2n+1)(A_n - A_n^s) P_n(\cos n\phi) = f_n - f_n^s, \quad (19b)$$

where  $P_n$  is a Legendre function.

The case of cylindrical or spherical *elastic shell* structures rather than *solid* structures is basically the same as above with larger determinants  $D_n^{(1)}$  and  $D_n^{(2)}$  in Eqs. (2a) and (2b). The case of an insonified *fluid* cylinders or spheres

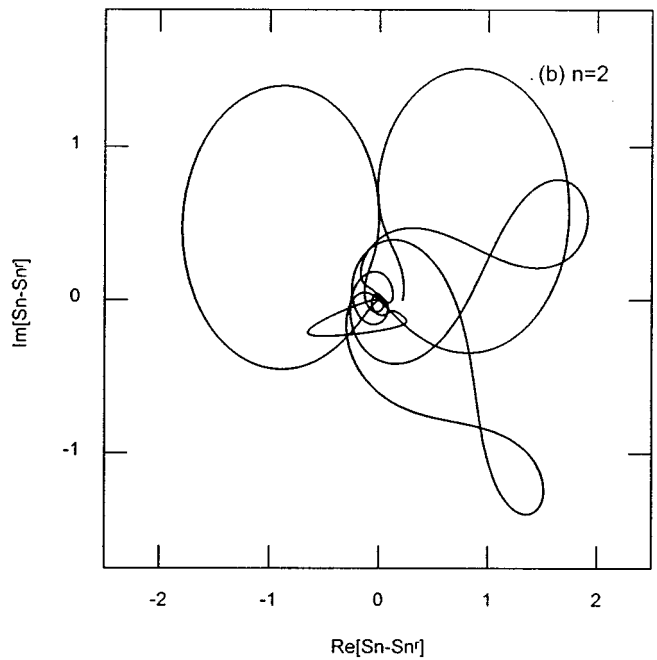
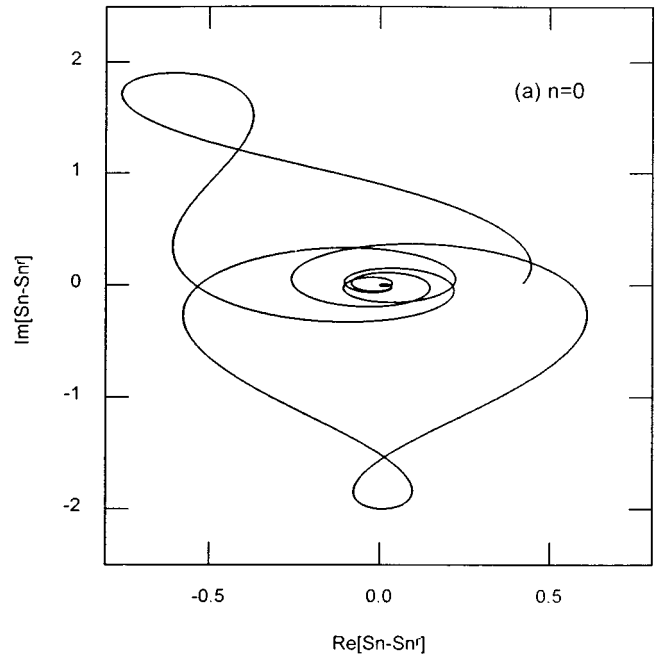


FIG. 6. Nyquist plot for  $S_n - S_n^r$  for  $n$ th scattered partial waves for a submerged aluminum cylinder with (a)  $n=0$ , (b)  $n=2$ , up to  $ka=25$ .

instead of *elastic* bodies is also very similar, in which case,  $F_n$  becomes the quotient of two cylindrical or spherical functions. However, the forms of expressions of Eqs. (18) and (19) still remain the same.

Equation (18) or (19) seems to give the correct resonance magnitude information. However, the phase behavior of isolated resonances obtained in this method is not physically explainable and, therefore, not useful although it is well known that the phase of a resonance term should shift by  $\pi$  radians as the frequency passes through the resonance frequency. The magnitudes and phases calculated using classi-

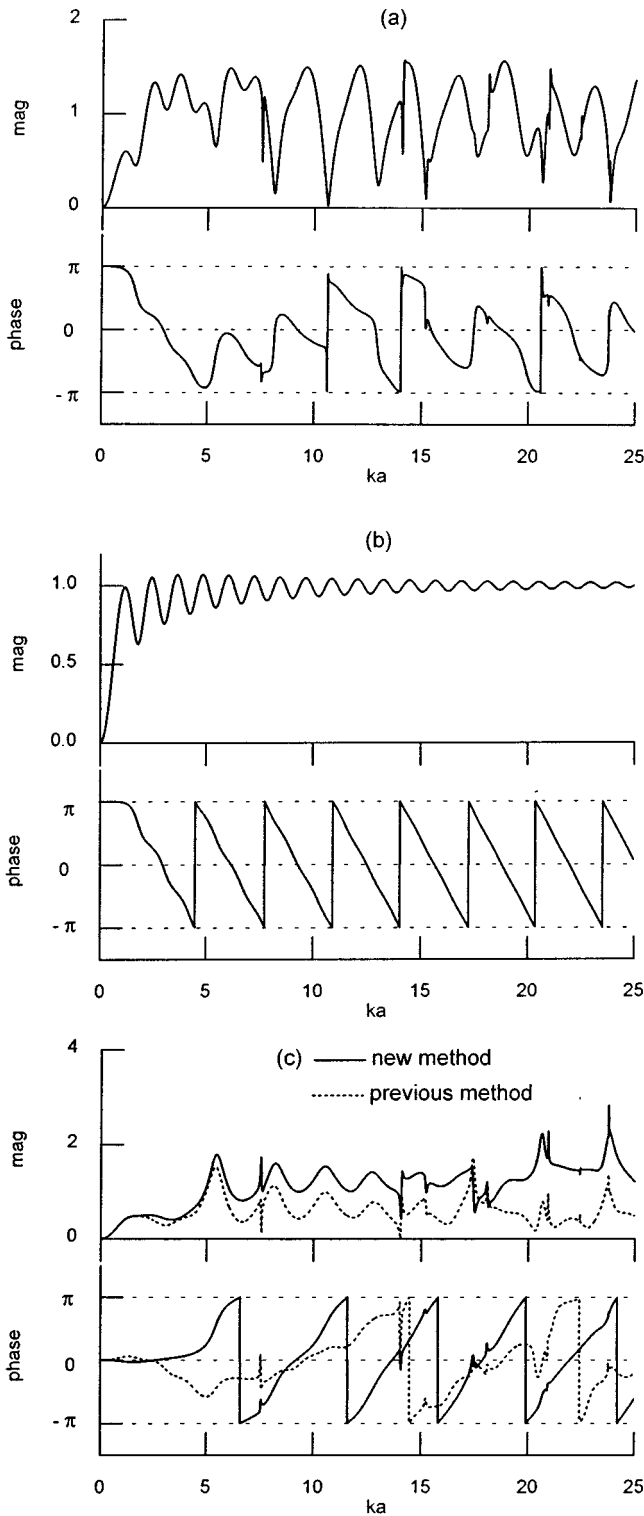


FIG. 7. Comparison of summed magnitudes and phases (for  $n=0$  to 30) of (a) total scattering pressure, (b) rigid background, and (c) isolated resonances by new method (solid curve) and previous method (dotted curve) for a submerged aluminum sphere.

cal resonance scattering theory will be presented and discussed further in Sec. IV.

## II. NOVEL RESONANCE FORMALISM

In this section, we attempt to establish a new formalism to extract the resonance information from the scattered

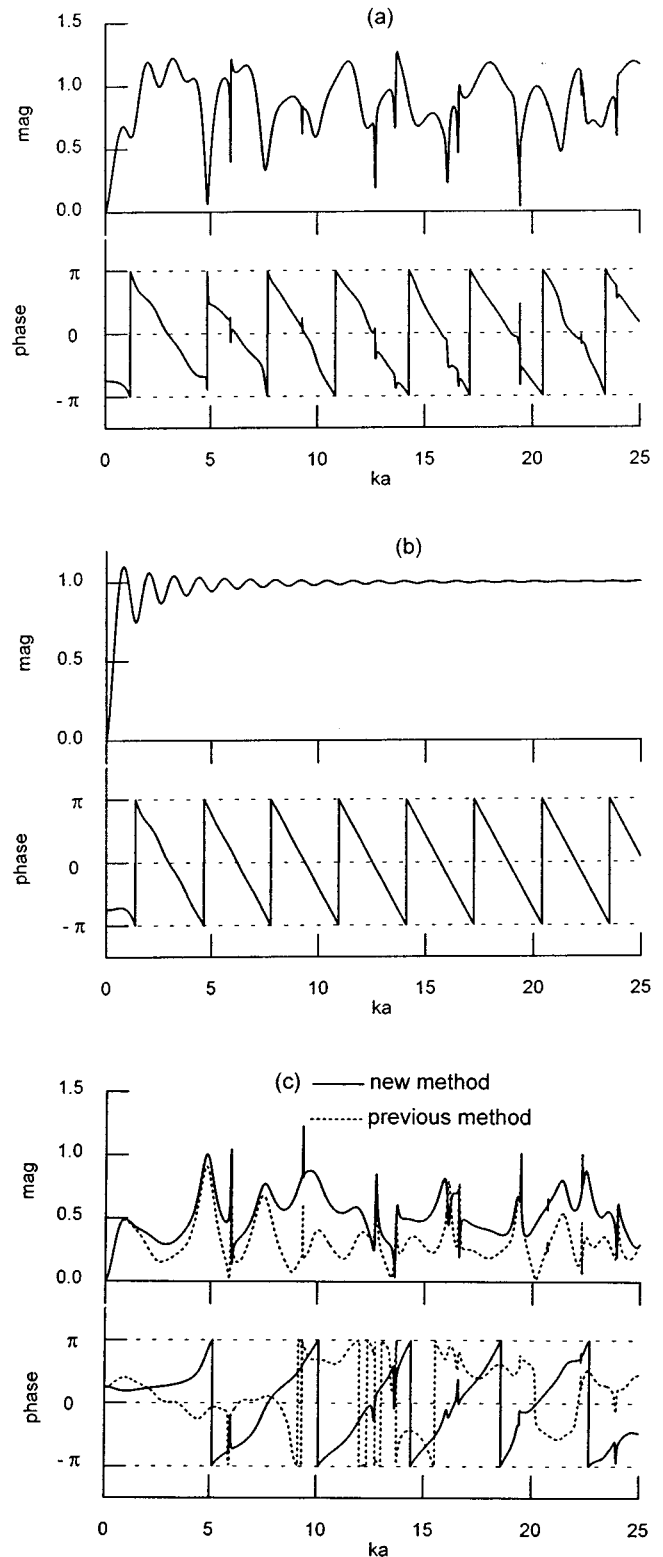


FIG. 8. Comparison of summed magnitudes and phases (for  $n = 0$  to 30) of (a) total scattering pressure, (b) rigid background, and (c) isolated resonances by new method (solid curve) and previous method (dotted curve, Ref. 8) for a submerged aluminum cylinder.

waves. The proposed new resonance formalism should compute physically meaningful phases as well as magnitudes of the isolated resonances of the scatterer.

Restarting with Eq. (16a), the scattering function  $S_n$  can be expressed as follows:

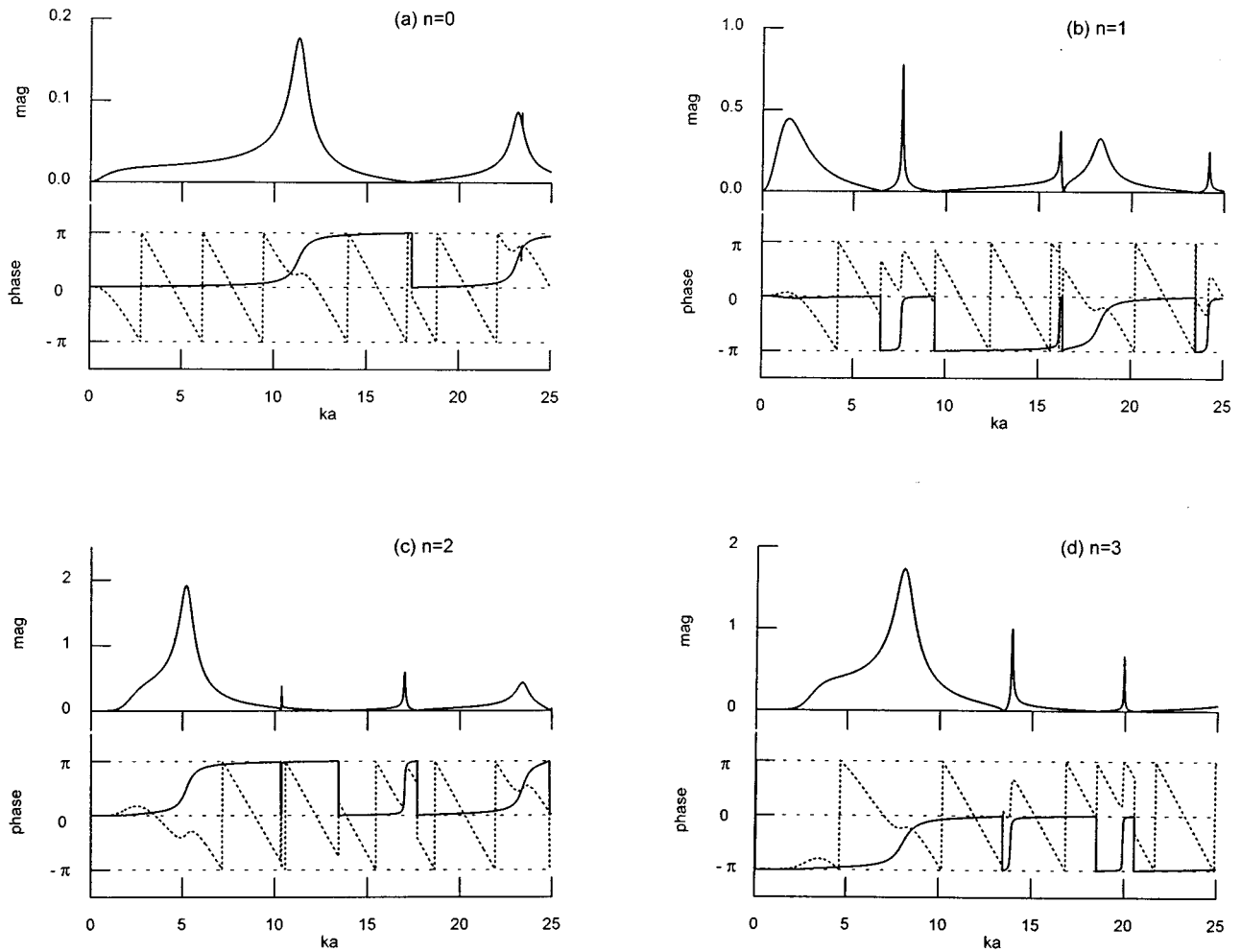


FIG. 9. Comparison of magnitudes and phases of isolated resonances by new method (solid curve) and previous method (dotted curve) for  $n$ th scattered partial waves for a submerged air-filled aluminum spherical shell (ratio of inner to outer radius=0.2) with (a)  $n=0$ , (b)  $n=1$ , (c)  $n=2$ , (d)  $n=3$ .

$$S_n = S_n^r S_n^* , \quad (20)$$

where

$$S_n^* = (F_n^{-1} - z_n^{(2)-1}) / (F_n^{-1} - z_n^{(1)-1}) .$$

Equation (20) states that  $S_n$  is the *product* of rigid background  $S_n^r$  and the remaining term  $S_n^*$ , which includes resonances. However,  $S_n^*$  is not a pure resonance term.  $S_n^*$  has a constant term which hides resonances unless it is removed. To see this,  $S_n^*$  may be written

$$\begin{aligned} S_n^* &= (F_n^{-1} - z_n^{(2)-1}) / (F_n^{-1} - z_n^{(1)-1}) \\ &= (z_n^{(1)-1} - z_n^{(2)-1}) / (F_n^{-1} - z_n^{(1)-1}) + 1 = S_n^{\text{res}} + 1, \end{aligned} \quad (21)$$

where  $S_n^{\text{res}}$  is defined as the resonance scattering function which consists purely of resonance information. By the definition in Eq. (20), the resonance scattering function  $S_n^{\text{res}}$  can be expressed as

$$S_n^{\text{res}} = \frac{S_n}{S_n^r} - 1 = \frac{z_n^{(1)-1} - z_n^{(2)-1}}{F_n^{-1} - z_n^{(1)-1}} = 2 \frac{A_n - A_n^r}{1 + 2A_n^r} , \quad (22)$$

where  $A_n = \frac{1}{2}(S_n - 1)$  and  $A_n^r = \frac{1}{2}(S_n^r - 1)$ .

In Eq. (11),  $S_n - 1$  contributes to the total response including both the background and the resonance.  $S_n^{\text{res}}$  is the

only resonance-related component of  $S_n$ . The unit constant cannot contribute to the resonance. The subtraction of a constant real number from a complex quantity results in a new complex quantity different from the original complex quantity. Therefore, from Eq. (11), the scattered wave due to resonance can be obtained by replacing  $S_n - 1$  with  $S_n^{\text{res}}$ :

$$\begin{aligned} P_{sc}^{\text{res}}(r, \phi) &= \frac{1}{2} \sum_{n=0}^{\infty} \epsilon_n i^n S_n^{\text{res}} H_n^{(1)}(kr) \cos n\phi \\ &= \sum_{n=0}^{\infty} \epsilon_n i^n \frac{A_n - A_n^r}{1 + 2A_n^r} H_n^{(1)}(kr) \cos n\phi. \end{aligned} \quad (23)$$

Then, the individual normal mode for resonances in the far field can be expressed as

$$f_n^{\text{res}}(\phi) = \frac{2}{\sqrt{\pi i x}} \epsilon_n \frac{A_n - A_n^r}{1 + 2A_n^r} \cos n\phi. \quad (24)$$

The expressions involving the corresponding soft background parameters are analogous:

$$\begin{aligned} S_n^* &= (F_n - z_n^{(2)}) / (F_n - z_n^{(1)}) \\ &= (z_n^{(1)} - z_n^{(2)}) / (F_n - z_n^{(1)}) + 1 = S_n^{\text{res}} + 1, \end{aligned} \quad (25)$$

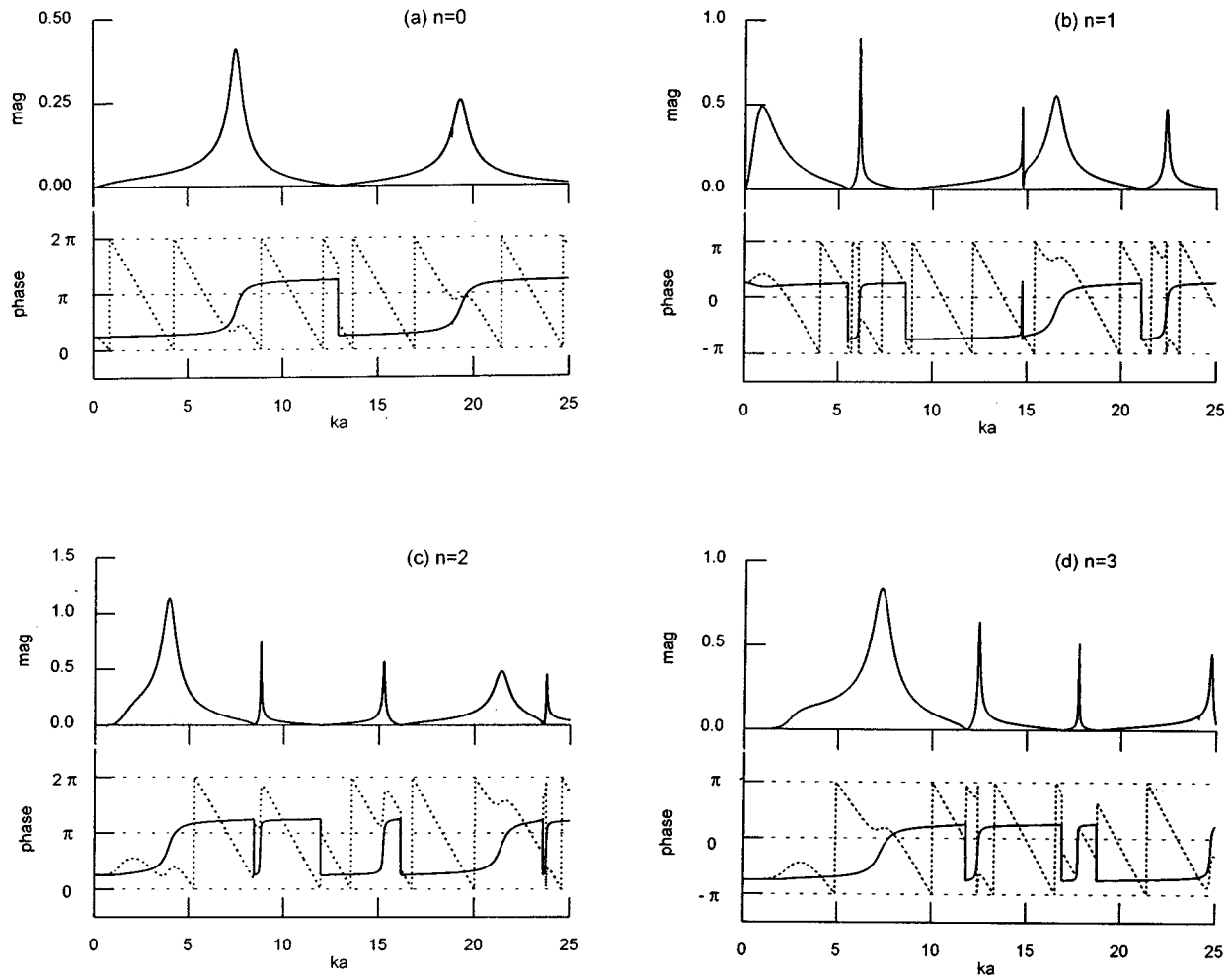


FIG. 10. Comparison of magnitudes and phases of isolated resonances by new method (solid curve) and previous method (dotted curve) for  $n$ th scattered partial waves for a submerged air-filled aluminum cylindrical shell (ratio of inner to outer radius = 0.2) with (a)  $n=0$ , (b)  $n=1$ , (c)  $n=2$ , (d)  $n=3$ .

$$S_n^{\text{res}} = \frac{S_n}{S_n^s} - 1 = \frac{z_n^{(1)} - z_n^{(2)}}{F_n - z_n^{(1)}} = 2 \frac{A_n - A_n^s}{1 + 2A_n^s}, \quad (26)$$

and

$$f_n^{\text{res}}(\phi) = \frac{2}{\sqrt{\pi i x}} \varepsilon_n \frac{A_n - A_n^s}{1 + 2A_n^s} \cos n\phi. \quad (27)$$

In case of a sphere instead of a cylinder,  $S_n^{\text{res}}$  contains spherical functions rather than cylindrical functions. The expressions corresponding to Eqs. (24) and (27) are, respectively,

$$f_n^{\text{res}}(\phi) = -\frac{2}{x} i(2n+1) \frac{A_n - A_n^r}{1 + 2A_n^r} P_n(\cos n\phi), \quad (28)$$

and

$$f_n^{\text{res}}(\phi) = -\frac{2}{x} i(2n+1) \frac{A_n - A_n^s}{1 + 2A_n^s} P_n(\cos n\phi). \quad (29)$$

The expressions in Eqs. (24), (27), (28), and (29) are also applicable to acoustic wave scattering from elastic cylindrical/spherical *shell* structures or *fluid* spheres/cylinders with the appropriate changes in  $F_n$  as explained in Sec. I.

By using Eqs. (24), (27), (28), and (29), the resonances which are mixed with the background in the total scattered pressure field can be uncovered perfectly. The only difference between these new equations and the old equations [Eqs. (18) and (19)] is the existence of the denominator  $1 + 2A_n^r$  or  $1 + 2A_n^s$ , which is respectively the scattering function  $S_n^r$  or  $S_n^s$  corresponding to the impenetrable targets in two extreme cases. In case of acoustic wave scattering, where no mode conversion occurs in the outside of scatterers because the medium supporting the scattered field is fluid, and with no material damping,  $S_n^r$  and  $S_n^s$  are unitary. Therefore these new and old equations can produce completely identical magnitudes. This perhaps induced so many previous studies to use the incorrect resonance formalism, Eqs. (18) and (19), with confidence. However, it should be noted that their phases are not the same because the scattering function  $S_n^r$  or  $S_n^s$  in the denominator has its own phase shift. If Nyquist plots (or Argand diagrams) rather than Bode type plots are examined, the new and old equations generate contrasting results. Moreover, in elastic wave scattering, where mode conversion occurs in the outside of scatterers because the elastic medium sustains not only longitudinal but also shear waves, it is not difficult to anticipate that both magnitude and phase in the old Eqs. (18) and (19) will be incorrect

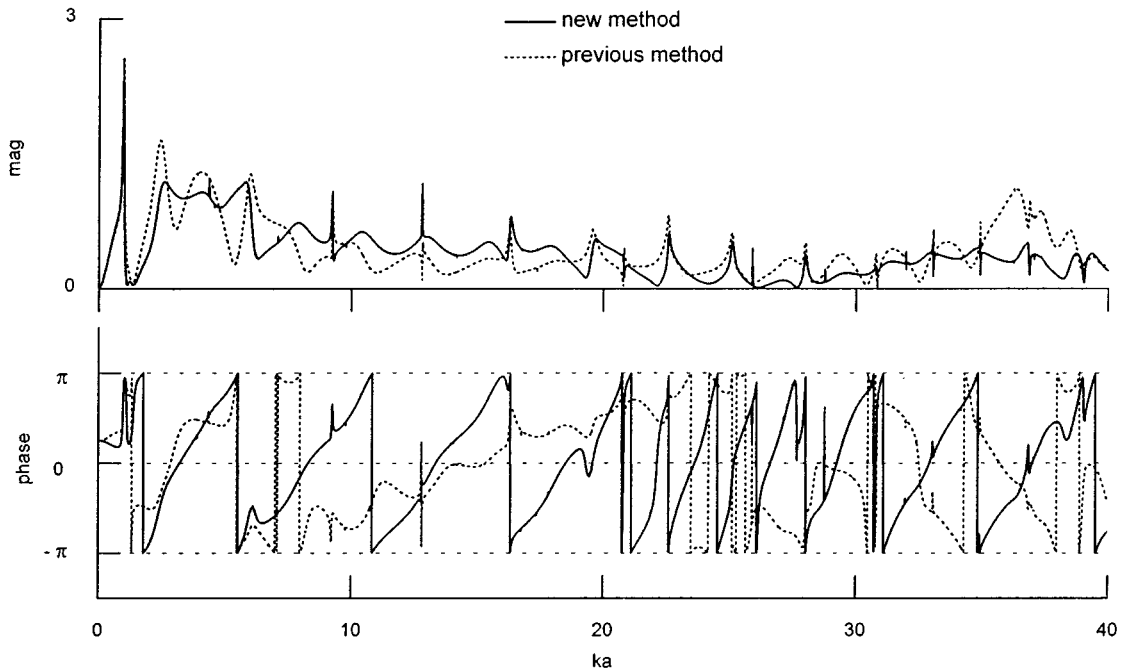


FIG. 11. Comparison of magnitudes and phases of summed resonance spectra (for  $n=0$  to 47) by new method (solid curve) and previous method (dotted curve, Ref. 4) for a submerged air-filled aluminum cylindrical shell (ratio of inner to outer radius=2/3).

because the unitary condition applies to the scattering matrix and cannot be extended to the individual scattering functions. Mode conversion is another complicated subject and will be discussed in detail in a separate paper.

### III. CONSISTENCY OF THE PROPOSED FORMALISM WITH RESONANCE SCATTERING THEORY

By considering Eq. (13) and following relationships:

$$S_n^r = e^{2i\delta_n^r} \quad (30)$$

and

$$S_n^r - 1 = 2ie^{i\delta_n^r} \sin \delta_n^r, \quad (31)$$

Eq. (17a) can be expressed as

$$A_n = A_n^r + (1 + 2A_n^r) \sum_{l=1}^{\infty} i \frac{\frac{1}{2}\Gamma_{nl}^r}{x_{nl}^r - x - \frac{1}{2}i\Gamma_{nl}^r}. \quad (32)$$

Now, if we approximate  $S_n^{\text{res}}$  near resonance frequencies as

$$S_n^{\text{res}} = \sum_{l=1}^{\infty} i \frac{\Gamma_{nl}^r}{x_{nl}^r - x - \frac{1}{2}i\Gamma_{nl}^r}, \quad (33)$$

and substitute into Eq. (32), Eq. (22) of the resonance scattering function is obtained.

In case of the soft background, Eq. (17b) can be expressed as

$$A_n = A_n^s + (1 + 2A_n^s) \sum_{l=1}^{\infty} i \frac{\frac{1}{2}\Gamma_{nl}^s}{x_{nl}^s - x - \frac{1}{2}i\Gamma_{nl}^s}. \quad (34)$$

We can also approximate

$$S_n^{\text{res}} = \sum_{l=1}^{\infty} i \frac{\Gamma_{nl}^s}{x_{nl}^s - x - \frac{1}{2}i\Gamma_{nl}^s}. \quad (35)$$

Substituting Eq. (35) into Eq. (34), Eq. (26) of the resonance scattering function is obtained.

Therefore, it is revealed that the novel formalism in Eqs. (24), (27), (28), and (29) is consistent with resonance scattering theory. One may argue that Eqs. (18) and (19) are merely an incorrect application of resonance scattering theory.

We note that Eqs. (33) and (35) are approximate expressions obtained by the linearization near resonance frequencies. Thus, these expressions are valid only near resonance frequencies because the interactions between resonances are not considered. Therefore, to compute the exact resonances, numerical solutions of Eqs. (24) and (27) for a cylinder [or Eqs. (28) and (29) for a sphere] are required.

### IV. NUMERICAL ANALYSIS AND DISCUSSION

All examples in this section are performed for back-scattering ( $\phi = \pi$ ). The acoustic properties of materials used for numerical calculations are listed in Table I. The background is assumed to be rigid for acoustic wave scattering from elastic bodies.

Acoustic plane wave scattering from solid elastic spheres and cylinders in water as an ambient medium is analyzed numerically in Figs. 2 and 3. Resonances in each partial wave are isolated and plotted separately by using the previous method [Eqs. (18) and (19)] and the new method [Eqs. (24) and (28)] so that comparisons can be made. As predicted in Sec. II, while the magnitudes are perfectly identical, the phases are very different. The new method gener-

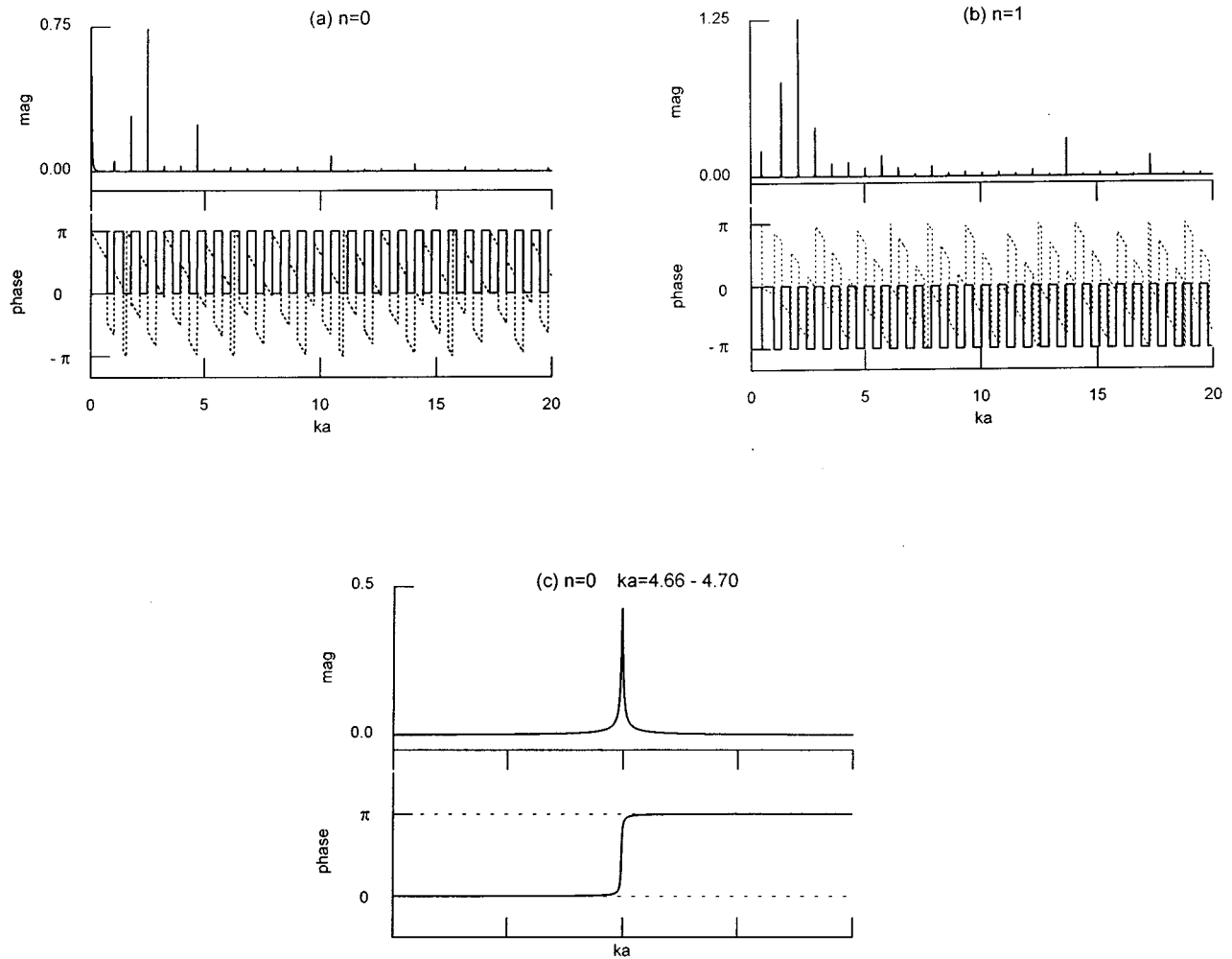


FIG. 12. Comparison of magnitudes and phases of isolated resonances by new method (solid curve) and previous method (dotted curve) for  $n$ th scattered partial waves for a submerged air sphere with (a)  $n=0$ , (b)  $n=1$ , (c)  $n=0$ ,  $ka=4.66-4.70$ .

ates exact  $\pi$ -phase shifts through the resonance. The shift occurs abruptly or gradually depending on radiation damping. If phase shift is close to but less than  $\pi$ , it signifies that higher resolution, i.e., smaller step size of  $\Delta ka$ , is necessary until the exact  $\pi$ -phase shift is obtained. Consequently, a more accurate determination of the peak magnitude can be obtained. The almost constant phase through the first thick peak of Fig. 2(b) or 3(b) shows clearly that it is not related to the scatterer's resonance. It is one example where the correct phase information is useful. The  $\pi$ -phase shift also occurs at the anti-resonance caused by the mutual interaction of adjacent resonances, which is consistent with the concept of the driving point transfer function.<sup>10</sup> Previous methods<sup>1-7</sup> calculate incorrect and nearly useless phase information as can be seen by the dotted lines in Figs. 2 and 3. If a Nyquist plot is constructed in the complex plane as a function of non-dimensionalized frequency  $ka$ , the new and previous methods produce contrasting trajectories because both the real and imaginary parts of the resonances are different.

Figure 4 shows a Nyquist plot for the resonance scattering function  $S_n^{\text{res}}$  defined in Sec. II. Regardless of mode number  $n$  and the shape of scatterer (spherical or cylindrical), the trajectory of  $S_n^{\text{res}}$  makes a circle with unit radius centered at

$(-1,0)$ . This can be explained as follows: By the definition of  $S_n^{\text{res}}$  in Eqs. (20) and (21) and by the fact that there is no mode conversion in acoustic wave scattering,  $|S_n| = |S_n^r| = |S_n^*| = 1$ , therefore,  $|S_n^{\text{res}}| = |S_n^* - 1|$ , which forms the circle in Fig. 4 in the complex plane as the non-dimensionalized frequency  $ka$  varies. This unit circle is physically related to the energy conservation during acoustic wave scattering.

Figures 5 and 6 are Nyquist plots of  $S_n - S_n^r$  for the cases of the sphere and the cylinder.  $S_n - S_n^r$  is equal to  $2(A_n - A_n^r)$  in Eqs. (18) and (19). Figures 5 and 6 are misleading and incorrect information for the purpose of obtaining the true resonances. Because of the difference in the phases of isolated resonances obtained by the two methods, one expects that the resonance spectrum, which is a total summation of isolated resonances, will not be the same. Figures 7 and 8 explicitly show the differences in summed magnitude and phase for the sphere and the cylinder. As can be seen in Fig. 8(c) efforts such as those of Maze<sup>8</sup> led to an incorrect resonance spectrum.

Aforementioned discussions are also applicable to spherical and cylindrical shell structures, of which inside is empty or filled with another material, instead of solid ones.

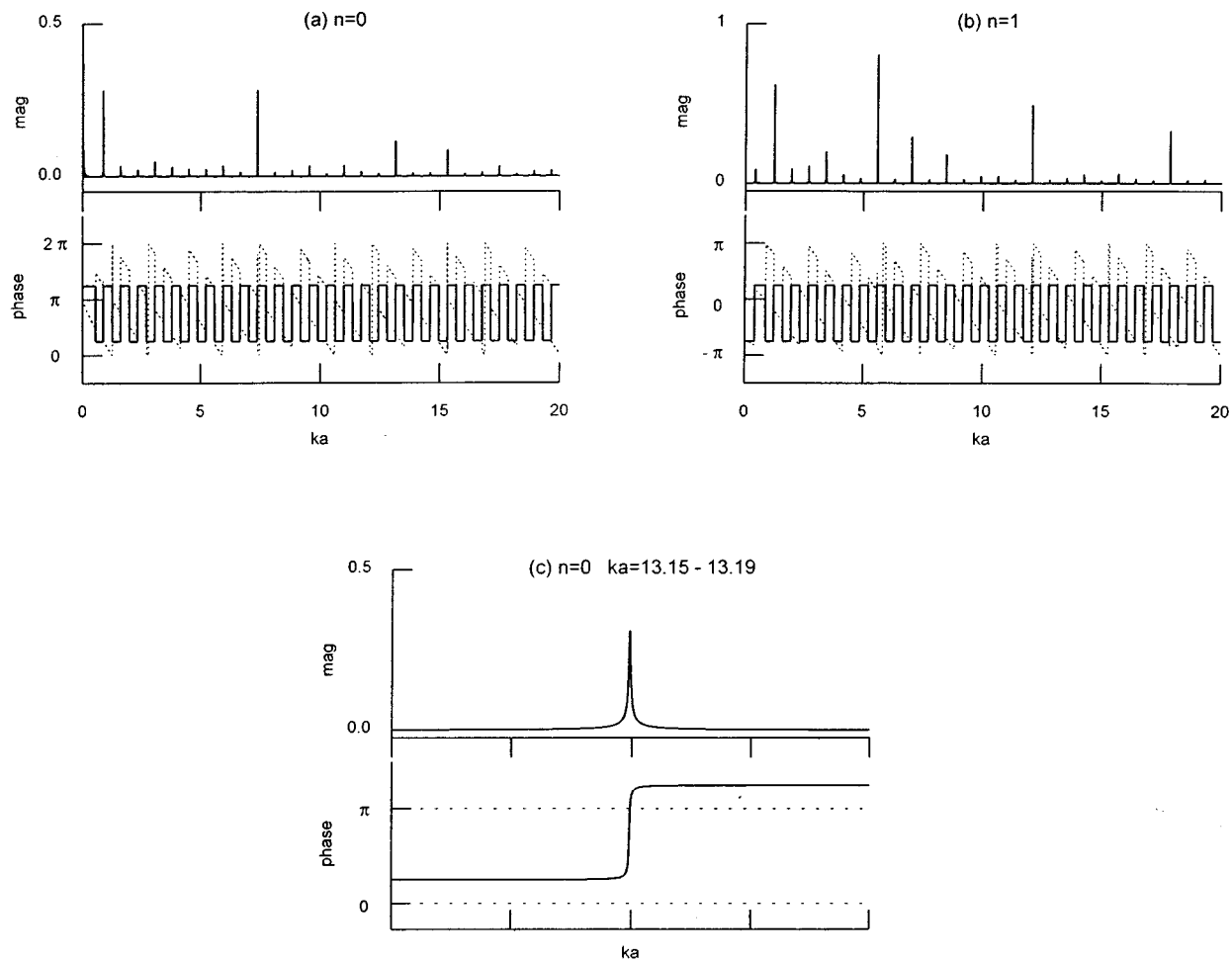


FIG. 13. Comparison of magnitudes and phases of isolated resonances by new method (solid curve) and previous method (dotted curve) for  $n$ th scattered partial waves for a submerged air cylinder with (a)  $n=0$ , (b)  $n=1$ , (c)  $n=0$ ,  $ka=13.15-13.19$ .

Figures 9 and 10 compare the resonances as calculated by two methods for air-filled spherical and cylindrical shells, respectively. The ratio of inner to outer radius of the shells is 0.2. Figure 11 compares the resonance spectrum up to  $ka=40$  calculated by the new method with that computed by Gaunard and Werby<sup>4</sup> for an air-filled aluminum cylindrical shell with inner to outer radius ratio 2/3.

Finally, it is mentioned that the proposed formalism can also be applied to acoustic wave scattering from fluid spheres or cylinders. Figures 12 and 13 show resonances for the air sphere and cylinder.

In these cases the proper background is the soft background rather than the rigid background. The new method [Eqs. (27) and (29)] generates correct phase information while the previous method [Eqs. (18b) and (19b)] does not.

So far, all the above numerical examples used the classical rigid or soft background as a proper background. However, any intermediate or mid-way background can be used with the proposed formalism once the corresponding expression to Eq. (20) is established.

## V. CONCLUSIONS

In this paper, a novel formalism for the exact isolation of resonances from partial waves for acoustic wave scattering is

proposed. The resonance scattering function consisting purely of resonance information is defined. Both magnitude and phase of isolated resonances can be correctly obtained using the proposed formalism. We have shown how previous works could obtain correct magnitude information for isolated resonances in the case of acoustic wave scattering. Plane compressive wave scattering from submerged bodies such as elastic solid spheres and cylinders, shell structures, and also fluid spheres and cylinders is analyzed numerically by utilizing the proposed resonance scattering function, and the isolated resonances are compared with previously published studies. The exact  $\pi$ -phase shifts through the resonance and at the anti-resonance caused by the interaction between adjacent resonances, which have never been reported clearly before, shows that the proposed formalism properly extracts the resonances from each partial wave. If a resonance-like peak in the magnitude plot is not accompanied with  $\pi$ -phase shift through the peak, we can clearly distinguish it from the genuine scatterer's eigenvibration. The summed resonance spectra computed by the proposed formalism show different magnitudes and phases from previous studies because phases of the resonances of each normal mode are corrected. Experimental results, once available, should be compared with the resonance spectra

computed by the proposed formalism. This paper has also shown that the physically unexplainable behavior of phase of the resonances extracted by classical resonance scattering theory for acoustic wave scattering was not due to the inexactness of the rigid or soft background, but due to the use of an incorrect resonance formalism. Extending the concept of the proposed resonance formalism to elastic wave resonance scattering is currently under study.

## ACKNOWLEDGMENT

The authors are grateful to the anonymous reviewers for their helpful comments.

<sup>1</sup>L. Flax, L. R. Dragonette, and H. Überall, "Theory of elastic resonance excitation by sound scattering," *J. Acoust. Soc. Am.* **63**, 723–731 (1978).

<sup>2</sup>L. Flax, G. Gaunard, and H. Überall, "Theory of resonance scattering," in *Physical Acoustics*, edited by W. P. Mason and R. N. Thurston (Academic, New York, 1981), Vol. XV, pp. 191–294.

<sup>3</sup>G. C. Gaunard, "Elastic and acoustic resonance wave scattering," *Appl. Mech. Rev.* **42**, 143–192 (1989).

<sup>4</sup>G. C. Gaunard and M. F. Werby, "Acoustic resonance scattering by submerged elastic shells," *Appl. Mech. Rev.* **43**, 171–208 (1990).

<sup>5</sup>N. D. Veksler, *Resonance Acoustic Spectroscopy* (Springer-Verlag, New York, 1993).

<sup>6</sup>*Acoustic Resonance Scattering*, edited by H. Überall (Gordon and Breach Science, Philadelphia, 1992).

<sup>7</sup>R. H. Hackman, "Acoustic scattering from elastic solids," in *Physical Acoustics*, edited by A. D. Pierce and R. N. Thurston (Academic, New York, 1993), Vol. XXII, pp. 1–194.

<sup>8</sup>G. Maze, "Acoustic scattering from submerged cylinders. MIIR Im/Re: Experimental and theoretical study," *J. Acoust. Soc. Am.* **89**, 2559–2566 (1991).

<sup>9</sup>M. C. Junger and D. Feit, *Sound, Structures and Their Interaction* (MIT, Cambridge, MA, 1986).

<sup>10</sup>D. J. Ewins, *Modal Testing: Theory and Practice* (Research Studies Press, Letchworth, England, 1986).

<sup>11</sup>P. McIntire, "Ultrasonic testing," in *Nondestructive Testing Handbook* (American Society for Nondestructive Testing, 1991), 2nd ed., Vol. 7.



# Vertical coherence of ambient noise in shallow water overlying a fluid seabed

Grant B. Deane and Michael J. Buckingham<sup>a)</sup>

*Marine Physical Laboratory, Scripps Institution of Oceanography, University of California, San Diego, 9500 Gilman Drive, La Jolla, California 92093-0238*

Christopher T. Tindle

*Physics Department, University of Auckland, Auckland, New Zealand*

(Received 30 January 1997; accepted for publication 15 August 1997)

Broadband (200 Hz–20 kHz) measurements of the vertical coherence of ambient noise in two well-surveyed, shallow-water channels with fluid, sedimentary seabeds are reported. The noise at one of the sites, the StrataForm natural laboratory off Eureka, northern California, was occasionally found to be exclusively wind generated, with negligible contributions from surface traffic and biological sources. Under these conditions, the theoretical coherence, computed using the known properties of the sediment at Eureka, closely follows the coherence data up to a frequency of 20 kHz. Subtle effects due to the finite depth of the sources, that is, the bubbles produced by wave breaking, are evident in both the theory and the data. At the second site, in Jellicoe Channel, New Zealand, some 64 km north of Auckland, wind noise again was a major factor, but much of the time local shipping also contributed to the overall noise field. Two sets of coherence data from the New Zealand site are examined, the first taken in near-isovelocity conditions, when the noise was due to wind plus a local ship, and the second recorded in the absence of shipping, when the channel showed a mildly linear, downward refracting profile. In both instances, the coherence data over a 5-kHz band compare well with theoretical curves computed using the known geoacoustic parameters of the sediment in the region. © 1997 Acoustical Society of America. [S0001-4966(97)02012-2]

PACS numbers: 43.30.Nb [DLB]

## INTRODUCTION

The vertical coherence of ambient noise in the deep ocean received considerable attention during the 1960's, when a number of measurements were reported,<sup>1–6</sup> although only over restricted frequency ranges below 2 kHz. Few data sets have been published on the vertical coherence of ambient noise in shallow water, and those that have are also restricted to a bandwidth of 2 kHz or less.<sup>7–9</sup>

Recently, we have collected high quality noise coherence data over an extended bandwidth, up to 20 kHz, from a number of open-ocean, shallow-water locations, including areas where the geophysical properties of the bottom are known from previous independent surveys. Two of these ‘‘calibrated’’ sites, one in New Zealand waters and the other off Eureka, northern California, both of uniform depth with fluidlike, sedimentary seabeds, offer near-ideal conditions for investigating the spatial, temporal, and spectral properties of ambient noise in a natural ocean waveguide. Indeed, under isovelocity conditions, both sites conform closely to a Pekeris channel,<sup>10</sup> that is to say, a homogeneous water column overlying a semi-infinite, homogeneous fluid basement.

A number of ambient noise data sets were collected at the New Zealand site over a period of several weeks during the (southern hemisphere) summer of 1995–96; and noise data were taken at the Eureka site in June 1996. At both

locations, two vertically aligned, low-noise hydrophones, with inter-element spacing adjustable between 0.73 m and 1.525 m, were deployed near the middle of the water column (Fig. 1). The noise data were recorded on a multi-channel digital audio tape (DAT) recorder over a bandwidth of 20 kHz. Expendable bathythermograph (XBT) casts were also taken, from which sound speed profiles were computed on the assumption of uniform salinity. At the New Zealand site, two types of sound-speed profile were encountered: isovelocity, associated with good mixing throughout most of the water column; and approximately linear with negative gradient ( $\approx 0.4$  m/s per m), giving rise to mild downward refraction. The profile at Eureka was very slightly downward refracting, but with a gradient so small ( $< 0.13$  m/s per m) that, as far as the vertical coherence of the noise is concerned, the water column acted as an isovelocity medium.

Now and again, at frequencies above several hundred hertz, the noise at the Eureka site was found to be almost entirely wind driven, created by bubbles produced by breaking surface waves. On those occasions, contributions to the noise from shipping, marine mammals, and other biological sources appear to have been negligible, since the coherence data conform very closely with the theoretical coherence of surface-generated noise, as derived from a model in which the sources are assumed to occupy a horizontal plane lying immediately beneath the sea surface. This agreement between theory and data lends support to the idea that the vertical structure of wind-generated noise in continental-shelf

<sup>a)</sup>Also affiliated to: Institute of Sound and Vibration Research, The University, Southampton SO17 1BJ, England.

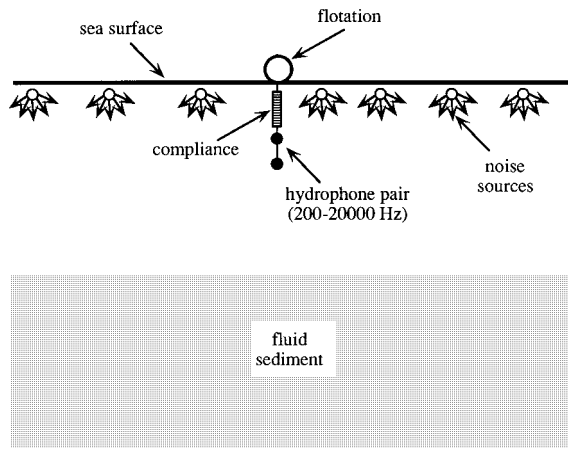


FIG. 1. Schematic showing the dual hydrophone configuration used to record ambient noise.

waters is not only stable but predictable, provided the geoaoustic parameters of the bottom are known.

The stability of the vertical coherence of wave-breaking noise in open-ocean shallow-water channels is attributed to the fact that the spatial structure of the noise field is largely controlled by the bottom boundary, whose properties are time invariant, at least over the timescales of the measurements. Compared with the intensity, which depends on such factors as wind speed and fetch, making it variable and difficult to predict, the vertical coherence is much less sensitive to changes in surface conditions.<sup>11</sup> This may be appreciated from the physical argument that the coherence is essentially a measure of the directionality of the noise, which is unaffected by the strength of the breaking-wave sources; or mathematically from the fact that the coherence is a relative measure in which the source strength cancels out as a result of the normalization.

Although the density of shipping around Australia and New Zealand is very low compared with typical shipping levels found in the northern hemisphere,<sup>12,13</sup> the noise measurement site, which was selected because of its known bottom conditions, is within about 10 km of a route used by commercial shipping into and out of Auckland harbor some 64 km to the south. At any given time, at least one ship was usually within audible range of the sensors, but this was sufficient to modify the spatial properties of the noise significantly. The main effect of the ship was to raise the overall level of the real part of the coherence function, but without modifying significantly the oscillatory structure of the curve.

A minor extension to the wind-noise model accurately accounts for the effect of local shipping on the noise field at the New Zealand site. By fitting the model to the data, the progress of a local ship can be identified as it approaches and then recedes from the sensors. Although the spatial structure of the noise field in this case is not time invariant, since it contains a component that varies with the passage of a local vessel, it is nevertheless predictable provided the bottom properties are known.

A technique for inverting the ambient noise field in the shallow ocean, nominally less than 200 m deep, to obtain the geoaoustic parameters of the seabed was introduced several

years ago by Buckingham and Jones.<sup>14</sup> Using a rather rudimentary inversion procedure, they demonstrated that the compressional speed of a fast, fluid sediment could be determined fairly reliably from the broadband vertical coherence of the water-borne noise. Of course, accurate forward modeling is a prerequisite of a reliable inversion technique for extracting seabed properties from shallow-water noise.

The main purpose of this paper is to present the broadband noise data acquired at the two calibrated sites, Eureka and New Zealand, and also to demonstrate that the measured vertical coherence can be represented accurately by a relatively simple noise model in which the input parameters represent the known geoaoustic properties of the (fluid) bottom. Only the forward problem is considered here, although the conclusions are relevant to the question of noise-coherence inversions. To begin, a brief account of the spatial properties of ambient noise fields is presented, and this is followed by a discussion of the noise data from the two experimental sites, which includes a comparison of the data with the theory.

## I. SPATIAL STATISTICS OF AMBIENT NOISE FIELDS

The coherence function of the noise pressure fluctuations at two hydrophones, designated 1 and 2, is a normalized quantity defined as

$$\Gamma_{12} = \frac{\bar{S}_{12}}{\sqrt{\bar{S}_{11}\bar{S}_{22}}}, \quad (1)$$

where the cross-spectral density,  $\bar{S}_{12}$ , and the power spectral densities,  $\bar{S}_{11}$  and  $\bar{S}_{22}$ , are ensemble averages, as indicated by the overbar. As a result of the normalization,  $\Gamma_{12}$ , is independent of the spectral shape of the sources, provided only one type of source is present. (If two spectrally distinct source mechanisms were present, say shipping and surface waves, then  $\Gamma_{12}$  would depend on the frequency-dependent relative weighting of the two source spectra.) In spatially homogeneous noise,  $\Gamma_{12}$  depends only on the separation and orientation of the sensors, but not their absolute positions in the water column. Strictly speaking, shallow-water noise is not spatially homogeneous but, away from the boundaries, the dependence of its second-order statistical measures ( $\bar{S}_{12}$ , etc.) on absolute position is weak, in which case the noise may be treated as quasi-homogeneous.<sup>15</sup> The concept of quasi-homogeneity is useful for gaining an intuitive appreciation of the relationship between vertical coherence and vertical directionality.

A noise field consisting of a random superposition of plane waves propagating in all directions is spatially homogeneous. Supposing that the quasi-homogeneous, shallow-water noise field is approximated as a superposition of plane waves with vertical directional density function,  $F(\theta)$ , where  $\theta$  is the polar angle measured from the upward vertical, then the coherence function,  $\Gamma_{12}$ , of the noise at two vertically separated sensors in the channel is given by the finite Fourier transform<sup>16</sup>

$$\Gamma_{12}(kd) = \frac{1}{2} \int_0^\pi F(\theta) \exp(-jkd \cos \theta) \sin \theta d\theta. \quad (2)$$

In this expression  $d$  is the sensor separation and  $k = \omega/c$  is acoustic wave number in the water column,  $\omega$  is angular frequency, and  $c$  is sound speed. The density function  $F(\theta)$ , representing the incident noise intensity per steradian integrated over azimuth, satisfies the normalization condition

$$\frac{1}{2} \int_0^\pi F(\theta) \sin \theta \, d\theta = 1, \quad (3)$$

which is equivalent to the requirement that the normalized intensity integrated over all solid angles should equal  $4\pi$ .

Any vertical directional density function can be expressed in the form

$$F(\theta) = F_e(\theta) + F_o(\theta), \quad (4)$$

where  $F_e(\theta)$  and  $F_o(\theta)$  are, respectively, even and odd functions about the horizontal. If  $F(\theta)$  were expanded in a sum of zonal harmonics, then  $F_e(\theta)$  and  $F_o(\theta)$  would correspond, respectively, to the even- and odd-order terms in the series. It follows from Eq. (2) that

$$\text{Re}[\Gamma_{12}(kd)] = \frac{1}{2} \int_0^\pi F_e(\theta) \cos(kd \cos \theta) \sin \theta \, d\theta \quad (5a)$$

and

$$\text{Im}[\Gamma_{12}(kd)] = -\frac{1}{2} \int_0^\pi F_o(\theta) \sin(kd \cos \theta) \sin \theta \, d\theta. \quad (5b)$$

Thus the symmetric component of the noise field is associated exclusively with the real part of the coherence function and the antisymmetric component with the imaginary part. In shallow water, distant sources such as breaking waves and surface shipping generate a discrete-mode acoustic field which is more or less symmetrical about the horizontal, and hence shows a coherence function that is essentially real. Overhead sources, on the other hand, including local wave-breaking events, give rise to a predominantly downward propagating field, which can be decomposed into a symmetrical and an asymmetrical component, with an associated coherence function in which the real and imaginary parts may be comparable in amplitude.

It is evident from Eqs. (5) that the vertical coherence of any spatially homogeneous noise field can be expressed explicitly, since the integrals are known forms<sup>17</sup> once the directional density function is expressed as a series of zonal harmonics. A particularly simple example is isotropic noise, for which  $F(\theta) = P_0(\cos \theta) = 1$ , giving the familiar result  $\Gamma_{12} = [\sin(kd)]/kd$ , which is real, consistent with the mirror-image symmetry of the field about the horizontal. An example of an asymmetrical density function is

$$F(\theta) = 4P_1(\cos \theta) = 4 \cos \theta, \quad 0 \leq \theta \leq \pi/2, \\ = 0, \quad \pi/2 < \theta \leq \pi, \quad (6)$$

which represents surface-generated noise in deep water, where the bottom is too remote for significant reflection to occur and there is therefore no upward traveling component in the noise field. The corresponding coherence function, from Eqs. (5), is

$$\Gamma_{12} = 2 \left\{ \left[ \frac{\sin kd}{kd} + \frac{\cos kd - 1}{k^2 d^2} \right] + j \left[ \frac{\cos kd}{kd} - \frac{\sin kd}{k^2 d^2} \right] \right\}, \quad (7)$$

which is the classic result for isovelocity, deep-water noise derived originally by Cron and Sherman.<sup>18,19</sup> Notice that when  $0 < kd \ll 1$  the imaginary part of  $\Gamma_{12}$  in Eq. (7) is negative, which is a characteristic of downward traveling noise.

In shallow water, the vertical coherence of surface-generated noise would be as given in Eq. (7) only if the bottom were transparent to sound incident from above, since there would then be no reflections from the seabed, which is equivalent to the situation where the seabed is infinitely remote. Realistic seabeds, however, are not nonreflective but in general are moderately efficient acoustic reflectors that introduce a significant upward traveling component into the noise field. The result is a coherence function that depends strongly on the reflectivity of the bottom interface; and the reflectivity is itself governed by the geoacoustic parameters of the seabed.

In general, the geoacoustic parameters of the bottom influence both parts, real and imaginary, of the coherence function; and, conversely, an inversion of shallow-water noise coherence to obtain the bottom parameters should, in some way, involve both the real and imaginary parts of the coherence function. Although, strictly, the relationship between coherence and directionality in Eq. (2) does not hold in a bounded environment, the concept of noise coherence is still perfectly valid in a shallow channel. Moreover, the vertical coherence function shows a number of advantages over the directional density function as the basis of an inversion procedure. For instance, from a practical point of view, the coherence can be measured over a broad bandwidth using just a pair of hydrophones, as opposed to the density function, which is measured over a narrow band of frequencies with a fully populated array. Thus noise inversions based on coherence exploit bandwidth rather than aperture.

## II. NOISE COHERENCE AND THE SEABED

If the vertical coherence of the noise is to be successfully inverted to obtain the properties of the seabed, it is necessary to establish some measure of the sensitivity of the inversion technique to different sediment types. The theoretical model described in the Appendix has been used to compute the coherence as a function of frequency for a representative selection of fluidlike sedimentary seabeds. An important input to the model is the compressional wave speed of the sediment, which, according to Hamilton,<sup>20</sup> shows a value ranging between approximately 1450 m/s (clayey silt) and 1800 m/s (coarse sand). Once the wave speed has been specified, the remaining parameters characterizing the sediment, that is, attenuation coefficient, grain size, density, porosity, and plane-wave reflection coefficient, can all be estimated uniquely using the theory of sediment acoustics recently developed by Buckingham.<sup>21-23</sup> Of these parameters, only the attenuation coefficient and density are required as inputs to the noise model to obtain the coherence function.

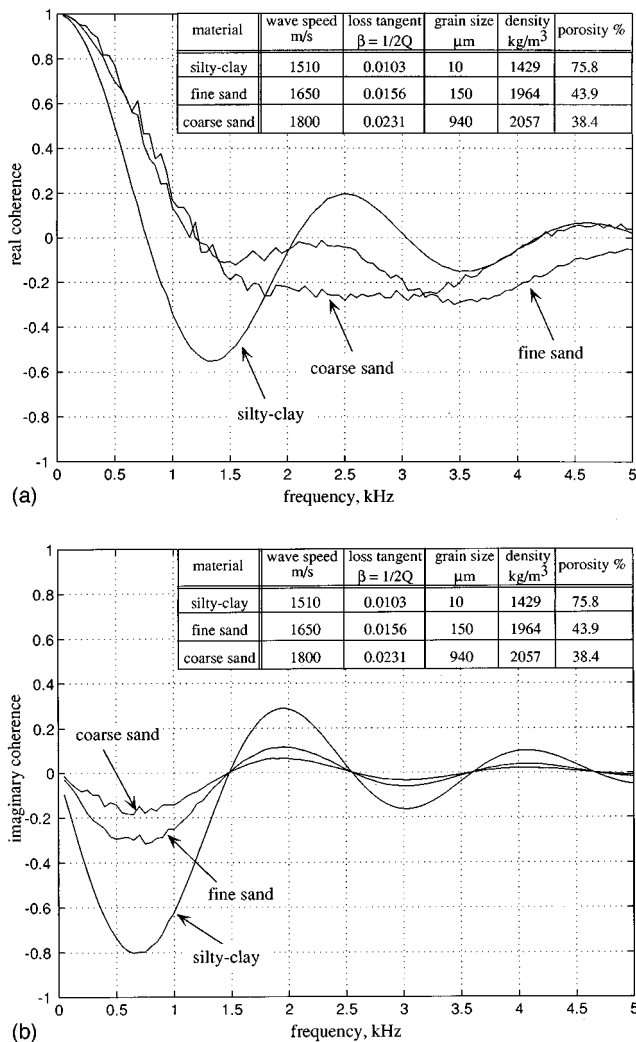


FIG. 2. (a) Real and (b) imaginary coherence curves, computed assuming a uniform sound speed in the water column of 1500 m/s. The curves correspond to three sediment types with geoacoustic properties as shown in the inset.

Figure 2 shows the computed noise coherence for three different types of fluid sediment, assuming an isovelocity channel of depth 50 m, and a sensor separation of 0.73 m. The table inset into the diagram shows the values of the parameters characterizing each of the three sediments, as determined from Buckingham's sediment model<sup>21</sup> assuming the wave speeds shown in the second column. The frequency-independent, dimensionless loss tangent  $\beta$ , as specified in the inset, is equal to  $1/2Q$ , where  $Q$  is the quality factor of the sediment. The attenuation coefficient is related to the loss tangent through the expression

$$\alpha = \frac{\omega\beta}{c_1}, \quad (8)$$

where  $\omega$  is angular frequency and  $c_1$  is the compressional wave speed in the sediment. Thus with  $\beta$  independent of frequency, the attenuation coefficient scales with the first power of frequency, in accord with numerous observations of the attenuation in unconsolidated marine sediments.<sup>20</sup> In the literature, the attenuation is often cited in terms of Hamil-

ton's coefficient  $k_H$ , or equivalently as dB/kHz m. The loss tangent,  $\beta$ , and  $k_H$  are related as follows:

$$\beta = 1.83 \times 10^{-5} c_1 k_H. \quad (9)$$

Of the three materials represented in Fig. 2, the silty clay sediment is the finest grained, showing the slowest sound speed, the lowest density and attenuation, and the highest porosity. In this case, the seabed is almost transparent to sound incident from above, most of which penetrates into the bottom and is thus lost from the water column. The resultant noise field in the channel is predominantly downward traveling, that is, it shows a high degree of asymmetry about the horizontal. This is evident from the relatively large excursions of the imaginary part of the coherence in Fig. 2(b). The real part also shows a high amplitude of oscillation about zero.

The coarse sand sediment represents the opposite extreme, being the coarsest grained of the three materials, with the highest sound speed and density, the lowest porosity and relatively high attenuation. Such a bottom is highly reflective, giving rise to a noise field that is fairly symmetrical about the horizontal. This is consistent with the small oscillations about zero exhibited by the imaginary part of the coherence in Fig. 2(b). It can also be seen in Fig. 2 that the sediment of fine sand, with properties intermediate between those of silty clay and coarse sand, gives rise to coherence curves which are distinguishable from those for the other two bottom types. Incidentally, most unconsolidated sediments exhibit some degree of rigidity and thus support shear waves, albeit only weakly. This has a minor effect on the vertical coherence of the noise, which is neglected in the present discussion.

It would appear from the theoretical results in Fig. 2 that the vertical coherence of shallow-water noise has the potential for providing a reasonable measure of the geoacoustic properties of a fluid seabed. To gain more confidence in this conclusion, it is necessary to compare measured noise data with theoretical predictions based on prior knowledge of the bottom properties. To this end, two shallow-water ambient noise data sets are discussed below, one taken at a site with a very fine grained, slow bottom (mud), and the other from an area with a moderately coarse, intermediate speed bottom (fine sand).

### III. WIND NOISE, EUREKA, NORTHERN CALIFORNIA

In June 1996, a set of ambient noise data was collected off Eureka, northern California, at a shallow-water site about 12 km out from the coast where the properties of the seabed have been extensively characterized as part of the Office of Naval Research's Strata Formation on Margins (StrataForm) research program.<sup>24</sup> The bottom in this region is essentially flat (slope less than  $0.4^\circ$ ), and is partly composed of fluvial mud, which has been deposited by the outflow from a number of rivers, but primarily the Eel and the Klamath. Also present are sandy marine sediments, creating a seabed that acts (acoustically) as a fluid, supporting negligible shear. More details of the site, including the geophysical properties of the bottom, are listed in Table I.

TABLE I. Details of the experimental sites at New Zealand and Eureka.

Site	Eureka, CA	Jellicoe Channel, NZ
Position	40°48'N, 124°20'W	36°15'S, 174°57'E
Water depth, m	70	50
Tidal range, m	...	3
Sediment type	fluvial mud	sand and broken shell
Mean grain diameter, $\mu\text{m}$	0.7 <sup>a</sup>	88 <sup>a</sup>
Sediment sound speed, m/s	1490	1610
Sediment density, $\text{kg/m}^3$	1179 <sup>a</sup>	1899 <sup>a</sup>
Sediment porosity	0.91 <sup>a</sup>	0.48 <sup>a</sup>
Sediment attenuation $\beta = 1/2Q$	0.0027 <sup>a</sup>	0.0072 <sup>a</sup>
Bottom water sound speed, m/s	1482	1506
Mean sensor depth, m	25	25

<sup>a</sup>Values estimated from Buckingham's theory of sediment acoustics.

During the noise measurements, ship traffic was present in the area some of the time, but not always, and in its absence surface wave breaking was the predominant source of noise. Data were collected when shipping sources were negligible, if not entirely absent, in light winds, with small spilling breakers forming visible whitecaps on top of a swell that occasionally reached a height of two meters peak-to-trough. The channel was fairly well mixed, showing a sound-speed profile that varied slowly with depth, with a negative gradient of less than 0.13 m/s per m. An example of the measured vertical coherence is shown in Fig. 3, and for comparison the solid line in the figure was computed for an isovelocity channel from the theoretical wind-noise model described in the Appendix. The geoacoustic parameters of the sediment (Table I) were used as inputs to the model. The data representing the real and imaginary parts of the coherence show smooth, slowly decaying oscillations out to a frequency of 5 kHz, and this behavior is matched reasonably faithfully by the theory. This agreement lends support to the view that the spatial coherence of shallow-water, wave-generated noise is stable and predictable, making it a good candidate for inversion to obtain the geoacoustic parameters of the bottom.

At frequencies above 5 kHz, other factors apart from the bottom affect the coherence of the noise, most notably the depth of the acoustic sources beneath the sea surface.<sup>25</sup> Figure 4 shows the same data set as in Fig. 3, but plotted over the full available bandwidth of 20 kHz. At about 6 kHz the coherence can be seen to change character from well-defined oscillations at the lower frequencies to bands of small ripples in the higher frequency range. Below 6 kHz the noise sources and their negative images in the sea surface act as acoustic dipoles (i.e., the separation between source and image is a small fraction of a wavelength), giving rise to the

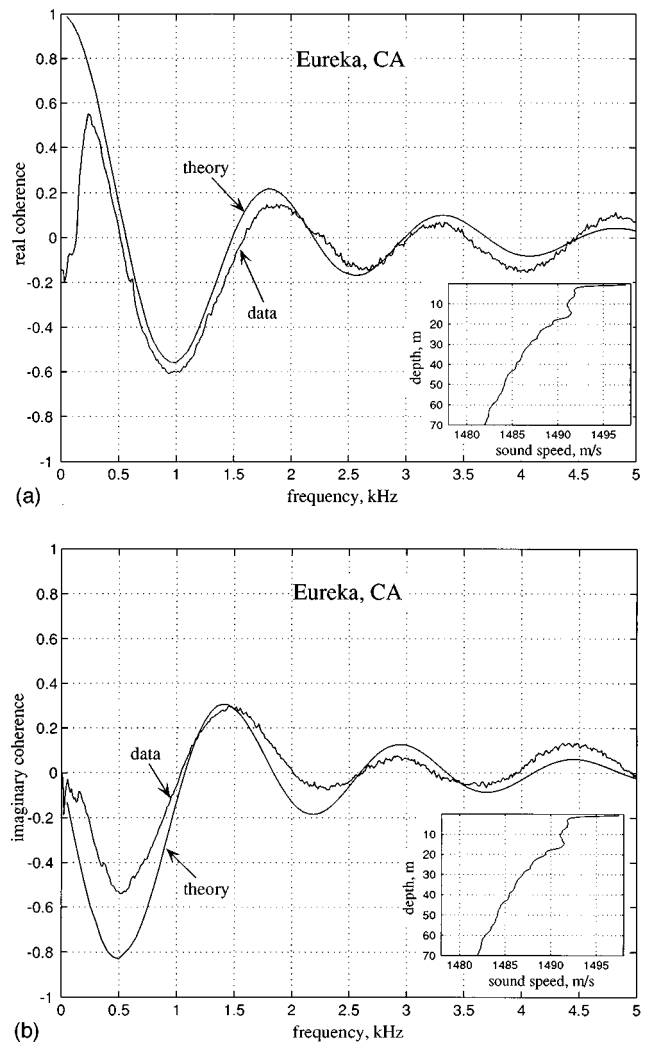


FIG. 3. Frequency dependence, over a 5-kHz band, of (a) the real and (b) the imaginary coherence of noise from wave-breaking off Eureka, northern California, as recorded on 21 June 1996 in near-isovelocity conditions (insets) with a sensor separation of 0.996 m. The spectral analysis was performed on approximately  $10^4$  time series records, each of duration 90 ms, corresponding to an averaging time of 15 min and a spectral resolution of 11 Hz. The theoretical curve was computed from the isovelocity wind-noise model described in the Appendix, using the environmental parameters for the site listed in Table I. Data below 200 Hz are excluded from the record, which accounts for the low-frequency discrepancy between theory and data in (a).

observed oscillatory form of the coherence. At higher frequencies, where the source–image separation is comparable with or greater than a wavelength, the dipole description fails and a Lloyd's mirror interpretation of the sources and their images is more appropriate. In this regime, the interference structure in the field from the noise sources tends to suppress the oscillations in the noise coherence, although bands of vestigial ripples survive out to a frequency of 15 kHz.

As in Fig. 3, the solid line in Fig. 4 has been computed from the isovelocity wind-noise theory in the Appendix, and includes the effect of the source depth, which is simply the displacement of the source plane below the sea surface. To fit the data, the source depth has been chosen as  $z' = 8.5$  cm, which may be interpreted as the depth of the acoustically active bubbles beneath the sea surface. It can be

seen that the theoretical transition from dipolar to Lloyd's mirror behavior matches the change in the data, and also that the higher-frequency bands of ripples appear in the theoretical curves very much as they do in the data. Although the ripples are a secondary effect, associated with constructive and destructive interference in the Lloyd's mirror field, the fact that they are so similar in the theory and the data lends credibility to the idea that the finite source depth is indeed responsible for the higher-frequency features in the coherence curves. Based on the quality of the fits in Figs. 3 and 4, it appears that the vertical noise coherence is a potential inversion tool not only for determining bottom parameters but also for acquiring quantitative information on sea surface processes.

#### IV. WIND AND SHIP NOISE, JELICOE CHANNEL, NEW ZEALAND

During the New Zealand summer, from mid-November 1995 to mid-January 1996, ambient noise measurements were performed in the shallow water of Jellicoe Channel, which is a tidal channel, about 22 km wide, between Cape Rodney on the New Zealand mainland and Little Barrier Island. The experimental site is some 64 km north of Auckland. From a previous geological survey of the area,<sup>26</sup> the seabed at the site is known to be more or less flat over an area of  $20 \times 12$  km, as illustrated by the contour map of the local bathymetry shown in Fig. 5(a). Echo soundings taken on the transit out to the noise measurement station [Fig. 5(b)] also indicate that the seafloor in the immediate vicinity of the sensors is smooth and horizontal.

According to Tindle *et al.*,<sup>27</sup> the seabed consists of a fluid-saturated sand layer about 100 m thick, below which is a basement of greywacke rock. This description is in accord with the geological chart of the bottom [Fig. 5(c)] around the measurement site. From several grab samples of the sedimentary bottom material collected during the course of our noise measurements, the sediment was found to consist of fine grained sand with an admixture of broken shell fragments (Fig. 6), which is consistent with the findings from the earlier geological survey of the bottom.<sup>26</sup> The geophysical and environmental properties of the site are summarized in Table I.

At this location, as in many areas around Australia and New Zealand,<sup>12,13</sup> the density of shipping is low compared with typical shipping levels found in the northern hemisphere. Not surprisingly, the sound produced by bubbles from wave breaking contributed significantly to the overall noise field at frequencies above a few hundred hertz. However, shipping is not entirely absent from the region. A shipping lane about 10 km from the measurement site serves Auckland Harbour some 64 km to the south, and for much of the time individual vessels (often just one) in transit along this route fell within audible range of the noise detection system. Although this surface ship traffic was often out of sight, nevertheless several of the data sets do contain a significant shipping noise component. The effect of the ship noise is to modify the spectrum and the vertical coherence of the overall noise field up to frequencies as high as 5 kHz.

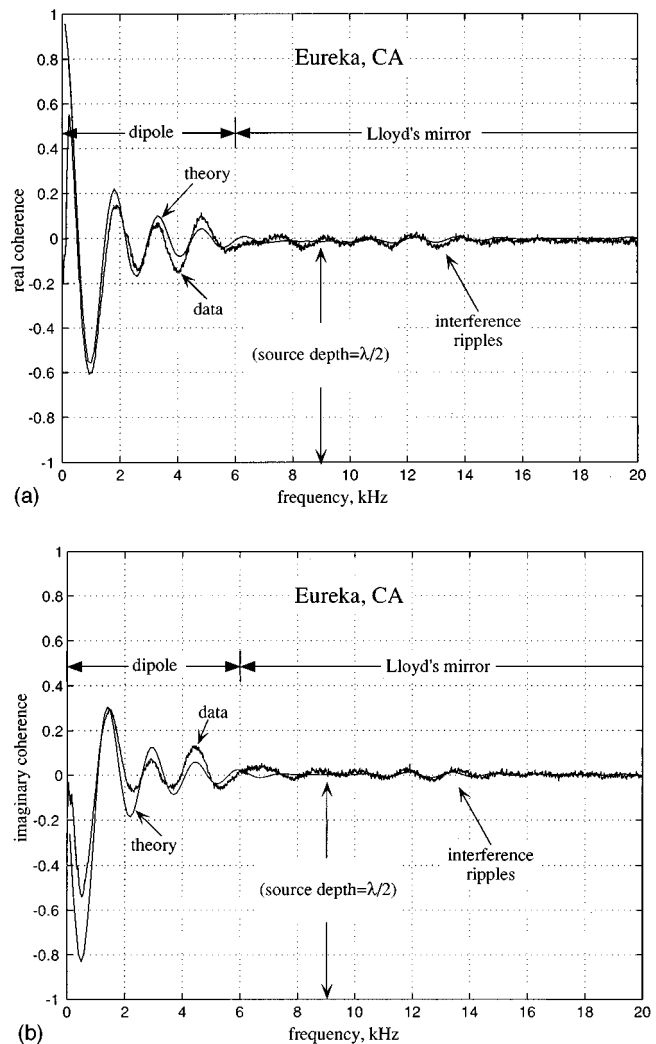
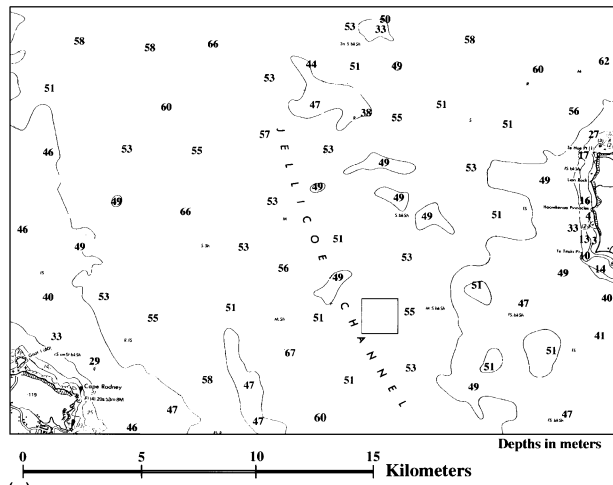


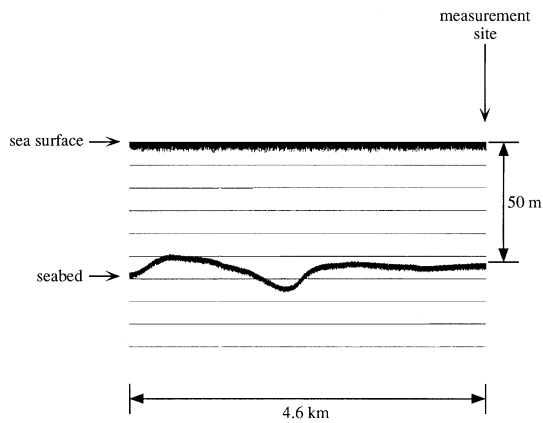
FIG. 4. (a) Real and (b) imaginary coherence of wave-breaking noise at Eureka, from the same time series as in Fig. 3, with the same spectral averaging, but shown over the extended bandwidth of 20 kHz. Note the transition from oscillatory behavior at low frequencies, associated with the dipole nature of the bubble sources, to Lloyd's mirror interference ripples at higher frequencies, which can be seen in both the theory and the data. The theoretical curve was computed from the isovelocity wind-noise model described in the Appendix, using the environmental parameters for the site listed in Table I.

Audible sounds from marine mammals were detected intermittently at frequencies above 6 kHz, but these signals were not significant during most of the recordings. Another biological source of sound, snapping shrimp, was occasionally present, producing very brief, extremely energetic acoustic pulses that are clearly evident in the time series, as illustrated in Fig. 7. These transient signals have a duration of no more than  $10 \mu\text{s}$ ,<sup>28</sup> a spectrum that extends up to at least 200 kHz, and a peak source strength in excess of 150 dB *re*:  $1 \mu\text{Pa}^2$ . Most of the energy in the pulses from the snapping shrimp lies above 5 kHz, but nevertheless, when these pulses are present, the residual energy at lower frequencies, between 2.5 and 5 kHz, is sufficient to affect slightly the coherence of the ambient noise. (The effect is illustrated in Fig. 9.)

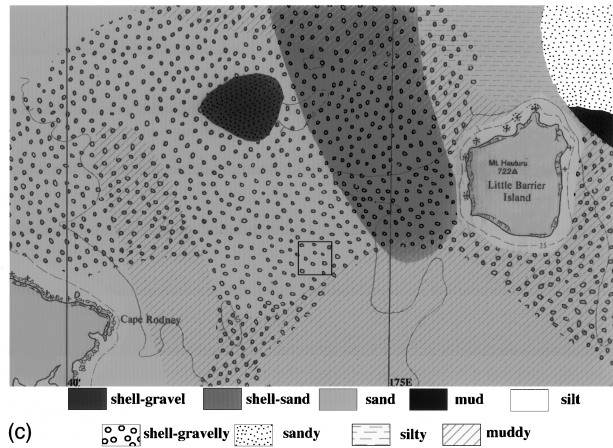
Figure 8 shows an example of the noise coherence, as measured on 28 November 1995 under well-mixed condi-



(a)



(b)



(c)

FIG. 5. Bottom conditions in the vicinity of the New Zealand experimental site. (a) Bathymetry in Jellicoe Channel, from: Hydrographic Office of the Royal New Zealand Navy, Chart No. N. Z. 522, Auckland (1974). (b) Echo sounder data taken during the transit out to station. (c) Map of the bottom geology, showing information from: L. Carter and J. V. Eade, Hauraki Sediments, New Zealand Oceanographic Institute Chart, Coastal Series 1:200,000 (1980). In (a) and (c) the square marks the position of the experimental site.

tions at the New Zealand site in Sea State 2 to 3. During the recording period the sound speed was essentially uniform throughout most of the water column. In comparison with Fig. 3, it is evident that the coherence differs significantly from that observed at the Eureka site off northern California.

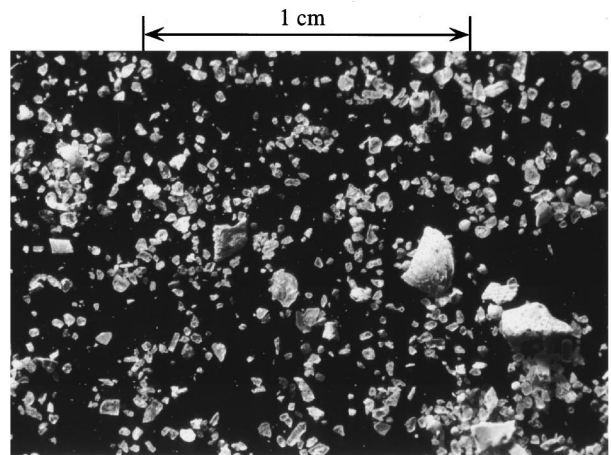
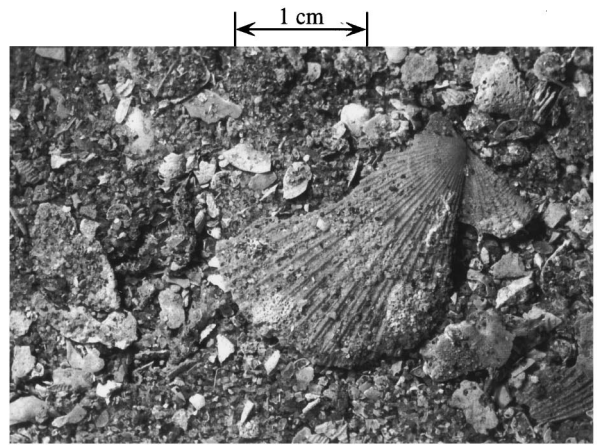


FIG. 6. Oven-dried sediment recovered from the experimental site in Jellicoe Channel. Top: aggregate sample showing a mixture of sand and broken shells. Bottom: separated sediment particles showing individual sand grains and fragments of shell. (Photographs by M. J. Buckingham.)

The difference is attributed, at least partially, to the faster sediment at Jellicoe Channel, as may be appreciated by comparing the theoretical curves for wind noise in Fig. 8 with the corresponding curves for the Eureka site in Fig. 3. It is clear,

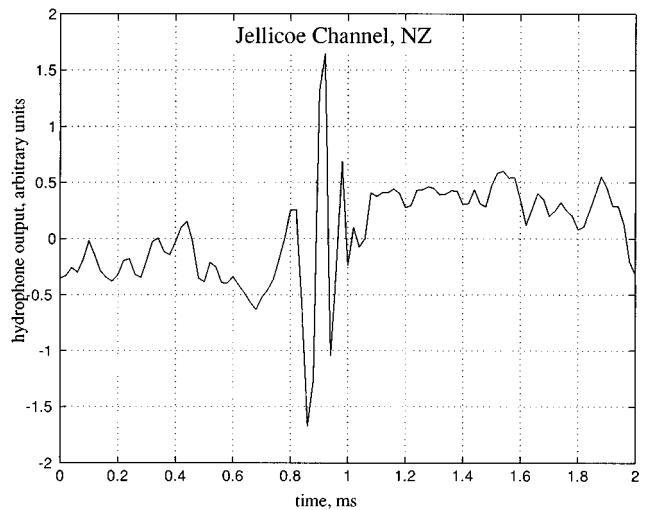


FIG. 7. Time series showing a very brief, energetic pulse from snapping shrimp in Jellicoe Channel. The pulse has been broadened considerably by the limited bandwidth (20 kHz) of the recording system.

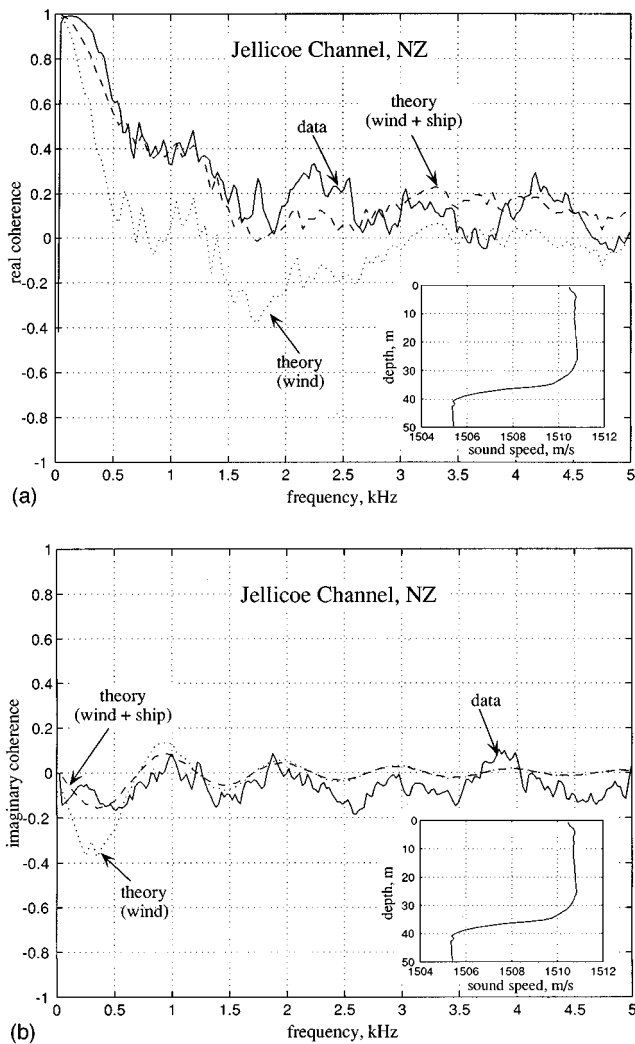


FIG. 8. (a) Real and (b) imaginary coherence of noise from a combination of wave-breaking and shipping around Jellicoe Channel, New Zealand, as recorded in near-isovelocity conditions (insets) on 28 November 1995 with a sensor separation of 1.525 m. A northerly wind was blowing at between 2.5 and 5 m/s. The spectral analysis was performed on approximately 4000 time series records, each of duration 43.5 ms, corresponding to an averaging time of 3 min and a spectral resolution of 23 Hz. The smooth, solid curve was computed from the wind- plus ship noise model outlined in the Appendix, and the dashed line is the computed coherence from wind-driven sources alone. The latter two curves were both calculated using the environmental parameters for the site listed in Table I.

however, that wind noise alone is not sufficient to explain the data in Fig. 8. On this occasion, an additional mechanism was at work in Jellicoe Channel, namely noise generation by a vessel that was within sight in the nearby shipping lane. When this noise component is included in the theoretical model, both the real and imaginary parts of the coherence are modified, to provide a much improved fit to the data over a bandwidth of 5 kHz (Fig. 8).

Theoretically, the ship noise has been represented by the lowest-order (first) mode from a single, broadband source at a range of 10 km and added incoherently to the noise contribution from the wind-driven surface sources. The first mode represents acoustic energy that propagates almost horizontally, and hence possesses a high degree of coherence in the vertical. Its main effect on the overall coherence is to

raise the real part but without introducing any new oscillatory structure into the curves. Such behavior is in accord with the data, as can be seen in Fig. 8. The spectral density of the ship noise component relative to the wave breaking spectrum was taken to be of the form  $(f/f_1)^2 + (f_1/f)^2$ , which has a maximum at frequency  $f_1 = 100$  Hz, with the shoulders either side rolling off at 6 dB per octave.

Conditions several weeks later, on the 9 January 1996, were somewhat different from those of the earlier measurements. Most of the water column was not well-mixed but showed a linear sound speed profile with negative gradient of approximately  $-0.42$  m/s per m, giving rise to mild downward refraction. On this occasion, there were periods when vessels in the nearby shipping lane were either absent or had a negligible effect on the noise field.

Figure 9 shows the vertical coherence recorded under such circumstances over a bandwidth of 5 kHz. For comparison, theoretical curves are included in the figure, as computed from the wind-noise model for a shallow channel with a linear sound-speed profile (see the Appendix). It is evident in this case that the wind-noise theory, without a shipping component, fits the data moderately well. In fact, for the imaginary part of the coherence [Fig. 9(b)], the match between theory and experiment is satisfactory across the 5-kHz band, indicating that the asymmetric component of the noise field is reasonably represented by the linear profile model. With regard to the real part of the coherence [Fig. 9(a)], the comparison between theory and experiment is reasonable up to about 3.5 kHz, in that the peaks and troughs match fairly well, but at higher frequencies the data begin to diverge from the theoretical prediction.

If it is assumed that the theory provides an accurate representation of the wind-generated noise coherence, then the implication of Fig. 9(a) and (b) is that at the time of the measurement an additional noise component must have been present which modified the field above 3.5 kHz. The discrepancy between theory and data at higher frequencies is even more evident in Fig. 10, which shows the coherence as a function of frequency over the full available bandwidth of 20 kHz. Whatever the additional component may have been, it affects the real and imaginary parts of the coherence above 5 kHz, indicating that the associated directional density function contains symmetrical and antisymmetrical components about the horizontal.

A possible explanation of the high-frequency discrepancy between the wind-noise theory and the data in Fig. 10 is snapping shrimp, since these creatures are known to produce sound above a few kHz. A fairly sparse distribution of snapping shrimp on the seabed would provide a set of spatially discrete acoustic sources, which may account for the observed high-frequency noise coherence. Below a few kHz, the snapping shrimp noise (or whatever the secondary noise component may be) is negligible, judging from the fact that the wind-noise theory follows the real and imaginary coherence data fairly faithfully.

## V. CONCLUDING REMARKS

Ambient noise in shallow water is modified by the proximity of the bottom boundary. The channel acts as an acous-



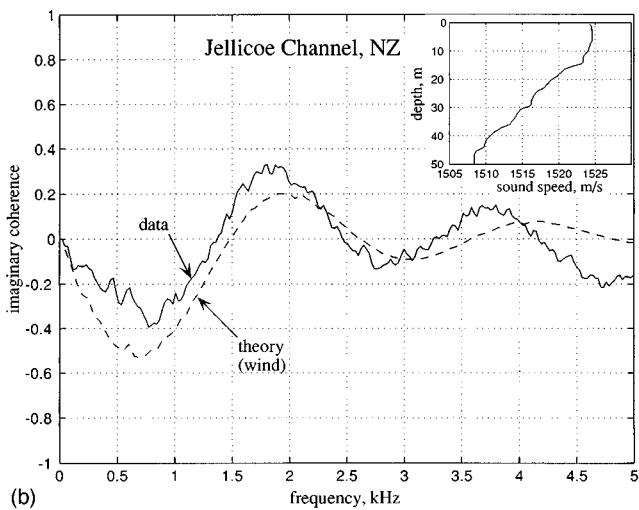
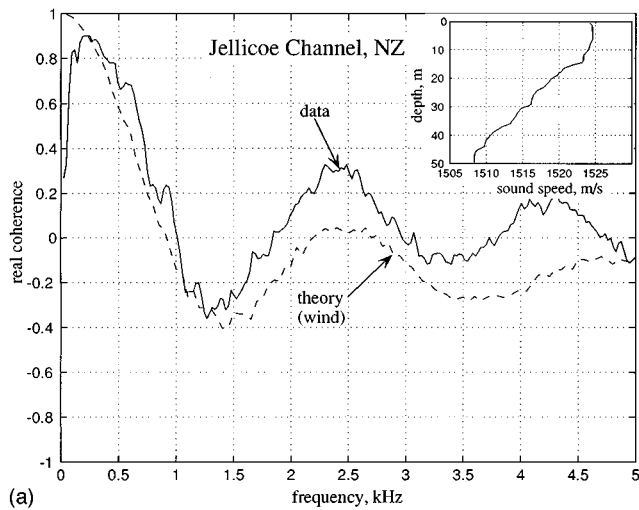


FIG. 9. (a) Real and (b) imaginary coherence of ambient noise in Jellicoe Channel, over a bandwidth of 5 kHz, as recorded in a nearly linear sound-speed profile (insets) on 9 January 1996 with a sensor separation of 0.73 m. The wind speed was between 7.5 and 10 m/s. The spectral analysis was performed on 250 records, each of duration 31.2 ms, corresponding to an averaging time of 7.8 s and a spectral resolution of 32.05 Hz. The theoretical curve was computed from the exponential profile model outlined in the Appendix, using the environmental parameters for the site listed in Table I. The  $e$ -folding depth used was  $d=4485.3$  m, giving an essentially linear profile through the 50-m water column with surface and bottom sound speeds matching the measured values.

tic waveguide supporting normal mode propagation and, since the noise originates in a number of discrete sources, it too exhibits a modal structure. Thus the intensity of the noise can be expressed in terms of normal modes plus a branch line integral or alternatively as an equivalent wave number integral, which may be evaluated numerically. Either way, the level of the noise is difficult to predict accurately because of the uncertainty about the distribution and intensity of the sources generating the field. The intensity also depends on the bottom type, but noise level inversions for the geoacoustic parameters of the seabed are made almost impossible by the strong variability of the sources.

The bottom affects not only the level of the noise but also its spatial structure (directionality and coherence) in the vertical. Unlike the noise level, however, the vertical coher-

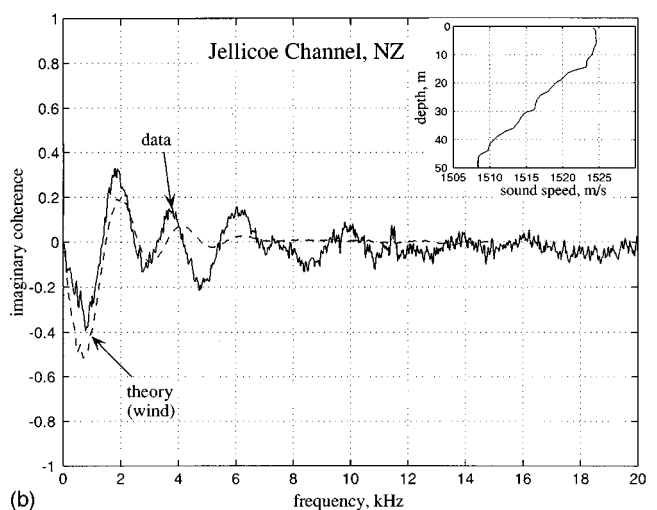
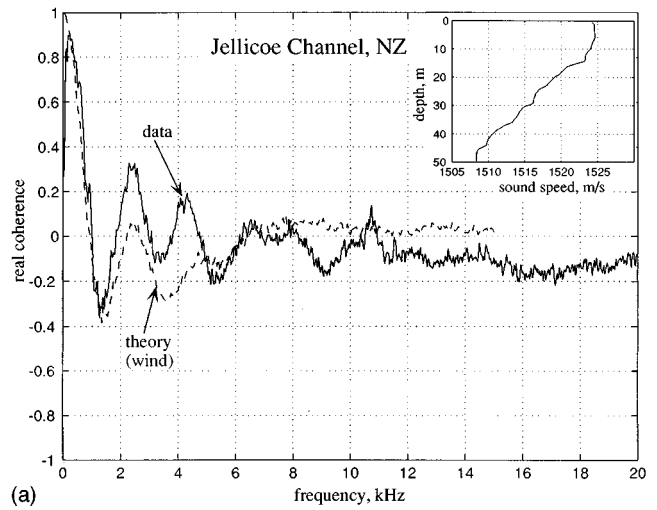


FIG. 10. (a) Real and (b) imaginary coherence of ambient noise in Jellicoe Channel, exactly as in Fig. 9 but over the full available bandwidth of 20 kHz.

ence is largely unaffected by the nature of the sources. The main factor determining the vertical coherence is the seabed, although at frequencies in excess of 5 kHz or so source depth effects may also be significant. To some extent the sound-speed profile in the channel influences the coherence, but often only weakly, besides which the profile is fairly easily incorporated into noise prediction models. Thus in principle at least, the noise coherence in the vertical is a statistical measure of the noise field which is relatively stable and predictable, suggesting that it is a good candidate for inversion, to yield the geoacoustic properties of the seabed.

The broadband noise measurements reported in this article, taken in ocean channels overlying fluid-saturated sediments, support the view that the vertical coherence of ambient noise in shallow water can be accurately predicted, provided the properties of the bottom are known. Different sedimentary types, ranging from coarse sand to silty clay, have been examined theoretically and shown to give rise to quite different noise coherence curves. These differences are sufficiently pronounced to provide an adequate basis for a noise inversion procedure to determine seabed parameters.

## ACKNOWLEDGMENTS

We wish to thank Dr. Michael Richardson and Dr. Kevin Briggs for the invitation to participate in the Eureka experiment on board the R. V. WECOMA; Dr. Nicholas Carbone for computing the coherence curves from the New Zealand time-series data; and Thomas Hahn and Thomas Berger for collecting the ambient noise data at the Eureka site. During the course of the New Zealand experiment, GBD was welcomed as a visiting scientist in the Physics Department, University of Auckland, which generously made available the R. V. PROTEUS as the trials vessel. This work was partially supported by the Office of Naval Research under Grant No. N00014-91-J-1118, for which we are grateful.

## APPENDIX: THEORETICAL MODEL FOR THE VERTICAL COHERENCE OF NOISE IN SHALLOW WATER

Wind-generated noise is generated mainly by breaking waves, which create bubbles that resonate radially, thereby acting as acoustic monopoles. For the purpose of modeling the noise field, the breaking events are usually represented as a random distribution (in time and space) of independent, discrete sources located in a plane lying immediately beneath the sea surface.<sup>15,18,19,29</sup> Each such source is in fact the superposition of all the individual bubble sources under a breaking wave, implying that the radiated acoustic pulse may persist for a period of several seconds. In general, the source spectrum will show considerable structure, but, if it is assumed that on average the pulses from all breaking events are identical, then the source spectrum cancels out of the coherence function. It is therefore satisfactory, in deriving the coherence function, to neglect the structure in the spectrum entirely and to treat the wave-breaking sources as impulses (delta functions). The source region is also assumed to be compact, that is, small in extent compared to a wavelength, allowing each breaking event to be treated as a point source. Thus the pulse arrival at a receiver from such a source, represented by delta functions in space and time, is simply the impulse response, or Green's function, of the channel.

In a horizontally stratified medium, the (harmonic) Green's function for the velocity potential can always be expressed in the form

$$G \equiv G(r, z, z', \omega) = \int_0^\infty p G_p(z, z', \omega) J_0(pr) dp, \quad (\text{A1})$$

where  $r$  is horizontal range between the source and receiver,  $(z, z')$  are receiver and source depths, respectively,  $\omega$  is angular frequency,  $p$  is horizontal wave number,  $J_0(\dots)$  is the Bessel function of the first kind of order zero, and  $G_p$  is the Hankel transform of the velocity potential  $G$ .  $G_p$  is a solution of the depth-dependent part of the wave equation, which depends on  $p$  as well as the boundary conditions and the sound-speed profile.

The noise sources within an annulus on the sea surface centred on the receiver and extending between radii  $r$  and  $r + dr$  all have the same Green's function, since the sound they generate propagates over identical transmission paths. It

follows from Carson's theorem<sup>30</sup> that the power spectral density of the noise at the receiver from all the sources within the annulus is

$$d\bar{S} = 4\pi\mu r |G|^2 dr, \quad (\text{A2})$$

where  $\mu$  is the mean rate of source events per unit area of surface and the overbar denotes an ensemble average. According to Eq. (A2), a stochastic quantity, in this case the power spectrum, is expressed in terms of the deterministic Green's function. The power spectral density of the noise from sources distributed across the whole sea surface is simply the integral of Eq. (A2) taken over all values of  $r$ :

$$\bar{S} = 4\pi\mu \int_0^\infty r |G|^2 dr. \quad (\text{A3})$$

When the integral for  $G$  in Eq. (A1) is substituted into this expression, a triple integral is obtained, which, by performing the integration over range first, reduces to the following single wave number integral

$$\bar{S} = 4\pi\mu \int_0^\infty p |G_p|^2 dp. \quad (\text{A4})$$

This result is obtained because the range integration is the delta-function identity

$$\int_0^\infty r J_0(pr) J_0(\bar{p}r) dr = \frac{\delta(p - \bar{p})}{\bar{p}}, \quad (\text{A5})$$

which immediately eliminates one of the two remaining wave number integrals, yielding the expression in Eq. (A4) for the power spectral density of the noise. The integral in Eq. (A4) may be evaluated numerically once  $G_p$  is known from a solution of the wave equation.

The result in Eq. (A4) may be readily extended to give the cross-spectral density of the noise at two hydrophones in the water column. If the separation between the sensors is  $s$  and the line connecting them is inclined at an angle  $\gamma$  to the vertical, then the cross-spectral density of the noise is

$$\bar{S}_{12} = 4\pi\mu \int_0^\infty p G_{1p} G_{2p}^* J_0(ps \sin \gamma) dp, \quad (\text{A6})$$

where the asterisk denotes complex conjugation. Clearly, when the two sensors are coincident, that is, when  $s$  goes to zero, the Bessel function is equal to unity and the expression in Eq. (A6) reduces to that for the power spectral density in Eq. (A4).

The coherence function is defined as

$$\Gamma_{12} = \frac{\bar{S}_{12}}{\sqrt{\bar{S}_{11}\bar{S}_{22}}} = \frac{\int_0^\infty p G_{1p} G_{2p}^* J_0(ps \sin \gamma) dp}{[\int_0^\infty p |G_{1p}|^2 dp \int_0^\infty p |G_{2p}|^2 dp]^{1/2}}, \quad (\text{A7})$$

where the normalizing terms,  $\bar{S}_{11}$  and  $\bar{S}_{22}$ , are just the power spectral densities of the noise at each of the sensors. In a homogeneous noise field,  $\bar{S}_{11}$  and  $\bar{S}_{22}$  would be the same, but this equality does not hold in shallow water, where the noise field is inhomogeneous. For the special case of vertically

separated sensors, the angle  $\gamma$  is zero and the Bessel function in the numerator of Eq. (A7) is unity, in which case the expression for the coherence function becomes

$$\Gamma_{12} = \frac{\int_0^\infty p G_{1p} G_{2p}^* dp}{[\int_0^\infty p |G_{1p}|^2 dp \int_0^\infty p |G_{2p}|^2 dp]^{1/2}}. \quad (\text{A8})$$

Equations (A7) and (A8) are generally valid for any profile but, of course, can be evaluated only when the Hankel transform of the velocity potential is known. The latter expression, Eq. (A8), is the basis of the models of the vertical

coherence of wind-generated noise in shallow water that are referred to in the text. This expression depends not only on the sound speed profile and the source depth but also on the sediment type, which determines the bottom boundary condition.

To evaluate the integrals in Eq. (A8), it is necessary to know the functions  $G_{1p}$  and  $G_{2p}$  representing the field at the two receivers. For an isovelocity water column overlying a homogeneous, fluid sediment (i.e., a Pekeris channel<sup>10</sup>), these functions are

$$G_{ip} = M \frac{\sin \eta_1 z'}{\eta_1} \left\{ \frac{(\eta_1 + b \eta_2) \exp[j \eta_1 z_i] + (\eta_1 - b \eta_2) \exp[j \eta_1 (2h - z_i)]}{(\eta_1 + b \eta_2) + (\eta_1 - b \eta_2) \exp[2j \eta_1 h]} \right\}, \quad (\text{A9})$$

where  $M$  is a simple scaling constant which cancels out of the coherence function,  $i = 1, 2$ ,  $z_i$  is the depth of the  $i$ th sensor, and  $h$  is the depth of the water column. ( $\eta_1, \eta_2$ ) are vertical wave numbers in the water (sound speed  $c_1$ ) and the sediment (sound speed  $c_2$ ), respectively:

$$\eta_1 = \sqrt{k_1^2 - p^2}, \quad \eta_2 = \sqrt{k_2^2 - p^2}, \quad (\text{A10})$$

where ( $k_1 = \omega/c_1$ ,  $k_2 = \omega/c_2$ ) are the acoustic wave numbers in the two media. To ensure convergence, the imaginary parts of  $\eta_1$  and  $\eta_2$  are constrained to be greater than zero everywhere in the complex  $p$  plane. The parameter  $b$  in Eq. (A9) is the ratio  $\rho_1/\rho_2$ , where  $\rho_1$  is the density of seawater and  $\rho_2$  is the density of the sediment.

With the expression for  $G_{ip}$  in Eq. (A9), the coherence function in Eq. (A8) is exact and complete in that it includes the discrete spectrum, the continuous spectrum and the lateral wave, although at the frequencies of interest here the last is negligible. The formulation of the coherence function embodied in Eqs. (A8) and (A9) is straightforward and rapid to evaluate numerically on a desktop computer, and it is this formulation that is referred to in the text as the isovelocity wind-noise model.

To include the effect of shipping in the isovelocity model, the field associated with the first normal mode from a single, deterministic source is added incoherently to the cross spectrum and autospectra. This field expression is determined in a standard fashion by solving for the eigenvalues from the dispersion relation [i.e., finding the roots of the denominator of Eq. (A9)] and then integrating around an appropriate contour in the complex  $p$  plane.

Returning to the question of the noise coherence, the situation is slightly more complicated in the case of a channel with an exponential sound-speed profile overlying a homogeneous, fluid basement. Based on a profile of the form

$$c_1 = c_s e^{-z/d}, \quad (\text{A11})$$

where  $c_s$  is the sound speed at the sea surface and  $d$  is the  $e$ -folding depth of the profile, a new set of variables is introduced:

$$x_i = k_s d e^{z_i/d}, \quad i = 1, 2; \quad x_s = k_s d; \quad x_h = k_s d e^{h/d}; \quad (\text{A12})$$

$$x' = k_s d e^{z'/d}.$$

The wave number in these expressions is  $k_s = \omega/c_s$ . It is convenient to define the following dimensionless functions:

$$A = j[J_v(x')Y_v(x_s) - J_v(x_s)Y_v(x')], \quad (\text{A13})$$

$$B(x) = jx_h[J_v'(x_h)Y_v(x) - J_v(x)Y_v'(x_h)], \quad (\text{A14})$$

$$C(x) = jx_h[J_v(x_h)Y_v(x) - J_v(x)Y_v(x_h)], \quad (\text{A15})$$

and

$$R = \frac{j \eta_2 db}{x_h}, \quad (\text{A16})$$

where  $b$  is as defined above in connection with an isovelocity profile. In Eqs. (A13) to (A15) the order of the Bessel functions of the first and second kinds,  $J_v$  and  $Y_v$ , respectively, is

$$v = pd, \quad (\text{A17})$$

and a prime on a Bessel function indicates a derivative with respect to the argument. Equations (A13) to (A17) emerge from a moderately lengthy analysis of the depth-separated part of the wave equation, which is transformed using Eqs. (A12) into Bessel's equation, which in turn is solved by the application of an appropriate Hankel transform. Eventually, the solution for the field at each of the hydrophones is expressed in terms of these functions as follows:

$$G_{ip} = NA \left\{ \frac{B(x_i) - RC(x_i)}{B(x_s) - RC(x_s)} \right\}, \quad i = 1, 2, \quad (\text{A18})$$

where  $N$  is a simple scaling constant which cancels out of the coherence function.

This result is a generally valid expression for the field in the presence of the exponential profile and can be substituted directly into Eq. (A8) to obtain the coherence function in this type of environment. For the situation where the depth of the channel,  $h$ , is such that  $h/d \ll 1$ , the exponential profile is essentially linear throughout the water column. This is the

case for those downward refracting profiles encountered at the New Zealand site which were linear, or nearly so, with a gradient of approximately  $-0.42$  m/s per m corresponding to an  $e$ -folding depth of  $d=3638$  m. Since the channel depth at this location is only 50 m, it is clear that the exponential profile is indistinguishable from linear in this particular case. In fact, the solution given by Eqs. (A18) and (A8) is referred to in the text as the linear-profile, wind-noise model, although in reality it is rather more general in its application.

- <sup>1</sup>E. M. Arase and T. Arase, "Correlation of ambient sea noise," J. Acoust. Soc. Am. **40**, 205–210 (1965).
- <sup>2</sup>T. Arase and E. M. Arase, "Deep-sea ambient-noise statistics," J. Acoust. Soc. Am. **44**, 1679–1684 (1968).
- <sup>3</sup>W. S. Liggett, Jr. and M. J. Jacobson, "Covariance of surface-generated noise in a deep ocean," J. Acoust. Soc. Am. **38**, 303–312 (1965).
- <sup>4</sup>W. S. Liggett, Jr. and M. J. Jacobson, "Noise covariance and vertical directivity in a deep ocean," J. Acoust. Soc. Am. **39**, 280–288 (1966).
- <sup>5</sup>B. F. Cron, B. C. Hassell, and F. J. Keltonic, "Comparison of theoretical and experimental values of spatial correlation," J. Acoust. Soc. Am. **37**, 523–529 (1965).
- <sup>6</sup>R. J. Urlick, "Correlative properties of ambient noise at Bermuda," J. Acoust. Soc. Am. **40**, 1108–1111 (1966).
- <sup>7</sup>P. Rudnick and E. D. Squier, "Fluctuations and directionality in ambient sea noise," J. Acoust. Soc. Am. **41**, 1347–1351 (1967).
- <sup>8</sup>P. Rudnick, V. C. Anderson, and B. A. Becken, "Directional distribution of ambient sea noise," J. Br. Inst. Radio Eng., 441–444 (May 1963).
- <sup>9</sup>H. M. Linnette and R. J. Thompson, "Directivity study of the noise field in the ocean, employing a correlative dipole," J. Acoust. Soc. Am. **36**, 1788–1794 (1964).
- <sup>10</sup>C. L. Pekeris, "Theory of propagation of explosive sound in shallow water," in *Geological Society of America Memoir 27: Propagation of Sound in the Ocean* (Geological Society of America, New York, 1948), pp. 1–117.
- <sup>11</sup>N. M. Carbone, "Inverting for Geoacoustic Seabed Parameters using Ambient Noise," Ph.D. thesis, Scripps Institution of Oceanography, University of California, pp. 1–246, 1996.
- <sup>12</sup>A. S. Burgess and D. J. Kewley, "Wind-generated surface noise source levels in deep water east of Australia," J. Acoust. Soc. Am. **83**, 201–210 (1983).
- <sup>13</sup>D. H. Cato, "Ambient sea noise in waters near Australia," J. Acoust. Soc. Am. **60**, 320–328 (1976).
- <sup>14</sup>M. J. Buckingham and S. A. S. Jones, "A new shallow-ocean technique for determining the critical angle of the seabed from the vertical directionality of the ambient noise in the water column," J. Acoust. Soc. Am. **81**, 938–946 (1987).
- <sup>15</sup>M. J. Buckingham, "A theoretical model of ambient noise in a low-loss, shallow water channel," J. Acoust. Soc. Am. **67**, 1186–1192 (1980).
- <sup>16</sup>H. Cox, "Spatial correlation in arbitrary noise fields with application to ambient sea noise," J. Acoust. Soc. Am. **54**, 1289–1301 (1973).
- <sup>17</sup>I. S. Gradshteyn and I. M. Ryzhik, *Tables of Integrals, Series, and Products* (Academic, New York, 1980), 1160 pp.
- <sup>18</sup>B. F. Cron and C. H. Sherman, "Spatial correlation functions for various noise models," J. Acoust. Soc. Am. **34**, 1732–1736 (1962).
- <sup>19</sup>B. F. Cron and C. H. Sherman, "Spatial correlation functions for various noise models," J. Acoust. Soc. Am. **38**, 885 (1965).
- <sup>20</sup>E. L. Hamilton, "Compressional wave attenuation in marine sediments," Geophysics **37**, 620–646 (1972).
- <sup>21</sup>M. J. Buckingham, "Theory of acoustic attenuation, dispersion and pulse propagation in granular materials including marine sediments," J. Acoust. Soc. Am. (in press).
- <sup>22</sup>M. J. Buckingham, "Theory of compressional and shear waves in fluid-like marine sediments," J. Acoust. Soc. Am. (in press).
- <sup>23</sup>M. J. Buckingham, "Theory of the interface wave in a marine sediment," J. Acoust. Soc. Am. (submitted).
- <sup>24</sup>C. A. Nittrouer and J. H. Kravitz, "Integrated continental margin research to benefit ocean and earth sciences," Eos, Transactions, American Geophysical Union **76**, 121, 124, 126 (1995).
- <sup>25</sup>M. J. Buckingham and N. M. Carbone, "Source depth and the spatial coherence of ambient noise in the ocean," J. Acoust. Soc. Am. (in press).
- <sup>26</sup>S. R. Ferguson, "The velocity structure of the sea bed and basement rocks between Leigh and Mokohinau," M.S. thesis, University of Auckland, 1974.
- <sup>27</sup>C. T. Tindle, K. M. Guthrie, G. E. J. Bold, M. D. Johns, K. O. Dixon, and T. G. Birdsall, "Measurements of the frequency dependence of normal modes," J. Acoust. Soc. Am. **64**, 1178–1185 (1978).
- <sup>28</sup>D. H. Cato and M. J. Bell, "Ultrasonic ambient noise in Australian shallow waters at frequencies up to 200 kHz," Technical Report No. MRL-TR-91-23, DSTO Materials Research Laboratory, Sydney, Australia (1992).
- <sup>29</sup>W. A. Kuperman and F. Ingenito, "Spatial correlation of surface generated noise in a stratified ocean," J. Acoust. Soc. Am. **67**, 1988–1996 (1980).
- <sup>30</sup>M. J. Buckingham, *Noise in Electronic Devices and Systems*, Ellis Horwood Series in Electrical and Electronic Engineering (Ellis Horwood, Chichester, 1983), pp. 1–372.

# Nonlinear tomographic inversion by using Wentzel–Kramers–Brillouin modal condition

E. C. Shang, Y. Y. Wang, and A. G. Voronovich

Cooperative Institute for Research in Environmental Sciences, University of Colorado/NOAA,  
Environmental Technology Laboratory, Boulder, Colorado 80303-3328

(Received 11 August 1996; revised 7 April 1997; accepted 1 September 1997)

In the horizontal refraction tomography (HRT) scheme [A. G. Voronovich and E. C. Shang, *J. Acoust. Soc. Am.* **98**, 2708–2716 (1995)], the 3-D tomographic inversion is performed in two stages: (1) retrieving the modal wave numbers  $k_m(x,y)$  in the horizontal plane, and (2) reconstructing the vertical sound-speed profile (SSP) at each node of the horizontal plane based on a set of retrieved modal wave numbers  $k_m(x,y)$ . Usually, a nonlinear approach must be considered for the 1-D vertical inversion of the second stage. In this paper, a nonlinear inversion method based on the WKB modal condition is proposed. Using the WKB modal condition has the following advantages: (a) it is efficient because the data  $k_m(x,y)$  can be matched directly to the SSP without a model-based replica calculation; (b) it works even when just a few modes are available; and (c) the error of the inversion can be estimated analytically. Some results of the simulation to verify the concept are presented. © 1997 Acoustical Society of America. [S0001-4966(97)04512-8]

PACS numbers: 43.30.Pc, 43.30.Qd [JHM]

## INTRODUCTION

The applicability of the standard linear inversion method of reconstructing the mesoscale variabilities is quite limited because the assumption that modal functions do not change significantly is not valid for many cases.<sup>1,2</sup> The matched-field processing (MFP) approach<sup>3</sup> can solve this problem, but it could be very time consuming if a 3-D tomographic inversion is considered. Recently, horizontal refraction tomography (HRT) has been proposed,<sup>4,5</sup> in which the 3D tomographic inversion is performed in two stages. At the first stage, modal wave numbers  $k_m(x,y)$  in the horizontal plane are retrieved from the measurement of a horizontal refraction angle of the horizontal modal rays. As the corresponding rays in the horizontal plane are almost straight lines (with great accuracy), the 2-D reconstruction of  $k_m(x,y)$  can be accomplished with a linear procedure. The second stage is to retrieve the vertical sound-speed profile (SSP) at each node of the horizontal plane where data  $k_m(x,y)$  can be used (see Fig. 1). Usually, a nonlinear approach should be considered for this 1-D vertical inversion; for example, the invariant imbedding method has been proposed.<sup>5</sup> In this paper, an inversion method based on the WKB modal dispersion condition is proposed, which has the following advantages: (a) it is very efficient because the data  $k_m(x,y)$  can be matched directly to the SSP without a model-based replica calculation; (b) it works even if just a few modes (say, three modes) are available; and (c) the error of the inversion can be estimated analytically. Numerical simulations on a mesoscale eddy in the deep ocean are presented.

## I. INVERSION USING THE WKB MODAL CONDITION

Now the problem is how to use data  $k_m(x,y)$  to reconstruct the vertical SSP at point  $(x,y)$ . The horizontal modal wave number  $k_m$  has been used for retrieving the SSP throughout the Abel transformation.<sup>6,7</sup> Numerically, we can

solve this problem by using the MFP approach in which the best estimation of the SSP is given by minimizing the following cost function:

$$F_c(\text{ssp}) = \sum_m [k_m(x,y) - k_m(\{\text{ssp}\})]^2, \quad (1)$$

where  $k_m(\{\text{ssp}\})$  is the replica calculated based on a model with the given  $\{\text{ssp}\}$  described by a set of parameters. However, the drawbacks of this procedure are that it is not efficient and it is model dependent. Here we propose to use the WKB modal dispersion condition to perform the SSP reconstruction. As is well known, the WKB dispersion condition for guided modes in the deep ocean is<sup>8</sup>

$$\int_{Z_l}^{Z_u} \sqrt{k^2(z;x,y) - k_m^2(x,y)} dz = (m - \frac{1}{2})\pi, \quad (2)$$

where  $Z_l$  and  $Z_u$  are the lower and upper turning points, and

$$k(z;x,y) = \frac{\omega_0}{c(z;x,y)}, \quad (3)$$

where  $\omega_0$  is the acoustic circular frequency, and  $c(z;x,y)$  is the SSP at point  $(x,y)$ ;  $(x,y)$  are parameters in the text that follows. We write the  $c(z;x,y)$  as a sum of the background  $c_0(z)$  plus a perturbation  $\Delta c(z;x,y)$ :

$$c(z;x,y) = c_0(z) + \Delta c(z;x,y). \quad (4)$$

The background part,  $c_0(z)$ , is assumed known, and the unknown part,  $\Delta c(z;x,y)$ , can be conveniently represented by an expansion of the empirical orthogonal functions (EOF).<sup>9</sup>

$$\Delta c(z;x,y) = \sum_j a_j(x,y) F_j(z), \quad (5)$$

where  $F_j(z)$  is the  $j$ th order of the EOF and is known when archival data are available or some *in situ* samples of SSP

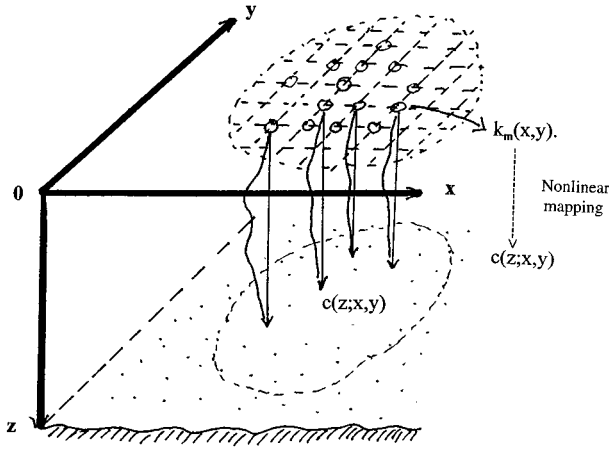


FIG. 1. Reconstructing the SSP at each node by using modal horizontal wave number data  $k_m(x, y)$ .

data are available. The EOFs are the most efficient basis functions for the expansion of the SSP. In many cases, a high degree of accuracy can be achieved with only a few EOFs. Thus, there are only a few unknown parameters  $\{a_j\}$  to be determined. From Eqs. (3) and (4), we have

$$k^2(z; x, y) = \left[ \frac{\omega_0}{c_0(z) + \Delta c(z; x, y)} \right]^2 = k_0^2(z) - \left[ \frac{2\omega_0^2}{c_0^3(z)} \right] \sum_j a_j F_j(z). \quad (6)$$

Substituting Eq. (6) into Eq. (2), we get

$$\int_{Z_l}^{Z_u} \sqrt{k_0^2(z) - \left[ \frac{2\omega_0^2}{c_0^3(z)} \right] \sum_j a_j F_j(z) - k_m^2(x, y)} dz = (m - \frac{1}{2})\pi. \quad (7)$$

We define

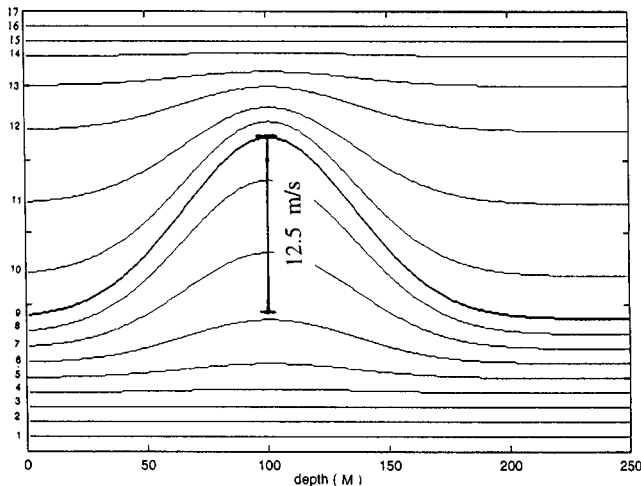


FIG. 2. The SSPs for different sections of the asymmetric Gaussian eddy. The range interval is 40 km.

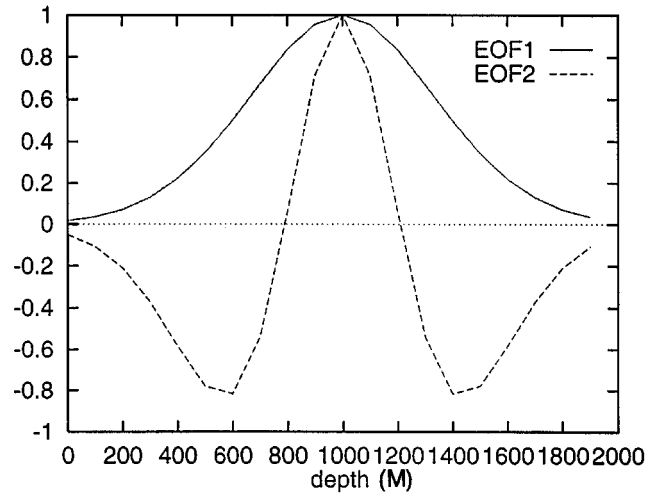


FIG. 3. The first two EOFs of the asymmetric Gaussian eddy.

$$S_m(\{a_j\}) = \int_{Z_l}^{Z_u} \sqrt{k_0^2(z) - \left[ \frac{2\omega_0^2}{c_0^3(z)} \right] \sum_j a_j F_j(z) - k_m^2(x, y)} dz. \quad (8)$$

Then, the reconstruction problem reduces to the determination of the set of parameters  $\{a_j\}$  that minimizes the following cost function:

$$F_c(\{a_j\}) = \sum_m [S_m(\{a_j\}) - (m - \frac{1}{2})\pi]^2. \quad (9)$$

## II. LINEARIZED FORMULA

For a weak enough perturbation, Eq. (2) can be linearized. Let

$$k^2(z; x, y) = k_0^2(z) + \Delta k_0^2(z; x, y) \quad (10)$$

and

$$k_m^2(x, y) = \{k_{m0} + \Delta k_m(x, y)\}^2 = k_{m0}^2 + 2k_{m0}\Delta k_m(x, y), \quad (11)$$

where  $k_{m0}$  satisfies the unperturbed WKB condition

$$\int_{Z_l}^{Z_u} \sqrt{k_0^2(z) - k_{m0}^2} dz = (m - \frac{1}{2})\pi. \quad (12)$$

Substituting Eqs. (10) and (11) into Eq. (2), we get

TABLE I. The WKB linear kernel matrix  $B_{mj}$ .

$m$	$j=1$	$j=2$
1	-1.2584009E-04	-5.9656177E-05
2	-1.2059656E-04	-3.9268714E-05
3	-1.1509480E-04	-2.2358547E-05
4	-1.0868657E-04	-7.6778006E-06
5	-1.0146108E-04	3.1919542E-06
6	-9.6470598E-05	9.5016912E-06
7	-9.2515773E-05	1.4024733E-05
8	-8.8249995E-05	1.7166711E-05
9	-8.4333180E-05	1.9293228E-05
10	-8.0494108E-05	2.0355850E-05

TABLE II. Simulated data  $k_m(x,y)$  for different sections, ir, of the ‘‘asymmetric’’ cold eddy (modes 1–10 at  $f=50$  Hz, DC = -12.5 m/s).

ir	Mode wave number									
	m1	m2	m3	m4	m5	m6	m7	m8	m9	m10
1	0.209363	0.209214	0.209066	0.208920	0.208775	0.208631	0.208489	0.208348	0.208209	0.208071
2	0.209364	0.209214	0.209066	0.208920	0.208775	0.208631	0.208489	0.208349	0.208209	0.208071
3	0.209367	0.209216	0.209068	0.208921	0.208776	0.208632	0.208490	0.208349	0.208210	0.208072
4	0.209387	0.209227	0.209075	0.208927	0.208781	0.208637	0.208495	0.208354	0.208214	0.208075
5	0.209480	0.209301	0.209133	0.208974	0.208821	0.208672	0.208526	0.208382	0.208240	0.208100
6	0.209728	0.209495	0.209284	0.209094	0.208920	0.208757	0.208601	0.208450	0.208303	0.208159
7	0.210193	0.209879	0.209595	0.209342	0.209118	0.208920	0.208742	0.208576	0.208417	0.208264
8	0.210795	0.210522	0.210259	0.210005	0.209761	0.209527	0.209303	0.209089	0.208885	0.208690
9	0.211048	0.210759	0.210479	0.210210	0.209951	0.209702	0.209464	0.209236	0.209019	0.208812
10	0.210795	0.210522	0.210259	0.210005	0.209761	0.209527	0.209303	0.209089	0.208885	0.208690
11	0.210243	0.210010	0.209786	0.209569	0.209361	0.209161	0.208969	0.208785	0.208608	0.208439
12	0.209755	0.209564	0.209379	0.209200	0.209026	0.208858	0.208695	0.208536	0.208382	0.208232
13	0.209490	0.209326	0.209166	0.209009	0.208854	0.208703	0.208555	0.208409	0.208265	0.208123
14	0.209393	0.209240	0.209089	0.208940	0.208793	0.208648	0.208505	0.208363	0.208222	0.208083
15	0.209368	0.209218	0.209070	0.208923	0.208778	0.208634	0.208492	0.208351	0.208211	0.208073
16	0.209364	0.209214	0.209066	0.208920	0.208775	0.208632	0.208489	0.208349	0.208209	0.208071
17	0.209363	0.209214	0.209066	0.208920	0.208775	0.208631	0.208489	0.208348	0.208209	0.208071

$$\int_{z_l}^{z_u} \sqrt{k_0^2(z) + \Delta k_0^2(z;x,y) - k_{m0}^2 - 2k_{m0}\Delta k_m(x,y)} dz = (m - \frac{1}{2})\pi, \quad (13)$$

$$\Delta k_m^{(L)}(x,y) = \frac{\int W_m(z)\Delta k_0^2(z;x,y) dz}{2k_{m0}\int W_m(z) dz}, \quad (16)$$

(13) where the weighting function  $W_m(z)$  is defined by

By linearizing the integrand of Eq. (13), we have

$$\int_{z_l}^{z_u} \sqrt{k_0^2(z) - k_{m0}^2} \left\{ 1 + \frac{(\Delta k_0^2 - 2k_{m0}\Delta k_m)}{2[k_0^2(z) - k_{m0}^2]} \right\} dz = (m - \frac{1}{2})\pi. \quad (14)$$

Taking into account Eq. (12), Eq. (14) becomes

$$\int_{z_l}^{z_u} \frac{\Delta k_0^2(z;x,y)}{\sqrt{k_0^2(z) - k_{m0}^2}} dz = \int_{z_l}^{z_u} \frac{2\Delta k_m(x,y)k_{m0}}{\sqrt{k_0^2(z) - k_{m0}^2}} dz. \quad (15)$$

Then, the linear perturbation of the modal wave number is given by

$$W_m(z) = \frac{1}{\sqrt{k_0^2(z) - k_{m0}^2}}. \quad (17)$$

This linear perturbation of the modal wave number given by Eq. (16) will be converted to the result given by the general perturbation theory<sup>10</sup> if we take the normalized eigenfunction  $\psi_m^2(z)$  as the weighting function instead of Eq. (17).

From Eqs. (6) and (10), we know that

$$\Delta k_0^2(z;x,y) = - \left[ \frac{2\omega_0^2}{c_0^3(z)} \right] \sum_j a_j F_j(z). \quad (18)$$

TABLE III. Simulated data  $k_m(x,y)$  for different sections, ir, of the ‘‘asymmetric’’ warm eddy (modes 1–10 at  $f=50$  Hz, DC = +12.5 m/s).

ir	Mode wave number									
	m1	m2	m3	m4	m5	m6	m7	m8	m9	m10
1	0.209363	0.209214	0.209066	0.208920	0.208775	0.208631	0.208489	0.208348	0.208209	0.208071
2	0.209363	0.209213	0.209066	0.208919	0.208775	0.208631	0.208489	0.208348	0.208209	0.208071
3	0.209359	0.209211	0.209064	0.208918	0.208773	0.208630	0.208488	0.208348	0.208208	0.208070
4	0.209340	0.209201	0.209056	0.208912	0.208768	0.208625	0.208484	0.208343	0.208204	0.208067
5	0.209250	0.209132	0.209002	0.208866	0.208729	0.208591	0.208452	0.208315	0.208178	0.208042
6	0.209046	0.208979	0.208875	0.208758	0.208634	0.208506	0.208376	0.208244	0.208113	0.207981
7	0.208879	0.208705	0.208679	0.208524	0.208455	0.208341	0.208227	0.208110	0.207988	0.207865
8	0.208405	0.208239	0.208088	0.208060	0.207961	0.207890	0.207808	0.207713	0.207614	0.207511
9	0.208346	0.208168	0.208002	0.207903	0.207849	0.207728	0.207688	0.207593	0.207504	0.207409
10	0.208405	0.208239	0.208088	0.208060	0.207961	0.207890	0.207808	0.207713	0.207614	0.207511
11	0.208603	0.208511	0.208459	0.208371	0.208277	0.208175	0.208067	0.207956	0.207842	0.207726
12	0.208981	0.208885	0.208777	0.208663	0.208543	0.208421	0.208296	0.208170	0.208043	0.207915
13	0.209237	0.209103	0.208969	0.208833	0.208697	0.208561	0.208425	0.208289	0.208154	0.208020
14	0.209333	0.209187	0.209043	0.208899	0.208756	0.208614	0.208474	0.208334	0.208196	0.208059
15	0.209358	0.209209	0.209062	0.208916	0.208771	0.208628	0.208486	0.208346	0.208207	0.208069
16	0.209363	0.209213	0.209065	0.208919	0.208774	0.208631	0.208489	0.208348	0.208209	0.208071
17	0.209363	0.209214	0.209066	0.208919	0.208775	0.208631	0.208489	0.208348	0.208209	0.208071

TABLE IV. The reconstruction results for different cases.

Case No.	Eddy	SSP No.	Formula	Data $k_m(r)$	Number of mode	Result		Illustration
						$a_1$	$a_2$	
1	cold	$r_9$	NL Eq. (9)	noise free	1,2	-13.0	0.3	Fig. 4
2	cold	$r_9$	NL Eq. (9)	noise free	1,2,...,9,10	-12.9	0.2	Fig. 4
3	cold	$r_9$	NL Eq. (9)	$n_m = +0.0001$	1,2	-13.9	0.5	Fig. 5
4	cold	$r_9$	NL Eq. (9)	$n_m = +0.0001$	1,2,3,4,5	-13.9	0.5	Fig. 5
5	cold	$r_9$	NL Eq. (9)	$n_m = -0.0001$	1,2,3	-12.1	0.1	Fig. 5
6	cold	$r_{11}$	NL Eq. (9)	noise free	1,2,3	-6.8	0.1	Fig. 6
7	cold	$r_7$	NL Eq. (9)	noise free	1,2,3	-5.0	-1.7	Fig. 7
8	warm	$r_9$	NL Eq. (9)	noise free	1,2,3	13.2	-0.1	Fig. 8
9	warm	$r_9$	NL Eq. (9)	noise free	6,7,8,9,10	12.8	-0.4	Fig. 8
10	warm	$r_9$	NL Eq. (9)	$n_m = +0.0001$	8,9,10	11.4	1.2	Fig. 9
11	warm	$r_9$	NL Eq. (9)	$n_m = +0.0001$	1,2,...,9,10	11.4	0.3	Fig. 9
12	warm	$r_9$	NL Eq. (9)	$n_m = -0.0001$	1,2,...,9,10	14.1	-0.9	Fig. 9
13	warm	$r_{11}$	NL Eq. (9)	noise free	1,2	6.8	0.0	Fig. 10
14	warm	$r_{11}$	NL Eq. (9)	noise free	1,2,...,9,10	6.8	0.0	Fig. 10
15	warm	$r_7$	NL Eq. (9)	noise free	1,2,3,4,5	5.0	1.8	Fig. 11
16	warm	$r_7$	L Eq. (20)	noise free	1,10	3.0	1.8	Fig. 12
17	warm	$r_6$	L Eq. (20)	noise free	1,10	1.6	1.9	Fig. 13

Substituting Eq. (18) into Eq. (16), we get

$$\Delta k_m^{(L)}(x,y) = \frac{\int W_m(z) \left[ \frac{-2\omega_0^2}{c_0^3(z)} \right] \sum a_j F_j(z) dz}{2k_{m0} \int W_m(z) dz}. \quad (19)$$

Now, if we use  $\{k_m(x,y) - k_{m0}\}$  as data and put it on the left-hand side of Eq. (19), then we will get a set of linear equations for solving the unknown parameters  $\{a_j\}$ :

$$\{k_m(x,y) - k_{m0}\} = \sum_j B_{mj} a_j, \quad (20)$$

where the matrix is given by

$$B_{mj} = \left( \frac{-\omega_0^2}{k_{m0}} \right) \frac{\int W_m(z) (1/c_0^3(z)) F_j(z) dz}{\int W_m(z) dz}. \quad (21)$$

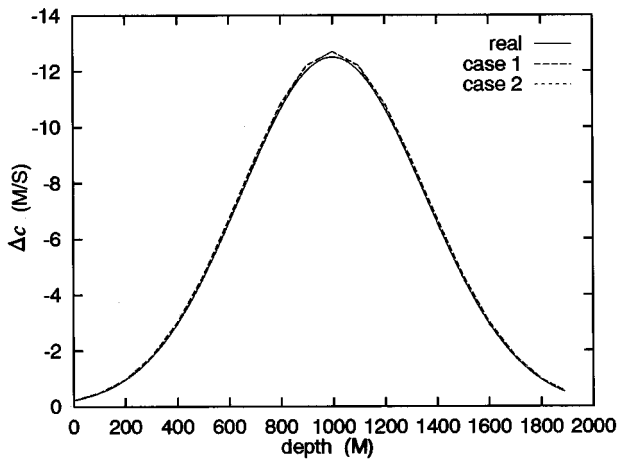


FIG. 4. The reconstructed cold eddy at eddy center (DC) = -12.5 (m/s) with noise free data. Case 1: modes 1, 2,  $a_1 = -13.0$  and  $a_2 = 0.3$ . Case 2: modes 1-10,  $a_1 = -12.9$  and  $a_2 = 0.2$ .

### III. ERROR ANALYSIS

One of the advantages of inversion by using the WKB condition is that the error can be estimated analytically. From Eq. (7), we have

$$\int_{z_l}^{z_u} \sqrt{k_0^2(z) - \frac{2\omega_0^2}{c_0^3(z)}} \Delta c(z;x,y) - k_m^2(x,y) dz = (m - \frac{1}{2})\pi. \quad (22)$$

If the data is contaminated by noise, then

$$k_m = k_m^R + n_m, \quad n_m \ll k_m, \quad (23)$$

where  $k_m^R$  is the true value and  $n_m$  is noise. The noise here is understood as errors in retrieving  $k_m(x,y)$ , resulting from the first stage of inversion.<sup>4,5</sup> Substituting Eq. (23) into Eq. (22), we get

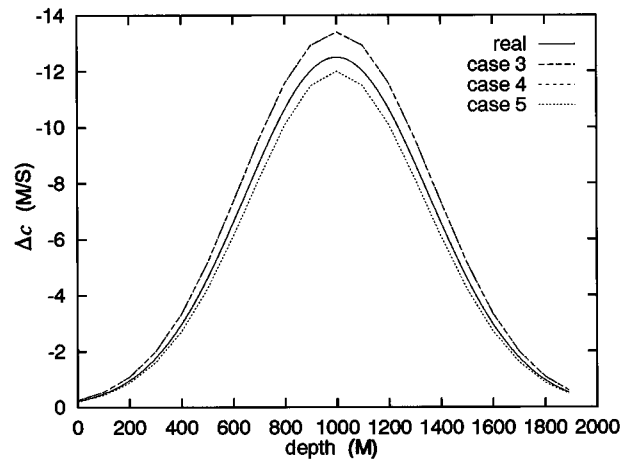


FIG. 5. The reconstructed cold eddy at eddy center (DC) = -12.5 (m/s), data with noise. Case 3: modes 1, 2,  $n_m = +0.0001$ ;  $a_1 = -13.9$  and  $a_2 = 0.5$ . Case 4: modes 1-5,  $n_m = +0.0001$ ;  $a_1 = -13.9$  and  $a_2 = 0.5$ . Case 5: modes 1, 2, 3,  $n_m = -0.0001$ ;  $a_1 = -12.1$  and  $a_2 = 0.1$ .



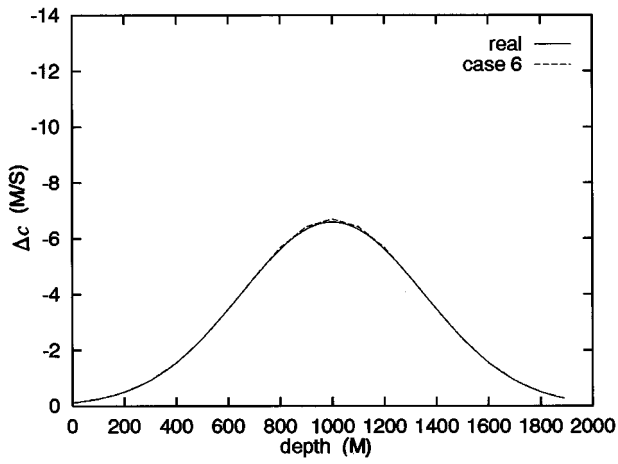


FIG. 6. The reconstructed cold eddy at  $r_{11}$  (wide side) with noise-free data. Case 6: modes 1, 2, 3,  $a_1 = -6.8$  and  $a_2 = 0.1$ .

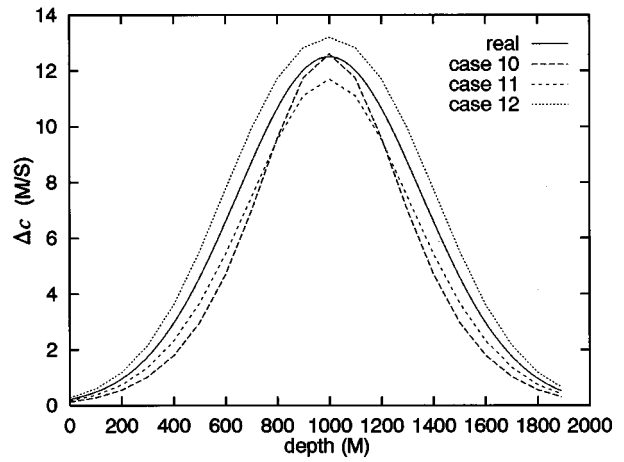


FIG. 9. The reconstructed warm eddy at eddy center (DC)=+12.5 (m/s), data with noise. Case 10: modes 8, 9, 10,  $n_m = +0.0001$ ;  $a_1 = 11.4$  and  $a_2 = 1.2$ . Case 11: modes 1-10,  $n_m = +0.0001$ ;  $a_1 = 11.4$  and  $a_2 = 0.3$ . Case 12: modes 1-10,  $n_m = -0.0001$ ;  $a_1 = 14.1$  and  $a_2 = -0.9$ .

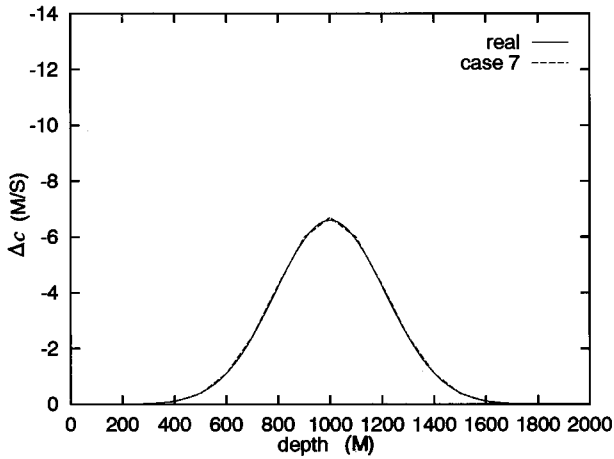


FIG. 7. The reconstructed cold eddy at  $r_7$  (narrow side) with noise-free data. Case 7: modes 1, 2, 3,  $a_1 = -5.0$  and  $a_2 = -1.7$ .

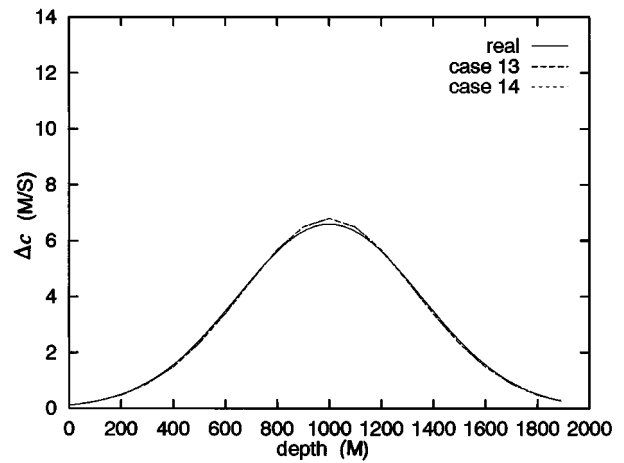


FIG. 10. The reconstructed warm eddy at  $r_{11}$  (wide side) with noise-free data. Case 13: modes 1, 2,  $a_1 = 6.8$  and  $a_2 = 0.0$ . Case 14: modes 1-10,  $a_1 = 6.8$  and  $a_2 = 0.0$ .

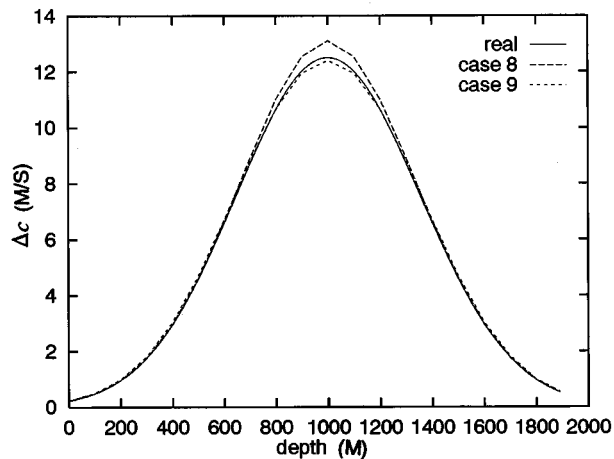


FIG. 8. The reconstructed warm eddy at eddy center (DC)=+12.5 (m/s) with noise-free data. Case 8: modes 1, 2, 3,  $a_1 = 13.2$  and  $a_2 = -0.1$ . Case 9: modes 6-10,  $a_1 = 12.8$  and  $a_2 = -0.4$ .

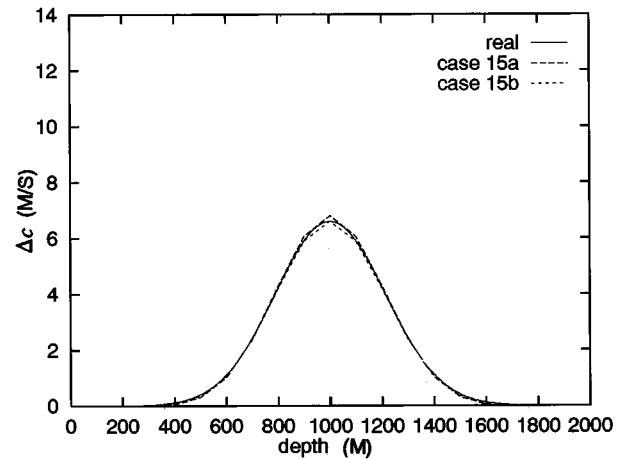


FIG. 11. The reconstructed warm eddy at  $r_7$  (narrow side) with noise-free data. Case 15a: modes 1-5,  $a_1 = 5.0$  and  $a_2 = 1.8$ . Case 15b: modes 1-5,  $a_1 = 4.9$  and  $a_2 = 1.7$ .

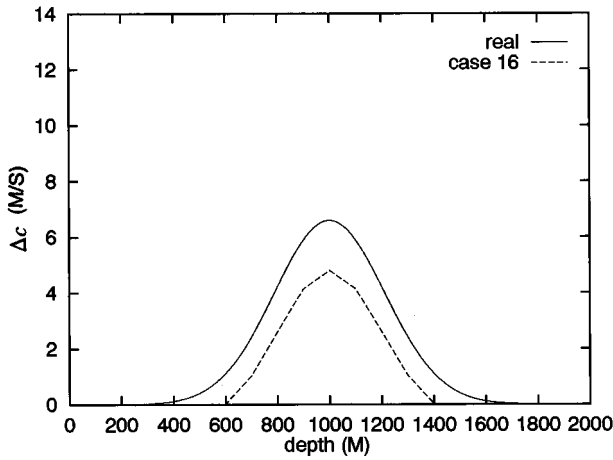


FIG. 12. The linear reconstruction of warm eddy at  $r_7$  (narrow side) with noise-free data. Case 16: mode 1, 10,  $a_1=3.0$  and  $a_2=1.8$ .

$$\int_{z_l}^{z_u} \sqrt{k_0^2(z) - \frac{2\omega_0^2}{c_0^3(z)} (\Delta c)^R - (k_m^R)^2 - 2k_m^R n_m} dz = (m - \frac{1}{2})\pi, \quad (24)$$

or, by rewriting,

$$\int_{z_l}^{z_u} \sqrt{k_0^2(z) - \frac{2\omega_0^2}{c_0^3(z)} (\Delta c)^c - (k_m^R)^2} dz = (m - \frac{1}{2})\pi, \quad (25)$$

where  $(\Delta c)^c$  is given by

$$(\Delta c)^c = (\Delta c)^R + \left(\frac{c_0^2}{\omega_0}\right) \left(\frac{k_m}{k_0}\right) n_m = (\Delta c)^R + \left(\frac{c_0^2}{\omega_0}\right) n_m. \quad (26)$$

Equation (25) indicates that by using the contaminated data, the reconstructed SSP is  $(\Delta c)^c$  instead of the true SSP,  $(\Delta c)^R$ . The reconstruction error induced by noise is

$$\varepsilon = (\Delta c)^c - (\Delta c)^R = \frac{c_0^2}{\omega_0} n_m \quad (27)$$

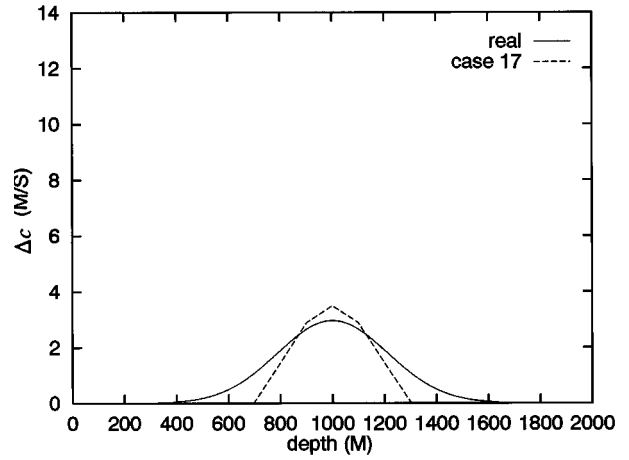


FIG. 13. The linear reconstruction of warm eddy at  $r_6$  (narrow side) with noise-free data. Case 17: mode 1, 10,  $a_1=1.6$  and  $a_2=1.9$ .

or

$$\frac{\varepsilon}{c_0} = \frac{n_m}{k_0}.$$

As an example, if we take  $n_m=10^{-4} \text{ m}^{-1}$ ,  $c_0=1500 \text{ m s}^{-1}$ , and  $f=50 \text{ Hz}$ , we get

$$\varepsilon = 0.7 \text{ m s}^{-1}.$$

## IV. NUMERICAL SOLUTIONS

### A. Ocean model

The ocean model is considered as a Munk's canonical profile<sup>11</sup> with a Gaussian eddy, and the EOFs corresponding to this eddy are also used.

(i) *Munk's canonical profile* as background:

$$c_0 = 1500\{1 + 0.0057[e^{-\eta} - (1 - \eta)]\}, \quad (28)$$

where  $\eta = 2(z - 1000)/1000$ .

(ii) *Gaussian eddy* (2D) (see Fig. 2):

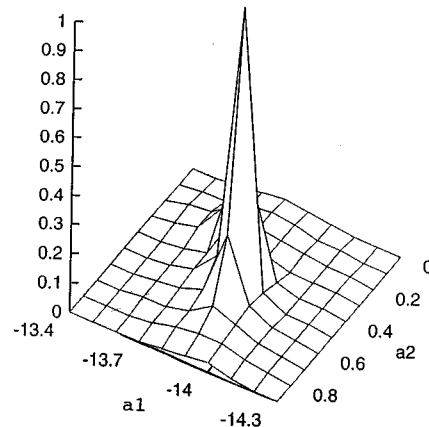
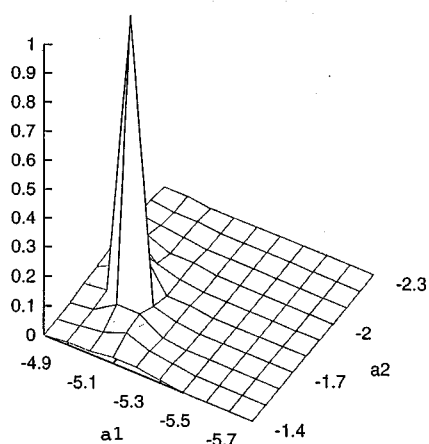


FIG. 14. Representative examples of ambiguity functions resulting from Eq. (9), least ambiguous results. (a) Case 4, cold eddy (center),  $n_m = +0.0001$  ( $m=1,2,3,4,5$ ). (b) Case 7, cold eddy (narrow side), noise-free ( $m=1,2,3$ ).

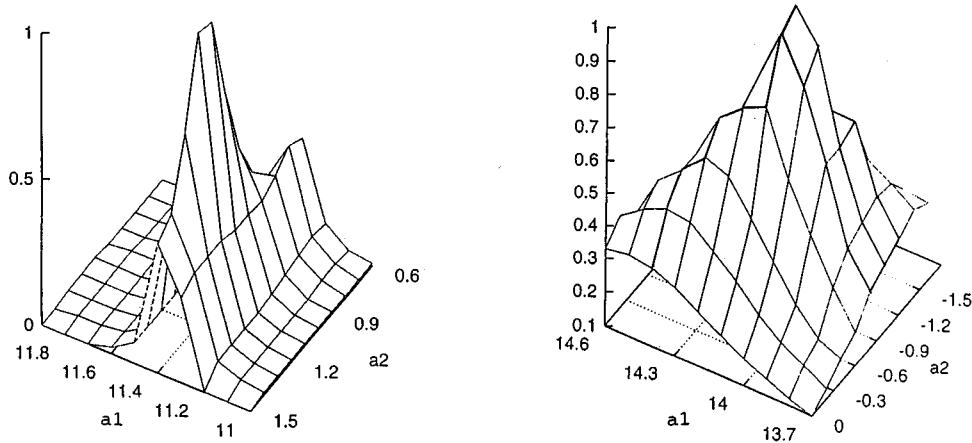


FIG. 15. Representative examples of ambiguity functions resulting from Eq. (9), most ambiguous results. (a). Case 10, warm eddy (center),  $n_m = +0.0001$  ( $m=8,9,10$ ). (b). Case 12, warm eddy (center),  $n_m = -0.0001$  ( $m$ =from 1 to 10).

$$\Delta c(z;r) = (\text{DC}) \exp \left\{ - \left[ \frac{r-r_9}{\text{DR}} \right]^2 - \left[ \frac{z-z_e}{\text{DZ}(r)} \right]^2 \right\}. \quad (29)$$

The eddy parameters are as follows:

$$(\text{DC}) = \pm 12.5 \text{ m s}^{-1}, \quad (\text{DR}) = 100 \text{ km},$$

$$r_9 = 320 \text{ km}, \quad z_e = 1000 \text{ m}.$$

Parameter (DZ) is range dependent and is given by

$$(\text{DZ}) = \begin{cases} 500 \text{ m}, & r \geq r_8, \quad r_8 = 280 \text{ km}, \\ 300 \text{ m}, & r_8 > r > r_5, \\ 200 \text{ m}, & r_5 \geq r, \quad r_5 = 160 \text{ km}. \end{cases}$$

(iii) The first two EOFs of this asymmetric Gaussian eddy are shown in Fig. 3. The first four eigenvalues are 182, 1.4,  $2.7 \times 10^{-4}$ , and  $7.4 \times 10^{-6}$ ; therefore, the first two EOFs dominate. The kernel matrix  $B_{mj}$  of the WKB linear inversion for 10 modes corresponding to these two EOFs is listed in Table I.

## B. Simulated data

Datasets of  $k_m(r)$  generated by KRAKEN<sup>12</sup> are listed in Tables II and III, for a cold and a warm eddy, respectively ( $m=1-10$ ;  $f=50$  Hz).

## C. Reconstruction results

The results of reconstruction are listed in Table IV and shown in Figs. 4–13. The ambiguities of the cost function for some cases are shown in Figs. 14 and 15 for the best and worst cases, respectively. For all the cases, the main peak offers the best estimation.

In principle, the necessary number of modes for getting a unique solution depends on the dimensions of parameter space  $\{a_j\}$ . Actually, Eq. (7) determines a surface in the parameter space  $\{a_j\}$  for each mode. In our 2-D case, Eq. (7) determines a curve in the  $(a_1, a_2)$  plane. In an ideal solution (with noise-free data), two modes will give a unique solution at the crossover point of the two corresponding lines. As an example, Fig. 16 illustrates the crossover point ( $a_1 = -12.9$  and  $a_2 = 0.2$ ) given by modes 1 and 8 for case 1.

## V. SUMMARY

- (1) The proposed inversion method is very efficient because there are no forward replica calculations as in the general MFP procedure. For a Gaussian cold eddy with a canonical profile, the first three modes give very good results.
- (2) On the other hand, for a warm eddy, higher modes give better results than lower modes (see Fig. 8, cases 8 and 9). The reason for this is most likely due to the double-channel effect; higher modes suffer less double-channel effect than lower modes.<sup>2</sup>
- (3) The noise impact illustrated by Figs. 5 and 9 is consistent (order of magnitude) with the theoretical analysis given by Eq. (27).
- (4) For this asymmetric Gaussian eddy, the first two EOFs dominate. The second EOF plays a more important role on the narrow side than the wide side (compare the coefficients  $a_2$  of case 13 with case 15).
- (5) The quality of the linear inversion is rather poor (see Fig.

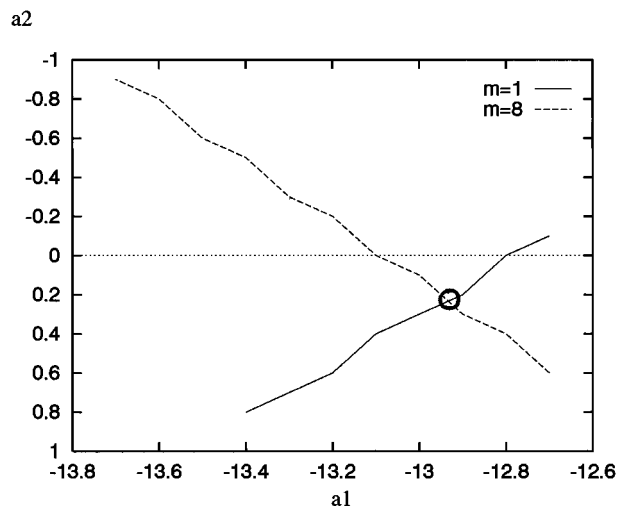


FIG. 16. The cross-over point given by the curves of modes 1 and 8, for case 1, cold eddy center:  $a_1 = -12.9$  and  $a_2 = 0.2$ .

12) compared with the nonlinear inversion (see Fig. 11) for a warm eddy at  $r_7$ .

## ACKNOWLEDGMENTS

This work was supported by the Office of Naval Research (ONR) and the National Oceanic and Atmospheric Administration (NOAA).

- <sup>1</sup>E. C. Shang and Y. Y. Wang, "The nonlinearity of modal travel time perturbation," in *Computational Acoustics*, edited by R. Lau, D. Lee, and A. Robinson (Elsevier Science, North-Holland, Amsterdam, 1993), Vol. 2, pp. 385–397.
- <sup>2</sup>E. C. Shang and Y. Y. Wang, "The impact of mesoscale oceanic structure on global-scale acoustic propagation," in *Theoretical and Computational Acoustics*, edited by D. Lee *et al.* (World Scientific, Singapore, 1996), pp. 409–431.
- <sup>3</sup>A. B. Baggeroer, W. Kuperman, and P. Mikhalevsky, "An overview of matched field methods in ocean acoustics," *IEEE J. Ocean Eng.* **18**, 401–424 (1993).

- <sup>4</sup>A. G. Voronovich and E. C. Shang, "A note on horizontal refraction-modal tomography," *J. Acoust. Soc. Am.* **98**, 2708–2716 (1995).
- <sup>5</sup>A. G. Voronovich and E. C. Shang, "Numerical simulations with horizontal-refraction-model tomography. Part I. Adiabatic propagation," *J. Acoust. Soc. Am.* **101**, 2636–2643 (1997).
- <sup>6</sup>K. D. Casey, "A modal/WKB inversion method for determining sound-speed profile in the ocean and ocean bottom," Ph.D. dissertation, MIT/Woods Hole Oceanographic Institute Joint Program, 1988.
- <sup>7</sup>R. M. Jones, E. C. Shang, and T. M. Georges, "Nonperturbation modal tomography inversion. Part 1. Theory," *J. Acoust. Soc. Am.* **94**, 2296–2302 (1993).
- <sup>8</sup>W. H. Munk, P. Worcester, and C. Wunsch, *Ocean Acoustic Tomography* (Cambridge U.P., Cambridge, 1995), Sec. 2.11, pp. 63–66.
- <sup>9</sup>A. Tolstoy, O. Diachok, and L. N. Frazer, "Acoustic tomography via matched field processing," *J. Acoust. Soc. Am.* **89**, 1119–1127 (1991).
- <sup>10</sup>E. C. Shang, "Ocean acoustic tomography based on adiabatic mode theory," *J. Acoust. Soc. Am.* **85**, 1531–1537 (1989).
- <sup>11</sup>W. H. Munk, "Sound channel in an exponential stratified ocean with application of SOFAR," *J. Acoust. Soc. Am.* **55**, 220–226 (1974).
- <sup>12</sup>M. Porter, "The KRAKEN normal mode program," SACLANT Memo. SM-245, 1991.

# Adaptive beamforming against reverberation for a three-sensor array

Joseph N. Maksym and Michael Sandys-Wunsch

*Defence Research Establishment Atlantic, 9 Grove St., Dartmouth, Nova Scotia B2Y 3Z7, Canada*

(Received 16 September 1996; revised 11 August 1997; accepted 22 August 1997)

Two algorithms for beamforming and bearing estimation of echoes from an active sonar transmission in a strongly reverberant bistatic environment are described. The receiving array consists of a single omnidirectional sensor and two collocated orthogonal dipole sensors, and is deployed in a bistatic configuration. Both beamforming algorithms are based on minimum-variance techniques. The first algorithm matches the pattern of the minimum-variance beamformed data with that expected from an impulse at a known bearing. The second algorithm reforms the sensor data from the minimum-variance beam response. Fixed-coefficient limaçon beamforming is then applied to estimate the beam power map with reduced reverberation. The detection performance of both techniques is evaluated by injection of a synthetic target echo into experimental reverberation data. The results suggest an enhanced array gain against reverberation of the order of 3 dB for reasonable values of signal strength and probability of false alarm, compared to a direct application of fixed-coefficient limaçon beamforming. The root-mean-squared bearing error for both techniques is reduced significantly, when compared to the limaçon beamformer, by factors varying from 2 to 5. [S0001-4966(97)03612-6]

PACS numbers: 43.30.Vh, 43.30.Bp, 43.30.Cq [SAC-B]

## INTRODUCTION

The problem of particular interest in this paper is the detection and bearing estimation of target echoes in strongly anisotropic reverberation fields characteristic of bistatic active sonars operating in shallow water.<sup>1-3</sup> Although bistatic reverberation models capable of predicting the average background in bistatic active sonar are now highly developed,<sup>4</sup> such models depend on knowledge of environmental parameters, and may not always provide the accuracy required for optimum beamforming and the setting of detection thresholds. As a consequence, there is much interest in data-adaptive methods that can estimate the reverberation background from the sensor signals themselves.

This work is an examination of two adaptive beamforming techniques in a reverberation-limited active sonar environment for a receiver consisting of an omnidirectional sensor and two collocated orthogonal dipole sensors. Both techniques are based on the minimum variance distortionless response (MVDR) beamformer.<sup>5</sup> The first is the pattern correlator (PATCOR) processor, which is a three-step process involving adaptive beamforming, response identification, and correlation. The second is the directional interference limited beamspace energy reformation technique (DILBERT) transform, a process for calculating a transformation matrix that reforms the sensor time series into equivalent time series with reduced directional interference. Of interest is the receiver performance for the detection of an echo in a given direction, as well as the root-mean-squared (rms) error of the estimate of the associated bearing.

The current literature in adaptive beamforming includes application of MVDR to topics as diverse as sonar performance prediction,<sup>6</sup> consideration of the detection process in a structured noise background,<sup>7</sup> and the general treatment of rank reduction and signal enhancement.<sup>8,9</sup> Here, we wish to

apply some of these concepts to the bistatic reverberation scenario illustrated schematically in Fig. 1 for a three-sensor receiving array consisting of an omnidirectional sensor and two orthogonal dipoles. With this configuration, apart from a possible signal arrival directly along the transmitter-receiver axis, reverberation at any particular instant during a ping arises from reflecting points on an ellipsoid that has the transmitter and receiver as the two foci. This fact, along with the strength and distribution of reflections from points on the ellipsoid, determines the directional character of bistatic sonar reverberation. Directionality of the reverberation field is important for the performance of the adaptive beamformers introduced in this paper. Bathymetric features complicate this reverberation distribution, but will not be considered in this work. It is convenient for analysis to estimate the direction of the transmitter-receiver axis, and to measure bearings relative to this reference axis as shown schematically in Fig. 2. One can then examine detection performance using data measured at receivers placed in a number of different locations by injecting signals at a known bearing relative to this reference axis.

To evaluate the two beamformers an experimental reverberation data set was recorded with receivers located over a wide area. A large number of transmissions, involving several waveforms over a wide band, were measured on each receiver. The transmitter-receiver geometries were diverse, ensuring that a variety of reverberation fields were included. Synthetic signals were then added at known values of bearing and signal-to-noise ratio (SNR). Receiver-operating characteristic (ROC) and rms bearing-estimation errors were directly measured with this data set. The fixed-coefficient limaçon beamformer described below was used as a benchmark both for the detection and for the bearing estimation problem.

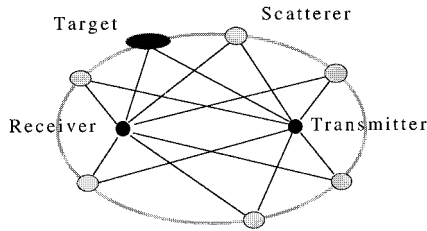


FIG. 1. Bistatic reverberation scenario.

For the long range bistatic sonar geometry that was used to gather the data (projector at least ten water depths from the sensor) it is reasonable to assume that almost all the reverberation arrives near the horizontal plane. This assumption allows us to simplify the subsequent development of the adaptive algorithms in this paper within a two-dimensional framework.

This paper is organized as follows. The fixed-coefficient limaçon beamformer and the two adaptive beamformers are outlined in Sec. I. The test data set and the results are described in Sec. II. Conclusions on the usefulness and limitations of these techniques are drawn in Sec. III.

## I. THEORY

The starting point for the discussion of the beamformers is the output of a matched filter, with the signal of interest showing up as a sharp peak against a slowly varying background of reverberation. In the implementation used in this work the sensor data are first bandpass filtered with a finite impulse response (FIR) filter, and then matched filtered with a replica of the waveform.

Data-adaptive beamforming of matched filter output, rather than the raw sensor time series, brings with it the important advantage that the contribution of ambient noise not correlated with the transmitted waveform is reduced by the bandwidth-time (BT) product of the waveform. If raw sensor data were used instead, isotropic ambient noise would likely dominate, resulting in MVDR beams similar to limaçons.

### A. The limaçon beamformer

The standard fixed-coefficient beamformer for the sensor configuration in this paper is the limaçon. Its power response is given by

$$p_{\xi} = \langle ([(1-\alpha), \alpha \sin \xi, \alpha \cos \xi] \mathbf{x})^2 \rangle_s, \quad (1)$$

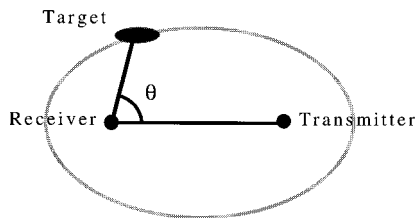


FIG. 2. Sensor geometry for the receiver. The angle of the direct arrival is used as a reference to realign the orthogonal dipole sensors.

where  $\langle \rangle_s$  denotes a time average over the expected duration of the signal,  $\xi$  is the steering direction, and  $\alpha$  is a parameter governing the shape of the response. With  $\alpha=0.5$  the result is a cardioid response pattern. We have found, for the experimental data in this paper, that  $\alpha=0.75$  is a good compromise, and this value will be used for the limaçon beamformer in this work. The resulting beam pattern has a broad main lobe somewhat narrower than that of the cardioid, and a backlobe that is 6 dB down from the main lobe.

A rough target bearing estimate  $\hat{\phi}$  is taken from the peak of the beam response,

$$\hat{\phi} = \max_{\xi} \{p_{\xi}\}. \quad (2)$$

In order to improve precision, at the expense of an increase in variance, a parabolic interpolator is applied. Suppose the power detected in beam  $\phi$  is  $p_1$ , and the power in the beams to either side is  $p_0$  and  $p_2$ . Then, in terms of these powers and the angular spacing  $\Delta\phi$  between beams the interpolated bearing estimate  $\hat{\phi}_i$  is given by

$$\hat{\phi}_i = \hat{\phi} + \frac{1}{2} \Delta\phi \frac{p_2 - p_0}{2p_1 - p_0 - p_2}. \quad (3)$$

A total of 24 beams were formed so as to be consistent with the number of beams used in the two adaptive beamformers, although this is considerably more than is necessary because the main lobe of the limaçon beamformer is quite broad.

### B. The PATCOR processor

The PATCOR processor is based on MVDR beamforming<sup>5</sup> in a number of equispaced steering angles  $\xi$ . Denote the response of the omnidirectional and the orthogonal dipole sensors to a plane wave incident at angle  $\xi$  by  $\mathbf{s}_{\xi}$ :

$$\mathbf{s}_{\xi} = [1, \sin \xi, \cos \xi]^T. \quad (4)$$

The MVDR beamforming vector  $\mathbf{w}_{\xi}^0$  steered to angle  $\xi$  is then obtained in terms of the correlation matrix  $\mathbf{Q}$  and the vector  $\mathbf{s}_{\xi}$ ,

$$\mathbf{w}_{\xi}^0 = \frac{\mathbf{Q}^{-1} \mathbf{s}_{\xi}}{\mathbf{s}_{\xi}^T \mathbf{Q}^{-1} \mathbf{s}_{\xi}}, \quad (5)$$

where  $\mathbf{Q} = \langle \mathbf{x}\mathbf{x}^T \rangle_t$  is the data correlation matrix. The angular brackets  $\langle \rangle_t$  denote a time average. Note that the reverberation background changes considerably over time, and it is necessary to consider this nonstationarity when selecting an interval over which to estimate the correlation matrix. The time interval for averaging this matrix should be short compared to that over which the reverberation directionality changes, which is of the order of the transmitter-receiver propagation time. It should, however, be long compared to the expected echo width, which for matched filter data is of the order of the reciprocal bandwidth. In this work the time constant for obtaining the  $\mathbf{Q}$  matrix is taken as 1500 independent samples. The MVDR coefficients are constant for a given window of data, but change as the next window is processed. For continuity, these data windows were overlapped by 50% in this work. In order to reduce the effect of strong reverberation peaks, we normalize the MVDR re-

sponse across bearing by dividing  $\mathbf{w}_\xi^0$  by the average long term root power,

$$\mathbf{w}_\xi = \frac{\mathbf{w}_\xi^0}{\sqrt{\mathbf{w}_\xi^{0T} \mathbf{Q} \mathbf{w}_\xi^0}}. \quad (6)$$

Normalization of the average background across bearing is similar to the spectral prewhitening commonly used in the design of matched filters for signals in colored noise. Its use here is, to the authors' knowledge, novel. Besides ensuring a more isotropic background for the detection and bearing estimation of target echoes, it normalizes the reverberation background with time during the ping.

Having obtained a set of beamformers  $\{\mathbf{w}_\xi\}$  indexed by equispaced bearings  $\xi$ , the next step is to calculate the power response for signal-direction vectors in the set  $\{\mathbf{s}_\theta\}$  indexed by equispaced bearings  $\theta$ . The response of the beamformer

steered at direction  $\xi$  to a signal incident at  $\theta$  is given by  $|\mathbf{w}_\xi^T \mathbf{s}_\theta|^2$ . We found by experiment that 24 values of  $\xi$  and an equal number for  $\theta$  was sufficient for stable response of the PATCOR processor.

In the final step sensor data are processed with the above beamformers in a time window matched to the signal duration, yielding the set of average power responses  $\{\langle |\mathbf{w}_\xi^T \mathbf{x}|^2 \rangle_s\}$ . This set, considered as a vector indexed by  $\xi$ , is compared by statistical correlation with each of the response vectors for signal directions in the set  $\{\mathbf{s}_\theta\}$ . A positive correlation for a particular  $\mathbf{s}_\theta$  is indicative of the presence of signal power in direction  $\theta$ . Since statistical correlation produces values in the range  $[-1, 1]$ , the correlator output was first shifted to the range  $[0, 2]$  and scaled by one-half the signal power  $\mathbf{w}_\theta^T \mathbf{Q}_s \mathbf{w}_\theta$ . The full expression for the PATCOR output  $p_\theta$  is given by

$$p_\theta = \frac{1}{2} \mathbf{w}_\theta^T \mathbf{Q}_s \mathbf{w}_\theta \left[ 1 + \frac{\sum_\xi (\langle |\mathbf{w}_\xi^T \mathbf{x}|^2 \rangle_s - \langle \langle |\mathbf{w}_\xi^T \mathbf{x}|^2 \rangle_s \rangle_\phi) (\langle |\mathbf{w}_\xi^T \mathbf{s}_\theta|^2 \rangle_s - \langle \langle |\mathbf{w}_\xi^T \mathbf{s}_\theta|^2 \rangle_s \rangle_\phi)}{\sqrt{\sum_\xi [\langle |\mathbf{w}_\xi^T \mathbf{x}|^2 \rangle_s - \langle \langle |\mathbf{w}_\xi^T \mathbf{x}|^2 \rangle_s \rangle_\phi]^2 \sum_\xi [|\mathbf{w}_\xi^T \mathbf{s}_\theta|^2 - \langle \langle |\mathbf{w}_\xi^T \mathbf{s}_\theta|^2 \rangle_s \rangle_\phi]^2}} \right], \quad (7)$$

where  $\langle \rangle_\phi$  denotes an average over all bearing terms. The bearing estimate is taken from the peak of  $p_\theta$  as in Eq. (2), and parabolic interpolation is applied as in Eq. (3).

### C. The DILBERT transform

The DILBERT transform is defined here. Essentially, it is a technique for "whitening" the average background interference across bearing, and is followed in this work by a limaçon beamformer. The MVDR coefficients defined by Eq. (6) provide a reverberation-normalized, minimum-variance estimate of the energy as a function of direction. We can recombine these bearing energies to produce sensor data with the dominant reverberation power reduced. Because the signal is of much smaller duration than the reverberation, it does not contribute significantly to the  $\mathbf{Q}$  matrix, and hence is not rejected by the resulting MVDR beamformer. In order to obtain a good bearing estimate, we impose the constraint of minimizing the rms deviation from a delta-function response to a unit amplitude signal incident from direction  $\theta$ . Such a sharp response is not possible with our receiver which has only three degrees of spatial freedom, but can be approximated in a least squares sense. This translates into minimizing the functional

$$F = \sum_\theta |\mathbf{v}_\theta^T \mathbf{w}_\theta^T \mathbf{s}_\theta - \delta(\xi - \theta) \sqrt{\mathbf{w}_\theta^T \mathbf{Q} \mathbf{w}_\theta \mathbf{s}_\theta \mathbf{s}_\theta^T}|^2, \quad (8)$$

where  $\mathbf{v}_\xi$  is the weighting vector for reforming the sensor data from energy in direction  $\xi$ , and  $\delta(\xi - \theta)$  is a Dirac delta function.

Minimizing  $F$  with respect to the beam weighting vector  $\mathbf{v}_\xi$  yields the equation

$$\mathbf{v}_\xi = \frac{\mathbf{s}_\xi}{\mathbf{w}_\xi^T \mathbf{Q}_i \mathbf{w}_\xi}, \quad (9)$$

where  $\mathbf{Q}_i$  is the normalized correlation matrix for two-dimensional isotropic noise:

$$\mathbf{Q}_i = \begin{bmatrix} 1 & 0 & 0 \\ 0 & 0.5 & 0 \\ 0 & 0 & 0.5 \end{bmatrix}. \quad (10)$$

Application of a set of MVDR beamformers indexed by  $\xi$  to the sensor data, followed by recombination of these beams by the weighting vectors  $\mathbf{v}_\xi$ , is equivalent to multiplication of the sensor data by the matrix  $\mathbf{H}$ ,

$$\mathbf{H} = \sum_\xi \frac{\mathbf{s}_\xi \mathbf{w}_\xi^T}{\mathbf{w}_\xi^T \mathbf{Q}_i \mathbf{w}_\xi}. \quad (11)$$

In this work 1000 bearing terms are used to form the sum in Eq. (11) in order to ensure a stable estimate of  $\mathbf{H}$ . The recombined sensor data can be subsequently beamformed with a limaçon beamformer as in Eq. (1), and the signal bearing estimated from the peak as before.

## II. TEST DATA SET AND RESULTS

For the evaluation of detection performance and bearing estimation error, a data set consisting of reverberation from a series of FM sweeps was collected on a number of three-sensor receivers. A large number of receivers in a variety of tactical geometries with respect to the transmitter, and several different transmitted waveforms were used to obtain a diverse data set.

Bandpass filtering and matched filtering were applied to the time series from each sensor. A smoothed estimate of the

power in the omni sensor was made in order to provide a basis for computing the SNR for purposes of synthetic signal injection. The bearing of the direct arrival of energy from the transmitter was measured by means of the limaçon beamformer, and used as a reference axis from which all bearings were measured in order to observe the effect of beamformer performance as a function of the angle off the main reverberation axis.

The time resolution of the matched filter output is approximately the reciprocal bandwidth. When considering the number of independent samples used in various stages of the processing, we have taken this resolution into account, assuming  $f_N/B$  samples are correlated, where  $f_N$  is the Nyquist frequency, and  $B$  the bandwidth. Data within a fixed window of 7500 independent samples were extracted from each transmission. For the purpose of the PATCOR processor and the DILBERT transform, 50% overlapped windows of 1500 samples duration were used to estimate the  $\mathbf{Q}$  matrices. For all three beamformers averaging of the outputs for signal detection was performed over 30 sample intervals.

In preparing the recorded reverberation data for the evaluation of performance the reverberation noise power in the omnidirectional sensor was first measured. Then, data examples were created at desired SNR by adding a constant power level signal to the reverberation data. As a consequence, the signal-plus-noise statistics of the test data set were those of fluctuating background plus a constant strength signal. The ROC curves were obtained by incrementing a counter if the signal-plus-noise power at a processor output exceeded an adjustable detection threshold (DT). The number of threshold crossings were then divided by the total number of trials to form an estimate of  $P_D$ . The probability of false alarm  $P_{FA}$  was estimated by recording the number of crossings of the noise level over the same DT. The rms bearing errors were obtained from the average squared difference between the measured bearing of the inserted signal and the true bearing.

### A. ROC curves

The ROC curves for all three beamformers are shown in Fig. 3. The false alarm probability  $P_{FA}$  is plotted in logarithmic scale along the  $x$  axis, and the detection probability  $P_D$  in increasing logarithmic scale along the  $y$  axis. The range of SNRs for the injected signal is from  $-6$  dB to  $+3$  dB with respect to reverberation power measured in the omni channel. Note that a smoothed estimate of power in the omni channel is used for this purpose, in order to avoid effects due to the large fluctuations characteristic of reverberation. The bearings of the synthetic signal vary from  $0$  to  $360$  degrees in  $60$ -degree increments. Because the results are symmetric about the transmitter–receiver axis, only the curves for signals at  $0, 60, 120,$  and  $180$  degrees are shown.

It should be pointed out that the reverberation background was nonstationary, so that these results represent an average over a time window, and it is likely that the distribution of reverberation fluctuations changed somewhat over this window. It should also be pointed out that the data set did not include anomalous reverberation returns, for example from large bathymetric features. The signal-plus-noise detec-

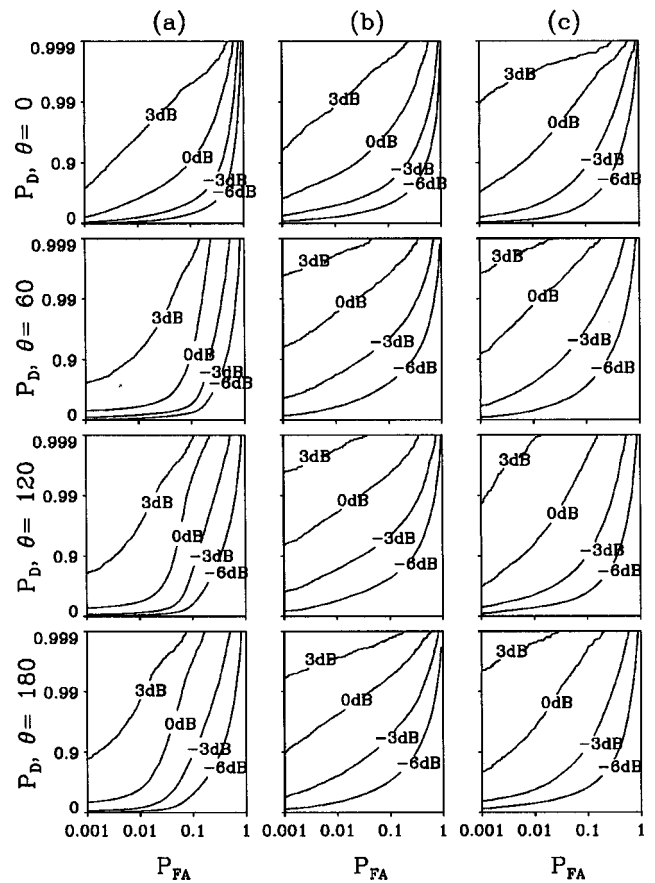


FIG. 3. ROC curves for the three beamformers; (a) limaçon; (b) PATCOR; and (c) DILBERT transform plus limaçon. The signal angle  $\theta$  is taken at  $0, 60, 120,$  and  $180$  degrees with respect to the transmitter–receiver axis. The SNR is with respect to the power measured in the omni sensor.

tion statistics were deduced for a signal injected in a single direction. This is a cued detection problem, appropriate when the beamformer performance in a given direction is to be optimized.

The ROC curves for the PATCOR processor show a considerable improvement over a processor employing a limaçon beamformer. They indicate an average performance gain of approximately  $3$  dB at a  $P_{FA}$  of  $0.01$ , with the caveat that at the lower SNRs the differences in performance is reduced. The ROC curves for the DILBERT transform followed by limaçon beamforming show similar improvements over those of the limaçon beamformer alone. Again, at very low SNRs the difference in performance is reduced.

Detection performance is illustrated as a function of SNR for  $P_{FA}=0.01$  in Fig. 4. Separate plots are made for signal bearings  $\theta$  at  $0, 60, 120,$  and  $180$  degrees. The two adaptive beamformers show the same  $P_D$  as the limaçon at SNRs that are lower by  $3$ – $6$  dB.

### B. rms bearing errors

We compare the bearing-estimation performance of the three beamforming systems in Fig. 5. The estimator based on the limaçon beamformer tends to lock onto the background reverberation, producing a bearing estimate independent of the signal, but with very low variance. The two adaptive beamformers exhibit low bias, but considerably higher vari-



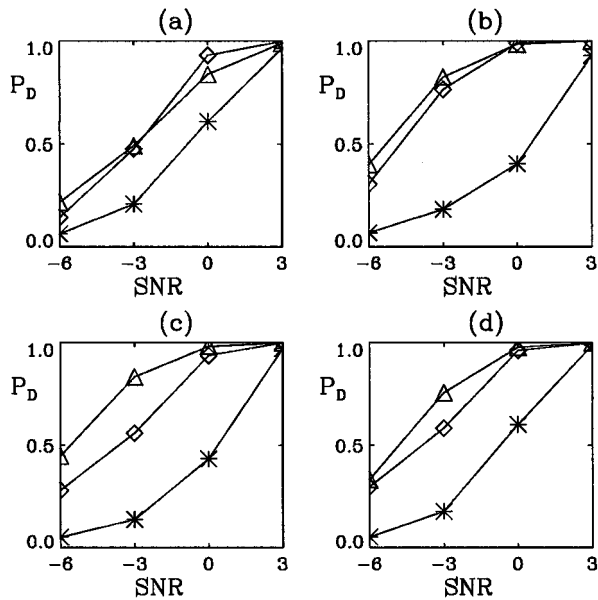


FIG. 4.  $P_D$  as a function of SNR, for a  $P_{FA}$  of 0.01. The symbols are as follows: \*—limaçon beamformer;  $\diamond$ —PATCOR processor;  $\triangle$ —DILBERT transform plus limaçon. The four panels correspond to signal bearings  $\theta$  at: (a) 0; (b) 60; (c) 120; and (d) 180 degrees.

ance, especially for low SNR signals. The rms bearing error takes both types of error into account and thus summarizes overall performance. A separate curve is plotted for each of four different values of signal bearing relative to the reference axis.

Using the limaçon-based estimator as a benchmark, Fig. 5 indicates variable and often large reductions in rms bearing error achieved by the adaptive systems. For signal bearings on the projector–receiver axis the adaptive systems show no improvement, while for the other signal directions reductions up to  $4\times$  for the PATCOR processor, and up to  $3\times$  for the

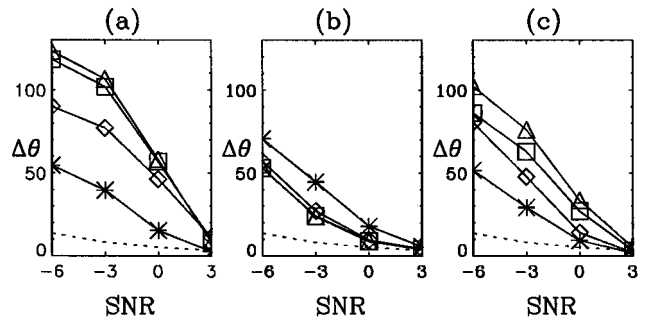


FIG. 5. rms bearing errors for the three beamformers; (a) limaçon beamformer; (b) PATCOR processor; and (c) DILBERT transform plus limaçon beamformer. The symbols are as follows: \*— $\theta=0$ ;  $\diamond$ — $\theta=60$ ;  $\triangle$ — $\theta=120$ ;  $\square$ — $\theta=180$ ;  $\cdots$ —CRLB.

DILBERT processor are achieved for SNRs below 0 dB. We also note in Fig. 5(b) that rms bearing error for the PATCOR processor is relatively independent of signal direction.

We also implemented the arctan bearing estimator (derived from the arctangent of the ratio of sine-channel and cosine-channel outputs). Its performance in terms of rms error was very similar to that of the limaçon estimator when applied to our dataset.

The Cramér–Rao lower bound (CRLB) for bearings in isotropic noise;<sup>10</sup> is shown as a dashed line for reference in Fig. 5. This bound is an estimate of the standard deviation, which should be close to the rms error for an unbiased estimator. We do not expect this bound to be achieved in the anisotropic reverberation field, but merely note that the CR bound appears to be approached by all the estimators at SNR of 3 dB or more. For the CRLB, it should be noted that the short-time averaging creates an effective BT product of approximately 30. The formula for the CRLB,  $\sigma_\theta$ , is taken from Eq. (14) in Ref. 10, albeit with a slight correction to the original formula:

$$\sigma_\theta \geq \left[ 2 \sum_{BT} \frac{s'^T Q^{-1} s' s'^T Q^{-1} s - s'^T Q^{-1} s - (s'^T Q^{-1} s)^2 - s'^T Q^{-1} s + 4 \frac{(s'^T Q^{-1} s)^2}{(1 + s'^T Q^{-1} s)}}{1 + s'^T Q^{-1} s} \right]^{-1/2}, \quad (12)$$

where  $s' = \partial s / \partial \theta$  and  $s'' = \partial^2 s / \partial \theta^2$ . Specializing to the case of the three-sensor array in two-dimensional isotropic noise, we find the CRLB to be

$$\sigma_\theta \geq \left[ \frac{12 \text{ BT SNR}^2}{1 + 3 \text{ SNR}} \right]^{-1/2}, \quad (13)$$

where SNR is expressed as an absolute ratio, rather than in decibels, and  $\sigma_\theta$  is in radians.

### III. CONCLUSIONS

Two adaptive beamforming techniques, the PATCOR and DILBERT transform, developed for signal detection and bearing estimation in strongly directional reverberation and interference, have been described. These techniques were

implemented and studied for a receiver consisting of an omnidirectional sensor and two collocated orthogonal dipole sensors. Performance was measured with recorded reverberation data. The detection performance of the PATCOR processor, as suggested by Fig. 4, was approximately 3 dB better than the benchmark limaçon beamformer at a  $P_{FA}$  of 0.01. That of the DILBERT transform, followed by a limaçon beamformer, was approximately 4 dB better, allowing for bearing variations.

The bearing-estimation performance of both the PATCOR and DILBERT processors was studied with rms error as the performance criterion. Except for signals incident on the projector–receiver axis, variable and often large reductions in rms error were observed relative to the limaçon

beamformer used as a bearing estimator. Reductions in rms bearing error up to  $4\times$  for the PATCOR processor, and up to  $3\times$  for the DILBERT processor were obtained.

As with all adaptive methods the cost of implementation must be balanced against the potential gain. The current implementation requires estimation of the data correlation matrix  $\mathbf{Q}$  every 1500 samples, as well as a considerable number of matrix multiplications to generate the PATCOR processor terms or DILBERT transform coefficients. At high SNRs the extra 3 dB or so that might be obtained may not be worth the need to generate the transformation matrix and multiply each sensor measurement. In addition, with only three spatial degrees of freedom in the measurement, it is very unlikely that strong interference from more than one direction can be handled by these techniques. These points notwithstanding, the two beamformers appear to be robust when faced with real experimental data, and the improvement in detection performance alone motivates further development.

<sup>1</sup>R. J. Urick, *Principles of Underwater Sound for Engineers* (McGraw-Hill, New York, 1967).

<sup>2</sup>H. L. Van Trees, *Detection, Estimation, and Modulation Theory, Part I* (Wiley, New York, 1968).

<sup>3</sup>R. O. Nielsen, *Sonar Signal Processing* (Artech House, Boston, 1991).

<sup>4</sup>D. D. Ellis, "A shallow-water normal-mode reverberation model," *J. Acoust. Soc. Am.* **97**, 2804–2814 (1995).

<sup>5</sup>D. A. Gray, "Formulation of the maximum signal-to-noise ratio array processor in beam space," *J. Acoust. Soc. Am.* **72**, 1195–1201 (1982).

<sup>6</sup>M. Wazenski, D. Alexandrou, and D. DeFatta, "ROC evaluation of adaptive beamforming in a simulated shallow water environment," *IEEE J. Ocean Eng.* **21**, 94–99 (1996).

<sup>7</sup>I. P. Kirsteins and D. W. Tufts, "On the probability density of signal-to-noise ratio in an improved adaptive detector," *ICASSP-85*, 572–575, Tampa, FL (1985).

<sup>8</sup>L. L. Scharf and D. W. Tufts, "Rank reduction for modeling stationary signals," *IEEE Trans. Acoust. Speech Signal Process.* **ASSP-35**, 350–355 (1987).

<sup>9</sup>L. L. Scharf, "The SVD and reduced rank signal processing," *Signal Process.* **25**, 113–133 (1991).

<sup>10</sup>J. N. Maksym, "Directional accuracy of small ring arrays," *J. Acoust. Soc. Am.* **61**, 105–109 (1977).

# Multipath compensation in shallow water environments using a virtual receiver

Martin Siderius,<sup>a)</sup> Darrell R. Jackson, Daniel Rouseff, and Robert Porter

*Applied Physics Laboratory, College of Ocean and Fishery Sciences, University of Washington, Seattle, Washington 98105*

(Received 5 March 1996; revised 16 May 1997; accepted 29 July 1997)

An acoustic technique for compensation of signal distortion due to propagation is developed in analogy with an astronomical technique in which light from a bright “guide star” is used to correct atmospheric aberration of weaker objects that are nearby in the angular sense. The acoustic technique investigated here uses a vertical array to receive both the signal from a broadband “guide source” and an unknown “objective source” which propagates over a partially shared path. The algorithm is a spatial–temporal cross correlation of the two signals and is termed a “virtual receiver” as the output approximates the signal that the unknown source would produce at the location of the guide source. By strategically locating the guide source, many of the distorting effects of an unknown propagation region can be removed, including mode coupling and multipaths. The virtual receiver can also be combined with matched field processing techniques to estimate the unknown source location. Results are given for a variety of numerical experiments in both the time and frequency domains. The numerical simulations are used to illustrate the virtual receiver algorithm in range-dependent shallow water environments exhibiting lossy propagation and mode coupling. © 1997 Acoustical Society of America. [S0001-4966(97)04011-3]

PACS numbers: 43.30.Wi, 43.30.Bp, 43.30.Vh, 43.60.Gk [JHM]

## INTRODUCTION

Guide source methods, widely used in astronomy, are related to techniques which estimate the transfer function (or Green’s function) describing propagation between two points.<sup>1</sup> The concept has considerable potential utility in shallow water acoustics where signals can become distorted due to inhomogeneities and multipathing. The virtual receiver method can be considered a degenerate type of the holographic processing method recently discussed in the underwater acoustics literature.<sup>2–4</sup> In holographic methods, multiple calibration sources are used together with a vertical receiving array to form an effective receiving array having elements at the location of the sources. For the virtual receiver, a single calibration source is used, removing the need for precise determination of relative source locations. An additional difference is that the virtual receiver calibration is applied instantaneously, so that time evolution of the environment is not a problem. The virtual receiver concept also shares some of the principles used in time-reversed processing. The “time-reversal mirror” also known as the “phase conjugate array” employs a probe source in much the same fashion as the guide source.<sup>5–9</sup> This probe transmission is then received at some distance and a time-reversed copy is retransmitted. At the location of the probe source, this time-reversed transmission is relatively free of multipath effects, as time reversal essentially employs the ocean channel as its own matched filter. Time reversal is equivalent to complex conjugation in the frequency domain, and as will be seen, complex conjugation is employed in the virtual receiver al-

gorithm. Mathematically, the two methods are nearly identical, but they are very different in practice, as reciprocal transmissions are employed in time reversal, necessitating the use of a receiver–transmitter array. In contrast, the virtual receiver only requires a receiving array. Because these two methods are so different in practice, they should not be considered as competing techniques.

In this article, a method is proposed that could potentially use simple, inexpensive guide sources. A vertical array is used to receive the signal from the guide source, and also any unknown signal from a target of interest. These measurements are used as input to an algorithm that creates a “virtual receiver” at the location of the known guide source. That is, the processor output approximates the target signal as it would appear at the location of the guide source. The guide source could be used as a remote probe in a bistatic sonar configuration as shown in Fig. 1. The known signal could be the “direct blast” while the unknown signal could be the target echo. Being relatively free of multipath effects, the output from the virtual receiver is ideally suited to echo classification applications. In Sec. I, the virtual receiver algorithm is defined and the performance is discussed for lossy range independent propagation. Section II introduces range dependence, including mode coupling effects and lossy sediments. The numerical results are discussed in Sec. III. The computational approach is to use a wide angle PE code and Fourier synthesis to simulate, time-domain results for broadband sources. Both downslope and upslope propagation with slope of 2° are considered. An example is also given for propagation over an obstacle producing strong mode coupling. To illustrate the utility of the concept, in Sec. IV, the virtual receiver data are used together with single receiver broadband matched field techniques for source localization.

<sup>a)</sup>Currently at: Saclant Undersea Research Centre, Viale S. Bartolomeo 400, 19138 La Spezia, Italy.

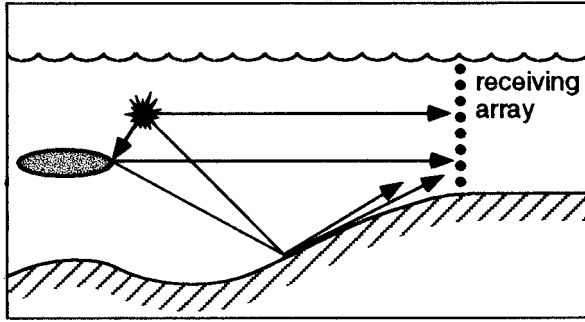


FIG. 1. Suggested here is a possible geometry for bistatic sonar using a guide source. The guide source insonifies the unknown object. The backscatter signal is processed with the guide source field to create a virtual receiver at the location of the guide source. The output of the processor looks like a true receiver at the location of the guide source.

A discussion of the restrictions placed on the relative positions of the guide and objective source is given in Sec. V, and in Sec. VI noise is considered.

### I. VIRTUAL RECEIVER ALGORITHM

Consider the geometry shown in Fig. 2. The source of interest, denoted the objective source, is located at range  $x = 0$ , depth  $z = z_0$ , and transmits the signal  $s(t)$ . The guide source, at  $(x_g, z_g)$ , transmits the signal  $g(t)$ . The resulting acoustic fields are measured along a distant vertical receiving array at  $x = x_j$ . This configuration is useful for illustrating the virtual receiver concept in a simple setting; the added complexity of analyzing the bistatic scenario in Fig. 1 can be avoided without affecting the operation of the virtual receiver algorithm. The configuration is useful in its own right in, for example, communications applications where the goal might be to recover the transmitted  $s(t)$  from the distant measurements.

Assume the pressure fields resulting from the objective source and the guide source can be separated, and are given by  $p_0(z; t)$  and  $p_g(z; t)$ , respectively. Requirements for separating the two signals is the topic of Sec. V. Define the temporal Fourier transform by

$$P(\omega) = \mathcal{F}\{p(t)\} = \int_{-\infty}^{\infty} p(t) e^{i\omega t} dt \quad (1)$$

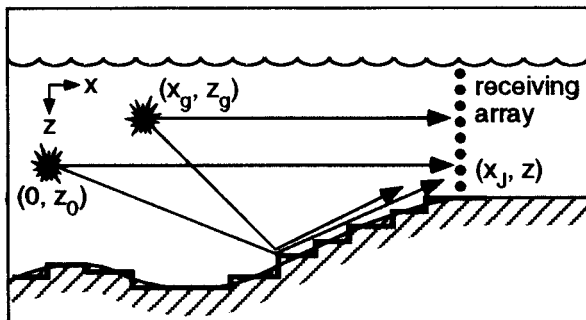


FIG. 2. Typical geometry: both the objective and guide source are active. The objective source is located in the first segment at  $(x_0, z_0)$ , the guide source in the  $G$ th segment at  $(x_g, z_g)$  and the receiving array in the  $J$ th segment at  $x = x_j$ .

with inverse transform,  $p(t) = \mathcal{F}^{-1}\{P(\omega)\}$ . The virtual receiver algorithm takes the transform of each signal at each depth, forms a spatial-temporal cross correlation in the same manner as the holographic techniques of Refs. 2, 3, and 4, and applies a filter with transfer function  $H(\omega)$ . In the frequency domain, the virtual receiver output is

$$V(\omega) = H(\omega) \int_0^h P_g^*(z; \omega) P_0(z; \omega) dz, \quad (2)$$

where  $*$  indicates complex conjugation and  $h$  is the water depth. It will later be assumed that the array spans the entire water column, Al-Kurd and Porter<sup>4</sup> showed a gradual degradation in performance for the holographic processor when the arrays only span part of the water column and we expect similar degradation for the virtual receiver algorithm. The time-domain virtual receiver output will resemble the output of an actual receiver placed at  $(x_g, z_g)$ . If the virtual receiver is sufficiently close to the objective source, distortion due to propagation effects can be removed and the desired signal,  $s(t)$  can be recovered. This follows from the work of Mourad *et al.*,<sup>2</sup> but a detailed explanation will be given in the following illustration for a range-independent environment. While Mourad *et al.* extended this result to the adiabatic range-dependent case, we provide a further extension to the nonadiabatic case in Sec. II.

Consider a range-independent environment. A normal mode expansion can be made at any frequency, and the time-domain pressure field then can be expressed by Fourier synthesis. In the frequency domain, the field measured at the array due to the guide source is<sup>10</sup>

$$P_g(z; \omega) = G(\omega) \sum_m \Psi_m(z_g) \Psi_m(z) H_0^{(1)}(k_m(x_j - x_g)), \quad (3)$$

where  $G(\omega)$  is the transform of  $g(t)$ , and the normal modes  $\Psi_m(z)$  and eigenvalues  $k_m$  are implicit functions of frequency. If the medium is lossless, both  $\Psi_m(z)$  and  $k_m$  are real. If the medium is slightly lossy, a perturbation approach can be used; to first order,  $\Psi_m(z)$  remains real while  $k_m = k'_m + i\alpha_m$ . A similar expansion can be made for  $P_0(z; \omega)$ . Substituting into Eq. (2), using the asymptotic expansion for the Hankel functions and the orthogonal property of the normal modes yields

$$V(\omega) = \frac{1}{\sqrt{(x_j - x_g)}} \tilde{S}(\omega) \sum_m \exp(-\alpha_m(2x_j - x_g)) \times \frac{\Psi_m(z_g) \Psi_m(z_0)}{|k_m|} \exp(ik'_m x_g), \quad (4)$$

where  $\tilde{S}(\omega) = H(\omega) G^*(\omega) S(\omega)$  and  $S(\omega) = \mathcal{F}\{s(t)\}$ . As mentioned earlier, in applying orthonormality it has been assumed that the array spans the region where the modes have significant amplitude. In addition, density gradients have been neglected. Numerical results to be presented later show that these idealizations have little effect on performance, as long as the array spans the water column. If the transmitted signal from the guide source is known, the filter in Eq. (2) can be designed to remove its effects so that  $\tilde{S}(\omega) \approx S(\omega)$ .

To verify that the processor is indeed a ‘‘virtual receiver,’’ consider the frequency response that would have been measured by a true receiver at  $(x_g, z_g)$ ,

$$V_T(\omega) = \frac{1}{\sqrt{x_g}} S(\omega) \sum_m \exp(-\alpha_m x_g) \times \frac{\Psi_m(z_g) \Psi_m(z_0)}{\sqrt{k_m}} \exp(ik'_m x_g). \quad (5)$$

Apart from a range-dependent scaling factor, the virtual receiver output  $V(\omega)$  closely resembles the output,  $V_T(\omega)$  of a true receiver. The extra factor of  $\sqrt{k_m}$  in the denominator of Eq. (4) has previously been interpreted<sup>11</sup> as a mode-dependent obliquity factor; the amplitude of each mode is perturbed depending on its corresponding grazing angle. More significantly, each mode is attenuated according to the actual propagation distances between sources and receiver. For lower-order modes that are weakly attenuated, however, it is expected that the virtual receiver will mimic what would have been measured by a true receiver at  $(x_g, z_g)$ .

## II. VIRTUAL RECEIVER ANALYSIS USING COUPLED MODES FOR RANGE-DEPENDENT ENVIRONMENTS

The range-independent result (4) is useful for illustrating some general properties of the virtual receiver algorithm. The same algorithm can be applied to more complicated propagation regimes. Consider again the geometry shown in Fig. 2. The objective source is located in the first segment at  $(0, z_0)$ , the guide source in the  $G$ th segment at  $(x_g, z_g)$  and the receiving array in the  $J$ th segment at  $(x_J, z)$ . The range-dependent medium is approximated by a series of range-independent segments and the propagation is modeled using one-way coupled modes.<sup>12</sup> For simplicity, the objective source, the guide source, and the receiving array are assumed to lie in the same vertical plane, and out-of plane propagation effects are ignored. The accuracy of the virtual receiver algorithm for more general geometries will clearly depend on the horizontal correlation length. Consider a general segment having index  $j$  with  $1 \leq j \leq J$ . Neglecting vertical density gradients and backscatter, the field due to the guide source is written as an expansion of the local modes in the  $j$ th segment,

$$P_g(x, z; \omega) = G(\omega) \sum_m a_m^j h_m^j(x) \Psi_m^j(z), \quad (6)$$

where  $x_{j-1} < x \leq x_j$  and  $h_m^j(x)$  is a ratio of Hankel functions. Using the asymptotic expansion for the Hankel functions,

$$h_m^j(x) = \sqrt{\frac{x_{j-1}}{x}} \exp(ik_m^j(x - x_{j-1})). \quad (7)$$

The modal coefficients between adjacent range segments are determined by recursion. In matrix form,

$$\mathbf{a}^{j+1} = \mathbf{R}^j \mathbf{a}^j = (\mathbf{C}^j \mathbf{H}^j) \mathbf{a}^j. \quad (8)$$

The latter form of Eq. (8) decomposes the transition matrix  $\mathbf{R}^j$  into two terms where the coupling matrix  $\mathbf{C}^j$  has elements,

$$C_{l,m}^j = \int \Psi_l^{j+1}(z) \Psi_m^j(z) dz, \quad (9)$$

and the propagation matrix  $\mathbf{H}^j$  is diagonal with elements  $h_m^j(x_j)$ . In the special case for the segment containing the source,  $x_{j-1} = x_1$ , and  $\mathbf{H}^j$  is replaced by the identity matrix  $\mathbf{I}$ . A similar expansion can be made for the objective source,

$$P_0(x, z; \omega) = S(\omega) \sum_m b_m^j h_m^j(x) \Psi_m^j(z). \quad (10)$$

Using Eq. (8) the coefficients at the receiving array are

$$\mathbf{a}^J = \mathbf{R}^{J-1} \mathbf{R}^{J-2} \dots \mathbf{R}^{G+1} \mathbf{R}^G \mathbf{a}^G, \quad (11)$$

$$\mathbf{b}^J = \mathbf{R}^{J-1} \mathbf{R}^{J-2} \dots \mathbf{R}^{G+1} \mathbf{R}^G \mathbf{R}^{OG} \mathbf{b}^1, \quad (12)$$

where  $\mathbf{R}^{OG} = \mathbf{R}^{G-1} \mathbf{R}^{G-2} \dots \mathbf{R}^1$ . Vectors  $\mathbf{a}^G$  and  $\mathbf{b}^1$  contain the coefficients for the objective and guide in the vicinity of their respective locations with elements,

$$a_m^G = \frac{1}{\sqrt{k_m^G(x_G - x_g)}} \Psi_m^G(z_g) \exp(ik_m^G(x_G - x_g)), \quad (13)$$

$$b_m^1 = \frac{1}{\sqrt{k_m^1 x_1}} \Psi_m^1(z_0) \exp(ik_m^1 x_1). \quad (14)$$

To calculate the virtual receiver output for the coupled mode environment, substitute the guide source field (6) and objective source field (10) into the virtual receiver algorithm (2). Using matrix notation and exploiting the orthonormal property of the local normal modes,

$$V(\omega) = \tilde{S}(\omega) (\mathbf{a}^J)^\dagger \mathbf{D}^J \mathbf{b}^J, \quad (15)$$

where  $\mathbf{D}^J$  is defined as

$$D_{m,m}^J = \exp(-2\alpha_m^J(x_J - x_{J-1})) \quad (16)$$

with  $\alpha_m^J$  is the imaginary part of  $k_m^J$ . The conjugate transpose operation is indicated by the  $\dagger$  symbol. To examine the virtual receiver output in more detail, consider first the special case where the medium is lossless. Matrix  $\mathbf{D}^J$  reduces to the identity matrix and, using the recursion relation for the guide source (11) and objective source (12), the virtual receiver given by (15) becomes

$$V(\omega) = \tilde{S}(\omega) \mathbf{a}^{G\dagger} \mathbf{R}^{G\dagger} \dots \mathbf{R}^{J-1\dagger} \mathbf{R}^{J-1} \dots \mathbf{R}^G \mathbf{R}^{OG} \mathbf{b}^1. \quad (17)$$

Expanding the inner multiplication using Eq. (8),

$$\mathbf{R}^{J-1\dagger} \mathbf{R}^{J-1} = \mathbf{H}^{J-1\dagger} \mathbf{C}^{J-1\dagger} \mathbf{C}^{J-1} \mathbf{H}^{J-1}. \quad (18)$$

The product  $\mathbf{C}^{J-1\dagger} \mathbf{C}^{J-1}$  reduces to the identity matrix  $\mathbf{I}$ , due to conservation of energy. For the lossless case,  $\mathbf{H}^{J-1\dagger} \mathbf{H}^{J-1}$  reduces to  $(x^{J-2}/x^{J-1}) \mathbf{I}$  giving  $\mathbf{R}^{J-1\dagger} \mathbf{R}^{J-1} = (x^{J-2}/x^{J-1}) \mathbf{I}$ . In general, this is true between any two range segments, that is,  $\mathbf{R}^{j\dagger} \mathbf{R}^j = (x_{j-1}/x_j) \mathbf{I}$ . Consequently, Eq. (17) reduces to

$$V(\omega) = N \mathbf{a}^{G\dagger} \mathbf{R}^{OG} \mathbf{b}^1 = N \mathbf{a}^{G\dagger} \mathbf{b}^G, \quad (19)$$

where  $N = \tilde{S}(\omega) \sqrt{x_G(x_G - x_g)/x_J(x_J - x_g)}$ . Finally, using Eq. (13), the virtual receiver output is written in summation form,

$$V(\omega) = \sqrt{\frac{x_G}{x_J(x_J - x_g)}} \tilde{S}(\omega) \times \sum_m \frac{\Psi_m^G(z_g) b_m^G}{\sqrt{k_m^G}} \exp(ik_m^G(x_g - x_G)). \quad (20)$$

To within a multiplicative constant, this is essentially what would have been measured by a receiver at  $(x_g, z_g)$ . This can be illustrated by putting the objective source in the same segment as the guide source. The virtual receiver is then written

$$V(\omega) = \frac{1}{\sqrt{x_J(x_J - x_g)}} \tilde{S}(\omega) \times \sum_m \frac{\Psi_m^G(z_g) \Psi_m^G(z_0)}{k_m^G} \exp(ik_m^G x_g). \quad (21)$$

The frequency response that would have been measured had a true receiver been placed at  $(x_g, z_g)$  is

$$V_T(\omega) = \frac{1}{\sqrt{x_J}} S(\omega) \sum_m \frac{\Psi_m^G(z_g) \Psi_m^G(z_0)}{\sqrt{k_m^G}} \exp(ik_m^G x_g). \quad (22)$$

These results are similar to the range-independent case; the virtual receiver output approximates what would have been measured by a true receiver. Again, the virtual receiver has a mode-dependent obliquity factor, and a range-dependent scaling factor.

When loss is included,  $\mathbf{D}^j$  no longer equals the identity matrix, and the matrix product between segments becomes

$$\mathbf{R}^{j\dagger} \mathbf{R}^j = \frac{x_{j-1}}{x_j} \mathbf{D}^j. \quad (23)$$

The virtual receiver given by Eq. (17) is written for lossy coupled mode propagation,

$$\text{error} = \begin{bmatrix} 0 & c_{12}(\epsilon_1 - \epsilon_2) & c_{13}(\epsilon_1 - \epsilon_3) & c_{14}(\epsilon_1 - \epsilon_4) & \cdots \\ c_{21}(\epsilon_2 - \epsilon_1) & 0 & c_{23}(\epsilon_2 - \epsilon_3) & c_{24}(\epsilon_2 - \epsilon_4) & \cdots \\ c_{31}(\epsilon_3 - \epsilon_1) & c_{32}(\epsilon_3 - \epsilon_2) & 0 & c_{34}(\epsilon_3 - \epsilon_4) & \cdots \\ c_{41}(\epsilon_4 - \epsilon_1) & c_{42}(\epsilon_4 - \epsilon_2) & c_{43}(\epsilon_4 - \epsilon_3) & 0 & \cdots \\ \vdots & \vdots & \vdots & \vdots & \ddots \end{bmatrix}. \quad (30)$$

The main diagonal has no error, and the off-diagonals have increasing error the farther from the main diagonal. However, the one-way coupled mode assumption requires energy to be confined near the main diagonal since coupling between distant modes implies large environmental variations between two segments (and significant backscatter). As long as the coupling is to nearby modes, the error term will be small. This is a plausibility argument that will be borne out in computer simulations to be presented. Using approximate commutation to “pull”  $\mathbf{D}^j$  through at each step segment results in the virtual receiver,

$$V(\omega) = \frac{x^{J-2}}{x^{J-1}} \tilde{S}(\omega) \mathbf{a}^G \mathbf{R}^{G\dagger} \mathbf{R}^{G\dagger} \cdots \mathbf{R}^{J-2\dagger} \mathbf{D}^{J-1} \mathbf{R}^{J-2} \cdots \mathbf{R}^G \mathbf{R}^{OG} \mathbf{b}^1. \quad (24)$$

The inner multiplication including the  $J-2$  segment is

$$\mathbf{R}^{J-2\dagger} \mathbf{D}^{J-1} \mathbf{R}^{J-2} = \mathbf{H}^{J-2\dagger} \mathbf{C}^{J-2\dagger} \mathbf{D}^{J-1} \mathbf{C}^{J-2} \mathbf{H}^{J-2}. \quad (25)$$

To simplify Eq. (25) assume that  $\mathbf{C}$  and  $\mathbf{D}$  commute so that, in general:

$$\mathbf{C}^{j-1\dagger} \mathbf{D}^j \approx \mathbf{D}^j \mathbf{C}^{j-1\dagger}. \quad (26)$$

The validity of this approximation is examined using the first two terms of a Taylor series to expand the weakly mode-dependent matrix  $\mathbf{D}^j$ ,

$$\mathbf{D}^j = \begin{bmatrix} 1 - \epsilon_1 & 0 & 0 & 0 & \cdots \\ 0 & 1 - \epsilon_2 & 0 & 0 & \cdots \\ 0 & 0 & 1 - \epsilon_3 & 0 & \cdots \\ \vdots & \vdots & 0 & \ddots & 0 \end{bmatrix}, \quad (27)$$

where  $\epsilon_m = 2\alpha_m^j(x_j - x_{j-1})$  is a small quantity giving the slowly varying relationship between mode number and attenuation. The matrix  $\mathbf{C}^{j-1\dagger}$  is represented as

$$\mathbf{C}^{j-1\dagger} = \begin{bmatrix} c_{11} & c_{12} & c_{13} & \cdots \\ c_{21} & c_{22} & c_{23} & \cdots \\ c_{31} & c_{32} & c_{33} & \cdots \\ \vdots & \vdots & \vdots & \ddots \end{bmatrix}. \quad (28)$$

Defining an error term to quantify the effect of the commut- ing operation,

$$\text{error} = \mathbf{C}^{j-1\dagger} \mathbf{D}^j - \mathbf{D}^j \mathbf{C}^{j-1\dagger}; \quad (29)$$

that is,

$$V(\omega) = N \mathbf{a}^G \mathbf{D}^{J-1} \mathbf{D}^{J-2} \cdots \mathbf{D}^G \mathbf{b}^G. \quad (31)$$

Once again assuming the objective and guide sources are in the same slab, the virtual receiver is

$$V(\omega) = \frac{1}{\sqrt{x_J(x_J - x_g)}} \tilde{S}(\omega) \sum_m \sum_{j=G}^J \exp(-2\alpha_m^j x_j - \alpha_m^G x_g) \frac{\Psi_m^G(z_g) \Psi_m^G(z_0)}{|k_m^G|} \exp(ik_m^G x_g). \quad (32)$$

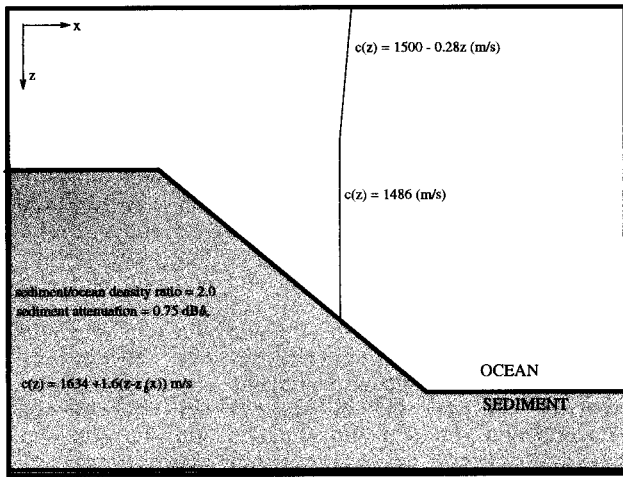


FIG. 3. Environmental parameters for numerical experiments.

The virtual receiver given by Eq. (32) can be compared with Eq. (21), the lossless coupled mode case, and Eq. (4), the range-independent lossy case. Again, the virtual receiver has a mode-dependent obliquity factor, and a range-dependent scaling factor. The additional term containing a summation over  $j$  is due to the lossy propagation. Similar to the range-independent case, the virtual receiver differs from the true receiver by the mode-dependent attenuation factor for propagation over the region between the sources and receiving array. The attenuation for range-dependent environments accumulates as a discrete summation over the range segments between the guide source and receiving array. As mentioned previously, the numerical simulations will be used to support the claims presented here.

### III. NUMERICAL RESULTS

Testing the virtual receiver algorithm by computer modeling requires a numerical technique which can simulate time-domain acoustic signals in range-dependent shallow water environments. The wide angle, finite element parabolic equation code FEPE is a frequency domain technique which is capable of simulating range-dependent environments and interactions with possibly lossy sediments.<sup>13</sup> Time-domain signals are simulated using Fourier synthesis and the algorithm is tested in a variety of range-dependent environments. The properties of the ocean and sediment used throughout are as follows (also shown diagrammatically in Fig. 3) with sound speed in m/s:

$$c(z) = \begin{cases} 1500 - 0.28z, & z < 50 \\ 1486, & 50 \leq z < z_b(x) \\ 1634 + 1.6(z - z_b(x)), & z_b(x) \leq z \end{cases} \quad (33)$$

The sound-speed ratio between sediment and water is 1.1 at the interface, the sediment/water density ratio is 2, and the attenuation in the sediment is 0.75 decibels per wavelength (dB/λ). The quantity,  $z_b(x)$ , is the range-dependent depth of the water sediment interface. The time-domain source signal is a Ricker wavelet with center frequency of 200 Hz for both the guide source and objective source, and is shown in Fig. 4. The Ricker wavelet, often used in seismic work, is the

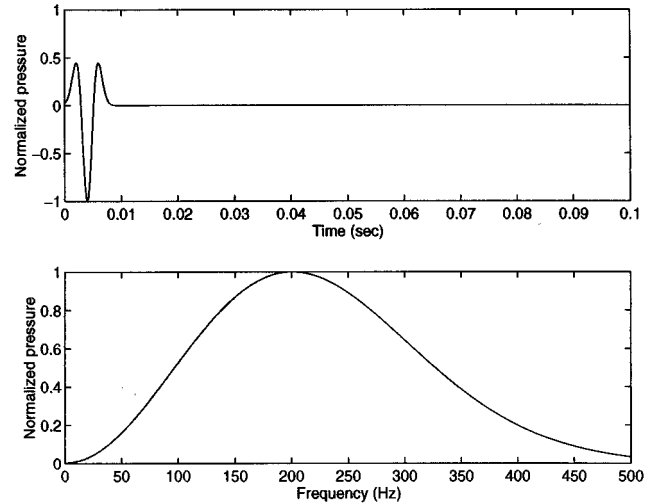


FIG. 4. Ricker wavelet used for source function in the time (top) and frequency (bottom) domains. Time and frequency axes are scaled for comparison with numerical results.

second derivative of the Gaussian function. The Ricker wavelet is used here primarily for convenience to provide a clear separation of multipaths without the confusing effects, e.g., of bubble pulses that arise with explosive sources. As the algorithm cross correlates the two receptions, matched filtering of the source signal is automatic. Thus the output of the virtual receiver will be a convolution of the source signal autocorrelation with an impulse response corresponding to mode-filtered propagation from the objective source location to the guide source location. Consequently, the results presented here should apply to any signals having similar autocorrelation.

The pressure field from the virtual receiver and true receiver will be shown for each geometry in both the frequency and time domain. To compare the true and virtual fields, the normalized complex correlation function is used in the frequency domain,

$$\Phi = \frac{\sum_n V^*(\omega_n) V_T(\omega_n)}{\sqrt{\sum_n V_T^*(\omega_n) V_T(\omega_n)} \sqrt{\sum_n V^*(\omega_n) V(\omega_n)}} \quad (34)$$

A perfect correlation results in  $|\Phi| = 1$ . For convenience,  $V_T(\omega)$  will be referred to as the true receiver “data” and  $V(\omega)$  as the virtual receiver “data.”

#### A. Downslope propagation with mode coupling

The geometry for the downslope simulation is given in Fig. 5. Over a majority of the propagation regime, the acoustic field travels down a 2° slope. The effect of multipath propagation for this geometry is evident from Fig. 6, which shows the pressure from the objective source at the receiving array element at depth 20 m. The received signal does not resemble the source function as propagation over 6 km has caused a considerable amount of time spreading due to multipath propagation. If the geometry between the receiving array and objective source is not well known, classification and localization of the objective source is extremely difficult. The goal of the virtual receiver processor is to obtain data that have suffered less distortion. The severity of the envi-

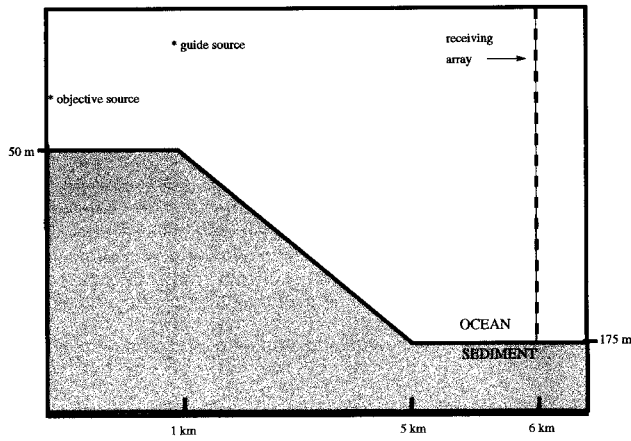


FIG. 5. Downslope example: the objective source and guide source are in 50-m water, receiving array is in 175-m water. The guide source is located 5 km from receiving array at a depth of 20 m and the objective source is located 6 km from receiving array at a depth of 30 m.

ronment can be illustrated by the cumulative coupling matrix  $\mathbf{R} = \mathbf{R}^{J-1} \mathbf{R}^{J-2} \dots \mathbf{R}^{G+1} \mathbf{R}^G$ , which represents the mode coupling due to propagation between the guide source and receiving array, and is shown in Fig. 7 for representative frequencies of 400 Hz and 100 Hz. Any off-diagonal terms indicate energy transfer between modes. Also shown in Fig. 7 is the matrix product  $\mathbf{R}^\dagger \mathbf{R}$  which has been predicted in Sec. II to be approximately diagonal with increasing attenuation for higher-order modes. The results shown in Fig. 7 show that this geometry induces mode coupling and the product  $\mathbf{R}^\dagger \mathbf{R}$  is approximately diagonal.

It has been predicted that the virtual receiver data will look similar to the true receiver data when  $\mathbf{R}^\dagger \mathbf{R}$  is diagonal, as described in Sec. II. For downslope propagation, some of the modes lose energy due to attenuation in the sediment, but no discrete modes are cut off (highly attenuated). In Fig. 8, the virtual receiver data  $v(t)$  and  $V(\omega)$  are plotted together with the true receiver data  $v_T(t)$  and  $V_T(\omega)$  (for clarity of viewing, the source function has been removed from the fre-

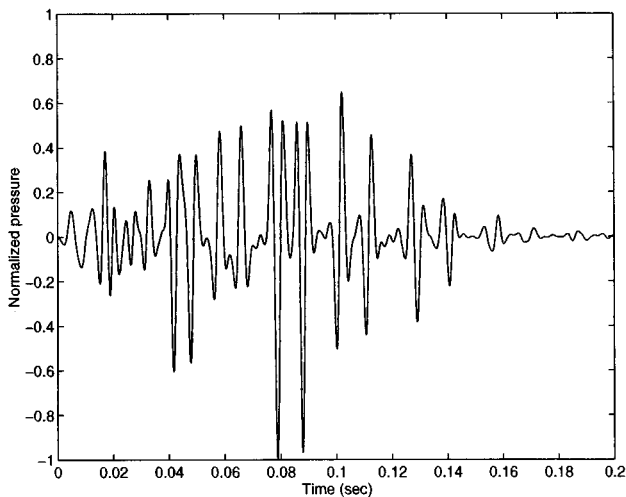


FIG. 6. Downslope example: pressure from the objective source at a receiver in array at depth of 20 m. Note the duration of the time axis in comparison to Fig. 4.

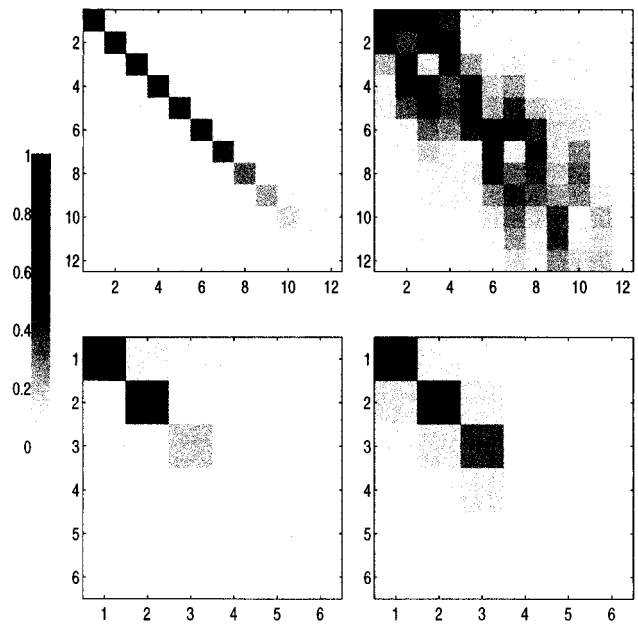


FIG. 7. Magnitude of coupling matrix  $\mathbf{R}$  for downslope propagation; top right—400 Hz, bottom right—100 Hz. Product  $\mathbf{R}^\dagger \mathbf{R}$  for downslope propagation; top left—400 Hz, bottom left—100 Hz. The off-diagonal terms indicate mode coupling has occurred. Product  $\mathbf{R}^\dagger \mathbf{R}$  is approximately diagonal. Axes correspond to row and column numbers.

quency data). Even though  $\mathbf{R}$  is not exactly unitary because of loss,  $\mathbf{R}^\dagger \mathbf{R}$  is approximately diagonal and the virtual receiver data agree well with the true receiver data. The correlation between true and virtual receivers is  $|\Phi| = 0.98$ . The benefit of the virtual receiver is evident; the multipath distortion to the signal is reduced as compared to propagation over the entire 6 km.

## B. Upslope propagation with mode coupling

For the upslope geometry, the sources are placed in deeper water, and the acoustic field propagates upslope to the receiving array as shown in Fig. 9. Many more modes are

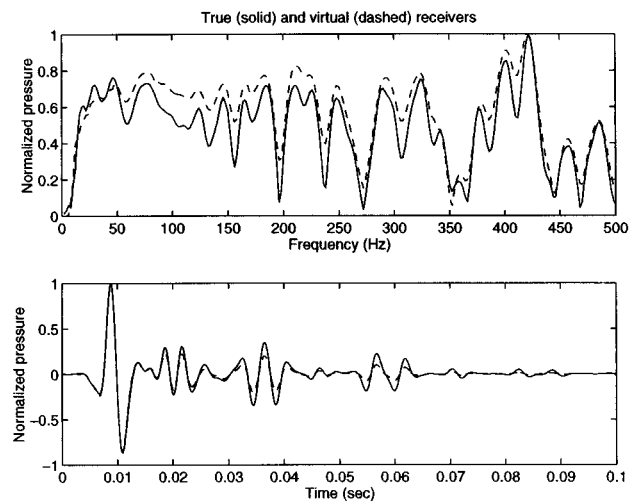


FIG. 8. Downslope example: pressure data for true and virtual receivers. Top is normalized pressure magnitude versus frequency with source function removed. Bottom is normalized pressure versus time.



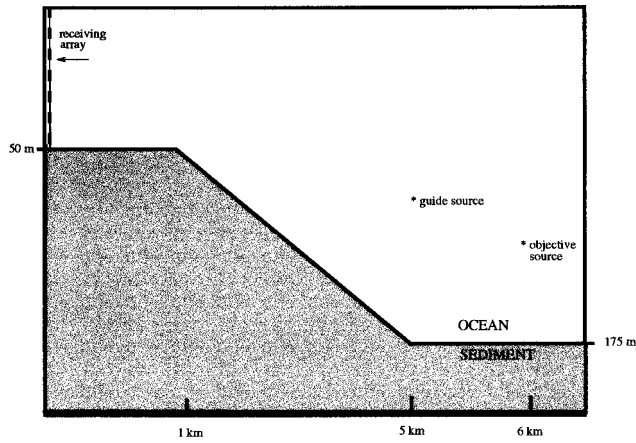


FIG. 9. Upslope example: the objective source and guide source are in 175-m water, receiving array is in 50-m water. The guide source is located 5 km from receiving array at a depth of 130 m, and the objective source is located 6 km from receiving array at a depth of 150 m.

excited in the deeper water than can be supported in the shallow water, and propagation upslope results in modes being cut off. The coupling matrix  $\mathbf{R}$  is the transpose of the coupling matrix for the downslope propagation. If the mode coupling is not too severe, the virtual receiver field should look like a mode-filtered version of the true field, as was described in Sec. II. The virtual receiver data  $v(t)$  and  $V(\omega)$  are plotted together with the true receiver data  $v_T(t)$  and  $V_T(\omega)$  in Fig. 10. While the virtual receiver seems to capture the trend of the true signal, the details are missing, because the virtual receiver is a mode filtered version of the true receiver with cut off modes removed. This will be discussed further in Sec. IV. Note the virtual receiver outperforms the true receiver in that mode filtering due to upslope propagation suppresses multipath arrivals which are significant even at the assumed 1-km range. The correlation for the upslope model is  $|\Phi|=0.7$ .

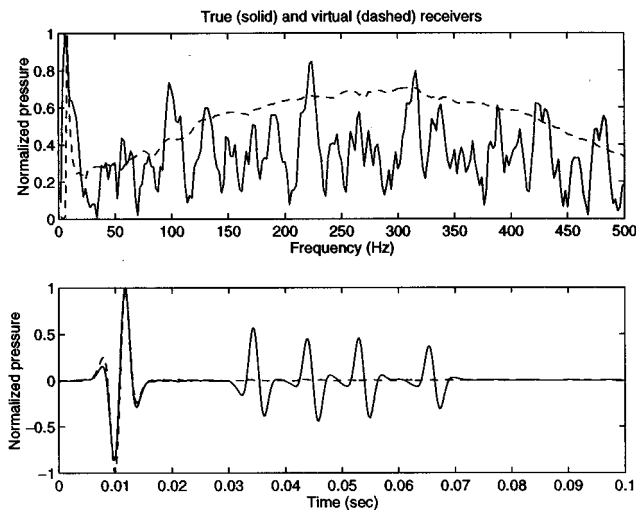


FIG. 10. Upslope example: pressure data for true and virtual receivers. Top is normalized pressure magnitude versus frequency with source function removed. Bottom is normalized pressure versus time.

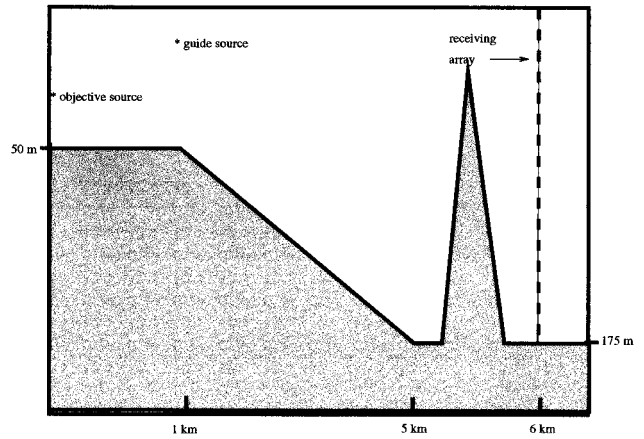


FIG. 11. Strong mode coupling example: the objective source and guide source are in 50-m water, receiving array is in 175-m water. The guide source is located 5 km from receiving array at a depth of 20 m and the objective source is located 6 km from receiving array at a depth of 30 m.

### C. Strong mode coupling

To induce strong mode coupling, a geometry is used which has a  $2^\circ$  slope followed by a  $14^\circ$  obstruction approximating a seamount<sup>18</sup> as illustrated in Fig. 11. While this geometry is not modeled after a particular site, the obstruction produces strong mode coupling and should give insight into the performance of the algorithm in severe environments. Figure 12 illustrates that the severe mode coupling with loss forms an  $\mathbf{R}^\dagger \mathbf{R}$  that is not as diagonal as for downslope propagation without the obstruction and the performance is expected to be worse. The virtual receiver is constructed and is shown together with the true receiver in Fig. 13. The correlation for the strong mode coupling model is  $|\Phi|=0.88$ .

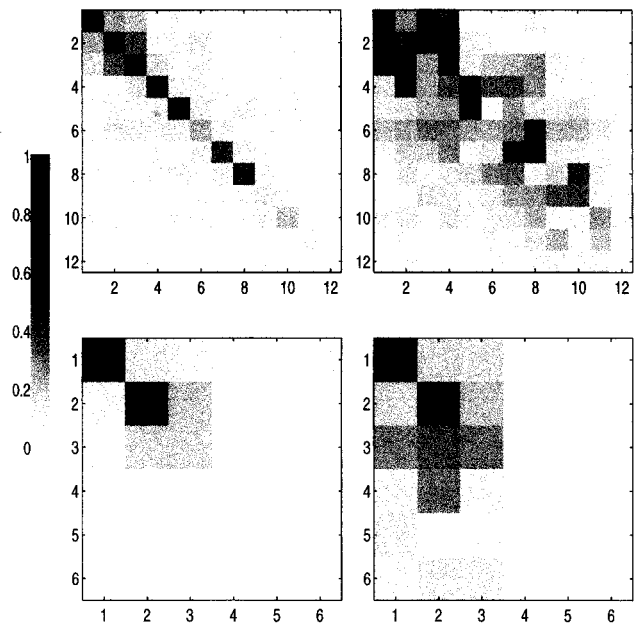


FIG. 12. Coupling matrix  $\mathbf{R}$  for downslope propagation with obstruction; top right—400 Hz, bottom right—100 Hz. Product  $\mathbf{R}^\dagger \mathbf{R}$  for downslope propagation with obstruction; top left—400 Hz, bottom left—100 Hz. Axes correspond to row and column numbers.

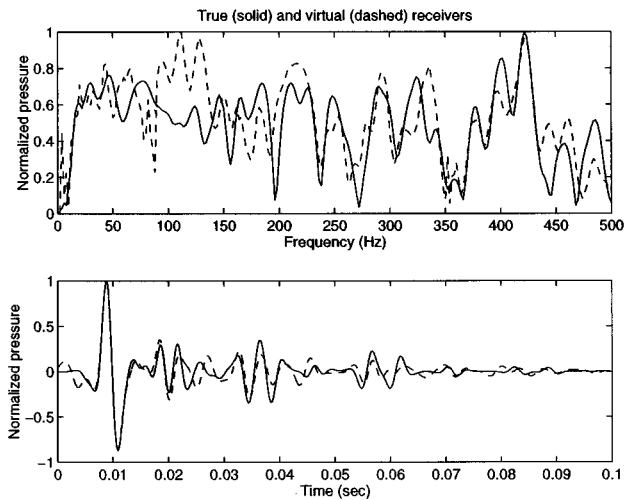


FIG. 13. Strong mode coupling example: pressure data for true and virtual receivers. Top is normalized pressure magnitude versus frequency with source function removed. Bottom is normalized pressure versus time.

#### IV. SOURCE LOCALIZATION BY MATCHED FIELD PROCESSING

The numerical simulations show the performance of the virtual receiver as compared to a true receiver at the location of the guide source. Another test of the algorithm is determining the objective source location given the virtual receiver “data.” Localization by single-receiver matched-field processing is used employing a method addressed in the literature.<sup>14,15</sup> The medium between the guide source and receiving array need not be considered, as the effects of this region have been removed by using the virtual receiver processor.

A normalized correlation function is used to compare the virtual receiver data to calculated candidate source locations in the vicinity of the virtual receiver,

$$\Phi(x, z) = \frac{\sum_n P^{c*}(\omega_n, x, z) V(\omega_n)}{\sqrt{\sum_n P^{c*}(\omega_n, x, z) P^c(\omega_n, x, z)} \sqrt{\sum_n V^*(\omega_n) V(\omega_n)}} \quad (35)$$

For discrete frequency,  $\omega_n$ , the candidate field is  $P^c(\omega_n, x, z)$  and the virtual receiver data is  $V(\omega_n)$ . The source function is removed for matched-field processing, which assumes knowledge of the objective source function. In practice, this may be an unknown quantity as well and may require additional processing. However, given the virtual receiver data, the objective source function can be estimated. The candidate fields are computed using the range-independent normal mode code Kraken.<sup>16</sup> The normal mode method is convenient because it is accurate and computationally efficient. The numerical experiments considered in the previous section are used to illustrate the source localization problem. Range and depth estimates for the objective source can be made using the computed candidate fields and correlation estimator (35). Figure 14 shows the correlation function in depth and range for the downslope geometry shown in Fig. 5. The true depth and range of the objective source are identified as expected. Figure 9 gives the geometry for

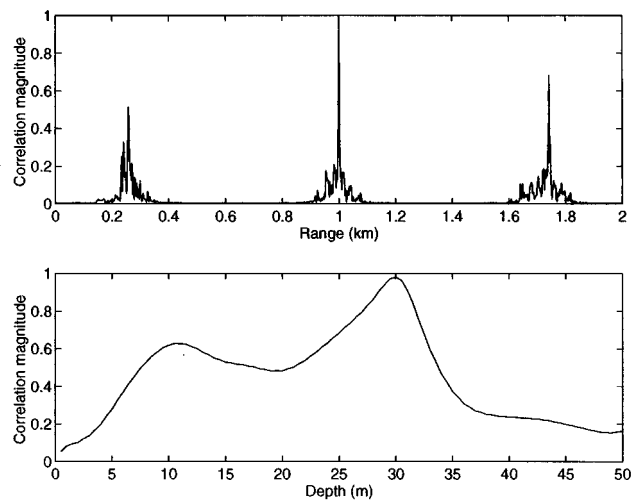


FIG. 14. Downslope results: top is range correlation  $|\Phi(x, z_0)|$  searching at depth of objective source. Bottom is depth correlation  $|\Phi(x_0, z)|$  searching at range of objective source. Objective source is located at range 1 km from guide source and depth 30 m.

the upslope experiment, and correlation giving the predicted objective source location is given in Fig. 15. Surprisingly, the objective source depth and range are still identifiable. When the candidate fields are recalculated using a subset of low-order modes (the candidate field modes are limited to those which are supported in 50-m water depth), the correlation magnitude approaches unity but the sidelobes increase as well. The new correlation function is shown in Fig. 16. This is consistent with the notion of mode stripping and the virtual receiver being a mode filtered version of the true field. Figure 17 shows the correlation for the strong mode coupled experiment which has geometry given in Fig. 11. Similar to the downslope experiment, the correlation is nearly unity, and the objective source range and depth are identified.

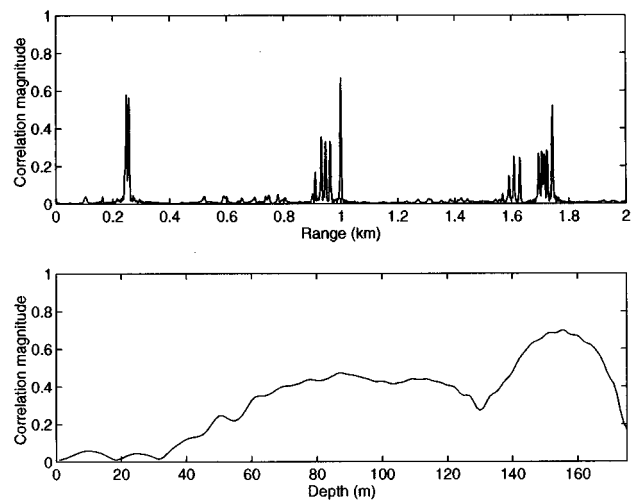


FIG. 15. Upslope results: top is range correlation  $|\Phi(x, z_0)|$  searching at depth of objective source. Bottom is depth correlation  $|\Phi(x_0, z)|$  searching at range of objective source. Objective source is located at range 1 km from guide source and depth 150 m.

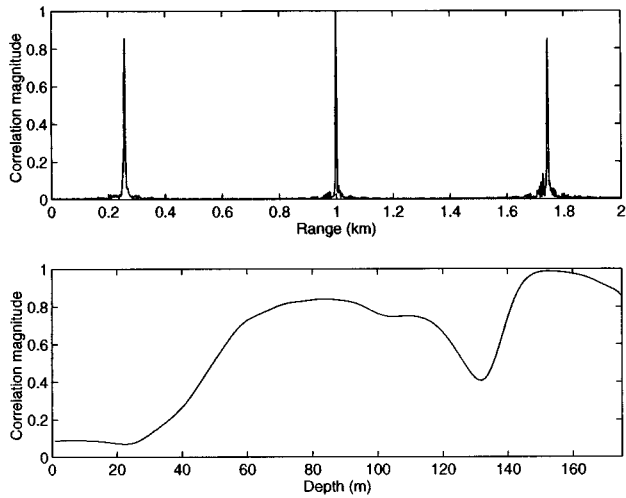


FIG. 16. Upslope results with reduced mode set: top is range correlation  $|\Phi(x, z_0)|$  searching at depth of objective source. Bottom is depth correlation  $|\Phi(x_0, z)|$  searching at range of objective source. Objective source is located at range 1 km from guide source and depth 150 m.

### V. RESTRICTIONS ON SPATIAL SEPARATION OF GUIDE AND OBJECTIVE SOURCES

Considering only the bistatic sonar application in which the guide source ensonifies the target and provides compensation for multipath, the guide source must be neither too near nor too far from the target. If the guide source is too near, its signal and the target echo will overlap at the receiving array and cannot be separated in the time domain. Separation is essential to the implementation of the virtual receiver (2). On the other hand, if the guide source is too far from the target, it will not properly sample the region between the target and the array. Rather simple considerations can be used to determine the minimum separation between guide source and target. Take  $c$  to be a nominal sound speed defined in terms of the time of arrival of the leading edge of the guide source transmission at the array. We assume that

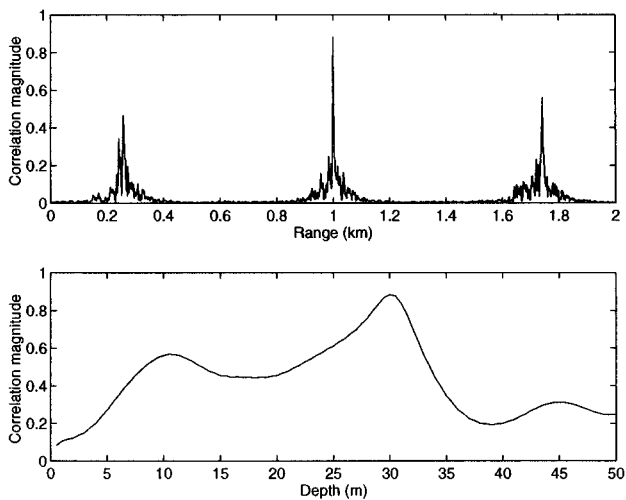


FIG. 17. Strong mode coupling results: top is range correlation  $|\Phi(x, z_0)|$  searching at depth of objective source. Bottom is depth correlation  $|\Phi(x_0, z)|$  searching at range of objective source. Objective source is located at range 1 km from guide source and depth 30 m.

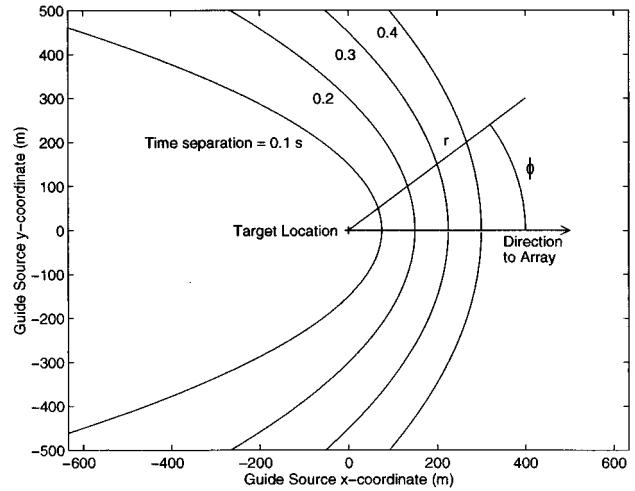


FIG. 18. Minimum guide source and target separations needed to separate the signals in the time domain.

this same speed will give a sufficiently accurate estimate of the arrival time of the target echo, even though somewhat different bathymetry and sound-speed profiles may be appropriate. Let  $T$  be the difference in arrival time at the array of the target echo and guide source “direct blast.” Then,

$$cT = 2r \cos^2(\phi/2), \quad (36)$$

where  $r$  and  $\phi$  are polar coordinates centered on the target, with  $r$  being the horizontal range to the guide source from the target and  $\phi$  being the angle subtended at the target location by lines connecting the target to the array and guide source (Fig. 18). It is assumed that the array–target range is much greater than  $r$ , the guide-source–target range. As an illustration, consider the case depicted in Fig. 6 for which the duration of the direct blast is about 0.2 s. Then, separation demands that  $cT$  must be greater than 300 m. If the guide source lies between the target and array ( $\phi = 0^\circ$ ), then the guide-source–target range must satisfy  $r > 150$  m. If the guide source and target ranges to the array are equal ( $\phi = 90^\circ$ ),  $r > 300$  m. The worst case occurs when the guide source is down range of the target and on a line through the array and target. Then  $\phi = 180^\circ$  and the condition for separation cannot be satisfied for any  $r$ .

Considering the maximum allowable separation between the guide source and target, the inhomogeneity of the environment is the determining factor and the variety of possibilities is too great to permit development of simple rules. It is useful, however, to compare the guide-source method with more standard sonar methods, which also suffer due to inhomogeneity of the environment. First consider the case in which the guide source lies between the target and array, so that the guide-source–array path coincides with a portion of the target–array path. In this case, the virtual receiver implementation (2) is useful even if the environment between the guide source and target is unknown and range dependent, provided cross-range variability of the environment is not severe enough to invalidate the two-dimensional propagation assumption. In this case, the output of the virtual receiver is a mode-filtered version of the output of a true receiver at the same location, and multipath effects will be

reduced compared to those seen at the array. As shown in examples presented earlier in this article, this will provide a “cleaner” target echo signature than seen at the array, assuming that environmental uncertainty does not permit accurate matched-field processing of the array output. A matched field processor can compensate for multipath in a fashion analogous to the guide source method, but this demands that the model environment used to compute replicas matches the true environment. This is precisely the problem that the virtual receiver concept addresses. If the application demands source localization, echo arrival time can be used to partially localize the target via Eq. (36). If better localization is required, the output of the virtual receiver can be used as the input to a single hydrophone method, such as that illustrated in Sec. IV. Note that the range-azimuth information provided by Eq. (36) and range determined by single hydrophone localization can be used to partially resolve range ambiguities and to obtain information on target azimuth. The success of this type of source localization depends on the degree of range independence between the guide source and target, and on knowledge of the ocean medium in this region. In any case, the virtual receiver should provide better source localization than could be obtained using a more distant single hydrophone.

A new issue arises if the guide source and target have azimuthal separation as viewed from the array. Then the guide source does not sample the target–array path, and cross-range variability of the environment may degrade the virtual receiver. This is a difficult issue whose resolution is beyond the scope of this article, but some understanding can be obtained by appealing to cross-range variability as it affects beamforming for conventional horizontal arrays. The virtual receiver algorithm (2) exploits the phase differences between the direct blast and target echo in that it employs a coherent cross correlation between these two signals. Thus the largest allowable cross-range separation between the guide source and target should be approximately equal to the largest horizontal aperture that can be formed. For example, in an experiment conducted in 1976, Williams measured coherence times of approximately 3–8 min allowing the formation of synthetic apertures of about 900 m at 400 Hz.<sup>17</sup> The correspondence between maximum horizontal aperture and maximum guide-source–target cross-range separation is not rigorous; however, as the guide source algorithm exploits signal coherence over the entire water column, the horizontal array occupies a single depth. The exact allowable cross-range separation of the guide and objective sources will depend on the particular environment.

## VI. NOISE

The noise performance of the virtual receiver has not been analyzed, but some general observations can be made. In applications where the guide source and objective source are of similar strength, the algorithm of Eq. (2) will treat noise nonlinearly, as it involves the product of the two signals. Assuming that the signal/noise ratio is large for both signals, the signal–noise cross terms will dominate the noise–noise term. In the bistatic sonar application, the direct blast will in most cases be much larger than the target echo,

and the guide source noise component can be neglected. In this case, the virtual receiver processor behaves linearly with respect to noise and in a fashion identical to a matched-field processor having the target echo as noisy input data and the direct blast as noiseless replica data. Note that the equivalent matched field processor has unequal source and replica locations; the former is at the guide source location and the latter is at the target location. Thus the noise at the output of the virtual receiver has been subjected to spatial and temporal filtering, with both filters matched to the guide source signal. If the output of the virtual receiver is subjected to further processing for the purpose of source localization, the noise output of the single hydrophone matched-field processor will also be linear in the input noise. In this case, there are two stages to the analysis of noise: (1) determination of the virtual receiver output noise, and (2) determination of the effect of this virtual receiver noise on the output of the single hydrophone matched-field processor.

## VII. DISCUSSION AND CONCLUSIONS

This paper has addressed two concerns, multipath distortion and source localization in lossy range-dependent shallow water environments. For situations where the details of the environment are not well known, a broadband guide source can be used to construct a virtual receiver. The numerical results show that when the guide source is near the objective source, the virtual receiver output has reduced multipath effects, as would be expected from a nearby true receiver. For source localization, use of the single guide source to create a virtual receiver can reduce the environmental mismatch problem and effectively localize targets. Mode coupling and lossy propagation, which are concerns relevant to shallow water acoustics, have been considered. The results for the virtual receiver algorithm seem promising for the typical shallow water geometries given here. The combination of strong mode coupling and loss can reduce the quality of the virtual receiver as compared with a true receiver at the same location. This was illustrated in the numerical results for acoustic simulation over an obstruction producing strong mode coupling. When modes have been cut off, such as for upslope propagation, the virtual receiver may represent a mode filtered version of the true field. This can, in some cases, improve suppression of multipath arrivals.

## ACKNOWLEDGMENTS

This work has been supported by the Naval Research Laboratory. The authors are indebted to Dr. David Drumheller and Dr. Charles Gaumont for suggesting an investigation based on the guide star concept. A preliminary version of the mode coupling analysis was supported by the Office of Naval Research, Code 3210A.

<sup>1</sup>R. Benedict, Jr., J. B. Breckinridge, and D. L. Fried, “Atmospheric-compensation technology (feature),” *J. Opt. Soc. Am. A* **11**, 257–451 (1994).

<sup>2</sup>P. D. Mourad, D. Rouseff, R. P. Porter, and A. Al-Kurd, “Source localization using a reference wave to correct for oceanic variability,” *J. Acoust. Soc. Am.* **92**, 1031–1039 (1992).

<sup>3</sup>A. Al-Kurd, “Holographic array processing in the ocean,” University of

- Washington, Applied Physics Laboratory Technical Report APL-UW-TR 9306 (1993).
- <sup>4</sup>A. Al-Kurd and R. P. Porter, "Performance analysis of the holographic array processing algorithm," *J. Acoust. Soc. Am.* **97**, 1747–1763 (1995).
- <sup>5</sup>A. Parvulescu and C. S. Clay, "Reproducibility of signal transmissions in the ocean," *Radio Electron. Eng.* **29**, 223–228 (1965).
- <sup>6</sup>A. Parvulescu, "Matched-signal (mess) processing by the ocean," *J. Acoust. Soc. Am.* **98**, 943–960 (1995).
- <sup>7</sup>D. R. Jackson and D. R. Dowling, "Phase conjugation in underwater acoustics," *J. Acoust. Soc. Am.* **89**, 171–181 (1991).
- <sup>8</sup>C. Prada, F. Wu, and M. Fink, "The iterative time reversal mirror: A solution to self-focusing in the pulse-echo mode," *J. Acoust. Soc. Am.* **90**, 1119–1129 (1991).
- <sup>9</sup>W. A. Kuperman, W. S. Hodgkiss, H. C. Song, T. Akal, C. Ferla, and D. R. Jackson, "Phase conjugation in the ocean: experimental demonstration of an acoustic time reversal mirror," *J. Acoust. Soc. Am.* (submitted).
- <sup>10</sup>F. B. Jensen, W. A. Kuperman, M. B. Porter, and Henrik Schmidt, *Computational Ocean Acoustics* (American Institute of Physics, New York, 1994).
- <sup>11</sup>D. Rouseff, M. Siderius, W. L. J. Fox, and R. P. Porter, "Acoustic calibration in shallow water using sparse data," *J. Acoust. Soc. Am.* **97**, 1006–1013 (1995).
- <sup>12</sup>R. B. Evans, "A coupled mode solution for acoustic propagation in a waveguide with stepwise depth variations of a penetrable bottom," *J. Acoust. Soc. Am.* **74**, 188–195 (1983).
- <sup>13</sup>M. D. Collins and E. K. Westwood, "A higher-order energy conserving parabolic equation for range-dependent ocean depth, sound speed, and density," *J. Acoust. Soc. Am.* **89**, 1068–1075 (1991).
- <sup>14</sup>N. L. Frazer and P. I. Pecholcs, "Single-hydrophone localization," *J. Acoust. Soc. Am.* **88**, 995–1002 (1990).
- <sup>15</sup>A. Tolstoy, *Matched Field Processing for Underwater Acoustics* (World Scientific, River Edge, NJ, 1993).
- <sup>16</sup>M. P. Porter, "The kraken normal mode program," Report SM-245, SACLANT Undersea Research Centre (1991).
- <sup>17</sup>R. E. Williams, "Creating an acoustic synthetic aperture in the ocean," *J. Acoust. Soc. Am.* **60**, 60–73 (1976).
- <sup>18</sup>N. R. Chapman and G. R. Ebbeson, "Acoustic shadowing by an isolated seamount," *J. Acoust. Soc. Am.* **73**, 1979–1984 (1983).

# Comparison between prediction and measurement of viscoelastic moduli in composite materials versus temperature using ultrasonic immersion technique with oil

Sandrine Baudouin and Bernard Hosten<sup>a)</sup>

Laboratoire de Mécanique Physique, Université de Bordeaux I, URA C.N.R.S. No. 867, 351, Cours de la Libération, 33405-Talence Cedex, France

(Received 24 October 1996; accepted for publication 29 July 1997)

An oil immersion ultrasonic method used for measuring elastic and viscoelastic properties of materials versus temperature is presented. From velocity and amplitude measurements, the complex viscoelastic tensor can be entirely determined from room temperature to temperatures near the glass transition temperature of the material. This tensor permits the computation of velocities and attenuations of heterogeneous or homogeneous modes in any direction of wave propagation. A micromechanics model is used to compare experimental results with theoretical ones and to analyze anisotropic elastic and viscoelastic behavior of composite materials. © 1997 Acoustical Society of America. [S0001-4966(97)01112-0]

PACS numbers: 43.35.Cg, 43.35.Mr [HEB]

## INTRODUCTION

Composite materials made of long fibers and a polymer matrix are commonly used in the aerospace, automotive, or naval industry. To predict the mechanical behavior, it is mandatory to measure the stiffness of these anisotropic materials. In the last two decades, ultrasonic methods have been shown to be appropriate for measuring the real<sup>1</sup> or complex<sup>2</sup> stiffness tensor of composites in their initial states or damaged states. Contact or water immersion methods provide precise measurements of the components of the tensor. Immersion methods are useful when the sample is unique and anisotropic. Noncontact methods using laser<sup>3</sup> or air-coupled transducers<sup>4-6</sup> are still in development and not yet easily adaptable for industrial applications.

The nondestructive measurement method presented here is a variation of the immersion ultrasonic method. A low-viscosity oil is used as the coupling medium instead of water. This method permits one to measure velocities and amplitudes of bulk waves propagating inside the material as temperature changes.

After describing the laboratory techniques, the procedures used to recover the elastic and viscoelastic properties of materials are presented. Preliminary stiffness measurements of the matrix used in composite materials will then be presented and used as the basic data in a micromechanics model.<sup>7,8</sup> Temperature-dependent composite material properties obtained experimentally will then be compared with the micromechanics model predictions.

## I. MATERIALS AND APPARATUS

Two materials are used in this study. The first one is a polymer matrix and the second one is the same matrix reinforced with long unidirectional glass fibers. The first material is assumed to be representative of the matrix used in the

composite material. The composite sample has 32 plies. Its density is 1.8 g/cm<sup>3</sup>, and its thickness is 5.72 mm. The matrix sample has a density of 1.20 g/cm<sup>3</sup>. Its thickness is 6.90 mm. The volume fraction of fibers in the composite material is 0.448.

Both samples are absorbent. Their mechanical properties can be represented by the complex viscoelastic tensor<sup>9</sup>

$$C_{ij}^* = \begin{bmatrix} C_{11}^* & C_{12}^* & C_{13}^* & 0 & 0 & 0 \\ & C_{22}^* & C_{23}^* & 0 & 0 & 0 \\ & & C_{33}^* & 0 & 0 & 0 \\ & & & C_{44}^* & 0 & 0 \\ \text{Sym} & & & & C_{55}^* & 0 \\ & & & & & C_{66}^* \end{bmatrix},$$

$$\text{where } [C_{ij}^*] = [C'_{ij}] + i[C''_{ij}]. \quad (1)$$

The real parts  $C'_{ij}$  of the tensor are the elastic moduli. The imaginary parts  $C''_{ij}$  are the viscoelastic moduli and represent the attenuative properties of the material. The signal reduction arising from diffraction is supposed to be negligible in the frequency domain were the wavelength is longer than the fibers size and ply thickness. These properties include viscoelasticity effects from the matrix and losses due to diffraction from the fibers. The attenuation is assumed to be small so that  $C''_{ij} \ll C'_{ij}$ .

When the orthotropic symmetry is assumed, nine moduli are independent and the material has three planes of mirror symmetry.<sup>10</sup> In the case of a unidirectional composite, only five moduli are independent due to transverse isotropy. These moduli are  $C_{11}^*$ , identified from axis 1 (see Fig. 1);  $C_{66}^*$ , identified from  $P_{12}$  plane; and  $C_{33}^*$ ,  $C_{55}^*$ , and  $C_{13}^*$ , identified from  $P_{13}$  plane. The  $P_{12}$  plane is quasi-isotropic, while  $P_{13}$  is highly anisotropic (Fig. 1). The isotropic symmetry of polymer materials is represented by only two moduli:  $C_{11m}^*$  and  $C_{66m}^*$ .

<sup>a)</sup>Electronic mail: hosten@lmp.u-bordeaux.fr

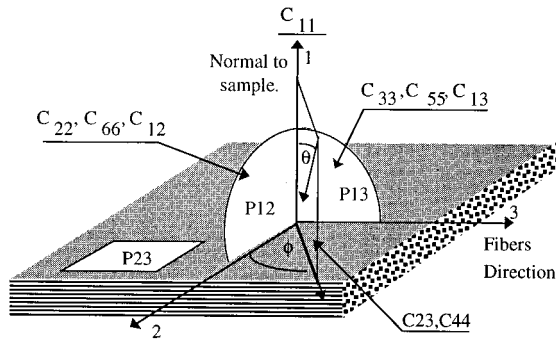


FIG. 1. Planes and axes of symmetry in a unidirectional composite.

To measure these quantities by the immersion technique, wave velocity and amplitudes are measured in several directions in the sample. The material properties are related to the acoustic parameters by complex Christoffel's equations:

$$|\Gamma_{ij}(*C_{ij}, *S_i * S_j) - \rho \delta_{ij}| = 0, \quad (2)$$

where  $\Gamma_{ij}$  is expressed as a function of  $C_{ij}$  and complex slowness vector components<sup>2</sup> and  $\rho$  is the mass density. The measurement method uses ultrasonic bulk waves transmitted in normal and oblique incidence through the sample immersed in a fluid. A plane wave propagating in the liquid generates three bulk modes in an anisotropic material at the liquid/solid interface and only two (QL: quasi-longitudinal and QT: quasi-shear modes) in a plane of symmetry.<sup>9</sup>

The usual fluid, water, is replaced by oil. This modification allows for measurements near the glass transition ( $\approx 130^\circ\text{C}$ ) of materials. A commercial regulation system suppresses temperature gradients in the tank. The stability of the velocity measurement in normal incidence, through the sample, attests that the sample is at the fluid temperature. Typically, this is reached in a few minutes and all of the measurements are done in a few hours. The sample is supported by a goniometer that allows one to change the angle of incidence (Fig. 2). The wave transmitted through the sample is received by a second transducer that is translated at the Snell's law position to minimize the effect of the limited size of the transducer. Both transducers can withstand temperatures up to  $250^\circ\text{C}$  and are broadband in frequency ( $\nu = 0.5\text{--}5\text{ MHz}$ ).

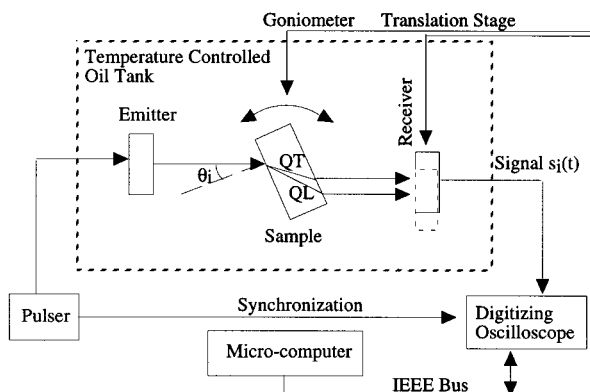


FIG. 2. System schematic diagram.

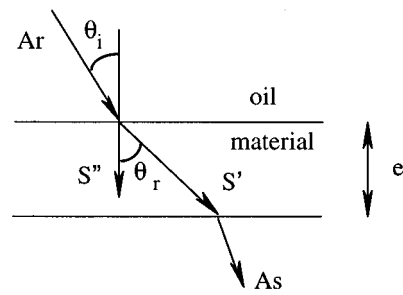


FIG. 3. Wave conversion at fluid/solid interface.

A signal, called the reference signal  $r(t)$ , corresponds to the wave transmitted without the sample between the transducers. Signals  $s_i(t)$  correspond to the waves transmitted through the sample for several angles of incidence  $\theta_i$ . The experiment is repeated for temperatures from  $40^\circ\text{C}$  to  $130^\circ\text{C}$ .

A transfer function  $H_i(\nu)$  can be computed for each angle  $\theta_i$  from the relation  $H_i(\nu) = S_i(\nu)/R(\nu) = A_i(\nu) \exp(i\varphi_i(\nu))$ , where  $S_i(\nu)$  and  $R(\nu)$  are the Fourier transforms of  $s_i(t)$  and  $r(t)$ , respectively.  $A_i(\nu)$  is the amplitude of the transfer function. The slope of the phase  $\varphi_i(\nu)$  furnishes the time of flight  $\tau_i$ . The wave velocity  $V_i$  in the sample can be determined from  $\tau_i$  and  $e$ , the thickness of the sample, with the following equation:

$$V_i = \frac{V_o}{\sqrt{1 + V_o \tau_i / e (V_o \tau_i / e - 2 \cos \theta_i)}}. \quad (3)$$

To use this relation, the wave velocity  $V_o$  in the incident medium (oil) needs to be known.

The incident wave is assumed to be a plane wave. Its displacement field  $\vec{U}$  is given by  $\vec{U} = \vec{P} \exp(i2\pi\nu\vec{S}\cdot\vec{M})$ , where  $\vec{P}$  is the polarization vector and  $\vec{M}$  is the position vector. The slowness complex vector  $*\vec{S}$  is composed of  $\vec{S}'$ , the propagation vector (its modulus is the inverse of the phase velocity), and  $\vec{S}''$ , the damping vector, such that  $*\vec{S} = \vec{S}' - i\vec{S}''$ . Since the incident medium is assumed to be a nonlossy material, Snell's law implies that  $\vec{S}''$  is perpendicular to the interface (Fig. 3) and the propagating wave inside the material is heterogeneous.<sup>2</sup>

From the amplitude loss  $A_i(\nu)$  of the signal, it is possible to know the wave attenuation. This attenuation is expressed with the modulus damping vector of heterogeneous modes:

$$S_i''(\nu) = -\frac{1}{2\pi\nu e} \ln\left(\frac{A_i(\nu)}{T_i'}\right). \quad (4)$$

The transmission coefficient  $T_i'$  of bulk modes through the two interfaces at the angle  $\theta_i$  is computed from the velocities of the QL and QT modes.<sup>2</sup>

The projection  $S_i'' \cos(\theta_r)$  of this vector can be related to the classical attenuation coefficient<sup>11-13</sup>  $\alpha_i(\nu) = 2\pi\nu S_i'' \cos(\theta_r)$ . This coefficient is nearly linear versus frequency. However, if a linear curve is used to fit experimental data, then the fitted curve does not go through the origin. To avoid this problem at the origin, a second-order polynomial

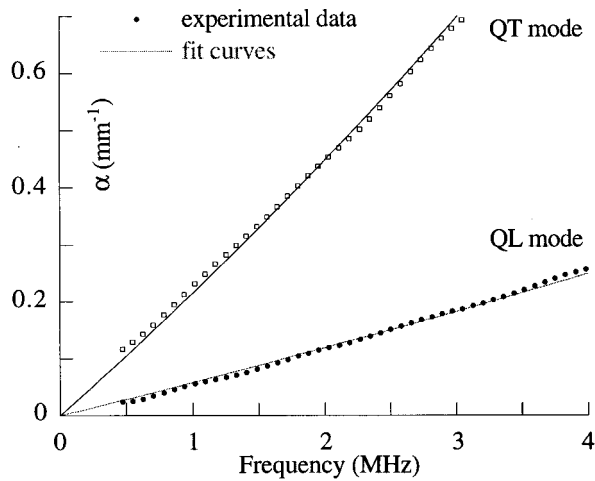


FIG. 4. Attenuation coefficient versus frequency in the matrix at 40 °C.

is used to model the attenuation coefficient versus frequency (Fig. 4). So,  $S''$  has small dependence on the frequency (Fig. 5).

Silicone oil, low in viscosity, is used as the coupling medium. The phase velocity of the oil needs to be known as a function of temperature. To make this measurement, a glass sample is placed in the tank. Longitudinal and transverse wave velocities in glass were previously measured at several temperatures, in a water tank. These velocities were found to be temperature independent. Once these parameters are known, Eq. (3) is used to express  $V_o$  as a function of  $V_i$ . Performing this procedure for different temperatures, one obtains the variation of  $V_o$  as a function of temperature (Fig. 6).

The relation  $V_o(\text{mm}/\mu\text{S}) = 1.66 - 0.0034T$  is obtained by a linear fit of experimental data and is used in Eq. (3). In the same way, the temperature dependence of the attenuation of oil is measured. Above 40 °C, it is negligible in comparison to the attenuation of the tested materials. The good reproducibility of the oil property measurements is a good check for the temperature stability.

The immersion technique with oil is first performed on the isotropic polymer. At 40 °C, the wave velocities of longitudinal and transverse modes in the matrix alone are measured in water and oil. Figure 7 shows very good agreement

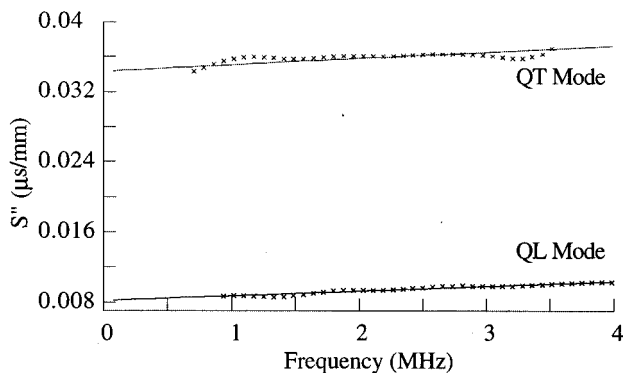


FIG. 5. Magnitude of the damping vector versus frequency in the matrix, at 40 °C.  $\times$ : experimental data. —: fit curve.

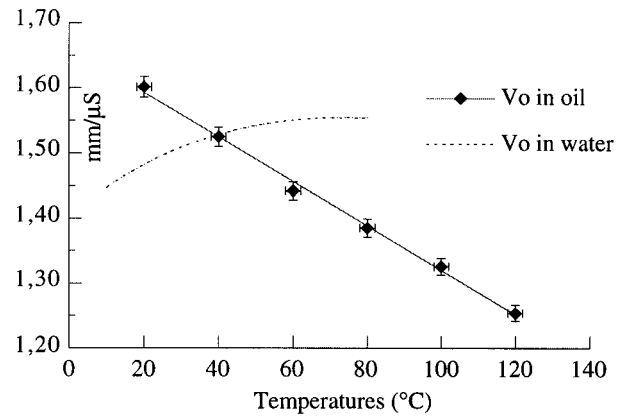


FIG. 6. Sound speed in the immersion medium versus temperature.

between both measurements for longitudinal waves as well as for transverse ones. Velocities are also measured in this material at 120 °C, with the oil coupling medium. The isotropy is preserved at 120 °C, which is near glass transition temperature. These results indicate that the immersion technique with oil can produce valid measurements in this range of temperatures. The attenuation curves presented in Fig. 8 for longitudinal and transverse modes at 40 °C are obtained from measurements (points) and computations (solid lines). The attenuations are calculated for any angle of incidence from the values of  $C_{ij}^*$  (Sec. II).

## II. COMPLETE VISCOELASTIC CHARACTERIZATION OF THE MATRIX

### A. Procedure of $C_{ij}^*$ identification and precision of results

Once the acoustic parameters of materials are measured in several propagation directions, the complex Christoffel equations [Eq. (2)] permit us to link them with the material properties of the medium.<sup>14</sup> When the propagation is along a symmetry axis  $i$ , the attenuation  $S''(\nu)$  is related to the viscoelastic moduli  $C_{ii}''$  and the loss tangent  $\tan \delta_{ii}$  by the equation

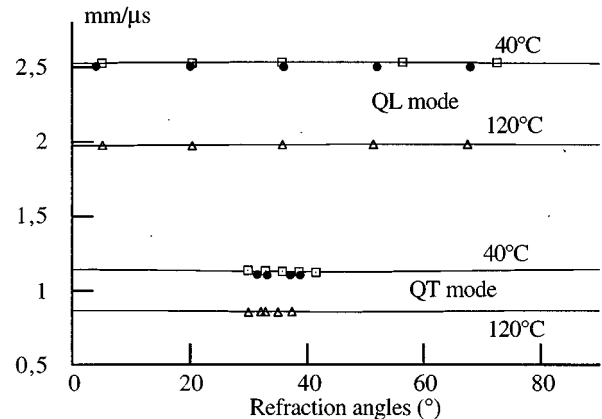


FIG. 7. Phase velocities in matrix.  $\square$ : velocities measured in oil (40 °C).  $\bullet$ : Velocities measured in water (40 °C).  $\triangle$ : Velocities measured in oil (120 °C). Solid lines: Velocities computed from  $C_{ij}^*$ , identified from data.



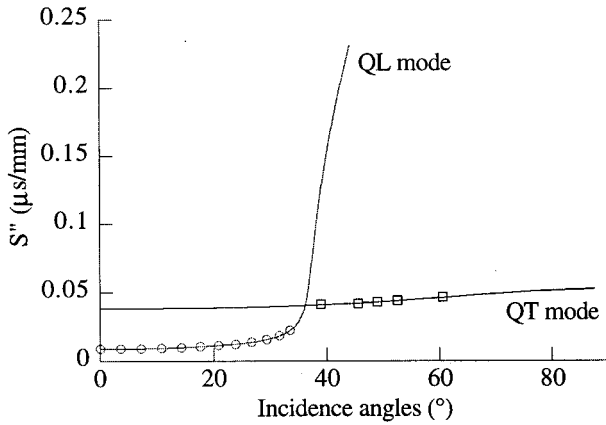


FIG. 8. Damping vector versus incidence angles in the matrix at 40 °C. ○: experimental data. —: computed  $S''$  from  $C'_{ijm}^*$  values.

$$\frac{2S''}{S'} = \frac{C''_{ii}}{C'_{ii}} = \tan \delta_{ii}. \quad (5)$$

Since it is difficult to identify 9 complex coefficients (18 real coefficients), the  $C'_{ij}$  are first identified from the real part measurement of the slowness vector by the following minimization procedure described in Appendix.

Let  $\mathcal{P}$  be a vector composed of  $p_i$  ( $i \in [1, \dots, n]$ ) unknown  $C'_{ij}$ . Along an axis of symmetry,  $\mathcal{P}$  has only one component. For example, in direction 1 (defined in Fig. 1),  $\vec{\mathcal{P}} = [C'_{11}]$ . In a plane of symmetry, there are three unknown components: in  $P_{12}$ ,  $\vec{\mathcal{P}} = [C'_{22}, C'_{66}, C'_{12}]$ , and in  $P_{13}$ ,  $\vec{\mathcal{P}} = [C'_{33}, C'_{55}, C'_{13}]$ . Since hexagonal symmetry is assumed for unidirectional composites,  $C'_{12} = 2 * C'_{66} - C'_{11}$  and  $C'_{11} = C'_{22}$ , which means that only five independent moduli exist.

The real part of the data vector  $*\tilde{S} = [*\tilde{S}_k]$  is then computed from the  $C'_{ij}$ . The components lying in the interface also are computed from Snell's law.

The imaginary parts of the viscoelasticity tensor are measured with a procedure similar to the one used for the real part. Only the imaginary component of  $S''$  perpendicular to the interface is measured. The unknown vector  $\mathcal{P}$  is simultaneously equal to  $[C''_{11}]$  in direction 1,  $[C''_{22}, C''_{66}, C''_{12}]$  in the plane  $P_{12}$ , and  $[C''_{33}, C''_{55}, C''_{13}]$  in the plane  $P_{13}$ . Like  $S''$ , the  $C''_{ij}$  also have small frequency dependence. Therefore,  $C''_{ij}$  and  $\tan \delta_{ij}$  will be specified for a specific frequency.

The upper bounds of the relative errors  ${}^+r_i$  for each of those parameters are then computed from the insensitivity matrix  $I_{ik}$  (see the Appendix):

$${}^+r_i \leq \sum_k |I_{ik} e_k|. \quad (6)$$

The terms  $e_k$  are the computed differences between the measurements and the computed values from identified parameters. From the  $*C'_{ij}$  and the Christoffel equations, it is possible to compute the values of  $S''$  for heterogeneous or homogeneous modes.<sup>2</sup> From the values of  $S''$ , the attenuation in each direction of the wave propagation in the material may be determined.

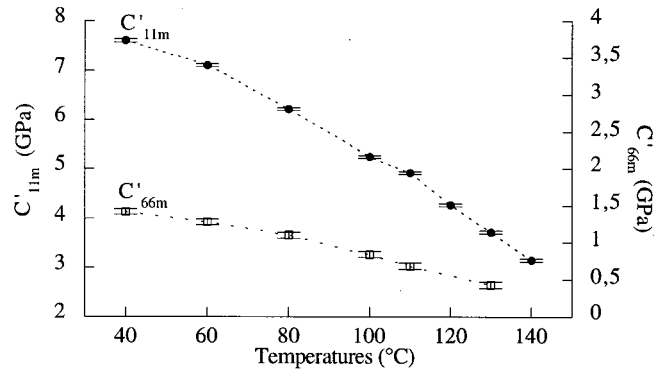


FIG. 9. Elastic moduli of the matrix versus temperature.

## B. Viscoelastic moduli of the matrix as a function of temperature

The measurement and identification procedures are performed for several temperatures between 40 °C and 130 °C for the matrix. The changes in the elastic moduli are shown in Fig. 9.

Like the velocities, these moduli decrease as temperature increases. The errors specified on the graph are computed by the previous procedure and represent only a few percent of each value. The two curves are fitted with a polynomial for  $C'_{11m}$ , and a linear curve for  $C'_{66m}$ , with the result

$$C'_{11m} = 7.7 + (3.8 \times 10^{-3})T - (2.4 \times 10^{-4})T^2 \text{ GPa},$$

$$C'_{66m} = 2.1 - (1.2 \times 10^{-2})T \text{ GPa}.$$

Similarly, the changes in the loss tangent,  $\tan \delta_{ii}$ , are shown in Fig. 10. The comparison between these curves and classical curves of loss tangent in polymers<sup>15</sup> suggests that the glass transition temperature is not reached, as curves grow without arriving at any peak. The most pronounced variation is of  $\tan \delta_{66m}$ . This amount of loss is expected since this loss tangent is related to the transverse mode, which is often more attenuated than the longitudinal one. The variations of  $C''_{11m}$  and  $C''_{66m}$  give two equations as a function of temperature.

## III. HASHIN'S MODEL FOR THE PREDICTION OF VISCOELASTIC MODULI

Several models<sup>16,17</sup> have been tested to predict the viscoelastic complex moduli of composite materials. Hashin's

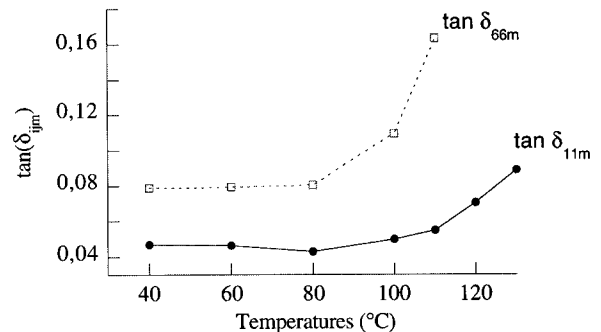


FIG. 10. Matrix loss tangents versus temperature.

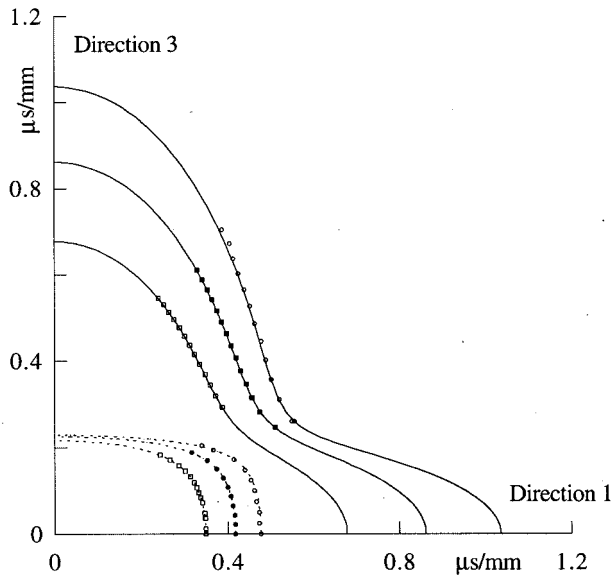


FIG. 11. Real part of slowness vector in plane P13. ---: QL modes. ○: 120 °C. —: QT modes. ●: 100 °C. □: 40 °C.

micromechanics model<sup>7,8</sup> seems to be the one that gives the best matching with experimental values of composite material properties. To use this model the previous equations of  $C'_{11m}(T)$ ,  $C'_{66m}(T)$ ,  $C''_{11m}(T)$ , and  $C''_{66m}(T)$  are introduced in the model as matrix data. Fibers' characteristics are also needed and are given by the manufacturer. They are assumed to be elastic and independent of temperature.

The main hypotheses made when using Hashin's model is that the matrix is the only source of attenuation in the composite. These assumptions are true to a good approximation for the frequency range used here to characterize materials.<sup>18,19</sup>

Hashin's model is expressed in terms of the following constants:  $k$  is the plane strain bulk modulus,  $E_l$  is the Young's modulus in the fiber direction,  $G_l$  is the axial shear modulus,  $G_t$  is the transverse shear modulus, and  $\nu_1$  is the axial Poisson ratio. All these parameters are expressed as a function of matrix and fiber constants, denoted below by the subscripts "m" and "f," respectively.

$$k = k_m(k_f + G_m)V_m + k_f(k_m + G_m)V_f / ((k_f + G_m)V_m + k_f(k_m + G_m)V_f), \quad (7)$$

$$G_t = G_m(G_m V_m + G_f(1 + V_f)) / (G_m(1 + V_f) + G_f V_m), \quad (8)$$

$$E_l = E_m V_m + E_f V_f + 4V_m V_f (v_f - v_m)^2 / (V_m/k_f + V_f/k_m + 1/G_m), \quad (9)$$

$$\nu_1 = v_m V_m + v_f V_f + V_m V_f (v_f - v_m) (1/k_m - 1/k_f) / (V_m/k_f + V_f/k_m + 1/G_m), \quad (10)$$

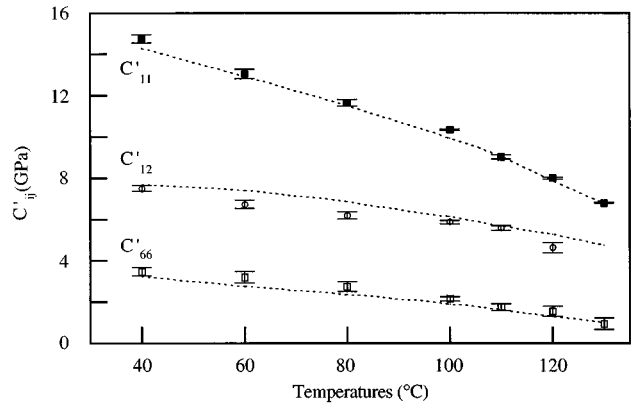


FIG. 12. Comparison between measured and computed elastic moduli in quasi-isotropic  $P_{12}$  plane (dashed lines: model; points: measurements).

$$G_t = G_m + \frac{V_f}{1/(G_f - G_m) + (k_m + 2G_m)V_m/2(k_m + G_m)G_m}, \quad (11)$$

where  $V_f$  and  $V_m (= 1 - V_f)$  represent the volume fraction of fiber and matrix, respectively.

The five independent complex viscoelastic moduli of the composite are computed using the following relations:

$$\begin{aligned} C_{11} &= k + G_t, & C_{66} &= G_t, & C_{13} &= 2\nu_1 k, \\ C_{33} &= 4\nu_1^2 k + E_1, & C_{55} &= G_1. \end{aligned} \quad (12)$$

## IV. RESULTS AND DISCUSSION

### A. Elastic moduli of the composite versus temperature

The real parts of slowness vectors are measured in various directions of propagation, in each plane of the sample and for several temperatures. In the  $P_{13}$  plane (Fig. 11), the slowness vectors change with propagation direction. This anisotropy increases with temperature. From these measurements, it is possible to deduce the elastic moduli. Results of measured and predicted elastic moduli for the glass-epoxy composite are presented for both  $P_{12}$  and  $P_{13}$  planes in Figs. 12 and 13. The rate of change in moduli with temperature is anisotropic. The  $C'_{33}$  modulus does not vary much with temperature. This result is expected since the modulus is mainly due to the fibers. Since good agreement seems to exist between measurements and predictions, the micromechanics model may be extended to viscoelastic composite moduli. Error bars shown on the graph correspond to a few percent for most of the values. Errors also exist on the predicted results since measured properties of the matrix are used for those predictions. For clarity, these errors are not reported in the predicted results, but it is clear that measurements and predictions agree over the range of temperature. Relative changes in the Young's moduli are plotted in Fig. 14. Since the modulus transverse to fibers  $E'_T$  is more influenced by the matrix properties variations, it changes more with temperature than the modulus parallel to the fibers  $E'_L$  does.

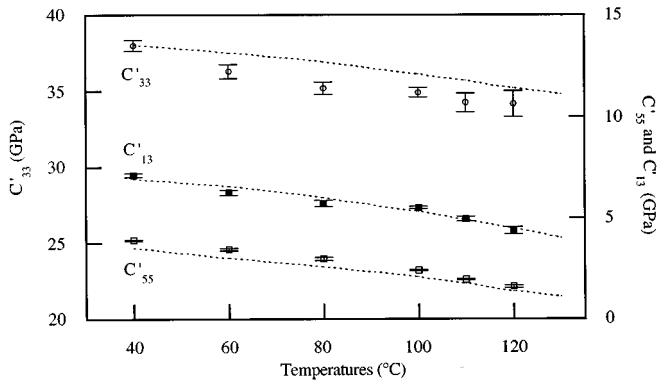


FIG. 13. Comparison between measured and computed elastic moduli in the anisotropic  $P_{13}$  plane (dashed lines: model; points: measurements).

### B. Viscoelastic moduli of the composite as a function of temperature

The damping vectors of the composite material are measured for quasi-longitudinal and quasi-transverse modes at several temperatures. From these measurements, the  $C''_{ij}$  are computed at 2 MHz and the damping vectors of the associated homogeneous modes are computed for each propagation angle. Figures 15 and 16 show these computed damping vectors for quasi-longitudinal and quasi-transverse modes as functions of the propagation angle. The attenuation is anisotropic for quasi-longitudinal modes as well as for quasi-transverse modes in the anisotropic  $P_{13}$  plane of the composite. Figure 16 shows that as the temperature increases, the anisotropy of quasi-transverse modes becomes more pronounced. As expected, transverse modes are more attenuated than longitudinal ones.

On both graphs, a range of refraction angles are notified. In this range, the attenuation of quasi-longitudinal modes (Fig. 15) is the highest and the attenuation of quasi-transverse modes (Fig. 16) is the lowest for an angle of refraction  $\theta_r$ , which depends on the temperature. At a fixed temperature, this angle is observed to be different for quasi-longitudinal and quasi-transverse modes. The computed polarization of both modes at this angle is about  $45^\circ$  to the fibers. These features need more explanations in a future work.

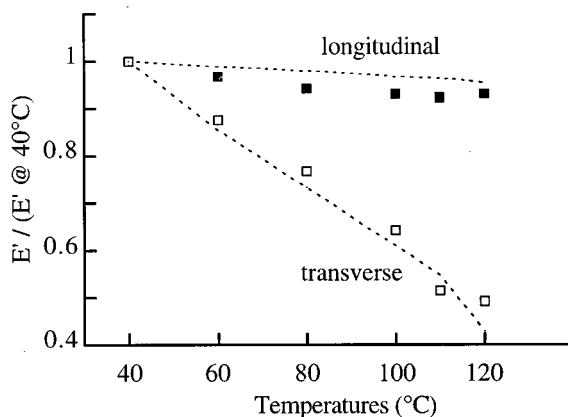


FIG. 14. Young's moduli of the composite material versus temperature.

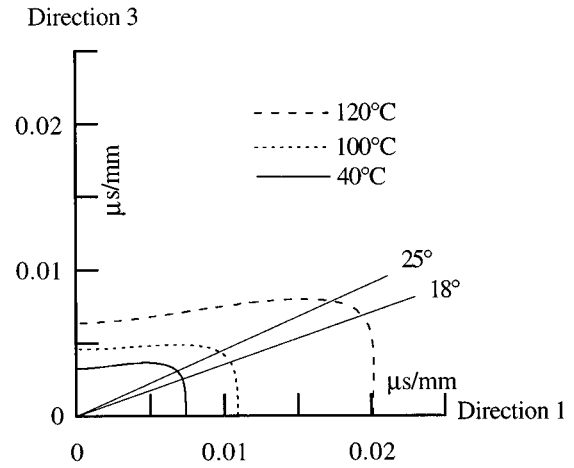


FIG. 15. Imaginary part of the slowness vector for quasi-longitudinal modes in the  $P_{13}$  plane.

Comparisons also are performed between the measured and predicted values of the composite loss tangent for each plane of the composite (Figs. 17 and 18). In the  $P_{12}$  plane, good agreement between measurements and computations is obtained for  $\tan \delta_{11}$  whatever the temperature. In that direction, attenuation in the composite is essentially controlled by the matrix, and this corresponds very well to the hypothesis made in the micromechanical model. For  $\tan \delta_{66}$ , some discrepancies can be observed as temperature grows. In both planes, the most pronounced variations are the ones of the loss tangent  $\tan \delta_{66}$  and  $\tan \delta_{55}$ , which correspond to transverse modes, as in the matrix. These curves may be related to the changes of the elastic and viscoelastic properties of the composite with temperature in a given direction. Possible errors on viscoelastic moduli are added to elastic ones, so this could be a reason for the discrepancies.

Good agreement can be observed in the  $P_{13}$  plane, with the exception of  $\tan \delta_{33}$ . In this case, the predicted results are much lower than measurements. This difference can be

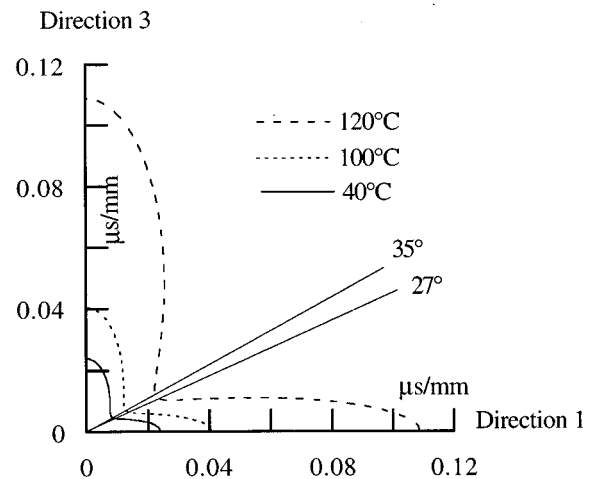


FIG. 16. Imaginary part of the slowness vector for quasi-transverse modes in the  $P_{13}$  plane.

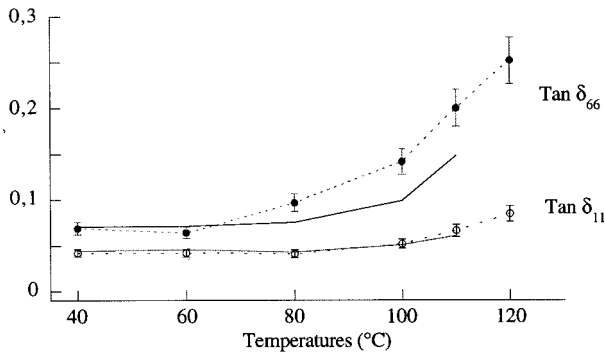


FIG. 17. Measured and computed viscoelastic moduli in the  $P_{12}$  plane (solid lines: model; points and dashed lines: measurements).

due to the hypothesis made in the model, which does not take into account the effect of fibers in the attenuation process.

## V. CONCLUSION

From an engineering point of view, it is interesting to measure material properties as a function of temperature. The immersion method permits one to measure complex viscoelastic properties of composite materials with varying temperature. Symmetries other than the transversely isotropic one have been tested successfully.

Relative errors are computed for measured results and permit one to have an estimation of the precision. The measurements of complex viscoelastic moduli are precise enough to be used to investigate the attenuation in composite materials that is intricate because it depends on the direction of propagation, nature of the mode, frequency, temperature, etc. All the phenomena related to the attenuation process are not explained yet, and the interpretation of the attenuation results in composite materials is still an open problem.

The micromechanics-model-based predictions are in good agreement with elastic material constants results and with some of the viscoelastic constants. It is possible that the hypothesis used in the model calculation of attenuation has to be improved. More comparisons at different frequencies are still to be done for a better understanding of the composite materials attenuation.

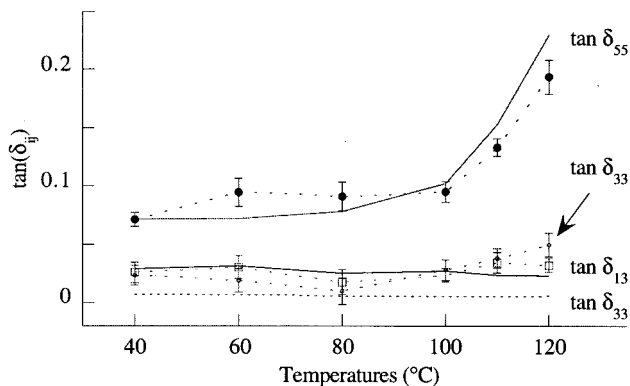


FIG. 18. Measured and computed viscoelastic moduli in the  $P_{13}$  plane (solid lines: model; points and dashed lines: measurements).

## APPENDIX: INSENSITIVITY MATRIX AND ERRORS

Let  $\tilde{V}_{k=1,\dots,m}$  denote  $m$  experimental values (velocities, slowness, attenuations, etc.).  $\tilde{V}_k$  is the true value  $V_k$  plus an experimental error  $\Delta V_k$ :  $\tilde{V}_k = V_k + \Delta V_k$ .

Let  $\vec{\mathcal{P}}$  be a vector composed of  $p_i$  ( $i \in [1, \dots, n]$ ) unknown components that we want to identify from the vector  $\tilde{V}_{k=1,\dots,m}$ , with  $m \gg n$ . According to the classical Newton-Raphson procedure, the inverse problem consists of finding the best estimate  $\vec{\mathcal{P}}$  of the  $p_i$  parameters that minimizes a quadratic, positive form:

$$F(\vec{\mathcal{P}}) = \sum_{k=1}^m (\tilde{V}_k - V(\vec{\mathcal{P}}))_k^2, \quad (\text{A1})$$

where  $\vec{\mathcal{P}} = \vec{\mathcal{P}} + \partial\vec{\mathcal{P}} = [p_i + \partial p_i]$  is the best estimated vector solution plus an error vector  $\partial\vec{\mathcal{P}}$ . Here  $V$  is a function of the unknown components that is given by the solution of the forward problem. At the minimum of this function, the vector  $\overrightarrow{\text{grad}}_{\vec{\mathcal{P}}}(F) = [\partial F / \partial p_i]$  is null. Consequently,

$$\overrightarrow{\text{grad}}_{\vec{\mathcal{P}}}(F) = \vec{0} + H \partial\vec{\mathcal{P}}, \quad (\text{A2})$$

where the operator  $H$  is defined by the matrix:  $[H] = [\partial^2 F / \partial p_i \partial p_j]$ . Therefore, the optimization step is given by

$$\partial p_i = \left[ \frac{\partial^2 F}{\partial p_i \partial p_j} \right]^{-1} \frac{\partial F}{\partial p_j}. \quad (\text{A3})$$

The minimization algorithm provides the best estimation of the parameters  $\tilde{p}_i = p_i + \Delta p_i$  with the errors  $\Delta p_i$ . Then,

$$V(\vec{\mathcal{P}})|_k = V(\vec{\mathcal{P}})|_k + \sum_i \frac{\partial V(\vec{\mathcal{P}})}{\partial p_i} \Big|_k \Delta p_i. \quad (\text{A4})$$

Between the forward solutions and the measurements, we can compute the differences

$$e_k = \tilde{V}_k - V(\vec{\mathcal{P}})|_k = \Delta V_k - \sum_i \frac{\partial V(\vec{\mathcal{P}})}{\partial p_i} \Big|_k \Delta p_i. \quad (\text{A5})$$

Let us introduce the absolute error vector,

$$\vec{E} = [\Delta V_k - e_k], \quad (\text{A6})$$

the **sensitivity** vector of  $V$  to the parameter  $p_i$ ,

$$\vec{S}_i = \left[ p_i \frac{\partial V(p_i)}{\partial p_i} \Big|_k \right], \quad (\text{A7})$$

the **sensitivity** matrix ( $m^*n$ ),

$$[S] = [\vec{S}_i], \quad (\text{A8})$$

the relative error vector,

$$\vec{r} = \left[ \frac{\Delta p_i}{p_i} \right]. \quad (\text{A9})$$

With these definitions, the previous relations become

$$[E] = [S][r]. \quad (\text{A10})$$

We have  $m$  equations to find  $n$  parameters. So,

$$[S]^t[E] = [S]^t[S][r]. \quad (\text{A11})$$

The matrix  $[M]$  ( $n \times n$ ) is defined by

$$[M_{ij}] = \sum_k S_{ik} S_{jk} \quad \text{and thus} \quad [r] = [M]^{-1} [S]^t [E]. \quad (\text{A12})$$

The inverse of the sensitivity matrix is called the **insensitivity matrix**:

$$[I] = [[S]^t[S]]^{-1} [S]^t, \quad \text{or} \quad [I] = [M]^{-1} [S]^t \quad \text{and} \quad (\text{A13})$$

$$I_{ik} = \sum_{j=1, \dots, n} M_{ij} S_{jk}.$$

The insensitivity vectors are defined by  $[I] = [\vec{I}_i]$ , and  $\langle \vec{I}_i, \vec{S}_j \rangle = 0$  if  $i \neq j$  and  $= 1$  if  $i = j$ . A larger insensitivity results in an increasing relative error:

$$[r] = [I][E]. \quad (\text{A14})$$

The computed difference  $e_k$  is the difference between the absolute error  $\Delta V_k$  of the measured data and the term  $\sum_i [\partial V(\vec{\mathcal{P}}) / \partial p_i]_k \Delta p_i$ , which includes the unknown errors  $\Delta p_i$ . The purpose of the minimization procedure is to obtain values of  $\vec{p}_i$  which make these terms as small as possible and smaller than  $\Delta V_k$  in Eq. (A2). The error  $\Delta V_k$  includes the measurement errors and the model errors. Consequently, for a large number of data,  $\Delta V_k$  is the main term in the error  $e_k$ . Both terms  $\Delta V_k$  and  $e_k$  have statistically the same sign and each component of vector  $\vec{E}$  is such that  $|E_k| = |\Delta V_k - e_k| < |e_k|$ . Therefore, the upper bounds of the relative errors  $r_i$

may be computed from the insensitivity matrix as follows:

$$r_i \leq \sum_k |I_{ik} e_k| \quad (\text{A15})$$

<sup>1</sup>J. E. Zimmer and J. R. Cost, "Determination of the elastic constants of a unidirectional fiber composite using ultrasonic velocity measurements," *J. Acoust. Soc. Am.* **47**, 795–803 (1970).

<sup>2</sup>B. Hosten, M. Deschamps, and B. R. Tittmann, "Inhomogeneous wave generation and propagation in lossy anisotropic solids. Application to the characterization of viscoelastic composite materials," *J. Acoust. Soc. Am.* **82**, 1763–1770 (1987).

<sup>3</sup>C. B. Scruby and L. E. Drain, *Laser Ultrasonics. Techniques and Applications* (Hilger, London, 1990).

<sup>4</sup>A. Safaeinili, O. I. Lobkis, and D. E. Chimenti, "Air-coupled ultrasonic characterization of composite plates" *Mater. Eval.* **53**(10), 1186–1190 (1995).

<sup>5</sup>R. Farlow, S. P. Kelly, and G. Hayward, "Advanced in air coupled NDE for rapid scanning applications," *Proc. IEEE Ultrasonics Symposium*, 1099–1102 (1994).

<sup>6</sup>B. Hosten, D. A. Hutchins, and D. W. Schindel, "Measurement of elastic constants in composite materials using air-coupled ultrasonic bulk waves," *J. Acoust. Soc. Am.* **99**, 2116–2123 (1996).

<sup>7</sup>Z. Hashin, "Analysis of composite materials. A survey," *J. Appl. Mech.* **50**, 481–504 (1983).

<sup>8</sup>Z. Hashin, "Complex moduli of viscoelastic composites. II. Fiber reinforced materials," *Int. J. Solids Struct.* **6**, 797–807 (1970).

<sup>9</sup>B. A. Auld, *Acoustic Fields and Waves in Solids* (Wiley-Interscience, New York, 1973), Vol. 1.

<sup>10</sup>M. J. P. Musgrave, "On an elastodynamic classification of orthorhombic media," *Proc. R. Soc. London, Ser. A* **374**, 401–429 (1981).

<sup>11</sup>H. A. Huang, C. E. Bakis, and H. T. Hahn, "Prediction of ultrasonic wave attenuation in fiber reinforced composite laminates," *Rev. Prog. in Quant. nondestruct. Eval.* **13**, 1181–1188 (1994).

<sup>12</sup>W. P. Mason and R. N. Thurston, *Physical Acoustics* (Academic, New York, 1976), Vol. XII.

<sup>13</sup>R. M. Christensen, *Mechanics of Composite Materials* (Pergamon, New York, 1982).

<sup>14</sup>B. Hosten, "Reflection and transmission of acoustic plane waves on an immersed orthotropic and viscoelastic solid layer," *J. Acoust. Soc. Am.* **89**, 2745–2752 (1991).

<sup>15</sup>I. M. Ward, *Mechanical Properties of Solid Polymers* (Wiley, New York, 1971).

<sup>16</sup>W. W. Stinchcomb, *Mechanics of Nondestructive Testing* (Plenum, New York, 1980).

<sup>17</sup>M. Hlavacek, "A continuum theory for fibre-reinforced composites," *Int. J. Solids Struct.* **11**, 199–211 (1975).

<sup>18</sup>V. K. Kinra and A. W. Wolfenden, *Mechanics and Mechanisms of Material Damping* (ASTM, Philadelphia, 1992).

<sup>19</sup>J.-Y. Kim, J.-G. Ih, and B.-H. Lee, "Dispersive wave propagation in a viscoelastic matrix reinforced by elastic fibers," *J. Acoust. Soc. Am.* **96**, 1213–1222 (1994).

# Comparison of elastic constant determination in anisotropic materials from ultrasonic group and phase velocity data

A. D. Degtyar and S. I. Rokhlin

The Ohio State University, Nondestructive Evaluation Program, 190 West 19th Avenue, Columbus, Ohio 43210

(Received 23 May 1997; accepted for publication 31 July 1997)

A comparative analysis of elastic constant determination from the angular dependence of group and phase velocity data in orthotropic and transversely isotropic materials is performed. A nonlinear least-squares optimization procedure is used for inversion. The method allows the use of group velocity data in a cuspidal region, where for a given ray direction there are more than three distinct wave modes propagating with different velocities. Exact analytical equations are derived relating group velocities to elastic constants for arbitrary planes in transversely isotropic materials. Approximate relations for nonsymmetry planes in orthotropic materials are obtained. The procedure is generalized for determination of elastic constants from group velocities measured in arbitrary incident planes in orthotropic materials. © 1997 Acoustical Society of America.

[S0001-4966(97)01312-X]

PACS numbers: 43.35.Cg, 43.35.Yb [HEB]

## INTRODUCTION

Ultrasonic measurements are widely used for elastic constant determination of anisotropic materials. If the samples can be cut in predetermined directions, elastic constants can be determined from velocity data in these directions with the number of measurements equal to the number of unknown independent elastic constants.<sup>1,2</sup> The accuracy of elastic constant measurement can be maximized by choosing an appropriate propagation direction and polarization. Six elastic constants of an orthotropic material can be determined from measurements along symmetry axes. Three others are obtained on samples which are cut in the off-axis directions.<sup>2</sup> Since velocities are stationary<sup>1</sup> along axes of symmetry, smaller measurement errors are associated with material axes misorientation. These traditional methods require access to different sample surfaces and sample cutting, thus they are inherently destructive. Often ultrasonic access is limited to one or two sides of the sample, normally in the through-thickness direction of the plate or shell and thus only measurement at one axis of symmetry can be done. Also it is often necessary to accompany measurements with sample scanning, so mapping of the elastic constants can be done. In this case special nondestructive ultrasonic velocity measurement techniques are required.

Most nondestructive techniques utilize obliquely incident phase velocity measurements<sup>3,4</sup> because it is easier to determine the elastic constants<sup>5</sup> from phase velocity than from group velocity. However, group velocity data can also be used to recover elastic constants. The data can be obtained using, for example, a point source–point receiver technique<sup>6</sup> which allows one to measure group velocities in different directions including those in a cuspidal region.<sup>7</sup> The advantage of this technique is that it does not require a sample rotation for velocity measurements in different directions. Also techniques with one-sided access to the sample can be utilized.<sup>8</sup> However, these group-velocity-measuring tech-

niques require accurate determination of the group velocity propagation direction.

Several methods to determine elastic constants from group velocity data have been proposed. Every and Sachse<sup>9</sup> use nonlinear least squares to determine three independent elastic constants of a cubic material from group velocity data outside cuspidal regions. Kim<sup>10</sup> shows that mixed-index elastic constants  $C_{12}$ ,  $C_{13}$ , and  $C_{23}$  in orthotropic materials can be determined by measuring the group velocity of a quasi-longitudinal or quasishear wave propagating obliquely in the symmetry plane assuming that pure-index elastic constants are known from measurements along symmetry axes. Kim *et al.*<sup>11</sup> apply this approach to determine all nine elastic constants of an orthotropic plate. Minachi *et al.*<sup>8</sup> use a perturbation method and a nonlinear least-squares procedure for a transversely isotropic material to determine  $C_{11}$  and  $C_{13}$  from measurements at oblique incidence in the symmetry plane, while the other elastic constants ( $C_{33}$ ,  $C_{44}$ , and  $C_{55}$ ) are assumed to be known from normal incidence measurements. In these techniques some or all pure-index elastic constants are determined from measurements along acoustic axes. As we mentioned above these measurements may not be always possible, as, for example, measurements along symmetry directions in the plane of a composite plate. For shear modulus measurement in the direction normal to the plate surface one needs to use a shear wave. Although it can be excited using electromagnetic transducers for metals in scanning modes, shear wave measurements using contact transducers are difficult to implement for scanning when nondestructive mapping of elastic constants is required. Therefore oblique excitation of shear waves is required.

In this paper we describe a method to determine the elastic constants of an orthotropic material from group velocity data of longitudinal and shear waves in different directions of symmetry and nonsymmetry planes using a nonlinear least-squares algorithm which minimizes the difference between experimental and calculated group veloc-

ity data. No elastic constants except one (determined from the longitudinal wave at normal incidence) are assumed to be known from measurements along symmetry axes. It is shown that experimental data in a cuspidal region can be utilized for the inversion. This eliminates the necessity of obtaining quasishear wave data away from folded regions. The reconstruction is performed for synthetic sets of experimental data corresponding to materials with different degrees of anisotropy. The results are compared to those obtained from phase velocity measurements also using nonlinear least-squares minimization as described in Ref. 12.

Seven of nine elastic constants for an orthotropic medium can be determined from group or phase velocity data in two symmetry planes perpendicular to the specimen plane. To determine the remaining two elastic constants velocity data in a nonsymmetry plane must be used. Such determination from phase velocity data is discussed in Ref. 13. Here we demonstrate that group velocity data can be used for this purpose. Also it is shown that the five independent elastic constants of a hexagonal material can be determined from group velocity data corresponding to one incident plane. Simple analytical formulas are presented for this case. It is also demonstrated that they provide good approximations for wave velocities in nonsymmetry planes of weakly orthotropic (with respect to transverse isotropy) materials.

### I. PHASE AND GROUP VELOCITIES IN SYMMETRY PLANES OF ORTHOTROPIC MATERIALS

The phase velocity of a wave propagating in a generally anisotropic medium is governed by the well-known Christoffel equation:<sup>11-14</sup>

$$[C_{ijkl}n_i n_l - \rho V_p^2 \delta_{jk}]P_k = 0, \quad (1)$$

where the  $C_{ijkl}$  are the elastic constants,  $\mathbf{n}$  is the wave normal,  $\mathbf{P}$  is the polarization unit vector, and  $\rho$  is the density. To have nontrivial solutions the determinant of Eq. (1) must vanish

$$|C_{ijkl}n_i n_l - \rho V_p^2 \delta_{jk}| = 0. \quad (2)$$

For a given propagation direction there are three solutions of Eq. (2), which represent one quasilongitudinal and two quasitransverse waves. The corresponding polarizations can be found from Eq. (1). The group velocity of the wave with known phase velocity ( $V_p$ ) and polarization ( $\mathbf{P}$ ) is determined from

$$V_{gi} = \frac{C_{imlj}P_l P_m n_j}{\rho V_p}. \quad (3)$$

Using Eqs. (2) and (3) one can show that the phase velocity is the projection of the group velocity onto the wave normal  $\mathbf{n}$  (Ref. 15)

$$\mathbf{V}_g \cdot \mathbf{n} = V_p. \quad (4)$$

Kim<sup>10</sup> derived closed-form analytical formulas for group velocities of quasilongitudinal and quasitransverse waves in symmetry planes of orthotropic materials. Below we present the resulting formulas for group velocities using a different form which makes them more convenient for subsequent use in the inversion method.

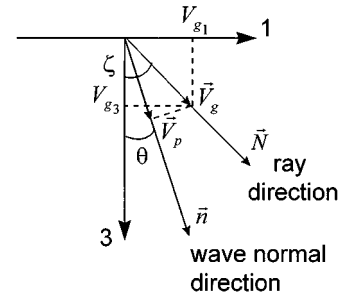


FIG. 1. (a) Wave propagation in the 1-3 symmetry plane of the orthotropic material; wave normal and group velocity directions.

We consider wave propagation in the 1-3 symmetry plane of an orthotropic material (Fig. 1). In this case Eq. (2) has the following form:

$$\begin{vmatrix} G_{11} - \rho V_p^2 & 0 & G_{13} \\ 0 & G_{22} - \rho V_p^2 & 0 \\ G_{13} & 0 & G_{33} - \rho V_p^2 \end{vmatrix} = 0, \quad (5)$$

where

$$\begin{aligned} G_{11} &= C_{11} \sin^2 \theta + C_{55} \cos^2 \theta, \\ G_{33} &= C_{55} \sin^2 \theta + C_{33} \cos^2 \theta, \\ G_{13} &= (C_{13} + C_{55}) \sin \theta \cos \theta, \\ G_{22} &= C_{66} \sin^2 \theta + C_{44} \cos^2 \theta. \end{aligned} \quad (6)$$

The angle  $\theta$  is between the direction of propagation and the 3-axis (Fig. 1). Equation (5) decomposes to a linear part for a pure transverse wave ( $T$ ) and a quadratic part for quasilongitudinal (QL) and quasishar (QT) waves. These solutions are

$$\begin{aligned} \rho V_{p(QL)}^2 &= \frac{G_{11} + G_{33}}{2} + \frac{\sqrt{(G_{11} - G_{33})^2 + 4G_{13}^2}}{2}, \\ \rho V_{p(QT)}^2 &= \frac{G_{11} + G_{33}}{2} - \frac{\sqrt{(G_{11} - G_{33})^2 + 4G_{13}^2}}{2}, \\ \rho V_{p(T)}^2 &= G_{22} \end{aligned} \quad (7)$$

and the polarizations of these waves are

$$\begin{aligned} \mathbf{P}_{(QL)} &= \begin{cases} (0,0,1)^T, \\ (1,0,0)^T, \\ \left( \frac{1}{\sqrt{1 + \xi_{(L)}^2}}, 0, \frac{\xi_{(QL)}^2}{\sqrt{1 + \xi_{(QL)}^2}} \right)^T, \end{cases} \\ \mathbf{P}_{(QT)} &= \begin{cases} (1,0,0)^T, & \text{for } \theta = 0^\circ, \\ (0,0,1)^T, & \text{for } \theta = 90^\circ, \\ \left( \frac{1}{\sqrt{1 + \xi_{(QT)}^2}}, 0, \frac{\xi_{(QT)}^2}{\sqrt{1 + \xi_{(QT)}^2}} \right)^T, & \text{otherwise,} \end{cases} \\ \mathbf{P}_{(T)} &= (0,1,0)^T, \end{aligned}$$

where

$$\xi_{(QL),(QT)} = \frac{\rho V_p^2 V_{p(Q),(QT)} - G_{11}}{G_{33}}. \quad (8)$$

Due to symmetry the group velocity vectors of all three waves lie in the same 1-3 plane. The nonzero components of the group velocity vectors for QL and QT waves (Fig. 1) are

$$V_{g1(Q),(QT)} = \frac{(C_{11}P_1^2 + C_{55}P_3^2)\sin\theta + (C_{13} + C_{55})P_1P_3\cos\theta}{\rho V_{p(Q),(QT)}}, \quad (9)$$

$$V_{g3(Q),(QT)} = \frac{(C_{13} + C_{55})P_1P_3\sin\theta + (C_{55}P_1^2 + C_{33}P_3^2)\cos\theta}{\rho V_{p(Q),(QT)}},$$

where  $\mathbf{P} = (P_1, P_2, P_3)^T$  is the polarization vector for QL and QT waves, respectively. For the pure transverse wave the nonzero group velocity components are

$$V_{g1(T)} = \frac{C_{66}\sin\theta}{\rho V_{p(T)}},$$

$$V_{g3(T)} = \frac{C_{44}\cos\theta}{\rho V_{p(T)}}. \quad (10)$$

The group velocity direction is defined by the angle  $\zeta$  between the vector  $\mathbf{V}_g$  and the 3-axis (Fig. 1). This angle equals

$$\zeta = \begin{cases} \tan^{-1}\left(\frac{V_{g1}}{V_{g3}}\right), & \text{when } V_{g3} \neq 0, \\ 90^\circ, & \text{when } V_{g3} = 0. \end{cases} \quad (11)$$

Equation (4) becomes

$$V_g \cos(\zeta - \theta) = V_p. \quad (12)$$

As one can see the QL and QT phase and group wave velocities depend on four elastic constants, namely  $C_{11}$ ,  $C_{33}$ ,  $C_{13}$ , and  $C_{55}$ , and both velocities of the pure transverse wave depend on  $C_{44}$  and  $C_{66}$ . It will be shown in the next section that from group velocity measurements on QL and QT waves in the 1-3 plane one can determine  $C_{11}$ ,  $C_{33}$ ,  $C_{13}$ , and  $C_{55}$ .

Wave propagation in the 2-3 symmetry plane is described by equations similar to Eqs. (5)–(12) with the index substitution  $1 \leftrightarrow 2$ ,  $55 \leftrightarrow 44$ . From group or phase measurements in the 2-3 plane it is possible to determine  $C_{22}$ ,  $C_{33}$ ,  $C_{23}$ , and  $C_{44}$ . From measurements in the 1-3 and 2-3 symmetry planes one can determine seven of the nine elastic constants of an orthotropic material (all except  $C_{12}$  and  $C_{66}$ , which can be determined from measurements in a nonsymmetry plane assuming that the other elastic constants are already known).

## II. PHASE AND GROUP VELOCITIES IN NONSYMMETRY PLANES OF ORTHOTROPIC AND IN TRANSVERSELY ISOTROPIC MATERIALS

In the case of wave propagation in a nonsymmetry plane the cubic Christoffel equation (2), presented in the coordinate system related to acoustical axes, cannot be decomposed in lower-order terms as was done for a plane of symmetry in

the previous section. But if the material is transversely isotropic, there exists a symmetry plane associated with any direction of wave propagation. If we consider the rotated coordinate system associated with this plane, the Christoffel equation can be decomposed into linear and quadratic parts. This factorization is well known in crystal acoustics<sup>15,16</sup> for hexagonal symmetry. A simple factorization method and analytical formulas for phase velocities and polarizations were derived by Chu *et al.*<sup>13</sup> In this section we review such a factorization and also present formulas for group velocities. The exact relation for transversely isotropic materials also provides a very good approximation for nonsymmetry planes in orthotropic materials.

Consider the 2-3 plane to be the plane of symmetry for the transversely isotropic material [Fig. 2(a) and (b)]. For a wave propagating in an arbitrary direction, the wave vector is characterized by polar angular coordinates  $\varphi$  and  $\theta$  [Fig. 2(a)]:

$$\mathbf{n} = (\cos\varphi \sin\theta, \sin\varphi \sin\theta, \cos\theta) \quad (13)$$

and the energy propagation direction is

$$\mathbf{N} = (\cos\Phi \sin\Theta, \sin\Phi \sin\Theta, \cos\Theta). \quad (14)$$

The incident plane as shown in Fig. 2(b) is not a symmetry plane. To simplify the wave propagation description let us introduce the rotated coordinate system  $(1', 2', 3')$  as shown in Fig. 2(b). It is associated with the symmetry plane  $(1'-3'$  plane in the rotated system) containing axis of symmetry 1 and wave normal  $\mathbf{n}$ . Due to symmetry the group velocity vector  $\mathbf{N}$  also lies in this plane. The  $3'$  axis of the rotated system is along the wave-vector direction. The  $2'$  axis is perpendicular to the  $1'-3'$  plane. The solution of the Christ-

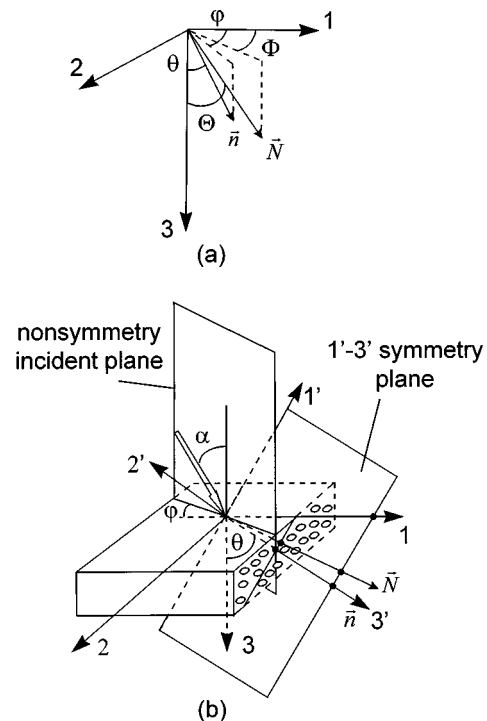


FIG. 2. (a) Ray ( $\mathbf{N}$ ) and wave normal ( $\mathbf{n}$ ) vectors for an arbitrary wave propagation direction. (b) Orientation of the rotated coordinate system.  $1'-3'$  is the plane of symmetry for transversely isotropic material.



offel equation for the ultrasonic phase velocities and their associated polarization unit vectors  $\mathbf{P}$  in the rotated coordinate system  $1'2'3'$  are given by<sup>13</sup>

$$\begin{aligned}\rho V_{\text{QL}}^2 &= C'_{33} + \frac{C'_{33} - C'_{55}}{2} f(\xi^2), \\ \rho V_{\text{QT1}}^2 &= C'_{55} - \frac{C'_{33} - C'_{55}}{2} f(\xi^2), \\ \rho V_{\text{QT2}}^2 &= C'_{44}\end{aligned}\quad (15)$$

and

$$\begin{aligned}\mathbf{P}_{\text{QL}} &= \left\{ \frac{p}{\sqrt{1+p^2}}, 0, \frac{1}{\sqrt{1+p^2}} \right\}^T; \\ \mathbf{P}_{\text{QT1}} &= \left\{ \frac{1}{\sqrt{1+p^2}}, 0, \frac{-p}{\sqrt{1+p^2}} \right\}^T, \\ \mathbf{P}_{\text{QT2}} &= \{0, 1, 0\}^T,\end{aligned}\quad (16)$$

where the function  $f$ , polarization factor  $\xi$ , and polarization component  $p$  are defined as

$$f(\xi^2) = \text{sgn}(C'_{33} - C'_{55}) \sqrt{1 + \xi^2} - 1, \quad (17)$$

$$\xi = \frac{2C'_{53}}{|C'_{33} - C'_{55}|}. \quad (18)$$

$$p = \frac{\xi}{\text{sgn}(C'_{33} - C'_{55}) + \sqrt{1 + \xi^2}} \quad (19)$$

and  $C'_{ij}$  are elastic constants in the rotated (prime) coordinate system (see the Appendix). The sign function  $\text{sgn}(x)$  is defined by

$$\text{sgn}(x) = \begin{cases} -1, & x < 0, \\ 1, & x > 0. \end{cases} \quad (20)$$

The group velocities are derived from Eq. (3):

$$\begin{aligned}\mathbf{V}_{g\text{QL}} &= \left\{ \frac{C'_{15}p^2 + (C'_{13} + C'_{55})p + C'_{35}}{(1+p^2)\rho V_{\text{QL}}}, 0, V_{\text{QL}} \right\}^T, \\ \mathbf{V}_{g\text{QT1}} &= \left\{ \frac{C'_{15} - (C'_{13} + C'_{55})p + C'_{35}p^2}{(1+p^2)\rho V_{\text{QT1}}}, 0, V_{\text{QT1}} \right\}^T, \\ \mathbf{V}_{g\text{QT2}} &= \left\{ \frac{C'_{46}}{\rho V_{\text{QT2}}}, 0, \frac{C'_{44}}{\rho V_{\text{QT2}}} \right\}^T,\end{aligned}\quad (21)$$

and the angular deviation  $\psi$  of the group velocity vector from the wave vector is

$$\psi = \tan^{-1} \left( \frac{V_{g1}}{V_{g3}} \right). \quad (22)$$

If the material is slightly anisotropic in the 2-3 plane, Eqs. (15)–(21) can be used as approximations, where exact equations for elastic constants  $C'_{ij}$  (see the Appendix) for the orthotropic material in the rotated coordinate system are used. The ray vector in this case will deviate slightly from the  $1'-3'$  plane. The difference between ray and phase di-

rections can be characterized by in-plane ( $\alpha$ ) and out-of-plane ( $\beta$ ) components:

$$\alpha = \tan^{-1} \left( \frac{N'_1}{N'_3} \right), \quad \beta = \sin^{-1} N'_2, \quad (23)$$

where  $\mathbf{N} = (N'_1, N'_2, N'_3)^T$  is the energy (group velocity) propagation direction in the rotated coordinate system. We call such materials weakly orthotropic. A wide range of materials including unidirectional composites possesses this property.

To investigate the accuracy of the approximation, we calculate phase and group velocities for graphite/epoxy composite. The elastic constants of the composite are taken from those of a transversely isotropic composite. The composite orthotropy is produced by decreasing  $C_{22}$ ,  $C_{12}$ , and  $C_{66}$  by 10% and increasing  $C_{33}$ ,  $C_{13}$ , and  $C_{55}$  by 10% ( $C_{22} \approx 0.8C_{33}$ ,  $C_{12} \approx 0.8C_{13}$ , and  $C_{66} \approx 0.8C_{55}$ ). Figure 3 shows the comparison for phase (a) and group (b) velocities. As one can see, the agreement between exact and approximate solutions is very good.

### III. DETERMINATION OF ELASTIC CONSTANTS FROM GROUP VELOCITY DATA IN A SYMMETRY PLANE

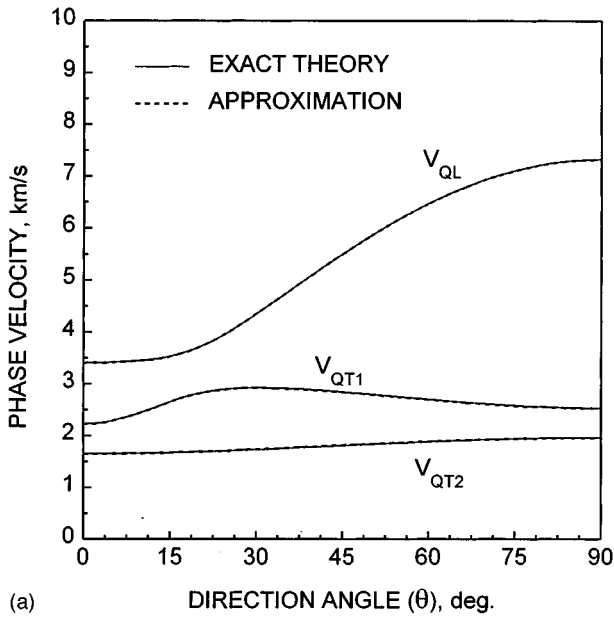
A schematic of the possible through-transmission arrangement for group velocity measurement is shown in Fig. 4. The ray (group velocity) direction  $\xi^{\text{exp}}$  is measured from the receiver position and group velocity  $V_g^{\text{exp}}$  from time of flight of the ultrasonic signal. The measurements described by Kim and Sachse<sup>7</sup> and by Minachi *et al.*<sup>8</sup> were performed by slightly different techniques.

From experimental QL and QT group velocity data  $\{V_g^{\text{exp}}(\xi^{\text{exp}})\}$  in the 1-3 plane four unknown elastic constants can be determined. Figure 5 shows a flow chart of the inversion procedure used in this study for elastic constant determination from group velocities. It is based on the nonlinear least-squares optimization algorithm. Initial guesses of the elastic constants are used to determine the wave normal directions  $\{\theta\}$  corresponding to the measured group velocity directions  $\{\xi^{\text{exp}}\}$  by solving Eq. (11):

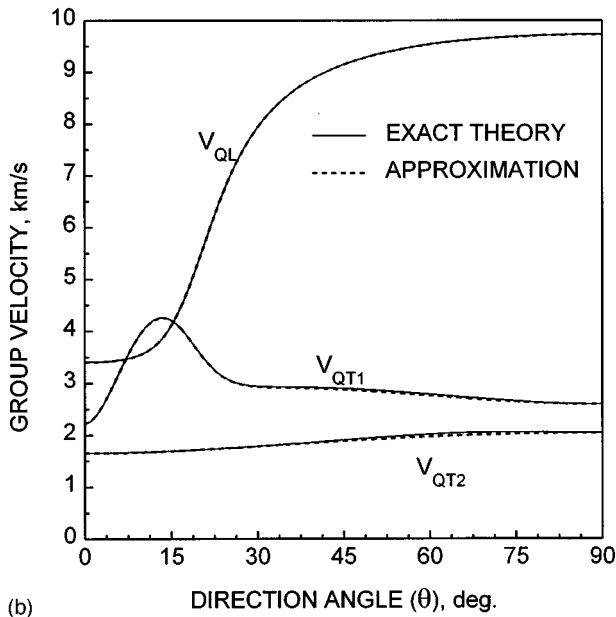
$$\frac{V_{g1}(\theta)}{V_{g3}(\theta)} = \tan(\xi^{\text{exp}}), \quad (24)$$

where  $V_{g1}$  and  $V_{g3}$  are calculated from initial guesses (9), on the interval  $\theta \in [-\pi/2, \pi/2]$ . The phase velocity can now be determined for this propagation angle using the initial guess of the elastic constants.

For a QT wave the solution of Eq. (11) is not unique in cuspidal regions, which means that there are several quasi-transverse waves propagating in the same direction with different velocities and wave normals. When Eq. (11) has multiple solutions  $(\theta_1, \theta_2, \theta_3)$  for the wave normal direction (this happens in a cuspidal region), we choose the one which gives the smallest deviation between the calculated phase velocity  $V_p(\theta_i)$  and the projection of the experimental group velocity on this direction  $V_g^{\text{exp}} \cos(\xi^{\text{exp}} - \theta_i)$  (for the exact set of elastic constants these values are equal according to Eq. (12), which represents the fact that the projection of the



(a)



(b)

FIG. 3. Comparison of exact (solid line) and approximate (dashed line) ultrasonic (a) phase and (b) group velocities for graphite/epoxy composite in a nonsymmetry plane  $\varphi = 45^\circ$  for weakly orthotropic material.

group velocity on the wave normal direction is equal to the phase velocity). We call this solution the calculated wave normal angle ( $\theta^{calc}$ ):

$$\left\{ \min_{i=1, \dots, 3} (V_g^{exp} \cos(\zeta^{exp} - \theta_i) - V_p(\theta_i)) \right\} \rightarrow V_g^{exp} \cos(\zeta^{exp} - \theta^{calc}). \quad (25)$$

Knowing the wave normal direction, the group velocity can be determined from Eq. (9). Repeating this procedure for each experimental group velocity direction we obtain the calculated set of group velocity data  $\{V_g^{calc}(\zeta^{exp})\}$  for a given set of initial guesses of the elastic constants.

Now, considering the elastic constants as variables in a four-dimensional space a nonlinear least-squares minimiza-

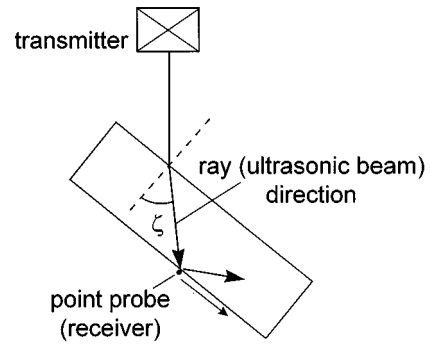


FIG. 4. Schematic of through-transmission technique for group velocity measurements.

tion of deviations between calculated and experimental group velocities is performed to determine the required set of elastic constants:

$$\min_{C_{11}, C_{33}, C_{13}, C_{55}} \frac{1}{2} \sum_{i=1}^m (V_{g_i}^{exp} - V_{g_i}^{calc})^2, \quad (26)$$

where  $m$  is the number of velocity measurements for different directions, and  $V_g^{exp}$  and  $V_g^{calc}$  are the experimental and calculated group velocities, respectively. Equations (7), (9), (11), and (12) are used to compute  $V_g^{calc}$ .

#### IV. COMPARISON OF THE RECONSTRUCTION RESULTS FROM GROUP AND PHASE VELOCITY DATA IN SYMMETRY PLANES

As an example elastic constants which correspond to zinc crystal (hexagonal) and graphite/epoxy composite (orthotropic) were used to simulate both QL and QT wave synthetic group  $[V_g^{exp}(\zeta^{exp})]$  and phase  $[V_p^{exp}(\theta)]$  velocity data for the 1-3 plane. These elastic constants are referred as "original values." Different levels of noise were introduced in the synthetic group and phase velocities and group veloc-

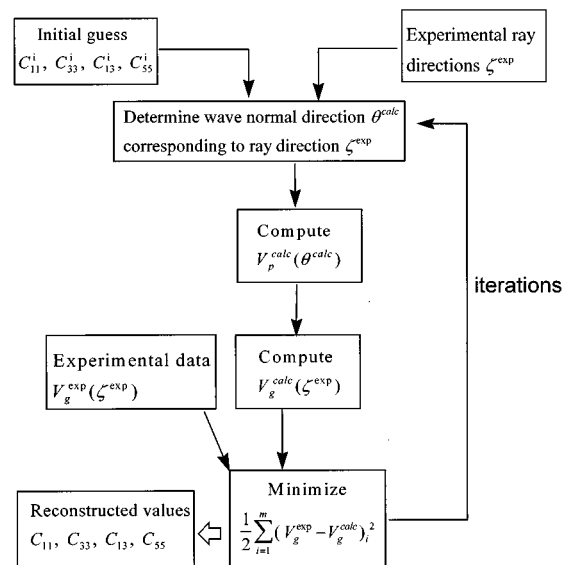


FIG. 5. Flow chart of the inversion procedure for determination of elastic constants from group velocity data in the 1-3 symmetry plane of an orthotropic material.

ity directions to simulate the effect of random scattering in measurements. It was assumed that wave normal and propagation directions can be determined with high precision. Four elastic constants ( $C_{11}$ ,  $C_{33}$ ,  $C_{13}$ , and  $C_{55}$ ) are determined from velocity data in the 1-3 plane.  $C_{33}$  can be determined from longitudinal wave velocity at normal incidence and then fixed for further reconstruction of the remaining three elastic constants. But our simulation results indicate that this does not improve the accuracy in determination of  $C_{33}$  itself, as well as of other elastic constants. Thus we consider simultaneous determination of all four elastic constants and since  $C_{33}$  is effectively decoupled in the equations, it is found most precisely.

For the zinc crystal, the angular range and the number of points for the group velocity data as well as original values for the elastic constants are taken from Ref. 7. Synthetic sets of group velocity "experimental" data with 1% scattering in both velocity values and directions of propagation were generated together with corresponding phase velocity data with 1% scattering. Here for simplicity we assume that the angle and the group velocity data have the same error. However, in an actual experiment the group velocity angle is difficult to measure accurately. In contrast to the group velocity measurement method, the wave normal angle is accurately determined from the incident angle in the phase velocity measurements.<sup>12</sup> Synthetic velocity data are presented in Fig. 6[(a) group and (b): phase]. The angular range and the number of "experimental" points for the graphite/epoxy composite are chosen such that the corresponding phase velocity data range is experimentally available using the double through-transmission technique described in Ref. 4. As an example simulated sets of group and phase "experimental" velocity data with 1% scattering for graphite/epoxy composite are presented in Fig. 7(a) and (b). Note that for both materials the group velocity data include a cuspidal region.

For each group velocity set of "experimental" data the reconstruction is performed using the procedure described above. The initial guess is taken to be 20% from the original elastic constants. One hundred inversions (runs) were made for randomly synthesized velocity data sets to compute the standard deviation of the reconstructed moduli from actual values. A similar reconstruction was performed from the phase velocity data. Several sets of the synthesized velocity data with scattering levels of 0.5%, 1%, 2%, and 5% were used. The standard deviation of the recovered elastic constants from the original ones is shown in Fig. 8(a) (zinc crystal) and (b) (graphite/epoxy composite). We see that the accuracy of determination of elastic constants from phase and group velocities is approximately the same for both the zinc crystal and the graphite/epoxy composite.

## V. RECONSTRUCTION FROM VELOCITY DATA IN NONSYMMETRY PLANES

In the nonsymmetry plane the ray vector deviates from the incident plane. The group velocity measurements can be performed by scanning the receiver to find the energy propagation direction and measuring the time of flight.

Here we demonstrate that for transversely isotropic material all five elastic constants can be determined from ex-

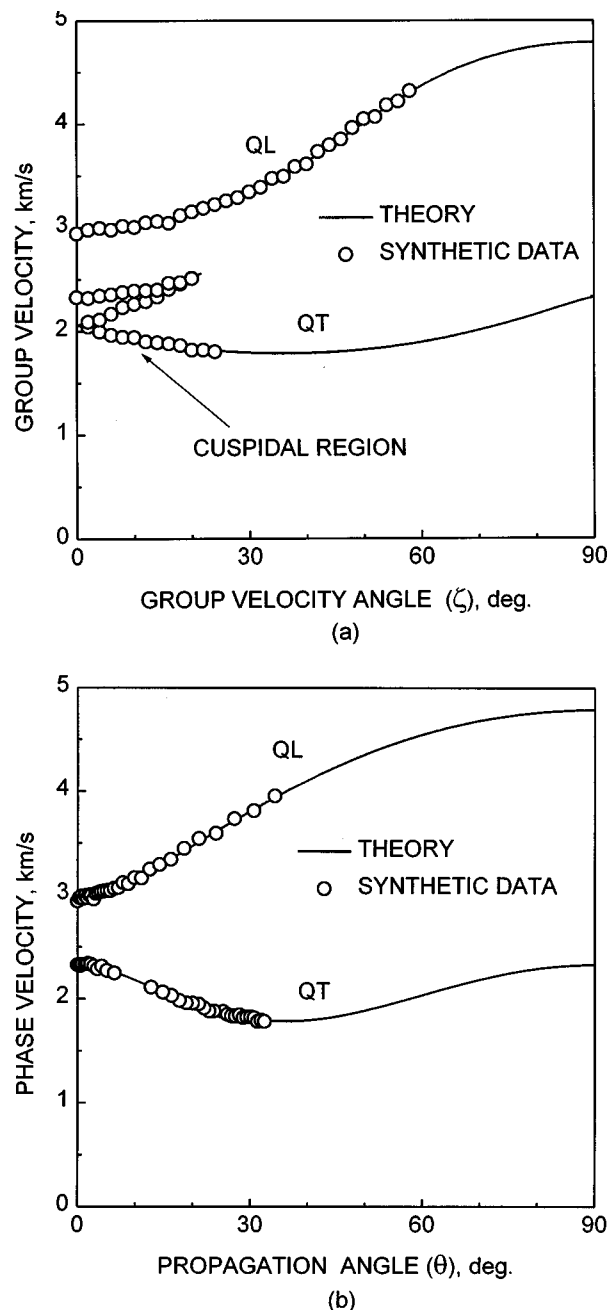


FIG. 6. (a) Group and (b) phase velocity computer-generated "experimental" data for zinc crystal.

perimental QL, QT1, and QT2 group velocity data  $\{V_g^{\text{exp}}(\Phi^{\text{exp}}, \Theta^{\text{exp}})\}$  in one incident plane (nonsymmetry 3-3' plane) as shown in Fig. 2(b). It was shown in Ref. 13 that similar reconstruction of nine elastic constants of an orthotropic material is not stable to scatter and selection of initial guesses. However, one can determine the remaining two elastic constants ( $C_{12}$  and  $C_{66}$ ) assuming that seven elastic constants ( $C_{11}$ ,  $C_{22}$ ,  $C_{33}$ ,  $C_{13}$ ,  $C_{23}$ ,  $C_{44}$ , and  $C_{55}$ ) were found from measurements in the 1-3 and 2-3 symmetry planes.

The inversion procedure is similar to the one described in Sec. III for determination of elastic constants from velocity data in symmetry planes. First, given the experimentally measured energy propagation direction ( $\Phi^{\text{exp}}, \Theta^{\text{exp}}$ ) and an

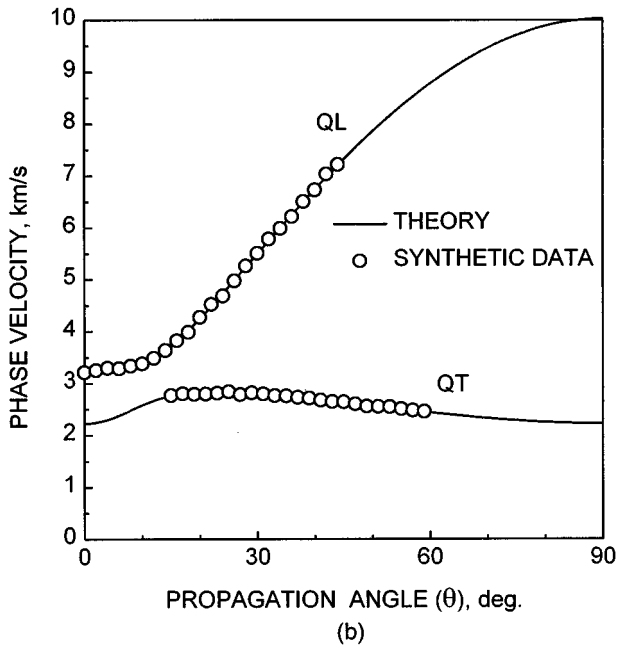
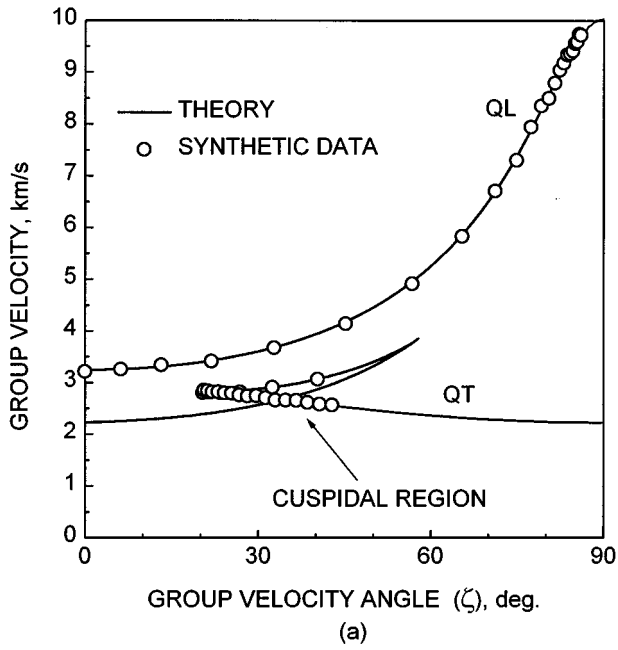


FIG. 7. (a) Group and (b) phase velocity computer-generated “experimental” data for graphite/epoxy composite.

initial guess for the elastic constants we determine the wave normal direction  $(\phi, \theta)$  by solving the system of equations:

$$\frac{V_{g3}(\phi, \theta)}{|\mathbf{V}_g(\phi, \theta)|} = \cos \Theta^{\text{exp}}, \quad (27)$$

$$\frac{V_{g2}(\phi, \theta)}{V_{g1}(\phi, \theta)} = \tan \Phi^{\text{exp}}$$

on the interval  $\phi \in [0, \pi]$ ,  $\theta \in [-\pi/2, \pi/2]$ . If the solution is not unique we choose the one which produces the smallest difference between calculated and experimental group velocity.

After the wave normal direction is found we employ nonlinear least-squares minimization, described in Sec. III.

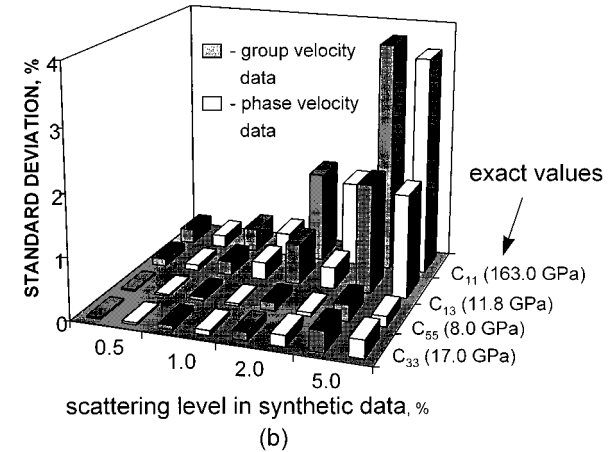
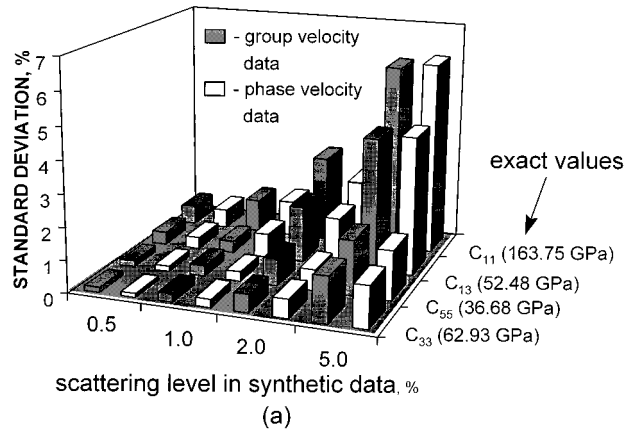


FIG. 8. Standard deviation of the reconstructed elastic constants from the original ones for (a) zinc crystal and (b) graphite/epoxy composite.

To calculate group velocities we use the analytical formulas in the rotated coordinate system, given in Sec. II for transversely isotropic materials, and the exact equation (3) for orthotropic materials.

As an example, we consider the determination of elastic constants from the synthetic velocity data in the  $\varphi=45^\circ$  plane in the ceramic composite material, which is assumed transversely isotropic. The range for the QL wave is  $0^\circ-50^\circ$ , for QT1  $35^\circ-75^\circ$ , and for QT2  $30^\circ-70^\circ$  in terms of the angle  $\theta$  which characterizes the wave normal direction. The energy propagation direction  $\mathbf{N}$  does not lie in the  $\varphi=45^\circ$  [Fig. 2(b)] plane and is computed to produce a synthetic set of experimental data  $\{V_g^{\text{exp}}(\Phi^{\text{exp}}, \Theta^{\text{exp}})\}$ . Synthetic group velocity data used for inversion are shown in Fig. 9. Open circles represent the data with ray direction angle  $\Phi \leq 45^\circ$  and closed circles correspond to the data with  $\Phi > 45^\circ$ . The total number of experimental points is 71. Scattering of 0.5%, 1%, 2%, and 5% is introduced into the group velocities using a random function generator. It is assumed that the energy propagation direction  $(\Phi^{\text{exp}}, \Theta^{\text{exp}})$  is known precisely. The inversion procedure described in the previous section is applied. The results of elastic constant determination from synthetic group velocity experimental data with different scattering levels for a transversely isotropic ceramic matrix composite are presented in Table I and compared with the reconstruction from phase velocity data  $\{V_p^{\text{exp}}(\theta^{\text{exp}})\}$ , which is

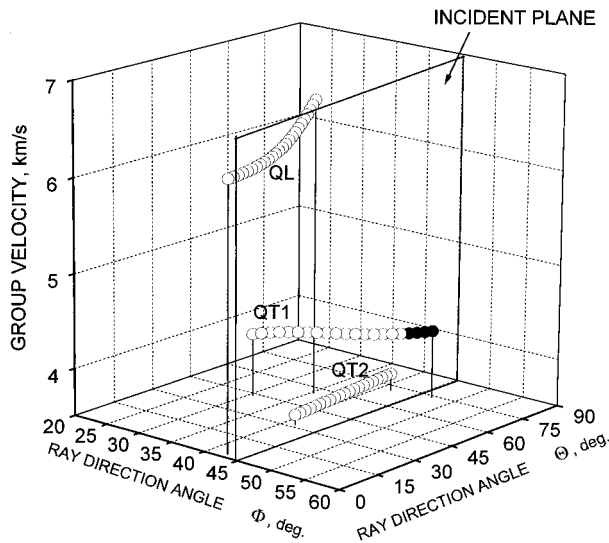


FIG. 9. Computer-generated “experimental” group velocity data in the  $\varphi = 45^\circ$  incident plane for the transversely isotropic ceramic composite. Data with angle  $\Phi \leq 45^\circ$  are shown by open circles and data with  $\Phi > 45^\circ$  by closed circles.

described in Ref. 13. Again we see that the accuracy of elastic constant determination from group and phase velocities is approximately the same.

In another example we determine two elastic constants ( $C_{12}$  and  $C_{66}$ ) from the synthetic velocity data in the  $\varphi = 45^\circ$  plane in the ceramic composite material, which this time is assumed orthotropic. The orthotropy is introduced by decreasing  $C_{22}$ ,  $C_{12}$ , and  $C_{66}$  by 10% and increasing  $C_{33}$ ,  $C_{13}$ , and  $C_{55}$  by 10%. It is assumed that other elastic constants are known from measurements in the (1-3) and (2-3) symmetry planes. The angular ranges and number of experimental points are taken the same as in the previous example. The inversion is performed from synthetic group velocity data using exact (Sec. I) and approximate (Sec. II) equations for group velocities. The reconstruction results are summa-

TABLE I. Standard deviations of the reconstructed elastic constants from the actual were computed using 100 runs for each level of velocity data scatter. The elastic constants were determined from group and phase velocity data in the  $\varphi = 45^\circ$  plane [Fig. 2(b)] for a transversely isotropic ceramic composite [ $C_{ij}(\text{reconstructed}) = C_{ij}(\text{exact}) \pm \sigma$ ].

Elastic constant (exact value, GPa)	Type of velocity data	Standard deviation $\sigma$ , GPa		
		0.5% scatter	1.0% scatter	2.0% scatter
$C_{11}$ (150)	phase	1.28	2.51	4.20
	group	1.38	2.66	5.62
$C_{33}$ (100)	phase	0.12	0.31	0.56
	group	0.15	0.33	0.54
$C_{13}$ (32)	phase	0.39	0.78	1.53
	group	0.45	0.86	1.83
$C_{55}$ (36)	phase	0.31	0.69	1.00
	group	0.13	0.25	0.50
$C_{23}$ (36)	phase	0.29	0.59	0.91
	group	0.19	0.39	0.75

TABLE II. Standard deviations of the reconstructed elastic constants from the actual were computed using 100 runs for each level of velocity data scatter. The elastic constants were determined from group velocity data in the  $45^\circ$  plane for an orthotropic ceramic composite. Exact and approximate equations for group velocities were used in the inversion procedure [ $C_{ij}(\text{reconstructed}) = C_{ij}(\text{exact}) \pm \sigma$ ].

Elastic constant (exact value, GPa)	Type of velocity data	Standard deviation, GPa		
		0.5% scatter	1.0% scatter	2.0% scatter
$C_{12}$ (25.6)	exact	1.67	2.89	3.45
	approximate	2.38	3.32	5.86
$C_{66}$ (28.8)	exact	1.23	1.68	2.56
	approximate	1.78	2.37	3.87

rized in Table II. The inversion results using approximate equations are comparable with those using the exact ones.

## VI. CONCLUSION

An inversion procedure based on a nonlinear least-squares method was used to determine elastic constants from group or phase velocity data in orthotropic and transversely isotropic materials. The algorithm described can utilize group velocity data in a cuspidal region. It was shown that for orthotropic material seven elastic constants (all except  $C_{12}$  and  $C_{66}$ ) can be determined from group velocity data in symmetry planes. The remaining two elastic constants of orthotropic materials can be determined from measurements in a nonsymmetry plane using approximated (closed-form expressions for velocities and polarizations in transversely isotropic materials) or exact equations. For hexagonal material all five independent elastic constants can be determined from a nonsymmetry plane.

It was found that for the same accuracy in phase and group velocity data the same accuracy in the elastic constants determined has been achieved. This conclusion assumes that the group velocity direction can be determined with the same precision as time delay measurements. However, in actual experiments the determination of the group velocity propagation direction requires scanning of the transmitted fields by the receiver. The error of angle determination in such experiments could be significant in this case. In phase velocity measurements, using, for example, the double through-transmission technique, the wave normal direction is calculated from Snell’s law and thus is determined very precisely. The issue of propagation direction determination for phase and group velocity needs to be carefully considered when one selects a method for elastic constant measurement.

## APPENDIX: ELASTIC CONSTANTS $C'_{ij}$ IN THE ROTATED COORDINATE SYSTEM FOR TRANSVERSELY ISOTROPIC MATERIALS

The elastic constants  $C'_{ij}$  used for the calculation of the phase and group velocities in transversely isotropic material (Sec. II) in the rotated coordinate system ( $1'2'3'$ ) are given by

$$C'_{11} = C_{11}c_1^4 + C_{33}s_1^4 + 2(C_{13} + 2C_{55})s_1^2c_1^2, \quad (\text{A1})$$

$$C'_{33} = C_{11}s_1^4 + C_{33}c_1^4 + 2(C_{13} + 2C_{55})s_1^2c_1^2, \quad (\text{A2})$$

$$C'_{13} = (C_{11} + C_{33})s_1^2c_1^2 + C_{13}(s_1^4 + c_1^4) - 4C_{55}s_1^2c_1^2, \quad (\text{A3})$$

$$C'_{44} = C_{44}c_1^2 + C_{66}s_1^2, \quad (\text{A4})$$

$$C'_{55} = (C_{11} + C_{33})s_1^2c_1^2 - 2C_{13}c_1^2s_1^2 + C_{55}(s_1^2 - c_1^2), \quad (\text{A5})$$

$$C'_{15} = C_{11}s_1c_1^3 - C_{33}s_1^3c_1 + (C_{13} + 2C_{55})s_1c_1(s_1^2 - c_1^2), \quad (\text{A6})$$

$$C'_{53} = C_{11}s_1^3c_1 - C_{33}s_1c_1^3 + (C_{13} + 2C_{55})s_1c_1(c_1^2 - s_1^2), \quad (\text{A7})$$

$$C'_{46} = (C_{55} - C_{44})s_1c_1, \quad (\text{A8})$$

where

$$s_1 = \cos \varphi \sin \theta, \quad c_1 = \sqrt{1 - s_1^2}. \quad (\text{A9})$$

The angles  $\theta$  and  $\varphi$  characterize the wave-vector direction [Eq. (13)] and are shown in Fig. 2.

The rotated elastic constants  $C'_{33}$ ,  $C'_{55}$ ,  $C'_{53}$ , and  $C'_{44}$  for an orthotropic material are given in Ref. 13. Here we provided the additional three elastic constants ( $C'_{13}$ ,  $C'_{15}$ ,  $C'_{46}$ ) which are used in the approximate Eqs. (15)–(21):

$$\begin{aligned} C'_{13} = & C_{11}s_1^2c_1^2 + C_{12}(s_1^4 + c_1^4)s_2^2 + C_{13}(s_1^4 + c_1^4)c_2^2 \\ & + C_{22}s_1^2s_2^2c_1^2 + C_{33}s_1^2c_1^2c_2^4 + 2(C_{23} + 2C_{44}) \\ & \times c_2^2s_1^2c_1^2s_2^2 - 4C_{55}s_1^2c_1^2c_2^2 - 4C_{66}s_1^2c_1^2s_2^2, \end{aligned} \quad (\text{A10})$$

$$\begin{aligned} C'_{15} = & C_{11}s_1c_1^3 + C_{12}(s_1^3c_1 - s_1c_1^3)s_2^2 + C_{13}(s_1^3c_1c_2^2 \\ & - s_1c_1^3c_2^2) - C_{22}s_1^3c_1s_2^4 - 2C_{23}s_1^3c_1s_2^2c_2^2 \\ & - C_{33}s_1^3c_1c_2^4 - 4C_{44}s_1^3s_2^2c_2^2 - 2C_{55}(c_1^2 - s_1^2)s_1c_1c_2^2 \\ & + 2C_{66}(s_1^2 - c_1^2)s_1c_1s_2^2, \end{aligned} \quad (\text{A11})$$

$$\begin{aligned} C'_{46} = & -C_{12}s_1c_1^2s_2c_2 + C_{13}s_1c_1^2s_2s_2 + C_{22}s_1c_1^2s_2^3c_2 \\ & + C_{23}(s_1c_1^2s_2c_2^3 - s_1c_1^2s_2^3c_2) + 2C_{44}(c_2^2 - s_2^2) \\ & \times s_1c_1^2s_2c_2 + (C_{55} - C_{66})(c_1^2 - s_1^2)s_1s_2c_2, \end{aligned} \quad (\text{A12})$$

where  $s_1$  and  $c_1$  are given by Eq. (A9) and

$$c_2 = \cos \theta / c_1, \quad s_2 = -\sin \theta \sin \phi / c_1. \quad (\text{A13})$$

<sup>1</sup>R. Truell, C. Elbaum, and B. B. Chick, *Ultrasonic Methods in Solid State Physics* (Academic, New York, 1969).

<sup>2</sup>R. D. Kritz and W. W. Stinchcomb, "Elastic moduli of transversely isotropic graphite fibers and their composites," *Exp. Mech.* **19**, 41–49 (1979).

<sup>3</sup>S. I. Rokhlin and W. Wang, "Ultrasonic evaluation of in-plane and out-plane elastic properties of composite materials," *Review of Progress in QNDE*, edited by D. O. Thompson and D. E. Chimenti (Plenum, New York, 1989), Vol. 8B, pp. 1489–1496.

<sup>4</sup>Y. C. Chu and S. I. Rokhlin, "Comparative analysis of through-transmission ultrasonic bulk wave methods for phase velocity measurements in anisotropic materials," *J. Acoust. Soc. Am.* **95**, 3204–3212 (1994).

<sup>5</sup>Y. C. Chu and S. I. Rokhlin, "Stability of determination of composite moduli from velocity data in planes of symmetry for weak and strong anisotropies," *J. Acoust. Soc. Am.* **95**, 213–225 (1994).

<sup>6</sup>W. Sachse and K. Y. Kim, "Novel approaches for the ultrasonic NDE of thick and other composites," *Review of Progress in QNDE*, edited by D. O. Thompson and D. E. Chimenti (Plenum, New York, 1989), Vol. 8B, pp. 1473–1480.

<sup>7</sup>K. Y. Kim and W. Sachse, "Direct determination of group velocity surfaces in a cuspidal region in zinc," *J. Appl. Phys.* **75**, 1435–1441 (1994).

<sup>8</sup>A. Minachi, D. K. Hsu, and R. B. Thompson, "Single-sided determination of elastic constants of thick composites using acoustoultrasonic technique," *J. Acoust. Soc. Am.* **96**, 353–362 (1994).

<sup>9</sup>A. G. Every and W. Sachse, "Determination of all the elastic constants of anisotropic solids from acoustic-wave group-velocity measurements," *Phys. Rev. B* **42**, 8196–8205 (1990).

<sup>10</sup>K. Y. Kim, "Analytic relations between the elastic constants and group velocity in an arbitrary direction of symmetry planes of media with orthorhombic or higher symmetry," *Phys. Rev. B* **49**, 3713–3724 (1994).

<sup>11</sup>K. Y. Kim, T. Ohtani, A. R. Baker, and W. Sachse, "Determination of all elastic constants of orthotropic plate specimens from group velocity data," *Res. Nondestruct. Eval.* **7**, 13–29 (1995).

<sup>12</sup>S. I. Rokhlin and W. Wang, "Double through-transmission bulk wave method for ultrasonic phase velocity measurement and determination of elastic constants of composite materials," *J. Acoust. Soc. Am.* **91**, 3303–3312 (1992).

<sup>13</sup>Y. C. Chu, A. D. Degtyar, and S. I. Rokhlin, "On determination of orthotropic material moduli from ultrasonic velocity data in nonsymmetry planes," *J. Acoust. Soc. Am.* **95**, 3191–3203 (1994).

<sup>14</sup>B. A. Auld, *Acoustic Fields and Waves in Solids* (Krieger, Malabar, FL, 1990).

<sup>15</sup>F. I. Fedorov, *Theory of Elastic Waves in Crystals* (Plenum, New York, 1968).

<sup>16</sup>M. J. P. Musgrave, *Crystal Acoustics* (Holden Day, San Francisco, 1970).

# Determination of elastic moduli, density, attenuation, and thickness of a layer using ultrasonic spectroscopy at two angles

Anton I. Lavrentyev<sup>a)</sup> and Stanislav I. Rokhlin

The Ohio State University, Nondestructive Evaluation Program, 190 West 19th Avenue, Columbus, Ohio 43210

(Received 11 February 1997; accepted for publication 30 July 1997)

An ultrasonic method for determination of the complete set of acoustical and geometrical properties of an isotropic layer embedded between two known materials (similar or dissimilar) is described. The method allows simultaneous determination of the layer thickness, density, elastic moduli, and attenuation (longitudinal and shear) from normal and oblique incidence reflection (transmission) frequency spectra. Reflection (transmission) from the layer is represented as a function of six nondimensional parameters which are determined from the two experimentally measured spectra: one at normal and one at oblique incidence. The introduction of the set of nondimensional parameters allows one to transform the reconstruction process from one search in a six-dimensional space to two searches in three-dimensional spaces (one search for normal incidence and one for oblique). Thickness, density, and longitudinal and shear elastic moduli of the layer are calculated from the nondimensional parameters determined. The sensitivity of the method to individual properties and its stability against experimental noise are studied and the inversion algorithm is accordingly optimized. Experimental examples are given for a layer immersed in water and for a thermoplastic joint. © 1997 Acoustical Society of America. [S0001-4966(97)01012-6]

PACS numbers: 43.35.Ns, 43.35.Zc, 43.20.Gp, 43.60.Pt [HEB]

## INTRODUCTION

Ultrasonic spectroscopy has long been thought promising for characterization of thin layers immersed in water or embedded between two known materials (similar or dissimilar).<sup>1</sup> The interphase layer between two substrates is usually used for their joining as, for example, in adhesive joints. Ultrasonic signals reflected from the front and back surfaces of a thin layer usually overlap in the time domain and interfere. Chang *et al.*<sup>2</sup> and Flynn<sup>3</sup> determined ultrasonic velocity and attenuation from the ultrasonic reflected signal and correlated them with the joint cohesive strength. The influence of frequency-dependent attenuation on amplitude and phase spectra of the signal reflected from the joint bond-line was studied in Ref. 4. An ultrasonic technique for the determination of elastic constants of anisotropic plates with thickness less than the ultrasonic wavelength is described in Ref. 5. An algorithm for determination of the moduli and thickness of a weak boundary layer is proposed in Ref. 6. Through-thickness resonance measurements were used in Refs. 7 and 8 to calculate both the thickness and the modulus of an adhesive layer. Inversion of leaky Lamb wave dispersion curves was used in Ref. 9 to determine the longitudinal and shear wave velocities and thickness of an adhesive layer inside a joint. A low-frequency through-transmission ultrasonic technique was proposed in Ref. 10 to determine the thickness or density of a thin layer. Normalized amplitude

spectra were used in Ref. 11 to measure attenuation. A comprehensive review of adhesive joint testing is given in Ref. 12.

A detailed analysis of application of the ultrasonic method for measurements of thin layer properties and adhesive joints was given by Kinra *et al.* in Refs. 13–17. The analysis was performed for an ultrasonic wave normally incident on the layer. The main attention was given to determination of one of the four properties of a thin plate (wave velocity, density, thickness, or attenuation) from the spectrum of the normally reflected or transmitted ultrasonic signal.<sup>14,15</sup>

In this paper we propose an ultrasonic method for simultaneous determination of all properties of the layer: density, thickness, and longitudinal and shear moduli and attenuations using ultrasonic measurements at only two angles: normal and oblique incidence. We assume the bond between the layer and substrates is perfect, the substrate properties are known, and the layer is isotropic. In the first section the ultrasonic wave interaction with a layer is described by six nondimensional parameters. This allows one to reduce the number of parameters to be measured. In the second section a two-step inversion algorithm to determine the layer properties is introduced. The algorithm is based on two consecutive inversion searches in two three-dimensional spaces of the layer parameters. The sensitivity of the algorithm to the layer parameters and stability against random noise is studied. Experimental techniques are described in Sec. III and the results of experiments to validate the method in Sec. IV.

<sup>a)</sup>Now with United Technologies Research Center, 411 Silver Lane, MS 129-86, East Hartford, CT 06108.

# I. PROBLEM STATEMENT AND THEORETICAL BACKGROUND

## A. Effect of layer properties on reflection and transmission at normal incidence

It is well known that it is impossible to determine modulus, density, thickness, and attenuation of an elastic layer using only ultrasonic measurement at normal incidence. To illustrate this let us consider a layer between two substrates indicating the substrates and layer, respectively, by subscripts 1 and 2. At normal incidence only longitudinal waves are present in this system. Reflection and transmission coefficients for the layer are given by<sup>18</sup>

$$R = \frac{R_{12}(1 - R_{12}e^{2ik_1h})}{1 - R_{12}^2e^{2ik_1h}}, \quad (1)$$

$$T = \frac{R_{12}e^{2ik_1h}}{1 - R_{12}^2e^{2ik_1h}}, \quad (2)$$

where  $k_1 = k_1' + ik_1''$  is the wave number,  $h$  is the layer thickness, and  $R_{12} = (Z_2 - Z_1)/(Z_2 + Z_1)$  is the coefficient of reflection from the adherend/adhesive interface. Here  $Z_2 = \rho\omega/k$  is the complex impedance. Attenuation inside the substrates is taken to be zero since it has negligible effect on the spectra; thus the substrate impedance  $Z_1$  is real.  $R$  and  $T$  depend on four independent layer properties: modulus ( $\lambda + 2\mu$ ), density  $\rho$ , thickness  $h$ , and attenuation  $\alpha_1$ . The number of independent parameters can be reduced. The reflection and transmission coefficients (1) and (2) can be rewritten so that they depend only on three nondimensional layer parameters:

$$R = \frac{Z_N - 1/Z_N + 1(1 - Z_N - 1/Z_N + 1e^{2i\bar{w}\bar{h}(1+i\alpha_1)})}{1 - (Z_N - 1/Z_N + 1)^2e^{2i\bar{w}\bar{h}(1+i\alpha_1)}}, \quad (3)$$

$$T = \frac{Z_N - 1/Z_N + 1e^{2i\bar{w}\bar{h}(1+i\alpha_1)}}{1 - (Z_N - 1/Z_N + 1)^2e^{2i\bar{w}\bar{h}(1+i\alpha_1)}}, \quad (4)$$

where impedance ratio  $Z_N$ , nondimensional thickness  $\bar{h}$ , and attenuation  $\alpha_1$  are given by

$$Z_N = \frac{Z_2}{Z_1}, \quad (5)$$

$$\bar{h}_1 = \frac{h}{V_1} \omega_0, \quad (6)$$

$$\alpha_1 = k_1''/k_1'. \quad (7)$$

Here  $V_1 = [(\lambda + 2\mu)/\rho]^{1/2}$  is the longitudinal velocity in the adhesive layer. We choose  $\omega_0 = 1$  MHz since for convenience we use  $h$  in mm and  $V$  in km/s. The reflection and transmission from the adhesive layer at normal incidence are functions of frequency and three independent nondimensional parameters:  $Z_N$ ,  $\bar{h}_1$ , and  $\alpha_1$ .

Figure 1 shows the effect of  $Z_N$  and  $\bar{h}_1$  on reflection spectrum at normal incidence. Calculations are done using parameters typical for an Al-to-Al adhesive joint. The minima observed in the reflection spectra are due to destructive interference of the wave reflected from the front surface

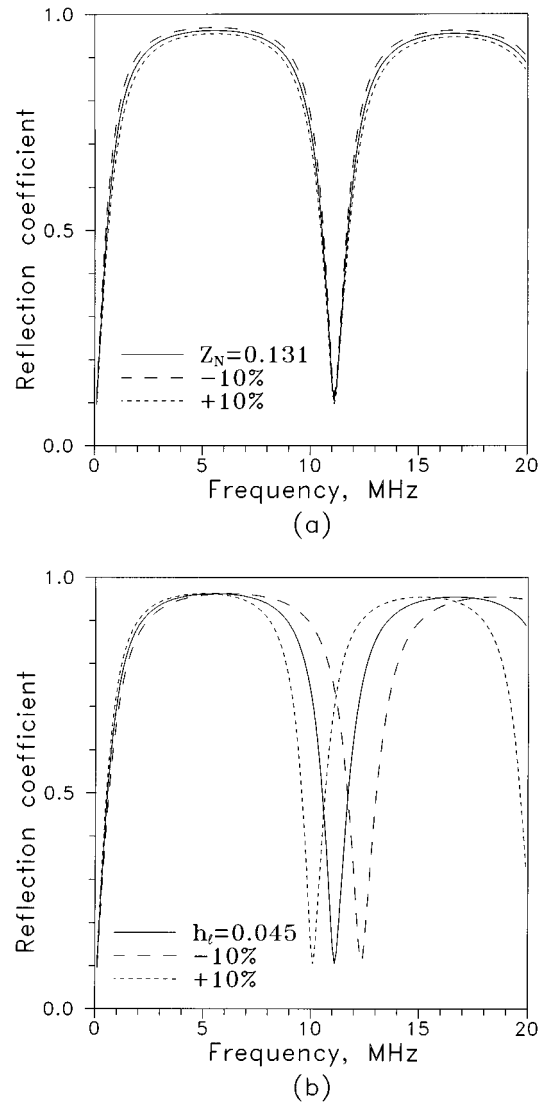


FIG. 1. Effect of (a) the impedance ratio  $Z_N = Z_2/Z_1$  and (b) the nondimensional thickness  $\bar{h}_1 = h/V_1 \cdot \omega_0$  ( $\omega_0$  is constant) on reflection from the adhesive layer inside the joint. Parameters used for calculation are  $Z_N = 0.131$ ,  $\bar{h}_1 = 0.045$ , and  $\alpha_1 = 0.01$ .

of the adhesive layer and waves multiply reflected inside the layer. The minima will reach zero when zero attenuation  $\alpha_1$  is used. One can see that for fixed  $\alpha_1$  and  $\bar{h}_1$  increase of the impedance ratio  $Z_N$  results in reflection amplitude decrease [Fig. 1(a)]. At fixed  $\alpha_1$  and  $Z_N$  nondimensional thickness  $\bar{h}_1$  increase results in resonance minima shifts towards lower frequency [Fig. 1(b)]. The  $\bar{h}_1$  increase does not change the maxima and minima amplitudes. The sensitivity of measurement is higher for  $\bar{h}_1$  than for  $Z_N$ . Attenuation does not change the position of the minima and maxima but it influences their depth and width and affects areas beyond antiresonance.<sup>19</sup>

It will be shown below that all three nondimensional parameters [ $Z_N$ ,  $\bar{h}_1$ , and  $\alpha_1$  given by (5), (6), and (7)] can be determined from the reflection or transmission frequency spectrum at normal incidence. However  $Z_N$  and  $\bar{h}_1$  are functions of three dimensional parameters: modulus ( $\lambda + 2\mu$ ), density  $\rho$ , and thickness  $h$ , and thus cannot be determined



uniquely from Eqs. (5) and (6). In some practical applications, one of the dimensional properties of the layer can be known: for example, the density of a properly cured adhesive layer inside an adhesive joint. In this case the layer thickness and modulus can be determined from  $Z_N$  and  $\bar{h}_1$  using (5) and (6). However, if none of the layer properties is known in advance, the nondimensional parameters cannot be determined: this is the principal limitation of normal incidence measurement. To find all four-dimensional properties [ $(\lambda + 2\mu)$ ,  $\rho$ ,  $h$ , and  $\alpha_1$ ] we propose to use an additional measurement at oblique incidence. In addition, the use of oblique incidence allows one to determine shear modulus  $\mu$  and shear wave attenuation  $\alpha_t$ , thus all six (longitudinal and shear) layer properties can be determined. This issue is addressed in the following sections.

## B. Definition of the unique set of material parameters

At oblique incidence both longitudinal and shear waves are excited inside the adhesive layer. Reflection and transmission coefficients depend on six layer parameters: elastic moduli, thickness, density, and longitudinal and shear wave attenuations:

$$\lambda + 2\mu, \quad \mu, \quad \rho, \quad h, \quad \alpha_1, \quad \alpha_t. \quad (8)$$

As shown in the previous section the reflection and transmission coefficients at normal incidence depend only on three nondimensional independent variables  $Z_N$ ,  $\bar{h}_1$ , and  $\alpha_1$  given by Eqs. (5), (6), and (7). It is convenient to use the same nondimensional parameters also to describe oblique incidence reflection and transmission. A full set of nondimensional parameters defining oblique incidence reflection and transmission includes  $Z_N$ ,  $\bar{h}_1$ , and  $\alpha_1$  and three more nondimensional parameters: nondimensional thicknesses at oblique incidence,

$$\bar{h}_{\theta l} = \frac{h \cos \theta_l}{V_l} \omega_0, \quad (9)$$

$$\bar{h}_{\theta t} = \frac{h \cos \theta_t}{V_t} \omega_0, \quad (10)$$

and shear wave attenuation

$$\alpha_t = k_t''/k_t', \quad (11)$$

where  $V_t = [\mu/\rho]^{1/2}$  is the shear wave velocity in the adhesive layer,  $\theta_l$  and  $\theta_t$  are longitudinal and shear wave propagation angles inside the layer, and  $\omega_0$  is a normalization constant. All six nondimensional parameters,

$$Z_N, \quad \bar{h}_1, \quad \bar{h}_{\theta l}, \quad \bar{h}_{\theta t}, \quad \alpha_1, \quad \alpha_t, \quad (12)$$

can be found from two measurements: one at normal and the other at oblique incidence, as will be shown below. Four nondimensional parameters from the set (12) ( $Z_N$ ,  $\bar{h}_1$ ,  $\bar{h}_{\theta l}$ ,  $\bar{h}_{\theta t}$ ) fully define the dimensional parameters from the set (12):

$$\lambda + 2\mu = \frac{Z_N Z_1}{\xi_0} \frac{\sqrt{\bar{h}_1^2 - \bar{h}_{\theta l}^2}}{\bar{h}_1}, \quad (13)$$

$$\mu = \frac{Z_N Z_1}{\xi_0} \frac{\bar{h}_1 \sqrt{\bar{h}_1^2 - \bar{h}_{\theta l}^2}}{\bar{h}_1^2 - \bar{h}_{\theta l}^2 + \bar{h}_{\theta t}^2}, \quad (14)$$

$$\rho = Z_N Z_1 \xi_0 \frac{\bar{h}_1}{\sqrt{\bar{h}_1^2 - \bar{h}_{\theta l}^2}}, \quad (15)$$

$$h = \frac{\sqrt{\bar{h}_1^2 - \bar{h}_{\theta l}^2}}{\xi_0 \omega_0}, \quad (16)$$

where  $\xi_0 = \sin \theta_0/V_0$ , and  $\theta_0$  and  $V_0$  are propagation angle and wave velocity in water. Attenuations  $\alpha_l$  and  $\alpha_t$  are part of both sets (12) and (8). Instead of elastic moduli longitudinal and shear wave velocities,  $V_l$  and  $V_t$ , can be used. They are related to the nondimensional parameters by

$$V_l = \frac{\sqrt{\bar{h}_1^2 - \bar{h}_{\theta l}^2}}{\xi_0 \bar{h}_1}, \quad V_t = \frac{\sqrt{\bar{h}_1^2 - \bar{h}_{\theta l}^2}}{\xi_0 \sqrt{\bar{h}_1^2 - \bar{h}_{\theta l}^2 + \bar{h}_{\theta t}^2}}. \quad (17)$$

## II. INVERSION ALGORITHM, ITS ANALYSIS, AND VALIDATION

### A. Inversion algorithm

As discussed in the previous section, the reflection spectrum at normal incidence is fully defined by two nondimensional parameters,  $Z_N$  and  $\bar{h}_1$  (and attenuation), which can be determined from experimental data by inversion.  $Z_N$  and  $\bar{h}_1$  are functions of three dimensional parameters:  $\lambda + 2\mu$ ,  $h$ , and  $\rho$ . Two of them can be determined only if the third is known: this is the main limitation of using only normal incidence measurements for the layer characterization. To determine all layer properties (8), oblique incidence measurements are also required.

Our goal is to determine six layer properties without any prior knowledge, as is often required in practice, using measurements of both normal and oblique incidence reflection (transmission) spectra. Oblique incidence reflection (transmission) coefficients depend on six layer parameters [(8) or (12)]. One finds that all six parameters cannot be reconstructed from a single oblique incidence measurement with reasonable precision. Also, one can try to determine six dimensional parameters from simultaneous least square minimization of the data for normal and oblique incidence. This requires search in a six-dimensional space which complicates finding the unique solution.

For the nondimensional set of parameters (12) the problem is factorized (decomposed) and a two-step algorithm for determination of the adhesive layer properties (Fig. 2) in a three-dimensional space of parameters can be used. First, we determine three nondimensional parameters,  $Z_N$ ,  $\bar{h}_1$ , and  $\alpha_1$ , from reflection (transmission) spectra at normal incidence. Next, considering  $Z_N$ ,  $\bar{h}_1$ , and  $\alpha_1$  as known, three more nondimensional parameters  $\bar{h}_{\theta l}$ ,  $\bar{h}_{\theta t}$ , and  $\alpha_t$  are determined from oblique incidence data (reflection or transmission). The corresponding dimensional parameters (8) are calculated using Eqs. (13)–(16).

Our algorithm assumes that the top and bottom substrates are much thicker than the interface layer and thus signal interference in the substrate is not considered. This is

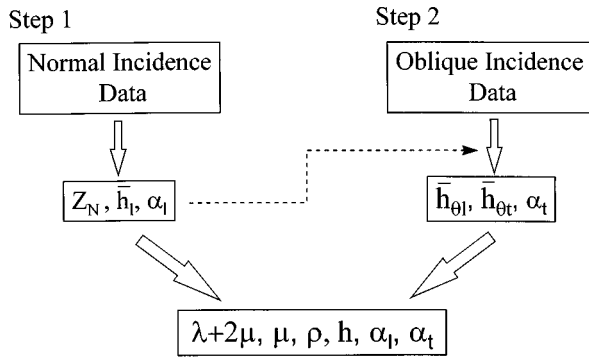


FIG. 2. Schematic of the algorithm for determination of adhesive layer properties from normal and oblique incidence reflection (transmission) spectra.

correct for the impulse regime when different reflections in the substrates are time resolved (the opposite case has been studied and results will be published elsewhere). The reflected signal from the interface layer is much longer than the incident signal due to multiple reflections in the layer (the signal ringing). For thinner substrates the signal doubly reflected in the substrate may interfere with the ringing part of the interface signal, thus appropriate gating of the interface signal should be made (Sec. III D). This is accounted for in our algorithm for normally reflected signals by selecting a limited number of the reverberations in the interface layer. For the oblique incident signal, due to increase in the acoustic path and the use of an incident shear wave (slower wave velocities) such an interference does not occur and does not need to be accounted for.

The frequency range for the experiment and calculations is selected based on the sensitivity analysis as discussed in the next section. Bandwidth is limited by the transducer characteristics and is carefully established in the experiments.

For inversion we employ the least squares method for the minimization of the sum of squared deviations between the calculated  $R^c$  and the experimental  $R^e$  reflection (transmission) coefficients considering nondimensional parameters (12) as variables in a multidimensional space:

$$\min_{X_i \in \mathcal{D}^n} \frac{1}{2} \sum_{i=1}^m (|R_i^e| - R_i^c)^2. \quad (18)$$

Here,  $X_i$  are nondimensional parameters (12),  $n=3$  is the number of parameters to be found,  $m$  is the number of data points at different frequencies, and  $R^e$  and  $R^c$  are the experimental and calculated reflection (transmission) coefficients, respectively. An approach for calculation of reflection and transmission coefficients is briefly discussed in the Appendix.

## B. Sensitivity of the reflection coefficient to the layer properties

In general, the inverse problem is *well posed* if its solution (a) exists, (b) is unique, and (c) is stable, i.e., to small changes of experimental data (input) correspond small changes of the solution (output). If the solution does not

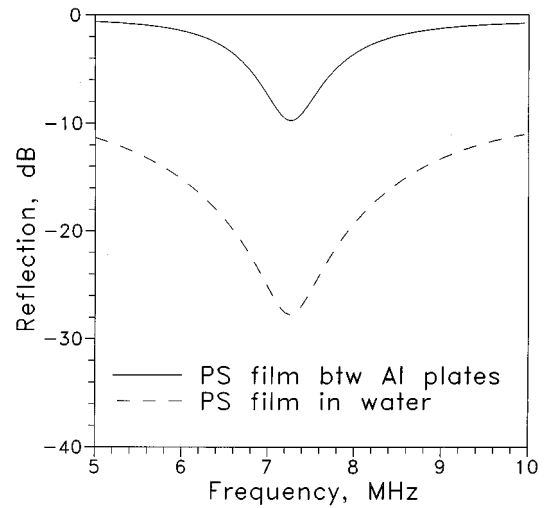


FIG. 3. Reflection spectra for a polystyrene film between aluminum semi-spaces (solid line) and in water (dashed line).

satisfy these conditions, the problem is called *ill posed* and its treatment requires special methods. The main focus of our further discussion is to demonstrate that the layer properties can be found using the proposed algorithm from the measured spectra at normal incidence and one at oblique incidence angle. We take a pragmatic approach. We consider the inverse solution unique if the least-squares minimization converges, whatever the initial guess, to the same solution. We consider the solution stable if it is weakly dependent on random scatter of the experimental data. Another stability consideration is the reflection (transmission) coefficient sensitivity to a parameter  $p$  of the layer. Let us assume explicit dependence of reflection (transmission) coefficient on the layer parameter  $p$ ,  $R=R(p)$ . Then the relative errors in  $p$  and  $R$ ,  $\epsilon_R = \delta|R|/|R|$ ,  $\epsilon_p = \delta p/p$ , are related by

$$\epsilon_p = \epsilon_R / X_{R,p}, \quad (19)$$

where  $X_{R,p}$  is the sensitivity of  $R$  to  $p$ ; it is defined as

$$X_{R,p} = \frac{p}{|R|} \frac{\partial |R|}{\partial p}. \quad (20)$$

If  $|X_{R,p}| \ll 1$ , then an amplification of error occurs. Thus, the sensitivity parameter is a good indicator of inversion stability. This is in line with the intuitive notion that if the reflection (transmission) coefficient is weakly dependent on one of the layer parameters, this parameter is difficult to find from the reflection (transmission) coefficient measurement.

Figure 3 shows spectra of a polystyrene film in water (dashed line) and between aluminum semi-spaces (solid line). Sensitivities of the reflections to  $Z_n$ ,  $\bar{h}_1$ , and  $\alpha_1$  are given in Fig. 4(a) and (b). Several conclusions can be drawn based on the figures presented.

First, the reflection coefficient is most sensitive to  $\bar{h}_1$ .  $X_{R,\bar{h}_1}$  has a distinctive frequency dependence with the sensitivity changing sign at  $f_{\min}$  and highest sensitivity in the vicinity of the minimum.

Second, the sensitivities to  $Z_N$  and  $\alpha_1$  are significantly smaller and have, at first sight, similar frequency dependencies. An important difference between them is that  $X_{R,Z_N}$  has

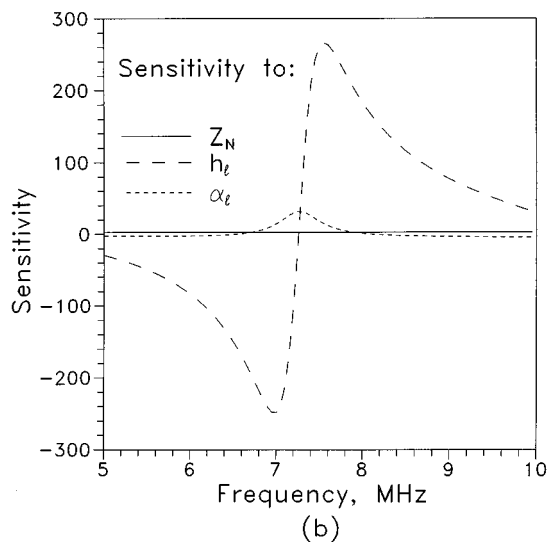
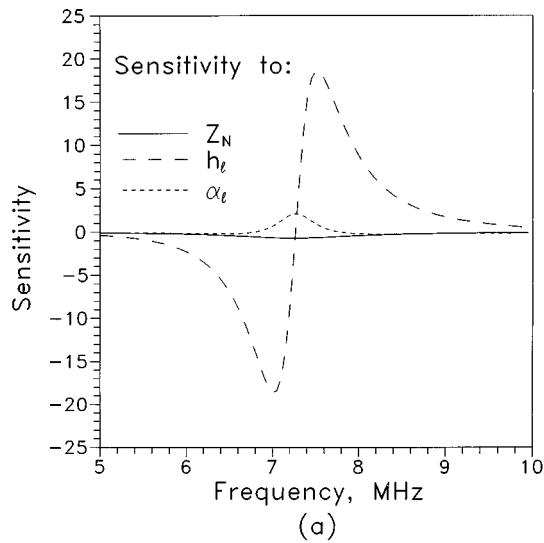


FIG. 4. Sensitivities of the reflection coefficient to  $Z_N$ ,  $\bar{h}_l$ , and  $\alpha_l$  calculated for polystyrene film (a) between aluminum plates and (b) immersed in water.

the same sign for any frequency while  $X_{R,\alpha_l}$  has opposite signs near minima and maxima. This is important for separation of the parameters during the inversion procedure.

Third, the sensitivity of the reflection from the film in water is significantly higher than that for the film between aluminum semispaces [Fig. 4(a) and (b)], which is explained by a much smaller impedance ratio for polystyrene/water than for polystyrene/aluminum. When the impedance ratio is small,  $|R|$  is small resulting in a large  $X_{R,p}$  [Eq. (20)]. This fact only reflects the effect on the relative error. However, in some cases, the absolute error is important, which is defined not by  $X_{R,p}$  [Eq. (20)], but by the derivative  $\partial|R|/\partial p$ . It must be noted here that the sensitivity parameter (20), although being a good indicator of the algorithm stability, does not fully reflect the accuracy of the reconstructed parameters. Other factors such as signal-to-noise ratio, transducer spectrum shape, and bandwidth used for reconstruction can significantly affect the result. In addition, since three parameters are being reconstructed simultaneously, the error in determi-

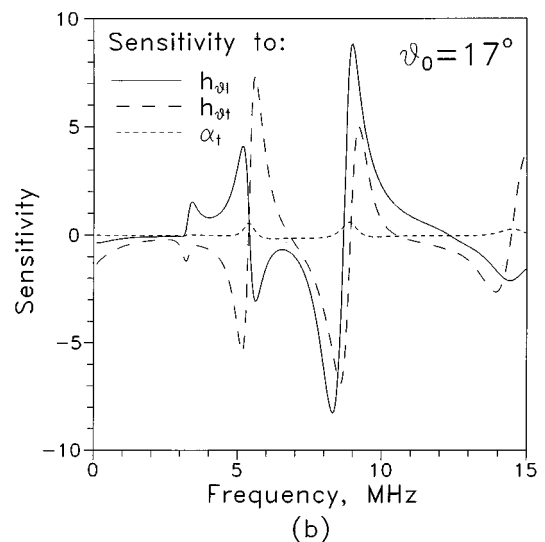
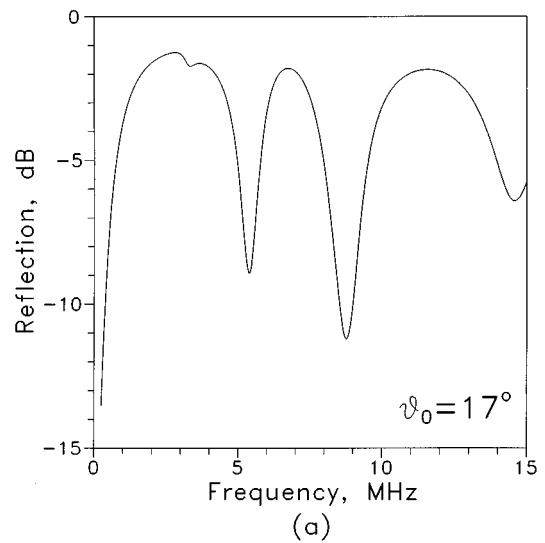


FIG. 5. Reflection from a polystyrene film between aluminum plates at  $\theta_0 = 17^\circ$ : (a) reflection spectrum and (b) sensitivities of  $\bar{h}_{\theta l}$ ,  $\bar{h}_{\theta t}$ , and  $\alpha_t$  determination.

nation of the one with the lowest sensitivity affects the other parameter errors.

Analogous trends are also observed for oblique incidence spectra. Reflectivity spectra and sensitivities to  $\bar{h}_{\theta l}$ ,  $\bar{h}_{\theta t}$ , and  $\alpha_t$  are shown in Fig. 5(a) and (b) for the incident angle  $\theta_0 = 17^\circ$ . Here  $\theta_0$  is the angle of ultrasonic wave incidence from water onto the aluminum plate;  $17^\circ$  is higher than the first critical angle of  $13.7^\circ$  and thus only a transverse wave propagates in aluminum and impinges on the embedded polymer film. At absolute measurements above the critical angle one should account for phase change<sup>20</sup> of the transmission coefficient. In current experiments we deconvolved the reflected signal from the interface layer with the signal from the bottom surface of the top plate (in the unbonded region), thus accounting for the possible phase change. Our analysis shows that at  $\theta_0 = 17^\circ$  the spectral minima are deeper and sensitivities to nondimensional parameters higher than at greater  $\theta_0$  (for example,  $\theta_0 = 20^\circ$ ). Although it can be concluded that for reconstruction of nondimensional param-

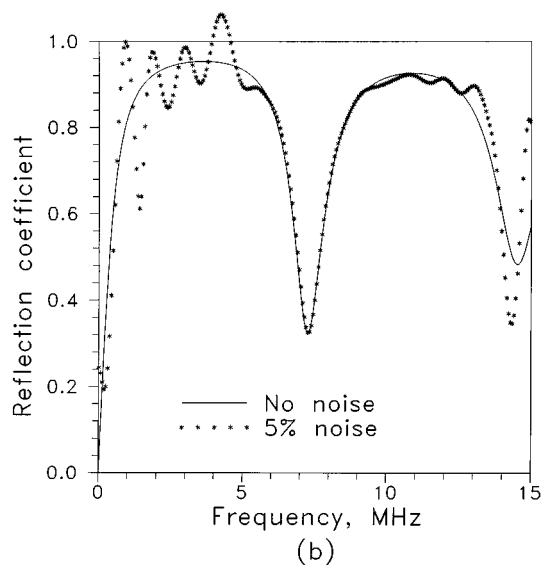
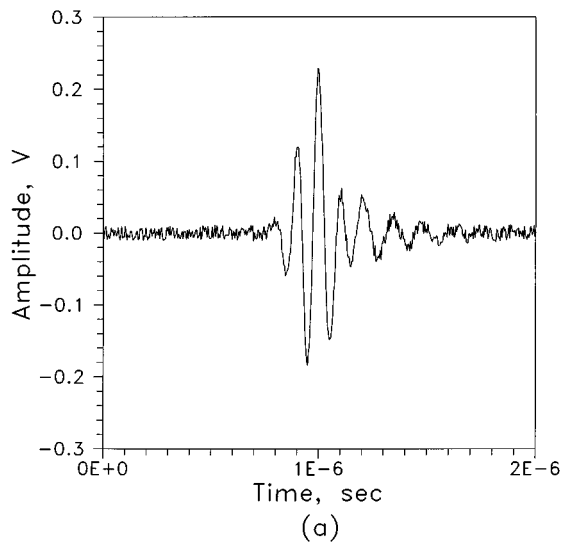


FIG. 6. (a) Typical synthetic time-domain signals at normal incidence with 5% noise and (b) corresponding frequency spectrum. (Solid line corresponds to the spectrum without noise.)

eters measurement at  $17^\circ$  is preferable, the issue is more complicated for the dimensional parameters (8) which are calculated using Eqs. (13)–(16). This is discussed in the next section.

### C. Stability of the inversion algorithm to the scatter in the experimental data

To take into account several factors affecting errors in the reconstructed layer parameters, the following numerical procedure is used to study the stability of the inversion algorithm. A set of polymer film properties (“original set”) is used to generate numerically synthetic reflection spectra at normal and oblique incidence. The spectra are overlapped with a typical transducer spectrum. A backward FFT procedure is used to calculate the corresponding synthetic time-domain signal. Next, different levels of random noise are introduced into the time-domain signals [Fig. 6(a)] to simulate possible experimental noise. A forward FFT procedure is applied to the “noisy” time-domain signals and decon-

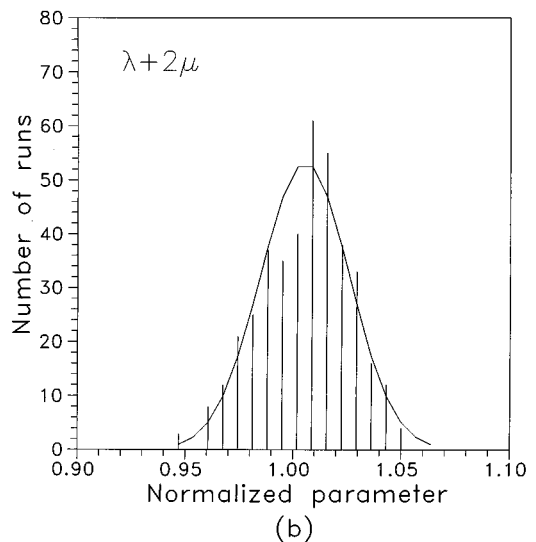
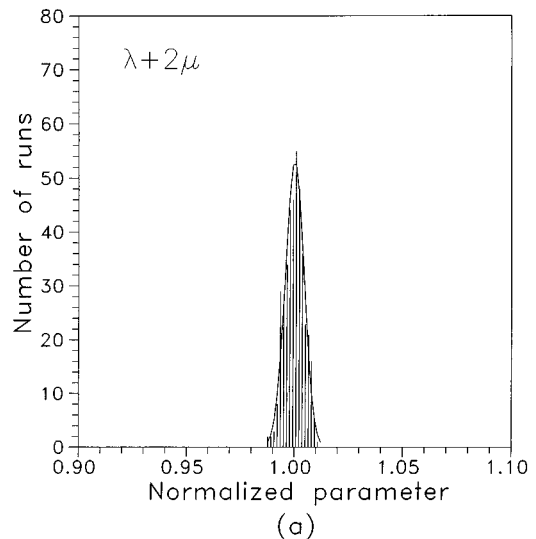


FIG. 7. The results of  $(\lambda + 2\mu)$  reconstruction from a synthetic “noisy” spectra with (a) 1% noise and (b) 5% noise.

involved with the transducer spectrum to obtain synthetic “noisy” reflection spectra [Fig. 6(b)]. These spectra are used to determine the elastic constants by the nonlinear least-square optimization method discussed previously. The spectral data from 5–10 MHz for normal incidence and from 3–12 MHz for oblique incidence are used for reconstruction which corresponds to the spectral minima position in our experiment (see below).

Due to the introduced noise the reconstructed set of the polymer film properties is not exactly equal to the original set. It is compared to the original set to study the effects of the noise level and initial guesses. For each noise level and initial guess the procedure is repeated 400 times, the reconstructed parameters (dimensional and nondimensional) are normalized to the original value, and average  $\bar{p}$  and standard deviation  $\sigma_p$  are calculated for the normalized values.

As an illustration, the results of  $(\lambda + 2\mu)$  reconstruction from synthetic “noisy” spectra are presented as histograms in Fig. 7(a) and (b). Each vertical line represents a number of reconstructed values in an interval of  $\sigma_{(\lambda+2\mu)}/3$ ; a corre-

TABLE I. Results of nondimensional parameter  $(Z_N, \bar{h}_1, \alpha_1)$  reconstruction using simulated “noisy” spectral data with different noise levels and initial guesses for a reflection from a polystyrene film between aluminum plates.  $\epsilon$  is a standard deviation of the normalized parameter. Original values of the nondimensional parameters are  $Z_N^0=0.126$ ,  $\bar{h}_1^0=0.0688$ , and  $\alpha_1^0=0.040$ .

Noise	Initial guess	$\bar{Z}_N/\bar{Z}_N^0$	$\epsilon_{Z_N}$	$\bar{h}_1/\bar{h}_1^0$	$\epsilon_{\bar{h}_1}$	$\bar{\alpha}_1/\bar{\alpha}_1^0$	$\epsilon_{\alpha_1}$
1%	+ 20%	1.000	0.4%	1.000	0%	1.001	1.2%
	0%	1.000	0.4%	1.000	0%	1.001	1.0%
	- 20%	1.000	0.4%	1.000	0%	1.001	1.1%
5%	+ 20%	1.003	1.7%	1.000	0.2%	0.998	5.4%
	0%	1.001	1.9%	1.000	0.2%	0.998	5.4%
	- 20%	1.001	1.8%	1.000	0.2%	0.997	5.1%

sponding normal distribution is shown by a solid line in the interval  $(\lambda + 2\mu - 3\sigma_{\lambda+2\mu}, \lambda + 2\mu + 3\sigma_{\lambda+2\mu})$ .

The effect of the initial guess on the results of reconstruction were studied for two different noise levels (for example, 5% noise level in the signal is illustrated in Fig. 6). The results for normal incidence are presented in Table I. One can see that for initial guesses within  $\pm 20\%$  of the originals, the results of inversion are practically identical. This indicates that the nonlinear least-square optimization is not affected by the initial guesses. The conclusion is valid even for 5% noise [Fig. 6(a)] which is unlikely for experimental data. The independence of the reconstruction results of the initial guesses suggests that the nonlinear least-square optimization procedure leads to unique values for the layer properties.

The results of the numerical simulations are summarized in Table II. This table presents statistics of the nondimensional (12) and dimensional (8) parameters reconstructed by the algorithm proposed earlier (Fig. 2). For completeness, results for longitudinal and shear wave velocities,  $V_1$  and  $V_t$ , are included. The results are presented for two oblique incidence angles ( $\theta_0=0^\circ$  and  $20^\circ$ ) for 1% noise. In addition, the results for  $\theta_0=0^\circ$  and 5% noise are presented. One can see that the error in nondimensional parameter determination (upper part of the table) is relatively small. The error for  $Z_N$  determination is larger than that for  $\bar{h}_1$ ,  $\bar{h}_{\theta_1}$ , and  $\bar{h}_t$  (parameters responsible for minima positions) which correlates with the sensitivity curves presented in Fig. 4. The  $\bar{h}_{\theta_1}$  is determined with better precision from the data measured at  $17^\circ$  than at  $20^\circ$ , again in accordance with corresponding sensitivities.

The error for dimensional parameters (lower part of the Table II) is several times larger than that for nondimensional parameters due to their recalculation by Eqs. (13)–(16). The source of the error increase is in  $\sqrt{\bar{h}_1^2 - \bar{h}_{\theta_1}^2}$ , where  $\bar{h}_1$  and  $\bar{h}_{\theta_1}$  are close to each other. The error in  $\rho$  and  $h$  determination is smaller when spectral data at  $\theta_0=20^\circ$  are used due to the larger difference between  $\bar{h}_1$  and  $\bar{h}_{\theta_1}$  at  $20^\circ$  as compared to  $17^\circ$ . The error in  $\mu$  determination is however larger for  $\theta_0=20^\circ$  due to the larger error in  $\bar{h}_{\theta_1}$ . In general, the relative error of nondimensional parameter determination is close to relative data scatter. At 5% noise level (which is an overestimation for actual experimental measurement) the largest error for density is 3.7% and attenuations 5.4% and 6.5%. When spectral data at  $\theta_0=20^\circ$  are used (column 2 in Table

II), an additional error is observed due to shift of the average from the original parameter value. The most pronounced effect is observed for  $\alpha_t$ . For this reason measurements at  $\theta_0=17^\circ$  were performed in the actual experiment.

### III. EXPERIMENTAL TECHNIQUES

#### A. Angle–beam reflection technique

The angle–beam reflection measurements were performed using a specially developed ultrasonic goniometer,<sup>21</sup> which can focus an obliquely incident ultrasonic wave on the adhesive–adherent interface by shifting the position of the adhesive joint along the cylinder radius [Fig. 8(a)]. The goniometer is unique in its ability to measure reflected interfacial signals at various incident angles with only one transducer. We used the angle of wave incidence on the water/aluminum interface greater than the first critical angle of  $13.8^\circ$ , thus only transverse waves propagated inside the joint. The diameter of the focusing point is a few millimeters.

The experiments have been done using a computer-controlled system. The reflected ultrasonic signals were am-

TABLE II. Results of reconstruction using simulated “noisy” spectral data with different noise levels for a reflection from a polystyrene film between aluminum plates.  $\epsilon$  is a standard deviation of the normalized parameter. Original values of the parameters are  $(\lambda + 2\mu)^0=4.464$  GPa,  $\mu^0=0.841$  GPa,  $\rho^0=1.054$  g/cm<sup>3</sup>,  $h=0.142$  mm,  $V_1=2.058$  km/s,  $V_t=0.893$  km/s,  $\alpha_1^0=0.040$ , and  $\alpha_t^0=0.063$ .

Noise	$\theta_0=20^\circ$		$\theta_0=17^\circ$	
	1%	1%	1%	5%
$\bar{Z}_N/\bar{Z}_N^0$ ( $\epsilon_{Z_N}$ )	1.000 (0.4%)	1.000 (0.4%)	1.001 (1.9%)	
$\bar{h}_1/\bar{h}_1^0$ ( $\epsilon_{\bar{h}_1}$ )	1.000 (0.0%)	1.000 (0.0%)	1.000 (0.2%)	
$\bar{h}_{\theta_1}/\bar{h}_{\theta_1}^0$ ( $\epsilon_{\bar{h}_{\theta_1}}$ )	0.998 (0.1%)	1.000 (0.1%)	0.999 (0.5%)	
$\bar{h}_t/\bar{h}_t^0$ ( $\epsilon_{\bar{h}_t}$ )	1.003 (0.2%)	1.000 (0.1%)	1.001 (0.5%)	
$\frac{(\lambda + 2\mu)}{(\lambda + 2\mu)^0}$ ( $\epsilon_{\lambda+2\mu}$ )	1.007 (0.4%)	1.000 (0.4%)	1.005 (2.1%)	
$\mu/\mu^0$ ( $\epsilon_\mu$ )	1.001 (0.5%)	1.000 (0.4%)	1.003 (2.0%)	
$\rho/\rho^0$ ( $\epsilon_\rho$ )	0.994 (0.6%)	1.001 (0.7%)	0.998 (3.7%)	
$h/h^0$ ( $\epsilon_h$ )	1.007 (0.4%)	1.000 (0.5%)	1.004 (2.3%)	
$V_1/V_1^0$ ( $\epsilon_{V_1}$ )	1.007 (0.4%)	1.000 (0.5%)	1.004 (2.3%)	
$V_t/V_t^0$ ( $\epsilon_{V_t}$ )	1.004 (0.3%)	1.000 (0.4%)	1.003 (1.8%)	
$\bar{\alpha}_1/\bar{\alpha}_1^0$ ( $\epsilon_{\alpha_1}$ )	1.001 (1.0%)	1.001 (1.0%)	0.998 (5.4%)	
$\bar{\alpha}_t/\bar{\alpha}_t^0$ ( $\epsilon_{\alpha_t}$ )	1.085 (1.9%)	1.005 (1.3%)	1.016 (6.5%)	

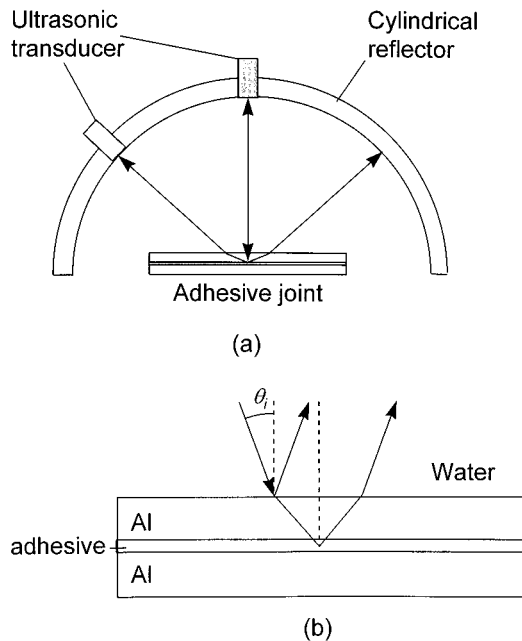


FIG. 8. Arrangement for ultrasonic measurements. (a) Schematic of ultrasonic reflection goniometer and (b) normal and oblique incidence transmission measurement.

plified, digitized, averaged by a HP 54504A 400-MHz digital oscilloscope, and collected by an IBM AT through an IEEE-488 interface. The data is then processed in the frequency domain using a FFT program and deconvolved with a reference signal taken from the aluminum-air interface (for the deconvolution a special sample with air gap was used). The rotation of the transducer, i.e., change of incident angle, and position of a sample using a translation table are controlled by a PC AT through an RS-232 interface using a CTC-283 DC Motor Controller, manufactured by Micro Kinetics Co. Resolution for the rotation table is  $0.01^\circ$  and for the translation table is 0.01 mm. The whole apparatus was immersed in water with temperature stabilized at  $29.8 \pm 0.02^\circ\text{C}$  using a Fisher Isotemp Circulator (Model 730).

## B. Measurements of transmission

Normal and oblique incidence transmission spectra were measured in the experimental setup shown schematically in Fig. 8(b). Data acquisition and analysis were done by the same system as for the reflection measurement experiments.

## C. Effect of pulse gating

Equations (1) and (2) and the general equations in the Appendix describe reflection and transmission for a plane harmonic wave. The equations account for an infinite number of reverberations inside the adhesive layer. In practice experiments are performed using pulse signals excited by an ultrasonic transducer. The pulse is characterized by a time domain signal and a corresponding spectrum. A signal of interest must be gated in the time domain to separate it from nonrelevant reflections inside the adherends. This is demonstrated in Fig. 9. One can see that only three (not an infinite number) signals reverberating inside the adhesive layer can

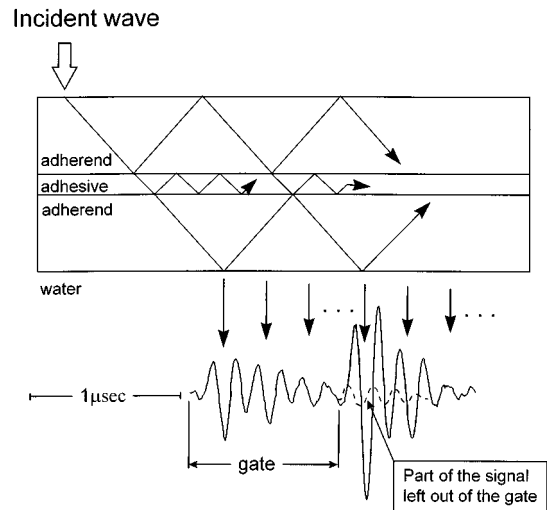


FIG. 9. Illustration of pulse gating for measurement of transmission through an adhesive layer.

be separated and related to the interface layer interactions. The rest of the signal due to interference with doubly reflected signal in the substrate is masked. The dashed line in the time domain signal shown in Fig. 9 indicates schematically the overlapping portion of the signal. This part of the signal is excluded by gating.

The effect of the number of reverberations gated is illustrated in Fig. 10. An experimentally measured transmission signal with only two reverberations gated is shown in Fig. 10(a). The solid line is calculated taking into account two reverberations inside the layer. We incorporate the number of reverberations into the inversion algorithm (Fig. 2) to obtain better fitting of the experimental data. The calculated results for two, four, and infinitely many reverberations are shown in Fig. 10(b). The spectra for four reverberations and for the complete signal are very close, indicating that Eqs. (1) and (2) can be used in this case.

## D. Sample preparation

Al-to-Al joints were prepared using thin polystyrene layers as a bonding material. Polystyrene was chosen because its properties were not expected to change significantly due to applied pressure and heat during joint preparation. In addition, the polystyrene film can easily be extracted from the joint and its properties measured directly and compared to the ultrasonic measurement results.

The joints were prepared using 6.4-mm-thick aluminum alloy coupons ( $9 \times 3$  cm) and 0.25-mm-thick polystyrene film. Prior to bonding the aluminum adherent surfaces were sandblasted and washed with acetone (AR, Mallinckrodt). The coupons were bonded by the polystyrene film: samples were heated in 15 min to  $170^\circ\text{C}$ , then held at this temperature for 30 min under pressure. Spacers 0.127 mm were used to ensure homogeneous thickness of the polystyrene layer. Then, the specimen was slowly cooled to room temperature and the pressure was released.

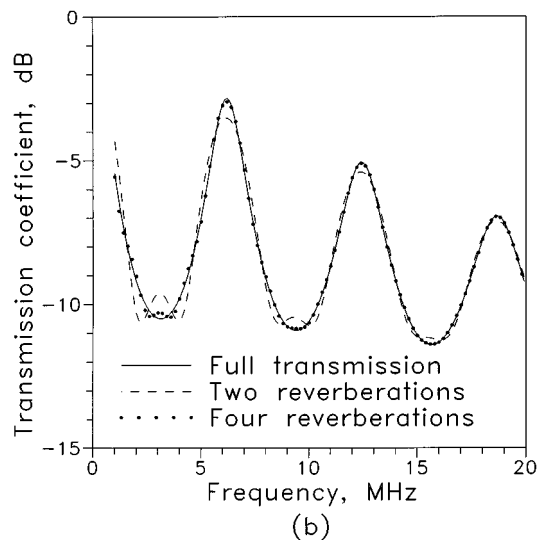
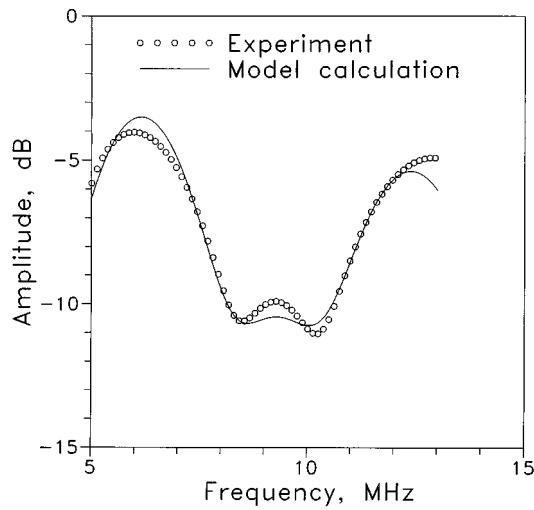


FIG. 10. Spectra of signals transmitted through an adhesive layer. Signal is gated with two reverberations in the layer: (a) points are measurements, solid line is theory. (b) Calculated transmitted signal with two (dashed line), four (points), and infinite number (solid line) reverberations.

#### IV. EXPERIMENTAL RESULTS AND DISCUSSION

The proposed method was applied for characterization of a thin polystyrene film and a polystyrene layer inside the Al-to-Al joint prepared as described in the previous section. After the ultrasonic measurement the film was extracted from the joint by peeling and its properties measured directly. The results of the ultrasonic measurements were also compared to the properties of the thick polystyrene plate exposed to the same heat treatment as during the joint preparation.

##### A. Determination of the polystyrene film properties in fluid at normal incidence

As mentioned above, in some practical applications one of the dimensional properties of the layer can be known. One example is given in this section: a thin polystyrene film whose thickness is measured to be 0.25 mm. The  $Z_N$ ,  $\bar{h}_1$ , and  $\alpha_1$  of the film were determined by inversion of the measured normal incidence reflection only. The normal incidence reflection spectrum of the film is shown in Fig. 11.

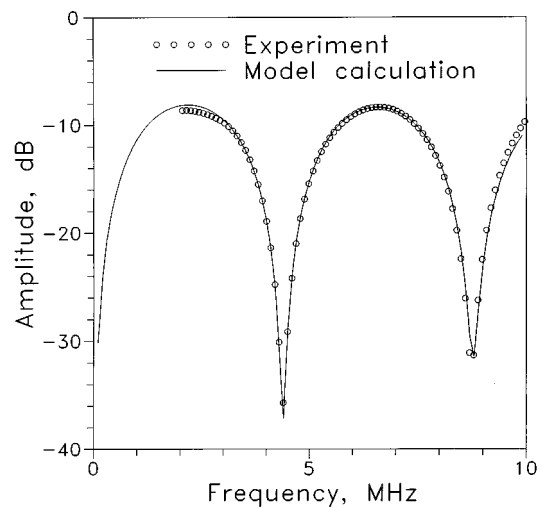


FIG. 11. Reflection spectrum of a 0.25-mm polystyrene film.

The experimental points are shown together with theoretical curves calculated using determined film properties. Since the film thickness is known, the film modulus, density, and attenuation can be determined from  $Z_N$  and  $\bar{h}_1$  using (5) and (6).

For comparison the elastic properties of a thick plate of the same material were determined from ultrasonic velocity angular dependence measured by a self-reference bulk wave method (SRBW) developed in our laboratory.<sup>22,23</sup> Longitudinal wave attenuation was estimated from the ratio of the amplitudes of the signals normally reflected from the front and back surfaces of the specimen. The polystyrene film properties determined are compared to the thick plate properties in Table III. The properties are in good agreement.

##### B. Determination of the full set of properties of a polystyrene film embedded between two solids

The polystyrene film properties inside the prepared Al-to-Al joint were determined using a combination of normal/oblique incidence measurements. The reflection coefficients were measured in two different locations (L and C) at 0° (normal incidence) and at 17° and 18° (oblique incidence). Figure 12 shows examples of the measured spectra. Since relatively thick adherends were used for the joint preparation (6.4 mm) the signals of interest were well separated in the time domain from the reverberations inside the adherends and thus they were treated as an interference of an infinite number of reverberations inside the polymer layer. Three nondimensional parameters,  $Z_n$ ,  $\bar{h}_1$  and  $\alpha_1$ , were determined from the reflection spectra at normal incidence. Three more nondimensional parameters,  $\bar{h}_{\theta_1}$ ,  $\bar{h}_{\theta_2}$ , and  $\alpha_1$ , were determined from the oblique incidence data (reflection or transmission) with  $Z_N$ ,  $\bar{h}_1$ , and  $\alpha_1$  taken as known. The corre-

TABLE III. Comparison of elastic properties of bulk and film polystyrene.

	$\lambda + 2\mu$ (GPa)	$\rho$	$\alpha_1$
Bulk	4.90	1.072	.012
Film	4.98	1.07	0.10

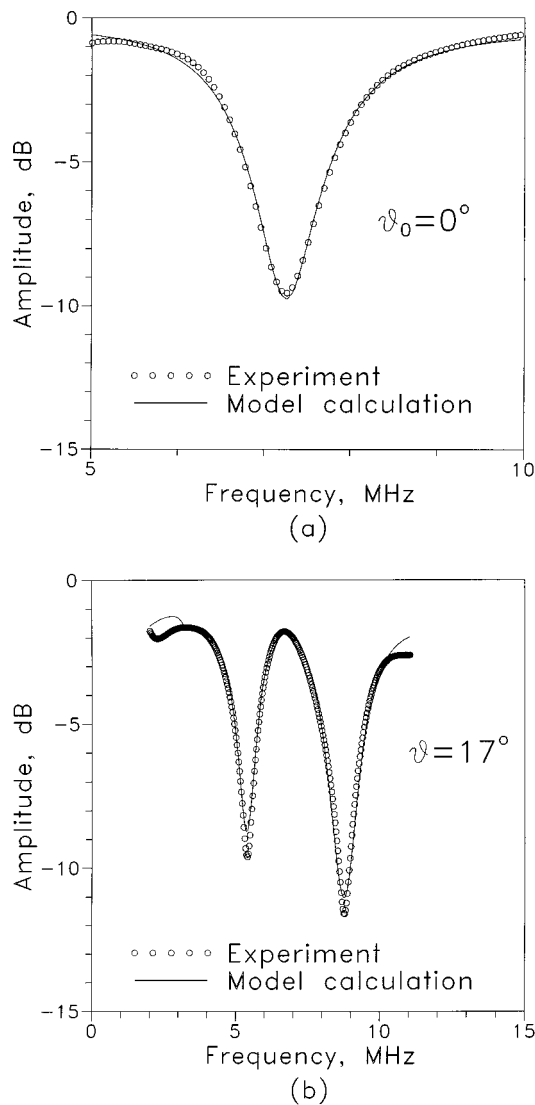


FIG. 12. Reflection from the polystyrene layer (point C) inside the Al-to-Al joint at (a)  $0^\circ$  and (b)  $17^\circ$ .

sponding dimensional parameters (8) were calculated using Eqs. (13)–(16). The solid lines in Fig. 12(a) and (b) represent spectra calculated from the parameters determined. Similar results were obtained for  $17^\circ$  and  $18^\circ$  incidence angles; averaged data is presented in Table IV for the two positions: L and C. The results for the two positions are very similar.

After experiment the polystyrene film was extracted from the joint and its density  $\rho$  and thickness  $h$  measured directly. To determine  $(\lambda + 2\mu)$  a normal incidence mea-

surement was performed and the position of the first spectral minimum  $f_{\min}$  determined. The modulus is then calculated from  $\lambda + 2\mu = 4h^2 \cdot \rho \cdot f_{\min}^2$ .

Table IV compares the film properties determined ultrasonically inside the joint to the extracted film properties and to the heat-treated thick polystyrene properties (measured by SRBW method). The data measured directly (i.e., thickness measured by micrometer and density by a water displacement method) is marked by an asterisk (\*). Relative error for direct density measurement is estimated to be 0.3% ( $\pm 0.003 \text{ g/cm}^3$ ), for thickness  $-2\%$  ( $\pm 3 \mu\text{m}$ ). This results in more than 4% error in the  $(\lambda + 2\mu)$  for the film extracted from the joint (or  $\pm 0.2 \text{ GPa}$ ). An additional source of error is in the nonhomogeneous thickness of the layer: up to  $5 \mu\text{m}$  difference in the ultrasonic beam diameter circle of  $\approx 4 \text{ mm}$ . Taking this into account the  $(\lambda + 2\mu)$  values measured inside and outside the joint are in good agreement. The shear modulus values are reasonably close to those of the heat-treated bulk polystyrene. The film thickness and density are in good agreement with the directly measured values. The properties measured for the two points (L and C) are close to each other with the difference attributed to variation of properties from point to point and to experimental error.

## V. SUMMARY AND CONCLUSIONS

This paper describes an ultrasonic method for determining the properties of an isotropic layer embedded between two known materials (similar or dissimilar). The method allows simultaneous determination of all properties—thickness, density, longitudinal and shear elastic moduli and attenuations—from two measured reflection spectra: one at normal and one at oblique incidence.

By introducing nondimensional parameters the number of parameters describing the normal incidence reflection (transmission) coefficient is reduced from four to three. The minimal set of six nondimensional parameters formed from the layer properties fully describes the reflection (transmission) at oblique incidence. To simplify the inversion the problem was decomposed by replacing an inversion in a six-dimensional space for the six parameters by two consecutive inversions in three-dimensional spaces: for three parameters from the normal incidence data and for the remaining three parameters from the oblique incidence data. The thickness, density, and elastic moduli of the layer are calculated from the nondimensional parameters determined using simple analytical expressions.

TABLE IV. Comparison of elastic properties of the film polystyrene inside the joint and extracted from the joint, and heat-treated bulk polystyrene.

		$\lambda + 2\mu$ (GPa)	$\mu$ (GPa)	$\rho$ (g/cm <sup>3</sup> )	$h$ (mm)	$\alpha_1$	$\alpha_t$
Polystyrene film inside joint	Point L	4.43	0.833	1.06	0.141	0.040	0.063
	Point C	4.50	0.860	1.08	0.140	0.038	0.045
Polystyrene film extracted from joint	Point L	4.54		1.072*	0.143*		
	Point C	4.41		1.072*	0.145*		
Heat-treated polystyrene		4.69	0.828	1.072*			

\*Direct measurement.



The sensitivity of the proposed method to the individual properties and the stability of the method against experimental noise are studied and the algorithm is optimized accordingly. It is shown that the results of reconstruction do not depend on the initial guess. For a randomly selected noise level in the time-domain signal in the  $\pm 5\%$  range (which overestimates the actual noise in experimental measurement) the standard deviation of a relative error for the elastic moduli determined is about 2%, for the layer thickness 2.3%, for density 3.7%, and for longitudinal and shear wave attenuation 5.4% and 6.5%. Thus magnification of the random scatter in the data inversion process does not occur.

It is shown that the effect of time gating has to be taken into account for joints with relatively thin adherends. The proposed method is validated experimentally using a polystyrene layer immersed in water and thermoplastic joint. The polystyrene film properties determined ultrasonically and by direct measurement are in good agreement.

## APPENDIX: REFLECTION AND TRANSMISSION THROUGH THE LAYER

To calculate the ultrasonic longitudinal or shear wave reflection (transmission) from a multilayered structure, we use a matrix algorithm described in Refs. 24 and 25. The matrix equation for reflection and transmission coefficients can be written in the form

$$\begin{bmatrix} A_1 \\ R_1 \\ A_t \\ R_t \end{bmatrix} = [D] \begin{bmatrix} T_1 \\ 0 \\ T_t \\ 0 \end{bmatrix}, \quad (\text{A1})$$

where  $R_1$  and  $R_t$  are the reflection coefficients of the longitudinal and transverse waves respectively,  $T_1$  and  $T_t$  are the corresponding transmission coefficients and  $A_1$  and  $A_t$  are the normalized potential amplitudes of the incident longitudinal and transverse waves:  $A_1=1$  and  $A_t=0$  for longitudinal incident wave and  $A_1=0$  and  $A_t=1$  for transverse. The matrix  $D$  is

$$[D] = [B^{(n+1)}][a^{(n)}][a^{(n-1)}] \cdots [a^{(2)}][a^{(1)}][A^{(0)}]. \quad (\text{A2})$$

The matrices  $A^{(0)}$  and  $B^{(n)}$  relate to the solid semispaces. Isotropic and anisotropic layers are represented by  $4 \times 4$  matrices  $[a^{(i)}]$  ( $i=1, \dots, n$ , where  $n$  is the number of layers) whose elements are given in Refs. 24 and 25. In this paper we consider an adhesive joint consisting of two solid semispaces and an adhesive layer (i.e.,  $n=1$ ) perfectly bonded to the adherends.

<sup>1</sup>L. Adler, K. V. Cook, and W. A. Simpson, "Ultrasonic frequency analysis," in *Research Techniques in Nondestructive Testing*, edited by R. S. Sharpe (Academic, New York, 1977), Vol. 3, pp. 1–49.

<sup>2</sup>F. H. Chang, P. L. Flynn, D. E. Gordon, and J. R. Bell, "Principles and application of ultrasonic spectroscopy in NDE of adhesive bonds," *IEEE Trans. Sonics Ultrason.* **SU-23**, 334–338 (1976).

<sup>3</sup>P. L. Flynn, "Cohesive bond strength prediction for adhesive joints," *J. Testing Eval.* **7**, 168–171 (1979).

<sup>4</sup>P. A. Meyer and J. L. Rose, "Ultrasonic attenuation effects associated with the physical modeling of adhesive bonds," *J. Appl. Phys.* **48**, 3705–3712 (1976).

<sup>5</sup>S. I. Rokhlin and W. Wang, "Measurements of elastic constants of very thin anisotropic plates," *J. Acoust. Soc. Am.* **94**, 2721–2730 (1993).

<sup>6</sup>W. Wang and S. I. Rokhlin, "Evaluation of interfacial properties in adhesive joints of aluminum alloys using angle-beam ultrasonic spectroscopy," *J. Adhesion Sci. Technol.* **5**, 647–666 (1991).

<sup>7</sup>C. C. H. Guyott and P. Cawley, "The ultrasonic vibration characteristics of adhesive joints," *J. Acoust. Soc. Am.* **83**, 632–640 (1988).

<sup>8</sup>C. C. H. Guyott and P. Cawley, "Evaluation of the cohesive properties of adhesive joints using ultrasonic spectroscopy," *NDT Int.* **21**, 233–240 (1988).

<sup>9</sup>P.-C. Xu, A. K. Mal, and Y. Bar-Cohen, "Inversion of leaky Lamb wave data to determine cohesive properties of bonds," *Int. J. Eng. Sci.* **28**, 331–346 (1990).

<sup>10</sup>W. Huang and S. I. Rokhlin, "Application of low frequency ultrasonic through-transmission method for thin film characterization," in *Review of Progress in QNDE*, edited by D. O. Thompson and D. E. Chimenti (Plenum, New York, 1994), Vol. 13, pp. 1485–1493.

<sup>11</sup>N. Guo, M. K. Lim, and T. Pialucha, "Measurement of attenuation using a normalized amplitude spectrum," *J. Nondestruct. Eval.* **14**, 9–19 (1995).

<sup>12</sup>R. B. Thompson and D. O. Thompson, "Past experience in the development of tests for adhesive bond strength," *J. Adhesion Sci. Technol.* **5**, 583–599 (1991).

<sup>13</sup>V. K. Kinra and V. Dayal, "A new technique for ultrasonic nondestructive evaluation of thin specimens," *J. Exp. Mech.* **28**, 288–297 (1988).

<sup>14</sup>V. K. Kinra and V. R. Iyer, "Ultrasonic measurement of the thickness, phase velocity, density or attenuation of a thin viscoelastic film. Part I: the forward problem," *Ultrasonics* **33**, 95–109 (1995).

<sup>15</sup>V. K. Kinra and V. R. Iyer, "Ultrasonic measurement of the thickness, phase velocity, density or attenuation of a thin viscoelastic film. Part II: the inverse problem," *Ultrasonics* **33**, 111–122 (1995).

<sup>16</sup>S. E. Hanneman and V. K. Kinra, "A new technique for ultrasonic non-destructive evaluation of adhesive joints: Part I. Theory" *J. Exp. Mech.* **32**, 323–331 (1992).

<sup>17</sup>S. E. Hanneman and V. K. Kinra, "A new technique for ultrasonic non-destructive evaluation of adhesive joints: Part II. Experiment" *J. Exp. Mech.* **32**, 332–339 (1992).

<sup>18</sup>L. M. Brekhovskikh, *Waves in Layered Media* (Academic, New York, 1960).

<sup>19</sup>A. I. Lavrentyev and S. I. Rokhlin, "Anomalous attenuation effect on reflectivity of an ultrasonic wave from a thin layer between dissimilar materials," *J. Acoust. Soc. Am.* **101**, 3405–3414 (1997).

<sup>20</sup>A. I. Lavrentyev and S. I. Rokhlin, "Phase correction for ultrasonic bulk wave measurements of elastic constant in anisotropic materials," in *Review of Progress in QNDE*, edited by D. O. Thompson and D. E. Chimenti (Plenum, New York, 1997), Vol. 16B, pp. 1367–1374.

<sup>21</sup>S. I. Rokhlin, W. Wang, Y. J. Wang, and J. L. Hamill, *NDE of Adhesive Bonds and Bondlines Track*, ASNT (1989), pp 41–50.

<sup>22</sup>S. I. Rokhlin and W. Wang, "Double through-transmission bulk wave method for ultrasonic phase velocity measurement and determination of elastic constants of composite materials," *J. Acoust. Soc. Am.* **91**, 3303–3312 (1992).

<sup>23</sup>Y. C. Chu and S. I. Rokhlin, "Comparative analysis of through-transmission ultrasonic bulk wave methods for phase velocity measurements in anisotropic materials," *J. Acoust. Soc. Am.* **95**, 3204–3212 (1994).

<sup>24</sup>S. I. Rokhlin and Y. J. Wang, "Analysis of boundary conditions for elastic wave interaction with an interface between two solids," *J. Acoust. Soc. Am.* **89**, 503–515 (1991).

<sup>25</sup>S. I. Rokhlin and Y. J. Wang, "Equivalent boundary conditions for thin orthotropic layer between two solids: reflection, refraction, and interface waves," *J. Acoust. Soc. Am.* **91**, 1875–1887 (1991).

# Why fluid loading has an opposite effect on the velocity of dilatational waves in thin plates and rods

Waled Hassan and Peter B. Nagy

*Department of Aerospace Engineering and Engineering Mechanics, University of Cincinnati, Cincinnati, Ohio 45221*

(Received 27 September 1997; accepted for publication 31 July 1997)

From almost every respect, the lowest-order dilatational waves in thin plates and rods are very similar. Therefore, it is rather intriguing that fluid loading increases the phase velocity of such waves in a plate, but decreases it in a rod. Although this difference can be easily demonstrated by inspection of the well-known exact dispersion equations, the underlying physics remains somewhat obscure. Simple physical models are introduced for thin immersed rods and plates that provide a better insight into the fundamental difference causing the opposite behavior of these otherwise analogous modes of wave propagation. It is shown that the inverse effect of fluid loading is caused by the fact that the radiation impedance exerted by the fluid on plates is purely real while it is dominantly imaginary in the case of thin rods. © 1997 Acoustical Society of America.

[S0001-4966(97)01212-5]

PACS numbers: 43.35.Pt [HEB]

## INTRODUCTION

At low frequencies, only the lowest-order symmetric longitudinal and antisymmetric flexural modes can propagate in thin plates. In rods a dispersion-free torsional mode can also propagate in addition to the longitudinal and flexural modes. The lowest-order longitudinal modes in thin plates and rods are physically very similar. Figure 1 shows the schematic diagram of a thin plate and a rod along with the coordinate system to be used in our analysis and the deformation pattern caused by the lowest-order dilatational mode. At sufficiently low frequencies, the displacement along the propagation ( $x$ ) direction dominates the vibration. In a thin plate the Poisson effect causes a weaker transverse vibration perpendicular to the surface of the plate, which is less than the longitudinal displacement by a factor proportional to  $\omega d\nu/(1-\nu)$ , where  $\omega$  denotes the angular frequency,  $d$  is the thickness of the plate, and  $\nu$  is the Poisson ratio. In other words, the Poisson effect causes the plate to breathe in a direction perpendicular to the direction of wave propagation as shown in Fig. 1(b). The lowest-order axisymmetric mode propagating in a thin rod exhibits a similar breathing behavior. The displacement along the axis of the rod dominates the vibration while the radial displacement caused by Poisson's effect is less than the longitudinal displacement by a factor proportional to  $\omega a\nu$ , where  $a$  is the radius of the rod. The only minor difference between these two modes is that in the case of a plate the Poisson effect is restricted to only one dimension normal to the plate, therefore, the dilatational wave velocity is  $\sqrt{1/(1-\nu^2)} \approx 1.05$  times higher in a plate than in a rod. As the frequency increases, in both cases the phase velocity first drops proportionally to the square of frequency and then asymptotically approaches the Rayleigh velocity. In spite of these common features of the dilatational vibrations in thin plates and rods, the effect of fluid loading on the phase velocity of these two modes is quite different. Although the magnitude of the relative change in the phase velocity due to fluid loading is very small and practically

negligible compared to the much stronger attenuation effect in both cases, the very fact that the sign of this velocity change is opposite deserves some attention. This fundamental difference in the effect of fluid loading on thin plates and rods can be easily demonstrated by inspection of the well-known exact dispersion equations found at numerous places in the scientific literature. Although the change in velocity is usually neglected, there are many indications that fluid loading causes the phase velocity of the lowest-order symmetric mode in a thin plate to slightly increase while the phase velocity of the lowest-order axisymmetric mode in a thin rod drops due to fluid loading. We will demonstrate these effects using both numerical solutions of the exact dispersion equations and simplified approximate models to understand the physical differences between the two cases that lead to such an opposite behavior.

## I. DISPERSION EQUATIONS AND NUMERICAL SOLUTIONS

First, we will demonstrate by numerically solving the respective exact dispersion equations that fluid loading has an opposite effect on the velocity of longitudinal waves in thin plates and rods. Wave propagation in fluid-loaded plates has been widely investigated. Schoch,<sup>1</sup> Osborne and Hart,<sup>2</sup> Merkulov,<sup>3</sup> Viktorov,<sup>4</sup> Pitts *et al.*,<sup>5</sup> and Selezov *et al.*<sup>6</sup> have studied the effect of water loading on plates under a variety of conditions. Their results indicated that most modes are strongly attenuated by leaking into the fluid but their phase velocity is essentially unaffected. More recent studies by Nayfeh and Chimenti<sup>7</sup> and Rokhlin *et al.*<sup>8</sup> showed that in some special cases of significant importance in nondestructive characterization of composite laminates, when the density ratio between the solid and the fluid is relatively low, the change in the phase velocity of the lowest-order symmetric mode is not negligible and, in extreme cases, even the topology of the mode structure might change.

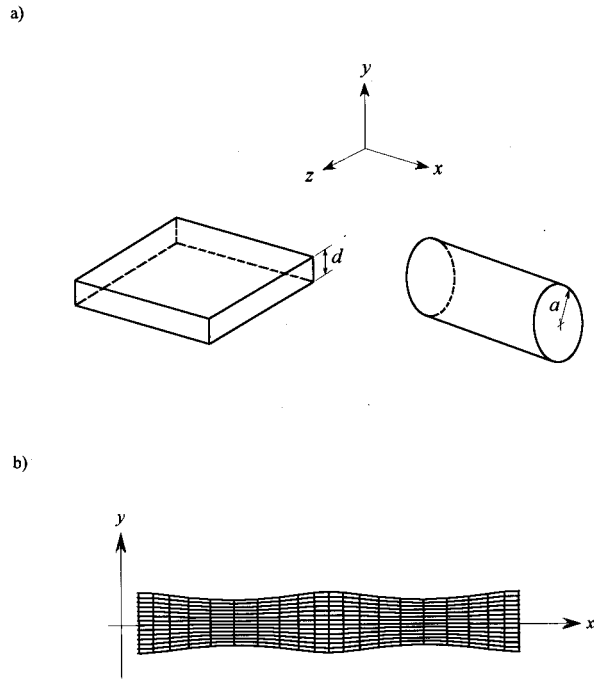


FIG. 1. The schematic diagram of a plate and a rod with the associated coordinate system (a) and the deformation pattern caused by the lowest-order dilatational mode (b).

The exact dispersion equation describing normal mode propagation in an unbounded, isotropic plate immersed in a fluid is given in Refs. 2–5. For the symmetrical mode, the equation can be written as follows:

$$(k^2 - \kappa_s^2)^2 \cot\left(\kappa_d \frac{d}{2}\right) + 4k^2 \kappa_s \kappa_d \times \cot\left(\kappa_s \frac{d}{2}\right) - i \frac{\rho \kappa_d k_s^4}{\kappa_f} = 0, \quad (1)$$

where  $\kappa_s = \sqrt{k_s^2 - k^2}$ ,  $\kappa_d = \sqrt{k_d^2 - k^2}$ ,  $\kappa_f = \sqrt{k_f^2 - k^2}$ ,  $k_s = \omega/c_s$ , and  $k_d = \omega/c_d$  are the wave numbers of the shear and longitudinal waves in the solid, and  $k_f = \omega/c_f$  is the wave number of the compressional wave in the fluid. Here  $\rho = \rho_f/\rho_s$  is the ratio of the fluid density to the density of the solid and  $d$  is the thickness of the plate. When numerically solving the dispersion equation, due care must be taken in choosing the physically allowable square root for  $\kappa_f$  (the signs of  $\kappa_d$  and  $\kappa_s$  do not affect the results). Using the  $e^{i(kx - \omega t)}$  convention, the attenuation coefficient of the guided wave is  $\alpha = \text{Im}\{k\}$ , i.e., the imaginary part of  $k$  must be positive. In contrast, the leaky field in the fluid must exponentially increase away from the plate, therefore the imaginary part of  $\kappa_f$  must be negative. Figure 2 shows a plot of the relative change in the phase velocity of the lowest-order symmetric mode in an aluminum plate immersed in water as a function of normalized frequency. The solid line represents the relative change in the phase velocity due to fluid loading as obtained by numerically solving the exact dispersion equation given in Eq. (1). The density and compressional wave velocity for water were taken as  $\rho_f = 1000 \text{ kg/m}^3$  and  $c_f = 1500 \text{ m/s}$ , respectively. The density

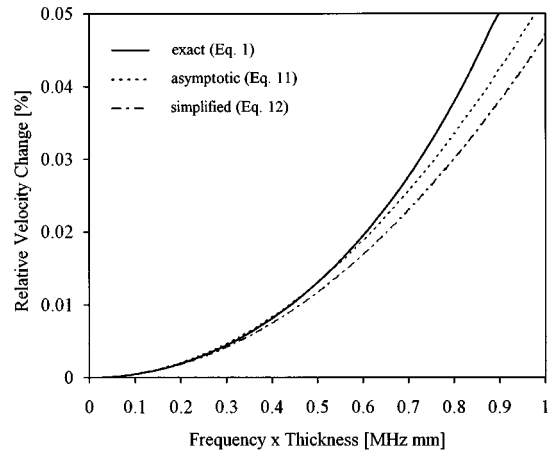


FIG. 2. Relative change in the phase velocity of the lowest-order symmetric Lamb mode propagating in a thin aluminum plate immersed in water.

and longitudinal and shear wave velocities for aluminum were taken as  $\rho_s = 2770 \text{ kg/m}^3$ ,  $c_d = 6323 \text{ m/s}$ , and  $c_s = 3100 \text{ m/s}$ , respectively. The relative velocity change is defined as the difference between the phase velocities of the fluid-loaded and free plates normalized to that of the low-frequency asymptotic value of the phase velocity in the free plate, i.e.,  $c_0 = \sqrt{E/[\rho_s(1 - \nu^2)]} = c_s \sqrt{2/(1 - \nu)}$ , where  $E$  denotes Young's modulus. Figure 2 clearly shows that, although the effect is obviously very small, the phase velocity of the lowest-order symmetric Lamb mode increases as a result of fluid loading on the plate.

Somewhat less attention has been given to the case of wave propagation in fluid-loaded rods. Most of the theoretical work in this area considered the more general cases of clad rods consisting of an isotropic core and an arbitrary number of isotropic coatings<sup>9</sup> or cylindrical shells.<sup>10,11</sup> Simmons *et al.*<sup>12</sup> studied both leaky and true axisymmetric modes in infinitely clad isotropic rods. Their results were adapted to fluid-loaded isotropic rods by Nagy and Kent in order to assess the leaky attenuation in immersed fibers and wires.<sup>13</sup> Recently, Liu *et al.*<sup>14</sup> presented a viscoelastic model for the coupled motion in a thin solid rod and an infinite viscous medium surrounding it.

The characteristic equation of the axisymmetric longitudinal mode of an immersed rod can be derived from the more general case of an isotropic rod embedded in a solid matrix<sup>12,13,15</sup>

$$(k_s^2 - 2k^2)^2 J(a\kappa_d) + 4k^2 \kappa_d^2 J(a\kappa_s) - k_s^2 \kappa_d^2 - \frac{1}{2} \rho a^2 k_s^4 \kappa_d^2 H(a\kappa_f) = 0, \quad (2)$$

where

$$J(\xi) = \xi J_0(\xi) / [2J_1(\xi)], \quad H(\xi) = H_0^{(1)}(\xi) / [\xi H_1^{(1)}(\xi)],$$

and  $J_0$ ,  $J_1$ ,  $H_0^{(1)}$ , and  $H_1^{(1)}$  are first-kind Bessel and Hankel functions of the zeroth and first order, respectively. Figure 3 shows a plot of the relative change in the phase velocity of the lowest-order axisymmetric mode in an aluminum rod immersed in water as a function of normalized frequency. The solid line represents the relative change in the phase velocity due to fluid loading as obtained by numeri-

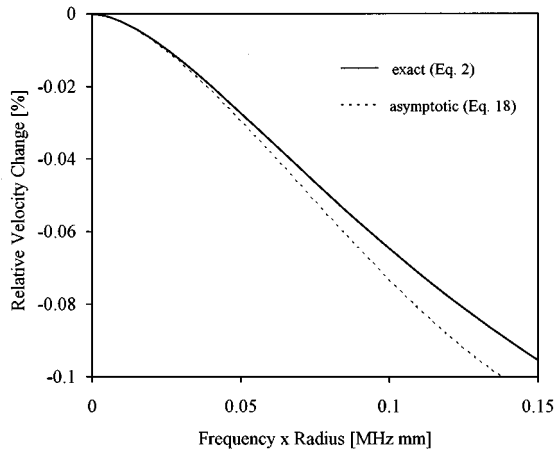


FIG. 3. Relative change in the phase velocity of the lowest-order axisymmetric mode propagating in a thin aluminum rod immersed in water.

cally solving the exact dispersion equation given in Eq. (2). The same material parameters were used as before, however the velocity change caused by fluid loading was normalized to the low-frequency asymptotic value of the phase velocity in the free rod, i.e.,  $c_0 = \sqrt{E/\rho_s} = c_s \sqrt{2/(1+\nu)}$ . Figure 3 clearly shows that the phase velocity of the lowest-order axisymmetric rod mode decreases as a result of fluid loading.

## II. LOW-FREQUENCY ASYMPTOTES

Although the opposite effect of fluid loading on the phase velocity of dilatational waves in thin plates and rods can be easily demonstrated by inspection of the respective exact dispersion equations given in Eqs. (1) and (2), the underlying physics remains somewhat hidden. A better understanding can be gained by considering the low-frequency asymptotic behavior of the modes. For low frequencies,  $\cot(\xi)$  may be approximated by  $1/\xi$ . Substituting this asymptotic value along with the expressions for  $\kappa_f$ ,  $\kappa_s$ , and  $\kappa_d$  into Eq. (1) yields

$$f \approx 4k^2(k_d^2 - k_s^2) + k_s^4 - i \frac{\rho d k_s^4 (k_d^2 - k^2)}{2\sqrt{k_f^2 - k^2}} = 0. \quad (3)$$

We can rewrite this approximate characteristic equation as  $f = f_0 - if_l$ , where

$$f_0 \approx 4k^2(k_d^2 - k_s^2) + k_s^4 \quad (4)$$

is the low-frequency asymptotic characteristic equation of the true mode in the free plate and

$$f_l \approx \frac{\rho d k_s^4 (k_d^2 - k^2)}{2\sqrt{k_f^2 - k^2}} \quad (5)$$

is the correction term which accounts for the loss via leakage into the fluid. When this leakage is weak, the characteristic equation can be approximated as follows:

$$f(k) \approx f(k_0) + (k - k_0)f'(k_0), \quad (6)$$

where the prime indicates differentiation with respect to  $k$ ,  $k_0 = \omega/c_0$  denotes the wave number of the true lowest-order symmetric Lamb mode in the free plate, and  $c_0$

$= \sqrt{E/[\rho_s(1-\nu^2)]} = c_s \sqrt{2/(1-\nu)}$  is the low-frequency asymptotic value of the phase velocity in the free plate. Substitution of  $f = f_0 - if_l$  into Eq. (6) gives

$$f_0(k_0) - if_l(k_0) + (k - k_0)[f'_0(k_0) - if'_l(k_0)] = 0, \quad (7)$$

where  $f_0(k_0) = 0$ . Equation (7) can be solved for  $(k - k_0)$  as

$$k - k_0 = \frac{if_l(k_0)}{f'_0(k_0) - if'_l(k_0)}. \quad (8)$$

The relative change in the phase velocity can now be written as

$$\begin{aligned} \Delta &= \frac{c_{\text{phase}} - c_0}{c_0} \approx -\frac{1}{k_0} \text{Re} \{k - k_0\} \\ &\approx \frac{1}{k_0} \text{Im} \left\{ \frac{f_l(k_0)}{f'_0(k_0) - if'_l(k_0)} \right\}. \end{aligned} \quad (9)$$

Since  $f_l(k_0)$  in the numerator is pure real, the imaginary part of the right side of Eq. (9) is due to the small imaginary part of its denominator. After some algebra, Eq. (9) can be further approximated to give

$$\Delta_{\text{plate}} \approx \frac{1}{k_0} \frac{f_l(k_0)f'_l(k_0)}{f_0'^2(k_0)}. \quad (10)$$

Using Eqs. (4), (5), and (10) we can obtain a low-frequency, weak-loading asymptote for the relative change in the phase velocity of the lowest-order symmetric mode in a plate as

$$\Delta_{\text{asymp}} \approx \frac{\rho^2 d^2 k_s^4 \nu^2 (2k_f^2 - k_d^2 - k_0^2)}{64 (k_f^2 - k_0^2)^2}. \quad (11)$$

If we further assume that  $c_f < c_0 < c_d$ , which is usually the case, the above expression simplifies to

$$\Delta_{\text{simpl}} \approx \frac{1}{32} \left[ \frac{\rho d \nu \omega c_f}{c_s^2} \right]^2. \quad (12)$$

The predictions of Eqs. (11) and (12) are also plotted in the previously shown Fig. 2. Because of the neglected terms in the simplified approximation, it underestimates the relative change in the phase velocity by approximately 10% in the case of an aluminum plate immersed in water. Clearly, these asymptotic approximations capture the main features of fluid loading quite well at low frequencies and at the same time they provide simple explicit formulas for the relative velocity change in terms of the principal parameters involved. The change in velocity is proportional to the square of the density ratio between the fluid and the solid, indicating that the phenomenon is only a second-order effect which is negligible for most fluid–solid combinations. Osborne and Hart<sup>2</sup> showed that a first-order approximation predicts that the phase velocity of the lowest-order symmetric Lamb mode is not affected by fluid loading but properly predicts the attenuation due to leakage of energy into the surrounding fluid. It should be mentioned that Viktorov<sup>4</sup> presented a weak-loading approximation for the relative change in the phase velocity of different Lamb modes. As an example, for the lowest-order symmetric mode in a thin aluminum plate immersed in water he cited a relative velocity change of  $\Delta$

$\approx -0.0005\bar{d}^2$ , where  $\bar{d}=k_s d/2$ . For this case, Eq. (11) can be written as

$$\Delta_{\text{asymp}} \approx \frac{1.1}{8} \left[ \frac{\rho \nu c_f}{c_s} \right]^2 \bar{d}^2 = 0.00049 \bar{d}^2. \quad (13)$$

Although, after rounding, Eq. (13) predicts the same value for the magnitude of velocity change caused by the fluid loading as given by Viktorov, the sign is opposite. We will confirm later via an independent physical model that the velocity change caused by fluid loading is actually positive as it is also shown elsewhere in the literature (see, for example, Fig. 5 in Ref. 8).

A similar asymptotic analysis can be carried out to obtain an explicit approximation for the relative change in phase velocity caused by fluid loading in a thin rod. For low frequencies, the exact dispersion equation given in Eq. (2) can be approximated by using  $J(\xi) \approx 1$  and  $H(\xi) \approx -\ln(\xi)$ .<sup>16</sup> Substituting these asymptotic values into Eq. 2 yields

$$f \approx (k_s^2 - 2k^2)^2 - \kappa_d^2(k_s^2 - 4k^2) + \frac{1}{2}\rho a^2 k_s^4 \kappa_d^2 \ln(\alpha \kappa_f), \quad (14)$$

which can be separated, as we did for the case of the plate above, to the free and fluid-loading terms

$$f_0 = (k_s^2 - 2k^2)^2 - \kappa_d^2(k_s^2 - 4k^2), \quad (15)$$

$$f_l = i \frac{1}{2} \rho a^2 k_s^4 \kappa_d^2 \ln(\alpha \kappa_f). \quad (16)$$

For a rod  $f_l(k_0)$  is essentially imaginary and  $f_l'(k_0)$  is negligible with respect to  $f_0'(k_0)$  in the denominator of the right side of Eq. (9), which simplifies the expression for the relative change in phase velocity to

$$\Delta_{\text{rod}} \approx \frac{1}{k_0} \text{Im} \left\{ \frac{f_l(k_0)}{f_0'(k_0)} \right\}, \quad (17)$$

where  $c_0 = \sqrt{E/\rho_s}$  in this case. Here, the denominator is pure real and the numerator can be made pure imaginary by taking the real part of the complex logarithmic function as  $\text{Re}\{\ln(\alpha \kappa_f)\} = \ln(|\alpha \kappa_f|)$ . Substituting Eqs. (15) and (16) into Eq. (17), and after some further algebraic manipulation, we obtain a low-frequency, weak-loading asymptote for the case of a thin rod immersed in fluid as

$$\Delta_{\text{asymp}} \approx \frac{\rho a^2 \omega^2 \nu^2}{2c_s^2(1+\nu)} \ln(|\alpha \kappa_f|), \quad (18)$$

where we can recognize the denominator as the square of the rod velocity, i.e.,  $c_0^2$ .

The prediction of Eq. (18) is also plotted in the previously shown Fig. 3. Again, the asymptotic approximation captures the main features of fluid loading quite well at low frequencies and provides a simple explicit formula for the relative velocity change in terms of the principal parameters. The change in velocity is linearly proportional to the density ratio between the fluid and the solid indicating that the phenomenon is a first-order effect which can be much stronger than the previously found second-order effect in the case of plates. More importantly for our immediate purposes, because of the logarithmic term, the change in velocity is always negative at low frequencies.

From many points of view, the above derived low-frequency asymptotic approximations provide a deeper insight into how fluid loading affects the velocity of the dilatational wave in thin plates and rods. In contrast to the implicit exact dispersion equations, these results clearly separate the roles of the various parameters involved in the velocity change. In both cases, the magnitude of the velocity change is roughly proportional to the square of the characteristic dimension, frequency, and Poisson ratio. The only significant difference, beside of course the opposite sign, was found in the dependence on the density ratio between the fluid and the solid, which indicated that the fluid loading produces a first-order perturbation of the dilatational wave velocity in thin rods but only a second-order effect in thin plates.

### III. PHYSICAL MODELS AND RADIATION IMPEDANCE

In order to obtain a better understanding of these differences, in this section we are going to introduce simple physical models that can directly relate the apparent change in the effective stiffness of thin plates and rods to the radiation impedance presented by the fluid loading. First let us consider how the effective complex stiffness  $\tilde{E} = \sigma_x / \varepsilon_x$  and the radiation impedance are related for a thin plate immersed in fluid. For an isotropic solid, the constitutive equations are given as

$$\varepsilon_x = \frac{\sigma_x}{E} - \frac{\sigma_y}{E} \nu - \frac{\sigma_z}{E} \nu, \quad (19a)$$

$$\varepsilon_y = -\frac{\sigma_x}{E} \nu + \frac{\sigma_y}{E} - \frac{\sigma_z}{E} \nu, \quad (19b)$$

$$\varepsilon_z = -\frac{\sigma_x}{E} \nu - \frac{\sigma_y}{E} \nu + \frac{\sigma_z}{E}. \quad (19c)$$

In the case of an infinite plate we have  $\varepsilon_z = 0$  and  $\sigma_y = -p$ , where  $p$  denotes the pressure in the fluid so that Eq. (19c) gives  $\sigma_z = (\sigma_x - p)\nu$ . The pressure in the fluid can be expressed in terms of the radiation impedance  $Z_{\text{rad}}$  as follows:

$$p = -i\omega Z_{\text{rad}} u_y|_{y=d/2} = -i \frac{1}{2} \omega \varepsilon_y Z_{\text{rad}} d. \quad (20)$$

Combining Eqs. (19) and (20) with the expression for  $\sigma_z$  we get the complex stiffness as

$$\tilde{E}_{\text{plate}} = \frac{E}{1-\nu^2} \frac{1 - (1-\nu^2)i\phi}{1 - [2\nu^2/(1-\nu)]i\phi}, \quad (21)$$

where  $\phi = \omega Z_{\text{rad}} d/2E$ . The first term is the well-known effective stiffness of the free plate while the second term is a weak perturbation caused by the fluid loading. The radiation impedance of a plate immersed in fluid is  $Z_{\text{rad}} = \rho_f \omega / \kappa_f$ , which is essentially real in the case of weak loading and can be approximated as  $Z_{\text{rad}} \approx \rho_f c_f / \cos(\theta)$ , where  $\sin(\theta) = c_f / c_0$ .<sup>17</sup> For  $c_f \ll c_0$ ,  $Z_{\text{rad}}$  can be further approximated as  $\rho_f c_f$ . Equation (21) is the effective complex stiffness in the low-frequency and weak-loading approximation. Since the radiation impedance of the plate is pure real, in a first-order approximation fluid loading does not affect the real part of

the effective stiffness, i.e., the velocity of the dilatational mode in the plate. In order to assess the velocity change in a thin plate due to fluid loading, a second-order approximation must be obtained by expanding Eq. (21) for small arguments using  $1/(1+\chi) \approx 1 - \chi + \chi^2 + 0(\chi^3)$ . After some algebraic manipulations, we can write the effective stiffness in the general form of

$$\tilde{E} \approx \frac{E}{1-\nu^2} (1 + \xi + i\eta), \quad (22)$$

where the real and imaginary parts of the correction term are

$$\xi = \left[ 1 - \frac{2\nu^2}{1-\nu} \right] \nu^2 \phi^2 \quad (23a)$$

and

$$\eta = -\nu^2 \frac{1+\nu}{1-\nu} \phi, \quad (23b)$$

respectively. The relative change in the phase velocity  $\Delta$  can be calculated from the effective stiffness as follows:

$$\Delta = \frac{1}{\text{Re} \left\{ 1/\sqrt{1+\xi+i\eta} \right\}} - 1 \approx \frac{\xi}{2} + \frac{3\eta^2}{8}. \quad (24)$$

From Eqs. (23a) and (23b) we notice that  $\xi$  and  $\eta^2$  are of the same order in  $\phi$ , therefore both terms must be retained in Eq. (24). When combined with Eqs. (23a) and (23b), Eq. (24) gives the relative change in the phase velocity for the lowest-order symmetric Lamb mode of a thin plate immersed in fluid as

$$\Delta = \frac{\delta}{32} \left[ \frac{\nu\omega\rho d c_f}{c_s^2} \right]^2, \quad (25)$$

where  $\delta = (4 - 8\nu + 3\nu^2)/[4(1-\nu)^2]$ . For aluminum of  $\nu=0.34$ ,  $\delta \approx 0.93$ , i.e., very close to unity. A Taylor series expansion of  $\delta$  in terms of the Poisson ratio yields  $\delta = 1 - \nu^2/4 - \nu^3/2 + 0(\nu^4)$ , i.e.,  $\delta$  approaches unity for low Poisson ratios. Retaining only the leading term in  $\delta$  reduces the expression for the relative phase velocity change given by Eq. (25) to that of Eq. (12) derived from a low-frequency, weak fluid-loading asymptotic analysis of the exact dispersion equation for a plate immersed in fluid. This result shows that, due to the pure real nature of the radiation impedance, fluid loading increases the effective stiffness of the plate. Our model also indicates that a second-order approximation is necessary to account for the change in velocity of the lowest-order symmetric Lamb mode in an immersed plate.

Similar calculations can be made to assess the effect of radiation loading on the effective stiffness of an immersed rod. For a fluid-loaded rod,  $\sigma_y = \sigma_z = -p$  and the pressure in the fluid is given as  $p = -i\omega a \varepsilon_r Z_{\text{rad}}$ . Substituting these equations into Eq. (19a) and assuming  $\varepsilon_r \approx -\nu \varepsilon_x$ , one can write the effective complex stiffness for a thin rod immersed in fluid as

$$\tilde{E}_{\text{rod}} = E \left( 1 - \frac{2\nu^2}{E} i\omega a Z_{\text{rad}} \right). \quad (26)$$

The radiation impedance of a pulsating cylinder is given as<sup>18</sup>

$$Z_{\text{rad}} = -i \frac{\omega \rho_f}{k_f} \frac{H_0^{(1)}(\kappa_f a)}{H_1^{(1)}(\kappa_f a)} = -i \omega \rho_f a H(\kappa_f a). \quad (27)$$

At low frequencies, the radiation impedance can be approximated by

$$Z_{\text{rad}} \approx i \omega \rho_f a \ln(\kappa_f a). \quad (28)$$

The real and imaginary components of the radiation impedance can be separated by using  $\ln(\kappa_f a) = \ln(|a\kappa_f|) + i \arg(a\kappa_f)$ . At low frequencies, the dominating imaginary part is always negative corresponding to the positive accession mass  $m_a \approx -\rho_f a \ln(|a\kappa_f|)$  of the fluid. Of course the real part of the radiation impedance  $-\omega \rho_f a \arg(a\kappa_f)$  is positive since the argument of the complex  $\kappa_f$  is always negative, as it was pointed out before. Since the radiation impedance is essentially pure imaginary, the relative change in the phase velocity can now be written as

$$\Delta \approx \text{Re} \left\{ \sqrt{\frac{\tilde{E}}{E}} \right\} - 1. \quad (29)$$

Using Eqs. (26), (28), and (29) we get

$$\Delta \approx \frac{\nu^2 \rho_f \omega^2 a^2}{E} \ln(|a\kappa_f|), \quad (30)$$

which is the same as the low-frequency, weak-loading asymptotic expression previously given in Eq. (18). This result shows that, due to the essentially imaginary nature of the radiation impedance, fluid loading decreases the effective stiffness of the rod.

In summary, it is well understood why transverse displacements due to the Poisson effect reduce the effective stiffness in a rod with respect to a plate and even more with respect to an infinite medium. It is also clear how mass loading reduces the effective stiffness of an immersed rod, thereby reducing the velocity of the longitudinal mode. It is less obvious why resistive loading increases the phase velocity of the longitudinal mode of a plate via a small imaginary component in the effective stiffness  $\tilde{E} \approx E(1 - i\eta)$ . The lack of lucidity is due to the fact that since resistive loading does not affect directly the wave velocity we had to consider second-order perturbation to determine the change in phase velocity. It further complicates the physical interpretation that this change can be attributed to the sum of two small effects. First, the velocity (or wave number) of an attenuated wave is inherently complex  $c = \sqrt{\tilde{E}/\rho} = c_r + ic_i$ , therefore its phase velocity  $c_{\text{phase}} \approx c_r + c_i^2/c_r$  is always higher than the real part of the velocity. Second, the real part of the complex velocity itself increases in the second order because of the square-root relationship between the complex velocity and the complex stiffness  $\sqrt{E(1 - i\eta)} \approx \sqrt{E}(1 - i\eta/2 + \eta^2/8 \dots)$ .

#### IV. CONCLUSIONS

In spite of the fundamental similarities between the dilatational vibrations of thin plates and rods, fluid loading exerts an opposite effect on their respective phase velocities. Although the magnitude of the relative change in the phase velocity due to fluid loading is usually very small and practically negligible compared to the much stronger attenuation

effect in both cases, the very fact that the sign of the velocity change is opposite motivated our effort. Both numerical and asymptotic analytical inspection of the known exact dispersion equations revealed that at low frequencies fluid loading slightly increases the phase velocity of the lowest-order symmetric Lamb mode propagating in a thin plate, while it decreases that of the lowest-order axisymmetric mode of a thin rod. These conclusions were also confirmed by a physical analysis that showed that the somewhat unexpected opposite effect of fluid loading on immersed rods and plates is caused by the different nature of radiation loading. First-order approximation of the effective complex stiffness, and therefore the relative change in the phase velocity, is sufficient in the case of a rod, whereas a second-order approximation is necessary to account for this effect in the case of a plate. This is due to the fact that, at very low frequencies, the rod possesses a complex radiation impedance with a dominating reactive part in contrast to the essentially resistive radiation impedance of a plate.

- <sup>1</sup>A. Schoch, "The transmission of waves through plates," *Acustica* **2**, 1–17 (1952) (in German).
- <sup>2</sup>M. F. M. Osborne and S. D. Hart, "Transmission, reflection, and guiding of an exponential pulse by a steel plate in water. I. Theory," *J. Acoust. Soc. Am.* **17**, 1–18 (1945).
- <sup>3</sup>L. G. Merkulov, "Damping of normal modes in a plate immersed in a liquid," *Sov. Phys. Acoust.* **10**, 169–173 (1964).
- <sup>4</sup>I. A. Viktorov, *Rayleigh and Lamb Waves* (Plenum, New York, 1967).
- <sup>5</sup>L. E. Pitts, T. J. Plona, and W. G. Mayer, "theoretical similarities of

- Rayleigh and Lamb modes of vibration," *J. Acoust. Soc. Am.* **16**, 374–377 (1976).
- <sup>6</sup>I. T. Selezov, V. V. Sorokina, and V. V. Yakovlev, "Wave propagation in a thickness-inhomogeneous elastic layer bounded by fluid media," *Sov. Phys. Acoust.* **31**, 220–223 (1985).
- <sup>7</sup>A. H. Nayfeh and D. E. Chimenti, "Propagation of guided waves in fluid-coupled plates of fiber-reinforced composite," *J. Acoust. Soc. Am.* **83**, 1736–1743 (1988).
- <sup>8</sup>S. I. Rokhlin, D. E. Chimenti, and A. H. Nayfeh, "On the topology of the complex wave spectrum in a fluid-coupled elastic layer," *J. Acoust. Soc. Am.* **85**, 1074–1080 (1989).
- <sup>9</sup>R. N. Thurston, "Elastic waves in rods and clad rods," *J. Acoust. Soc. Am.* **64**, 37 (1978).
- <sup>10</sup>J. F. M. Scott, "The free modes of propagation of an infinite fluid-loaded thin cylindrical shell," *J. Sound Vib.* **125**, 241–280 (1988).
- <sup>11</sup>D. M. Photiadis, "The propagation of axisymmetric waves on a fluid-loaded cylindrical shell," *J. Acoust. Soc. Am.* **88**, 239–250 (1990).
- <sup>12</sup>J. A. Simmons, E. D. Krasicka, and H. N. G. Wadley, "Leaky axisymmetric modes in infinite clad rods, I," *J. Acoust. Soc. Am.* **92**, 1061–1090 (1992).
- <sup>13</sup>P. B. Nagy and R. M. Kent, "Ultrasonic assessment of Poisson's ratio in thin rods," *J. Acoust. Soc. Am.* **98**, 2694–2701 (1995).
- <sup>14</sup>Y. Liu, M. Viens, and D. Cheeke, "Behavior of extensional modes in a thin rod immersed in a viscous medium," *J. Acoust. Soc. Am.* **99**, 706–712 (1996).
- <sup>15</sup>A. H. Nayfeh and P. B. Nagy, "General study of axisymmetric waves in layered anisotropic fibers and their composites," *J. Acoust. Soc. Am.* **99**, 931–941 (1996).
- <sup>16</sup>M. Abramowitz, and I. A. Stegun, *Handbook of Mathematical Functions* (Dover, New York, 1972).
- <sup>17</sup>A. Pierce, *Acoustics, an Introduction to Its Physical Principles and Applications* (Acoustic Society of America, New York, 1989), p. 108.
- <sup>18</sup>M. C. Junger and D. Feit, *Sound, Structures and Their Interaction* (MIT, Cambridge, MA, 1986), pp. 168–172.

# A simplified model for linear and nonlinear processes in thermoacoustic prime movers. Part I. Model and linear theory

M. Watanabe,<sup>a)</sup> A. Prosperetti, and H. Yuan

Department of Mechanical Engineering, The Johns Hopkins University, Baltimore, Maryland 21218

(Received 12 December 1995; accepted for publication 30 July 1997)

A simplified quasi-one-dimensional model of thermoacoustic devices is formulated by averaging the conservation equations over the cross section. Heat transfer and drag effects are introduced by means of suitable coefficients. While the primary motivation for this work is the development of a model approximately valid in the nonlinear regime, the focus of this paper is the proper formulation of the transfer coefficients and the analysis of the linear problem. The accuracy of the model is demonstrated by comparison with existing more precise theories and data. Examples of devices with variable cross section demonstrate the flexibility of the approach. © 1997 Acoustical Society of America. [S0001-4966(97)01412-4]

PACS numbers: 43.35.Ud [HEB]

## INTRODUCTION

In recent years there has been a renewal of interest in thermoacoustic devices, both prime movers and heat pumps (for reviews see Wheatley, 1986; Swift, 1988). The foundations of the linear theory were firmly established in a well-known series of papers by Rott (1969, 1976, 1980, 1983, and others) and further developed by a number of authors (Merkli and Thomann, 1975; Yazaki *et al.*, 1980, 1987; Arnott *et al.*, 1991, 1992, 1996; Atchley, 1992, 1994; Atchley and Kuo, 1994; Atchley *et al.*, 1990a, 1990b, 1992; Olson and Swift, 1994; Raszpet *et al.*, 1993; Swift, 1992; Swift and Keolian, 1993; Wheatley *et al.*, 1983). As a consequence of this work, the linear analytical theory of such devices is now well developed although, due to the complexities of the process, it appears doubtful that much progress can be made into the nonlinear realm along similar lines (Gaitan and Atchley, 1993).

Progress in the direction of nonlinear phenomena clearly requires a time-domain formulation. For this purpose, we use a method very common in the study of nonlinear compressible flows and shock waves, namely the integration of the governing equations over the cross section of the device (see, e.g., Crocco, 1958; Landau and Lifshitz, 1959). This procedure leads us to a quasi-one-dimensional model that, although approximate, appears useful to further an understanding of thermoacoustic devices in the nonlinear regime.

Briefly, the novelty of the model described in this paper consists in: (i) its nonlinear nature; (ii) its formulation in the time domain necessary for the study of nonlinear effects; and (iii) its ability to account for changes of the cross section of the device also in the nonlinear regime.

In spite of its approximate nature, the present model is still very complex and its full study is a nontrivial matter. In the present paper we consider the prime mover case. We develop the model and compare it with the existing linear theory. Part II of this study (Yuan *et al.*, 1997) addresses the

issue of the numerical integration of the nonlinear problem and presents some results. Future work will be devoted to improved approximations, the weakly nonlinear regime, the refrigerator case, and other related topics.

## I. SIMPLIFIED MODEL OF THERMOACOUSTIC DEVICES

Most thermoacoustic devices consist of an acoustic resonator containing different heat transfer components (stack, heat exchangers, etc.). Typically the dimensions along the direction of the particle displacement, the resonator "axis," is much longer than the transverse one and this circumstance suggests the basis for our approximation. We recast the governing equations in an integrated form over the cross section of the device thus reducing the model to one dimension in space (along the tube axis) and time. Effects taking place in the orthogonal directions (friction, heat transfer, etc.) are to be accounted for approximately by the introduction of suitable terms in the equations.

Consider a thermoacoustic device consisting of a duct of variable area  $S(x)$ . The coordinate  $x$  is taken along the axis of the device that is not necessarily straight. Upon integrating the equation of continuity over the volume delimited by two neighboring cross sections  $S(x)$  and  $S(x+dx)$  we find the well-known relation

$$\frac{\partial \langle \rho \rangle}{\partial t} + \frac{1}{S} \frac{\partial S \langle \rho u \rangle}{\partial x} = 0, \quad (1)$$

where  $\rho$  is the gas density,  $u$  the velocity in the  $x$  direction, and the angle brackets indicate the cross sectional average,

$$\langle \cdots \rangle = \frac{1}{S(x)} \int_{S(x)} dS (\cdots). \quad (2)$$

The vanishing of the exact normal velocity on the lateral walls of the duct has been applied to obtain (1).

Similarly, the momentum equation in the  $x$  direction becomes

<sup>a)</sup>Present address: Department of Mechanical Engineering, Kyushu University, 5-10-1 Hakozeki, Higashi-ku, Fukuoka, Japan 812.



$$\begin{aligned} \frac{\partial \langle \rho u \rangle}{\partial t} + \frac{1}{S} \frac{\partial}{\partial x} (S \langle \rho u^2 \rangle) + \frac{\partial \langle p \rangle}{\partial x} + \frac{1}{S} (\langle p \rangle - \bar{p}) \frac{dS}{dx} \\ = - \frac{\mathcal{P}}{S} \overline{(\boldsymbol{\tau} \cdot \mathbf{n})}_x. \end{aligned} \quad (3)$$

Here,  $p$  is the gas pressure,  $\boldsymbol{\tau}$  the viscous stress tensor, and the overline denotes the average over the “wetted perimeter”  $\mathcal{L}$ , i.e., the lines along which the cross-section  $S$  is cut by solid boundaries,

$$\bar{p} = \frac{1}{\mathcal{P}} \oint_{\mathcal{L}} p \, dl, \quad (4)$$

where  $\mathcal{P}$  is the length of  $\mathcal{L}$ . The unit normal  $\mathbf{n}$  is directed into the fluid region. The viscous component  $\tau_{xx}$  has been neglected in deriving (3).

Before turning to the energy equation we introduce an assumption widely used in gas dynamics (see e.g., Crocco, 1958 for a discussion), namely that the fields are approximately uniform over the cross section. [The assumption of uniform pressure over the cross section has already been used in thermoacoustics, e.g., by Tominaga (1995) and can be traced at least as far back as Lord Rayleigh.] As a consequence of the cross-sectional uniformity,  $\langle p \rangle \approx \bar{p}$  and we may disregard correlation terms writing the average of products as products of averages. This approximation is addressed quantitatively in Sec. IV. The effects of nonuniformities, such as wall drag, are accounted for in an approximate manner. For the wall shear stress we write

$$\frac{\mathcal{P}}{S} \overline{(\boldsymbol{\tau} \cdot \mathbf{n})}_x \equiv \mathcal{D}(u), \quad (5)$$

where  $\mathcal{D}$  is a suitable operator the exact form of which can only be found in the linear case as shown later in Sec. III, Eq. (45). As made evident from this relation, in the linear domain,  $\mathcal{D}(u)/\langle u \rangle$  is a complex, frequency-dependent quantity. The first feature implies that the wall drag has a component in phase with the velocity and one in phase with the acceleration, while the second one implies that an exact representation of the action of  $\mathcal{D}(u)$  requires a convolution integral in time. The latter feature would render the integration of the equations over the many thousands of cycles necessary to reach steady state completely impractical. We are therefore forced to neglect memory effects assuming the form

$$\mathcal{D}(u) = \rho D \left[ 1 + \theta_V \left( \frac{\partial}{\partial t} + \langle u \rangle \frac{\partial}{\partial x} \right) \right] \langle u \rangle, \quad (6)$$

where  $D$  and  $\theta_V$  are quantities to be specified later. The latter parameter accounts for the phase relation between velocity and acceleration. Truncated to the linear terms, this form approximates the correct action of  $\mathcal{D}$  in the case of single-frequency oscillations. The convective term  $\langle u \rangle \partial \langle u \rangle / \partial x$  is an educated guess of a form suitable for the nonlinear regime. With these assumptions, and the omission henceforth of explicit indication of cross-sectional averages, the continuity (1) and momentum (3) equations become

$$\frac{\partial \rho}{\partial t} + \frac{1}{S} \frac{\partial}{\partial x} (S \rho u) = 0, \quad (7)$$

$$\frac{\partial \rho u}{\partial t} + \frac{1}{S} \frac{\partial}{\partial x} (S \rho u^2) + \frac{\partial p}{\partial x} = - \mathcal{D}(u). \quad (8)$$

The cross-sectional averaging procedure applied to the energy equation of a perfect gas gives

$$\begin{aligned} \frac{\partial}{\partial t} \left[ \frac{1}{\gamma-1} p + \frac{1}{2} \rho u^2 \right] + \frac{1}{S} \frac{\partial}{\partial x} \left[ u S \left( \frac{\gamma}{\gamma-1} p + \frac{1}{2} \rho u^2 \right) \right] \\ = \frac{\mathcal{P}}{S} \overline{\mathbf{q} \cdot \mathbf{n}}, \end{aligned} \quad (9)$$

where  $\mathbf{q}$  is the heat flux and  $\gamma$  is the ratio of specific heats. The most intense heat transfer occurs in the directions normal to  $x$  and, accordingly, the effect of axial conduction  $q_x$  has been disregarded. This approximation is of course invalid at the ends of the tube. We return on this point below. Note also that the viscous dissipation term has been neglected here because it is small in comparison with the wall heat transfer.

Similar to (5), we introduce two heat transfer operators  $\mathcal{H}$ ,  $\mathcal{Q}$  by writing

$$\frac{\mathcal{P}}{S} \overline{\mathbf{q} \cdot \mathbf{n}} \equiv \mathcal{H}(T_w - T) - \frac{dT_w}{dx} \mathcal{Q}(u), \quad (10)$$

where  $T_w(x)$  is the temperature of the solid structure (e.g., the stack plates) at  $x$ . In this paper this quantity is taken to be prescribed, e.g., on the basis of experiment. A refinement of the model enabling  $T_w$  to be calculated will be presented in a future paper. The second term in (10) accounts for the distortion of the temperature distribution due to the flow in the presence of a mean temperature gradient. This ansatz is suggested by the structure of the temperature distribution given by the exact linear theory as will be seen below in connection with Eq. (51). As for  $\mathcal{D}$ , the form for the operators  $\mathcal{H}$ ,  $\mathcal{Q}$  assumed here is

$$\mathcal{H}(T_w - T) = \rho c_p H \left[ 1 + \theta_T \left( \frac{\partial}{\partial t} + u \frac{\partial}{\partial x} \right) \right] (T_w - T), \quad (11)$$

$$\mathcal{Q}(u) = \rho c_p Q \left[ 1 - \theta_Q \left( \frac{\partial}{\partial t} + u \frac{\partial}{\partial x} \right) \right] u, \quad (12)$$

where  $c_p$  is the gas specific heat at constant pressure. The time derivatives have been introduced for the same reason as previously in connection with  $\mathcal{D}(u)$ , i.e., to account for phase relations. The convective derivative in (11) is taken to operate on  $T_w - T$ , rather than  $T$  alone, as what matters physically is the temperature difference between the fluid particle and the solid structure it is in contact with. If a particle has moved from  $x$  to  $x + udt$ , it will “see” a temperature  $T_w(x + udt)$  rather than  $T_w(x)$ . The determination of the parameters  $H$ ,  $Q$ ,  $\theta_T$ , and  $\theta_Q$  will be considered in Sec. III.

Now, upon using (7) and (8) to eliminate the time derivatives of  $\rho$  and  $u$ , the energy equation (9) becomes

$$\frac{\partial p}{\partial t} + u \frac{\partial p}{\partial x} + \frac{\gamma p}{S} \frac{\partial}{\partial x} (Su) = (\gamma - 1) \left[ \mathcal{H}(T_w - T) - \frac{dT_w}{dx} Q(u) + u \mathcal{L}(u) \right]. \quad (13)$$

The third term in the right-hand side represents the rate of conversion of mechanical to thermal energy by friction.

The last step to close the system (7), (8), (13) is to specify an equation of state. We assume that the averaged variables are related by the perfect gas equation

$$p = R\rho T, \quad (14)$$

where  $R$  is the universal gas constant divided by the gas molecular mass.

In Part II of this study (Yuan *et al.*, 1997), devoted to the nonlinear problem, it will prove desirable to change slightly the form of  $\mathcal{H}$  shown above by adding a second-order spatial derivative. In this way it will be possible to bring the spectra of the approximate and exact linear problems in better agreement, which is important when nonlinearities cause a mixing of different modes. Since the remainder of this paper is devoted to the linear case, and for brevity, we postpone the discussion of this point until then.

In the present paper we consider only the prime mover problem in which the end walls of the tube are fixed. Therefore, we must require that the velocity vanish at  $x=0$  and  $x=L$ . As a consequence of (8), this implies

$$\frac{\partial p}{\partial x} = 0 \quad (15)$$

as well. Equations (7) and (13) written at the end points give then

$$\left[ \frac{\partial \rho}{\partial t} + \rho \frac{\partial u}{\partial x} \right]_{x=0,L} = 0, \quad (16)$$

$$\left[ \frac{\partial p}{\partial t} + \gamma p \frac{\partial u}{\partial x} = \gamma \frac{p}{T} H \left( 1 + \theta_T \frac{\partial}{\partial t} \right) (T_w - T) \right]_{x=0,L}. \quad (17)$$

Upon eliminating  $\partial u / \partial x$  one finds

$$\left[ \frac{\partial}{\partial t} + H \left( 1 + \theta_T \frac{\partial}{\partial t} \right) \right]_{x=0,L} T = \left[ \frac{\gamma - 1}{\gamma} \frac{T}{p} \frac{\partial p}{\partial t} + H \left( 1 + \theta_T \frac{\partial}{\partial t} \right) T_w \right]_{x=0,L}. \quad (18)$$

This relation shows that a knowledge of  $p$  at the boundary completely specifies the gas temperature perturbation provided  $T_w$  is known, as assumed in this paper. No additional boundary conditions are therefore necessary. In order to understand this result it may be useful to rewrite it in the exact equivalent form

$$\frac{\partial}{\partial t} \left( \frac{T}{p^{\gamma-1/\gamma}} \right) = \frac{1}{p^{\gamma-1/\gamma}} H \left( 1 + \theta_T \frac{\partial}{\partial t} \right) (T_w - T), \quad (19)$$

which shows that the gas would behave adiabatically if  $H$  vanished, i.e., in the absence of heat exchange with the wall.

It is evident that, in general, the relation (18) implies a temperature jump at the left and right boundaries from the  $T$  given by this relation to the end-wall temperatures. This is a consequence of the neglect of axial conduction in the derivation of the energy equation (9). Axial conduction would introduce a term  $\partial^2 T / \partial x^2$ , important only near the end walls, the role of which would be to reestablish continuity of temperature by means of a thin boundary layer. The temperature in this layer would adjust itself so as to match the value given by (18). This is an essentially passive process with negligible effects on the temperature distribution elsewhere in the device and can therefore be disregarded. Alternatively, the value of  $H$  at  $x=0, L$  can be adjusted to account for heat transfer with the terminations of the tube.

## II. LINEARIZATION

The model described by Eqs. (7), (8), (13), and (14) is general. For the rest of this article we focus, however, only on its linear aspects.

We assume that, at equilibrium, the device contains gas at a uniform pressure  $p_0$  and in thermal equilibrium with the solid boundaries with which it is in contact, so that its temperature is  $T_w(x)$ . Let now

$$p = p_0 + p', \quad \rho = \rho_0 + \rho', \quad T = T_w + T', \quad (20)$$

where the subscript 0 and the prime indicate unperturbed and perturbed quantities, respectively. The unperturbed quantities satisfy the equation of state with  $p_0$  independent of  $x$  so that  $\rho_0 = \rho_0(x)$  must compensate for the  $x$  dependence of  $T_w$ . Upon assuming a time dependence proportional to  $\exp i\omega t$  and neglecting quadratic and higher terms in the primed quantities and in  $u$ , we readily find:

$$i\omega \rho' + \frac{1}{S} \frac{d}{dx} (\rho_0 S u) = 0, \quad (21)$$

$$\rho_0 i\omega u + \frac{dp'}{dx} = -\rho_0 D (1 + i\omega \theta_V) u, \quad (22)$$

$$i\omega \rho' + \gamma \frac{p_0}{S} \frac{d(Su)}{dx} = -\gamma \frac{p_0}{T_w} H (1 + i\omega \theta_T) T' - (\gamma - 1) \rho_0 c_p \frac{dT_w}{dx} \times Q (1 - i\omega \theta_Q) u. \quad (23)$$

From the momentum equation (22) we have

$$u = -\frac{1}{1 + (1 + i\omega \theta_V)(D/i\omega)} \frac{1}{\rho_0 i\omega} \frac{dp'}{dx}, \quad (24)$$

and, upon substituting into the continuity equation (21),

$$\rho' = -\frac{1}{\omega^2 S} \frac{d}{dx} \left[ \frac{S}{1 + (1 + i\omega \theta_V)(D/i\omega)} \frac{dp'}{dx} \right]. \quad (25)$$

By substituting these relations into the energy equation (23) and using the linearized form of the equation of state we find the following equation for the pressure:

$$\begin{aligned} & \frac{1}{S} \frac{d}{dx} \left[ \frac{Sc_A^2}{1+(1+i\omega\theta_V)(D/i\omega)} \frac{dp'}{dx} \right] \\ & + \omega^2 p' + \gamma \frac{H}{i\omega} (1+i\omega\theta_T) \\ & \times \left\{ \frac{c_I^2}{S} \frac{d}{dx} \left[ \frac{S}{1+(1+i\omega\theta_V)(D/i\omega)} \frac{dp'}{dx} \right] + \omega^2 p' \right\} \\ & + \frac{(\gamma-1)c_p}{1+(1+i\omega\theta_V)(D/i\omega)} \frac{dT_w}{dx} Q(1-i\omega\theta_Q) \frac{dp'}{dx} = 0, \end{aligned} \quad (26)$$

where

$$c_A^2 = \gamma RT_w, \quad c_I^2 = RT_w, \quad (27)$$

are the adiabatic and isothermal sound speeds, respectively. The associated boundary conditions are the vanishing of the first derivative at the two ends of the tube as given in Eq. (15).

If drag is disregarded so that  $D=0$ , the previous equation may be written in the time domain in the form

$$\begin{aligned} & \frac{\partial}{\partial t} \left[ \frac{1}{S} \frac{\partial}{\partial x} \left( Sc_A^2 \frac{\partial p'}{\partial x} \right) - \frac{\partial^2 p'}{\partial t^2} \right] + \gamma H \left( 1 + \theta_T \frac{\partial}{\partial t} \right) \\ & \times \left[ \frac{c_I^2}{S} \frac{\partial}{\partial x} \left( S \frac{\partial p'}{\partial x} \right) - \frac{\partial^2 p'}{\partial t^2} \right] + (\gamma-1)c_p \frac{dT_w}{dx} Q \\ & \times \left( 1 - \theta_Q \frac{\partial}{\partial t} \right) \frac{\partial^2 p'}{\partial x \partial t} = 0. \end{aligned} \quad (28)$$

This equation may be considered as falling in the class of the ‘‘wave hierarchies’’ studied, among others, by Whitham (1974). This remark is, however, of limited usefulness as the standard theory of wave hierarchies applies to propagating, rather than standing, waves.

Once the pressure has been found, the temperature disturbance can be calculated by eliminating  $\partial(Su)/\partial x$  between the continuity and the energy equation. The result is

$$\begin{aligned} & \left[ 1 + \frac{H}{i\omega} (1+i\omega\theta_T) \right] T' \\ & = \frac{p'}{\rho_0 c_p} + i \frac{u}{\omega} [1+Q(1-i\omega\theta_Q)] \frac{dT_w}{dx}. \end{aligned} \quad (29)$$

With (24) for  $u$  and (25) for  $p'$ , the determination of  $p'$  gives then a complete solution of the problem.

It is evident from (28) that, if no heat transfer occurs so that  $H=0$ ,  $Q=0$ , the equation describes adiabatic sound waves in an imposed temperature distribution. In the opposite limit of very large heat transfer, but again with  $Q=0$ , the waves propagate isothermally in the sense that each fluid ‘‘slice’’ retains the temperature of the solid surface in contact with it. More generally, Eq. (28) describes the competition of processes occurring on three time scales, the acoustic one of the wave oscillation, that associated to heat transfer, and that associated to convection. These time scales can be estimated as follows. Let

$$\bar{c}, \quad \bar{H}, \quad \bar{T}_w \quad (30)$$

be suitable average values of the sound speed, heat transfer coefficient, and gas temperature. Then the acoustic time scale  $t_a$  is of order  $\omega^{-1} \sim L/\bar{c}$ , while for the thermal time scale, from the coefficient of the second group of terms in (28), we have

$$t_h \sim \frac{1}{\gamma \bar{H}}. \quad (31)$$

From the definition (11) of  $H$  we can clearly write

$$\rho c_p \bar{H} \Delta T \sim \frac{1}{l} k \frac{\Delta T}{\delta_K}, \quad (32)$$

where  $\Delta T$  is of the order of the temperature difference between gas and solid surfaces in the stack,  $k$  is the gas thermal conductivity,  $\delta_K$  defined by

$$\delta_K = \sqrt{\frac{2\alpha}{\omega}}, \quad (33)$$

with  $\alpha$  the thermal diffusivity of the gas is the thermal diffusion length, and  $l$  is the plate spacing in the stack. Upon substitution into (31) we thus have

$$t_h \sim \frac{l \delta_K}{\gamma \alpha}, \quad (34)$$

The ratio of the thermal and acoustic time scales is then

$$\frac{t_h}{t_a} \sim \frac{l}{\gamma \delta_K}. \quad (35)$$

At low frequencies  $\delta_K$  is large and the motion in the stack is dominated by the terms multiplied by  $H$  in (28). At high frequencies, the terms in the first square brackets prevail.

For the coefficient  $Q$ , it is simple to obtain the estimate  $Q \sim 1$  so that, in order of magnitude, the ratio between the first and the last group of terms of (28) is

$$\frac{(\gamma-1)c_p Q (dT_w/dx) (\partial^2 p'/\partial x \partial t)}{c_A^2 (\partial^3 p'/\partial x^2 \partial t)} \sim \frac{T_H - T_C}{\bar{T}_w} \frac{L}{L_S}, \quad (36)$$

where  $T_H - T_C$  is the temperature difference over the length  $L_S$  of the stack. This estimate indicates that this convective term is not small in typical applications.

Viscous effects introduce an additional time scale  $t_v \sim 1/D$  that affects equally the ‘‘isothermal’’ and the ‘‘adiabatic’’ components. From the definition (6) we expect that  $D \sim \nu/l\delta_V$ , where  $\nu$  is the gas kinematic viscosity and  $\delta_V$  the viscous diffusion length defined by

$$\delta_V = \sqrt{\frac{2\nu}{\omega}} = \sqrt{\sigma} \delta_K, \quad (37)$$

with  $\sigma$  the Prandtl number. The condition for viscous effects to be negligible is that  $t_v \omega \ll 1$ , which is verified at low frequencies. Since, for gases, diffusivities are of the order of the speed of sound times the molecular mean free path  $s$  (see, e.g., Chapman and Cowling, 1952), we have

$$\omega t_v \sim \frac{l}{s} \frac{\delta_V}{L}. \quad (38)$$

This quantity can assume a wide range of values depending on pressure, temperature, and nature of the gas. The ratio of  $t_h$  and  $t_v$  is

$$\frac{t_h}{t_v} \sim \frac{1}{\gamma} \frac{\nu}{\alpha} \frac{\delta_K}{\delta_V} = \frac{\sqrt{\sigma}}{\gamma}. \quad (39)$$

Since the Prandtl number has a value close to 1 for most gases, this relation implies that viscous effects are normally just as important as heat transfer ones.

### III. DRAG AND HEAT TRANSFER PARAMETERS

In the linear regime, appropriate expressions for the drag and heat transfer coefficients can be found from their definitions (6) and (10) upon comparison with the exact linear results.

Swift (1988, Eq. A4) gives the following expression for the velocity field in a plane channel of width  $l$ :

$$u_1 = \frac{i}{\omega \rho_0} \frac{dp'}{dx} \left( 1 - \frac{\cosh(1+i)y/\delta_V}{\cosh(1+i)l/2\delta_V} \right), \quad (40)$$

where  $y$  is measured from the center plane of the channel and the diffusion length  $\delta_V$  is given by (37). From this equation we have

$$(\boldsymbol{\tau} \cdot \mathbf{n})_x = -\mu \left. \frac{\partial u_1}{\partial y} \right|_{y=l/2} = -\frac{i(1+i)\mu}{\omega \rho_0 \delta_V} \frac{dp'}{dx} \tanh \frac{(1+i)l}{2\delta_V}. \quad (41)$$

The mean velocity in the channel (to be identified with our  $u$ ) is

$$u = \frac{1}{l} \int_{-l/2}^{l/2} u_1 dy = \frac{i}{\omega \rho_0} (1-f_V) \frac{dp'}{dx}, \quad (42)$$

where

$$f_V = \frac{\tanh(1+i)l/2\delta_V}{(1+i)l/2\delta_V}. \quad (43)$$

From these two expressions we find

$$\frac{\mathcal{P}}{S} \overline{(\boldsymbol{\tau} \cdot \mathbf{n})_x} = -i\omega \rho_0 \frac{f_V}{1-f_V} u. \quad (44)$$

Comparison with (6) then gives

$$D(1 + \omega \theta_V) = i\omega \frac{f_V}{1-f_V}. \quad (45)$$

Upon separating real and imaginary parts, explicit expressions for  $D$  and  $\theta_V$  are readily obtained.

For later reference it is useful to note the following asymptotic behaviors of the function  $f_V(\eta)$ , with  $\eta = 2\delta_V/l$ , defined by (43). In the thin viscous layer limit  $\eta \rightarrow 0$  and one has

$$f_V \approx \frac{1}{2}(1-i)\eta, \quad (46)$$

while, for  $\delta_V \gg l$ ,

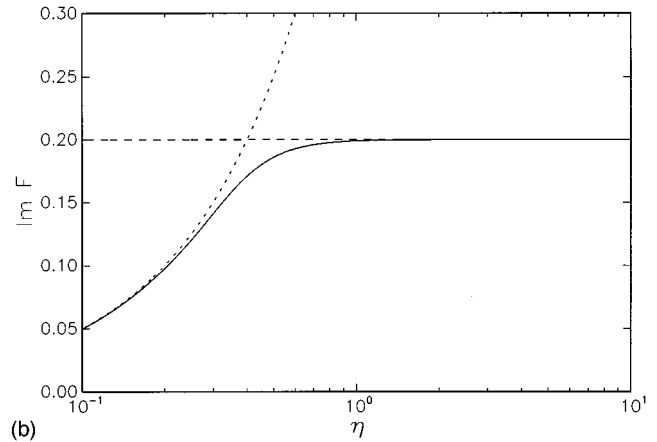
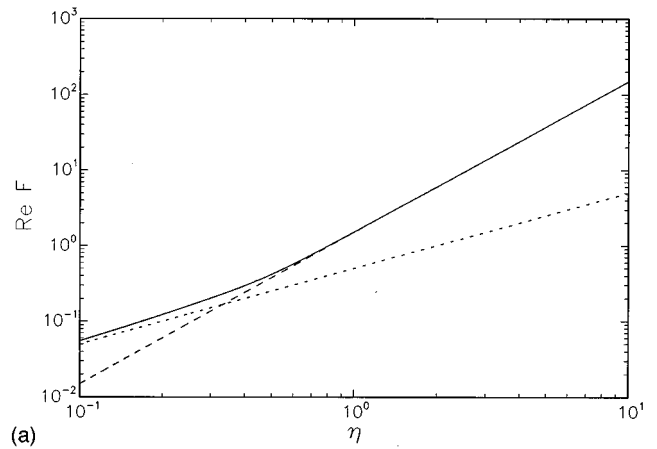


FIG. 1. The real, (a), and imaginary, (b), parts of the function  $F(\eta)$  defined in (48). The dashed line is the asymptotic approximation (50) for  $\eta \rightarrow \infty$ , and the dotted line the approximation (49) for  $\eta \rightarrow 0$  truncated to the term linear in  $\eta$ .

$$f_V \approx 1 - \frac{2i}{3\eta^2} - \frac{8}{15\eta^4}. \quad (47)$$

With these results it is easy to establish the asymptotic behavior of

$$F = \frac{if_V}{1-f_V}, \quad (48)$$

namely

$$F \approx \frac{1}{2}(1+i)\eta + \frac{1}{2}\eta^2 + \frac{1}{4}(1-i)\eta^3, \quad \eta \rightarrow 0, \quad (49)$$

and

$$F \approx \frac{3}{2}\eta^2 + \frac{i}{5} - \frac{338}{175}\frac{1}{\eta^2}, \quad \eta \rightarrow \infty. \quad (50)$$

Graphs of the real and imaginary parts of  $F$  are shown in Fig. 1.

We now proceed in a similar fashion to calculate the heat transfer coefficient. From Eq. (A10) in Swift (1988), neglecting the small term  $\epsilon_s$  involving the conductivity and heat capacity of the solid, we have the temperature perturbation in the channel as

$$T_1 = \frac{p'}{\rho_0 c_p} \left[ 1 - \frac{\cosh(1+i)y/\delta_K}{\cosh(1+i)l/2\delta_K} \right] + \frac{1}{\omega^2 \rho_0} \frac{dp'}{dx} \frac{dT_w}{dx} \left[ \frac{\sigma}{\sigma-1} \frac{\cosh(1+i)y/\delta_V}{\cosh(1+i)l/2\delta_V} - \frac{1}{\sigma-1} \frac{\cosh(1+i)y/\delta_K}{\cosh(1+i)l/2\delta_K} - 1 \right], \quad (51)$$

where the thermal diffusion length  $\delta_K$  has been defined in (33). The structure of this result, with dependence on both  $\delta_V$  and  $\delta_K$ , shows that the temperature disturbance is determined by both convection and conduction processes. This is the reason for our ansatz (10) to express the mean energy transport.

Using (51), we can calculate the mean of  $T_1$  over the channel width, to be identified with the temperature disturbance  $T'$  of our theory:

$$T' = (1-f_K) \frac{p'}{\rho_0 c_p} + \frac{1}{\omega^2 \rho_0 (1-\sigma)} \times [\sigma(1-f_V) - (1-f_K)] \frac{dT_w}{dx} \frac{dp'}{dx}, \quad (52)$$

where, as in (43),

$$f_K = \frac{\tanh(1+i)l/2\delta_K}{(1+i)l/2\delta_K}. \quad (53)$$

Again from (51), one can calculate the heat flux into the boundaries:

$$-\mathbf{q} \cdot \mathbf{n} = \frac{kl}{\delta_K^2} \left[ if_K \frac{p'}{\rho_0 c_p} + \frac{f_V - f_K}{(1-f_V)(1-\sigma)} \frac{dT_w}{dx} u \right]. \quad (54)$$

Upon using (42) and (52), we then find

$$-\frac{\mathcal{P}}{S} \mathbf{q} \cdot \mathbf{n} = \frac{i\omega k}{\alpha} \frac{f_K}{1-f_K} T' + \frac{k}{\alpha(1-\sigma)} \frac{dT_w}{dx} \times \left( \sigma - 1 + \frac{1}{1-f_V} - \frac{\sigma}{1-f_K} \right) u, \quad (55)$$

from which, comparing with (11) and (12), we deduce

$$H(1+i\omega\theta_T) = i\omega \frac{f_K}{1-f_K}, \quad (56)$$

$$Q(1-i\omega\theta_Q) = \frac{1}{1-\sigma} \left( \frac{1}{1-f_V} - \frac{\sigma}{1-f_K} \right) - 1. \quad (57)$$

The functions  $f_V$ ,  $f_K$  defined in (43), (53) are appropriate for a plane channel geometry. As shown by Rott (1969), for a circular tube with radius  $r_0$  one has

$$f_V = 2 \frac{J_1((i-1)(r_0/\delta_V))}{(i-1)(r_0/\delta_V)J_0((i-1)(r_0/\delta_V))}, \quad (58)$$

with a corresponding expression for  $f_K$ . Asymptotic approximations for large and small tube radii now are, with  $\eta = 2\delta_V/r_0$ ,

$$f_V \approx \frac{1}{2}(1-i)\eta, \quad (59)$$

and

$$f_V \approx 1 - \frac{i}{2\eta^2} - \frac{1}{6\eta^4}, \quad (60)$$

respectively. Note that the two asymptotic expressions for small  $\eta$  are the same for the plane channel and the cylindrical tube. More generally, the same expression holds provided  $\eta$  is defined as the ratio of  $2\delta_V$  to the hydraulic radius.

Upon substituting (45), (56), and (57) into the wave equation (26), we find

$$\frac{1}{S} \frac{d}{dx} \left[ (1-f_V)S \frac{dp'}{dx} \right] + \frac{1}{T_w} \frac{dT_w}{dx} \left( 1 + \frac{\sigma f_V - f_K}{1-\sigma} \right) \frac{dp'}{dx} + \frac{\omega^2}{c_A^2} [1 + (\gamma-1)f_K] p' = 0. \quad (61)$$

If  $S$  is a constant, this equation is identical to that given by Swift [1988, his Eq. (54)] provided his wall parameter  $\epsilon_s$  is neglected and the gas is treated as perfect. If the spatial variation of  $S$  is retained, it coincides with a result given by Rott [1976, his Eq. (6)]. With the choices (45), (56), and (57), the present theory thus reproduces exactly the eigenfrequency and pressure eigenfunction of the standard linear theory. The velocity and temperature eigenfunction are only reproduced in the cross-sectional mean as indicated by (42) and (52).

Upon substituting (45) for  $D$  into the expression (24) for  $u$ , we recover (42) as expected. The expression (29) for the (cross-sectional mean) temperature disturbance becomes

$$T' = \frac{1-f_K}{\rho_0 c_p} p' + \frac{i}{1-\sigma} \left( \frac{1-f_K}{1-f_V} - \sigma \right) \frac{u}{\omega} \frac{dT_w}{dx} = \frac{1-f_K}{\rho_0 c_p} p' - \frac{1}{\rho_0 \omega^2} \left( 1 + \frac{\sigma f_V - f_K}{1-\sigma} \right) \frac{dT_w}{dx} \frac{dp'}{dx}, \quad (62)$$

while from (25) for the density disturbance we find

$$\rho' = -\frac{1}{\omega^2 S} \frac{\partial}{\partial x} \left[ (1-f_V)S \frac{\partial p'}{\alpha x} \right]. \quad (63)$$

Upon substitution of the expression (56) for the heat transfer parameter into the linearized boundary condition (18) for the temperature we find

$$\frac{T'}{T_w} = (1-f_K) \frac{\gamma-1}{\gamma} \frac{p'}{\rho_0}. \quad (64)$$

This relation is identical to (62) evaluated at the end walls where  $u=0$ .

When the stack plates are widely separated, from (43) and (53), we have  $f_V, f_K \approx 0$  and as a consequence, from (57),  $Q \approx 0$ . The temperature disturbance (62) becomes then

$$T' = \frac{1}{\rho_0 c_p} p' - \frac{1}{\rho_0 \omega^2} \frac{\partial T_w}{\partial x} \frac{dp'}{dx}. \quad (65)$$

Setting the right-hand side to zero we find the well-known expression of the critical temperature gradient (see, e.g., Swift, 1988):

$$\left. \frac{dT_w}{dx} \right|_{\text{crit}} = \frac{\omega^2 p'}{c_p (dp'/dx)}. \quad (66)$$

In general, however, only the component of  $T'$  in phase with the second term of Eq. (62) can be made to vanish by a suitable choice of  $dT_w/dx$ . The component in quadrature with this term will not normally be zero. We conclude that, in general, the gas temperature disturbance cannot vanish.

The procedure followed in this section has led to expressions for the viscous and heat transfer terms of the approximate model that match those of the exact linear theory for oscillations at one fixed frequency. Thus in the linear case where the different modes can be considered independently of each other, results such as Eq. (61) are exact. For example, Eq. (61) can be solved exactly to produce eigenfrequencies and eigenfunctions for all the modes. If many modes are present at the same time, as with a time-dependent nonlinear calculation, the need to use one specific value for each of the exchange parameters forces one to make some compromises. It turns out that in most practical cases only the lowest-frequency mode is unstable, and it is therefore reasonable to use the frequency of this mode to evaluate the parameters. The (real part of this) frequency can be approximated by

$$\bar{\omega} = \frac{\bar{c}}{L}, \quad (67)$$

where  $\bar{c} = (\gamma R \bar{T}_w)^{1/2}$  and

$$\bar{T}_w = \frac{1}{L} \int_0^L T_w(x) dx. \quad (68)$$

We will make use of  $\bar{\omega}$  thus defined in some of the examples that follow. An unwelcome feature of committing oneself to one value of the frequency is, however, that the spectrum of the linear problem is altered. We shall pursue this point in Part II of this study devoted to the nonlinear problem (Yuan *et al.*, 1997).

The dependence of the boundary layer thicknesses (37), (33) on  $\sqrt{\omega}$  implies that the diffusive transfers of momentum and energy to the solid boundaries are affected by the history of the flow and are therefore nonlocal in time. This feature is of course well recognized in the literature (see, e.g., Achard and Lespinard, 1981). The representations of the exchange operators assumed in (6), (11), and (12) are local in time and therefore can only be approximations. Conceivably, these approximations can be improved in the manner suggested by Achard and Lespinard by introducing, in place of explicit relations such as (10), differential ones connecting the time derivative of  $\mathbf{q}$ , in addition to  $\mathbf{q}$  itself, to the quantities in the right-hand side. In this way a nonlocal nature in time would be reintroduced, if with a kernel different from the exact one. This matter will be examined in a future study.

#### IV. CORRELATION TERMS

As pointed out in Sec. I, the major approximation underlying the present model consists in the neglect of the correlation terms, i.e., in setting the cross-sectional average of the product of two quantities equal to the product of the averages. Of course, the error associated with this procedure only affects the nonlinear calculations to be reported in subsequent papers as the choice of the drag and heat transfer

parameters made in the previous section insures that the linear results are reproduced exactly. Nevertheless this remains an important point that we can examine approximately using exact linear-theory results such as (40) and (51).

The most interesting quantity to consider is the product  $u_1 T_1$  as it enters in the expression for the energy flow in the device (see, e.g., Rott, 1975; Swift, 1988). In the special case of  $\sigma = 1$ ,  $dT_w/dx = 0$ , the result of this calculation also gives the correlation term for  $u_1^2$ . It may be noted that the neglect of correlation terms can be expected to be much more accurate for products involving the pressure field as, contrary to velocity, temperature, and density, the latter does not have a boundary layer structure.

By using (40) and (51), a straightforward calculation gives

$$\begin{aligned} \langle u_1 T_1 \rangle &\equiv \frac{1}{l} \int_0^l dy u_1(y) T_1(y) \\ &= \frac{i}{\omega \rho_0^2 c_p} p' \frac{dp'}{dx} \Phi_e(\zeta, \sigma) \\ &\quad + \frac{i}{(1-\sigma)\omega^3 \rho_0^2} \left( \frac{dp'}{dx} \right)^2 \frac{dT_w}{dx} \Psi_e(\zeta, \sigma), \end{aligned} \quad (69)$$

where

$$\zeta = \frac{l/2}{\delta_V} \quad (70)$$

is the ratio of the channel half-width to the boundary layer thickness and

$$\Phi_e = 1 + \frac{\sigma f_V - f_K}{1-\sigma}, \quad (71)$$

$$\begin{aligned} \Psi_e &= 1 - \sigma + \frac{1}{2} \sigma \frac{5-3\sigma}{1-\sigma} f_V - \frac{1}{1-\sigma} f_K \\ &\quad - \frac{\sigma}{2 \cosh^2(1+i)(l/2\delta_V)}. \end{aligned} \quad (72)$$

Here  $f_V$  and  $f_K$  are as defined in the previous section, Eq. (43), and we use the subscript  $e$  to indicate that these are exact expressions.

By taking the product of the averages (42) and (52) of  $u$  and  $T'$  we find an expression with the same structure as (69), but with the following approximate values of  $\Phi$  and  $\Psi$ :

$$\Phi_{\text{app}} = (1-f_V)(1-f_K), \quad (73)$$

$$\Psi_{\text{app}} = (1-\sigma + \sigma f_V - f_K)(1-f_V). \quad (74)$$

It may be noted that, for  $\sigma = 0$ , the boundary layer structure of the velocity field disappears and the exact and approximate expressions of  $\Phi$  and  $\Psi$  become identical for any  $\delta_K$ .

Figures 2 and 3 show the real and imaginary parts of the ratios  $\Phi_e/\Phi_{\text{app}}$  and  $\Psi_e/\Psi_{\text{app}}$  for  $\sigma = 0.71$  (helium) and  $\sigma = 0.392$  (60% helium and 40% argon mixture), respectively, as functions of  $\zeta = (l/2)/\delta_V$ . The range of interest of  $\zeta$  for existing thermoacoustic engines with a gas medium is typically from a low value of 4 to 5 in the stack region to many tens or more away from the stack. The figures show that,

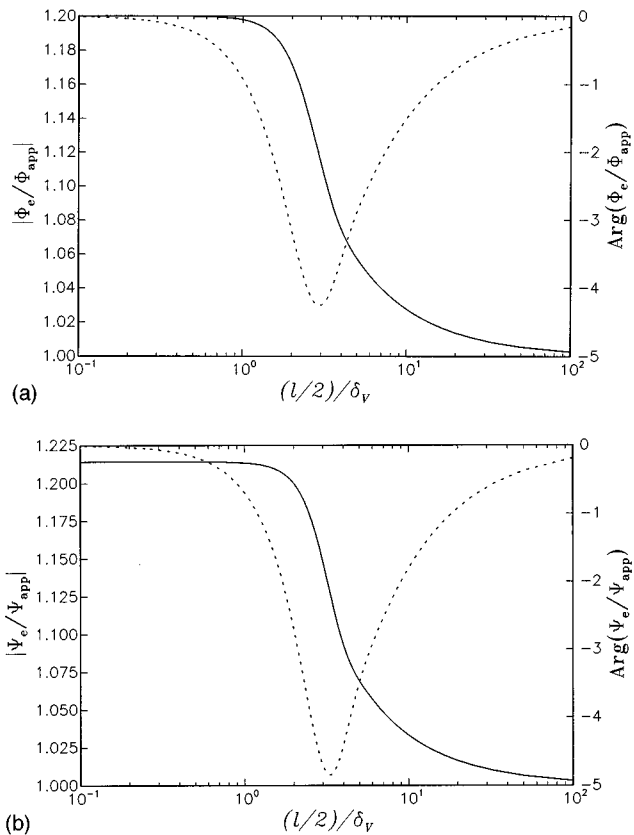


FIG. 2. The ratios  $\Phi_e/\Phi_{app}$ , (a), and  $\Psi_e/\Psi_{app}$ , (b), of the correlation coefficients appearing in the approximate and exact expressions of the velocity-temperature correlation (69) as functions of the ratio of the viscous penetration length  $\delta_v$  to the channel half-width  $\frac{1}{2}l$  for  $\sigma=0.71$  (helium). The solid lines are the modulus and the dashed lines the argument in degrees. The range of interest of the ratio  $(l/2)/\delta_v$  for existing thermoacoustic engines with a gas medium is typically from a low value of 4 to 5 up.

over this range, the moduli of the approximate and exact expressions differ by less than 6% and the phases by less than  $5^\circ$ .

These results suggest that the negative impact of cross-sectional averaging is limited. In particular, the model should be able to reproduce correctly the trends of real thermoacoustic prime movers resulting from different values of parameters or operating conditions.

## V. NUMERICAL RESULTS

We now turn to some numerical results obtained from the linearized equations of Sec. II. The expressions for the drag and heat transfer parameters found in Sec. III are used throughout. Although obtained from the linear theory, results of the type considered here do not seem to have been shown before. Most of the previous studies, and in particular the analysis of data that we consider here, have been based on approximations rather than on the exact theory.

As another point, we want to demonstrate the ability of the model to deal with devices with a variable cross section. By assuming a linear growth of the cross-sectional area with distance from  $x=0$ , we could readily adapt our model to the case of a cylindrical resonator. Since, however, a cylindrical system can be treated exactly by separation of variables, as

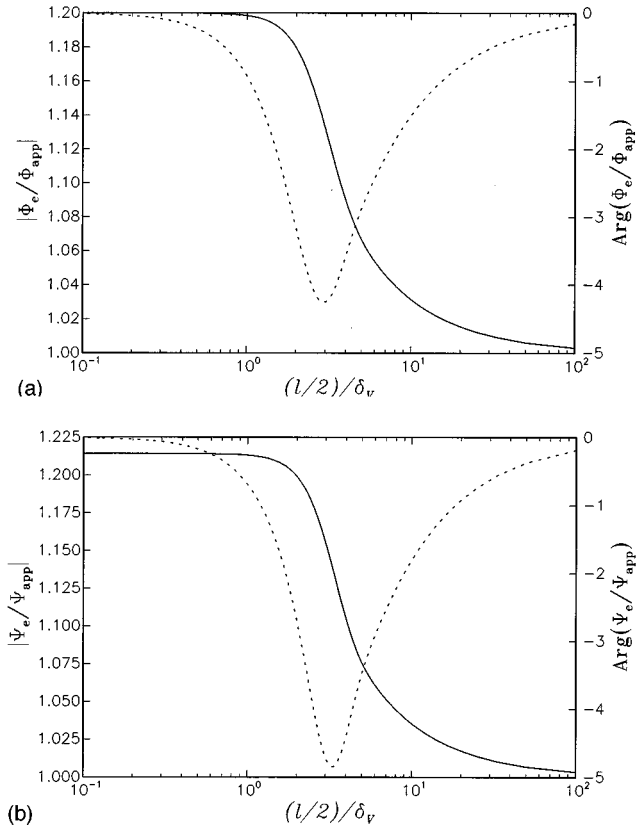


FIG. 3. The ratios  $\Phi_e/\Phi_{app}$ , (a), and  $\Psi_e/\Psi_{app}$ , (b) of the correlation coefficients appearing in the approximate and exact expressions of the velocity-temperature correlation (69) as functions of the ratio of the viscous penetration length  $\delta_v$  to the channel half-width  $\frac{1}{2}l$  for  $\sigma=0.392$  (60% helium and 40% argon mixture). The solid lines are the modulus and the dashed lines the argument in degrees. The range of interest of the ratio  $(l/2)/\delta_v$  for existing thermoacoustic engines with a gas medium is typically from a low value of 4 to 5 up.

recently demonstrated by Arnott *et al.* (1996), we prefer to focus on cases for which no exact method is available to demonstrate the specific strengths of our approach in this particular respect. For this reason, we consider a linear device with a contraction or expansion at its midsection.

We start by comparing the results of the model with the data of Atchley (1992) who measured the damping of oscillations in a thermoacoustic tube for different values of the imposed temperature difference across the stack. His results are expressed in terms of the inverse quality factor  $1/Q$  of the oscillations that is related to the real and imaginary parts of the eigenfrequency  $\omega$  appearing in our analysis by

$$\frac{1}{Q} = 2 \frac{\text{Im } \omega}{\text{Re } \omega}. \quad (75)$$

Below the stability threshold  $1/Q$  is positive, while it becomes negative above. At the threshold,  $1/Q=0$ .

The gas used in the experiment was helium. Over the temperature range of interest here, from 300 to 650 K, we fit thermal conductivity data (Vargaftik, 1975) by a linear function of temperature as  $k=0.151+3.228 \times 10^{-4}(T-300)$ , with  $k$  in W/m K and  $T$  in K, which provides a better fit than a power law. We have included this effect in our calculation as the value of  $k$  determines the boundary layer thickness,

and therefore the heat transfer parameters. For the specific heat we use the constant value 5.2 kJ/kg K and  $\gamma=5/3$ ,  $\sigma=0.71$ .

For Atchley's experiment, the tube length was 99.87 cm, its radius was 3.82 cm, the stack length  $L_S=3.5$  cm, and the stack was positioned at  $x_S=87.95$  cm from the cold end. The cold heat exchanger, consisting of two equal parts separated by 1.04 mm and 10.2-mm long, is to the left of the stack and the hot heat exchanger, 7.62-mm long, to the right. The combined cross-sectional area of the stack plates was 3.1 cm<sup>2</sup>, i.e., 27% of the entire cross section. Atchley reports that the temperature was approximately constant and equal to its cold and hot values to the left and right of the stack, respectively, and linear in the stack so that  $T=T_C$  for  $0 \leq x \leq x_S$ ,  $T=T_H$  for  $x_S+L_S \leq x \leq L$ , and

$$T = T_C + \frac{x - x_S}{L_S} (T_H - T_C), \quad (76)$$

for  $x_S < x < x_S + L_S$ .

To solve Eq. (61) numerically we multiply by  $S$  and discretize by centered differences on an equispaced grid. This procedure requires the values of  $(1 - f_v)S$  at the half-integer nodes, that are calculated as simple arithmetic averages. Typically 2000 cells were used along the tube length, with approximately 100 in the stack region. The eigenvalues were searched by the inverse iteration method (Press *et al.*, 1992).

The specification of the cross-sectional area and wall temperature according to the data given before leads to strong spatial discontinuities of the cross section and heat flux. In principle this causes no difficulties, as Eq. (61) is in conservation form and the corresponding jump conditions on  $p'$  are automatically satisfied. However, such discontinuities cannot give a realistic representation of the actual physical situation. Small-scale thermal transport processes (conduction between the stack ends and the heat exchangers, natural convection, etc.) must cause the wall temperature distribution to become smoother than the mathematical idealization given by (76). Similarly, flow separation phenomena must prevent the streamlines from precisely expanding to follow the discontinuities of the cross-sectional area mentioned before. Unfortunately the published information does not give a characterization of the system sufficiently precise to enable us to use more realistic distributions. Therefore we decided to mimic the action of these unknown, but certainly present, diffusive processes by smoothing the discontinuous distributions of  $S(x)$  and  $T_w(x)$ . We accomplish this by effecting a series of sweeps in which  $S_i$  and  $T_{wi}$ , the values of  $S(x)$  and  $T_w(x)$  at the node  $x_i$ , are replaced by

$$\frac{1}{4}(S_{i+1} + 2S_i + S_{i-1}), \quad (77)$$

and similarly for  $T_w$ . The same prescription is applied to the exchange parameters  $D$ ,  $H$ ,  $Q$ ,  $\theta_V$ ,  $\theta_K$ , and  $\theta_Q$ . It will be seen that this smoothing procedure has a rather strong impact on the final results. A comparison between the smoothed and nonsmoothed distributions is shown graphically in Part II for one example. It may be remarked that something corresponding to our smoothing operation is implicit in all earlier treat-

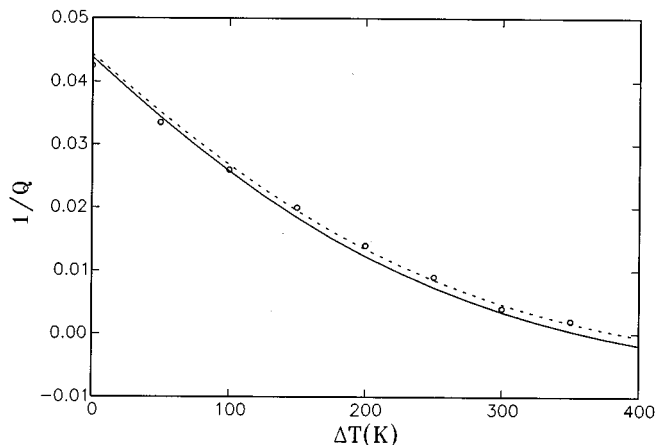


FIG. 4.  $1/Q$  versus the temperature difference  $\Delta T = T_H - T_C$  along the stack for an undisturbed pressure of 170 kPa. The circles are the data of Atchley (1992). The solid line is the result for discontinuous cross-sectional area and wall temperature distributions given in the text. The dashed line is the result with the same quantities smoothed by effecting the operation (77) 50 times.

ments of the problem where it is introduced (with limited control) through the spatial discretization.

Figures 4 and 5 show  $1/Q$  versus the temperature difference  $\Delta T = T_H - T_C$  along the stack for pressures of 170 and 500 kPa, respectively. The data are shown by circles. The solid lines are the result given by the full solution of the eigenvalue problem associated with Eq. (61) with the discontinuous area and temperature distributions as mentioned before. The dashed lines are the results corresponding to smoothed distributions with the smoothing procedure explained before applied 50 times in Fig. 4 and 200 times in Fig. 5.

Since Eq. (61) coincides with the exact linear theory, these results are to be considered exact solutions to the problem. In the past, the same data had only been analyzed on the basis of approximations to the eigenfunction and real part of the eigenfrequency (Atchley, 1992). It can be seen that, particularly in the unstable region where the temperature differ-

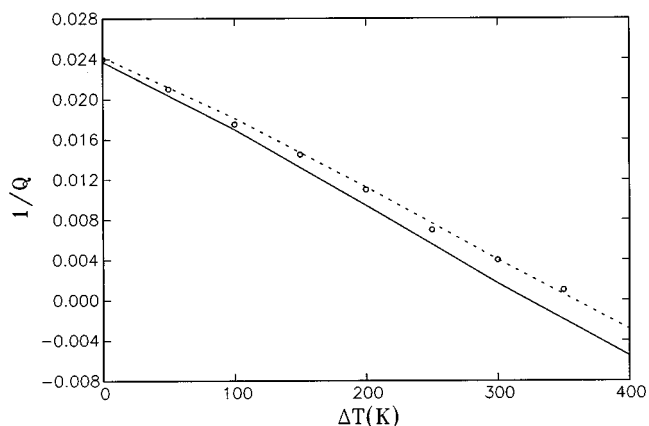


FIG. 5.  $1/Q$  versus the temperature difference  $\Delta T = T_H - T_C$  along the stack for an undisturbed pressure of 500 kPa. The circles are the data of Atchley (1992). The solid line is the result for discontinuous cross-sectional area and wall temperature distributions given in the text. The dashed line is the result with the same quantities smoothed by effecting the operation (77) 200 times.



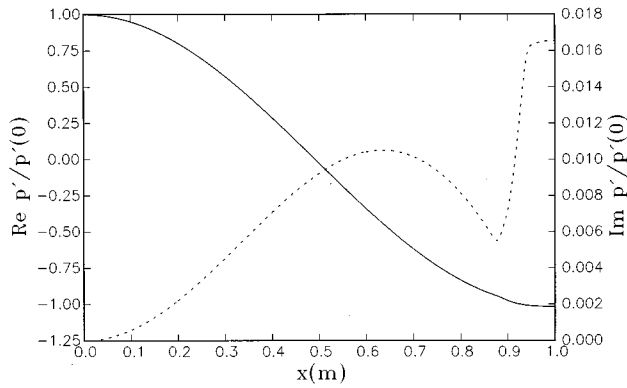


FIG. 6. Real (solid line) and imaginary part of the pressure eigenfunction for  $\Delta T=350$  K,  $p_0=500$  kPa, and the situation of Atchley's (1992) experiment.

ence is large, the smoothing has a significant effect on the results. By smoothing only the wall temperature or only the cross-sectional area, it is found that the latter affects the  $Q$  value more than the former. In both figures, and particularly at the higher pressure and temperatures, the data lie above the  $Q$  values calculated from the discontinuous distributions (solid lines). The smoothed distributions (dashed lines) give instead larger  $Q$  values and results generally closer to the data. The implication is that the thermoacoustic energy conversion process is stronger in the case of sharp discontinuities. At the higher pressure the density is larger and the effect of area discontinuities on the mass flux correspondingly greater. Of course, our smoothed profiles are simply a conjecture about the conditions prevailing in the experiment. Other causes may produce a larger  $Q$ , i.e., a greater damping. One may mention the mismatch between the number of plates in the heat exchangers and in the stack, or other factors as discussed by Atchley (1992). In spite of these elements of uncertainty, however, theory and experiment seem to be in good overall agreement. Only smoothed distributions are used in the calculations shown in the rest of the paper.

Figures 6 and 7 show the real and imaginary part of the normalized pressure and velocity eigenfunctions for  $\Delta T=350$  K,  $p_0=500$  kPa. The quantities plotted are

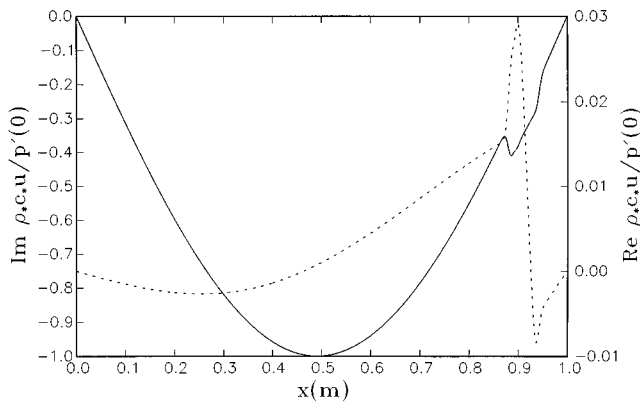


FIG. 7. Imaginary (solid line) and real part of the normalized velocity eigenfunction for  $\Delta T=350$  K,  $p_0=500$  kPa, and the situation of Atchley's (1992) experiment. The oscillations in the stack region occur in correspondence of the area changes.

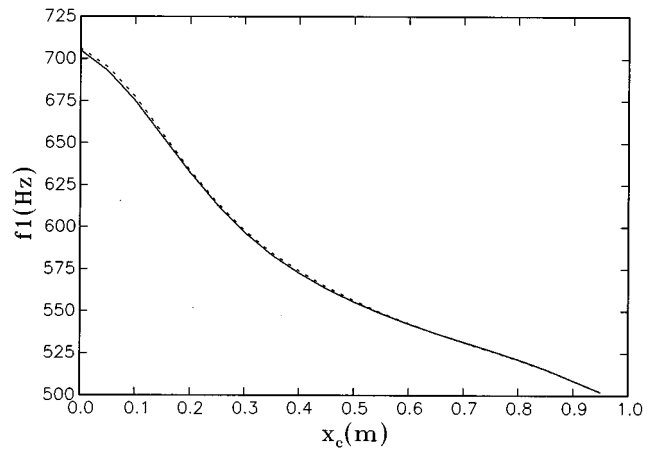


FIG. 8. Real part of the eigenfrequency of the fundamental mode  $f_1 = \text{Re } \omega/2\pi$  as a function of the position of the cold end of the stack at 170 kPa for  $\Delta T=300$  K. Other conditions as in Atchley's (1992) experiment. The gas temperature equals  $T_C$  in the entire region to the left of the stack and  $T_H$  to the right. In the stack region a linear dependence is assumed. The solid line is the exact result. The dashed line is obtained by using the approximation (67) for the parameter  $\bar{\omega}$  entering the expression of the expression of the exchange coefficients  $D$ ,  $H$ , and  $Q$ .

$$\frac{p'(x)}{p'(0)}, \quad \frac{u'(x)\rho_*c_*}{p'(0)} = \frac{p_0}{p'(0)} \sqrt{\frac{\gamma}{RT_C}} u'(x). \quad (78)$$

The real part of  $p'$  (solid line, Fig. 6) and the imaginary part of  $u'$  (solid line, Fig. 7) are very close to the corresponding results for an unobstructed isothermal tube. The quantity affected most is the velocity, where the fluctuations in the stack region correspond to the rapid area variations. The imaginary part of  $p'$  and real part of  $u'$  (dashed lines) are much smaller.

Figure 8 is the real part of the eigenfrequency  $\text{Re } \omega/2\pi$  as a function of the position of the cold end of the stack, at a pressure of 170 kPa for  $\Delta T=300$  K. The solid line is the exact value, and the dashed line the value calculated by approximating the exchange coefficients in terms of the effective angular frequency  $\bar{\omega}$  defined in (67). The approximation is seen to be quite good. The significant change in the frequency is due to the fact that, in this calculation, the gas temperature has been taken equal to  $T_H$  in the entire region to the right of the stack.

Information on  $\text{Im } \omega$  as a function of the stack position is given in Fig. 9 in the form of a graph of  $1/Q$  for 170 and 500 kPa and  $\Delta T=300$  K. The solid lines are the exact results and the dashed lines those obtained by using  $\bar{\omega}$  in the exchange coefficients. The system is seen to be most unstable for a stack position in the neighborhood of the  $3/4$  point as is well known (see, e.g., Swift, 1988). For this example, the lower pressure leads to a stronger maximum growth rate of the instability.

We now turn to a system with a cross-sectional area given by

$$S(x) = S_0 \left[ 1 + C \cos^2 \pi \left( \frac{2x}{L} - 1 \right) \right]^2, \quad \text{for } \frac{1}{4}L \leq x \leq \frac{3}{4}L, \quad (79)$$

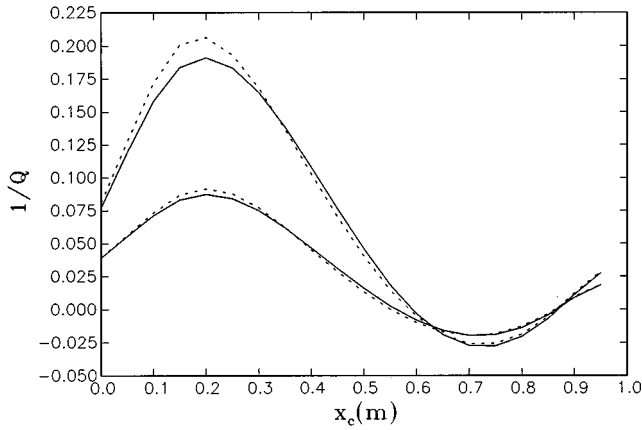


FIG. 9.  $1/Q$  as a function of the stack position at two pressures from the exact linear theory with  $\Delta T=300$  K for Atchley's (1992) experiment. The dotted lines are the approximations due to the use of  $\bar{\omega}$  defined in (67) in the expressions of the exchange coefficients  $D$ ,  $H$ , and  $Q$ . The system is most unstable for a stack position in the neighborhood of the 3/4 point. The pair of lines with the smallest oscillation is for 500 kPa, the other pair for 170 kPa.

while  $S=S_0$  elsewhere other than in the stack region which is the same as before. With  $S_0=24$  cm<sup>2</sup> and  $C=0$ , this is the same system considered up to now. With  $C>0$ , the tube's cross section is thicker in the central region, and with  $C<0$  it is thinner. The stack region has the same geometry as before independently of the value of  $C$ . Figures 10–12 show the effect of the cross-sectional area change on the  $Q$  value of the fundamental mode, the first, and the second harmonic. In all the figures, the dashed line is for  $C=0$ , the dotted line for the smallest value of  $C$  considered,  $C=-0.4$ , and the dash-dot line for the largest one,  $C=0.4$ . It is seen that thicker and thinner cross sections, respectively, increase and decrease the frequency of the fundamental and second harmonic, while they have the opposite effect on the first harmonic. The dependence of the corresponding frequencies on the temperature difference along the stack is rather weak, increasing with the order of the harmonic.

The  $Q$  value tends to become negative, implying insta-

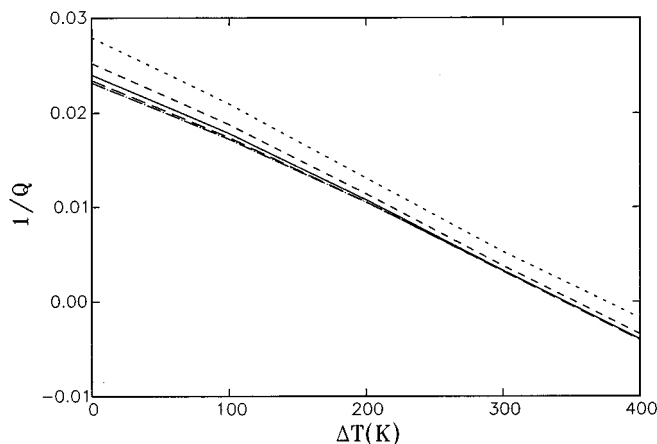


FIG. 10. Effect on the damping parameter  $1/Q_1$  of the fundamental mode of a narrowing or expanding cross section of the tube. ———  $C=0$ , constant cross section; ---  $C=0.2$ ; -·-·-  $C=0.4$ ; - - -  $C=-0.2$ ; ·····  $C=-0.4$ .

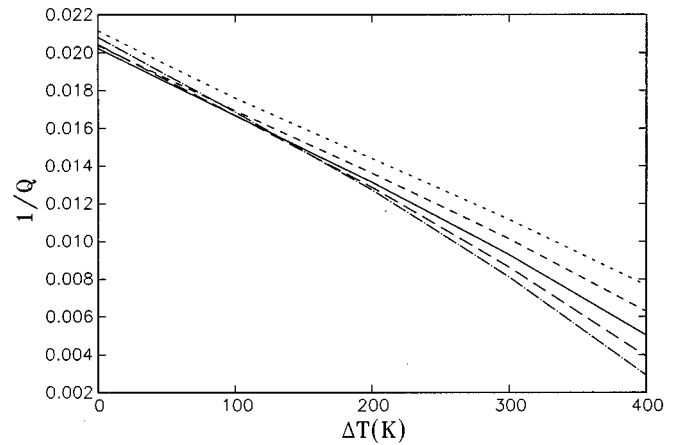


FIG. 11. Effect on the damping parameter  $1/Q_2$  of the first harmonic mode of a narrowing or expanding cross section of the tube. ———  $C=0$ , constant cross section; ---  $C=0.2$ ; -·-·-  $C=0.4$ ; - - -  $C=-0.2$ ; ·····  $C=-0.4$ .

bility, at smaller  $\Delta T$ 's for a thickening cross section than for a thinning one for the fundamental and first harmonic mode. A thickening cross section, however, has a stabilizing effect on the third harmonic at the higher  $\Delta T$ 's. These results can be interpreted by considering the eigenfunctions, two examples of which are shown in Figs. 13 and 14 for the fundamental mode. In all cases, the pressure distribution (solid line, left vertical scale) is very similar to the usual sinusoidal one. There is, however, a marked effect on the velocity distribution (dashed line, right vertical scale) as a consequence of the constraint arising from mass conservation. With a narrowing tube, the velocity is relatively large in the narrow part and has a long distance over which to decrease to zero at the left and right boundaries. It is therefore small in the stack region with a consequent reduction in the thermoacoustic effect. For a thickening cross section, on the other hand, the velocity starts decreasing closer to the ends, and therefore it is larger in the stack region. Another feature evident from these figures is the asymmetry, caused by the stack, of the

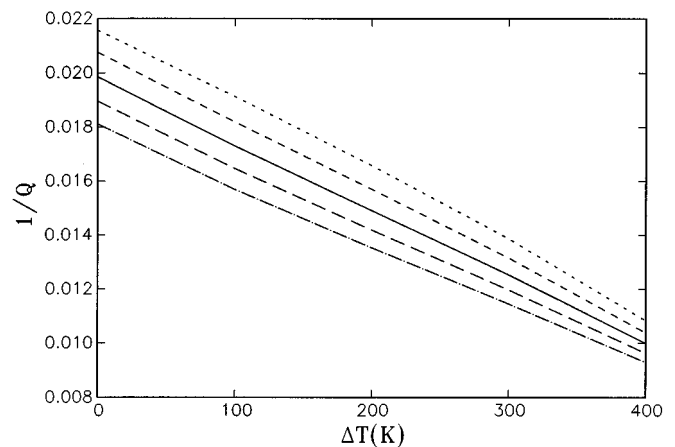


FIG. 12. Effect on the damping parameter  $1/Q_3$  of the second harmonic mode of a narrowing or expanding cross section of the tube. ———  $C=0$ , constant cross section; ---  $C=0.2$ ; -·-·-  $C=0.4$ ; - - -  $C=-0.2$ ; ·····  $C=-0.4$ .

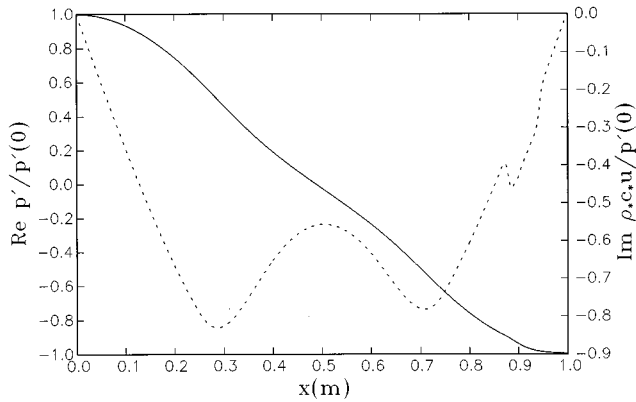


FIG. 13. Real part of the pressure eigenfunction (solid line, left vertical scale) and imaginary part of the normalized velocity eigenfunction (dashed line, right vertical scale) for a thickening tube with  $C=0.2$ ;  $\Delta T=350$  K and  $p_0=500$  kPa.

velocity eigenfunction with respect to the tube's midpoint. It is found that, the larger  $\Delta T$ , the steeper the eigenfunction near the hot end. Similar trends are found in the eigenfunctions of the first harmonic mode. For the second mode, however, the stack is close to the optimal position of 1/4 wavelength from the velocity node. Therefore for  $\Delta T$  greater than about 500 K, the thickening of the cross section causes the antinode to move toward the stack thus decreasing the magnitude of the thermoacoustic destabilization. Conversely, narrowing the cross section displaces the antinode in the favorable direction and decreases the damping. The opposite occurs at lower  $\Delta T$ 's due to interplay between this effect and the asymmetrical nature of the eigenfunction.

As a final item of interest we show in Fig. 15 the ratios  $f_2/f_1$  (solid line) and  $f_3/f_1$  as a function of the cross-sectional area parameter  $C$  in Eq. (79) for  $\Delta T=300$  K and a pressure of 500 kPa. For a straight tube  $C=0$  and these ratios are extremely close to 2 and 3, respectively. Evidently, the detuning of the system resulting from the presence of the stack and of the heated region has a very small effect on the harmonic structure of the modes. Area changes do, however,

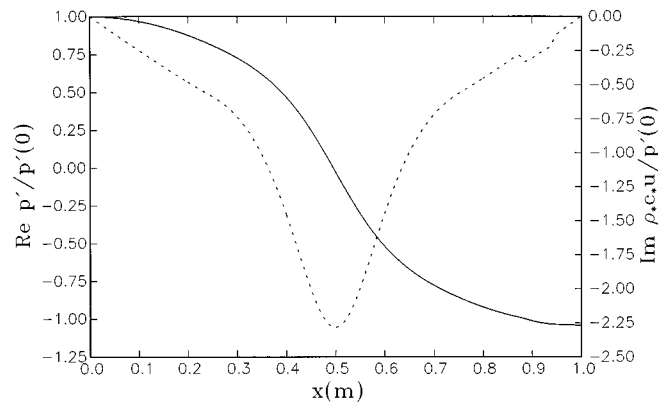


FIG. 14. Real part of the pressure eigenfunction (solid line, left vertical scale) and imaginary part of the normalized velocity eigenfunction (dashed line, right vertical scale) for a thickening tube with  $C=-0.2$ ;  $\Delta T=350$  K and  $p_0=500$  kPa.

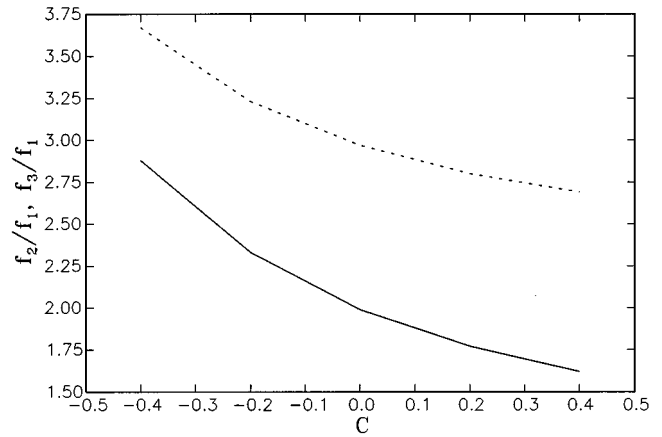


FIG. 15. Ratios  $f_2/f_1$  (solid line) and  $f_3/f_1$  of the first and second harmonic frequencies to the fundamental as a function of the cross-section parameter  $C$ , Eq. (79) for  $\Delta T=300$  K,  $p_0=500$  kPa. Positive  $C$  corresponds to an area increase.

result in a considerable detuning, with contractions relatively more effective than expansions.

## VI. CONCLUSIONS

We have presented an approximate theory of a thermoacoustic prime mover based on a quasi-one-dimensional approximation. Primarily, the theory differs from available ones in the following respects:

- (1) It is nonlinear in nature.
- (2) It is formulated in the time domain.
- (3) It can readily account for changes of the device's cross section in the direction normal to the wavefronts also in the nonlinear case.

This paper has dealt with the linear version of the model and has shown that, in those situations where the exact theory available in the literature applies, the approximate theory gives results for the pressure eigenfunctions and frequency eigenvalues that are identical to the exact ones. The cross-sectional averages of the other primary fields—velocity, temperature, and density—are reproduced exactly, but not the pointwise structure in the cross section. As a consequence, the mean value of fields nonlinear in the primary ones, such as the energy flux, is not reproduced exactly in the model. A preliminary analysis given in Sec. IV would seem to indicate that this error is not serious in many cases.

We have applied the theory to data that had, in the past, only been examined on the basis of an approximate model and we have found a very good agreement. We have also shown some results for tubes of axially varying cross section finding a tendency to greater instability for a tube that widens in its midsection.

The present model can be made more realistic by including heat conduction in the stack and other effects. Furthermore, it can equally well be adapted to the refrigerator case. Work in these directions is currently under way.

The study of the nonlinear regime with the present model still remains a rather complex matter and will be carried out in subsequent papers. Some results are shown in Part II of this work (Yuan *et al.*, 1997).

## ACKNOWLEDGMENTS

The original idea to develop a quasi-one-dimensional model was suggested by Professor Lev Ostrovsky to whom the authors express their gratitude. Thanks are also due to the referees and to the Office of Naval Research for support of this study.

- Achard, J. L., and Lespinard, G. M. (1981). "Structure of the transient wall-friction law in one-dimensional models of laminar pipe flows," *J. Fluid Mech.* **113**, 283–298.
- Arnott, W. P., Bass, H. E., and Raspet, R. (1991). "General formulation of thermoacoustics for stacks having arbitrarily shaped pore cross sections," *J. Acoust. Soc. Am.* **90**, 3228–3237.
- Arnott, W. P., Bass, H. E., and Raspet, R. (1992). "Specific acoustic impedance measurements of an air-filled thermoacoustic prime mover," *J. Acoust. Soc. Am.* **92**, 3432–3434.
- Arnott, W. P., Lightfoot, J. A., Raspet, R., and Moosmüller, H. (1996). "Radial wave thermoacoustic engines: Theory and examples for refrigerators and high-gain narrow-bandwidth photoacoustic spectrometers," *J. Acoust. Soc. Am.* **99**, 734–45.
- Atchley, A. A. (1992). "Standing wave analysis of a thermoacoustic prime mover below onset of self-oscillation," *J. Acoust. Soc. Am.* **92**, 2907–2914.
- Atchley, A. A. (1994). "Analysis of the initial build-up of oscillations in a thermoacoustic prime mover," *J. Acoust. Soc. Am.* **95**, 1661–1664.
- Atchley, A. A., and Kuo, F. M. (1994). "Stability curves for a thermoacoustic prime mover," *J. Acoust. Soc. Am.* **95**, 1401–1404.
- Atchley, A. A., Bass, H. E., and Hoffer, T. J. (1990a). "Development of nonlinear waves in a thermoacoustic prime mover," in *Frontiers in Nonlinear Acoustics*, edited by M. F. Hamilton and D. T. Blackstock (Elsevier, New York), pp. 603–608.
- Atchley, A. A., Bass, H. E., Hoffer, T. J., and Lin, H.-T. (1992). "Study of a thermoacoustic prime mover below onset of self-oscillation," *J. Acoust. Soc. Am.* **91**, 734–743.
- Atchley, A. A., Hoffer, T. J., Muzzerall, M. L., Kite, M. D., and Ao, C. (1990b). "Acoustically generated temperature gradients in short plates," *J. Acoust. Soc. Am.* **88**, 251–263.
- Chapman, S., and Cowling, T. G. (1952). *Mathematical Theory of Nonuniform Gases* (Cambridge U.P., Cambridge, England), 2nd ed.
- Crocchio, L. (1958). "One-dimensional treatment of steady gas dynamics," in *Fundamentals of Gas Dynamics*, edited by H. W. Emmons (Princeton U.P., Princeton, NJ), pp. 64–349.
- Gaitan, D. F., and Atchley, A. A. (1993). "Finite amplitude standing waves in harmonic and anharmonic tubes," *J. Acoust. Soc. Am.* **93**, 2489–2495.
- Landau L. D., and Lifshitz, E. M. (1959). *Fluid Mechanics* (Pergamon, London).
- Merkli, P., and Thomann, H. (1975). "Thermoacoustic effects in a resonance tube," *J. Fluid Mech.* **70**, 161–177.
- Olson, J. R., and Swift, G. W. (1994). "Similitude in thermoacoustics," *J. Acoust. Soc. Am.* **95**, 1405–1412.
- Press, W. H., Vetterling, W. T., Teukolsky, S. A., and Flannery, B. P. (1992). *Numerical Recipes in FORTRAN* (Cambridge U.P., Cambridge, England), 2nd ed.
- Raspet, R., Bass, H. E., and Kordomenos, J. (1993). "Thermoacoustics of traveling waves: Theoretical analysis for an inviscid ideal gas," *J. Acoust. Soc. Am.* **94**, 2232–2239.
- Rott, N. (1969). "Damped and thermally driven acoustic oscillations in wide and narrow tubes," *Z. Angew. Math. Phys.* **20**, 230–243.
- Rott, N. (1975). "Thermally driven acoustic oscillations, Part III: Second-order heat flux," *Z. Angew. Math. Phys.* **26**, 43–49.
- Rott, N. (1976). "Thermally driven acoustic oscillations, Part IV: Tubes with variable cross section," *Z. Angew. Math. Phys.* **27**, 197–224.
- Rott, N. (1980). "Thermoacoustics," *Adv. Appl. Mech.* **20**, 135–175.
- Rott, N. (1983). "Thermally driven acoustic oscillations, Part VI: Excitation and power," *Z. Angew. Math. Phys.* **34**, 609–626.
- Swift, G. W. (1988). "Thermoacoustic engines," *J. Acoust. Soc. Am.* **84**, 1145–1180.
- Swift, G. W. (1992). "Analysis and performance of a large thermoacoustic engine," *J. Acoust. Soc. Am.* **92**, 1551–1563.
- Tominaga, A. (1995). "Thermodynamic aspects of thermoacoustic theory," *Cryogenics* **35**, 427–440.
- Vargaftik, N. B. (1975). *Handbook of Physical Properties of Liquids and Gases* (Wiley, New York).
- Wheatley, J. (1986). "Intrinsically irreversible or natural heat engines," in *Frontiers in Physical Acoustics*, edited by D. Sette (North-Holland, Amsterdam), pp. 35–475.
- Wheatley, J., Hoffer, T., Swift, G. W., and Migliori, A. (1983). "An intrinsically irreversible thermoacoustic engine," *J. Acoust. Soc. Am.* **74**, 153–170.
- Whitham, G. B. (1974). *Linear and Nonlinear Waves* (Wiley, New York).
- Yazaki, T., Takashima, S., and Mizutani, S. (1987). "Complex quasiperiodic and chaotic states observed in thermally induced oscillations of gas columns," *Phys. Rev. Lett.* **58**, 1108–1111.
- Yazaki, T., Tominaga, A., and Narahara, Y. (1980). "Experiments on thermally driven acoustic oscillations of gaseous helium," *J. Low Temp. Phys.* **41**, 45–60.
- Yuan, H., Karpov, S., and Prosperetti, A. (1997). "A simplified model for linear and nonlinear processes in thermoacoustic prime movers. Part II. Nonlinear oscillations," *J. Acoust. Soc. Am.* **102**, 3497–3506.

# A simplified model for linear and nonlinear processes in thermoacoustic prime movers. Part II. Nonlinear oscillations

H. Yuan, S. Karpov, and A. Prosperetti

*Department of Mechanical Engineering, The Johns Hopkins University, Baltimore, Maryland 21218*

(Received 27 September 1996; accepted for publication 30 July 1997)

The simplified quasi-one-dimensional model of thermoacoustic devices formulated in Part I [Watanabe *et al.*, *J. Acoust. Soc. Am.* **102**, 3484–3496 (1997)] is studied in the nonlinear regime. A suitable numerical method is described which is able to deal with the steep waveforms that develop in the system without inducing spurious oscillations, appreciable numerical damping, or numerical diffusion. The results are compared with some experimental ones available in the literature. Several of the observed phenomena are reproduced by the model. Quantitative agreement is also reasonable when allowance is made for likely temperature nonuniformities across the heat exchangers. © 1997 Acoustical Society of America. [S0001-4966(97)01512-9]

PACS numbers: 43.35.Ud [HEB]

## INTRODUCTION

The literature contains evidence of the presence of nonlinear processes in thermoacoustic devices already at relatively low oscillation amplitudes (Atchley *et al.*, 1990a, 1990b). The available linear theory, although quite well developed (see, e.g., Rott, 1980; Wheatley, 1986; Swift, 1988), is incapable of dealing with these phenomena, nor does its extension into the nonlinear realm appear easy. Furthermore, even if such an attempt were successful, one would most likely end up with a very complex model that would not lend itself to the ready exploration of parameter space and the evaluation of different design alternatives.

These considerations motivated Part I of this study (Watanabe *et al.*, 1997), in which an approximate quasi-one-dimensional model of thermoacoustic devices was developed by integrating over the cross-sectional area. Although simplified, the model is nonlinear. Furthermore, upon linearization, it reproduces the pressure field and the eigenfrequencies of the linear theory exactly.

In the present paper we continue the analysis of the model extending it into the nonlinear regime. Our initial attempts in this direction (Prosperetti and Watanabe, 1994) encountered numerical difficulties due to the ready appearance of quasi-shock waves in the system. Overcoming this obstacle has required the adoption of a rather complex numerical method that is described in detail in Sec. III of this paper. In Sec. IV a comparison between the numerical results and some available experimental data is presented. Experimentally observed phenomena such as unstable growth of the wave and eventual saturation are well reproduced in qualitative terms. The computed wave amplitude tends to be higher than the measured one, probably due, among others, to an effectively lower temperature difference than the nominal value and to other dissipation phenomena not included in the model.

## I. MODEL

We summarize here the equations of the present model. Their derivation can be found in Part I.

The equation of continuity is

$$\frac{\partial \rho}{\partial t} + \frac{1}{S} \frac{\partial}{\partial x} (S \rho u) = 0. \quad (1)$$

Here,  $x$  is the coordinate along the axis of the device (not necessarily rectilinear),  $S(x)$  is the local cross sectional area, and  $\rho$  and  $u$  are the gas density and axial velocity averaged over the cross-sectional area. The momentum equation takes the form

$$\frac{\partial}{\partial t} (\rho u) + \frac{1}{S} \frac{\partial}{\partial x} (S \rho u^2) + \frac{\partial p}{\partial x} = -\mathcal{D}(u), \quad (2)$$

where  $p$  is the cross-sectional average of the gas pressure and the drag operator  $\mathcal{D}$  will be specified shortly. The energy equation is used in the form

$$\begin{aligned} \frac{\partial}{\partial t} \left( \frac{1}{\gamma-1} p + \frac{1}{2} \rho u^2 \right) + \frac{1}{S} \frac{\partial}{\partial x} \left[ u S \left( \frac{\gamma}{\gamma-1} p + \frac{1}{2} \rho u^2 \right) \right] \\ = \mathcal{H}(T_w - T) - \frac{dT_w}{dx} \mathcal{Q}(u), \end{aligned} \quad (3)$$

where  $\gamma$  is the ratio of the specific heats of the gas,  $T$  the cross-sectional average of the gas temperature,  $T_w(x)$  the surface temperature of the solid surfaces in contact with the gas, and the operators  $\mathcal{H}$ ,  $\mathcal{Q}$  will be specified below. In the present model, the temperature distribution  $T_w$  along the stack will be taken as given and independent of time. Work on an improved model in which this quantity is calculated is currently under way. The set of equations is closed by assuming the validity of the equation of state of perfect gases, namely,

$$p = R \rho T, \quad (4)$$

where  $R$  is the universal gas constant divided by the gas molecular mass.

A key aspect of the model is the specification of the terms  $\mathcal{D}$ ,  $\mathcal{H}$ , and  $\mathcal{Q}$ . On the basis of the results of Part I we set

$$\mathcal{D}(u) = D \rho \left[ 1 + \theta_v \left( \frac{\partial}{\partial t} + u \frac{\partial}{\partial x} \right) \right] u, \quad (5)$$

$$\mathcal{H}(T_w - T) = H\rho c_p \left[ 1 + \theta_T \left( \frac{\partial}{\partial t} + u \frac{\partial}{\partial x} \right) \right] (T_w - T) + k_n \frac{\partial^2}{\partial x^2} \left( \frac{1}{\gamma - 1} p + \frac{1}{2} \rho u^2 \right), \quad (6)$$

$$\mathcal{Q}(u) = c_p \rho \mathcal{Q} \left[ 1 - \theta_Q \left( \frac{\partial}{\partial t} + u \frac{\partial}{\partial x} \right) \right] u, \quad (7)$$

where  $c_p$  is the gas specific heat at constant pressure. In the version of the model presented in Part I the term with the second spatial derivative in (6) was omitted. It is introduced here for reasons discussed in the next section; the quantity  $k_n$  is a constant. In Part I the other parameters have been estimated by imposing that the results of the linear version of the model reproduce those of the exact linear theory. In this way it was determined that

$$D(1 + i\omega\theta_V) = i\omega \frac{f_V}{1 - f_V}, \quad (8)$$

$$H(1 + i\omega\theta_T) = i\omega \frac{f_K}{1 - f_K}, \quad (9)$$

$$Q(1 - i\omega\theta_Q) = \frac{1}{1 - \sigma} \left( \frac{1}{1 - f_V} - \frac{\sigma}{1 - f_K} \right) - 1, \quad (10)$$

with  $\sigma$  the gas Prandtl number. For a stack consisting of plane parallel plates spaced by an amount  $l$  one has

$$f_V = \frac{\tanh(1 + i)l/2\delta_V}{(1 + i)l/2\delta_V}, \quad (11)$$

where  $\delta_V$  is the viscous boundary layer thickness given by

$$\delta_V = \sqrt{\frac{2\mu}{\omega\rho}}. \quad (12)$$

Outside the stack region,  $l$  should be taken as the hydraulic diameter of the local cross section. The function  $f_K$  has the same expression (11) with  $\delta_V$  replaced by the thermal boundary layer thickness  $\delta_K = \delta_V/\sqrt{\sigma}$ . Graphs of  $if/(1 - f)$  are given in Part I. Upon separating real and imaginary parts, the coefficients in the left-hand sides of (8)–(10) are readily determined.

If the parameter  $\omega$  is chosen as one of the linear eigenmodes of the system, a linearization of the present model will reproduce the exact pressure eigenequation of the linear theory (Rott, 1976). In a nonlinear, time-dependent calculation, frequencies cannot be easily separated and a definite single value of  $\omega$  must be committed to. We address this point in the next section.

For the present prime mover case, the velocity must vanish at the tube ends:

$$u = 0 \quad \text{at } x = 0, \quad x = L. \quad (13)$$

The momentum equation (2) then implies that

$$\frac{\partial p}{\partial x} = 0 \quad \text{at } x = 0, \quad x = L. \quad (14)$$

As shown in I, it follows from the energy and continuity equations that the temperature satisfies, at both ends,

$$\left[ \frac{\partial}{\partial t} + H \left( 1 + \theta_T \frac{\partial}{\partial t} \right) \right] T = \frac{\gamma - 1}{\gamma} \frac{T}{p} \frac{\partial p}{\partial t} + H \left( 1 + \theta_T \frac{\partial}{\partial t} \right) T_w + \frac{k_n}{\gamma} \frac{T}{p} \frac{\partial^2 p}{\partial x^2}. \quad (15)$$

We assume that  $\partial T/\partial x = 0$  at the end points. Since the constant  $k_n$  will be taken to be very small and, away from the stack region,  $H$  is also very small, this relation then essentially implies the adiabatic pressure–temperature relation of perfect gases.

The velocity boundary condition (13) at  $x = 0$  will be modified for the simulation of a piston-driven tube described later in Sec. IV.

## II. THE LINEAR SPECTRUM

As shown in Part I if, in the expressions (5)–(7) for the momentum and energy transfer terms  $\mathcal{D}$ ,  $\mathcal{H}$ , and  $\mathcal{Q}$ ,  $\omega$  is chosen as the exact eigenfrequency of any one mode, the linear version of the present model with  $k_n = 0$  gives the pressure equation of the exact Rott theory for that mode [see Eq. (6) in Rott (1976) or Eq. (60) in Part I]. In a time-dependent nonlinear calculation as the one of present concern the separation of modes, although not impossible, is a nontrivial task that we have not attempted. For the purposes of this study we shall use a single value of  $\omega$  that we denote by  $\omega_0$ . While this will be treated as an adjustable parameter, it will always be close to the (real part of the) fundamental mode of the system for which an approximation can be given as

$$\bar{\omega} = \frac{\sqrt{\gamma R \bar{T}_w}}{L}, \quad (16)$$

where  $\bar{T}_w$  is the average wall temperature:

$$\bar{T}_w = \frac{1}{L} \int_0^L T_w(x) dx. \quad (17)$$

The need to fix the parameter  $\omega$  has a strong effect on the linear spectrum of the problem, that is reflected in the nonlinear calculations.

To illustrate this point, we show in Fig. 1 the imaginary part  $\text{Im } \omega_n$  of the exact linear eigenvalues as a function of the mode number  $n$ , with  $1 \leq n \leq 20$ . The circles are connected by a solid line as an aid to the eye. The conditions here are as specified in Sec. IV below in connection with Fig. 7, but the general behavior is typical. The eigenvalue problem was solved by the inverse iteration method (Press *et al.*, 1992). It is seen that only the first mode is unstable ( $\text{Im } \omega_1 < 0$ ). The second one has a relatively small damping (with a  $Q$  value of approximately 170), and all the other ones are heavily damped. If one calculates the linear eigenvalues keeping  $\omega_0$  equal to  $\bar{\omega} = 3327.7 \text{ s}^{-1}$ , instead, the results shown by the triangles and the dashed line are found. Although the first few eigenvalues are not very different, the approximation renders several of the higher-order modes unstable as well. The consequence of this is that, while a numerical calculation with a coarse discretization (and a consequently large numerical damping) would superficially look acceptable, an

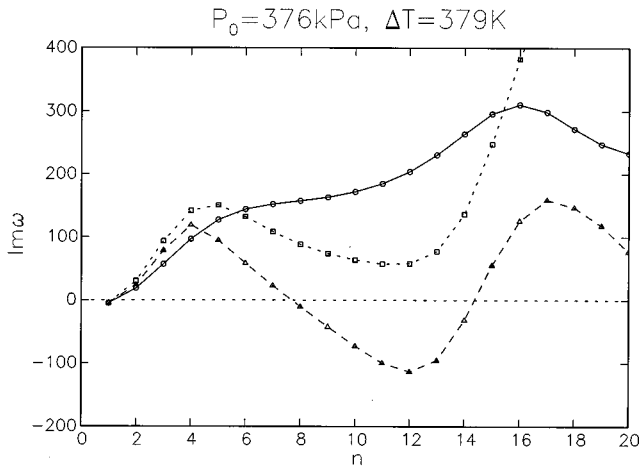


FIG. 1. Imaginary part of the first 20 eigenvalues for the system and conditions of Fig. 7 below. The circles connected by the solid line are the exact results of the linear theory. Note that only the first mode is unstable ( $\text{Im } \omega_1 < 0$ ). The results shown by the triangles and the dashed line correspond to setting the parameter  $\omega$  in Eqs. (5)–(7) equal to  $\bar{\omega}$  defined in (16) that here has the value  $3327.7 \text{ s}^{-1}$ . The higher modes become unstable with this approximation. The squares and the dotted line are the linear spectrum for  $\omega = \omega_0 = 2762.0 \text{ s}^{-1}$  and  $k_n = 0.25 \text{ m}^2/\text{s}$ .

attempt to refine the grid would lead to the rapid growth of short-wavelength instabilities that destroy the calculation. The thermoacoustic effect requires a very delicate balance and does not easily survive approximations.

This is the reason why we have introduced a second-derivative in the exchange term  $\mathcal{H}$ . With a suitable adjustment of  $\omega_0$  and of the “pseudo-thermal conductivity”  $k_n$ , we can approximate the important first few linear modes and dampen the higher ones. As an example we show (dotted line, squares) the effect of choosing  $\omega_0 = 2762.0 \text{ s}^{-1}$  and  $k_n = 0.25 \text{ m}^2/\text{s}$ . It is seen that the only large differences between the exact and the approximate results are relegated to the high-order modes that are heavily damped anyway and should therefore not have a large effect on the results. It might appear that treating both  $\omega_0$  and  $k_n$  as adjustable parameters makes the formulation of the model nonunique. In practice, however, we find that the two requirements of matching the growth rate of the unstable mode and requiring the higher modes to be all damped leaves little room to adjust the values of these two quantities. In particular, as will be seen in Sec. IV, the nonlinear steady-state amplitudes are not greatly affected.

Figure 2 is similar to Fig. 1 and shows some examples for the case of Fig. 8 below. The circles and the solid line are again the exact spectrum, for which  $\text{Im } \omega_1 = -4.73 \text{ s}^{-1}$ . The other lines, in descending order, correspond to  $\omega_0 = 2658.6 \text{ s}^{-1}$ ,  $k_n = 0.42 \text{ m}^2/\text{s}$  ( $\text{Im } \omega_1 = -4.71 \text{ s}^{-1}$ ),  $\omega_0 = 2791.5 \text{ s}^{-1}$ ,  $k_n = 0.31 \text{ m}^2/\text{s}$  ( $\text{Im } \omega_1 = -4.73 \text{ s}^{-1}$ ),  $\omega_0 = 2858.0 \text{ s}^{-1}$ ,  $k_n = 0.26 \text{ m}^2/\text{s}$  ( $\text{Im } \omega_1 = -4.72 \text{ s}^{-1}$ ),  $\omega_0 = 2924.4 \text{ s}^{-1}$ ,  $k_n = 0.21 \text{ m}^2/\text{s}$  ( $\text{Im } \omega_1 = -4.72 \text{ s}^{-1}$ ). All these curves differ by very little for the first few modes which carry most of the energy. The main differences are in the higher modes, which have a minor effect on the waveform of the steady-state solution as will be seen in Sec. IV.

In principle, one can avoid the approximations just de-

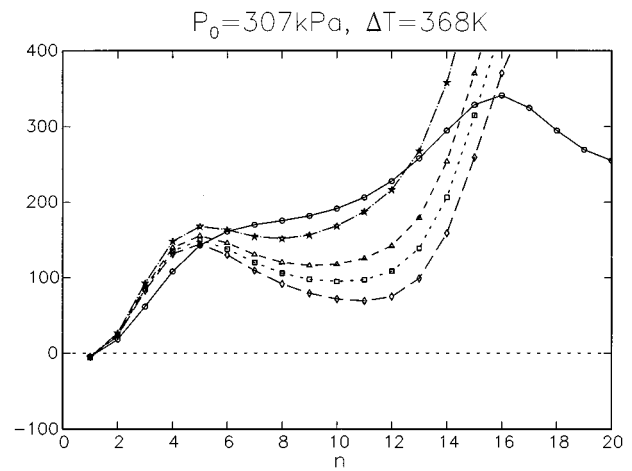


FIG. 2. (a) Imaginary part of the first 20 eigenvalues for the system and conditions of Fig. 8 below. The circles connected by the solid line are the exact results of the linear theory. The other lines, in descending order, correspond to  $\omega_0 = 2658.6 \text{ s}^{-1}$ ,  $k_n = 0.42 \text{ m}^2/\text{s}$ ,  $\omega_0 = 2791.5 \text{ s}^{-1}$ ,  $k_n = 0.31 \text{ m}^2/\text{s}$ ,  $\omega_0 = 2858.0 \text{ s}^{-1}$ ,  $k_n = 0.26 \text{ m}^2/\text{s}$ ,  $\omega_0 = 2924.4 \text{ s}^{-1}$ ,  $k_n = 0.21 \text{ m}^2/\text{s}$ .

scribed by calculating the exchange terms by means of convolutions in time with kernels given by the inverse Fourier transforms of (8)–(10). This procedure would, however, add further complexity to the calculation. Another approximate scheme, possibly better than the one used here, could be to specify the exchange terms by means of differential equations rather than explicitly as done above. This approach has been advocated by Achard and Lespinard (1981) for the similar problem of the time-dependent flow in a tube.

We plan to pursue this idea in future work. For the time being we proceed in the manner described. Even though this is an approximation, it enables us to gain some insight into the time-dependent problem, nonlinear growth, and eventual saturation, for which no theoretical framework is currently available.

### III. NUMERICAL METHOD

With the expressions (5)–(7), and the definitions

$$m = \rho u, \quad e = \frac{1}{\gamma - 1} p + \frac{1}{2} \rho u^2, \quad (18)$$

for the momentum flux  $m$  and total energy  $e$  it is easy to verify that the continuity, momentum, and energy equations (1), (2), and (3) may equivalently be written as

$$\frac{\partial \rho}{\partial t} + \frac{\partial m}{\partial x} + \frac{m}{S} \frac{\partial S}{\partial x} = 0, \quad (19)$$

$$\begin{aligned} \frac{\partial m}{\partial t} + \frac{\partial}{\partial x} (mu + p) + \frac{mu}{S} \frac{\partial S}{\partial x} \\ = 0 = -D \left[ m + \theta_V \left( \frac{\partial m}{\partial t} + \frac{1}{S} \frac{\partial}{\partial x} (muS) \right) \right], \quad (20) \end{aligned}$$

$$\frac{\partial e}{\partial t} + \frac{\partial}{\partial x} [u(e+p)] + \frac{u}{S} (e+p) \frac{\partial S}{\partial x} \quad \mathbf{w} = \begin{bmatrix} \rho \\ m \\ e \end{bmatrix}, \quad (23)$$

$$\begin{aligned} &= Hc_p \rho (T_w - T) - \gamma H \theta_T \left[ \frac{\partial e}{\partial t} + \frac{\partial}{\partial x} (ue) - u \frac{\partial m}{\partial t} - \frac{1}{2} u^2 \right. \\ &\quad \left. \times \frac{\partial \rho}{\partial t} - \frac{1}{2} \frac{\partial}{\partial x} (mu^2) \right] - m \frac{dT_w}{dx} c_p (H \theta_T + Q) \\ &\quad + \frac{dT_w}{dx} c_p Q \theta_Q \left[ \frac{\partial m}{\partial t} + \frac{\partial}{\partial x} (um) \right] + k_n \frac{\partial^2 e}{\partial x^2}. \end{aligned} \quad (21)$$

We rewrite this system of equations in vector form as

$$\frac{\partial \mathbf{w}}{\partial t} + \frac{\partial \mathbf{F}}{\partial x} + \mathbf{s} = \mathbf{B} \frac{\partial \mathbf{w}}{\partial t} + \mathbf{b}, \quad (22)$$

where  $\mathbf{w}$  is given by

the flux vector  $\mathbf{F}$  by

$$\mathbf{F} = \begin{bmatrix} \rho u \\ \rho u^2 + p \\ (e+p)u \end{bmatrix} \quad (24)$$

the vector  $\mathbf{s}$  accounting for the effect of changes in the cross-sectional area by

$$\mathbf{s} = \begin{bmatrix} \rho u \\ \rho u^2 \\ (e+p)u \end{bmatrix} \frac{1}{S} \frac{\partial S}{\partial x}, \quad (25)$$

and

$$\mathbf{B} = \begin{bmatrix} 0 & 0 & 0 \\ 0 & -D \theta_V & 0 \\ H \theta_T \left( c_p T_w - \frac{1}{2} \gamma u^2 \right) & \gamma H \theta_T u + \frac{dT_w}{dx} c_p Q \theta_Q & -\gamma H \theta_T \end{bmatrix}, \quad (26)$$

$$\mathbf{b} = \begin{bmatrix} 0 \\ -D \left[ m + \frac{\theta_V}{S} \frac{\partial}{\partial x} (Sum) \right] \\ Hc_p \left[ \rho (T_w - T) + \frac{\theta_T}{S} \frac{\partial}{\partial x} [\rho u S (T_w - T)] \right] - \frac{dT_w}{dx} c_p Q \left[ m - \frac{\theta_Q}{S} \frac{\partial}{\partial x} (umS) + k_n \frac{\partial^2 e}{\partial x^2} \right] \end{bmatrix}. \quad (27)$$

Our first attempt at solving Eq. (22) was based on a straightforward centered-difference spatial discretization with a predictor-corrector time stepping procedure (Prosperetti and Watanabe, 1994). We found that, whenever conditions were such that quasi-shocks developed, a series of spurious grid-dependent oscillations also appeared. Such oscillations are a well-known numerical artifact affecting computations in the presence of steep gradients (see, e.g., Roe, 1986; Fletcher, 1988), and their elimination has motivated a large amount of research. While a complete bibliography would be out of place here, it may be useful to cite the review by Roe (1986) and a few other papers (Sod, 1978; Harten, 1983; Osher, 1984; Osher and Chakravarthy, 1984; Sweby, 1984; Harten *et al.*, 1986; Harten and Osher, 1987). This effort has led to a new family of schemes for hyperbolic equations known as total variation diminishing (TVD) schemes. The name is a consequence of the definition of the *total variation*  $\text{TV}(u^n)$  of a grid function  $\{u_i^n\}$ ,  $i = 1, 2, \dots, N+1$  at time  $t^n$ :

$$\text{TV}(u^n) = \sum_{i=1}^N |u_{i+1}^n - u_i^n|, \quad (28)$$

and of the fact that these schemes have the property that  $\text{TV}(u^n)$  is a nonincreasing function of time:

$$\text{TV}(u^n) \geq \text{TV}(u^{n+1}). \quad (29)$$

Evidently, a TVD scheme cannot produce an oscillatory solution starting from monotonic initial data. We have found that the scheme proposed by Harten (1983) proved suitable for our problem.

The system (22) is first discretized explicitly in time as

$$(\mathbf{I} - \mathbf{B}_i^n) \frac{\mathbf{w}_i^{n+1} - \mathbf{w}_i^n}{\Delta t} + \frac{\hat{\mathbf{F}}_{i+1/2}^n - \hat{\mathbf{F}}_{i-1/2}^n}{\Delta x} + \mathbf{s}_i^n = \mathbf{b}_i^n, \quad (30)$$

where superscripts indicate time levels and subscripts spatial nodes. The spatial derivatives appearing in  $\mathbf{B}$  and  $\mathbf{s}$  are discretized by central differences. The essential aspect of the numerical method is the manner in which the modified fluxes  $\hat{\mathbf{F}}$  are specified in terms of some auxiliary quantities that we now define.

Let

$$\mathbf{R}^{(1)} = \begin{bmatrix} 1 \\ u - c \\ \frac{e+p}{\rho} - uc \end{bmatrix}, \quad \mathbf{R}^{(2)} = \begin{bmatrix} 1 \\ u \\ \frac{1}{2} u^2 \end{bmatrix}, \quad (31)$$

$$\mathbf{R}^{(3)} = \begin{bmatrix} 1 \\ u + c \\ \frac{e+p}{\rho} + uc \end{bmatrix}.$$

where  $c = \sqrt{\gamma RT}$ , and



$$a^{(1)}=u-c, \quad a^{(2)}=u, \quad a^{(3)}=u+c. \quad (32)$$

Furthermore, let

$$\alpha_i^{(1)} = \frac{1}{2c_{i+1/2}^2} \left[ (p_{i+1}-p_i) - \rho_{i+1/2}c_{i+1/2}(u_{i+1}-u_i) + \frac{\rho_{i+1/2}u_{i+1/2}c_{i+1/2}^2}{(u_{i+1/2}-c_{i+1/2})S_{i+1/2}} (S_{i+1}-S_i) \right], \quad (33)$$

$$\alpha_i^{(2)} = \frac{1}{c_{i+1/2}^2} [c_{i+1/2}^2(\rho_{i+1}-\rho_i) - (p_{i+1}-p_i)], \quad (34)$$

$$\alpha_i^{(3)} = \frac{1}{2c_{i+1/2}^2} \left[ (p_{i+1}-p_i) + \rho_{i+1/2}c_{i+1/2}(u_{i+1}-u_i) + \frac{\rho_{i+1/2}u_{i+1/2}c_{i+1/2}^2}{(u_{i+1/2}+c_{i+1/2})S_{i+1/2}} (S_{i+1}-S_i) \right], \quad (35)$$

where the quantities carrying a half-integer subscript are calculated as arithmetic averages, e.g.,  $u_{i+1/2} = 1/2(u_{i+1} + u_i)$ . Then

$$\hat{\mathbf{F}}_{i+1/2} = \frac{1}{2} (\mathbf{F}_{i+1} + \mathbf{F}_i) + \frac{\Delta t}{2\Delta x} \sum_{l=1}^3 [g_i^{(l)} + g_{i+1}^{(l)} - Q(v_{i+1/2}^{(l)} + \gamma_i^{(l)})\alpha_i^{(l)}] \mathbf{R}_{i+1/2}^{(l)}, \quad (36)$$

where

$$v^{(l)} = \frac{\Delta t}{\Delta x} a^{(l)}, \quad \gamma_i^{(l)} = \frac{g_{i+1}^{(l)} - g_i^{(l)}}{\alpha_i^{(l)}}. \quad (37)$$

The quantities  $g_i^{(l)}$  appearing in these definitions are a correction to the components of the flux  $\mathbf{F}$  along the characteristic directions and are the smaller one in modulus between

$$[Q(v_{i+1/2}^{(l)} - v_{i+1/2}^{(l)})\alpha_{i+1/2}^{(l)}, \quad (38)$$

and

$$[Q(v_{i-1/2}^{(l)} - v_{i-1/2}^{(l)})\alpha_{i-1/2}^{(l)}].$$

This flux correction is introduced to account for the discretization error and guarantees second-order accuracy in space.

The last quantity to be defined is the function  $Q(x)$  that may be considered as a modified  $|x|$ . Specifically, following Harten (1983), we take

$$Q(x) = \frac{x^2}{4\epsilon} + \epsilon, \quad \text{for } |x| < 2\epsilon, \\ = |x|, \quad \text{for } |x| \geq 2\epsilon, \quad (39)$$

with  $\epsilon = 0.1$ . This quantity plays the role of an artificial viscosity.

Since the integration is explicit in time, the preceding formulas are sufficient to construct the solution at all the interior nodes at time level  $t^{n+1}$  starting from the known values at  $t^n$ . The solution at the two boundary nodes is calculated from the boundary conditions (13)–(15).

#### IV. RESULTS

As a first test of the numerical method, we consider the thermoviscous damping of the lowest linear acoustic mode in a rigid-walled, empty, isothermal tube. Since an exact solu-

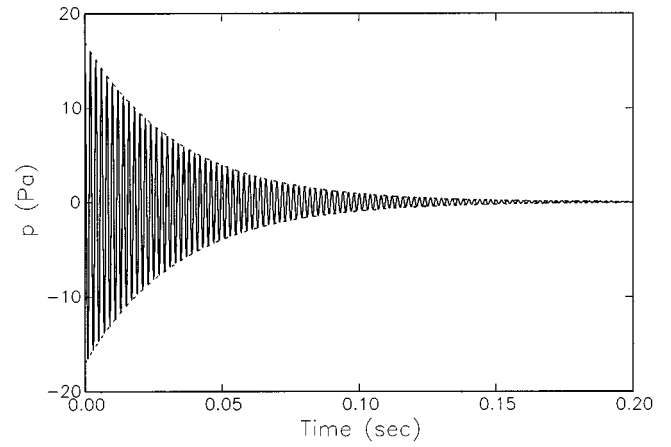


FIG. 3. Decay of pressure oscillations in a rigid isothermal tube for the conditions described in the text. The solid line is the result of the numerical computation. The dashed lines are the exponential envelope proportional to  $\pm \exp(-bt)$  with  $b$  given by (40).

tion to this problem is available, this simulation is a useful test of the numerical method. Theoretically the solution consists of exponentially damped oscillations with a decay rate  $b$  given by (see, e.g., Pierce, 1989, p. 534; the spatial decay rate given in this text can be converted to a temporal one by dividing by the sound speed  $c = \sqrt{\gamma RT_w}$ ):

$$b = \frac{c}{2a\gamma} \left[ (\gamma - 1) \frac{\omega_0 \sigma k}{2p_0 R} \right]^{1/2} \left( 1 + \frac{\gamma - 1}{\sqrt{\sigma}} \right), \quad (40)$$

where  $a$  is the tube radius,  $k$  the gas thermal conductivity,  $p_0$  the undisturbed pressure, and  $\omega_0 = \pi c/L$  the natural frequency of the eigenmode.

The pressure at one of the tube's rigid terminations given by the numerical method described in the previous section is shown in Fig. 3 as a function of time. The tube has a length of 99.9 cm and a diameter of 3.82 cm. The gas is helium at a static pressure  $p_0 = 170$  kPa and temperature  $T_w = 293$  K. For this case there are no unstable modes and we set  $k_n = 0$  in Eqs. (8) and (9) and fix  $\omega$  as in Eq. (16).

At time 0 the system is at rest with an initial pressure disturbance consisting of the lowest eigenmode with an amplitude of 17 Pa. The dashed lines in Fig. 3 are the exponential envelope  $\propto \exp(-bt)$  with  $b$  given by (40). The agreement between the analytical and numerical results is remarkably good, which gives some confidence on our computer code. For these calculation 500 nodes proved sufficient for a good resolution and the time step was adjusted so that the maximum Courant number  $\Delta t |a^{(i)}| / \Delta x$ , with the  $a^{(i)}$  defined in Eq. (32), remained below 0.8.

As another test, we consider the nonlinearly driven tube studied by Gaitan and Atchley (1993). The tube contained air at ambient pressure and temperature and was 82.55 cm long with a diameter of 5.82 cm. For this simulation we excite the tube by prescribing a sinusoidal gas velocity at  $x=0$ . The boundary conditions on pressure and temperature are still given by (14) and (15). Again there are no unstable modes and we set  $k_n = 0$ .

In the experiment the driving frequency was chosen so as to match the pipe's frequency. We found that by using the

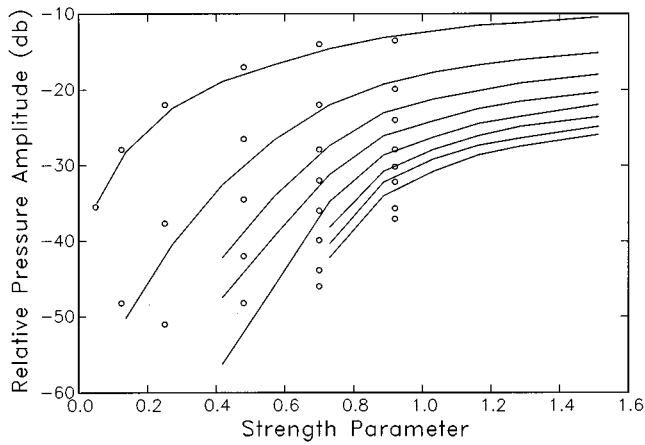


FIG. 4. Level of the harmonics of order 2–8 of a tube driven at resonance by a piston as a function of the level of the fundamental normalized according to (41). The lines are the present computational results. The data the experimental points of Gaitan and Atchley (1993).

reported value  $f=209$  Hz, our “numerical pipe” was not in exact resonance conditions. To match the resonance it was necessary to use  $f=207$  Hz. This sensitivity is not surprising in view of the rather large  $Q$  value of this system that, on the basis of our numerical results, is approximately 134. Gaitan and Atchley (1994) show in their Fig. 4 the dependence of the higher harmonic pressure amplitudes on the strength parameter, i.e., the amplitude  $P_1$  of the fundamental normalized by

$$P_1^* = \frac{\beta Q}{\gamma p_0} P_1, \quad (41)$$

where  $\beta$  is the nonlinearity parameter equal to 1.2 for air. They do not report a value for  $Q$  and we used the one deduced from our computations quoted above. A comparison of the calculated (lines) and measured (circles) results is shown in Fig. 4. The comparison is very good especially for the lower harmonics that have a higher level and are therefore less sensitive to noise and parasitic damping. For these calculations we used 500 nodes and a maximum Courant number of 0.4.

We now turn to thermoacoustic prime movers, specifically the helium system used in the experiments of Atchley *et al.* (1992) and Atchley (1994). As described in these references, the tube length was 99.89 cm and the diameter 3.82 cm. The cold portion of the tube was 87.5 cm long. At the end of this section was the cold heat exchanger consisting of two identical structures separated by 1.5 mm. Each structure consisted of 25 nickel plates 0.45-mm thick, spaced by 1.04 mm and 1.02 cm long. Attached to the second part of the cold heat exchanger was the stack consisting of 3.5-cm-long stainless-steel plates spaced by 0.77 mm, with a thickness of 0.28 mm. The hot heat exchanger was attached to the other end of the stack. This heat exchanger was equal to the cold one except that it consisted of only one section 7.62 mm long. The hot section of the tube was 5.5 cm long. The area blockage fraction was approximately 30% in the heat exchangers and 27% in the stack.

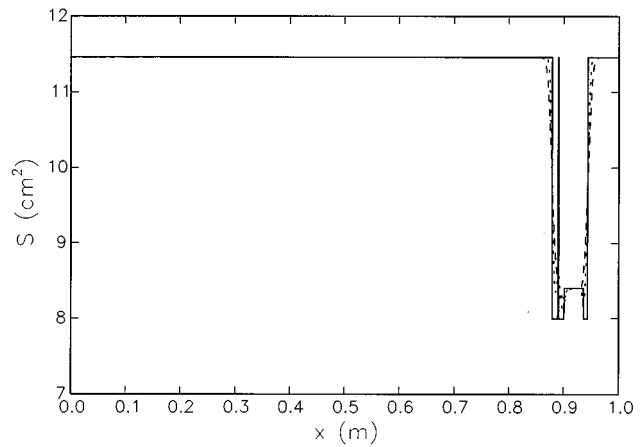


FIG. 5. The solid line is the cross-sectional area of the thermoacoustic prime mover of Atchley *et al.* (1992) and Atchley (1994) according to the geometrical specifications given in the papers. The dotted and dashed lines are the cross-sectional area after applying the smoothing operation of Part I 100 and 310 times, respectively.

We have pointed out in Part I the effect on the linear growth rate of the instability of using discontinuous versus smoothed prescriptions for the axial variation of the cross-sectional area and of the wall temperature. The discontinuities in area and axial derivative of the wall temperature are certainly not a realistic approximation to the actual spatial distribution of these parameters and their presence depends on features (such as natural convection, microstreaming, etc.) that are not included in the model. In Part I we have used a smoothing prescription

$$T_w(x_i) \rightarrow \frac{1}{4} [T_w(x_{i-1}) + 2T_w(x_i) + T_w(x_{i+1})] \quad (42)$$

(where  $x_i$  is the  $i$ th spatial node) iterated a number of times so as to have results in agreement with reported data, and we follow the same approach here. From the data reported by Atchley (1994) for a mean pressure of 376 kPa and a temperature difference of 379 K along the stack (and, presumably, an ambient temperature of 293 K), one finds that the temporal growth rate of the perturbation is  $5.0 \text{ s}^{-1}$ . Upon assuming discontinuous distributions for  $S(x)$  and  $T_w(x)$  we find from the exact linear theory  $11.7 \text{ s}^{-1}$ . By repeating the smoothing operation 310 times, the calculated linear growth rate becomes  $5.13 \text{ s}^{-1}$ . The cross-sectional area and wall temperature distributions resulting from smoothing 100 and 310 times are shown in Figs. 5 and 6. The corresponding initial unsmoothed distributions are shown by the solid lines. The difference is not large, which gives an indication of the sensitivity of the thermoacoustic energy conversion process. In all the calculations shown in this section we have used area and temperature distributions smoothed 310 times.

After matching the linear growth rate with the exact linear theory, in order to proceed with the time-dependent nonlinear calculation, we must select values of the parameter  $\omega_0$  and pseudoconductivity  $k_n$ . By a process of trial and error we find that, with  $k_n=0.25 \text{ m}^2/\text{s}$  and  $\omega_0=2762.0 \text{ s}^{-1}$ , the linear growth rate becomes  $5.01 \text{ s}^{-1}$  to be compared with the measured one of  $5.0 \text{ s}^{-1}$ . On the basis of a convergence

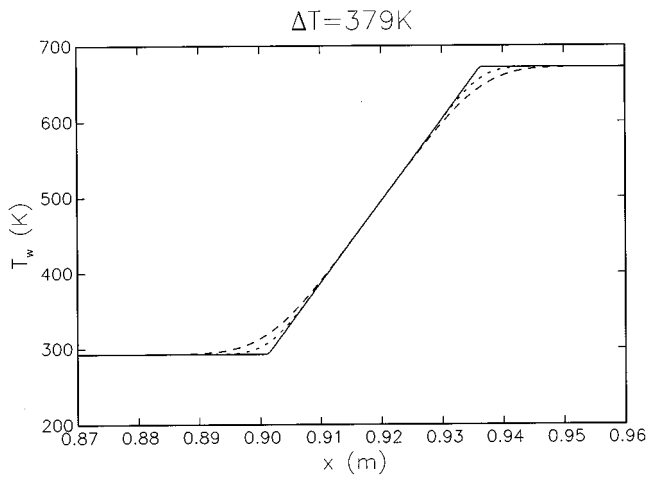


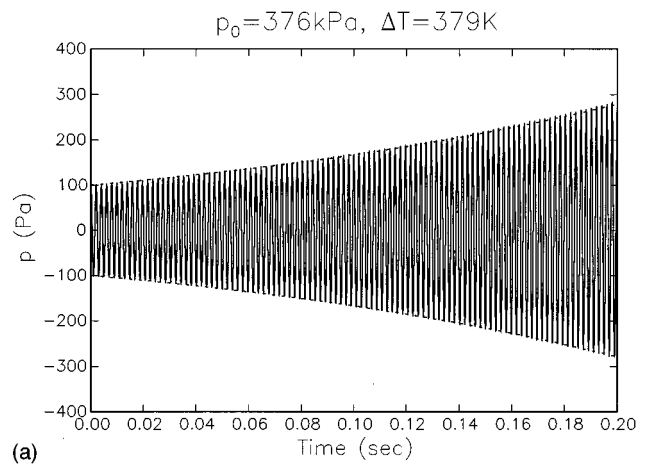
FIG. 6. Unsmoothed (solid line) and smoothed temperature distributions for the simulation of the case studied by Atchley (1994) and shown in Fig. 7. The dotted and dashed lines are the distributions after applying the smoothing operation of Part I 100 and 310 times, respectively.

study we found that 2000 spatial nodes are sufficient for a grid-independent solution. The maximum Courant number allowed was 0.4.

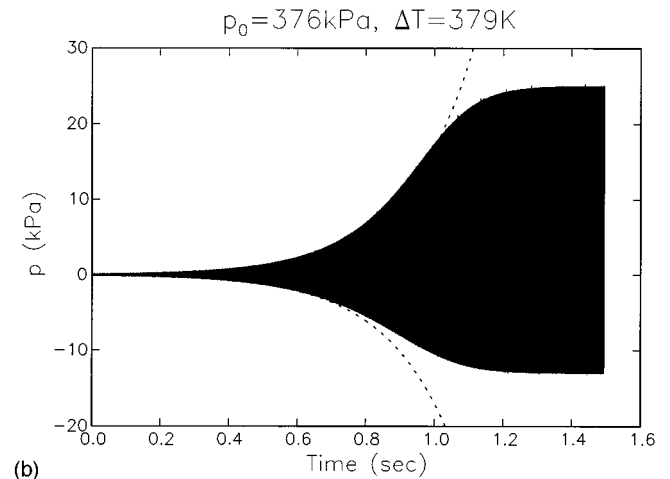
Figure 7 shows the numerically computed pressure at the cold end of the tube versus time for these conditions. The initial disturbance is taken to be the fundamental linear eigenmode, with an amplitude of 100 Pa. The dashed lines are graphs of an exponential growth with the growth rate of  $5.13 \text{ s}^{-1}$  of the exact linear theory. Figure 7(a) shows the initial buildup of the oscillations. The initial growth rate as deduced from these results is exponential, but at a rate of  $5.25 \text{ s}^{-1}$ , just slightly higher than the exact linear result of  $5.13 \text{ s}^{-1}$ . We consider this 2.3% difference as an acceptable consequence of the numerical error affecting the time-dependent calculation. At first the numerical results track with great precision the exponential growth. Soon thereafter, however, nonlinear effects set in as evidenced by the growing asymmetry between positive and negative pressure peaks. Figure 7(b) (note the change in the vertical scale) shows the same results over a longer time interval. Here one sees the eventual divergence of the linear result as opposed to the finite-amplitude stabilization of the nonlinear one.

Figure 7(b) shows that the system saturates at a positive pressure amplitude of approximately 25.0 kPa, i.e., about 6.6% of the static pressure. If the same calculation is repeated with cross-sectional area and wall temperature distributions smoothed only eight times instead of 301 (i.e., very nearly discontinuous), the saturation value for the positive pressure amplitude is approximately 41.0 kPa. Again, this is an indication of the sensitivity of the process.

We have found two papers in the literature where data are presented for nonlinear steady oscillations. One is by Atchley *et al.* (1990), and the other by Swift (1992). The stack used by the latter was of the honeycomb, rather than parallel plate, type and therefore cannot be simulated in the framework of the present model. Hence we focus on the results of Atchley *et al.*, and in particular on those corresponding to a nominal temperature difference along the stack of 368 °C that are documented in good detail in their paper.



(a)



(b)

FIG. 7. Pressure versus time at the cold end of the prime mover for the case studied by Atchley (1994) described in the text. (a) shows the initial buildup of the oscillations. (b) shows the long-term evolution of the system to steady state. The dashed lines portray an exponential growth with the growth rate of  $5.13 \text{ s}^{-1}$  of the exact linear theory.

The experimental setup used in this work was the same described before in connection with Fig. 7.

Figure 8 shows the computed steady-state pressure disturbance at the cold end of the tube for a mean pressure of 307 kPa and a temperature difference along the stack  $\Delta T = 368 \text{ K}$ . The solid line is for  $\omega_0 = 2658.6 \text{ s}^{-1}$ ,  $k_n = 0.42 \text{ m}^2/\text{s}$  and the dashed line for  $\omega_0 = 2924.4 \text{ s}^{-1}$ ,  $k_n = 0.21 \text{ m}^2/\text{s}$ . The corresponding linear spectra are shown by the curves marked with stars and diamonds, respectively, in Fig. 2. The two waveforms are very similar to each other, in particular for what concerns the period and the amplitudes of the positive and negative portions. The main difference is the greater amount of fine structure present in the dashed curve that reflects the weaker attenuation of the higher modes evident from Fig. 2. The corresponding spectra are shown in Fig. 9, where also one observes mainly differences in the high-frequency components.

These results should be compared with those shown in Figs. 4 and 5 of Atchley *et al.* (1990). Qualitatively, the numerical results are close to the experimental ones. The period, 1.95 ms, is identical within the precision with which it can be read from the figure. The waveform exhibits a strong

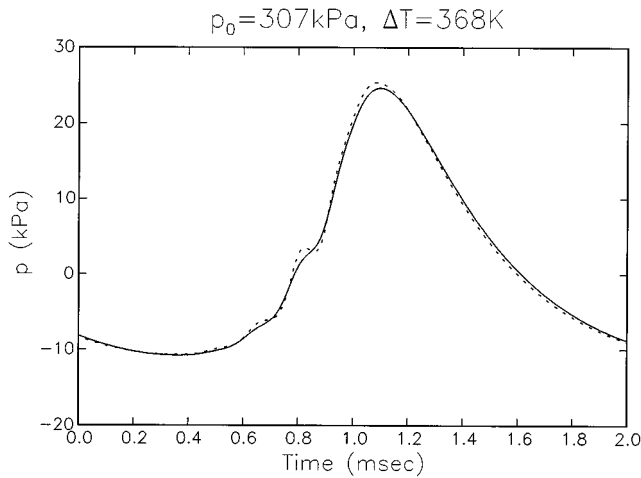


FIG. 8. Steady pressure waveform for a temperature difference between the hot and cold ends of the stack  $\Delta T = 368$  K and the conditions of the experiment of Atchley *et al.* (1990) described in the text. The solid line is for  $\omega_0 = 2658.6 \text{ s}^{-1}$ ,  $k_n = 0.42 \text{ m}^2/\text{s}$ , the dashed line for  $\omega_0 = 2924.4 \text{ s}^{-1}$ ,  $k_n = 0.21 \text{ m}^2/\text{s}$ . The corresponding linear spectra are shown, respectively, by the stars and the diamonds in Fig. 2.

asymmetry, with the negative amplitude much smaller than the positive one. The general spectral shapes also compare favorably with the spectrum flattening out 35–40 dB below the fundamental around the 6th to 7th harmonic. The major difference between calculations and experiment is the amplitude, that is about 24.7 kPa according to Fig. 8, but 13.5 kPa in the data.

Atchley (private communication) has pointed out to us that his temperature data were obtained from a thermocouple near the outer wall of the tube and, at such high power, a substantial temperature nonuniformity across the hot stack could be expected, as large as 50 K, with a likely value of 20–30 K. The present model is below the instability threshold if  $\Delta T$  is reduced by 50 K. The result for a reduction of 25 K is shown in Fig. 10. Now the maximum pressure disturbance is 14.6 kPa, with the period (1.97 ms) hardly affected. However, the waveform shown in Fig. 10 exhibits a front less steep than the experimental one.

Other features of the results that can be compared with experiment are the ratio of the positive and negative amplitude, and the time interval between the zero crossings, e.g., of the positive part of the wave. The data for these quantities are 1.53 and 0.77 ms. (The latter quantity may, however, be affected by the fact that the experimental waveform exhibits some dc bias as the net area under the curve does not seem to vanish.) For the two computations of Fig. 8 the positive/negative ratio is 2.29 and 2.37, while the interval between zero crossings is 0.82 ms. For the smaller  $\Delta T$  case of Fig. 10, the corresponding values are 1.97 and 0.90 ms.

Clearly, there are discrepancies between data and theory. Unfortunately, on the basis of the available information it is not clear whether the origin of the observed differences resides in the approximations of the present model or in the data. More detailed experiments would be highly desirable to help resolve the matter.

Atchley *et al.* (1990) also report results for a smaller

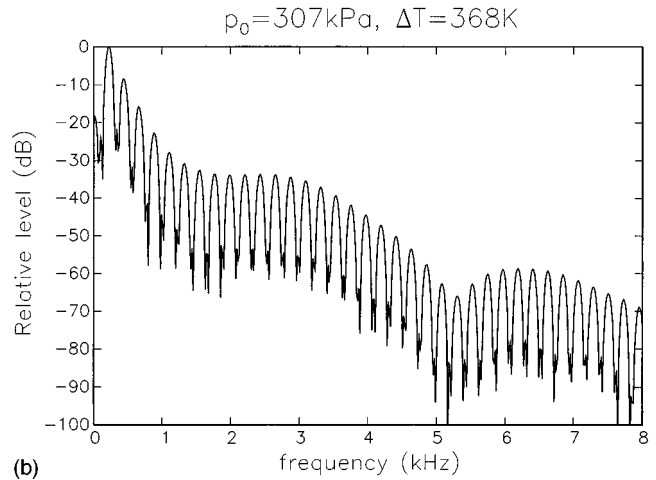
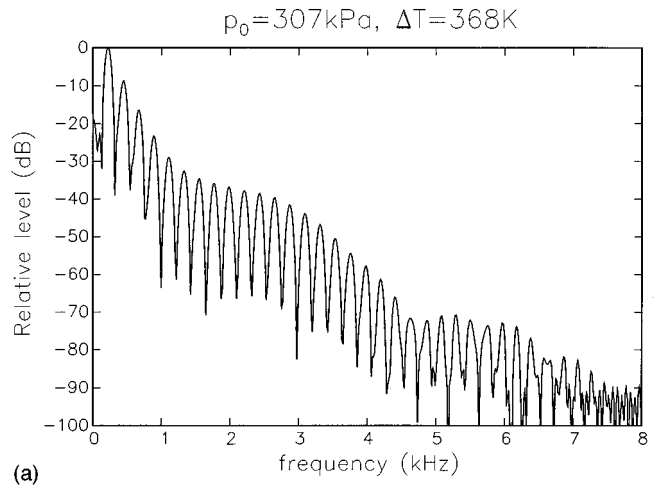


FIG. 9. Spectra of the pressure waveforms of the previous figure; (a) is for  $\omega_0 = 2658.6 \text{ s}^{-1}$ ,  $k_n = 0.42 \text{ m}^2/\text{s}$ , (b) for  $\omega_0 = 2924.4 \text{ s}^{-1}$ ,  $k_n = 0.21 \text{ m}^2/\text{s}$ . The corresponding linear spectra are shown, respectively, by the stars and the diamonds in Fig. 2.

temperature gradient, with  $\Delta T = 325$  K. In our model this is just below threshold, with  $\text{Im } \omega_1 = 0.44 \text{ s}^{-1}$ . In view of the extreme sensitivity of a system so close to threshold to even minute adjustments of parameters or operating conditions, we do not feel that a comparison with these data would be meaningful.

As a last topic we give two examples that illustrate the effect of the tube's cross-sectional area distribution. The conditions and the system simulated are the same as in Fig. 8 except that the cross-sectional area of the midsection of the tube, for  $\frac{1}{2}L < x < \frac{3}{4}L$ , is given by

$$S(x) = S_0 \left[ 1 + C \cos^2 \pi \left( \frac{2x}{L} - 1 \right) \right]^2, \quad \text{for } \frac{1}{4}L \leq x \leq \frac{3}{4}L. \quad (43)$$

while  $S = S_0 = \frac{1}{4}\pi(3.82)^2 \text{ cm}^2$  elsewhere (except for the stack region). Figure 11 shows the steady-state pressure distribution at the cold end of the tube for  $C = 0.2$ . The pressure amplitude is now about five times that found for the constant-area case. The formation of a shock is also evident from the figure. If the tube is narrower in its central region,

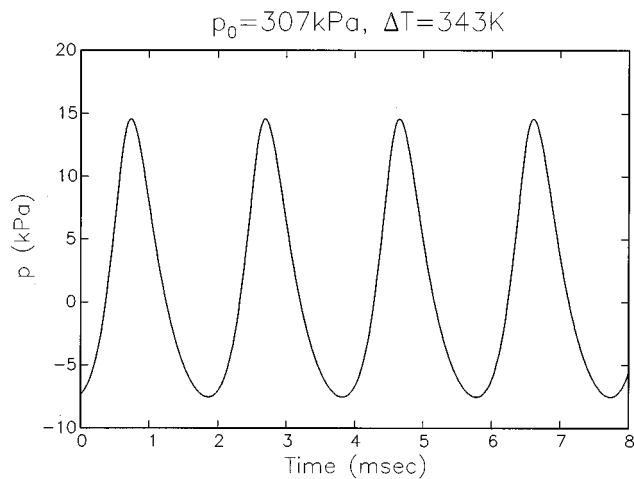


FIG. 10. Steady pressure waveform for  $\Delta T=343$  K and the other conditions as in Fig. 8. Time in ms.

on the other hand, we have the result shown in Fig. 12 for  $C=-0.2$ . The amplitude of the wave is now reduced by about 3% to approximately 24.4 kPa with respect to the constant area case. While the amplitude is not much different, the waveform is strongly affected with a markedly smaller steepening. These results are consistent with the corresponding linear ones presented in Part I.

## V. CONCLUSIONS

In this paper we have adapted the model introduced in Part I to the nonlinear regime and we have described a reliable numerical method for its integration. The numerical results agree very well with experiment for the case of a resonantly driven tube. For a thermoacoustic prime mover, the model has been shown to describe the growth and eventual saturation of the oscillations. While the qualitative predictions match observation, the computed wave amplitude for a case studied by Atchley *et al.* (1990) exceeds the experimentally reported one. It does not seem possible to reach definite

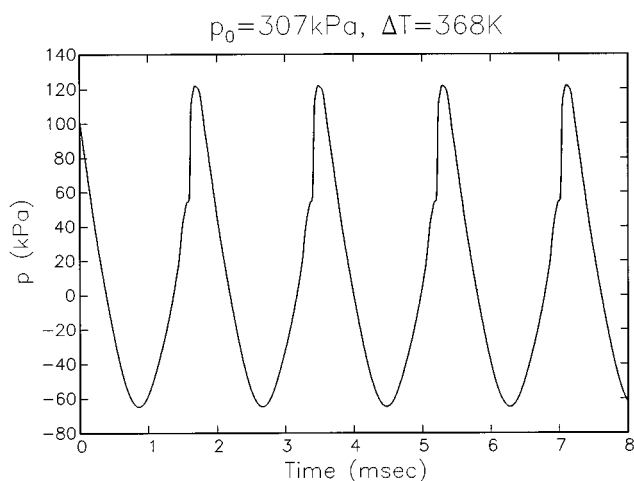


FIG. 11. Steady pressure waveform for the same conditions as in Fig. 8, except that the tube's cross section is enlarged in the midsection according to (43) with  $C=0.2$ . Time in ms.

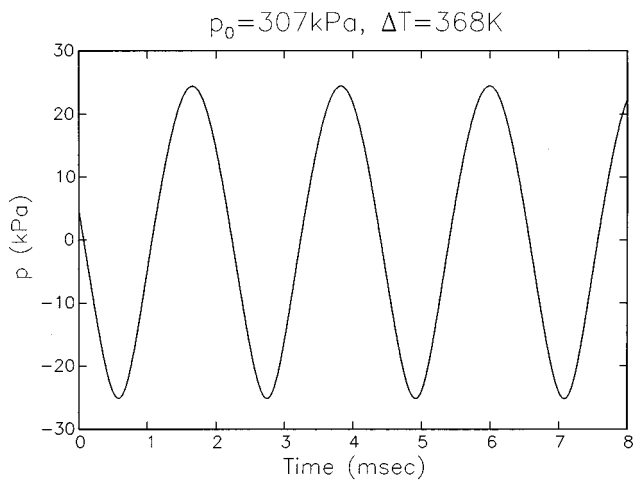


FIG. 12. Steady pressure waveform for the same conditions as in Fig. 8, except that the tube's cross section is decreased in the midsection according to (43) with  $C=-0.2$ . Time in ms.

conclusions on the reason for this discrepancy at this time. It is possible that in the experiment the actual temperature difference along the stack was less than the nominal value. It would also appear from the reported experimental waveform (Fig. 4 of Atchley *et al.*) that the mean of the pressure over the wave is not zero. We have also found that the simulation of this case is very sensitive to details of the temperature and cross-sectional area distribution. Lastly, the model requires the introduction of a certain number of approximations concerning critical terms that govern the energy exchange between the stack and the wave, and it is possible that the results are negatively affected by these approximations.

A more detailed characterization of future experiments would be desirable to resolve some of these points. Hopefully, this paper will stimulate such further experimental work. On the theoretical side, better approximations of the energy exchange terms of the model should be sought. To this end we are currently pursuing the idea mentioned at the end of Sec. II.

Even with the limitations and uncertainties that affect it, the simplified mathematical model that we have developed is of some interest. In the first place, it is the only model to date capable of describing the time-dependent behavior of thermoacoustic prime movers. Second, it can be used to compare design options. For example we have found that, under identical conditions in the stack, a device with a thicker cross section in the central part will develop a much stronger wave than one with a constant cross section.

Clearly, the present formulation can be extended in several directions. In the first place, we can account for heat conduction in the stack. Second, we can extend the model to the refrigerator case. Third, we can pursue the nonlinear aspects at the analytical level by using the techniques of weakly nonlinear stability theory. Efforts in all these directions are currently under way.

## ACKNOWLEDGMENTS

The authors wish to express their gratitude to Dr. M. Watanabe who performed the initial computations and to

Professor A. Atchley for his help and advice. The Office of Naval Research is also gratefully thanked for the support of this study.

- Achard, J. L., and Lespinard, G. M. (1981). "Structure of the transient wall-friction law in one-dimensional models of laminar pipe flows," *J. Fluid Mech.* **113**, 283–298.
- Atchley, A. A. (1992). "Standing wave analysis of a thermoacoustic prime mover below onset of self-oscillation," *J. Acoust. Soc. Am.* **92**, 2907–2914.
- Atchley, A. A. (private communication).
- Atchley, A. A. (1994). "Analysis of the initial build-up of oscillations in a thermoacoustic prime mover," *J. Acoust. Soc. Am.* **95**, 1661–1664.
- Atchley, A. A., Bass, H. E., and Hoffer, T. J. (1990). "Development of nonlinear waves in a thermoacoustic prime mover," in *Frontiers in Non-linear Acoustics*, edited by M. F. Hamilton and D. T. Blackstock (Elsevier, New York), pp. 603–608.
- Atchley, A. A., Hoffer, T. J., Muzzerall, M. L., Kite, M. D., and Ao, C. (1990b). "Acoustically generated temperature gradients in short plates," *J. Acoust. Soc. Am.* **88**, 251–263.
- Fletcher, C. A. J. (1988). *Computational Techniques for Fluid Dynamics* (Springer-Verlag, Berlin).
- Gaitan, D. F., and Atchley, A. A. (1993). "Finite amplitude standing waves in harmonic and anharmonic tubes," *J. Acoust. Soc. Am.* **93**, 2489–2495.
- Harten, A. (1983). "High resolution schemes for hyperbolic conservation laws," *J. Comput. Phys.* **49**, 357–393.
- Harten, A., and Osher, S. (1987). "Uniformly high-order accurate nonoscillatory schemes. i," *SIAM (Soc. Ind. Appl. Math.) J. Numer. Anal.* **24**, 279–309.
- Harten, A., Osher, S., Engquist, B., and Chakravarthy, R. (1986). "Some results on uniformly high-order accurate essentially nonoscillatory schemes," *Appl. Numer. Math.* **2**, 347–377.
- Osher, S. (1984). "Riemann solvers, the entropy condition, and difference approximation," *SIAM (Soc. Ind. Appl. Math.) J. Numer. Anal.* **21**, 217–235.
- Osher, S., and Chakravarthy, R. (1984). "High resolution schemes and the entropy condition," *SIAM (Soc. Ind. Appl. Math.) J. Numer. Anal.* **21**, 955–984.
- Pierce, A. D. (1989). *Acoustics* (American Institute of Physics, Woodbury), 2nd ed.
- Press, W. H., Vetterling, W. T., Teukolsky, S. A., and Flannery, B. P. (1992). *Numerical Recipes in FORTRAN* (Cambridge U.P., Cambridge, England), 2nd ed.
- Prosperetti, A., and Watanabe, M. (1994). "Simplified model for the study of nonlinear processes in thermoacoustic engines," *J. Acoust. Soc. Am.* **96**, 3220.
- Roe, P. L. (1986). "Characteristic-based schemes for the euler equations," *Annu. Rev. Fluid Mech.* **18**, 337–365.
- Rott, N. (19xx). "Thermally driven acoustic oscillations, Part IV: Tubes with variable cross section," *Z. Angew. Math. Phys.* **27**, 197–224.
- Rott, N. (1980). "Thermoacoustics," *Adv. Appl. Mech.* **20**, 135–175.
- Sod, G. A. (1978). "A survey of several finite difference methods for systems of nonlinear hyperbolic conservation laws," *J. Comput. Phys.* **27**, 1–31.
- Sweby, P. K. (1984). "High resolution schemes using flux limiters for hyperbolic conservation laws," *SIAM (Soc. Ind. Appl. Math.) J. Numer. Anal.* **21**, 995–1011.
- Swift, G. W. (1988). "Thermoacoustic engines," *J. Acoust. Soc. Am.* **84**, 1145–1180.
- Swift, G. W. (1992). "Analysis and performance of a large thermoacoustic engine," *J. Acoust. Soc. Am.* **92**, 1551–1563.
- Watanabe, M., Prosperetti, A., and Yuan, H. (1997). "A simplified model for linear and nonlinear processes in thermoacoustic prime movers. Part I. Model and linear theory," *J. Acoust. Soc. Am.* **102**, 3484–3496.
- Wheatley, J. (1986). "Intrinsically irreversible or natural heat engines," in *Frontiers in Physical Acoustics*, edited by D. Sette (North-Holland, Amsterdam), pp. 35–475.

# Characterization of porous piezoelectric ceramics: The length expander case

Tomás E. Gómez Alvarez-Arenas<sup>a)</sup> and Francisco Montero de Espinosa  
*Instituto de Acústica, C.S.I.C., C/Serrano 144, 28006 Madrid, Spain*

(Received 24 March 1997; accepted for publication 31 July 1997)

Porous piezoelectric ceramics and 0–3/3–3 connectivity piezoelectric composites are normally characterized following the Standards on Piezoelectricity. Nevertheless, these materials are not homogeneous and losses are significant. New constitutive and wave equations have been obtained recently for these kind of materials. The objective of this paper is to derive new definitions for the electromechanical coupling coefficients and a suitable characterization procedure according to the new constitutive and wave equations previously mentioned. In particular, the case of the length expander bar mode is analyzed in detail. The study of resonant elements requires the use of suitable boundary conditions. In this case the boundary conditions are borrowed from the theory of poroelasticity and extended for a piezoelectric material. Finally the procedure is applied to characterize a commercial porous piezoelectric ceramic. © 1997 Acoustical Society of America. [S0001-4966(97)05211-9]

PACS numbers: 43.38.Ar, 43.20.Jr, 43.38.Fx [SLE]

## INTRODUCTION

A number of papers<sup>1–3</sup> have introduced a new theoretical frame to study porous piezoelectric ceramics and 0–3/3–3 connectivity piezoelectric composites. A new system of constitutive equations for these types of two-phase materials was presented in Refs. 1–3. These constitutive equations consider the interaction between the phases that build up the material and therefore permit a better understanding of the behavior of such materials.

The theory was applied to different porous commercial ceramics which are actually a particular case of a 3–3 connectivity biphasic material<sup>1,2</sup> and to highly loaded epoxy-ceramic powder composites<sup>3</sup> whose real electrical and mechanical connectivity should be located somewhere between the 0–3 and 3–3 ideal configurations. It was shown that the behavior of these materials can be better explained within the frame of this new theoretical scenario than if they are considered homogeneous.

The application of the Standards on Piezoelectricity<sup>4</sup> to characterize porous piezoelectric ceramics and 0–3/3–3 connectivity piezoelectric composites is not straightforward because these materials are not homogeneous as the standards suppose. This limitation was shown in Ref. 5 where different electromechanical coefficients were measured for different minor phases in the same porous piezoelectric ceramic. Unexpected changes of the piezoelectric constant of the samples were observed and forbidden mechanical resonances of the thickness vibrations appeared. Nevertheless it is possible to find a reasonable explanation of these measurements in terms of the interaction between the phases that constitute the sample.

The first problem to solve in order to study the resonant modes of a finite and porous piezoelectric sample is the de-

termination of suitable boundary conditions. To this end, the theory of poroelasticity is used and extended to be applied to a piezoelectric material. Once wave equations and boundary conditions are established, the sample can be characterized.

It is the objective of this paper to present a characterization procedure for porous piezoelectric ceramics consistent with the theoretical frame obtained from Refs. 1–3. Section I presents a short review of the constitutive equations of 0–3 and 3–3 piezoelectric composites. Section II briefly reviews the derivation of wave equations for this problem. Section III analyzes the boundary conditions suitable for a porous piezoelectric ceramic. In Sec. IV a new definition of the electromechanical coupling coefficients is introduced accordingly with the new constitutive equations. Sections V and VI analyze the length expander case: vibration modes and electrical impedance. A new characterization procedure is then proposed and applied to some experimental cases. The results are compared with those obtained from the standard characterization procedure.

## I. CONSTITUTIVE RELATIONS FOR POROUS PIEZOELECTRIC CERAMICS

Constitutive relations for 3–3 and 0–3/3–3 connectivity composites were obtained in Refs. 2 and 3. The Gibbs energy is presented as an addition of the contributions due to each phase. Constitutive relations and thermodynamical definitions of the properties of the material are obtained from the expansion of the Gibbs free energy up to second derivatives order. The result is a set of linear and coupled constitutive equations. The main feature of these relations is that the properties of the composite are not a linear combination of the properties of each component. On the contrary, new terms appear in which different ways of interaction between phases are considered.

If only one component of the composite has piezoelectric properties, the constitutive relations can be written as:<sup>2</sup>

<sup>a)</sup>Present address: Ultrasonic Research Group, E&EE Department, University of Strathclyde, 204 George Street, G1 1XW Glasgow, U.K.

$$\begin{aligned}
S_{ij} &= T^* E^* s_{ijkl} T_{kl} + E^* m_{ijk} T_{kl}^* + ET^* \widetilde{\delta}_{nij} E_n^* \\
S_{ij}^* &= E^* m_{ijk} T_{kl} + TE^* s_{ijkl} T_{kl}^* + ET d_{nij}^* E_n^* \\
D_i^* &= ET d_{ikl}^* T_{kl}^* + ET^* \widetilde{\delta}_{ikl} T_{kl} + TET^* \epsilon_{il}^* E_l^* + TT^* A_{il} E_l \\
D_i &= TT^* A_{il} E_l^* + E^* \epsilon_{il} E_l,
\end{aligned} \tag{1}$$

where  $s_{ijkl}$  are the elastic compliances,  $\epsilon_{ij}$  the dielectric permittivities, and  $d_{ijk}$  the piezoelectric coefficients. The piezoelectric coefficients couple the dielectric and elastic energy systems. In addition, some new coupling parameters appear in Eqs. (1). These parameters link the properties of the phases:  $m$  (elastic coupling parameter),  $A$  (dielectric coupling parameter), and  $\delta$  (new piezoelectric coupling parameter).

The superscripts ( $T$ ,  $D$ ,  $E$ , and  $S$ ) mean that the affected magnitude ( $m$ ,  $s$ ,  $d$ ,  $A$ , and  $\epsilon$ ) is measured at such conditions that those magnitudes appearing as superscripts are kept constant. In addition, the asterisk over the magnitudes  $S$ ,  $T$ ,  $D$ , or  $E$  is used to denote the two different components of the medium (the asterisk is used for the piezoelectric solid).

Another useful representation of the constitutive relations is shown in Eqs. (2):<sup>2</sup>

$$\begin{aligned}
T_{ij} &= S^* E^* c_{ijkl} S_{kl} + E^* n_{ijk} S_{kl}^* - ES^* \zeta_{nij} E_n^* \\
T_{ij}^* &= E^* n_{ijk} S_{kl} + SE^* c_{ijkl}^* S_{kl}^* - ES e_{nij}^* E_n^* \\
D_i^* &= ES e_{ikl}^* S_{kl}^* + ES^* \zeta_{ikl} S_{kl} + SES^* \epsilon_{il}^* E_l^* + SS^* A_{il} E_l \\
D_i &= SS^* A_{il} E_l^* + E^* \epsilon_{il} E_l,
\end{aligned} \tag{2}$$

where  $c_{ijkl}$  are the elastic compliances,  $n_{ijk}$  are the elastic parameters that couple the phases,  $e_{ijk}$  are the piezoelectric constants, and  $\zeta_{ikj}$  are the new piezoelectric parameters that couple the phases.

## II. WAVE EQUATION FOR A FLUID-SATURATED POROUS PIEZOELECTRIC CERAMIC

The constitutive relations presented in the previous section are quite general and suitable for any 3–3 or 0–3/3–3 connectivity piezoelectric composite. Nevertheless, the interest is now focused on the study of wave equations for the particular case of a fluid-saturated 3–3 connectivity porous piezoelectric ceramic. Different reasons can be given to support the study of this particular case. From the theoretical point of view, this case is particularly interesting for the parallelism that can be traced with Biot's theory.<sup>6,7</sup> From the experimental point of view, porous piezoelectric ceramics are more easily handled than 0–3/3–3 connectivity nonporous piezoelectric composites and the piezoelectric properties can be measured more accurately for porous piezoelectric ceramics than for 0–3/3–3 nonporous piezoelectric composites.

In 1956 M. A. Biot<sup>6,7</sup> developed a theory of sound propagation in fluid-saturated porous solids. This theory has been widely applied to a great number of very different cases. More recently this theory has been extended to consider the interaction of acoustic waves with electric fields in

relationship to electroseismic waves<sup>8</sup> and finally, as mentioned previously, to the piezoelectric effect.<sup>2,3</sup>

The main hypothesis of the Biot's theory are also assumed here: (1) There is an interconnected pore space (3–3 connectivity) filled by a fluid; (2) The fluid can move inside the pores; (3) The wavelength of the acoustic wave is much greater than the typical pore or grain size so that scattering effects are neglected and displacements in each phase are defined as an average displacement over a volume much higher than the volume associated to individual pores or grains. With these assumptions Biot developed his theory from: (1) A system of constitutive equations for the whole material (fluid and solid); (2) Darcy's law and the calculation of viscous friction between the solid and fluid; and (3) A coupled system of momentum equations for the whole material. For a porous piezoelectric ceramic it is supposed that the same procedure can be followed but instead of using the constitutive equations derived by Biot, Eqs. (1) are used. Then, the one-dimensional momentum equations derived by Biot in 1956 can be written in this case as

$$\begin{aligned}
\rho^* \frac{\partial^2}{\partial t^2} \xi_i^* + \rho_c \frac{\partial^2}{\partial t^2} \xi_i + b \frac{\partial}{\partial t} (\xi_i^* - \xi_i) &= \frac{\partial T_{1i}^*}{\partial x_1} \\
\rho_c \frac{\partial^2}{\partial t^2} \xi_i^* + \rho \frac{\partial^2}{\partial t^2} \xi_i - b \frac{\partial}{\partial t} (\xi_i^* - \xi_i) &= \frac{\partial T_{1i}}{\partial x_1},
\end{aligned} \tag{3}$$

where  $\xi$  and  $\xi^*$  are the displacement vectors of the fluid and the piezoelectric solid, respectively, and are defined as  $S_1 = \partial \xi_1 / \partial x_1$  and  $S_1^* = \partial \xi_1^* / \partial x_1$ . The right-hand side terms are the generalized forces over fluid and solid parts of the composite, respectively. The third term in the left-hand side of the equations (containing the coefficient  $b$ ) represents the friction force in the  $x_1$  direction per unit volume of bulk material. These terms originate from viscous drag between the solid and fluid. Finally,  $\rho^*$ ,  $\rho$ , and  $\rho_c$  are density coefficients related to the density of the solid, the density of the fluid, and the inertial coupling between the phases. In particular,  $\rho_c$  is given by  $\rho_c = \rho \phi (1 - \theta)$  where  $\theta$  is the pore tortuosity. The calculation of this parameter is discussed in Appendix B.

The majority of the problems of interest deal with purely longitudinal or purely shear propagating waves. Biot shows<sup>6</sup> that both waves are also decoupled in the propagation through an infinite porous medium. Without loss of generality, the wave equations for longitudinal waves propagating along the  $x_1$  axis can be written as

$$\begin{aligned}
\rho^* \frac{\partial^2}{\partial t^2} \xi_i^* + \rho_c \frac{\partial^2}{\partial t^2} \xi_i + b \frac{\partial}{\partial t} (\xi_i^* - \xi_i) &= SE^* c_{1i1k}^* \frac{\partial^2 \xi_k^*}{\partial x_1^2} + E^* n_{1i1k} \frac{\partial^2 \xi_k}{\partial x_1^2} - ES e_{k1i}^* \frac{\partial E_k^*}{\partial x_1} \\
\rho_c \frac{\partial^2}{\partial t^2} \xi_i^* + \rho \frac{\partial^2}{\partial t^2} \xi_i - b \frac{\partial}{\partial t} (\xi_i^* - \xi_i) &= E^* n_{1i1k} \frac{\partial^2 \xi_k^*}{\partial x_1^2} + S^* E^* c_{1i1k} \frac{\partial^2 \xi_k}{\partial x_1^2} - ES^* \zeta_{k1i} \frac{\partial E_k^*}{\partial x_1}.
\end{aligned} \tag{4}$$



Since the waves are assumed plane, all partial derivatives with respect to  $x_2$  and  $x_3$  are zero and an electric field can exist only along  $x_1$ . In addition, it is supposed that both phases are electrical insulators. Then, with the use of Eqs. (1), Eqs. (4) become (longitudinal and unidirectional case):

$$\begin{aligned} & \rho_c^* \frac{\partial^2}{\partial t^2} \xi_1^* + \rho_c \frac{\partial^2}{\partial t^2} \xi_1 + b \frac{\partial}{\partial t} (\xi_1^* - \xi_1) \\ &= {}^{SE^*} c_{11}^* \left( 1 + \frac{({}^{SE} e_{11}^*)^2}{\epsilon_{11}^{\text{eff}} {}^{SE^*} c_{11}^*} \right) \frac{\partial^2 \xi_1^*}{\partial x_1^2} \\ &+ {}^{E^*} n_{11} \left( 1 + \frac{{}^{SE} e_{11}^* {}^{S^*E} \zeta_{11}}{\epsilon_{11}^{\text{eff}} {}^{E^*} n_{11}} \right) \frac{\partial^2 \xi_1}{\partial x_1^2}, \\ & \rho_c \frac{\partial^2}{\partial t^2} \xi_1^* + \rho \frac{\partial^2}{\partial t^2} \xi_1 - b \frac{\partial}{\partial t} (\xi_1^* - \xi_1) \\ &= {}^{E^*} n_{11} \left( 1 + \frac{{}^{SE} e_{11}^* {}^{S^*E} \zeta_{11}}{\epsilon_{11}^{\text{eff}} {}^{E^*} n_{11}} \right) \frac{\partial^2 \xi_1^*}{\partial x_1^2} \\ &+ {}^{S^*E^*} c_{11} \left( 1 + \frac{{}^{S^*} \zeta_{11}^2}{\epsilon_{11}^{\text{eff}} {}^{S^*E^*} c_{11}} \right) \frac{\partial^2 \xi_1}{\partial x_1^2}, \end{aligned} \quad (5)$$

where

$$\epsilon_{11}^{\text{eff}} = {}^{SDS^*} \epsilon_{11}^* = {}^{SES^*} \epsilon_{11}^* \left( 1 - \frac{({}^{SS^*} A_{11})^2}{E^* \epsilon_{11} {}^{SES^*} \epsilon_{11}^*} \right), \quad (6)$$

and the matrix notation has been employed.

### III. BOUNDARY CONDITIONS IN THE INTERFACE BETWEEN A POROUS MEDIUM AND AN ELASTIC CONTINUUM

The characterization of piezoelectric materials usually involves the study of the resonances of certain sample geometries such as plates, bars, or disks. In order to apply the constitutive equations and wave equations previously developed, it is necessary, first, to derive boundary conditions suitable for the problem. Two different kinds of boundary conditions have to be studied: mechanical and electrical boundary conditions.

The mechanical boundary conditions at the interface between a fluid-saturated porous solid and an elastic continuum were first studied by Deresiewicz *et al.*<sup>9,10</sup> In this case the interest is focused on the acoustic wave interaction with a plane interface separating a fluid (air) and a fluid-saturated porous ceramic. This interaction is governed by four boundary conditions.<sup>11</sup> Three of them, namely the continuity of normal stress and displacements and the disappearance of the transverse stress at the interface, are the usual conditions required at ordinary fluid/solid interfaces. The only conceptual difference in the case of permeable solids is that the continuity of the normal displacements has to be modified to express the conservation of fluid volume ( $\xi_n'$ ):

$$\xi_n' = \phi \xi_n + (1 - \phi) \xi_n^*, \quad (7)$$

where  $\phi$  is the porosity and the subindex  $n$  specifies normal displacements components.

The fourth boundary condition is Darcy's law applied to the surface pores of the porous solid:

$$p - p' = i \omega Z_s \phi (\xi_n - \xi_n^*), \quad (8)$$

where  $p$  and  $p'$  are the pressures of the fluid in the pores and in the free space, respectively, and  $Z_s$  is a surface impedance defined as the ratio between the discontinuity in pressure and the relative volume velocity of the fluid with respect to the porous solid.

Two limiting cases are normally considered: (a) open-pore surface and (b) sealed-pore surface. In the first case it is supposed that the fluid inside the porous solid can flow out and into the porous solid without any resistance ( $Z_s = 0$ ). On the other hand, for the sealed-pore surface case, it is supposed that the fluid meets an infinite resistance to flow out or into the porous solid ( $Z_s = \infty$ ). Intermediate cases lay in between these limits, yet the main problem is the determination of  $Z_s$ . Some experimental results and analytical calculations were shown in Ref. 11 but there is a lack of experimental data on this specific point and normally one of the two approximations is considered.

In this paper, open-pore conditions are considered. In fact, in the system considered the size of the pore is large enough to ensure that viscous skin effects are negligible at the working frequencies used in this work. In addition, as the samples can be saturated or dried out easily, it is known that the fluid can flow in and out of the porous media without difficulties.

The electric boundary conditions are obtained by considering that at the interfaces where the boundary conditions must be applied there is an uniform metallization (i.e., the interface is covered by a thin layer of a perfect electrical conductor). The same boundary conditions as in the homogeneous case are, therefore, used here.

### IV. DEFINITION OF THE ELECTROMECHANICAL COUPLING COEFFICIENTS OF A POROUS PIEZOELECTRIC CERAMIC

The electromechanical coupling coefficients provide an important measure of the performance of piezoelectric materials as electroacoustic transducers. These coefficients are nondimensional factors related to the ratio of mechanical work available to electrical energy stored. In order to obtain a definition of the electromechanical coefficients of a porous ceramic, the same procedure as that employed in the IEEE Standard on Piezoelectricity<sup>4</sup> is now followed.

Let us consider the sample geometry and electrode configuration depicted in Fig. 1. In particular, the element is silverplated on faces perpendicular to  $x_3$  (the polar axis). Cross-sectional dimensions are small compared with its length. Due to its geometry this is, essentially, a one-dimensional problem. Open-pore conditions are considered at the surfaces. On the electroded surfaces:  $E_1^* = E_2^* = E_1 = E_2 = 0$  and since the thickness  $t$  is very small  $E_1^* = E_2^* = E_1 = E_2 = 0$  is considered throughout the bar along with  $E_3^* = E_3$ . In a similar way,  $T_3 = T_2 = 0$  and  $T_1 \neq 0$  represent the stress conditions along the propagation throughout the bar. Therefore for this particular case, the constitutive equations (1) can be written as

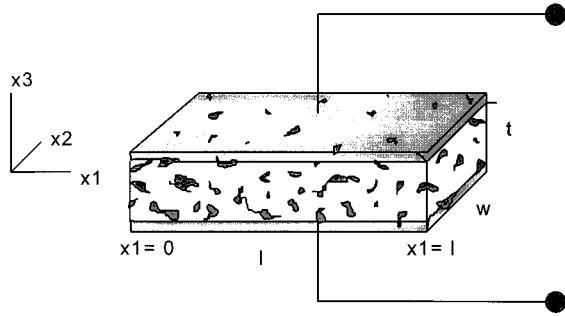


FIG. 1. Schematic representation of the geometry of the sample and electrode configuration for the calculation of the  $k_{31}$  electromechanical coupling coefficient of a porous piezoelectric ceramic.

$$S_1 = T^* E^* S_{11} T_1 + E^* m_{11} T_1^* + ET^* \tilde{\delta}_{31} E_3^* \quad (9)$$

$$S_1^* = E^* m_{11} T_1 + TE^* s_{11}^* T_1^* + ET d_{31}^* E_3^*$$

$$D_3^{\text{total}*} = ET d_{31}^* T_1^* + ET^* \tilde{\delta}_{31} T_1 + TT^* \epsilon_{33}^{\text{eff}} E_3,$$

where  $TT^* \epsilon_{33}^{\text{eff}} = (TT^* \epsilon_{33}^* + 2TT^* A_{33} + TT^* \epsilon_{33})$  and matrix notation was used.

The sample is subjected to the electromechanical cycle shown in Fig. 2. It is placed under electrical short circuit as a stress  $T_1$  is applied to both phases [leg AB in Fig. 2(a)]. The element is free to expand so that  $T_1$  is the only nonzero stress component. The total stored energy per unit volume at point B is  $W_1 + W_2$ . Prior to removal of the lateral stress  $T_1$ , the element is open circuited and connected to an ideal electric load to complete the cycle (leg BC). As work is done on the electrical load, the strain returns to its initial state. For the idealized cycle shown, the work  $W_1$  done on the electric load and the part of the energy unavailable to the electric load  $W_2$  are related to the coupling factor  $k_{31}$  as follows:

$$k_{31}^2 = \frac{W_1}{W_1 + W_2}. \quad (10)$$

Using the procedure outlined before (Fig. 2) and Eqs. (9), quantities  $W_1$  and  $W_2$  are calculated. From this results and Eq. (10) we obtain

$$k_{31}^2 = \frac{(ET d_{31}^*)^2}{\pi^* \epsilon_{33}^{\text{eff}} TE^* s_{11}^*} \frac{1 - 2\alpha(E^* m_{11}/T^* s_{11}) + \alpha^2(T s_{11}^*/T^* s_{11})}{[1 - (E^* m_{11})^2/(T^* s_{11} T s_{11}^*)]}, \quad (11)$$

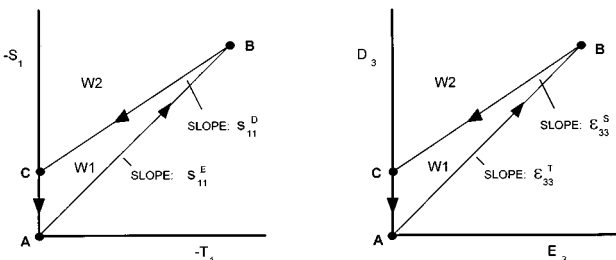


FIG. 2. Ideal and quasi-static electromechanical cycle for the determination of the electromechanical coupling coefficients.

where  $\alpha$  is defined as the ratio of the two piezoelectric constants:  $\alpha = ET^* \tilde{\delta}_{31}/ET d_{31}^*$ .

Following a similar procedure, the  $k_{33}$  electromechanical coupling coefficient is obtained:

$$k_{33}^2 = \frac{(ET d_{33}^*)^2}{TT^* \epsilon_{33}^{\text{eff}} TE^* s_{33}^*} \frac{1 - 2\alpha(E^* m_{33}/T^* s_{33}) + \alpha^2(T s_{33}^*/T^* s_{33})}{[1 - (E^* m_{33})^2/(T^* s_{33} T s_{33}^*)]}, \quad (12)$$

where  $\alpha$  in this case is defined as  $\alpha = ET^* \tilde{\delta}_{33}/ET d_{33}^*$ .

The expressions obtained for the electromechanical coupling coefficients resemble the classical expressions, affected by a factor that depends on the coupling mechanisms between the components of the sample.

## V. LOW-FREQUENCY EXTENSIONAL VIBRATIONS OF POROUS PIEZOELECTRIC BARS: LENGTH EXPANDER MODE WITH FIELD PERPENDICULAR TO LENGTH

For this particular case, the wave equations are easily obtained if the strains in Eqs. (9) are expressed as the independent variable:

$$T_1^* = \frac{T^* s_{11} S_1^* - E m_{11} S_1 - (T^* s_{11} d_{31}^* - E m_{11} \tilde{\delta}_{31}) E_3}{T^* s_{11} T s_{11}^* - (E m_{11})^2} \quad (13)$$

$$T_1 = \frac{T s_{11}^* S_1 - E m_{11} S_1^* - (T s_{11}^* \tilde{\delta}_{31} - E m_{11} d_{31}^*) E_3}{T^* s_{11} T s_{11}^* - (E m_{11})^2}.$$

Substituting Eqs. (13) into momentum equations (3), considering plane wave propagation:  $\xi_1 = \xi_0 \exp[i(kx + \omega t)]$  and  $\xi_1^* = \xi_0^* \exp[i(kx + \omega t)]$  (where  $k$  is the wave vector and  $\omega$  the angular frequency) and the insulating case:  $\partial D_3/\partial x = 0$ , the following system of equations is obtained:

$$\frac{T^* s_{11} \xi_0^* - E m_{11} \xi_0}{T^* s_{11} T s_{11}^* - (E m_{11})^2} k^2 = \omega^2 \rho^* \xi_0^* + \omega^2 \rho_c \xi_0 - i \omega b (\xi_0 - \xi_0^*) \quad (14)$$

$$\frac{T s_{11}^* \xi_0 - E m_{11} \xi_0^*}{T^* s_{11} T s_{11}^* - (E m_{11})^2} k^2 = \omega^2 \rho \xi_0 + \omega^2 \rho_c \xi_0^* + i \omega b (\xi_0 - \xi_0^*).$$

Solving this system of equations, two different values for  $k$  are obtained, which correspond to two different longitudinal modes (fast and slow) that are equivalent to the two Biot's longitudinal modes in a nonpiezoelectric fluid-saturated porous solid. An useful parameter to look at the physics of the problem is the ratio between the displacements in each phase for every propagating mode:

$$\Phi_{F,S} = \frac{-E m_{11} k_{F,S}^2 - \omega^2 \rho_c \Omega + i \omega b \Omega}{T^* s_{11} k_{F,S}^2 - \omega \rho^* \Omega - i \omega b \Omega}, \quad (15)$$

where  $\Omega$  is given by

$$\Omega = T^* s_{11} T s_{11}^* - (E m_{11})^2. \quad (16)$$

In general, solid and fluid parts of the material are moved nearly in phase under the action of the fast longitu-

dinal wave. On the contrary, the oscillation of solid and fluid components tends to be out of phase (180°) when the slow longitudinal wave is considered. In addition, the oscillation amplitude in the fluid particles is much higher in the case of the slow longitudinal wave, while the fast longitudinal wave generates amplitudes of oscillation of similar magnitude in both phases.

Considering sinusoidal excitation  $E_3 = E_0 \exp(i\omega t)$  then the displacements inside the bar of Fig. 1 are given by

$$\xi_1 = \left( A \sin \frac{x\omega}{\nu_F} + B \cos \frac{x\omega}{\nu_F} + C \sin \frac{x\omega}{\nu_S} + D \cos \frac{x\omega}{\nu_S} \right) \quad (17)$$

$$\xi_1^* = \left( A\Phi_F \sin \frac{x\omega}{\nu_F} + B\Phi_F \cos \frac{x\omega}{\nu_F} + C\Phi_S \sin \frac{x\omega}{\nu_S} + D\Phi_S \cos \frac{x\omega}{\nu_S} \right),$$

where  $\nu_F$  and  $\nu_S$  are the velocities of propagation of the fast ( $F$ ) and slow ( $S$ ) longitudinal modes, respectively.

From the previous discussion it is clear that for the uni-dimensional bar case and open pore conditions, the boundary conditions to be imposed at  $x=0$  and  $x=L$  are  $T_1^* = T_1 = 0$ . Considering these boundary conditions the coefficients  $A$ ,  $B$ ,  $C$ , and  $D$  can be calculated and the problem is completely solved. Analytical expressions for these coefficients are given in Appendix A.

The admittance of a piezoelectric and homogeneous vibrating bar is given by

$$\frac{1}{Z} = \frac{1}{V} = \frac{w \int_0^L \dot{D}_3 dx}{\int_0^L E_3 dz}. \quad (18)$$

For the case considered here the total electric displacement field must be considered:  $D_3^T = D_3 + D_3^*$ , which was defined in Eqs. (9)

From Eqs. (13), the definitions of  $S_1$  and  $S_1^*$  and the solutions for  $\xi_1$  and  $\xi_1^*$  [Eqs. (16) and (A1)–(A4)], the following expression for the electric displacement field is obtained:

$$D_3^T = TT^* \epsilon_{33}^{\text{eff}} (1 - k_{31}^2) E_0 + TT^* \epsilon_{33}^{\text{eff}} k_{31}^2 \kappa_F \left( \cos \frac{x\omega}{\nu_F} - \sin \frac{x\omega}{\nu_F} \frac{\cos(l\omega/\nu_F) - 1}{\sin(l\omega/\nu_F)} \right) E_0$$

+ slow wave contribution, (19)

where

$$\kappa_F = \frac{1 - \Phi_S \alpha}{\Phi_F - \Phi_S} \frac{\Phi_F T^* s_{11} + \alpha^T s_{11}^* - (\alpha \Phi_F + 1) E m_{11}}{T^* s_{11} - 2 E m_{11} \alpha + T s_{11}^* \alpha^2}, \quad (20)$$

and the definition of  $k_{31}$  given by Eq. (11) has been used. The slow wave contribution is easily obtained by swapping the  $F$  and  $S$  indices.

Finally, substituting the expression for the electric displacement field (19) into (18), the expression of the admittance of the piezoelectric and porous bar is obtained:

$$\frac{1}{Z} = i\omega \frac{l w}{t} TT^* \epsilon_{33}^{\text{eff}} \left[ (1 - k_{31}^2) + \kappa_F k_{31}^2 \frac{\tan(l\omega/2\nu_F)}{l\omega/2\nu_F} \right]$$

+ slow wave contribution. (21)

In many real cases the slow wave becomes negligible and is not observed. This fact is due to many different factors<sup>12</sup> with the high attenuation of this mode the most important one. In these cases, the contribution of the slow wave can be neglected, and the characterization procedure is based only on the contribution of the fast wave. Nevertheless, if the slow wave is observed then more information about the properties of the sample are obtained. In the following section a characterization procedure for the most common but restrictive case of negligible slow wave is presented.

Before moving forward to the characterization procedure it is important to point out that expression (21) reduces to the expression used in the Standards on Piezoelectricity<sup>4</sup> when the sample behaves as an homogeneous material and the coupling between the phases disappears. If the coupling mechanisms become negligible then:  $E m_{11} = \delta_{31} = b = \rho_a = 0$ . As the material behaves as an homogeneous sample and fluid and solid moves equally; that means  $\Phi_F = 1$ ,  $\Phi_S = 0$ . Then the following is finally obtained:

$$\kappa_F = 1 \quad (22)$$

$$k_{31}^2 = \frac{(d_{31}^*)^2}{TT^* \epsilon_{33}^{\text{eff}} TE^* s_{11}^*},$$

and these expressions give rise to the following impedance:

$$\frac{1}{Z} = i\omega \frac{l w}{t} \epsilon_{33}^{\text{eff}} \left[ (1 - k_{31}^2) + k_{31}^2 \frac{\tan(l\omega/2\nu_F)}{l\omega/2\nu_F} \right], \quad (23)$$

which is similar to the homogeneous case.

## VI. CHARACTERIZATION PROCEDURE FOR POROUS PIEZOELECTRIC BARS AND EXPERIMENTAL RESULTS

The mechanical resonance frequency  $f_r$  of the bar is obtained at the frequency at which the admittance [Eq. (21)] becomes infinite. When the contribution of the slow wave can be neglected (as indicated in the previous section), this frequency ( $f_r$ ) is obtained from:

$$f_r = \frac{\nu_F}{2l}, \quad \text{and} \quad \tan \frac{l\omega}{2\nu_F} = \infty. \quad (24)$$

This resonance is followed by an antiresonance frequency ( $f_a$ ) defined as the frequency at which the admittance is zero. Using these definitions, the next expression is obtained from Eq. (23):

$$\frac{k_{31}^2 - 1}{\kappa_F k_{31}^2} = \frac{\tan[\pi/2(f_a/f_r)]}{\pi/2(f_a/f_r)}. \quad (25)$$

The electromechanical coupling coefficient ( $k_{31}$ ) can be obtained by measuring the resonance and antiresonance frequencies. The difference in comparison to the standard procedure is that now a correction factor applies. This factor takes into account the influence of the coupling mechanism

between the phases as well as the effects of the dynamics of the two propagating modes. The following characterization procedure is proposed:

(1) The sample is characterized at empty pore condition (air saturation). In this case the coupling mechanisms between the phases are negligible. The following parameters are measured: the electric capacity at 1 kHz, the resonance and antiresonance frequencies ( $f_a$  and  $f_r$ ) of the impedance, and the weight. From these measurements, the following parameters are calculated:  $T_{s11}^*$ ,  $\epsilon_{33}^*$ , and  $d_{31}^*$ .

(2) The sample is saturated with a fluid (e.g., an oil, a polymer before curing, etc.) and the same procedure as before is repeated. The following parameters are calculated: the velocity of the fast wave,  $\nu_F$ , the dielectric permittivity,  $\epsilon_{33}^{\text{eff}}$ , and the porosity,  $\phi$ . In some cases it could be possible to measure the velocity of the slow longitudinal case. Nevertheless, as this mode is considered negligible, this measurement is not considered.

(3) If the fluid used to saturate the porous ceramic is not known, the following parameters must be measured: density, velocity of sound, and viscosity. The parameter  $T_{s11}^*$  is obtained from

$$T_{s11}^* \cong \frac{1}{\phi \nu_{\text{fluid}}^2 \rho_{\text{fluid}}}, \quad (26)$$

which corresponds to the effective elastic parameter of the fluid space obtained from the simple Voigt mixture rule (parallel connection).

(4) The porous structure is characterized: pore size and shape. The parameters  $b$  (flux resistivity) and  $\rho_a$  are obtained from the expressions provided from Biot's theory;<sup>8-15</sup> see Appendix B for a brief explanation.

(5) The wave equations (14) are applied to the data previously calculated, and the following parameters are obtained:  $E_{m11}$ ,  $\nu_s$ ,  $\Phi_F$ , and  $\Phi_S$  (if the slow wave is observed, then  $\nu_s$  can be experimentally obtained). The procedure involves the solution of Eqs. (14) for  $E_{m11}$  using the data of the measured velocity of the fast longitudinal mode. Once  $E_{m11}$  has been determined, this value is used to calculate the velocity of the slow wave and the  $\Phi_F$  and  $\Phi_S$  coefficients.

(6) Finally the expression for the admittance (23) and the definition of the electromechanical coupling coefficient (6a) are applied.  $\delta_{31}$  and  $k_{31}$  are obtained and the material is completely characterized. The calculation of these parameters is performed by means of an iterative method as it is not possible to obtain an exact expression for them. An initial guess for  $\delta_{31}$  is used and steps (5) and (6) are repeated until the convergence is found. Usually, the convergence is met before 15 iterations. Appendix C shows some of the aspects to consider for the numerical solution of the problem.

To illustrate the procedure, it is now applied to characterize a bar of a porous piezoelectric ceramic. The dimensions are 19 mm × 2 mm × 0.34 mm. The material is a commercial modified lead metaniobate, manufactured by Keramos. Two fillers were used, first a silicone oil and then an epoxy resin. In the case of the epoxy resin the cure process of the resin inside the pores was monitored, and the sample was characterized at a number of points. Details about the curing process of the resin are explained in Ref. 2.

The first step is to verify the assumption that the slow wave contribution is negligible. Using an HP 4194A impedance analyzer, the admittance of the saturated bar was displayed within a wide frequency range. Additional resonance peaks at low frequency due to the appearance of an additional slow longitudinal mode cannot be observed in this material either at air saturation or at oil/epoxy saturation. This fact led us to assume that in this case it is reasonable to ignore the presence of the slow wave in order to calculate the admittance of the porous bar.

Now it is possible to follow the characterization steps previously described. The HP 4194 A impedance analyzer was used for the electrical measurements. The results of the measurements for oil saturation and epoxy(fluid) saturation are shown in Table I.

In order to characterize the porous structure, SEM micrographs were taken and analyzed in a computer. Pore size and geometry can be obtained from the micrographs. Nevertheless, and due to the very irregular geometry of the pores, it is impossible to provide exact values for those magnitudes and therefore pore size and pore tortuosity cannot be determined with absolute accuracy. It is observed that the pore size changes between 1 and 5 micrometers. In addition, the tortuosity must be determined from theoretical expressions that depend on the shape of the pores or the grains. As actual pores and grains do not have an ideal shape, then the theoretical predictions provide a range of variation for the tortuosity rather than an exact value (Appendix B). In Appendix B it is shown that the sensitivity of the final output ( $k_{31}$ ) is very low or negligible to the actual variations of the pore size and that the use of different expressions to evaluate the tortuosity do not lead to different results. However, these are not the only parameters subjected to experimental errors (although they are those for which the errors are thought to be the highest) and any other of the material properties that must be measured beforehand is subjected to a certain degree of uncertainty. These errors may propagate during the iterative procedure proposed to solve the problem. This should be checked as it has been done here for the pore size and the tortuosity (Appendix B) to find out the influence of these errors over the accuracy of the final output.

Wave equations (14) are solved by the procedure outlined in Appendix C for the data shown in Table I. The results are summarized in Table II. The value of the electromechanical coupling coefficient obtained from the standard method is also shown. The most interesting effect is that the values of the  $k_{31}$  coefficient calculated by means of the standard procedure are much higher (40% for the oil saturation and 56% for the epoxy saturation) than the figures obtained by the new technique presented here. The overestimation of the classical results originates from the fact that the two-phase nature of the sample is not considered and, therefore, the interactions between the components are neglected. It is known from Refs. 1 to 3 that the effect of the new coupling mechanisms is that the conversion of energy from mechanical to electrical can take place also through the minor and passive phase and not exclusively through the piezoelectric effect in the active phase. Therefore, not all the converted energy from mechanical to electrical and vice versa can be

TABLE I. Experimental measurements for the characterization of an oil-saturated and an epoxy-saturated porous piezoelectric ceramic.

	Porous ceramic	Saturated ceramic		Filler	
		Fluid epoxy	Oil	Fluid epoxy	Oil
Relative dielectric constant	603	699	625	6.0	3.0
Density (kg/m <sup>3</sup> )	5472	5555	5549	1100	950
Resonance frequency (kHz)	74.63	93.81	79.65	***	***
Antiresonance frequency (kHz)	76.85	96.7	81.85	***	***
Piezoelectric constant $d_{31}$ (C/m)	$-6.5 \times 10^{-11}$	***	***	***	***
Velocity of sound propagation (m/s)	2835	3190	3027	1830	1000

attributed exclusively to the piezoelectric effect in the active phase. This is the main reason to explain why the corrected values provide a lower  $k_{31}$  electromechanical coefficient compared with the value measured using the standard procedure and the assumption that the sample is homogeneous.

Figure 3 shows the evolution of the electromechanical coupling coefficient ( $k_{31}$ ) during the curing of the epoxy embedded in the porous ceramic. The results obtained with the new technique (closed circles) are compared with those obtained from the standard technique (closed squares). In order to quantify the curing process the velocity of sound in the sample is considered. This parameter is easily measured and reflects very well the real state of the epoxy in the pores.<sup>2</sup>

As before, it is observed that the classical values are much higher than the values obtained by the new procedure. In addition, the classical values present a rather strange evolution. In the first stages of the curing process, the electromechanical coupling coefficient increases, but after a steady state, it decreases again so that the  $k_{31}$  coefficient of the epoxy-saturated ceramic is lower when the epoxy is solid than when it is fluid. This result is not confirmed by the new procedure. In this case, the electromechanical coupling coefficient increases continuously due to the stiffening of the epoxy inside the pores. When, finally, the epoxy solidifies, both results are quite close. This could be produced by the fact that the high stiffness of the epoxy produces a lower mechanical and piezoelectric coupling between the phases.

TABLE II. Obtained results from the characterization of the saturated porous ceramic (Table I). Both the Standard and the new technique results are shown.

	Oil saturation	Epoxy (fluid) saturation
$m_{11} \times 10^{-10}$ (m <sup>2</sup> /N)	-1.58	-1.10
$\tilde{d}_{31} \times 10^{-10}$ (C/N)	2.05	1.76
$k_{31}$	0.183	0.171
$k_{31}$ (standard)	0.256	0.269

The gel transition can be observed in the evolution of the  $k_{31}$  as a slight change of the shape in Fig. 3 ( $v \approx 3250$  m/s). Finally, it must be pointed out that for the final point, where the epoxy is fully solidified, the procedure explained here is working beyond the initial assumptions, as the minor phase is not a fluid.

As a first verification of this procedure, the obtained  $E_{m_{11}}$  parameter for the points presented in Fig. 3 were analyzed. As is explained in Appendix C, the parameter  $E_{m_{11}}$  only depends on the structure of the porous ceramic, and not on the fluid saturating it. Therefore it is expected that the calculated  $E_{m_{11}}$  parameter at each step in the curing process should be the same. The averaged value and deviation of  $E_{m_{11}}$  at 19 points during the cure process (as shown in Fig.

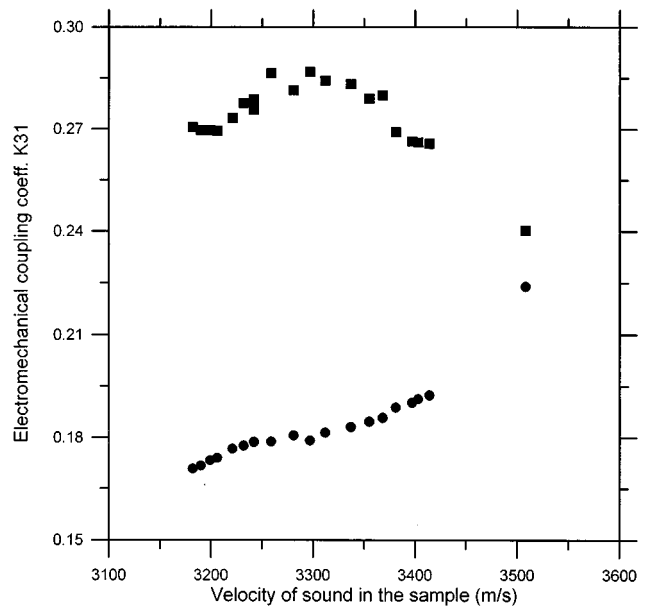


FIG. 3. Electromechanical coupling coefficient of an epoxy-saturated porous piezoelectric ceramic  $k_{31}$  versus the velocity of sound propagation. Standard results (closed squares). Proposed procedure (closed circles).

3) is  $(-1.06 \pm 0.06) \times 10^{-10} \text{ m}^2/\text{N}$ . That is, the fluctuations in the determination of  ${}^E m_{11}$  with the procedure presented here are about 6%.

## VII. CONCLUSIONS

A characterization procedure for porous piezoelectric ceramic bars has been developed. Suitable wave equations and boundary conditions considering the porous and biphasic nature of the material have been developed and used to derive a characterization procedure. Despite the complexity of the study of porous piezoelectric ceramics, the theoretical analysis gives rise to a characterization procedure that can be applied in a relative easy way. The method was applied to a commercial piezoelectric porous ceramic: modified lead metaniobate (k85 ceramic manufactured by KERAMOS). It was shown that the  $k_{31}$  obtained with the new characterization procedure differs by 40%–50% from the calculations of the standardized expressions. The standard value is overestimated due to the fact that energy conversion from mechanical to electrical and vice versa that takes place through interactions between the components is attributed only to the piezoelectric effect in the solid because the biphasic nature of the sample is neglected.

This new procedure permits the calculation of the effective electromechanical coupling coefficients of porous or composite piezoelectric materials very accurately and without errors due to the biphasic nature of the sample. This fact could be of particular importance in the modeling of ultrasonic transducers whose performance is strongly affected by errors in the estimation of their electromechanical coupling coefficients.

## ACKNOWLEDGMENT

The authors are grateful to Professor Gordon Hayward for his helpful suggestions.

## APPENDIX A: CALCULATION OF THE AMPLITUDES OF THE WAVES INSIDE THE RESONANT BAR

Considering the following boundary conditions at  $x=0$  and  $x=1$ , that correspond to the open-pore and free-surface case, for the geometry depicted in Fig. 1:

$$T_1^* = T_1 = 0,$$

and substituting into Eqs. (17), the following expressions for the parameters  $A$ ,  $B$ ,  $C$ , and  $D$  are obtained:

$$A = \frac{\nu_R}{\omega} \frac{d_{31}^* - \tilde{\delta}_{31} \Phi_S}{\Phi_F - \Phi_S} E_0, \quad (\text{A1})$$

$$C = \frac{\nu_S}{\omega} \frac{d_{31}^* - \tilde{\delta}_{31} \Phi_F}{\Phi_S - \Phi_F} E_0, \quad (\text{A2})$$

$$B = \frac{\nu_F}{\omega} (d_{31}^* - \tilde{\delta}_{31} \Phi_S) E_0 \frac{\cos(\omega l / \nu_F) - 1}{(\Phi_F - \Phi_S) \sin(\omega l / \nu_F)}, \quad (\text{A3})$$

$$D = \frac{\nu_S}{\omega} (d_{31}^* - \tilde{\delta}_{31} \Phi_F) E_0 \frac{\cos(\omega l / \nu_S) - 1}{(\Phi_S - \Phi_F) \sin(\omega l / \nu_S)}. \quad (\text{A4})$$

## APPENDIX B: CALCULATION OF FLUX RESISTIVITY AND INERTIAL COUPLING COEFFICIENTS

The flux resistivity ( $b$ ) and the inertial coupling ( $\rho_c$ ) coefficients are obtained by means of the same methods that are normally used in the study of sound propagation in liquid saturated porous solids. The flux resistivity is given by

$$b = \frac{3 \eta \phi \zeta}{a^2}, \quad (\text{B1})$$

where  $\eta$  is the fluid viscosity,  $\phi$  is the porosity, and  $a$  is the radius of the pore. This result is obtained for circular cross-section pores. The parameter  $\zeta$  is called the sinuosity and is introduced to take into account the variation of the cross section of the real pores in comparison with the idealized model. The main problem in this case is the determination of the effective pore size. The porous ceramics used in this work exhibit a pore size between  $1 \mu\text{m}$  and  $5 \mu\text{m}$ . That means that the flux resistivity could vary between  $4.5 \times 10^6 \text{ kg}/(\text{m}^3 \text{ s})$  and  $1.8 \times 10^7 \text{ kg}/(\text{m}^3 \text{ s})$ .

The calculation of the  $\rho_c$  coefficient involves another structural parameter, very important in the study of porous materials. This parameter is the tortuosity that takes account for the apparent increase of inertial mass of the fluid due to the constrains imposed to its movement by the presence of the solid frame. For some idealized structures it is possible to obtain an analytical expression for this parameter. A good review of the different structures and expressions for the tortuosity can be found in Ref. 13. For a self-similar random array of spheres, the tortuosity ( $\theta$ ) is given by

$$\theta = \phi^{-1/2}, \quad (\text{B2})$$

while for a self-similar random array of needles the result is

$$\theta = \phi^{-2/3}. \quad (\text{B3})$$

The porosity of the ceramics used in this work is 7.5%. A reasonable range for the tortuosity is from 2 to 6, which produces a variation of the  $\rho_a$  coefficient from  $-68 \text{ kg}/\text{m}^3$  to  $-300 \text{ kg}/\text{m}^3$ .

Table BI shows the calculated  $k_{31}$  of the oil-saturated porous piezoceramic for different values of the analyzed input parameters. From Table BI it can be observed that the final results remain unchanged for almost all cases, and that a small variation is always observed within range of the possible experimental error. Therefore, it is possible to conclude that the degree of accuracy of the determination of the input parameters is enough for the particular case here considered.

## APPENDIX C: CALCULATION OF $k_{31}$ : NUMERICAL AND ITERATIVE METHOD

Given the procedure outlined in Sec. VI, the numerical calculation of the electromechanical coupling coefficient is carried out as follows. Initially, a guess value for the  $\tilde{\delta}_{31}$  coefficient is considered. The number of iterations to be made until the convergence is found is not affected very much by the initial guess. The first step is to solve Eqs. (14) to obtain  ${}^E m_{11}$ . This requires the calculation of the roots of a fourth-order polynomial. The procedure is notably simplified by the fact that two of these roots correspond to the values

TABLE BI. Calculated electromechanical coupling coefficient ( $k_{31}$ ) of the oil-saturated porous piezoelectric ceramic for different values of the input parameters.

	$k_{31}$
Medium case	0.1834
$b = 1.8 \times 10^7$	0.1835
$b = 4.5 \times 10^6$	0.1834
$\rho_a = -70$	0.1834
$\rho_a = -300$	0.1834

that makes zero the determinant of the system of equations shown in Eq. (14); obviously these roots do not have physical sense and can be removed. These roots are:  $E m_{11} = \pm \sqrt{T} s_{11}^* T^* s_{11}$ . Once these roots are removed (the polynomial is twice deflated), the solutions are easily found as the order of the polynomial is reduced to two.

Two solutions are obtained for  $E m_{11}$ . It can be demonstrated from the Biot's theory, and from the relation of  $s_{ij}^*$ ,  $s_{ij}$ , and  $m_{ij}$  with the Biot's elastic coefficients  $P$ ,  $Q$ , and  $R$ , that  $E m_{11} \leq 0$ . Hence only one root for  $E m_{11}$  can be chosen.

Once  $E m_{11}$  has been obtained, the wave equations (14) are solved again to obtain the velocity of the slow wave compatible with the previous values of  $E m_{11}$  and  $\nu_F$ . These results are introduced in Eq. (15) and the oscillation relations between solid and fluid are obtained.

The electromechanical coupling coefficient is obtained from its definition Eq. (11) and from the measurements of the impedance [Eq. (25)]. The value of  $\tilde{\delta}_{31}$  that makes these two results agree is calculated. This value is used to restart the calculations again. The convergence for the electromechanical coupling coefficient is found, normally, before 20 iterations.

It is important to point out here that the coefficient  $E m_{11}$  only depends on the structure and not on the fluid saturating it. This result appears clear from the definition of this parameter and is confirmed if the Biot-Willis expressions (Ref. 14)

are used to work out the matrix of elastic coefficients of the fluid-saturated porous sample ( $P$ ,  $N$ ,  $Q$ , and  $R$ ) and it is then inverted to obtain the equivalent parameters of  $s_{ij}^*$ ,  $s_{ij}$ , and  $m_{ij}$ . Therefore, the procedure explained here should provide the same result for the  $E m_{11}$  coefficient when the same porous ceramic is saturated by different fluids, or the properties of the fluid change.

<sup>1</sup>T. E. Gómez and F. Montero, "Highly coupled dielectric behaviour of porous ceramics embedding a polymer," *Appl. Phys. Lett.* **68**, 263–265 (1996).

<sup>2</sup>T. E. Gómez and F. Montero, "New constitutive relations for piezoelectric composites and porous piezoelectric ceramics," *J. Acoust. Soc. Am.* **100**, 3104–3114 (1996).

<sup>3</sup>T. E. Gómez and F. Montero, "Piezocomposites of complex microstructure: Theory and experimental assessment of the coupling between phases," *IEEE Ultrason. Ferroelectr. Freq. Control* **44**, 208–217 (1997).

<sup>4</sup>IEEE Standard on Piezoelectricity ANSI/IEEE Std. 176–1987.

<sup>5</sup>T. E. Gómez, A. M. Gonzalez, J. de Frutos, and F. Montero, "Piezoelectric characterisation of porous piezoceramics," 1996 IEEE Ultrasonics Symposium Conference Proceedings, San Antonio, Texas, 519–522.

<sup>6</sup>M. A. Biot, "Theory of propagation of elastic waves in a fluid-saturated porous solid. I. Low-frequency range," *J. Acoust. Soc. Am.* **28**, 168–178 (1956).

<sup>7</sup>M. A. Biot, "Theory of propagation of elastic waves in a fluid-saturated porous solid. II. Higher frequency range," *J. Acoust. Soc. Am.* **28**, 179–191 (1956).

<sup>8</sup>S. R. Pride and M. W. Haartsen, "Electroseismic wave properties," *J. Acoust. Soc. Am.* **100**, 1301–1315 (1996).

<sup>9</sup>H. Deresiewicz and J. T. Rice, "The effect of boundaries on wave propagation in a liquid-filled porous solid: III. Reflection of plane waves at a free plane boundary (General case)," *Bull. Seismol. Soc. Am.* **52**, 595–625 (1962).

<sup>10</sup>H. Deresiewicz and R. Skalak, "On uniqueness in dynamic poroelasticity," *Bull. Seismol. Soc. Am.* **53**, 783–788 (1963).

<sup>11</sup>P. Nagy and G. Blaho, "Experimental measurements of surface stiffness on water-saturated porous solids," *J. Acoust. Soc. Am.* **95**, 828–835 (1994).

<sup>12</sup>T. E. Gómez, L. Elvira, and E. Riera, "Generation of the slow wave to characterise air filled porous fabrics," *J. Appl. Phys.* **78**, 2843–2845 (1995).

<sup>13</sup>S. G. Kargl and R. Lim, "A transition-matrix formulation of scattering in homogeneous, saturated, porous media," *J. Acoust. Soc. Am.* **94**, 1527–1550 (1993).

<sup>14</sup>M. A. Biot and D. G. Willis, "The elastic coefficients of the theory of consolidation," *J. Appl. Mech.* **24**, 594–601 (1957).

# Vibration and dynamic response control of cantilevers carrying externally mounted stores

L. Librescu and S. S. Na

*Engineering Science and Mechanics Department, Virginia Polytechnic Institute & State University, Blacksburg, Virginia 24061-0219*

(Received 31 October 1996; accepted for publication 19 August 1997)

The vibrational and dynamic response control of cantilevers carrying externally mounted stores is investigated. The cantilevered structure is modeled as a thin-walled beam of arbitrary cross section and incorporates a number of nonclassical effects such as transverse shear, secondary warping, anisotropy of constituent materials, and heterogeneity of the construction. The control is carried out via a dynamic bending moment applied at the tip of the structure. A feedback control law relating the boundary moment with one of the kinematical variables characterizing the response of the beam is implemented, and its results upon the closed-loop eigenfrequencies and dynamic response are highlighted. The obtained numerical results emphasize the efficiency of this control methodology to enhance, without weight penalties, vibrational and dynamic response behavior and inhibit and even suppress the occurrence of the resonance phenomenon. © 1997 Acoustical Society of America. [S0001-4966(97)01712-8]

PACS numbers: 43.40.Cw, 43.40.Vn [PJR]

## INTRODUCTION

The cantilever beams carrying externally mounted stores can serve as a basic model for a number of structures used in the aeronautical, aerospace, as well as in other fields of the advanced technology.

Civil and military airplane wings are designed to carry heavy external mounted stores along their span. Depending on their magnitude and location, drastic reduction of natural eigenfrequencies and modification of the eigenmodes are experienced (e.g., see Refs. 1 and 2). These modifications can result in a deterioration of the dynamic response to time-dependent excitations and can also precipitate the occurrence of the flutter instability (e.g., see Refs. 3 and 4).

As robot manipulator arms, space booms, or antennas operating in space, they are required to be lightweight, strong, and of high precision in their mission. Uncontrolled vibrations can result in drastic reductions of the accuracy and precision of their operations. In order to be able to control the dynamic response of these structures under time-dependent external excitations and inhibit the damaging effects of vibrations without weight penalties, new technologies have to be implemented.

Toward this end, in this paper a number of results related with the vibrational and dynamic response control of cantilevered beams carrying externally mounted stores is addressed. The control mechanism is achieved through the action of a bending moment applied at the tip of the beam. This boundary moment is related, via a linear functional relationship, with the kinematical response quantities, appropriately selected. Such a feedback control methodology was mathematically substantiated quite recently, see, e.g., Refs. 5 and 6. Consistent with the approach in Refs. 7 and 8, in this paper, the implemented feedback control law features a dynamic character. This constitutes a basic departure from the ones in Refs. 9–14, where the adopted control law has a

static character and which should be much less efficient than the dynamic one.

In the forthcoming developments, the theory of cantilevers incorporating dynamic feedback control capabilities will be addressed and its implications upon their free vibration and dynamic response will be investigated.

## I. GENERAL CONSIDERATIONS. BASIC ASSUMPTIONS

The case of the cantilevered thin-walled beams of arbitrary closed cross section is considered. It is assumed that the beam is symmetrically composed of transversely isotropic material layers (the surface of isotropy in each material layer being parallel to the reference surface of the beam structure).

It is assumed that, in addition to a system of concentrated stores of mass  $m_j$  and mass moment of inertia  $I_j$  (about their centroid) located at  $z = z_j$ , ( $j = 1, J$ ), the beam carries also a tip mass of characteristics  $M$  and  $I_M$ . In the case of an airplane wing/robot arm the tip mass can simulate the presence of a tank/payload (see Fig. 1). Herein  $J$  denotes the total number of wing-mounted stores.

Two systems of coordinates are used in the forthcoming developments, namely: (i) a global Cartesian system  $(x, y, z)$ , where  $(x, y)$  denote the cross-section beam coordinates while the spanwise  $z$  axis is assumed to coincide with the locus of symmetrical points of the cross sections along the wing span, and (ii) a local orthogonal coordinate system  $(n, s, z)$  where  $n$  denotes the thicknesswise coordinate normal to the beam midsurface and  $s$  the tangential coordinate along the contour line of the beam cross section.

The equations governing the motion of cantilever beams are established in the context of the following assumptions:

(i) The cross sections of the beam do not deform in their own planes, (ii) The effects of transverse shear flexibility featured by the advanced composite materials are taken into consideration, (iii) The hoop stress resultant  $N_{ss}$  is consid-



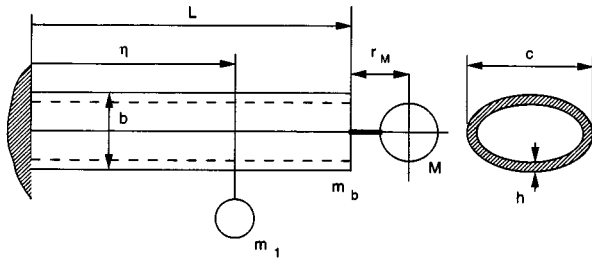


FIG. 1. Geometry of the cantilever beam carrying a unistore and a tip-mass.

ered negligibly small with respect to the remaining ones, (iv) The centroids of the attached masses are distributed along the  $z$  axis

As a result of the transverse-isotropy of the constituent materials and in the light of assumption (iv), an exact decoupling of transverse bending (expressed in terms of variables  $v_0$  and  $\theta_x$ ), lateral bending (expressed in terms of  $u_0$  and  $\theta_y$ ), and twist ( $\Theta$ ) is obtained. For the problem studied herein only transverse bending will be considered. However, since secondary warping induces transverse bending (See Ref. 16), this effect will also be incorporated.

## II. GOVERNING EQUATION

Based upon the previously stipulated assumptions, the one-dimensional (1-D) version of the equations governing the flexural motion about the equilibrium position as derived in Refs. 11 and 12 are

$$a_{55}(v_0'' + \theta_x') - \left[ b_1 \ddot{v}_0 + \sum_{j=1}^J m_j \ddot{v}_0 \delta(z - z_j) \right] + p_y = 0, \quad (1a)$$

$$a_{33} \theta_x'' - a_{55}(v_0' + \theta_x) - \left[ (b_4 + b_{14}) \ddot{\theta}_x + \sum_{j=1}^J I_j \ddot{\theta}_x \delta(z - z_j) \right] = 0, \quad (1b)$$

For the beam considered to be clamped at the root and free at the tip, the associated boundary conditions are

$$v_0 = \theta_x = 0 \quad \text{at } z=0 \quad (2)$$

and

$$a_{55}(v_0' + \theta_x) + M \ddot{v}_0 - M r_M \ddot{\theta}_x = 0, \quad (3a)$$

$$a_{33} \theta_x' + I_M \ddot{\theta}_x - M r_M \ddot{v}_0 = \hat{M}_x. \quad (3b)$$

In these equations  $v_0(z,t)$  and  $\theta_x(z,t)$  denote the transverse deflection and rotation about the  $x$  axis, respectively,  $\delta(\cdot)$  denotes the Dirac's distribution, and  $a_{33}$  and  $a_{55}$  denote the bending and transverse shear stiffness, respectively. They are defined as

$$a_{33} = \oint_C \left[ \bar{K}_{11} y^2 + \hat{K}_{11} \left( \frac{dx}{ds} \right)^2 \right] ds, \quad (4a)$$

$$a_{55} = \oint_C \left[ A_{66} \left( \frac{dy}{ds} \right)^2 + A_{44} \left( \frac{dx}{ds} \right)^2 \right] ds, \quad (4b)$$

where

$$\bar{K}_{11} = A_{11} - \frac{A_{12}^2}{A_{11}}, \quad (5a)$$

$$\hat{K}_{11} = D_{11} \quad (5b)$$

while

$$(A_{ij}, D_{ij}) = \sum_{k=1}^N \int_{n_{(k-1)}}^{n_{(k)}} C_{ij}^{(k)}(1, n^2) dn \quad (6)$$

denote the stretching and bending stiffness quantities, respectively, while  $N$  denotes the number of constituent layers.

In Eq. (6),  $C_{ij}$  denotes the elastic coefficients, which, for the present type of anisotropy, are expressed in terms of the engineering constants as

$$C_{11} = (E\nu'^2 - E')E/\Delta, \quad (7a)$$

$$C_{12} = -(E\nu'^2 + E'\nu)E/\Delta, \quad (7b)$$

$$C_{13} = -\nu'(1 + \nu)EE'/\Delta, \quad (7c)$$

$$C_{33} = -(1 - \nu^2)E'^2/\Delta, \quad (7d)$$

$$C_{44} = G', \quad (7e)$$

$$\frac{C_{11} - C_{12}}{2} = G \left( \equiv \frac{E}{2(1 + \nu)} \right). \quad (7f)$$

In these expressions  $\Delta = (1 + \nu)(2E\nu'^2 + E'\nu - E')$ ;  $E$ ,  $\nu$ , and  $E'$ ,  $\nu'$  denote Young's modulus and Poisson's ratio in the plane of isotropy and transverse to the plane of isotropy, respectively, while  $G'$  and  $G$  denote the transverse shear and in-plane shear modulus, respectively.

In addition to these notations,

$$(b_1, b_4) = \oint_C m_0(1, y^2) ds, \quad (8a)$$

$$b_{14} = \oint_C m_2 \left[ \frac{dx}{ds} \right]^2 ds, \quad (8b)$$

stand for the mass terms, where

$$(m_0, m_2) = \sum_{k=1}^N \int_{h_{(k-1)}}^{h_{(k)}} \rho_{(k)}(1, n^2) dn, \quad (9)$$

$\rho$  denotes the mass density of the constituent materials,  $p_y(\equiv p_y(z,t))$  is the distributed transverse load (per unit span of the beam), while  $r_M$  denotes the offset between the beam extremity and the centroid of the tip mass.

The primes denote derivatives with respect to the spanwise  $z$  coordinate while the superposed dots denote derivatives with respect to time  $t$ ,  $\oint_C(\cdot) ds$  denotes the integral around the circumference of the midline contour of the beam.

In the boundary condition [Eq. (3b)],  $\hat{M}_x$  stands for the boundary moment control.

## III. SPECIAL CASE OF GOVERNING EQUATIONS

The Bernoulli-Euler counterpart of the governing equations (1) and boundary conditions, Eqs. (2) and (3), is ob-

tained through the elimination of  $a_{55}(v'_0 + \theta'_x)$  in Eqs. (1) and (3), operation followed by consideration of  $\theta_x = -v'_0$ . In such a way, the classical equations governing the transverse bending of thin-walled beams carrying concentrated masses are

$$a_{33}v_0'''' - \left[ (b_4 + b_{14})\ddot{v}_0 + \sum_{j=1}^J I_j \ddot{v}_0'' \delta(z - z_j) \right] + \left[ b_1 \ddot{v}_0 + \sum_{j=1}^J m_j \ddot{v}_0 \delta(z - z_j) \right] = p_y, \quad (10)$$

while the boundary conditions to be prescribed are

$$v_0 = v'_0 = 0 \quad \text{at } z = 0 \quad (11)$$

and

$$\left. \begin{aligned} a_{33}v_0''' &= M\ddot{v}_0 + Mr_M\dot{v}_0', \\ a_{33}v_0'' - I_M\ddot{v}_0' + Mr_M\ddot{v}_0 &= \hat{M}_x \end{aligned} \right\} \quad \text{at } z = L. \quad (12)$$

It should be remarked that both the shearable and the classical nonshearable thin-walled beam models provide fourth-order governing equation systems (see Ref. 12).

In Eqs. (1) and (3) as well as in Eqs. (10) and (12), the terms identifying the rotatory inertia effect are underscored by a dotted line.

#### IV. THE CONTROL LAW

The adaptive nature of the cantilevered beam is introduced by requiring that the applied electric field  $\mathcal{E}_3$ , or in other words the piezoelectrically induced bending moment at the beam tip, be related to one of the mechanical quantities characterizing its static or dynamic response. With this in mind, a number of feedback control laws featuring a static or a dynamic character have been implemented.

The static-type of control laws have been formulated by stating that the induced bending moment at the beam tip is proportional either with the mechanical bending moment at the beam root, or with the vertical deflection at the wing tip (see Refs. 9–14).

In contrast to the previously mentioned feedback control laws the one referred to as the velocity feedback control appears (see Refs. 7, 8, and 15) to be a good candidate for the problem at hand.

Within this control law, the moment  $\hat{M}_x$  at the beam tip is proportional to the velocity  $\dot{\theta}_x(L)$  at the same location. A more explicit expression of this feedback control law is derived from Eq. (3b) as

$$\begin{aligned} \theta'_x(L) + I_M/(a_{33})\ddot{\theta}_x(L) + Mr_M/(a_{33})\ddot{v}_0(L) \\ = (k_v/a_{33})\dot{\theta}_x(L), \end{aligned} \quad (13)$$

where  $k_v$  denotes the (dimensional) feedback gain.

In contrast to the previously mentioned control laws, the present one has a dynamic character and, as a result of it, damping is adaptively induced. Consequently, enhanced dynamic response performances are expected from its application.

Related with the bending moment at the beam tip, this can be generated via the use of the converse piezoelectric effect featured by these devices. In Refs. 7–13 it was shown that, in the case of piezoactuators spread over the entire beam span, polarized in the thickness direction, and featuring in-plane isotropy, under an applied electrical field  $\mathcal{E}_3$ , a bending moment at the beam tip is generated.

It should be mentioned that the piezoelectric induced moment  $\hat{M}_x$  is different from zero only if external voltages, of opposite signs, are applied in the upper and bottom piezo-actuator layers (out of phase activation).

For feedback control, the electric field  $\mathcal{E}_3$  on which the induced bending moment depends should be related through a prescribed functional relationship with the mechanical quantities characterizing the wing's response. In the present case, the relationship is established with the rotational velocity at the beam tip.

#### V. PROBLEMS STUDIED

For the sake of numerical illustration, the case of a cylindrical thin-walled beam of a biconvex cross-section profile is adopted. The geometry of the cantilevered beam is shown in Fig. 1.

It is also considered, unless otherwise stated, that the beam carries a store of mass  $m_1$  located along the beam span  $\eta$  ( $\equiv z/L$ ) and a tip mass  $M$  as well. The beam mass is  $m_b \equiv b_1L$ , where  $b_1$  is the beam mass per unit length.

Within this paper two problems will be analyzed: the control of free vibration (problem I) and the dynamic response control to external excitation (problem II).

To analyze problem I, the external load term has to be discarded and all field variables, generically denoted as  $F(z, t)$ , have to be represented as

$$F(z, t) = \bar{F}(z)\exp(\lambda t), \quad (14)$$

where  $\lambda$  is the closed-loop eigenvalue.

Since the eigenvalue is contained in both the governing equations and boundary conditions, it becomes apparent that the solution of the closed-loop eigenvalue and of that of the dynamic problems constitute a rather involved task.

The results obtained within the study of problem I are useful not only as a basic ingredient in the approach of problem II, but also in the study of the flutter instability of adaptive aircraft wings carrying external stores.

For problem II, one considers that the beam is excited by a concentrated harmonically time-dependent load located along the beam  $z$  axis. Hence the load  $p_y$  is represented as

$$p_y(z, t) = F_0\delta(z - z_0)\exp(i\omega t), \quad (15)$$

where  $z_0$ ,  $F_0$ , and  $\omega$  denote spanwise location of the load, and its amplitude and excitation frequency, respectively.

Both problems are solved via the extended Galerkin method (EGM) extensively used in Refs. 9–13.

As a matter of fact, the accuracy of this solution methodology was checked by comparing its predictions with the

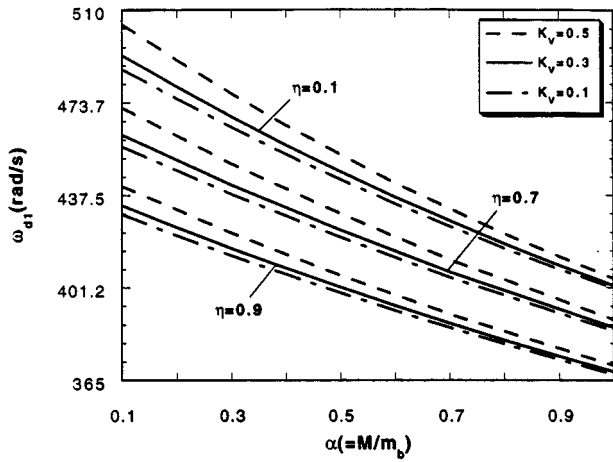


FIG. 2. The first closed-loop eigenfrequency versus the parameter  $\alpha$ , for three values of the feedback gain and of the position of the unistore along the beam span ( $m_1/m_b=0.1$ ).

ones based on an exact method, i.e., Laplace transform method (see Ref. 17) and the agreement was excellent. Once the frequency response functions corresponding to a given excitation frequency are determined [i.e.,  $v_0(z_0, \omega)$  and  $\theta_x(z_0, \omega)$ ], their time-domain counterparts can be obtained as

$$\begin{aligned} \begin{Bmatrix} v_0(z_0, t) \\ \theta_x(z_0, t) \end{Bmatrix} &= \mathcal{F}^{-1} \begin{Bmatrix} v_0(z_0, \omega) \\ \theta_x(z_0, \omega) \end{Bmatrix} \\ &= \frac{1}{2\pi} \int_{-\infty}^{+\infty} \begin{Bmatrix} v_0(z_0, \omega) \\ \theta_x(z_0, \omega) \end{Bmatrix} \exp(i\omega t) d\omega, \end{aligned} \quad (16)$$

where  $\mathcal{F}^{-1}$  denotes the inverse Fourier transform.

The results of the study of problem II can constitute a good basis for a more reliable design of advanced structural systems as, e.g., aircraft wings or robot arm manipulators working in space which can carry stores and are exposed to external excitations.

## VI. NUMERICAL APPLICATIONS AND DISCUSSION

Within this section, numerical results pertaining to control of free vibration and dynamic response will be supplied and discussed.

### A. Free vibration control

The closed-loop eigenfrequencies are obtained from Eqs. (1) and their associated boundary conditions Eqs. (2) and (3) considered in conjunction with the control law, Eq. (13). Within this problem the external load term is discarded and the field variables are represented in the form of Eq. (14). For the controlled structure, implying  $k_v \neq 0$ , the eigenvalues  $\lambda$  are complex valued quantities expressible as

$$\lambda = \sigma \pm i\omega_d. \quad (17)$$

Based on their expressions one can determine the damped frequency  $\omega_d$  and the damping ratio  $\zeta$  defined as the imagi-

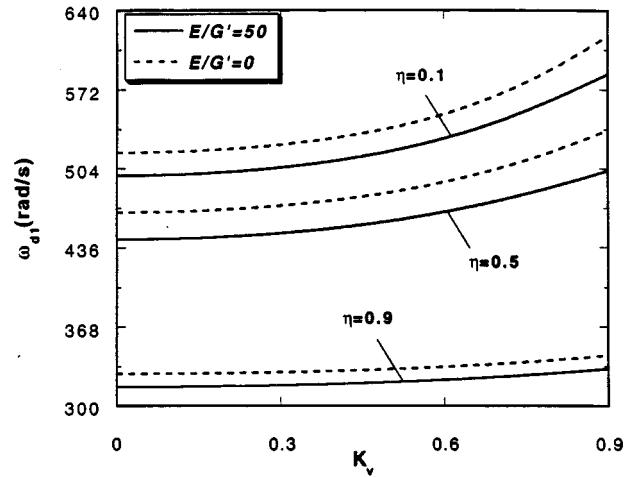


FIG. 3. The first closed-loop eigenfrequency versus the velocity feedback gain, for three positions of the unistore along the beam span and for the shearable and nonshearable beam. ( $M=0$ ,  $AR=8$ ).

nary and the negative of the normalized real part of Eq. (17), respectively, i.e.,

$$\zeta = -\sigma / (\sigma^2 + \omega_d^2)^{1/2}. \quad (18)$$

Throughout the numerical illustrations, unless otherwise stated, it was considered that  $E/G' = 50$ ,  $M/m_b = 0.1$ ,  $r_M = 0.05L$ ,  $L = 1$  m,  $b = 0.068$  m, and  $c = 0.25$  m. These dimensions correspond to a beam of aspect ratio,  $AR = 8$  where  $AR = 2L/c$ .

Figure 2 displays the influence of a tip mass characterized by the mass ratio  $\alpha = M/m_b$  on the first closed-loop eigenfrequency of a shear deformable beam carrying an unistore at various locations  $\eta (=z/L)$  along the beam span.

From this graph it becomes apparent that with the increase of the nondimensional feedback gain  $K_v$  ( $\equiv k_v L \bar{\omega} / a_{33}$ ), the decay of the eigenfrequency resulting from the increase of  $\alpha$  and location of the store towards the beam tip can be counteracted. At the same time, the results

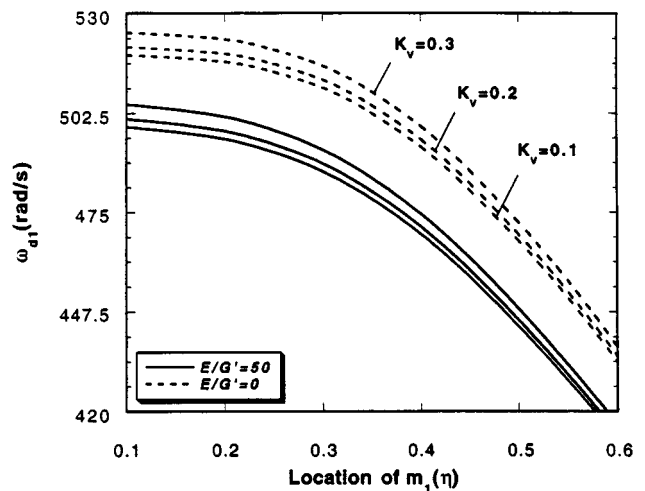


FIG. 4. The first closed-loop eigenfrequency versus the location  $\eta$  of the unistore for the shearable and nonshearable and controlled and uncontrolled beam ( $m_1/m_b=0.5$ ,  $AR=8$ ,  $M=0$ ).

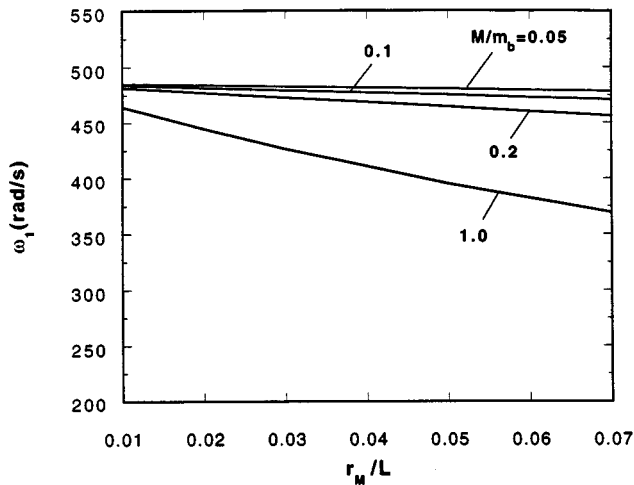


FIG. 5. The first open-loop eigenfrequency versus the dimensionless offset between the beam tip and the centroid of the tip-mass for four values of the ratio  $M/m_b$  ( $E/G' = 50$ ,  $m_1/m_b = 0.1$ ,  $\eta = 0.5$ ).

reveal that with the increase of  $\alpha$ , a decay in the efficiency of the control capability is experienced. Herein  $\bar{\omega} (= 128.16 \text{ rad/s})$  is the fundamental eigenfrequency of the uncontrolled beam characterized by  $E/G' = 50$  and  $AR = 16$ .

Figure 3 depicts the variation of the first damped eigenfrequency versus the feedback gain  $K_v$ , for three values of the location of the unistore and for the shearable and nonshearable beam models. The results reveal that: (a) as expected, the Bernoulli–Euler beam model (i.e., the model corresponding to  $E/G' = 0$ ) overestimates the frequencies predicted by the actual shearable one and (b) the frequencies and control efficiency diminish with the increase of the distance of the store location, towards the beam tip.

The effect of location of the unistore along the beam span upon the closed-loop first eigenfrequency is highlighted in Fig. 4. Herein, the behavior resulting from the consideration of both shearable and nonshearable beam models are illustrated. The results presented in this figure enforce the previously obtained conclusions regarding the influence, on the closed-loop first eigenfrequencies, of transverse shear

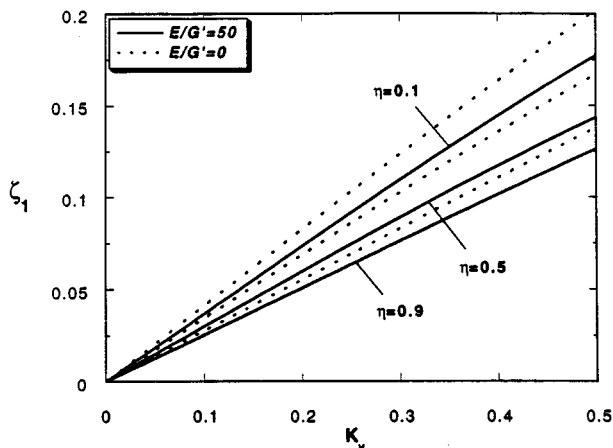


FIG. 6. Induced damping versus the feedback gain for three values of the unistore location and shearable and nonshearable beam ( $m_1/b_m = 0.5$ ,  $AR = 8$ ,  $M = 0$ ).

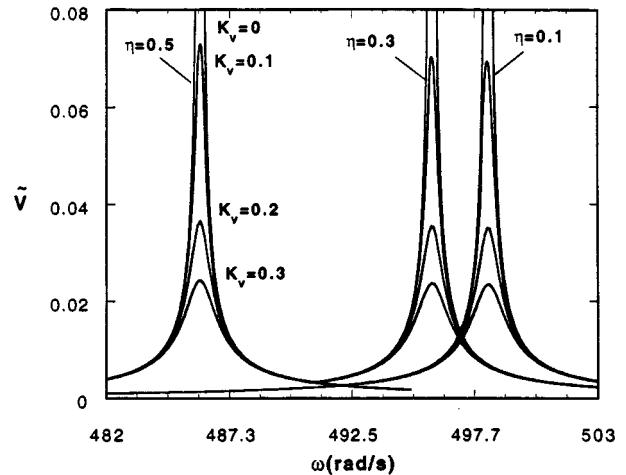


FIG. 7. Normalized steady-state deflection amplitude versus the excitation frequency for three locations of the unistore and for the controlled and uncontrolled beam ( $m_1/m_b = 0.1$ ,  $M = 0$ ).

flexibility and position of the store along the beam span.

Figure 5 highlights the influence of the distance  $r_M$  on the first eigenfrequency of the uncontrolled beam. The results obtained from this figure reveal that for smaller ratios  $M/m_b$  the conclusions in Ref. 18 regarding the negligible influence of  $r_M$  on the eigenfrequency are in perfect agreement with the present ones. However, with the increase of the ratio  $M/m_b$ , as is usual in space applications (see Ref. 19), this quantity can play a non-negligible influence on the decay of eigenfrequencies.

Figure 6 displays the variation of the first mode induced damping  $\zeta_1$  as a function of the feedback gain in the case of a beam carrying a unistore located at different locations. The results reveal that: (a) the increase in the induced damping varies almost linearly with the increase of the feedback gain  $K_v$ , a trend which is consistent with that in Ref. 20; (b) as expected, the Bernoulli–Euler beam model overestimates the actual damping induced in the shear deformable beam coun-

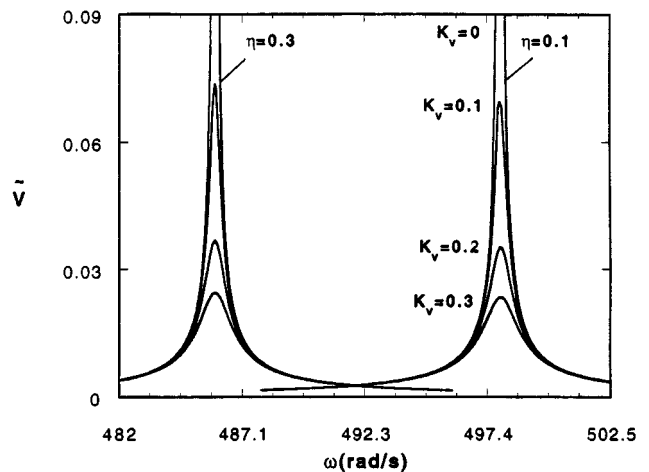


FIG. 8. Normalized steady-state deflection amplitude versus the excitation frequency for two locations of the unistore and for the controlled and uncontrolled beam ( $M = 0$ ,  $m_1/m_b = 0.5$ ).

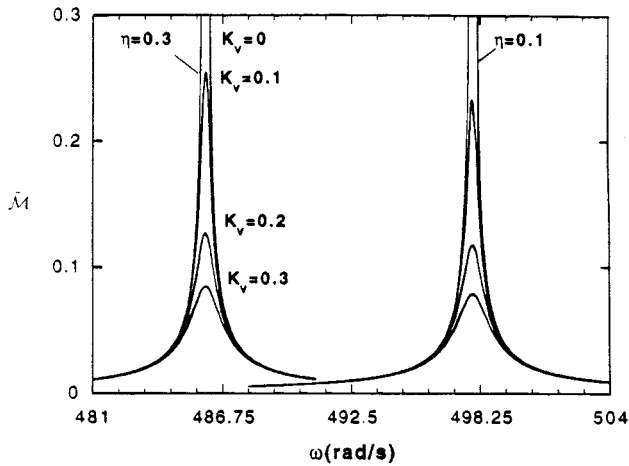


FIG. 9. Steady-state dimensionless root moment amplitude versus the excitation frequency for values of the location of the unistore ( $m_1/m_b=0.5$ ) and for the controlled and uncontrolled beam ( $M=0$ ).

terpart, overestimation which is exacerbated by the increase of  $K_v$  and shift of the store toward the beam root.

### B. Dynamic response control

Related with the dynamic response problem the variation of the dimensionless steady-state response amplitude  $\tilde{V}$  ( $\equiv \bar{v}_0/L$ ) of the beam tip, for the noncontrolled and controlled beam, as a function of the excitation frequency is depicted in Figs. 7 and 8, where the case of the unistore of  $m_1/m_b=0.1$  and 0.5, respectively, differently located along the beam span is considered.

In these graphs a shearable beam model is considered. The results reveal: (a) the capability of the control methodology to contain the level of vibration at the beam tip via the generation of damping, (b) the effect played by the location of the unistore along the beam span consisting of the shift of the resonance frequency towards larger frequencies when the unistore is located closer to the beam root, and, towards lower frequencies when the store is located closer to the beam tip. The results not displayed here reveal that the latter

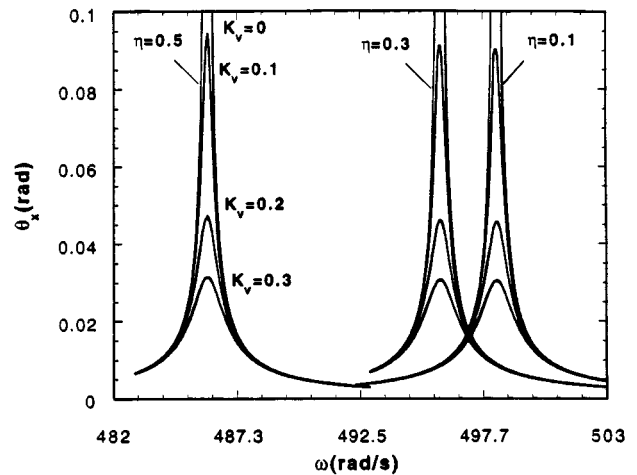


FIG. 11. Steady-state rotation amplitude versus the excitation frequency for three values of the location of the unistore ( $m_1/m_b=0.1$ ), and for controlled and uncontrolled beam ( $M=0$ ).

shift is further exacerbated when, in addition to the unistore, a tip mass is carried by the beam.

Figures 9 and 10 display the variation of steady-state dimensionless moment amplitude  $\tilde{\mathcal{M}}(\equiv \theta'_x(0))$  at the beam root versus the excitation frequency. The results reveal that while the location along the beam span of the unistore has little effect upon the amplitude of the response, the shift towards lower or larger resonance frequencies (depending on the location of the store toward the beam tip or beam root, respectively) remains the most important effect in the context of the beam with attached stores or tip mass.

In this case, the shift of the resonance frequencies follows the same trend with respect to the ratio  $m_1/m_b$  and the presence of the tip mass, as in the case of the dynamic response deflection amplitude (see Figs. 7 and 8). For the sake of completeness, Fig. 11 presents the variation of the steady-state rotation amplitude  $\theta_x$  versus the excitation frequency. In this respect, similar conclusions to the ones highlighted by the behaviors of  $\tilde{V}$  and  $\tilde{\mathcal{M}}$  can be outlined in this case as well.

## VII. CONCLUSIONS

A control methodology carried out via the boundary moment and of a dynamic feedback control law aimed at enhancing the free vibration and dynamic response of cantilever beams carrying heavy concentrated masses was developed. The obtained results reveal that by using this control methodology, it is possible to modify in a beneficial and predictable way the vibration and dynamic response of these structures, as well to inhibit and even avoid, without weight penalties, the occurrence of the resonance phenomenon.

It should also be remarked that the control laws used in Refs. 9–13 and in the present paper are complementary to each other, in the sense that a combination of them can be used towards a more efficient static and dynamic control of such structures.

Finally, it should be added that use of segmented piezoelectric actuators, and specially of piezoelectric patches conveniently

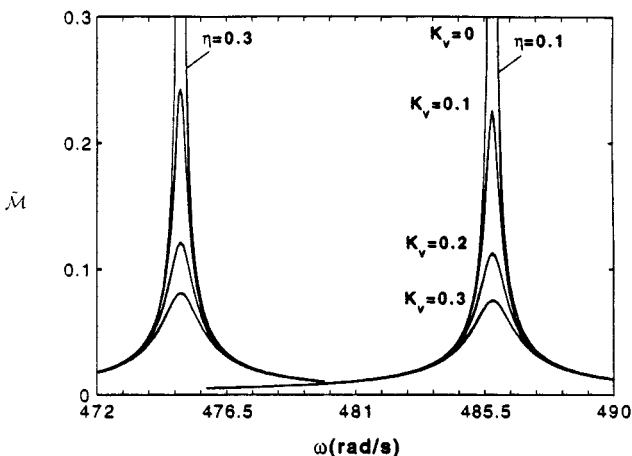


FIG. 10. The counterpart of Fig. 9 for the case when  $M \neq 0$ .

located, while resulting in a significant weight saving, would not yield a less control efficiency as compared to that provided by piezoactuators spread over the entire beam span. The preliminary results obtained so far, fully justify this statement.

- <sup>1</sup>J. C. Bruch, Jr. and T. P. Mitchell, "Vibrations of a mass-loaded clamped-free Timoshenko beam," *J. Sound Vib.* **114**, 341–345 (1987).
- <sup>2</sup>H. Abramovich and O. Hamburger, "A vibration of a cantilever Timoshenko beam with a tip mass," *J. Sound Vib.* **148**, 162–170 (1991).
- <sup>3</sup>W. E. Triplett, H. P. F. Kappus, and R. J. Landy, "Active flutter control-An adaptable application to wing/store flutter," *J. Aircr.* **10**(11), 669–678 (1973).
- <sup>4</sup>H. Zimmerman and S. Vogel, "Influence of main design parameters on flutter behavior of large aircraft configurations with heavy concentrated masses," Report No. AGARD-CP-354, pp. 6-1 to 6-11 (1983).
- <sup>5</sup>J. E. Lagnese and J. L. Lions, "Boundary stabilization of thin plates," in *Collection RMA* (Masson, Paris, 1988).
- <sup>6</sup>J. E. Lagnese, "Boundary stabilization of thin plates," *SIAM Studies in Applied Mechanics* (SIAM, Philadelphia, 1989).
- <sup>7</sup>T. Bailey and J. E. Hubbard, Jr., "Distributed piezoelectric-polymer active vibration control of a cantilever beam" *J. Guid. Control. Dyn.* **8**, 605–611 (1985).
- <sup>8</sup>H. S. Tzou, *Piezoelectric Shells, Distributed Sensing and Control of Continua* (Kluwer Academic, Dordrecht, 1993).
- <sup>9</sup>O. Song, L. Librescu, and C. A. Rogers, "Application of adaptive technology to static aeroelastic control of wing structures," *AIAA J.* **30**, 2882–2889 (1992).
- <sup>10</sup>L. Librescu, O. Song, and C. A. Rogers, "Adaptive vibrational behavior of cantilevered structures modeled as composite thin-walled beams," *Int. J. Eng. Sci.* **31**, 775–792 (1993).
- <sup>11</sup>O. Song, L. Librescu, and C. A. Rogers, "Adaptive response control of cantilevered thin-walled beams carrying heavy concentrated masses," *J. Intell. Mater. Syst. Struct.* **5**, 42–48 (1994).
- <sup>12</sup>O. Song and L. Librescu, "Bending vibrations of adaptive cantilevers with external stores," *Int. J. Mech. Sci.* **38**, 483–498 (1996).
- <sup>13</sup>L. Librescu, L. Meirovitch, and O. Song, "Integrated structural tailoring and adaptive materials control for advanced aircraft wings," *J. Aircr.* **33**, 203–213 (1996).
- <sup>14</sup>H. S. Tzou and J. R. Zhong, "Adaptive piezoelectric structures: Theory and experiment," *Active Materials and Adaptive Structures, Proceedings of the ADPA/AIAA/ASME/APIE Conference on Active Materials and Adaptive Structures*, Alexandria, VA, edited by G. J. Knowles, pp. 719–724.
- <sup>15</sup>A. Baz, "Boundary control of beams using active constrained layer damping," *J. Vib. Acoust., Trans. ASME* **9**, 166–172 (1997).
- <sup>16</sup>A. Gjelsvik, *The Theory of Thin Walled Bars* (Wiley, New York, 1981).
- <sup>17</sup>O. Song and L. Librescu, "Bending vibration of cantilevered thin-walled beams subjected to time-dependent external excitations," *J. Acoust. Soc. Am.* **97**, 313–319 (1995).
- <sup>18</sup>M. W. D. White and G. R. Heppler, "Dynamics of Timoshenko beams with attached masses," *Dynamics and Control of Structures in Space II*, edited by C. L. Kirk and R. C. Hughes (Computational Mechanics, Southampton, Boston, 1993), pp. 209–224.
- <sup>19</sup>R. Kumar, "Vibrations of space booms under centrifugal force field," *Can. Aeronaut. Space Inst. (CASI) Trans.* **7**, 1–6 (1974).
- <sup>20</sup>H. S. Tzou, J. P. Zhong, and J. J. Hollkamp, "Spatially distributed orthogonal piezo-electric shells actuators: Theory and applications" *J. Sound Vib.* **177**, 363–378 (1994).

# Frequency derivative approach for identification of the wave resonances on immersed elastic bodies

Bertrand Dubus, Antoine Lavie, and Naum D. Veksler<sup>a)</sup>

*Institut d'Electronique et de Microélectronique du Nord, U.M.R. C.N.R.S. 9929, Département I.S.E.N., 41 boulevard Vauban, 59046 Lille Cedex, France*

(Received 7 April 1997; accepted for publication 25 August 1997)

Acoustic scattering by elastic bodies is usually analyzed in terms of resonances, the frequency, width, and order of which should be determined. In this paper, a simple approach based on a frequency derivative of the scattered pressure is proposed for resonance order identification on bodies of arbitrary shape. The method is applied to the acoustic scattering of a plane wave by a spherical shell for validation and by a cylindrical shell bounded by hemispherical end caps. In both cases, the  $A$  and  $S_0$  wave resonances are identified. © 1997 Acoustical Society of America. [S0001-4966(97)03812-5]

PACS numbers: 43.40.Rj, 43.20.Fn, 43.20.Tb, 43.30.Jx [CBB]

## INTRODUCTION

In the analysis of scattering of an acoustic wave by elastic bodies of spherical and cylindrical shapes, different approaches can now be used to isolate and identify the resonance components of partial waves: the resonance scattering theory<sup>1,2</sup> with classical (rigid and soft) and intermediate<sup>3-6</sup> backgrounds, the phase gradient method,<sup>7</sup> the Argand diagram method,<sup>8</sup> and the computation of the pole positions of the partial scattering function in the complex frequency plane.<sup>9</sup> The resonance component of the total form function can be found for scatterers of arbitrary shape as well,<sup>10</sup> but some procedure is needed for the resonance identification. We propose a simple approach based on a frequency derivative of the scattered pressure for this identification. This approach called the frequency derivative approach (FDA) is presented in Sec. I. An identification of the resonances of the  $A$  and  $S_0$  waves on a spherical shell is carried out in Sec. II to validate the method. Finally, the FDA is applied to identify the resonances of a cylindrical shell bounded by hemispherical end caps in Sec. III.

## I. THE FREQUENCY DERIVATIVE APPROACH

Let us consider an elastic body immersed in an infinite fluid. The parameters of the elastic medium are the density  $\rho$  and the velocities of the longitudinal and transverse waves  $c_l$  and  $c_t$ , respectively. For the fluid,  $\rho_f$  is the density and  $c_f$  is the sound velocity. The body is impinged by an incident plane wave with the pressure  $p_i$  given by

$$p_i = p_0 \exp[i(kz - \omega t)], \quad (1)$$

where  $p_0$  is the amplitude of the incident pressure,  $\omega$  is the circular frequency,  $k = \omega/c_f$  is the wave number in the fluid,  $z$  is the Cartesian coordinate, and  $t$  is the time. In the following, we shall use the reduced frequency  $x = ka$ , where  $a$  is a length characterizing the size of the body.

According to the resonant scattering theory (RST),<sup>1,2</sup> the scattered far-field pressure (or the form function)  $p_s$  can be split into the resonance  $p_r$  and the background  $p_b$  components

$$p_s(\theta, \varphi, x) = p_r(\theta, \varphi, x) + p_b(\theta, \varphi, x), \quad (2)$$

where  $\theta$  and  $\varphi$  are the spherical coordinates. At small or moderate  $x$  (lower than the first thickness resonance<sup>11</sup>), it is usually assumed that the background component varies slowly with frequency. Considering an isolated resonance at  $x = x_r$  and a small frequency shift  $\Delta x$ , we write

$$\begin{aligned} p_s(\theta, \varphi, x_r + \Delta x) - p_s(\theta, \varphi, x_r) \\ \approx p_r(\theta, \varphi, x_r + \Delta x) - p_r(\theta, \varphi, x_r) \\ \approx \Delta x \left( \frac{\partial p_r(\theta, \varphi, x)}{\partial x} \right) \Big|_{x=x_r}, \end{aligned} \quad (3)$$

where the last term is obtained from a Taylor expansion of  $p_r$  at  $x = x_r$ . For an isolated resonance, we assume that the resonance component can be presented as

$$p_r(\theta, \varphi, x) = F(\theta, \varphi)G(x), \quad (4)$$

where  $F(\theta, \varphi)$  is the angular pattern, which characterizes spatially the resonance contribution and  $G(x)$  describes the variation of the resonance component with frequency. Equation (4) relies upon a separation of the variables for the resonance component, which has been demonstrated for partial waves of canonical (spherical, cylindrical) shapes.<sup>1,2</sup>

For a body of arbitrary shape, the validity of the factorization in Eq. (4) can be verified considering some properties of the  $S$  matrix already discussed by Waterman.<sup>12</sup> The incident wave is expanded in the regular spherical (or cylindrical) wave function

$$p_i = \sum_{n=1}^{\infty} a_n \text{Re}(\Psi_n(\mathbf{r})), \quad (5)$$

where  $\mathbf{r}$  denotes the position, and the scattered pressure is expanded in a spherical (or cylindrical) partial wave  $\Psi_n(\mathbf{r})$  basis

<sup>a)</sup>Permanent address: Institute of Cybernetics, Akadeemia 21, Tallinn, EE-0026, Estonia.

$$p_s = \sum_{n=1}^{\infty} f_n \Psi_n(\mathbf{r}). \quad (6)$$

The  $[T]$  matrix relates the known quantities  $a_n$  to the unknown ones  $f_n$

$$f_n = \sum_{m=1}^{\infty} T_{nm} a_m. \quad (7)$$

The  $[S]$  matrix is defined as

$$[S] = [I] + 2[T], \quad (8)$$

where  $[I]$  is the identity matrix. The total field can be written as

$$\begin{aligned} p_i + p_s &= \sum_{n=1}^{\infty} \sum_{m=1}^{\infty} [a_n \operatorname{Re}(\Psi_n(\mathbf{r})) + T_{mn} a_m \Psi_m(\mathbf{r})] \\ &= \frac{1}{2} \sum_{n=1}^{\infty} \sum_{m=1}^{\infty} [a_n \Psi_n^*(\mathbf{r}) + S_{mn} a_m \Psi_m(\mathbf{r})], \end{aligned} \quad (9)$$

where the asterisk denotes the complex conjugate. When the geometry of the scatterer differs from the spherical (or cylindrical) one, coupling occurs between partial modes resulting in nondiagonal terms in the  $[S]$  matrix.  $[S]$  is a unitary matrix; its eigenvalues lie on the unit circle and are denoted by  $e^{i\lambda_j}$  (where  $j$  labels the number of the eigenvalue). The eigenvectors  $v^j$  constitute a real orthonormal set. Eigenfunctions  $\Phi_n(\mathbf{r})$  are constructed using the eigenvectors, as expansion coefficients with the basis function

$$\Phi_j(\mathbf{r}) = \sum_{n=1}^{\infty} v_n^j \Psi_n(\mathbf{r}). \quad (10)$$

After expanding the pressure in the incident wave in regular eigenfunctions

$$p_i = \sum_{j=1}^{\infty} c_j \operatorname{Re}(\Phi_j(\mathbf{r})), \quad (11)$$

one obtains the solution of the scattering problem in terms of eigenfunctions

$$p_s = \sum_{j=1}^{\infty} \frac{1}{2} (e^{i\lambda_j} - 1) c_j \Phi_j(\mathbf{r}). \quad (12)$$

Equation (12) is similar to the relation obtained for the scattered pressure in the RST,<sup>1,2</sup> when replacing partial scattering functions  $S_n$  by eigenvalues  $e^{i\lambda_j}$  and partial waves  $\Psi_n$  by eigenfunctions. For a frequency close to a resonance frequency, corresponding to eigenfunction  $\Phi_k$ , Eq. (12) is written by separating the contribution of  $\Phi_k$  and the contribution of all the other eigenfunctions

$$p_s = \frac{1}{2} (e^{i\lambda_k} - 1) c_k \Phi_k(\mathbf{r}) + \sum_{\substack{j=1 \\ j \neq k}}^{\infty} \frac{1}{2} (e^{i\lambda_j} - 1) c_j \Phi_j(\mathbf{r}). \quad (13)$$

The first term corresponds to the resonance component of the eigenfunction and the second term corresponds to the background contribution. In the formula for the resonance com-

ponent, spatial and frequency variables are separated, justifying Eq. (4) for objects of arbitrary shape.

Finally, Eqs. (3) and (4) are combined to give

$$p_s(\theta, \varphi, x_r + \Delta x) - p_s(\theta, \varphi, x_r) \approx \Delta x F(\theta, \varphi) \left( \frac{\partial G(x)}{\partial x} \right) \Big|_{x=x_r}. \quad (14)$$

Equation (14) shows that the frequency derivative of the scattered pressure gives access to the directivity pattern of the resonance component and can therefore be used for resonance identification. It can be noted that usually, at resonance, the frequency derivative of the magnitude of  $G$  fades out and the main contribution in the derivative comes from the phase variation.

The separation between resonance and background components can be extended to the near-field pressure

$$p_s(\mathbf{r}, x) = p_r(\mathbf{r}, x) + p_b(\mathbf{r}, x), \quad (15)$$

and to the displacement field in the body

$$\mathbf{u}_s(\mathbf{r}, x) = \mathbf{u}_r(\mathbf{r}, x) + \mathbf{u}_b(\mathbf{r}, x). \quad (16)$$

The application of FDA to near-field pressure and body displacements is carried out by applying the procedure described previously to Eqs. (15) and (16). The separation of the variables for the resonance contribution is performed on  $\mathbf{r}$  and  $x$ . The result obtained from the frequency derivative is a spatial characterization of the resonance component of the near-field pressure (or body displacements) and can be used to identify the resonance.

Practically, the absolute amplitude of the result obtained from Eq. (14) has no physical interest. Therefore results are normalized to the maximal value of the function. The application of FDA to near-field or far-field pressures gives only access to the order of the resonance. When the resonances are isolated and the resonance orders determined, the resonances are gathered into families corresponding to propagating waves. Finally, the application of FDA to surface displacement together with the dispersion curves of the phase and group velocities, as well as the half-width variation with order (or frequency), can be used for resonance classification.

## II. IDENTIFICATION OF THE RESONANCES OF A SPHERICAL SHELL

For validation purpose, the FDA is applied to identify the resonances of the  $A$  and  $S_0$  waves for an aluminum spherical shell immersed in water. The following parameters are used

$$\begin{aligned} \rho &= 2780 \text{ kg/m}^3, & c_1 &= 6339 \text{ m/s}, & c_t &= 3091 \text{ m/s}, \\ \rho_f &= 1000 \text{ kg/m}^3, & c_f &= 1490 \text{ m/s}, & b/a &= 0.97, \end{aligned} \quad (17)$$

where  $a$  and  $b$  are the external and internal radii of the sphere, respectively. For an incident plane wave, the scattered far-field pressure is expressed as in Ref. 13.



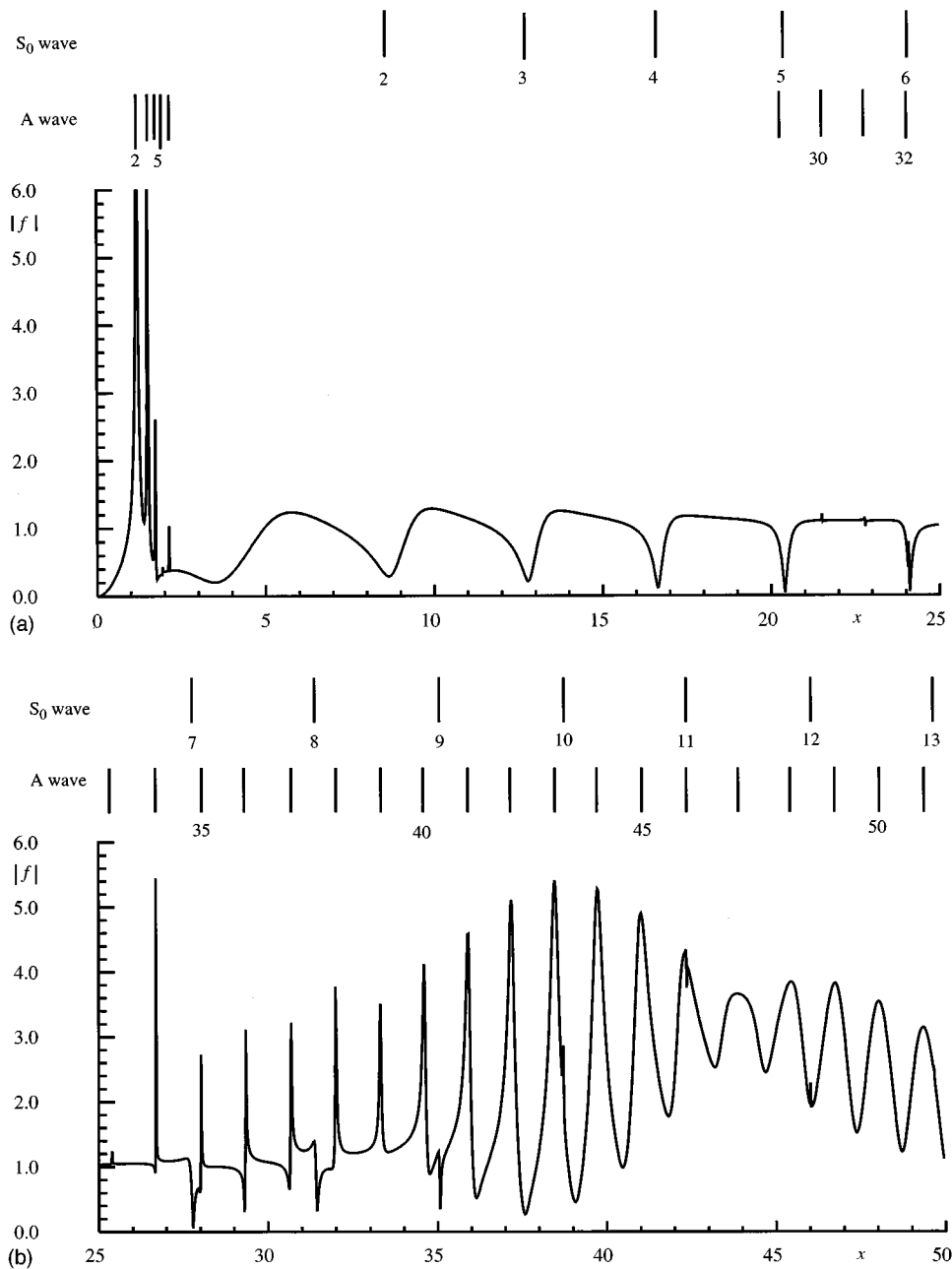


FIG. 1. The backscattered form function modulus and the acoustic spectrogram for a spherical aluminum shell. The form function is computed with a frequency step size of 0.02.

$$\begin{aligned}
 p_s(r, \theta, x) &= \frac{p_0 a}{2r} \exp[i(kr - \omega t)] \left[ \frac{2}{x} \sum_{n=0}^{\infty} (2n+1) P_n(\cos \theta) c_n \right] \\
 &= \frac{p_0 a}{2r} \exp[i(kr - \omega t)] f(\theta, x), \quad (18)
 \end{aligned}$$

where  $r$  and  $\theta$  are the spherical coordinates (with the origin at the center of the spherical shell),  $P_n$  are Legendre polynomials,  $c_n$  are coefficients determined from the boundary conditions, and  $f$  is the form function. The magnitude of the form function is displayed in Fig. 1 for  $0 < ka < 50$ . The

identification of the resonances is carried out in three steps. First, the resonance frequency  $x_n$  and width  $\Gamma_n$  are obtained by using the intermediate background.<sup>6,11</sup> Second, the FDA is applied to the form function given by Eq. (18). Finally, the directivity pattern  $F(\theta)$  is drawn and the identification is performed by counting the number of lobes. By definition, the theoretical curve is known to be  $P_n(\cos \theta)$  for a resonance of  $n$ th order. Figures 2 and 3 display examples of directivity patterns obtained for resonances of the A and  $S_0$  waves, respectively. The symmetry of the pattern is a first verification of the validity of the method. Identification is possible after applying FDA to the far-field scattered pressure or to displacement of the external shell surface. The

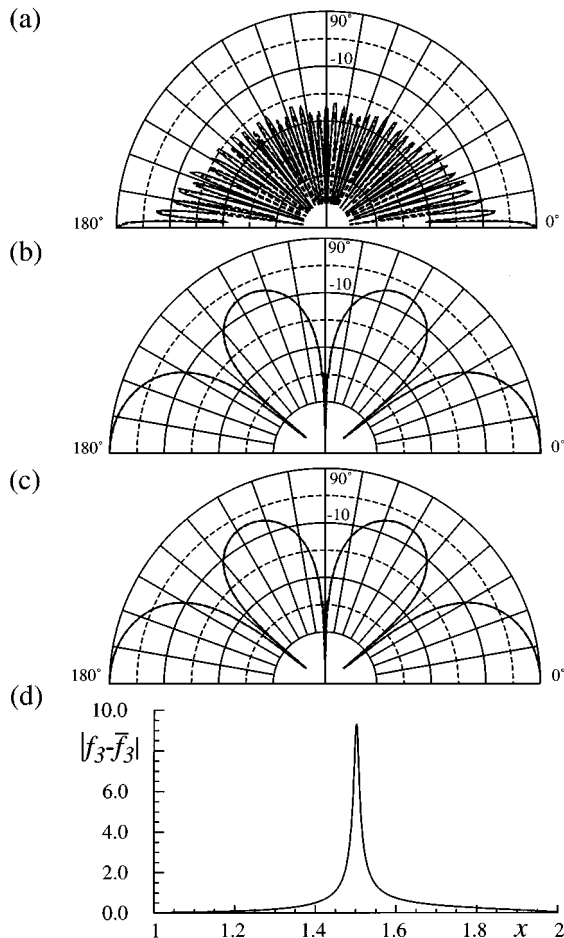


FIG. 2. Identification of the  $A$  wave resonances for plane-wave scattering by the spherical aluminum shell. Solid line: FDA with  $\Delta x=0.004$ , dotted line: the Legendre polynomial. (a) the 42nd modal resonance ( $x_{42}=37.20$ ), the pressure magnitude in the far field. (b)–(d) the third modal resonance ( $x_3=1.50$ ). (b) the pressure magnitude in the far field, (c) the normal displacement magnitude on the outer surface of the shell, (d) the Breit–Wigner curve (Refs. 1 and 2) computed with the intermediate background. The mode order is equal to one half of the number of lobes on the shell circumference. In (b) and (c) solid and dotted lines coincide.

effectiveness of FDA to identify the resonances of  $A$  and  $S_0$  waves is shown in Tables I and II. It is related to the value of  $\Gamma_n$ . FDA succeeds when  $\Gamma_n < 0.2$  and fails for  $\Gamma_n > 0.4$ . The success or failure of FDA is directly related to the validity of

TABLE I. The resonance frequencies of the  $A$  wave revolving around aluminum spherical shell.  $n$  is the order of the partial mode. The last column indicates the success (s) or failure (f) of FDA to identify the resonance.

$n$	$x_n$	$\Gamma_n$	FDA
2	1.18	0.05	s
3	1.50	0.017	s
4	1.73	<0.01	s
5	1.93	<0.01	s
6	2.13	<0.01	s
...	...	...	...
40	34.62	0.076	s
41	35.91	0.12	s
42	37.20	0.17	s
43	38.47	0.24	s
44	39.73	0.32	s
45	40.98	0.42	f
46	42.22	0.55	f

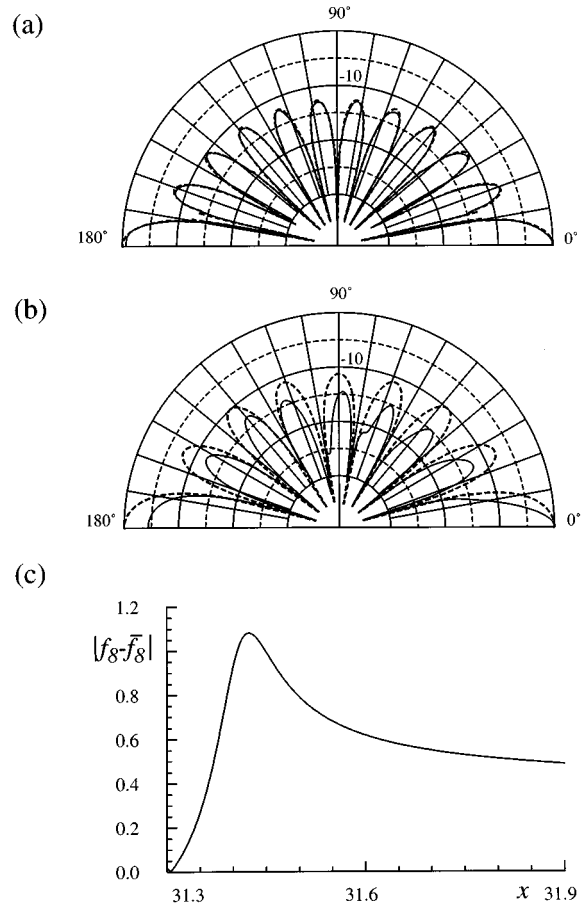


FIG. 3. Identification of the  $S_0$  wave resonances for plane-wave scattering by the spherical aluminum shell. Solid line: FDA with  $\Delta x=0.004$ , dotted line: the Legendre polynomial. (a) the 11th modal resonance ( $x_{11}=42.36$ ), the pressure magnitude in the far field. (b) and (c) the 8th modal resonance ( $x_8=31.42$ ). (b) the pressure magnitude in the far field, (c) the Breit–Wigner curve (Refs. 1 and 2) computed with the intermediate background. The mode order is equal to one-half of the number of lobes on the shell circumference.

the hypothesis of isolated resonance. Thus for the  $A$  wave, when  $n > 40$ ,  $\Gamma_n$  strongly increases with  $n$ . When  $n > 45$ , only the superposition of  $A$  wave resonances of successive orders is obtained and the identification is impossible. Resonances 5, 6, and 7 of the  $S_0$  wave are very close in frequency to resonances 29, 32, and 35 of the  $A$  wave, respectively. We observe a superposition of two resonances of different waves. Note that the superposition only affects the identification of the resonance of large width. This difficulty arises because FDA does not directly compute the eigenmodes but

TABLE II. The resonance frequencies of the  $S_0$  wave revolving around aluminum spherical shell.  $n$  is the order of the partial mode. The last column indicates the success (s) or failure (f) of FDA to identify the resonance.

$n$	$x_n$	$\Gamma_n$	FDA
5	20.53	0.70	f
6	24.15	0.40	f
7	27.78	0.22	f
8	31.42	0.12	s
9	35.07	0.06	s
10	38.71	0.025	s
11	42.36	0.007	s

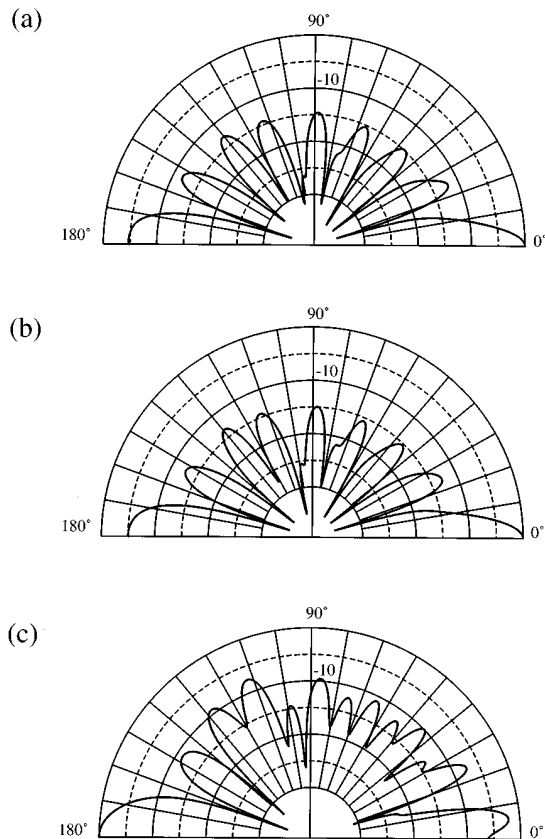


FIG. 4. Effect of  $\Delta x$  value on the effectiveness of the FDA. The 8th resonance of the  $S_0$  wave for plane-wave scattering by the spherical aluminum shell. The pressure magnitude in the far field for different  $\Delta x$  values. (a)  $\Delta x = 10^{-5}$ , (b)  $\Delta x = 10^{-2}$ , and (c)  $\Delta x = 10^{-1}$ .

the superposition of all the resonances. The eigenmode of interest is properly extracted only if the resonance is isolated, i.e., if the contribution of all the other eigenmodes varies much slower with frequency than the contribution of the

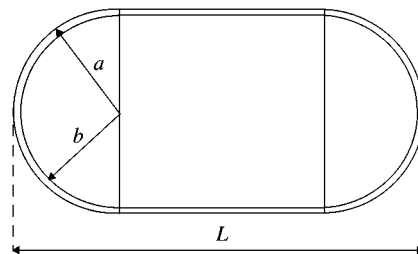


FIG. 5. Geometry of the cylindrical shell with hemispherical end caps.

eigenmode of interest. The choice of  $\Delta x$  has little effect on the directivity pattern as long as  $\Delta x < \Gamma_n/10$ , as shown in Fig. 4.

### III. IDENTIFICATION OF THE RESONANCES OF A CYLINDRICAL SHELL BOUNDED BY HEMISPHERICAL END CAPS

We now consider a cylindrical shell bounded by hemispherical end caps made of stainless steel and immersed in water (Fig. 5). The parameters used in the computation are

$$\begin{aligned} \rho &= 7900 \text{ kg/m}^3, & c_1 &= 5790 \text{ m/s}, & c_t &= 3100 \text{ m/s}, \\ \rho_f &= 1000 \text{ kg/m}^3, & c_f &= 1470 \text{ m/s}, \end{aligned} \quad (19)$$

$$b/a = 0.97, \quad L/2a = 2.$$

The scattering of an acoustic wave by a similar target has already been studied using coupled finite element/boundary element (FEM/BEM) or finite element/superposition methods.<sup>14</sup> Identification was made for resonances of flexural wave by plotting the displacement on the shell surface.

In this work, the far-field and near-field scattered pressures and the body displacements are computed using a nu-

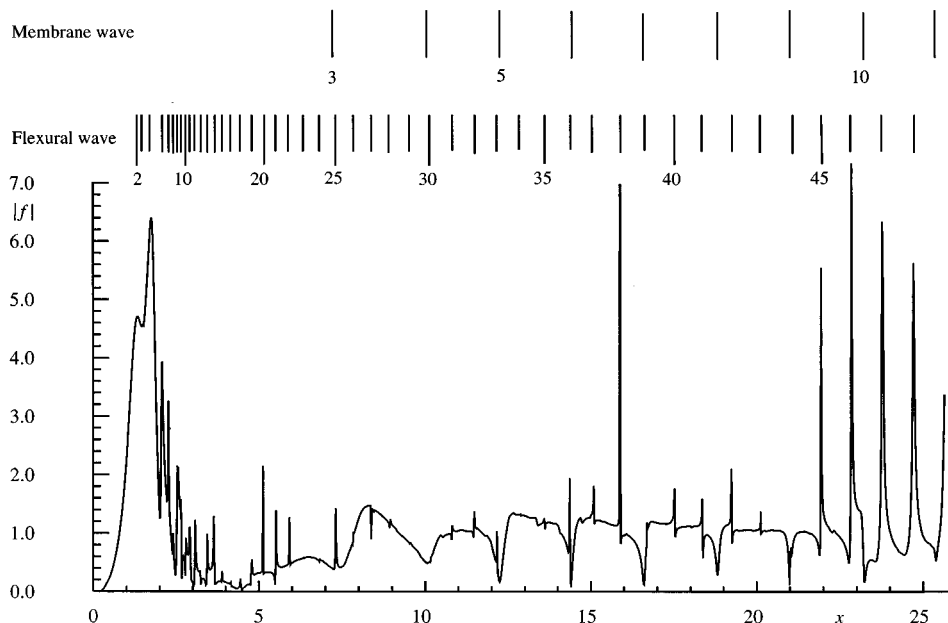


FIG. 6. The backscattered form function modulus for end-on incidence from the cylindrical shell with hemispherical end caps and the acoustic spectrogram. The form function is computed using the FEM/BEM method with a frequency step size of 0.04.

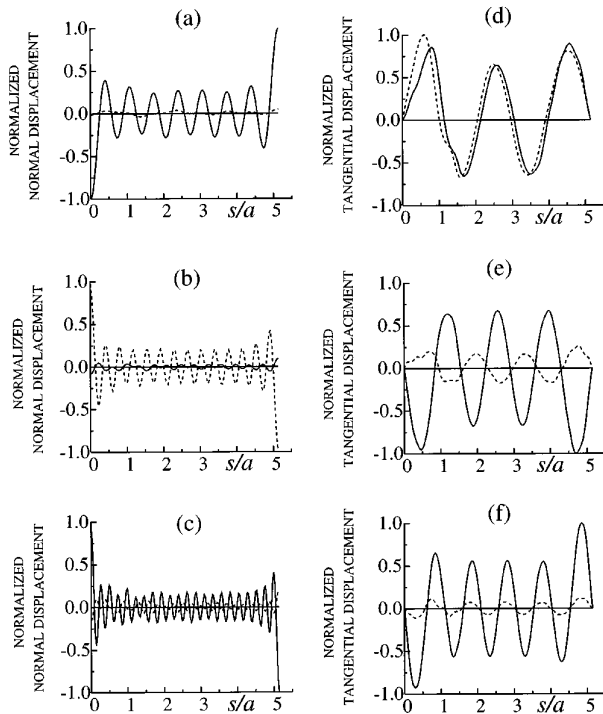


FIG. 7. The resonance components of the normal and tangential displacements on the outer surface of the shell computed by the FDA ( $\Delta x = 0.004$ ). Solid line: real part (displacement in phase with the incident pressure at the origin), dashed line: imaginary part (displacement shifted in phase by  $\pi/2$ ).  $s$  is the curvilinear abscissa. Only half of the perimeter is shown. *Left column*, normal displacements of the flexural wave. (a) the 15th resonance ( $x_{15} = 3.63$ ), (b) the 27th resonance ( $x_{27} = 8.38$ ), and (c) the 43rd resonance ( $x_{43} = 20.11$ ). *Right column*, tangential displacements of the membrane wave. (d) the 5th resonance ( $x_5 = 12.25$ ), (e) the 7th resonance ( $x_7 = 16.58$ ), and (f) the 10th resonance ( $x_{10} = 23.21$ ). The order of the resonance ( $l$ ) is equal to the number of extrema of the real (or imaginary) part on the half perimeter of the shell.

merical finite element–boundary element method.<sup>15</sup> The shell is modeled using a thin shell finite element.<sup>16</sup> Therefore the resonances are interpreted in terms of flexural and membrane waves rather than Lamb waves. Figure 6 displays the backscattered form function of the shell for end-on incidence. Two types of resonances are observed associated with flexural and membrane waves. No background is used here.

TABLE III. The resonance frequencies of the flexural wave revolving around the steel cylindrical shell with hemispherical end caps.  $l$  is the number of wavelengths in the meridian plane.

$l$	$x_l$	$l$	$x_l$	$l$	$x_l$	$l$	$x_l$
2	1.32	14	3.44	26	7.82	38	15.88
3	1.50	15	3.63	27	8.38	39	16.69
4	1.75	16	3.89	28	8.95	40	17.50
5	2.07	17	4.15	29	9.55	41	18.35
6	2.27	18	4.45	30	10.17	42	19.19
7	2.41	19	4.79	31	10.81	43	20.11
8	2.54	20	5.13	32	11.48	44	21.00
9	2.65	21	5.51	33	12.18	45	21.90
10	2.80	22	5.92	34	12.87	46	22.80
11	2.91	23	6.35	35	13.59	47	23.79
12	3.08	24	6.84	36	14.36	48	24.73
13	3.23	25	7.31	37	15.13		

TABLE IV. The resonance frequencies of the membrane wave revolving around the steel cylindrical shell with hemispherical end caps.  $l$  is the number of wavelengths in the meridian plane.

$l$	$x_l$	$l$	$x_l$
3	7.26	8	18.81
4	10.06	9	21.03
5	12.25	10	23.21
6	14.40	11	25.41
7	16.58		

The resonance frequencies correspond to the extrema of the form function. Identification of flexural and membrane wave resonances is performed by applying FDA to shell displacements and by plotting normal (or tangential) displacements of the shell versus curvilinear abscissa (Fig. 7). Again, the symmetry (or antisymmetry) of the displacements is a first verification of the validity of the method. Figure 7 can also be used to obtain the velocity of the peripheral waves. Tables III and IV give the complete identification of the flexural and membrane wave resonances. Using surface displacement, direct identification (without FDA) is possible for resonances clearly observed on the form function whose amplitude is much higher than one or whose width is sufficiently small. However, only FDA can give access to the resonant contribution of the far-field pressure.

#### IV. CONCLUSION

In this paper, a steady-state axisymmetrical scattering problem of a plane acoustic wave by an elastic shell has been considered. An approach has been proposed to interpret the form function. The procedure has been tested on a model problem (scattering by a spherical shell), the exact solution of which is well known. As an example of the approach utilization, the numerically (FEM/BEM) computed form function of a cylindrical shell closed by two hemispherical end caps has been analyzed. In a restricted, but sufficiently representative, frequency domain, all the resonances of two peripheral waves (membrane and flexural) have been identified. In the test problem the motion of the shell is governed by the equations of elasticity theory, and in the example it is governed by the thin shells theory equations. The model used to describe the motion of the elastic body has no influence on the effectiveness of the procedure. The main limitation of the method lies in the hypothesis of isolated resonance which breaks down for resonances of large width (where classical methods also fail). The proposed approach can be used for two-dimensional scattering problems by thickwalled and solid elastic bodies as well. It has already been successfully applied to ellipsoidal shells and ribbed cylindrical shells with hemispherical end caps for peripheral wave resonance identification. Finally, it can be noted that the FDA which has been applied to analytically and numerically computed form functions in this paper, can also be used for resonance identification from measured data.

## ACKNOWLEDGMENTS

This work was performed with the financial support of Direction des Recherches Etudes et Techniques and of Conseil Régional Nord-Pas de Calais. The authors wish to acknowledge the stimulating discussion with Dr. J.-M. Conoir.

- <sup>1</sup>L. Flax, L. R. Dragonette, and H. Uberall, "Theory of elastic resonance excitation by sound scattering," *J. Acoust. Soc. Am.* **63**, 723–731 (1978).
- <sup>2</sup>J. D. Murphy, E. D. Breitenbach, and H. Uberall, "Resonance scattering of acoustic waves from cylindrical shells," *J. Acoust. Soc. Am.* **64**, 677–683 (1978).
- <sup>3</sup>M. F. Werby, "The acoustical background for a submerged elastic shell," *J. Acoust. Soc. Am.* **90**, 3279–3287 (1991).
- <sup>4</sup>G. C. Gaunard, "Hybrid background coefficients to isolate the resonance spectrograms of submerged shells," *J. Acoust. Soc. Am.* **92**, 1981–1984 (1992).
- <sup>5</sup>A. Norris and N. Vasudevan, "Acoustic wave scattering from thin shell structures," *J. Acoust. Soc. Am.* **92**, 3320–3336 (1992).
- <sup>6</sup>N. D. Veksler, "Intermediate background in problems of sound wave scattering by elastic shells," *Acustica* **76**, 1–10 (1992).
- <sup>7</sup>J.-M. Conoir, J.-L. Izbicki, and O. Lenoir, "Phase gradient method applied to scattering by an elastic shell," *Ultrasonics* **35**, 157–169 (1997).
- <sup>8</sup>P. Rembert, S. Derible, and J.-L. Izbicki, "Experimental measurement of resonance width of a cylindrical elastic shell," *Acust. Acta Acust.* **82**, Suppl. 1, S239 (1996).
- <sup>9</sup>N. D. Veksler and J.-L. Izbicki, "Modal resonances of peripheral waves," *Acust. Acta Acust.* **82**, 401–410 (1996).
- <sup>10</sup>N. D. Veksler, "Isolation of resonances in problems of acoustic waves scattering by elastic shells," *Sov. Phys. Acoust.* **38**, 231–234 (1992).
- <sup>11</sup>S. G. Kargl and P. L. Marston, "Longitudinal resonances in the form function for backscattering from a spherical shell: fluid shell case," *J. Acoust. Soc. Am.* **88**, 1114–1122 (1990).
- <sup>12</sup>P. C. Waterman, "New formulation of acoustic scattering," *J. Acoust. Soc. Am.* **45**, 1417–1429 (1969).
- <sup>13</sup>R. Hickling, "Analysis of echoes from a hollow metallic sphere in water," *J. Acoust. Soc. Am.* **36**, 1124–1137 (1964).
- <sup>14</sup>R. D. Miller, E. Thomas Moyer, Jr., H. Huang, and H. Uberall, "A comparison between the boundary element method and the wave superposition approach for the analysis of the scattered fields from rigid bodies and elastic shells," *J. Acoust. Soc. Am.* **89**, 2185–2196 (1991).
- <sup>15</sup>B. Dubus, A. Lavie, D. Décultot, and G. Maze, "Coupled finite element/boundary element method for the analysis of the acoustic scattering from elastic targets," in *ASME 15th Biennial Conference on Mechanical Vibration and Noise, Acoustics of Submerged Structures and Transduction Systems* (ASME, New York, 1995), Vol. 3, part B, pp. 25–32.
- <sup>16</sup>J. J. Webster, "Free vibrations of shells of revolution using ring finite elements," *Int. J. Mech. Sci.* **9**, 559–570 (1967).

# An analytical investigation of the active attenuation of the plate flexural wave transmission through a reinforcing beam

Nicole J. Kessissoglou and Jie Pan

*Department of Mechanical and Materials Engineering, The University of Western Australia,  
Western Australia, 6907 Australia*

(Received 3 July 1996; accepted for publication 19 August 1997)

The transmission of plate flexural waves through a reinforcing beam is related to the coupling between the plate flexural waves and the flexural and torsional waves in the beam. The beam–plate coupling and the energy transmission through the beam can be described in terms of the trace wave matching of the flexural waves in the plate with the flexural and torsional waves in the beam. For a given incident flexural wave from the plate to the beam interface, the amount of trace matching is determined by the flexural and torsional wave numbers in the beam. It is shown in this paper that the reinforcing beam of an infinite beam–plate system serves as a good passive device in attenuating wave transmission except at two coincidences corresponding to the optimal wave trace-matching conditions. The maximum power flow across the beam at the optimal trace wave matching conditions can be reduced by a feedforward active control system using the information on the wave numbers at the coincidence conditions. In this paper, the coupling mechanisms involved with the wave transmission in a coupled beam–plate structure is used to explain the coincidence conditions of the wave transmission. The active control is applied to the reinforcing beam to attenuate the transmitted waves at the coincidences. Results demonstrate that it is possible to achieve a significant reduction of the transmitted energy by using an array of point forces and point moments, and the biologically inspired control strategy for the control actions. © 1997 Acoustical Society of America. [S0001-4966(97)01612-3]

PACS numbers: 43.40.Vn [PJR]

## INTRODUCTION

There are many practical applications of ribbed plate structures, for example, in submarine hulls, aircraft, and aerospace craft. Although there has been extensive research on the coupling interaction between ribbed plates and the surrounding fluid, and the sound radiation from such structures,<sup>1–3</sup> there has been very little consideration given to the attenuation of the wave vibration and the acoustic radiation from such structures by active control means.

Active control of the flexural waves and the power flow in single beam and plate structures has been widely reviewed for many different types of control applications and arrangements.<sup>4,5</sup> However, it is only more recently that the active control of flexural waves in stiffened plates is being investigated. Hansen and Young<sup>6</sup> investigate the application of a new type of actuator which provides both a control force and moment, for the control of the flexural vibrations in a semi-infinite plate. Their approach is to replace the conventional actuators which are usually in the form of piezoelectric crystals, by using a stack of piezoceramic actuators placed between the stiffener flange and thin plate. These stack actuators generate a point force, a line force, and a line moment to minimize the flexural vibration in the plate at the error sensors, which are located on the opposite side of the stiffener flange to the primary excitation. They use the traveling wave approach to determine the flexural displacement at any location in the plate, and the stiffener flange is modeled as lumped mass and stiffness with constant values. Maidanik and Dickey<sup>7</sup> present an analytical model to actively control the response of ribbed panels based on an impulse response

function. The impulse response function is used to describe the structural response, and the control system is described by an external control drive. The analytical model is simplified to a one-dimensional system, and they use a finite number of ribs which are described by a lumped-mass approximation.

Infinite structures are represented in the physical world by structures with sufficient absorption at the boundary edges, achieved by absorbing most of the incident waves towards the boundaries. This paper gives an initial insight into the theoretical modeling of infinite ribbed plates, with an approach to the application of an active control system. The entire ribbed plate system is modeled by a continuous system, using equations of motion to describe the plate in flexure and the beam in both flexure and torsion. The approach to the design of the active control system involves using the dynamic nature of the physical structure in order to obtain the best use of both passive and active control, and thereby optimizing the attenuation of the flexural vibration in the plate. In this paper, the analysis of the dynamic nature of the beam-reinforced plate pays special attention to the wave motion at the boundary interfaces of the beam and plate, resulting in an understanding of the transmission, reflection, and near-field effects observed at the beam–plate interconnections. It is shown that the maximum energy transmission through the beam occurs at the coincidence or optimal trace wave matching conditions between the flexural waves in the plate and the flexural and torsional waves in the beam. The coincidence conditions occur when the trace wavelength of the plate flexural waves matches the natural spatial wave-

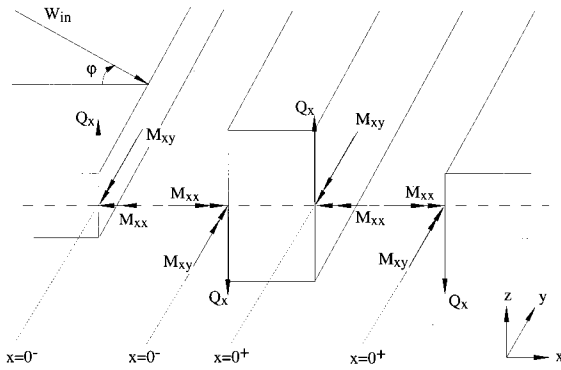


FIG. 1. Three subsystems of the beam–plate model: plate 1, beam, and plate 2, showing the plane flexural wave incident at the beam boundary.

length of the flexural waves in the beam (flexural trace matching), and similarly, when the trace wavelength of the plate flexural waves matches the natural wavelength of the torsional waves in the beam (torsional trace matching).

When a point control force is applied to the beam of the infinite system, the far-field propagating waves in the plate is contributed by the supersonic wave number components of the radiating secondary flexural waves from the beam to the plate. If the beam stiffness is much greater than that of the plate, then the radiated waves are dominated by the beam flexural wave number component at the excitation frequency. Similarly, the greatest amount of flexural wave radiation from the beam by a point moment corresponds to the beam torsional wave number component at the excitation frequency. These characteristics of the wave radiation from the beam driven by point force and point moment indicate that point forces and moments may result in effective attenuation of plate flexural wave transmission at the coincidence conditions.

## I. BEAM-PLATE INTERCONNECTIONS

An extensive analysis on the behavior of the wave motions in an infinite beam-reinforced plate has already been developed by Ungar and Cremer.<sup>8,9</sup> It is useful to review the analysis for a better understanding of the active control strategy. The beam–plate structure consists of an infinite uniform plate symmetrically reinforced by two identical uniform narrow straight beams of rectangular cross section. The attachment between the plate and beams is assumed to be perfect and continuous. For the mathematical modeling, the structure can be divided into three subsystems: plate 1, beam, and plate 2; with the centroidal axis of the system lying in the midplane of the plate and coinciding with the beam centre of twist. The geometry and coordinates of the subsystems may be visualized in Fig. 1. The incident flexural wave,  $W_{in}$ , traveling in the  $x$ - $y$  plane at an angle  $\varphi$ , is also shown in Fig. 1.

$Q_x$ ,  $M_{xy}$ , and  $M_{xx}$  represent the shear forces, bending moments, and twisting moments acting along the unit length of the plates in the  $y$  direction, respectively, and are described by the following classical relations:

$$Q_x = -D \frac{\partial}{\partial x} \left[ \frac{\partial^2 W}{\partial x^2} + \frac{\partial^2 W}{\partial y^2} \right], \quad (1)$$

$$M_{xy} = D \left[ \frac{\partial^2 W}{\partial x^2} + \nu \frac{\partial^2 W}{\partial y^2} \right], \quad (2)$$

$$M_{xx} = -D(1 - \nu) \frac{\partial^2 W}{\partial x \partial y}, \quad (3)$$

where  $D = E_p h^3 / 12(1 - \nu^2)$  is the flexural rigidity of the plate, and  $h$ ,  $E_p$ , and  $\nu$  are, respectively, the thickness, Young's modulus, and Poisson's ratio of the plate. The internal distributed damping in the structure is included in the complex Young's modulus by  $E_p^* = E_p(1 + j\eta)$ , where  $\eta$  is the structural loss factor.  $W(x, y, t)$  is the plate flexural displacement in the  $z$  direction. The flexural displacement of the beam in the  $z$  direction is denoted by  $u(y, t)$  and the rotation of the beam about its  $y$  axis is described by the torsional angular displacement  $\theta(y, t)$ .

When the flexural motion in plate 1 impinges on the beam boundary, it induces both flexural and torsional motions in the beam, and subsequently radiates flexural motion in plate 2. Ignoring rotary inertia and using the sign notation corresponding to Fig. 1, the equations of motion for the beam flexure and torsion are derived as

$$E_b I \frac{\partial^4 u}{\partial y^4} + \rho_b A \frac{\partial^2 u}{\partial t^2} = \left( Q_x + \frac{\partial M_{xx}}{\partial y} \right)_{x=0^+} - \left( Q_x + \frac{\partial M_{xx}}{\partial y} \right)_{x=0^-}, \quad (4)$$

$$GJ \frac{\partial^2 \theta}{\partial y^2} - \rho_b I_p \frac{\partial^2 \theta}{\partial t^2} = (M_{xy})_{x=0^+} - (M_{xy})_{x=0^-}, \quad (5)$$

where  $E_b I$  and  $GJ$  are the flexural and torsional stiffness of the beam, respectively, and  $\rho_b A$ ,  $\rho_b I_p$  are, respectively, the beam mass and polar mass moment of inertia per unit length of beam.

The plate flexural displacements are governed by the plate classical equation of motion:

$$D \nabla^2 W + \rho_p h \frac{\partial^2 W}{\partial t^2} = 0, \quad (6)$$

where  $\nabla^2 = (\partial^2 / \partial x^2) + (\partial^2 / \partial y^2)$  is the Laplace operator, and  $\rho_p$  is the density of the plate.

For the displacement continuity of the three subsystems at the boundary interfaces, the beam flexural displacement is equal to the plate flexural displacements, and the torsional displacement of the beam is equal to the rotation of the plates about the  $y$  axis. The following coupling equations correspond to the sign notation in the equations of motion:

$$u(y, t) = W_1(x, y, t)|_{x=0^-} = W_2(x, y, t)|_{x=0^+}, \quad (7)$$

$$\theta(y, t) = - \frac{\partial W_1}{\partial x} \Big|_{x=0^-} = - \frac{\partial W_2}{\partial x} \Big|_{x=0^+}. \quad (8)$$

## II. PRIMARY FLEXURAL WAVE MOTION IN THE PLATES

### A. Plate flexural plane wave incident on the beam discontinuity

Consider a plane flexural wave propagating in the positive  $x$  direction in plate 1, where the direction of the propagation is inclined at an angle  $\varphi$  to the  $x$  axis. This incident plane wave of frequency  $\omega$  and wave number  $k_p$  in the direction of its propagation impinges on the beam boundary as shown in Fig. 1, and can be described by

$$W_{in}(x, y, t) = A_p e^{-j(k_p \cos \varphi)x} e^{j(k_p \sin \varphi)y} e^{j\omega t}, \quad (9)$$

where  $A_p$  is the amplitude of the incident wave. The plate wave number  $k_p$  is related to the plate parameters by

$$k_p = \sqrt{\omega \left( \frac{\rho_p h}{D} \right)^{1/4}}. \quad (10)$$

When the incident wave impinges on the beam boundary, the scattering of the structural wave field generates both reflective and transmitted waves. For an infinite plate, no waves are reflected from the infinities; the resulting plate displacement in plate 1 (on the same side of the boundary as the incoming wave) consists of three components along the  $x$  direction; the incident wave, the reflected propagating wave and the near-field reflection:

$$W_1(x, y, t) = [A_p e^{-jk_x x} + R_p e^{jk_x x} + R_n e^{k_n x}] e^{jk_y y + j\omega t}, \quad (11)$$

where  $k_x = \sqrt{k_p^2 - k_y^2} = k_p \cos \varphi$  and  $k_y = k_p \sin \varphi$  are, respectively, the wave number components of the incident wave in the  $x$  and  $y$  directions, and  $k_n = \sqrt{k_p^2 + k_y^2} = k_p \sqrt{1 + \sin^2 \varphi}$  is the decay constant of the near-field wave component. The coefficients  $R_p$  and  $R_n$  are the amplitudes of the reflected and near-field waves, respectively.

Similarly, the total flexural displacement in plate 2 can be described by two components—the transmitted propagating wave and the near-field transmission:

$$W_2(x, y, t) = [T_p e^{-jk_x x} + T_n e^{-k_n x}] e^{jk_y y + j\omega t}, \quad (12)$$

where  $T_p$  and  $T_n$  are the amplitudes of the transmitted and transmitted near-field waves in the  $x$  direction on the “right” side of the beam boundary in plate 2. For the continuity of the plane waves in the  $y$  direction, both plates have the same periodicity of motion along the  $y$  direction.

The induced beam flexural and torsional vibrations are described by

$$u(y, t) = u_0 e^{jk_y y + j\omega t}, \quad (13)$$

$$\theta(y, t) = \theta_0 e^{jk_y y + j\omega t}, \quad (14)$$

where  $u_0$  and  $\theta_0$  are the amplitudes of the flexural and torsional motions in the beam, respectively.

### B. Coincidence conditions

The relationship between the wave number  $k$  and the wavelength  $\lambda (k = 2\pi/\lambda)$  allows the explanation of the coincidence or optimal trace wave matching conditions. The plane wave in plate 1 at a frequency  $\omega$  has wavelength  $\lambda_p$  as

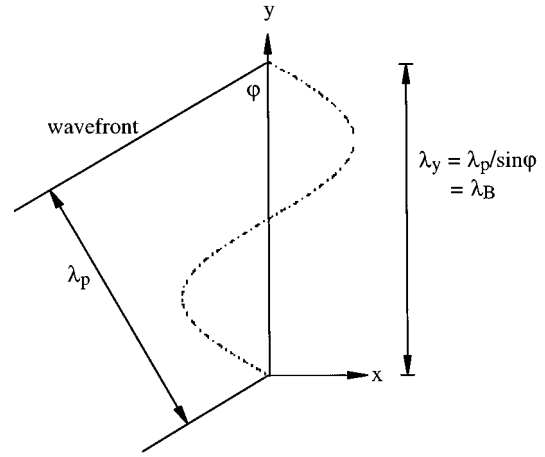


FIG. 2. Optimal trace wave matching between the plate flexural waves and the beam flexural waves.

determined by Eq. (10), while the wavelength of the flexural wave in the beam  $\lambda_B$  at frequency  $\omega$  is determined by  $\lambda_B = (2\pi/\omega)(E_b I / \rho_b A)^{1/4}$ .  $\lambda_p$  and  $\lambda_B$  are not necessarily equal. If the intercepts of the incident wave on the  $y$  axis  $\lambda_y = \lambda_p / \sin \varphi$  equals the natural flexural wavelength of the beam  $\lambda_B$ , as shown in Fig. 2; then optimal flexural trace wave matching between the plate flexural waves and the beam flexural waves occurs. We call this phenomenon *flexural coincidence*. Similarly, if  $\lambda_y$  matches the natural torsional wavelength of the beam,  $\lambda_T$ , where  $\lambda_T = (2\pi/\omega) \times (GJ / \rho_b I_p)^{1/2}$ , then optimal trace wave matching occurs between the plate flexural waves and the beam torsional waves. This is called *torsional coincidence*. It is at these coincidence conditions that the greatest coupling between the plate and beam motions occurs, resulting in the maximum transmission of the flexural wave motion through the reinforcing beam.

From Ungar's work,<sup>8</sup> solutions for the coefficients  $T_p$ ,  $R_p$ ,  $T_n$ , and  $R_n$  have been determined by making use of the equations of motions and the boundary conditions, and that the beam–plate structure is constructed entirely of the same material, resulting in the following expressions:

$$T_p = A_p [1 - (\text{tors} + \text{flex})], \quad (15)$$

$$R_p = A_p (\text{tors} - \text{flex}), \quad (16)$$

$$T_n = A_p \left[ j \frac{\cos \varphi}{\sqrt{1 + \sin^2 \varphi}} \text{flex} - \text{tors} \right], \quad (17)$$

$$R_n = T_n - 2A_p \text{tors}, \quad (18)$$

where

$$\text{tors} = \left( \frac{1}{1 + j\beta} \right), \quad (19)$$

$$\text{flex} = \left( \frac{1}{1 + j\alpha} \right), \quad (20)$$

and

$$\beta = \frac{U \sqrt{1 + \sin^2 \varphi} - 4}{U \cos \varphi}, \quad (21)$$



$$\alpha = \left( \frac{4}{S} - \frac{1}{\sqrt{1 + \sin^2 \varphi}} \right) \cos \varphi, \quad (22)$$

$$S = \frac{Ak_p^2}{h} \left[ \left( \frac{c_B}{c_p} \sin \varphi \right)^4 - 1 \right], \quad (23)$$

$$U = \frac{I_p k_p}{h} \left[ 1 - \left( \frac{c_T}{c_p} \sin \varphi \right)^2 \right], \quad (24)$$

where  $c_p$  is the bending wave speed of the plates and  $c_B$ ,  $c_T$  are the bending and torsional wave speeds of the beam, respectively. From Eqs. (21)–(24) it can be shown that the symbols tors and flex indicate the amount of torsional and flexural trace wave matching, respectively.<sup>8</sup>

To investigate the flexural wave transmission in the far field of plate 2, it is sufficient to only obtain the solution for the coefficient  $T_p$  in Eq. (15). If the amplitude of the incident wave is unity ( $A_p = 1$ ), then  $T_p T_p^*$  represents the energy transmission coefficient, where  $T_p T_p^*$  is the ratio of the transmitted energy per unit length to the incident energy per unit length, and can simply be described by

$$T_p T_p^* = 1 - \text{tors}(\text{tors})^* - \text{flex}(\text{flex})^* + \text{tors}(\text{flex})^* + \text{flex}(\text{tors})^*, \quad (25)$$

where  $T_p^*$  denotes the complex conjugate of  $T_p$ .

For flexural trace wave matching only the above expression reduces to

$$T_p T_p^* = 1 - \text{flex}(\text{flex})^*, \quad (26)$$

that is, the far-field flexural wave transmission in plate 2 is a direct result of the optimal coupling between the plate flexural waves and the beam flexural waves. Since the trace wave number of the plate,  $k_y$ , and the natural bending wave number of the beam,  $k_B$ , vary with frequency the same way, this coincidence condition becomes frequency independent, and occurs for a single angle of incidence only [ $\varphi_B = \sin^{-1}(k_B/k_p)$ ]. For torsional trace wave matching only, the expression for the wave transmission reduces to:

$$T_p T_p^* = 1 - \text{tors}(\text{tors})^*, \quad (27)$$

where the energy transmission is solely due to the trace matching between the plate flexural and beam torsional waves. This coincidence condition is dependent on both angle and frequency, that is, the angle at which this coincidence condition occurs increases with the corresponding coincidence frequency [ $\varphi_T = \sin^{-1}(k_T/k_p)$ ].

### III. ACTIVE CONTROL OF THE PLATE FLEXURAL WAVE TRANSMISSION

The active control of the flexural wave transmission in plate 2 may be realized with the application of point control forces and point control moments to the reinforcing beam, as shown in the Fig. 3. The point forces are arranged to excite only flexural motion in the beam, and similarly, the point control moments excite only torsional motion in the beam.

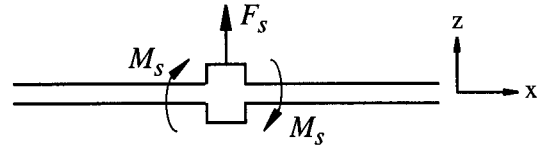


FIG. 3. Application of a single point control force and a single point control moment to the reinforcing beam.

#### A. Point force control

For simplicity, we initially consider single channel control with the application of a single point force only to the beam. The total force acting on the beam consists of two parts; the exciting control force given by a point force  $F_s$  applied at a location  $y_0$  on the beam, and a force  $F_{BR}$  which is a result of the backward reaction from the plates on either side of the beam.

The equation of motion for the secondary flexural displacement of the beam,  $u_s$ , to the point control force and backward reaction force is<sup>10</sup>

$$E_b I \frac{\partial^4 u_s}{\partial y^4} + \rho_b A \frac{\partial^2 u_s}{\partial t^2} = F_{BR} + F_s \delta(y - y_0). \quad (28)$$

$F_{BR}$  is the net vertical shear force acting at the boundaries between the beam and the plates, that is:

$$F_{BR} = \left( Q_{x_s} + \frac{\partial M_{xx_s}}{\partial y} \right) \Big|_{x=0^+} - \left( Q_{x_s} + \frac{\partial M_{xx_s}}{\partial y} \right) \Big|_{x=0^-}, \quad (29)$$

where the secondary shear forces  $Q_{x_s}$  and twisting moments  $M_{xx_s}$  are described by Eqs. (1) and (3), and are a result of the secondary flexural displacement in the plates.

Due to the symmetry under the control force application, the secondary flexural displacements in plates 1 and 2 should be symmetric.<sup>11</sup> At the boundary interfaces between the plates and beam, the secondary coupling conditions can be described by Eqs. (7) and (8), with the rotation of the beam and in the plates about the  $y$  axis equal to zero for beam flexural excitation only. Using the wave number transformation of Eq. (29) in the  $y$  direction into the  $\gamma_y$  domain, Eqs. (1) and (3) to describe the plate motions, and the boundary conditions to describe the coupling between the plate and

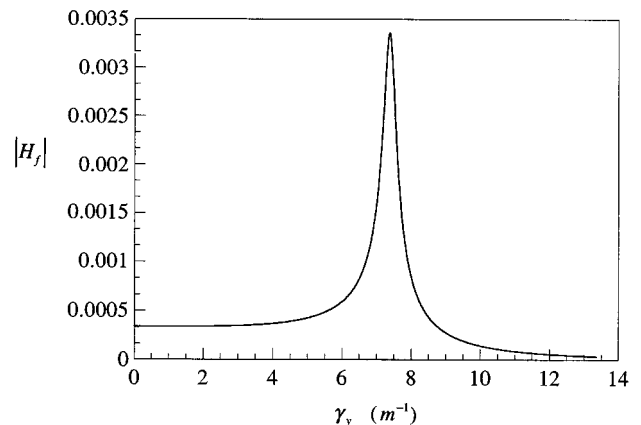


FIG. 4. Pole location of  $H_f$  in the supersonic wave number spectrum.

beam motions, it is possible to describe  $F_{BR}$  in terms of the beam secondary flexural displacement  $\tilde{u}_s(\gamma_y)$  by

$$\begin{aligned} \tilde{F}_{BR}(\gamma_y) = & 2jD(k_p^4 - \gamma_y^4)[(k_p^2 - \gamma_y^2)^{-1/2} \\ & + j(k_p^2 + \gamma_y^2)^{-1/2}]\tilde{u}_s(\gamma_y). \end{aligned} \quad (30)$$

The wave number transformation of Eq. (28) involves multiplying by  $e^{-j\gamma_y y}$  and integrating over the range  $(-\infty \leq y$

$\leq \infty)$ . Using Eq. (30) and the Fourier transformation of Eq. (28) results in the following expression for the beam secondary flexural displacement:

$$\tilde{u}_s(\gamma_y) = \frac{F_s}{E_b I} H_f(\gamma_y) e^{-j\gamma_y y_0}, \quad (31)$$

where

$$H_f(\gamma_y) = \frac{1}{k_y^4 - k_B^4 + (2jD/E_b I)(k_p^4 - \gamma_y^4)[(k_p^2 - \gamma_y^2)^{-1/2} + j(k_p^2 + \gamma_y^2)^{-1/2}]}. \quad (32)$$

It was mentioned earlier that although the coupling conditions between the plates and the beam are the same as those described in Eqs. (7) and (8), for secondary structural displacements due to point force application, the angular displacements at the plate and beam boundaries are zero. This allows an expression for the secondary displacement of plate 2 in the wave number space described by

$$\begin{aligned} \tilde{W}_2^s(x, \gamma_y) = & [A_1(\gamma_y) e^{-j\sqrt{k_p^2 - \gamma_y^2} x} \\ & + A_2(\gamma_y) e^{-\sqrt{k_p^2 + \gamma_y^2} x}] \tilde{u}_s(\gamma_y), \end{aligned} \quad (33)$$

where

$$A_1(\gamma_y) = \frac{\sqrt{k_p^2 + \gamma_y^2}}{\sqrt{k_p^2 + \gamma_y^2} - j\sqrt{k_p^2 - \gamma_y^2}} \quad (34)$$

and

$$A_2(\gamma_y) = -j \frac{\sqrt{k_p^2 - \gamma_y^2}}{\sqrt{k_p^2 + \gamma_y^2} - j\sqrt{k_p^2 - \gamma_y^2}}$$

are, respectively, the amplitudes of the secondary traveling waves and near-field decay waves. The resultant secondary displacement response can be obtained by the following wave number integration:

$$\begin{aligned} W_2^s(x, y) = & \frac{F_s}{2\pi E_b I} \int_{-\infty}^{\infty} [A_1(\gamma_y) e^{-j\sqrt{k_p^2 - \gamma_y^2} x} + A_2(\gamma_y) \\ & \times e^{-\sqrt{k_p^2 + \gamma_y^2} x}] H_f(\gamma_y) e^{-j\gamma_y(y_0 - y)} d\gamma_y. \end{aligned} \quad (35)$$

If the error sensors are located in the far field of the transmitted waves (at  $x = 10\lambda_p$ ), then the only portion of the wave number spectrum which contributes to the far-field propagating waves is the supersonic wave number component of the spectrum, where the wave number component  $\gamma_y$  has magnitude less than the plate wave number  $k_p$ , (that is,  $|\gamma_y| < k_p$ ).<sup>12</sup> Therefore the limits of the integral can be reduced to the range from  $-k_p$  to  $k_p$ , where the real part of  $k_p$  is approximately  $35 \text{ m}^{-1}$  at an excitation frequency of 500 Hz, and hence the flexural wave motion in the far field of plate 2 due to the point control force on the beam can be approximated as

$$\begin{aligned} W_2^s(x, y) = & \frac{F_s}{2\pi E_b I} \int_{-k_p}^{k_p} A_1(\gamma_y) e^{-j\sqrt{k_p^2 - \gamma_y^2} x} H_f(\gamma_y) \\ & \times e^{-j\gamma_y(y_0 - y)} d\gamma_y. \end{aligned} \quad (36)$$

Initial examination of the supersonic wave number spectrum of the radiated flexural waves in plate 2 found that the waves are dominated by the wave number component which is determined by the pole location of  $H_f(\gamma_y)$  in the range of  $|\gamma_y| \leq k_p$ . If the plate-to-beam flexural stiffness ratio  $D/E_b I$  is small (that is, the beam is considerably stiffer than the plate), the dominant component will be in the vicinity of  $k_B$ , where  $k_B = 7.2 \text{ m}^{-1}$ , as illustrated in Fig. 4. This coincides with the results of the primary wave transmission, where for beam flexural motion, the maximum plate flexural wave transmission occurs at the flexural coincidence condition, corresponding to when the wave number component of the plate in the  $y$  direction  $k_y$ , is equal to the beam natural flexural wave number  $k_B$ .

The single point force is located at a position  $y_0 = 0$  on the beam. The corresponding secondary flexural waves in the beam generated by the single control force have a decaying magnitude after a distance of approximately  $0.3\lambda_B$  from the origin along the  $\pm y$  directions. Therefore, in order to achieve global attenuation of the transmitted primary plane waves, it is necessary to generate a secondary plane wave with a nondecaying magnitude along the  $y$  direction. As a result, multiple channel control was employed where multiple point control forces are used to excite the beam. For  $2N+1$  point forces equally spaced in the  $y$  direction by a distance  $\Delta$ , the superimposed secondary flexural displacement in plate 2 can be expressed as

$$\begin{aligned} W_2^s(x, y) = & \frac{1}{2\pi E_b I} \int_{-k_p}^{k_p} A_1(\gamma_y) e^{-j\sqrt{k_p^2 - \gamma_y^2} x} H_f(\gamma_y) \\ & \times \sum_{n=-N}^N F_n^s e^{-jk_y(n\Delta - y)} d\gamma_y. \end{aligned} \quad (37)$$

The determination of the magnitudes and phases of the point control forces poses a minimization problem with multiple variables to optimize. To gain the initial physical insight of the control feasibility, the control forces are arranged to have the same magnitudes and prefixed phases as follows:

$$F_n^s = F_s e^{j\phi_n}, \quad n = -N, \dots, N. \quad (38)$$

For example, if  $\phi_n = 0$ , a uniform amplitude of the radiated secondary waves along the  $y$  direction can be generated by the control forces, but the spatial phase in the region of interest does not match that of the primary transmitted waves.

From the observation of the flexural wave transmission through the beam, it has been shown that the transmitted primary plane waves are generated by the nondecaying flexural and torsional vibrations in the beam as described by Eqs. (13) and (14). If the phases of the point control forces are arranged to have the same spatial phase variation to that of the primary flexural waves in the beam, as shown in Eq. (13), it is expected that the beam secondary flexural response to the control forces will also have the same spatial phase variation in the spatial range where the forces are located. Hence the secondary flexural waves in plate 2 from the beam vibration will have a wave feature with spatial phase in the  $y$  direction determined by that of the primary flexural waves in the beam. Also, we know that the primary flexural waves in the plates have their maximum transmission at the flexural coincidence (that is, at  $k_y = k_B$ ), and if the control forces are arranged to have the spatial phase relationship at the flexural coincidence, then the radiated secondary flexural waves in plate 2 will have the optimal spatial phase match with transmitted primary waves at the flexural coincidence. For this case, the phases of the control forces in Eq. (37) become

$$\phi_n = k_B n \Delta, \quad n = -N, \dots, N, \quad (39)$$

where  $\Delta = 0.3\lambda_B$  and  $\lambda_B = 0.87$  m. This arrangement is similar to the biologically inspired control strategy, where a group of actuators are connected together with certain phase and amplitude relationship, and only one control signal is needed to drive them.<sup>12</sup> Using this spatial phase relationship and the following expression:<sup>13</sup>

$$\sum_{n=-N}^N e^{-j\omega n \Delta} = \frac{\sin[\omega(2N+1)\Delta/2]}{\sin[\omega\Delta/2]}. \quad (40)$$

Equation (36) becomes

$$W_2^s(x, y) = F_s G_f, \quad (41)$$

where

$$G_f = \frac{1}{2\pi E_b I} \int_{-k_p}^{k_p} A_1(\gamma_y) e^{-j\sqrt{k_p^2 - \gamma_y^2} x} H_f(\gamma_y) \times \frac{\sin[(\gamma_y - k_B)(2N+1)\Delta/2]}{\sin[(\gamma_y - k_B)\Delta/2]} e^{j\gamma_y y} d\gamma_y. \quad (42)$$

For an infinite number of control forces, that is,  $2N+1 \rightarrow \infty$ , and using the following expressions:

$$\lim_{M \rightarrow \infty} \frac{\sin Mx}{x} = \pi \delta(x), \quad (43)$$

$$\lim_{x \rightarrow 0} \frac{\sin x}{x} = 1, \quad (44)$$

the expression for  $G_f$  in Eq. (42) can be simplified to

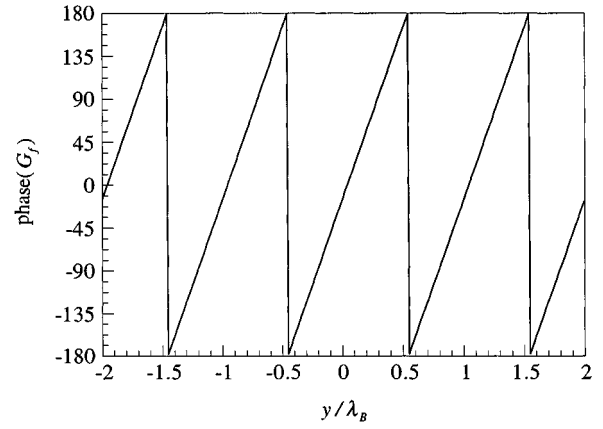


FIG. 5. Spatial phase variation of  $G_f$  along the  $y$  direction.

$$G_f = \frac{A_1(k_B) H_f(k_B) e^{-j\sqrt{k_p^2 - k_B^2} x} e^{jk_B y}}{2E_b I}. \quad (45)$$

A uniformly distributed magnitude of  $G_f$  corresponding to Eq. (45) along the  $y$  direction in the far field of plate 2 is now attained. Also, the spatial phase variation of  $G_f$  matches with the phase variation at the flexural coincidence condition (at  $e^{jk_B y}$ ), as the wavelength between each consecutive wave in the  $y$  direction  $\lambda_y$ , matches the natural flexural wavelength of the beam,  $\lambda_B$ , as shown in Fig. 5.

The displacement at the error sensor locations is the superposition of the primary transmitted waves and secondary flexural waves generated by the control forces, that is,

$$W_2^{\text{total}}(x, y) = W_2^p(x, y) + W_2^s(x, y), \quad (46)$$

where the primary transmitted wave in the far field of plate 2 is approximated as

$$W_2^p(x, y) = T_p e^{-j(k_p \cos \varphi)x + j(k_p \sin \varphi)y}. \quad (47)$$

The cost function used for the control optimization is the averaged squared plate flexural displacement  $J^F$  at the error sensor location  $x_0 = 10\lambda_p$ , and at  $M$  discrete locations along the  $y$  direction:

$$J^F = \frac{1}{M} \sum_{i=1}^M W_2^{\text{total}}(x_0, y_i) [W_2^{\text{total}}(x_0, y_i)]^*. \quad (48)$$

By standard methods, the cost function can be expressed as a quadratic function of the control force  $F_s$ .<sup>14</sup>

$$J^F = F_s A_f F_s^* + B_f F_s^* + F_s B_f^* + C_f, \quad (49)$$

where

$$A_f = \frac{1}{M} \sum_{i=1}^M G_f(x_0, y_i) [G_f(x_0, y_i)]^*, \quad (50)$$

$$B_f = \frac{1}{M} \sum_{i=1}^M T_p e^{-j(k_p \cos \varphi)x_0} e^{j(k_p \sin \varphi)y_i} [G_f(x_0, y_i)]^*, \quad (51)$$

and

$$C_f = T_p T_p^*. \quad (52)$$

The optimal control force can be obtained by differentiating the cost function with respect to the real and imaginary components of the control force. The optimal force corresponds to the force value when both derivatives are zero. The solution for the optimal control force for the minimum averaged plate flexural displacement can therefore be obtained as<sup>14</sup>

$$F_s|_{\text{opt}} = -\frac{B_f}{A_f}. \quad (53)$$

The corresponding maximum attenuation level can be expressed (in dB) by taking the ratio between the controlled and uncontrolled averaged plate displacements, that is,

$$P^F|_{\text{atten}} = -10 \log_{10} \left| \frac{J_{\min}^F}{C_f} \right| = -10 \log_{10} \left| 1 - \frac{B_f^* B_f}{C_f A_f} \right|. \quad (54)$$

## B. Point moment control

Similar arrangements can be applied to the point moment control to achieve large attenuation of the flexural wave transmission in the far field of plate 2 at the torsional coincidence. With the application of a single point moment to the beam, the total moment acting on the beam also consists of two parts: the exciting moment  $M_s$  acting at a location  $y_b$  on the beam, and a moment  $M_{\text{BR}}$  to include the backward reaction from the plates. The equation of motion for the beam secondary torsional displacement  $\theta_s$  becomes

$$GJ \frac{\partial^2 \theta}{\partial y^2} - \rho_b I_p \frac{\partial^2 \theta}{\partial t^2} = M_{\text{BR}} - M_s \delta(y - y_b). \quad (55)$$

$M_{\text{BR}}$  is the net bending moment acting at the boundaries of the plates and beam, that is,

$$M_{\text{BR}} = (M_{x_y_s})_{x=0^+} - (M_{x_y_s})_{x=0^-}, \quad (56)$$

where the secondary bending moments,  $M_{x_y_s}$ , result from the secondary flexural displacements in the plates as described by Eq. (2).

Due to the symmetry of the applied control moment, the secondary vibrations in both plates are also symmetric. At the boundary interfaces, the rotation in the plates about the  $y$  axis are equal to the beam secondary torsional displacement. However, for beam torsional excitation only, the secondary flexural displacements in both the plates and beam are equal to zero. Using this information,  $M_{\text{BR}}$  can be obtained in wave number space in terms of the beam secondary torsional displacement  $\tilde{\theta}_s(\gamma_y)$  as

$$\tilde{M}_{\text{BR}}(\gamma_y) = 2jD(\sqrt{k_p^2 + \gamma_y^2} + j\sqrt{k_p^2 - \gamma_y^2})\tilde{\theta}_s(\gamma_y). \quad (57)$$

Using Eq. (57), the wave number transformation of Eq. (55) gives rise to

$$\tilde{\theta}_s(\gamma_y) = \frac{M_s}{GJ} H_m(\gamma_y) e^{-j\gamma_y y_b}, \quad (58)$$

where

$$H_m(\gamma_y) = \frac{1}{\gamma_y^2 - k_T^2 + \frac{2jD}{GJ}(\sqrt{k_p^2 + \gamma_y^2} + j\sqrt{k_p^2 - \gamma_y^2})}. \quad (59)$$

Under point moment application the structural flexural displacements are equal to zero. Using this information and the boundary conditions defined by Eqs. (7) and (8), it is possible to obtain an expression for the secondary flexural displacement response of plate 2 due to the point moment only, described by wave number integration in the  $\gamma_y$  domain:

$$W_2^s(x, y) = \frac{M_s}{2\pi GJ} \int_{-\infty}^{\infty} B_1(\gamma_y) [e^{-j\sqrt{k_p^2 - \gamma_y^2} x} - e^{-\sqrt{k_p^2 + \gamma_y^2} x}] H_m(\gamma_y) e^{-j\gamma_y(y_b - y)} dy_y, \quad (60)$$

where

$$B_1 = \frac{1}{j\sqrt{k_p^2 - \gamma_y^2} - \sqrt{k_p^2 + \gamma_y^2}}. \quad (61)$$

and  $B_1$  is the amplitude of both the traveling and near-field secondary waves in the plate under the point moment application. By similar analysis for the point force application, the radiated flexural waves in the far field of plate 2 due to the point control moment on the beam are found to be directly contributed by the supersonic wave number spectrum, and therefore the limits of the integration in Eq. (60) can be limited to the range from  $-k_p$  to  $k_p$ :

$$W_2^s(x, y) = \frac{M_s}{2\pi GJ} \int_{-k_p}^{k_p} B_1(\gamma_y) e^{-j\sqrt{k_p^2 - \gamma_y^2} x} H_m(\gamma_y) \times e^{-j\gamma_y(y_b - y)} d\gamma_y. \quad (62)$$

Examination of the pole location of  $H_m(\gamma_y)$  in the relevant wave number spectrum, ( $|\gamma_y| < k_p$ ) and at 500 Hz, reveals that if the plate flexural-to-beam torsional stiffness ratio  $D/GJ$  is small, then the dominant wave number component of  $\gamma_y$  is in the vicinity of  $k_T$ , where  $k_T = 1.4 \text{ m}^{-1}$ . This confirms the torsional coincidence phenomenon where the maximum primary transmission occurs when  $k_y = k_T$ .

Multiple point moments, equally spaced along the  $y$  direction by a distance  $\Delta$ , are used to generate a nondecaying secondary wave in plate 2 along the  $y$  direction. Biologically inspired control is employed where the array of moments are arranged to have the same magnitudes and prefixed phases. For optimal results, the phases of the control moments are arranged to have the same spatial phase variation to that of the primary torsional waves in the beam. As a result, the beam secondary torsional response will have the same spatial phase variation as the primary torsional motion in the beam. Also, we know that for beam torsional motion, the primary flexural waves in plate 1 have their maximum transmission at the torsional coincidence, that is, at  $k_y = k_T$ . Therefore, if the control moments are arranged to have their spatial phase relationship at the torsional coincidence, then the secondary flexural waves in plate 2 will have the optimal spatial phase match with the primary transmitted waves. For this case, the phases of the control moments become:

$$\phi_n = k_T n \Delta. \quad (63)$$

Using  $2N+1$  control moments separated by a distance  $\Delta$ , and the expressions in Eqs. (40), (43), and (44), the second-

ary flexural wave displacement for point moment control becomes

$$W_2^s(x, y) = M_s G_m, \quad (64)$$

where

$$G_m = \frac{B_1(k_T) H_m(k_T) e^{-j\sqrt{k_p^2 - k_T^2} x} e^{jk_T y}}{2GJ}. \quad (65)$$

The distance between the point moments used in this simulation is  $\Delta = 0.5\lambda_T$ , where  $\lambda_T = 4.4$  m, a uniformly distributed magnitude of the radiated secondary plate waves along the  $y$  direction is attained. The spatial phase variation along the  $y$  direction matching that at the torsional coincidence (at  $e^{jk_T y}$ ), that is, for this spatial phase arrangement, the wavelength of the secondary plate waves along the  $y$  direction is equal to the natural torsional wavelength of the beam,  $\lambda_T$ .

Now it is only necessary to optimize a single variable  $M_s$  in order to minimize the total flexural displacement in plate 2 at the error sensor locations. The total displacement at the error sensor locations (also at  $x_0 = 10\lambda_p$  for point moment control) is the superposition of the primary transmitted waves and the secondary flexural waves generated by the control moments:

$$W_2^{\text{total}}(x, y) = W_2^p(x, y) + W_2^s(x, y), \quad (66)$$

where  $W_2^p(x, y)$  represents the primary transmitted wave as in Eq. (47) and  $W_2^s(x, y)$  represents the secondary flexural waves generated by the control moments as in Eq. (64). Using the same cost function for the control force application, and at  $M$  discrete locations along the  $y$  direction, we can express the cost function as a quadratic function of the control moment:

$$J^M = M_s A_m M_s^* + B_m M_s^* + M_s B_m^* + C_m, \quad (67)$$

where

$$A_m = \frac{1}{M} \sum_{i=1}^M G_m(x_0, y_i) [G_m(x_0, y_i)]^*, \quad (68)$$

$$B_m = \frac{1}{M} \sum_{i=1}^M T_p e^{-j(k_p \cos \varphi)x_0 + j(k_p \sin \varphi)y_i} [G_m(x_0, y_i)]^*, \quad (69)$$

and

$$C_m = C_f = T_p T_p^*. \quad (70)$$

The solution for the optimal control moment for the minimum averaged plate displacement is obtained as

$$M_s|_{\text{opt}} = -\frac{B_m}{A_m}, \quad (71)$$

and the corresponding maximum attenuation level is

$$P^M|_{\text{atten}} = -10 \log_{10} \left| 1 - \frac{B_m^* B_m}{C_m A_m} \right|. \quad (72)$$

## IV. RESULTS AND DISCUSSION

### A. Results of the primary flexural wave transmission

As the theoretical analysis in this paper is based on the requirement that the beam–plate system is constructed of the

same material throughout, the properties of aluminium were selected for the materials parameters, using  $\rho = 2700$  kg/m<sup>3</sup>,  $E = 6.9 \times 10^{10}$  N/m<sup>2</sup>,  $\nu = 0.33$ , and  $\eta = 0.001$ . The regions of the maximum transmission occur at the coincidence conditions, and can be described in terms of the stiffness of the structure. The flexural rigidities of the beam and plate are  $E_b I$  and  $D$ , respectively, and the torsional rigidity  $GJ$  of the beam was calculated using the analysis of Wang.<sup>15</sup> In his analysis on the input impedance of a beam coupled to a plate, Lamb<sup>16</sup> introduced a coupling parameter,  $D/E_b I k_B$ , which describes the frequency dependent degree of plate–beam coupling in terms of the flexural rigidities of the plate and beam. For beam stiffness which is significantly greater than the plate stiffness, the regions of the maximum transmission of the plate flexural waves through the beam become more clearly defined, as the beam increases its ability to act as an effective passive device. These regions of maximum transmission correspond to the coincidence conditions determined by the trace wave matching phenomenon described earlier.

In Fig. 6(a)–(c), the characteristics of the transmission of the plate flexural waves through the reinforcing beam are illustrated for a frequency range up to 2000 Hz, and for a relevant range of angles of the incident waves from 0° to 20°. Using a plate thickness of 1.6 mm, and reinforcing beams of both width and height of 2 cm, results in a very small coupling parameter  $D/E_b I k_B$  of  $4.4 \times 10^{-4}$ . Figure 6(a) corresponds to the wave transmission due to the flexural coincidence condition only, as described by Eq. (26). The flexural coincidence condition is independent of frequency and occurs for a single incident angle corresponding to  $\varphi_B = \sin^{-1}(k_B/k_p)$ , where  $\varphi_B = 11.5^\circ$  for this beam–plate model. As the beam stiffness decreases, the incident angle for flexural coincidence increases, and also the region of maximum transmission increases as the beam loses its ability to act as a passive control device.

Figure 6(b) shows the flexural wave transmission for the torsional trace wave matching condition only, as described in Eq. (27). It demonstrates that the angle of incidence at torsional coincidence increases with the corresponding coincidence frequency. Similarly, as the beam stiffness decreases, the angle of incidence at torsional coincidence gradually increases, and the region of maximum transmission surrounding the coincidence angle is also increased.

The total flexural wave transmission in plate 2 through a reinforcing beam, as described by Eq. (25), is shown in Fig. 6(c). It can be observed that the maximum transmission occurs at the coincidence conditions. Away from the coincidences, there is very little transmission which concludes that the beam itself acts as an effective passive attenuation device. The contribution of the interference terms in Eq. (25) displays no extra information to the general shape of the total wave transmission in Fig. 6(c).

In the regions of maximum transmission, the spatial phase of the plate flexural waves in the  $y$  direction is controlled by the corresponding coincidences, that is, at  $e^{jk_B y}$  for flexural coincidence, and  $e^{jk_T y}$  for torsional coincidence.

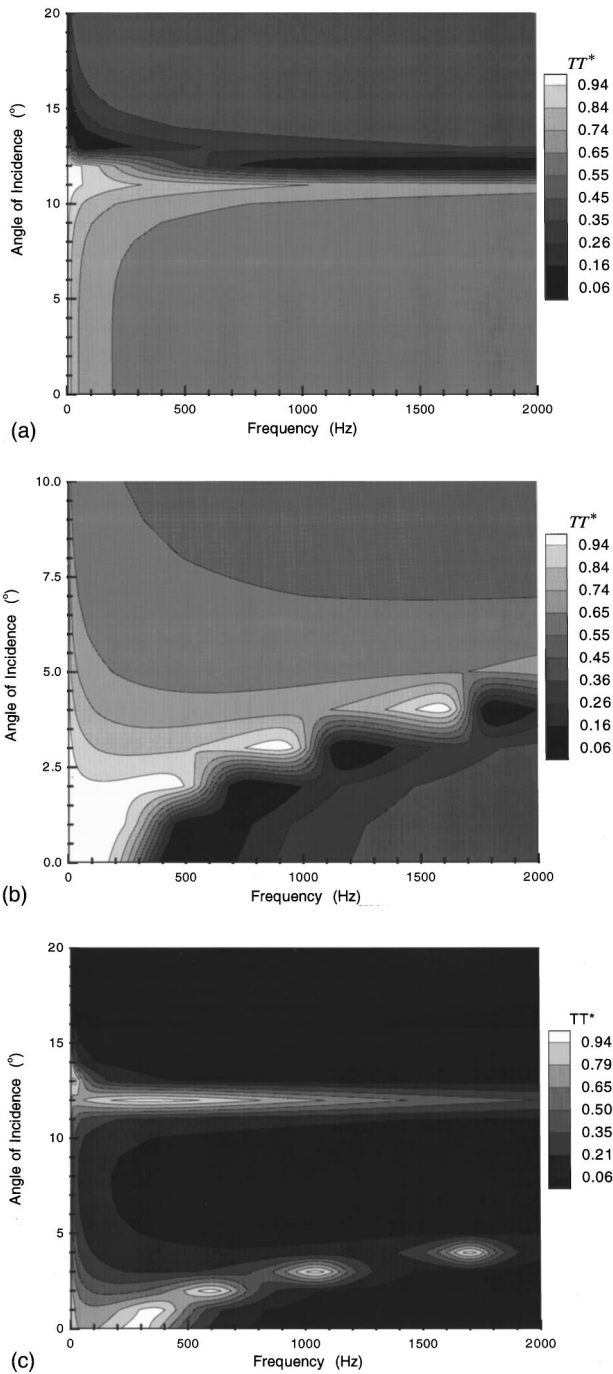


FIG. 6. (a) Flexural wave transmission in the far field of plate 2 for flexural coincidence only. (b) Flexural wave transmission in the far field of plate 2 for torsional coincidence only. (c) The total flexural wave transmission in the far field of plate 2.

### B. Control results

Figure 7 shows the flexural wave attenuation level at the error sensor location ( $x_0 = 10\lambda_p$ ), and for 401 discrete locations along the  $y$  direction corresponding to the range  $(-2\lambda_B, 2\lambda_B)$ . Examination of a relevant range for the incident angle from  $0^\circ$  to  $20^\circ$  at excitation frequencies of 500 Hz and 1000 Hz shows that a significant attenuation level of approximately 14.3 dB has been achieved at the flexural coincidence angle of  $\varphi_B = 11.5^\circ$ . The level of attenuation at both frequencies is the same. Due to the nature of the ar-

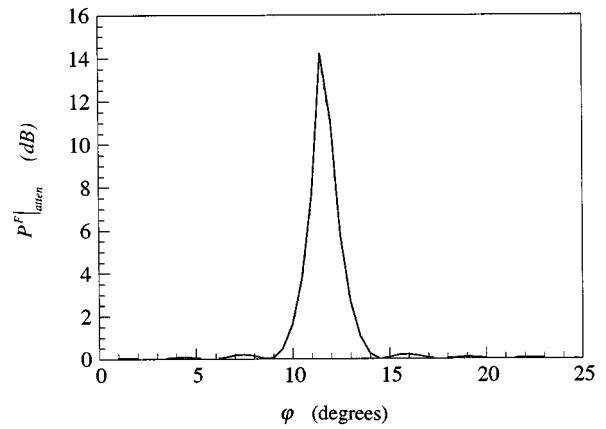


FIG. 7. Attenuation levels of the flexural wave transmission at excitation frequencies of 500 Hz (—) and 1000 Hz (----) using point control forces.

anged control force excitation, the radiated secondary flexural waves have poor spatial phase correlation with the transmitted primary waves away from the flexural coincidence angle, which results in poor global attenuation. However, away from the coincidence, the beam itself acts as an effective passive device, as shown in Fig. 6(a). Changing the frequency of excitation has no effect on the attenuation level attained or the angle at which attenuation is achieved, as the flexural coincidence condition is independent of frequency. Figure 8 shows the corresponding dimensionless magnitude of the optimal control force  $F_{s,opt}$ , for an amplitude of the incident wave  $A_p$  of  $10^{-4}$  m, where a large force is required at the flexural coincidence angle. At lower frequencies, the plate adds an additional stiffness susceptance to the input impedance of a beam-stiffened plate excited by a point force applied to the beam.<sup>16</sup> As the frequency increases, the beam is able to vibrate more freely, and the primary flexural energy level in the beam slightly decreases. Hence, at higher frequencies, a smaller amplitude of the control forces is required in order to generate secondary vibrational levels in the beam to match the primary energy level in the beam.

The plate flexural attenuation level under the control moment application is achieved for the same number of discrete locations along the  $y$  direction as for the point control

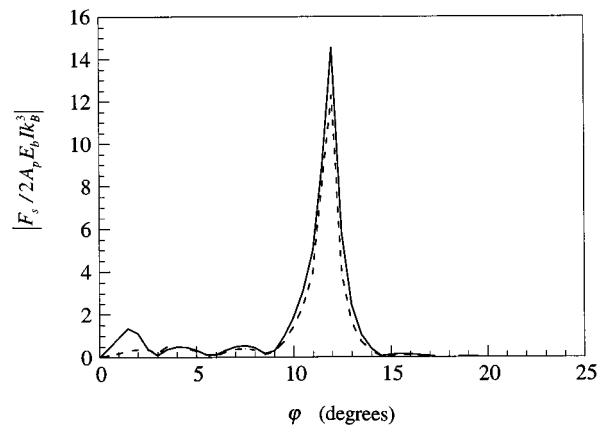


FIG. 8. Dimensionless magnitudes of the optimal control forces,  $F_s$ , for an amplitude of the incident wave,  $A_p$ , of  $10^{-4}$  m at 500 Hz (—) and 1000 Hz (----).

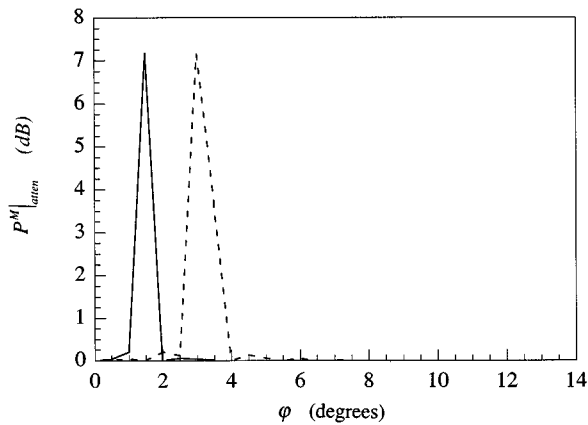


FIG. 9. Attenuation levels of the flexural wave transmission at excitation frequencies of 500 Hz (—) and 1000 Hz (----) using point control moments.

force arrangement, corresponding to the range  $(-2\lambda_T, 2\lambda_T)$ . Figure 9 shows the attenuation levels of the flexural wave transmission using point control moments at excitation frequencies of 500 Hz and 1000 Hz. The peaks of the attenuation levels occur at the corresponding torsional coincidence angles of  $1.5^\circ$  and  $3.0^\circ$ , respectively. Although significant attenuation levels at the torsional coincidence angles have been achieved, the amount of attenuation is not as significant as for the control force application. Shown in Fig. 10 are the dimensionless magnitudes of the optimal control moments,  $M_s|_{\text{opt}}$ , which occur at the corresponding torsional coincidence angles for the frequencies of 500 Hz and 1000 Hz, respectively. Figure 10 shows that at higher frequencies, the magnitudes of the control moments required for the same level of attenuation increases. Also, as the frequency increases, the primary energy level in the beam due to torsional displacement is increased at the corresponding torsional coincidence angle. This is because at higher frequencies, the beam torsional stiffness relative to the plate bending stiffness increases.<sup>17</sup> As a result, a larger magnitude of the control moments is required in order to generate the sufficient displacement to match that of the primary transmitted waves.

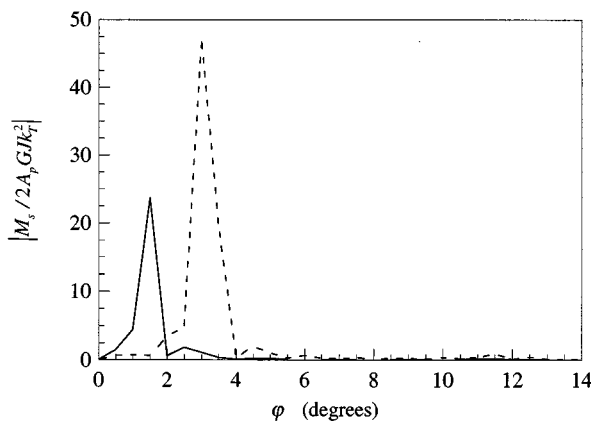


FIG. 10. Dimensionless magnitudes of the optimal control moments,  $M_s$ , for an amplitude of the incident wave,  $A_p$ , of  $10^{-4}$  m at 500 Hz (—) and 1000 Hz (----).

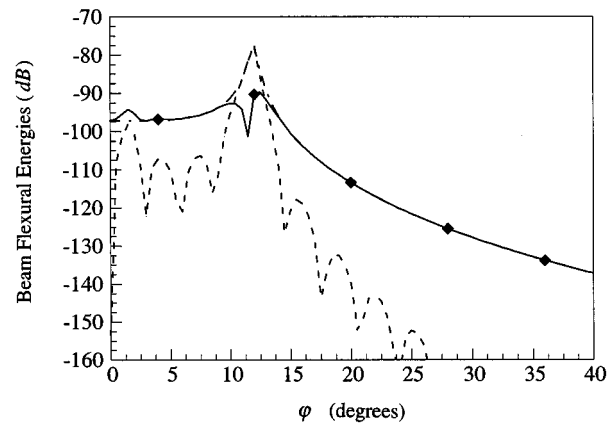


FIG. 11. Total beam flexural energy (—◆—◆—) showing the contributions by the primary (----) and secondary (---) beam flexural displacements.

## V. EFFECT OF THE ACTIVE CONTROL ON THE BEAM VIBRATION AND NEAR-FIELD PLATE DISTRIBUTION

For the application of multiple point control forces to the reinforcing beam, it is of interest to investigate the total beam flexural energy and the near-field distribution of the plate vibration, to determine whether there has been significant increase in the vibration levels in these areas. For the same control force arrangement used earlier in the analysis, the beam flexural energy under control and the primary and secondary beam flexural energies are shown in Fig. 11 as a function of the incident angle and at 500 Hz. The flexural energies are obtained from the averaged beam displacements over the given number of discrete locations along the  $y$  direction corresponding to the range  $(-2\lambda_B, 2\lambda_B)$ . The beam secondary flexural displacement is obtained using the solution for the optimal control force derived in the minimisation of the flexural energy transmission at the error sensor locations ( $x = 10\lambda_p$ ) in the far field of plate 2 as shown in Fig. 8. The results in Fig. 11 show that around the flexural coincidence angle, the primary and secondary beam flexural energies are almost equal, and at a maximum of  $-77$  dB at the flexural coincidence angle of  $\varphi_B = 11.5^\circ$ . The corresponding beam flexural energy under control at the flexural coincidence angle is  $-91$  dB, resulting in a 14 dB reduction of the beam flexural energy at the flexural coincidence angle. Similar results are found in examining the beam torsional energy distributions for the application of point control moments to the beam, where the primary and secondary beam torsional energies are both a maximum and are equal at the torsional coincidence angle, and the corresponding beam torsional energy under control at the torsional coincidence angle is attenuated.

In order to investigate the near-field distribution in plate 2 for the control force application, the primary and total squared plate displacements were averaged over the given number of discrete locations along the  $y$  direction, and then examined as a distance away from the beam along the  $x$  direction. The expressions for both the primary and secondary flexural plate displacements include the terms describing the near-field waves. The primary flexural energy distribution was obtained for an incident angle at the flexural coin-

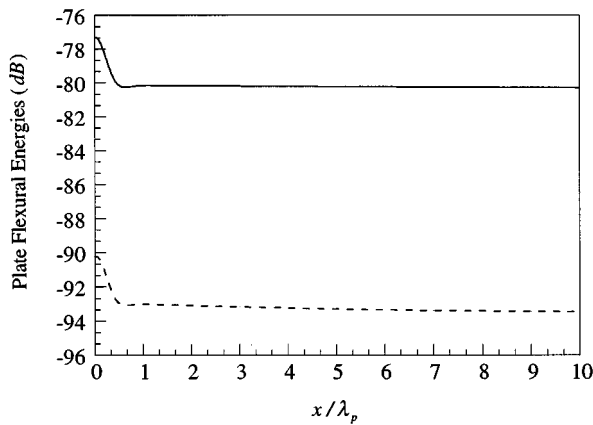


FIG. 12. Primary (—) and controlled (----) flexural energy distributions along the  $x$  direction in plate 2, for the optimal control force obtained at the error sensor locations ( $x=10\lambda_p$ ).

cidence condition, and the secondary flexural energy was determined using the same optimal control force obtained at the error sensor locations as shown in Fig. 8. Figure 12 shows the primary and controlled energy distributions along the  $x$  direction beginning at  $x=0$  at the boundary interface between the beam and plate 2, up to the error sensor locations at  $x=10\lambda_p$ . At the boundary interface ( $x=0$ ), the primary flexural energy in the plate is equal to  $-77$  dB, corresponding to the primary flexural energy in the beam, and the attenuated flexural energy in the plate is  $-91$  dB, which confirms the results obtained for the beam flexural energies in Fig. 11. In Fig. 12, it can be seen that the near-field region for the primary vibrations in the plates is significant for  $x < 0.5\lambda_p$ , after which the propagating waves dominate the response. The near-field decay waves increase the primary and controlled flexural energy levels in the plate by as much as 3 dB. Attenuation of the total flexural energy transmission in the far field of plate 2 also attenuates the near-field energy distribution in the plate. For the control arrangement described in this paper, active control of the far-field flexural energy transmission results in a global attenuation level of the total plate flexural energy distribution of approximately 14 dB. Investigation of the near-field flexural energy distribution due to the control moment application also results in global attenuation in both the near-field and far-field regions of plate 2, although the level of attenuation achieved is not as significant as for the control force application. Mechanisms of the global control of the plate vibration are due to the significant reduction of the beam flexural vibration by using point control forces. Similarly, global control of the plate flexural energy transmission can be achieved with the application of point control moments to the beam, which reduces the beam torsional energy level.

## VI. CONCLUSIONS

The active attenuation of the plate flexural wave transmission through a reinforcing beam has been investigated for an infinite beam–plate system. It has been shown that the maximum flexural wave transmission occurs at the optimal trace wave matching between the flexural waves in the plate and the flexural and torsional waves in the beam, described

as flexural and torsional coincidence respectively. At incident angles away from these coincidence conditions, the wave transmission is not significant as the beam itself acts as an effective attenuation device. The active control was realized with the application of point control forces and moments to the reinforcing beam. The control forces were arranged to excite only flexural motion in the beam, and similarly, the control moments were arranged to excite only torsional motion in the beam. It was possible to optimize the attenuation results with the arrangement of the control forces and moments using information at the coincidence conditions. It was shown that with the application of multiple point forces, arranged so as to have the same spatial phase variation as the flexural waves in the beam at the flexural coincidence condition, the resulting secondary waves in the far field of plate 2 generated by the control forces had the optimal spatial phase match with the primary transmitted waves. Hence, maximum attenuation of the flexural wave transmission was achieved for the transmission occurring at flexural coincidence, making use of both active and passive control techniques. Similarly, the arrangement of point control moments so as to have the same spatial phase variation as the torsional waves in the beam at the torsional coincidence, resulted in the secondary flexural waves in the far field of plate 2 having the optimal phase match with the primary transmitted waves, and thereby achieving maximum attenuation of the flexural wave transmission at torsional coincidence. Global attenuation of the plate flexural wave transmission is achieved in both the near-field and far-field regions of plate 2. Mechanisms of the global control of the plate vibration are due to the significant reduction of the beam flexural vibration by using point control forces. Similarly, global control of the plate flexural energy transmission can be achieved with the application of point control moments to the beam, which reduces the beam torsional energy level.

- <sup>1</sup>R. H. Lyon, "Sound radiation from a beam attached to a plate," *J. Acoust. Soc. Am.* **34**, 1265–1268 (1962).
- <sup>2</sup>G. Maidanik, "Response of ribbed panels to reverberant acoustic fields," *J. Acoust. Soc. Am.* **34**, 809–824 (1962).
- <sup>3</sup>D. J. Mead, "Plates with regular stiffening in acoustic media: Vibration and radiation," *J. Acoust. Soc. Am.* **88**, 391–401 (1980).
- <sup>4</sup>J. Pan and C. H. Hansen, "Active control of total vibratory power flow in a beam," in *Proceedings from the International Congress on Recent Developments in Air and Structure-Borne Sound and Vibration*, Auburn University, pp. 229–236 (1990).
- <sup>5</sup>X. Pan and C. H. Hansen, "Active control of vibratory power transmission along a semi-infinite plate," *J. Sound Vib.* **184**, 585–610 (1994).
- <sup>6</sup>C. H. Hansen and A. J. Young, "Active control of vibration transmission in a stiffened semi-infinite plate," in *Proceedings from the International Congress on Air- and Structure-Borne Sound and Vibration*, Montreal, Canada, pp. 1485–1494 (1994).
- <sup>7</sup>J. Dickey and G. Maidanik, "Active control of response of ribbed panels," in *Proceedings of the Conference on Recent Advances in Active Control of Sound and Vibration*, Virginia Polytechnic Institute and State University, Blacksburg, Virginia, pp. 525–533 (1991).
- <sup>8</sup>E. E. Ungar, "Transmission of plate flexural waves through reinforcing beams: Dynamic stress concentrations," *J. Acoust. Soc. Am.* **33**, 633–639 (1961).
- <sup>9</sup>L. Cremer, M. Heckl, and E. E. Ungar, *Structure-Borne Sound* (Springer-Verlag, New York, 1988), 2nd ed., pp. 442–447.
- <sup>10</sup>G. L. Lamb, "Input impedance of a beam coupled to a plate," Bolt Beranek and Newman Inc., Report No. 603 (1958).



- <sup>11</sup>M. A. Heckl, "Compendium of Impedance Formulas," Bolt Beranek and Newman Inc., Report No. 774 (1961).
- <sup>12</sup>C. R. Fuller and J. P. Carneal, "A biologically inspired control approach for distributed elastic systems," *J. Acoust. Soc. Am.* **93**, 3511–3513 (1993).
- <sup>13</sup>D. G. Crighton, A. P. Dowling, J. E. Ffowcs Williams, M. Heckl, and F. G. Leppington, *Modern Methods in Analytical Acoustics, Lecture Notes* (Springer-Verlag, New York, 1992), pp. 109–110, 513.
- <sup>14</sup>J. Pan and C. H. Hansen, "Active control of total vibratory power flow in a beam: I. Physical system analysis," *J. Acoust. Soc. Am.* **89**, 200–209 (1991).
- <sup>15</sup>C. T. Wang, *Applied Elasticity* (McGraw-Hill, New York, 1953), pp. 85–89.
- <sup>16</sup>G. L. Lamb, "Input impedance of a beam coupled to a plate," *J. Acoust. Soc. Am.* **33**, 628–633 (1961).
- <sup>17</sup>H. G. D. Goyder and R. G. White, "Vibrational power flow from machines into built-up Structures, Part II: Wave propagation and power flow in beam-stiffened plates," *J. Sound Vib.* **68**, 77–96 (1980).

# Analysis of ceramic thickness shear piezoelectric gyroscopes

J. S. Yang

Department of Engineering Mechanics, University of Nebraska, Lincoln, Nebraska 68588

(Received 16 September 1996; accepted for publication 19 August 1997)

Equations for linear piezoelectricity are formulated in a reference frame rotating at a constant angular velocity and are simplified by a perturbation procedure when the angular velocity of the reference frame is small. The equations thus obtained are then employed in the analysis of a rectangular ceramic plate piezoelectric gyroscope operating with thickness shear modes. Approximate analytical solutions to the equations resulted from the perturbation procedure are obtained based on Mindlin's two-dimensional equations for a piezoelectric plate which are simplified by the thickness shear long wave approximation. Free-vibration frequencies and mode shapes, as well as the condition for double resonance, are obtained. Forced vibration is also studied which leads to a simple expression for the voltage sensitivity of the gyroscope. The analysis is approximate and qualitative mainly with the purpose of exhibiting some most basic characteristics of the gyroscope. Some of the results are compared with finite element numerical method. © 1997 Acoustical Society of America. [S0001-4966(97)01812-2]

PACS numbers: 43.40.Yq, 43.38.Fx [PJR]

## INTRODUCTION

Piezoelectric materials can be used to make gyroscopes (angular rate sensors)<sup>1</sup> to measure the angular velocity of a rotating body. Piezoelectric gyroscopes can be made of quartz or ceramics.<sup>2</sup> They make use of two modes of a vibrating piezoelectric body in which material particles move in perpendicular directions and the natural frequencies of the two modes must be very close. Examples are flexure-flexure vibrations of beams and thickness shear-thickness shear vibrations of plates.<sup>2</sup>

When a piezoelectric gyroscope is used to measure the angular velocity  $\Omega$  of a rotating body, the gyroscope is attached to the rotating body and is excited into mechanical vibration by applied alternating voltage through piezoelectric coupling. Then, in the reference frame attached to the rotating body, Coriolis force causes the gyroscope to vibrate in the direction perpendicular to the piezoelectrically excited motion. This motion caused by Coriolis force is related to  $\Omega$  and can be used to detect it. In the rotating reference frame, piezoelectric gyroscopes undergo small vibrations. The governing equations are more complicated than the equations of linear piezoelectricity in an inertial frame because of Coriolis force terms. These equations can be analyzed analytically or numerically. A numerical analysis can usually give quick and accurate results for gyroscopes working with low-frequency vibration modes like the flexure of beams. However, for high-frequency modes like the thickness shear of plates finite element numerical analysis is difficult and remains a challenging problem.<sup>3</sup> For gyroscopes of regular geometry, analytical analysis is possible which provides more insight into the problem and results can be used to compare with numerical analysis. For beam piezoelectric gyroscopes in flexure both numerical<sup>4,5</sup> and analytical<sup>6-8</sup> results are available. For plate thickness shear gyroscopes, only finite element numerical results from a supercomputer are available.<sup>9</sup> Therefore it is purposeful to perform some ana-

lytical analysis on plate thickness shear gyroscopes for a better understanding of the problem.

In this work, a perturbation procedure is established for the equations of linear piezoelectricity in a rotating frame when the angular velocity of the rotating frame is small. The perturbation procedure breaks the time harmonic motion of the piezoelectric body into two steps. In the first step the piezoelectric body behaves as if the reference frame were not rotating. In the second step the motion of the piezoelectric body is driven by Coriolis force corresponding to the motion obtained in the first step. Based on the equations resulting from the perturbation procedure, an approximate analytical analysis is performed on a rectangular ceramic plate gyroscope operating with thickness shear modes. Mindlin's equations for a piezoelectric plate<sup>10</sup> are employed with the thickness shear long wave approximation.<sup>11</sup> Resonant frequencies, mode shapes, double resonance condition, output sensing signal, and voltage sensitivity are obtained which are important in the design of the gyroscope. Some of the analytical results are compared with finite element numerical method.

## I. EQUATIONS FOR A PIEZOELECTRIC BODY IN A ROTATING FRAME

Let the piezoelectric body rotate at a constant angular velocity  $\Omega$ . A reference frame is attached to the body and rotated with it. We study the small vibration of the body in the rotating reference frame. Let the region occupied by the piezoelectric body in the rotating frame be denoted by  $V$  and its boundary surface by  $S$  with unit outward normal  $n_i$  and the following partitions (Fig. 1):

$$S = S_u \cup S_T = S_\phi^f \cup S_\phi^s \cup S_D, \quad (1a)$$

$$\emptyset = S_u \cap S_T = S_\phi^f \cap S_\phi^s = S_\phi^f \cap S_D = S_\phi^s \cap S_D, \quad (1b)$$

where  $S_u$  is the part of the surface  $S$  on which the mechanical displacement is prescribed and  $S_T$  the part of  $S$  where the traction vector is prescribed. Here,  $S_\phi^f$  represents the forcing

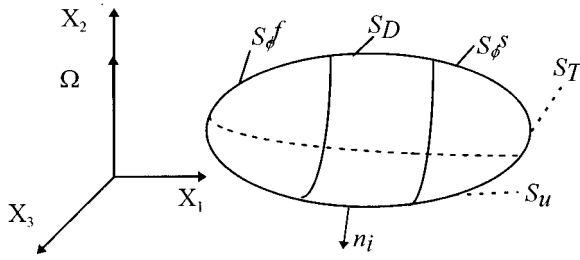


FIG. 1. A piezoelectric body in a rotating reference frame.

electrodes on which known values of the electric potential or voltage is applied and  $S_\phi^s$  represents the sensing electrodes on which values of the electric potential are unknown constants (may be functions of time). We note that  $S_\phi^f$  or  $S_\phi^s$  may each have several disjoint parts with different values of the electric potential on each individual part.  $S_D$  is the unelectroded part of the surface. Without loss of generality we orient the  $x_2$  axis along the axis of rotation. The angular velocity vector is represented by  $\Omega_j = \Omega s_j$ , where  $(s_1, s_2, s_3) = (0, 1, 0)$  is the unit vector along the rotation axis. Then the equations of balance of linear momentum for a linear piezoelectric body in the rotating frame can be obtained from the equations for linear piezoelectricity in an inertial frame<sup>11</sup> by adding Coriolis and centrifugal forces as

$$T_{ji,j} + \rho[f_i - 2\epsilon_{ijk}\Omega\zeta_j\dot{u}_k + O(\Omega^2)] = \rho\ddot{u}_i \text{ in } V, \quad (2)$$

where  $u_i$  is the mechanical displacement vector,  $T_{ij}$  the stress tensor,  $\epsilon_{ijk}$  the permutation tensor,  $\rho$  the mass density, and  $f_i$  the ordinary body force. The term that is linear in  $\Omega$  is the Coriolis force which is responsible for the detection of  $\Omega$  for piezoelectric gyroscopes.  $O(\Omega^2)$  is the centrifugal force which is proportional to the square of  $\Omega$  and the detailed expression of which is not shown because it will be neglected later within the approximation of this analysis. Summation convention for repeated tensor indices and the convention that a comma followed by an index denotes partial differentiation with respect to the coordinate associated with the index are used. A superimposed dot represents the time derivative. The equations of electrostatics, piezoelectric constitutive relations, the strain-displacement, and electric field-potential relations remain the same as those in an inertial frame<sup>11</sup>

$$D_{i,i} = 0 \text{ in } V, \quad (3a)$$

$$T_{ij} = c_{ijkl}S_{kl} - e_{kij}E_k \text{ in } V, \quad (3b)$$

$$D_i = e_{ijk}S_{jk} + \epsilon_{ij}E_j \text{ in } V, \quad (3c)$$

$$S_{ij} = (u_{i,j} + u_{j,i})/2 \text{ in } V, \quad (3d)$$

$$E_i = -\phi_{,i} \text{ in } V, \quad (3e)$$

$$u_i = \bar{u}_i \text{ on } S_u, \quad (3f)$$

$$T_{ji}n_j = \bar{t}_i \text{ on } S_T, \quad (3g)$$

$$\phi = \bar{V} \text{ on } S_\phi^f, \quad (3h)$$

$$\phi = \bar{\phi} \text{ on } S_\phi^s, \quad (3i)$$

$$D_i n_i = \bar{d} \text{ on } S_D, \quad (3j)$$

where we have included appropriate boundary conditions (3f)–(3j). In Eq. (3)  $S_{ij}$  is the strain tensor,  $E_i$  the electric field,  $D_i$  the electric displacement,  $\phi$  the electric potential, and all quantities are with respect to the rotating frame.  $c_{ijkl}$ ,  $e_{kij}$ , and  $\epsilon_{ij}$  are the elastic, piezoelectric, and dielectric constants, respectively. Barred quantities are boundary data which are assumed known, except the values of the electric potential  $\bar{\phi}$  on the sensing electrodes  $S_\phi^s$ . Since  $\bar{\phi}$  is unknown on the sensing electrodes, some circuit condition joining the sensing electrodes is needed to determine the value of  $\bar{\phi}$ . The simplest condition is the open circuit condition which will be used in this analysis and will be shown in detail in the analysis of the rectangular ceramic plate piezoelectric gyroscope later. For the particular purpose of this study, we consider the case when there is no body force  $f_i$  and all the boundary conditions are homogeneous except those on the electrodes  $S_\phi^f$  and  $S_\phi^s$ . On the forcing electrodes  $S_\phi^f$  the piezoelectric body is forced by a time harmonic voltage

$$\phi = \bar{V}e^{i\omega t}. \quad (4)$$

Then for steady state vibrations the unknowns  $u_i$  and  $\phi$  in  $V$  as well as  $\bar{\phi}$  on  $S_\phi^s$  have the same time dependence and the whole set of equations and boundary conditions (2) and (3) reduce to

$$c_{ijkl}u_{k,lj} + e_{kij}\phi_{,kj} + \rho[-2i\omega\epsilon_{ijk}\Omega\zeta_j u_k + O(\Omega^2)] = -\rho\omega^2 u_i \text{ in } V, \quad (5a)$$

$$e_{kij}u_{i,jk} - \epsilon_{ki}\phi_{,ik} = 0 \text{ in } V, \quad (5b)$$

$$u_i = 0 \text{ on } S_u, \quad (5c)$$

$$(c_{ijkl}u_{k,l} + e_{kij}\phi_{,k})n_j = 0 \text{ on } S_T, \quad (5d)$$

$$\phi = \bar{V} \text{ on } S_\phi^f, \quad (5e)$$

$$\phi = \bar{\phi} \text{ on } S_\phi^s, \quad (5f)$$

$$(e_{kij}u_{i,j} - \epsilon_{ki}\phi_{,i})n_k = 0 \text{ on } S_D, \quad (5g)$$

where we have made some substitutions and eliminated some intermediate variables. We note that, although the forcing voltage  $\bar{V}$  can be assumed real for simplicity, the unknowns  $u_i$ ,  $\phi$ , and  $\bar{\phi}$  are usually complex. The value of  $\bar{\phi}$  on the sensing electrodes  $S_\phi^s$  depends on the angular velocity  $\Omega$  of the rotating frame, hence it can be used to measure  $\Omega$ . Solutions to the above equations can be attempted directly. However, when the angular velocity  $\Omega$  is small in a sense that will become clear later, a perturbation procedure can be established which simplifies the problem and reveals the sensing mechanism more clearly without losing much accuracy.

## II. A PERTURBATION PROCEDURE

When the piezoelectric gyroscope is used to measure the angular velocity of a rotating body, the forcing frequency  $\omega$  is very close to a resonant frequency of the gyroscope which

is much larger than the angular velocity of the rotating frame or  $\omega \gg \Omega$ . Hence a small, dimensionless parameter can be introduced as

$$\lambda = \Omega/\omega \ll 1, \quad (6)$$

and with which we have, from Eq. (5a)

$$c_{ijkl}u_{k,lj} + e_{kij}\phi_{,kj} + \rho\omega^2[-2i\lambda\epsilon_{ijk}\zeta_j u_k + O(\lambda^2)] = -\rho\omega^2 u_i. \quad (7)$$

We then expand all the unknowns as

$$u_j = u_j^{(0)} + \lambda u_j^{(1)} + O(\lambda^2), \quad (8a)$$

$$\phi = \phi^{(0)} + \lambda \phi^{(1)} + O(\lambda^2), \quad (8b)$$

$$\bar{\phi} = \bar{\phi}^{(0)} + \lambda \bar{\phi}^{(1)} + O(\lambda^2), \quad (8c)$$

which, when substituted into Eq. (5), leads to the following perturbation problems of successive orders. For the zeroth-order problem we have

$$c_{ijkl}u_{k,lj}^{(0)} + e_{kij}\phi_{,kj}^{(0)} = -\rho\omega^2 u_i^{(0)} \quad \text{in } V, \quad (9a)$$

$$e_{kij}u_{i,jk}^{(0)} - \epsilon_{ki}\phi_{,ik}^{(0)} = 0 \quad \text{in } V, \quad (9b)$$

$$u_i^{(0)} = 0 \quad \text{on } S_u, \quad (9c)$$

$$(c_{ijkl}u_{k,l}^{(0)} + e_{kij}\phi_{,k}^{(0)})n_j = 0 \quad \text{on } S_T, \quad (9d)$$

$$\phi^{(0)} = \bar{V} \quad \text{on } S_\phi^f, \quad (9e)$$

$$\phi^{(0)} = \bar{\phi}^{(0)} \quad \text{on } S_\phi^s, \quad (9f)$$

$$(e_{kij}u_{i,j}^{(0)} - \epsilon_{ki}\phi_{,i}^{(0)})n_k = 0 \quad \text{on } S_D. \quad (9g)$$

The zeroth-order problem is the forcing problem. It is seen that the zeroth-order problem does not have the effect of  $\Omega$ . The piezoelectric body is forced into a time harmonic motion by the applied voltage on  $S_\phi^f$ . The forcing frequency  $\omega$  should be close to a particular resonant frequency  $\omega_f$  at which resonance of the forced motion occurs for effective forcing. We note that in this forced vibration without  $\Omega$  there still may be an output  $\bar{\phi}^{(0)}$  on the sensing electrodes  $S_\phi^s$ . This output is not related to  $\Omega$  and it can usually be eliminated by a proper choice of material orientation, resonant mode of  $\omega_f$ , or positions and connections of the sensing electrodes. When  $\bar{V}$  is real, the zeroth-order response can also be written in real form. For the first-order problem we have

$$c_{ijkl}u_{k,lj}^{(1)} + e_{kij}\phi_{,kj}^{(1)} - \rho\omega^2 2i\epsilon_{ijk}\zeta_j u_k^{(0)} = -\rho\omega^2 u_i^{(1)} \quad \text{in } V, \quad (10a)$$

$$e_{kij}u_{i,jk}^{(1)} - \epsilon_{ki}\phi_{,ik}^{(1)} = 0 \quad \text{in } V, \quad (10b)$$

$$u_i^{(1)} = 0 \quad \text{on } S_u, \quad (10c)$$

$$(c_{ijkl}u_{k,l}^{(1)} + e_{kij}\phi_{,k}^{(1)})n_j = 0 \quad \text{on } S_T, \quad (10d)$$

$$\phi^{(1)} = 0 \quad \text{on } S_\phi^f, \quad (10e)$$

$$\phi^{(1)} = \bar{\phi}^{(1)} \quad \text{on } S_\phi^s, \quad (10f)$$

$$(e_{kij}u_{i,j}^{(1)} - \epsilon_{ki}\phi_{,i}^{(1)})n_k = 0 \quad \text{on } S_D. \quad (10g)$$

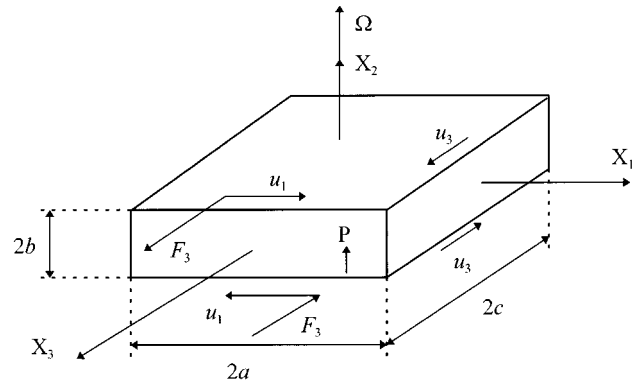


FIG. 2. A rectangular ceramic plate piezoelectric gyroscope.

The first-order problem is the sensing problem. The third term on the left hand side of Eq. (10a) is the Coriolis force due to the zeroth-order motion. The centrifugal force does not show up in the first-order problem because it is of higher order in  $\lambda$ . It can be seen that the first-order motion is driven by the Coriolis force due to the zeroth-order motion. For effective sensing  $\omega$  should also be close to another resonant frequency  $\omega_s$  of the piezoelectric body at which resonance of the sensing motion occurs. Hence we must have  $\omega \approx \omega_f \approx \omega_s$  which is called double resonance.<sup>5</sup>  $\bar{\phi}^{(1)}$  on  $S_\phi^s$  is the quantity that shows the effect of the angular velocity  $\Omega$  of the reference frame. When the zeroth-order solution is real, the first-order solution can be written in a pure imaginary form.

### III. EQUATIONS FOR A CERAMIC PIEZOELECTRIC PLATE

Consider a rectangular ceramic plate poled in the thickness direction as shown in Fig. 2. The plate can vibrate at thickness shear modes. Thickness shear modes are usually coupled with flexural deformations. For a ceramic plate poled in the thickness direction  $x_2$ , these thickness shear modes can be excited or detected by lateral electrodes on the sides  $x_1 = \pm a$  or  $x_3 = \pm c$  of the plate because of the specific forms of the following material constant matrices<sup>12</sup>

$$\begin{pmatrix} c_{11} & c_{13} & c_{12} & 0 & 0 & 0 \\ c_{13} & c_{33} & c_{13} & 0 & 0 & 0 \\ c_{12} & c_{13} & c_{11} & 0 & 0 & 0 \\ 0 & 0 & 0 & c_{44} & 0 & 0 \\ 0 & 0 & 0 & 0 & c_{66} & 0 \\ 0 & 0 & 0 & 0 & 0 & c_{44} \end{pmatrix}, \quad (11a)$$

$$\begin{pmatrix} 0 & 0 & 0 & 0 & 0 & e_{15} \\ e_{31} & e_{33} & e_{31} & 0 & 0 & 0 \\ 0 & 0 & 0 & e_{15} & 0 & 0 \end{pmatrix}, \quad (11b)$$

$$\begin{pmatrix} \epsilon_{11} & 0 & 0 \\ 0 & \epsilon_{33} & 0 \\ 0 & 0 & \epsilon_{11} \end{pmatrix}, \quad (11c)$$

where  $c_{66} = (c_{11} - c_{12})/2$ . In Eq. (11) the compact matrix notation<sup>11</sup> has been used.  $c_{pq}$  and  $e_{ip}$  correspond to  $c_{ijkl}$  and

$e_{ijk}$  for  $p, q = 1, \dots, 6$ . We note that in Ref. 12 the material matrices are for ceramics poled in the  $x_3$  direction. Here we consider the case of ceramics poled in the  $x_2$  direction whose material matrices can be obtained from the matrices in Ref. 12 by rotating rows and columns properly. Mindlin<sup>10</sup> derived two-dimensional equations for a piezoelectric plate with coupled flexural, thickness shear, thickness twist, and contour (plane stress) modes. For the particular plate in Fig. 2, we exclude contour modes because they will not be excited by lateral electric fields and specialize Mindlin's equations for a ceramic plate as

$$\kappa^2 c_{44}(u_{2,aa}^{(0)} + u_{a,a}^{(1)}) + \kappa e_{15} \phi_{,aa}^{(0)} = \rho \ddot{u}_2^{(0)}, \quad (12a)$$

$$\kappa e_{15}(u_{2,aa}^{(0)} + u_{a,a}^{(1)}) - \epsilon_{11} \phi_{,aa}^{(0)} = 0, \quad (12b)$$

$$\begin{aligned} \bar{c}_{11} u_{1,11}^{(1)} + c_{66} u_{1,33}^{(1)} + (\bar{c}_{13} + c_{66}) u_{3,13}^{(1)} - 3b^{-2} \kappa^2 c_{44}(u_1^{(1)} + u_{2,1}^{(0)}) \\ - 3b^{-2} \kappa e_{15} \phi_{,1}^{(0)} = \rho \ddot{u}_1^{(1)}, \end{aligned} \quad (12c)$$

$$\begin{aligned} c_{66} u_{3,11}^{(1)} + \bar{c}_{11} u_{3,33}^{(1)} + (\bar{c}_{13} + c_{66}) u_{1,13}^{(1)} - 3b^{-2} \kappa^2 c_{44}(u_3^{(1)} + u_{2,3}^{(0)}) \\ - 3b^{-2} \kappa e_{15} \phi_{,3}^{(0)} = \rho \ddot{u}_3^{(1)}, \end{aligned} \quad (12d)$$

where  $\phi^{(0)}$ ,  $u_2^{(0)}$ , and  $u_a^{(1)}$  ( $a=1,3$ ) are the two-dimensional zeroth-order electric potential, zeroth-order displacement of deflection, and first-order displacements of shear, respectively. They are functions of  $x_a$  ( $a=1,3$ ) and time  $t$ . Repeated indices are summed over 1, 3. Equation (12a) is the equation for flexure, Eq. (12b) the equation for electrostatics, and Eqs. (12c) and (12d) the equations for shear. We note that, beginning with this section, superscripts are no longer related to orders of perturbation. They are orders of various quantities in the plate theory. Once the perturbation procedure is understood, it can be carried out without superscripts for perturbation orders. In Eq. (12)

$$\bar{c}_{11} = c_{11} - c_{13}^2/c_{33}, \quad \bar{c}_{13} = c_{12} - c_{13}^2/c_{33}, \quad (13)$$

and

$$\kappa^2 = \pi^2/12, \quad (14)$$

is the thickness shear correction factor which is determined by requiring the thickness shear frequencies obtained from the two-dimensional plate equations and the three-dimensional equations to be the same for an infinite ceramic plate. We note that the general two-dimensional equations for piezoelectric plates have two correction factors  $\kappa_1$  and  $\kappa_3$  for thickness shears in the  $x_1$  and  $x_3$  directions separately.<sup>10</sup> Since ceramics are transversely isotropic, the two correction factors are equal. To apply boundary conditions, we also need the following:<sup>10</sup>

$$T_{2a}^{(0)} = 2b[\kappa^2 c_{44}(u_{2,a}^{(0)} + u_a^{(1)}) + \kappa e_{15} \phi_{,a}^{(0)}], \quad (15a)$$

$$D_a^{(0)} = 2b[\kappa e_{15}(u_{2,a}^{(0)} + u_a^{(1)}) - \epsilon_{11} \phi_{,a}^{(0)}], \quad (15b)$$

$$T_{11}^{(1)} = \frac{2}{3} b^3 (\bar{c}_{11} u_{1,1}^{(1)} + \bar{c}_{13} u_{3,3}^{(1)}), \quad (15c)$$

$$T_{33}^{(1)} = \frac{2}{3} b^3 (\bar{c}_{13} u_{1,1}^{(1)} + \bar{c}_{11} u_{3,3}^{(1)}), \quad (15d)$$

$$T_{13}^{(1)} = \frac{2}{3} b^3 c_{66}(u_{1,3}^{(1)} + u_{3,1}^{(1)}), \quad (15e)$$

which are the shearing force (15a), zeroth-order electric displacement (15b), bending moment in the  $x_1$  direction (15c),

bending moment in the  $x_3$  direction (15d), and twisting moment (15e), respectively. Analytical solutions to the above system of Eqs. (12) can be attempted. However, we will simplify the problem a little more before we proceed to solve it.

#### IV. THICKNESS SHEAR APPROXIMATION

Thickness shear modes are usually accompanied by weak flexural deformations. This weak flexural deformation can be eliminated by the so called thickness shear approximation which further simplifies the problem. Enlightened by the thickness shear approximation for a system of one-dimensional equations for quartz,<sup>11</sup> we proceed as follows. From Eqs. (12a) and (12b), we obtain, by eliminating  $\phi^{(0)}$

$$\kappa^2 \left( c_{44} + \frac{e_{15}^2}{\epsilon_{11}} \right) (u_{2,aa}^{(0)} + u_{a,a}^{(1)}) = \rho \ddot{u}_2^{(0)}. \quad (16)$$

Substitution of the following wave solution in Eq. (16):

$$u_2^{(0)} = A_2 \exp[i(\omega t + \xi_a x_a)], \quad (17)$$

$$u_b^{(1)} = A_b \exp[i(\omega t + \xi_a x_a)],$$

results in the dispersion relation

$$\kappa^2 \left( c_{44} + \frac{e_{15}^2}{\epsilon_{11}} \right) (-A_2 \xi_a \xi_a + A_a i \xi_a) = -\rho \omega^2 A_2. \quad (18)$$

Since we are interested in long waves with small wave number  $\xi_a$ , the term quadratic in  $\xi_a$  in the above equation can be dropped. Also, since the frequency  $\omega$  is very close to the thickness shear frequency of an infinite plate, we make the following substitution in Eq. (18);

$$\omega^2 \approx \omega_\infty^2 = \frac{\pi^2 c_{44}}{4\rho b}, \quad (19)$$

where  $\omega_\infty$  is the infinite plate thickness shear frequency. This leads to the simplified dispersion relation

$$A_2 = -\frac{b^2}{3} \left( 1 + \frac{e_{15}^2}{c_{44} \epsilon_{11}} \right) i \xi_a A_a, \quad (20)$$

which is equivalent to the differential relation

$$u_2^{(0)} = -\frac{b^2}{3} (1 + k_{15}^2) u_{a,a}^{(1)}, \quad (21)$$

where we have denoted

$$k_{15}^2 = \frac{e_{15}^2}{c_{44} \epsilon_{11}}. \quad (22)$$

Substituting Eq. (21) into (12c) and (12d), neglecting the  $u_2^{(0)}$  term in (12b) under the long wave approximation, we obtain the following equations we need to solve under the thickness shear approximation:

$$\kappa e_{15} u_{a,a}^{(1)} - \epsilon_{11} \phi_{,aa}^{(0)} = 0, \quad (23a)$$

$$c_{11}^* u_{1,11}^{(1)} + c_{66} u_{1,33}^{(1)} + c_{13}^* u_{3,13}^{(1)} - 3b^{-2} \kappa^2 c_{44} u_1^{(1)} - 3b^{-2} \kappa e_{15} \phi_{,1}^{(0)} = \rho \ddot{u}_1^{(1)}, \quad (23b)$$

$$c_{66} u_{3,11}^{(1)} + c_{11}^* u_{3,33}^{(1)} + c_{13}^* u_{1,13}^{(1)} - 3b^{-2} \kappa^2 c_{44} u_3^{(1)} - 3b^{-2} \kappa e_{15} \phi_{,3}^{(0)} = \rho \ddot{u}_3^{(1)}, \quad (23c)$$

where

$$c_{11}^* = \bar{c}_{11} + \kappa^2 c_{44} (1 + k_{15}^2), \quad (24a)$$

$$c_{13}^* = \bar{c}_{13} + c_{66} + \kappa^2 c_{44} (1 + k_{15}^2). \quad (24b)$$

Once  $u_a^{(1)}$  are known,  $u_2^{(0)}$  can be obtained through Eq. (21). Corresponding to Eqs. (15a) and (15b), under the thickness shear approximation, we have

$$T_{2a}^{(0)} = 2b(\kappa^2 c_{44} u_a^{(1)} + \kappa e_{15} \phi_{,a}^{(0)}), \quad (25a)$$

$$D_a^{(0)} = 2b(\kappa e_{15} u_a^{(1)} - \epsilon_{11} \phi_{,a}^{(0)}), \quad (25b)$$

which are useful when specifying boundary conditions for Eq. (23). Equations (15c)–(15e) remain the same under thickness shear approximation. We note that the infinite plate thickness shear frequency  $\omega_\infty$  may have more than one value depending on whether the edges at infinity are shorted or open. This difference is neglected in the present analysis.

## V. DRIVING IN THE $X_1$ DIRECTION

Thickness shear in the  $x_1$  direction can be driven by a voltage  $2V_1$  applied across a pair of electrodes at  $x_1 = \pm a$ . Since the main motion is  $u_1^{(1)}$ , we neglect  $u_3^{(1)}$  and the small variation along  $x_3$ . Then from Eqs. (23a), (23b), and (25a) we have

$$\kappa e_{15} u_{1,1}^{(1)} - \epsilon_{11} \phi_{,11}^{(0)} = 0, \quad -a < x_1 < a, \quad (26a)$$

$$c_{11}^* u_{1,11}^{(1)} - 3b^{-2} \kappa^2 c_{44} u_1^{(1)} - 3b^{-2} \kappa e_{15} \phi_{,1}^{(0)} = \rho \ddot{u}_1^{(1)}, \quad -a < x_1 < a, \quad (26b)$$

$$T_{21}^{(0)} = 2b(\kappa^2 c_{44} u_1^{(1)} + \kappa e_{15} \phi_{,1}^{(0)}) = 0, \quad x_1 = \pm a, \quad (26c)$$

$$\phi^{(0)} = \pm V_1 \sin \omega t, \quad x_1 = \pm a. \quad (26d)$$

Equation (26c) physically represents free edges at  $x_1 = \pm a$ . As an approximation, we neglect the piezoelectric coupling term to  $u_1^{(1)}$  in the electrostatic equation (26a). We still keep the piezoelectric coupling term to  $\phi^{(0)}$  in Eq. (26b). Once  $\phi^{(0)}$  is obtained approximately from Eq. (26a) by neglecting the piezoelectric coupling term in Eq. (26a), it is substituted into Eq. (26b) through the piezoelectric coupling term in Eq. (26b). This type of approximation of neglecting piezoelectric coupling at certain places is common in piezoelectric analysis.<sup>13</sup> For materials with weak piezoelectric coupling, quartz for example, this approximation causes very little error. For ceramics the piezoelectric coupling is not weak. However, this approximation will not affect the qualitative behavior of the problem which is the purpose of this paper. Under this approximation, we obtain the approximate solution of the driving electric potential as

$$\phi^{(0)} = \frac{x_1}{a} V_1 \sin \omega t \approx \frac{8}{\pi^2} V_1 \sin \frac{\pi x_1}{2a} \sin \omega t, \quad (27)$$

which satisfies the electric boundary condition (26d). Note that in Eq. (27) we have approximated a linear function of  $x_1$  over  $[-a, a]$  by a sine function. It can be considered as a one term approximation by Fourier series. Substituting Eq. (27) into (26b), we then obtain the following expression for  $u_1^{(1)}$ :

$$u_1^{(1)} = B_1 \cos \frac{\pi x_1}{2a} \sin \omega t, \quad (28)$$

where

$$B_1 = \frac{2\sqrt{3}}{\omega^2 - \omega_\infty^2 (1 + c_{11}^* b^2 / c_{44} a^2)} \frac{e_{15} V_1 / a}{\rho b^2}. \quad (29)$$

We note that the mechanical boundary conditions (26c) are satisfied approximately because  $u_1^{(1)}(x_1 = \pm a) = 0$  from Eq. (28).

## VI. SENSING IN THE $X_3$ DIRECTION

With the driving solution  $u_1^{(1)}$  known, we have the displacement field

$$u_1 = x_2 u_1^{(1)} = B_1 x_2 \cos \frac{\pi x_1}{2a} \sin \omega t, \quad (30)$$

which leads to a Coriolis force field

$$\mathbf{F} = -2\Omega \mathbf{e}_2 \times \dot{u}_1 \mathbf{e}_1 = 2\Omega \dot{u}_1 \mathbf{e}_3, \quad (31)$$

or

$$F_3 = 2\Omega \omega B_1 x_2 \cos \frac{\pi x_1}{2a} \cos \omega t \approx \frac{4}{\pi} \Omega \omega B_1 x_2 \cos \omega t \approx 2\Omega \omega B_1 x_2 \cos \frac{\pi x_3}{2c} \cos \omega t, \quad (32)$$

where we have approximated a cosine function over  $[-a, a]$  by a constant, and similarly a constant over  $[-c, c]$  by a cosine function. To apply the Coriolis force in the plate equations, we need to find the following quantity<sup>10</sup>

$$F_3^{(1)} = \int_{-b}^b x_2 F_3 dx_2 = \frac{2b^3}{3} 2\Omega \omega B_1 \cos \frac{\pi x_3}{2c} \cos \omega t. \quad (33)$$

Then from Eqs. (23a), (23c), and (25), with (33), we have the following sensing problem

$$c_{11}^* u_{3,33}^{(1)} - 3b^{-2} \kappa^2 c_{44} u_3^{(1)} - 3b^{-2} \kappa e_{15} \phi_{,3}^{(0)} + \frac{3}{2b^3} \rho F_3^{(1)} = \rho \ddot{u}_3^{(1)}, \quad -c < x_3 < c, \quad (34a)$$

$$\kappa e_{15} u_{3,3}^{(1)} - \epsilon_{11} \phi_{,33}^{(0)} = 0, \quad -c < x_3 < c, \quad (34b)$$

$$T_{23}^{(0)} = 2b(\kappa^2 c_{44} u_3^{(1)} + \kappa e_{15} \phi_{,3}^{(0)}) = 0, \quad x_3 = \pm c, \quad (34c)$$

$$\phi^{(0)} = \pm V_3 \cos \omega t, \quad x_3 = \pm c, \quad (34d)$$

$$D_3^{(0)} = 2b(\kappa e_{15} u_3^{(1)} - \epsilon_{11} \phi_{,3}^{(0)}) = 0, \quad x_3 = \pm c, \quad (34e)$$

where, since the sensing motion is  $u_3^{(1)}$ , we have neglected  $u_1^{(1)}$  and the small variation along  $x_1$ . Equation (34c) physically represents free edges at  $x_3 = \pm c$ . We note that in Eq. (34), since  $V_3$  is unknown, we need some circuit condition joining the sensing electrodes to determine  $V_3$ . We consider the simple case of open circuit in which  $D_3^{(0)}$  or the charge and hence the current on the sensing electrodes vanish in Eq. (34e). As an approximation, we neglect the piezoelectric coupling term to  $\phi^{(0)}$  in Eq. (34a) while keeping the piezoelectric coupling term to  $u_3^{(1)}$  in Eq. (34b). Then, under the driving of the Coriolis force  $F_3^{(1)}$ , we obtain, from Eq. (34a),

$$u_3^{(1)} = B_3 \cos \frac{\pi x_3}{2c} \cos \omega t, \quad (35)$$

where

$$B_3 = \frac{-2\Omega\omega}{\omega^2 - \omega_\infty^2(1 + c_{11}^*b^2/c_{44}c^2)} B_1. \quad (36)$$

With  $u_3^{(1)}$  known, from Eq. (34b), we obtain

$$\phi^{(0)} = A_3 \sin \frac{\pi x_3}{2c} \cos \omega t \approx \frac{\pi^2}{8} A_3 \frac{x_3}{c} \cos \omega t, \quad (37)$$

where

$$A_3 = \frac{ce_{15}}{\sqrt{3}\epsilon_{11}} B_3, \quad (38)$$

and we note that the mechanical boundary conditions (34c) and the open circuit condition (34e) are satisfied because  $u_3^{(1)}(x_3 = \pm c) = 0$  and  $\phi_3^{(0)}(x_3 = \pm c) = 0$  from Eqs. (35) and (37). The electric boundary condition (34d) will give the sensing voltage, as shown in the next section.

## VII. DISCUSSION

From Eqs. (37), (34d), (29), (36), and (38), the sensing voltage is

$$\begin{aligned} V_3 &= \phi^{(0)}(x_3 = c) \\ &= \left[ \frac{\pi^2 ce_{15}}{8\sqrt{3}\epsilon_{11}} \left[ \frac{-2\Omega\omega}{\omega^2 - \omega_\infty^2(1 + c_{11}^*b^2/c_{44}c^2)} \right] \right. \\ &\quad \times \left. \left[ \frac{2\sqrt{3}}{\omega^2 - \omega_\infty^2(1 + c_{11}^*b^2/c_{44}a^2)} \frac{e_{15}V_1/a}{\rho b^2} \right] \right] \cos \omega t, \end{aligned} \quad (39)$$

or, for voltage sensitivity

$$\begin{aligned} \frac{V_3}{V_1\Omega} &= \left[ -2k_{15}^2 \frac{c}{a} \left[ \frac{\omega}{\omega^2 - \omega_\infty^2(1 + c_{11}^*b^2/c_{44}c^2)} \right] \right. \\ &\quad \times \left. \left[ \frac{\omega_\infty^2}{\omega^2 - \omega_\infty^2(1 + c_{11}^*b^2/c_{44}a^2)} \right] \right] \cos \omega t, \end{aligned} \quad (40)$$

where

$$\begin{aligned} c_{11}^* &= \bar{c}_{11} + \kappa^2 c_{44}(1 + k_{15}^2), \quad \bar{c}_{11} = c_{11} - c_{13}^2/c_{33}, \\ \kappa^2 &= \frac{\pi^2}{12}, \quad k_{15}^2 = \frac{e_{15}^2}{c_{44}\epsilon_{11}}, \quad \omega_\infty^2 = \frac{\pi^2 c_{44}}{4\rho b^2}. \end{aligned} \quad (41)$$

In Eq. (39), the three pairs of brackets on the right hand side represent, from right to left, respectively, the driving of the

thickness shear motion in the  $x_1$  direction by the applied voltage  $V_1$  in the  $x_1$  direction, the driving of the thickness shear motion in the  $x_3$  direction by the Coriolis force due to the thickness shear motion in the  $x_1$  direction, and the sensing of the thickness shear motion in the  $x_3$  direction. Roles of various material constants and geometric parameters are clearly exhibited. At resonant frequencies of the sensor, the above expressions become singular. This singularity will disappear when damping is included in the analysis. We note that the forcing voltage is a sine function of time while the sensing voltage is a cosine function. Hence a phase shift is involved. This is because that the Coriolis force, being proportional to the particle velocity, appears like a damping term which causes phase shift although it in fact does not work here since it is perpendicular to the particle velocity. In Eq. (40), the driving dimension  $a$  and the sensing dimension  $c$  appear in the form of a ratio  $c/a$ . Hence the sensitivity depends on the length to width ratio but not the absolute size of the gyroscope. This implies that miniaturization does not lead to lower sensitivity. It is important to note that the driving dimension  $a$  is in the denominator and the sensing dimension  $c$  is in the numerator in Eq. (40). Therefore better sensitivity can be expected if a gyroscope is designed to be driven at the smaller dimension (plate thickness, for example) and to sense at the larger dimension (plate length or width). The quartz plate thickness shear gyroscope in Ref. 9 has this advantage. From Eq. (40) it can be seen that for large voltage sensitivity the driving frequency and the two natural frequencies of the thickness shear motions in two directions must all be very close. This is the condition of double resonance<sup>5</sup> which implies, from Eq. (39) or (40), that  $a$  must be very close to  $c$  and the plate is almost square. When that is the case, we can write

$$\omega_\infty^2 \left( 1 + \frac{c_{11}^*b^2}{c_{44}a^2} \right) \approx \omega + \Delta\omega_1, \quad (42a)$$

$$\omega_\infty^2 \left( 1 + \frac{c_{11}^*b^2}{c_{44}c^2} \right) \approx \omega + \Delta\omega_3, \quad (42b)$$

which implies

$$\frac{V_3}{V_1\Omega} \approx -\frac{k_{15}^2}{2} \frac{\omega}{(\Delta\omega_1)(\Delta\omega_3)}. \quad (43)$$

Equation (43) is very simple and it shows that materials with larger electromechanical coupling coefficients ( $k_{15}$  here) give higher sensitivity. The commonly used quartz is not a good material in this respect. Equation (43) also shows that the sensitivity is linear in  $\omega$ . This is natural because from Eq. (32) it can be seen that the Coriolis force, through which the gyroscope is measuring the rotation, is linear in  $\omega$ . Thickness shear modes have a nodal central plane at  $x_2 = 0$  where the gyroscope can be mounted. Some contouring (variable thickness) may also be considered so that the vibration will be confined in the central portion of the plate because of the energy trapping<sup>14</sup> phenomenon related to thickness shear modes. Then the gyroscope can be supported any where on the edges without affecting its performance. Although the main purpose of the above approximate analysis is to present some qualitative results for the gyroscope, we will compare

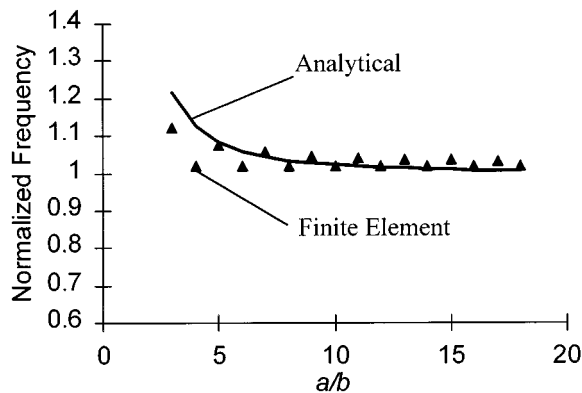


FIG. 3. Normalized thickness shear resonant frequency  $\omega/\omega_\infty$ .

the resonant frequencies predicted by the analytical analysis with finite element numerical analysis. Consider a gyroscope made of PZT-5H. We have<sup>12</sup>

$$\begin{aligned}
 c_{11} &= 12.6, & c_{33} &= 11.7, & c_{44} &= 2.30, \\
 c_{12} &= 7.95, & c_{13} &= 8.41 \times 10^{10} \text{ N/m}^2, \\
 c_{66} &= (c_{11} - c_{12})/2, \\
 e_{15} &= 17.0, & e_{31} &= -6.5, & e_{33} &= 23.3 \text{ C/m}^2, \\
 \epsilon_{11}^s &= 1700\epsilon_0, & \epsilon_{33}^s &= 1470\epsilon_0, \\
 \epsilon_0 &= 8.854 \times 10^{-12} \text{ farads/m}, & \rho &= 7500 \text{ kg/m}^3.
 \end{aligned} \tag{44}$$

The results of resonant frequencies from the above analytical solution and finite element solution as a function of the length–thickness ratio are shown in Fig. 3. The analytical solution is shown by a curve while the finite element solution is represented by small triangles. The frequencies are normalized by  $\omega_\infty$ . We note that the finite element solution can not be represented by one single curve. The small triangles are in fact points on a family of curves.<sup>15</sup> This detailed structure of the frequency spectra is neglected in the analytical analysis, therefore the analytical solution can be represented by one single curve. The analytical solution is obtained by letting the denominator in Eq. (39) vanish. The finite element analysis is done on a supercomputer under the plane strain assumption because both the driving modes (26) and the sensing modes (34) are essentially plain strain. The two end electrodes are shorted. The two solutions agree very well. They both approach the infinite plate solution with the value of 1 as the aspect ratio  $a/b$  becomes very large. When  $a/b$  decreases, the difference between the two solutions increases. This is because that for small aspect ratios flexural deformation becomes more important in thickness shear modes. (For an infinite ceramic plate with  $a/b = \infty$ , the thickness shear mode is pure, without flexural deformation.) While finite element method can take care of this flexural deformation without any additional inaccuracy, the above analytical method can only handle this flexural deformation approximately under the thickness shear approximation. Another reason is that for an infinite ceramic plate the thickness shear mode we have been computing is pure elastic without

piezoelectric coupling. For a finite plate, piezoelectric coupling exists and the finite element method takes the piezoelectric coupling into full account but the above analytical method treats the piezoelectric coupling approximately.

## VIII. CONCLUSION

Equations for the small vibration of a rotating piezoelectric body are simplified by a perturbation procedure which reveals the mechanism of piezoelectric gyroscopes. It is a general formulation and can be used in conjunction with various numerical and analytical methods for the analysis of beam or plate piezoelectric gyroscopes. The approximate analytical solution on the ceramic plate thickness shear gyroscope given in this work presents some simple results which exhibit the effect of various geometrical and material parameters on the sensitivity of the gyroscope. The two-dimensional equations for piezoelectric plates can be employed effectively in the analysis of plate piezoelectric gyroscopes. These equations can be further simplified by the thickness shear long wave approximation. The present analysis can be performed on thickness shear gyroscopes made of quartz or other materials.

## ACKNOWLEDGMENTS

The author would like to thank Dr. J. Mattson of Motorola for a discussion on the perturbation procedure, and Dr. W. Zhang of Motorola for discussions on coupled thickness shear and flexural vibrations of plates.

- <sup>1</sup>W. D. Gates, "Vibrating angular rate sensor may threaten the gyroscope," *Electronics* **41** (10), 130–134 (10 June 1968).
- <sup>2</sup>J. Soderkvist, "Micromachined gyroscopes," *Sens. Actuators A* **43**, 65–71 (1994).
- <sup>3</sup>Y.-K. Yong, Z. Zhang, and J. Hou, "On the accuracy of plate theories for the prediction of unwanted modes near the fundamental thickness shear mode," *Proc. IEEE Frequency Control Symp.* 755–760 (1995).
- <sup>4</sup>M. Rodamaker and C. R. Newell, "Finite element analysis of a quartz angular rate sensor," *ANSYS Conference Proceedings*, 3.35–48 (1989).
- <sup>5</sup>S. Kudo, S. Sugawara, and N. Wakatuki, "Finite element analysis of single crystal tuning forks for gyroscopes," *Proceedings of the IEEE Frequency Control Symposium*, 640–647 (1996).
- <sup>6</sup>C. S. Chou, J. W. Yang, Y. C. Huang, and H. J. Yang, "Analysis on vibrating piezoelectric beam gyroscope," *Int. J. Appl. Electromagn. Mater.* **2**, 227–241 (1991).
- <sup>7</sup>J. Soderkvist, "Piezoelectric beams and vibrating angular rate sensors," *IEEE Trans. Ultrason. Ferroelectr. Freq. Control* **38**, 271–280 (1991).
- <sup>8</sup>I. A. Ulitko, "Mathematical theory of the fork-type wave gyroscope," *Proceedings of the IEEE Frequency Control Symposium*, 786–793 (1995).
- <sup>9</sup>G. M. Reese, E. L. Marek, and D. W. Lobitz, "Three dimensional finite element calculations of an experimental quartz rotation sensor," *Proceedings of the IEEE Ultrasonics Symposium*, pp. 419–422 (1989).
- <sup>10</sup>R. D. Mindlin, "High frequency vibrations of piezoelectric crystal plates," *Int. J. Solids Struct.* **8**, 895–906 (1972).
- <sup>11</sup>H. F. Tiersten, *Linear Piezoelectric Plate Vibrations* (Plenum, New York, 1969).
- <sup>12</sup>B. A. Auld, *Acoustic Fields and Waves in Solids* (Wiley, New York, 1973), Vol. 1, pp. 357–382.
- <sup>13</sup>Y. Kagawa, T. Tsuchiya, and T. Kawashima, "Finite element simulation of piezoelectric vibrator gyroscopes," *IEEE Trans. Ultrason. Ferroelectr. Freq. Control* **43**, 509–518 (1996).
- <sup>14</sup>D. Salt, *Hy-Q Hand Book of Quartz Crystal Devices* (Van Nostrand Reinhold, UK, 1987), pp. 45–62.
- <sup>15</sup>R. D. Mindlin and W. J. Spencer, "Anharmonic, thickness-twist overtones of thickness-shear and flexural vibrations of rectangular, AT-cut quartz plates," *J. Acoust. Soc. Am.* **42**, 1268–1277 (1967).



# An experimental-numerical technique for evaluating the bulk and shear dynamic moduli of viscoelastic materials

R. Lance Willis, T. Shane Stone, and Yves H. Berthelot

Woodruff School of Mechanical Engineering, Georgia Institute of Technology, Atlanta, Georgia 30332-0405

Walter M. Madigosky

Vector Research Company, 3206 Tower Oaks Boulevard, Suite 400, Rockville, Maryland 20852

(Received 22 January 1997; revised 7 July 1997; accepted 13 August 1997)

An experimental/numerical technique has been implemented to determine simultaneously the bulk and shear dynamic moduli (and loss factor) of viscoelastic materials of arbitrary shape under low-frequency (0.5–2.5 kHz) harmonic excitation. The method consists of measuring the dynamic response of the sample at several points on the surface with a set of five independent laser interferometers, and matching the response with the predictions from a finite element code in which the two complex elastic moduli are the adjustable parameters. Results are presented for measurements made in air, under standard pressure and temperature conditions, and compared with predictions based on Kerner's model. © 1997 Acoustical Society of America. [S0001-4966(97)06711-8]

PACS numbers: 43.58.Dj, 43.35.Mr, 43.35.Cg, 43.20.Jr [SLE]

## INTRODUCTION

Viscoelastic polymers have become widely used in many areas involving water-borne transmission and attenuation of acoustic waves. In order to use these materials effectively, it is critical to determine accurately their complex, bulk and shear moduli.<sup>1</sup> A standard approach is to measure the reflection and transmission of sound with the sample placed either in a free-field water tank or inside an impedance tube.<sup>2–6</sup> A simpler experimental method is the resonance technique proposed by Madigosky and Lee<sup>7,8</sup> in which a longitudinal wave is transmitted down a rod of material with accelerometers attached at both ends. The complex modulus of elasticity can be calculated at each resonance frequency from the phase interference of the extensional waves in the bar. The technique works throughout the audio range but is limited to a specific one-dimensional sample geometry, a discrete set of resonance frequencies, and it measures only the complex Young's modulus. A similar technique has been developed by Garrett<sup>9</sup> to measure both the Young's and shear moduli in a rod in which torsional, longitudinal, and flexural resonant modes are selectively excited by a pair of coils placed at the end of the rod in a magnetic field. Again, the technique is limited to a one dimensional geometry and a discrete set of frequencies. A system developed by Polymer Laboratories (now Rheometric Scientific, NJ) is the Dynamic Mechanical Thermal Analyzer (DMTA). This elaborate system measures automatically Young's modulus as a function of temperature, in a small sample, over a limited range of frequency, typically 0.3–30 Hz. The master curve covering the entire frequency range is then obtained by using the time-temperature superposition principle and the associated WLF shift constant.<sup>10</sup> This principle states that measurements made within a narrow frequency range at several temperatures are equivalent to measurements made over a wide frequency range at a single temperature.

We propose a new, direct method for measuring the two

complex elastic moduli simultaneously, with a sample of arbitrary shape, over a continuous frequency range. The method consists of measuring the dynamic response of a sample with a set of five independent laser interferometers, and matching the response with the predictions from a finite element code in which the two complex elastic moduli are the adjustable parameters. This material characterization inverse problem has been studied in detail by McCollum *et al.*<sup>11</sup> at the Underwater Sound Reference Detachment in Orlando. The experimental arrangement is presented in Sec. I, the inversion procedure is described in Sec. II, the results are presented and discussed in Sec. III, and summarized in Sec. IV.

## I. EXPERIMENTAL SYSTEM

Measurements are made in air at ambient conditions. The sample is excited harmonically at the base by a shaker (Ling Dynamic Systems, model 556) between 500 and 2500 Hz. A block diagram of the experimental arrangement is shown in Fig. 1. The sample is glued to an aluminum base with a cyanoacrylate bond. The base is designed to minimize the amount of wobble and the presence of flexural waves, so that the base motion can be modeled as uniform. Measurements on the unloaded base indicate that this assumption is valid (within 5%) in the frequency range of interest with the Ling dynamic shaker. (With a small B&K 4810 shaker, the nonuniformity of the base motion reaches 10% in the 0.3–2 kHz range and 20% in the 2–4 kHz range.)

The surface dynamics of the sample were measured in the time domain, in real time, simultaneously at four points and referenced (amplitude and phase) to the motion of the base. To do so, five independent laser interferometers were built, calibrated, and tested. Two of the interferometers were used in the out-of-plane configuration to measure the vertical component of the velocity at the top-center of the sample (point #5) and at the base (point #4). The other three interferometers were used in the in-plane configuration to mea-

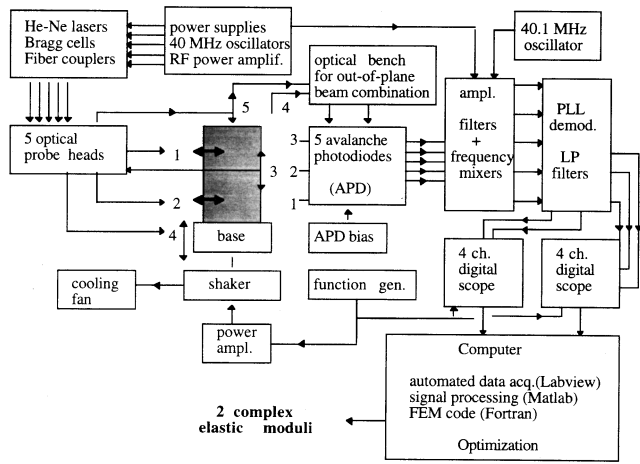


FIG. 1. Experimental arrangement.

sure the in-plane component of the surface velocity of the sample as indicated in Fig. 1. Probe #1 and #2 measured in-plane surface velocity (horizontally polarized), close to the edge of the sample, at a height  $z=H/3$  and  $z=2H/3$ , respectively, where  $H=7.58$  cm is the sample height and  $z$  is the vertical axis ( $z=0$  denotes the base). Probe #3 measured the in-plane surface velocity (vertically polarized) at a height  $z=H/2$ , on the edge of the sample. Each probe is very compact<sup>12</sup> (about  $3.2\text{ cm}\times 1.5\text{ cm}\times 1\text{ cm}$ ).

Each interferometer was powered by a 10 mW He:Ne laser. For convenience, single mode fibers were used to bring the light to the probe heads which were positioned close to the sample (1 cm for the in-plane configuration, and 4.4 cm for the out-of-plane configuration). Each probe was mounted on a small aluminum arm secured to a series of optical stages (two translations and one tilt) for precise alignment.

The principle of laser interferometry for in-plane and out-of-plane measurements is well understood.<sup>13,14</sup> In our experiment, five optical benches with lasers and associated optics lead separately to the five optical probe heads. On each optical bench, the light from the laser passes through an acousto-optic Bragg cell driven by a precision quartz oscillator at  $f_B=40.0$  MHz. The Bragg cell splits the beam into two beams, one of which is frequency shifted by 40 MHz while the other remains unaffected at the optical frequency,  $f_L$ . Each beam is then launched into a single mode optical fiber. Figure 2 shows the geometry associated with either in-plane or out-of-plane detection. To detect the in-plane surface displacement,  $u(t)$ , the two arms of the interferometer illuminate the surface at an angle  $\alpha=30^\circ$  symmetrically with respect to the normal to the surface. The two beams are focused to a tight spot ( $\approx 75\ \mu\text{m}$ ) by two cylindrical rod lenses with graded index of refraction (GRIN lenses). At the surface, the two beams interfere at 40 MHz, and light is scattered in all direction because of surface roughness. Some of it is collected by a large core (1000  $\mu\text{m}$  diameter) fiber and fed into an avalanche photodiode (EG&G C30950EL). In this configuration, the detected signal is of the form  $\cos[2\pi f_B t + 2k \sin \alpha u(t)]$ , where  $k$  is the optical wave number. To increase the amount of scattered light, a small patch (1 mm $\times$ 1 mm) of scattering film (retroreflective tape series

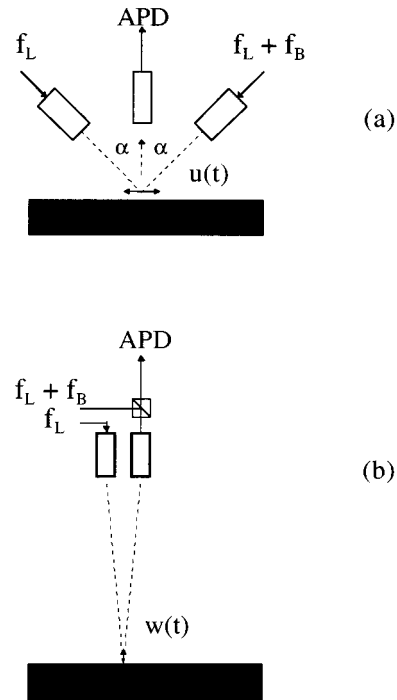


FIG. 2. Optical configuration for (a) in-plane and (b) out-of-plane measurements.

680 from 3M) is placed at the focusing point on the surface. In the out-of-plane configuration, only one beam illuminates the surface at an angle very close to the normal ( $< 3^\circ$ ). Some of the light is reflected to a large core multimode fiber (also 1000  $\mu\text{m}$  diameter) and combined with the second arm of the interferometer (reference signal) to produce the interference signal at 40 MHz which, in this configuration, is of the form  $\cos[2\pi f_B t + 2kw(t)]$ , where  $w(t)$  is the out-of-plane displacement. To increase the amount of reflected light, a small patch (1 mm $\times$ 1 mm) of reflective mylar is placed at the focal point on the surface of the sample.

Each signal is then downshifted from a 40-MHz carrier to a 100-kHz carrier by mixing the output of the photodiodes with a 40.1-MHz signal generated by another precision quartz oscillator. The in-plane and out-of-plane signals are demodulated with a phase-locked loop (PLL). Basically, a PLL produces a voltage proportional to the instantaneous frequency deviation from the nominal carrier frequency. Its output is therefore proportional to the instantaneous surface velocity components,  $\dot{u}(t)$  or  $\dot{w}(t)$ , which are then displayed on a digital oscilloscope and transferred to a computer via a GPIB interface controlled by Labview. In our experiment, the PLL's (National Semiconductor LM565) are designed to have a flat frequency response up to 10 kHz. In our design, each probe head can be configured either for in-plane or for out-of-plane detection. The system performance and characteristics are shown in Table I.

Two four-channel digital oscilloscopes are used to capture the seven waveforms in real time: five surface velocities+one reference signal for each oscilloscope. The reference signal for each oscilloscope is the output from the signal generator driving the shaker. The Labview software controls the data acquisition as follows. The waveform gen-

TABLE I. Typical performance and characteristics of the interferometers.

	In-plane	Out-of-plane
Noise floor (w/o ave.)	65 $\mu\text{m/s}$ —rms	35 $\mu\text{m/s}$ —rms
Noise floor (w/ 64 ave.)	5 $\mu\text{m/s}$ —rms	3.5 $\mu\text{m/s}$ —rms
Maximum velocity	35 mm/s—peak	17 mm/s—peak
Maximum displacement	18 $\mu\text{m}$ —peak	125 $\mu\text{m}$ —peak
Sensitivity	23.7 ( $\mu\text{m/s}$ )/mV	11.7 ( $\mu\text{m/s}$ )/mV
Bandwidth	dc—10 kHz	dc—10 kHz

erator scans successively throughout the frequency range from 500 to 2500 Hz (usually by steps of 100 Hz). At each frequency, 7 waveforms of 5000 data points each are acquired 64 times successively, and converted to 64 files in ASCII format. At this point, the signals are processed under the Matlab environment as follows. The waveforms are slightly truncated to contain an integer number of cycles. A discrete Fourier transform (DFT) is used to find the peak complex amplitude of each of the  $7 \times 64$  waveforms at each frequency. No special windowing is needed if one uses an integer number of cycles in the waveform. Then, each complex amplitude is multiplied by the appropriate calibration constant of each interferometer (PLL calibrations and probe geometry) and compensated for the phase difference between the two reference signals of each scope which may have slightly different trigger levels. All signals are phase referenced to the oscilloscope on which probe #4 (the base) is displayed. Subsequently, the mean and the standard deviation over the 64 samples (at each frequency) in amplitude and phase is calculated. These values characterize the average and the spread of the amplitude and the phase of the surface velocities at points #1, #2, #3, and #5, relative to point #4, at each frequency. As indicated in the next section, the values can be compared with numerical predictions to infer the values of the elastic moduli of the sample.

## II. MATERIAL CHARACTERIZATION

The viscoelastic material under investigation is usually assumed to be macroscopically homogeneous and isotropic<sup>15–18</sup> in which case the dynamics are governed by the wave equation

$$(\lambda + \mu)\nabla\nabla \cdot \mathbf{u} + \mu\nabla^2\mathbf{u} = \rho \frac{\partial^2 \mathbf{u}}{\partial t^2} \quad (1)$$

subject to the appropriate boundary conditions. Here,  $\lambda$  and  $\mu$  are the (complex) effective Lamé constants,  $\mathbf{u}$  is the vector displacement, and  $\rho$  is the effective density of the sample. The term “effective” is used to denote the macroscopic behavior of the sample, matrix (neat material) and voids combined. The effective Lamé constants are related to the effective shear and bulk moduli,  $G$  and  $K$ , by  $G = \mu$  and  $K = \lambda + (2\mu/3)$ . The effective shear and longitudinal complex sound speeds are related to the elastic moduli by

$$c_s = \sqrt{\frac{G}{\rho}} \quad (2)$$

and

$$c_L = \sqrt{\frac{K + \frac{4}{3}G}{\rho}} \quad (3)$$

The lossy properties of the material are usually described by the loss tangents,  $\tan \delta_K$  and  $\tan \delta_G$ , defined by

$$\tan \delta_K = \frac{K''}{K'} \quad \text{with } K = K' + iK'' = K'(1 + i \tan \delta_K), \quad (4a)$$

$$\tan \delta_G = \frac{G''}{G'} \quad \text{with } G = G' + iG'' = G'(1 + i \tan \delta_G). \quad (4b)$$

The loss tangents of the sample under consideration are typically around 0.3. For void fraction  $\Phi$  less than 0.45, the Kerner model<sup>19</sup> is the best theory available<sup>20</sup> to calculate the effective moduli of the sample in terms of the complex moduli of the neat material,  $K_0$  and  $G_0$ , and the void fraction  $\Phi$  using

$$K = \frac{K_0(1 - \Phi)}{1 + 3K_0\Phi/4G_0} \quad \text{and} \quad G = \frac{G_0}{1 + 5\Phi/3}. \quad (5)$$

By definition,  $K_0 = \lambda_0 + \frac{2}{3}\mu_0$ , and  $G_0 = \mu_0$ . For our sample, it is reasonable to assume that  $\lambda_0 = \rho_0 c_{L_0}^2$  with  $\rho_0 = 1076 \text{ kg/m}^3$  and  $c_{L_0} = 1750 \text{ m/s}$ , and that the frequency dependence and the losses in the viscoelastic material come into play only through the shear modulus of the neat material. Since  $|K_0| \gg |G_0|$ , the phase of  $K_0$  is identical to that of  $G_0$  and  $G$ , and the effective bulk modulus is approximated by

$$K = \frac{4(1 - \Phi)G_0}{3\Phi}, \quad (6)$$

and the ratio of the longitudinal to shear sound speeds becomes

$$\frac{c_L}{c_s} = \sqrt{C} \quad \text{where} \quad C = \frac{K}{G} + \frac{4}{3} = \frac{4(1 - \Phi)(1 + \frac{5}{3}\Phi)}{3\Phi} + \frac{4}{3}. \quad (7)$$

This ratio is independent of the material moduli and thus it is a direct measure of void fraction. Note that the ratio of sound speeds can also be expressed in terms of the effective Poisson’s ratio of the material,  $\nu$ , as follows:

$$\frac{c_L}{c_s} = \sqrt{\frac{2(1 - \nu)}{1 - 2\nu}}, \quad (8)$$

and therefore

$$\nu = \frac{C - 2}{2(C - 1)}, \quad (9)$$

where  $C$  is given explicitly in terms of the void fraction,  $\Phi$ , in Eq. (7). Note that the assumption used to derive Eq. (6) implies that the imaginary part of  $K$  (i.e., the lossy part) is due entirely to the shear modulus. The loss factors of  $K$ ,  $G$ , and  $G_0$  are identical, so that the ratio of sound speeds, the constant  $C$ , and the Poisson’s ratio are all real. Physically, it means that all the losses are due to the conversion of dilatational to shear energy at the boundaries of the air inclusions, with a corresponding dissipation of the shear waves into heat in the polymer.<sup>17</sup>

In our experiment; the boundary conditions are such that all faces of the sample are free except for the bottom face which is driven harmonically and uniformly. With such a simple geometry and boundary conditions, the problem is

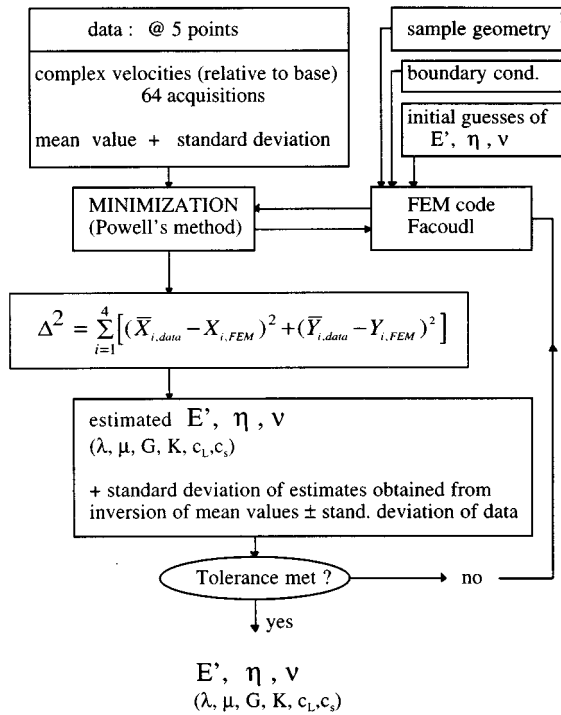


FIG. 3. Block diagram of the experimental/numerical procedure for determining the material properties.

ideally suited for an efficient and accurate computation of the surface dynamics by the finite element method (FEM). Our numerical code (FAcoudl) uses the quarter symmetry of the sample geometry with 825 nodes and 36 elements: 6 along the height, 3 along the half-length, and 2 along the half-width. The algorithm used to extract the material properties from the data consists in minimizing the difference between the data and the predicted values. It turns out that, in practice, the imaginary part of the Poisson's ratio is often assumed to be negligible. The finite element code is therefore written in terms of only three material parameters: the Young's modulus,  $E'$ , the loss factor,  $\eta$ , and the Poisson's ratio,  $\nu$ . As usual, the complex Young's modulus is defined as  $E = E'(1 + i\eta)$ . From these three values, we compute the complex Lamé constants according to the standard relations:

$$\lambda = \frac{E\nu}{(1+\nu)(1-2\nu)} \quad \text{and} \quad \mu = \frac{E}{2(1+\nu)}, \quad (10)$$

from which one can evaluate the bulk and shear moduli and the longitudinal and shear sound speeds using Eq. (3). (Alternatively, the complex bulk and shear moduli can also be expressed directly as  $K = E/[3(1-2\nu)]$  and  $G = E/[2(1+\nu)]$ , respectively.)

The search for these three parameters ( $E'$ ,  $\eta$ ,  $\nu$ ) is obtained by a three-dimensional direction set method (Powell's method),<sup>21</sup> a robust, classical method in optimization theory. The method requires initial estimates of the three parameters and a step size for the search procedure. The function that is minimized is the mean-square error defined by

$$\Delta^2 = \sum_{i=1}^4 [(\bar{X}_{i,data} - X_{i,FEM})^2 + (\bar{Y}_{i,data} - Y_{i,FEM})^2], \quad (11)$$

where  $X$  and  $Y$  are the real and imaginary parts, respectively, of the complex amplitude of the surface velocity of either the measured data or the FEM prediction. (The overbar indicates an average value over the 64 samples.) The summation in Eq. (11) is over the four surface points (#1, #2, #3, #5) normalized to point #4 (the base) in both amplitude and phase. This function (and the minimization algorithm) is evaluated for one frequency at a time. The algorithm converges toward the optimum values of  $E'$ ,  $\eta$ , and  $\nu$ , from which one calculates the shear and bulk moduli (and also the Young's modulus and Poisson's ratio, the Lamé constants, and the shear and longitudinal sound speeds) at that frequency. The process is repeated at each frequency over the range of interest. A block diagram of the procedure is shown in Fig. 3. The material inversion procedure takes typically 15 min per frequency on a Pentium Pro computer.

### III. RESULTS

Measurements were made on a sample of rectangular shape (width=1.42 cm, length=5.00 cm, and height=7.88 cm). The sample is a black, soft polymer which has not been

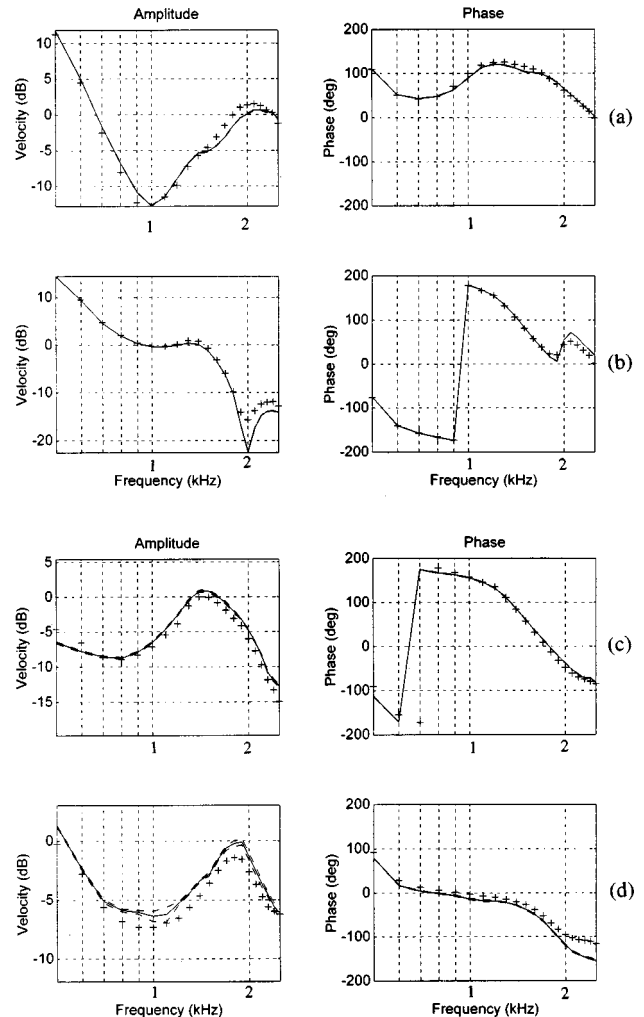


FIG. 4. Amplitude and phase at four points as a function of frequency. (a) probe #3; (b) probe #5; (c) probe #1; and (d) probe #2, all referenced to the base excitation probe #4. Solid line: average of 64 samples; dashed lines: average  $\pm$  a standard deviation (64 samples); +: FEM prediction.

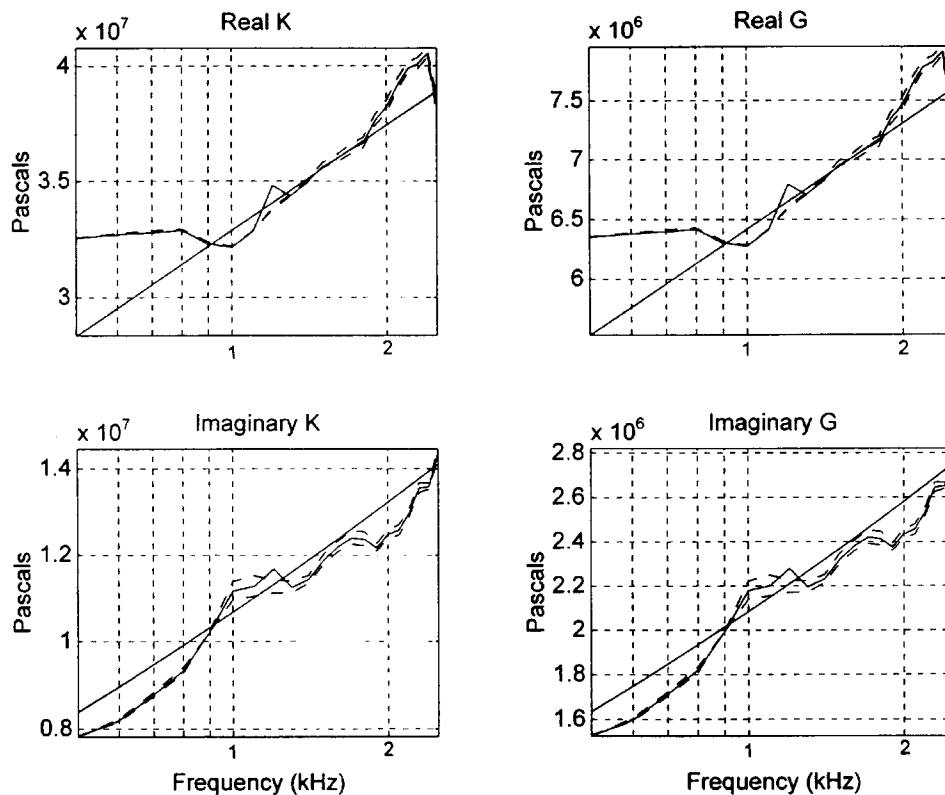


FIG. 5. Real and imaginary parts of the bulk and shear moduli as functions of frequency. Solid line: average of 64 samples; dashed line: average  $\pm$  a standard deviation (64 samples). The straight line is a prediction based on Kerner's model and DMTA data.

pressure cycled. It contains closed cell, voided microspheres, with nominal void fraction of about 32% and an average density of  $736.3 \text{ kg/m}^3$ . The matrix "neat" density is  $1076 \text{ kg/m}^3$  and the "neat" sound speed is  $1750 \text{ m/s}$ . Figure 4 shows the amplitude and phase (normalized at each frequency to the amplitude and phase of the motion of the base at point #4) measured at each of the four locations of interest, as a function of frequency. The amplitude is given in decibels referenced to the base velocity. The solid line represents the measurements obtained after 64 averages (mean value) while the two dashed lines represent the mean value plus or minus one standard deviation, also after 64 averages. The dashed lines are barely distinguishable from the solid line, thus indicating excellent repeatability of the measured waveforms. The "+" symbols denote the numerical predictions from the finite element model in which the material parameters were calculated with the inversion technique in which the input surface displacements were the mean values (over the 64 averages). The results clearly show the first resonances with the corresponding amplitudes and phases (measured relative to the base motion) characterizing the sample dynamics. At very low frequencies (below  $500 \text{ Hz}$ ), the sample is undergoing rigid body motion and the predicted dynamic response of the sample is insensitive to the material parameters. Probe #5 which measures the vertical motion at the top center of the sample shows a sharp drop at  $2 \text{ kHz}$ . This is not a spurious data point. Indeed, the finite element code shows that, at the frequency, the sample is also subject to a resonance along the lateral dimension, so that the total vertical displacement at the top center of the sample remains zero.

The measured surface displacements were then used to infer the effective bulk moduli of the sample using the inversion procedure described above. The results indicated some rather large peaks as a function of frequency which were unlikely to be physical. The source of these large fluctuations was found to be some relatively small variations in the Poisson's ratio as a function of frequency. Based on physical consideration, as well as on Eqs. (9) and (7) which show that the Poisson's ratio should be independent of frequency, we calculated an average value of the Poisson's ratio over the frequency range of interest of  $\nu=0.408$ . This value is in good agreement with the value of  $\nu=0.393$  predicted by the Kerner model, Eq. (9), with a void fraction  $\Phi=0.32$ . The inversion procedure was repeated again, with a fixed value of  $\nu=0.408$  over all frequencies to determine  $E'$  and  $\eta$ , and therefore the bulk and shear moduli. As expected, this technique reduced the large fluctuations observed earlier. The results are shown in Fig. 5 which shows the real and imaginary parts of the bulk and shear moduli as functions of frequency. The solid line represents the elastic moduli obtained after the inversion procedure in which the input displacements are the mean values over 64 averages (i.e., the solid lines in Fig. 4). The two dashed lines represent elastic moduli obtained after the inversion procedure when the input to the inversion code is the mean value of the data plus or minus one standard deviation, also after 64 averages (i.e., the dashed lines in Fig. 4). Therefore, the dashed lines in Fig. 5 are not the standard deviation of the bulk and shear moduli, but rather a somewhat qualitative representation of the confidence in the mean value that one can expect at a given

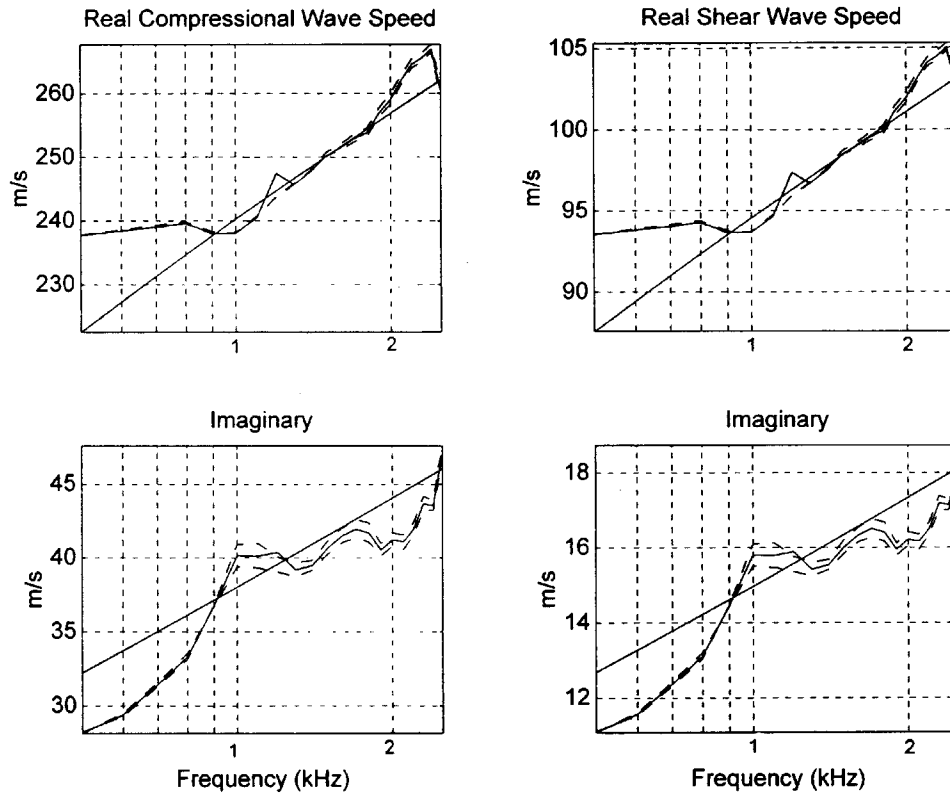


FIG. 6. Real and imaginary parts of the shear and compressional sound speeds as a function of frequency. solid line: average of 64 samples; dashed line: averaged  $\pm$  a standard deviation (64 samples). The straight line is a prediction based on Kerner's model and DMTA data.

frequency. The results are also compared with predictions based on the Kerner model<sup>19</sup> [see Eq. (5)] in which  $G_0$  (frequency dependence and loss tangent) are determined experimentally by a totally different method: the Dynamic Mechanical and Thermal Analyzer (DMTA) and Universal Temperature Programmer (UTP) apparatus from Rheometric Scientific, NJ. The result of this independent measurement is shown in the appendix. From the values of  $K$  and  $\nu$ , one computes  $E = 3K(1 - 2\nu)$  and  $G = E/2(1 + \nu)$ . The real and imaginary parts of the complex shear and compressional sound speeds are then computed from the complex elastic bulk and shear moduli using Eq. (3). The results are shown in Fig. 6. (Note that the scales of the shear and compressional sound speeds are very different.) Clearly, the shear and bulk complex moduli exhibit a relatively strong frequency dependence but the ratio  $K/G$  is independent of frequency, as predicted by Eq. (7). The Kerner model predicts a ratio of 4.34 for a void fraction  $\Phi = 0.32$ , i.e., a Poisson's ratio of  $\nu = 0.393$ . The Kerner model somewhat underestimates the ratio  $K/G = 2(1 + \nu)/3(1 - 2\nu) = 5.10$  for the Poisson ratio  $\nu = 0.408$  determined by the LDV numerical technique.

The LDV numerical data show good agreement with the predictions based on Kerner's model for the complex bulk modulus and the complex compressional sound speed, especially between 1 and 2 kHz. Differences between measured and predicted values can be attributed to several factors which remain to be investigated to determine the accuracy of the proposed new method. In particular, the shift factors used in estimating the shear modulus of the neat material by the

DMTA technique may be imprecise; the sample used in the LDV numerical experiment was different from the one used in the DMTA apparatus, albeit from the same strip of material; it is possible that the sample exhibits some anisotropy or even that there are some large air bubbles inside the sample; also, the base may have some nonuniform motion. In addition, there are several assumptions built into the Kerner model. Also, the LDV numerical method is not expected to work at low frequencies. Well below the first resonance, when the sample is undergoing essentially rigid body motion, the material inversion routine is extremely inaccurate.

#### IV. SUMMARY

A laser-based numerical/experimental technique suitable for laboratory studies has been designed and tested to measure simultaneously the bulk and shear complex dynamic moduli of a viscoelastic sample excited harmonically in the 0.5–2.5 kHz range. The method consists in measuring the dynamic response (amplitude and phase) of the sample at four points and at the base using noncontact laser Doppler interferometry. This method eliminates the inherent loading of the sample that occurs when using accelerometers. In addition, in-plane surface dynamics can be accurately measured by laser interferometry, thus providing additional valuable information. To determine the bulk and shear moduli as functions of frequency, the measured dynamic surface response is matched to the predictions obtained from a finite element model of the sample in which the two complex elastic moduli are the adjustable parameters. This inversion pro-

cedure is based on a classical multidimensional direction set method (Powell's method) of optimization theory. The results were found to be very sensitive to small changes in the value of the Poisson's ratio as a function of frequency. Better results were obtained by computing an average value of the Poisson's ratio over the frequency range of interest, and repeating the inversion procedure with Young's modulus and the loss factor as adjustable parameters. The results were compared with predictions based on Kerner's theory and independent measurements with the DMTA apparatus with a reasonable degree of agreement especially in the 1–2 kHz range. At low frequencies, when the sample is undergoing essentially rigid body motion, the method is not expected to work. At high frequencies, the method is currently limited by the nonuniform motion of the base below the sample. The results presented in this paper are for measurements made in air under standard pressure and temperature conditions. However, work is under way toward a similar system that would allow for measurements under static pressure and controlled temperature.

## ACKNOWLEDGMENTS

This work is based on the Master theses of the first two authors. The research was supported by the Office of Naval Research, Structural Acoustics Program, Code 334, Dr. G. L. Main Scientific Officer. The authors would like to thank Steve Hahn for his help with the finite element code; and Jacek Jarzynski, Michele McCollum, Steve Black, and Pat Klippel, and Geoff Main for many insightful discussions during the course of this project.

## APPENDIX

A similar sample of viscoelastic material was tested with the Dynamic Mechanical Thermal Analyzer (DMTA) to determine its complex shear modulus. The DMTA actually measures the Young's modulus of a small sample at a given temperature over a narrow frequency band (0.3–30 Hz). It repeats the measurements over a large temperature range (–20 °C–+50 °C) and builds a master curve over a large frequency range based on the time-temperature equivalence

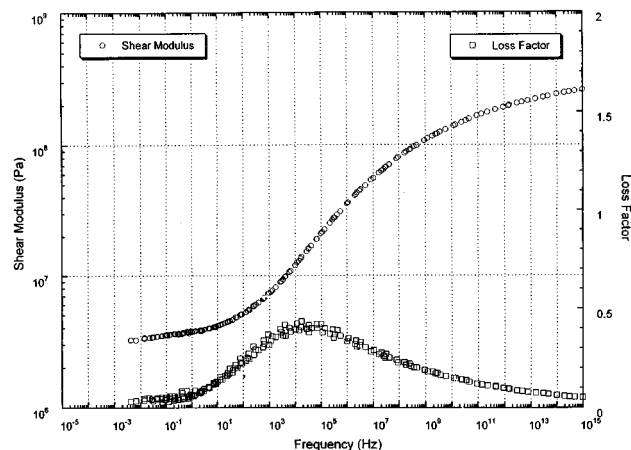


FIG. A1. Shear modulus and loss tangent of the voided polymer. Measurement made with the Dynamic Mechanical Testing Apparatus.

principle and the associated WLF shift constant.<sup>10</sup> This principle states that measurements made within a narrow frequency range at several temperatures are equivalent to measurements made over a wide frequency range at a single temperature. The shear modulus is then obtained by dividing the Young modulus by 3, i.e., by assuming a Poisson's ratio of 0.5. The results are shown in Fig. A1 which shows the measured shear modulus,  $G_{\text{meas}}$  and the measured loss tangent,  $\tan \delta_G$ . To relate the measured values (voided polymer) to the modulus of the neat material, we use Kerner's model [Eq. (5)], i.e., we multiply the measured value by a factor  $(1 + \frac{5}{3}\Phi)$ . The frequency dependence is calculated only between 500 and 2500 Hz by linear interpolation for both the shear modulus and the loss tangent.

- <sup>1</sup>B. E. Read and G. D. Dean, *The Determination of Dynamic Properties of Polymers and Composites* (Wiley, New York, 1978).
- <sup>2</sup>R. J. Bobber, *Underwater Electroacoustics Measurements* (Peninsula, Los Altos, CA, 1988), pp. 287–314.
- <sup>3</sup>S. S. Sattinger, "Direct method for measuring the dynamic shear properties of damping polymers," in *Sound and Vibration Damping with Polymers*, edited by R. D. Corsaro and L. H. Sperling (The American Chemical Society, Washington, DC, 1990), pp. 79–91.
- <sup>4</sup>G. A. Sabin, "Acoustic-impedance measurements at high hydrostatic pressures," *J. Acoust. Soc. Am.* **40**, 1345–1353 (1966).
- <sup>5</sup>R. Harrison, "Guided-Wave tube technique for materials characterization," in *Sound and Vibration Damping with Polymers*, edited by R. D. Corsaro and L. H. Sperling (The American Chemical Society, Washington, DC, 1990), pp. 248–259.
- <sup>6</sup>M. P. Hagelberg and R. D. Corsaro, "A small pressurized vessel for measuring the acoustic properties of materials," *J. Acoust. Soc. Am.* **77**, 1222–1228 (1985).
- <sup>7</sup>W. M. Madigosky and G. F. Lee, "Automated dynamic Young's modulus and loss factor measurements," *J. Acoust. Soc. Am.* **66**, 345–349 (1979).
- <sup>8</sup>W. M. Madigosky and G. F. Lee, "Improved resonance technique for material characterization," *J. Acoust. Soc. Am.* **73**, 1374–1377 (1983).
- <sup>9</sup>S. L. Garrett, "Resonant acoustic determination of elastic moduli," *J. Acoust. Soc. Am.* **88**, 210–221 (1990).
- <sup>10</sup>J. Ferry, *Viscoelastic Properties of Polymers* (Wiley, New York, 1970).
- <sup>11</sup>M. McCollum, "Surface-measurement-based acoustic materials characterization using MIME," Structural dynamics and structural acoustics program review (part II), Office of Naval Research, 12–15 February 1996.
- <sup>12</sup>R. L. Willis, "A five channel laser interferometer for use in non-invasive acoustic material characterization," MS thesis, Georgia Institute of Technology, Mechanical Engineering (1995).
- <sup>13</sup>L. E. Drain, *The Laser Doppler Technique* (Wiley, Chichester, 1980).
- <sup>14</sup>D. Lee, J. Jarzynski, and Y. H. Berthelot, "A study of wave propagation on a cylindrical shell using optic fiber Doppler velocimetry," *J. Acoust. Soc. Am.* **94**, 196–212 (1993).
- <sup>15</sup>R. Kingman, W. Madigosky, and J. Barlow, "Effective dynamic properties of composites viscoelastic materials," *J. Acoust. Soc. Am.* **70**, 1437–1444 (1981).
- <sup>16</sup>I. A. Chaban, "Calculation of the effective parameters of microinhomogeneous media by the self consistent field method," *Sov. Phys. Acoust.* **11**, 81–86 (1965).
- <sup>17</sup>J. Jarzynski, "Mechanisms of sound attenuation in materials," in *Sound and Vibration Damping with Polymers*, edited by R. D. Corsaro and L. H. Sperling (The American Chemical Society, Washington, DC, 1990), pp. 167–207.
- <sup>18</sup>W. Madigosky and K. Scharnhorst, "Acoustic wave propagation in materials with inclusions or voids," in *Sound and Vibration Damping with Polymers*, edited by R. D. Corsaro and L. H. Sperling (The American Chemical Society, Washington, DC, 1990), pp. 229–247.
- <sup>19</sup>E. H. Kerner, "The elastic and thermoelastic properties of composite media," *Proc. Phys. Soc. London* **69**, 808–813 (1956).
- <sup>20</sup>W. Madigosky, R. W. Harrison, and K. Scharnhorst, "Effect of air inclusions on absorption and velocity of sound in viscoelastic materials," *Polymeric Materials: Sci. Eng.* **60**, 489–496 (1989).
- <sup>21</sup>W. H. Press, B. P. Flannery, S. A. Teukolsky, and W. T. Vetterling, *Numerical Recipes* (Cambridge U.P., Cambridge, 1986), Sec. 10.5.

# An experimental evaluation of split-beam processing as a broadband bearing estimator for line array sonar systems

Stergios Stergiopoulos<sup>a)</sup>

Defence and Civil Institute of Environmental Medicine, P.O. Box 2000, North York, Ontario M3M 3B9, Canada

Anthony T. Ashley

Defence Research Establishment Atlantic, P.O. Box 1012, Dartmouth, Nova Scotia B2Y 3Z7, Canada

(Received 20 May 1996; accepted for publication 3 July 1997)

This paper examines the potential improvements in bearing estimation performance of split-beam processing over full-aperture beamforming for broadband signals. It presents theoretical results in order to define the details of the signal flow in a split-beam processor, and it provides theoretical performance predictions by using Cramer–Rao lower bound (CRLB) analysis. The split-beam processing scheme was implemented in a real-time line array system. Good agreement between the theoretical performance predictions and the associated experimental broadband results were obtained. The experimental results indicate that the advantage of improved bearing estimation performance of the split-beamformer over the conventional full-aperture beamformer may be practically insignificant for passive line array applications because of the split-beamformer's poor performance in detecting very weak broadband signals. © 1997 Acoustical Society of America. [S0001-4966(97)01311-8]

PACS numbers: 43.60.Gk, 43.30.Wi [JLK]

## INTRODUCTION

Sonar array processing includes a large number of algorithms that are quite diverse in concept. However, a common element in most sonar systems is the beamforming process which provides both array gain and target bearing estimation.

Previous theoretical studies<sup>1–4</sup> have addressed two important points regarding the beamforming problem. First, Cramer–Rao lower bound (CRLB) analysis has been used to set an absolute lower bound for the minimum variance achievable by a maximum-likelihood (ML) estimator. Second, CRLB estimates have been used to determine the optimum position configuration for the hydrophones of a line array in order to get optimum estimates for a target's bearing or range or position. When quantifying bearing performance, MacDonald and Schultheiss<sup>1</sup> and Carter<sup>2</sup> have shown that, when placing half the towed array sensors exactly at one end and half exactly at the other end, the theoretical lower limit is achieved indicating optimum array configuration for bearing estimates. However, the above optimum array configuration is useful only under the assumed condition that signal and noise are stationary Gaussian processes embodied in an isovelocity medium. Furthermore, several hydrophone elements could never be physically located at the identical spot on both ends of the line array. In practice, the sensors would be placed at moderate fraction of a half-wavelength spacing. As a result of this kind of practical constraint, it has been shown<sup>1</sup> that a nearly optimal technique for bearing estimation is the *split-beam processing method*.

In split-beam processing a linear array is assumed to consist of two subarrays placed towards each end of a hydrophone array configuration. At each subarray, beams are

steered simultaneously in the same direction by means of conventional beamforming. Then, the corresponding output pairs of beam time-series are cross correlated in order to derive time delay measurements for bearing estimates. Theoretically, split-beam processing can provide better broadband bearing resolution than conventionally beamforming the full aperture.<sup>1,4</sup>

Even though the improved bearing estimation performance of the split-beam processing over full aperture beamforming is more pronounced for broadband signals located in the endfire directions of a towed array, this advantage may be practically insignificant for passive towed array applications because of the split-beamformer's poor performance in detecting very weak signals.<sup>2,3,5,13,14</sup> However, despite these performance problems, the split-beamforming concept was considered, until very recently, as an attractive option by the sonar system designers. The reason is that hardware restrictions and computing architecture limitations favored suggestions<sup>2</sup> that included the placing of two or three subarrays widely spaced over a baseline of a fixed length. The aim of this paper is to address these concerns experimentally and to assess their importance with respect to system applications.

The material in Secs. I–III of this paper addresses the theoretical principles<sup>1–5,13–15</sup> to provide the details of an optimum split-beamformer's signal processing flow and to assess its performance. The poor performance of the split-beam processing versus the full-aperture beamforming, predicted in Secs. II and III, is verified experimentally in Sec. IV by (i) implementing the broadband split-beamforming concept in a real-time line array system as shown in Fig. 3, and (ii) comparing the split-beamformer's performance with that of the full-aperture beamformer's output, which is shown in Fig. 11.

<sup>a)</sup>Electronic mail: stergios@dcie.dnd.ca



## I. BACKGROUND

Consider a horizontal line array with  $N$  omnidirectional hydrophones equally spaced at distance  $\delta$  in an anisotropic ocean. Furthermore, assume an incoming acoustic signal from a distant source with bearing  $\theta$ , measured from the broadside direction of the line array. The signal is sampled at time increment  $\Delta t$  with  $t_i = i\Delta t$ , where  $i = 1, 2, \dots, K$ ,  $K$  being the number of data samples for each one of the hydrophone time series. The time series are expressed by

$$x_n(t_i) = s(t_i + n\tau) + \varepsilon_{n,i}(0, \sigma_\varepsilon), \quad (1)$$

where  $n = 0, 1, \dots, N-1$ ,  $N$  is the number of hydrophones and  $\tau$  is the time delay between two successive hydrophones of the signal wavefront arrival. Here  $X_n(f) = \sum_{i=1}^K x_n(t_i) \times \exp(-j2\pi f t_i)$  is the Fourier transform of  $x_n(t_i)$  at frequency  $f$ ,  $c = f\lambda$  is the speed of sound in the ocean, and  $\lambda$  is the wavelength;  $\varepsilon_{n,i}(0, \sigma_\varepsilon)$  are independent, zero mean, Gaussian random variables with standard deviation  $\sigma_\varepsilon$ .

Quantitative estimates of the spatial coherence for signals from a line array are provided by the cross-spectral density matrix between any set  $(n, m)$  of two hydrophone time series of the line array with spatial separation  $\delta_{nm} = (n - m)\delta$ . An estimate of the cross-spectral density matrix<sup>2,3</sup> in the frequency domain is given by

$$R_{nm}(f, \delta_{nm}) = E[X_n(f)X_m^*(f)], \quad (2)$$

where  $E[\dots]$  denotes the expectation operator and  $*$  denotes complex conjugate. The above space-frequency correlation function can be related to the angular power directivity pattern of the source,  $\Psi_s(f, \theta)$ , via a Fourier transformation<sup>6</sup> by using a generalization of Bello's concept<sup>7</sup> of time-frequency correlation function  $[t \leftrightarrow 2\pi f]$  into space  $[\delta_{nm} \leftrightarrow 2\pi f \sin \theta/c]$ . The correlation function,  $R_{nm}(f, \delta_{nm})$ , has numerous uses in other areas such as time delay estimation, beamforming, and determination of array gain.

Previous studies<sup>8</sup> have shown that for a signal embedded in a spatially white noise field, the *conventional beamformer* (CBF) without shading is an optimum beamformer for bearing estimation and its variance achieves the theoretical CRLB bound. When there are multiple signals, however, the deterioration of performance for the CBF is well-known and well documented with defects of "spatial beam leakage" and degradation in spatial resolution.<sup>16</sup> The narrow-band CBF is defined by  $B(f, \theta_s) = D^*(f, \theta_s)X(f)$ , where the  $n$ th element of the steering vector  $D(f, \theta_s)$  is

$$\eta_n(f, \theta_s) = \exp[j2\pi f \delta_{1n} \sin \theta_s/c]$$

and  $X(f)$  is an  $N$ -dimensional vector of hydrophone data  $X_n(f)$  at frequency  $f$ . The term  $\tau_s = \delta_{1n} \sin \theta_s/c$ , in the steering vector  $\eta_n(f, \theta_s)$ , represents the time delay between the first and  $n$ th hydrophones of the array for an incoming plane wave with direction of propagation  $\theta_s$ .

Cross correlation of the corresponding pairs of beam time series in split-beam processing is the main processing step to provide time delay estimates  $\tau_s$ , which can be interpreted as bearing angles  $\theta_s$ , expressed by

$$\theta_s = \cos^{-1}(c\tau_s/\Delta L), \quad (3)$$

where  $\Delta L$  is the distance between the two acoustic subarray centers. A tutorial review on time delay estimation is provided by Carter.<sup>2-4</sup> Practical issues of robustness for cross-correlation processing are also discussed by Ferguson.<sup>5</sup>

For bandwidth-limited signals the cross-correlation output of the split-beam processing is a cosine function modulated by a sinc function [see Eq. (5)], therefore the time spreading increases as the bandwidth decreases. As the signal bandwidth becomes a small fraction of the center frequency, then the time delay estimate from the cross-correlator's output becomes more ambiguous.<sup>13,14</sup> For temporally white noise the cross-correlation output  $R_\theta(\tau)$  of the corresponding pairs of beam time series in split-beamforming is expressed by

$$R_\theta(\tau) \propto \delta(\tau), \quad (4)$$

for bandwidth limited signals is expressed by

$$R_\theta(\tau) = B_w \left[ \frac{\sin(\pi B_w \tau)}{\pi B_w \tau} \right] \cos(2\pi f_0 \tau), \quad (5)$$

where  $B_w$  is the bandwidth of the signal and  $0 < f_0 - (B_w/2) \leq f \leq f_0 + (B_w/2)$ , and for a monochromatic signal is expressed by

$$R_\theta(\tau) \propto \cos(2\pi f_0 \tau). \quad (6)$$

Furthermore, for signals close to broadside ( $\theta_s = 0$ ) the resolution properties of the split-beamformer are governed by the width of the main lobe of the correlator's output. Thus, for two detected signals with bearings  $\theta_1$  and  $\theta_2$  the corresponding time delay estimates,  $\tau_1$  and  $\tau_2$ , provided at the output of the split beamformer, will be resolvable if their difference satisfies the relation

$$\tau_2 - \tau_1 = \frac{\Delta L}{c} (\cos \theta_2 - \cos \theta_1) \geq \frac{\mu}{B_w}, \quad (7)$$

where  $\mu$  is a constant that depends on the definition of resolution. Assume for simplicity ( $\theta_1 = 0$ , i.e., broadside) then  $\cos \theta_2 = \mu c/(B_w \Delta L)$  or, more general,

$$\theta = \cos^{-1} \left( \frac{\mu c}{B_w \Delta L} \right), \quad (8)$$

which is Eq. (3) with  $\tau_s = \mu/B_w$ . Based on Eq. (8) and for  $\mu = 1$ , which assumes ideal bandpass signals, numerical results in Figs. 1 and 2 illustrate the effects of the signal bandwidth and the subaperture separation  $\Delta L$  on the effective angular resolution performance of the split-beamformer. In particular, Fig. 1 plots for two cases of subaperture separation,  $\Delta L$ , the angular resolution performance of a split beamformer as a function of the signal's bandwidth,  $B_w$ . Figure 2 shows the effects of subaperture separation,  $\Delta L$ , on the minimum signal bandwidth,  $B_w$ , which is required to achieve the indicated angular resolution.

## II. SIGNAL PROCESSING FLOW FOR A SPLIT-BEAMFORMER

Before we present the signal processing flow of a split beamformer implemented in a real-time line array system, it is important to discuss briefly prefiltering operations that im-

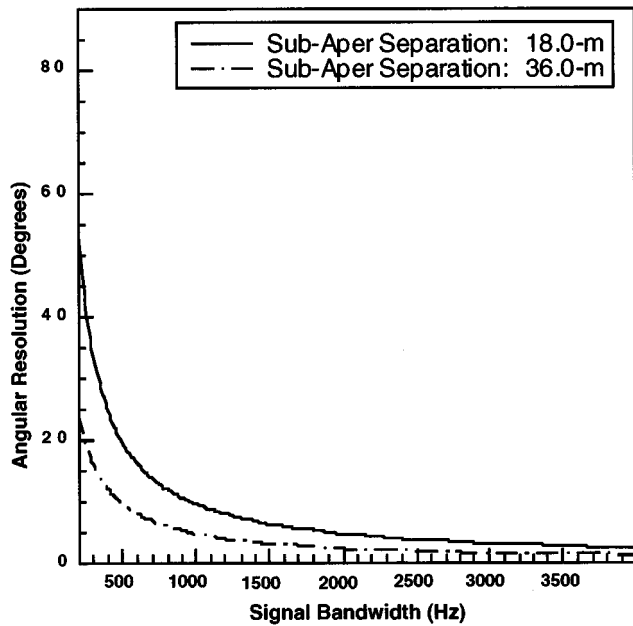


FIG. 1. Effects of signal bandwidth versus angular resolution for a split-beamforming process. Two cases have been considered having subaperture separation of 18 m (shown by the solid line) and 36 m (shown by the dashed line).

prove the cross-correlation processing performance and, as a result, the time delay and bearing estimation process associated with split-beam processing.

Improvements in the time delay estimation process can be obtained through the application of various prefilterers in order to accentuate the signal passed to the correlator at those frequencies at which the SNR is highest.<sup>4</sup> In other words, the highest weighting will be applied to cross-spectral estimates with the least variance in the phase error estimates. The same type of prefiltering is provided by the generalized Eckart filter,<sup>15</sup> which maximizes the SNR of the correlator output. In practice, however, the Eckart filter requires knowledge or estimation of the signal and noise spectra.

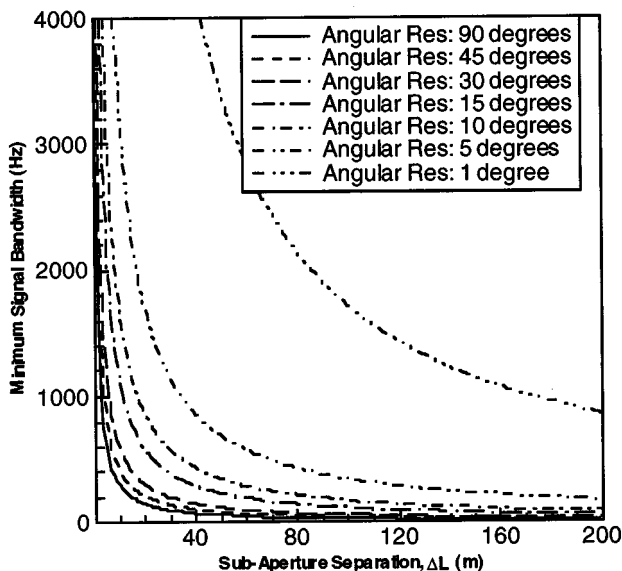


FIG. 2. Effects of subaperture separation and signal bandwidth on selected cases of angular resolution performance by a split-beamforming process.

In the time domain, prefiltering includes the application of filters to the two time series prior to their cross-correlation, while in the frequency domain, prefiltering includes the application of windows or weighting functions to the cross-spectral density function before the inverse FFT process. Therefore, if  $R_{nm}(f, \delta_{nm})$  is the correlation output in the frequency domain between two hydrophone time series with  $\delta_{nm}$  being the hydrophone separation,  $f$  is in the frequency range of  $0 < f_0 - (B_w/2) \leq f \leq f_0 + (B_w/2)$ ,  $B_w$  is the signal bandwidth, and  $f_0$  is the center frequency, then the prefiltered cross-correlation output is

$$R_{\theta_s}(f) = W(f) \times R_{nm}(f, \delta_{nm}), \quad (9)$$

where  $W(f)$  is a filter defined below by Eq. (10). The inverse FFT of  $R_{\theta_s}(f)$  provides the cross-correlation time series  $r_{\theta_s}(\tau)$ . Since estimates of  $W(f)$  are a function of the signal and noise spectra, the signal's coherence properties must be either known *a priori* or estimated. Ferguson<sup>5</sup> has examined experimentally the performance characteristics of three different filters and has discussed practical aspects associated with this kind of prefiltering process. One of the above three prefilterers is the *phase transform* processor,<sup>4</sup> which is an *ad hoc* technique that uses only the cross-spectral phase information and it is defined by

$$W(f) = |R_{nm}(f, d_{nm})|^{-1/2}. \quad (10)$$

The Eckart filter<sup>15</sup> unlike the phase transform processor attaches zero weight,  $W(f) = 0$ , to bands where  $R_{nm}(f, d_{nm}) = 0$ . However, the Eckart filter requires knowledge or estimation of the signal and noise characteristics to be integrated in the signal processing flow of a real time split-beam processor, which is a very difficult requirement to fulfill. For the present real time system application, we have chosen to use the *phase transform* as a filter, because it does not require knowledge or estimation of the shape of the signal and noise spectra.

Shown in Fig. 3 is the processing configuration of split-beam processing for a line array system. At each subarray, beams are steered simultaneously in the same direction by means of frequency domain conventional beamforming without spatial shading. The frequency domain beamforming outputs are made equivalent to the FFT of the time domain beamformers' outputs by applying proper selection of beamforming weights and careful data partitioning. This equivalence corresponds to implementing FIR filters via circular convolution.<sup>9</sup>

Then, the corresponding output pairs of frequency domain beams  $[B^F(f, \theta_s)$  and  $B^A(f, \theta_s)]$  are cross correlated to form the beam cross spectra,  $\Phi(f, \theta_s) = B^F(f, \theta_s) \times B^{A*}(f, \theta_s)$ , for all the frequency bins of the signal's bandwidth  $B_w$ , where  $0 < f_0 - (B_w/2) \leq f \leq f_0 + (B_w/2)$ . Prefiltering is applied next by weighting the terms  $\Phi(f, \theta_s)$  by the phase transform  $W(f) = |\Phi(f, \theta_s)|^{-1/2}$ . The inverse FFT of  $\{W(f) \times \Phi(f, \theta_s)\}$  provides a cross-correlation time series for each beam steered at  $\theta_s$ . The peaks associated with the cross-correlation outputs provide differential time delay estimates and, as a result, bearing estimates according to Eq. (3). Integration of the bearing estimates from all the cross-

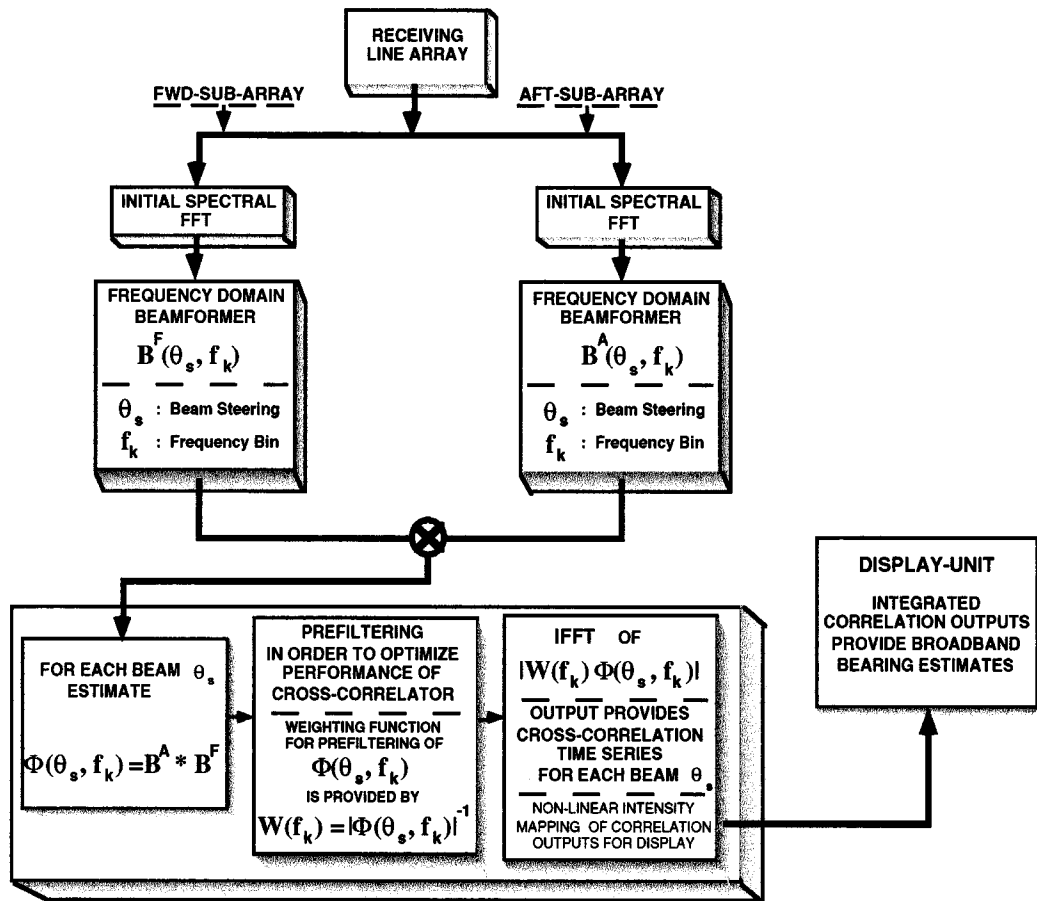


FIG. 3. Signal processing flow of a split-beamformer implemented in a real time system.

correlated beams and their display as a function of time produces the main output of the split-beamformer.

### III. THRESHOLD EFFECTS

In this section, the CRLB analysis and computer simulations are used to define and compare quantitatively the performance of the split-beamformer (defined in Sec. II) versus the full aperture beamformer.

Typically, the performance of an unbiased estimator is represented as the variance in the estimated parameters. If the *a priori* probability of detection is close to unity, the minimum variance achievable by any unbiased estimator is provided by the *Cramer-Rao Lower Bound* (CRLB).<sup>10,11</sup> In this case, if there exists a signal processor to achieve the CRLB, it will be the maximum-likelihood estimation (MLE) technique. The above requirement associated with the *a priori* probability of detection is essential because if it is less than one, then the estimation is biased and the theoretical CRLBs do not apply.<sup>10</sup> This general framework of optimality is essential in order to account for Middleton's (Ref. 10, p. 787) warning that a system optimized for the one function (detection or estimation) may not be necessarily optimized for the other.

Let  $\theta_i$  denote the *maximum likelihood estimate* (MLE) of the parameter of interest and  $\sigma_{\theta_i}^2$  denote the variance of the estimate  $\tilde{\theta}_i$  for the parameter  $\theta_i$  that is described by a model, such as the one in Eq. (1). The Cramer-Rao<sup>10,11</sup>

bound states that the variance  $\sigma_{\theta_i}^2$  of the best unbiased estimate  $\tilde{\theta}_i$  of the parameter of  $\theta_i$  has a CRLB, which is given by the diagonal elements of the Fisher information matrix.<sup>10,11</sup> This CRLB is used as a standard of performance and provides a good measure for the performance of a signal processing algorithm. Furthermore, for each estimator it is well known that there is a range of *Signal-to-Noise Ratio* (SNR) in which the variance of the estimates rises rapidly as SNR decreases. This effect, which is called the *threshold effect of the estimator*, determines the range of SNR of the received signals for which the parameter estimates can be accepted. Thus, estimation of the threshold effect is essential in the selection of practical robust sonar signal processing.

At this point it is important to note that the CRLB applies to small or local errors only, hence it is not useful below threshold where large errors occur. Other bounds are thus needed to characterize the large error region. One such bound is the Zik-Zakai lower bound (ZZLB).<sup>13,14</sup>

In this study, the CRLB analysis and computer simulations have been used to define and compare quantitatively the performance of the split-beam processing for different cases of effective signal bandwidth and subaperture separation. Shown by the three curves in Fig. 4 are the theoretical CRLB,  $\sigma_{\theta_{\text{CRLB}}}^2$  for the bearing as a function of SNR for the case of one source. These theoretical CRLB estimates were derived from MacDonald and Schultheiss [Ref. 1, Eq. (20)] and are for a split-beam processor including two subaper-

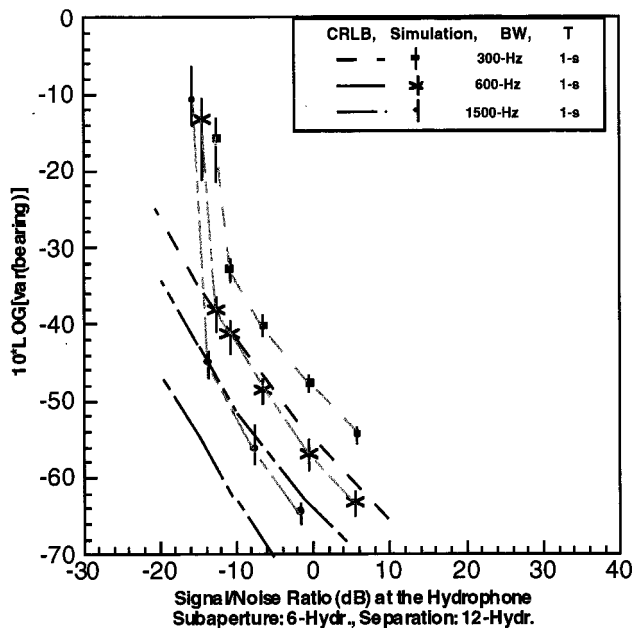


FIG. 4. Performance analysis of a split-beamformer for three different cases of effective signal bandwidth. Curves show the corresponding theoretical CRLB estimates.

tures each having 6 hydrophones. The separation between the two subapertures is 12 hydrophone spacings as this is illustrated in Fig. 5. Moreover, the geometric configuration of the above figure shows the concept of this study of forming the two subapertures at both ends of an equi-spaced line array. For the above three CRLB estimates,  $\sigma_{\theta_{\text{CRLB}}}^2$ , the corresponding signal bandwidths are 300, 600, 1500 Hz; and for all of them the processing period was the same and equal to 1 s.

For the same signal bandwidths and subaperture configuration, computer simulations were also considered for the calculation of the variance  $\sigma_{\theta_s}^2$  of bearing estimates. Figure 4 presents the estimates of  $\sigma_{\theta_s}^2$  derived by a split-beam processor with a signal processing flow, which is shown in Fig. 3. The ocean model for the simulations is a direct path isovelocity environment.

In Fig. 4, the difference between the theoretical CRLB estimates,  $\sigma_{\theta_{\text{CRLB}}}^2$  and the simulations,  $\sigma_{\theta_s}^2$  is approximately 7.8 dB and agrees with predictions discussed in Ref. 1, Eq. (35). It is apparent by the above results that the performance of the split-beamformer improves as the signal bandwidth

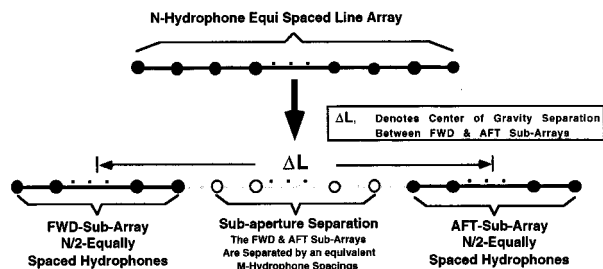


FIG. 5. Geometric configuration showing the concept of this study of forming the two sub-apertures at both ends of an equi-spaced line array.

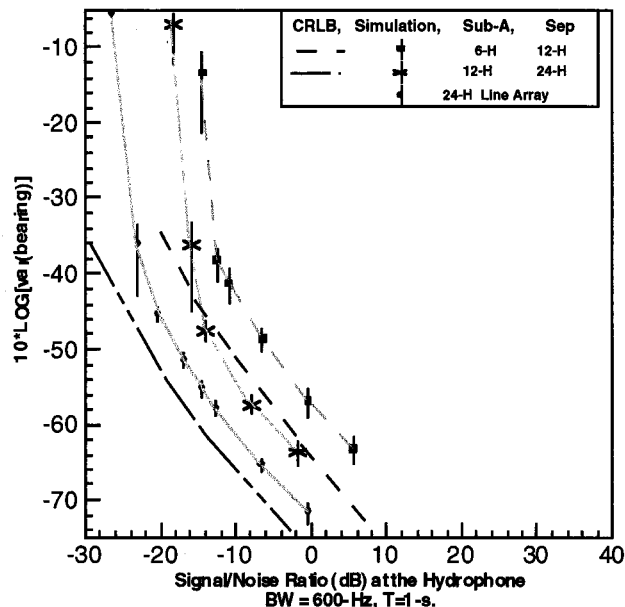


FIG. 6. Performance analysis of a split-beamformer for two different cases of subaperture sizes and for a full aperture beamformer. The signal bandwidth was 600 Hz and the observation period was 1 s. Curves show the theoretical CRLB estimates.

increases. The threshold effect is also shown by the rapid rise of the variance of the bearing estimates for SNR values in the range of  $-12$  dB at the hydrophone.

The results depicted in Fig. 6, from the same kind of computer simulations as those of Fig. 4, show how bearing variance depends upon aperture size. The curves in Fig. 6 provide the theoretical CRLB,  $\sigma_{\theta_{\text{CRLB}}}^2$ , [Ref. 1, Eqs. (19), (20)] for the bearing as a function of SNR for the case of one source with effective signal bandwidth of 600 Hz. These theoretical CRLB estimates are for two different kinds of subaperture configurations, shown in Fig. 6. Results indicated by solid circles are from computer simulations derived by full aperture beamforming a 24-hydrophone line array. The processing period for this signal was equal to 1 s. In this case of full aperture beamforming, the threshold effect is shown to be in the range of  $-22$  dB at the hydrophone. Solid squares in the same figure present the variance estimates  $\sigma_{\theta_s}^2$  for the same 600-Hz signal bandwidth and 1-s integration period. These estimates were derived by applying split-beam processing on two subarrays of 6 hydrophones each and separated by 12 hydrophones. The threshold effect of the split-beam processing is in the range of  $-12$  dB at the hydrophone.

In order to quantify the effects of larger subapertures, this split-beamforming analysis was also applied to the same signal and for subarrays of 12 hydrophones each and separated by 24 hydrophones for an extended array. The simulation results of  $\sigma_{\theta_s}^2$ , in this case, are shown by the star symbols in Fig. 6 and indicate inferior performance than that of the fully populated 24-hydrophone array, shown by the solid circles in the same figure. In the simulation, the conventional beamformer included uniform spatial shading across the hydrophone samples. Thus, although the two subarrays of 12 hydrophones each have in total the same number of hydro-

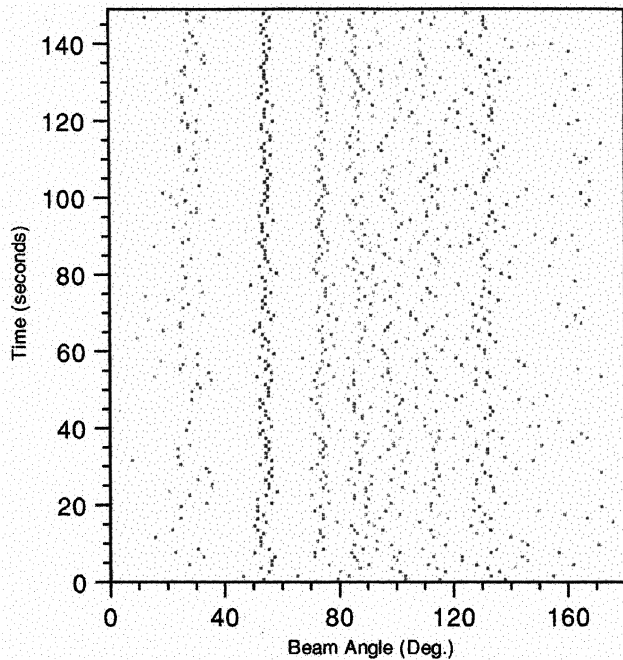


FIG. 7. Bearing estimates as a function of time from real sea data and for a split-beam processing scheme shown in Fig. 3. The signal bandwidth was 200 Hz and the coherent processing period was 1 s. The two subapertures (with size of 6 hydrophones each) were separated by 12 hydrophone spacings.

phones as the 24-hydrophone fully populated array, the threshold value of the split-beam processing is worse than that of the full aperture beamformer.

#### IV. REAL EXPERIMENTAL RESULTS

The set of experimental data of this study represents an acoustic field consisting of radiated noise including strong narrowband and broadband features from distant ships and geological equipment in acoustic conditions typical of a North Atlantic sea state 4. The data were collected over 150 s on a 24 hydrophone line array with 2-m spacing. The velocity profile was a typical North Atlantic summer ocean environment.

The subaperture configuration for split-beam processing included two subarrays with 6 hydrophones each at both ends of the deployed array and separated by 12 hydrophones spacing. Application of the split-beam processing scheme on the above subarray configuration provided broadband bearing results shown in the following figures. The length of the processed time series was 1 s and the signal bandwidth was 200 Hz. Figure 7 shows the bearing estimates as a function of time provided by the output of the split-beamformer of Fig. 3, which utilizes prefiltering. In Fig. 8 the cross-correlation output is presented from one snapshot of the corresponding pairs of beams steered simultaneously in the same direction of  $60^\circ$ , with respect to the line array axis, where a loud broadband target was known to exist. The cross-correlation peaks in this figure indicate the differential time delays, which provide the associated bearing estimates according to Eq. (6).

In order to illustrate the influence of the prefiltering process on the performance of the split-beamformer, the weight-

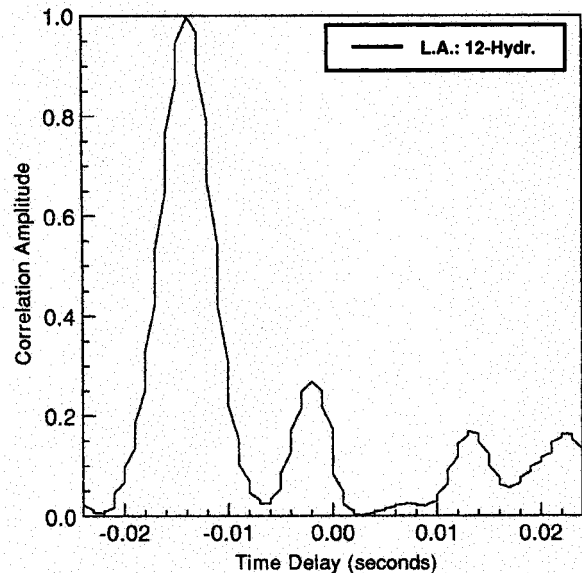


FIG. 8. Cross-correlation output from the corresponding pair of subaperture beams steered simultaneously in the same direction of  $60^\circ$ . The cross-correlation peaks in this figure indicate the differential time delays that provide the associated bearing estimates shown in the previous Fig. 7.

ing coefficients  $W(f)$  of the prefilter were set to unity. That is prefiltering was “off.” In this case, split-beam processing of the same data set of Fig. 8 provided poor bearing results which are shown in Fig. 9. Another way to demonstrate the relative performance of the prefiltering process is to examine the corresponding cross-correlation output from one snapshot of the corresponding pairs of beams steered simultaneously in the same direction of  $60^\circ$ , as those of Fig. 8. The associated cross-correlation output, for split-beam processing

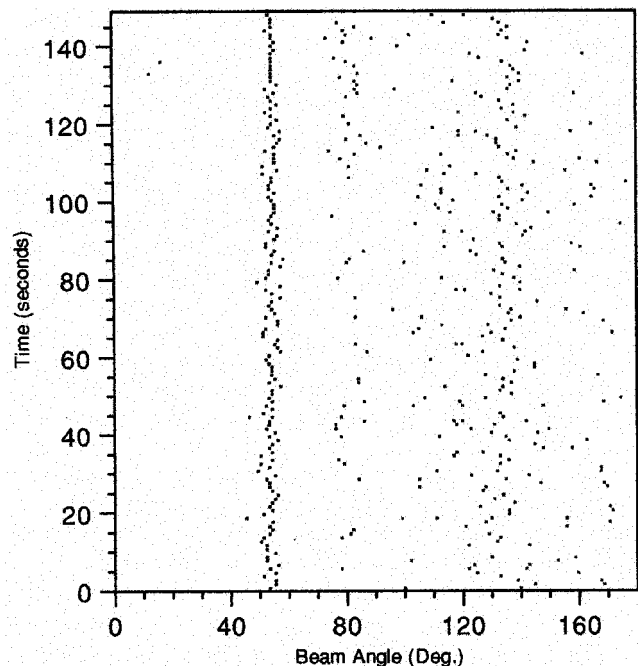


FIG. 9. Bearing estimates as a function of time for a split-beam processing scheme shown schematically in Fig. 3. In this case the weighting coefficients  $W(f)$  of the prefilter were set to unity. The pronounced difference in performance between the results of this figure with those of Fig. 7 indicates the necessity to include the prefiltering process in the split-beamformer.

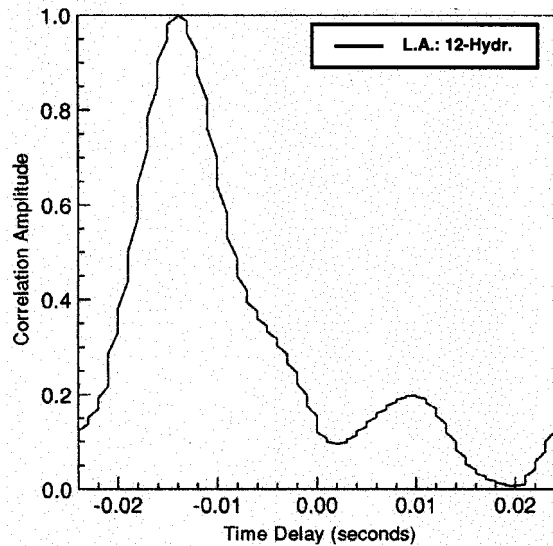


FIG. 10. Cross-correlation output from the corresponding pair of subaperture beams steered simultaneously in the same direction of  $60^\circ$ . In this case the weighting coefficients  $W(f)$  of the prefilter were set to unity. The cross correlation peaks in this figure indicate the differential time delays that provide the associated bearing estimates shown in the previous Fig. 9.

with prefilter weighting coefficients set to unity, is shown in Fig. 10. This figure shows fewer correlations peaks (or targets) than the results of Fig. 8.

The correlation peaks in Figs. 7–10 refer to distant multiple targets and their associated multipath characteristics.

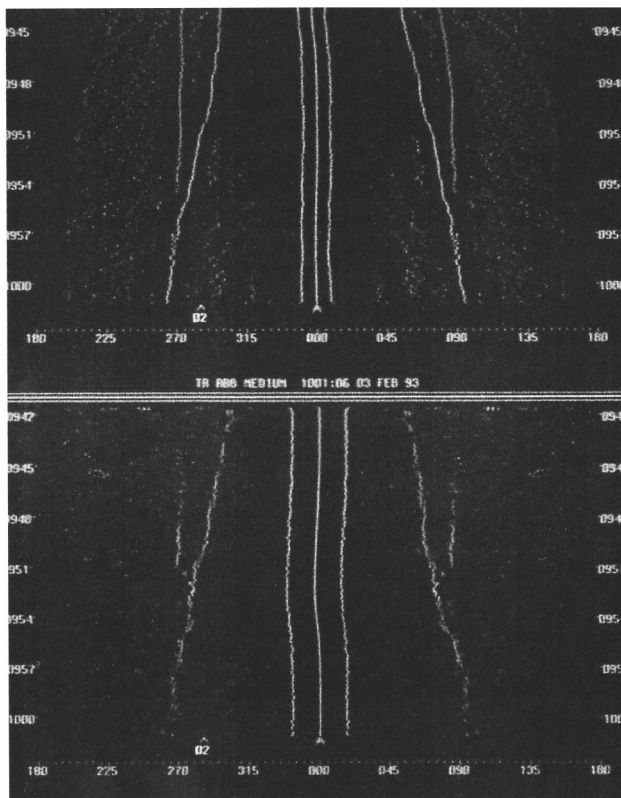


FIG. 11. Bearing estimates as a function of time from real line array data, including both split-beam and full-aperture conventional beamforming processing schemes under a parallel configuration. The upper part shows the bearing estimates from a full-aperture conventional beamformer and the lower part from the corresponding split-beamformer.

Since Figs. 8 and 10 refer to the same set of real data, their pronounced difference indicates the necessity to include the prefiltering process in split-beam processing. Furthermore, the above real data results confirm theoretical predictions on prefiltering process, which are discussed in Refs. 1–4.

Figure 11 shows broadband bearing results from a split-beam and a full aperture conventional beamformer implemented for a real experimental array system. The array configuration was as described above. The upper part of this figure shows broadband bearing results derived by beamforming all 24 hydrophones of the array. The lower part in the same figure shows the broadband bearing estimates provided by the output of the split-beamformer. Both the split-beam and full aperture beamforming operations were applied simultaneously on the same set of data. The middle solid line in both displays shows the heading of the tow ship. The two almost vertical traces, which appear to be parallel with the heading of the tow ship, are the bearing estimates of the tow vessel detected at the forward endfire of the towed array.

Differences in the bearing estimates of the tow vessel between the upper and lower displays indicate the superior performance of the split beam processor to provide better accuracy in bearing estimates at the endfire beams of the towed array than that of the full aperture conventional beamformer. This confirms predictions<sup>1–4</sup> that the bearing estimates located at the endfire of the towed array are biased when are provided by the full aperture beamformer. In fact this was the main argument and driving force to pursue this implementation study. The objective was to quantify experimentally that the split-beam processor provides significant angular resolution improvement over that of the full aperture beamformer for targets located at the endfire beams of a towed array.

In conclusion, the results in Fig. 11 are in agreement with those of Figs. 4 and 6, which predicted the characteristics and the performance difference between the full and subaperture beamforming. As discussed in Sec. III, a dramatic performance difference associated with the detection of weak signals should be expected to be in favor of the full aperture beamforming over the split-beam processing. This prediction has been confirmed by the results of Fig. 11. The only advantage that the split-beam processing has with respect to the full aperture beamforming is a better angular resolution performance at the end-fire beams, which is restricted only for cases with very strong signals.<sup>1–4</sup>

## V. CONCLUSION

In conclusion, this study has shown that the improved bearing estimation performance of the split-beam processing over the full aperture beamforming is practically insignificant for passive line arrays because of the split-beamformer's poor performance in detecting very weak signals.

Furthermore, in practical sonar applications the acoustic signals of interest are embedded in spatially and temporally partially correlated noise fields, which is in sharp contrast with the assumption of this study that the noise field is spatially and temporally white. The general case of broadband and narrowband signals embedded in a spatially and temporally anisotropic noise field requires that the spatial filtering

operation for optimum detection should include adaptation of the sonar signal processing according to the noise characteristics. This last argument suggests a need for adaptive beamforming in sonar systems.

In summary, the results of this experimental study verify that the theoretical developments play an important role in assisting the sonar system designers to define optimum signal processing concepts and in predicting the performance of a sonar line array system incorporating split-beamformers.

- <sup>1</sup>V. H. MacDonald and P. M. Schulteiss, "Optimum passive bearing estimation in a spatially incoherent noise environment," *J. Acoust. Soc. Am.* **46**, 37–43 (1969).
- <sup>2</sup>G. C. Carter, "Coherence and Time Delay Estimation," *Proc. IEEE* **75**(2), 236–255 (1987).
- <sup>3</sup>G. C. Carter and E. R. Robinson, "Ocean Effects on Time Delay Estimation Requiring Adaptation," *IEEE J. Ocean Eng.* **18**, 367–378 (1993).
- <sup>4</sup>C. H. Knapp and G. C. Carter, "The generalized correlation method for estimation of time delay," *IEEE Trans. Acoust. Speech Signal Process.* **ASSP-24**, 320–327 (1976).
- <sup>5</sup>B. G. Ferguson, "Improved time-delay estimates of underwater acoustic signals using beamforming and prefiltering techniques," *IEEE J. Ocean Eng.* **14**(3), 238–244 (1989).
- <sup>6</sup>S. Stergiopoulos, "Limitations on towed-array gain imposed by a non

isotropic ocean," *J. Acoust. Soc. Am.* **90**, 3161–3172 (1991).

- <sup>7</sup>P. A. Bello, "Characterization of randomly time-variant linear channels," *IEEE Trans. Commun. Syst.* **10**, 360–393 (1963).
- <sup>8</sup>W. M. X. Zimmer, "High resolution beamforming techniques, performance analysis," SACLANTCEN SR-104, La Spezia, Italy, SACLANT Undersea Research Centre (1986).
- <sup>9</sup>A. Mohammed, "A high-resolution spectral analysis technique," DREA Memorandum 83/D, Defence Research Establishment Atlantic, Dartmouth, N.S., Canada (1983).
- <sup>10</sup>D. Middleton, *Introduction to Statistical Communication Theory* (McGraw-Hill, New York, 1960), p. 787.
- <sup>11</sup>H. L. Van Trees, *Detection, Estimation and Modulation Theory* (Wiley, New York, 1968).
- <sup>12</sup>S. Stergiopoulos and A. T. Ashley, "Editorial," Special issue on Sonar System Technology, *IEEE J. Ocean Eng.* **18**(4), 361–366 (1993).
- <sup>13</sup>J. P. Ianniello, "Lower Bounds on Worst Case Probability of Large Error for Two Channel Time Delay Estimation," *Trans. Acoust. Speech Signal Process.* **ASSP-33**(4), 1102–1110 (1985).
- <sup>14</sup>J. Ziv and M. Zakai, "Some Lower Bounds on Signal Parameter Estimation," *IEEE Trans. Inf. Theory* **IT-15**, 386–391 (1969).
- <sup>15</sup>C. Eckart, "Optimal Rectifier Systems for the Detection of Steady Signals," Univ. California, Scripps Inst. Oceanography, Marine Physical Lab., Rep. SIO 12692, SIO Ref. 52-11, 1952.
- <sup>16</sup>S. Haykin, *Advances in Spectrum Analysis and Array Processing* (Prentice-Hall, Englewood Cliffs, NJ, 1991).

# Growth rate of simultaneous masking in cat auditory-nerve fibers: Relationship to the growth of basilar-membrane motion and the origin of two-tone suppression

Xiao Dong Pang

*Eaton-Peabody Laboratory of Auditory Physiology, Department of Otolaryngology, Massachusetts Eye and Ear Infirmary, 243 Charles Street, Boston, Massachusetts 02114 and Department of Electrical Engineering and Computer Science, and Research Laboratory of Electronics, Massachusetts Institute of Technology, Cambridge, Massachusetts 02139*

John J. Guinan, Jr.

*Eaton-Peabody Laboratory of Auditory Physiology, Department of Otolaryngology, Massachusetts Eye and Ear Infirmary, 243 Charles Street, Boston, Massachusetts 02114 and Department of Electrical Engineering and Computer Science, and Research Laboratory of Electronics, Massachusetts Institute of Technology, Cambridge, Massachusetts 02139 and Department of Otology and Laryngology, Harvard Medical School, Boston, Massachusetts 02115*

(Received 9 December 1996; revised 21 July 1997; accepted 22 July 1997)

Although many aspects of the mechanisms by which low-frequency sounds exert their powerful masking on responses to high-frequency sounds are well documented and understood, there are few data on the *growth of masking* for signal frequencies near, but not necessarily at, auditory-nerve-fiber characteristic frequency (CF). Masking of responses to 6- or 8-kHz tones by a continuous 300-Hz band of noise centered at 500 Hz was measured in single auditory-nerve fibers with various CFs. The growth rate of maskings averaged approximately 2 dB/dB, was typically largest for tones about 10% above fiber CF, and decreased at higher and lower frequencies. This pattern of masking versus frequency relative to CF resembles the pattern of compression of the growth of basilar membrane motion versus frequency at a fixed cochlear place. This correspondence supports the hypothesis that the high growth rate of masking by low-frequency sounds is due to the same mechanisms which produce the compression in the growth of basilar membrane motion. © 1997 Acoustical Society of America. [S0001-4966(97)03112-3]

PACS numbers: 43.64.Kc, 43.64.Pg, 43.66.Dc [RDF]

## INTRODUCTION

Intense low-frequency sounds powerfully mask responses to high-frequency sounds, particularly the information-rich high-frequency components of speech (Stevens *et al.*, 1946; Miller, 1947). Low-frequency sounds are also important as maskers because most natural environmental noise, many kinds of industrial and traffic noise, and the energy content of human speech are predominantly low frequency (e.g., Fletcher, 1953; Ono *et al.*, 1983).

The physiological mechanisms underlying psychophysical masking have been extensively studied so that many aspects of masking are well understood (Kiang and Moxon, 1974; Abbas and Sachs, 1976; Abbas, 1978; Geisler and Sinex, 1980; Schmiedt, 1982; Javel *et al.*, 1983; Costalupes *et al.*, 1984, 1987; Fahey and Allen, 1985; Young and Barta, 1986; Delgutte, 1990a, b; Ruggero *et al.*, 1992; Nuttall and Dolan, 1993; Rhode and Cooper, 1993; Cooper, 1996; Cai and Geisler, 1996; Cooper and Rhode, 1997). Masking can be excitatory (via the line-busy effect), adaptive (excitation produces adaptation which lowers sound-evoked responses), and suppressive (masking without excitation). Generally speaking, excitatory and adaptive masking compress neural rate versus sound level functions by increasing the background rate and reducing the plateau (or saturated) rate; in contrast, suppressive masking shifts neural rate-level functions to higher sound levels.

One aspect of masking which is not fully understood is the high growth rate of masking for simultaneous maskers that are much lower in frequency than the signal. For such maskers, both psychophysical and physiological studies have found high growth rates of masking, typically 2 dB/dB (Wegel and Lane, 1924; Egan and Hake, 1950; Abbas and Sachs, 1976; Geisler and Sinex, 1980; Javel *et al.*, 1983; Fahey and Allen, 1985; Costalupes *et al.*, 1987; Delgutte, 1990a, b). Although with a low-frequency suppressor there is a clear within-cycle variation of the suppression (e.g., Javel *et al.*, 1983; Ruggero *et al.*, 1992; Rhode and Cooper, 1993), in the present paper we are concerned only with masking manifested in responses averaged over many cycles.

For understanding the origin of growth rate of simultaneous masking, it seems relevant that the growth rates of basilar-membrane motion are different for signal-frequency versus masker-frequency tones. Near the signal-frequency place (the cochlear place with the largest basilar-membrane motion at the signal frequency), basilar membrane motion in response to a signal-frequency tone grows more slowly than sound level (i.e., shows a compressive nonlinearity) throughout much of the normal range of hearing (Rhode, 1971, 1978; Patuzzi and Sellick, 1983; Robles *et al.*, 1986; Cooper and Rhode, 1992; Nuttall and Dolan, 1993, 1996; Ruggero *et al.*, 1997). In contrast, basilar membrane motion increases linearly at all sound levels in response to a suppressor tone at



a frequency an octave or more lower than the signal frequency. Thus near the signal-frequency place in the cochlea, basilar membrane motion in response to a low-frequency masker grows much faster than basilar membrane motion in response to a signal-frequency tone.

For simultaneous maskers much lower in frequency than the signal, masking appears to be predominately suppressive (reviewed by Delgutte, 1990a, 1996; see also Fahey and Allen, 1985; Smoorenburg and Kloppengurg, 1986; Costalupes *et al.*, 1987). Suppressive masking has been hypothesized to be due to the masker causing saturation of outer hair cell (OHC) mechanical-to-electrical transduction channels, thereby reducing the gain of the cochlear amplifier at the signal frequency, and the same mechanism may be responsible for the compressive growth of basilar membrane motion (Zwicker, 1986; Geisler *et al.*, 1990; Kanis and de Boer, 1994; Nobili and Mammano, 1997; Geisler and Nuttall, in press). Thus the properties of the cochlear amplifier and those of suppressive masking may be tied closely together.

If the compressive growth of basilar membrane motion is produced by a mechanism in which the amplitude of the resulting motion controls the gain of the cochlear amplifier at the signal frequency, then, for a masker much lower in frequency than the signal, the different growth rates of basilar membrane motion at signal and masker frequencies will produce a high growth rate of masking. To see this, consider that to produce a 1-dB increase in motion at the signal-frequency place, the masker need only be increased 1 dB, but a tone at the signal frequency must be increased  $1/S$  dB (where "S" is the slope of the growth of basilar-membrane motion and is less than unity). Thus if the resulting motion controls the cochlear-amplifier gain, then the masker will be much more efficient than the signal in lowering the gain. With this kind of mechanism, the growth rate of masking is strongly (and inversely) related to the growth rate of basilar-membrane motion for the tone alone.

In light of the above putative relationship, the observation that the lowest slopes of the growth of basilar membrane motion are for signal frequencies slightly above the characteristic frequency of the cochlear place (Rhode, 1971, 1978; Patuzzi and Sellick, 1983; Robles *et al.*, 1986; Cooper and Rhode, 1992; Nuttall and Dolan, 1996; Ruggero *et al.*, 1997) implies that the greatest growth of masking will be for signal frequencies slightly above the characteristic frequency. Although many response properties of single auditory-nerve fibers relevant to masking are well documented, the dependence of the growth rate of masking on signal frequency for frequencies near, but not necessarily at, the fiber characteristic frequency (CF) has been explored very little. Several studies have varied signal frequency and found that for low-frequency maskers, the greatest masking is for signals at CF (Kiang and Moxon, 1974; Abbas and Sachs, 1976; Abbas, 1978; Geisler and Sinex, 1980; Fahey and Allen, 1985). However, these studies only reported data from a few fibers with relatively coarse frequency spacings and/or without measurements of the growth rate of masking as a function of frequency.

In addition to its implications for the mechanisms in-

involved, the growth rate of masking at frequencies near CF is interesting because in psychophysical tasks listeners use auditory-nerve fibers with CFs over a range of frequencies, not just fibers with CFs at the signal frequency. Intense maskers can change the tuning of single auditory-nerve fibers producing changes in the effective CF of half an octave, although usually much less (Kiang and Moxon, 1975; Fahey and Allen, 1985; Delgutte, 1990a). In such cases, listeners may most easily hear a tone by using auditory-nerve fibers normally tuned to a nearby frequency, a phenomenon known as "off-frequency" listening (Johnson-Davies and Patterson, 1979; Glasberg and Moore, 1990). Thus to fully understand the physiological basis of masking, it is necessary to know how maskers affect responses of auditory-nerve fibers at a variety of frequencies near the CF, e.g., within one-half octave of CF.

In this paper, we present data on the masking by low-frequency noise of auditory-nerve fiber responses to signals at a variety of frequencies near fiber CF. We studied low-frequency maskers because they are important in many circumstances and because of our interest in the effects of stapedius contractions in reducing masking (see Pang and Guinan, 1997). We have focused on measuring the growth rate of masking produced by continuous, low-frequency noise (center frequency 500 Hz, 300 Hz bandwidth) on responses of auditory-nerve fibers to 6- or 8-kHz tones. These parameters were chosen to correspond to those used by Borg and Zakrisson (1974) in psychophysical measurements in humans. With our paradigm, signal frequency was varied relative to CF by using a fixed-frequency tone with CF varied as different auditory-nerve fibers were contacted.

We measured masking in several ways because one statistic may not provide all the relevant information. From the point of view of statistical detection theory, the detectability index  $d'$  provides a summary of the information in the firing pattern for a signal processed by an ideal detector. However, Relkin and Pelli (1987) and others have provided evidence which indicates that the central nervous system does not use the information in auditory-nerve spike trains in the optimal signal-processing way. Considering this, it is relevant to measure masking in several ways to indicate how sensitive the measurements are to the method used. We measured the growth rate of masking using three measures of masking: changes in tuning curves, changes in sound-level functions, and changes in the detectability index  $d'$ . These measures provide criteria which are calculated in different ways, and they measure the masking at different points on the sound-level functions so that they are relevant to both threshold and suprathreshold masking.

## I. METHODS

### A. Surgery

Treatment of experimental animals was in accordance with regulations of the Committees on Animal Care at the Massachusetts Institute of Technology and the Massachusetts Eye and Ear Infirmary. Thirty-two normal-hearing adult cats were anesthetized by intraperitoneal injection (0.75 ml/kg) of Dial-Urethane (100-mg diallylbarbituric acid, 400-mg

Urethane, and 400-mg monoethylurea per ml). Additional anesthesia was given as needed to maintain the animal without a toe-pinch withdrawal reflex. Observations of the stapedius tendon and the head of the stapes (as in Pang and Peake, 1986) demonstrated that this level of anesthesia abolished sound-evoked middle-ear-muscle reflexes for 1-kHz binaural tones up to 115 dB SPL. The methods for animal preparation, generation of acoustic stimuli, and recording from auditory-nerve fibers are similar to those described by Kiang *et al.* (1965). Important points and differences are noted here.

## B. Sound stimulation

An acoustic assembly consisting of a 1-in. condenser earphone (Bruel & Kjaer 4144) as a sound source and a 1/4-in. condenser microphone (B&K 4136) was fitted into the cut ear canal. The acoustic system was calibrated on each animal so that all sound levels refer to the sound pressure level (SPL) near the tympanic membrane. The square-law characteristic of the condenser earphone produced second-harmonic and intermodulation distortion in the acoustic signal. For 6- or 8-kHz tones, the second-harmonic was approximately twice the SPL of the fundamental, minus 132 dB. For a 6- or 8-kHz tone plus a 500-Hz noise, the levels of the sum and difference intermodulation components were approximately the sum of the SPLs of the signal and the masker, minus 132 dB. Thus the second-harmonic and intermodulation components were each 68 dB SPL (32 dB below the signal) with signal and masker at maximum (100 dB SPL), and 48 dB SPL (42 dB below the signal) with signal and masker at 90 dB SPL. These distortion components would be expected to evoke little additional excitation or masking and should have negligible influence on the results.

## C. Monitoring

Auditory-nerve compound action potentials (CAPs) were monitored with an electrode on, or near, the round window. An automated tone-pip audiogram determined the sound level at 0.5, 1, 2, 4, 8, 16, and 32 kHz which evoked criterion CAPs. An ear was not used if its thresholds were 20 dB or more above normal (the average from >30 ears of early experiments) in the frequency regions of concern to this study (0.5, 4, 8 kHz). All data presented in this paper are from the ears in which the threshold at the end of data collection remained within 15 dB of the level at the beginning of data collection.

## D. Recording

Auditory-nerve-fiber responses were recorded with glass micropipettes filled with 1 M KCl (40–80 mΩ). The search stimuli were acoustic clicks and sometimes broadband noise bursts. Once a fiber was isolated, an automated tuning curve was obtained (Lieberman, 1978) with 50-ms tone bursts presented at 10 bursts/s, 30 points per octave, a sound-level step size of 0.75 dB, and a threshold criterion rate increase over background of approximately 20 spikes/s. The spontaneous firing rate (SR) was measured and the fiber was classified as lower SR (SR < 1 spikes/s) or higher SR (SR ≥ 1 spikes/s). A

fiber was studied if it had an adequate dynamic range over which to obtain a masking function, i.e., if its threshold at 6 or 8 kHz was ≤ 75 dB SPL (in almost all cases, the threshold at CF was much lower than this). Measurements typically included firing rate versus tone-level functions in quiet and with several levels of masking noise. Many of these measurements were also done with and without shock-induced stapedius contractions for use in another study (Pang and Guinan, 1997).

Rate-level functions used tone bursts of 100-ms duration, 2.5-ms rise–fall times, presented once per second, and had 5- or 10-dB steps from near the fiber threshold to a maximum of 100 dB SPL. When masking noise (50–100 dB SPL) was added, it was turned on at least 15 s prior to the tone bursts and was on throughout the level function so that a steady state of noise-evoked activity was present (Costalupes *et al.*, 1984). Each point in a rate-level function was determined from the responses of at least ten tone bursts. The average and variance of the spike rate were calculated using the spikes in a window 80-ms long starting at 20 ms after each tone burst onset, so that an approximately “steady-state” rate response was sampled (Costalupes, 1985). The mean and variance of the spike rates were also measured for spontaneous activity and for responses to the masking noise alone. Average firing rates were used, thereby ignoring the information in spike times relative to sound phase, because at the high-signal frequencies used (≥ 6 kHz) there is little synchrony in auditory-nerve responses (Johnson, 1980). Rate-level functions and tuning curves were smoothed by a three-point triangular moving average (weight: 1/4, 1/2, 1/4) before the masking-induced shift was measured.

From each rate-level function and the corresponding variance measurements, we calculated a  $d'$  versus sound function, where  $d' = (M_{n+t} - M_n) / s_{n+t}$ ,  $M$  is the mean rate,  $s$  is the standard deviation, and the subscript  $n$  is for noise and  $n+t$  is for noise plus tone. A tone was considered “detectable” when the  $d'$  value of an auditory-nerve fiber’s response reached unity ( $d' = 1$  corresponds to approximately 75% correct in a two-interval forced-choice paradigm). The use of the detectability measure  $d'$  assumes that auditory-nerve-fiber discharge rates can be characterized as a normal random variable or a variable that is monotonically convertible to normal (Teich and Khanna, 1985; Relkin and Pelli, 1987).

For data compilations across fibers (e.g., Figs. 2, 7, and Table I), the growth of masking was determined from the lowest to the highest masking level at which complete data were obtained, excluding points at which there was less than 5 dB of masking. We avoided using masker noises which produced less than 5 dB of masking because near masking threshold the growth rate of masking depended strongly on masker level, whereas for masking greater than 5 dB, the growth rate of masking was relatively constant (see Results).

## II. RESULTS

### A. Masking effects on tuning curves

To obtain masking functions at many frequencies from one set of measurements, we measured the effects of mask-

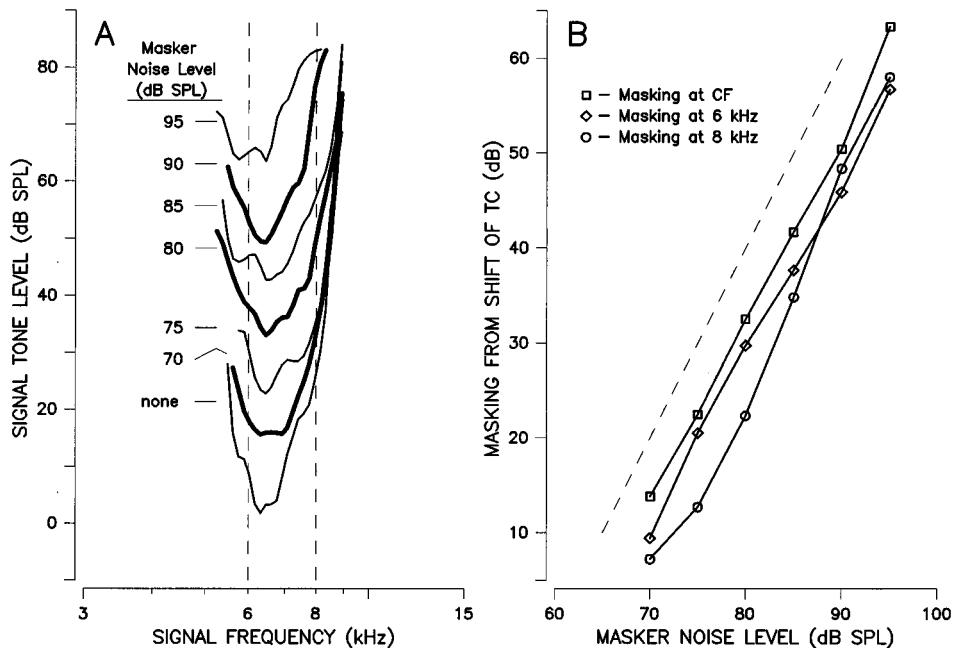


FIG. 1. Masking measured from tuning curves. (A) Tuning curves for various masking-noise levels. Dashed lines mark 6 and 8 kHz. (B) Masking functions obtained from the data in panel (A). The growth rates of masking (GRs) at the characteristic frequency (CF), 6 kHz, and 8 kHz, are 1.99, 1.90, and 2.03 dB/dB, respectively. Fiber 87-73: CF=6.31 kHz; threshold at CF=1.8 dB SPL; SR=51 spikes/s.

ing noise on tuning curves. For high-CF fibers, the tuning-curve tip region is the most sensitive to masking by low-frequency noise (Kiang and Moxon, 1974), so this is the region we focused on.

For a higher-SR auditory-nerve fiber, the masking produced by low-frequency noise on tuning-curve tips is shown in Fig. 1. As the masker level was increased, there was a monotonic increase in the fiber's threshold for frequencies near the CF, an effect typical of all fibers observed (also see Fahey and Allen, 1985). Figure 1(B) shows masking functions for tones at 6 and 8 kHz, and fiber CF, calculated from the data of Fig. 1(A). For all noise levels, the masking was larger near the CF than at frequencies substantially below or above the CF (i.e., in Fig. 1, the squares are always above the diamonds and circles). At CF, the masking was over 60 dB with 95 dB SPL noise. At all three frequencies, the growth-rate of masking had a value close to 2 dB/dB.

Figure 2 shows the relationship between the growth rate of masking and test signal frequency relative to fiber CF from 25 auditory-nerve fibers in seven animals with fiber CFs ranging from 4.5 to 11 kHz. On the average, the growth rate was largest when the test frequency was slightly higher (0.1 to 0.2 oct) than the fiber CF. Another way to view the data of Fig. 2 is that for a fixed test frequency, the maximum growth rate was from fibers whose CFs were near or slightly below the test frequency. Other features of the data (not shown in Fig. 2) include: (1) the growth rate at fiber CF, averaged over all noise levels and all fibers, was 2.30 dB/dB [range: 1.55–3.44, standard deviation (s.d.)=0.43]. (2) The average growth rates at 6 and 8 kHz were 2.03 and 1.69 dB/dB, respectively. (3) The largest measured masking was almost 80 dB.

Since masking was typically largest and the growth rate

of masking highest near the fiber CF, the sharpness of tuning must have been reduced. Figure 3 shows the relationship between noise-induced elevation of threshold at the fiber CF and the change in tuning-curve sharpness as measured by the change in  $Q_{10}$  ( $Q_{10}$  is the CF divided by the bandwidth of the tuning curve at 10 dB above the threshold at CF). In general,  $Q_{10}$  decreased with increasing elevation in tuning-curve threshold, reaching a 60% decrease at about 75 dB elevation of the threshold (Fig. 3).

The noise masking sometimes produced an apparent shift of the tuning-curve "CF." The typical value of such a shift was rather small (0.03 oct up or down), and no system-

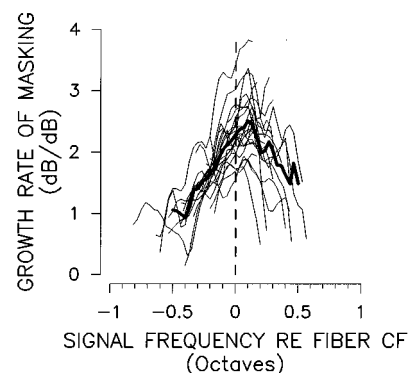


FIG. 2. The growth rate of masking from all tuning-curve measurements as a function of the signal frequency relative to fiber CF. Each thin line corresponds to one fiber. The thick line is the mean at each frequency in the range  $\pm 0.5$  oct relative to CF. The dashed line is at CF. For each fiber, the growth rate was measured between the most and the least intense noise levels, excluding noise levels which did not elevate the tuning curve by at least 5 dB. Data are from 25 auditory-nerve fibers (CF range: 4.5–11 kHz) from seven animals.

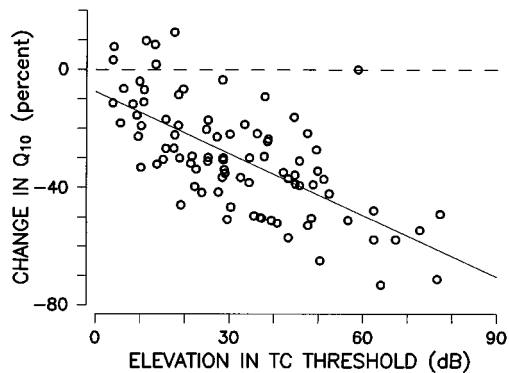


FIG. 3. The masking-induced change in tuning-curve (TC) sharpness as a function of the change in TC threshold. Sharpness is measured by  $Q_{10}$ , the CF divided by the bandwidth of the tuning curve at 10 dB above the threshold at CF. All available data are shown (88 data points from 25 fibers from six animals, fiber CFs 4.5–11 kHz). The solid, linear-regression line has a slope of  $-0.7$  and an intercept of  $-7.45$ . The correlation coefficient is  $-0.67$ . The dashed line marks no change in TC sharpness.

atic trend was observed in the direction or magnitude of the shift with increasing noise level.

### B. Masking patterns from rate-level functions

Tuning curves provide information only at fiber threshold, but suprathreshold responses are also of interest for their relevance in a variety of psychophysical tasks and for understanding the mechanisms involved in masking. Suprathreshold masking was measured using firing rate versus tone-level functions.

An example of the masking produced by a low-frequency noise on rate-level functions for a high-frequency tone is shown in Fig. 4(A). Although this example is for a lower-SR auditory-nerve fiber, two features typical of all fi-

bers can be seen: (1) as the noise level was increased there was a monotonic shift of the rate-level function towards higher tone levels, and (2) when the increasing noise level started to excite the fiber, there was a monotonic increase in the background discharge rate (most easily seen with the tone at 10 dB SPL). This fiber also showed a decreased response to the noise as the tone was increased from 20 to 60 dB SPL (most easily seen in responses from the 90 dB SPL noise at tone levels 30–60 dB SPL). Such masking of the noise response by the tone was observed in some fibers, but it was much smaller than the masking of the tone response by the noise and is not the focus of the present study.

An example of masking from a higher-SR fiber is shown in Fig. 5(A). In addition to the features noted above, Fig. 5(A) shows a plateau rate (sometimes called “saturated rate”) that decreased with increasing noise level. Such a depression of plateau rate was seen more frequently in higher-SR than in lower-SR fibers, but was not seen in all higher-SR fibers. Presumably, this depression of plateau rate is due to adaptation produced by the noise-evoked increase in background discharge rate, with lower-SR fibers being more resistant to this form of adaptation (Costalupes *et al.*, 1984, 1987).

As an index of masking, we used the amount that rate-level functions are shifted toward higher sound levels by the masking noise (Geisler and Sinex, 1980). Because of the nonlinear shape of rate-level functions, with both thresholds and saturations, level shift provides a better overall description of the effects of masking than the rate difference at a constant tone level. To provide a single-number characterization of masking over the widest possible range of conditions, we measured masking using a “midrate” criterion (“midrate” is the mean of the fiber’s spontaneous and plateau rates, both measured without masking noise). One ad-

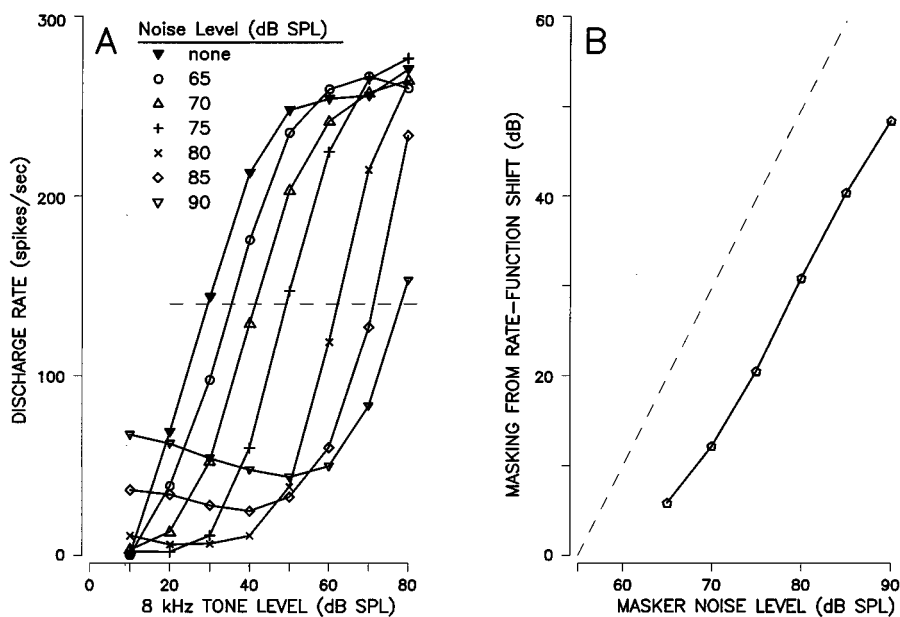


FIG. 4. Masking in a lower-SR auditory-nerve fiber. (A) Firing rate versus tone-level functions for various noise levels (key at upper left). The dashed line is at the “midrate” (the mean of the spontaneous and plateau rates). (B) The masking function at the midrate from the data in panel (A). GR is 1.72 dB/dB. The dashed line has a slope of 2. Fiber 80–71: CF=8.04 kHz, threshold at CF=14.2 dB SPL; SR=0.4 spikes/s.

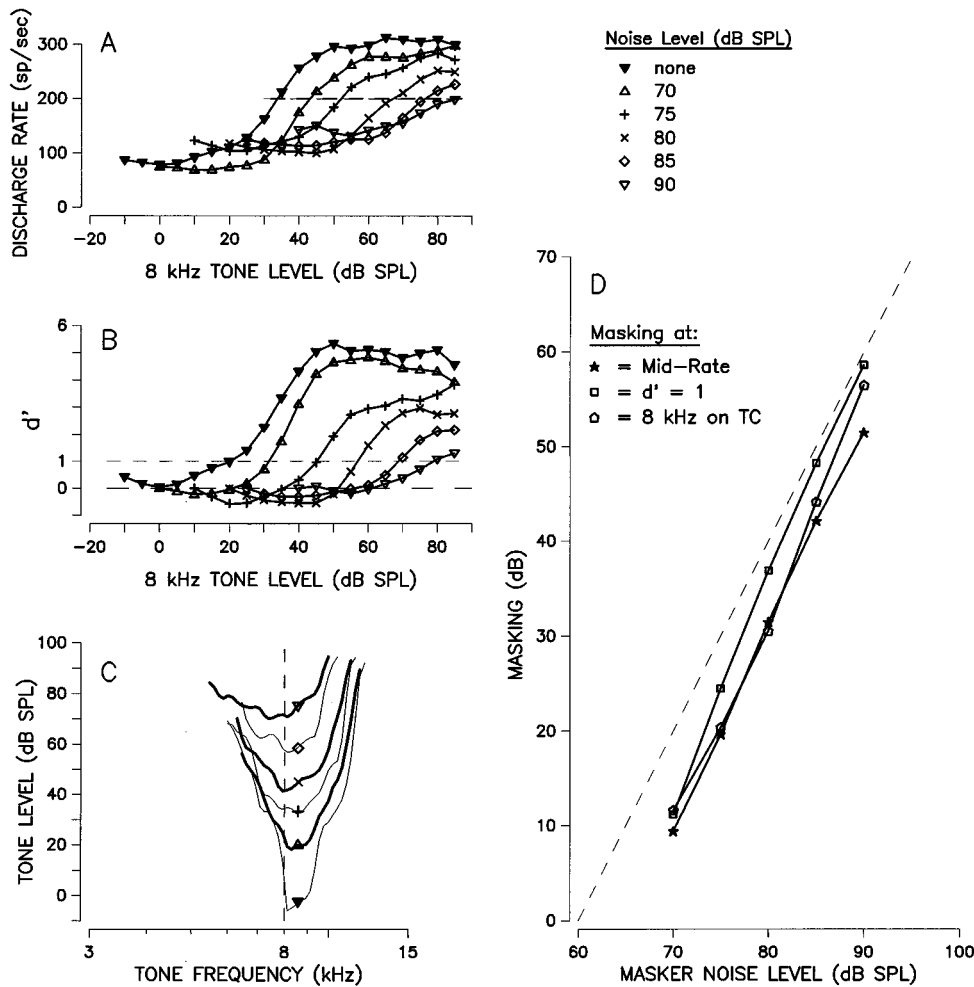


FIG. 5. Masking in a higher-SR auditory-nerve fiber. (A) Firing rate versus tone-level functions for various noise levels (key at upper right). The dashed line is at the “midrate.” (B) Detectability index  $d'$  versus tone-level functions. Data from the same responses as in panel (A). Dashed lines at  $d'=0$  and 1. The small negative values of the  $d'$  functions are probably due to masking by the tone of the fiber’s response to the noise. (C) Tuning curves for various masking-noise levels (key at upper right). The dashed line marks 8 kHz. (D) Masking functions obtained from each of the three data sets at left. GR is 2.1 dB/dB at midrate, 2.4 dB/dB at  $d'=1$ , and 2.2 dB/dB from the tuning curves at 8 kHz. The dashed line has a slope of 2. Fiber 76–105: CF=8.13 kHz; threshold at CF=−5.9 dB SPL; SR=79 spikes/s.

vantage of the midrate criterion is that it is robust against small variations in the criterion because the noise-induced shifts of tonal rate-level functions are usually close to parallel in the midrate region [Figs. 4(A) and 5(A)]. Using midrate criteria, the masking functions determined from the data in Figs. 4(A) and 5(A) are shown as pentagons in Figs. 4(B) and 5(D). For both fibers, the highest noise level (90 dB SPL) masked the tone response by 50 dB, or more, at the midrate.

Since the growth rate of masking was usually relatively constant across noise levels above the threshold for masking [Figs. 4(B) and 5(D)], we normally characterized the growth rate of masking for a fiber by the average across all noise levels used. For the fibers in Figs. 4 and 5, the growth rates of masking were 1.72 and 2.1 dB/dB, respectively. Considering all of our masking measurements from rate-level functions at either 6 or 8 kHz (82 fibers with a CF range of 4.5–12.5 kHz from ten animals), the maximum masking was 75 dB, and the mean growth rate (GR) of masking was 1.9 dB/dB (range: 0.43–3.8, s.d.=0.72).

Masking patterns from rate-level functions are compared

to those from tuning-curves in Fig. 5 for the same fiber at the same frequency and the same noise levels. There was slightly more masking and a slightly higher growth rate of masking with tuning-curve “threshold” measurements than with “midrate” measurements [Fig. 5(D)]. This was typically the case, but the differences were never very large. For the 14 cases in which we have comparable data available on the same fiber, the growth rate of masking averaged 0.2 dB/dB higher for the tuning curve measurement than at midrate.

### C. Masking measured by the elevation of detection threshold

As a masking noise is increased in level, it not only shifts the tonal rate-level function upward, it also raises the background discharge rate, and it may also change the variance of the rate. The true separability or detectability of the tone from the background noise is determined by both the separation of the mean rates and by the variances of the spike distributions. Thus measuring masking only as the shift at the midrate does not completely characterize the masking

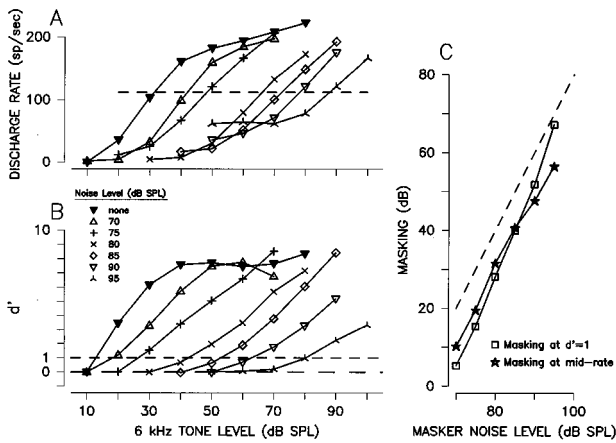


FIG. 6. Masking in a lower-SR auditory-nerve fiber. (A) Firing rate versus tone-level functions for various noise levels [key in panel (B)]. The dashed line is at “midrate.” (B) Detectability index  $d'$  versus tone-level functions. Data from the same responses as in panel (A). Dashed lines are at  $d'=0$  and 1. (C) Masking functions obtained from the data in panels (A) and (B). GR is 1.85 dB/dB at midrate, and 2.48 dB/dB at  $d'=1$ . The dashed line has a slope of 2. Fiber 87–28; CF=5.96 kHz; threshold at CF=22.6 dB SPL; SR=0.1 spikes/s.

and may tend to underestimate the effective growth rate of masking. The detectability index  $d'$  (see Methods) takes into account the variability in the spike response and, at least theoretically, is more “complete” than masking measured directly from tuning curves or rate-level functions. Masking measured from  $d'$  is also more comparable to masking measured psychophysically.

Figure 5(B) shows  $d'$  versus level functions for the measurements that were shown in Fig. 5(A) as rate versus level functions. The  $d'$  versus level functions and the rate versus level functions are similar in overall shape, but in the  $d'$  functions, the different background discharge rates (due to the different noise intensities) are taken into account according to their effect on tone detectability. Since the  $d'$  functions take into account the noise-produced elevation of background discharge rate, it is not surprising that the growth-rate of masking measured from  $d'$  functions was somewhat larger than the growth rate from the midrate functions [Fig. 5(D)]. Rate and  $d'$  versus level functions for a lower-SR fiber are shown in Fig. 6. Again the growth rate of masking from  $d'$ -level functions was larger than that from rate-level functions [Fig. 6(C)]. This was generally the case but the

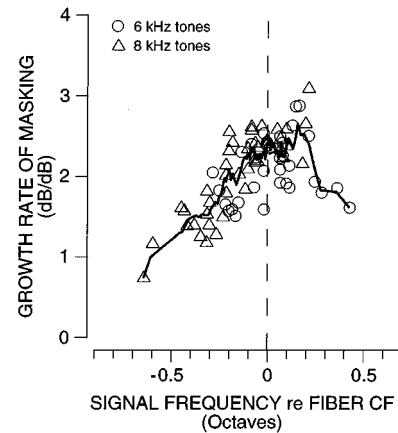


FIG. 7. The growth rate of masking from all  $d'$ -level functions as a function of the separation between the signal frequency and fiber CF. Each point corresponds to a fiber (91 fibers from eleven animals, CF range 4.5–12.5 kHz) with the growth rate averaged over all noise levels used. The continuous line is a five-point rectangular moving average of all data points.

differences were usually small, averaging only 0.2 dB/dB.

Data from all of the masking functions from  $d'$  measurements are summarized in Table I. This shows that there were no significant differences in the growth rates of masking due to the presence of efferent innervation (see Pang and Guinan, 1997, for the methods for cutting the efferents), the SR category of the fibers, or whether the tone was at 6 or 8 kHz. Tests performed with and without the assumption of equal-variance for the subpopulations gave the same results, and tests of whether the variances were equal revealed no significant differences at the 0.2 level.

The relationship between the growth rate of masking measured from  $d'$  functions and the test-tone frequency relative to fiber CF is shown in Fig. 7. With masking measured from  $d'$  functions, the maximum growth rate was typically from tone frequencies slightly greater (0.1 to 0.2 oct) than fiber CF, which is consistent with Fig. 2.

### III. DISCUSSION

#### A. The growth rate of masking as a function of frequency

Our data clearly show that the growth rate of masking is a function of signal frequency relative to CF with the peak growth rate being not at CF, but slightly above CF. In both

TABLE I. Growth rates (dB/dB) of masking measured from  $d'$ -level functions.

Category	Growth rate				Probability that the two groups have the same growth rate <sup>a</sup>
	mean	range	s.d.	<i>n</i>	
All fibers	2.09	0.72–3.52	0.65	91	
Intact efferents	2.1	0.72–3.52	0.66	82	
Severed efferents	2.02	1.14–3.10	0.62	9	0.7
Lower SR	2.05	0.72–3.27	0.63	36	
Higher SR	2.15	0.99–3.52	0.63	55	0.4
6 kHz	2.10	0.93–3.32	0.58	40	
8 kHz	2.04	0.72–3.52	0.69	51	0.6

<sup>a</sup>More specifically, to assume that the two groups have different growth rates, one would be wrong with a probability larger than the number given.

the data from tuning curves (Fig. 2) and the data from  $d'$  versus tone-level functions (Fig. 7), the peak growth rate was at a frequency approximately 10% above the fiber CF. Above and below this peak, the growth rate fell relatively steeply with frequency (i.e., it decreased approximately a factor of 2 for a half octave change in frequency). This pattern has not been reported before. However, it is consistent with previous reports that the greatest masking is at fiber CF, if one takes into account that previous investigations did not make growth-rate measurements as closely spaced in frequency at, and near, fiber CF (Kiang and Moxon, 1974; Abbas and Sachs, 1976; Geisler and Sinex, 1980; Fahey and Allen, 1985; Delgutte, 1990a, b).

### B. The observed masking is mostly due to suppression

The mechanisms by which our low-frequency noise masked responses to the high-frequency tones are almost certainly a combination of suppressive, excitatory, and adaptive masking. The mark of suppressive masking is a shift of rate versus sound-level functions to higher sound levels, consistent with the suppression turning down the gain of the cochlear amplifier (Geisler *et al.*, 1990). In our masking data, upward shifts of the rate versus level functions were the most noticeable feature and occurred for noise levels at which there was no increase in background rate (Figs. 4–6) indicating that this masking was due to suppression. However, there were also increases in background rate and depressions of plateau rate which indicate that excitatory and adaptive masking were also present.

The relatively small difference between the growth rate of masking measured at the midrate versus that measured from tuning curves or  $d'$  indicates that our masking was mostly suppressive. Masking measured at midrate can be expected to emphasize suppressive masking because it measures primarily shifts of neural rate-level functions to higher sound levels, and it is affected little by increases in background rate or decreases in the saturated rate [see Figs. 4(A), 5(A), and 6(A)]. On the other hand, masking measured with tuning curves or  $d'$  will be affected by all three factors. Although we did find a higher growth rate of masking with tuning curves and  $d'$  measurements, the increase over masking measured at the midrate averaged only about 10%. In somewhat similar measurements on cats, Fahey and Allen (1985) saw masking that extended over a 40-dB range and was produced by tones that were below the threshold for excitation, i.e., it was suppressive masking. All in all, the data are consistent with the conclusion of Delgutte (1990b) that for signal tones more than a decade higher than the masker frequency, masking is mostly due to suppression.

### C. Comparison of the growth of masking with the growth of basilar membrane motion

Our observation that the peak growth rate of masking is not at CF, but is slightly above CF, supports the hypothesis that the high growth rate of masking is strongly related to the slope of basilar-membrane motion versus sound-pressure level for a signal-frequency tone. To enable a more direct

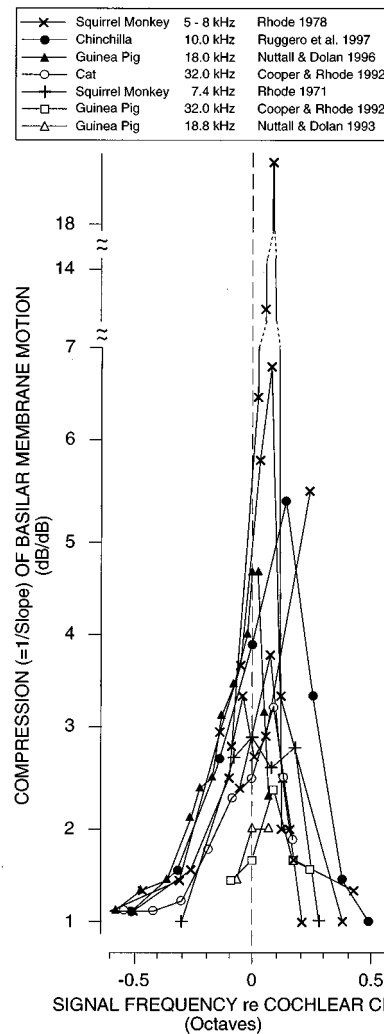


FIG. 8. The “compression” of the growth of basilar-membrane motion as a function of normalized signal frequency. “Compression” is the reciprocal of the slope of the amplitude of basilar-membrane motion versus sound level (with both plotted on log scales so that linear growth has a slope of 1). The key in the figure shows the species, the characteristic frequency (CF) of the cochlear place, and the paper from which the data were obtained. Slope was measured over the range of sound levels which showed the largest compressions of basilar-membrane motion in each case. The number of cases and details of the data extraction for each paper are Rhode (1971, Fig. 7), 1 case, slopes from the constant slope region at the highest SPL; Rhode (1978, Fig. 10) (CFs from Table 1), 4 cases, slopes from the lowest-slope lines that encompass more than a single pair of data points; Cooper and Rhode (1992, Figs. 13 and 14), 2 cases (1 cat, 1 guinea pig), slopes from points  $\geq 65$  dB SPL; Nuttall and Dolan (1993, Fig. 2B), 1 case, slopes from points at 30–60 dB SPL. Nuttall and Dolan (1996, Fig. 2), 1 case, slopes from points with stapes velocity  $> 1 \mu\text{s}$ ; Ruggero *et al.* (1997, Figs. 6 and 7), 1 case, points from the constant slope part between 40–80 dB SPL.

comparison of the growth rate of masking and the growth of basilar membrane motion, in Fig. 8 we have compiled data from many studies of basilar membrane motion. This figure shows the “compression” of basilar membrane motion with “compression” defined as  $1/\text{slope}$  in a log-log plot of basilar membrane motion versus sound level. Most of these data are for cochlear regions with higher CFs than our 6- and 8-kHz measurements. Since tuning curves generally become sharper as frequency goes up, data from higher frequency regions may be more compressed along the frequency axis

than data from lower frequencies. Although there is considerable scatter in the data from the different preparations, there is an overall resemblance of the basilar-membrane compression data (Fig. 8) and the growth rate of masking data (Figs. 2 and 7) in that the frequency of peak compression, or growth rate of masking, is slightly above the CF in both sets of data.

In addition to the similarity in shape, data on the growth rate of masking and the "compression" of basilar membrane motion are numerically consistent. In particular, if the compressive growth of basilar membrane motion is produced by a mechanism in which the resulting motion controls the gain of the cochlear amplifier at the signal frequency, then, a region with compression  $C$  (where  $C=1/\text{slope of basilar membrane growth}$ ) will produce a growth rate of masking of  $C-1$ .<sup>1</sup> We found peak growth rates of masking mostly in the range of 2 to 3 for the 6- and 8-kHz regions of the cat cochlea which would correspond to basilar-membrane peak compressions of 3 to 4. Our data (Figs. 2 and 7) and the basilar membrane data (Fig. 8) are consistent bearing in mind that (1) our measurements were seldom on the most sensitive ears because of our use of intense maskers and test tones, but much of the basilar-membrane data may also be from compromised ears, (2) our masking may include line-busy and adaptive components in addition to suppression, and (3) there may be species and CF differences [the one set of squirrel-monkey data which was usually compressive in Fig. 8 may be due to species differences, but the three other sets of data from this same paper (Rhode, 1978) are much less compressive].

The hypothesis that the amplitude of basilar membrane motion controls the gain of the cochlear amplifier at the signal frequency explains several additional aspects of low-frequency suppression. For suppressor frequencies an octave or more below CF, the growth rate of masking is constant as a function of suppressor frequency but increases with fiber CF (Delgutte, 1990b). According to the hypothesis, this implies that the growth of basilar-membrane motion at CF becomes more compressive with increasing CF. The few data available on the growth of basilar membrane motion at different CF regions are consistent with this (Cooper and Rhode, 1997). The prediction also fits with auditory-nerve-fiber data (rate-versus-level functions) which indicate that the growth of basilar-membrane motion at CF becomes more compressive as CF increases (Cooper and Yates, 1994). Finally, for suppressor frequencies within an octave below CF, as suppressor frequency is increased toward CF, the growth rate of basilar-membrane motion in response to the suppressor tone slowly becomes more compressive (at CF becoming the same as the CF tone), so that the hypothesis predicts that the growth rate of suppression should gradually decrease from the value for very low-frequency suppressors to unity at CF. Our masking data (Figs. 2 and 7) and the basilar membrane data (Fig. 8) agree in showing that this change takes place over approximately 1/2 octave.

The hypothesis that the amplitude of basilar membrane motion controls the gain of the cochlear amplifier provides a very general explanation for two-tone rate suppression (Zwicker, 1986; Geisler *et al.*, 1990; Kanis and de Boer,

1994; Nobili and Mammano, 1996; Geisler and Nuttall, 1997). In addition to explaining the high growth rate of suppression for low-frequency suppressors, it can also explain why, for suppressor frequencies greater than CF, the growth rate of masking is less than one and decreases as suppressor frequency increases above CF (Delgutte, 1990b). Presuming that the cochlear amplifier is spread over a region (e.g., a half-octave to octave) basal to the CF place (i.e., places tuned to higher frequencies), fractional growth rates of suppression can be understood by the fact that basilar-membrane motion in response to the high-frequency suppressor tone only reaches a fraction of the cochlear region containing the amplifier for the signal frequency. Thus amplification is reduced only in the narrow cochlear region where there is overlap of signal-frequency cochlear amplification and a high-amplitude response to the masker, but amplification continues in the remaining region involved in signal-frequency cochlear amplification. Thus overall signal-frequency cochlear amplification decreases as masker level increases, but since only a fraction of the cochlear amplifier is suppressed, the overall growth rate of masking is less than one. As the suppressor frequency increases above CF, there is a progressively smaller region in which the response to the suppressor tone overlaps the region of signal-frequency cochlear amplification, so the growth rate of masking decreases as the suppressor frequency increases. An additional factor is that basilar membrane motion for the suppressor grows approximately as slowly as the response to the signal (even though the response to the suppressor may grow linearly at the signal-frequency CF place, it grows slowly at the higher-frequency region where its amplitude is big enough to produce the suppression). With the suppressor and signal-frequency tones both growing slowly, the growth rate of suppression is lower than unity because the suppressor frequency response overlaps very little with the region of amplification at the signal frequency.

The above analysis was stated in terms of the amplitude of basilar membrane motion controlling the gain of the cochlear amplifier because there are data on basilar membrane motion, but the relevant mechanical variable which controls the gain of the cochlear amplifier may be something else, e.g., the mechanical drive to the OHCs. Since the compressive nonlinearity of basilar membrane motion in response to a near CF tone is presumably created by the OHCs in some sort of feedback system with basilar membrane motion, the mechanical drive to OHCs may not show the same degree of compressive nonlinearity as basilar membrane motion. The above analysis will hold as long as the mechanical drive that controls the gain of the cochlear amplifier shows a pattern of compressive nonlinearity similar to that of basilar membrane motion.

Considerable evidence indicates that saturation of OHC receptor currents is a major source of two-tone suppression (Geisler *et al.*, 1990; see also Zwicker, 1986; Kanis and de Boer, 1994; Nobili and Mammano, 1996), but it may not be the only mechanism involved. Nonlinearity in the OHC electric to mechanical transduction (Evans *et al.*, 1991) may also play a role. In addition, the motion that drives the cochlear amplifier for a particular signal frequency is likely to be



basal to the signal CF place. Thus there will not be a simple correspondence between the degree of suppression and amplitude of the response to the suppressor tone at the CF place (Kanis and de Boer, 1994). Finally, it appears that the suppression of low-SR fibers is not fully accounted for by the suppression of basilar membrane motion (Cai and Geisler, 1996; Geisler and Nuttall, in press).

In summary, while saturation of OHC receptor currents may be the major source of both two-tone suppression and the compression of basilar-membrane motion, there are aspects of these phenomena which are not understood. It seems likely that appreciating the relationship between the growth rate of suppression and the compression of basilar-membrane motion will provide insight into these important facets of cochlear mechanics.

There are reports of individuals with normal-hearing thresholds but no suppression (see Thibodeau, 1996). In the light of the above hypothesis, these people would be expected to have an abnormal growth of basilar-membrane motion with increasing sound level. It would be interesting to determine whether such individuals have abnormal loudness growth functions.

#### D. Comparison of our data with previous data

Most aspects of our data are consistent with previous reports on masking in single auditory-nerve fibers (Kiang and Moxon, 1974; Abbas and Sachs, 1976; Abbas, 1978; Geisler and Sinex, 1980; Schmiedt, 1982; Costalupes *et al.*, 1984, 1987; Fahey and Allen, 1985; Young and Barta, 1986; Delgutte, 1990a, b). In agreement with these reports, for masking of responses to high-frequency sounds by low-frequency maskers we found that the threshold of masking is high (typically greater than 60 dB SPL) as is the growth rate of masking (2 dB/dB or more) so that large maskings (over 60 dB) can be produced (Figs. 1 and 4–6). In our data, the most prominent effect of the masker is to shift the signal sound-level functions to higher sound levels, but the masker normally also increases the background firing rate (i.e., the rate for below-threshold signals) and can decrease the slope and the plateau rate so that the firing-rate dynamic range is reduced (Figs. 4–6). In general, our experiments provide more extensive quantitative data for a narrower range of conditions than previous studies, but both are in agreement.

We found little consistent change in fiber CF even though we found large values of masking. This is in agreement with the data of Fahey and Allen (1985) and the findings of Delgutte (1990a) that for signal frequencies which are more than ten times the masker frequency, there was little change in fiber CF.

We found a systematic decrease in tuning curve sharpness as masking increased (Fig. 3). Such a masking-induced decrease in tuning curve sharpness has been reported previous (Kiang and Moxon, 1974; Delgutte, 1990a; see also Fahey and Allen, 1985). Stimulation of medial olivocochlear efferents produces a similar decrease in tuning-curve sharpness (Guinan and Gifford, 1988). If both low-frequency maskers and efferents act by similar or identical mechanisms to depress the gain of the cochlear amplifier, one would ex-

pect the relationship between the change in tuning and the reduction in sensitivity to be similar in both cases.

Although efferents influence masking under certain circumstances, we found no substantial effect on the growth rate of masking from cutting the efferents. This is consistent with reports that efferents influence masking in a frequency selective fashion with the influence being close to the frequency band of the sound that evoked the efferent activity. Thus a high-frequency sound may evoke efferent activity which increases forward masking (Liberman *et al.*, 1996) or decreases the masking of transients by steady backgrounds (Winslow and Sachs, 1987; Kawase *et al.*, 1993), but this action is close in frequency to the sound that evoked the efferent activity. In contrast, we have studied masking which goes across frequency bands (the masking of responses to high-frequency sounds by low-frequency maskers). Our cut-efferent results indicate that such across-frequency masking is mediated by intracochlear processes, not by sound-evoked efferent activity.

#### E. Comparison of our data with psychophysical masking in humans

Studies in humans have found masking similar to the masking we have found in cats. In humans masking grows at close to 1 dB/dB for a masker close in frequency to the test frequency, but for maskers which are much lower in frequency than the test tone, the growth rate of masking is high, approaching 2 dB/dB (Wegel and Lane, 1924; Egan and Hake, 1950). Studying masking over very wide sound-level ranges in humans is complicated by the presence of the acoustic stapedius reflex. As masker level increases above the reflex threshold, stapedius contractions slow the growth of masker energy reaching the cochlear, thereby lowering the growth rate of masking. Wegel and Lane (1924) and Egan and Hake (1950) avoided this problem by only using sound intensities below the threshold of the acoustic stapedius reflex. Our work used acoustic intensities up to 100 dB SPL but did not evoke stapedius contractions because of the anesthesia.

Data comparable to ours, from subjects without a functioning acoustic stapedius reflex, were obtained by Borg and Zakrisson (1974) on human subjects who had Bell's Palsy. These investigators measured masking at frequencies up to 8 kHz using the same low-frequency masking noise as ours. The growth-rate of masking from ears with active Bell's Palsy were similar to those in cat auditory-nerve fibers, with the average growth rate (above 5 dB of masking) approximately 2 dB/dB for frequencies 4–8 kHz. However, the human threshold of masking at 6 and 8 kHz was about 15 dB higher than the average threshold of masking in cat auditory-nerve fibers. This difference may originate from a difference in the acoustic calibrations or from the difference in tonal audibility thresholds between the human and cat. Cat hearing thresholds at 6 and 8 kHz are lower than those of humans and are more comparable to human thresholds at 3 and 4 kHz (Sivian and White, 1933; Miller *et al.*, 1963). Whatever the cause of the threshold difference, the data of Borg and Zakrisson (1974) show that high growth rates of masking in

humans persist above the normal threshold for stapedius contractions, as they do in cats.

In certain psychophysical tasks, subjects hear the signal tone by using responses from auditory-nerve fibers that do not have CFs at the signal frequency (Johnson-Davies and Patterson, 1979). It seems likely that such "off-frequency listening" will be influenced by the different growth rates of masking above and below fiber CF (Figs. 2 and 7). If a subject is making use of fibers with CFs below the signal frequency, then one would expect the growth rate of masking to be higher than for a subject using fibers with CFs at or above the signal frequency.

#### IV. CONCLUSIONS

(1) Over all noise levels and fibers, the growth rate of masking averaged approximately 2 dB/dB.

(2) The growth-rate of masking was typically largest for tones about 10% above fiber CF and decreased over about 1/2 octave above and below this frequency.

(3) Masking as large as 70 dB was measured either at tuning-curve threshold, at the middle of rate-level functions, or in  $d'$  versus sound-level functions.

(4) We found no significant difference between the growth rate of masking for higher-SR versus lower-SR fibers, or at 6 versus 8 kHz.

(5) For a tone near CF, the high growth rate of masking by low-frequency maskers and the compressive growth of basilar membrane motion may be due to a common mechanism, one in which the amplitude of basilar-membrane motion controls the gain of the cochlear amplifier at the signal frequency. Such a mechanism may explain the growth rate of two-tone suppression under a wide range of conditions.

#### ACKNOWLEDGMENTS

We thank Dr. B. Delgutte and Dr. M. C. Liberman for comments on the manuscript and the members of the Eaton-Peabody Laboratory for help throughout this work. This work was supported by Grant No. PO1 DC000119 from the National Institute on Deafness and Other Communication Disorders, National Institutes of Health, and by a Sherman Fairchild Fellowship to X.D.P.

<sup>1</sup>Consider a log-log plot of basilar membrane motion versus sound level which has a slope  $S$  at the signal frequency. For an increase in signal level of  $C=1/S$  dB, there will be an increase in basilar membrane motion of 1 dB, and a corresponding decrease in cochlear amplifier gain of  $C-1$  dB (the motion would have increased  $C$  dB if the gain stayed the same, but since the motion increased only 1 dB, the gain must have decreased  $C-1$  dB). If the amplitude of basilar membrane motion controls the gain, then a 1 dB increase in motion produced by a low-frequency masker will also decrease the cochlear amplifier gain by  $C-1$  dB, so the response to the signal frequency will decrease (i.e., be "suppressed") by  $C-1$  dB.

Abbas, P. J. (1978). "Effects of stimulus frequency on two-tone suppression: A comparison of physiological and psychophysical results," *J. Acoust. Soc. Am.* **63**, 1878-1886.

Abbas, P. J., and Sachs, M. B. (1976). "Two-tone suppression in auditory-nerve fibers: Extension of a stimulus-response relationship," *J. Acoust. Soc. Am.* **59**, 112-122.

Borg, E., and Zakrisson, J.-E. (1974). "Stapedius reflex and monaural maskings," *Acta Oto-Laryngol.* **78**, 155-161.

Cai, Y., and Geisler, C. D. (1996). "Suppression in auditory-nerve fibers of cats using low-side suppressors. II. Effect of spontaneous rates," *Hearing Res.* **96**, 113-125.

Cooper, N. P. (1996). "Two-tone suppression in cochlear mechanics," *J. Acoust. Soc. Am.* **99**, 3087-3098.

Cooper, N. P., and Rhode, W. S. (1992). "Basilar membrane mechanics in the hook region of cat and guinea-pig cochleae: Sharp tuning and nonlinearity in the absence of baseline position shifts," *Hearing Res.* **63**, 163-190.

Cooper, N. P., and Rhode, W. S. (1997). "Two-tone suppression in apical cochlear mechanics," *Aud. Neurosci.* **3**, 123-134.

Cooper, N. P., and Yates, G. K. (1994). "Nonlinear input-output functions derived from the responses of guinea-pig cochlear nerve fibers: Variations with characteristic frequency," *Hearing Res.* **78**, 221-234.

Costalupes, J. A. (1985). "Representation of tones in noise in the responses of auditory nerve fibers in the cats: I. Comparisons with detection thresholds," *J. Neurosci.* **5**, 3261-3269.

Costalupes, J. A., Rich, N. C., and Ruggero, M. A. (1987). "Effects of excitatory and nonexcitatory suppressor tones on two-tone suppression in auditory nerve fibers," *Hearing Res.* **26**, 155-164.

Costalupes, J. A., Young, E. D., and Gibson, D. J. (1984). "Effects of continuous noise backgrounds on rate response of auditory nerve fibers in cat," *J. Neurophysiol.* **51**, 1326-1344.

Delgutte, B. (1990a). "Physiological mechanisms of psychophysical masking: Observations from auditory-nerve fibers," *J. Acoust. Soc. Am.* **87**, 791-809.

Delgutte, B. (1990b). "Two-tone rate suppression in auditory-nerve fibers: Dependence on suppressor frequency and level," *Hearing Res.* **49**, 225-246.

Delgutte, B. (1996). "Physiological models for basic auditory percepts," in *Auditory Computation*, edited by H. Hawkins *et al.* (Springer-Verlag, New York), pp. 157-220.

Egan, J. P., and Hake, H. W. (1950). "On the masking pattern of a simple auditory stimulus," *J. Acoust. Soc. Am.* **22**, 622-630.

Evans, B. N., Hallworth, R., and Dallos, P. (1991). "Outer hair cell electromotility: The sensitivity and vulnerability of the DC component," *Hearing Res.* **52**, 288-304.

Fahey, P. F., and Allen J. B. (1985). "Nonlinear phenomena as observed in the ear canal and the auditory nerve," *J. Acoust. Soc. Am.* **77**, 599-612.

Fletcher, H. (1953). *Speech and Hearing in Communication* (Van Nostrand, Princeton, NJ).

Geisler, C. D., and Nuttall, A. L. (1997). "Two-tone 'Low Side' suppression in responses of basal basilar membrane," in *Diversity in Auditory Mechanics*, edited by E. R. Lewis *et al.* (World Scientific, Singapore), pp. 305-311.

Geisler, C. D., and Sinex, D. G. (1980). "Responses of primary auditory fibers to combined noise and tonal stimuli," *Hearing Res.* **3**, 317-334.

Geisler, C. D., Yates, G. K., Patuzzi, R. B., and Johnstone, B. M. (1990). "Saturation of outer hair cell receptor currents causes two-tone suppression," *Hearing Res.* **44**, 241-256.

Glasberg, B. R., and Moore, B. C. (1990). "Derivation of auditory filter shapes from notched-noise data," *Hearing Res.* **47**, 103-38.

Guinan, Jr., J. J., and Gifford, M. L. (1988). "Effects of electrical stimulation of efferent olivocochlear neurons on cat auditory-nerve fibers. III. Tuning curves and thresholds at CF," *Hearing Res.* **37**, 29-46.

Javel, E., McGee, J. A., Walsh, E. J., Farley, G. R., and Gorga, M. P. (1983). "Suppression of auditory nerve responses. II. Suppression threshold and growth, iso-suppression contours," *J. Acoust. Soc. Am.* **74**, 801-813.

Johnson-Davies, D., and Patterson, R. D. (1979). "Psychophysical tuning curves: Restricting the listening band to the signal region," *J. Acoust. Soc. Am.* **65**, 765-770.

Johnson, D. H. (1980). "The relationship between spike rate and synchrony in responses of auditory-nerve fibers to single tones," *J. Acoust. Soc. Am.* **68**, 1115-1122.

Kanis, L. J., and de Boer, E. (1994). "Two-tone suppression in a locally active nonlinear model of the cochlea," *J. Acoust. Soc. Am.* **96**, 2156-2165.

Kawase, T., Delgutte, B., and Liberman, M. C. (1993). "Anti-masking effects of the olivocochlear reflex, II: Enhancement of auditory-nerve response to masked tones," *J. Neurophysiol.* **70**, 2533-2549.

Kiang, N. Y. S., and Moxon, E. C. (1974). "Tails of tuning curves of auditory-nerve fibers," *J. Acoust. Soc. Am.* **55**, 620-630.

Kiang, N.Y. S., Watanabe, T., Thomas, E. C., and Clark, L. F. (1965).

- Discharge Patterns of Single Fibers in the Cat's Auditory Nerve* (MIT, Cambridge, MA).
- Lieberman, M. C. (1978). "Auditory-nerve response from cats raised in a low-noise chamber," *J. Acoust. Soc. Am.* **63**, 442–455.
- Lieberman, M. C., Puria, S., and Guinan, Jr., J. J. (1986). "The ipsilaterally evoked olivocochlear reflex causes rapid adaptation of the  $2f_1-f_2$  distortion product otoacoustic emission," *J. Acoust. Soc. Am.* **99**, 3572–3584.
- Miller, G. A. (1947). "The masking of speech," *Psychol. Bull.* **44**, 105–129.
- Miller, J. D., Watson, C. S., and Covell, W. P. (1963). "Deafening effects of noise on the cat," *Acta Oto-Laryngol. Suppl.* **176**, 1–93.
- Nobili, R., and Mammano, F. (1996). "Biophysics of the cochlea. II: Stationary nonlinear phenomenology," *J. Acoust. Soc. Am.* **99**, 2244–2255.
- Nuttall, A. L., and Dolan, D. F. (1993). "Two-tone suppression of inner hair cell and basilar membrane responses in the guinea pig," *J. Acoust. Soc. Am.* **93**, 390–400.
- Nuttall, A. L., and Dolan, D. F. (1996). "Steady-state sinusoidal velocity responses of the basilar membrane in guinea pig," *J. Acoust. Soc. Am.* **99**, 1556–1565.
- Ono, H., Kanzaki, J., and Mizoi, K. (1983). "Clinical results of hearing aid with noise-level-controlled selective amplification," *Lancet* **22**, 494–515.
- Pang, X. D., and Guinan, J. J. Jr. (1997). "Effects of stapedius-muscle contractions on the masking of auditory nerve responses," *J. Acoust. Soc. Am.* **102**, 3576–3586.
- Pang, X. D., and Peake, W. T. (1986). "How do contractions of the stapedius muscle alter the acoustic properties of the ear?," in *Peripheral Auditory Mechanisms*, edited by J. B. Allen *et al.* (Springer-Verlag, New York), pp. 36–43.
- Patuzzi, R., and Sellick, P. M. (1983). "A comparison between basilar membrane and inner hair cell receptor potential input-output functions in the guinea pig cochlea," *J. Acoust. Soc. Am.* **74**, 1734–1741.
- Relkin, E. M., and Pelli, D. G. (1987). "Probe tone thresholds in the auditory nerve measured by two-interval forced-choice procedures," *J. Acoust. Soc. Am.* **82**, 1679–1691.
- Rhode, W. S. (1971). "Observations of the vibration of basilar membrane in squirrel monkeys using the Mössbauer technique," *J. Acoust. Soc. Am.* **49**, 1218–1231.
- Rhode, W. S. (1978). "Some observations on cochlear mechanics," *J. Acoust. Soc. Am.* **64**, 158–176.
- Rhode, W. S., and Cooper, N. P. (1993). "Two-tone suppression and distortion production on the basilar membrane in the hook region of cat and guinea pig cochlea," *Hearing Res.* **66**, 31–45.
- Robles, L., Ruggero, M. A., and Rich, N. C. (1986). "Basilar membrane mechanics at the base of the chinchilla cochlea. I. Input-output functions, tuning curves, and response phases," *J. Acoust. Soc. Am.* **80**, 1364–1374.
- Ruggero, M. A., Robles, L., and Rich, N. C. (1992). "Two-tone suppression in the basilar membrane of the cochlea: Mechanical basis of auditory-nerve rate suppression," *J. Neurophysiol.* **68**, 1087–1099.
- Ruggero, M. A., Rich, N. C., Recio, A., Narayan, S. S., and Robles, L. (1997). "Basilar-membrane responses to tones at the base of the chinchilla cochlea," *J. Acoust. Soc. Am.* **101**, 2151–2163.
- Schmiedt, R. A. (1982). "Boundaries of two-tone rate suppression of cochlear-nerve activity," *Hearing Res.* **7**, 335–351.
- Sivian, L. J., and White, S. D. (1933). "On minimum audible sound fields," *J. Acoust. Soc. Am.* **4**, 288–321.
- Smoorenburg, G. F., and Kloppenburg, B. A. M. (1986). "Single-neuron tuning curves measured with psychoacoustic paradigms," in *Auditory Frequency Selectivity*, edited by B. C. J. Moore and R. D. Patterson (Plenum, London), pp. 179–186.
- Stevens, S. S., Miller, J., and Truscott, I. (1946). "The masking of speech by sine waves, square waves, regular and modulated pulses," *J. Acoust. Soc. Am.* **18**, 418–424.
- Teich, M. C., and Khanna, S. M. (1985). "Pulse-number distribution for the neural spike train in the cat's auditory nerve," *J. Acoust. Soc. Am.* **77**, 1110–1128.
- Thibodeau, L. M. (1996). "Evaluation of auditory enhancement and auditory suppression in listeners with normal hearing and reduced speech recognition in noise," *J. Speech Hear. Res.* **39**, 947–956.
- Wegel, R. L., and Lane, C. E. (1924). "The auditory masking of one pure tone by another and its probable relation to the dynamics of the inner ear," *Phys. Rev.* **23**, 266–285.
- Winslow, R. L., and Sachs, M. B. (1987). "Effect of electrical stimulation of the crossed olivocochlear bundle on auditory nerve response to tones in noise," *J. Neurophysiol.* **57**, 1002–1021.
- Young, E. D., and Barta, P. E. (1986). "Rate responses of auditory nerve fibers to tones in noise near masked threshold," *J. Acoust. Soc. Am.* **79**, 426–442.
- Zwicker, E. (1986). "Suppression and ( $2F_1-F_2$ ) difference tones in a nonlinear cochlear preprocessing model with active feedback," *J. Acoust. Soc. Am.* **80**, 163–176.

# Effects of stapedius-muscle contractions on the masking of auditory-nerve responses

Xiao Dong Pang

*Eaton-Peabody Laboratory of Auditory Physiology, Department of Otolaryngology, Massachusetts Eye and Ear Infirmary, 243 Charles Street, Boston, Massachusetts 02114 and Department of Electrical Engineering and Computer Science, and Research Laboratory of Electronics, Massachusetts Institute of Technology, Cambridge, Massachusetts 02139*

John J. Guinan, Jr.

*Eaton-Peabody Laboratory of Auditory Physiology, Department of Otolaryngology, Massachusetts Eye and Ear Infirmary, 243 Charles Street, Boston, Massachusetts 02114 and Department of Electrical Engineering and Computer Science, and Research Laboratory of Electronics, Massachusetts Institute of Technology, Cambridge, Massachusetts 02139 and Department of Otology and Laryngology, Harvard Medical School, Boston, Massachusetts 02115*

(Received 9 December 1996; revised 21 July 1997; accepted 22 July 1997)

There has been little exploration of the mechanisms by which stapedius muscle contractions reduce the masking of responses to high-frequency sounds by low-frequency sounds. To fill this gap in knowledge, controlled stapedius contractions were elicited with direct shocks in anesthetized cats, and measurements were made of the effects of these contractions on the masking of single auditory-nerve fibers and on the attenuation of middle-ear transmission. The results show that the stapedius-induced reductions of masking can be much larger than the attenuations of low-frequency sound. With a 300-Hz band of masking noise centered at 500 Hz, and signal tones at 6 or 8 kHz, unmasking effects over 40 dB were observed for sounds 100 dB SPL or less. The data suggest that much larger unmasking might occur. The observed unmasking can be explained completely by a linear stapedius-induced attenuation of sound transmission through the middle ear and a nonlinear growth rate of masking for auditory-nerve fibers. No central effects are required. It is argued that the reduction of the upward spread of masking is probably one of the most important functions of the stapedius muscle. © 1997 Acoustical Society of America. [S0001-4966(97)03212-8]

PACS numbers: 43.64.Kc, 43.64.Bt, 43.64.Ha, 43.64.Pg [RDF]

## INTRODUCTION

One effect of the stapedius muscle is to reduce masking. An important example of this is the stapedius-induced reduction of masking during the perception of high-level speech. At levels over 90–100 dB SPL, speech recognition in ears lacking a working stapedius reflex is worse than normal, presumably because the low-frequency components of the speech mask responses to the high-frequency components (Borg and Zakrisson, 1973, 1975b; Dorman *et al.*, 1987; Colletti and Fiorino, 1994; Wormald *et al.*, 1995).

With current knowledge, we can formulate a plausible hypothesis for the mechanism responsible for the “unmasking” effect of the stapedius. The stapedius provides significant “unmasking” in situations in which low-frequency sounds mask responses to high-frequency sounds. One line of evidence for this comes from experiments on patients with Bell’s palsy who lacked a functioning stapedius on one side (Borg and Zakrisson, 1974). In these patients, the “unmasking” attributed to the stapedius was as much as 50 dB when the masker was a 300-Hz band of noise centered at 500 Hz and the masked signal was a tone in the 4–8-kHz range. Furthermore, the amount of stapedius “unmasking” paralleled the attenuation produced by the stapedius at the frequency of the masker (Borg and Zakrisson, 1974). A stapedius-induced attenuation of the low-frequency noise would be expected to exert a powerful “unmasking” effect

because the masking of responses to high-frequency tones by low-frequency maskers grows at a high (e.g., 2 dB/dB) rate (Wegel and Lane, 1924; Egan and Hake, 1950; Geisler and Sinex, 1980; Delgutte, 1990; Pang and Guinan, 1997). Considering this evidence, we hypothesize that the “unmasking” produced by the stapedius can be explained by (1) a stapedius-induced change in the middle-ear transfer function which is equivalent to inserting a linear filter, followed by (2) a nonlinear cochlea in which intense low-frequency sounds strongly mask responses to high-frequency sounds. Despite the fact that the background elements of this hypothesis are well established, the mechanisms by which stapedius contractions reduce masking have never been directly tested experimentally.

The goal of this paper is to test the above hypotheses and thereby to understand the mechanism responsible for the “unmasking” effect of the stapedius. Understanding the mechanisms by which the stapedius reduces masking will help us to predict the magnitude of the effect and the circumstances under which it is important. Ultimately, this will help us to understand the role of stapedius “unmasking” in hearing. It should also indicate the usefulness of incorporating into hearing aids an action like that of the stapedius acoustic reflex.

The unmasking (UM) produced by contraction of the stapedius when a high-frequency signal is masked by a low-

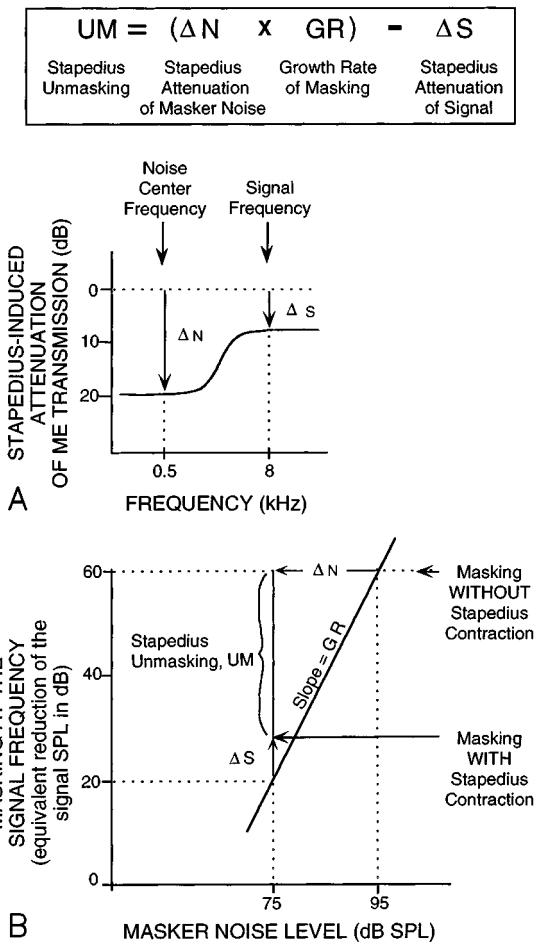


FIG. 1. The relationship of stapedius “unmasking” to the growth rate of masking and to the stapedius-induced attenuations at masker and signal frequencies. (A) A schematized typical example of the stapedius-induced attenuation of middle ear (ME) transmission showing the attenuation at the frequency of the masking noise ( $\Delta N$ ) and the signal tone ( $\Delta S$ ). (B) A schematized typical example of stapedius unmasking. The thick diagonal line is the auditory-nerve-fiber masking function, i.e., the amount in dB that the signal sound level must be increased in the presence of the masking noise to equal the response without the masking noise *versus* the masking noise level. This line shows a growth rate of masking (GR) of 2 dB/dB which is close to the average of our data (Pang and Guinan, 1997). The stapedius contraction reduces the effective masker noise by 20 dB ( $\Delta N$  line) which would reduce the masking by  $\Delta N \times GR = 40$  dB, except that the stapedius contraction also reduces the signal frequency by  $\Delta S$ , so the net unmasking  $UM = (\Delta N \times GR) - \Delta S$ .

frequency noise is illustrated in Fig. 1. GR is the growth rate of neuronal masking at the signal frequency produced by the low-frequency noise in the absence of stapedius contractions, and  $\Delta N$  is the stapedius-induced attenuation of the low-frequency noise. The stapedius-induced reduction of the low-frequency noise will reduce the masking by  $\Delta N \times GR$  [Fig. 1(B)]. However, the stapedius contraction also reduces middle-ear transmission at the signal frequency by  $\Delta S$  [Fig. 1(A)], so the total reduction of masking is<sup>1</sup>

$$UM = (\Delta N \times GR) - \Delta S. \quad (1)$$

Note that with this hypothesis, the only attribute of the single auditory-nerve fiber needed for the prediction of stapedius unmasking is the growth rate of masking, GR.

To test the hypothesis, we monitored responses of single auditory-nerve fibers and measured the “unmasking” produced by fixed stapedius contractions in responses to high-frequency tones masked by low-frequency noise. To be comparable to the experiments of Borg and Zakrisson (1974), we used a tone at 6 or 8 kHz as the signal and a 300-Hz band of noise centered at 500 Hz as the masker. We compared the measured “unmasking” results with “unmasking” predicted by Eq. (1) from (a) measurements of GR obtained from the same auditory-nerve fiber as the stapedius unmasking measurements, and (b) measurements of the middle-ear-transmission attenuations at the frequencies of the signal and masker ( $\Delta S$  and  $\Delta N$ ) obtained by monitoring the change in cochlear microphonic (CM) from the same fixed stapedius contraction.

## I. METHODS

### A. General experimental approach

We blocked activation of the stapedius through the central nervous system by deep anesthesia and evoked controlled stapedius contractions by directly stimulating the muscle with electric shocks. From a signal-flow point of view, the anesthesia opens the loop of the middle-ear-muscle acoustic reflex. Although the hypothesis applies to both open- and closed-loop stapedius contractions, the hypothesis is more easily tested in the open-loop condition. Direct stapedius stimulation had several other advantages: (1) we could evoke stable contractions at a desired time and strength, (2) since it is not necessary to use intense sounds to evoke stapedius contractions, the hypothesis could be tested at any sound level, and (3) we could reduce the desensitization of the cochlea produced by intense sounds. With an open-loop reflex, we are able to test the hypothesis up to high effective sound levels because the drive to the cochlea in the open-loop condition at the highest noise level used (100 dB SPL) is equivalent to a close-loop drive to the cochlea with a noise level of 110–120 dB SPL (the exact value depends on the reflex regulation factor).

A potential complication might come from the olivocochlear efferents which are also activated by sounds, inhibit the responses of auditory-nerve fibers, and can have unmasking effects (see Guinan, 1996). However, since the stapedius loop is opened, the olivocochlear efferents have no influence on the activation of the stapedius. For this study, efferent effects can be treated as part of the cochlear processing of the signal, as long as the preparation is stable and activation of the efferents depends only on the sound drive to the cochlea. This will not be true, however, if the stapedius shocks directly excite efferent fibers. Direct, shock-excitation of efferents appears to be a possibility because our shock electrode is not far from the round window and high-level shocks on the round window (RW) can excite efferents (Rajan and Johnstone, 1983). However, Rajan and Johnstone used monopolar stimulation on the RW to maximize current flow into the cochlea, but we used bipolar stimulation to minimize current spread and electrodes at least 1 mm from the RW. As a partial test for shock-evoked efferent effects, a control experiment was carried out in the same way as the others, but

with the olivocochlear efferents severed at the anastomosis of Oort. This provided no evidence of shock excitation of the olivocochlear efferents (see Sec. II). The cut is only a partial control because it is not clear how far the damage to efferent axons extends from the cut, or where along the fibers efferents are excited by the round-window shocks. In addition, we found no sign of auditory-nerve fiber activity being directly evoked, or spontaneous activity being modified, by the stapedius shocks.

Our hypothesis assumes that the stapedius-induced change in the middle-ear transfer function<sup>2</sup> is equivalent to inserting a linear filter. Experiments that confirm that the attenuation produced by the stapedius is not a function of sound level are reported elsewhere (Pang, 1988; Pang and Guinan, unpublished).

## B. Animal preparation

Treatment of experimental animals was in accordance with regulations of the Committees on Animal Care at the Massachusetts Institute of Technology and the Massachusetts Eye and Ear Infirmary. Normal-hearing adult cats were anesthetized by intraperitoneal injection (0.75 ml/kg) of Dial-Urethane (100-mg diallylbarbituric acid, 400-mg urethane, and 400-mg monoethylurea per ml). Additional anesthesia was given as needed to maintain the animal without a toe-pinch withdrawal reflex. Methods for the preparation of the animal, the acoustic system, the recording from auditory-nerve fibers, and the data analysis for obtaining  $d'$  were described previously (Pang, 1988; Pang and Guinan, 1997). The data in this paper are from 103 auditory-nerve fibers from nine cats. Fibers were classified as lower spontaneous rate (SR) ( $SR < 1$  spikes/s) or higher SR ( $SR \geq 1$  spikes/s).

After the experiment in which olivocochlear efferents were cut, the cochlea was injected with horseradish peroxidase and the tissue was processed as described by Joseph *et al.* (1985). No olivocochlear-neuron labeling was found [hundreds are routinely labeled if the fibers are not cut (Joseph *et al.*, 1985)], confirming that the efferents were completely severed.

## C. Electric stimulation of the stapedius muscle

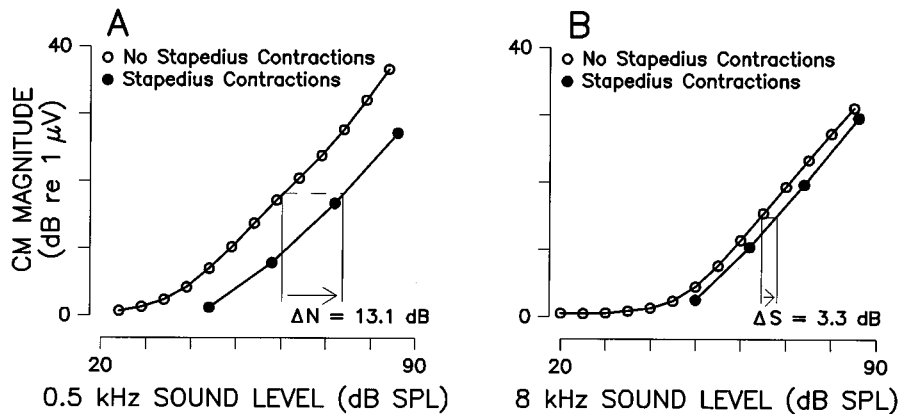
The stapedius was stimulated with a bipolar electrode placed either (1) in the bony notch just dorsal and lateral to the round-window (the notch often provided direct access to the ventral surface of the muscle), or (2) on the dorso-lateral surface of the muscle after the stapedius was exposed by drilling a small hole through the temporal bone posterior and dorsal to the external ear canal (Vacher *et al.*, 1989). Since the latter approach required drilling through (and then resealing) the external semicircular canal, it was used only if the "notch approach" produced a high threshold for muscle contraction and intolerable shock artifact (presumably, cases when the notch electrode was not directly on the muscle). Ears in which the muscle exposure produced a threshold loss of 15 dB or more (assessed by measurements of compound action potentials) were not used. No difference in results

appeared attributable to which approach was used. The tendon of the tensor tympani was cut to prevent it from affecting middle-ear transmission.

Shocks were delivered through an isolation transformer to two platinum wires 1 to 2 mm apart. In early experiments, these wires were pointed, but ball-tipped electrodes produced more stable results and were used in most experiments. The relationship between shock current intensity (monitored by a Tektronix P6016) and stapedius contractions (monitored by stapes head displacements; Pang and Peake, 1986) was normally stable during the experiment. Shock artifacts were minimized by an aluminum-foil shield between the shock electrode and the microelectrode and by cancellation using a reference artifact from an electrode near the auditory nerve (as in Guinan and McCue, 1987). The remaining shock artifact was less than 10% of the neuronal spike amplitude in the shock range normally used, but was much larger at shock levels that produced maximum stapedius contractions. Shock artifacts limited our ability to use the largest stapedius contractions. The artifact in the recording of CM produced by electric stimulation of the stapedius muscle could be adequately eliminated by the use of bandpass and tracking filters.

The stapedius was stimulated by sinusoids or low-pass-filtered pulse trains. Pulse stimuli had lower peak currents at the threshold for evoking stapedius contractions, but the artifact from sinusoids was easier to remove. In each cat, we chose the waveform which gave the smaller artifact at stapedius threshold. Pulse stimulation used 0.3-ms pulse durations and 5-ms interpulse intervals; these values gave the lowest threshold currents. With sinusoidal stimulation, the current at threshold decreased as shock frequency increased from 50 to 200 Hz. However, sinusoidal shocks to the stapedius produce an undesirable vibration (i.e., sound) in the middle ear at the shock frequency, so it was important to keep the shock frequency low to avoid producing a potential masking sound. We usually chose 100 Hz as the sinusoidal shock frequency.

Stapedius shocks were either continuous or in bursts. Bursts were usually used when the acoustic stimulation was also in repeated bursts, e.g., in rate-level functions. Each shock burst was 200-ms duration with a 1-s repetition period to maintain stable stapedius excitability. To ensure that the stapedius contractions were in the steady state, tone bursts began at least 100 ms after shock onset, and spikes were counted only during the last 80 ms of the shock burst. For most auditory-nerve fibers, rate-level functions with stapedius shocks were measured before other rate-level functions to obtain the best spike-to-artifact ratio (the spike size usually decreased with time). A few auditory-nerve fibers were held for long times with large spikes enabling us to redo measurements and confirm that the results were not order dependent. Continuous shocks were used when long continuous stapedius contractions were needed, i.e., in obtaining tuning curves from auditory-nerve fibers. With continuous shocks, all measurements were made during the period of constant stapedius contraction, and the minimum time between stapedius stimulations (up to 4 min) was adjusted to maintain consistent stapedius excitability [based on measure-



Growth Rate of Masking,  
 $GR = \frac{\Delta m}{\Delta L} = \frac{26.4}{10} = 2.64$

Predicted Unmasking:  
 $UM_p = \Delta N \times GR - \Delta S$   
 $= 13.1 \times 2.64 - 3.3$   
 $= 31.3 \text{ dB}$

Measured Unmasking:  
 $UM_M = 31.7 \text{ dB}$

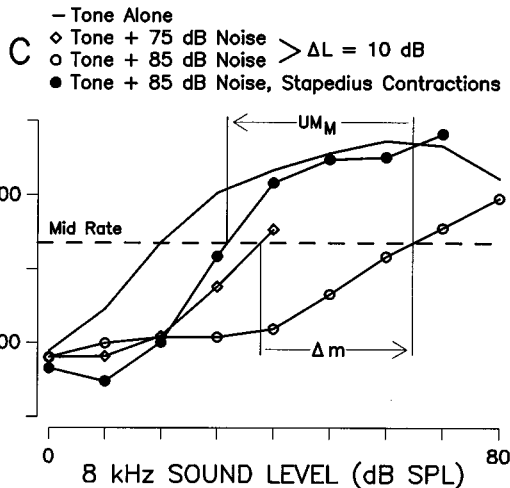


FIG. 2. A comparison of predicted and measured stapedius unmasking using neural rate versus sound-level functions. Top: The magnitude of CM versus sound level for (A) tones at 0.5 kHz, the center frequency of the masker noise, and (B) 8 kHz, the signal frequency. The sound attenuations produced by stapedius contractions,  $\Delta N$  and  $\Delta S$ , were obtained from the differences between the curves obtained without and with stapedius contractions, as indicated in the figure. (C) Firing rate versus 8-kHz sound level functions for various combinations of noise levels and stapedius contractions (key in figure). Measured stapedius unmasking,  $UM_M$  was the difference between the signal levels which produced midrate responses with and without stapedius contractions. The growth rate of masking, GR, was calculated from  $\Delta m$ , the change in masking measured at midrate, due to the change in masking noise  $\Delta L$  from 75 dB SPL to 85 dB SPL. Inset: Comparison of predicted unmasking  $UM_p$  and measured unmasking  $UM_M$ . Fiber 86-79: CF=7.5 kHz, threshold at CF=7.3 dB SPL, spontaneous rate (SR)=90 sp/s.

ments of cochlear microphone (CM) attenuations made before contacting the auditory-nerve fiber].

We determined  $\Delta N$  and  $\Delta S$  [Fig. 1(A)] immediately after losing contact with an auditory-nerve fiber using constant-response measures of CM with and without stapedius contractions [e.g., Figs. 2(A), and (B) and 3(A) and (B)]. The same shock-current level was used as in the auditory-nerve measurements. The stapes head displacement was also measured to confirm that the strength of the stapedius contractions had not changed. Since the stapedius-induced change in middle-ear transmission is relatively flat near 500 Hz (Pang and Peake, 1986),  $\Delta N$  was measured at its center frequency instead of over the octave band of the noise. In some cases (all of which had an almost linear growth of CM with sound level), we measured  $\Delta N$  and  $\Delta S$  from short frequency sweeps at a constant sound level, with and without stapedius contractions [e.g., Fig. 4(A)]. Since the attenuation produced by the stapedius is not a function of sound level (Pang, 1988; Pang and Guinan, unpublished),

$\Delta N$  and  $\Delta S$  measured at one sound level will hold for all sound levels.

#### D. Controls for artifacts

Electrical stimulation of the stapedius produced two kinds of sound in the middle ear, a very low-frequency transient sound at the onset and offset of stimulation, and a continuous sound at the stimulation frequency. The low-frequency transient sound was produced both by pulse and sinusoidal stimulation, was generally <45 dB SPL, and typically lasted less than 100 ms. It may be generated by a step displacement of the stapes at the onset and offset of stapedius contraction. This transient sound occasionally evoked activity in nerve fibers with CFs < 0.2 kHz, but did not evoke activity in nerve fibers with CFs > 0.5 kHz. Since our counts of auditory-nerve spikes began 120 ms after shock onset, this transient sound should have negligible effects on the measurements.

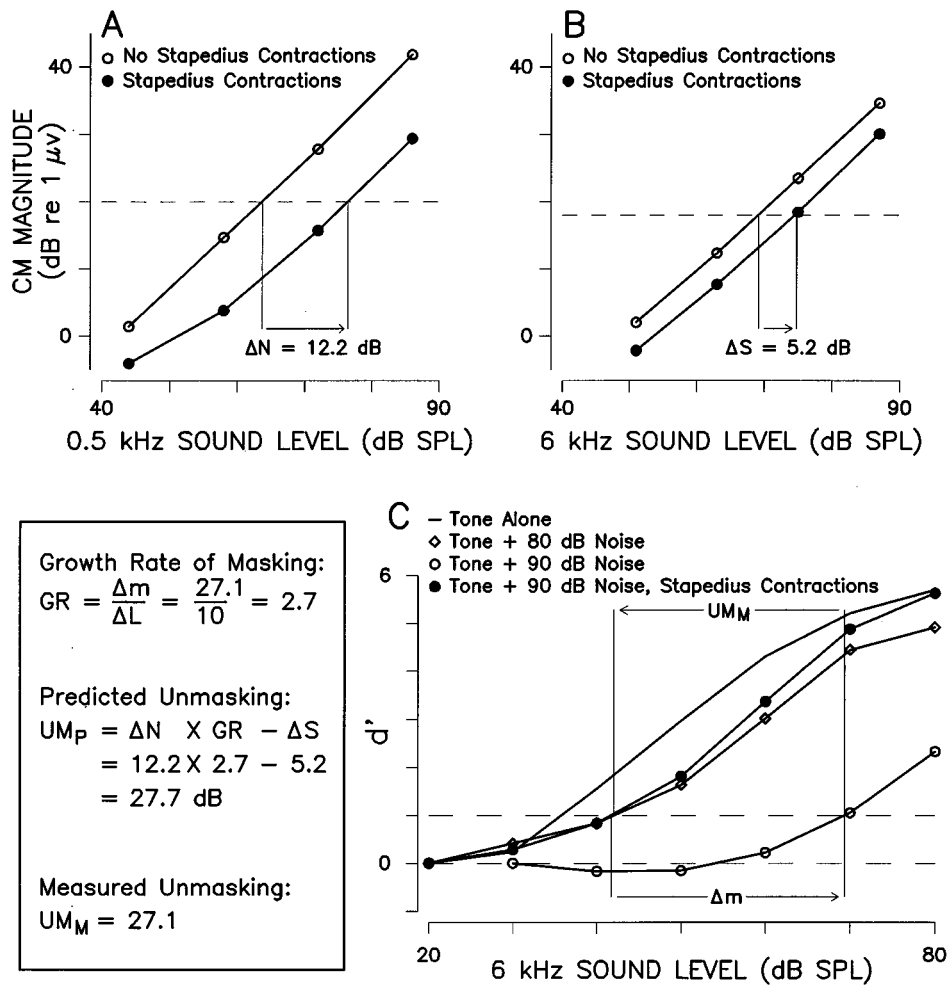


FIG. 3. A comparison of predicted and measured stapedius unmasking using neural  $d'$  versus sound-level functions. Format as in Fig. 2 except that panel (C) shows  $d'$  versus sound level functions and the signal frequency is 6 kHz. Fiber 86–104: CF=7.0 kHz, threshold at CF=10.3 dB SPL, SR=75 sp/s.

The sustained sound produced by stapedius shocks should also have a negligible effect on our measurements. With shock-pulse stimulation of the stapedius, we were unable to detect sustained sound in the ear canal. With sinusoidal shock currents at 100 Hz, the sound in the ear canal was typically less than 20 dB SPL, although the effective sound level reaching the cochlea may have been more. We found no effect of this sound in the high-CF auditory-nerve fibers used in this study. In particular, there was no evoked activity and no modulation at 100 Hz of responses to 6- or 8-kHz tones. Finally, when the stapedius tendon was cut, electric stimulation of the muscle produced no change in the CM response to acoustic stimuli.

## II. RESULTS

Tests of the “linear-transmission-change plus nonlinear-cochlea” hypothesis of Eq. (1) were made with the masking of single auditory-nerve fibers measured in three ways: from rate versus level functions (Fig. 2), from  $d'$  versus level functions (Fig. 3), and from tuning curves (Fig. 4). Testing with three different criteria is useful because each measure is in a somewhat different position of the response versus sound level functions and the three criteria represent different aspects of the neural responses that the brain might use in

making threshold and/or suprathreshold judgments. In Figs. 2–4, panel (C) shows the single-fiber response data used to measure stapedius unmasking,  $UM_M$ , and to calculate the growth rate of masking, GR. The stapedius unmasking,  $UM_M$  was measured from the difference between the signal levels which produced a criterion response with and without stapedius contractions. Our criteria were the midrate (for rate versus level functions, Fig. 2) (midrate is the average of the spontaneous and maximum rates),  $d' = 1$  (for  $d'$  versus level functions, Fig. 3), and tuning-curve threshold (for tuning curves, Fig. 4). The growth rate of masking was calculated from data without stapedius contractions as  $GR = \Delta m / \Delta L$ , with the change in masking  $\Delta m$  being the difference between the signal levels which produced criterion responses for two masker levels separated by  $\Delta L$ . We measured GR in the noise intensity range which corresponded as closely as possible to the range over which the stapedius unmasking was measured. In all cases, we chose sound levels which ensured that the noise drive to the cochlea remained above the threshold of masking (in almost all cases the noise drive to the cochlea was kept at least 5 dB above the threshold of masking to avoid the region of gradual onset of masking). In Figs. 2–4, the top panels show determinations of  $\Delta N$  and  $\Delta S$ , the stapedius-induced attenuations at the center fre-



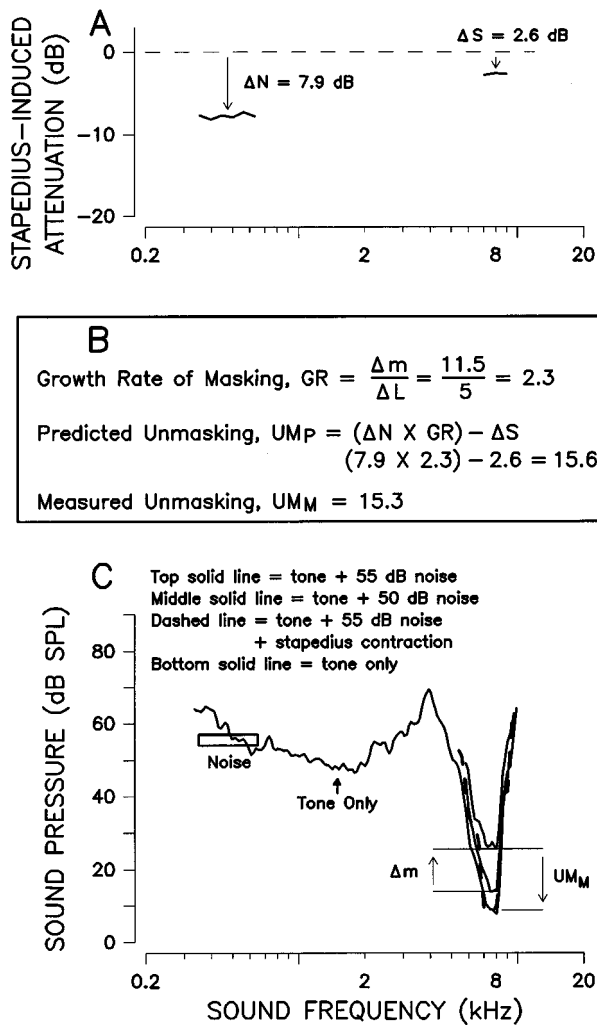


FIG. 4. A comparison of predicted and measured stapedius unmasking using neural tuning curves. (A) The magnitudes of the stapedius-induced attenuations in the frequency regions of the noise ( $\Delta N$ ) and the signal ( $\Delta S$ ). In this case,  $\Delta N$  and  $\Delta S$  were calculated from the difference (in dB) of CM-level versus tone-frequency sweeps at constant SPL with and without stapedius shocks (at the sound levels used, 60–70 dB SPL, the CM-level functions had approximately unity slopes). (B) Comparison of predicted unmasking  $UM_P$  and measured unmasking  $UM_M$ . (C) Threshold tuning curves for various combinations of noise level and stapedius contractions (key in figure). At a given frequency, the measured stapedius unmasking  $UM_M$  was the difference between the tuning-curve threshold levels with and without stapedius contractions in the presence of 55 dB SPL noise. The growth rate of masking, GR, was calculated from  $\Delta m$ , the change in tuning-curve threshold due to the change in masking noise  $\Delta L$  from 55 dB SPL to 60 dB SPL. Fiber 65–3: CF=8.04 kHz, threshold at CF=7.8 dB SPL, SR=65 sp/s.

quency of the masking noise and at the signal frequency. From these, and the measured GR, we calculated the stapedius unmasking predicted by the hypothesis  $UM_P$ .

In each of Figs. 2–4,  $UM_P$  was very close to the measured unmasking  $UM_M$ . This was true no matter whether the criteria applied were in terms of rate (Fig. 2),  $d'$  (Fig. 3), or tuning-curve threshold (Fig. 4). In each of these cases, the stapedius contraction produced a moderate  $\Delta N$  (8–13 dB) and a larger stapedius unmasking (15–32 dB). As can be seen in each figure, unmaskings larger than the stapedius attenuations came about because the growth rates of masking were over 2 dB/dB.

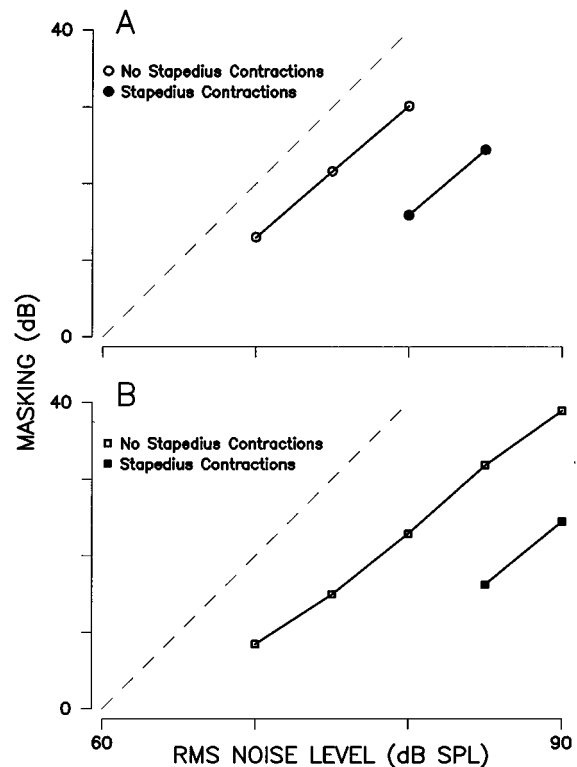


FIG. 5. The effects of stapedius contractions on masking functions from two auditory-nerve fibers, (A) and (B). Masking criteria were  $d'$  (top) and midrate (bottom). (A) Fiber 83–123: CF=8.04 kHz, threshold at CF=6.4 dB SPL, SR=116 sp/s. (B) Fiber 83–117: CF=8.61 kHz, threshold at CF=19.1 dB SPL, SR=9.2 sp/s.

Figure 5 shows examples of the effects of fixed stapedius contractions on masking functions (i.e., masking as a function of masker-noise level) using  $d'$  (top) and midrate (bottom) criteria. If the masking function in the absence of stapedius contractions is a straight line, then the hypothesis predicts that the effect of a fixed stapedius contraction would be a parallel shift of the masking function towards higher noise levels. Although there are not many points in the masking functions, the data of Fig. 5 are consistent with the hypothesis.

#### A. The effect of cutting the olivocochlear efferents

As a control, in one experiment we measured masking and stapedius unmasking in an animal with cut olivocochlear efferents. In this animal, masking level functions were obtained from rate-level functions from nine fibers with CFs 5.7–7.5 kHz. The growth rate of masking (mean=1.9 dB/dB, s.d.=0.48,  $n=9$ ) was almost identical to the growth rate from all animals with intact efferents (see Pang and Guinan, 1997). The average masking at a given noise level, however, was less than the average from other animals. This might be due to an increase in the masking threshold (the noise level at which masking begins) on the order of 5 dB, but the sample size with cut efferents is not large enough to warrant a detailed analysis or a definitive conclusion on the source of this small difference.

Figure 6 shows data for a comparison of predicted and measured stapedius unmasking from the cat with cut olivocochlear efferents. As in the earlier examples, the predicted

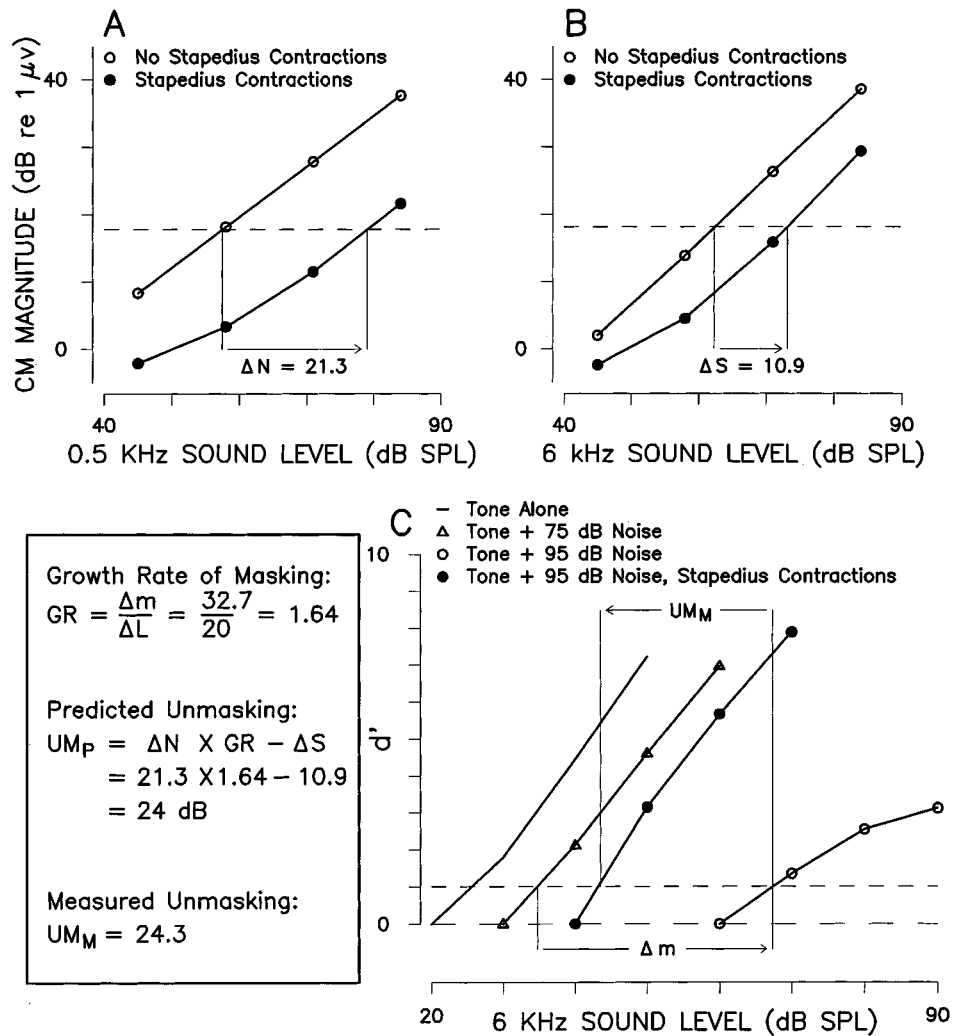


FIG. 6. A comparison of predicted and measured stapedius unmasking from neural  $d'$  versus sound level functions from a cat with cut olivocochlear efferents. Format as in Fig. 2 except that panel (C) shows  $d'$  versus sound level functions and the signal frequency is 6 kHz. Fiber 89-22: CF=6.92 kHz, threshold at CF=21.2 dB SPL, SR=1.6 sp/s.

and measured unmasking are very similar, indicating that cutting the efferents did not affect the validity of the hypothesis. This is consistent with the interpretation that the shocks do not directly excite efferent fibers and with the expectation that whatever unmasking effects the efferents produce (e.g., Kawase *et al.*, 1993), the hypothesis of Eq. (1) should hold both with and without efferent activity.

### B. Measured and predicted stapedius unmasking in all fibers

A comparison of measured and predicted stapedius unmasking is shown in Fig. 7 for all the available data from rate-level functions,  $d'$ -level functions, and tuning curves. In the data from each type of measurement, and in the combined data, there are no statistically significant systematic differences between the measured and predicted unmasking. The largest difference between the measured and predicted unmasking was 8.3 dB. Since that point was from a very early experiment where sharp-tipped shock electrodes were used, one possibility is that the strength of the stapedius con-

tractions evoked by the shocks changed over the 19 min between the single-fiber and the CM measurements.

In Fig. 7 there is only one stapedius unmasking point over 40 dB, but we measured stapedius unmasking over 40 dB in five fibers. Four of these five cases are not shown in the figure because we did not obtain sufficient data to calculate a predicted stapedius unmasking for them. In all five cases, stapedius shocks were used that produced only 20 dB of low-frequency attenuation. With maximum stapedius contractions, stapedius unmaskings well in excess of 40 dB would be expected.

## III. DISCUSSION

### A. Validity of the hypothesis as tested by the physiologic data

Our tests show that the "linear-transmission-change plus nonlinear-cochlear" hypothesis, of Eq. (1), provides a good quantitative accounting of the stapedius unmasking data. In almost all cases, the predicted unmasking was close to the measured unmasking (Fig. 7). Although there are a

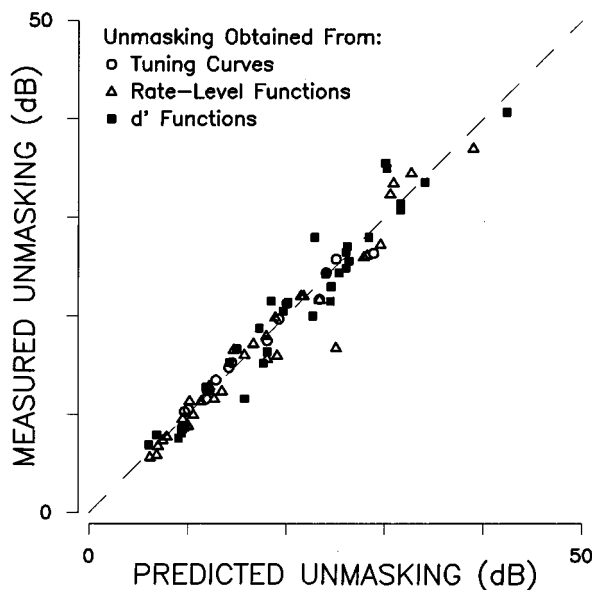


FIG. 7. Comparison of predicted and measured stapedius unmasking using all data from rate-level functions,  $d'$ -level functions and tuning curves. 80 points from 58 auditory-nerve fibers from eight animals, CFs 4.3–9.9 kHz. Statistics for the differences between prediction ( $p$ ) and measurement ( $m$ ) are (in dB): For  $(p-m)$ , mean=0.2, range: -5.4 to 8.3, standard deviation (s.d.)=1.96. For  $|p-m|$  (the absolute values of the difference), mean=1.4, s.d.=1.38.

few outliers in Fig. 7, there does not appear to be any trend toward a systematic difference between the predicted and measured unmasking. Furthermore, the validity of the stapedius-unmasking hypothesis does not depend on any particular measure of the masking effect. For all three measures (firing rate,  $d'$ , and tuning curves), the predicted unmasking equals the measured unmasking (Fig. 7).

### B. Extension of the hypothesis to psychophysical performance in humans

Although the hypothesis was tested with physiological data from cats, it is reasonable to believe that it applies to psychophysical performance in humans. First, the frequency dependence and magnitude of the middle-ear transmission changes produced by stapedius contractions are similar in cats and humans (Møller, 1962, 1965; Borg, 1968; Teig, 1973; Rabinowitz, 1977; Pang and Peake, 1986). Second, psychophysical masking of tones by noise is similar for cats and humans with respect to the growth rate of masking (Watson, 1963) and the critical bandwidth (Costalupes, 1983). Masking measurements at sound levels above the stapedius acoustic-reflex threshold must be interpreted carefully because the reflex is usually blocked in the cat data but intact in normal humans. Comparable, high-sound-level, reflex-blocked measurements show similar masking growth rates (over 2 dB/dB up to very high sound levels) in anesthetized cats (Pang and Guinan, 1997) and in subjects with Bell's Palsy<sup>3</sup> (Borg and Zakrisson, 1974). Finally, similar maximum values of stapedius unmasking have been found in cats (40–45 dB, this paper) and in humans (47 dB, Borg and Zakrisson, 1974). Although it is possible that there is a central component to stapedius unmasking (whatever activates

the stapedius could also activate fibers to central auditory nuclei and change their signal processing), our data show that peripheral mechanisms alone are sufficient to produce stapedius unmasking quantitatively similar to that observed psychophysically in humans. All in all, our hypothesis is consistent with available data from humans.

### C. Implications of the hypothesis

The hypothesis, combined with previous data, has implications regarding the contributions to unmasking from various classes of auditory-nerve fibers. Since noise-induced masking of a fiber's response to a signal is most powerful when the signal frequency is near the fiber's CF (Kiang and Moxon, 1974; Geisler and Sinex, 1980; Pang and Guinan, 1997), stapedius unmasking should be largest in fibers with CFs near (or just below) the signal frequency. Since, on the average, there is no significant difference between the growth rate of masking in higher-SR *versus* lower-SR auditory-nerve fibers (Pang and Guinan, 1997), there should be no significant difference between the stapedius-unmasking effect for higher-SR *versus* lower-SR auditory-nerve fibers. Since it appears likely that all fibers with similar CFs (i.e., fibers that innervate a narrow region of the cochlea) are affected by stapedius unmasking to the same extent, and there is no reason to think that the central nervous system uses information from various auditory-nerve fibers differently when the stapedius is contracting, the unmasking seen in individual single auditory-nerve fibers should be close in value to the unmasking which would be measured psychophysically.

Although we observed 40–45 dB of stapedius unmasking in cats, and unmaskings as high as 47 dB were found in humans (Borg and Zakrisson, 1974), the largest possible stapedius unmasking might be even higher. In cats, the maximum growth rate of masking measured over a large noise range was in excess of 3 dB/dB (Pang and Guinan, 1997), and the largest measured stapedius-induced attenuation of low-frequency sound was 30 dB, with a corresponding high-frequency attenuation of about 15 dB (Pang and Peake, 1986). Thus the hypothesis predicts a maximum stapedius unmasking of  $[3 \times 30] - 15 = 75$  dB. Although 75 dB is probably too optimistic, it seems realistic to think that stapedius contractions might produce unmaskings in excess of the 40–47 dB measured so far.

Although we measured stapedius unmasking only at 6 and 8 kHz, it is interesting to consider how much stapedius unmasking might be produced across a wide range of signal frequencies. Large stapedius unmaskings will be obtained for maskers 1 kHz or lower (i.e., frequencies at which stapedius-induced attenuation is high) and for signals above about 2 kHz (i.e., frequencies at which stapedius-induced attenuation is low). Although growth rates of masking of 3 dB/dB have been obtained, growth rates are normally closer to 2, so that with the largest stapedius-induced attenuations of Pang and Peake (1986) there would be unmaskings of 40–50 dB by Eq. (1). For stapedius contractions to produce 40–50 dB of unmasking, there must be at least that much masking produced without the stapedius contractions. Low-frequency maskers at 80 dB SPL produce masking of 40–50 dB up to

signal frequencies of a few kHz (Wegel and Lane, 1924; Egan and Hake, 1950) and sufficiently high-level maskers should produce 40–50 dB of masking up to the highest audible frequencies. Measurements in Bell's Palsy patients (e.g., during versus after stapedius reflex block) show stapedius unmaskings over 40 dB for signal frequencies up to 8 kHz, the highest frequency tested (Borg and Zakrisson, 1974). All considered, it seems likely that stapedius unmasking of 40–50 dB is present up to the highest audible frequencies.

#### D. Significance for hearing

In order to assess the significance of the stapedius unmasking we have studied, we must know how relevant our masker and signal frequencies are to sounds normally heard by cats and humans. A lot of environmental noise and many kinds of industrial and traffic noise are predominantly low frequency with strong components in the frequency region of our masker (Kryter, 1970; White, 1975; Harris, 1979). In addition, maskers in this low-frequency region are among the most powerful and bothersome in terms of effects on responses to high-frequency sounds (Stevens *et al.*, 1946; Miller, 1947). Our signal frequencies, 6 and 8 kHz, are well within the acoustic spectrum of cat vocalizations as well as some of its prey's vocalizations (such as mice and rats) (Busnel, 1963). These signal frequencies are relatively high for humans, but the corresponding frequencies for humans (about an octave lower, i.e., 3 and 4 kHz) are in the range of frequencies important for speech communication (Fletcher, 1953; Licklider and Miller, 1951) and it seems likely that the hypothesis applies for these lower frequencies. Borg and Zakrisson, 1974 found sizable stapedius unmasking for frequencies down to about 2 kHz. We conclude that stapedius unmasking must operate and be important in many real world situations both in cats and humans.

The "unmasking" effect of the stapedius is likely to be important both while listening and while talking. Although stapedius contractions produced by the acoustic reflex have received the most attention in the literature, the stapedius may well be active more often *without* intense external sound. Stapedius activity is associated with vocalization, mastication, and head and body movement (Carmel and Starr, 1963; Simmons, 1964; Borg and Zakrisson, 1975a).

One way to appreciate the significance of stapedius unmasking on hearing is by looking at unmasking in terms of the difference in the detectability of a fixed tone in a fixed noise level. (We have been using the increase in signal needed to counteract the masking produced by the noise.) Changes in signal detectability are shown by receiver operating characteristic (ROC) curves obtained from the difference in the  $d'$  values and the corresponding variability in the responses with and without contractions of the stapedius. Figure 8 gives an example of the effects of stapedius contractions on the  $d'$  value of an auditory-nerve fiber's response to an 8-kHz tone masked by an 85 dB SPL low-frequency noise [Fig. 8(A)], and the calculated effects on the detectability of the tonal signal [Fig. 8(B)]. Although the 1.8 difference in  $d'$  might seem small, it indicates that the stapedius contraction produces a remarkable increase in detect-

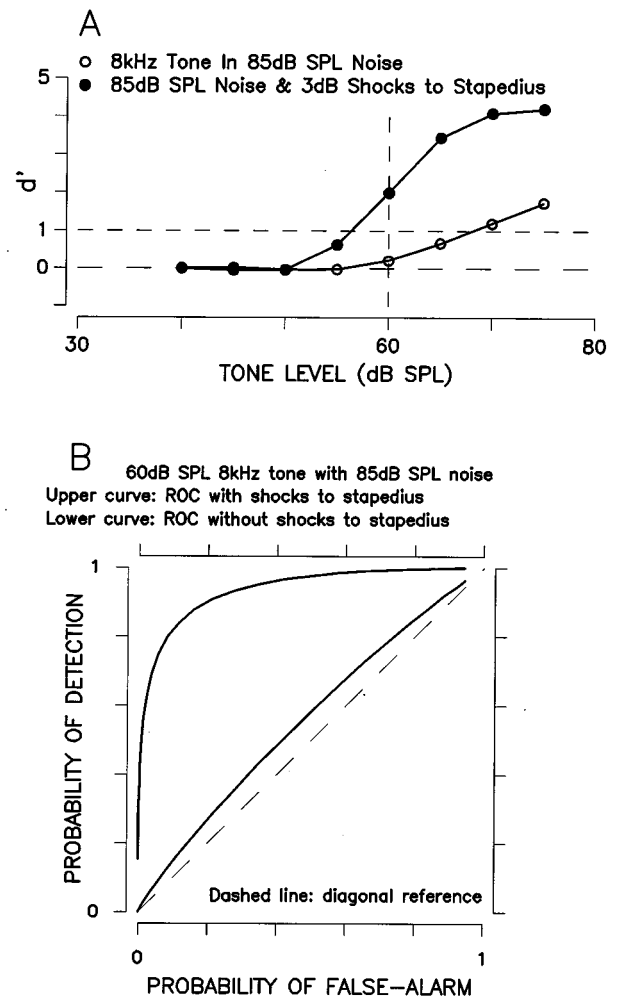


FIG. 8. Stapedius unmasking in terms of  $d'$  (A) and receiver-operating-characteristics (ROCs) (B) with and without stapedius contractions. (A)  $d'$  versus tone level functions measured with 8-kHz tones in 85 dB SPL masking noise, with and without stapedius contractions. (B) The difference in the "best possible detection performance" as seen from the difference in receiver-operating-characteristics (ROCs) with and without stapedius contractions. The ROCs were derived from the  $d'$  values at the 60 dB SPL tone level [vertical dashed line in (A)], and the sample variances of the fiber's discharge rates with noise alone and with noise+tone, both with and without stapedius shocks. The ratio  $r$  of the sample variance with noise alone over that with noise+tone was 0.987 without shocks and 0.838 with shocks. The area under each ROC curve equals the percentage correct in a two-alternative forced-choice detection task. The fiber's discharge rate was assumed to have a normal distribution in all cases. Fiber 86–93; CF=7.08 kHz, threshold at CF=4.3 dB SPL, SR=80 sp/s.

ability. For example, for a probability of false alarm of 0.1, the probability of detection increased from 0.15 to 0.82. Practically speaking, this is the difference between not detecting the tone and detecting it.

#### E. Clinical implications

The results presented here help bolster the case for preserving stapedius function in clinical situations. There is already good evidence that preserving stapedius function in stapedectomy or stapedotomy provides better speech intelligibility (Lidén *et al.*, 1964; Rasmay, 1986; Colletti and Fiorino, 1994). There might also be considerable benefit in building stapedius-like function into hearing aids (e.g., Ono

*et al.*, 1983) but some of this benefit might be blunted by growth rates of masking which are lower in patients with sensory-neural hearing loss than in normals (Murnane and Turner, 1991; Dubno and Ahlstrom, 1995).

## F. Comparison of stapedius and olivocochlear efferent effects

It is interesting to compare the effects of stapedius contractions with the effects of medial olivocochlear efferents because several putative functions of these feedback systems are similar. Both systems can be activated by sound and form acoustic reflexes which attenuate auditory-nerve responses to tones in a quiet background [see Guinan (1996) for a review of efferent physiology]. Both systems may function to reduce masking of a signal by noise, albeit in very different ways. The stapedius produces a predominantly low-frequency attenuation, no matter what the activating stimulus, and reduces the masking of responses to high-frequency sounds by low-frequency sounds. In contrast, individual medial olivocochlear efferents innervate an octave or less of cochlear length and can attenuate different frequencies selectively. When activated by sound, medial efferents attenuate responses in each frequency band according to how much sound energy is received in that frequency band. Medial efferents appear to reduce masking principally by reducing responses to low-level sounds thereby reducing the ongoing adaptation in auditory-nerve fibers and allowing these fibers to respond more vigorously to intense transients (Winslow and Sachs, 1987; Kawase *et al.*, 1993). Considering the differences in the mechanisms and frequency range of action, these two systems appear to be complementary.

## IV. CONCLUSIONS

Our results demonstrate that:

(1) Stapedius unmasking can be explained completely by a linear stapedius-produced attenuation of sound transmission through the middle ear and a nonlinear growth rate of masking for auditory-nerve fibers.

(2) Even though a contraction of the stapedius muscle produces an *attenuation* of acoustic transmission through the middle ear that primarily affects low-frequency sounds, it can strongly *enhance* responses of auditory-nerve fibers to high-frequency sounds when low- and high-frequency sounds are both present.

(3) The unmasking produced by stapedius contractions can be more than twice as large as the stapedius-induced attenuation of low-frequency sounds.

(4) Unmasking is probably one of the most important functions of the stapedius.

## ACKNOWLEDGMENTS

We thank Dr. B. Delgutte, and Dr. M. C. Liberman for comments on the manuscript and the members of the Eaton-Peabody Laboratory, particularly Dr. W. T. Peake, for help throughout this work. This work was supported by Grant No. PO1 DC00119 from the National Institute on Deafness and Other Communication Disorders, National Institutes of Health, and by a Sherman Fairchild Fellowship to XDP.

<sup>1</sup>The formula applies when the stapedius contraction does not reduce the noise below the threshold of masking. If it does, then the amount by which the noise had exceeded the threshold of masking before the stapedius contraction should be used in place of  $\Delta N$  in Eq. (1).

<sup>2</sup>The "stapedius-induced change in the middle-ear transfer function" measured in this paper is from earphone drive to cochlear response and includes both the attenuation of acoustic transmission through the middle ear and the change in sound pressure at the tympanic membrane due to the stapedius contraction changing the input impedance of the middle ear. Alternately, one could measure just the change of transmission through the middle ear. Both measures provide an equally valid test of the hypothesis as long as the same measure is used throughout. With the sound source used in this study, a stapedius contraction that produced a 15-dB low-frequency attenuation also produced an increase in sound pressure at the tympanic membrane of about 1 dB for frequencies below 1 kHz, and close to zero dB at higher frequencies.

<sup>3</sup>The usefulness of data from subjects with Bell's Palsy was called into question by Wormald *et al.* (1995) who argued that Bell's Palsy may involve the auditory nerve as well as the facial nerve. If so, then perceptual deficits from Bell's Palsy may not be due entirely to the lack of an acoustic stapedius reflex. However, their tests were flawed because, among other things, they compared normal speech and speech filtered to simulate a paralyzed stapedius muscle (frequencies below 1 kHz emphasized by 30 dB) at equal hearing levels instead of at equal levels of the high-frequency components (the way the Bell's Palsy patients would hear the speech). Thus Wormald *et al.* (1995) do not present a convincing case that would make us reinterpret the data of Borg and Zakrisson, (1974).

Borg, E. (1968). "A quantitative study of the effect of the acoustic stapedius reflex on sound transmission through the middle ear of man," *Acta Oto-Laryngol.* **66**, 461–472.

Borg, E., and Zakrisson, J.-E. (1973). "Stapedius reflex and speech features," *J. Acoust. Soc. Am.* **54**, 525–527.

Borg, E., and Zakrisson, J.-E. (1974). "Stapedius reflex and monaural masking," *Acta Oto-Laryngol.* **78**, 155–161.

Borg, E., and Zakrisson, J.-E. (1975a). "The activity of the stapedius muscle in man during vocalization," *Acta Oto-Laryngol.* **79**, 325–333.

Borg, E., and Zakrisson, J.-E. (1975b). "The stapedius muscle and speech perception," *Symp. Zool. Soc. London* **37**, 51–68.

Busnel, R. G., ed. (1963). *Acoustic Behavior of Animals* (Elsevier, New York).

Carmel, P. W., and Starr, A. (1963). "Acoustic and non-acoustic factors modifying middle-ear muscle activity in walking cats," *J. Neurophysiol.* **26**, 598–616.

Colletti, V., and Fiorino, F. G. (1994). "Stapedotomy with stapedius tendon preservation: technique and long-term results," *Otolaryngol-Head-Neck Surg.* **111**, 181–188.

Costalupes, J. A. (1983). "Broadband masking noise and behavioral pure-tone thresholds in cats," *J. Acoust. Soc. Am.* **74**, 758–764.

Delgutte, B. (1990). "Two-tone rate suppression in auditory-nerve fibers: Dependence on suppressor frequency and level," *Hearing Res.* **49**, 225–246.

Dorman, M. F., Lindholm, J. M., Hannley, M. T., and Leek, M. R. (1987). "Vowel intelligibility in the absence of the acoustic reflex: performance-intensity characteristics," *J. Acoust. Soc. Am.* **81**, 562–564.

Dubno, J. R., and Ahlstrom, J. B. (1995). "Growth of low-pass masking of pure tones and speech for hearing-impaired and normal-hearing listeners," *J. Acoust. Soc. Am.* **98**, 3113–3124.

Egan, J. P., and Hake, H. W. (1950). "On the masking pattern of a simple auditory stimulus," *J. Acoust. Soc. Am.* **22**, 622–630.

Fletcher, H. (1953). *Speech and Hearing in Communication* (Van Nostrand, Princeton, NJ).

Geisler, C. D., and Sinex, D. G. (1980). "Responses of primary auditory fibers to combined noise and tonal stimuli," *Hearing Res.* **3**, 317–334.

Guinan, Jr., J. J. (1996). "The Physiology of Olivocochlear Efferents," in *The Cochlea*, edited by P. J. Dallos, A. N. Popper, and R. R. Fay (Springer-Verlag, New York), pp. 435–502.

Guinan, Jr., J. J., and McCue, M. P. (1987). "Asymmetries in the acoustic reflexes of the cat stapedius muscle," *Hearing Res.* **26**, 1–10.

Harris, C. M. E. (1979). *Handbook of Noise Control* (McGraw-Hill, New York).

Joseph, M. P., Guinan, Jr., J. J., Fullerton, B. C., Norris, B. E., and Kiang, N. Y. S. (1985). "Number and distribution of stapedius motoneurons in cats," *J. Comp. Neurol.* **232**, 43–54.

- Kawase, T., Delgutte, B., and Liberman, M. C. (1993). "Anti-masking effects of the olivocochlear reflex, II: Enhancement of auditory-nerve response to masked tones," *J. Neurophysiol.* **70**, 2533–2549.
- Kiang, N. Y. S., and Moxon, E. C. (1974). "Tails of tuning curves of auditory-nerve fibers," *J. Acoust. Soc. Am.* **55**, 620–630.
- Kryter, K. D. (1970). *The Effects of Noise on Man* (Academic, New York).
- Licklider, J. C. R., and Miller, G. A. (1951). "The perception of speech," in *Handbook of Experimental Psychology*, edited by S. S. Stevens (Wiley, New York), pp. 1040–1074.
- Lidén, G., Nordlund, B., and Hawkins, J. E. (1964). "Significance of the stapedius reflex for the understanding of speech," *Acta Oto-Laryngol. Suppl.* **188**, 275–279.
- Miller, G. A. (1947). "The masking of speech," *Psychol. Bull.* **44**, 105–129.
- Möllner, A. R. (1962). "Acoustic reflex in man," *J. Acoust. Soc. Am.* **34**, 1524–1534.
- Möllner, A. R. (1965). "An experimental study of the acoustic impedance of the middle ear and its transmission properties," *Acta Oto-Laryngol.* **60**, 129–149.
- Murnane, O., and Turner, C. W. (1991). "Growth of masking in sensorineural hearing loss," *Audiology* **30**, 275–285.
- Ono, H., Kanzaki, J., and Mizoi, K. (1983). "Clinical results of hearing aid with noise-level-controlled selective amplification," *Lancet* **22**, 494–515.
- Pang, X. D. (1988). "Effects of stapedius-muscle contractions on masking of tone responses in the auditory nerve," Sc. D. thesis, MIT, Cambridge, MA.
- Pang, X. D., and Guinan, Jr., J. J. (1997). "Growth rate of simultaneous masking in cat auditory-nerve fibers: Relationship to the growth of basilar-membrane motion and the origin of two-tone suppression," *J. Acoust. Soc. Am.* **102**, 3564–3575.
- Pang, X. D., and Guinan, Jr., J. J. (unpublished).
- Pang, X. D., and Peake, W. T. (1986). "How do contractions of the stapedius muscle alter the acoustic properties of the ear?," in *Peripheral Auditory Mechanisms*, edited by J. B. Allen *et al.* (Springer-Verlag, New York), pp. 36–43.
- Rabinowitz, W. M. (1977). "Acoustic-reflex effects on the input admittance and transfer characteristics of the human middle-ear," Ph. D. thesis, MIT, Cambridge, MA.
- Rajan, R., and Johnstone, B. M. (1983). "Efferent effects elicited by electrical stimulation at the round window of the guinea pig," *Hearing Res.* **12**, 405–417.
- Rasmy, E. (1986). "Stapedius reflex after stapedectomy with preservation of the stapedius tendon," *J. Laryngol. Otol.* **100**, 512–527.
- Simmons, F. B. (1964). "Perceptual theories of middle ear muscle function," *Ann. Otol. Rhinol. Laryngol.* **73**, 724–740.
- Stevens, S. S., Miller, J., and Truscott, I. (1946). "The masking of speech by sine waves, square waves, regular and modulated pulses," *J. Acoust. Soc. Am.* **18**, 418–424.
- Teig, E. (1973). "Differential effect of graded contraction of middle ear muscles on the sound transmission of the ear," *Acta Physiol. Scand.* **88**, 382–391.
- Vacher, S. R., Guinan, Jr., J. J., and Kobler, J. B. (1989). "Intracellularly labeled stapedius-motoneuron cell bodies in the cat are spatially organized according to their physiologic responses," *J. Comp. Neurol.* **289**, 401–415.
- Watson, C. S. (1963). "Masking of tones by noise for cat," *J. Acoust. Soc. Am.* **35**, 167–172.
- Wegel, R. L., and Lane, C. E. (1924). "The auditory masking of one pure tone by another and its probable relation to the dynamics of the inner ear," *Phys. Rev.* **23**, 266–285.
- Winslow, R. L., and Sachs, M. B. (1987). "Effect of electrical stimulation of the crossed olivocochlear bundle on auditory nerve response to tones in noise," *J. Neurophysiol.* **57**, 1002–1021.
- White, F. A. (1975). *Our Acoustic Environment* (Wiley, New York).
- Wormald, P. J., Rogers, C., and Gatehouse, S. (1995). "Speech discrimination in patients with Bell's palsy and a paralyzed stapedius muscle," *Clin-Otolaryngol.* **20**, 59–62.

# Frequency-dependent enhancement of basilar membrane velocity during olivocochlear bundle stimulation

David F. Dolan<sup>a)</sup>

*Kresge Hearing Research Institute, University of Michigan Medical School, Ann Arbor, Michigan 48109-0506*

Meng He Guo

*Department of Otolaryngology, Xijing Hospital, Xi'An ShaanXi 710032, People's Republic of China*

Alfred L. Nuttall

*Kresge Hearing Research Institute, University of Michigan Medical School, Ann Arbor, Michigan 48109-0506 and Oregon Hearing Research Center, Oregon Health Sciences University, Portland, Oregon*

(Received 5 February 1997; revised 1 August 1997; accepted 5 September 1997)

Basilar membrane (BM) velocity responses were measured in the presence of olivocochlear bundle (OCB) stimulation. Frequency threshold tuning curves (FTCs) were derived from tone-evoked input-output (I/O) functions. Efferent nerve activation produced decreases in velocity amplitude for frequencies around best frequency (BF) at low stimulus levels with little or no effect for stimuli well below the BF. A level-dependent efferent reduction/enhancement of BM velocity was found for certain stimulus frequencies above the BF. Efferent activation either had no effect or caused small reductions in the velocity response produced by low level sound, whereas, at higher stimulus levels, efferent activation *increased* the velocity response. The derived FTCs, therefore, showed criterion-dependent changes with efferent activation. For low BM criterion velocities, FTCs showed the classic desensitization of the tip region without a shift of BF. Some BM velocity criterion values showed FTCs with an expanded high-frequency response area, also without a shift of BF. The results suggest that the effect of OCB activation changes the gain of the voltage-dependent outer hair cell motility such that BM velocity response near BF is decreased while increasing the response for tones well above BF. © 1997 Acoustical Society of America. [S0001-4966(97)06112-2]

PACS numbers: 43.64.Me, 43.64.Kc 43.64.Ri [RDF]

## INTRODUCTION

The source of efferent innervation of the mammalian cochlea is bilaterally from lateral and medial locations within the brainstem (Rasmussen, 1946; Warr, 1975, 1978; Warr and Guinan, 1979; Guinan *et al.*, 1983; Robertson, 1985). The efferent innervation is divided into two systems based on site of origin within the brainstem and axon destination within the organ of Corti (Warr and Guinan, 1979; Guinan *et al.*, 1983). The lateral system gives rise to the small-diameter, unmyelinated neurons that project primarily to the afferent terminals under the inner hair cell. The medial brainstem gives rise to the large diameter, myelinated fibers that terminate directly on the outer hair cell (OHC) (Altschuler and Fex, 1986). Electrical activation of the medial system, the crossed olivocochlear bundle (OCB) at the floor of the fourth ventricle, causes a decrease in the endocochlear potential (Fex, 1967) and reduces the cochlear whole-nerve action potential (CAP) (Galambos, 1956) and the underlying discharge rate of auditory nerve fibers (Wiederhold, 1970). OCB activation alters the level of the acoustic distortion products recorded in the ear canal (Mountain, 1980; Siegel and Kim, 1982; Guinan, 1986; Long, 1989; Mott *et al.*, 1989; Whitehead *et al.*, 1991; Kujawa *et al.*, 1992). The re-

duction of neural output can be accounted for by an efferent-induced reduction of mechanical stimulation of the inner hair cell (IHC) (Brown and Nuttall, 1984).

More recently, the effect of OCB stimulation has been shown to reduce the basilar membrane velocity and displacement responses (Dolan and Nuttall, 1994; Murugasu and Russell, 1996). Dolan and Nuttall (1994) showed that the effect of OCB stimulation reduced the velocity response of the basilar membrane to transient (click) stimulation, while Murugasu and Russell (1996) showed reductions in BM displacement responses to tonal stimulation. The effects of OCB stimulation on the basilar membrane, auditory nerve, and IHC responses are frequency specific in that the responses to acoustic stimuli at and near the characteristic frequency (CF) are affected most. In general, the effects are restricted to low stimulus intensities (Dolan and Nuttall, 1994; Murugasu and Russell, 1996; Wiederhold, 1970; Brown and Nuttall, 1984). The exception to this general rule of effects being confined to low-level responses has been reported by Guinan and colleagues (Gifford and Guinan, 1983; Guinan and Gifford, 1988; Guinan and Stankovic, 1996). They showed that OCB activation can reduce auditory nerve fiber discharge rates to tonal stimulation well above threshold. The driven discharge rate of auditory nerve fibers with low or medium spontaneous discharge rates can be reduced by OCB activation up to 100 dB SPL for tones presented at CF.

<sup>a)</sup>Electronic mail: ddolan@umich.edu

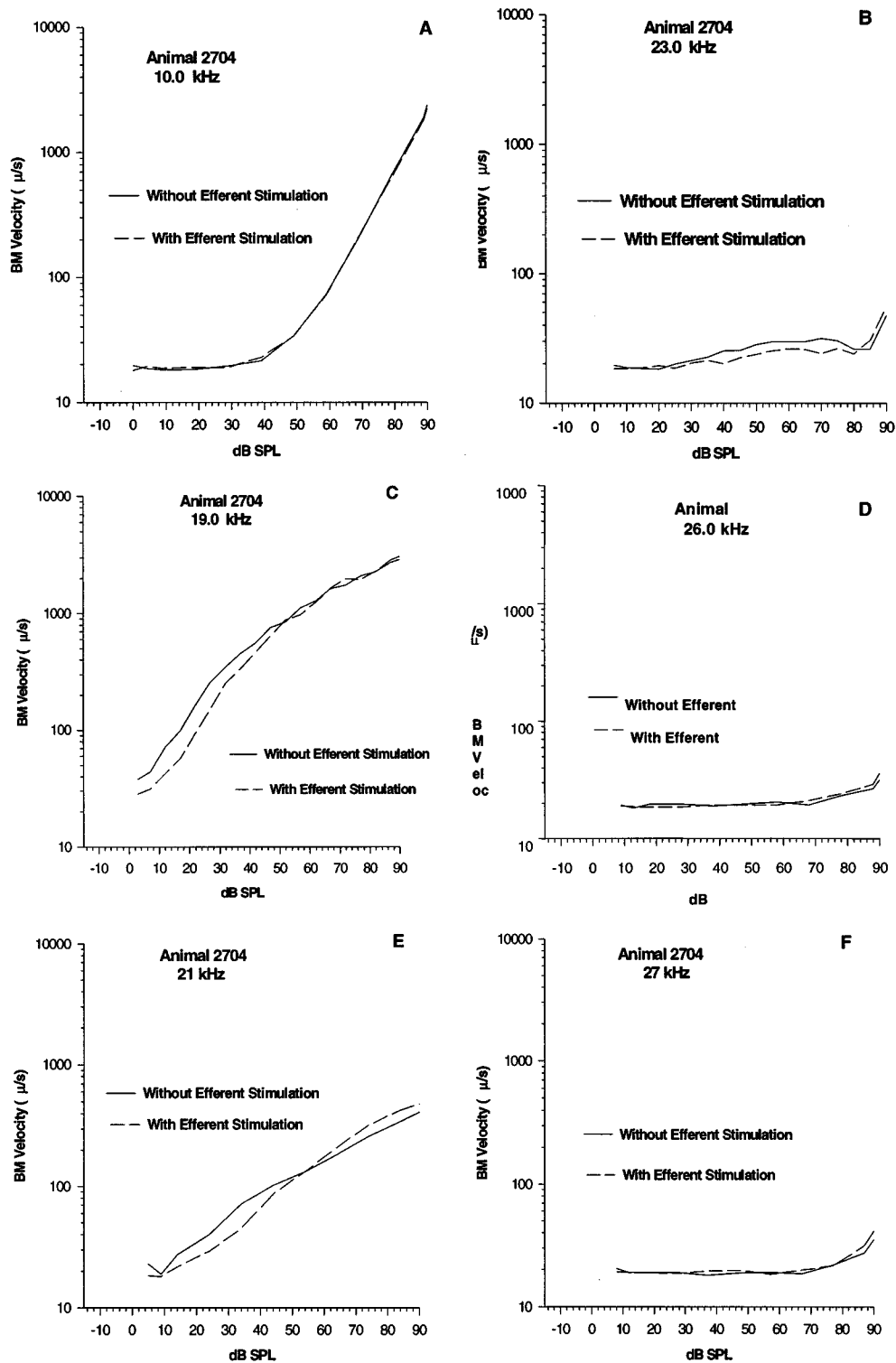


FIG. 1. (A)–(F) Selected basilar membrane velocity I/O functions to tones below (A), near (C) and above (B,D,E,F) best frequency are shown for animal 2704. The OCB stimulation (dashed line) has little effect for tones below best frequency (A) compared to the control function (solid line). Near the best frequency, OCB activation reduces the velocity response for tones near threshold (C). For tones well above best frequency, OCB activation can decrease the velocity magnitude at low stimulus levels and increase the values at high stimulus levels (E). At even higher stimulus frequencies OCB stimulation causes small increases in velocity amplitude (B,D,F).

In this study we have found another phenomenon related to higher level sound stimulation. The OCB activation can have effects on BM velocity responses at stimulus levels well above threshold. The effects of OCB stimulation at the best tonotopic frequency are greatest at low stimulus levels. The effects of OCB activation can increase the BM velocity

response at high stimulus levels for frequencies well above the tonotopic best frequency.

## I. METHODS

Pigmented guinea pigs, with body weights between 200 and 400 g, were anesthetized xylazine (5 mg/kg) and ket-



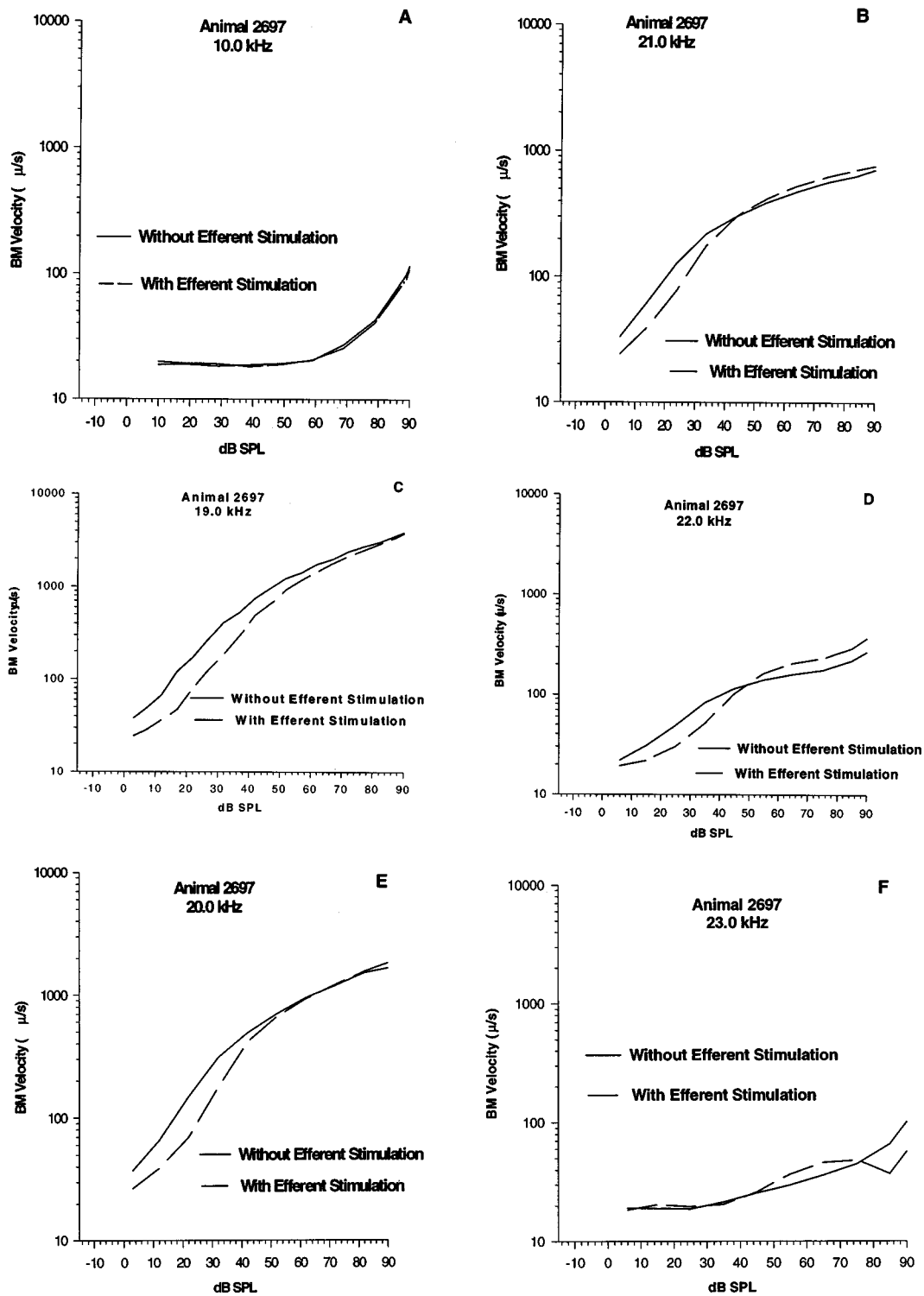


FIG. 2. (A)–(F) Selected basilar membrane velocity I/O functions to tones below (A), near (C,E) and above (B,D,E,F) best frequency are shown for animal 2697. OCB stimulation (dashed line) has little effect for tones below best frequency (A) compared to the control function (solid line). Near the best frequency, OCB activation reduces the velocity response for tones near threshold (C,E). For tones above best frequency, OCB activation can decrease the velocity magnitude at low stimulus levels and increase the values at high stimulus levels (B,D). At even higher stimulus frequencies OCB stimulation causes small increases in velocity amplitude at moderate intensities and decreases the response at higher levels (F).

amine (30 mg/kg) and placed in a head holder. The anesthetic state was maintained with additional doses given approximately every hour after the initial dose. The EKG was monitored and rectal temperature was maintained near 37° with a heating blanket. To preserve cochlear sensitivity, a

head holder heater and heat lamp were used to maintain cochlear temperature near body temperature (Brown *et al.*, 1983; Shore and Nuttall, 1985).

A postauricular incision exposed the bulla. The tensor tympani and stapedius muscles were cut. An electrode was

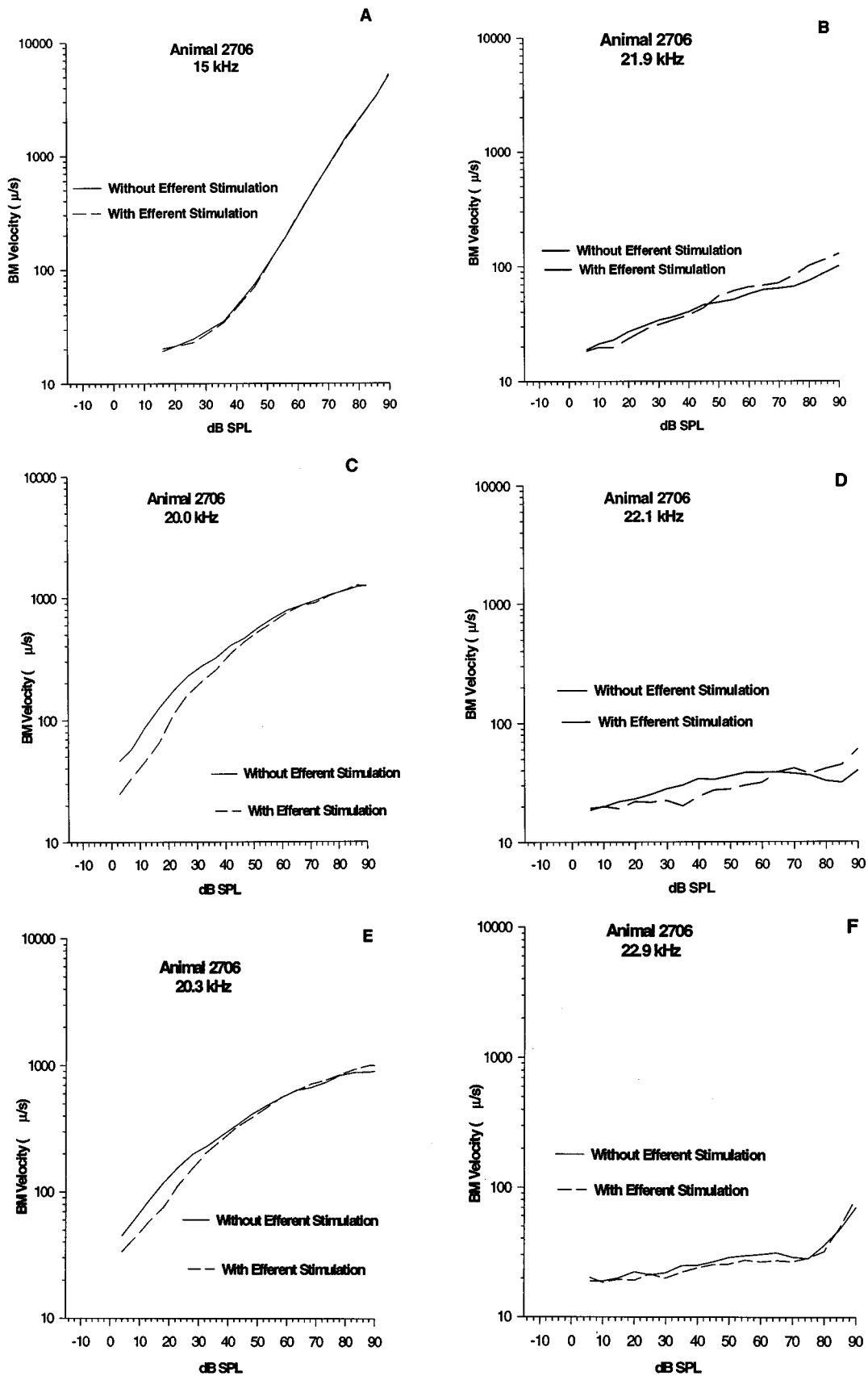


FIG. 3. (A)–(F) Selected basilar membrane velocity I/O functions to tones below (A), near (C) and above (B,D,E,F) best frequency are shown for animal 2706. The OCB stimulation (dashed line) has little effect for tones below best frequency (A) compared to the control function (solid line). Near the best frequency, OCB activation reduces the velocity response for tones near threshold (C,E). For tones above best frequency, OCB activation can decrease the velocity magnitude at low stimulus levels and increase the values at high stimulus levels (B,D,F).

cemented on the round window to record CAPs. Tone bursts (1.0-ms rise/fall time, 15-ms duration) ranging in frequency from 2.0–40.0 kHz were delivered from a  $\frac{1}{2}$ -in. condenser microphone (B & K) to assess auditory sensitivity. The microphone was housed in a custom-designed speculum and inserted into the external auditory meatus as a closed field. The CAP was measured after signal averaging, using custom software with a PC-AT-type computer (512 samples, 25- $\mu$ s bin width, 64 responses).

The animal was then rotated and prepared for stereotaxic placement (Brown and Nuttall, 1984) of a bipolar electrode (insulated 32-gauge stainless steel wire) into the floor of the fourth ventricle where the OCB crosses between the genua of the facial nerve. The stimulating electrode was insulated to the cut end, with a tip separation of approximately 1 mm. Electrical stimuli, generated by the computer, were bipolar pulses (0.2 ms each phase) delivered at a rate of 250/s for 250 ms. Stimulating current values were measured with a 1.0-kOhm resistor in series with the electrode and ranged from 50–200  $\mu$ A. The animals were then paralyzed with curare (0.3 mg, i.m.). Each animal was artificially respired via intubation of the trachea. The acoustic and efferent activation epoch rate was 1/s. The stimulus to evoke the CAP was temporally placed 10–15 ms after the offset of the OCB activation.

The optimal placement of the bipolar stimulating electrode was judged successful by the effect of OCB activation on CAP response to a tone burst (10 kHz) set 10–15 dB above threshold. The typical effect of OCB activation on the CAP to this stimulus is a complete reduction to baseline.

The bipolar electrode was securely cemented to the head and the animal rotated. A small hole was carefully made in the bone over scala tympani of the first cochlear turn (Brown *et al.*, 1983). The mechanical activity (velocity) of the BM was measured using a laser Doppler velocimeter (LDV) (Polytec Corp. OFV 1102). Laser reflections from gold-coated glass microbeads (10–30  $\mu$ m diameter) were measured with the LDV through a compound microscope. A dissecting microscope was used to insure that the microbeads were placed on the BM. The locations of the microbeads on the BM ranged radially between the spiral osseous lamina and the outer hair cells. Tones (300 ms) for BM velocity responses were controlled by a microcomputer using Wilsonics (PATT digital) attenuators and tone switches (BSIT). Tone intensity was increased in eight to ten steps of 10 dB each from the lowest to highest sound levels. The epoch rate was 1/s. For each I/O function, the OCB was stimulated continuously for 10–12 s. The electrical stimulation of the OCB was controlled by an independent microcomputer. After each I/O function, the OCB stimulation was terminated for 2–3 mins. Signals from the LDV were sent to a lock-in amplifier (Stanford, model SR530) (Nuttall *et al.*, 1991). To derive BM velocity I/O functions, the output of the lock-in amplifier was sent to the input of an A/D converter where custom software plotted the response amplitudes. The I/O functions were then analyzed off line.

## II. RESULTS

The results presented here are from three of the four animals in which the enhancement phenomenon was observed. The enhancement was observed in animals in which hearing sensitivity was maintained through the experimental procedures for frequencies at the tonotopic location. Loss of sensitivity resulted in a reduction of any OCB-induced effect. Figures 1–3 show representative I/O BM velocity output functions at frequencies below, near, and above the BF for the given BM location. In each figure, the solid line and dashed lines represent the BM velocity without and with OCB stimulation, respectively. For each animal, the OCB effect on frequencies below the BF has little or no effect on the I/O function at any stimulus level [Figs. 1(A), 2(A), and 3(A)]. For frequencies at or near the BF the OCB activation reduces the BM velocity response over a 30–40-dB range of stimulus level [Figs. 1(C), 2(C) and (E), and 3(C)]. For each animal, stimulus frequencies well above the best tonotopic frequency are affected differently depending on stimulus intensity. At low levels, the OCB activation either has no effect or slightly reduces the velocity response [Figs. 1(B), 2(B) and (F), and 3(B), (D), and (F)]. At high stimulus intensities, OCB activation increases the velocity response [Figs. 1(B), (D), (E), and (F), 2(B), (D), and (F), and 3(B), (D), (E), and (F)]. The intensity level at which the enhancement occurs varies across the three animals; in general, the enhancement was only observed above 50 dB SPL.

Tuning curves generated from the I/O functions show OCB stimulation can alter the high-frequency slope of the tuning curve. Figures 4 and 5 show threshold tuning curves for animal 2706 (data from Fig. 3) and 2697 (data from Fig. 2). Each figure shows an isovelocity tuning curve at a low to moderate velocity response criterion level. IsovLOCITY tuning curves, with (solid line) and without (dashed line) OCB stimulation, are shown for velocity criterion values of 35 and 30  $\mu$ s. In each figure, OCB stimulation broadens the high-frequency slope of the tuning curve. The OCB-induced in-

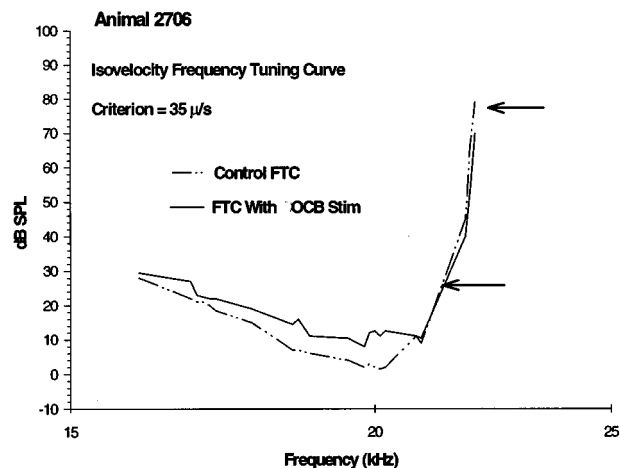


FIG. 4. Isovelocity tuning curve (criterion=35  $\mu$ s) from animal 2706. The OCB activation reduces the tip of the tuning curve and, to a lesser extent, velocity responses below best frequency. Above best frequency, OCB activation actually broadens the response area. The arrows indicate area of the expanded high-frequency region.

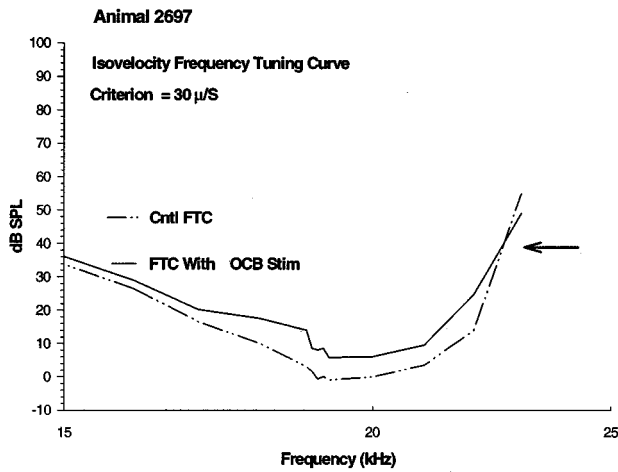


FIG. 5. This figure is similar to Fig. 4 except the data is from a different animal (2697). The velocity criterion is  $30 \mu/s$ . The OCB activation reduces the tip of the tuning curve and, to a lesser extent, velocity responses below best frequency. Above best frequency, OCB activation causes a slight broadening of the response area. The arrow indicates area of the expanded high-frequency region.

crease in the high-frequency slope is restricted to moderate level criterion. No significant change in the high frequency slope was observed for tuning curves derived at very low or very high criterion values.

In general, tuning curves showed no enhancement when using higher criterion levels. Figure 6(A)–(C) shows tuning curves generated from a  $100\text{-}\mu/s$  velocity response criterion. Using this criterion level, two tuning curves from different animals [Fig. 6(A) and (B)] showed no enhancement. The tuning curve from animal 2706 [Fig. 6(C)] did show a large enhancement at this criterion level.

Figure 7(A)–(C) shows the shift in velocity, in dB, induced by OCB stimulation as a function of velocity amplitude for several stimulus frequencies for three animals. A shift of the velocity I/O functions to the right (a reduction in velocity response) is indicated by negative values and is restricted to frequencies near the tonotopic best frequency. A shift to the left (an increase in velocity response) is indicated by positive values and occurs for frequencies above best frequency. The enhancement, in general, is gone at the highest stimulus intensities. Some enhancement remains at the highest stimulus levels for restricted frequencies.

Strychnine, known to block the effects of efferent activity (Bobbin and Konishi, 1974; Klinke and Galley, 1974), was given (1.0 mg/kg, i.p.) to one animal (Fig. 8) that showed a clear enhancement as described above. The velocity response was measured directly from a chart recorder (CNTL) during OCB stimulation and 1 h after administration of strychnine. Strychnine eliminates the OCB-induced reduction of BM velocity responses for frequencies near BF as well as the enhancement of velocity responses for frequencies above BF.

One concern in these experiments is the duration of the OCB stimulation. In these experiments the BM velocity responses were measured while the OCB was stimulated continuously for 10–12 s. The effect of this duration of OCB stimulation on repeated measurement of BM velocity is

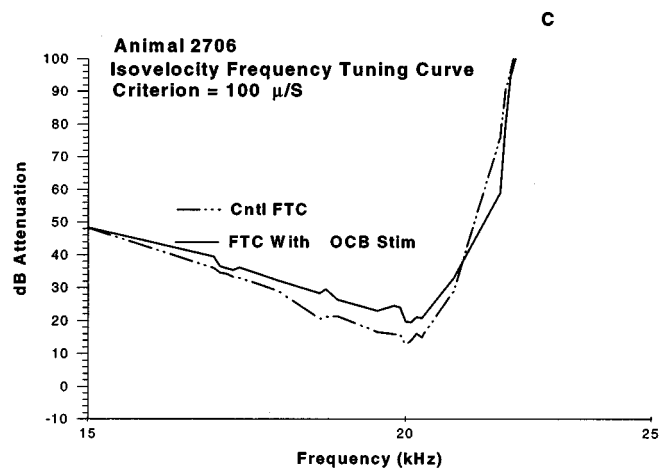
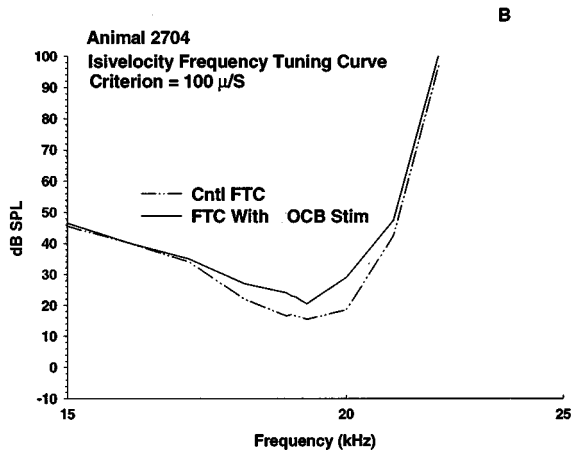
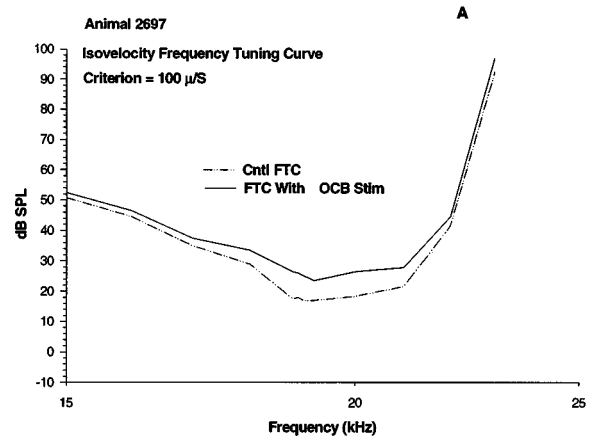


FIG. 6. (A)–(C) These figures are similar to Figs. 3–5 except that the velocity criterion for the tuning curve is  $100 \mu/s$ . In general, at this response criterion, OCB activation does not increase the BM velocity response. The result is a narrowing of the tuning curve (A and B). However, at this response criterion, OCB activation did cause a slight broadening of the BM response area for animal 2706 (C).

shown in Fig. 9. The I/O functions measured within 1 min of the termination of the previous OCB stimulation showed no effect. None of the velocity measurements in this study were obtained at time periods less than 1 min from the previous OCB stimulation. The duration of OCB stimulation used in this study had no effect on repeated measures of the observed enhancement.

Table I(A–C) lists the BF, threshold,  $Q(10 \text{ dB})$ ,  $Q(20$

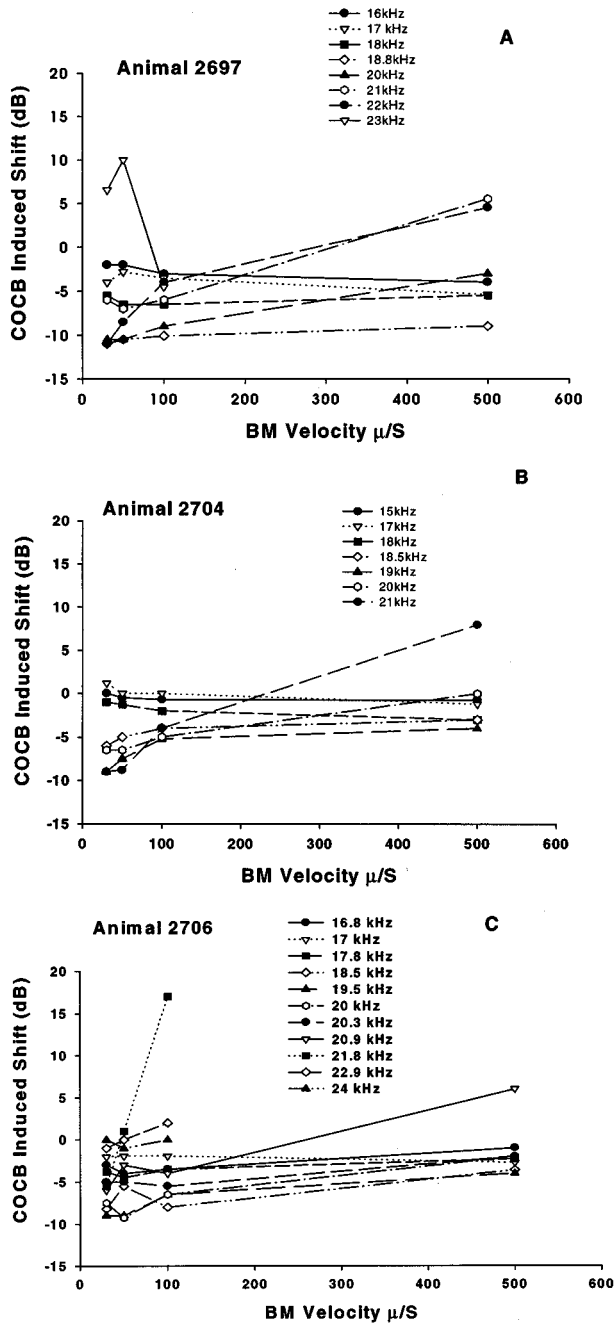


FIG. 7. (A)–(C) These figures show the OCB-induced shift of the basilar membrane velocity I/O function for three different animals. Negative numbers indicates a shift of the I/O function to the right (decrease in velocity) whereas an increase in velocity (a shift of the I/O function to the left) is shown as positive numbers.

dB),  $Q(30\text{ dB})$ , and  $Q(40\text{ dB})$  for isovelocity tuning curve condition for each animal.  $Q$  is defined as  $\text{BF}/\text{bandwidth at } X\text{ dB}$ . The OCB activation increased the BF for all criterion values for animal 2706. In general, OCB stimulation did not change the BF. The majority of decreases in  $Q$  with OCB activation are for the  $Q$  values above  $Q(10)$ . This is consistent with the earlier observation that the velocity enhancement occurs at moderate to high intensities.

### III. DISCUSSION

To the best of our knowledge, the enhancement phenomenon reported here has not been described previously. The

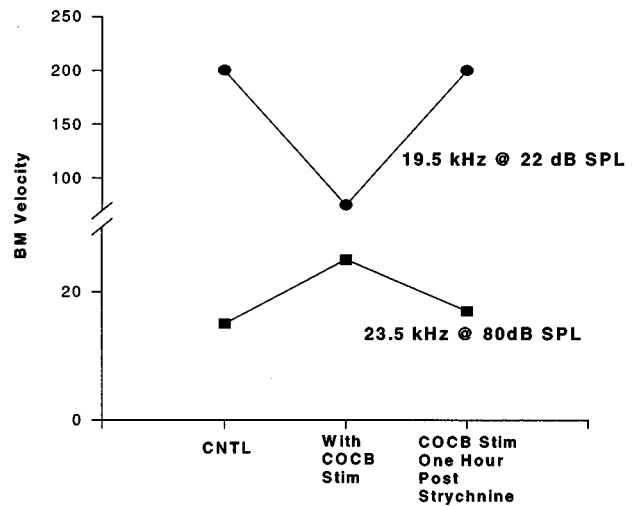


FIG. 8. This figure shows the uncorrected BM velocity amplitudes read from a chart recorder before and after systemic application of strychnine. Strychnine eliminates the OCB-induced reduction in BM velocity for tones near best frequency and the enhancement of BM velocity for a tone well above best frequency.

absence of a similar description of this enhancement phenomenon in auditory nerve fiber responses suggests that it may be specific either to the guinea pig BM response or to the extreme high-frequency region of the cochlea. The response measure used in this study, BM velocity, is restricted to measurements at a location with tonotopic BF of 17–20 kHz. The enhancement of velocity responses occurred for frequencies between 21–27 kHz. It is possible that a similar phenomenon occurs in auditory nerve fibers but has been missed because of the relatively few fibers studied with high characteristic frequencies or a lack of detailed study of the high-frequency slope. A similar study (Murugasu and Russell, 1996) to that reported here did not report any enhancement of BM velocity in the presence of OCB stimulation. In their study, most measurements were made near 15 kHz. The highest frequency I/O function reported is 18 kHz (Muru-

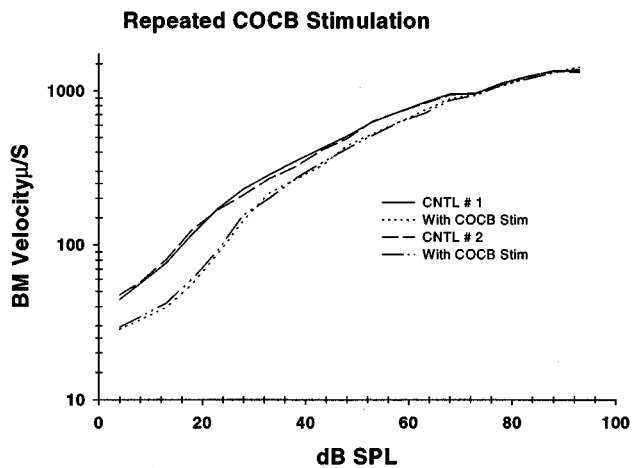


FIG. 9. The unusually long duration of OCB stimulation used in these experiments has no effect on repeated measures of the BM velocity I/O functions. The second control I/O and OCB conditions were each measured less than 1 min after the previous electrical stimulation of the OCB.

TABLE I. (A–C) Each table lists the results for a different animal. The best frequency, threshold at best frequency for the control, and OCB conditions are given.  $Q_{(x \text{ dB})}$  is given for 10, 20, 30, and 40 dB above threshold. \*\* indicates an increase in  $Q$  as a result of OCB stimulation. There is a tendency for OCB stimulation to increase the sharpness of tuning for the  $Q(10)$  condition for each animal. \* indicates that there was insufficient data to compute a data point.

A. Animal 2704	FTC 30 $\mu/s$	FTC 40 $\mu/s$	FTC 50 $\mu/s$	FTC 60 $\mu/s$	FTC 100 $\mu/s$
BF Control	19.2	19.2	19.2	19.1	19.2
Threshold-3 dB SPL					
BF OCB	19.2	19.2	19.2	19.2	19.2
Threshold-4 dB SPL					
$Q(10)$ Control	8.53	7.97	7.13	6.9	7.52
OCB	6.99	7.06	7.16**	7.14**	7.74**
$Q(20)$ Control	4.77	5.01	4.54	4.41	4.85
OCB	3.7	3.82	4.04	3.87	4.07
$Q(30)$ Control	3.25	3.37	3.2	3.14	3.17
OCB	2.83	2.81	2.81	2.76	2.83
$Q(40)$ Control	2.53	2.38	2.57	2.56	2.56
OCB	2.46	6.65**	2.45	2.44	2.46
B. Animal 2697	FTC 30 $\mu/s$	FTC 40 $\mu/s$	FTC 50 $\mu/s$	FTC 60 $\mu/s$	FTC 100 $\mu/s$
BF Control	19.2	19.2	19.1	19.1	19.1
Threshold-1 dB SPL					
BF OCB	19.2	19.2	19.1	19.1	19.2
Threshold 5.7 dB SPL					
$Q(10)$ Control	5.63	6.1	4.81	6.19	6.1
OCB	6.4**	6.1	5.5**	5.85	5.75
$Q(20)$ Control	3.57	3.76	3.91	3.74	3.83
OCB	3.39	3.37	4.4**	3.41	3.42
$Q(30)$ Control	2.86	3.01	2.99	2.99	2.97
OCB	2.59	2.63	2.67	2.68	2.69
$Q(40)$ Control	2.3	2.73	2.42	2.42	2.4
OCB	2.08	2.12	2.2	2.19	2.2
C. Animal 2706	FTC 30 $\mu/s$	FTC 40 $\mu/s$	FTC 50 $\mu/s$	FTC 60 $\mu/s$	FTC 100 $\mu/s$
BF Control	19.8	19.8	19.8	19.8	20.0
Threshold-4.5 dB SPL					
BF OCB	20.3	20.3	20.3	20.3	20.1
Threshold 1.5 dB SPL					
$Q(10)$ Control	7.57	6.39	8.1	7.88	8.66
OCB	8.2**	7.8**	7.5	7.12	9.44**
$Q(20)$ Control	4.67	3.48	4.9	4.9	5.35
OCB	4.25	4.4**	4.4	3.59	4.65
$Q(30)$ Control	3.27	3.48	3.48	*	*
OCB	3.03	3.08	3.02	*	*
$Q(40)$ Control	*	*	*	*	*
OCB	*	*	*	*	*

gasu and Russell, 1996, Fig. 3). As stated above, only frequencies well above BF showed the enhancement. The OCB-induced alterations of the tuning curves reported here was only observed for velocity criteria well above threshold and frequencies well above BF. It is likely that no enhancement was observed in Murugasu and Russell (1996) due to the fact that their isoresponse tuning curves were generated with a 2-nm criterion. In their study, the 2-nm criterion was just above the noise floor of 1–1.5 nm. All enhancement observed in this report occurred at levels well above the noise floor.

There is other evidence from this laboratory, though not described, showing enhancement of the high-frequency slope of tuning curves recorded from IHCs (Brown and Nuttall, 1984). The measurement technique of recording from IHCs is similar to the BM measurements reported here in that they are made at a similar location in the cochlea. Brown and Nuttall (1984) showed one tuning curve (their Figure 9B)

with an expanded high-frequency slope in the presence of OCB stimulation. The tuning curve reported in their study (Brown and Nuttall, 1984) was derived from I/O functions to tonal stimulation. The tuning curve is based on the acoustic stimulus level that evoked a 2-mV d.c. receptor potential. It is possible that higher criterion values, comparable to those used in the present study, may have shown the expansion of the high-frequency slope in other IHCs.

How can OCB-induced enhancement of the velocity response occur? There are at least two possibilities that are associated with the recipient of the medial efferent neural system: the OHC.

The role that the OHC plays in the efferent-induced effects is probably based on the dynamic nature of this receptor cell. The OHC has a major role in determining the active micromechanical response of the cochlea. The effects of OCB activation are mediated through the OHC. Acetylcholine (ACh) is thought to be the neurotransmitter released by

the medial efferent fibers (see Eybalin, 1993, for review). The ACh receptor is unusual in that neither nicotine nor muscarine activates the receptor but the receptor is blocked by nicotinic and muscarinic antagonists (Housley and Ashmore, 1991; Erostequi *et al.*, 1994). A likely candidate for the ACh receptor is the  $\alpha 9$  subunit cloned by Elgoyhen *et al.* (1994). The pharmacological characteristics of the  $\alpha 9$  subunit are similar to the cholinergic receptor in the OHCs in terms of the order of receptor antagonist potency (Sridhar *et al.*, 1995).

A speculative notion is that two different ACh receptors exist in the OHC (for a review see Guth and Norris, 1996). Briefly, one receptor is described as strychnine-preferring, nicotiniclike ionotropic, and mediates hair cell hyperpolarization (Guth *et al.*, 1994). The other receptor is atropine-preferring and muscariniclike. The receptor is metabotropic and mediates depolarization in the hair cell (Guth *et al.*, 1986; Norris *et al.*, 1988). In the vestibular system, there is evidence for the two different receptor types based on the opposite responses of the vestibular nerve fibers to ACh application. ACh caused an increase in afferent semicircular canal fibers and reduction in frog saccule afferent fibers (Guth *et al.*, 1986; Norris *et al.*, 1988; Guth *et al.*, 1994). Although no evidence exists that efferent activation facilitates auditory nerve activity in mammals, there is strong evidence that the same receptors found on the frog semicircular canal hair cells exist in the cochlear OHCs. A comparison of the effects of application of ACh on frog vestibular afferents is difficult because in the mammalian system, the lateral and medial components of the efferent system provide dual innervation of the cochlea. Although the mechanisms underlying the effects of ACh on the OHCs is not completely understood, ACh appears to hyperpolarize the OHC by activating a  $\text{Ca}^{2+}$ -dependent  $\text{K}^{+}$  current (Housley and Ashmore, 1991; Doi and Ohmori, 1993; Kakehata *et al.*, 1993; Erostequi *et al.*, 1994). The ACh-induced rise in  $\text{Ca}^{2+}$  may result by  $\text{Ca}^{2+}$  crossing the OHC membrane through a cation channel gated by a nicotiniclike receptor (Housley and Ashmore, 1991; Evans, 1996) or a release of  $\text{Ca}^{2+}$  from inside the OHC through the action of a muscarinic receptor linked to a G protein (Kakehata *et al.*, 1993). The net effect of OHC hyperpolarization is a reduction in the response of the BM, IHC, and the auditory nerve.

Although the results presented here may be explained by activation of a different ACh receptor in the OHC, the action of ACh must be interpreted as a mechanical one involving the OHC. The OHC clearly provides the sensitivity and exquisite tuning of the IHC, BM, and auditory nerve fibers. In the absence of the OHC, the motion of the BM becomes a more broadly tuned filter. The OHC influences the organ of Corti in an unknown but in a very frequency-specific manner. The mechanical increase in sensitivity provided by the OHC is tonotopic for each location along the BM. The frequency-specific influence of the OHC is now a hallmark of OHC function. The efferent influence on cochlear physiology is specific in that it affects only the frequency region in which the OHC provides gain. The enhancement observed in this report is also frequency specific and level dependent. The enhancement is observed only for frequencies well

above the BF and at levels of moderate to loud intensities. At BF, OCB activation alters the mechanical response of the system such that there is a reduction of the velocity amplitude. Efferent activation may also alter the mechanical response of the system to frequencies above BF by increasing the velocity response. There is *in vitro* evidence for ACh-induced increases in the OHC motility response. In isolated OHCs, the transfer function of electromotility showed gain decreases with hyperpolarization and gain increases with cell depolarization with application of ACh to the synaptic end of the OHC (Sziklai and Dallos, 1993). *In vivo* it is possible the velocity reduction at BF is associated with OHC hyperpolarization while enhancement is a result of OHC depolarization. Dallos *et al.* (1996) showed that ACh applied to isolated OHCs increases the axial but reduces the radial motile response. They (Dallos *et al.*, 1996) suggest that ACh acts on the motors within the OHCs or their mechanical load. It is not known by what means this happens in the ear but the enhancement may involve a change in axial or radial motile response, such that OCB activation causes an enhancement.

An upward shift in BF was observed in one animal in this study (animal 2706, Table IC). In this study we used a resolution of 100 Hz around the BF to characterize the tuning. This would seem to be sufficient to detect any significant changes in BF with OCB stimulation. No changes in IHC characteristic frequencies were noted during OCB stimulation (Brown and Nuttall, 1984). It is likely that the use of relatively coarse 1-kHz frequency steps in the Brown and Nuttall (1984) study would have been too large to detect an upward or downward shift in characteristic frequency. Murugasu and Russell (1996) also used relatively coarse frequency steps (500 Hz) but found a reduction in BF in three of their seven animals. The small upward shift in BF for animal 2706 was caused by a smaller OCB effect on BM responses to frequencies slightly above the control BF. Therefore the increase in BF may be an anomaly related to the strength of efferent fiber activation since the other two animals had similar best frequencies and thresholds but showed no change in BF (up or down).

What we find significant in this study is that OCB stimulation can enhance the velocity amplitude for tones well above the tonotopic location. The functional advantage or role of an efferent-induced broadening of the high-frequency slope is unknown. Further study in other animals showing similar findings in auditory nerve fiber responses would make it more likely that such an expansion does indeed play some role in the processing of acoustic stimuli.

## ACKNOWLEDGMENTS

This research was supported by NIH Grant No. DC0141. The authors gratefully acknowledge N. Brown for proofreading this manuscript. Portions of these data were presented at the midwinter ARO meeting, St. Petersburg Beach, FL, 1997.

Altschuler, R. A., and Fex, J. (1986). "Efferent transmitters," in *Neurobiology of Hearing: The Cochlea*, edited by R. A. Altschuler, R. P. Bobbin, and D. W. Hoffman (Raven, New York).

- Bobbin, R. P., and Konishi, T. (1974). "Action of cholinergic and anticholinergic drugs at the crossed olivocochlear bundle-hair cell junction," *Acta Oto-Laryngol.* **77**, 56–65.
- Brown, M. C., and Nuttall, A. L. (1984). "Efferent control of cochlear inner hair cell responses in the guinea pig," *J. Phys.* **354**, 625–646.
- Brown, M. C., Smith, D. I., and Nuttall, A. L. (1983). "The temperature dependency of neural and hair cell responses evoked by high frequencies," *J. Acoust. Soc. Am.* **73**, 1662–1670.
- Dallos, P., He, D. Z. Z., Lin, X., Evans, M. G., and Sziklai, I. (1996). "Efferent control of cochlear hair cells," *Diversity in Auditory Mechanics* (Univ. of California Berkeley, CA).
- Doi, T., and Ohmori, H. (1993). "Acetylcholine increases intracellular Ca<sup>2+</sup> concentration and hyperpolarizes the guinea pig outer hair cell," *Hearing Res.* **67**, 179–188.
- Dolan, D. E., and Nuttall, A. L. (1994). "Basilar membrane movement evoked by sound is altered by electrical stimulation of the crossed olivocochlear bundle," Seventeenth Association for Research in Otolaryngology, St. Petersburg Beach, FL.
- Elgoyhen, A. B., Johnson, D. S., Boulter, J., Vetter, D. E., and Heinemann, S. (1994). "9: An acetylcholine receptor with novel pharmacological properties expressed in rat cochlear hair cells," *Cell* **79**, 705–715.
- Erostegui, C., Norris, C. H., and Bobbin, R. P. (1994). "In vitro pharmacologic characterization of a cholinergic receptor on outer hair cells," *Hearing Res.* **74**, 135–147.
- Evans, M. G. (1996). "Acetylcholine activates two currents in guinea-pig outer hair cells," *J. Physiol. (London)* **491**(2), 563–578.
- Eybalin, M. (1993). "Neurotransmitters and neuromodulators of the mammalian cochlea," *Physiol. Rev.* **73**, 309–373.
- Fex, J. (1967). "Efferent inhibition in the cochlea related to hair-cell dc activity: study of postsynaptic activity of the crossed olivocochlear fibers in the cat," *J. Acoust. Soc. Am.* **41**, 666–675.
- Galambos, R. (1956). "Suppression of auditory nerve activity by stimulation of efferent fibers to the cochlea," *J. Neurophysiol.* **19**, 424–437.
- Gifford, M. L., and Guinan, J. J. (1983). "Effects of crossed-olivocochlear-bundle stimulation on cat auditory nerve fiber response to tones," *J. Acoust. Soc. Am.* **74**, 115–123.
- Guinan, J. J. (1986). "Effect of efferent neural activity on cochlear mechanics," *Scand Audiol. Suppl.* **25**, 53–62.
- Guinan, J. J., and Gifford, M. L. (1988). "Effects of electrical stimulation of efferent olivocochlear neurons on cat auditory-nerve fibers. I. Rate-level functions," *Hearing Res.* **33**, 97–114.
- Guinan, J. J., and Stankovic, K. M. (1996). "Medial efferent inhibition produces the largest equivalent attenuations at moderate to high sound levels in cat auditory-nerve fibers," *J. Acoust. Soc. Am.* **100**, 1680–1690.
- Guinan, J. J., Warr, W. B., and Norris, B. E. (1983). "Differential olivocochlear projections from lateral versus medial zones of the superior olivary complex," *J. Comp. Neurol.* **221**, 358–370.
- Guth, P. S., and Norris, C. H. (1996). "The hair cell acetylcholine receptors: A synthesis," *Hearing Res.* **98**, 1–8.
- Guth, P. S., Dunn, A., Kronomer, K., and Norris, C. H. (1994). "The cholinergic pharmacology of the frog sacculle," *Hearing Res.* **75**, 225–232.
- Guth, P. S., Norris, C. H., Guth, S. L., Quine, D. B., and Williams, W. H. (1986). "Cholinomimetics mimic efferent effects on semicircular canal afferents activity in the frog," *Acta Oto-Laryngol. (Stockh.)* **102**, 194–203.
- Housley, G. D., and Ashmore, J. F. (1991). "Direct measurement of the action of acetylcholine on isolated outer hair cells of the guinea pig cochlea," *Proc. R. Soc. London, Ser. B* **244**, 161–167.
- Takehata, S., Nakagawa, T., Takasaka, T., Akaike, N. (1993). "Cellular mechanism of acetylcholine-induced response in dissociated outer hair cells of guinea-pig cochlea," *J. Physiol. (London)* **463**, 227–244.
- Kujawa, S. G., Glatke, T. J., Fallon, M., Bobbin, R. P. (1992). "Intracochlear application of acetylcholine alters sound-induced mechanical events within the cochlear partition," *Hearing Res.* **61**, 106–116.
- Long, G. R. (1989). "Modification of the frequency and level of otoacoustic emissions by contralateral stimulation, in a subject with no acoustic reflexes in one ear." (Assoc. for Res. in Otolaryngol., St. Petersburg Beach, FL).
- Mott, J. B., Norton, S. J., Neely, S. T., Warr, W. B. (1989). "Changes in spontaneous emissions produced by acoustic stimulation of the contralateral ear," *Hearing Res.* **38**, 229–242.
- Mountain, D. C. (1980). "Changes in endolymphatic potential and crossed olivocochlear bundle stimulation alter cochlear mechanics," *Science* **210**, 71–72.
- Murugasu, E., Russell, I. J. (1996). "The effect of efferent stimulation on basilar membrane displacement in the basal turn of the guinea pig cochlea," *J. Neurosci.* **16**(1), 325–332.
- Norris, C. H., Housley, G. D., Williams, W. H., Guth, S. L., and Guth, P. S. (1988). "The acetylcholine receptors of the semicircular canal in the frog (*Rana pipiens*)," *Hearing Res.* **32**, 197–206.
- Nuttall, A. L., Dolan, D. F., and Avinash, G. B. (1991). "Laser Doppler velocimetry of basilar membrane vibration," *Hearing Res.* **51**, 203–214.
- Rasmussen, G. L. (1946). "The olivary peduncle and other fiber connections of the superior olivary complex," *J. Comp. Neurol.* **84**, 141–219.
- Robertson, D. (1985). "Brainstem location of efferent neurons projecting to the guinea pig cochlea," *Hearing Res.* **20**, 79–84.
- Shore, S. E., and Nuttall, A. L. (1985). "The effects of cochlear hypothermia on compound action potential tuning," *J. Acoust. Soc. Am.* **77**, 590–598.
- Siegel, J. H., and Kim, D. O. (1982). "Efferent neural control of cochlear mechanics? Olivocochlear bundle stimulation affects cochlear biomechanical nonlinearity," *Hearing Res.* **6**, 171–182.
- Sridhar, T. S., Liberman, M. C., Brown, M. C., and Sewell, W. F. (1995). "A novel cholinergic 'slow effect' of efferent stimulation on cochlear potentials in the guinea pig," *J. Neurosci.* **15**(5), 3667–3678.
- Sziklai, I., and Dallos, P. (1993). "Acetylcholine controls the gain of the voltage-to-movement converter in isolated outer hair cells," *Acta Oto-Laryngol. (Stockh.)* **113**, 326–329.
- Warr, W. B. (1975). "Olivocochlear and vestibular efferent neurons of the feline brain-stem: Their location, morphology and number determined by retrograde axonal transport and acetylcholinesterase histochemistry," *J. Comp. Neurol.* **161**, 159–182.
- Warr, W. B. (1978). "The olivocochlear bundle: its origins and termination in the cat," in *Evoked Electrical Activity in the Auditory Nervous System*, edited by R. F. Naunton and Fernandez (Academic, New York).
- Warr, W. B., and Guinan, J. J., Jr. (1979). "Efferent innervation of the organ of Corti: Two separate systems. *Brain Res.* **173**, 152–155.
- Whitehead, M. L., Martin, G. K., and Lonsbury-Martin, B. L. (1991). "Effects of the crossed acoustic reflex on distortion-product otoacoustic emissions in awake rabbits, *Hearing Res.* **51**, 55–72.
- Wiederhold, M. L. (1970). "Variation in the effects of electrical stimulation of the crossed olivocochlear bundle on cat single auditory nerve fiber responses to tone bursts," *J. Acoust. Soc. Am.* **48**, 966–977.



# Frequency specificity of the human auditory brainstem and middle latency responses to brief tones.

## I. High-pass noise masking<sup>a)</sup>

Peggy Oates

*Auditory Evoked Potentials Research Laboratory, Albert Einstein College of Medicine, Bronx, New York and Doctoral Program in Speech and Hearing Sciences, CUNY Graduate Center, New York, New York*

David R. Stapells<sup>b)</sup>

*School of Audiology and Speech Sciences, The University of British Columbia, 5804 Fairview Avenue, Vancouver, British Columbia V6T 1Z3, Canada*

(Received 15 August 1996; revised 22 August 1997; accepted 2 September 1997)

This study investigated the frequency specificity of the auditory brainstem (ABR) and middle latency (MLR) responses to 500- and 2000-Hz brief tones using high-pass noise masking. Stimuli were linear- (2-1-2 cycles) and exact-Blackman- (5 cycles) gated tones presented at 80 dB peak-to-peak equivalent (ppe) SPL. Cochlear contributions to ABR wave V-V' and MLR wave Na-Pa were assessed by the effects of high-pass noise masking on response amplitudes and latencies. The high-pass noise results demonstrate that the ABR and the MLR to the 80 dB ppe SPL brief tones show good frequency and place specificity. Changes in ABR or MLR amplitude and latency with high-pass noise masking did not occur as the masker cutoff was decreased from 2 to 3 octaves above the stimulus nominal frequency until it was within one-half octave of this frequency, below which amplitudes rapidly decreased (500- and 2000-Hz tones) and latencies increased (500-Hz tones). No significant differences existed in the frequency specificity of the ABR versus MLR, or in these evoked potentials to exact-Blackman- versus linear-gated tones. © 1997 Acoustical Society of America. [S0001-4966(97)06212-7]

PACS numbers: 43.64.Qh, 43.64.Ri [RDF]

## INTRODUCTION

The auditory brainstem (ABR) and the middle latency (MLR) responses to tonal stimuli have both been suggested for use in estimating pure-tone behavioral thresholds in infants and children, thus highlighting the importance of defining the frequency and place specificity of these responses. The frequency specificity of an audiometric measure is a term generally applied to threshold evaluations and refers to how independent a threshold at one stimulus frequency is of contributions from surrounding frequencies (Stapells *et al.*, 1994, 1985). Cochlear place specificity, in contrast, refers to the portion of the basilar membrane contributing to the response. Three areas of controversy with respect to the frequency and place specificity of these evoked potentials to tonal stimuli are: (1) the use of low-frequency stimuli (i.e., 500 Hz) at high stimulus intensities for recording the ABR; (2) the suggestion that the MLR provides a more frequency-specific response to low-frequency tones compared to the ABR; and (3) the use of nonlinear-gated stimuli (e.g., Blackman-gated tone) versus conventional linear-gated tones to improve the frequency specificity of the ABR and/or MLR.

The controversial issues in the literature regarding the use of the ABR to 500-Hz brief tones for estimating low-

frequency hearing sensitivity arise from a small number of studies which suggest that: (1) the ABR to high-intensity nonmasked 500-Hz tonal stimuli is primarily generated from the basal end of the cochlea; (2) waveform identification of the ABR to 500-Hz stimuli is problematic in quiet, and even more so in the presence of high-pass (HP) noise masking; and (3) ABR thresholds to 500-Hz stimuli have poor frequency specificity and thus are poor predictors of low-frequency behavioral thresholds (e.g., Davis and Hirsh, 1976; Laukli, 1983a, 1983b; Laukli *et al.*, 1988; Laukli and Mair, 1986; Scherg and Volk, 1983; Sohmer and Kinarti, 1984; Weber, 1987). Contrary to these results, many studies have been successful in recording replicable and clearly identifiable ABRs to air-conducted 500-Hz stimuli both in quiet and in the presence of ipsilateral notched noise and/or HP noise masking, down through 55 dB peak-to-peak equivalent (ppe) SPL and lower (Davis and Hirsh, 1979; Hyde, 1985; Hyde *et al.*, 1987; Jacobson, 1983; Kileny, 1981; Kodera *et al.*, 1977a; Munnerley *et al.*, 1991; Purdy *et al.*, 1989; Sininger *et al.*, 1997; Stapells, 1984, 1989; Stapells *et al.*, 1995; Stapells and Picton, 1981; Stapells *et al.*, 1994, 1990; Suzuki *et al.*, 1977, 1981, 1984; Wu and Stapells, in preparation). In addition, high correlations (i.e.,  $\geq 0.9$ ) between ABR thresholds to 500-Hz air-conducted tones in notched noise and/or HP noise and 500-Hz pure-tone behavioral thresholds have been demonstrated for normal and hearing-impaired subjects (e.g., Kileny and Magathan, 1987; Munnerley *et al.*, 1991; Stapells *et al.*, 1995, 1990).

<sup>a)</sup>Portions presented at American Speech-Language-Hearing Association Convention, Seattle, WA, 21 November 1996.

<sup>b)</sup>Author to whom correspondence should be addressed. Electronic mail: stapells@audiospeech.ubc.ca

In view of the disagreement regarding the use of the ABR to 500-Hz tones to estimate low-frequency hearing sensitivity, the MLR has been proposed to be a better indicator of 500-Hz sensitivity (e.g., Kavanagh *et al.*, 1984; Kileny and Shea, 1986; Palaskas *et al.*, 1989; Scherg and Volk, 1983). This suggestion has been based on the observation that larger peak-to-peak amplitudes are measured for the MLR compared to the ABR in response to 500-Hz tones, leading to better detectability of the MLR (Scherg and Volk, 1983; Wu and Stapells, 1994, in preparation). A commonly held belief is that the MLR may be recorded using tones with longer rise times than the ABR without causing a significant decrease in the amplitude of the response. Tones with longer rise times have greater acoustic frequency specificity (Burkard, 1984; Gorga and Thornton, 1989; Jacobson, 1983; Stapells and Picton, 1981). The current literature on the effects of rise time on the MLR, however, shows significant decreases in MLR amplitude when rise times exceed 5 ms (Beiter and Hogan, 1973; Vivion *et al.*, 1980), similar to that reported for the ABR (e.g., Stapells and Picton, 1981).

To date, only three published studies have directly compared the frequency specificity of the ABR to the MLR to tonal stimuli and these have reported conflicting results (Mackersie *et al.*, 1993; Smith *et al.*, 1990; Wu and Stapells, 1994). Smith and colleagues employed forward masking of 2000-Hz probe tones with gerbils and reported that the MLR is less frequency specific than the ABR. In contrast, Stapells and co-workers (Mackersie *et al.*, 1993; Wu and Stapells, 1994), who tested human subjects with a simultaneous masking paradigm, reported no significant differences in the frequency and place specificity of the ABR and MLR to low-intensity (60 dB ppe SPL) 500- and 2000-Hz probe tones. The inconsistencies between the findings of Smith *et al.* and these two later studies may be related to the differences in masking techniques used, differences in adaptation characteristics between the ABR and MLR, and/or species differences in the neural generators of the MLR. No published research, however, has addressed the question of how frequency specific the MLR is to higher intensity 500- and 2000-Hz tones. This information is clearly needed to determine the potential benefit of the MLR for threshold evaluations.

Currently, the most widely used tonal stimuli for recording evoked potentials are linear-gated brief tones. There are, however, a number of nonlinear gating functions (e.g., cosine, exponential, Gaussian, Hanning, Kaiser-Bessel, exact-Blackman) which can theoretically yield frequency spectra that are more narrow than those for linear-gated tones, while maintaining the rapid stimulus onset needed for eliciting both the ABR and MLR (Gorga and Thornton, 1989; Harris, 1978; Nuttal, 1981). The differences between the frequency spectra of the linear and nonlinear stimuli are in the width of the main energy lobe, the amplitudes of the sidelobes of energy, and the rate of decay of the sidelobes with frequency.

Some investigators have claimed that the frequency specificity of the ABR will be improved by using a Blackman-gated tone (Gorga *et al.*, 1992; Gorga and Thornton, 1989; Telian and Kileny, 1989). It has been suggested that the reduction of energy in the sidelobes of the

Blackman-gated tone may have the advantage of removing contributions to the evoked potentials from frequencies other than the nominal frequency and thus yield more frequency-specific responses than would have been obtained with a linear-gated signal (Gorga and Thornton, 1989). This may not be the case, however, as the wider main lobe of the exact-Blackman-gated tone likely stimulates a broader region of the basilar membrane. To date, no published studies in humans have investigated how these frequency spectra differences between the exact-Blackman- and linear-gated tones are reflected by either of these evoked potentials.

Several noise masking techniques have been used to investigate the frequency and place specificity of evoked potentials to different stimuli. These include: pure-tone masking (Folsom, 1984, 1985; Folsom and Wynne, 1987; Klein, 1983; Klein and Mills, 1981a, b; Mackersie *et al.*, 1993; Wu and Stapells, 1994); notched-noise masking (Abdala and Folsom, 1995; Beattie and Kennedy, 1992; Jacobson, 1983; Picton *et al.*, 1979; Stapells, 1984; Stapells and Picton, 1981); and high-pass noise masking (Don and Eggermont, 1978; Eggermont, 1976; Eggermont and Don, 1980; Kramer, 1992; Noursak and Stapells, 1992). Of these three types of noise masking, high-pass noise yields the most frequency and place specific evaluation of a response as there is little or no downward spread of masking, as reflected by the steep high-frequency edge of the VIIIth nerve action potential tuning curves (Stapells *et al.*, 1994, 1985).

Using high-pass noise masking, the purposes of this study were to assess: (1) the frequency specificity and cochlear contributions to the ABR and MLR to 80 dB ppe SPL 500- and 2000-Hz tones; (2) the differences, if any, in the frequency and place specificity of the ABR (wave V) versus MLR (wave Na-Pa); and (3) the differences, if any, in the frequency and place specificity of these responses to exact-Blackman- versus linear-gated tones.

## I. METHODS

### A. Subjects

Twelve normal-hearing adults (4 males and 8 females) participated in this study. The age range of the subjects was 18–40 years of age, with a mean age of 27.25 years. All had behavioral pure-tone audiometric thresholds of 15 dB HL (ANSI, 1989) or better at octave frequencies of 250 through 8000 Hz in the test ear, and no significant otologic or neurologic histories. On each day of testing, type A tympanograms (220-Hz probe tone) and a present ipsilateral acoustic reflex to a 90 dB HL 1000-Hz tone were obtained.

### B. Stimuli

The stimuli were generated and presented by a Neuroscan “STIM” system. The stimuli were 500- and 2000-Hz brief tones which were presented in two conditions: (1) “2-1-2” linear tones, consisting of a linear two-cycle rise and two-cycle fall time, and a plateau time of one cycle, and (2) exact-Blackman-gated tones, with a five-cycle total duration and no plateau (Harris, 1978, formula 32). Figure 1 displays the acoustic spectra of these stimuli. The stimuli were of alternating-onset polarity and were presented at a rate of

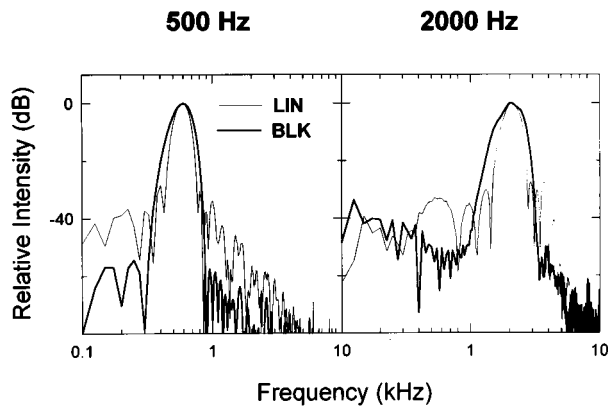


FIG. 1. Acoustic spectra for exact-Blackman (thick line, "BLK") versus linear-gated (thin line, "LIN") tones for 500 Hz (left) and 2000 Hz (right). These spectra were obtained by coupling the ER-2 insert earphone to a Brüel & Kjaer 2-cc adaptor and 4152 coupler, a 1-in. condenser microphone (type 4144), and a 2209 sound level meter. The ac output of the sound level meter was routed to the "SCAN" system of the Neuroscan. The spectra were obtained from FFTs of 200-trial time-domain averages, using a sampling rate of 25 600 Hz over an analysis time of 20 ms, with the stimulus waveforms centered in this window. The averaged waveforms were not windowed prior to FFT.

9.4/s using Etymotic Research ER-2 insert earphones. Alternating-onset-polarity stimuli were employed because stimulus-related electrical artifacts and the cochlear microphonic may be recorded, especially at moderate-to-high stimulus intensities, and are effectively canceled by the polarity alternation (Davis, 1976). The use of alternate-onset-polarity stimuli also cancelled out the frequency following response which may occur in ABRs to 500-Hz stimuli presented at stimulus intensities of 65 dB ppe SPL and above (Davis and Hirsh, 1976; Gerken *et al.*, 1975). The stimuli were presented to one ear per subject, randomly selected for each subject, and were presented at 80 dB ppe SPL. The stimuli were calibrated daily using a Brüel & Kjaer DB0138 2-cc adaptor and 4152 coupler, 1-in. condenser microphone (type 4144) and a 2209 sound-level meter. The 80 dB ppe SPL value corresponds to levels of 53 dB nHL for the 500-Hz stimuli and 52 dB nHL for the 2000-Hz stimuli, as determined from a pilot study conducted on 10 subjects with normal hearing.

### C. Broadband and HP noise masking

Broadband pink noise was generated by a white-noise masking module (Coulbourn model S81-02) and pink noise audio filter (Coulbourn S86-05), and then high-pass filtered (Stanford Research System, model SR650, nominally 115 dB/octave slope), and attenuated (Coulbourn S85-08). The actual slope of the filter, measured from the frequency spectra using a Wavetek 804A spectrum analyzer, was 94 dB/octave, with a stopband attenuation of 63.25 dB. The intensity of the broadband pink noise required to mask the ABR and MLR to the 80 dB ppe SPL exact-Blackman- and linear-gated tones was initially determined behaviorally from a pilot study conducted on ten normal-hearing adults. For each subject in the present study, the maximum of the masker intensity measured from the pilot study was increased in 1-dB steps until the ABR and MLR was judged to be com-

pletely masked. The mean pink noise masker intensity actually employed in this study was 92 dB SPL (range = 90–93 dB SPL), measured prior to filtering through a Brüel & Kjaer 2-cc adaptor and 4152 coupler, using a Brüel & Kjaer 1-in. pressure microphone (type 4144) and sound level meter (model 2209) set to slow normal (linear).

The HP noise cutoff frequencies employed for the 500-Hz stimuli were: 4.0, 2.83, 2.0, 1.41, 1.0, 0.707, 0.5, 0.354, and 0.25 kHz; the HP cutoff frequencies for the 2000-Hz stimuli were: 8.0, 5.66, 4.0, 2.83, 2.0, 1.41, 1.0, 0.707, and 0.5 kHz.

### D. Evoked potential recordings

All recordings and waveform analyses were carried out using a Neuroscan "SCAN" system. Simultaneous recordings of the ABR and MLR were obtained using gold-plated electrodes placed on the vertex (Cz) and earlobe (A1 or A2) of each subject, with a forehead electrode (Fpz) serving as ground. Interelectrode impedances were 2000 Ohms or less. The electroencephalographic (EEG) signals were amplified (gain=100 000) and analog filtered (10–3000 Hz, 6 dB/octave, Grass model 12). The EEG signals were digitized (12-bit converter) using a sampling rate of 12 128 Hz over an analysis time of 84 ms (including a pre-stimulus baseline of 3 ms), and stored as averages of 1000 trials each. Trials containing amplitudes exceeding  $\pm 25 \mu\text{V}$  were automatically rejected. The calibration of the EEG amplifier was checked daily before each test session. The averaged responses were digitally filtered *post hoc* in the frequency domain (forward and inverse FFTs; data not windowed) using a HP filter setting of 20 Hz (24 dB/octave) and a low-pass (LP) filter setting of 1000 Hz (96 dB/octave). After digital filtering, average waveforms representing the overall average of 8000 sweeps were calculated, as were two replications of 4000 sweeps each and four replications of 2000 sweeps each.

### E. Procedure

All testing was performed in a double-walled sound attenuating room (Industrial Acoustics Corporation). Subjects were seated in a reclining chair, resting or reading quietly during the testing. Subjects were instructed to remain awake during testing, and their EEG activity was monitored on an oscilloscope. All of the subjects were tested with the exact-Blackman- and linear-gated stimuli at both 500 and 2000 Hz in quiet and simultaneously with broadband pink noise, and the nine HP noise cutoff frequency conditions for each stimulus. Each stimulus frequency was tested over two sessions with the HP noise conditions being presented in a different order for the second session. Four replications of 1000 sweeps each were collected within a test session yielding a total (over the two sessions) of 8000 sweeps for the non-masked, broadband noise and HP noise conditions for each stimulus. The orders of the stimulus test frequencies, linear versus nonlinear stimuli, and the HP noise cutoff frequencies, were all randomized for each subject.

## F. Response identification

The decision regarding the presence or absence of ABR wave V and MLR wave Pa was made by combining the ratings of three judges experienced in the identification of ABRs and MLRs to tonal stimuli. All three judges had knowledge of the frequency of the stimulus, however, they were blind to the type of stimulus (exact-Blackman- versus linear-gated tone) and to the HP noise cutoff frequency. The order of rating the various HP noise conditions, as well as the order of the subjects, were randomized for each rater. Each judge scored the ABR and MLR waveforms independently of the other judges. The three judges showed high interjudge reliability, with Gamma probabilities ranging from 0.844 to 0.922.

Each rater independently assigned a score of "1" to "4" to ABR wave V and MLR wave Pa in each subject's grand averages (8000 sweeps) for the various HP noise conditions, based on the replicability of the wave in question. The significance of the scores was as follows: a score of "4" indicated a "definite response", a "3" indicated a "probable response", a "2" indicated a "probable no-response," and a "1" indicated "definite no response." The ratings were then averaged, and mean ratings across the judges of 2.5 or higher were considered "response present" (Stapells, 1984; Stapells *et al.*, 1990).

## G. Response measurements

Peak-to-peak amplitude measures of ABR wave V-V' and MLR wave Na-Pa for each subject were obtained from each subject's grand average waveforms (8000 trials) for those peaks judged to contain a response in the various HP noise masking conditions. Peaks judged as no response, as determined by a mean rating of less than 2.5, were assigned an amplitude value of zero  $\mu\text{V}$ .<sup>1</sup>

Wave V was defined as the maximum vertex-positive peak occurring between 6 and 20 ms following stimulus onset. If several peaks of equal amplitude occurred within this range, the peak preceding the largest negative shift was selected. Wave V' was defined as the greatest negativity occurring within 8 ms after wave V (Stapells and Picton, 1981; Nousak and Stapells, 1992). MLR wave Na was defined as the largest negativity following wave V and occurring between 10 and 30 ms; wave Pa was the largest positivity following wave Na and occurring between 20 and 50 ms (Mackersie *et al.*, 1993). Latency values were corrected for the delay introduced by the insert earphones.

## H. Statistical analyses

Peak-to-peak amplitudes and latencies were analyzed using descriptive statistics and repeated measures analyses of variance (ANOVAs). Greenhouse-Geisser epsilon corrections for the degrees of freedom for repeated measures were employed when appropriate (Greenhouse and Geisser, 1959). Probabilities reported reflect these adjustments. Results were considered statistically significant if  $p < 0.01$ . When significant results were found in the ANOVAs, Newman-Keuls

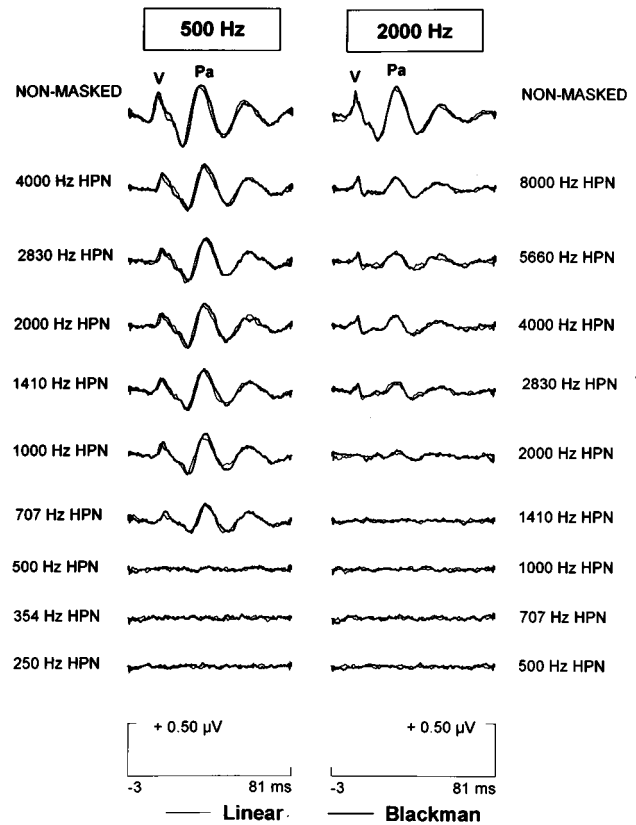


FIG. 2. Grand mean ( $N=12$ ) waveforms recorded to 80 dB ppe SPL 500- and 2000-Hz exact-Blackman- and linear-gated tones recorded in nine HP noise conditions.

*post hoc* tests were performed to determine the pattern of the significant differences. Results of these *post hoc* analyses were considered significant if  $p < 0.05$ .

## II. RESULTS

### A. Nonmasked responses

The waveforms on the top of Fig. 2 represent the grand mean ( $N=12$ ) nonmasked ABRs and MLRs recorded to 80 dB ppe SPL 500- and 2000-Hz exact-Blackman- and linear-gated tones. ABR wave V and MLR wave Pa are labeled.

Mean ( $\pm$  standard deviation) peak-to-peak amplitude values for the nonmasked responses to the 500-Hz stimuli are:  $0.36 \pm 0.10 \mu\text{V}$ ,  $0.40 \pm 0.12 \mu\text{V}$ ,  $0.65 \pm 0.20 \mu\text{V}$ , and  $0.67 \pm 0.23 \mu\text{V}$  for wave V to linear tones, wave V to exact-Blackman tones, wave Pa to linear tones, and wave Pa to exact-Blackman tones, respectively. The mean ( $\pm$  standard deviation) amplitudes for the responses to the nonmasked 2000-Hz tones are:  $0.41 \pm 0.12 \mu\text{V}$ ,  $0.37 \pm 0.08 \mu\text{V}$ ,  $0.55 \pm 0.17 \mu\text{V}$ , and  $0.57 \pm 0.18 \mu\text{V}$  for wave V to linear tones, wave V to exact-Blackman tones, wave Pa to linear tones, and wave Pa to the exact-Blackman tones, respectively. A three-way repeated measures ANOVA (stimulus frequency  $\times$  wave  $\times$  window) calculated on the amplitude results for the quiet condition revealed that the peak-to-peak amplitude of MLR Na-Pa is significantly larger compared to the amplitude of ABR V-V' [ $p = 0.0001$ ]. There are no statistically significant differences between the amplitudes of the responses to the exact-Blackman- versus linear-gated

tones [ $p=0.385$ ], or to the responses to 500- vs 2000-Hz tones [ $p=0.132$ ]. No interactions reached statistical significance [ $p=0.012-0.496$ ], however, there is a trend [ $p=0.012$ ] for wave Na-Pa to be slightly larger to the 500-Hz tones compared to the 2000-Hz tones.

The mean ( $\pm$  standard deviation) absolute latency values obtained for the responses to the nonmasked 500-Hz tones are:  $9.91 \pm 0.96$  ms,  $10.84 \pm 0.83$  ms,  $31.97 \pm 1.57$  ms, and  $32.31 \pm 1.21$  ms for wave V to linear tones, wave V to exact-Blackman tones, wave Pa to linear tones, and wave Pa to exact-Blackman tones, respectively. The mean ( $\pm$  standard deviation) latencies for the responses to the nonmasked 2000-Hz tones are:  $7.08 \pm 0.34$  ms,  $7.29 \pm 0.60$  ms,  $27.88 \pm 1.16$  ms, and  $28.62 \pm 1.49$  ms for wave V to linear tones, wave V to exact-Blackman tones, wave Pa to linear tones, and wave Pa to exact-Blackman tones, respectively. A three-way repeated measures ANOVA (stimulus frequency  $\times$  wave  $\times$  window) calculated on the absolute latency values revealed expected significant main effects for stimulus frequency [ $p < 0.0001$ ] and wave [ $p < 0.0001$ ], with later latencies for the responses to the 500-Hz stimuli and for MLR wave Pa. There is also a significant latency difference between the responses to exact-Blackman- versus linear-gated tones [ $p = 0.0003$ ], with the responses to the exact-Blackman-gated tones having a longer latency. No interactions reached statistical significance [ $p = 0.035-0.915$ ].

## B. HP noise masking

The grand mean waveforms recorded to 80 dB ppe SPL 500- and 2000-Hz exact-Blackman- and linear-gated tones for the nine HP noise masking conditions are also displayed in Fig. 2. In response to the 500-Hz tones, clear ABRs and MLRs are present in each of the HP noise masking conditions down through 707 Hz, with no responses present at the lowest HP noise cutoff frequencies (i.e., 500, 354, and 250 Hz). For the 2000-Hz stimuli, ABR wave V and MLR wave Pa are clearly evident down to a HP noise masking cutoff frequency of 2830 Hz and both waves disappear at cutoff frequencies of 1410 Hz and below. MLR wave Pa is present in the recordings obtained in the presence of HP noise with a 2000-Hz cutoff, however, there is no clear wave V in this condition. There are no obvious differences in the responses to the exact-Blackman- versus linear-gated tones at either stimulus frequency.

The ABRs and MLRs recorded in the presence of HP noise masking are smaller in amplitude and longer in latency than the nonmasked responses. The decrease in amplitudes and increase in latencies are evident even at the highest HP noise cutoff frequency 2–3 octaves above each stimulus frequency (i.e., 4000 Hz for the 500-Hz tones, and 8000 Hz for the 2000-Hz tones). The responses then remain essentially unchanged as the cutoff frequency of the masking noise is lowered until it is within a half octave of the nominal stimulus frequencies. When the cutoff frequency of the HP noise is a half octave above the nominal stimulus frequencies, a significant decrease in the amplitudes and increase in the latencies of the ABR and MLR occurs prior to the waveforms disappearing when the cutoff frequency is less than or equal to the nominal stimulus frequency.

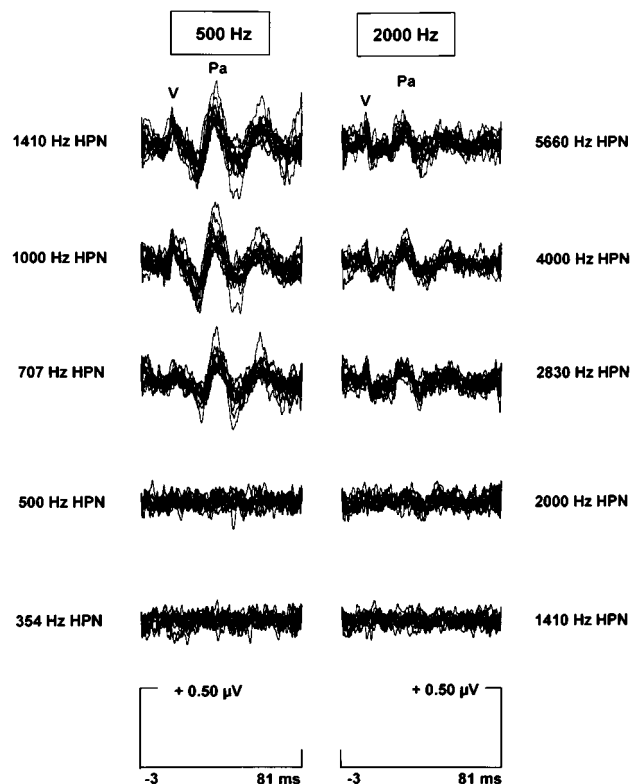


FIG. 3. ABRs and MLRs recorded from each individual subject ( $N=12$ ) to 80 dB ppe SPL 500- and 2000-Hz linear-gated tones presented in HP noise (“HPN”) with cutoffs ranging from 1410 to 354 Hz for the 500-Hz tones, and from 5660 to 1410 Hz for the 2000-Hz tones.

Figure 3 presents the ABRs and MLRs recorded in the presence of HP noise masking to 80 dB ppe SPL 500- and 2000-Hz linear-gated tones superimposed for each of the 12 subjects. The HP noise conditions displayed in half-octave steps range from 1410 through 354 Hz for the responses to the 500-Hz tones, and from 5660 to 1410 Hz for the responses to the 2000-Hz tones. These HP noise conditions were selected as they show the greatest changes in response amplitude and latency for each of the stimulus frequencies. The response changes with HP noise cutoff frequency seen in the grand mean waveforms (Fig. 2) are also clearly reflected in the individual subjects’ results.

Amplitudes for the responses recorded in HP noise were normalized to a percentage of their nonmasked amplitudes. Mean normalized ABR V-V’ and MLR Na-Pa amplitudes (and standard deviations) are plotted in Fig. 4 as a function of HP noise cutoff frequency. There is little or no change in the amplitudes of waves V-V’ and Na-Pa as the cutoff frequency of the HP noise is lowered to within a half octave above the stimulus frequency, where there is a sharp dropoff in response amplitude. The normalized amplitudes of ABR V-V’ and MLR Na-Pa to the 2000-Hz stimuli are lower (in percent) than those for the 500-Hz tones. This is especially evident for MLR Na-Pa, as indicated by a significant ANOVA main effect for wave shown at this stimulus frequency (see Table I).

Three-way repeated measures ANOVAs were calculated separately for the 500- and 2000-Hz amplitude profiles for the HP noise conditions. The results of these ANOVAs, sum-

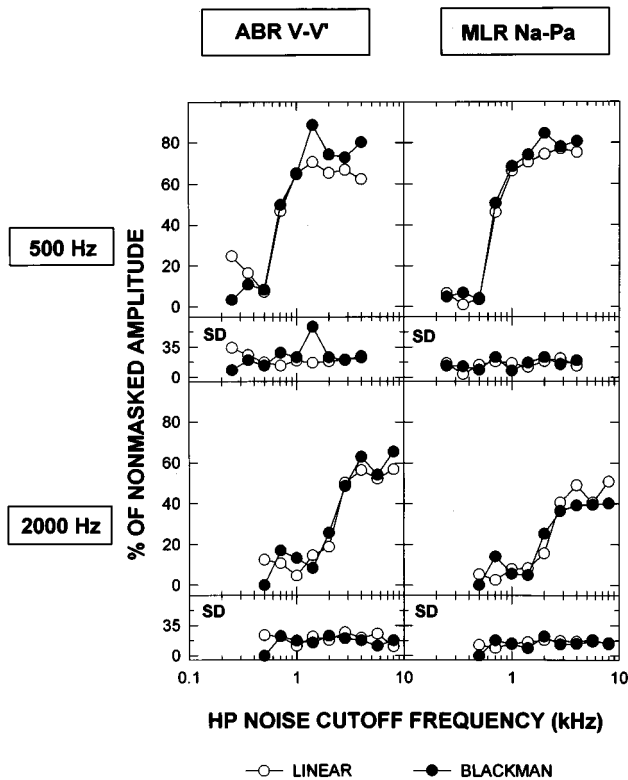


FIG. 4. Mean and standard deviation (s.d.) response amplitude profiles for ABR wave V-V' and MLR wave Na-Pa to 500- and 2000-Hz exact-Blackman- versus linear-gated tones recorded in the HP noise masking conditions.

marized in Table I (left side), reveal a significant main effect for HP noise cutoff frequency for both the 500- and 2000-Hz stimuli. Neuman-Keuls *post hoc* testing of the amplitude profiles for the 500-Hz tones reveal the ABRs and MLRs recorded at HP noise cutoff frequencies of 1000–4000 Hz are significantly larger in amplitude than those recorded at cutoff frequencies of 707 Hz and below. *Post hoc* comparisons of the amplitude profiles for 2000-Hz tones show that the main effect for HP noise cutoff frequency is due to the fact that the ABR/MLR recorded at cutoff frequencies of 2830–8000 Hz has significantly larger normalized amplitudes than those recorded at cutoff frequencies of 2000 Hz and below. The amplitudes for the nonmasked condition were excluded in these analyses. The results of the *post hoc* analyses indicate that there is little contribution of stimulus energy from the frequencies greater than one or more octaves above nominal frequencies to the ABRs and MLRs to the 80 dB ppe SPL 500- and 2000-Hz tones.<sup>2</sup> The significant main effect for wave indicates that the amplitude of ABR wave V-V' to the 2000-Hz stimuli is significantly larger than for MLR wave Na-Pa, relative to their nonmasked amplitudes. There is no significant HP noise  $\times$  wave interaction, however, demonstrating that there is no difference in the frequency specificity of these evoked potentials. There are no significant differences between the amplitude profiles for responses to exact-Blackman- versus linear-gated tones [i.e., no main effect for window] for either stimulus frequency, nor any significant interactions involving window. Both the ABR and MLR in response to the 2000-Hz tones show greater de-

TABLE I. Results of three-way repeated measures analyses of variance for amplitude and latency profiles for the HP noise conditions.

Source of variance	Amplitude <sup>a</sup>				Latency			
	500 Hz		2000 Hz		500 Hz		2000 Hz	
	df	P <sup>b</sup>	df	P	df	P	df	P
Wave	1	0.923	1	0.006 <sup>c</sup>	1	0.0 <sup>c</sup>	1	0.0 <sup>c</sup>
Error term	11		11		9		7	
Window	1	0.234	1	0.945	1	0.002 <sup>c</sup>	1	0.005 <sup>c</sup>
Error term	11		11		9		7	
HP noise cutoff frequency (CF)	8	0.0 <sup>c</sup>	8	0.0 <sup>c</sup>	5	0.0 <sup>c</sup>	3	0.61
Error term	88		88		45		21	
Wave $\times$ Window	1	0.958	1	0.188	1	0.516	1	0.104
Error term	11		11		9		7	
Wave $\times$ HP noise CF	8	0.028	8	0.056	5	0.539	3	0.248
Error term	88		88		45		21	
Window $\times$ HP noise CF	8	0.223	8	0.326	5	0.167	3	0.763
Error term	88		88		45		21	
Wave $\times$ Window $\times$ HP noise CF	8	0.32	8	0.163	5	0.484	3	0.773
Error term	88		88		45		21	

<sup>a</sup>ANOVAs for amplitude profiles were based on percent of the nonmasked amplitudes.

<sup>b</sup>Probabilities reflect Greenhouse-Geisser epsilon corrections for degrees of freedom for repeated measures.

<sup>c</sup> $p < 0.01$ .

creases by masking compared to the responses to the 500-Hz tones. This difference, however, was not tested statistically. These findings show that there are no significant differences in the frequency specificity of the ABR versus the MLR, or in the responses to exact-Blackman- versus linear-gated tones. These results also suggest that the responses to the 500- and 2000-Hz tones are equally place specific. Significant changes in response amplitudes to both frequencies only occur when the HP masker cutoff was within a half octave of the nominal stimulus frequencies.<sup>2</sup>

Each subject's latencies for ABR wave V and MLR wave Pa were measured in the various HP noise conditions. Mean absolute latency values for the 500- and 2000-Hz stimuli are plotted as a function of the cutoff frequency of the HP noise in Fig. 5. Mean latencies for the Quiet condition are also plotted. Each symbol in the figure represents a minimum of ten subjects' data for the responses to the 500-Hz tones, and 11 subjects' data for the responses to the 2000-Hz tones. The latencies of waves V and Pa are longer to the 500-Hz tones compared to the 2000-Hz tones. As indicated above and discussed below, latencies of the ABR and MLR are longer with introduction of the HP noise with a cutoff 2–3 octaves above the stimulus nominal frequency. The latencies of waves V and Pa then remain essentially unchanged as the cutoff frequency of the HP noise is lowered, until the HP noise cutoff reaches within approximately a half to one octave above the stimulus nominal frequency. The increases in latency are greater for the responses to the

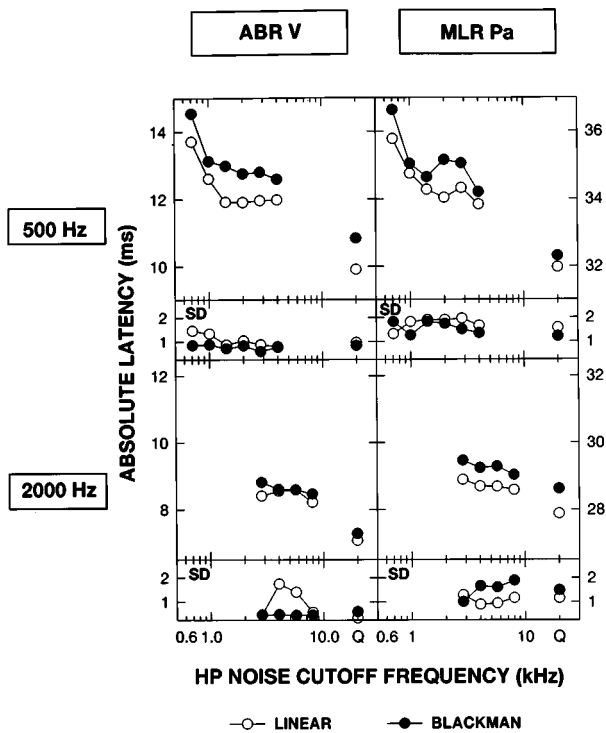


FIG. 5. Mean waves V and Pa absolute latencies and standard deviations (s.d.) to the 500- and 2000-Hz stimuli as a function of HP noise cutoff frequency. Results for the nonmasked QUIET condition, indicated by "Q," are also plotted. Each symbol represents a minimum of 10 subjects for the 500-Hz tones and 11 subjects for the 2000-Hz tones.

500-Hz stimuli compared to the responses to the 2000-Hz tones, reflecting the longer cochlear delays associated with apical cochlear activation.

Latency data were analyzed in a similar manner for responses to each stimulus frequency (i.e., down to within one-half octave above the nominal stimulus frequency). Responses at lower HP cutoff frequencies were few and thus were not included. Specifically, the HP noise cutoff frequencies analyzed for the 500-Hz stimuli were from 707 to 4000 Hz; the cutoff frequencies evaluated for the 2000-Hz tones were from 2830 to 8000 Hz. Results for the Quiet condition were not included. Separate three-way repeated measures ANOVAs were carried out on the absolute latency values from 10 subjects' responses to the 500-Hz tones and eight subjects' responses to the 2000-Hz tones. The remaining subjects' data were excluded from the analyses because their waveforms did not contain replicable responses to the exact-Blackman- and/or linear-gated tones in the lowest HP noise conditions included in the analyses (i.e., 707 Hz for the 500-Hz tones; 2830 Hz for the 2000-Hz tones). The results of the ANOVAs, presented in Table I (right side), reveal an expected significant main effect for wave for both stimulus frequencies, with longer latencies for MLR wave Pa. A significant main effect for HP noise cutoff frequency is seen for the 500-Hz stimuli only. *Post hoc* comparisons reveal that the latencies of the responses recorded to the 500-Hz tones in the presence of 707 and 1000 Hz HP noise masking are significantly longer than those recorded in HP noise with higher cutoff frequencies (i.e., 1410–4000 Hz). Small but nonsignificant latency increases are seen for the responses to

the 2000-Hz tones as the cutoff frequency of the HP noise is lowered. The results of the ANOVAs also demonstrate that the latencies of the responses to the exact-Blackman-gated tones are significantly longer in comparison to the responses to the linear-gated tones (significant main effect for window). No interactions involving wave reached statistical significance for either of the stimulus frequencies.

### III. DISCUSSION

#### A. Frequency specificity of evoked potentials to brief tones

The results of this HP noise study suggest that the ABR and the MLR show reasonably good frequency and place specificity to 500- and 2000-Hz brief tones presented at 80 dB ppe SPL. The amplitude profiles for the HP masking conditions illustrate that there are no significant decreases in response amplitudes until the cutoff frequency of the noise is lowered to 707 Hz for the 500-Hz stimuli, and to 2000 Hz for the 2000-Hz tones. This indicates that any spread of stimulus energy or cochlear excitation to frequency regions more than one-half octave above the nominal frequency does not contribute to these responses.

Similarly, significant increases in the response latencies to the 500-Hz tones occurred in this study only when the cutoff frequency of the HP noise was within a half to one octave of the nominal stimulus frequency. Lowering of the cutoff frequency of the noise from 8000 to 2830 Hz produced small but nonsignificant increases in latencies to the 2000-Hz tones. Significant latency changes for the responses to 2000-Hz tones are less likely compared to the responses to the 500-Hz tones because: (1) removing contributions to the response from more basal regions of the cochlea produce very small changes in the response latencies to the 2000-Hz tones due to the better neural synchrony of responses to stimulation of the higher frequency regions of the cochlea (Kiang, 1975); (2) an equivalent latency shift corresponds to a greater distance along the basilar membrane in the 2000-Hz region compared to the 500-Hz region (Tonndorf, 1970); and (3) the longer cochlear delay times associated with apical versus basal cochlear activation (Békésy, 1960). When the cutoff frequency of the noise was equal to or lower than the nominal stimulus frequency (i.e., 500 and 2000 Hz), the evoked potentials completely disappear, suggesting that cochlear contributions to these responses come from a relatively narrow region along the cochlear partition.

Our interpretation of the changes in the amplitudes and latencies of the responses as a function of the cutoff frequency of the HP noise seen in this study is supported by physiological data obtained from direct cochlear nerve fiber recordings in cats to moderate-intensity click stimuli (Evans and Elberling, 1982). Evans and Elberling's results show a sharp dropoff, or transition, in the amplitude profiles from nonmasked to totally masked cochlear fiber response when the cutoff frequency of the HP noise is either equal to or within one-half to one octave of the fiber's characteristic frequency (CF). They also showed that lowering the cutoff frequency of the HP noise had no effect on the absolute latencies of the peaks in the cochlear fiber histograms until

the cutoff frequency was within a half octave of the CF of the cochlear fiber (Evans and Elberling, 1982).

In contrast to the findings of the current study, Burkard and Hecox (1983) reported an increase in mean absolute wave V latencies of approximately 1.5 ms as the cutoff frequency of HP noise was lowered from 8000 to 1000 Hz for responses to 82 dB ppe SPL 1000-Hz tones presented in 63 dB SPL broadband noise. Based on these latency changes, Burkard and Hecox concluded that the nonmasked response to the moderate-intensity 1000-Hz tones lacked frequency specificity and predominately reflected contributions to the response from the basal regions of the cochlea. Latency profiles, however, tend to reflect any higher frequency contributions to a response to a greater extent than coexisting lower frequency contributions. Amplitude profiles tend to give a different picture. For example, compare the latency and amplitude pure-tone masking profiles presented by Folsom (Folsom, 1984, Figures 2a and 3a): the latency profile shows that only the 3000- and 4000-Hz regions of the basilar membrane contribute to ABR wave V to 40-dB nHL nonmasked clicks. In contrast, Folsom's amplitude profile indicates cochlear contributions to the nonmasked response arise from a broader range of frequencies (1000–8000 Hz). Similarly, Don and Eggermont, employing the high-pass noise derived response (HP/DR) technique, have demonstrated that ABR wave V latencies to 40–60 dB SL (sensation level) nonmasked clicks reflect cochlear contributions from the higher frequencies even though the response contains contributions from nearly the entire cochlear partition (Don and Eggermont, 1978; Eggermont and Don, 1980).

Burkard and Hecox (1983) did not provide amplitude results for their various HP noise conditions, making comparisons to the current as well as other studies difficult. Methodological differences (e.g., differences in the intensity of the masking noise) as well as the differences in criteria used to determine frequency and place specificity (amplitude versus latency changes) may explain why Burkard and Hecox (1983) reached different conclusions regarding the frequency specificity of responses to moderate-intensity tonal stimuli. The present study's results—amplitude and latency—are quite different from their results. It is, therefore, appropriate to consider the results of other studies employing different masking paradigms.

Studies which have investigated the frequency specificity of the ABR to tonal stimuli by comparing the responses recorded in quiet to those recorded in notched noise maskers have shown that the responses are frequency specific when tones are presented at 70 dB ppe SPL or lower. When stimulus intensities are greater than 70 dB ppe SPL, however, the response is in part influenced by contributions from frequencies away from the nominal stimulus frequency (Beattie and Kennedy, 1992; Jacobson, 1983; Picton *et al.*, 1979; Stapells, 1984; Stapells and Picton, 1981). That is, above 70 dB ppe SPL, the introduction of notched noise masking significantly increases the latency and decreases the amplitude of ABR wave V compared to the nonmasked response, with larger changes in wave V latency occurring for the responses to the 500-Hz tones compared to responses to the 2000-Hz tones. The early notched-noise investigations, however, did

not determine which specific frequency regions along the basilar membrane were contributing to the nonmasked response. This is because the center frequency of the notch was fixed at the nominal stimulus frequency. Recently, Abdala and Folsom (1995) varied the location of the notch along the basilar membrane in order to more directly assess cochlear contributions to ABR wave V to moderate intensity (77–86 dB ppe SPL) nonmasked tonal stimuli. They centered their one-octave-wide notch at 1/3-octave intervals above and below the stimulus test frequencies (e.g., for the 1000-Hz tones, the center frequencies of the notched noise were: 666, 833, 1000, 1333, and 1666 Hz). Abdala and Folsom (1995) reported that the maxima in their response amplitude profiles occurred at the nominal stimulus frequencies, indicating that the nonmasked ABRs are frequency and place specific. They also calculated bandwidth as well as low- and high-frequency slope measures on the amplitude profiles, and confirmed the sharp tuning of the tonal ABRs.

Finally, a number of studies have employed pure-tone masking to investigate the frequency and place specificity of evoked potentials to tonal stimuli (Brown and Abbas, 1987; Dolan and Klein, 1987; Folsom, 1984, 1985; Folsom and Wynne, 1987; Klein, 1983; Klein and Mills, 1981a, 1981b; Mackersie *et al.*, 1993; Wu and Stapells, 1994). The results of these pure-tone masking studies have shown that ABRs and MLRs to low- and moderate-intensity (60–80 dB ppe SPL) 500–8000 Hz tonal stimuli have good frequency and place specificity, with maximal masking (latency and amplitude profiles) occurring either at the nominal stimulus frequency or within less than a half octave of this frequency. The pure-tone masking profiles also have steep low- and high-frequency slopes, indicating little or no contributions to the nonmasked response from regions of the basilar membrane one or more octaves away from the nominal stimulus frequency. Considered together, the findings in the present study and the results from previous notched noise and pure-tone masking studies strongly suggest that ABRs and MLRs to 80 dB ppe SPL nonmasked tonal stimuli have good frequency and place specificity.

The pure-tone masking studies by Folsom (1984) have also shown that higher stimulus intensities can degrade the frequency and place specificity of ABRs to lower-frequency tonal stimuli. His wave V amplitude and latency profiles to 1000-Hz stimuli (filtered clicks) presented at 75 dB peak SPL (measured in a 6-cc coupler) are sharply tuned to the nominal stimulus frequency. When these same stimuli are presented at 95 dB peak SPL, however, the profiles (amplitude and latency) peak at 1500 Hz with significant cochlear contributions to the response from the 2000–4000 Hz regions. Folsom's findings suggest that there is a critical stimulus intensity, located between 75 and 95 dB peak SPL, above which the responses to nonmasked low-frequency tones becomes substantially less frequency and place specific. The results of our current study indicate that this critical level likely occurs between 81 and 92 dB ppe SPL—approximately 55–65 dB nHL (Purdy *et al.*, 1989; Stapells *et al.*, 1990)—for both the ABR and MLR. Future masking studies, however, are needed to carefully define this critical level.



## B. Frequency specificity of the ABR versus the MLR

No significant differences were found in the frequency specificity of ABR wave V-V' versus that of MLR wave Na-Pa, as illustrated by the amplitude and latency profiles for the HP noise conditions. The lack of significance for the differences in frequency specificity of the ABR versus the MLR is in agreement with studies by Mackerse *et al.* (1993) and Wu and Stapells (1994), which demonstrated that the ABR and MLR are equally frequency specific for low-intensity (i.e., 60 dB ppe SPL) 500- and 2000-Hz tones. The results of the present study, however, are not in agreement with those of Smith *et al.* (1990), who concluded that the MLR is less frequency specific compared to the ABR because their MLR frequency tuning curves had a similar V-shape but wider width than the ABR curves and that the MLRs were more susceptible to effects of pure-tone masking than the ABR. The contradictory findings between Smith *et al.* (1990) and the present results may be due to differences in the masking procedures employed (HP noise versus pure-tone masking), differences in generators between the species (humans versus gerbils), or differences in adaptation characteristics for the ABR versus the MLR (simultaneous versus forward masking).

## C. Responses to exact-Blackman- versus linear-gated tones

The mean amplitude and latency profiles for the responses recorded in HP noise show no significant differences exist in the frequency specificity of the evoked potentials to the exact-Blackman- versus linear-gated tones. This finding is in agreement with unpublished results of Purdy and Abbas (1989), and does not provide support for the recommendation to use Blackman-gated tones specifically to improve the frequency specificity of the ABR (e.g., Gorga *et al.*, 1992; Gorga and Thornton, 1989; Telian and Kileny, 1989).

## D. ABRs and MLRs to 500- vs 2000-Hz tones

ABRs and MLRs recorded to 80 dB ppe SPL 500-Hz tones in quiet are longer in latency compared to the responses recorded to the same intensity 2000-Hz tones. The longer latency of the nonmasked 500-Hz responses is due to the greater cochlear delay times associated with apical cochlear activation. Latency delays of approximately 3–4 ms are seen for waves V and Pa as stimulus frequency is changed from 2000 to 500 Hz. There is no significant difference in the frequency-based latency delay for the ABR versus MLR. The size of the latency shift for waves V and Pa as a function of stimulus frequency reported in this study are in general agreement with the latency shifts reported by previous investigations (Stapells, 1984; Stapells and Picton, 1981; Wu and Stapells, in preparation). The longer latencies for the nonmasked responses to the 500-Hz tones may also be, in part, due to their longer rise times (4–5 ms) compared to the 2000-Hz tones (1–1.25 ms). Previous studies have shown longer rise times result in later wave V latencies (Jacobson, 1983; Kodera *et al.*, 1977b; Stapells and Picton, 1981).

In the present study, no differential effects of stimulus frequency were found on the nonmasked amplitudes of

waves V-V' and Na-Pa, although there was a nonsignificant trend for wave Na-Pa to be slightly larger for the responses to the 500-Hz tones compared to the 2000-Hz tones. This finding is in agreement with the results of Wu and Stapells who also report no significant wave V-V' amplitude differences for responses to 500- vs 2000-Hz tones (Wu and Stapells, in preparation). Those authors, however, did find slightly but significantly larger Na-Pa amplitudes for the 500- versus 2000-Hz tonal stimuli (Wu and Stapells, in preparation). The current study also showed that the nonmasked amplitude of MLR wave Na-Pa is significantly larger compared to ABR wave V-V'. This finding is in agreement with previous studies (Scherg and Volk, 1983; Wu and Stapells, 1994; in preparation) and this amplitude effect is likely a reflection of the nature of the measurement (i.e., determining where the ABR wave V ends and the MLR wave Na begins).

In the current study, the noise masking had a greater impact on the amplitudes of the ABRs and MLRs recorded to the 2000-Hz tones compared to those recorded to the 500-Hz stimuli, with this effect especially evident for MLR wave Na-Pa (see Fig. 2). Several studies of the ABR have shown that broadband, high-pass, or notched-noise masking produce greater decreases in the amplitude of responses to higher- versus lower-frequency stimuli (Beattie and Kennedy, 1992; Burkard and Hecox, 1983, 1987; Purdy *et al.*, 1989; Stapells, 1984; Stapells *et al.*, 1994, 1985). This greater masking effect on responses to the 2000-Hz tones is likely related, at least in part, to the larger behavioral threshold shifts produced by broadband noise for higher- versus lower-frequency tonal stimuli (Hawkins and Stevens, 1950).

## E. Response changes seen with the introduction of the HP masker

The evoked potentials recorded in HP noise masking were smaller in amplitude and longer in latency than the nonmasked responses. This occurred for responses to both stimulus frequencies. These changes in response amplitudes and latencies are evident at the highest HP noise cutoff frequency for each tonal stimulus (i.e., HP 4000 Hz for the 500-Hz tones and HP 8000 Hz for the 2000-Hz tones).

One possible explanation for these changes is a low-level (approximately 30 dB SPL) broadband noise masking effect resulting from the input broadband noise intensity (mean=92 dB SPL) being higher than the maximum stop-band attenuation of the HP filter (measured attenuation=63.25 dB). Burkard and Hecox (1983) have demonstrated that broadband masker intensities of 23 dB SPL and above produce decreases in the amplitude of wave V to moderate intensity 1000- and 4000-Hz tones, and increases in wave V latency when noise levels are 33 dB SPL or greater. Consistent with this "broadband masking" explanation, no further changes in amplitude or latency were seen in the present study until the HP masker cutoff approached (i.e., within one-half to one octave) the tone's nominal frequency.

An alternative or, more likely, an additional factor accounting for some of the changes in the amplitude and la-

tency with the introduction of the high-pass noise at the highest cutoff frequency may be a central masking effect. The MLR has been shown to be more susceptible than the ABR to masking noise delivered to the ear contralateral to stimulation (Galambos and Makeig, 1992) [as well as to masking delivered ipsilaterally (Gott and Hughes, 1989)]. This greater effect of “central masking” on the MLR would be consistent with the findings of the present study.

Finally, there may be a third explanation for the shift in latencies and amplitudes which occurred with the introduction of high-pass masking noise 2–3 octaves above the stimulus frequency. The nonmasked response may actually receive substantial contributions from the high-frequency regions of the cochlea located above the highest cutoff frequency of the noise, and well above (2–3 octaves) the stimulus frequencies. Although it cannot be definitely ruled out, this third explanation appears unlikely for the following reasons. First, there are no significant changes in the amplitude or latency of the response as the HP noise cutoff frequency is lowered from 2 to 3 octaves above the nominal stimulus frequency until the HP cutoff frequency is within 0.5–1.0 octaves above the stimulus nominal frequency. If this explanation were correct, one would expect there to be amplitude decreases and latency increases with each HP cutoff change. Second, at an equivalent number of octaves above the stimulus frequency, the decreases in amplitude are greater for responses to 2000-Hz tones compared to responses to 500-Hz tones. For example, the mean normalized wave V-V' amplitudes (averaged across exact-Blackman and Linear windows) are: 61% for responses to 2000-Hz tones with a 8-kHz HP cutoff, and 70% for responses to 500-Hz tones with a 2-kHz HP cutoff. Such a finding, if not related to a simple low-level broadband noise masking and/or central masking effect, would suggest poorer frequency and place specificity of the ABR to 2000-Hz tones compared to 500-Hz tones. Such a view is not supported by previous electrophysiologic research, auditory nerve physiology [higher Q10 values are consistently reported for cochlear nerve fibers with higher versus lower CFs, indicating sharper tuning (for review, see Pickles, 1988)], nor current beliefs regarding the frequency specificity of the ABR (for reviews, see Stapells *et al.*, 1995, 1985). Third, the approximately 3-ms latency shift for the responses to 2-kHz tones seen with the introduction of the 8-kHz HP masker must be explained by mechanism(s) other than a shift in cochlear place, since 3 ms is much greater than the time required to travel from the base to 2-kHz cochlear place. Fourth, many studies employing pure-tone or notched-noise masking in adults and infants have shown that ABRs to 500-, 1000-, 2000-, 4000-, and 8000-Hz air-conducted tones presented at stimulus intensities ranging from 60 to 86 dB ppe SPL show quite good frequency and place specificity (Abdala and Folsom, 1995; Dolan and Klein, 1987; Folsom, 1984, 1985; Folsom and Wynne, 1987; Klein, 1983; Mackersie *et al.*, 1993; Wu and Stapells, 1994). These studies have demonstrated that the maximum reductions or peaks in the ABR amplitude and latency profiles occurred either at the nominal stimulus frequency or within a narrow range (half-octave) of this frequency. This final explanation for the shift in latencies and amplitudes which occurred with the intro-

duction of high-pass masking noise 2–3 octaves above the stimulus frequency therefore seems the least plausible of the three possibilities.

#### IV. CONCLUSIONS

The mean amplitude and latency profiles for the responses recorded in HP noise indicate that ABR V-V' and MLR Na-Pa to moderately intense (80 dB ppe SPL) exact-Blackman- and linear-gated tones are frequency and place specific. There are no significant differences in the frequency and place specificity of the ABR versus MLR or for responses to exact-Blackman- versus linear-gated tones. If one assumes that contributions from frequencies *lower* than the tones' nominal frequencies are equal to (or, more likely, less than) those from higher frequencies, cochlear contributions to these responses come from narrow regions along the basilar membrane (i.e., within one-half octave above and below the nominal stimulus frequency). Contributions from frequency regions below the stimulus' nominal frequencies, however, were not directly assessed by the use of high-pass noise masking alone. In order to assess these lower frequency contributions at and above the nominal frequencies, narrow-band “derived” responses must be calculated. These derived response analyses are presented in our following paper (Oates and Stapells, 1997).

The present results apply only to moderate intensity (80 dB ppe SPL) nonmasked tonal stimuli. It is likely that responses to higher stimulus intensities ( $\geq 90$  dB ppe SPL) will show increased cochlear contributions from frequencies away from the nominal stimulus frequency due to the increased effects of spectral splatter as well as the upward spread of cochlear excitation. Future research is needed to better define the frequency and place specificity of evoked potentials to nonmasked high-intensity tones and thus their potential application in the clinical evaluation of hearing sensitivity, especially with the hearing-impaired population.

#### ACKNOWLEDGMENTS

This manuscript is based on the Ph.D. dissertation of the first author, submitted to the City University of New York Ph.D. Program in Speech and Hearing Sciences. This research was funded in part by an American Speech-Language-Hearing Foundation Student Research grant (1993) to the first author, as well as by NIDCD Grant No. 8P50 DC00223 to the second author. We would also like to express our appreciation for the insightful feedback and suggestions we received on this manuscript from Dr. William H. Martin, Dr. Arthur Boothroyd, and Dr. Terence W. Picton, as well as to two reviewers for their very helpful suggestions.

<sup>1</sup>An evaluation of the lowest amplitude values recorded for “response present” waveforms was made to determine whether these values were close to 0  $\mu$ V. Of the 960 possible amplitude measures for ABR wave V-V' and MLR wave Na-Pa (480 values each), 134 of the wave V and 154 of the wave Na-Pa were scored as zero  $\mu$ V. At least 90% of these 0- $\mu$ V values for the ABR and MLR occurred when the HP cutoff frequency was at or below the nominal stimulus frequencies. The smallest recorded values were 0.07  $\mu$ V for wave V-V' and 0.11  $\mu$ V for wave Na-Pa, both of which are close to zero. Thus the insertion of a 0- $\mu$ V value for waves judged as “no response” appears to have been a reasonable estimate. It is possible,

however, that the use of 0- $\mu$ V values for responses judged as “no response” violated the assumptions of the ANOVA regarding normal distributions and heterogeneity of variance, even though the ANOVA is quite robust to such violations (Glass and Hopkins, 1996). Therefore, we re-analyzed the amplitude data by re-calculating the ANOVAs eliminating those conditions containing “no-response” results. The pattern of the results remained the same (see Sec. II).

<sup>2</sup>Possible explanations for the changes in response amplitude and latency which occurred at both stimulus frequencies with the introduction of HP noise masking at the highest cutoff frequencies (i.e., HP 4000 Hz for the responses to 500-Hz tones and HP 8000 Hz for responses to 2000-Hz tones) are presented in Sec. III.

Abdala, C., and Folsom, R. C. (1995). “The development of frequency resolution in humans as revealed by the auditory brain-stem response recorded with notched noise masking,” *J. Acoust. Soc. Am.* **98**, 921–930.

ANSI (1989). ANSI S3.6-1989, “Specification for Audiometers,” ANSI, New York.

Beattie, R. C., and Kennedy, K. M. (1992). “Auditory brainstem response to tone bursts in quiet, notch-noise, high-pass noise, and broadband noise,” *J. Am. Acad. Audiol.* **3**, 349–360.

Beiter, R. C., and Hogan, D. D. (1973). “Effects of variations in stimulus rise-decay time upon the early components of the auditory evoked response,” *Electroencephalogr. Clin. Neurophysiol.* **34**, 203–206.

Békésy, G. von (1960). *Experiments in Hearing* (McGraw-Hill, New York).

Brown, C. J., and Abbas, P. J. (1987). “A comparison of AP and ABR tuning curves in the guinea pig,” *Hearing Res.* **25**, 193–204.

Burkard, R. (1984). “Sound pressure level measurement and spectral analysis of brief acoustic transients,” *Electroencephalogr. Clin. Neurophysiol.* **57**, 83–91.

Burkard, R., and Hecox, K. (1983). “The effect of broadband noise on the human auditory evoked response. II. Frequency specificity,” *J. Acoust. Soc. Am.* **74**, 1214–1223.

Burkard, R., and Hecox, K. E. (1987). “The effect of broadband noise on the human brain-stem auditory evoked response. III. Anatomic locus,” *J. Acoust. Soc. Am.* **81**, 1050–1063.

Davis, H. (1976). “Principles of electronic response audiometry,” *Ann. Otol. Rhinol. Laryngol.* **85** (Suppl. 28), 1–96.

Davis, H., and Hirsh, S. K. (1976). “The audiometric utility of brain stem responses to low-frequency sounds,” *Audiology* **15**, 181–195.

Davis, H., and Hirsh, S. K. (1979). “A slow brainstem response for low-frequency audiometry,” *Audiology* **18**, 445–461.

Dolan, T. G., and Klein, A. J. (1987). “Effect of signal temporal shaping on the frequency specificity of the action potential in gerbils,” *Audiology* **26**, 20–30.

Don, M., and Eggermont, J. J. (1978). “Analysis of the click-evoked brainstem potentials in man using high-pass masking,” *J. Acoust. Soc. Am.* **63**, 1084–1092.

Eggermont, J. J. (1976). “Electrocochleography,” in *Handbook of Sensory Physiology*, edited by W. D. Keidel and W. D. Neff (Springer-Verlag, New York), Vol. 5(3), pp. 625–705.

Eggermont, J. J., and Don, M. (1980). “Analysis of the click-evoked brainstem potentials in humans using high-pass noise masking. II. Effect of click intensity,” *J. Acoust. Soc. Am.* **68**, 1671–1675.

Evans, E. F., and Elberling, C. (1982). “Location specific components of the gross cochlear action potential. An assessment of the validity of the high-pass noise masking technique by cochlear nerve fiber recording in the cat,” *Audiology* **21**, 204–227.

Folsom, R. C. (1984). “Frequency specificity of human auditory brainstem responses as revealed by pure-tone masking profiles,” *J. Acoust. Soc. Am.* **75**, 919–924.

Folsom, R. C. (1985). “Auditory brain stem responses from human infants: Pure-tone masking profiles for clicks and filtered clicks,” *J. Acoust. Soc. Am.* **78**, 555–562.

Folsom, R. C., and Wynne, M. K. (1987). “Auditory brain stem responses from human adults and infants: Wave V tuning curves,” *J. Acoust. Soc. Am.* **81**, 412–417.

Galambos, R., and Makeig, S. (1992). “Physiological studies of central masking in man. I: The effects of noise on the 40-Hz steady-state response,” *J. Acoust. Soc. Am.* **92**, 2683–2690.

Gerken, G. M., Moushegian, G., Stillman, R. D., and Rupert, A. L. (1975). “Human frequency-following responses to monaural and binaural stimuli,” *Electroencephalogr. Clin. Neurophysiol.* **38**, 379–386.

Glass, G. V., and Hopkins, K. D. (1996). *Statistical Methods in Education and Psychology* (Allyn and Bacon, Boston), 3rd ed., pp. 402–405.

Gorga, M. P., Beauchaine, K. L., Kaminski, J. R., and Bergman, B. M. (1992). “Use of tone bursts in ABR evaluations,” *Am. J. Audiol.* **1**, 11–12.

Gorga, M. P., and Thornton, A. R. (1989). “The choice of stimuli for ABR measurements,” *Ear Hear.* **10**, 217–230.

Gott, P. S., and Hughes, E. C. (1989). “Effect of noise masking on the brain-stem and middle-latency auditory evoked potentials: Central and peripheral components,” *Electroencephalogr. Clin. Neurophysiol.* **74**, 131–138.

Greenhouse, S. W., and Geisser, S. (1959). “On methods in the analysis of profile data,” *Psychometrika* **24**, 95–112.

Harris, F. J. (1978). “On the use of windows for harmonic analysis with the discrete Fourier transform,” *Proc. IEEE* **66**, 51–84.

Hawkins, J. E., and Stevens, S. S. (1950). “The masking of pure tones and of speech by white noise,” *J. Acoust. Soc. Am.* **22**, 6–13.

Hyde, M. L. (1985). “Frequency-specific BERA in infants,” *J. Otolaryngol.* (Suppl. 14), 19–27.

Hyde, M. L., Matsumoto, N., and Alberti, P. W. (1987). “The normative basis for click and frequency-specific BERA in high-risk infants,” *Acta Oto-Laryngol.* **103**, 602–611.

Jacobson, J. T. (1983). “Effects of rise time and noise masking on tone pip auditory brainstem responses,” *Sem. Hear.* **4**, 363–372.

Kavanagh, K. T., Harker, L. A., and Tyler, R. S. (1984). “Auditory brainstem and middle latency responses. II. Threshold responses to a 500-Hz tone pip,” *Ann. Otol. Rhinol. Laryngol.* **93** (Suppl. 108), 8–12.

Kiang, N. Y. S. (1975). “Stimulus representation in the discharge patterns of auditory neurons,” in *The Nervous System, Vol. 3: Human Communication and Its Disorders*, edited by D. B. Tower (Raven, New York), pp. 81–96.

Kileny, P. (1981). “The frequency specificity of tone-pip evoked auditory brain stem responses,” *Ear Hear.* **2**, 270–275.

Kileny, P. R., and Magathan, M. G. (1987). “Predictive value of ABR in infants and children with moderate to profound hearing impairment,” *Ear Hear.* **8**, 217–221.

Kileny, P., and Shea, S. L. (1986). “Middle-latency and 40-Hz auditory evoked responses in normal-hearing subjects: Click and 500-Hz thresholds,” *J. Speech Hear. Res.* **29**, 20–28.

Klein, A. J. (1983). “Properties of the brain-stem response slow-wave component. II. Frequency specificity,” *Arch. Otolaryngol.* **109**, 74–78.

Klein, A. J., and Mills, J. H. (1981a). “Physiological (waves I and V) and psychophysical tuning curves in human subjects,” *J. Acoust. Soc. Am.* **69**, 760–767.

Klein, A. J., and Mills, J. H. (1981b). “Physiological and psychophysical measures from humans with temporary threshold shift,” *J. Acoust. Soc. Am.* **70**, 1045–1053.

Kodera, K., Yamane, H., Yamada, O., and Suzuki, J.-I. (1977a). “Brain stem response audiometry at speech frequencies,” *Audiology* **16**, 469–479.

Kodera, K., Yamane, H., Yamada, O., and Suzuki, J.-I. (1977b). “The effect of onset, offset and rise-decay times of tone bursts on brain stem response,” *Scand. Audiol.* **16**, 205–210.

Kramer, S. J. (1992). “Frequency-specific auditory brainstem responses to bone-conducted stimuli,” *Audiology* **31**, 61–71.

Laukli, E. (1983a). “Stimulus waveforms used in brainstem response audiometry,” *Scand. Audiol.* **12**, 83–89.

Laukli, E. (1983b). “High-pass and notch noise masking in suprathreshold brainstem response audiometry,” *Scand. Audiol.* **12**, 109–115.

Laukli, E., Fjermedal, O., and Mair, I. W. S. (1988). “Low-frequency auditory brainstem response threshold,” *Scand. Audiol.* **17**, 171–178.

Laukli, E., and Mair, I. W. S. (1986). “Frequency specificity of the auditory brainstem responses. A derived-band study,” *Scand. Audiol.* **15**, 141–146.

Mackersie, C., Down, K. E., and Stapells, D. R. (1993). “Pure-tone masking profiles for human auditory brainstem and middle latency responses,” *Hearing Res.* **65**, 61–68.

Munnerley, G. M., Greville, K. A., Purdy, S. C., and Keith, W. J. (1991). “Frequency-specific auditory brainstem responses: Relationship to behavioral thresholds in cochlear-impaired adults,” *Audiology* **30**, 25–32.

Nousak, J. M. K., and Stapells, D. R. (1992). “Frequency specificity of the auditory brain stem response to bone-conducted tones in infants and adults,” *Ear Hear.* **13**, 87–95.

Nuttall, A. H. (1981). “Some windows with very good sidelobe behavior,” *IEEE Trans. Acoust., Speech, Signal Process.* **29**, 84–91.

- Oates, P. A., and Stapells, D. R. (1997). "Frequency specificity of the human auditory brainstem and middle latency responses to brief tones. II. Derived response analyses." *J. Acoust. Soc. Am.* **102**, 3609–3619.
- Palaskas, C. W., Wilson, M. J., and Dobie, R. A. (1989). "Electrophysiologic assessment of low-frequency hearing: Sedation effects," *Otolaryngol. Head Neck Surg.* **101**, 434–441.
- Pickles, J. O. (1988). *An Introduction to the Physiology of Hearing* (Academic, New York), 2nd ed.
- Picton, T. W., Ouellette, J., Hamel, G., and Smith, A. D. (1979). "Brainstem evoked potentials to tonepips in notched noise," *J. Otolaryngol.* **8**, 289–314.
- Purdy S., and Abbas, P. J. (1989). "Auditory brainstem response audiometry using linearly and Blackman gated tonebursts," *ASHA* **31**, 115–116.
- Purdy, S. C., Houghton, J. M., Keith, W. J., and Greville, K. A. (1989). "Frequency-specific auditory brainstem responses. Effective masking levels and relationship to behavioral thresholds in normal hearing adults," *Audiology* **28**, 82–91.
- Scherg, M., and Volk, S. A. (1983). "Frequency specificity of simultaneously recorded early and middle latency auditory evoked potentials," *Electroencephalogr. Clin. Neurophysiol.* **56**, 443–452.
- Sininger, Y. S., Abdala, C., and Cone-Wesson, B. (1997). "Auditory threshold sensitivity of the human neonate as measured by the auditory brainstem response," *Hearing Res.* **104**, 27–38.
- Smith, D. I., Mills, J. H., and Schmiedt, R. A. (1990). "Frequency selectivity of the middle latency response," *Hearing Res.* **43**, 95–106.
- Sohmer, H., and Kinarti, R. (1984). "Survey of attempts to use auditory evoked potentials to obtain an audiogram," *Br. J. Audiol.* **18**, 237–244.
- Stapells, D. R. (1984). "Studies in evoked potential audiometry," Doctoral Dissertation, University of Ottawa, Ontario, Canada.
- Stapells, D. R. (1989). "Auditory brainstem response assessment of infants and children," *Sem. Hear.* **10**, 229–251.
- Stapells, D. R., Gravel, J. S., and Martin, B. A. (1995). "Thresholds for auditory brain stem responses to tones in notched noise from infants and young children with normal hearing or sensorineural hearing loss," *Ear Hear.* **16**, 361–371.
- Stapells, D. R., and Picton, T. W. (1981). "Technical aspects of brainstem evoked potential audiometry using tones," *Ear Hear.* **2**, 20–29.
- Stapells, D. R., Picton, T. W., and Durieux-Smith, A. (1994). "Electrophysiologic measures of frequency-specific auditory function," in *Principles and Applications in Auditory Evoked Potentials*, edited by J. T. Jacobson (Allyn and Bacon, Needham Heights), pp. 251–283.
- Stapells, D. R., Picton, T. W., Durieux-Smith, A., Edwards, C. G. and Moran, L. M. (1990). "Thresholds for short-latency auditory-evoked potentials to tones in notched noise in normal-hearing and hearing-impaired subjects," *Audiology* **29**, 262–274.
- Stapells, D. R., Picton, T. W., Pérez-Abalo, M., Read, D., and Smith, A. (1985). "Frequency specificity in evoked potential audiometry," in *The Auditory Brainstem Response*, edited by J. T. Jacobson (College-Hill, San Diego), pp. 147–177.
- Suzuki, T., Hirai, Y., and Horiuchi, K. (1977). "Auditory brain stem responses to pure tone stimuli," *Scand. Audiol.* **6**, 51–56.
- Suzuki, T., Hirai, Y., and Horiuchi, K. (1981). "Simultaneous recording of early and middle components of auditory electric response," *Ear Hear.* **2**, 276–282.
- Suzuki, J.-I., Kodera, K., and Yamada, O. (1984). "Brainstem response audiometry in newborns and hearing-impaired infants," in *Sensory Evoked Potentials. An International Conference on Standards for Auditory Brainstem Response (ABR) Testing*, edited by A. Starr, C. Rosenberg, M. Don, and H. Davis (CRS Amplifon, Milan, Italy), pp. 85–93.
- Telian, S. A., and Kileny, P. R. (1989). "Usefulness of 1000 Hz tone-burst-evoked responses in the diagnosis of acoustic neuroma," *Otolaryngol. Head Neck Surg.* **101**, 466–471.
- Tonndorf, J. (1970). "Cochlear mechanics and hydro-dynamics," in *Foundations of Modern Auditory Theory*, Vol. 1, edited by J. V. Tobias (Academic, New York), pp. 205–254.
- Vivion, M. C., Hirsch, J. E., Frye-Osier, J. L., and Goldstein, R. (1980). "Effects of stimulus rise-fall time and equivalent duration on middle components of AER," *Scand. Audiol.* **9**, 223–232.
- Weber, B. A. (1987). "Assessing low frequency hearing using auditory evoked potentials," *Ear Hear.* **8** (Suppl. 4), 49–54.
- Wu, C.-Y., and Stapells, D. R. (1994). "Pure-tone masking profiles for human auditory brainstem and middle latency responses to 500-Hz tones," *Hearing Res.* **78**, 169–174.
- Wu, C.-Y., and Stapells, D. R. (in preparation). Detection of auditory brainstem and middle latency responses to clicks and brief tones. I: Expert human observers.

# Frequency specificity of the human auditory brainstem and middle latency responses to brief tones.

## II. Derived response analyses<sup>a)</sup>

Peggy Oates

*Auditory Evoked Potentials Research Laboratory, Albert Einstein College of Medicine, Bronx, New York and Doctoral Program in Speech and Hearing Sciences CUNY Graduate Center, New York, New York*

David R. Stapells<sup>b)</sup>

*School of Audiology and Speech Sciences, The University of British Columbia, 5804 Fairview Avenue, Vancouver, British Columbia V6T 1Z3, Canada*

(Received 15 August 1996; revised 22 August 1997; accepted 2 September 1997)

This study investigated the frequency specificity of the auditory brainstem (ABR) and middle latency (MLR) responses to 500- and 2000-Hz brief tones using narrow-band derived response analyses of the responses recorded in high-pass masking noise [Oates and Stapells, *J. Acoust. Soc. Am.* **102**, 3597–3608 (1997)]. Stimuli were linear- and exact-Blackman-gated tones presented at 80 dB ppe SPL. Cochlear contributions to ABR wave V-V' and MLR wave Na-Pa were assessed by response amplitude profiles as a function of derived band center frequency. The largest amplitudes of waves V and Na-Pa occurred in the 500- and 707-Hz derived bands in response to the exact-Blackman- and linear-gated 500-Hz tones. The peak in the response amplitude profiles for wave V to both 2000-Hz stimuli was seen in the 2000-Hz derived band. For wave Na-Pa, the maxima in the amplitude profiles occurred in the 2000- and 1410-Hz derived bands for the exact-Blackman- and linear-gated tones. Smaller cochlear contributions to the ABR/MLR were also present at 0.5–1 octave above and below the nominal stimulus frequencies. The ABR/MLR to 500- and 2000-Hz 80 dB ppe SPL tones thus shows good frequency specificity, with no significant differences in the frequency specificity of: (1) ABR versus MLR; (2) these evoked potentials to 500- versus 2000-Hz tones; and (3) responses to exact-Blackman- versus linear-gated tones. © 1997 Acoustical Society of America. [S0001-4966(97)06312-1]

PACS numbers: 43.64.Qh, 43.64.Ri [RDF]

## INTRODUCTION

In our previous paper, high-pass (HP) noise masking was used to investigate the regions of the cochlea that contribute to the nonmasked auditory brainstem (ABR) and middle latency (MLR) responses to moderate-intensity brief-tone stimuli (Oates and Stapells, 1997). If one assumes that cochlear contributions from frequencies lower than the tones' nominal frequencies are equal to (or, more likely, less than) those from higher frequencies, then the results of that study suggest that cochlear contributions to the nonmasked ABR and MLR to 80 dB peak-to-peak equivalent (ppe) SPL 500- and 2000-Hz brief tones come from a narrow region along the basilar membrane (i.e., within one-half to one octave above and below the nominal stimulus frequency). A disadvantage of using HP noise masking alone, however, is that it only directly assesses contributions to these evoked potentials from frequency regions located at and above the nominal stimulus frequencies. In order to determine cochlear contributions to the nonmasked response from regions of the basilar membrane below, as well as at and above, the tones'

nominal frequencies, narrow-band "derived" responses are calculated. Cochlear contributions to the derived responses may be assessed by plotting the amplitudes of the derived responses as a function of derived-band center frequency (Eggermont, 1976a, b; Eggermont *et al.*, 1976). The area below the response amplitude curves represent the frequency regions of the basilar membrane that are contributing to the nonmasked evoked potential.

The high-pass noise/derived response (HP/DR) technique has been used to investigate the frequency specificity of evoked potentials to specific stimuli, including brief tones of high- and low-frequency (Eggermont, 1976a, b; Kramer, 1992; Nousak and Stapells, 1992). In comparison to other noise-masking techniques (e.g., pure-tone masking and notched-noise masking), the HP/DR technique likely yields the most frequency- and place-specific evaluation of a response due to its use of HP noise masking, where, as a result of the steep high-frequency edge of the auditory nerve tuning curves, little or no downward spread of masking occurs (for reviews, see: Stapells *et al.*, 1994, 1985b).

In the HP/DR technique, the evoked potential to a stimulus is recorded in quiet and then simultaneously with broadband noise of sufficient intensity to completely mask the response. This broadband noise is then high-pass filtered, and the evoked potential is then recorded in the presence of the HP noise. The response obtained in HP noise at one

<sup>a)</sup>Portions presented at the 18th Midwinter Research Meeting of the Association for Research in Otolaryngology, St. Petersburg, FL, 7 February 1995; and at the 14th Biennial Symposium of the International Evoked Response Audiometry Study Group, Lyon, France, 29 August 1995.

<sup>b)</sup>Author to whom correspondence should be addressed. Electronic mail: stapells@audiospeech.ubc.ca

cutoff frequency is subtracted from the response obtained in the presence of HP noise with a higher cutoff frequency. The result is a “derived response” to the frequencies approximately between the two cutoff frequencies.<sup>1</sup> The assumptions underlying this technique are that: (1) the HP masker prevents contributions to the responses from cochlear fibers with characteristic frequencies above the HP cutoff frequency, leaving those fibers with characteristic frequencies below the HP cutoff frequency unaffected; (2) the subtraction procedure yields “derived responses” which represent cochlear activity limited to the frequency regions approximately between the two HP noise cutoff frequencies; and (3) the subtraction procedure is linear (i.e., that individual derived responses resulting from contributions of adjoining sections of the cochlea add up to the nonmasked response). Studies by Don and Eggermont (1978), Evans and Elberling (1982), and Parker and Thornton (1978a, b) have provided evidence that these assumptions are valid.

Derived response amplitude profiles may be determined for any frequency region along the cochlear partition, depending on the spacing of the HP noise cutoff frequencies. Typically, one-octave-wide or half-octave-wide regions along the basilar membrane have been studied (e.g., Burkard and Hecox, 1983; Don and Eggermont, 1978; Don *et al.*, 1979; Eggermont, 1976a, b; Eggermont and Don, 1980; Kramer, 1992; Nousak and Stapells, 1992; Ponton *et al.*, 1992a, b). The derived-band center frequencies (CFs) which contain the maximum response amplitudes provide a measure of the frequency specificity of the evoked potential to the specific stimulus. There are differences in the literature, however, concerning how specifically to determine the CF of the derived band (this issue is described in further detail in Sec. III). In the present study, the lower high-pass noise cutoff frequency has been selected as the CF of the derived band, similar to many previous derived response studies (Don *et al.*, 1979; Eggermont and Don, 1980; Kramer, 1992; Nousak and Stapells, 1992; Picton *et al.*, 1981; Stapells, 1984).

The purposes of this study were to evaluate derived response amplitude profiles (full- and half-octave-wide analyses) in order to assess: (1) cochlear contributions to the ABR and MLR to 80 dB ppe SPL 500- and 2000-Hz tones and differences, if any, in the frequency specificity of these responses across stimulus frequency; (2) the frequency and place specificity of ABR (wave V) versus MLR (wave Na-Pa); and (3) the frequency and place specificity of these responses to exact-Blackman versus linear-gated tones.

## I. METHODS

### A. Subjects, stimuli, noise masking, recordings, and procedure

Information regarding subject criteria, the generation, presentation, and calibration of the stimuli and the noise masking, the recording of the evoked potentials, and the testing procedures employed in the study have been presented in greater detail in our first paper (Oates and Stapells, 1997), and will be presented only briefly below. The ABR/MLR was recorded from 12 normal-hearing subjects with elec-

trodes placed on their vertex (Cz, noninverting), ipsilateral earlobe (A1 or A2, inverting), and forehead (Fpz, ground). Alternating-onset polarity 500- and 2000-Hz brief tones were presented in two conditions: (1) “2-1-2” linear-gated tones, consisting of a linear 2-cycle rise and 2-cycle fall time, and a plateau time of 1 cycle, and (2) exact-Blackman-gated tones, with a 5-cycle total duration and no plateau (Harris, 1978, formula 32). The stimuli were presented to one ear per subject at a rate of 9.4/s using Etymotic Research ER-2 insert earphones. Stimulus intensity was 80 dB ppe SPL, which corresponds to levels of 53 dB nHL for the 500-Hz stimuli and 52 dB nHL for the 2000-Hz stimuli.

Ipsilateral broadband pink noise was presented at an intensity of 92 dB SPL (mean across 12 subjects). Using half-octave steps, the HP noise cutoff frequencies employed for the 500-Hz stimuli ranged from 4.0 to 0.25 kHz; the HP cutoff frequencies for the 2000-Hz stimuli ranged from 8.0 to 0.5 kHz.

After amplification (gain=100 000), the electroencephalographic (EEG) signals were analog filtered (10–3000 Hz, 6 dB/octave) and digitized using a sampling rate of 12 128 Hz over an analysis time of 84 ms (including a prestimulus baseline of 3 ms). Averages of 1000 trials each were stored, with trials containing amplitudes exceeding  $\pm 25 \mu\text{V}$  automatically rejected. The averaged responses were digitally filtered *post hoc* in the frequency domain (forward and inverse FFTs; data not windowed) using a HP filter setting of 20 Hz (24 dB/octave) and a low-pass (LP) filter setting of 1000 Hz (96 dB/octave). Following digital filtering, average waveforms representing the overall average of 8000 sweeps were calculated, as were two replications of 4000 sweeps each and four replications of 2000 sweeps each.

All subjects were tested with the exact-Blackman- and linear-gated 500- and 2000-Hz stimuli in quiet, and simultaneously with broadband pink noise, and the nine HP noise conditions. Each stimulus frequency was tested over two sessions, with the HP noise conditions being presented in a different order for the second session. The orders of the stimulus frequencies, linear versus nonlinear stimuli, and the HP noise cutoff frequencies, were all randomized for each subject.

### B. Derived responses

Narrow-band derived responses were obtained by subtracting, in succession, individual recordings of the response to the tone in HP noise at one cutoff frequency from the response to the same frequency tone recorded in HP noise at a higher cutoff frequency. This technique was applied to determine the one-octave-wide and half-octave-wide contributions to the evoked potentials. The HP/DR subtraction technique resulted in seven separate derived responses for the full-octave analyses, and eight derived responses for the half-octave analyses. Only responses in the various HP noise conditions recorded within the same test session were subtracted from each other to obtain the derived responses.

The frequency of the lower of the two HP cutoff frequencies used in the subtraction was considered the CF of the derived band (Don *et al.*, 1979; Eggermont and Don, 1980; Kramer, 1992; Nousak and Stapells, 1992; Oates,

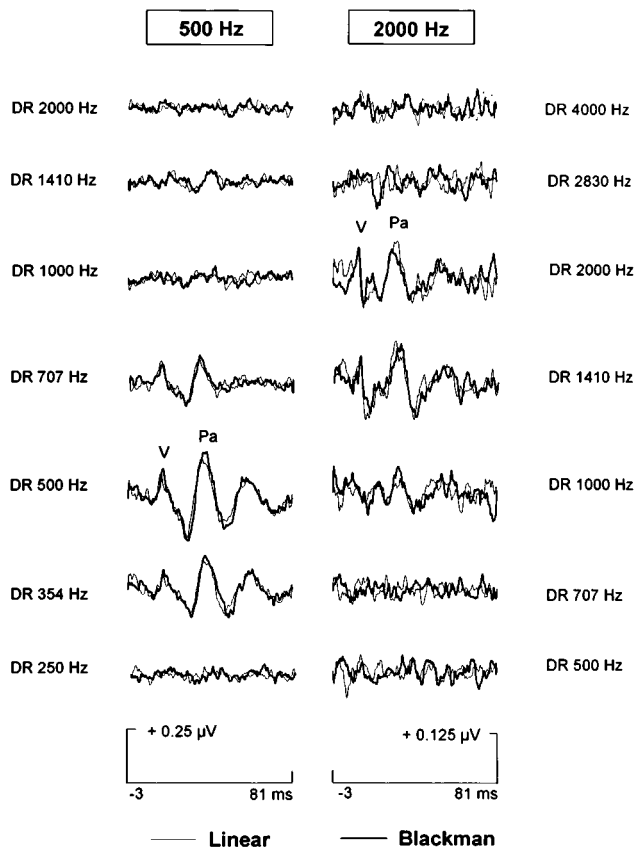


FIG. 1. Grand mean ( $N=12$ ) full-octave derived response waveforms to 80 dB ppe SPL exact-Blackman- and linear-gated 500- and 2000-Hz tones. Amplitude scale is  $+0.25 \mu\text{V}$  for responses to 500-Hz tones (left) and  $+0.125 \mu\text{V}$  for responses to 2000-Hz tones (right).

1996; Picton *et al.*, 1981; Stapells, 1984). The CFs for the full-octave derived responses are: 2.0, 1.41, 1.0, 0.707, and 0.50 kHz for both stimulus frequencies; as well as 0.354 and 0.25 kHz for the 500-Hz tones and 4.0 and 2.83 kHz for the 2000-Hz tones. The CFs for the half-octave derived responses are: 2.83, 2.0, 1.41, 1.0, 0.707, and 0.50 kHz for the two stimulus frequencies; as well as 0.354 and 0.25 kHz for the 500-Hz stimuli and 5.66 and 4.0 kHz for the 2000-Hz stimuli.

### C. Data analyses

Detailed descriptions of the criteria used to identify the responses as well as the response measurements taken are provided in the previous paper (Oates and Stapells, 1997) and therefore are not repeated here. Peak-to-peak amplitudes were analyzed using descriptive statistics and repeated-measures analyses of variance (ANOVAs).<sup>2</sup> Results for the full- and half-octave derived response profiles were analyzed independently. Greenhouse-Geisser epsilon corrections for the degrees of freedom for repeated measures were employed when appropriate (Greenhouse and Geisser, 1959). Probabilities reported reflect these corrections. Results were considered statistically significant if  $p < 0.01$ . When significant results were found in the ANOVAs, Newman-Keuls *post*

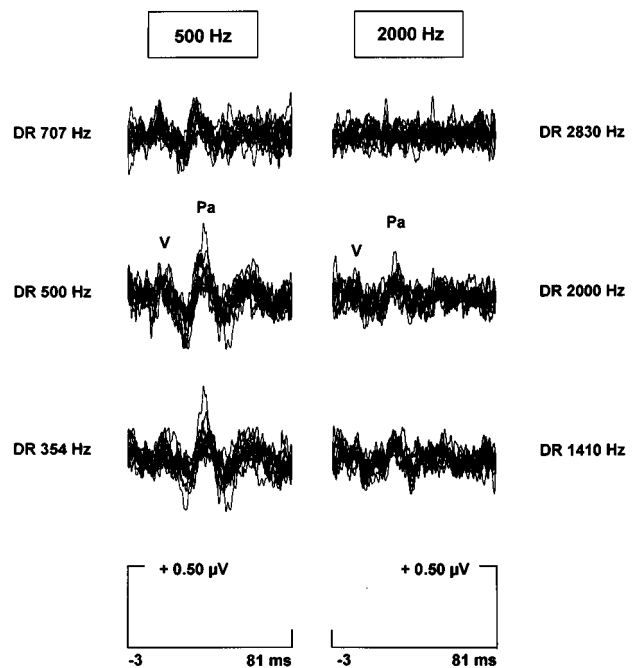


FIG. 2. Responses for all individual subjects' superimposed full-octave derived bands located within  $\frac{1}{2}$ -octave of the nominal stimulus frequencies for 80 dB ppe SPL linear-gated tones. Amplitude scales are  $+0.50 \mu\text{V}$  for responses to both stimulus frequencies.

*hoc* tests were performed to determine the pattern of the significant differences. Results of these *post hoc* analyses were considered significant at  $p < 0.05$ .

## II. RESULTS

### A. Full-octave derived responses

Figure 1 presents the grand mean derived response waveforms representing one-octave-wide regions along the basilar membrane for the exact-Blackman- and linear-gated tones at both stimulus frequencies. The largest amplitude ABR waves V-V' and MLR waves Na-Pa to the 500-Hz total stimuli are located in the responses in the 500-Hz derived band. Waves V and Pa are also present in the derived bands a half-octave above and below this nominal test frequency. The largest amplitude waves V-V' and Na-Pa to the 2000-Hz stimuli are in the responses from the 1410- and 2000-Hz derived bands. ABRs and/or MLRs are inconsistently present to either the 500- or 2000-Hz tones in the other derived bands.

The waveforms for each individual subject are superimposed in Fig. 2. Plotted are the full-octave derived bands containing the largest ABR wave V-V' and MLR wave Na-Pa amplitudes to the linear-gated 500- and 2000-Hz tones. These derived responses were selected for each stimulus frequency because they show the greatest changes in response amplitude and latency as a function of the CF of the derived band. A clear ABR wave V and MLR wave Pa can be identified in all of the derived bands with the exception of the 2830-Hz derived band for the 2000-Hz stimuli. The derived response waveforms are noisier than those seen for the HP noise conditions (Oates and Stapells, 1997, Fig. 3) due to the waveform subtraction technique, which increases

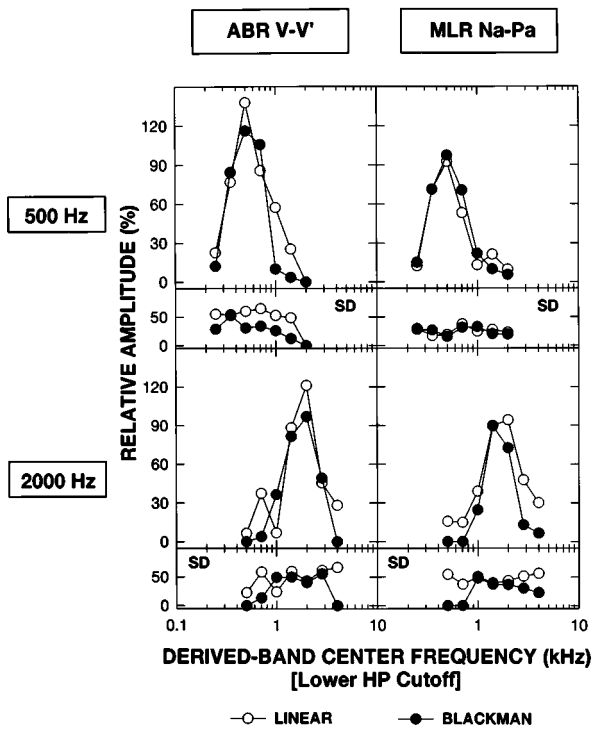


FIG. 3. Mean and standard deviation (sd) amplitude profiles for one-octave-wide derived responses (ABR wave V-V'; MLR wave Na-Pa) to 80 dB ppe SPL 500- and 2000-Hz exact-Blackman- versus linear-gated tones.

the root-mean-square value of the waveform's residual noise by 1.4 (i.e.,  $\sqrt{2}$ ) (Stapells *et al.*, 1994, 1985b). The changes in response amplitude and latency as a function of CF of the derived band seen in the grand mean waveforms (Fig. 1) are also clearly evident in the individual subjects' responses.

Peak-to-peak amplitudes of waves V-V' and Na-Pa were measured for each subject's derived responses. These amplitude values were then normalized to a percentage of the amplitudes of the subject's waves V-V' and Na-Pa recorded in the highest HP noise-masking condition (i.e., 4000 Hz for the 500-Hz stimuli, and 8000 Hz for the 2000-Hz stimuli). The amplitude values were normalized in this manner to correct for the decrease in amplitude which occurred with the introduction of the HP noise (Oates and Stapells, 1997). The mean relative amplitude values for ABR V-V' and MLR Na-Pa are plotted in Fig. 3 as a function of derived-band center frequency for each stimulus frequency and for each stimulus envelope. The peak in the mean amplitude profiles for the 500-Hz stimuli occurs at 500 Hz for waves V-V' and Na-Pa for both the exact-Blackman- and linear-gated tones. The peak in the mean amplitude profiles for the 2000-Hz stimuli occurs at 2000 Hz for ABR V-V' for both stimuli. For MLR Na-Pa, the peak occurs at 2000 Hz for responses to the linear-gated tone and at 1410 Hz for responses to the exact-Blackman tone. There are cochlear contributions to both of these responses from one-half to one-octave above and below the nominal stimulus frequencies. For individual subjects, the peaks in the derived response ABR and MLR amplitude profiles for the 500-Hz exact-Blackman- and linear-gated tones were seen within one-half-octave of the nominal stimulus frequency for 11 out of 12 subjects. For the

TABLE I. Probabilities from three-way repeated measures analyses of variance for full- and half-octave derived responses (DR).

Source of variance	Full-octave DR				Half-octave DR			
	500 Hz		2000 Hz		500 Hz		2000 Hz	
	df	$P^a$	df	$P$	df	$P$	df	$P$
Wave	1	0.019	1	0.183	1	0.004 <sup>b</sup>	1	0.639
Error term	11		11		11		11	
Window	1	0.472	1	0.149	1	0.349	1	0.37
Error term	11		11		11		11	
Derived response frequency (Hz)	6	0.0 <sup>b</sup>	6	0.0 <sup>b</sup>	7	0.0 <sup>b</sup>	7	0.0 <sup>b</sup>
Error term	66		66		77		77	
Wave×Window	1	0.93	1	0.312	1	0.168	1	0.991
Error term	11		11		11		11	
Wave×DR freq	6	0.025	6	0.076	7	0.146	7	0.168
Error term	66		66		77		77	
Window×DR freq	6	0.151	6	0.456	7	0.685	7	0.089
Error term	66		66		77		77	
Wave×Window ×DR freq	6	0.141	6	0.183	7	0.461	7	0.694
Error term	66		66		77		77	

<sup>a</sup>Probabilities reflect Greenhouse-Geisser epsilon corrections for degrees of freedom for repeated measures.

<sup>b</sup> $p < 0.01$ .

responses to the 2000-Hz tones, at least nine out of 12 subjects showed maximum derived response ABR and MLR amplitudes for both the exact-Blackman- and linear-gated tones within one-half-octave of the stimulus frequency.

Three-way repeated measures ANOVAs were calculated separately for the 500- and 2000-Hz derived response amplitude profiles. These results, displayed in Table I (left side), show the expected significant main effects for derived-band center frequency for the 500- and 2000-Hz tones. There are no significant differences, however, between results for ABR versus MLR, exact-Blackman- versus linear-gated tones, nor any significant interactions at either stimulus frequency. These results demonstrate that the ABR and MLR are equally frequency specific and that there are no significant differences in the frequency specificity of these evoked potentials to exact-Blackman- versus linear-gated tones.

## B. Half-octave derived responses

In an attempt to obtain a more frequency-specific evaluation of the contributions to the evoked potentials, derived responses representing half-octave-wide bands were calculated. The grand mean derived responses representing half-octave-wide derived bands for both stimulus frequencies are shown in Fig. 4. The half-octave waveforms appear noisier because the signal-to-noise ratio of the derived responses with the half-octave-wide bands is lower in comparison to the full-octave-wide bands. Compared to the full-octave derived responses, the half-octave derived response amplitudes are smaller and more difficult to detect in the background residual noise of the waveforms. The decrease in amplitude



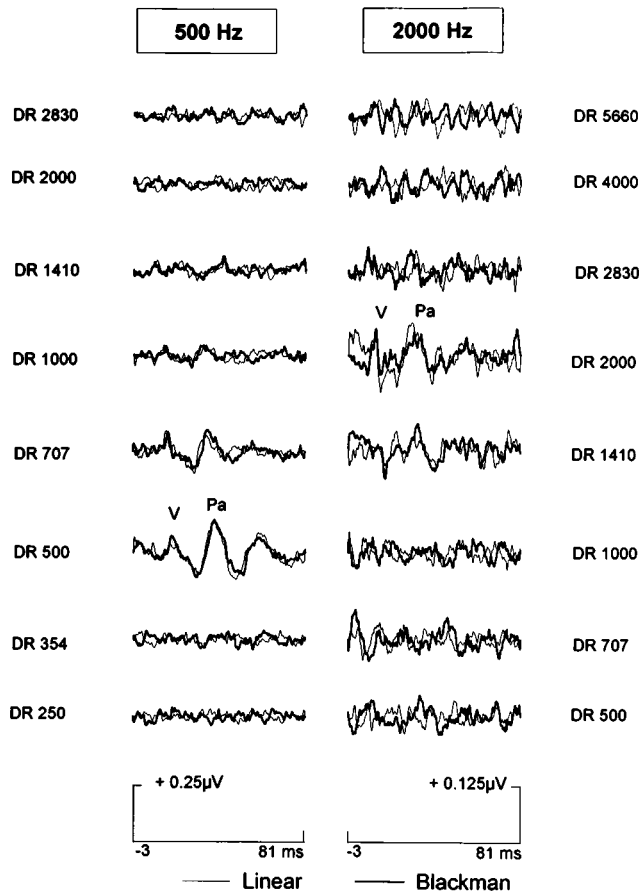


FIG. 4. Grand mean ( $N=12$ ) half-octave derived response waveforms to 80 dB ppe SPL exact-Blackman- and linear-gated 500- and 2000-Hz tones. Amplitude scale is  $+0.25 \mu\text{V}$  for the responses to the 500-Hz tones (left) and  $+0.125 \mu\text{V}$  for the responses to the 2000-Hz tones.

is due to the responses originating from a smaller portion of the basilar membrane (i.e., a half-octave-wide area versus a full-octave-wide area). The residual electrical noise in the waveforms is approximately the same in the half- and full-octave derived responses.

The maximum amplitudes for waves V and Pa to the 500-Hz stimuli occur in the 500-Hz derived band, with the 707-Hz derived band also containing ABRs and MLRs to both the exact-Blackman- and linear-gated stimuli. For the 2000-Hz stimuli, the largest amplitudes for waves V and Pa are seen in the 2000-Hz derived band. Cochlear contributions to wave Pa are also present in the derived bands one-half-octave above and below 2000 Hz. Either very small or absent peaks in response to either stimulus frequency are seen in the other derived bands.

Mean (and standard deviation) amplitude profiles for the 12 subjects' half-octave-wide derived responses are shown in Fig. 5. The 500- and 707-Hz derived bands contribute equally to wave V-V' for the exact-Blackman- and linear-gated 500-Hz stimuli. For MLR Na-Pa, the largest amplitude occurs in the 500-Hz derived band for both of the 500-Hz tones, with significant cochlear contributions also coming from the 707-Hz band. The peak in the amplitude profiles for both of the 2000-Hz stimuli occurs in the 2000-Hz derived band for wave V-V'. The maximum amplitude for MLR

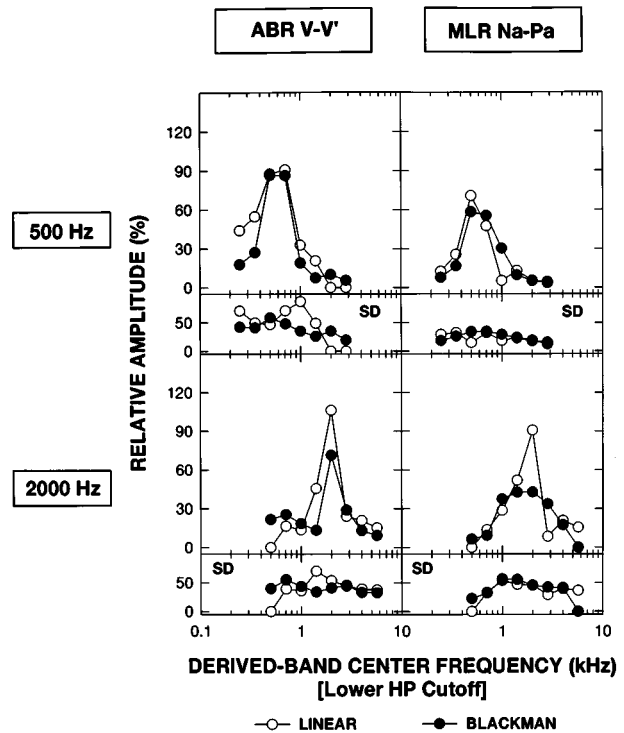


FIG. 5. Mean and standard deviation (sd) amplitude profiles for half-octave-wide derived responses (ABR wave V-V'; MLR wave Na-Pa) to 80 dB ppe SPL 500- and 2000-Hz exact-Blackman- versus linear-gated tones.

Na-Pa occurs at 2000 Hz in response to the linear tone and at 1410 and 2000 Hz in response to the exact-Blackman tone. The peak in the individual subjects' ABR and MLR amplitude profiles for the 500- and 2000-Hz tones occurred within a half-octave of the nominal stimulus frequencies for at least 7 out of 12 subjects. Although the waveforms are more difficult to analyze in the individual subjects, the mean half-octave derived response amplitude profiles suggest even better frequency specificity for these evoked potentials than indicated by the full-octave profiles.

Three-way repeated measures ANOVAs were calculated separately for the 500- and 2000-Hz half-octave derived responses. The results of these ANOVAs, displayed in Table I (right side), reveal the expected significant main effect for derived response center frequency for both stimulus frequencies. For the 500-Hz stimuli, the relative amplitude of ABR V-V' is significantly larger compared to MLR Na-Pa, indicating MLR Na-Pa is decreased by the masking to a greater extent than ABR V-V', even after normalizing the amplitudes to the highest HP cutoff frequency. There are no significant wave $\times$ derived band interactions, however, indicating that the ABR and MLR are equally frequency specific in response to the 500- or 2000-Hz tones. There are no significant differences in the response amplitude profiles for responses to exact-Blackman- versus linear-gated tones at either stimulus frequency, nor any significant interactions.

### C. Full- and half-octave derived response latencies

Individual subjects' derived response latencies were examined in order to determine whether the earlier latencies for the responses to the nonmasked linear-gated tones in com-

TABLE II. Mean ABR wave V and MLR wave Pa latencies (ms) for nonmasked responses (top) and derived responses (bottom) to 80 dB ppe SPL 500- and 2000-Hz exact-Blackman- versus linear-gated tones.

	500-Hz tones				2000-Hz tones			
	Wave V		Wave Pa		Wave V		Wave Pa	
	Linear <sup>a</sup>	Blk <sup>b</sup>	Linear	Blk	Linear	Blk	Linear	Blk
Nonmasked latencies								
Nonmasked <sup>c</sup>	9.91	10.84	31.97	32.31	7.08	7.29	27.88	28.62
s.d.	0.96	0.83	1.57	1.21	0.34	0.60	1.16	1.49
N <sup>d</sup>	12	12	12	12	12	12	12	12
DR latencies at nominal stimulus frequency (i.e., 500-Hz DR and 2000-Hz DR)								
Full-octave	12.33	13.06	33.26	34.94	8.02	8.64	28.01	28.43
s.d.	0.82	0.80	1.83	1.24	0.82	0.59	1.58	1.57
N	12	12	12	12	12	11	12	11
Half-octave	13.46	14.18	34.76	35.37	8.36	8.81	27.75	28.46
s.d.	1.53	0.48	1.22	1.12	0.53	0.39	1.57	1.40
N	10	10	12	11	12	10	11	8

<sup>a</sup>Linear-gated tone.

<sup>b</sup>Exact-Blackman-gated tone.

<sup>c</sup>All latency values have been corrected for ER-2 insert earphone delay.

<sup>d</sup>N= number of subjects.

parison to the exact-Blackman tones (Oates and Stapells, 1997) are due to differences in ‘‘place’’ of cochlear excitation or to differences in the rise times of the linear and exact-Blackman windows (i.e., 2.0 cycles for the linear-gated tones versus 2.5 cycles for the exact-Blackman-gated tones). ABR wave V and MLR wave Pa latencies in response to the 500- and 2000-Hz tones were measured from both the one-octave-wide and half-octave-wide derived bands corresponding to the nominal stimulus frequencies. Mean latencies for the derived bands representing one-octave-wide regions along the basilar membrane, as well as for the nonmasked responses, are presented in Table II (middle and top, respectively). A three-way repeated measures ANOVA (stimulus frequency $\times$ wave $\times$ window) was calculated on 11 subjects’ full-octave derived response latencies (one subject, who had responses in the 1410-Hz derived band, did not have an ABR or MLR to the 2000-Hz exact-Blackman-gated tone in the 2000-Hz derived band). The results of the ANOVA reveal expected significant main effects for stimulus frequency [ $p < 0.0001$ ] and wave [ $p < 0.0001$ ], with longer latencies for the responses to the 500-Hz tones and for MLR wave Pa. There is a significant main effect for exact-Blackman- versus linear-gated tones [ $p < 0.0021$ ], with the responses to the exact-Blackman-gated tones having a longer latency. No interactions reach statistical significance [ $p < 0.023$ – $0.462$ ].

Mean half-octave-wide derived response latencies for ABR wave V and MLR wave Pa to the 500- and 2000-Hz exact-Blackman- and linear-gated tones are presented in the bottom of Table II. The latencies of the responses to both stimulus envelopes are longer for the half-octave-wide derived responses at each of the nominal stimulus frequencies compared to the full-octave-wide derived responses. These latency differences between the full- versus half-octave derived bands were not evaluated statistically, as not all subjects showed responses in all conditions for the half-octave analyses. Two-way repeated-measures ANOVAs (wave $\times$ window) were calculated independently for the re-

sponses to 500- vs 2000-Hz tones. The analyses were calculated on nine subjects’ data for the 500-Hz tones and eight subjects’ data for 2000-Hz tones (the remainder of the subjects did not show ABRs and/or MLRs in the half-octave-wide derived responses for the nominal frequencies of the stimuli). The expected main effect for wave is seen for the responses to the 500-Hz tones [ $p < 0.0001$ ] and to the 2000-Hz tones [ $p < 0.0001$ ], with longer latencies for MLR wave Pa. A significant main effect is also seen for window for the responses recorded to the 500-Hz tones [ $p = 0.004$ ], with the responses to the exact-Blackman-gated tones having a longer latency compared to responses to the linear-gated tones. Although not statistically significant, there was a trend for the responses to the 2000-Hz exact-Blackman-gated tones to be slightly longer than the responses to the 2000-Hz linear-gated tones [ $p = 0.011$ ]. The wave $\times$ window interaction did not reach statistical significance for either the 500- [ $p = 0.713$ ] or 2000-Hz [ $p = 0.101$ ] tones.

### III. DISCUSSION

#### A. Frequency specificity of the tone-evoked ABR and MLR

The mean derived response (full- and half-octave) amplitude profiles demonstrate that the ABR (wave V-V’) and the MLR (wave Na-Pa) to 80 dB ppe SPL brief tones show good frequency specificity, as indicated by maxima in the amplitude profiles occurring either at the nominal stimulus frequency or within a narrow range (i.e., one-half-octave) of this frequency. The ABR and MLR amplitude profiles show a sharp dropoff in the amplitudes of the responses on the low- and high-frequency sides of the profile peak, indicating little or no contributions to these evoked potentials from regions of the basilar membrane one or more octaves away from the probe frequency.

The results of the present study are in agreement with previous studies which have investigated, in normal-hearing

adults, the frequency specificity of the ABR to moderately intense nonmasked tonal stimuli using either pure-tone or notched-noise-masking paradigms (e.g., Abdala and Folsom, 1995; Folsom, 1984, 1985; Folsom and Wynne, 1987; Jacobson, 1983; Klein, 1983; Klein and Mills, 1981a, b; Mackersie *et al.*, 1993; Oates, 1996; Oates and Stapells, 1997; Picton *et al.*, 1979; Stapells, 1984; Stapells and Picton, 1981; Wu and Stapells, 1994). Employing a pure-tone masking paradigm, Klein demonstrated that the ABR slow-wave component (V-V' in the present paper) to 77 dB ppe SPL 500- and 1000-Hz tones is best tuned to narrow cochlear regions surrounding the nominal stimulus frequency (e.g., for the 500-Hz tone, the tip of the tuning curve occurred at 500–600 Hz), illustrating that the response has a good degree of frequency and place specificity. Subsequent pure-tone masking studies by Folsom (1984, 1985), Folsom and Wynne (1987), and by Stapells and colleagues (Mackersie *et al.*, 1993; Wu and Stapells, 1994) also report that ABRs to 60–75 dB ppe SPL tonal stimuli show masking profiles which are narrow and centered on the nominal stimulus frequency. Lastly, ABR response amplitude profiles to moderate intensity (77–86 dB ppe SPL) 1000-, 4000-, and 8000-Hz brief-tone stimuli, determined using notched-noise-masking, peaked at the nominal stimulus frequencies, again indicating the good frequency and place specificity of these responses (Abdala and Folsom, 1995).

The present study's findings on the frequency specificity of the MLR are in agreement with those of Mackersie *et al.* (1993) and Wu and Stapells (1994). All three studies show that the largest cochlear contributions to MLR wave Na-Pa come from regions of the basilar membrane corresponding to the stimulus probe frequencies and thus exhibit good frequency specificity. The derived response amplitude profiles in the present study also show contributions to the MLR to the 500-Hz tones from the 354- and 707-Hz cochlear regions and from the 1410- and 2830-Hz regions for the MLR to the 2000-Hz tonal stimuli (i.e., one-half-octave on either side of the tone frequency). Cochlear contributions to MLRs from a slightly wider region along the basilar membrane for 80 (present study) versus 60 (Mackersie *et al.*, 1993; Wu and Stapells, 1994) dB ppe SPL tones is not surprising in view of the increased spread of cochlear excitation that occurs with higher stimulus intensities (e.g., Anderson *et al.*, 1970; Kiang *et al.*, 1967; Rose *et al.*, 1971), as well as the effects of increased spectral splatter.

## B. Determination of derived band center frequency

There is some ambiguity in the derived response literature as to the dominant cochlear place with the derived band (i.e., which specific frequencies the response comes from). The ambiguity is due, in part, to the fact that at least three methods have been employed for *estimating* the CFs of the narrow-band regions contributing to the derived responses. In the first method, labeled here as the “calculated” CF, estimates of the CF are obtained from the acoustic noise spectra. An estimate of the derived band and its CF is obtained by subtracting the spectrum of the HP noise at one cutoff frequency from the spectrum of the HP noise at the higher cutoff frequency (Don and Eggermont, 1978; Nousak

and Stapells, 1992; Oates, 1996). In the second method, labeled here as the “nominal” CF and employed in the present study, the frequency of the lower of the two HP cutoff frequencies used in the subtraction procedure is considered the CF of the derived response. This is due to masking occurring below the HP cutoff frequency as a result of the finite slope of the HP filter. For half-octave-wide derived bands, the CF may actually be *below* the lower of the two HP cutoff frequencies (Don and Eggermont, 1978; Eggermont, 1976a; Oates, 1996). The nominal CF was originally validated using the calculated CF technique (Don *et al.*, 1979; Eggermont and Don, 1980; Kramer, 1992; Nousak and Stapells, 1992; Oates, 1996; Picton *et al.*, 1981; Stapells, 1984). In the third method, the CF of the derived band is determined by calculating the geometric mean of the two HP noise cutoff frequencies used in the subtraction procedure. The geometric mean =  $\sqrt{F_L} \times \sqrt{F_H}$ , where  $F_L$  = the lower HP noise cutoff and  $F_H$  = the higher HP noise cutoff (Don and Eggermont, 1978; Don *et al.*, 1993; Eggermont, 1976; Eggermont *et al.*, 1976; Parker and Thornton, 1978a, 1978b; Ponton *et al.*, 1992a, b).

A comparison of estimates of CF of the derived band obtained using these three methods reveals relatively small differences, with all three CF values located within a half-octave of each other (Oates, 1996). For example: the various estimated CFs of the one-octave-wide derived band for HP 4000-Hz condition minus HP 2000-Hz condition are: nominal CF = 2.0 kHz; geometric mean CF = 2.83 kHz; calculated CF = 2.2 kHz. The estimates for the half-octave-wide bands are even closer (Oates, 1996).

All three CF estimates are somewhat arbitrary and have limitations. The use of the geometric mean does not take into account characteristics of the HP noise, such as its slope. (Indeed, use of the geometric mean assumes a slope of infinite steepness.) Neither the geometric mean nor the CF calculated from the noise spectra take into account cochlear physiology. Use of the lower HP noise cutoff frequency (“nominal” CF) as an estimate of the CF of the derived band is supported by the following physiological data: First, Evans and Elberling (1982) obtained single-unit cochlear nerve action potential recordings in cats, and compared whole nerve derived compound action potentials (CAPs) to the mapping of the single-unit results. Their physiological data suggest that the derived responses obtained from subtracting responses recorded to clicks in 500-Hz HP noise masking from those recorded in 1000-Hz HP noise masking have a center frequency of 600 Hz. Results for higher-frequency derived bands also peaked either at the lower of the two HP noise cutoff frequencies or within a half-octave of the lower cutoff frequency (Evans and Elberling, 1982). Second, ABR threshold estimations obtained from the HP/DR technique in individuals with sensorineural hearing loss suggest that the effective CF of the derived band is located at or close to the lower of the two cutoff frequencies (Don *et al.*, 1979; Stapells *et al.*, 1985a). For example, Don and colleagues present results for an individual with a moderate notched hearing loss at 4000 Hz, restricted to just this audiometric frequency (Don *et al.*, 1979). The derived-ABR threshold estimate from the HP 8000 minus HP 4000-Hz

derived band closely (i.e., within 5 dB) approximated that subject's 4000-Hz behavioral threshold. If, in fact, this patient's derived responses had been more influenced by the higher frequencies within the derived band, one would have expected an underestimation of the degree of his hearing loss.

Ambiguity concerning the dominant or center frequency of the derived band is further increased since the dominant frequency is likely to be dependent on the metric employed: latencies may reflect higher frequencies than do amplitudes; different evoked potential peaks may show different patterns for latency versus amplitude measures; etc. Finally, the CF of the derived band may differ for different stimulus intensities, shifting to higher frequencies for higher stimulus intensities. For example, because cochlear contributions to ABRs to high-intensity ( $\geq 90$  dB ppe SPL) low-frequency tonal stimuli will likely include more basal regions of the basilar membrane (e.g., Folsom, 1984), the dominant frequencies *within* a derived band may shift to the higher frequencies within the band. Thus our choice of the lower HP noise cutoff frequency to estimate the CF of the derived band may represent the "best case" choice for the argument that the response is place specific. One solution for this shifting is to use narrower (e.g., half-octave) derived bands (Figs. 4 and 5).

### C. Frequency specificity of the ABR versus the MLR

No significant differences were found in the frequency specificity of ABR wave V-V' versus that of MLR wave Na-Pa, as illustrated by the full- and half-octave-wide derived response amplitude profiles. The lack of significance for the differences in frequency specificity of the ABR versus MLR is in agreement with previous studies (Mackersie *et al.*, 1993; Oates and Stapells, 1997; Wu and Stapells, 1994), which demonstrated that the ABR and MLR are equally frequency specific for low to moderate intensity (i.e., 60–80 dB ppe SPL) 500- and 2000-Hz tones. A similar conclusion was reached from the effects of high-pass noise masking on the ABR and MLR (Oates and Stapells, 1997). The results of the present study, however, are not in agreement with those of Smith *et al.* (1990), who concluded that, in gerbils, the MLR is less frequency specific than the ABR, as indicated by wider tuning curves and greater susceptibility to the effects of pure-tone (forward) masking.

### D. Frequency specificity of responses to 500- versus 2000-Hz tones

An additional measure of the frequency specificity of the evoked potential may be obtained by calculating the bandwidths (Hz) of the amplitude profiles (e.g., Dauman *et al.*, 1988; Mackersie *et al.*, 1993; Portmann *et al.*, 1983; Wu and Stapells, 1994). Comparisons of the bandwidths between different frequencies, however, are best made when stimulus frequency has been normalized (i.e., bandwidth in Hz divided by the stimulus frequency), reflecting the logarithmic basis of frequency representation along the basilar membrane (e.g., Tonndorf, 1970), especially above 1000 Hz.

Bandwidths of the derived response profiles at 50% amplitude, when normalized for stimulus frequency ("Q50%", Oates, 1996), are nearly identical at both stimulus frequencies, with only slightly better results for 2000 Hz compared to 500 Hz (Oates, 1996). This finding of essentially no difference in the frequency specificity of the ABR/MLR to 500- vs 2000-Hz tonal stimuli agrees well with several studies which have shown equally high correlations at 500 and 2000 Hz between tone-evoked ABRs and pure-tone behavioral thresholds for normal and hearing-impaired subjects (Mun-nerley *et al.*, 1991; Stapells *et al.*, 1995, 1990).

### E. Responses to exact-Blackman- versus linear-gated tones

As discussed in our previous paper (Oates and Stapells, 1997), the absolute latencies of the nonmasked ABR wave V and MLR wave Pa are significantly longer at both stimulus frequencies in response to the exact-Blackman-gated tones compared to the linear-gated tones. The latency differences between the responses to the stimulus envelopes are more pronounced for the 500- versus 2000-Hz tones. Significant latency differences between the exact-Blackman- versus linear-gated tones remain in the derived responses (full and half-octave) from cochlear regions corresponding to the nominal stimulus frequencies (Table II). Because the latency differences between these stimulus envelopes remain when place of cochlear excitation is held constant, these differences are likely due to differences in the rise time of the stimuli (i.e., 2 cycle rise time for the linear-gated tones versus 2.5 cycle rise time for the exact-Blackman-gated tones) rather than differences in place of cochlear excitation. The larger latency difference for the lower frequency stimuli may be explained by the 0.5-cycle rise time difference between the stimuli being equal to 1.0 ms at 500 Hz compared to 0.25 ms at 2000 Hz.

The derived response (full- and half-octave-wide) amplitude profiles, as well as the mean amplitude and latency profiles for the responses recorded in HP noise (Oates and Stapells, 1997), indicate no significant differences exist in the frequency specificity of the evoked potentials to the exact-Blackman- versus linear-gated tones. This finding is in agreement with unpublished results of Purdy and Abbas (1989), and does not provide support for the recommendation to use Blackman-gated tones specifically to improve the frequency specificity of the ABR (e.g., Gorga *et al.*, 1992; Gorga and Thornton, 1989; Telian and Kileny, 1989). The lack of significance for the differences in the frequency specificity of the ABR and MLR to exact-Blackman- versus linear-gated tones indicates the inability of the auditory system to reflect the small temporal differences present in the acoustic waveforms of these stimuli. The acoustic spectra of these brief tones may therefore not reflect their "effective" spectra. The effective spectrum of the stimuli is determined by the interaction of the characteristics of the stimuli, the transducer and the transfer characteristics of the ear canal, middle ear, and the inner ear (Fowler and Durrant, 1994), as well as more central structures (e.g., VIIIth nerve, brainstem, and cortex). Several investigators have suggested that there is a limited effective portion of the brief tone which elicits

the ABR (e.g., Kodera *et al.*, 1983; Suzuki and Horiuchi, 1981). If true, the acoustic spectra, which reflect the total duration of the brief tone, present a misleading picture of the energy as a function of frequency present in the effective portion of the tonal stimulus.

The HP/DR technique employed in the present study provides a direct measure of the physiological effective spectra of the stimuli (i.e., the frequencies in the stimuli which actually contribute to the response). The results of this study clearly show that the large differences between the sidelobe energy in the acoustic spectra of the exact-Blackman- versus linear-gated stimuli (Fig. 1, Oates and Stapells, 1997) do not accurately reflect the effective spectra of the stimuli for the ABR or the MLR. The major cochlear contributions to these evoked potentials to 80 dB ppe SPL exact-Blackman- and linear-gated brief tones come from the nominal stimulus frequency or within a narrow range (i.e., about one-half-octave) of this frequency, with no differences between the two gating functions.

The present findings for the exact-Blackman- versus linear-gated tones may apply only to moderately intense (80 dB ppe SPL) stimuli. It remains to be investigated whether there would be differences in the frequency specificity of the ABR and/or MLR to these stimuli at higher stimulus intensities. The unpublished data from the Purdy and Abbas (1989) study (which investigated responses of hearing-impaired subjects to high-intensity tones), however, do not suggest any significant differences in the frequency specificity of the ABR to these exact-Blackman- versus linear-gated tones at stimulus intensities of 90 dB ppe SPL or greater.

## F. Octave-wide versus half-octave-wide analyses

The inclusion of full- and half-octave derived responses in this study allowed us to investigate the following questions: (1) "Do half-octave-wide derived responses provide a similar assessment of the frequency and place specificity of the evoked potentials as do full-octave derived responses?" an issue not previously addressed in the literature; and (2) "Does the addition of individual half-octave derived responses resulting from adjoining sections of the cochlea ( $\frac{1}{2}$ -octave separations) equal the summed response resulting from the addition of full-octave derived responses (1-octave separations)?" For example, for the 500-Hz derived responses, does the sum of the 250-, 500-, 1000-, and 2000-Hz full-octave derived responses equal the sum of the 250-, 354-, 500-, 707-, 1000-, 1410-, 2000-, and 2830-Hz half-octave derived responses?

In the present study, the amplitudes of the half-octave derived responses were smaller in comparison to the full-octave derived responses. The decrease in response amplitude is most likely due to the responses originating from a smaller portion of the basilar membrane (i.e., a half-octave wide area versus a full-octave wide area). This decline in amplitude leads to a lower signal-to-noise ratio (SNR) for the half- versus full-octave wide derived bands (the residual electrical noise present in the waveforms is approximately the same in the full- and half-octave derived responses). When the individual full-octave derived responses resulting from contributions of adjoining sections of the cochlea (one-

octave separations) were added together, they were found to equal the summed response resulting from the addition of the half-octave derived responses (Oates, 1996). This finding indicates that the derived response linear subtraction procedure (full- or half-octave) is roughly similar to the physiological subtraction achieved by the masking (Oates, 1996).

The derived response waves V and Pa latencies from the full-octave-wide bands corresponding to the nominal stimulus frequencies are shorter compared to those from the half-octave-wide bands. Seen for responses to both stimulus frequencies, this latency effect was nevertheless more pronounced for the responses to the 500-Hz stimuli. These latency differences for the full- versus half-octave derived responses are probably due to the fact that the full-octave-wide band contains all of the frequencies contributing to the half-octave-wide band plus contributions from frequencies one-quarter octave above and below the edges of the half-octave band. Assuming higher frequencies determine response latency, cochlear contributions to the evoked potentials from the  $\frac{1}{4}$ -octave-wide region located above (i.e., basal to) the half-octave-wide band would yield shorter latencies. The difference in mean wave V latencies for the full- and half-octave derived responses reported in this study (i.e., approximately 1.1 ms for the 500-Hz tones and 0.3 ms for the 2000-Hz tones) represents an estimate of the cochlear time delay between the 1000–707 Hz regions of the cochlea for the responses to the 500-Hz tones, and the 4000–2830 Hz regions for the responses to the 2000-Hz tones. These shifts in wave V latency as a function of change in the area of cochlear excitation are in general agreement with the wave V latency shifts of approximately 0.95 ms and 0.16 ms reported by Don and Eggermont (1978) for the same cochlear regions.

The latency effect of the derived response bandwidth was more pronounced for the low- versus high-frequency tonal stimuli because: (1) the better neural synchrony of the higher frequency regions of the cochlea; (2) the longer cochlear delay times associated with apical versus basal cochlear activation; and (3) the half-octave-wide differences between the full- versus half-octave derived bands correspond to larger distance along the basilar membrane for the low- versus high-frequency tones.

The latency differences between the two derived response bandwidths may also be a reflection of the differences in their areas of cochlear excitation. The area of the basilar membrane, and thus the number of auditory nerve fibers free to respond to the stimulus, is greater for the full- versus half-octave-wide bands. Responses from the full-octave bands would therefore have shorter latencies (and larger amplitudes).

The results of this study indicate that either full- or half-octave steps may be used to evaluate the frequency specificity of the evoked potentials. Narrower bandwidths make shifts in the dominant frequency of the derived band less likely and determination of band CF less prone to error. A major disadvantage with the smaller bandwidths, however, is a lower SNR, making waveforms more difficult to analyze. The noisier half-octave waveforms resulted in some subjects providing incomplete data, thus reducing the power of the statistical comparisons (e.g., see Table II). For example,

Q50% bandwidths could only be determined for a limited number of subjects' half-octave profiles ( $N=9$  and 7 for 500- and 2000-Hz profiles, respectively) in comparison to all subjects' ( $N=12$ ) for the full-octave profiles at each stimulus frequency (Oates, 1996). Thus even though the mean half-octave derived response profiles suggest better frequency specificity of the evoked potentials in comparison to the full-octave profiles, the use of half-octave derived responses is recommended with caution as individual subject's half-octave HP/DR waveforms may be quite noisy, making waveform identification difficult.

## G. Implications

This study's results, and those of our previous study (Oates and Stapells, 1997), demonstrate that the ABR and MLR to 80 dB ppe SPL 500- and 2000-Hz brief tones show good frequency and place specificity. There are no significant differences in the frequency specificity of: (1) ABR wave V-V' versus MLR wave Na-Pa; (2) the evoked potentials to 500- vs 2000-Hz tones; and (3) the evoked potentials to exact-Blackman- versus linear-gated tones. ABRs and MLRs to moderately intense nonmasked tonal stimuli may therefore be used to accurately assess both low- and high-frequency hearing sensitivity, given that appropriate technical factors are considered in recording these evoked potentials. Either exact-Blackman- or linear-gated brief tones may be employed.

The present study investigated the frequency specificity of these evoked potentials to moderately intense (i.e., 80 dB ppe SPL) brief tones. As stimulus intensity is increased above 80 dB ppe SPL there will likely be greater contributions to the evoked potentials from frequencies outside of the nominal stimulus frequency, thus reducing the frequency specificity of the responses (Burkard and Hecox, 1983, 1987; Folsom 1984, 1985; Picton *et al.*, 1979; Stapells, 1984; Stapells and Picton, 1981). The reduced frequency specificity of the ABR and/or MLR to high-intensity nonmasked tonal stimuli may have detrimental effects on ABR/MLR estimates of pure-tone behavioral threshold in hearing-impaired subjects. It is therefore important for future studies to better define the frequency specificity of these evoked potentials at higher stimulus intensities. Masking techniques, such as notched noise masking (Stapells *et al.*, 1994, 1985b), may be required to ensure the frequency specificity of responses to tonal stimuli presented at 90 dB ppe SPL or higher.

## ACKNOWLEDGMENTS

This manuscript is based on the Ph.D. dissertation of the first author, submitted to the City University of New York Ph.D. Program in Speech and Hearing Sciences. This research was funded in part by an American Speech-Language-Hearing Foundation Student Research grant (1993) to the first author, as well as by NIDCD Grant No. 8P50 DC00223 to the second author. We would also like to express our appreciation for the insightful feedback and suggestions we received on this manuscript from Dr. William H. Martin, Dr. Arthur Boothroyd, and Dr. Terence W. Picton, as well as to two reviewers for their very helpful suggestions.

<sup>1</sup>Due to the finite slope of the HP filter, some masking below the HP cutoff frequency occurs. The derived band resulting from the subtraction of two HP noise-masked responses will therefore include frequencies below, as well as above, the lowest HP cutoff (e.g., Don and Eggermont, 1978; Eggermont, 1976a; Nousak and Stapells, 1992; Picton *et al.*, 1981).

<sup>2</sup>In analyses where all subjects showed "no response" for particular conditions, thus resulting in 0- $\mu$ V amplitude and a standard deviation of zero, the ANOVA was calculated a second time with the associated condition(s) removed. The results of all of the recalculated ANOVAs remained consistent with the original ANOVAs, and are not further reported.

- Abdala, C., and Folsom, R. C. (1995). "The development of frequency resolution in humans as revealed by the auditory brain-stem response recorded with notched noise masking," *J. Acoust. Soc. Am.* **98**, 921–930.
- Anderson, D. J., Rose, J. E., Hind, J. E., and Brugge, J. F. (1970). "Temporal position of discharges in single auditory nerve fibers within the cycle of a sine-wave stimulus: Frequency and intensity effects," *J. Acoust. Soc. Am.* **49**, 1131–1139.
- Burkard, R., and Hecox, K. (1983). "The effect of broadband noise on the human auditory evoked response. II. Frequency specificity," *J. Acoust. Soc. Am.* **74**, 1214–1223.
- Burkard, R., and Hecox, K. E. (1987). "The effect of broadband noise on the human brain-stem auditory evoked response. III. Anatomic locus," *J. Acoust. Soc. Am.* **81**, 1050–1063.
- Dauman, R., Cazals, Y., and Aran, J.-M. (1988). "Frequency selectivity: Reliability of electrocochleographic measure with iso-intensity masking," *Acta Oto-Laryngol.* **105**, 50–55.
- Don, M., and Eggermont, J. J. (1978). "Analysis of the click-evoked brain-stem potentials in man using high-pass masking," *J. Acoust. Soc. Am.* **63**, 1084–1092.
- Don, M., Eggermont, J. J., and Brackmann, D. E. (1979). "Reconstruction of the audiogram using brain stem responses and high-pass noise masking," *Ann. Otol. Rhinol. Laryngol.* **88** (Suppl. 57), 1–20.
- Don, M., Ponton, C. W., Eggermont, J. J., and Masuda, A. (1993). "Gender differences in cochlear response time: An explanation for gender amplitude differences in the unmasked auditory brain-stem response," *J. Acoust. Soc. Am.* **94**, 2135–2148.
- Eggermont, J. J. (1976a). "Analysis of the compound action potential responses to tone bursts in the human and the guinea pig cochlea," *J. Acoust. Soc. Am.* **60**, 1132–1139.
- Eggermont, J. J. (1976b). "Electrocochleography," in *Handbook of Sensory Physiology*, Vol. 5, edited by W. D. Keidel and W. D. Nelf (Springer-Verlag, New York), pp. 625–705.
- Eggermont, J. J., and Don, M. (1980). "Analysis of the click-evoked brain-stem potentials in humans using high-pass noise masking. II. Effect of click intensity," *J. Acoust. Soc. Am.* **68**, 1671–1675.
- Eggermont, J. J., Spoor, A., and Odenthal, D. W. (1976). "Frequency specificity of tone-burst electrocochleography," in *Electrocochleography* edited by R. J. Ruben, C. Elberling, and G. Salomon (University Park, Baltimore), pp. 215–246.
- Evans, E. F., and Elberling, C. (1982). "Location specific components of the gross cochlear action potential. An assessment of the validity of the high-pass masking technique by cochlear nerve fiber recording in the cat," *Audiology* **21**, 204–227.
- Folsom, R. C. (1984). "Frequency specificity of human auditory brainstem responses as revealed by pure-tone masking profiles," *J. Acoust. Soc. Am.* **75**, 919–924.
- Folsom, R. C. (1985). "Auditory brain stem responses from human infants: Pure-tone masking profiles for clicks and filtered clicks," *J. Acoust. Soc. Am.* **78**, 555–562.
- Folsom, R. C., and Wynne, M. K. (1987). "Auditory brain stem responses from human adults and infants: Wave V tuning curves," *J. Acoust. Soc. Am.* **81**, 412–417.
- Fowler, C. G., and Durrant, J. D. (1994). "The effects of peripheral hearing loss on the auditory brainstem response," in *Principles and Applications in Auditory Evoked Potentials*, edited by J. T. Jacobson (Allyn and Bacon, Needham Heights), pp. 237–250.
- Gorga, M. P., Beauchaine, K. L., Kaminski, J. R., and Bergman, B. M. (1992). "Use of tone bursts in ABR evaluations," *Am. J. Audiol.* **1**, 11–12.
- Gorga, M. P., and Thornton A. R. (1989). "The choice of stimuli for ABR measurements," *Ear Hear.* **10**, 217–230.
- Greenhouse, S. W., and Geisser, S. (1959). "On methods in the analysis of profile data," *Psychometrika* **24**, 95–112.

- Harris, F. J. (1978). "On the use of windows for harmonic analysis with the discrete Fourier transform," *Proc. IEEE* **66**, 51–84.
- Jacobson, J. T. (1983). "Effects of rise time and noise masking on tone pip auditory brainstem response," *Semi. Hear.* **4**, 363–372.
- Kiang, N. Y. S., Sachs, M. B., and Peake, W. T. (1967). "Shapes of tuning curves for single auditory-nerve fibers," *J. Acoust. Soc. Am.* **42**, 1341–1342.
- Klein, A. J. (1983). "Properties of the brain-stem response slow-wave component. II. Frequency specificity," *Arch. Otolaryngol.* **109**, 74–78.
- Klein, A. J., and Mills, J. H. (1981a). "Physiological (waves I and V) and psychological tuning curves in human subject," *J. Acoust. Soc. Am.* **69**, 760–767.
- Klein, A. J., and Mills, J. H. (1981b). "Physiological and psychophysical measures from humans with temporary threshold shift," *J. Acoust. Soc. Am.* **70**, 1045–1053.
- Kodera, K., Marsh, R. R., Suzuki, M., and Suzuki, J.-I. (1983). "Portions of tone pips contributing to frequency-selective auditory brain stem responses," *Audiology* **22**, 209–218.
- Kramer, S. J. (1992). "Frequency-specific auditory brainstem responses to bone-conducted stimuli," *Audiology* **31**, 61–71.
- Mackersie, C., Down, K. E., and Stapells, D. R. (1993). "Pure-tone masking profiles for human auditory brainstem and middle latency responses," *Hearing Res.* **65**, 61–68.
- Munnerley, G. M., Greville, K. A., Purdy, S. C., and Keith, W. J. (1991). "Frequency-specific auditory brainstem responses: Relationship to behavioral thresholds in cochlear-impaired adults," *Audiology* **30**, 25–32.
- Nousak, J. M. K., and Stapells, D. R. (1992). "Frequency specificity of the auditory brain stem response to bone-conducted tones in infants and adults," *Ear Hear.* **13**, 87–95.
- Oates, M. A. (1996). "Frequency specificity of the auditory brainstem and the middle latency responses," Doctoral Dissertation, Graduate Center, City University of New York, New York, N.Y.
- Oates, P., and Stapells, D. R. (1997). "Frequency specificity of the human auditory brainstem and middle latency responses to brief tones. I. High-pass noise masking," *J. Acoust. Soc. Am.* **102**, 3597–3608.
- Parker, D. J., and Thornton, A. R. D. (1978a). "The validity of the derived cochlear nerve and brainstem evoked responses of the human auditory system," *Scand. Audiol.* **7**, 45–52.
- Parker, D. J., and Thornton, A. R. D. (1978b). "Derived cochlear nerve and brainstem evoked responses of the human auditory system. The effect of masking in the derived band," *Scand. Audiol.* **7**, 73–80.
- Picton, T. W., Ouellette, J., Hamel, G., and Smith, A. D. (1979). "Brainstem evoked potentials to tonepips in notched noise," *J. Otolaryngol.* **8**, 289–314.
- Picton, T. W., Stapells, D. R., and Campbell, K. B. (1981). "Auditory evoked potentials from the human cochlea and brainstem," *J. Otolaryngol.* **10** (Suppl. 9), 1–41.
- Ponton, C. W., Don, M., and Eggermont, J. J. (1992a). "Place-specific derived cochlear microphonics from human ears," *Scand. Audiol.* **21**, 131–141.
- Ponton, C. W., Eggermont, J. J., Coupland, S. G., and Winkelaar, R. (1992b). "Frequency-specific maturation of the eighth nerve and brainstem auditory pathway: Evidence from derived auditory brain-stem responses (ABRs)," *J. Acoust. Soc. Am.* **91**, 1576–1586.
- Portmann, M., Harrison, R. V., Negrevergne, M., Dauman, R., and Aran, J.-M. (1983). "Electrocochleographic measures of cochlear frequency selectivity in hearing loss of cochlear origin," *Acta Oto-Laryngol.* **95**, 657–663.
- Purdy S., and Abbas P. J. (1989). "Auditory brainstem response audiometry using linearly and Blackman gated tonebursts," *ASHA* **31**, 115–116.
- Rose, J. E., Hind, J. E., Anderson, D. J., and Brugge, J. F. (1971). "Some effects of stimulus intensity on response of auditory nerve fibers in the squirrel monkey," *J. Neurophysiol.* **34**, 685–699.
- Smith, D. I., Mills, J. H., and Schmiedt, R. A. (1990). "Frequency selectivity of the middle latency response," *Hearing Res.* **43**, 95–106.
- Stapells, D. R. (1984). "Studies in evoked potential audiometry," Doctoral Dissertation, University of Ottawa, Ontario, Canada.
- Stapells, D. R., Gravel, J. S., and Martin, B. A. (1995). "Thresholds for auditory brain stem responses to tones in notched noise from infants and young children with normal hearing or sensorineural hearing loss," *Ear Hear.* **16**, 361–371.
- Stapells, D. R., and Picton, T. W. (1981). "Technical aspects of brainstem evoked potential audiometry using tones," *Ear Hear.* **2**, 20–29.
- Stapells, D. R., Picton, T. W., and Durieux-Smith, A. (1994). "Electrophysiologic measures of frequency-specific auditory function," in *Principles and Applications in Auditory Evoked Potentials*, edited by J. T. Jacobson (Allyn and Bacon, Needham Heights), pp. 251–283.
- Stapells, D. R., Picton, T. W., Durieux-Smith, A., Edwards, C. G., and Moran, L. (1985a). "An evaluation of eight electric response audiometry techniques," *ERA Newsletter* **2**, 36.
- Stapells, D. R., Picton, T. W., Durieux-Smith, A., Edwards, C. G., and Moran, L. M. (1990). "Thresholds for short-latency auditory-evoked potentials to tones in notched noise in normal-hearing and hearing-impaired subjects," *Audiology* **29**, 262–274.
- Stapells, D. R., Picton, T. W., Pérez-Abalo, M., Read, D., and Smith, A. (1985b). "Frequency specificity in evoked potential audiometry," in *The Auditory Brainstem Response*, edited by J. T. Jacobson (College-Hill, San Diego), pp. 147–177.
- Suzuki, T., and Horiuchi, K. (1981). "Rise time of pure-tone stimuli in brain stem response audiometry," *Audiology* **20**, 101–112.
- Telian, S. A., and Kileny, P. R. (1989). "Usefulness of 1000 Hz tone-burst-evoked responses in the diagnosis of acoustic neuroma," *Otolaryngol. Head Neck Surg.* **101**, 466–471.
- Tonndorf, J. (1970). "Cochlear mechanics and hydro-dynamics," in *Foundations of Modern Auditory Theory*, edited by J. V. Tobias (Academic, New York), Vol. 1, pp. 205–254.
- Wu, C.-Y., and Stapells, D. R. (1994). "Pure-tone masking profiles for human auditory brainstem and middle latency responses to 500-Hz tones," *Hearing Res.* **78**, 169–174.

# The effects of click level, click rate, and level of background masking noise on the inferior colliculus potential (ICP) in the normal and carboplatin-treated chinchilla

Robert Burkard,<sup>a)</sup> Patricia Trautwein, and Richard Salvi

Center for Hearing & Deafness, 215 Parker Hall, SUNY—Buffalo, Buffalo, New York 14214-3007

(Received 16 April 1997; revised 22 July 1997; accepted 5 September 1997)

Carboplatin produces a selective loss of inner hair cells in chinchilla, substantially reducing the amplitude of the compound action potential. A key question that arises from these experiments is: What effect does a reduction in IHC-eighth-nerve fiber input have on the central auditory nervous system? This investigation evaluated the inferior colliculus potential (ICP) in chinchillas treated with carboplatin. The left ear was surgically destroyed and a recording electrode was placed in the left inferior colliculus. Following thirteen days of recovery time, the ICP was recorded in the awake animal. Click level was varied from 10–20 to 80 dB pSPL. Click rate was varied from 10 to 1000 Hz using both conventional averaging and a cross-correlation procedure. Broadband masking noise was varied from 30 to 70 dB SPL with click level held constant at 80 dB pSPL. The dependent variables were the positive peak latency and peak-to-following trough amplitude of the evoked potential. Following baseline studies, the animals were administered carboplatin (50 mg/kg IP) and retested two weeks later. Prior to carboplatin administration, there was an increase in ICP latency and a decrease in ICP amplitude with decreasing stimulus level, increasing rate and increasing noise level. Mean ICP threshold was 30 dB pSPL. Following carboplatin administration, there was little change in threshold or peak latencies. In contrast, the amplitude of the ICP was reduced on average by one-third, although this effect varied considerably across animals. The magnitude of this amplitude decrement was not strongly dependent on click level, click rate, or the level of background noise. © 1997 Acoustical Society of America. [S0001-4966(97)05912-2]

PACS numbers: 43.64.Wn, 43.64.Ri, 43.64.Qh [RDF]

## INTRODUCTION

Carboplatin, a second-generation, platinum-based anti-cancer drug, produces a selective loss of inner hair cells (IHCs) in the chinchilla (Wake *et al.*, 1993, 1994; Takeno *et al.*, 1994a, b; Jock *et al.*, 1996; Trautwein *et al.*, 1996; Liberman *et al.*, 1997). Interestingly, distortion product otoacoustic emissions (DPOAEs) are of normal amplitude (Trautwein *et al.*, 1996; Liberman *et al.*, 1997) or are slightly larger than normal (Jock *et al.*, 1996) following carboplatin treatment. A recent report by Wake *et al.* (1996a) also demonstrated larger transient-evoked otoacoustic emissions in cochlear regions where IHCs were extensively damaged, but OHCs were intact. There is some disagreement across studies concerning the effects of IHC loss on auditory-evoked potential thresholds, with several studies (Trautwein, 1996; Jock *et al.*, 1996) showing little or no threshold shift following moderate IHC loss, and other studies (Takeno *et al.*, 1994a; Wake *et al.*, 1993) showing a substantial threshold shift. One study has shown that the compound action potential (CAP) amplitude is reduced in carboplatin-treated animals with mild-to-moderate IHC loss, but the CAP was eliminated with large IHC lesions (Trautwein *et al.*, 1996).

The present investigation extends the results of these studies by investigating the effects of IHC loss on the near-field response from the inferior colliculus (inferior colliculus potential, ICP). We investigated the behavior of the ICP to

manipulations of click level, click rate, and level of background noise following carboplatin treatment. We wished to determine whether carboplatin caused a decrease in ICP amplitude. Significant IHC loss would be expected to reduce the number of inputs to central auditory neurons. This could conceivably lead to changes in the magnitude of spatial and/or temporal summation of inputs in the central auditory nervous system. Increasing click rate and level of a background masking noise produces changes in evoked potentials that appear to reflect the stressing of synaptic events (Burkard *et al.*, 1996a, b). The use of rate and masking-noise manipulations in this study are intended to investigate any changes in synaptic dynamics following IHC loss and subsequent loss of a subset of type I afferent inputs to the cochlear nuclei.

## I. METHODS

Five adult chinchillas were anesthetized with Ketamine (60 mg/kg) and acepromazine (0.6 mg/kg) and the left cochlea was surgically destroyed. The skin overlying the posterior cranium was cut midsagittally, and a tungsten electrode was stereotaxically placed in the left inferior colliculus. To ensure placement within the IC, the electrode was advanced until a large amplitude-evoked potential could be recorded in response to acoustic stimulation of the right ear. A reference electrode was implanted just beneath the dura at a site approximately 1 cm anterior to the IC electrode (McFadden *et al.*, 1997). Following a two-week recovery period, baseline distortion product otoacoustic emissions (DPOAEs)

<sup>a)</sup>Electronic mail: RFB@ACSU.BUFFALO.EDU



and ICPs were obtained from the awake animal resting comfortably in a custom-built animal restraint (Snyder and Salvi, 1994) inside a sound-attenuating chamber. The DPOAEs were recorded with a custom-designed system composed of two Etymotic ER-2 earphones and an Etymotic ER-10B microphone. Stimuli were produced and recorded with TMS320C25-based DSP boards housed in a personal computer. The DPOAE input/output (I/O) functions were measured with equal-level primary tones ranging in level from 0 to 70 dB SPL in 5-dB steps. The  $f_2/f_1$  ratio was 1.2, and  $f_1$  frequencies were 1, 2, 3, 4, 6, and 8 kHz. The acoustic signal in the ear canal was digitized for 2000 ms at a sampling frequency of 31 kHz. Spectral components were derived by discrete Fourier transform at frequencies equal to  $f_1$ ,  $f_2$ ,  $2f_1 - f_2$  and  $fn = 0.7(2f_1 - f_2)$ . The level of  $fn$  was used to check for movement artifacts. If  $fn > 10$  dB SPL, the sample was rejected and a new sample collected. The ICPs were recorded from the IC electrode, with the more anterior electrode as common. The ICP was amplified ( $10\,000 \times -20\,000 \times$ ) and filtered from 100–3000 Hz by a Grass P511 bioamplifier, and digitized at 20 kHz by the 16-bit A/D of an Ariel DSP-16 board housed in a personal computer. For conventional averaging, each response was the averaged response to 250 stimulus presentations. For maximum length sequence (MLS) stimuli, ICPs were the averaged response to 15 MLS trains, with each train composed of 64 clicks. The MLS ICPs were obtained following cross correlation of the averaged response with an appropriate recovery sequence (Eysholdt and Schreiner, 1982; Burkard *et al.*, 1990a,b; Burkard, 1994a). Condensation clicks (Global Specialties model 4001 pulse generator) were 50 microsecond electrical pulses, which were attenuated (TDT model PATT) and input to one port of a passive mixer. Broadband noise (Koep Precision Standards CNM-1000B) was routed through an attenuator (Tucker Davis model PATT) and input to the second port of the passive mixer, whose output was amplified (MacIntosh power amplifier) and transduced by an Etymotic ER-2 earphone. The SPL was monitored with an Etymotic ER-10B microphone.

Stimulus manipulations included click level, click rate, and level of background masking noise. Click level was varied in 10-dB steps from 10 or 20 dB pSPL to 80 dB pSPL, with a click rate of 25 Hz. Click rate studies used click levels of 60 and 80 dB pSPL. For conventional averaging, click rates included 10, 25, 50, 75, and 100 Hz. Using MLS trains combined with cross-correlation, MLS ICPs were obtained at minimum pulse intervals (MPIs) of 5, 3, 2, 1 and 0.5 ms, corresponding to average rates of 100, 167, 250, 500, and 1000 Hz, respectively. For noise-level studies, the click was presented at 80 dB pSPL at a rate of 25 Hz. Noise-level conditions included a no-noise condition, and noise levels of 30, 40, 50, 60, and 70 dB pSPL.

Immediately following the above protocol, each chinchilla was injected IP with 50 mg/kg of carboplatin, and the above protocol was repeated 13 days later. Two weeks following this second evaluation, several animals were sacrificed by Nembutal overdose, their cochleas were harvested, and cochleograms were obtained by counting outer hair cells (OHCs) and inner hair cells (IHCs), as described by Hofstet-

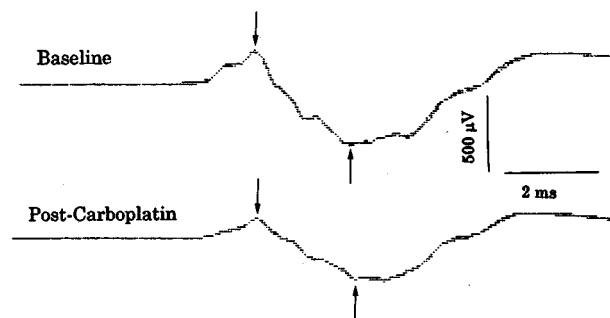


FIG. 1. Examples of the inferior colliculus potential (ICP) from one chinchilla before (upper) and following (lower) carboplatin injection. Stimuli were 80-dB pSPL clicks presented at a rate of 25 Hz. Downward pointing arrows indicate the latency of the ICP, while the ICP amplitude is the amplitude difference between the points indicated by the downward- and upward-pointing arrows.

ter *et al.* (1997). Briefly, cochleas were removed, the oval window opened, and the cochleas were perfused with 2.5% glutaraldehyde in veronal acetate buffer ( $pH\ 7.2$ ). Cochleas were postfixed in osmium tetroxide and dehydrated with a series of ethanol solutions with a final concentration of 70%. The cochleas were then dissected out and the organ of Corti carefully removed and mounted in glycerin on glass slides. Specimens were viewed with a microscope at  $400\times$  and the number of missing IHCs and OHCs counted to obtain a cochleogram showing the percent of IHC and OHC loss as a function of percent total distance from the apex and as a function of frequency (Greenwood, 1990).

For all stimulus manipulations, the dependent variables were the latency of the initial positive peak of the ICP response, and the amplitude of this response from the positive peak to the following negative trough (see Fig. 1). All latency measures have been corrected for the 0.9-ms acoustic delay through the ER-2 earphone.

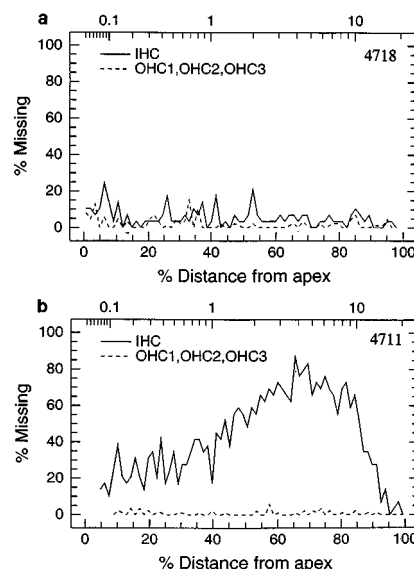


FIG. 2. Cochleograms from two chinchillas following carboplatin injection.

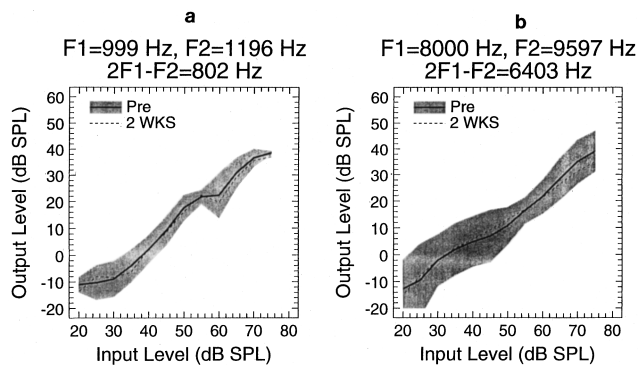


FIG. 3. Distortion product otoacoustic emission input/output functions for  $f_1$  frequencies of 1000 Hz (a) and 8000 Hz (b). The solid line shows the mean DPOAE amplitude across chinchillas, while the shaded area shows the 95% confidence interval. The dashed line shows mean DPOAE amplitude two weeks following carboplatin injection.

## II. RESULTS

### A. Anatomy/DPOAEs

Cochleograms were obtained from two ears one month following carboplatin injection. These cochleograms are shown in Fig. 2. Figure 2(a) shows little loss of IHCs, with a minimal loss of OHCs. Figure 2(b) shows a cochlea with IHC loss ranging from about 10% to 80%, with minimal OHC loss. Figure 3 shows the effects of hair cell loss on DPOAEs for several  $f_1$  frequencies. The solid line and hatched area shows the mean and 95% confidence interval of CDT amplitude pre-carboplatin. The dashed line shows the mean CDT amplitude two weeks following carboplatin. It is clear that DPOAEs are unaffected by carboplatin, in agreement with previous results from our laboratory (Trautwein *et al.*, 1996; Hofstetter *et al.*, 1997).

### B. Inferior colliculus potential (ICP)

#### 1. ICP minimum response levels

Table I shows the lowest click level at which an ICP was observed for each chinchilla pre- and post-carboplatin. We will call this the minimum response level (MRL). In three of five cases, MRL remained constant, in one case MRL improved by 10 dB, and in one case MRL worsened by 10 dB. This 10-dB change in two animals reflects the intensity steps used in this study. On average, MRL remained the same following carboplatin administration, consistent with previ-

TABLE I. Minimum response levels of the ICP before and after carboplatin injection.

Animal	Baseline (dB pSPL)	Post-carboplatin (dB pSPL)
4718	30	30
4713	20	30
4711	30	30
4719	40	30
4709	30	30
Mean	30	30

ous results following carboplatin doses that produce mild-to-moderate IHC losses (Trautwein *et al.*, 1996; Jock *et al.*, 1996).

#### 2. Effect of click level

Mean ICP latency is plotted across click level in Fig. 4. Baseline latency measures show the expected decrease in latency with increasing click level. The slope of the latency/intensity function was  $-15.1 \mu\text{s}/\text{dB}$ . Following carboplatin, there was a small increase (roughly  $50 \mu\text{s}$ ) in mean ICP latency for all click levels. However, the latency/intensity function parallels the baseline function, demonstrating a very similar slope ( $-16.2 \mu\text{s}/\text{dB}$ ). The  $50\text{-}\mu\text{s}$  mean latency shift post-carboplatin translates into a 3-dB shift in the latency/intensity function. To explore ICP latency shift in more detail, Table II shows latency shift (postcarboplatin minus baseline) for each chinchilla across click level. These data show that one chinchilla (4713) consistently showed a roughly 0.2-ms increase in ICP latency following carboplatin, two others (4711, 4709) showed a small increase at most click levels, one (4718) showed little change in latency, and one (4719) consistently showed a decrease in ICP latency. Mean ICP amplitude data across click level are shown in Fig. 5. Baseline ICP data showed the expected increase in response amplitude with increasing click level. Following carboplatin injection, there was a substantial reduction in response amplitude, which was most evident for the higher click levels.

In order to evaluate in more detail the effects of carboplatin on ICP amplitude in each chinchilla at different click levels, we calculated the ratio of the ICP amplitude post-carboplatin relative to the amplitude pre-carboplatin. These data are shown in Table III. Note that at the higher click levels, the ratio varied from 0.5 (the post-carboplatin amplitude is half that of baseline) to 1.0 (no change). On average, at the higher click levels, the post-carboplatin ICP amplitude was approximately 70% of that pre-carboplatin. This amplitude ratio appears to increase somewhat with decreasing click level. At the lower click levels, several ratios increased to values

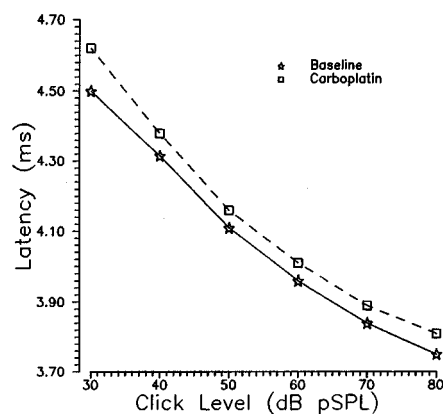


FIG. 4. Mean response latency is plotted across click level. The stars show baseline data, while the squares show the post-carboplatin data. For each condition, standard deviations were approximately 0.2 ms, ranging from 0.156 ms (50 dB pSPL, post-carboplatin) to 0.243 ms (30 dB pSPL, post-carboplatin).

TABLE II. Latency shift (in microseconds) of the ICP across click level. Each value represents the ICP latency post-carboplatin minus the ICP latency pre-carboplatin.

Animal	dB pSPL					
	80	70	60	50	40	30
4718	0	0.05	0	-0.05	0.05	0.05
4713	0.2	0.2	0.25	0.25	0.325	0.225
4711	0.05	0.1	0.05	0	0.2	0.20
4719	-0.05	-0.1	-0.1	-0.2	-0.3	<sup>a</sup>
4709	0.1	0	0.05	0.25	0.05	0.225

<sup>a</sup>ICP minimum response level for this chinchilla was 40 dB pSPL for the baseline condition.

greater than 1. It is likely that these large ratios are the result of small response amplitudes at these click levels combined with response variability, rather than a true enhancement of response amplitude.

### C. Click rate

Figure 6 plots ICP latency across click rate. Open symbols show conventional ICP data and filled symbols show data obtained using MLS trains. Figure 6(a) shows the data for 60-dB pSPL clicks; while Fig. 6(b) shows data to 80-dB pSPL clicks. For baseline data, increasing click rate produces a substantial increase in ICP latency. Following carboplatin, we again see a small (but consistent) increase in ICP latency (approximately 50  $\mu$ s) for all click rates, but the change in ICP latency with rate is similar pre- and post-carboplatin.

The effects of click rate on ICP amplitude is shown in Table IV. For both click levels, baseline ICP responses show an increase in amplitude with increasing click rate from 10 to 100 Hz for conventional averaging. This response enhancement is likely to reflect an overlap of long-latency activity at high stimulation rates, as this enhancement disappears with the use of MLS trains combined with cross correlation, which eliminates potential response overlap. For MLS trains, there is a decrease in response amplitude with increasing click rate. Following carboplatin injection, there is a substantial decrease in response amplitude at all rates, for both click levels. This decrease in mean response amplitude is seen at all click rates.

The effects of carboplatin on the ICP amplitude versus click rate function are difficult to evaluate because response

amplitude is reduced even for the lowest rate used. To control for this, ICP amplitude was normalized to the ICP amplitude at the 10-Hz rate. Figure 7 plots the mean relative amplitude across click rate, both pre- and post-carboplatin. For both click levels, the amplitude of the conventional ICP increases for click rates up to 100 Hz. There is a monotonic decrease in ICP amplitude for MLS click rates from 100 to 1000 Hz. Note the close correspondance of the pre- and post-carboplatin functions.

### D. Noise level

The effects of background noise level on ICP response latency are shown in Fig. 8. The data for the no-noise control condition is plotted at 0 dB SPL. For baseline data, there is a monotonic increase in ICP latency with increasing noise level from 30 to 70 dB SPL. Post-carboplatin, there is again a small increase in response latency for all noise conditions. However, the post-carboplatin function closely parallels the baseline function.

Mean ICP amplitude is shown across noise level in Table V. For both the pre- and post-carboplatin data, there is a monotonic decrease in ICP amplitude with increasing noise level. The mean response amplitude post-carboplatin is clearly smaller than pre-carboplatin values at all noise levels. To assess the effect of masker level independent of the amplitude reduction from carboplatin, pre- and post-carboplatin ICP amplitudes at each noise level were normalized relative to the ICP amplitude for the no-noise condition. The average relative amplitudes across masker level are shown in Fig. 9. For both pre- and post-carboplatin data, there is a small decrease in relative amplitude for the 30-dB SPL noise level,

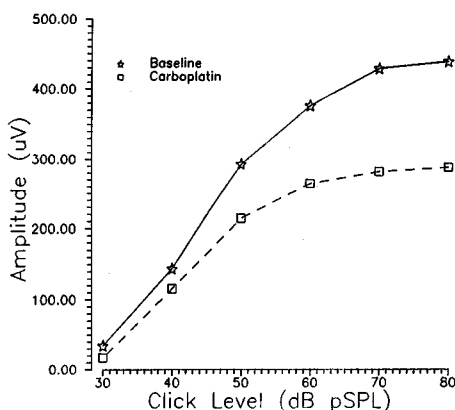


FIG. 5. Mean response amplitude is plotted across click level. The stars show baseline data, while the squares show the post-carboplatin data.

TABLE III. Relative amplitude of the ICP across click level. Each value represents the amplitude ratio of the post-carboplatin amplitude to the pre-carboplatin amplitude.

Animal	dB pSPL					
	80	70	60	50	40	30
4718	0.72	0.70	0.80	0.82	1.06	1.77
4713	0.51	0.50	0.52	0.50	0.29	0.20
4711	0.64	0.67	0.70	0.71	0.86	0.88
4719	0.63	0.63	0.66	0.83	2.69	<sup>a</sup>
4709	1.0	1.0	1.14	1.27	2.87	0.29
Mean	0.70	0.70	0.76	0.83	1.55	0.79
s.d.	0.18	0.19	0.23	0.28	1.16	0.72

<sup>a</sup>ICP minimum response level for this chinchilla was 40 dB pSPL for the baseline condition.

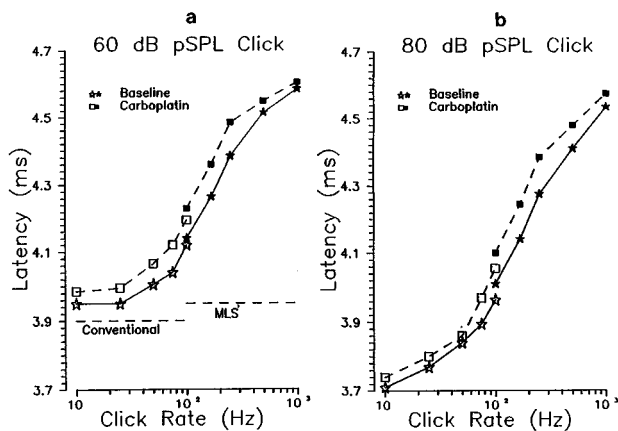


FIG. 6. Mean response latency is plotted across click rate. The stars show baseline data, while the squares show the post-carboplatin data. (a) shows data to 60-dB pSPL clicks, while (b) shows 80-dB pSPL clicks.

with a monotonic decrease in relative response amplitude with increasing noise level. Each 10-dB increase in noise level produced a 10%–20% reduction in response amplitude. Note the similarity of the functions pre- and post-carboplatin.

### III. DISCUSSION

#### A. Normative ICP data

Little data are available concerning the effects of click level, click rate, and background masking noise on the chinchilla ICP. Our results demonstrate an increase in ICP latency and a decrease in ICP amplitude with decreasing click level, increasing click rate, and increasing masking noise level. These findings are in fundamental agreement with ABR reports for other mammals, including humans (Burkard and Hecox, 1983, 1987; Burkard *et al.*, 1990a, b) and gerbils (Burkard, 1994b; Burkard and Voigt, 1989a, b, 1990).

The slope of the latency/intensity function was  $-16 \mu\text{s}/\text{dB}$ . This value is substantially less than the  $-40 \mu\text{s}/\text{dB}$  observed in wave V of the human ABR (Burkard and Hecox, 1983), but is larger than that reported in the ABR of other rodents such as gerbil ( $-6 \mu\text{s}/\text{dB}$ ; Burkard and Voigt, 1989a) or rat ( $-10 \mu\text{s}/\text{dB}$ ; Burkard *et al.*, 1990c), and similar to the cat

( $-16 \mu\text{s}/\text{dB}$ ; Huang and Buchwald, 1978). These data suggest an inverse relationship between body size and slope of the ABR (or ICP) latency/intensity function.

#### B. Effects of carboplatin: DPOAEs

The cochleograms obtained for the two animals shown in Fig. 2 demonstrate minimal loss of OHCs and a range of IHC loss from about 10% to 80%. These anatomical results are similar to those reported for a dosage of 38 mg/kg of carboplatin (Hofstetter *et al.*, 1997), i.e., that in moderate doses, carboplatin spares OHCs and damages IHCs in the chinchilla. There was little effect of carboplatin on DPOAE amplitude, consistent with earlier reports (Trautwein *et al.*, 1996; Jock *et al.*, 1996). Since DPOAEs remained normal, it is likely that OHCs were intact (Trautwein *et al.*, 1996; Brown *et al.*, 1989).

#### C. ICP minimum response level

We found little effect of carboplatin on the lowest click level at which an ICP response could be elicited. It should be noted that we only defined minimum response level with a 10-dB resolution, and that a small threshold shift would not be observed. Trautwein *et al.* (1996) reported no change in CAP threshold following carboplatin injections that produced mild-to-moderate IHC loss, and thus our findings are in fundamental agreement with theirs. In contrast, Harrison and colleagues (Takeno *et al.*, 1994a, b; Wake *et al.*, 1993, 1994) reported substantial elevations in chinchilla CAP and ABR thresholds following carboplatin. It is possible that differences in carboplatin dosage that result in different degrees of IHC loss may be a contributing factor. For example, when IHC loss exceeds about 80%, or when OHC loss is observed, then threshold shifts have been reported (Trautwein *et al.*, 1996).

Wang *et al.* (1997) investigated eighth nerve fiber responses in carboplatin-treated animals. In those animals with intact OHCs and moderate IHC loss, most neurons showed normal (or near-normal) thresholds and normal tuning. Interestingly, spontaneous and maximum discharge rates were reduced relative to values observed in control animals. Wake *et al.* (1996b) reported normal thresholds and tuning from neurons from the central nucleus of the IC following carbo-

TABLE IV. Amplitude (in microvolts) of ICP response across click rate and click level, pre- and post-carboplatin. Means and standard deviations are rounded to the nearest microvolt.

		Rate (Hz)					MPI (ms)				
		10	25	50	75	100	5	3	2	1	0.5
60 dB pSPL click											
Baseline	Mean:	393	386	409	433	414	370	299	241	100	34
	s.d.:	152	164	165	179	154	157	122	114	43	13
Post-carbo	Mean:	260	261	285	294	302	257	203	163	70	25
	s.d.:	43	39	40	45	46	41	32	37	22	8
80 dB pSPL click											
Baseline	Mean:	417	436	457	490	493	383	313	247	94	25
	s.d.:	158	162	151	180	174	131	110	101	36	6
Post-carbo	Mean:	285	287	314	329	336	267	215	174	69	22
	s.d.:	76	64	39	33	33	36	23	27	18	9

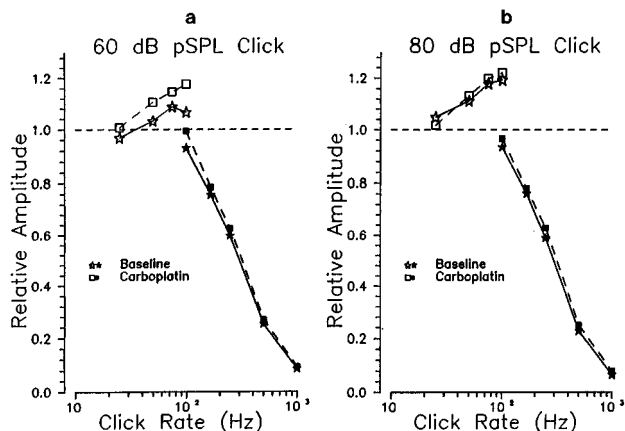


FIG. 7. Mean proportional response amplitude (*re*: amplitude at a 10-Hz rate) is plotted across click rate. The stars show baseline data, while the squares show the post-carboplatin data. (a) shows data to 60-dB pSPL clicks, while (b) shows 80-dB pSPL clicks.

platin treatment that spared OHCs, but produced substantial IHC loss. Under ideal conditions, if only a small proportion of type I afferents fire to a near-threshold stimulus, then a near-field or far-field evoked response should be observed. However, the reduction in the number of type I afferents responding to the transient stimulus would reduce the amplitude of the evoked potential. If one used a criterion response amplitude to determine response “threshold,” then the reduction in response amplitude following IHC loss would result in an elevation in “threshold” once IHC loss exceeded some minimum value. For example, Liberman *et al.* (1997) report that CAP threshold was elevated when IHC loss in a given cochlear region of carboplatin-treated chinchillas exceeded roughly 50%. However, this statement is based on “threshold” estimation using a 10- $\mu$ V criterion. It seems likely that the amount of IHC loss required to produce a “threshold” shift would depend on the amplitude criterion used. Perhaps the differences in reports concerning threshold shift following carboplatin-induced IHC loss reflect differences in threshold-determining criteria as well as differences in the amount of IHC loss.

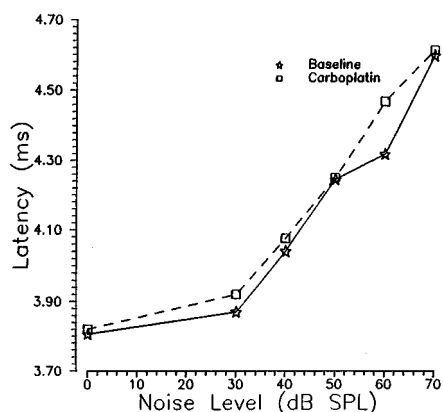


FIG. 8. Mean response latency is plotted across noise level. The stars show baseline data, while the squares show the post-carboplatin data.

TABLE V. Amplitude (in microvolts) of ICP response across noise level, pre- and post-carboplatin. Means and standard deviations are rounded to the nearest microvolt. Responses were obtained from all five animals for all noise conditions except for the 70-dB SPL noise condition, for the baseline measure, in which only four animals showed an identifiable response.

		Noise level (dB SPL)					
		No noise	30	40	50	60	70
Baseline	Mean	473	404	351	251	108	19
	s.d.	176	112	79	51	14	3
Post-carbo	Mean	310	290	244	160	77	13
	s.d.	59	50	31	26	20	3

#### D. Amplitude reduction

There is a clear reduction in ICP amplitude following carboplatin. This is consistent with the reduction in CAP amplitude reported previously (Trautwein *et al.*, 1996). Our data show that the amplitude reduction observed in the peripheral nerve response is reflected in the response from the inferior colliculus. The loss in IHCs results in a loss of type I fiber excitation, which in turn leads to a net reduction in CAP amplitude, and this loss of peripheral input is reflected downstream in the evoked potential response amplitude from the IC. In two animals, we have both cochleograms (Fig. 2) and ICP amplitude data (Table III). Animal 4718 showed a small (5%–10%) loss of IHCs and an ICP amplitude reduction of 28% at the 80-dB pSPL click level. Animal 4711 showed a much larger (20%–80%) IHC loss, and yet showed an ICP amplitude reduction of 36% at the 80-dB pSPL click. A firm conclusion concerning the relationship between IHC loss and ICP amplitude awaits a study with a larger number of chinchillas.

#### E. Latency shift

There was a small increase in ICP response latency following carboplatin treatment. The mean latency increase was on the order of 50  $\mu$ s. Only a subset of the animals showed this latency increase post-carboplatin; indeed, one consistently showed a latency decrease. It would appear that an ICP latency increase occurs in a subset of chinchillas exposed to carboplatin. A study varying the dosage of carbopl-

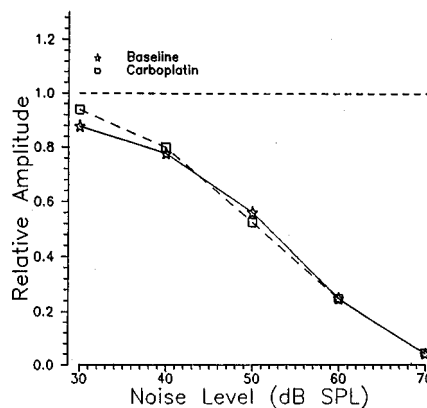


FIG. 9. Mean proportional response amplitude (*re*: amplitude for the no-noise condition) is plotted across noise level. The stars show baseline data, while the squares show the post-carboplatin data.

atin and relating the magnitude of OHC loss with ICP latency shift would be required to shed light on the relationship between IHC loss and ICP latency shift.

## F. Effects of click level

The slope of the ICP latency/intensity function was similar pre- and post-carboplatin. In the human ABR, sensorineural hearing loss, thought to reflect primarily OHC loss, results in threshold elevation and often a steepening of the slope of the latency/intensity function (Galambos and Hecox, 1978). For the sake of discussion, let us accept a homology between the chinchilla ICP response and human ABR wave V. It then appears that IHC loss produces minimal threshold shift and minimal changes in the latency/intensity function, while what is likely to be an OHC loss produces threshold elevation and a steeper latency/intensity function. These results suggest that OHC loss leads to a steepening of the latency/intensity function, while IHC loss does not. Alternatively, the steepening of the latency/intensity function only occurs if there is a substantial threshold elevation.

The loss in response amplitude post-carboplatin was larger at higher click levels than at low click levels (see Table III). At high click levels, IHCs are maximally stimulated and lead to a high probability of type I fiber discharge. The loss of IHCs post-carboplatin should clearly be reflected in response amplitude under these stimulus conditions. As click amplitude is reduced, there is a net reduction in IHC excitation and type I fiber discharge probability, and this less deterministic excitation may lead to a reduced effect of carboplatin on response amplitude. This function may also be affected by the convergence pattern of type I fibers in the cochlear nuclei and in more rostral auditory centers. Finally, it may be that as stimulus level decreases, and ICP response amplitude decreases, the net contribution of residual noise in the averaged response becomes more dominant (both pre- and post-carboplatin), reducing the difference in the estimated response amplitudes pre- and post-carboplatin. The similarity in ICP amplitude reduction post-carboplatin across click rate and noise level (see below) argues against this latter explanation.

## G. Effects of click rate and masker level

Change in ICP response latency with increasing click rate was similar pre- and post-carboplatin. Click rate is thought to stress synaptic mechanisms (Burkard *et al.*, 1996a, b). Increasing click rate produces greater ABR latency and interwave interval increases in animals with immature synaptic machinery (Burkard *et al.*, 1996a; Lasky, 1984) and in those with compromised neural function, such as in patients with multiple sclerosis (Jacobson *et al.*, 1987). The failure to observe a greater increase in ICP latency with increasing click rate following carboplatin injection suggests that the effects of carboplatin are limited to the periphery, and have little or no neurotoxic effects on the central auditory system.

The latency increase and proportional amplitude decrease with increasing level of a broadband noise are similar pre- and post-carboplatin. Burkard and Hecox (1987)

showed that both increasing click rate and noise level produced an increase in the human ABR interwave intervals. This is consistent with a central (synaptic) mechanism of these stimulus manipulations on ABR peak latency shifts. Burkard and Hecox (1983) showed a nonadditivity of click rate and noise level on human ABR wave V latency shift. They interpreted these findings as suggesting that the mechanisms producing rate- and masking-induced ABR peak latency shifts were produced by overlapping mechanisms. The similarity in ICP latency shift and amplitude reduction with noise level pre- and post-carboplatin is consistent with similar findings with click rate and with a purely peripheral effect of carboplatin on auditory function.

## ACKNOWLEDGMENTS

This work was supported by NIH-NIDCD 5R01DC00166-13. We thank Sandra L. McFadden for her careful review of an earlier draft of this manuscript.

- Brown, A., McDowell, B., and Forge, A. (1989). "Acoustic distortion products can be used to monitor the effects of chronic gentamicin treatment," *Hearing Res.* **42**, 143–156.
- Burkard, R. (1994a). "The use of maximum length sequences to obtain brainstem auditory evoked responses at rapid rates of stimulation," *Am. J. Audiol.* **Nov.**, 16–20.
- Burkard, R. (1994b). "Gerbil brainstem auditory evoked responses (BAERs) to maximum length sequences," *J. Acoust. Soc. Am.* **95**, 2126–2135.
- Burkard, R., and Hecox, K. (1983). "The effect of broadband noise on the human brainstem auditory evoked response. I. Rate and intensity effects," *J. Acoust. Soc. Am.* **74**, 1204–1213.
- Burkard, R., and Hecox, K. (1987). "The effect of broadband noise on the human brainstem auditory evoked response. III. Anatomic locus," *J. Acoust. Soc. Am.* **81**, 1050–1063.
- Burkard, R., and Voigt, H. (1989a). "Stimulus dependencies of the gerbil brainstem auditory evoked response (BAER). I. Effects of click level, rate and polarity," *J. Acoust. Soc. Am.* **85**, 2514–2525.
- Burkard, R., and Voigt, H. (1989b). "Stimulus dependencies of the gerbil brainstem auditory evoked response (BAER). II. Effects of broadband noise level and high-pass masker cutoff frequency across polarity," *J. Acoust. Soc. Am.* **85**, 2526–2536.
- Burkard, R., and Voigt, H. (1990). "Stimulus dependencies of the gerbil brainstem auditory evoked response. III. Additivity of click level and rate with noise level," *J. Acoust. Soc. Am.* **88**, 2222–2234.
- Burkard, R., Feldman, M., and Voigt, H. (1990c). "Brainstem auditory-evoked response in the rat. Normative studies, with observations concerning the effects of ossicular disruption," *Audiology* **29**, 146–162.
- Burkard, R., McGee, J., and Walsh, E. (1996a). "The effects of stimulus rate on the feline BAER during development. I. Peak latencies," *J. Acoust. Soc. Am.* **100**, 978–990.
- Burkard, R., McGee, J., and Walsh, E. (1996b). "The effects of stimulus rate on the feline BAER during development. II. Peak amplitudes," *J. Acoust. Soc. Am.* **100**, 991–1002.
- Burkard, R., Shi, Y., and Hecox, K. (1990a). "A comparison of maximum length and Legendre sequences to derive BAERs at rapid rates of stimulation," *J. Acoust. Soc. Am.* **87**, 1656–1664.
- Burkard, R., Shi, Y., and Hecox, K. (1990b). "The effects of masking noise on BAERs obtained by deconvolution," *J. Acoust. Soc. Am.* **87**, 1665–1672.
- Eysholdt, V., and Schreiner, C. (1982). "Maximum length sequences. A fast method for measuring the auditory brainstem response," *Audiology* **21**, 242–250.
- Galambos, R., and Hecox, K. (1978). "Clinical applications of the auditory brainstem response," *Otolaryngol. Clin. N. Am.* **11**, 709–722.
- Greenwood, D. (1990). "A cochlear frequency-position function for several species—29 years later," *J. Acoust. Soc. Am.* **87**, 2592–2604.
- Hofstetter, P., Ding, D., Powers, N., and Salvi, R. (1997). "Quantitative

- relationship of carboplatin dose to magnitude of inner and outer hair cell loss and the reduction in distortion product otoacoustic emission amplitude in chinchilla," *Hearing Res.* **112**, 199–215.
- Huang, C., and Buchwald, J. (1978). "Factors that affect the amplitude and latencies of the vertex short latency acoustic responses in the cat," *Electroencephalogr. Clin. Neurophysiol.* **44**, 179–186.
- Jacobson, J., Murray, T., and Deppe, U. (1987). "The effects of ABR stimulus repetition rate in multiple sclerosis," *Ear Hear.* **8**, 115–120.
- Jock, B., Hamernik, R., Aldrich, L., Ahroon, W., Petriello, K., and Johnson, A. (1996). "Evoked-potential thresholds and cubic distortion product otoacoustic emissions in the chinchilla following carboplatin treatment and noise exposure," *Hearing Res.* **96**, 179–190.
- Lasky, R. (1984). "A developmental study on the effect of stimulus rate on the auditory evoked brain-stem response," *Electroencephalogr. Clin. Neurophysiol.* **59**, 119–130.
- Liberman, M., Chesney, C., and Kujawa, S. (1997). "Effects of selective inner hair cell loss on DPOAE and CAP in carboplatin-treated chinchillas," *Aud. Neurosci.* **3**, 255–268.
- McFadden, S., Henderson, D., and Quaranta, A. (1997). "Remote masking in normal-hearing and noise-exposed chinchillas," *Audiol. Neurootol.* **2**, 128–138.
- Snyder, D., and Salvi, R. (1994). "A novel chinchilla restraint device," *Lab Animal* **23**, 42–44.
- Takeno, S., Harrison, R., Ibrahim, D., Wake, M., and Mount, R. (1994a). "Cochlear function after selective inner hair cell degeneration induced by carboplatin," *Hearing Res.* **75**, 93–102.
- Takeno, S., Harrison, R., Mount, R., Wake, M., and Harada, Y. (1994b). "Induction of selective inner hair cell damage by carboplatin," *Scanning Microsc.* **8**, 97–106.
- Trautwein, P., Hofstetter, P., Wang, J., Salvi, R., and Nostrand, A. (1996). "Selective inner hair cell loss does not alter distortion product otoacoustic emissions," *Hearing Res.* **96**, 71–82.
- Wake, M., Takeno, S., Ibrahim, D., and Harrison, R. (1994). "Selective inner hair cell ototoxicity induced by carboplatin," *Laryngoscope* **104**, 488–493.
- Wake, M., Takeno, S., Mount, R., and Harrison, R. (1996b). "Recording from the inferior colliculus following cochlear inner hair cell damage," *Acta Oto-Laryngol.* **116**, 714–720.
- Wake, M., Takeno, S., Ibrahim, D., Harrison, R., and Mount, R. (1993). "Carboplatin ototoxicity: an animal model," *J. Laryngol. Otol.* **107**, 585–589.
- Wake, M., Anderson, J., Takeno, S., Mount, R., and Harrison, R. (1996a). "Otoacoustic emission amplification after inner hair cell damage," *Acta Oto-Laryngol.* **116**, 374–381.
- Wang, J., Powers, N., Hofstetter, P., Trautwein, P., Ding, D., and Salvi, R. (1997). "Effects of selective inner hair cell loss on auditory nerve fiber threshold, tuning and spontaneous and driven discharge rate," *Hearing Res.* **107**, 67–82.

# Modeling the relation between the intensity just-noticeable difference and loudness for pure tones and wideband noise

Jont B. Allen

AT&T Labs Research, Florham Park, New Jersey 07932

Stephen T. Neely

Boys Town National Research Hospital, Omaha, Nebraska 68131

(Received 8 August 1995; revised 17 July 1997; accepted 17 July 1997)

A classical problem in auditory theory is the relation between the loudness  $L(I)$  and the intensity just-noticeable difference (JND)  $\Delta I(I)$ . The intensity JND is frequently expressed in terms of the Weber fraction defined by  $J(I) \equiv \Delta I/I$  because it is anticipated that this ratio should be a constant (i.e., Weber's law). Unfortunately,  $J(I)$  is not a constant for the most elementary case of the pure tone JND. Furthermore it remains unexplained why Weber's law holds for wide-band stimuli. We explore this problem and related issues. The loudness and the intensity JND are defined in terms of the first and second moments of a proposed random *decision variable* called the *single-trial loudness*  $\tilde{L}(I)$ , namely the loudness is  $L(I) \equiv \mathcal{E}\tilde{L}(I)$ , while the variance of the single trial loudness is  $\sigma_L^2 \equiv \mathcal{E}(\tilde{L} - L)^2$ . The JND is given by the signal detection assumption  $\Delta L = d' \sigma_L$ , where we define the loudness JND  $\Delta L(I)$  as the change in loudness corresponding to  $\Delta I(I)$ . Inspired by Hellman and Hellman's recent theory [J. Acoust. Soc. Am. **87**, 1255–1271 (1990)], we compare the Riesz [Phys. Rev. **31**, 867–875 (1928)]  $\Delta I(I)$  data to the Fletcher and Munson [J. Acoust. Soc. Am. **5**, 82–108 (1933)] loudness growth data. We then make the same comparison for Miller's [J. Acoust. Soc. Am. **19**, 609–619 (1947)] wideband noise JND and loudness match data. Based on this comparison, we show empirically that  $\Delta L(L) \propto L^{1/p}$ , where  $p=2$  below  $\approx 5$  sones and is 1 above. Since  $\Delta L(I)$  is proportional to  $\sigma_L$ , when  $p=2$  the statistics of the single-trial loudness  $\tilde{L}$  are Poisson-like, namely  $\sigma_L^2 \propto L$ . This is consistent with the idea that the pure tone loudness code is based a neural discharge rate (not the auditory nerve). Furthermore, when  $p=1$  (above about 5 sones), the internal loudness signal-to-noise ratio is constant. It is concluded that Ekman's law ( $\Delta L/L$  is constant) is true, rather than Weber's law, in this loudness range. One of the main contributions of this paper is its attempt to integrate Fletcher's neural excitation pattern model of loudness and signal detection theory. © 1997 Acoustical Society of America. [S0001-4966(97)02411-9]

PACS numbers: 43.66.Ba, 43.66.Cb, 43.66.Fe [WJ]

## INTRODUCTION

When modeling human psychophysics we must carefully distinguish the external *physical* variables, which we call  $\Phi$  variables, from the internal *psychophysical* variables, which we refer to as  $\Psi$  variables.<sup>1</sup> Psychophysical modeling seeks a transformation from the  $\Phi$  domain to the  $\Psi$  domain. The  $\Phi$  intensity of a sound is easily quantified by direct measurement. The  $\Psi$  intensity is the loudness. The idea that loudness could be quantified was first suggested by Fechner (1966) in 1860, which raised the question of the quantitative transformation between the physical and psychophysical intensity. For a recent review of this problem, and a brief summary of its long history, see Schlauch *et al.* (1995).

An increment in the intensity of a sound that results in a *just-noticeable difference* (JND) is called an intensity JND. Fechner suggested quantifying the intensity-loudness growth transformation by counting the number of the *loudness JNDs* between two intensity values. However, after many years of work, the details of the relationship between loudness and the intensity JNDs have remained unclear (Zwislocki and Jordan, 1986; Viemeister, 1988; Plack and Carlyon, 1995).

The contribution of this paper is that it takes a fresh view of the whole problem of the intensity JND and loudness

by merging the 1953 Fletcher neural excitation pattern model of loudness (Allen, 1995, 1996a) with auditory signal detection theory (Green and Swets, 1966). It is generally accepted that the intensity JND is the physical correlate of the psychological-domain uncertainty corresponding to the psychological intensity representation of a signal. Along these lines, for long duration pure tones and wideband noise, we assume that the  $\Psi$ -domain intensity is the loudness, and that the loudness JND results from loudness "noise" due to its stochastic representation.

To model the intensity JND we must define a *decision variable* associated with loudness and its random fluctuations. We call this loudness random decision variable the *single-trial loudness*. Accordingly we define the loudness and the loudness JND in terms of the first and second moments of the single-trial loudness, corresponding to the mean and variance of the distribution of the intensity decision variable. Because of its fundamental importance, we define the ratio of the mean loudness to the loudness standard deviation as the *loudness signal-to-noise ratio* ( $\text{SNR}_L$ ).

We will show that a transformation of the  $\Phi$ -domain JND data into the  $\Psi$  domain unifies tonal-stimuli JND data, which do not obey the Weber's law ("near-miss results"),



and wideband noise data, for which Weber's law holds. We show that  $\text{SNR}_L(L)$  is functionally the same for both the tone and noise cases. To help understand these results, we introduce the concept of a near-miss to Stevens' law, which we show cancels the near-miss to Weber's law, giving the invariance in  $\text{SNR}_L$  for the tone case. Our ultimate goal in this work is to use signal detection theory to unify masking and the JND, following the 1947 outline of this problem by Miller (1947). This work has applications in speech and audio coding.

For the case of tones, we have chosen to illustrate our theoretical work using the classical intensity modulation measurements of Riesz (1928). Riesz measured the intensity JND using small, low-frequency (3-Hz), sinusoidal modulation of tones. "Modern" methods generally use "pulsed" tones which are turned on and off somewhat abruptly, to make them suitable for a two-alternative, forced-choice (2AFC) paradigm. Riesz's modulation method has a distinct advantage for characterizing the internal signal detection process, because it maintains a nearly steady-state small-signal condition within the auditory system. The interpretation of intensity JNDs is therefore simplified since the underlying stochastic processes are stationary.

An outline of the paper is as follows: After some basic definitions in Sec. I, and a review of some previous models in Sec. II, in Sec. III we explore issues surrounding the relation between the intensity JND and loudness, for the special case of tones in quiet and for wideband noise. First, we look at formulas for counting the number of intensity and loudness JNDs and we use these formulas, together with decision-theoretic principles, to relate loudness to the intensity JND. We then review the loudness-JND theory developed by Hellman and Hellman (1990), which provided the inspiration for the present work. Next, we empirically estimate the loudness SNR as a function of both intensity and loudness, using the tonal JND data of Riesz (1928) and the loudness growth function of Fletcher and Munson (1933). We then repeat this calculation for Miller's wideband noise JND and loudness data. Finally we propose a model of loudness that may be used to compute the JND. This model merges Fletcher's neural excitation pattern model of loudness with signal detection theory.

## I. DEFINITIONS

We need a flexible yet clear notation that accounts for important time fluctuations and modulations that are present in the signals, such as beats and gated signals. Toward this end, we propose the following definitions. We include a definition of *masked threshold* because we view the intensity JND as a special case of the masked threshold (Miller, 1947). We include a definition of *beats* so that we can discuss their influence on Riesz's method for the measurement of intensity JNDs.

### A. Basic definitions

#### 1. Intensity

In the time domain, it is common to define the  $\Phi$  *intensity* in terms of the time-integrated squared signal pressure  $s(t)$ , namely,<sup>2</sup>

$$I_s(t) \equiv \frac{1}{\rho c T} \int_{t-T}^t s^2(t) dt, \quad (1)$$

where  $T$  is the integration time and  $\rho c$  is the specific acoustic impedance of air. The *intensity level* is defined as  $I_s/I_{\text{ref}}$ , and the *sound-pressure level* as  $s/s_{\text{ref}}$  where the reference intensity is  $I_{\text{ref}}$  or  $10^{-10} \mu\text{W}/\text{cm}^2$  and the reference pressure  $s_{\text{ref}} = 20 \mu\text{Pa}$ . These two reference levels are equivalent at only one temperature,<sup>3</sup> but both seem to be in use.

### 2. Intensity of masker+probe

The JND is sometimes called "self-masking," to reflect the view that it is determined by the internal noise of the auditory system. To model the JND it is useful to define a more general measure called the *masked threshold*, which is defined in the  $\Phi$  domain in terms of a pressure scale factor  $\alpha$  applied to the probe signal  $p(t)$  that is then added to the masking pressure signal  $m(t)$ . The relative intensity of the probe and masker is varied by changing  $\alpha$ . Setting  $s(t) = m(t) + \alpha p(t)$ , we denote the combined intensity as

$$I_{m+p}(t, \alpha) \equiv \frac{1}{\rho c T} \int_{t-T}^t (m(t) + \alpha p(t))^2 dt. \quad (2)$$

The unscaled probe signal  $p(t)$  is chosen to have the same long-term average intensity as the masker  $m(t)$ , defined as  $I$ . Let  $I_m(t)$  be the intensity of the masker with no probe ( $\alpha=0$ ), and  $I_p(t, \alpha) = \alpha^2 I$  be the intensity of the scaled probe signal with no masker. Thus<sup>4</sup>

$$I \equiv I_{m+p}(t, 0) = I_m(t) = I_p(t, 1).$$

### 3. Beats

Rapid fluctuations having frequency components outside the bandwidth of the  $T$  second rectangular integration window are very small and will be ignored. Accordingly we drop the time dependence in terms  $I_m$  and  $I_p$ . Because of beats between  $m(t)$  and  $p(t)$  (assuming the spectra of these signals are within a common critical band) one must proceed carefully. Slowly varying correlations between the probe and masker having frequency components within the bandwidth of the integration window may *not* be ignored, as with beats between two tones separated in frequency by a few Hz. Accordingly we keep the time dependence in the term  $I_{m+p}(t, \alpha)$  and other slow-beating time-dependent terms. In the  $\Phi$  domain these beats are accounted for with a probe-masker correlation function  $\rho_{mp}(t)$  (Sydorenko and Allen, 1994; Green and Swets, 1966, p. 213).

### 4. Intensity increment $\delta I(t, \alpha)$

Expanding Eq. (2) and solving for the *intensity increment*  $\delta I$  we find

$$\delta I(t, \alpha) \equiv I_{m+p}(t, \alpha) - I \quad (3)$$

$$= (2\alpha\rho_{mp}(t) + \alpha^2)I, \quad (4)$$

where

$$\rho_{mp}(t) = \frac{1}{\rho c T I} \int_{t-T}^t m(t)p(t) dt \quad (5)$$

defines a normalized cross correlation function between the masker and the probe. The correlation function must lie between  $-1$  and  $1$ .

### 5. Detection threshold

As the probe to masker ratio  $\alpha$  is slowly increased from zero, the probe can eventually be detected. We specify the *detection threshold* as  $\alpha_*$ , where the asterisk indicates the threshold value of  $\alpha$  where a subject can discriminate intensity  $I_{m+p}(t, \alpha_*)$  from intensity  $I_{m+p}(t, 0)$  50% of the time, corrected for chance [i.e., obtain a 75% correct score in a direct comparison of the two signals (Yost, 1994; Green and Swets, 1966, p. 129)]. The quantity  $\alpha_*(t, I)$  is the probe to masker rms pressure ratio at the detection threshold. It is a function of the masker intensity  $I$  and, depending on the experimental setup, time.

### 6. Masked threshold intensity

The *masked threshold intensity* is defined in terms of  $\alpha_*$  as

$$I_p^*(I) \equiv I_p(\alpha_*) = \alpha_*^2 I,$$

which is the threshold intensity of the probe in the presence of the masker.

The masked threshold intensity is a function of the stimulus modulation parameters. For example, tone maskers and narrow-band noise maskers of equal intensity, and therefore approximately equal loudness, give masked thresholds that are about 20 dB different (Egan and Hake, 1950). As a second example, when using the method of beats (Riesz, 1928), the just-detectable modulation depends on the beat frequency. With ‘‘modern’’ 2AFC methods, the signals are usually gated on and off (100% modulation) (Jesteadt *et al.*, 1977). According to Stevens and Davis (p. 142, 1983)

A gradual transition, such as the sinusoidal variation used by Riesz, is less easy to detect than an abrupt transition; but, as already suggested, an abrupt transition may involve the production of unwanted transients.

One must conclude that the *relative masked threshold* [i.e.,  $\alpha_*(t, I)$ ] is a function of the modulation conditions.

### 7. $\Psi$ -domain temporal resolution

When modeling time varying psychological decision variables, the relevant integration time  $T$  is not the duration defined by the  $\Phi$ -intensity Eq. (1), rather the integration time is determined in the  $\Psi$  domain. This important  $\Psi$ -domain model parameter is called *loudness temporal integration* (Yost, 1994). It was first explicitly modeled by Munson in 1947.

The  $\Phi$ -domain temporal resolution ( $T$ ) is critical to the definition of the JND in Riesz’s experiment (see Appendix A) because it determines the measured intensity of the beats. The  $\Psi$ -domain temporal resolution plays a different role. Beats cannot be heard if they are faster than, and therefore ‘‘filtered’’ out by, the  $\Psi$  domain response. The  $\Psi$ -domain temporal resolution also impacts results for gated stimuli,

such as in the 2AFC experiment, though its role is poorly understood in this case. To model the JND as measured by Riesz’s method of just-detectable beats, one must know the  $\Psi$ -domain resolution duration to calculate the probe-masker effective correlation  $\rho_{mp}(t)$  in the  $\Psi$  domain. It may be more practical to estimate the  $\Psi$ -domain resolution from experiments that estimate the degree of correlation, as determined by the beat modulation detection threshold as a function of the beat frequency  $f_b$  (Sydorenko and Allen, 1994).

In summary, even though Riesz’s modulation detection experiment is technically a masking task, we treat it, following Riesz (1928), Miller (1947), and Littler (1965), as characterizing the intensity JND.

It follows that the  $\Psi$ -domain temporal resolution plays a key role in intensity JND and masking models.

### 8. The intensity JND $\Delta I$

The intensity *just-noticeable difference* (JND) is<sup>5</sup>

$$\Delta I(I) \equiv \delta(t, \alpha_*), \quad (6)$$

the intensity increment at the masked threshold, for the special case where the probe signal is equal to the masking signal [ $p(t) = m(t)$ ]. From Eq. (4) with  $\alpha$  set to threshold  $\alpha_*$  and  $\rho_{mp}(t) = 1$

$$\Delta I(I) = (2\alpha_* + \alpha_*^2)I. \quad (7)$$

An important alternative definition for the special case of the *pure-tone JND* is to let the masker be a pure tone, and let the probe be a pure tone of a slightly different frequency (e.g., a beat frequency difference of  $f_b = 3$  Hz). This was the definition used by Riesz in 1928. Beats are heard at  $f_b = 3$  Hz, and assuming the period of 3 Hz is within the passband of the  $\Psi$ -temporal resolution window,  $\rho_{mp}(t) = \sin(2\pi f_b t)$  and

$$\Delta I(t, I) = [2\alpha_* \sin(2\pi f_b t) + \alpha_*^2]I. \quad (8)$$

If the beat period is less than the  $\Psi$  temporal resolution window, the beats are ‘‘filtered’’ out by the auditory brain (the effective  $\rho_{mn}$  is small) and we do not hear the beats. In this case  $\Delta I(I) = \alpha_*^2 I$ .

### 9. Internal noise

It is widely accepted that the pure tone intensity JND is determined by the *internal noise* of the auditory system (Siebert, 1965; Raab and Goldberg, 1975), and that  $\Delta I$  is proportional to the standard deviation of the  $\Psi$ -domain decision variable that is being discriminated in the intensity detection task, reflected back into the  $\Phi$  domain. The usual assumption, from signal detection theory, is that  $\Delta I = d' \sigma_I$ , where  $d' \equiv \Delta I / \sigma_I$  is a constant that depends on the experimental design, and  $\sigma_I$  is the intensity standard deviation of the  $\Phi$ -domain intensity due to  $\Psi$ -domain auditory noise (Yost, 1994).

### 10. Hearing threshold

The *hearing threshold* (or unmasked threshold) *intensity* may be defined as the intensity corresponding to the first (lowest intensity) JND. The hearing threshold is represented

as  $I_p^*(0)$  to indicate the probe intensity when the masker intensity is small (i.e.,  $I \rightarrow 0$ ). It is believed that internal noise is responsible for the hearing threshold, however, there is no reason to assume that this noise is the same as the internal noise that produces the JND.

## 11. Loudness $L$

The loudness  $L$  of a sound is the  $\Psi$  intensity. The loudness growth function  $L(I)$  depends on the stimulus conditions. For example  $L(I)$  for a tone and for wideband noise are not the same functions. Likewise the loudness growth function for a 100-ms tone and a 1-s tone differ. When defining a loudness scale it is traditional to specify the intensity, frequency, and duration of a tone such that the loudness growth function is one [i.e.,  $L(I_{\text{ref}}, f_{\text{ref}}, T_{\text{ref}}) = 1$  defines a loudness scale]. For the sone scale, the reference signal is a  $I_{\text{ref}} = 40$  dB SPL tone at  $f_{\text{ref}} = 1$  kHz with duration  $T_{\text{ref}} = 1$  s. For Fletcher's LU scale the reference intensity is the hearing threshold, which means that 1 sone = 975 LU (Fletcher, 1953) for a "normal" hearing person. In the next section we shall show that Fletcher's LU loudness scale is a more natural scale than the sone scale (the ANSI and ISO standard scales).

## 12. The single-trial loudness

A fundamental postulate of psychophysics is that all decision variables (i.e.,  $\Psi$  variables) are random variables, drawn from some probability density function (Green and Swets, 1966, Chap. 5). For early discussions of this point see Montgomery (1935) and page 144 of Stevens and Davis (1983). To clearly indicate the distinction between random and nonrandom variables, a tilde ( $\sim$ ) is used to indicate a random variable.<sup>6</sup>

We define the loudness decision variable as the single-trial loudness  $\tilde{L}$ , which is the sample loudness heard on each stimulus presentation. The loudness  $L$  is then the expected value of the single-trial loudness  $\tilde{L}$

$$L(I) \equiv \mathcal{E}\tilde{L}(I). \quad (9)$$

The second moment of the single-trial loudness

$$\sigma_{\tilde{L}}^2 \equiv \mathcal{E}(\tilde{L} - L)^2 \quad (10)$$

defines the loudness variance  $\sigma_{\tilde{L}}^2$  and standard deviation  $\sigma_{\tilde{L}}$ .

## B. Derived definitions

The definitions given above cover the basic variables. However, many normalized forms of these variables are used in the literature, and these also need to be defined. These derived variables were frequently formed with the hope of finding an invariance in the data. This could be viewed as a form of modeling exercise that has largely failed (e.g., the near-miss to Weber's law). The sheer number of combinations has led to serious confusions (Yost, 1994, p. 152). Each normalized variable is usually expressed in dB, adding an additional unnecessary layer of confusion to the picture.

## 1. Weber fraction $J$

The intensity JND is frequently expressed as a relative JND called the Weber fraction defined by

$$J(I) \equiv \Delta I(I)/I. \quad (11)$$

From the signal detection theory premise that  $\Delta I = d' \sigma_I$  (Yost, 1994),  $J$  is just the reciprocal of an effective signal-to-noise ratio defined as

$$\text{SNR}_I(I) \equiv I/\sigma_I(I) \quad (12)$$

since

$$J = d' \sigma_I / I = d' / \text{SNR}_I. \quad (13)$$

One conceptual problem with the Weber fraction  $J$  is that it is an effective noise-to-signal ratio, expressed in the  $\Phi$  (physical) domain, but determined by a  $\Psi$  (psychophysical) domain mechanism (internal noise).

## 2. Loudness JND $\Delta L$

Any superthreshold  $\Psi$ -domain increments may be quantified by corresponding  $\Phi$ -domain increments. The loudness JND  $\Delta L(I)$  is defined as the change in loudness  $L(I)$  corresponding to the intensity JND  $\Delta I(I)$ . While it is not possible to measure  $\Delta L$  directly, we assume that we may expand the loudness function in a Taylor series, giving

$$L(I + \Delta I) = L(I) + \Delta I \left. \frac{dL}{dI} \right|_I + \text{HOT},$$

where HOT represents higher-order terms, which we shall ignore. If we solve for

$$\Delta L \equiv L(I + \Delta I) - L(I) \quad (14)$$

we find

$$\Delta L = \Delta I \left. \frac{dL}{dI} \right|_I. \quad (15)$$

We call this expression the small-JND approximation. The above shows that the loudness JND  $\Delta L(I)$  is related to the intensity JND  $\Delta I(I)$  by the slope of the loudness function, evaluated at intensity  $I$ . According to the signal detection model, the standard deviation of the single trial loudness is proportional to the loudness JND, namely

$$\Delta L = d' \sigma_L. \quad (16)$$

A more explicit way of expressing this assumption is

$$\frac{\Delta L}{\Delta I} = \frac{\sigma_L}{\sigma_I}. \quad (17)$$

## 3. Loudness SNR

In a manner analogous to the  $\Phi$ -domain  $\text{SNR}_I$ , we define the  $\Psi$ -domain loudness SNR as  $\text{SNR}_L(L) \equiv L/\sigma_L(L)$ . Given Eq. (16), it follows that

$$\text{SNR}_I = \nu \text{SNR}_L, \quad (18)$$

where  $\nu$  is the slope of the log-loudness function with respect to log-intensity, namely

$$\nu(\beta) \equiv \left. \frac{dL_{\log}}{d\beta} \right|_{\beta}, \quad (19)$$

where  $\beta \equiv 10 \log_{10}(I/I_{\text{ref}})$  is the *intensity level* in dB, and  $L_{\log}(\beta) \equiv 10 \log_{10}(L(10^{\beta/10}))$ .

The derivation of Eq. (18) is as follows: If we express the loudness as a power law

$$L(I) = I^{\nu}$$

and let  $x = \log(I)$  and  $y = \log(L)$ , then  $y = \nu x$ . If the change of  $\nu$  with respect to dB SPL is small, then  $dy/dx \approx \Delta y/\Delta x \approx \nu$ . Since  $d \log(y) = dy/y$  we get

$$\Delta L/L = \nu \Delta I/I. \quad (20)$$

From Eq. (17), Eq. (18) follows.

Equation (18) is important because (a) it tells us how to relate the SNRs between the  $\Phi$  and  $\Psi$  domains, (b) every term is dimensionless, (c) the equation is simple, since  $\nu$  is approximately constant above 40 dB SL (i.e., Stevens' law), and because (d) we are used to seeing and thinking of loudness, intensity, and the SNR, on log scales, and also the slope on log-log scales.

#### 4. Counting JND's

While the concept of counting JNDs has been frequently discussed in the literature, starting with Fechner, unfortunately the actual counting formula (i.e., the equation) is rarely provided. As a result of a literature search, we found the formula in Nutting (1907), Fletcher (1923a), Wegel and Lane (1924), Riesz (1928), Fletcher (1929), and Miller (1947).

To derive the JND counting formula, Eq. (15) is rewritten as

$$\frac{dI}{\Delta I} = \frac{dL}{\Delta L}. \quad (21)$$

Integrating over an interval gives

$$\int_{I_1}^{I_2} \frac{dI}{\Delta I} = \int_{L_1}^{L_2} \frac{dL}{\Delta L}, \quad (22)$$

where  $L_1 = L(I_1)$  and  $L_2 = L(I_2)$ . Each integral counts the total number of JND's between  $I_1$  and  $I_2$  (Riesz, 1928; Fletcher, 1929). For example

$$N_{12} \equiv \int_{I_1}^{I_2} \frac{dI}{\Delta I(I)} \quad (23)$$

defines  $N_{12}$ , the number of intensity JNDs between  $I_1$  and  $I_2$ . Equivalently

$$N_{12} \equiv \int_{L_1}^{L_2} \frac{dL}{\Delta L} \quad (24)$$

defines the number of loudness JNDs between  $L_1$  and  $L_2$ . The number of JNDs must be the same regardless of the domain (i.e., the abscissa variable),  $\Phi$  or  $\Psi$ .

## II. EMPIRICAL MODELS

This section reviews some earlier empirical models of the JND and its relation to loudness relevant to our development.

### A. Weber's law

In 1846 it was suggested by Weber that  $J(I)$  is independent of  $I$ . According to Eq. (7),

$$J(I) = 2\alpha_* + \alpha_*^2.$$

If  $J$  is constant, then  $\alpha_*$  must be constant, which we denote by  $\alpha_*(I)$  (we strike out  $I$  to indicate that  $\alpha_*$  is not a function of intensity). This expectation, which is called Weber's law (Weber, 1988), has been successfully applied to many human perceptions. We refer the reader to the helpful and detailed review of these questions by Viemeister (1988), Johnson *et al.* (1993), and Moore (1982).

Somewhat frustrating is the empirical observation that  $J(I)$  is not constant for the most elementary case of a pure tone (Riesz, 1928; Jesteadt *et al.*, 1977). This observation is referred to as *the near-miss to Weber's law* (McGill and Goldberg, 1968b). It remains unexplained why Weber's law holds as well as it does (Green, 1988, 1970, p. 721), or even why it holds at all. Given the complex and nonlinear nature of the transformation between the  $\Phi$  and  $\Psi$  domains, coupled with the belief that the noise source is in the  $\Psi$  domain, it seems unreasonable that a law as simple as Weber's law, could hold in any general way. A transformation of the JND from the  $\Phi$  domain to the  $\Psi$  domain might clarify the situation.

Weber's law does make one simple prediction that is potentially important. From Eq. (23) along with Weber's law  $J_0 \equiv J(I)$  we see that the formula for the number of JNDs is

$$N_{12} = \int_{I_1}^{I_2} \frac{dI}{J_0 I} \quad (25)$$

$$= \frac{1}{J_0} \ln\left(\frac{I_2}{I_1}\right). \quad (26)$$

### B. Fechner's postulate

In 1860 Fechner postulated that the loudness JND  $\Delta L(I)$  is a constant<sup>7</sup> (Stevens, 1951; Fechner, 1966; Luce, 1993; Plack and Carlyon, 1995). We shall indicate such a constancy with respect to  $I$  as  $\Delta L(I)$  (as before, we strike out the  $I$  to indicate that  $\Delta L$  is *not* a function of intensity). As first reported by Stevens (1961), we shall show that Fechner's postulate is not generally true.

#### 1. The Fechner JND counting formula

From Eq. (24), along with Fechner's postulate  $\Delta L(I)$ , we find

$$N_{12} = \int_{L_1}^{L_2} \frac{dL}{\Delta L(I)} \quad (27)$$

$$= \frac{L_2 - L_1}{\Delta L}. \quad (28)$$

This says that if the loudness JND were constant, one could calculate the number of JNDs by dividing the length of the interval by the step size. We call this relation the *Fechner JND counting formula*.

## 2. The Weber–Fechner law

It is frequently stated (Luce, 1993) that Fechner’s postulate  $[\Delta L(I)]$  and Weber’s law  $[J_0 \equiv J(I)]$  lead to the conclusion that the difference in loudness between any two intensities  $I_1$  and  $I_2$  is proportional to the logarithm of the ratio of the two intensities, namely

$$\frac{L(I_2) - L(I_1)}{\Delta L} = \frac{1}{J_0} \log\left(\frac{I_2}{I_1}\right). \quad (29)$$

This is easily seen by eliminating  $N_{12}$  from Eq. (26) and (28). This result is called *Fechner’s law*, and was called the *Weber–Fechner law* by Fletcher and his colleagues (as it is today by the Vision community) because Eq. (29) results when one assumes that both Fechner’s postulate and Weber’s law are simultaneously true.

Even though Weber’s law is approximately true, because Fechner’s postulate Eq. (28) is not true<sup>8</sup> (Stevens, 1961), Fechner’s law cannot be true. The arguments on both sides of this proposal have been weakened by the unclear relation between loudness and the intensity JND. For example, it has been argued that since the relation between  $L(I)$  and  $\Delta I(I)$  depends on many factors, there can be no simple relation between the two (Zwislocki and Jordan, 1986). It has even been suggested that loudness and the intensity JND may be independent.<sup>9</sup> For a recent discussion of loudness and psychophysical scaling, see Marks (1974), Gescheider (1976), Luce (1993), and Plack and Carlyon (1995).

## C. Poisson noise

Starting in 1923, Fletcher and Steinberg studied loudness coding of pure tones, noise, and speech (Fletcher, 1923a, 1923b; Fletcher and Steinberg, 1924; Steinberg, 1925), and proposed that loudness was related to neural spike count (Fletcher and Munson, 1933), and even provided detailed estimates of the relation between the number of spikes and the loudness in sones (Fletcher, 1953, p. 271). In 1943 De Vries first introduced a photon counting Poisson process model as a theoretical basis for the threshold of vision (De Vries, 1943). Siebert (1965) proposed that Poisson-point-process noise, resulting from the neural rate code, acts as the internal noise that limits the frequency JND (Green, 1970; Jesteadt *et al.*, 1977). A few years later (Siebert, 1968), and independently<sup>10</sup> McGill and Goldberg (1968a) proposed that the Poisson internal noise (PIN) model might account for the intensity JND, but they did not find a reasonable loudness growth function. Hellman and Hellman (1990) further refined the argument that Poisson noise may be used to relate the loudness growth to the intensity JND, and they found good agreement between the JND and realistic loudness functions.

As we shall show, the PIN model requires that  $\Delta L(L) \propto \sqrt{L}$ , which may be written as  $\sigma_L^2 \propto L$ . The proportionality constant depends on the loudness scale.

## D. Hellman and Hellman’s alternative to Fechner

In 1990 Hellman and Hellman proposed an alternative to Fechner’s hypothesis, that  $\Delta L$  is constant, by showing that the PIN model could give reasonable loudness growth functions. Their paper concludes that the relation between the intensity JND and loudness is

$$\sqrt{L(I_2)} - \sqrt{L(I_1)} = \frac{h}{2} \int_{I_1}^{I_2} \frac{dI}{\Delta I(I)}. \quad (30)$$

In the next section we discuss the underlying principles behind Eq. (30), and discuss its generalization to other conditions, such as higher intensities, noise, complex tones, and pulsed signals of various duty cycles.

**The PIN JND counting formula.** Given the definition of the number of JNDs [Eq. (23)] we may rewrite the Hellman and Hellman formula [Eq. (30)] as

$$N_{12} = \frac{2}{h} (\sqrt{L_2} - \sqrt{L_1}). \quad (31)$$

We call this relation the *PIN JND counting formula*. It specifies the number of JNDs between two loudness values, where the factor  $h$  depends on the reference intensity  $I_{\text{ref}}$  for the loudness scale. Equation (31) was first described by Stevens in 1936 (Stevens and Davis, 1983, p. 149) in a slightly modified form as  $L_2 = N_{02}^{2.2}$ , where  $L_0 = 0$  is the loudness for  $I_0 = 0$ , and again by Miller (1947) for white noise as  $L_2 = N_{02}^3$ . Equation (31) (i.e.,  $L_2 \approx N_{02}^2$ ) should be compared and contrasted to Fechner’s JND counting formula Eq. (28). In the next section we show that for long duration tones, below about 20 dB SL, Eq. (31) is essentially correct; however, when the PIN model does not hold [e.g., when  $\Delta L(L) \neq \sqrt{L}$ , such as for continuous tones at high intensities], a different relation must apply.

## III. RESULTS

In the following we directly compare the loudness-growth function of Fletcher and Munson to the number of JNDs  $N_{12}$  from Riesz, as described in Appendix A. The Fletcher and Munson loudness data (Munson, 1932) were determined for long duration tonal stimuli using the loudness balance method (Fletcher and Munson, 1933), the method of *constant stimuli* (Yost, 1994), and the assumption of additivity of partial loudness. Riesz’s data were also determined for long duration stimuli with just-detectable modulation (i.e., they were tonelike sounds). Since the JND depends on the modulation depth, as discussed in the *Definitions* section, Riesz’s JND data seem to be ideal for this comparison since both the loudness data and the JND data have minimal (and similar) modulation parameters (Riesz’s continuous tonal stimuli, which have just-detectable modulations, are more tonelike than gated 2AFC stimuli).

### A. Determination of the JND counting formula

Motivated by Eq. (31), in Fig. 1 we have compared the number of JNDs to the square root of the loudness at all 11 frequencies that Fletcher and Munson used to define the loudness, requiring the reconstruction of the loudness curves from the raw data given in Table I of the 1933 paper. The

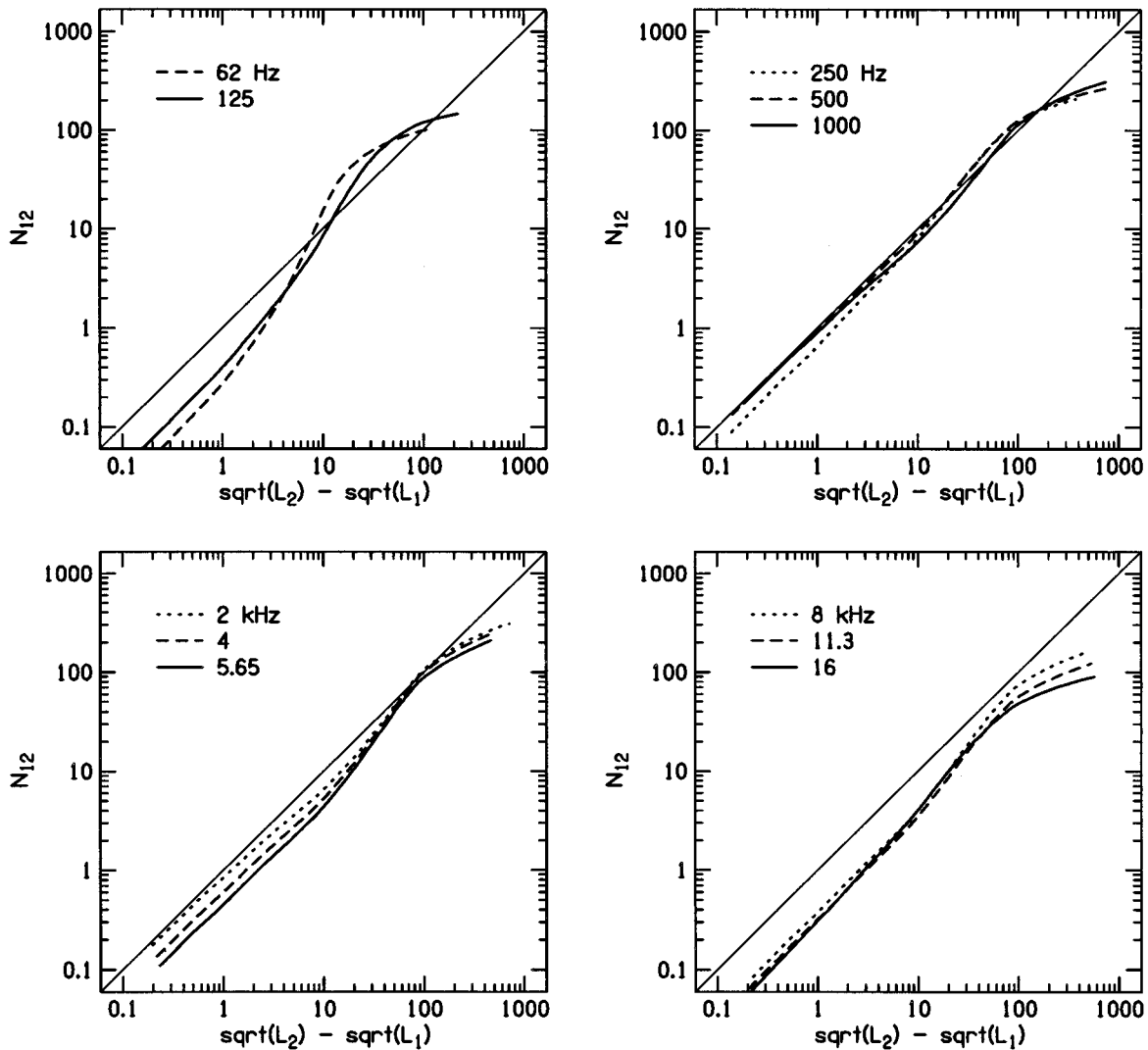


FIG. 1. Observed versus predicted number of JNDs. In this figure  $\sqrt{L_2} - \sqrt{L_1}$  is the abscissa, using the loudness  $L(I)$  from Fletcher and Munson (1933), versus the number of JNDs  $N_{12}$  from Riesz (1928) on the ordinate, for intensities  $I_2$  from 1 dB to 120 dB SL (above the threshold intensity  $I_1$ ). The 11 curves, corresponding to the frequencies 0.062 to 16 kHz, are distributed among the four panels for clarity. Except at low frequencies and high levels, the resulting plots are nearly parallel to the 45° line, in support of the Hellman and Hellman PIN model.

procedure for doing this is described in Appendix B. The figure is divided into four panels to separate the results across frequency. The abscissa gives the difference between the square root of loudness above threshold and the square root of the loudness at threshold  $\sqrt{L_2} - \sqrt{L_1}$ , while the ordinate gives the corresponding number of JNDs above threshold  $N_{12}$ . The results for 62 and 125 Hz clearly depart from straight-line behavior. Also at high levels for all frequencies, for  $L > 10^4$  LU (i.e.,  $> 10$  sones), the results deviate from a straight-line. However, over the rest of the range, Eq. (31) is an excellent summary of the curves of Fig. 1.

Figure 2 shows an alternative way of presenting the data that estimates  $2/h$  and provides a more sensitive indication of the deviations from Eq. (31). In this figure we plot the ratio of  $N_{12}$  divided by  $\sqrt{L_2} - \sqrt{L_1}$ , as a function of the intensity expressed in dB SL. Equation (31) says that this ratio should be independent of intensity. The deviation from a constant value shown in Fig. 2 is greatest at low frequencies, but is small in comparison to the large range of values spanned by both the numerator and denominator of this ratio.

Again we see reasonable agreement between the Hellman and Hellman theory and the tonal data.

## B. An alternative to Fechner's postulate

If one treats Eq. (31) as an exact representation of Fig. 2, thereby ignoring any deviations with intensity and frequency, one may draw several interesting conclusions. First it follows that

$$\Delta L = h\sqrt{L}, \quad (32)$$

where  $h$  is a proportionality constant, as may be seen by direct substitution of Eq. (32) into the JND counting formula Eq. (24):

$$N_{12} = \int_{L_1}^{L_2} \frac{dL}{h\sqrt{L}} \quad (33)$$

$$= \frac{2}{h} (\sqrt{L_2} - \sqrt{L_1}), \quad (34)$$

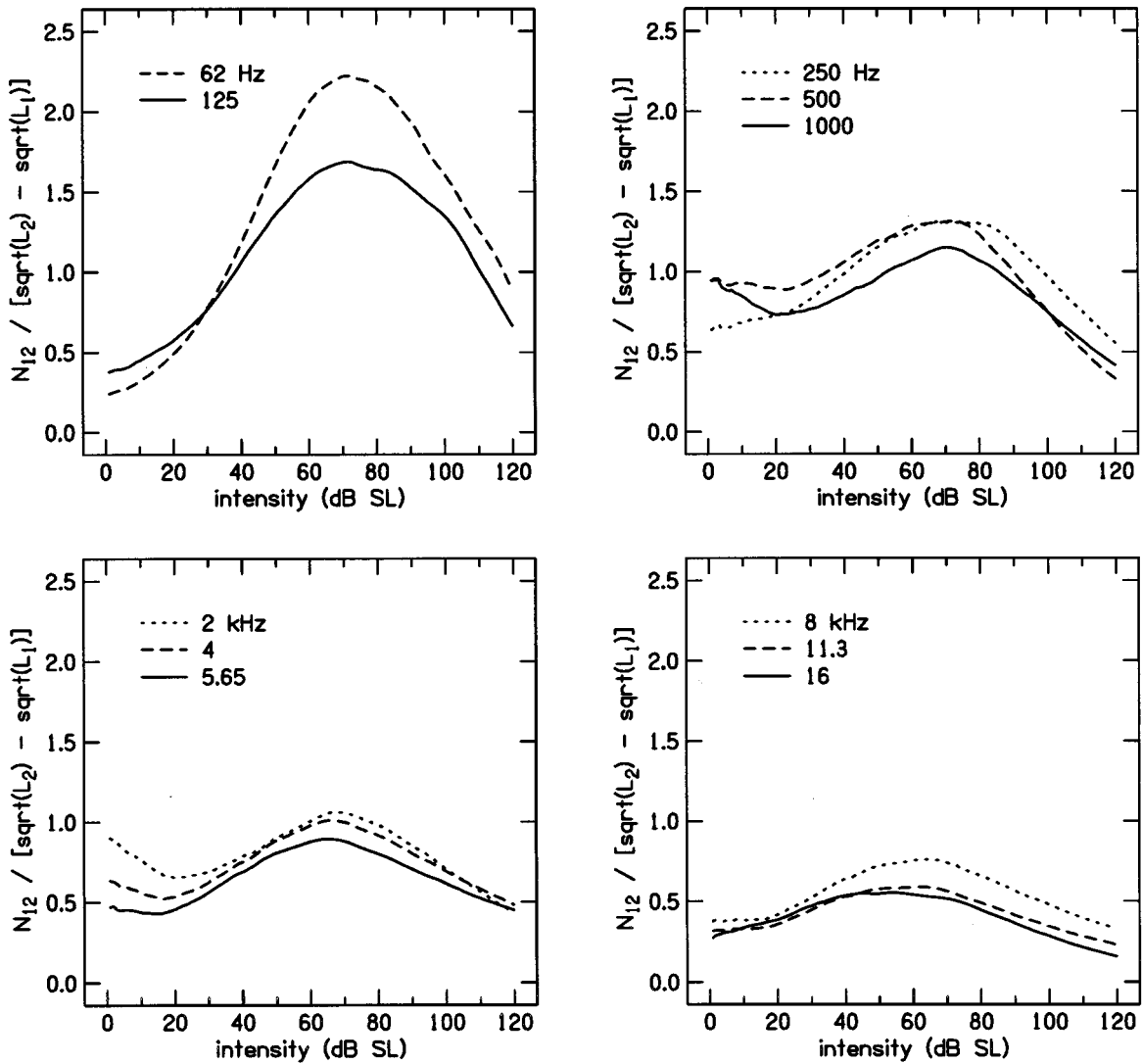


FIG. 2. These data are the same as that of Fig. 1 except the ordinate has been normalized by the abscissa. On the abscissa is the sound intensity, in dB SL, and on the ordinate is  $N_{12}/(\sqrt{L_2}-\sqrt{L_1})$ . This allows the estimation of the parameter  $2/h$ , as described by Eq. (31). The 11 curves represent the same frequencies shown in the previous figure.

which is Eq. (31). In summary, Fechner's postulate cannot be true since  $\Delta L = h\sqrt{L}$ , which is *not* constant.

As discussed in Sec. I, a basic tenant of signal detection theory is that the standard deviation of the decision variable is proportional to the change in the mean, which is Eq. (16) in the present case, since the decision variable is the single-trial loudness.

If we eliminate  $\Delta L$  from Eqs. (32) and (16), we recover the fundamental assumption of the PIN model (Sec. II C),

$$L = \left(\frac{d'}{h}\right)^2 \sigma_L^2, \quad (35)$$

which says that *the mean of the single-trial loudness  $L$  is proportional to  $\sigma_L^2$ , the variance of the single-trial loudness*, where the *single-trial loudness* is the loudness decision variable. By the proper choice of the reference intensity  $I_{\text{ref}}$  corresponding to unity loudness (i.e.,  $L_{\text{ref}}=1$ ), along with knowledge of  $d'$ , which depends on the experimental conditions, the proportionality constant  $(d'/h)$  may be set to 1. In fact, Fletcher's LU loudness scale, which is based on spike

counts, is just such a scale (Fletcher and Munson, 1933) since  $L(I_{\text{ref}})=1$  when  $I_{\text{ref}}$  is the threshold intensity  $I_p^*(0)$ . The one scale is not such a loudness scale since in that case  $I_{\text{ref}}$  corresponds to 40 dB SPL.

Since for the PIN model we know both  $\Delta I(I)$  and  $\Delta L(L)$ , we may evaluate Eq. (22) and obtain a usable alternative to Fechner's ill-founded loudness law Eq. (29). For example based on Eqs. (32) and (A1), Eq. (22) gives  $L(I)$  for tones by equating Eqs. (31) and (A5), leading to

$$L(I) = \left[ \sqrt{L_{\text{ref}}} + \frac{h}{2\kappa J_{\infty}} \ln \left( \frac{(I/I_{\text{ref}})^{\kappa} J_{\infty} + (J_{\text{ref}} - J_{\infty})}{J_{\text{ref}}} \right) \right]^2. \quad (36)$$

The parameters  $\kappa$ ,  $J_{\infty}$ , and  $J_{\text{ref}}$  are described in Appendix A. Equation (36) provides a good description of the tonal loudness functions over the range of intensities where the PIN model is valid. A similar use of Eq. (22) should give a reasonable fit to any loudness growth function once  $\Delta I(I)$  and  $\Delta L(L)$  have been estimated.

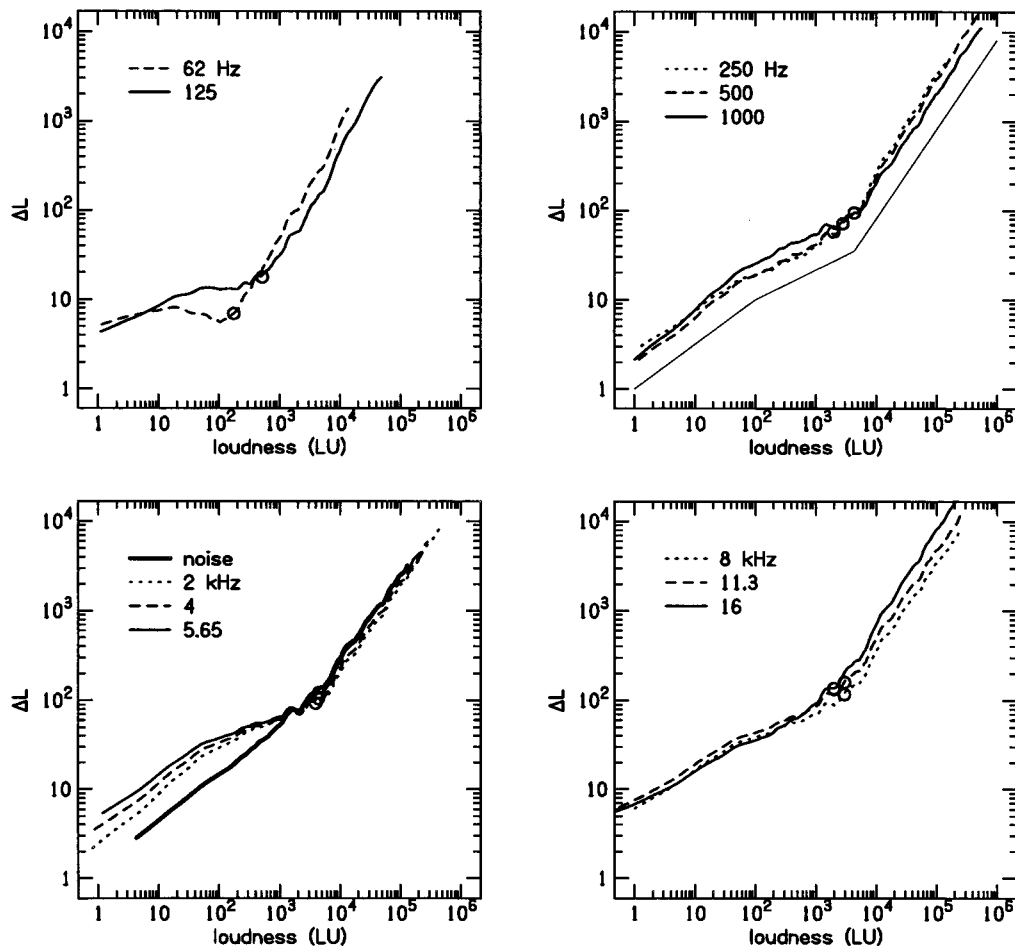


FIG. 3. In this figure we show  $\Delta L(L, f)$  computed directly from Eq. (14) using Riesz's JND data and the Fletcher–Munson loudness-intensity curve, for levels between 0 and 120 dB SL. A  $\odot$  has been placed on the curves at an intensity of 55 dB SL, for 62 and 125 Hz, 60 dB SL for 0.25 to 1 kHz, 55 dB SL for 2–5.65 kHz, and 50 dB SL for 8–16 kHz. In the upper-right panel we have added a straight line for reference, having slopes of 1/2, 1/3, and 1, for levels between 0–20, 20–60, and above 60 dB SL, respectively. From these plots it is clear that  $\Delta L(L)$  is described by a power law in  $L$  having three straight line segments. Between 0 and 20 dB SL, the slope is close to 0.5. Between 20 and 60 dB SL the slope is close to 1/3 ( $\Delta L \propto L^{1/3}$ ) for tones, and 2/3 for noise. Above 60 dB SL, the slope is 1 ( $\Delta L \propto L$ ). Fechner's law [ $\Delta L(I)$ ] appears to hold only for 62 and 125 Hz below 50 dB SL. One extra curve, labeled with a thick solid line, has been added to the lower-left panel, showing  $\Delta L(L)$  for the wideband noise data of Miller (1947). This curve has a slope of approximately 1/2 below 25 dB SL, 2/3 between 25 and 55 dB SL, and then merges with the tone data up to a loudness of  $10^5$  (LU), the upper limit of Miller's data. Note that 1 sone is 975 LU.

### C. The direct estimate of $\Delta L$

The above discussion has (a) drawn out the fundamental nature of the JND, (b) shown the critical nature of the dependence of  $\Delta L(L)$  on  $L$ , and (c) has shown that below 10 sones the PIN model, Eq. (32), approximately holds. Given its importance, it is reasonable to estimate  $\Delta L$  directly from its definition Eq. (14), using Riesz's  $\Delta I(I)$  and Fletcher and Munson's (1933) estimate of  $L(I)$ .

In Fig. 3 we show an estimate of  $\Delta L(L)$  computed using all 11 tonal frequencies that Fletcher and Munson used to define the loudness. Each of the four panels displays a different frequency range. As indicated in the figure caption we have marked the point on the curve where the slope changes. For the 62 Hz data in the upper-left panel we see that  $\Delta L$  is constant for levels below about 50 dB SL. Over most of the frequency range, below 20 dB SL,  $\Delta L \propto \sqrt{L}$ . Between 20 and 60 dB SL,  $\Delta L \propto L^{1/3}$ . Above 60 dB SL,  $\Delta L \propto L$ .

Miller's (1947) famous JND paper also includes wideband noise loudness-level results. We transformed these data

to loudness using Fletcher and Munson's (1933) reference curve (i.e., Fig. 6 upper left). In Fig. 3 (thick line, lower-left panel) we show  $\Delta L(L)$  for Miller's (1947) wideband noise JND<sub>I</sub> data. Between 25 and 55 dB SL, the slope of  $\Delta L(L)$  on a log–log plot is close to 2/3. Above 55 dB SL,  $\Delta L(L)$  is the same as that for tones.

### D. Determination of the loudness SNR

The pure tone and wideband noise JND results may be summarized in terms of the loudness SNR<sub>L</sub>( $I$ ) data shown in Fig. 4 where we show  $L/\Delta L = \text{SNR}_L/d'$  as a function of intensity. As before we separate frequencies into separate panels. The SNR<sub>L</sub> for the wide band noise data of Miller is shown in the lower-left panel.

For noise below 55 dB SL the loudness signal-to-noise ratio  $\text{SNR}_L \equiv L/\sigma_L$  increases as the cube root ( $1 - 2/3 = 1/3$ ) of the loudness; namely the noise increases by a factor of 2 when the loudness increases by a factor of 8. For levels above about 55 dB SL, SNR<sub>L</sub>( $L$ ) remains approxi-



mately constant with a value between 20 and 60 for both tones and noise. For tones, between threshold and 60 dB SL  $\sigma_L \propto L^{1/p}$  with  $2 \leq p \leq 3$ . Above 60 dB SL,  $\sigma_L \propto L$  (i.e.,  $p=1$ ).

To the extent that the curves are all approximately the same across frequency, Fig. 4 provides a stimulus independent description of the relation between the intensity JND and loudness. This invariance in  $\text{SNR}_L$  seems significant. Where the high level segment of  $\text{SNR}_L$  is constant, the intensity resolution of the auditory system has a fixed internal *relative* resolution (Ekman, 1959). The obvious interpretation is that as the intensity is increased from threshold, the neural rate-limited SNR increases until it saturates due to some *other* dynamic range limit, such as that due to some form of central nervous system (CNS) noise.

**Near-miss to Stevens' law.** In Fig. 5 we show a summary of  $L(I)$ ,  $\nu(I)$ ,  $J(I)$ , and  $\Delta L/L = d'/\text{SNR}_L$  for the tone and noise data. For tones the intensity exponent  $\nu(I)$  varies systematically between 0.3 and 0.4 above 50 dB SL, as shown by the solid line in the upper-right panel. We have highlighted this change in the power law with intensity for a 1 kHz tone in the upper-right panel with a light-solid straight line. It is logical to call this effect the *near-miss to Stevens' law*, since it cancels the near-miss to Weber's law, giving a constant relative loudness JND  $\Delta L/L$  for tones.

In the lower-right panel we provide a functional summary of  $\Delta L/L$  for both tones and noise with the light-solid line described by

$$\frac{\Delta L(L)}{L} = h[\min(L, L_0)]^{-1/2}, \quad (37)$$

where  $h = \sqrt{2}$  and  $L_0 = 5000$  LU ( $\approx 5$  sones). We call this relation the Saturated Poisson Internal Noise (SPIN) model. With these parameter values, Eq. (37) appears to be a lower bound on the relative loudness JND<sub>L</sub> for both tones and noise.

### E. Weber-fraction formula

In this section we derive the relation between the Weber fraction  $J(I)$  given the loudness  $L(I)$  starting from the *small-JND approximation*

$$\Delta L = \Delta I L'(I), \quad (38)$$

where  $L'(I) \equiv dL/dI$ . If we solve this equation for  $\Delta I$  and divide by  $I$  we find

$$J(I) \equiv \frac{\Delta I}{I} = \frac{\Delta L}{I L'(I)}. \quad (39)$$

Finally we substitute the SPIN model Eq. (37)

$$J(I) = \frac{hL(I)}{I L'(I)} [\min(L(I), L_0)]^{-1/2}. \quad (40)$$

This formula is the same as that derived by Hellman and Hellman (1990) when  $L \leq L_0$ . In Fig. 6 we plot Eq. (40) in the lower two panels labeled "SPIN model." From the lower-left panel of this figure,  $h=2.4$  and  $L_0=10\,000$  LU. For levels between 0 and 100 dB SL, the SPIN model (solid

curve) fit to Riesz's data and Riesz's formula is excellent. Over this 100 dB range the curve defined by the loudness function fits as well as the curve defined by Riesz's formula given in Appendix A (the dashed curve). The excellent fit gives us further confidence in the basic assumptions of the model.

In the lower-right panel we have superimposed the JND data of Jesteadt *et al.* (1977) with  $h=3$  and  $L_0=10\,000$  LU for comparison to Eq. (40). The Jesteadt *et al.* data were taken with gated stimuli (100% modulation) and 2AFC methods. It is expected that the experimental method would lead to a different value of  $h$  than the valued required for Riesz's data set. The discrepancy between 0 and 20 dB may be due to the 100% modulation for these stimuli. The fit from 20 to 80 dB SL is less than a 5% maximum error, and much less in terms of rms error. Note the similarity in slope between the model and the data.

### F. Riesz's counting ratio

According to Eq. (31), the frequency dependence of the number of intensity JNDs between any two values of loudness must be isolated to the coefficient  $h(f)$ . This was first observed empirically by Riesz in 1933 in a different form when he pointed out that for levels below approximately 70 dB SL the JND counting-ratio

$$N_{1X}/N_{1R} \quad (41)$$

is independent of frequency (Riesz, 1933; Houtsma *et al.*, 1980). In this equation,  $N_{1X}$  and  $N_{1R}$  are given by Eq. (23). The index 1 corresponds to the threshold intensity  $I_1 = I_p^*(0)$ , the  $R$  index indicates some reference intensity  $I_R$  [e.g.,  $L_R(I_R) = 1$  sone at  $I_R = 40$  phons], while  $X$  indicates an arbitrary intensity  $I_X$ . The data of Fig. 2 show a slight frequency dependence of  $h(f)$  on  $f$ . In the ratio given by Eq. (41), this dependence cancels, making the counting ratio independent of frequency.

Riesz's observation about the JND counting ratio is interesting because the isoloudness contours depend significantly on frequency,  $\Delta I(I, f)$  depends significantly on frequency, and yet the ratio Eq. (41), which depends only on  $\Delta I(I, f)$ , shows little variation with frequency.

By assuming that the counting ratio is independent of frequency, Riesz was able to mimic Munson's loudness curves (Munson, 1932) (i.e., the Fletcher–Munson isoloudness curves) below a critical level of approximately 70 dB SL, given two isolevel contours (e.g.,  $L_1$  and  $L_R$ ) and his 1928 measurements of  $\Delta I(I)$  expressed in terms of  $N$  using Eq. (23).

From ratio Eq. (41) and Eq. (31) we obtain

$$\frac{N_{1X}}{N_{1R}} = \frac{\sqrt{L_X} - \sqrt{L_1}}{\sqrt{L_R} - \sqrt{L_1}}. \quad (42)$$

Thus we see that the frequency independence of Eq. (42) [namely Riesz's (1933) observation] follows directly from Eq. (32) and the definition of the number of JNDs Eq. (24).

A more general statement may be made. If  $\Delta L(L, f)$  has no direct dependence on intensity and is either independent of frequency or contains a frequency dependence which is

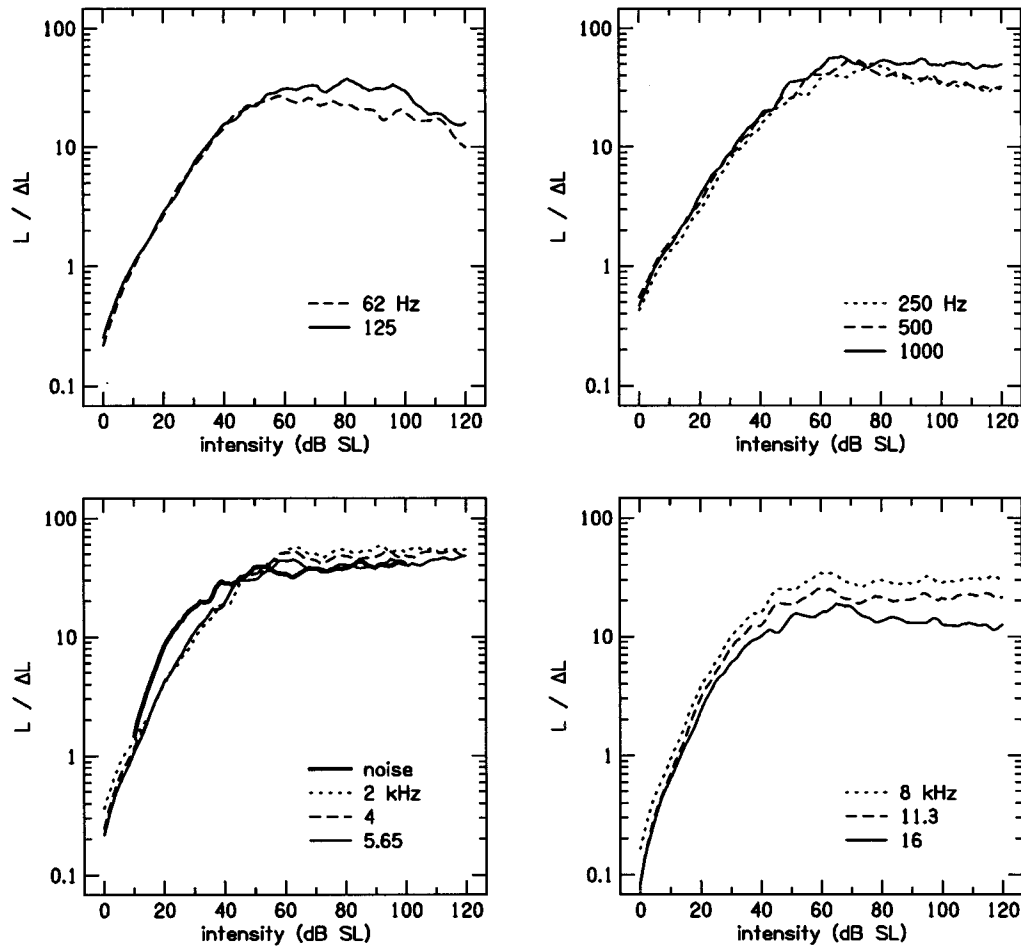


FIG. 4. In this figure we plot  $L(I)/\Delta L = \text{SNR}_L/d'$  for intensities between 0 and 120 dB SL. Below about 55 dB SL the internal signal-to-noise ratio  $\text{SNR}_L(I)$  is increasing and is proportional to  $L^{1-1/p}$ , where  $2 \leq p \leq 3$  for tones and  $p \approx 3/2$  for noise. Above 60 dB SL the  $\text{SNR}_L$  saturates at about 50 linear units. At 62 and 125 Hz the  $\text{SNR}_L$  decreases at high levels.

separable [i.e.,  $\Delta L(L, f) = \varphi_1(L, f)\varphi_2(f, f)$ ], then the frequency independence of Riesz's counting ratio follows from Eq. (24), regardless of the detailed form of the dependence of  $\Delta L$  on  $L$ .

### G. Summary

Riesz's (1933) observation that the counting ratio is independent of frequency for intensities below 70 dB SL tells us that the loudness JND has no direct dependence on intensity [i.e.,  $\Delta L(L, f, f)$ ], and that its dependence on loudness can be separated from any possible dependence on frequency. Turning the argument around, when Riesz's counting ratio is independent of intensity, it follows that  $\Delta L(L, f, f)$  (i.e., that  $\Delta L$  does not depend on  $I$ ). This observation supports Fechner's idea that  $L(I)$  may be found by counting JNDs; he simply had the wrong formulas for  $\Delta I(I)$  and  $\Delta L(L)$ .

## IV. A MODEL OF TONAL LOUDNESS CODING

In this section the SPIN model [Eq. (37)] is merged with Fletcher's loudness theory. Fletcher was the first to describe the neural excitation pattern model of partial loudness and propose that the summation of the total spike activity could account for the loudness. Since the variance of the spike

count is equal to the mean count for a Poisson process (the PIN model), Fletcher's neural rate model of loudness predicts the JND when the neural spike train obeys Poisson statistics. Above 60 dB, where the  $\text{SNR}_L$  is saturated, a different explanation is required (e.g., CNS noise).

### A. Assumptions about loudness for pure tones

To understand all these relations we need a model, and we make the following model assumptions about the single-trial pure-tone loudness:

(1) The *single-trial pure-tone loudness*  $\tilde{L}(I, f)$  is given by the total number of neural spikes that result from the presentation of the tone of duration  $\mathcal{T}$  seconds. Namely

$$\tilde{L}(I, t, f) = \int_0^{x_L} \int_{t-\mathcal{T}}^t \tilde{\mathcal{R}}(I, t, f, x) dt dx,$$

where  $\tilde{\mathcal{R}}(I, t, f, x)$  is a random variable that describes the neural spike rate at time  $t$  associated with place  $x$  on the basilar membrane, given a tone of frequency  $f$  and intensity  $I$ . The length of the basilar membrane is  $x_L$ . The additivity (i.e., the integral over place and time) is based on Fletcher's analysis of 10 years of loudness measurements by Munson

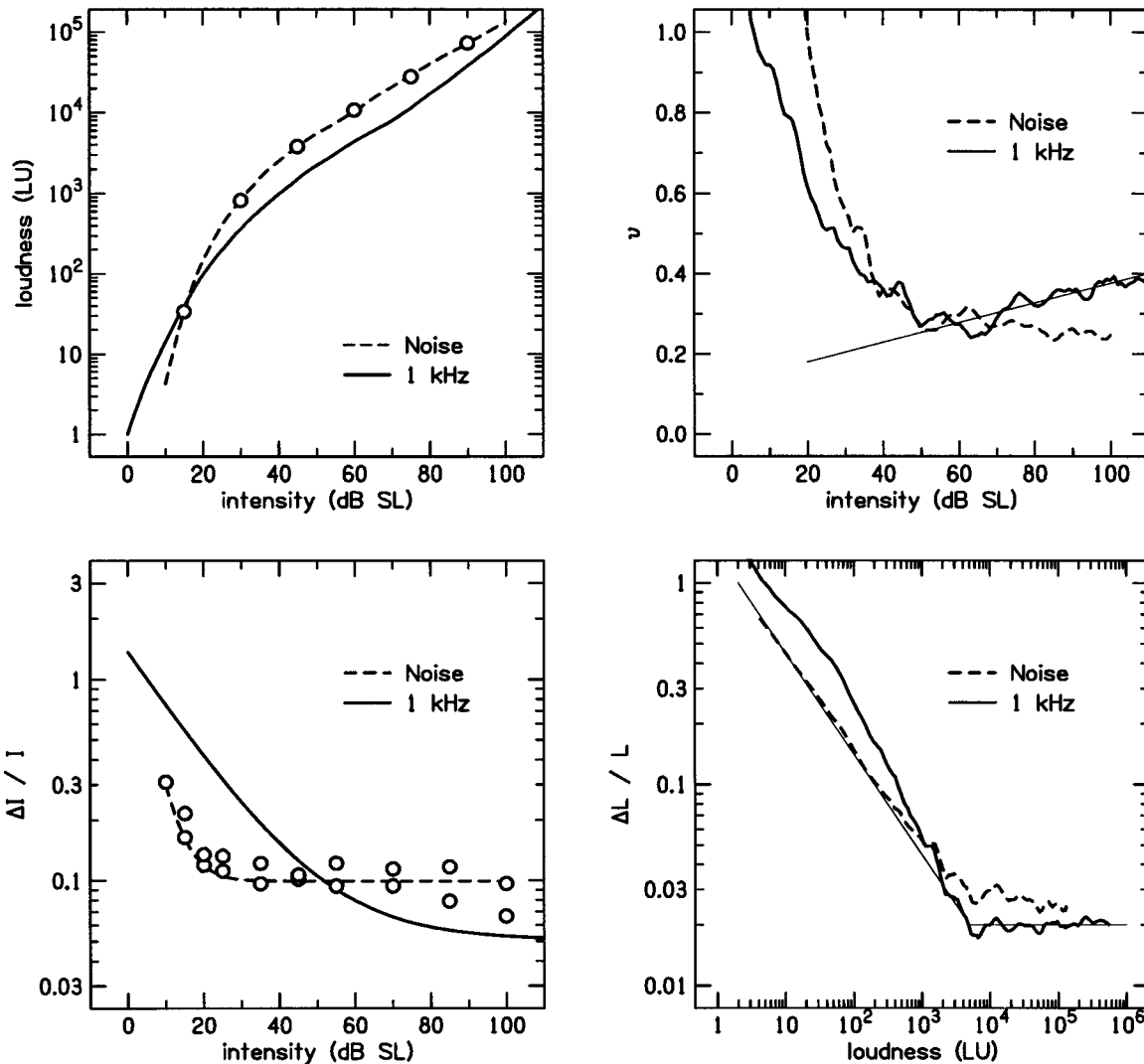


FIG. 5. In 1947 Miller measured the  $JND_I$  and the loudness level for two subjects using wide band noise (0.15–7 kHz) for levels between 3 and 100 dB SL. The intensity of the noise was modulated with a ramped square wave that was high for 1.5 s and low 4.5 s. The loudness, computed from Miller's phon data (dashed curve) using Fletcher and Munson's (1933) 1-kHz tone loudness-growth curve are shown in the upper-left panel, along with the Fletcher Munson tonal loudness-growth function (solid curve). The upper-right panel shows the exponent  $\nu(I) \equiv dL_{\log}/d\beta$  for both Fletcher and Munson's and Miller's (average of two subjects) loudness-growth function. In the lower-left panel we plot  $\Delta I/I$  vs  $I$  for Miller's two subjects, Miller's equation, and Riesz's equation. In the bottom-right panel we show the  $\Delta L/L$  vs  $L$  for the noise and tones cases. From Eq. (20)  $\Delta L/L = \nu(I)J(I)$ . Note how the product of  $\nu(I)$  and  $J(I)$  is close to a constant for tones above 65 dB SL. This invariance justifies calling the variations in the power-law exponent  $\nu(I)$  for tones the "near-miss to Stevens' law." For reference, 1 sone is 975 LU.

(Fletcher and Munson, 1933), as well as more recent observations.

(2) From signal detection theory, the relation between the loudness JND  $\Delta L$  and the standard deviation of the single-trial loudness [Eq. (10)] is  $\Delta L = d' \sigma_L$ .

(3) The single-trial loudness is Poisson below 60 dB SL. A second independent noise source limits the  $L/\Delta L$  ratio to a fixed maximum of about 50 for levels above 60 dB.

(4) The loudness-growth function  $L(I, f)$  has a slope  $dL/dI$  which is a good local approximation to the ratio of the loudness JND to the intensity JND  $\Delta L/\Delta I(I, f)$ .

## B. Model discussion

Fletcher's model (assumption 1) has been heavily and widely criticized (e.g., Licklider, 1959). Clearly, the auditory nerve response is the input to such loudness calculations, but

the auditory nerve response may not be claimed to be loudness *per se*. We have shown in this paper that a point-process representation of loudness appears to be a realistic assumption. It is remarkable, given the primitive state of knowledge in 1923 about auditory neurophysiology, that Fletcher associated neural rate with loudness (Fletcher, 1923a; Fletcher and Steinberg, 1924). Unfortunately this association receives only tenuous acceptance today (Viemeister, 1988; Smith, 1988; Delgutte, 1995; Doucet, 1995). Our assumption of a uniform time weighting having duration  $T$  is not realistic, and a more realistic weighting function needs further study.

Assumption 2 is widely accepted, and works well for the 2AFC JND task, but is not correct for the modulation-detection task such as Riesz's method of beats. When modulation detection is the task,  $\Delta L \approx 0$ . This is best seen from Eq. (8). Since  $\alpha_*$  is small, the mean change in intensity

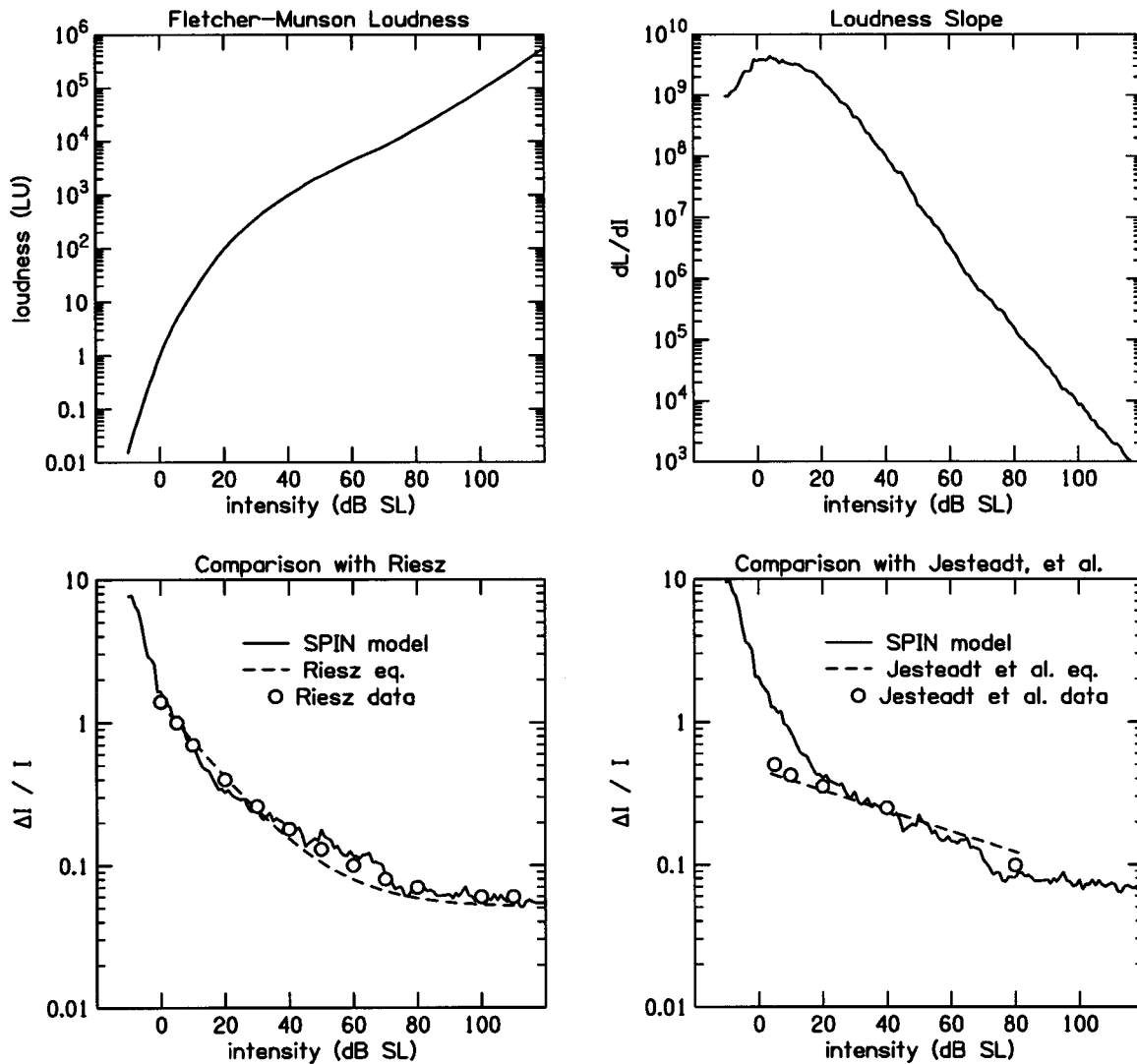


FIG. 6. Comparison between loudness data and intensity JND data at 1 kHz using the SPIN model. The upper-left panel shows the Fletcher–Munson loudness data from their Table III (Fletcher and Munson, 1933). The upper-right panel is a plot of the slope of the loudness with respect to intensity (LU-cm/W). In the lower-left we show the relation between the SPIN-model [Eq. (40) with  $h=2.4$ ] relative JND (solid line), calculated from the Fletcher–Munson loudness data, and the measured relative JND obtained by Riesz (1928) at 1 kHz. We display both Riesz’s formula (dashed line) and Riesz’s raw data (circles), which may be found in Fletcher (1953, 1995). In the lower right we compare the SPIN-model relative JND [Eq. (40), with  $h=3.0$ ], and the relative JND computed from the Jesteadt *et al.* formula (dashed line) and data from their Table B-I (circles). They measured the JND using pulsed tones for levels between 5 and 80 dB. For reference, 1 sone is 975 LU.

defined by the second term  $\alpha_*^2 I$  is not what is detected by the listener. The beating term  $2\alpha_* \sin(2\pi f_b t)$  is responsible for detection. From basic detection theory we know that the width of the distribution is responsible for modulation detection rather than the change in the mean. Riesz avoided this problem with the empirical definition of  $J$  described in Appendix A.

Assumption 4 is easily tested by direct comparison of the two sides of Eq. (15).

## V. DISCUSSION

Inspired by the Poisson internal noise (PIN) based theory of Hellman and Hellman (1990), we have developed a theoretical framework that can be used to explore the relationship between the pure-tone loudness and the intensity JND. The basic idea is to combine Fletcher’s neural excitation response pattern model of loudness with signal detection

theory. We defined a random decision variable called the single-trial loudness. The *mean* of this random variable is the loudness, while its *standard deviation* is proportional to the loudness JND. We define the loudness signal-to-noise ratio  $SNR_L$  as the ratio of loudness (the signal) to standard deviation (a measure of the noise).

### A. Model validation

To evaluate the model we have compared the loudness data of Fletcher and Munson (1933) with the intensity JND data of Riesz (1928) for tones. A similar comparison was made for noise using loudness and intensity JND data from Miller (1947). We were able to unify the tone and noise data by two equivalent methods. First, since the loudness SNR is proportional to the ratio of the loudness to the JND  $L/\Delta L$ , the SNR is also a piecewise power-law function we call the SPIN model. All the data are in excellent agreement with the

SPIN model, providing support for the validity of this theory. Second, we found that the loudness JND  $\Delta L(L)$  is a piecewise power law, namely

$$\Delta L(L) = L^{1/p},$$

where  $p$  is a piecewise intensity-independent constant. Next we discuss the various piecewise regions for long-duration tones.

### 1. Below 20 dB SL

In this intensity range we have found that the pure-tone loudness JND is proportional to the square root of the loudness, that is  $p=2$ . One interpretation of this dependence is that the single-trial loudness obeys Poisson statistics (the PIN model is valid, which says that  $\sigma_L^2=L$ ), and that the tonal loudness is the average count of the total number of spikes.

From the data of Figs. 1 and 2, we conclude that the PIN JND counting formula Eq. (31) is in excellent agreement with Riesz's (1928) JND data and Fletcher and Munson's (1933) loudness data between 250 Hz and 16 kHz. We take these results as a direct demonstration of the validity of the theory presented in Sec. IV, which implies that the theory's underlying assumptions are correct. Most important is assumption 1 which says that the loudness is equal to the total neural spike count. This same assumption inspired Fletcher's model of loudness and led to the *loudness unit* (LU) scale, which predates the sone scale by 10 years. However, other than for setting the reference intensity corresponding to unit loudness, Fletcher did not actually use the neural counting assumption in his derivation. The success of the PIN theory supports the view that it is Poisson noise that limits our ability to discriminate pure tone intensity below 70 dB (10 sones). In other words, the source of uncertainty that gives rise to the intensity JND is due to the granularity of the neural spikes in the counting representation of loudness, as reflected by assumption 3.

### 2. Between 20 and 60 dB SL

In this region, for the tone case,  $p$  increases from 2 to 3. We have no way of judging the statistical significance of this change to evaluate the significance of this change in exponent. Is it a result of a spread of the excitation pattern, primary neural saturation, or a more central effect? Could it be an anomaly of Riesz's formula for  $\Delta I$ , or Fletcher and Munson's 1 kHz loudness-growth curve? The only safe conclusion is that we need more data.

### 3. Above 60 dB SL

Above 60 dB SL the PIN counting formula Eq. (32) begins to fail—above 80 dB it fails dramatically as  $p$  approaches 1. At high rates the variance could depend on “dead-time” effects (Teich and Khanna, 1985; Young and Barta, 1986) which introduce a correlation between spikes. One problem with the dead-time model is that it does not seem consistent with a  $p$  of 1. A more likely possibility is that this high level “CNS noise” is due to the variability in

spike amplitude, assuming that the output cell soma voltage is sensitive to the area under each spike input.

The direct estimate of  $\Delta L(L)$  from Fig. 4 shows that  $\sigma_L(I) \propto L$  (Ekman, 1959), leading to a loudness  $\text{SNR}_L$  of  $\approx 50$ . We may understand better what is happening in this region by looking at the model. If we combine Eqs. (13) and (18), we find

$$J(I) = \frac{d'}{\nu(I) \text{SNR}_L(I)}. \quad (43)$$

From this equation it appears that the near-miss to Weber's law above 60 dB SL results from the variations in  $\nu(I)$  with  $I$ , since  $\text{SNR}_L$  is independent of  $I$  in this region. We call this small variation in  $\nu(I)$  the near-miss to Stevens law.

**An example.** As a sanity check on Eq. (43), we calculate  $\text{SNR}_L$  for Miller's wideband JND data. As shown in Fig. 5 lower- $L$  panel, dashed line, Miller<sup>11</sup> found  $J=0.1$ . From Eq. (13), assuming  $d' \approx 1$ ,  $\text{SNR}_L$  is therefore 10. As shown in Fig. 5, upper right, the power-law exponent is  $\nu \approx 1/4$  at 60 dB SL for noise, which means  $\text{SNR}_L \approx 40$ . This estimate is in reasonable agreement with the measured values of Fig. 4.

## B. The noise model

### 1. The SPIN model

Equation (37) summarizes our results on the relative loudness JND for both tones and noise. Using this formula along with Eq. (18), the JND may be estimated for tones and noise once the loudness has been determined, by measurement, or by model. Fechner's postulate, that the loudness JND is constant, is not supported by our analysis, in agreement with Stevens (1961).

### 2. The PIN model

The success of the PIN model is consistent with the idea that the pure-tone loudness code is based on neural discharge rate. This theory should apply between threshold and moderate intensities (e.g., <60 dB) for “frozen stimuli” where the JND is limited by internal noise.

### 3. CNS noise

Above 60 dB SL we find that the loudness signal-to-noise ratio saturated with a constant loudness SNR between 30 and 50 for both the tone and noise conditions, as summarized by Ekman's law (Ekman 1959). We conclude that the Hellman and Hellman theory must be modified to work at these higher intensities.

### 4. Weber's law

It is significant that while both  $J(I)$  and  $\nu(I)$  vary with intensity, the product is constant above 60 dB SL. Given that  $J = d'/\nu \text{SNR}_L$ , the saturation in  $\text{SNR}_L$  explains Weber's law for wideband signals (since  $\nu$  and  $\text{SNR}_L$  for that case are constant) as well as the near-miss to Weber's law for tones,

where  $\nu$  is not constant (the near-miss to Stevens' law, Fig. 5).

### 5. Generalization to other data

If  $\sigma_L(L, I)$  depends on  $L$ , and is independent of  $I$ , then the  $\text{SNR}_L(L)$  should not depend on the nature of the function  $L(I)$  [i.e., it should be true for any  $L(I)$ ]. This prediction is supported by our analysis summarized by Eq. (37). It will be interesting to see how  $\text{SNR}_L$  depends on  $L$  and  $I$  for subjects having a hearing-loss-induced recruitment, and how well this theory explains other data in the literature, such as loudness and JNDs with masking-induced recruitment (Schlauch *et al.*, 1995).

### 6. Conditions for model validity

To further test the SPIN model, several conditions must be met. First the loudness and the JND must have been measured under the same stimulus conditions. Second, the internal noise must be the dominant factor in determining the JND. This means that the stimuli must be frozen (or have significant duration and bandwidth), and the subjects well trained in the task. As the signal uncertainty begins to dominate the internal noise, as it does in the cases of roving the stimulus, the intensity JND will become independent of the loudness.

As discussed by Stevens and Davis (Stevens and Davis, 1983, pp. 141–143), JND data are quite sensitive to the modulation conditions. The Riesz (1928) and Munson (1932) data make an interesting comparison because they are taken under steady-state conditions and are long duration tonal signals. Both sets of experimental data (i.e., Riesz and Munson) were taken in the same laboratory within a few years of each other.<sup>12</sup> Riesz (1928) states that he used the same methods as Wegel and Lane (1924), and it is likely that Munson (1932) did as well.

Differences in the signal conditions are the most likely explanation for the differences observed in the intensity JND measurements of Riesz and Jesteadt shown in Fig. 6. One difference between the data of Riesz (1928) and Jesteadt *et al.* (1977) is that Riesz varied the amplitude of the tones in a sinusoidal manner with a small (i.e., just detectable) modulation index, while Jesteadt *et al.* alternated between two intervals of different amplitude, requiring that the tones be gated on and off (i.e., a 100% modulation index).

The neural response to transient portions of a stimulus is typically larger than the steady-state response (e.g., neural overshoot) and, therefore, may dominate the perception of stimuli with large abrupt changes in amplitude. The fact that the intensity JND is sensitive to the time interval between two tones of different amplitude (Stevens and Davis, 1983) is another indication that neural overshoot may play a role.

It would be interesting to check the SPIN model on loudness and JND data taken using gated signals, given the observed sensitivity to the modulation. While these JND data are available (Jesteadt *et al.*, 1977), one would need loudness data taken with identical (or at least similar) modulations. We are not aware of such data.

## C. Discussion of the model

### 1. Does Weber's law hold in a single channel?

It has been observed that Weber's law holds for wide-band stimuli (Florentine and Buus, 1981; Viemeister, 1988). This observation has led to the conclusion that Weber's law must hold in a single auditory channel. Because  $\text{SNR}_L$  is approximately the same for both tones and noise, we are led to the conclusion that the source of noise for Miller's JND experiment is the same internal noise as that for tones. Important questions are: If the noise is internal, and both  $\text{SNR}_L(L)$  and  $\nu(L)$  depend on  $L$ , why is  $\nu(L) \text{SNR}_L$  constant when many channels are excited? Does this observation hold true for both frozen as well as random stimuli? What is the physical mechanism that determines the value of  $\nu$  in the normal cochlea?

Miller's data shows that  $J$  is constant from 20 to 80 dB SL. Above 80 the relative JND seems to decrease slightly, and below 20 it dramatically increases. Between 20 and 50 dB SL both  $\nu(I)$  and  $\text{SNR}_L(I)$  change by a factor of 4, but in such a way that their product is constant. While the source of this covariation is presently unknown, it may be related to the compressive role of outer hair cell feedback (Allen, 1996b).

### 2. Near-miss and the spread of excitation

Based on the results presented here it seems that  $\Delta L/L$  is the invariant (Ekman's law) above about 5 sones (5 000 LU) rather than  $\Delta I/I$ . As a result of Eq. (18), when  $\nu(I)$  is constant, Weber's law must hold. In this view, the "near-miss" to Weber 1988's law results from the range of  $\nu(I, x)$  values that contribute to the specific loudness (i.e.,  $\mathcal{N}$ ) for pure tones. If  $\nu$  were independent of intensity [i.e., if Stevens' law strictly held and  $L(I)$  was exactly a power law], the addition of components of differing intensities leads to a power law, that is

$$(I + aI)^\nu = (1 + a)^\nu I^\nu. \quad (44)$$

When  $\nu(I)$  depends on intensity, the sum is no longer strictly a power law (i.e., the near-miss). According to this view, the near-miss results from the large spread of intensities, and therefore of exponents  $\nu(I)$ , in the tonal excitation pattern. This explanation seems different than the 1981 spread of masking explanation of the near-miss offered by Florentine and Buus.

### 3. A correlation with other cochlear measures

It seems to be more than coincidence that 60 dB is where the cochlear microphonic saturates, two-tone suppression neural threshold sets in (Fahey and Allen, 1985), the upward spread of masking becomes important (Wegel and Lane, 1924), and the internal noise of the SPIN model saturates. If the saturation of the  $\text{SNR}_L$  (Ekman's law) seen in Fig. 4 is found for other experimental conditions, then it is an important result that could lead to a great simplification of our understanding of neural coding. It is important to establish the source of the saturation, which might be viewed as some form of CNS noise. This saturated region, which is an example of Ekman's law, supersedes Weber's law. Ekman's

law is similar to Weber's law, but instead of the  $\Phi$  relative JND being constant, it is the  $\Psi$  relative JND that is constant. Schlauch *et al.* (1995) tested Ekman's law and found it did not provide a good fit to their data.

Some measurements of the relative intensity JND<sub>I</sub> have shown a discontinuity around 60 dB SL (Rabinowitz *et al.*, 1976; Greenwood, 1993), which is not apparent in the data of Riesz (1928) and Jesteadt *et al.* (1977). This intensity JND<sub>I</sub> discontinuity may be related to saturation of the loudness JND<sub>L</sub>.

## VI. SUMMARY

A summary list of some of the main conclusions of this paper is:

—Fechner's postulate is not valid, except perhaps below 125 Hz and 50 dB SPL.

—Fechner's idea that the *number* of JNDs may be useful in defining a basic psychophysical scale which quantifies supra-threshold loudness seems correct if modified to allow  $\Delta L$  to depend on  $L$ .

—Once  $\Delta I(I)$  and  $\Delta L(L)$  are known,  $L(I)$  may be determined from Eq. (22).

—The near-miss to Weber's law for tones covaries with the near-miss to Stevens' law, defined as a deviation from a power-law dependence of loudness on intensity for tones.

—Above 125 Hz, a possible replacement for Fechner's law for tones is given by Eq. (36). This formula assumes that  $\Delta L = \sqrt{L}$ , and therefore should be valid for tones between 0 and 60 dB SL.

—The variance of the single-trial loudness is strictly proportional to the mean of the single trial loudness ( $\sigma_L^2 = L$ ) for  $I < 20$  dB for frequencies between 250 Hz and 16 kHz.

—The variance of the single-trial loudness is approximately proportional to the mean of the single-trial loudness ( $\sigma_L^2 \approx L$ ) for  $I < 60$  dB, for frequencies between 250 Hz and 16 kHz.

—The observation that  $\sigma_L^2 \approx L$  for  $I < 60$  dB (Fig. 3) is not inconsistent with the near-miss to Weber's law for tones or Weber's law for wide band stimuli.

—The standard deviation of the single trial loudness is proportional to the mean of the single-trial loudness ( $\sigma_L \propto L$ ) for  $I > 60$  dB SL, for all frequencies.

—The PIN model is easily merged with Fletcher's neural counting model of loudness.

—At 1 kHz the loudness SNR<sub>L</sub> of the auditory system seems to saturate at a value of  $\approx 50$  (linear units) at an intensity of  $\approx 60$  dB SL.

—When  $L(I) \propto I^p$ ,  $\text{SNR}_I = \nu \text{SNR}_L$ .

—When  $L(I) \propto I^p$ , the Weber fraction is  $J = d' / (\nu \text{SNR}_L)$ .

—We interpret the invariance of Riesz's JND counting ratio with frequency in terms of Eq. (22) as showing that the loudness JND for tones is a separable function of loudness and frequency, and is not a function of intensity [i.e.,  $\Delta L(f, L, I) = \phi(f)\psi(L)$ ].

## ACKNOWLEDGMENTS

We would like to thank Don Sinex, Donna Neff, Walt Jesteadt, Stefan Launer, Mohan Sondhi, and Joe Hall for many helpful comments and corrections and for the extensive *Journal of the Acoustical Society of America* reviews by Ken Norwich, Rhona and Bill Hellman, and one anonymous review, and for their excellent suggestions, and for putting up with our endless revisions. We would like to thank those who helped in very specific ways: Mark Sydorenko worked extensively on narrow-band JND and masking experiments, and worked out a signal detection theory model which provided important insights into the JND problem described here. Patricia Jeng led us to the Fletcher data and provided us with the computer program we used to reconstruct the loudness curves. Neal Viemeister helped us to clarify assumptions and understand the meaning of loudness growth. Duncan Luce helped us to understand better the controversy created by Fechner's law, and Jennifer Melcher did some helpful detective work. Finally George Zweig challenged us to solve the problem.

## APPENDIX A: RIESZ'S EXPERIMENT

The Riesz intensity JND data were measured by modulation detection. Two tones, separated by small "beat" frequency difference (e.g., 3 Hz), were presented to the subject, who was asked to vary the level of the lower-level, higher-frequency tone, until the 3-Hz beat was just detectable. The Weber fraction was computed from the relative levels of the tones using the relation

$$J(I) = \frac{(a_1 + a_2)^2 - (a_1 - a_2)^2}{(a_1 - a_2)^2},$$

where  $a_1(f_1)$  and  $a_2(f_2)$  are the *peak* amplitudes of the two tones at  $f_1$  and  $f_2$ , with  $f_2 - f_1 > 0$ .

The first series was taken at 25 and 50 dB SL at  $f_1 = 1$  kHz for eight beat frequencies ranging from 0.2 to 30 Hz. The best-beats detection frequency was found to be 3 Hz. A second series of measurements was made using a beat frequency of 3 Hz, as a function of frequency  $f_1$  between 35 and 10 000 Hz and levels of  $a_1$  between threshold and 110 dB SL (the upper limit depended on frequency). Twelve male subjects were used.

Riesz summarized his data using a formula for  $J(I, f) \equiv \Delta I(I)/I$ , that fit the mean data points. This important formula is repeated here for convenience

$$J(I, f) = J_\infty(f) + (J_0(f) - J_\infty(f))(I_0/I)^{\kappa(f)}. \quad (\text{A1})$$

It has three frequency-dependent parameters

$$J_\infty(f) = 15 \times 10^{-6} f + \frac{126}{(80f^{1/2} + f)}, \quad (\text{A2})$$

$$J_0(f) = 0.3 + 0.3 \times 10^{-3} f + \frac{193}{f^{0.8}}, \quad (\text{A3})$$

$$\kappa(f) = \frac{0.244 \times 10^6}{(0.358 \times 10^6 f^{1/8} + f^2)} + \frac{0.65f}{(3500 + f)}, \quad (\text{A4})$$

where  $J_0(f) = J(I_0, f)$  and  $J_\infty(f) = J(I \rightarrow \infty, f)$ .

Riesz also evaluated the integral for the number of JNDs between  $I_0$  and  $I_1$  Eq. (23),

$$N_{01} = \frac{1}{\kappa(f)J_\infty(f)} \ln \left( \frac{J_\infty(f)(I_1/I_0)^{\kappa(f)} + (J_0(f) - J_\infty(f))}{J_0(f)} \right). \quad (\text{A5})$$

It is interesting to compare Riesz's  $N_{01}$  to Eq. (26). A table of  $\Delta a = a_1 - a_2$  values (i.e., Riesz's raw data) may be found in Fletcher (1953, Table 24, page 146).

## APPENDIX B: RECONSTRUCTION OF THE LOUDNESS CURVES

The isoloudness data were first reported in 1932 by Munson at 11 different frequencies, for 11 subjects, using earphones (Munson, 1932; Fletcher and Munson, 1933). In this Appendix we describe the procedure and the assumptions required to reconstruct the loudness-growth curves  $L(I, f)$  at any frequency  $f$  (Jeng, 1992).

It is helpful to have a notation to describe the isoloudness curves. The pressure of a test tone at test frequency  $f$  is defined as  $P(f)$ . The reference frequency is 1 kHz and the reference tone pressure is  $P_r = P(1000)$ . The average hearing threshold at the reference frequency is defined as  $P_0$ . We use the superscript asterisk on  $P(f)$  to indicate that the test tone pressure corresponds to the isoloudness condition. Thus  $P^*(P_r, f)$  is defined by the condition  $L(P^*, f) = L(P_r, 1000)$ , which says that the loudness of the test tone at frequency  $f$  and pressure  $P^*(P_r, f)$  is equal to the loudness of the reference tone at 1 kHz. Equally loud sounds define the *phon* scale of loudness level. Thus  $P^*(P_r, f)$  is said to be at  $20 \log_{10}(P_r/P_0)$  phons. Loudness level, in phons, is *not* a loudness scale (loudness is measured in *sones*).

The raw data are given in Table I of Fletcher and Munson (1933), which provides rms voltages on the earphone at ten frequencies from 62 Hz to 16 kHz, expressed in dBV. Since the earphone is linear, the voltage across the earphone and the ear canal pressure are related by a scale factor. Thus the values (Fletcher and Munson, 1933, Table I) provide estimates of  $20 \log_{10}(P^*(P_r, f)/P_r)$ , namely the relative intensity of a test tone in dB that is equal in loudness to the reference tone. We have reduced this data to a frequency dependent regression. Thus to find the phon value  $P^*(P_r, f)$  at frequency  $f$ , one may use the regression coefficients of our Table BI, derived in the next section.

Fletcher and Munson's Table III gives the loudness  $G(P_r) \equiv L(1000, P_r)$ , which is plotted in the upper-left panel of our Fig. 6. Today loudness is defined using the sone scale. One sone is the loudness at 40 dB SPL at 1 kHz. In 1933 Fletcher and Munson used the Loudness-Unit (LU) scale. One LU is the loudness at 0 dB SL at 1 kHz. These scales differ in ratio by 975, namely 975 LUs is 1 sone.

To compute  $L(P, f)$  for any  $f$  and  $P(f)$  there are two ways to proceed. The first method is to compute  $G(P_r)$  and  $P^*(P_r, f)$  using the reference pressure  $P_r$  as the independent variable. One can then plot  $G$  vs  $P^*$ . While this method is

TABLE BI. Regression coefficients used to calculate the phon value at the frequency defined by the first column. This regression relates the ear canal sound pressure in dB at 1 kHz to the ear canal sound pressure in dB at the measurement frequency, that is equally loud, as measured by Munson (1932) and Fletcher and Munson (1933).

$f$	$c_3$	$c_2$	$c_1$	$c_0$
0.062	7.46169e-05	-0.00984189	0.74629	0.425879
0.125	5.2594e-05	-0.00654132	0.800557	0.295663
0.25	0	0.00124457	0.720323	0.780066
0.5	0	0.00209933	0.761911	0.467849
1	0	0	1	0
2	0	-0.0011956	1.14141	-0.622967
4	0	-0.00240718	1.2314	-0.393083
5.65	0	-0.00272458	1.24014	0.481007
8	0	-0.00232339	1.20659	0.0426691
11.3	0	-0.002439	1.24474	-1.51871
16	0	-0.000566296	1.03446	-1.82771

simple, it does not directly give the loudness for any value of  $P(f)$ , as  $P_r$  is the independent variable, but can be used to build a "look-up" table. The second method, which is logically more direct, is to define the *inverse* of the phon function  $P^*(P_r, f)$  corresponding to the test pressure  $P(f)$ , which we define as  $P_r^*(P, f)$ . Using this notation,  $G(P, f) = L(P_r^*(P, f))$ . If you think this is confusing, you have a greater than average attention span. We used the first method. Linear interpolation was then used to obtain the loudness for phon values between the tabulated values, which were computed in 1-dB steps from -10 to 129 dB.

### 1. Phon estimation

We used polynomial regression (Jeng, 1992, p. 27) on the raw data (Fletcher and Munson, 1933, Table I) of isoloudness measurements to define  $P^*(f, P_r)$ . The measurements of the subject's threshold, given in the lower portion of their Table I, were also used in the regression to increase the accuracy of regression estimate at threshold. It was also important to use the 1-kHz reference values as the abscissa, when setting up the regression, since these are unaffected by the subject's loudness estimate variability (Jeng, personal communication).

The resulting regression coefficients, given in Table BI, are defined by the cubic polynomial

$$y = c_3 x^3 + c_2 x^2 + c_1 x^1 + c_0,$$

where the abscissa  $x = 20 \log_{10}(P_r/P_0)$  represents the 1-kHz reference earphone voltage in dB and the ordinate  $y = 20 \log_{10}(P^*/P_0)$  is the earphone voltage at the frequency where the phon value is being specified. For the two lowest frequencies, at 62 and 125 Hz, it was necessary to use third-order polynomials, while second-order regressions were adequate for the remaining frequencies.

<sup>1</sup>It may be helpful to note that  $\Phi$  and  $\Psi$  sound similar to the initial syllable of the words *physical* and *psychological*, respectively (Boring, 1929).

<sup>2</sup>The symbol  $\equiv$  denotes "equivalence." It means that the quantity to the left of the  $\equiv$  is defined by the quantity on the right.

<sup>3</sup>Equivalence of the pressure and intensity references requires that  $\rho c = 40$  cgs Rayls. At standard atmospheric pressure, this is only true when the temperature is about 39 °C.



- <sup>4</sup>Because of small fluctuations in  $I_m$  and  $I_p$  due to the finite integration time  $T$ , this equality cannot be exactly true. We specifically ignore these small rapid fluctuations—when these rapid fluctuations are important, our conclusions and model results must be reevaluated.
- <sup>5</sup>It is traditional to define the intensity JND to be a function of  $I$ , rather than a function of  $\alpha(I)$ , as we have done here. We shall treat both notations as equivalent [i.e.,  $\Delta I(I)$  or  $\Delta I(\alpha(I))$ ].
- <sup>6</sup>As a mnemonic, think of the  $\sim$  as a “wiggle” associated with randomness.
- <sup>7</sup>We are only considering the auditory case of Fechner’s more general theory.
- <sup>8</sup>Except, as we shall show, in the limited region below 125 Hz and 50 dB SL.
- <sup>9</sup>For example, when the signal is roved, the JND will be determined by the magnitude of the rove, and the loudness and the JND must be independent.
- <sup>10</sup>W. Siebert, personal communication.
- <sup>11</sup>Miller used  $10 \log(1+J)$  as the measure of the JND rather than  $J$ .
- <sup>12</sup>In 1928 Wegel, Riesz, and Munson were all members of Fletcher’s department.
- Allen, J. B. (1996a). “Harvey Fletcher’s role in the creation of communication acoustics,” *J. Acoust. Soc. Am.* **99**, 1825–1839.
- Allen, J. B. (1996b). “OHCs shift the excitation pattern via BM tension,” in *Diversity in Auditory Mechanics*, edited by E. Lewis, G. Long, R. Lyon, P. Narins, and C. Steel (World Scientific, Singapore).
- Allen, J. B. (1995). “Harvey Fletcher 1884–1981,” in *The ASA edition of Speech, Hearing in Communication*, edited by J. B. Allen (Acoustical Society of America, Woodbury, New York).
- Boring, E. (1929). *History of Psychophysics* (Appleton–Century, New York).
- De Vries, H. (1943). “The quantum character of light and its bearing upon the threshold of vision, the differential sensitivity and the acuity of the eye,” *Physica* **10**, 553–564.
- Delgutte, B. (1995). “Physiological models for basic auditory percepts,” in *Auditory Computation*, edited by H. Hawkins and T. McMullen (Springer-Verlag, New York).
- Doucet, J. R. (1995). “The perstimulus compound action potential and intensity coding in the chinchilla auditory nerve,” Technical Report No. ISR-S-32, Institute for Sensory Research, Syracuse University, Syracuse, New York.
- Egan, J., and Hake, H. (1950). “On the masking pattern of a simple auditory stimulus,” *J. Acoust. Soc. Am.* **22**, 662–630.
- Ekman, G. (1959). “Weber’s law and related functions,” *Psychology* **47**, 343–352.
- Fahey, P. F., and Allen, J. B. (1985). “Nonlinear phenomena as observed in the ear canal, at the auditory nerve,” *J. Acoust. Soc. Am.* **77**, 599–612.
- Fechner, G. (1966). “Translation of: Elemente der psychophysik,” in *Elements of Psychophysics, Volume I*, edited by H. Adler (Holt, Rinehart, and Winston, New York).
- Fletcher, H. (1923a). “Physical measurements of audition and their bearing on the theory of hearing,” *J. Franklin Inst.* **196**, 289–326.
- Fletcher, H. (1923b). “Physical measurements of audition and their bearing on the theory of hearing,” *Bell Syst. Tech. J.* **ii**, 145–180.
- Fletcher, H. (1929). *Speech and Hearing* (Van Nostrand, New York).
- Fletcher, H. (1953). *Speech and Hearing in Communication* (Krieger, Huntington, NY).
- Fletcher, H. (1995). “Speech and Hearing in Communication,” in *The ASA edition of Speech and Hearing in Communication*, edited by J. B. Allen (Acoustical Society of America, New York).
- Fletcher, H., and Munson, W. (1933). “Loudness, its definition, measurement, and calculation,” *J. Acoust. Soc. Am.* **5**, 82–108.
- Fletcher, H., and Steinberg, J. (1924). “The dependence of the loudness of a complex sound upon the energy in the various frequency regions of the sound,” *Phys. Rev.* **24**, 306–317.
- Florentine, M., and Buus, S. (1981). “An excitation-pattern model for intensity discrimination,” *J. Acoust. Soc. Am.* **70**, 1646–1654.
- Gescheider, G. (1976). *Psychophysics: Method and Theory* (Erlbaum, Hillsdale, NJ).
- Green, D. (1970). “Application of detection theory in psychophysics,” *Proc. IEEE* **58**, 713.
- Green, D. (1988). “Audition: Psychophysics and perception,” in *Stevens’ Handbook of Experimental Psychology*, edited by R. Atkinson, R. Herrnstein, G. Lindzey, and R. Luce (Wiley, New York), Chap. 6, pp. 327–376.
- Green, D., and Swets, J. (1966). *Signal Detection Theory and Psychophysics* (Wiley, New York).
- Greenwood, D. (1993). “The intensive DL of tones: Dependence of signal/masker ratio on tone level and on spectrum of added noise,” *Hearing Res.* **65**, 1–39.
- Hellman, W., and Hellman, R. (1990). “Intensity discrimination as the driving force for loudness. Application to pure tones in quiet,” *J. Acoust. Soc. Am.* **87**, 1255–1271.
- Houtsma, A., Durlach, N., and Braida, L. (1980). “Intensity perception XI. Experimental results on the relation of intensity resolution to loudness matching,” *J. Acoust. Soc. Am.* **68**, 807–813.
- Jeng, P. (1992). “Loudness predictions using a physiologically based auditory model,” Ph.D. thesis, City University of New York, Ann Arbor, MI.
- Jeng, P. (personal communication).
- Jesteadt, W., Wier, C., and Green, D. (1977). “Intensity discrimination as a function of frequency and sensation level,” *J. Acoust. Soc. Am.* **61**, 169–177.
- Johnson, J., Turner, C., Zwislocki, J., and Margolis, R. (1993). “Just noticeable differences for intensity and their relation to loudness,” *J. Acoust. Soc. Am.* **93**, 983–991.
- Licklider, J. (1959). “Three auditory theories,” in *Psychology: A Study of a Science. Study I, Volume I*, edited by S. Koch (McGraw-Hill, New York), pp. 41–144.
- Littler, T. (1965). *The Physics of the Ear* (Pergamon, Oxford, England).
- Luce, R. (1993). *Sound and Hearing* (Earlbaum, Hillsdale, NJ).
- Marks, L. (1974). *Sensory Processes: The New Psychophysics* (Academic, New York).
- McGill, W., and Goldberg, J. (1968a). “Pure-tone intensity discrimination as energy detection,” *J. Acoust. Soc. Am.* **44**, 576–581.
- McGill, W., and Goldberg, J. (1968b). “A study of the near-miss involving Weber’s law and pure tone intensity discrimination,” *Percept. Psychophys.* **4**, 105–109.
- Miller, G. A. (1947). “Sensitivity to changes in the intensity of white noise and its relation to masking and loudness,” *J. Acoust. Soc. Am.* **19**, 609–619.
- Montgomery, H. (1935). “Influence of experimental technique on the measurement of differential intensity sensitivity of the ear,” *J. Acoust. Soc. Am.* **7**, 39–43.
- Moore, B. (1982). *An Introduction to the Psychology of Hearing* (Academic, London), 2nd ed.
- Munson, W. (1932). “An experimental determination of the equivalent loudness of pure tones,” *J. Acoust. Soc. Am.* **4**, 7 (Abstract).
- Munson, W. (1947). “The growth of auditory sensation,” *J. Acoust. Soc. Am.* **19**, 584–591.
- Nutting, P. (1907). “The complete form of Fechner’s law,” *Bull. Bureau Stand.* **3**, 59–64.
- Plack, C., and Carlyon, R. (1995). “Loudness perception and intensity coding,” in *Hearing, Handbook of Perception and Cognition*, edited by B. Moore (Academic, San Diego), Chap. 4, pp. 123–160.
- Raab, D., and Goldberg, I. (1975). “Auditory intensity discrimination with bursts of reproducible noise,” *J. Acoust. Soc. Am.* **57**, 473–447.
- Rabinowitz, W., Lim, J., Braida, L., and Durlach, N. (1976). “Intensity perception: VI. Summary of recent data on deviations from Weber’s law for 1000-Hz tone pulses,” *J. Acoust. Soc. Am.* **59**, 449–450.
- Riesz, R. (1928). “Differential intensity sensitivity of the ear for pure tones,” *Phys. Rev.* **31**, 867–875.
- Riesz, R. (1933). “The relationship between loudness and the minimum perceptible increment of intensity,” *J. Acoust. Soc. Am.* **4**, 211–216.
- Schlauch, R., Harvey, S., and Lanthier, N. (1995). “Intensity resolution and loudness in broadband noise,” *J. Acoust. Soc. Am.* **98**, 1895–1902.
- Siebert, W. (1965). “Some implications of the stochastic behavior of primary auditory neurons,” *Kybernetik* **2**, 205–215.
- Siebert, W. (1968). “Stimulus transformations in the peripheral auditory system,” in *Recognizing patterns*, edited by P. Kolers and M. Eden (MIT, Cambridge, MA), Chap. 4, pp. 104–133.
- Siebert, W. (personal communication).
- Smith, R. L. (1988). “Encoding of sound intensity by auditory neurons,” in *Auditory Function*, edited by G. Edelman, W. Gall, and W. Cowan (Wiley, New York), Chap. 7, pp. 243–274.
- Steinberg, J. (1925). “The loudness of a sound and its physical stimulus,” *Phys. Rev.* **26**, 507.
- Stevens, S. (1951). “Mathematics, measurement, and psychophysics,” in *Handbook of Experimental Psychology*, edited by S. Stevens (Wiley, New York), Chap. 1, pp. 1–49.

- Stevens, S. (1961). "To honor Fechner and repeal his law," *Science* **133**, 80–86.
- Stevens, S., and Davis, H. (1983). *Hearing, Its Psychology and Physiology* (The Acoustical Society of America, Woodbury, New York).
- Sydorenko, M., and Allen, J. B. (1994). "The relationship between the difference limen (DL) in intensity and the masked threshold of sub-critical bandwidth signals," *J. Acoust. Soc. Am.* **95**, 2942.
- Teich, M., and Khanna, S. (1985). "Pulse-number distribution for the neural spike train in the cat's auditory nerve," *J. Acoust. Soc. Am.* **77**, 1110–1128.
- Viemeister, N. F. (1988). "Psychophysical aspects of auditory intensity coding," in *Auditory Function*, edited by G. Edelman, W. Gall, and W. Cowan (Wiley, New York), Chap. 7, pp. 213–241.
- Weber, E. H. (1988). "Der tastsinn und das gemainfüll," in *Handwörterbuch der Physiologie*, edited by R. Wagner (Vieweg, Braunschweig), Vol. 3, Chap. 7, pp. 481–588.
- Wegel, R., and Lane, C. (1924). "The auditory masking of one pure tone by another and its probable relation to the dynamics of the inner ear," *Phys. Rev.* **23**, 266–285.
- Yost, W. (1994). *Fundamentals of Hearing, An Introduction* (Academic, San Diego).
- Young, E. D., and Barta, P. E. (1986). "Rate responses of auditory nerve fibers to tones in noise near masked threshold," *J. Acoust. Soc. Am.* **79**, 426–442.
- Zwislocki, J., and Jordan, H. (1986). "On the relation of intensity JNDs to loudness and neural noise," *J. Acoust. Soc. Am.* **79**, 772–780.

# Auditory discrimination of material changes in a struck-clamped bar

Robert A. Lutfi

*Department of Communicative Disorders and Waisman Center, University of Wisconsin, Madison, Wisconsin 53706*

Eunmi L. Oh

*Department of Psychology, University of Wisconsin, Madison, Wisconsin 53706*

(Received 25 April 1997; revised 21 August 1997; accepted 21 August 1997)

The principles of theoretical acoustics were applied to approximately reconstruct the sound pressure waveform at the ear as would be generated by an idealized struck-clamped bar. The result is an inharmonic sum of damped sinusoids whose individual acoustic parameters (frequency, intensity, and decay modulus) are, for a fixed geometry and fixed driving force, uniquely determined by the material composition of the bar. In the standard 2IFC procedure, listeners were asked to discriminate changes in material composition based on their perception of the acoustic waveform. Listener strategies for discriminating such changes were estimated by perturbing slightly the individual acoustic parameters from trial to trial and computing correlations with the listener's response [cf. R. A. Lutfi and E. Oh, *J. Acoust. Soc. Am.* **95**, 2963(A) (1994)]. In general, the correlations reveal that listeners fail to make optimal use of the information in the acoustic waveform by tending to give undue weight, for a given material change, to changes in component frequency. In some cases, the accompanying reduction in performance efficiency amounted to 80%. © 1997 Acoustical Society of America. [S0001-4966(97)03312-2]

PACS numbers: 43.66.Ba, 43.66.Fe [WJ]

## INTRODUCTION

How is it that we are able to identify physical properties of an object from the sound it produces when it is struck? If the physical properties are known in advance, then theoretically it is possible to determine the sound that would be produced. But, if the physical properties are in question, then recovering these properties from the sound can prove quite difficult. This is referred to as the problem of sound-source determination. It is a problem that the human auditory system must solve everyday often in the face of considerable uncertainty regarding possible sources.

At present, little is known regarding how, in everyday listening, the auditory system solves the problem of sound-source determination, even for the simplest of resonant sources. There is general agreement that the acoustic signal is rich in information regarding basic physical attributes such as size and material, but there are different views regarding what aspect of the acoustic information is used to evaluate these attributes. One reason for the difference among views is the failure to agree exactly on what constitutes a condition of "everyday listening." Consider the simple case of determining the material of a bar from the sound it produces when it is struck. The equations of motion for the bar are well known, and the solution to the problem is well defined given certain constraints. But such constraints are not typical of everyday listening. Real bars come in various shapes and sizes, and they may be struck at different places, with different mallets, and with different force. These factors naturally conspire to make the task of determining material more difficult as they produce changes in the acoustic signal that are confounded with those accompanying changes in material.

Indeed, without any constraints on bar geometry and the manner in which the bar is struck there is no unique solution to the equations for motion—two bars of different material can thus produce perfectly identical sounds. This is why specific assumptions regarding the conditions of listening are so important, and why one may be given to different views regarding how material is determined depending on one's assumptions regarding the conditions of everyday listening.

The present study was intended as a small incursion on this problem. We begin by recognizing that everyday listening includes not one, but many possible conditions of listening, and moreover, that particular individuals may be better or worse at making determinations under different conditions depending on experience and prior knowledge of these conditions. We therefore take as a logical starting point for our study the "best case scenario." We attempt to determine precisely what acoustic information is used to distinguish bars of different material when listeners are highly practiced and when the only difference between the bars is in their material composition. To determine how listeners solve the problem in this case a correlational procedure is used (Lutfi, 1995; Lutfi and Oh, 1995). In the standard two-interval, forced-choice trial the listener must choose from two sounds the one corresponding to the bar made of a prespecified material. The sounds are synthesized according to the principles of theoretical acoustics such that nominal values of frequency, amplitude, and decay uniquely identify each material. In practice, however, these parameters are randomly perturbed such they deviate slightly from their nominal values from one presentation to the next. The manner in which a listener makes use of the acoustic information is then evaluated from correlations between this listener's response

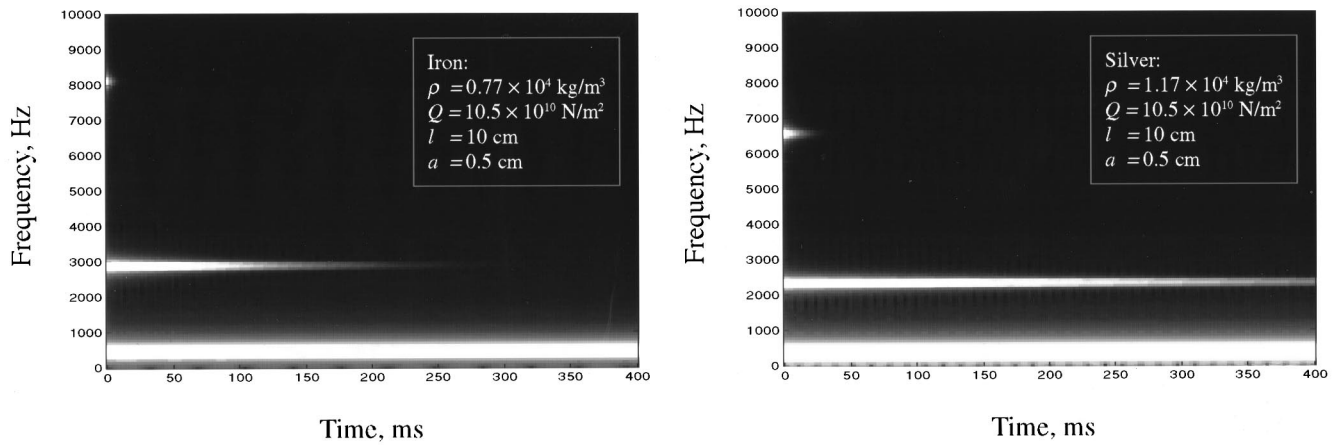


FIG. 1. Example spectrograms of the sounds used in this study corresponding to a struck, clamped bar made of iron and silver. The frequency, amplitude, and decay of individual partials maintain the same orderly relation to one another, as is shown in the figure. Amplitude decreases in proportion to frequency ( $-6$  dB per octave), decay modulus decreases in proportion to frequency cubed, and frequency ratios between partials are constant.

and the value of each acoustic parameter as it varies from trial to trial.

## II. GENERAL METHODS

### A. Stimuli

The principles of theoretical acoustics were applied to synthesize over headphones the airborne sound of a struck bar, rigidly clamped at one end. The solution to the equation for motion for the struck-clamped bar is reviewed in the Appendix, but a more thorough treatment can be found in texts by Morse and Ingard (1968), pp. 175–191 or Kinsler and Frey (1962), pp. 55–78. The solution is a sum of exponentially damped sinusoids whose individual frequencies ( $\nu_n$ ), amplitudes ( $C_n$ ), and decay moduli ( $\tau_n$ ) are joint functions of the elasticity and mass density of the bar, its specific geometry, and the manner in which the bar is struck,

$$y = \sum_n C_n e^{-t/\tau_n} \sin(2\pi\nu_n t). \quad (1)$$

All of these factors were held constant in these experiments except for the elasticity and mass density which are specific to each material. A solid round bar was used either 10 cm in length ( $l$ ) and 0.5 cm in radius ( $a$ ), or 11 cm in length and 0.5 cm in radius. An ideal 50- $\mu$ s impulse of constant force was applied to the free end. Using a fixed geometry and driving force insures that the values of  $\nu_n$ ,  $C_n$ , and  $\tau_n$  are uniquely determined by material. Specific values were chosen to allow sounds from a variety of materials without exceeding the normal range of hearing. Also, as a practical matter it was necessary to truncate signals as the first partial remained audible for several seconds after the bar was struck. Hence, 5-ms, cosine-squared offset ramps were used to truncate signals after 400 ms, allowing in most cases adequate time for the second and third partial to decay to inaudibility. All signals were played over a 16-bit DAC at a 20-kHz sampling rate. The output of the DAC was low-pass filtered at a 10-kHz cutoff (120 dB/octave) and amplified before being delivered to the right ear of listeners over Sennheiser Model 520 II headphones. All signals were pre-

sent to individual listeners seated in a double-walled, IAC sound-attenuation chamber.

Example spectrograms of two of these stimuli, iron and silver, are shown in Fig. 1. Some features common to all of these sounds are evident in this figure. First for all sounds only a few of the partials are audible. In fact, for the conditions of our experiments only the first three partials were typically audible so only the first three were synthesized. Second, the frequency, amplitude, and decay of individual partials maintain the same orderly relation to one another, as is shown in the figure. Amplitude always decreases in proportion to frequency ( $-6$  dB per octave), decay modulus decreases in proportion to frequency cubed, and frequency ratios between partials are constant at values of  $\nu_2/\nu_1=6.26$  and  $\nu_3/\nu_1=17.5$ . These constant relations make the information in the different partials redundant and allow material to be determined from the information in any one partial alone.

Table I gives the nominal values of frequency, amplitude, and decay for the second partial associated with each material used in this study. Iron and glass were identified as targets in these experiments as they tend to occupy opposite corners of the elasticity-density plane (see Kinsler and Frey, p. 502). Immediately below iron and glass are listed the three materials that served as their nominal comparisons in different conditions. Each comparison involves the discrimination of a change in one or both of the physical parameters of mass density and/or elasticity. The values of these parameters were selected to yield discriminable changes in each of the three acoustic parameters, and performance levels typically within the range of 70–85% correct. Note, for frequency the change amounts to many just-noticeable-differences (Wier *et al.*, 1977), whereas for intensity and decay the number of just-noticeable-differences is much smaller (Jesteadt *et al.*, 1977; Van Heuven and Van Den Broecke, 1979).

As an informal check on the stimulus synthesis, we compared spectrograms from a real clamped bar (tuning fork) and the sounds we synthesized on computer. Small differences in the way the tuning fork was struck could produce noticeable differences in excitation of the different

TABLE I. Physical and acoustic parameters associated with material for the struck-clamped bar. Entries for acoustic parameters pertain to the second partial. Targets are indicated by asterisk. Material labels are not to be taken literally, but are included as reference to different conditions. In particular, the values of mass density and elasticity used in these experiments correspond more accurately to alloys of these materials (our copper and silver, for example, could have some gold). More typical values associated with these labels are given in parentheses (Kinsler and Frey, 1962).

Closest common material	Physical parameters			Acoustic parameters		
	Geom, $l \times a$ cm	Density, $\rho$ $\text{k/m}^3$	Elasticity, $Q$ $\text{N/m}^2 \times 10^{11}$	Frequency, $\nu$ Hz	Amp, $ C $ dB SPL	Decay, $\tau$ ms
Iron*	10×0.5	7700 (7700)	1.05 (1.05)	3237	55.0	46
Silver	10×0.5	11700 (10 500)	1.05 (0.78)	2626	53.2	130
Steel	10×0.5	7700 (7700)	1.35 (1.95)	3670	53.9	31
Copper	10×0.5	11 700 (8900)	1.35 (1.22)	2977	52.1	89
Glass*	11×0.5	2300 (2300)	0.62 (0.62)	3761	55.0	9
Crystal	11×0.5	3700 (3100)	0.62 (0.60)	2965	53.0	29
Quartz	11×0.5	2300 (2650)	0.77 (0.79)	4191	54.1	6
Aluminum	11×0.5	3700 (2700)	0.77 (0.71)	3305	52.0	21

modes of vibration, but with some care it was possible to strike the fork in such a way as to produce a nearly identical spectrogram. We also had several colleagues attempt to discriminate blindfold the tuning fork sound from one that we synthesized on computer. Again, because of small variations in the way the tuning fork was struck and its ringing was terminated, a same-different discrimination was often possible. Even so, not all participants correctly identified which of the two sounds corresponded to the real tuning fork. As a final test, we conducted a more rigorous study in which four highly trained listeners were asked to discriminate the synthesized bar sounds from “barlike” sounds for which the lawful relations among acoustic parameters were systematically violated, in particular where the frequency ratio and decay moduli of partials were allowed to deviate substantially from their correct values (see Lutfi and Oh, 1994). Under these conditions, listeners could achieve the discrimination significantly above chance only if the deviation was at least 20–30%. Since our measurements of the spectrograms indicated that we were well within the 20–30% range of error, we felt satisfied that our synthesis was adequate for experiments we wished to undertake.

## B. Procedure

To apply the correlational procedure it is necessary, upon each presentation, to introduce a random perturbation in each of the acoustic parameters. This was achieved in two ways. In the first case, the values of mass density and elasticity were perturbed about their nominal values such that all lawful relations among acoustic parameters were maintained. In the second case, the values of mass density and elasticity were again perturbed about their nominal values, but this time independently for each acoustic parameter.<sup>1</sup> The second

procedure slightly disrupts the lawful relations among acoustic parameters, but it has the advantage of decreasing correlations that might otherwise make the separate influence of these parameters difficult to assess. For each material and procedure a set of 100 waveforms was synthesized where the values of mass density and elasticity for each waveform were selected independently and at random from normal distributions. The means of these distributions are given by the nominal values in Table I. When iron was used as the target, standard deviations were  $2000 \text{ kg/m}^3$  for density and  $0.3 \text{ N/m}^2 \times 10^{11}$  for elasticity. When glass was used as the target, standard deviations were  $700 \text{ kg/m}^3$  for density and  $0.15 \text{ N/m}^2 \times 10^{11}$  for elasticity.

Listeners discriminated between only two materials within any single block of trials. A two-interval, forced-choice procedure was used with sounds separated by 500 ms. The sound corresponding to the target material occurred with equal probability in the second or first interval. The listener’s task was to indicate by button press which interval contained the target (either iron or glass in different trial blocks). Correct feedback was given after each trial. Trials were run in blocks of 50 with short breaks between blocks. A total of 4000 trials was run for each listener for each condition. The first half of all trials was discarded as practice and the remaining half was used for subsequent analysis. Six musically trained volunteers participated as listeners. The listeners were students at the University of Wisconsin–Madison, and were between the ages of 20–24 yrs. All had normal hearing by standard audiometric tests, and all were paid at an hourly rate for their participation. The listeners were instructed that the sounds corresponded to bars made of different material, and that in different conditions their task was to choose the sound corresponding to iron or glass. They were also told

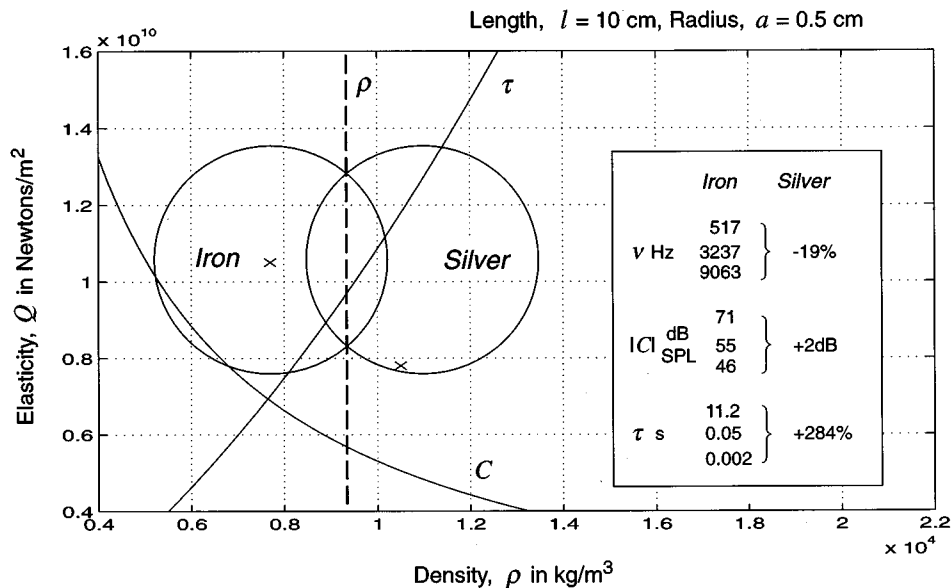


FIG. 2. Representation of material discrimination as a bivariate detection problem. Typically reported values of each material are indicated by the  $\times$ s (see Kinsler and Frey, 1962). The two circles correspond to arbitrary equal probability contours for each material. The distributions differ in mean density alone, hence, the maximum-likelihood decision boundary is a vertical line representing a single value of density  $\rho_c$  (dashed line). The two continuous curves correspond to constant decay,  $\tau$ , and constant amplitude,  $C$ , decision boundaries. These are arbitrarily selected from many such possible boundaries and are only presented by way of example. An observer basing decisions only on decay would discriminate significantly better than chance, but an observer basing decisions on the intersection of decay and amplitude boundaries for each signal on each trial would do as well as the maximum-likelihood detector.

that the sounds would differ in loudness, pitch, and decay, and that their goal was to use any combination of these cues to maximize detection of the target material.

### C. Analysis

Given the constraints on bar geometry and driving force, the task of discriminating material in these experiments reduces to a simple bivariate detection problem, as is shown for the discrimination of iron and silver in Fig. 2. The two circles in this figure correspond, for each material, to equal probability contours of bivariate gaussian distributions in the elasticity-density plane. The distributions differ in mean density alone, hence, the decision boundary corresponding to a likelihood ratio of one is a vertical line on this plane representing a single value of density  $\rho_c$  halfway between the means of the two distributions (dashed line). The ideal decision rule for maximizing the probability of a correct detection is

$$\text{Respond } R=0 \text{ if } \rho > \rho_c \text{ else } R=1. \quad (2)$$

The ideal decision rule is achievable, in theory, because any permissible combination of frequency, amplitude, and decay maps uniquely to one and only one point on the elasticity-density plane (see the Appendix).

Our goal is to determine in what manner, if any, the listener's decision rule deviates from the ideal. Consider, for example, the listener whose decisions are based solely on tone decay. The decision boundary is a contour of constant decay,  $\tau_c$ , an example of which is given by the continuous line in Fig. 2. The listener's decision rule is

$$\text{Respond } R=0 \text{ if } \tau > \tau_c \text{ else } R=1. \quad (3)$$

One might attempt to determine whether this rule is actually used by comparing precisely any deficits in listener performance to that expected based on this rule. This test would not be conclusive, however, inasmuch as very different rules can give rise to similar performance deficits. Our approach is to combine performance measures with estimates of listener weights computed from the trial-by-trial data of the two-interval, forced-choice task. The weights are given as correlations between the listener's trial-by-trial responses  $R$  and the difference between intervals in the values of frequency, amplitude, and decay. In practice, we apply the regression model

$$R = \dot{r}_{R\nu}Z_\nu + \dot{r}_{RC}Z_C + \dot{r}_{R\tau}Z_\tau + \epsilon, \quad (4)$$

where  $Z$  gives the difference in parameter values in standard deviation units, the  $\dot{r}$  are partial correlations representing the weights, and  $\epsilon$  is the regression error (see Lutfi, 1995). The partial correlation, in this case, gives the correlation of  $R$  with a given acoustic parameter after the correlation of this parameter with each of the remaining two parameters has been partialled out. For the decision rule described by Eq. (3) we expect a strong partial correlation with decay ( $\dot{r}_{R\tau}$  significantly greater than 0), and little or no correlation with the other two acoustic parameters,  $\dot{r}_{RC} \approx \dot{r}_{R\nu} \approx 0$ .<sup>2</sup> The degree to which these weights differ from the ideal weights is determined by comparison to the partial correlations resulting from the application of the decision rule described by Eq. (2) to the same trial-by-trial data.

## III. RESULTS

### A. Listener weights

Table II lists the ideal and obtained partial correlations for the discrimination of a change in mass density with law-

TABLE II. Obtained and ideal partial correlations for the discrimination of a change in mass density  $\rho$  (iron versus silver, glass versus crystal), where acoustic parameters covary lawfully. Entries are partial correlations between response  $R$  and acoustic parameters of frequency  $\nu$ , amplitude  $C$ , and decay  $\tau$ . Values between  $\pm 0.06$  are not significantly greater than 0 ( $p < 0.01$ ). Next to the correlations are listed the obtained performance levels in  $d'$  for each condition.

Target: Observer	Iron				Glass			
	$\dot{r}_{R\nu}$	$\dot{r}_{RC}$	$\dot{r}_{R\tau}$	$d'$	$\dot{r}_{R\nu}$	$\dot{r}_{RC}$	$\dot{r}_{R\tau}$	$d'$
CAS	-0.45	0.02	-0.01	0.84	-0.30	-0.15	0.11	1.08
JAL	-0.61	0.02	0.00	1.04	-0.42	-0.04	0.24	1.08
NKY	-0.49	0.01	0.03	0.90	-0.30	-0.03	0.13	0.97
RJU	-0.57	-0.02	0.00	1.03	-0.28	-0.02	-0.05	0.45
JRL	-0.58	-0.07	0.09	1.09	-0.43	-0.05	0.23	1.29
YYL	-0.61	-0.02	0.15	0.90	*	*	*	*
PAW	*	*	*	*	-0.41	-0.04	0.19	1.20
Ideal	-0.23	-0.51	0.26	2.00	-0.10	-0.40	0.30	2.00

ful covariation of acoustic parameters. Nominally, this is the discrimination between iron and silver, or glass and crystal. There is remarkable agreement in the pattern of weights among listeners. For iron as the target all six listeners give greatest weight, by far, to tone frequency. By comparison, the weights given to amplitude and decay are so small that they are rarely significantly greater than 0 ( $p < 0.01$ ). For glass as the target, listeners continue to give greatest weight to tone frequency, although five of the six listeners now also give a significant nonzero weight to tone decay.

The good agreement among listener weights contrasts markedly with the deviation of these weights from the ideal. This can be seen most clearly by comparing the “relative importance” of the weights as in Fig. 3. Here, relative importance is defined as the proportional contribution of each weight in Eq. (4) independent of its sign. It is computed by taking the absolute values of the correlations and then normalizing to sum to one. Each symbol in Fig. 3 designates the

TABLE III. Same as Table II, except partial correlations are for the discrimination of a change in mass density  $\rho$  (iron versus brass, glass versus crystal), where acoustic parameters are jittered independently.

Target: Observer	Iron				Glass			
	$\dot{r}_{R\nu}$	$\dot{r}_{RC}$	$\dot{r}_{R\tau}$	$d'$	$\dot{r}_{R\nu}$	$\dot{r}_{RC}$	$\dot{r}_{R\tau}$	$d'$
CAS	-0.48	-0.02	0.13	0.88	-0.31	-0.03	0.46	0.93
JAL	-0.61	0.02	0.21	1.05	0.55	-0.03	0.27	1.21
NKY	-0.57	0.00	0.14	0.89	-0.47	-0.06	0.16	0.92
RJU	0.63	-0.04	0.15	1.07	-0.47	-0.05	0.13	0.85
JRL	-0.60	0.04	0.25	1.02	-0.58	-0.08	0.17	1.06
YYL	-0.64	-0.07	0.14	1.09	*	*	*	*
PAW	*	*	*	*	-0.52	-0.11	0.07	0.88
Ideal	-0.36	-0.24	0.50	1.73	-0.31	-0.23	0.51	1.73

relative importance of the three acoustic parameters for a single listener, for a single condition. The dashed lines are drawn from each corner of the plot so as to intersect at the point of relative importance for the ideal. Any deviation of the data from the intersection point along one of these lines indicates a disproportionate weighting of one of the three acoustic parameters relative to the ideal. What is clear from this figure is that the ideal decision rule places greatest importance on tone amplitude and least importance on tone frequency—this is exactly the reverse of our listeners. For listeners, the extent of the disproportionate weighting on tone frequency is indicated by the near total convergence of the data in the lower right-hand corner of the plot.

The disproportionate weighting on tone frequency is evident in all remaining conditions of the study. Tables III–VI give the ideal and obtained partial correlations, Figs. 4–7 give the corresponding relative importance of the weights. Performance was near perfect for the case in which density and elasticity were perturbed independently. Hence, this condition was rerun with the differences in mass density and elasticity reduced by one standard deviation (in this case,

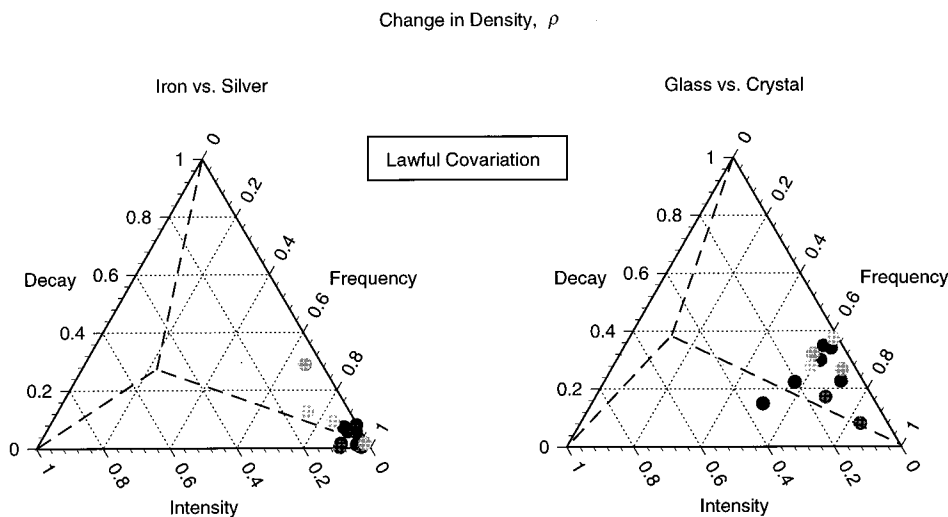


FIG. 3. Proportional contribution of each weight in Eq. (4) independent of its sign. Each symbol designates the relative importance of the three acoustic parameters for a single listener with replication (1000 or more trials/point). A symbol in the bottom-right corner, for example, indicates weight of 1 on frequency and weight of 0 on intensity and decay. The dashed lines are drawn from each corner of the plot so as to intersect at the point of relative importance for the ideal. Any deviation of the data from the intersection point along one of these lines indicates a disproportionate weighting of one of the three acoustic parameters relative to the ideal. Data are for the discrimination of iron vs. silver, and glass vs. crystal, lawful covariation of parameters.

TABLE IV. Same as Table II, except that partial correlations are for the discrimination of a change in elasticity  $Q$  (iron versus steel), where acoustic parameters covary lawfully.

Target Observer	Iron				Glass			
	$\dot{r}_{R\nu}$	$\dot{r}_{RC}$	$\dot{r}_{R\tau}$	$d'$	$\dot{r}_{R\nu}$	$\dot{r}_{RC}$	$\dot{r}_{R\tau}$	$d'$
CAS	0.18	-0.40	-0.02	0.94	0.13	-0.15	-0.14	0.69
NKY	0.31	-0.14	-0.00	0.84	*	*	*	*
RJU	0.51	-0.18	-0.01	0.99	*	*	*	*
JAL	*	*	*	*	0.01	-0.07	-0.09	0.85
HCL	*	*	*	*	0.11	-0.17	-0.20	0.78
Ideal	0.40	-0.57	-0.02	1.00	0.01	-0.04	-0.06	1.00

silver has now become brass). These data are shown in Tables III and V, and in Figs. 4 and 6. Both the pattern and relative importance of the ideal weights varies greatly from one type of discrimination to the next, but in a manner consistent with expectations based on the corresponding changes in acoustic parameters (see the Appendix). Changes in the listener weights follow to some extent the changes in the ideal weights. In each case, however, the tendency to give disproportionate weight to tone frequency is evident as a displacement from the ideal towards the lower right-hand corner of each plot. This is true even when frequency is nearly useless as a cue, as is evident in Fig. 7 where the task is to discriminate iron from copper, and glass from aluminum.

### B. Effect of weights on discrimination performance

To evaluate the effect of listener weights on discrimination performance, weighting efficiencies  $\eta_{\text{wgt}}$  were computed for each listener following the procedure described by Berg (1990). The weighting efficiencies, in this case, indicate the degree to which listener weights on frequency, amplitude, and decay approximate those of the ideal decision rule. The exact expression is  $\eta_{\text{wgt}} = (d'_{\text{wgt}}/d'_{\text{ideal}})^2$ , where  $d'_{\text{wgt}}$  is performance limited only by the particular values of weights obtained from each listener. The comparable measure of overall performance is performance efficiency which expresses overall  $d'$  relative to ideal,  $\eta = (d'/d'_{\text{ideal}})^2$ . The two measures are plotted against one another for all listeners and all conditions in Fig. 8. Note first that there is no indication of a difference in either performance or weighting efficiency be-

TABLE V. Same as Table II, except that partial correlations are for the discrimination of a change in elasticity  $Q$  (iron versus steel, glass versus quartz), where acoustic parameters are jittered independently.

Target: Observer	Iron				Glass			
	$\dot{r}_{R\nu}$	$\dot{r}_{RC}$	$\dot{r}_{R\tau}$	$d'$	$\dot{r}_{R\nu}$	$\dot{r}_{RC}$	$\dot{r}_{R\tau}$	$d'$
CAS	0.35	-0.13	-0.23	0.76	0.20	-0.28	-0.23	0.82
JAL	0.68	-0.01	-0.02	0.90	0.70	-0.01	-0.02	0.95
NKY	0.45	-0.05	-0.03	0.61	0.50	-0.00	-0.01	0.68
RJU	0.57	-0.12	-0.13	0.91	0.66	0.02	-0.03	0.82
JRL	0.68	-0.01	-0.20	1.03	0.68	-0.11	-0.14	1.01
YYL	0.62	-0.09	-0.17	1.01	*	*	*	*
PAW	*	*	*	*	0.62	-0.08	-0.06	0.91
Ideal	0.44	-0.32	-0.26	1.73	0.41	-0.32	-0.33	1.73

TABLE VI. Same as Table II, except that partial correlations are for the discrimination of a combined change in mass density  $\rho$ , and elasticity  $Q$  (iron versus copper, glass versus aluminum), where acoustic parameters covary lawfully.

Target: Observer	Iron				Glass			
	$\dot{r}_{R\nu}$	$\dot{r}_{RC}$	$\dot{r}_{R\tau}$	$d'$	$\dot{r}_{R\nu}$	$\dot{r}_{RC}$	$\dot{r}_{R\tau}$	$d'$
CAS	-0.18	-0.29	-0.06	0.63	0.20	0.04	0.17	0.60
NKY	-0.17	-0.33	-0.00	0.48	0.14	0.08	0.07	0.69
RJU	-0.26	-0.35	-0.17	0.55	*	*	*	*
JRL	*	*	*	*	0.23	0.15	0.22	0.76
PAW	*	*	*	*	0.06	0.19	0.18	0.65
Ideal	0.02	-0.70	0.20	2.24	0.09	0.64	0.20	2.24

tween lawful and independent perturbation conditions. This result is in keeping with our previous experiments showing that rather large deviations from lawful variation are required before listeners can distinguish lawful from unlawful perturbations in these sounds (Lutfi and Oh, 1994). The weighting efficiencies  $\eta_{\text{wgt}}$  vary widely from a minimum value of 0.2 to near the maximum value of 1.0. Over this range there is only a weak relation of  $\eta_{\text{wgt}}$  to  $\eta$ . Indeed, if weighting efficiency were the only factor affecting performance one should expect all data to fall along the veridical. The fact that many of these data fall below the veridical means that other factors, possibly related to limits in sensitivity or various sources of internal noise, also play a role in limiting performance in these conditions. Nonetheless, the effect of weights is highly significant, amounting to nearly an 80% reduction in performance efficiency in some cases.

### IV. DISCUSSION

The basic result of this study is that the ability of listeners to discriminate changes in the material composition of a struck-clamped bar is far less than ideal, and that this is largely because of the listener's tendency to give greater weight than is warranted to changes in signal frequency, regardless of the type of discrimination. This result was obtained for all eight listeners participating in this study—all experienced musicians who received extensive training with feedback in each condition prior to data collection.

Before one can properly interpret this result, it is necessary to consider some possible effects of procedural factors on performance in these conditions. The first is the effect of stimulus uncertainty due to the random perturbation of the acoustic parameters. The detrimental effect of stimulus uncertainty on discrimination performance is well documented (Watson, 1987; Lutfi, 1993) and may have partly affected the results obtained here. It is doubtful, however, that this effect would substantially change the interpretation of the results. First, the effect of stimulus uncertainty is generally found to be quite small when, as in the present study, the uncertainty is associated with the change to be discriminated. Indeed, for single tones, the discrimination of changes in frequency, intensity, and duration has been found to be hardly affected at all by uncertainty due to random trial-by-trial variation in these parameters (Watson, 1987; Lutfi, 1989, 1990). Second, even if a sizable effect were determined in these experi-



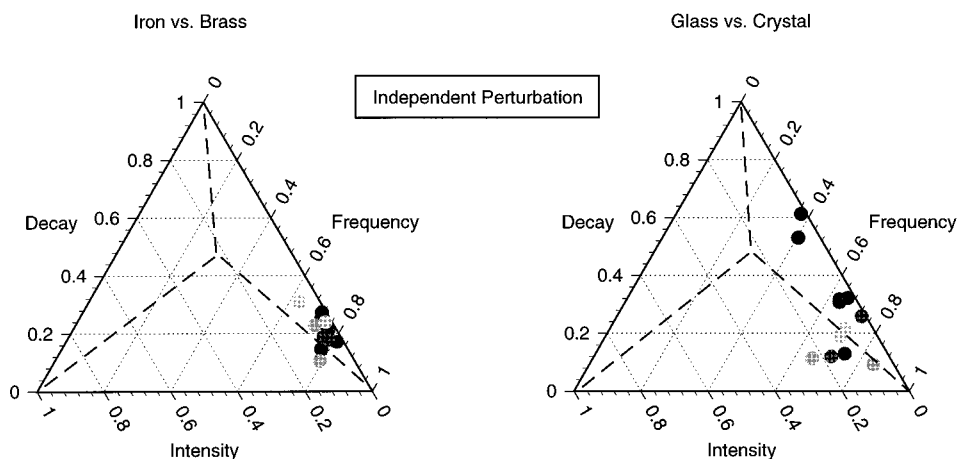


FIG. 4. Same as Fig. 3, except that data are for the condition in which parameters vary independently (Note: to avoid perfect performance in the discrimination between iron and silver it was necessary to reduce the mean difference in density. Hence the comparison is now iron and brass.)

ments, it would still be necessary to explain the main result which is why frequency is given such a disproportionate weighting by listeners.

Another factor, more likely to affect interpretation, is reductions in sensitivity due to the perturbations in parameters. Consider, in particular, tone intensity. The normal intensity difference limen at these moderate sound levels is about 1 dB, while for most conditions in Table II the difference in mean intensity between sounds to be discriminated is only 2 dB. With perturbation the difference in intensity would have been difficult or impossible to discriminate on some proportion of trials. This should force greater weight on tone frequency and tone decay, where the difference in means relative to the difference limen is much larger. Such an effect seems likely, but it cannot entirely explain the disproportionate weighting on tone frequency. A generous approach to estimating this effect is to reduce the weight on tone intensity (and increase the weight on frequency and decay) in proportion to the percentage of trials in which the

intensity difference is less than 1 dB. Consider, for example, the case of discriminating iron from copper (Fig. 7). Here the ideal weights for intensity, frequency, and decay are respectively 0.75, 0.03, and 0.22. From the trial by-trial data, the intensity difference is found to be less than 1 dB in 25% of all trials. Hence, the adjusted ideal weights, when normalized to sum to one, are respectively 0.69, 0.04, and 0.27. The ideal weight on frequency, which is quite small to begin with, increases only slightly to 0.04. By comparison, listener weights on frequency are nearly an order of magnitude larger (approximately 0.36), far in excess of what would be predicted based on reduced sensitivity for intensity.

To further evaluate the effect of differences in sensitivity we reran the discrimination between iron and silver, and glass and crystal as before. This time, however, only one of the three acoustic parameters was allowed to vary within each block of trials, the other two parameters were fixed at the nominal values for iron. In this way, a  $d'$  was obtained separately for each acoustic parameter. These  $d'$  values con-

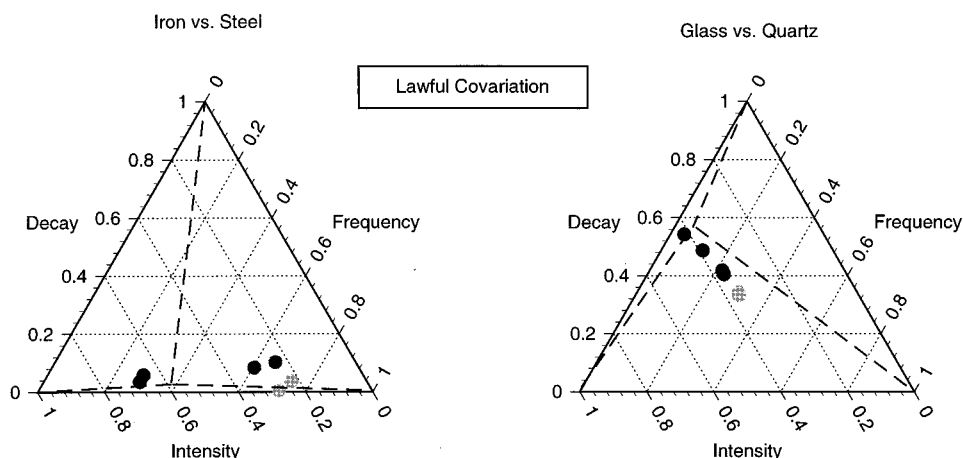


FIG. 5. Same as Fig. 3, except that data are for the discrimination of iron versus steel, and glass versus quartz, lawful covariation of parameters.

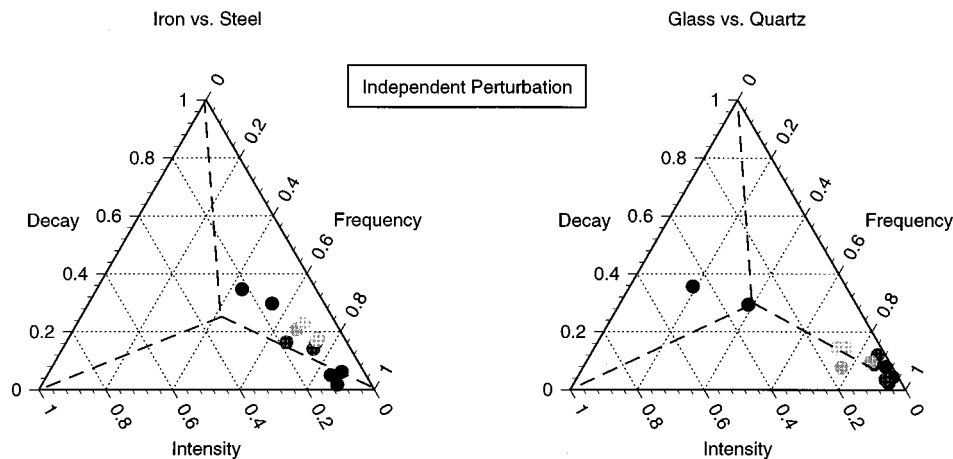


FIG. 6. Same as Fig. 3, except that data are for the discrimination of iron versus steel, and glass versus quartz, independent variation of parameters.

stitute in a maximum-likelihood sense, the optimal weights for each observer, hence, they can be compared directly to those of the ideal decision rule. This comparison is made in Fig. 9. As to be expected, there is a deviation from the ideal toward frequency, and this is largely due to the reduction in sensitivity to intensity. As can be seen from this figure, however, the effect is not nearly as large as required to account for the disproportionate weight on frequency when all acoustic parameters vary simultaneously.

As one last consideration, it must be noted that our method of synthesizing sounds is not exact. Whereas our synthesis required that sounds be truncated after 400 ms, real bars of iron or silver can “ring” for many seconds after this. The 400-ms duration allowed adequate time for the second and third partials to decay in these experiments, but had we selected a much longer duration, listeners might have placed greater weight on decay of the first partial (see the Appendix). This does not diminish the outcome of these experiments, for it still remains to be explained why listeners

would ignore so much information that could have aided discrimination during the first 400 ms of the sound.

### A. Theoretical implications

Notwithstanding the limits of procedure, it is of interest to consider the possible implications of these results for current theories of sound source determination. There are generally two views on this topic. On the one hand, there is the view that the perception of physical attributes is “direct,” or at least that it is closely tied to the physical dynamics of the source (Gibson, 1966; Fowler, 1990). This is a somewhat optimistic view of an observer who recovers near complete information regarding the source. On the other hand, there is the less optimistic view that source attributes are inferred from partial acoustic information, perhaps from as little as one acoustic parameter (Wilde and Richards, 1988). To say that the observer perceives the material of the bar directly implies that the observer’s determinations will be highly correlated with specific values of mass density and elasticity

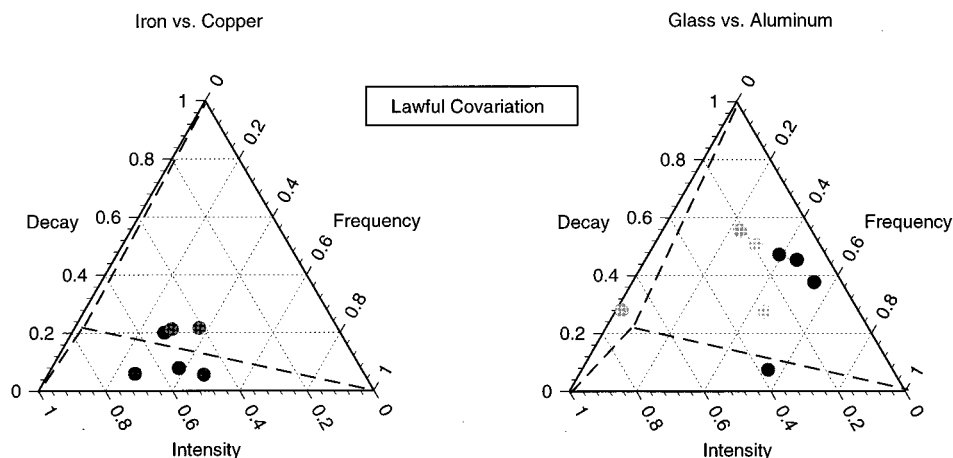


FIG. 7. Same as Fig. 3, except that data are for the discrimination of iron versus copper and glass versus aluminum, lawful covariation of parameters.

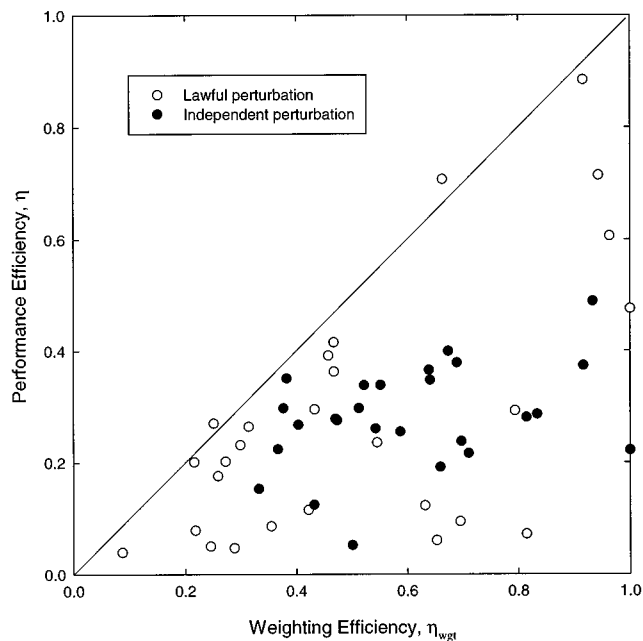


FIG. 8. Overall performance efficiency  $\eta$  is plotted against weighting efficiency  $\eta_{\text{wgt}}$  for all listeners and all conditions. Open symbols designate the condition for which stimulus parameters were perturbed in a lawful manner, filled symbols designated the condition for which parameters were perturbed independently. The veridical corresponds to hypothetical observer whose performance is limited only by weights. (See text for further details.)

unique to each material. Moreover, since these parameters determine all relevant acoustic information for material, this observer would appear as one that optimizes decisions based on appropriate combinations of frequency, amplitude, and decay. In this sense, at least, the present results seem to support the less optimistic view of the listener.

Of course, the present results reflect the outcome of a single and highly constrained listening situation, using highly trained listeners, so their theoretical relevance could be questioned. Even so, a different outcome with inexperi-

enced listeners and sources that vary seems unlikely, since these factors would, if anything, be expected to make the task harder not easier. Indeed, such factors might generally explain the disproportionate weighting on frequency. Frequency after all is a very salient cue, if not always the most informative regarding changes in material. The changes in frequency that accompany changes in material can amount to hundreds of jnds, whereas corresponding changes in intensity and decay may amount to only a few jnds. Salience is likely to be an important factor in everyday listening where there are typically sources of interference that can mask small changes in the signal. It is also likely to be an important factor given the ambiguities that exist when discriminating material of sources of different geometry, or sources whose vibration may be forced. Where two sources of different material and different geometry can produce identical sounds, there may be no distinct advantage to processing anything more than the most salient features of the acoustic signal. Whatever the explanation, the results indicate that the discrimination of material is poor, largely because of the failure to make use of any information except frequency. In this regard, the results are not different from many studies using non-natural sounds that in the past have shown basic limits on a listener's ability to process information in two or more acoustic dimensions simultaneously.

#### ACKNOWLEDGMENTS

The authors wish to thank Mr. Ewan Macpherson, Mr. Wen Wang, and Dr. Amjad Javaid for helpful consultations regarding the physical model underlying signal synthesis. Dr. Adrian Houtsma, Dr. Walt Jesteadt, and an anonymous reviewer also provided helpful comments on an earlier version of this manuscript. This research was supported by a grant from the NIDCD (R01 CD01262-04).

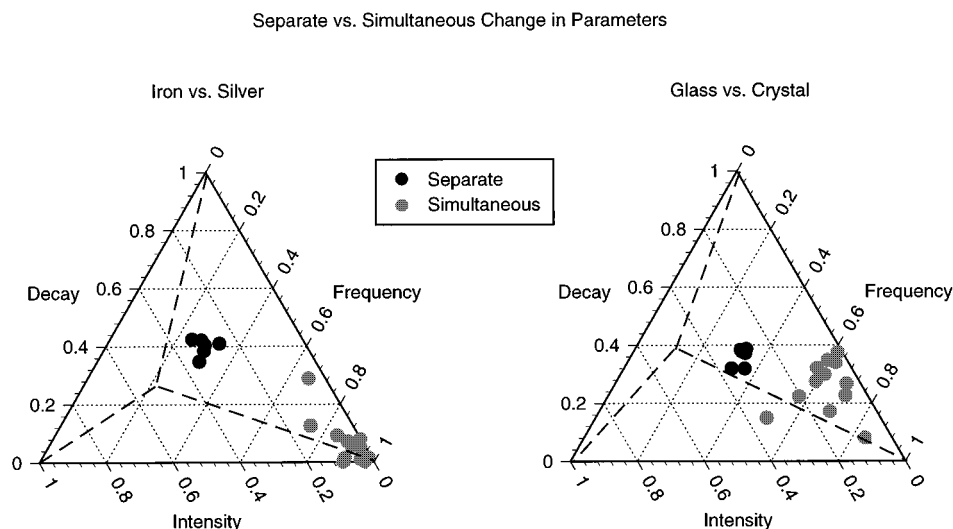


FIG. 9. Dark symbols: Ideal relative importance based on measured sensitivity to each acoustic parameter varied separately (three listeners with replication, 500 trials/point). Light symbols: Obtained relative importance when all acoustic parameters vary simultaneously (replotted from Fig. 3).

## APPENDIX: SOLUTION TO THE EQUATION OF MOTION FOR THE STRUCK-CLAMPED BAR

In this section, we give only the results of the solution to the equation of motion for the struck clamped bar. For a complete development the reader is referred to the chapters by Morse and Ingard (1968), pp. 175–191 and Kinsler and Frey (1962), pp. 55–78. The equation of motion for the homogeneous bar is

$$\frac{\partial^4 y}{\partial x^4} = \frac{\rho}{Q\kappa^2} \frac{\partial^2 y}{\partial t^2}, \quad (\text{A1})$$

where  $x$  is displacement parallel to the length of the bar,  $y$  is displacement perpendicular to length,  $\rho$  is the mass density of the bar,  $Q$  is Young's modulus of elasticity, and  $\kappa$  is the radius of gyration. For the solid round bar  $\kappa$  is just half the radius of the bar.

For the damping of the motion we include only radiation loss due to the loading on the bar of surrounding air molecules (see Morse and Ingard, p. 222). We did not include additional damping by friction of bar molecules rubbing against each other internally. Internal friction, unlike radiation loss, varies nonmonotonically with the frequency of vibration for solids, but, for  $(\nu\tau)^2 \gg 1$  both experiment and theory indicate that the resultant damping is essentially independent of frequency (Zenner, 1965, p. 55). The damping due to radiation loss, by comparison, increases in proportion to frequency cubed and so dominates at higher frequencies. This means that the significance of internal friction would have been greatest for the lowest-frequency partial. However, since the lower-frequency partial was allowed to ring for only 400 ms, the experiments could not have provided a valid test of the effects of internal friction (cf. Wildes and Richards, 1988).

For these conditions the solution to the equation of motion at any point  $x$  is given as a sum of damped sinusoids,

$$y = \sum_n C_n e^{-t/\tau_n} \sin(2\pi\nu_n t), \quad (\text{A2})$$

where  $|C|$  is amplitude,  $\nu$  is frequency, and  $\tau$  is decay modulus. We consider the solid round bar of length  $l$  and radius  $a$ , where the vibration is propagated through air. The bar is rigidly clamped at one end and an ideal impulse is applied to the free end  $x=l$  with force  $P$ . The specific solution for motion at  $x=l$  is then Eq. (A2) where

$$\nu_n = \frac{\pi}{4l^2} \sqrt{\frac{Qa^2}{\rho}} \beta_n^2, \quad (\text{A3})$$

$$C_n = (-1)^{n-1} \frac{lP}{\pi^3 a^3 \beta_n^2} \sqrt{\frac{32}{\rho Q}}, \quad (\text{A4})$$

$$\tau_n = 16 \times 10^8 (\pi\rho/a^2 \nu_n^3), \quad (\text{A5})$$

and  $\beta_1 = 0.597$ ,  $\beta_2 = 1.494$ ,  $\beta_{n>2} = n - \frac{1}{2}$ . Hence, with these

constraints, all acoustic parameters are described by just three equations, (A3)–(A5), in two unknowns,  $\rho$  and  $Q$ . Since  $\rho$  and  $Q$  uniquely determine the material of the bar, and since the acoustic parameters are monotonic with  $\rho$  and  $Q$ , it is, in theory, possible to recover material with certainty from exact knowledge of any two acoustic parameters of a single partial. The problem, in effect, reduces to one of solving two equations in two unknowns.

<sup>1</sup>In this case only the value of the one physical parameter that changed with material was perturbed independently for each acoustic parameter. The other physical parameter was fixed at its nominal value. This was necessary so that a solution to the discrimination problem, as given in the Appendix, would be preserved as one of solving two equations in two unknowns.

<sup>2</sup>Note however that  $r_{Rr}$  is a point-biserial correlation and, depending on the form of the underlying distribution, has a value somewhat less than 1.0 as its maximum (Thorndike, 1978).

- Berg, B. G. (1990). "Observer efficiency and weights in a multiple observation task," *J. Acoust. Soc. Am.* **88**, 149–158.
- Fowler, C. A. (1990). "Sound-producing sources as objects of perception: Rate normalization and nonspeech perception," *J. Acoust. Soc. Am.* **88**, 1236–1249.
- Gibson, J. J. (1966). *The Senses Considered as Perceptual Systems* (Houghton-Mifflin, Boston).
- Jesteadt, W., Wier, C. C., and Green, D. M. (1977). "Intensity discrimination as a function of frequency and sensation level," *J. Acoust. Soc. Am.* **61**, 169–177.
- Kinsler, L. E., and Frey, A. R. (1962). *Fundamentals of Acoustics* (Wiley, New York), pp. 55–78.
- Lutfi, R. A. (1989). "Informational processing of complex sound. I: Intensity discrimination," *J. Acoust. Soc. Am.* **86**, 934–944.
- Lutfi, R. A. (1990). "Informational processing of complex sound. II: Cross-dimensional analysis" *J. Acoust. Soc. Am.* **87**, 2141–2148.
- Lutfi, R. A. (1993). "A model of auditory pattern analysis based on component relative-entropy," *J. Acoust. Soc. Am.* **94**, 748–758.
- Lutfi, R. A. (1995). "Correlation coefficients and correlation ratios as estimates of observer weights in multiple-observation tasks," *J. Acoust. Soc. Am.* **97**, 1333–1334.
- Lutfi, R. A., and Oh, E. (1994). "Auditory discrimination based on the physical dynamics of a tuning fork," *J. Acoust. Soc. Am.* **95**, 2967.
- Lutfi, R. A., and Oh, E. (1995). "Auditory detection of changes in mass density and elasticity of a tuning fork," *J. Acoust. Soc. Am.* **97**, 3330.
- Morse, P. M., and Ingard, K. U. (1968). *Theoretical Acoustics* (Princeton U. P., Princeton, NJ), pp. 175–191.
- Thorndike, R. M. (1978). *Correlational Procedures for Research* (Gardner, New York).
- Van Heuven, V. J., and Van Den Broecke, M. P. R. (1979). "Auditory discrimination of rise and decay times in tone and noise bursts," *J. Acoust. Soc. Am.* **66**, 1308–1315.
- Watson, C. S. (1987). "Uncertainty, informational masking and the capacity of immediate auditory memory," in *Auditory Processing of Complex Sounds*, edited by W. A. Yost and C. S. Watson (Erlbaum, Hillsdale, NJ), pp. 267–277.
- Wier, C. C., Jesteadt, W., and Green, D. M. (1977). "Frequency discrimination as a function of frequency and sensation level," *J. Acoust. Soc. Am.* **61**, 178–184.
- Wildes, R., and Richards, W. (1988). "Recovering material properties from sound," in *Natural Computation*, edited by W. Richards (MIT, Cambridge, MA), pp. 356–363.
- Zenner, C. (1965). *Elasticity and Anelasticity of Metals* (University of Chicago, Chicago).

# Effect of the relative phase of amplitude modulation on the detection of modulation on two carriers

Shigeto Furukawa<sup>a)</sup> and Brian C. J. Moore

*Department of Experimental Psychology, University of Cambridge, Downing Street, Cambridge CB2 3EB, England*

(Received 30 January 1997; revised 8 August 1997; accepted 25 August 1997)

This study examined how effectively information about amplitude modulation (AM) on two carriers is combined, and whether the detection of AM depends on the relative phase of the AM across carriers. Psychometric functions were measured for detecting 5-Hz sinusoidal AM of carriers with frequencies 1100 and 1925 Hz, with a mean level 65 dB SPL for each carrier. The carriers had a duration of 400 ms with 50-ms raised-cosine ramps on either side of this. A single cycle of 5-Hz sinusoidal AM (200 ms in duration) was imposed on the temporal center of the stimulus, with 100-ms steady-state fringes before and after the modulation. The modulators for the two carriers were either in phase or in antiphase. The modulation of each carrier was equally detectable, as determined in a preliminary experiment. A continuous pink noise background was used to mask the outputs of auditory filters tuned between the two carrier frequencies. There was no effect of relative modulator phase. However, performance was consistently better than predicted from the assumption that information about AM from the two carriers is processed independently and combined optimally. The results are discussed in terms of (1) predictions using Dau's "modulation filter bank model" [T. Dau *et al.*, in *Psychoacoustics, Speech and Hearing Aids*, edited by B. Kollmeier (World Scientific, Singapore, 1996), pp. 45–48], and (2) the fact that relative modulator phase does have an effect on the detection of *frequency* modulation on two carriers, as found by Furukawa and Moore [J. Acoust. Soc. Am. **100**, 2299–2311 (1996)]. © 1997 Acoustical Society of America. [S0001-4966(97)04012-5]

PACS numbers: 43.66.Fe, 43.66.Mk, 43.66.Nm [JWH]

## INTRODUCTION

In everyday life we are often exposed simultaneously to sounds from several different sources. The auditory system has the ability to "group" together the different frequency components in the mixture, so as to achieve a percept of separate sound sources. The way in which frequency components change in amplitude has been suggested to be a cue that contributes to this grouping (Bregman *et al.*, 1985). The auditory system may group together frequency components that change in amplitude in a correlated way; this is the Gestalt principle of "common fate." This would imply the existence of mechanism(s) that can compare the pattern of amplitude change at the outputs of auditory filters with different center frequencies, corresponding to different places along the basilar membrane.

Several studies have presented evidence that the auditory system is sensitive to the relative phase of amplitude modulation (AM) on separate carrier frequencies, using a variety of different paradigms (Hall *et al.*, 1984; Bregman *et al.*, 1985; Strickland *et al.*, 1989). For example, Strickland *et al.* (1989) presented listeners with stimuli consisting of two sinusoidal carriers, both of the carriers being amplitude modulated, and measured the listeners' ability to detect a disparity of modulator phase across the carriers. Strickland *et al.* found that listeners can detect such a disparity with

reasonable accuracy. This was true even though the listeners were prevented from using information from single auditory filters tuned between the two carriers. This was achieved by using carrier frequencies more than 2 octaves apart and by adding a band of noise to mask the outputs of auditory filters tuned between the two carriers.

However, some studies using different paradigms, such as modulation detection/discrimination interference (MDI) (Yost and Sheft, 1989; Yost *et al.*, 1989), failed to show sensitivity to the relative phase of AM across carriers. For example, Moore *et al.* (1991) measured thresholds for detecting a change in the modulation depth of AM on a sinusoidal carrier (target), in the presence of two amplitude-modulated sinusoids with different carrier frequencies (interferers). The carrier frequencies were well separated (1000 Hz for the target; 230 and 3300 Hz for the interferers) and the carriers had moderate levels, so there was little or no interaction of the carriers within single auditory filters. Thresholds were generally highest when the modulation rates of the target and the interferers were the same. However, there was no effect of relative modulator phase on detectability. This result suggests that the mechanism(s) involved in detecting changes in AM depth is not sensitive to the relative phase of the AM across carriers.

The present study examines the extent to which listeners can combine information about amplitude modulation (AM) imposed on two widely spaced carrier frequencies. More specifically, it seeks to answer two questions: (1) is the detection of AM on two carriers influenced by the relative

<sup>a)</sup>Present address: Kresge Hearing Research Institute, University of Michigan, 1301 East Ann Street, Ann Arbor, MI 48109-0506.

phase of the modulator across carriers and (2) how does performance compare to what would be expected from signal detection theory on the basis of the optimal combination of independent sources of information? The results were also intended to be useful in evaluating certain aspects of a “modulation filter bank” model proposed by Dau and co-workers (Dau, 1996; Dau *et al.*, 1996a, 1997a, b) and in evaluating a hypothesis proposed by Furukawa and Moore (1996) to explain their finding that the detection of *frequency* modulation (FM) on two carriers depended on the relative phase of the modulation across carriers. The following sections briefly review these earlier studies.

### A. Dau’s model of a “modulation filter bank”

Several physiological studies (Langner and Schreiner, 1988; Palmer, 1995) and psychophysical studies (Martens, 1982; Bacon and Grantham, 1989; Houtgast, 1989; Fassel and Püschel, 1993; Münkner and Püschel, 1993; Dau, 1996; Dau *et al.*, 1996a, 1997a, b) support the hypothesis of a “modulation filter bank.” It is assumed that the (central) auditory system contains an array of neurons each tuned to a different modulation rate. Each neuron can be considered as a filter in the modulation domain. The physiological data have shown that most neurons with tuning in the modulation-frequency domain are also tuned in the carrier-frequency domain.

As a functional realization of a modulation filter bank, Dau (1996) and Dau *et al.* (1996a, 1997a, b) have proposed a model that contains a modulation filter bank for the output of each peripheral filter. The model assumes that (1) an independent internal noise is added to the output of each modulation filter, and listeners base their decision on the combined information across filters; and (2) information about modulator phase for each carrier frequency is lost at the stage where information is combined across modulation filters. The decision process is implemented using an “optimal detector” that is based on a template (Dau *et al.*, 1996b, 1997a). The model can explain the results of experiments on the detectability of AM imposed on carriers of various types, including sinusoids, narrowband noises, and broadband noises.

The experiment in the present study was intended to evaluate one aspect of this model. The model predicts that if the modulation of each carrier is equally detectable (detectability  $d'_{\text{ind}}$ ), then the detectability of the combined modulation should be no greater than  $\sqrt{2}d'_{\text{ind}}$  (from assumption 1). Also, the detectability of modulation on two widely spaced carriers should be independent of the relative modulator phase (from assumption 2).

### B. Detection of FM on two carriers

Furukawa and Moore (1996) investigated the detectability of FM imposed on two inharmonically related carriers. The modulation on each carrier was equally detectable, as determined in preliminary experiments, and a pink noise background was used to mask the outputs of auditory filters tuned between the two carriers. They found that detectability was generally better when the FM was in phase (or “coher-

ent”) across carriers than when the FM was in anti-phase (or “incoherent”); we refer to this as “the effect of FM coherence.”

Furukawa and Moore (1996) discussed some possible mechanisms that might underlie the effect of FM coherence. One is that the auditory system is sensitive to the coherence or relative phase of AM at the outputs of the auditory filters where the changes in excitation level evoked by the FM are greatest. This mechanism is referred to as the “FM-induced-AM mechanism.” It is based on two assumptions: (1) when detecting FM on two carriers, the listener attends to the low-frequency side of the excitation pattern of each carrier, i.e., to auditory filters with center frequencies just below the carrier frequencies, whose outputs give the largest FM-induced *amplitude* fluctuation (Zwicker and Fastl, 1990); and (2) there is a mechanism that is more sensitive to coherent amplitude changes than to incoherent ones, and that mechanism enhances the detection of FM when the outputs of the selected auditory filters are coherent. The amplitude changes at the outputs of the filters that produce the largest amplitude fluctuation (i.e., the filters centered just below the two carrier frequencies) are coherent when the FM is coherent across carriers. For example, when the carrier frequencies both go down, the outputs of the relevant filters go up. Similarly, the amplitude changes at the outputs of the filters that produce the largest amplitude fluctuation are incoherent when the FM is incoherent. Hence, coherent FM is expected to be more detectable than incoherent FM.

Furukawa and Moore (1997) attempted to explore the importance of this mechanism by randomly varying the carrier frequencies for every stimulus presentation, keeping the ratio of the carrier frequencies fixed. This random variation was introduced so as to disrupt the ability of listeners to attend to the auditory filters whose outputs changed the most; the appropriate center frequencies changed randomly from trial to trial. If the FM-induced-AM mechanism plays an important role, then we would expect this random variation of the carrier frequencies to reduce the effect of FM coherence. The effect of FM coherence was slightly greater when the carrier frequencies were fixed throughout a block of trials than when they were roved. This may indicate a sensitivity to the coherence of FM-induced AM. However, an effect of FM coherence still remained even when the carriers were roved. Thus, Furukawa and Moore (1997) were not able to rule out the hypothesis that the FM-induced-AM mechanism contributes to the effect of FM coherence.

The FM-induced-AM hypothesis is only plausible if the auditory system has different sensitivities to coherent (in-phase) and incoherent (antiphase) AM at the outputs of widely separated auditory filters (assumption 2 above). The present experiment provides a direct test of whether this is the case. A failure to find an effect of relative modulator phase across carriers would indicate that the FM-induced-AM mechanism was invalid, and that some other mechanism leads to the dependence of FM detection on relative modulator phase across carriers.

## I. EXPERIMENT: DETECTION OF AM ON TWO CARRIERS

### A. Method

The experiment had two stages: In stage 1, psychometric functions were determined for the detection of AM on only one of the two carrier frequencies, using a two-alternative forced-choice (2AFC) method. In stage 2, psychometric functions were measured for the detection of AM on the two carriers. The modulation depth for each carrier was determined, on the basis of the results of stage 1, so that the AM would be equally detectable when presented on each carrier separately.

#### 1. Stimuli

The carriers had frequencies of 1100 and 1925 Hz, and were presented simultaneously in both stages 1 and 2, and gated synchronously. Each carrier had a mean level of 65 dB SPL. The carriers had a duration of 400 ms with 50-ms raised-cosine ramps on either side of this. A single cycle of 5-Hz sinusoidal AM (200 ms in duration) was imposed on the temporal center of the stimulus, with 100-ms steady-state fringes before and after the modulation. The steady-state fringes were used to prevent any confusion between the amplitude modulation to be detected and the raised-cosine envelope at the onset and offset of the stimuli. The waveform,  $w(t)$ , of the modulated part of a modulated carrier was

$$w(t) = A[1 \pm m \sin(2\pi f_m t)] \sin(2\pi f_c t + \phi), \quad (1)$$

where  $A$  is the mean amplitude,  $m$  is the modulation depth,  $f_m$  is the modulator frequency or modulation rate,  $f_c$  is the carrier frequency, and  $t$  is time relative to the point when the modulation starts. The value of  $\phi$  determined the phase of the carrier, and was fixed at a single, randomly determined, value. The sign determined the starting direction of the modulation. The interstimulus interval in the 2AFC task was 500 ms. In stage 2, both of the carriers were modulated in the signal interval of the 2AFC trial.

The modulation always started with a positive- or negative-going zero-crossing of one cycle of AM, denoted  $\langle + \rangle$  or  $\langle - \rangle$ , respectively, corresponding to the signs in Eq. (1). In stage 2, there were four patterns in the direction of amplitude changes for the two carriers, and they are denoted by combinations of the symbols  $\langle + \rangle$  and  $\langle - \rangle$  (e.g.,  $\langle + - \rangle$ ). The first symbol of a pair indicates the modulation direction for the higher carrier, and the second symbol indicates the modulation direction for the lower carrier. Conditions with the same modulator starting directions ( $\langle ++ \rangle$  or  $\langle -- \rangle$ ) had in-phase AM across frequencies, and conditions with opposite modulator starting directions ( $\langle +- \rangle$  or  $\langle -+ \rangle$ ) had antiphase AM.

The signals were digitally generated at a sampling rate of 10 kHz, using a Masscomp 5400 computer system and a 16-bit digital-to-analog converter (DAC, model DA04H). The output of the DAC was low-pass filtered (Kemo, type VBF 8/03, 48 dB/oct) with a cutoff frequency of 4 kHz and mixed with a filtered (Kemo, type VBF 8/03, 48 dB/oct) pink noise with a passband from 100 to 2000 Hz and with a spectrum level of 25 dB at 1000 Hz. This noise was used to reduce within-channel cues associated with combination

tones and with the outputs of auditory filters that respond to both carrier frequencies. The noise level was chosen so as to give a good signal-to-noise ratio for center frequencies close to the two carrier frequencies, while being high enough to eliminate within-channel effects. It was determined as follows. First, the excitation pattern produced by each (unmodulated) carrier was calculated, using the procedure described by Glasberg and Moore (1990); second, the range of CFs over which the excitation levels for the two carriers were different by less than 15 dB was determined; finally, the level of the pink noise was chosen so that, over this range of CFs, the pink noise would produce an excitation level greater than or equal to that produced by either carrier alone. When the excitation levels evoked by the two carriers differed by more than 15 dB, then the noise would have completely masked the excitation produced by the carrier with the lower excitation level, for any frequency within the pass band of the noise. The levels of the sinusoidal and noise stimuli were adjusted by manual attenuators. The stimuli were delivered to one earpiece of a Sennheiser HD 414 headset.

#### 2. Procedure

A 2AFC task was used to measure psychometric functions for AM detection. Detectability indices,  $d'$ , were calculated from the results for 200 trials (four blocks of 50 trials) for each modulation depth, using standard tables (Hacker and Ratcliff, 1979). In both stages 1 and 2, the subject's task was to indicate whether the first or the second interval in a trial contained a modulated tone. For stage 1, five modulation depths were chosen for each subject on the basis of pilot experiments, so that the resulting detectability indices,  $d'$ , were reasonably evenly spread over the range 0 to 2.5. For stage 2, the modulation depth for each carrier was chosen, on the basis of stage 1, so that the modulation would be equally detectable for each carrier when presented alone; the modulation depths used were calculated so as to give  $d'$  values of 0.2, 0.45, 0.7, 0.95, and 1.2 for the individual carriers. For both stages 1 and 2, the conditions were fixed for a block of 55 trials. The first five trials used the highest modulation depth and were treated as practice. The rest of a block consisted of ten subblocks, each of which started with the highest modulation depth and decreased progressively to the lowest. In stage 1, both modulation directions,  $\langle + \rangle$  and  $\langle - \rangle$ , were tested within a block of trials. The order of the modulation directions was random, but the number of upwards and downwards stimuli for each modulation depth was balanced in a block, except for the practice trials where the numbers of upwards and downwards stimuli were not balanced. In stage 2, one combination of AM directions was presented in a block.

Subjects were tested in a double-walled sound-attenuating chamber. Correct answer feedback was provided by lights on the response box.

#### 3. Subjects

Three subjects with normal hearing were used. One was author SF. The other two subjects were paid for their ser-

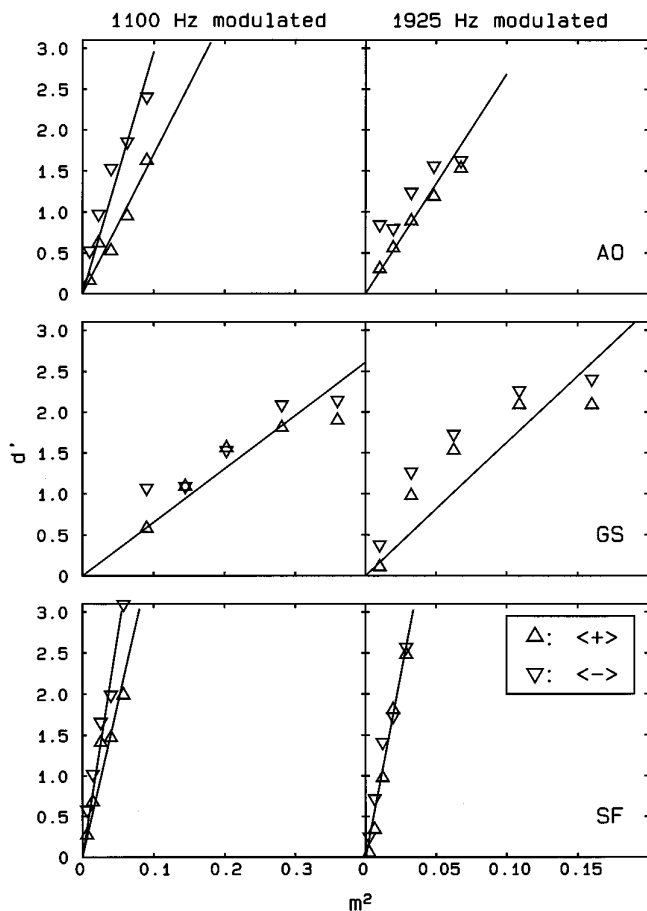


FIG. 1. Results of stage 1 of the experiment, showing psychometric functions for the detection of AM on only one carrier frequency. Detectability,  $d'$ , is plotted as a function of the squared modulation depth,  $m^2$ . Up-pointing symbols indicate that the modulation started in the  $\langle + \rangle$  direction and down-pointing symbols indicate that the modulation started in the  $\langle - \rangle$  direction (see text). The left column shows results when the 1100-Hz carrier was modulated, and the right column shows results when the 1925-Hz carrier was modulated. Each row shows results for one subject. Best fitting lines to the data points are also shown (see text).

vices. Two subjects (AO and SF) were highly experienced in similar psychoacoustical experiments. All subjects were trained until their performance appeared to be stable. This took about 6 h.

## B. Results and discussion

The results of stage 1 are shown in Fig. 1. Each column shows the results for one carrier frequency. Each row shows the results for one subject. Since, in most cases, the  $d'$  values seemed to be linearly related to the squared modulation depth,  $m^2$ , as found by Moore and Sek (1992), values of  $d'$  are plotted as a function of  $m^2$ , for each modulated carrier (recall that the other carrier was present, but unmodulated, in both intervals of a trial). Different symbols indicate the modulation starting direction. Straight lines were fitted to the values of  $d'$  as a function of  $m^2$ , so as to minimize the sum of squared errors. The lines were constrained to pass through the origin. In most cases a single straight line was fitted to the data for both modulation directions. However, for sub-

jects AO and SF for the carrier frequency 1100 Hz,  $t$  tests showed that the slopes of the lines fitted separately to the data for the two modulation directions were different with a significance level of 1%. Here, the variances of the slopes were estimated from the sum of the squared deviations of the data from each regression line (Snedecor and Cochran, 1967, p. 153). In these cases, two separate lines were fitted to the data. The obtained slopes were used to calculate the modulation depths used in stage 2, so as to give the same  $d'$  values for the two individual carriers. For subject GS, a ‘‘ceiling’’ effect was found; performance did not improve with increasing modulation depth once the value of  $d'$  exceeded about 2. This may have been due to occasional loss of attention; if the subject made four errors in a block of 50 trials even when the signal was highly discriminable, then  $d'$  would never exceed 2. Because the lines for GS were fitted to all of the data points, the values of  $d'_{\text{ind}}$  in stage 2 may have been underestimated. We will return to this point later.

The slopes of the psychometric functions were markedly greater for the 1925-Hz carrier than for the 1100-Hz carrier; note the different abscissa scales in Fig. 1. This can be attributed to the use of the pink noise, which would have masked the high-frequency side of the excitation pattern of the 1100-Hz carrier but not of the 1925-Hz carrier. We would expect markedly better performance for the 1100-Hz carrier if the noise background had not been used (Moore and Sek, 1994). The detection of AM at medium and high levels is optimal when information from the high-frequency side of the excitation pattern is available, owing to the non-linear (expansive) growth of excitation on that side of the pattern (Zwicker and Fastl, 1990; Moore and Sek, 1994; Moore, 1997).

The slopes of the psychometric functions varied markedly across subjects. In particular, the slopes for subject GS were small relative to those for the other two subjects. For example, for the 1100-Hz carrier, the slope for subject SF ( $\langle - \rangle$  direction) was larger than the slope for GS by a factor of about 8. This large variation may be due to a difference in the degree of experience in psychoacoustical experiments. However, it should be noted that the crucial points for this experiment were (1) the extent to which the detectability of AM improved when AM was presented on two carriers relative to when AM was presented on only one carrier, and (2) the effect of the relative phase of the AM across carriers. Since the modulation depths of the AM in stage 2 were chosen for each carrier and subject so that the AM would be equally detectable, results in stage 2 were reasonably similar across subjects despite the variability in detection performance for AM on one carrier.

The results of stage 2 are shown in Fig. 2. Each panel shows the results for one subject or the average data collapsed across subjects. The detectability index,  $d'$ , for AM on the two carriers is plotted as a function of  $d'$  for AM on only one carrier. Different symbols represent the patterns of modulation direction as indicated in the key. In each panel, the upper dashed line, which has a slope of  $\sqrt{2}$ , shows the detectability predicted on the basis of signal detection theory, on the assumption that information about AM from each carrier is processed independently and combined optimally



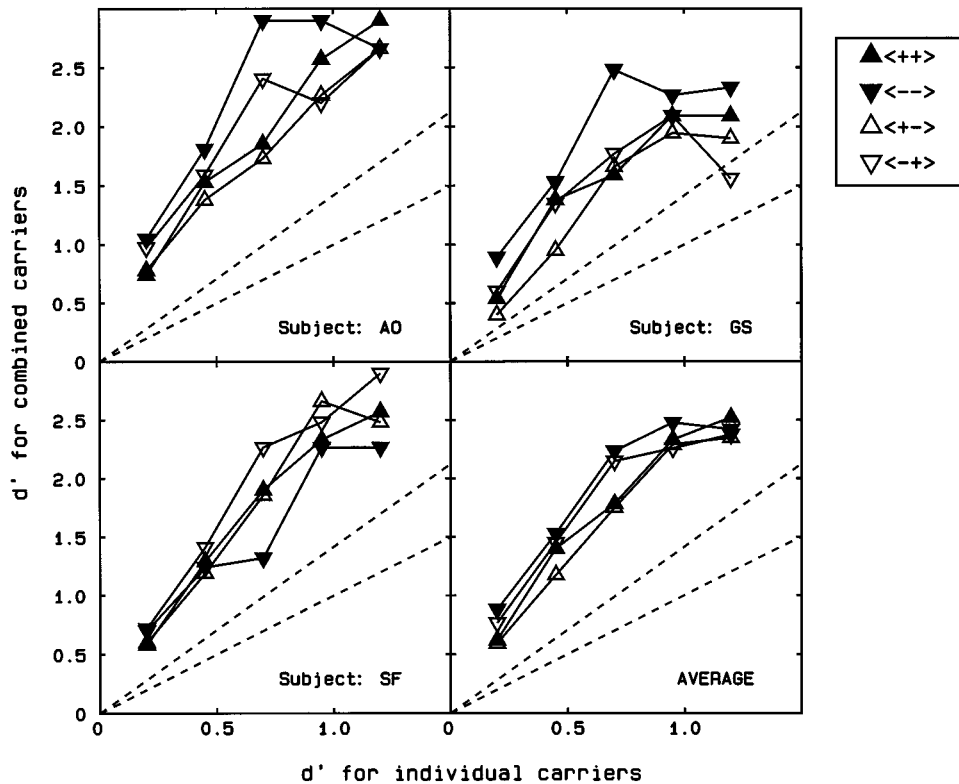


FIG. 2. Results of stage 2 of the experiment, showing psychometric functions for the detection of AM on both carrier frequencies. Each panel shows results for one subject or the average data across subjects. The abscissa shows the value of  $d'$  for AM of one carrier. The ordinate shows the value of  $d'$  for AM on both carriers. The parameter is the combination of modulation direction. The lower dashed line shows where the points would lie if  $d'$  for AM on both carriers were equal to  $d'$  for AM on a single carrier. The upper dashed line shows the value of  $d'$  predicted by signal detection theory on the assumption that information about AM from each carrier is processed independently and combined optimally.

(Green and Swets, 1974). Dau's model predicts that the data should lie on this line. The lower dashed line shows where the data would lie if the value of  $d'$  for the combination was the same as that when only one carrier was modulated. As in stage 1, a "ceiling" effect was apparent for subject GS, and also, less clearly, for subject AO. As suggested earlier, this may reflect occasional lapses of attention.

There seemed to be no consistent difference in performance for the different patterns of modulation direction. To assess whether there was a significant effect of modulation direction, the slopes of the best-fitting straight lines to the psychometric functions were determined and were subjected to an ANOVA. The best fitting lines were calculated to give the least mean squared deviation of the points from the fitted lines (in the orthogonal direction), with the constraint that they passed through the origin. The root-mean-square deviation of the points from the fitted values was 0.135. The maximum deviation for a single line was 0.211. The slope values are given in Table I. A one-way within-subjects ANOVA was carried out with factor the combination of modulation direction ( $\langle ++ \rangle$ ,  $\langle +- \rangle$ ,  $\langle -+ \rangle$ ,  $\langle -- \rangle$ ). The effect of the combination of modulation direction was not significant [ $F(3,6) = 0.85$ ,  $p = 0.52$ ], indicating that the detectability of AM did not depend on the pattern of AM across carriers. Thus, the relative phase of the AM across carriers did not affect the detectability of the AM.

The psychometric functions were generally well above the upper dashed line. This may indicate that information

about AM for each carrier is not processed independently, but is processed in a common channel. However, some caution is needed in interpreting the absolute values of the slopes of the lines, for two reasons. First, in stage 1, the two different modulation directions were mixed within a block of trials. This may have made the task more difficult than if only a single direction were used within a block. In stage 2, only a single combination of modulation directions was used within a block. This may partly account for the relatively good performance in stage 2. We believe, however, that this effect was probably small. Furukawa (1996) carried out an experiment measuring the detectability of FM instead of AM on two carriers using a method similar to that of the present experiment. He tested two conditions: (1) only a single combination of modulation directions was used within a block, and (2) different combinations of modulation directions were mixed within a block of trials. The results showed no signifi-

TABLE I. Slopes of the psychometric functions for stage 2.

Subject	Modulation direction			
	In-phase AM		Anti-phase AM	
	$\langle ++ \rangle$	$\langle -- \rangle$	$\langle +- \rangle$	$\langle -+ \rangle$
AO	2.65	3.12	2.41	2.67
GS	2.11	2.60	1.92	2.04
TP	2.41	2.15	2.47	2.70
Mean	2.39	2.62	2.27	2.47

cant difference in the detectability of FM between the fixed and mixed modulation directions within a block. This result indicates that it is of little relevance to the detectability of FM whether one block of trials includes fixed or mixed modulation directions. However, we cannot be certain that the same applies for AM detection.

A second factor that may have influenced the slopes of the psychometric functions in stage 2 is that, especially for GS, the values of  $d'_{\text{ind}}$  (i.e., the  $d'$  values for the single carriers) may have been underestimated, because these values were derived from lines fitted to all the data obtained in stage 1, including some data for which a ceiling effect was observed. The size of this effect can be estimated in the following way. Consider the case for GS where the nominal value of  $d'_{\text{ind}}$ , based on the fitted lines, was 0.7; the values of  $m^2$  required to give these nominal values of  $d'_{\text{ind}}$  were about 0.1 for the 1100-Hz carrier and 0.04 for the 1925-Hz carrier. Using the same values of the modulation index, the values of  $d'_{\text{ind}}$  based on lines fitted to the data for the three smallest modulation depths (i.e., excluding ceiling effects) are 0.83 for the 1100-Hz carrier and 1.12 for the 1925-Hz carrier. Hence, using the higher values of  $d'_{\text{ind}}$ , the predicted value of  $d'$  in stage 2, if information from the two carriers were processed independently and combined optimally, is  $(0.83^2 + 1.12^2)^{0.5} = 1.39$ . This is a factor of 1.4 greater than predicted using the nominal value of  $d'_{\text{ind}}$ . In fact, the value of  $d'$  obtained by GS in stage 2 for this case averaged about 1.9. This represents a "worst case." For the other two subjects, it made much less difference whether predictions were based on lines fitted to all the data in stage 1 or lines fitted to the data for the three smallest modulation depths.

The two factors discussed above may have increased the slopes of the psychometric functions in stage 2. However, it seems unlikely that they would account for the whole of the difference between the obtained psychometric functions and the upper dashed lines. The former have an initial slope of about 3, as compared to the slope of  $\sqrt{2}$  for the latter. Possibly, the "true" initial slope, allowing for the two factors, may be closer to 2 than to 3, but it is unlikely to be as small as  $\sqrt{2}$ .

Overall, the results of this experiment suggest that information about AM for each carrier is processed partly in a common central channel (i.e., detectability is determined by internal noise common to both carriers). This channel is not sensitive to the relative phase of AM across carriers.

## II. DISCUSSION

### A. Implications for the processing of amplitude modulation

The results showed that there was no difference in detectability between in-phase and antiphase AM across carriers. This is consistent with Dau's model (assumption 2 described in the Introduction). The model assumes that information about the phase of modulation for each carrier frequency is lost at the stage where information is combined across modulation filters.

However, the present experiment also showed that the psychometric functions generally had slopes larger than the

value of  $\sqrt{2}$  which would be predicted by signal detection theory on the assumption that information about AM from each carrier is processed independently and combined optimally. This is not consistent with Dau's model (assumption 1), since the "optimal detector" should only make use of information from active modulation filters, and since the only source of noise in his model is an independent noise added to the output of each modulation filter. Our results suggest that, if a modulation filter bank is involved in AM detection, then there is an internal noise at the stage *after* information from the different modulation filters is combined.

The maximum expected value for the slopes of the psychometric functions in stage 2 depends upon assumptions made about the internal representation of the modulation and about sources of internal noise. For example, if the internal representations of the modulation on each carrier were added at an early stage of processing, and there was negligible internal noise prior to the point of addition, then combining the information from two equally detectable carriers would lead to an effective doubling of the information. This might be expected to lead to a value of  $d'$  double that for the individual carriers. However, if the information was in a "raw" form, for example, a direct neural representation of the modulation itself, this could lead to a  $d'$  value as much as four times that for the individual carriers, since  $d'$  for a single carrier is roughly proportional to the modulation index squared. This seems unlikely, since if information about the modulation was represented in such a raw form, one would expect detectability in stage 2 to depend on the relative modulator phase of the two carriers. In fact, no such dependence was found. Probably, the "true" slopes of the psychometric functions in stage 2, allowing for the factors discussed earlier, are close to 2. This is consistent with a model in which information about the modulation on each carrier is represented in a processed form (for example as the envelope at the output of the appropriate modulation filter) at the point where information is combined across carriers, and the dominant source of internal noise occurs after the point of combination.

It is of interest that other data on AM detection for stimuli exciting auditory filters with widely spaced center frequencies *are* consistent with Dau's model. For example Eddins (1993) measured thresholds for detecting AM on noise carriers as a function of carrier bandwidth and upper cutoff frequency. The thresholds improved with increasing bandwidth but were almost independent of upper cutoff frequency. For the stimuli with the widest bandwidth (1600 Hz), auditory filters with a range of center frequencies would have been excited, especially for the lowest upper cutoff frequency. Dau and co-workers (Dau, 1996; Dau *et al.*, 1997b) showed that his model could account for these data (and their own comparable data) very well.

It seems likely that Dau's model works well for noise carriers but not for tonal carriers (as used by us) because performance for noise carriers is largely determined by the inherent fluctuations in the noise. These fluctuations are independent in different frequency regions. In contrast, performance for tonal carriers must be limited by internal noise as

the inherent variability in the stimuli is negligible. Our results suggest that this noise is not independent across different frequency regions, at least for the detection of AM.

In the discussion above, we have assumed that analysis in terms of a modulation filter bank is appropriate. However, this concept is still controversial, and other mechanisms for processing modulation remain possible. For example, a low-pass filter could be applied to the (rectified) output of each auditory filter (Viemeister, 1979). Whatever model is assumed, our results suggest that significant internal noise occurs after the point where information from different peripheral channels is combined.

## B. The plausibility of the FM-induced-AM model

As described earlier, Furukawa and Moore (1997) showed that the detectability of FM on two widely spaced carriers was better when the carriers were modulated in phase than when they were modulated in antiphase. They showed further that roving the carrier frequencies across trials reduced but did not eliminate the effect of FM coherence and suggested that this result might indicate that the FM-induced-AM mechanism is (partly) involved in the effect of FM coherence. The present experiment showed that the detectability of AM on two carriers did not depend on the relative phase of the AM across the carriers. This indicates that the FM-induced-AM mechanism almost certainly does not play a role in the effect of FM coherence. That is, the mechanism that is responsible for the effect of FM coherence does not rely on information about FM coded in the form of excitation level changes.

If we abandon the FM-induced-AM hypothesis, then another explanation is needed for the fact that roving the carrier frequencies slightly reduced the effect of FM coherence. One possibility derives from another mechanism suggested by Furukawa and Moore to explain the effect of FM coherence. This is that judgments were partly based on fluctuations in the residue pitch evoked by the two carriers; these fluctuations would be bigger when the modulation was coherent across carriers. The large pitch changes induced by roving the carriers might have made it more difficult to detect the smaller fluctuations in residue pitch produced by the FM. Consistent with this, Furukawa and Moore (1997) found that the detectability of FM on a *single* carrier was markedly reduced by roving the carrier frequency from trial to trial.

## C. Implications for perceptual grouping processes

As discussed in the introduction, there is evidence that the auditory system can compare the relative phase of AM on two different carriers when the depth of the AM is well above threshold values. Hence, we were somewhat surprised by our finding that the detectability of AM on two carriers is not influenced by relative modulator phase. However, our results are not inconsistent with the finding of sensitivity to relative modulator phase for supra-threshold amounts of AM. They merely indicate a dissociation between processes involved in detection of AM and processes involved in discrimination of the relative phase of AM. In a sense, our results are the converse of those found for FM. Listeners are

insensitive to the relative phase of supra-threshold amounts of FM on different carriers (Carlyon, 1991, 1994), but relative modulator phase does influence the detectability of FM (Furukawa and Moore, 1996, 1997). For AM, the opposite is true.

The role of the relative AM phase of sinusoidal modulators in perceptual grouping remains unclear. Although changes in relative modulator phase on two carriers can be detected (Strickland *et al.*, 1989), there is not strong evidence that relative AM phase across frequencies plays a role in perceptual grouping, at least for low modulation rates. Bregman *et al.* (1985) reported that the perceptual fusion of two sinusoidal carriers modulated at a 100-Hz rate was stronger when the tones were modulated in phase than when they were modulated 180° out of phase. However, the effect was weak, and they noted that "... about two out of three subjects failed to pass a pretest in which they were required to discriminate stimuli in which the AM of tones B and C was in-phase versus out-of-phase." For lower modulation rates, several studies have failed to find a role for AM phase in perceptual grouping (Summerfield and Culling, 1992; Moore and Alcántara, 1996). Perhaps AM phase does not play a strong role because it would not be a reliable cue for many everyday sounds. For example, when the fundamental frequency of a vowel sound is frequency modulated, this results in AM of the individual harmonics. However, the AM would be out of phase for harmonics on either side of a formant frequency.

## III. SUMMARY

The following conclusions can be drawn from the present study:

- (1) The detectability of AM on two carriers did not depend on the relative phase of the AM across the carriers.
- (2) The detectability of AM on two carriers was generally above the value predicted by signal detection theory on the assumption that information about FM from each carrier is processed independently and combined optimally. This result indicates that information about AM from each carrier is processed in a common channel. This is not consistent with Dau's model (Dau, 1996; Dau *et al.*, 1997a).
- (3) These results imply that the FM-induced-AM model cannot explain the effect of FM coherence. Probably, there is no mechanism that has higher sensitivity to in-phase AM across auditory filters than to anti-phase AM. The mechanism responsible for the effect of FM coherence does not appear to rely on information about FM coded in the form of excitation level changes.

## ACKNOWLEDGMENTS

This work was supported by the Medical Research Council (UK). S. Furukawa was supported by the British Council and an ORS award. We thank Thomas Baer, Yoshito Nejime, Bob Carlyon, Torsten Dau, and an anonymous reviewer for helpful comments on earlier versions of this paper.

- Bacon, S. P., and Grantham, D. W. (1989). "Modulation masking: effects of modulation frequency, depth and phase," *J. Acoust. Soc. Am.* **85**, 2575–2580.
- Bregman, A. S., Abramson, J., Doehring, P., and Darwin, C. J. (1985). "Spectral integration based on common amplitude modulation," *Percept. Psychophys.* **37**, 483–493.
- Carlyon, R. P. (1991). "Discriminating between coherent and incoherent frequency modulation of complex tones," *J. Acoust. Soc. Am.* **89**, 329–340.
- Carlyon, R. P. (1994). "Further evidence against an across-frequency mechanism specific to the detection of frequency modulation (FM) incoherence between resolved frequency components," *J. Acoust. Soc. Am.* **95**, 949–961.
- Dau, T. (1996). "Modeling auditory processing of amplitude modulation," Ph.D. thesis, University of Oldenburg.
- Dau, T., Kollmeier, B., and Kohlrausch, A. (1996a). "Modeling modulation perception: modulation low-pass filter or modulation filter bank?," in *Psychoacoustics, Speech and Hearing Aids*, edited by B. Kollmeier (World Scientific, Singapore).
- Dau, T., Kollmeier, B., and Kohlrausch, A. (1997a). "Modeling auditory processing of amplitude modulation: I. Detection and masking with narrowband carriers," *J. Acoust. Soc. Am.* **102**, 2892–2905.
- Dau, T., Kollmeier, B., and Kohlrausch, A. (1997b). "Modeling auditory processing of amplitude modulation: II. Spectral and temporal integration," *J. Acoust. Soc. Am.* **102**, 2906–2919.
- Dau, T., Püschel, D., and Kohlrausch, A. (1996b). "A quantitative model of the "effective" signal processing in the auditory system. I. Model structure," *J. Acoust. Soc. Am.* **99**, 3615–3622.
- Eddins, D. A. (1993). "Amplitude modulation detection of narrow-band noise: Effects of absolute bandwidth and frequency region," *J. Acoust. Soc. Am.* **93**, 470–479.
- Fassel, R., and Püschel, D. (1993). "Modulation detection and masking using deterministic and random maskers," in *Contributions to Psychological Acoustics*, edited by A. Schick (Biblioteks-und Informationssysteme der Universität Oldenburg, Oldenburg).
- Furukawa, S. (1996). "Across-frequency processes in modulation detection," Ph.D. thesis, Cambridge.
- Furukawa, S., and Moore, B. C. J. (1996). "Across-frequency processes in frequency modulation detection," *J. Acoust. Soc. Am.* **100**, 2299–2312.
- Furukawa, S., and Moore, B. C. J. (1997). "Dependence of frequency modulation (FM) detection on FM coherence across carriers: Effects of modulation rate, harmonicity and roving of the carrier frequencies," *J. Acoust. Soc. Am.* **101**, 1632–1643.
- Glasberg, B. R., and Moore, B. C. J. (1990). "Derivation of auditory filter shapes from notched-noise data," *Hearing Res.* **47**, 103–138.
- Green, D. M., and Swets, J. A. (1974). *Signal Detection Theory and Psychophysics* (Krieger, New York).
- Hacker, M. J., and Ratcliff, R. (1979). "A revised table of d' for M-alternative forced choice," *Percept. Psychophys.* **26**, 168–170.
- Hall, J. W., Haggard, M. P., and Fernandes, M. A. (1984). "Detection in noise by spectro-temporal pattern analysis," *J. Acoust. Soc. Am.* **76**, 50–56.
- Houtgast, T. (1989). "Frequency selectivity in amplitude-modulation detection," *J. Acoust. Soc. Am.* **85**, 1676–1680.
- Langner, G., and Schreiner, C. E. (1988). "Periodicity coding in the inferior colliculus of the cat. I. Neuronal mechanisms," *J. Neurophysiol.* **60**, 1799–1822.
- Martens, J.-P. (1982). "A new theory for multi-tone masking," *J. Acoust. Soc. Am.* **72**, 397–405.
- Moore, B. C. J. (1997). *An Introduction to the Psychology of Hearing* (Academic, San Diego), 4th ed.
- Moore, B. C. J., and Alcántara, J. I. (1996). "Vowel identification based on amplitude modulation," *J. Acoust. Soc. Am.* **99**, 2332–2343.
- Moore, B. C. J., and Sek, A. (1992). "Detection of combined frequency and amplitude modulation," *J. Acoust. Soc. Am.* **92**, 3119–3131.
- Moore, B. C. J., and Sek, A. (1994). "Effects of carrier frequency and background noise on the detection of mixed modulation," *J. Acoust. Soc. Am.* **96**, 741–751.
- Moore, B. C. J., Glasberg, B. R., Gaunt, T., and Child, T. (1991). "Across-channel masking of changes in modulation depth for amplitude- and frequency-modulated signals," *Q. J. Exp. Psychol.* **43A**, 327–347.
- Münkner, S., and Püschel, D. (1993). "A psychoacoustical model for the perception of nonstationary sounds," in *Contributions to Psychological Acoustics*, edited by A. Schick (Biblioteks-und Informationssysteme der Universität Oldenburg, Oldenburg).
- Palmer, A. R. (1995). "Neural signal processing," in *Hearing*, edited by B. C. J. Moore (Academic, San Diego).
- Snedecor, G. W., and Cochran, W. G. (1967). *Statistical Methods* (Iowa U. P., Ames, Iowa).
- Strickland, E. A., Viemeister, N. F., Fantini, D. A., and Garrison, M. A. (1989). "Within-versus cross-channel mechanisms in detection of envelope phase disparity," *J. Acoust. Soc. Am.* **86**, 2160–2166.
- Summerfield, Q., and Culling, J. F. (1992). "Auditory segregation of competing voices: absence of effects of FM or AM coherence," *Philos. Trans. R. Soc. London, Ser. B* **336**, 357–366.
- Viemeister, N. F. (1979). "Temporal modulation transfer functions based on modulation thresholds," *J. Acoust. Soc. Am.* **66**, 1364–1380.
- Yost, W. A., and Sheft, S. (1989). "Across-critical-band processing of amplitude-modulated tones," *J. Acoust. Soc. Am.* **85**, 848–857.
- Yost, W. A., Sheft, S., and Opie, J. (1989). "Modulation interference in detection and discrimination of amplitude modulation," *J. Acoust. Soc. Am.* **86**, 2138–2147.
- Zwicker, E., and Fastl, H. (1990). *Psychoacoustics—Facts and Models* (Springer-Verlag, Berlin).

# Infants' pitch perception: Masking by low- and high-frequency noises

Christine Rogers Montgomery and Marsha G. Clarkson

*Department of Psychology, Neuropsychology and Behavioral Neuroscience Program,  
Georgia State University, University Plaza, Atlanta, Georgia 30303*

(Received 21 October 1996; accepted for publication 11 August 1997)

The present research employed an operant conditioning procedure typically used with infants to test noise masking of pure tones and tonal complexes in adults and in 7-month-old infants. Adults and infants were presented with either pure tones of 160 and 200 Hz or harmonic tonal complexes with pitches equivalent to 160 and 200 Hz. The tonal complexes did not contain energy at the fundamental frequency. After learning these tasks, subjects in the tonal complex group categorized spectrally varying tonal complexes according to the pitch of the missing fundamental. Stimuli were subsequently presented in combination with either a low- or a high-frequency noise. Both age groups successfully discriminated pure tones when combined with a high-frequency noise but not when combined with a low-frequency noise in the same frequency range as the pure tone. Infants, like adults, successfully categorized harmonic tonal complexes based on the pitch of the missing fundamental when those stimuli were combined with a low-frequency noise in the range of the missing fundamental but not when combined with a high-frequency noise which covered the frequency range of the harmonics themselves. These results suggest that infants rely primarily on a central process and not peripherally generated combination tones to hear the pitch of the missing fundamental. © 1997 Acoustical Society of America. [S0001-4966(97)00112-4]

PACS numbers: 43.66.Hg [JWH]

## INTRODUCTION

Much of the large pitch perception literature has addressed the spectral and temporal bases of pitch perception and has identified a number of classic phenomena that have constrained subsequent models of pitch perception. The present research is one of a series of studies that has looked at those phenomena in 7-month-old infants. Measuring infants' responses to classic stimulus manipulations allows us to understand the nature and limits of infants' pitch perception abilities. In other words, do infants rely on the same spectral and temporal information as do adults to discriminate the pitches of complex spectra? To date, our findings reveal that infants respond to a variety of the classic stimulus manipulations in a manner similar to adults. These parallels suggest that infants' perception of pitch may be based on the same acoustic cues as that of adults and that adult models may be applicable to perception during development.

In a first attempt to study infants' perception of pitch, Clarkson and Clifton (1985) demonstrated that 7-month-old infants could categorize harmonic tonal complexes on the basis of their missing fundamental frequencies, despite variations in the spectra of the sounds. This performance suggested that infants did, in fact, hear the pitch of the missing fundamental. Subsequently, Clarkson and Rogers (1995) found that the strength of pitch for infants, like that for adults (Carlyon and Shackleton, 1994; Ritsma, 1962), is greater for sounds containing relatively low-frequency energy (i.e., below 5000 Hz) than for those having only high-frequency energy. Although adults could hear the pitch of the missing fundamental for stimuli containing only high-frequency, unresolvable harmonics (e.g., Carlyon and Shackleton, 1994), infants failed to do so. For both adults (Goldstein *et al.*,

1978; Houtsma and Goldstein, 1972; Houtsma and Smurzynski, 1990) and infants (Clarkson *et al.*, 1996), perception of the missing fundamental improves as the number of harmonics in a tonal complex increases. However, 7-month-old infants, unlike adults (Smoorenburg, 1970), did not hear the pitch of sounds containing only two harmonics of a missing fundamental. The results of these studies emphasize the importance of the power spectrum for both infants' and adults' perception of the pitch of the missing fundamental for harmonic sounds.

Research with inharmonic tonal complexes provides additional evidence of the importance of the power spectrum for pitch perception. Like adults (e.g., Schouten *et al.*, 1962), 7-month-old infants appear to recognize the pitch of at least some inharmonic tonal complexes (Clarkson and Clifton, 1995). At the same time, infants' performance deteriorated progressively as sounds became increasingly inharmonic, paralleling the decreased salience of pitch for increasingly inharmonic sounds reported for adults (deBoer, 1976; Wightman, 1973). Because the strength of the simple difference tone is unlikely to differ for harmonic and inharmonic sounds (cf. Clarkson and Clifton, 1995; Hall, 1972), differential performance for these two types of sounds suggests that combination tones are not responsible for infants' perception of the pitch of the missing fundamental.

The most compelling, direct evidence that adults' perception of the missing fundamental does not rely on combination tones came first from a demonstration by Licklider (1954) and subsequently from a detailed report by Patterson (1969). In Patterson's experiment, listeners heard sinusoids and pulse trains lacking the fundamental frequency in the presence of a low- or a high-frequency noise. The low-

frequency noise overlapped the spectral region of the pure tones as well as the simple difference tones and missing fundamentals of the pulse trains, whereas the high-frequency noise corresponded to the harmonics of the pulse trains. Although the low-frequency noise did not affect detection of the pitch of the missing fundamental, it did mask a change in the pitch of the pure tones (Patterson, 1969). Conversely, the high-frequency noise impaired discrimination of the pitch of the missing fundamental but not of the pure tones. The fact that subjects still heard the pitch of the missing fundamental in the presence of the low-frequency noise indicates that combination tones do not provide the basis for success in the task. However, combination tones do appear to influence adults' perception of the missing fundamental by increasing the strength of the pitch percept (Houtsma and Goldstein, 1972).

Although infants' perception of inharmonic complexes suggests that they do not rely on combination tones to hear the pitch of complex spectra, direct evidence in the form of masking data does not exist. To determine whether infants use combination tones to perceive the pitch of the missing fundamental, we tested 7-month old infants and adults under stimulus conditions analogous to those used by Patterson (1969). The adults were tested first to assure that the stimulus and noise levels were appropriate to replicate Patterson's data.

In a conditioning procedure, subjects progressed through several experimental stages in which the bases for responding to tonal complexes were successively narrowed. Subjects first learned to discriminate either two tonal complexes or two pure tones. For subjects who heard tonal complexes, we introduced variations in the harmonic components of the stimuli to assure that they were attending to the pitch of the missing fundamental. Finally, the tonal complexes were presented in combination with either a low- or a high-frequency noise. Subjects who heard pure tones proceeded to a final stage in which they were asked to discriminate the pure tones in the presence of low- or high-frequency noise. In accordance with Patterson's (1969) findings, we anticipated that both adults and infants would hear the pitch of the missing fundamental when the tonal complexes were combined with low-frequency noise but not when combined with high-frequency noise. We also predicted that listeners would discriminate pure tones when combined with high-frequency noise but fail to discriminate them when combined with low-frequency noise.

## I. METHOD

### A. Subjects

Infants were recruited through letters distributed by hospitals and physicians and through various public service announcements. All infants met criteria for experiencing an uncomplicated term birth (within 2 weeks of anticipated birthdate), having good health on the day of testing, having no cold and taking no medications, and having no history of chronic ear infections or suspicion of hearing loss. Eighteen (10 male, 8 female) 7- to 8-month-old infants ( $M=32.47$  weeks; range=30.71–34.86 weeks) completed the experi-

ment. The data for an additional 88 infants were excluded because of equipment malfunction (2), incomplete data (73), scheduling conflicts (6), and poor state (7).

Adult subjects were recruited through introductory psychology courses at a large, urban university. All adults met criteria for having no suspicion of hearing loss, having good health on the day of testing, and taking no medications known to influence hearing. Thirty-two (12 male, 20 female) 18- to 30-year-old college students (mean=19.8 years) completed testing, and the data for an additional 5 adults were excluded because of equipment malfunction (1), failure to learn the task (2), and failure to follow instructions (2).

Subjects were randomly assigned to one of four experimental groups formed from the factorial combination of two stimuli (tonal complex and pure tone) and two noises (low frequency and high frequency), until at least three infants and eight adults in each group completed both stages of the experiment. Assignment to two directions of pitch change (160 to 200 Hz and 200 to 160 Hz) was counterbalanced across subjects, but direction of pitch change was not used as a separate grouping variable because previous studies with infants have never demonstrated an effect of this factor (e.g., Clarkson and Clifton, 1985, 1995; Clarkson *et al.*, 1996; Clarkson and Rogers, 1995).

### B. Stimuli and apparatus

Two pure tones, having frequencies of 160 and 200 Hz, and two sets of seven tonal complexes, all of which lacked energy at the fundamental frequency, were generated. One set of tonal complexes was based on a missing fundamental frequency of 160 Hz, whereas the other set was based on a missing fundamental frequency of 200 Hz. Although the complexes differed in the number and frequencies of the harmonics they contained, all harmonics were equal in amplitude and combined in cosine phase. The right side of Table I lists the harmonic structures for each of the seven basic tonal complexes used in various stages of the experiment. The tonal complexes, which were used to shape initial responding and to establish discrimination, contained eight consecutive harmonics of a missing fundamental (i.e., harmonics 2–9). The number of harmonics was limited to eight because the tonality of complex spectra decreases as high harmonic numbers are included (Ritsma and Hoekstra, 1974). Because the frequencies of the components were unique to each tonal complex, discrimination could have been based on detection of either the pitch of the missing fundamental or the frequencies of individual components. Therefore, three tonal complexes having different ranges of six harmonics represented each pitch in a missing fundamental stage. Varying the range of the frequencies in the sounds minimized the usefulness of pitch cues formed by the frequencies of the components and by the upper and lower spectral edges of the sounds. Three additional tonal complexes containing six harmonics represented each pitch in the masked missing fundamental stage. The ranges of harmonics differed for the stimuli presented in the last two stages so that subjects could not rely on memory for specific stimulus frequencies in one stage as a basis for responding in the subsequent one.

TABLE I. Experimental stages and harmonic structures of stimuli.

Stage	Stimuli:	Stimuli:	Stimuli:	Stimuli:
	Pure tone group Low-frequency noise	Pure tone group High-frequency noise	Tonal complex group Low-frequency noise	Tonal complex group High-frequency noise
Shaping	$f_0$	$f_0$	H2–H9	H2–H9
Discrimination	$f_0$	$f_0$	H2–H9	H2–H9
Missing fundamental	not applicable	not applicable	H3–H8 H5–H10 H7–H12	H3–H8 H5–H10 H7–H12
Masking	$f_0$ + noise (60–260 Hz)	$f_0$ + noise (260–2600 Hz)	H2–H7 H4–H9 H6–H11 + noise (60–260 Hz)	H2–H7 H4–H9 H6–H11 + noise (260–2600 Hz)

Two bandpass noises were generated: a low-frequency noise having a low-frequency cutoff of 60 Hz and a high-frequency cutoff of 260 Hz and a high-frequency noise having a low-frequency cutoff of 260 Hz and a high-frequency cutoff of 2600 Hz. As for Patterson's (1969) stimuli, the low-frequency noise occupied the spectral region of the pure tones and of the missing fundamental frequencies and simple difference tones of the tonal complexes. The high-frequency noise corresponded to the frequencies of the harmonics in the tonal complexes but did not overlap with the pure tones.

Stimuli were digitized on a Gateway computer at a sampling rate of 10 kHz via customized software and stored on a hard disk. Stimuli were read from the hard disk, played through a D/A converter, sent through a 5-kHz anti-imaging filter, routed through a programmable attenuator and then sent through a summer, where they were combined with the noises. Bandpass noises were synthesized by a noise generator, filtered by a programmable filter, fed through a programmable attenuator, and then sent through the summer. The stimuli and noise maskers were led through a power amplifier to a JBL 4208 loudspeaker. All stimuli and noises were 500 ms long with a 50-ms rise/fall time.

Sound pressure levels were measured at the position of the infant's or adult's head with a Bruel & Kjaer model 2231 sound level meter via a type 4155 condenser microphone with random incidence corrector. All A-weighted stimulus levels were 50 dB, except for a second set of 60-dB stimuli that were used to shape initial responding in the infants. The bandpass noises were 65 dB. In previous studies with infants (Clarkson and Clifton, 1985, 1995; Clarkson and Rogers, 1995) tonal complexes ranged from 55 to 60 dB, but the level of noise required to mask such stimuli made the overall sound level noxious. To limit the overall stimulus level, we reduced the level of the stimuli to 50 dB. Because Nozza (1987) has reported that infants' perception of speech deteriorates significantly when the sound level is reduced from 60 to 50 dB we expected that group performance would be poorer in this study than in the previous studies. Nonetheless, we anticipated that an adequate number of infants would meet the individual criterion of performance to allow interpretation of results in each experimental stage. Thus the resulting stimulus and noise levels reflect a compromise to keep the stimulus detectable without letting the masker become noxious.

The infant sat on a parent's lap in the center of a double-

walled IAC booth, while an experimenter, who entertained the infant with silent toys, sat opposite them. Adults were tested alone in the IAC booth seated on the same chair as the parents. A Panasonic video camera provided a frontal view of the subject, which was fed to a Panasonic video recorder for presentation on a video monitor. The loudspeaker was placed on a 114-cm-high pedestal, which stood at a 45-degree angle to the subject's right about 100 cm from him or her. A Sony Trinitron video monitor was placed in front of the loudspeaker on a 61-cm-high pedestal, and a Sony laserdisc player fed the monitor to present audiovisual reinforcement for correct responses when the pitch of the sounds changed.<sup>1</sup>

The computer in an adjoining room controlled the subject's progress through the experiment. For infants, the computer detected the start of trials from a button, which was pressed by the experimenter in the IAC chamber. Throughout each trial, the computer activated a small light behind the infant and out of his or her view to inform the experimenter when a trial was in progress. For adults, the experimenter initiated trials by pressing the space bar on the computer's keyboard. The computer detected both the experimenter's votes of infants' head turning (via a small footpedal) and the adult's responses (via a button), recorded those votes, and activated the reinforcer at the appropriate times.

## C. Procedure

### 1. General procedure

Subjects were tested in a single interval, go/no-go operant conditioning procedure. Background sounds, which represented one pitch, played repeatedly at a rate of one per second. On signal trials, sounds with a different pitch replaced the background sounds (i.e., the pitch changed), but on no-signal trials the background pitch continued. Trials lasted 6 s and occurred at 6–10 s intertrial intervals. Infants were taught to turn their heads in the direction of the sound when the pitch of the sounds changed, whereas adults were instructed to press the button to activate the television monitor and to press the button only when they thought the television would be activated. When adults responded repeatedly and randomly, they were further instructed to minimize the number of times that they pressed the button and nothing occurred.

If the experimenter voted that the infant turned his or her head at any time during a signal trial or if the adult pressed

the button, the computer credited the subject with a hit, stopped presentation of the sounds, and activated a reinforcer for 5 s. Responses during no-signal trials were coded as false alarms and were not reinforced. Those trials ended if the subject responded, and the background sounds resumed with the appropriate interstimulus interval immediately thereafter. If the subject did not respond, the trial ended after the 6-s presentation of stimuli.

## 2. Shaping stage

Infants progressed through two shaping stages: an initial one in which stimuli were presented at an A-weighted sound level of 60 dB followed by one in which stimuli were presented at an A-weighted sound level of 50 dB. The initial shaping stage was added because pilot subjects did not attend to the stimuli when they were presented at 50 dB.<sup>2</sup> By contrast, adults received shaping stimuli that were presented at an A-weighted sound level of 50 dB. In the shaping stages, only signal trials were presented so that the subject would have a high level of reinforcement. Details of the infants' shaping procedure can be found in Clarkson and Clifton (1995) or Clarkson and Rogers (1995). If the adult did not begin responding on his or her own within four or five trials, the experimenter activated the reinforcer for several trials. Each subject received from 15 to 30 trials to meet a criterion of unassisted responses on three consecutive trials in each shaping stage, after which testing proceeded to the next stage.

## 3. Experimental stages

During the experimental stages, half the trials were no-signal trials on which the pitch did not change. Trial order was randomized with the restriction that no more than two consecutive trials of a given type occurred. When infants were tested, the parent and experimenter wore headphones over which they listened to music. Because they could not hear the stimuli over the music, neither adult could cue the infant to pitch changes. In addition, the type of trial could not alter the experimenter's criterion for judging head turns or her way of entertaining the infant.

Testing in each stage continued for 30 trials or until the subject reached the criterion to pass the stage. This criterion was a hit rate of 0.8 or higher *in combination* with a false-alarm rate of 0.2 or lower across ten consecutive trials. With this relatively stringent criterion, the probability of an infant reaching criterion by chance is 0.056 (Bakeman, 1992, Chap. 2). Although a less stringent criterion (e.g., 60% correct) might have resulted in more subjects reaching criterion, the likelihood of their doing so by chance would increase to 0.337. Minimizing the likelihood of a subject progressing through stages by chance was deemed important because interpretation of performance in the latter stages of the experiment depends on the subject being under stimulus control in the preceding stages. Consequently, we chose to adopt the more stringent criterion we have employed in the past (Clarkson and Clifton, 1995; Clarkson *et al.*, 1996; Clarkson and Rogers, 1995). Testing was ended for subjects who failed to meet criterion within 30 consecutive trials.

*a. Tonal complex groups.* For subjects in the tonal complex groups, three experimental stages followed shaping. In the discrimination stage, listeners heard the same sounds as they did during shaping. The spectra of these stimuli provided multiple bases for discrimination. Listeners could have heard the pitch of the missing fundamental. Alternatively, they could have attended to differences in the frequencies of individual components of the complexes, and finally, they could have responded to differences in the spectral locus of the signals. To clarify these bases of responding, listeners who met criterion for discriminating the tonal complexes moved to a missing fundamental stage.

In the missing fundamental stage, three spectrally differing tonal complexes represented each pitch. A random sequence of background stimuli repeated, and on signal trials sounds having the other pitch were presented in a random sequence. The subject's task was to ignore spectral variations and respond only when the pitch of the sounds changed. Individuals who successfully completed this stage perceived the pitch of the missing fundamental, as variations in the frequencies of individual harmonics and in the spectral profiles of the signals eliminated other bases of responding.

In the masked missing fundamental stage, the procedure was the same as for the missing fundamental stage. However, the three tonal complexes which represented each pitch were combined with either the low-frequency or the high-frequency noise.

The introduction of frequency variations in the missing fundamental and masked missing fundamental stages confused some subjects. To remind listeners of their task, we employed a procedure similar to that used by Clarkson and Clifton (1995). If subjects did not respond on four consecutive signal trials or if they responded on two of three consecutive no-signal trials, they were returned to the preceding stage. Thus individuals heard discrimination stimuli if they became confused during the missing fundamental stage, and they were reminded with missing fundamental stimuli if they had difficulty with the masked missing fundamental stage. Subjects were expected to reorient to the task quickly because they had already successfully discriminated or categorized the reminder stimuli. They received up to 12 trials in which to meet a criterion of correct responding on 5 of 6 consecutive trials. When this occurred, testing resumed in the following stage. If a subject did not reach criterion with the reminder stimuli, we ended testing for the day and scheduled a return visit. Because the subject failed with the same stimuli he or she had just discriminated, we assumed that he or she was no longer attending to the stimuli. On the return visit, shaping stimuli from the last stage completed were presented and testing continued with the subsequent stage.

During testing, each subject received up to four runs through the missing fundamental and masked missing fundamental stages with reminder stimuli presented between each run. If a subject met criterion with the reminder stimuli on three occasions but still did not successfully complete the stage, we concluded that the individual failed the task. Thus the procedure assured that a listener's failure to categorize the tonal complexes was based not on boredom with the task but rather on perceptual grounds.



*b. Pure tone groups.* For subjects in the pure tone groups, two experimental stages followed shaping. The discrimination stage was identical to shaping except for the introduction of no-signal trials. In the masked discrimination stage listeners were presented with the pure tones in combination with either the low-frequency noise or the high-frequency noise. If subjects were confused by the introduction of the noise the reminder procedure described above was employed. Across both the tonal complex and the pure tone groups, all infants who completed testing did so in 1–3 visits ( $M=1.31$ ), and all adults completed testing in one visit.

## II. RESULTS

### A. Data analyses

To evaluate individual performance, we determined the number of listeners meeting criterion in each stage. Because we were interested in subjects' best performance under different task demands, analyses of group performance tested responses on the last five signal and the last five no-signal trials in each stage. A principal analysis of variance (ANOVA) compared the number of responses on those trials with stage (discrimination/masking) and type of trial (signal/no-signal) as within-subjects factors and stimulus (tonal complex/pure tone) and noise (low frequency/high frequency) as between-subjects factors. Significant interactions were followed up with simple effects tests. These analyses included data only for those individuals who completed all experimental stages. To assure that the subjects in the tonal complex groups actually heard the pitch of the missing fundamental, a further analysis compared the number of responses on signal and no-signal trials for the missing fundamental stage only.

### B. Individual performance

#### 1. Adults

In the tonal complex group, all 18 adults met criterion in the shaping stage. Sixteen out of 18 adults (88.9% of those tested) met criterion in the discrimination stage within 12 to 17 trials ( $M=12.3$ ). The two adults who failed discrimination were the first to do so in a series of several experiments with similar stimuli (e.g., Clarkson and Rogers, 1995; Clarkson and Clifton, 1995). Reportedly, the students deliberately responded on all trials in order to end testing quickly. In the missing fundamental stage, all 16 adults who heard the sounds met criterion within 12–50 trials ( $M=21.6$ ). Only one of the eight adults (12.5%) receiving the tonal complexes in combination with the high-frequency noise successfully categorized the sounds, whereas all of the eight adults hearing the low-frequency noise did so.

In the pure tone group, 16 of 18 adult listeners (88.9%) reached criterion in the shaping stage, and all subjects tested met criterion in the discrimination stage within 12–17 trials (mean=12.3). All of the eight adults receiving the pure tones in combination with the high-frequency noise successfully discriminated the sounds, whereas none of the eight adults hearing the low-frequency noise did so. These results indicate that the stimulus and masker levels were appropriate to replicate Patterson's (1969) findings.

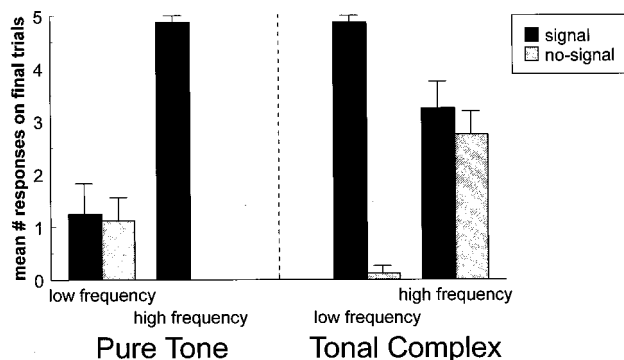


FIG. 1. Mean number of trials on which adults responded for the last five signal (solid bars) and the last five no-signal (striped bars) trials in the masking stage for the pure tone and the tonal complex groups. Note that for subjects in the pure tone group with the high-frequency noise, no turns occurred on no-signal trials.

#### 2. Infants

In the tonal complex groups, 44 of 49 (89.8%) infants met criterion in the first shaping stage, and 37 of 44 (84.1%) passed the second shaping stage. Thus across the two shaping stages 76% of the infants learned the task. Twelve of the 37 (32.4%) infants tested met criterion in the discrimination stage within 12–28 trials ( $M=18.7$ ), and six of those 12 infants met criterion in the missing fundamental stage within 14–36 trials ( $M=25.3$ ). All three of the three infants receiving the tonal complexes in combination with the low-frequency noise successfully categorized the sounds, whereas none of the three infants hearing the high-frequency noise did so.

In the pure tone group, 33 of 42 (78.6%) infants passed the first shaping stage, and 26 of those infants (78.8%) also met criterion in the second shaping stage. Thus 62% of the infants who started the testing proceeded to the discrimination stage. Six of 26 (23.1%) infants met criterion in the discrimination stage within 13–27 trials (mean=19.2). In the masked discrimination stage, all three infants receiving the pure tones in combination with the high-frequency noise successfully discriminated the sounds, whereas none of the three infants hearing the low-frequency noise did so.

### C. Group performance

#### 1. Adults

*a. Masking.* The principal ANOVA confirmed the individual performance at a group level by revealing a significant stimulus $\times$ noise $\times$ stage $\times$ type of trial interaction,  $F(1,28) = 24.4, p < 0.001$ . Follow-up simple effects tests for the discrimination stages revealed that adults responded more often on signal ( $M=4.97$ ) than on no-signal ( $M=0.0$ ) trials,  $F(1,28) = 259.027, p < 0.001$ . In the masking stages, simple effects tests yielded stimulus $\times$ noise $\times$ type of trial interaction,  $F(1,28) = 53.12, p < 0.001$ . As can be seen in Fig. 1, the means were in the predicted direction, with adults responding more often on signal than on no-signal trials for tonal complexes in the presence of the low-frequency noise and for pure tones combined with the high-frequency noise. Responding did not differ as a function of type of trial for tonal

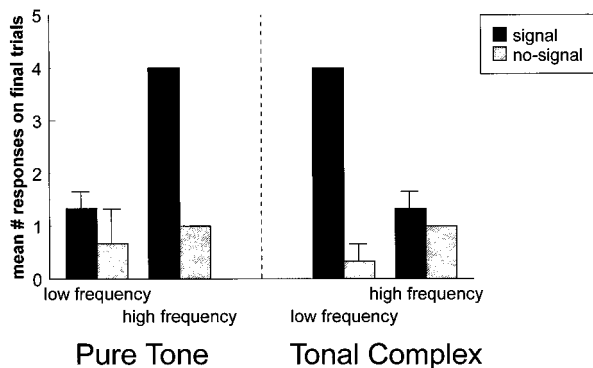


FIG. 2. Mean number of trials on which infants turned for the last five signal (solid bars) and the last five no-signal (striped bars) trials in the masking stage for the pure tone and the tonal complex groups. Where error bars are absent, there was no variability in the number of head turns.

complexes when combined with the high-frequency noise or for pure tones in the presence of the low-frequency noise.

*b. Missing fundamental.* For the missing fundamental stage, a separate ANOVA compared the number of responses for all subjects tested in that stage with type of trial (signal/no-signal) as a within-subjects factor and noise (low-frequency/high-frequency) as a between-subjects factor. This analysis yielded only a significant main effect of type of trial,  $F(1,15) = 1101.36$ ,  $p < 0.001$ , with adults responding more often on signal ( $M = 4.9$ ) than on no-signal ( $M = 0.6$ ) trials.

## 2. Infants

*a. Masking.* Infants' results paralleled those of adults with the principal ANOVA yielding a stimulus  $\times$  noise  $\times$  stage  $\times$  type of trial interaction,  $F(1,8) = 66.67$ ,  $p < 0.001$ . Follow-up simple effects tests for the discrimination stage revealed that infants turned more often on signal ( $M = 4.2$ ) than on no-signal ( $M = 0.8$ ) trials,  $F(1,8) = 711.11$ ,  $p < 0.001$ . For the masking stage, follow-up tests yielded a stimulus  $\times$  noise  $\times$  type of trial interaction,  $F(1,8) = 96.33$ ,  $p < 0.001$ , and the means for the various conditions were in the predicted direction. As can be seen in Fig. 2, infants who completed all stages turned more often on signal than on no-signal trials for tonal complexes in the presence of the low-frequency noise and for pure tones combined with the high-frequency noise. Infants responded in the same manner for tonal complexes when combined with the high-frequency noise or for pure tones in the presence of the low-frequency noise. The low variability in infants' responding, as indicated by the error bars in Fig. 2, increases confidence in these results despite the small number of infant subjects.

*b. Missing fundamental.* Infants turned more often on signal ( $M = 2.92$ ) than on no-signal ( $M = 1.58$ ) trials, but that difference failed to reach statistical significance,  $p = 0.105$ .

*c. Stimulus level.* To assess the possibility that infants' relatively poor performance resulted from the low stimulus level, we calculated proportion correct for all subjects in the discrimination and missing fundamental stages. This statistic permits us to compare our data more directly with Nozza's (1987) data for speech discrimination at various stimulus

levels. For infants who heard the tonal complexes, proportion correct averaged 0.63 for the discrimination stage. Infants in the pure tone groups responded correctly on 0.62 of the discrimination trials. In the missing fundamental stage, proportion of correct responses averaged 0.63.

## III. DISCUSSION

These findings demonstrate that adults and infants tested in an operant conditioning paradigm discriminate the pitch of the missing fundamental in the presence of a low-frequency noise and the pitch of pure tones in the presence of a high-frequency noise. This performance is consistent with that previously reported for adults (Patterson, 1969) and suggests that infants, like adults, do not rely upon combination tones to hear the pitch of the missing fundamental.

To the extent that the present results eliminate the simple difference tone,  $f_2 - f_1$ , and other combination tones as the basis for infants' pitch perception, these data are consistent with the conclusions drawn from infants' perception of inharmonic complexes (Clarkson and Clifton, 1995). Although infants can hear the pitch of some inharmonic signals, their performance deteriorates as signals become increasingly inharmonic. As such, infants' performance parallels the decreasing salience of increasingly inharmonic signals for adults (deBoer, 1976; Wightman, 1973). Because the strength of the combination tones should remain constant regardless of the degree of inharmonicity in a tonal complex (Hall, 1972), these findings suggested that combination tones are unlikely to provide the basis for infants' perception of pitch for inharmonic or harmonic complexes.

Although combination tones do not provide the basis for hearing the pitch of the missing fundamental, distortion products do influence adults' pitch perception. Houtsma and Goldstein (1972) compared the strength of pitch for monotic and dichotic presentation of tonal complexes. Under monotic conditions, two successive harmonics of a missing fundamental were presented to one ear, which introduced combination tones into the internal spectrum of the listeners. The presentation of one harmonic to each ear in the dichotic condition prohibited the peripheral generation of combination tones. Under both conditions, listeners identified a pitch corresponding to the missing fundamental of the two harmonics, but the strength of the pitch percept was greater for the monotic than for the dichotic presentation, suggesting that combination tones might contribute to pitch. When components equal in frequency, amplitude, and phase to the combination tones were added back into the dichotic stimuli, performance improved to equal that in the monotic condition. Thus combination tones, while not the primary determinant of pitch, do contribute to perception of the missing fundamental.

The generation and perception of combination tones by infants has never been studied. Hence, we do not know whether combination tones exist for infants and, if so, whether they are similar to those perceived by adults. If combination tones do exist and are consistent with those of adults, then presumably those distortions would add to the internal spectra of sounds and increase the strength of the pitch of harmonic tonal complexes relative to inharmonic

complexes. To the extent that infants' frequency resolution appears to be similar to that of adults (Spetner and Olsho, 1990), the generation of combination tones might be similar for adults and infants. Future research must determine the contribution of combination tones in infants to explain what appears to be a decreased salience of pitch for infants relative to adults.

Infants' overall performance in the present experiment was poorer than that reported in previous research. This relatively poor performance is likely due to the lower level of the stimuli in this study (50 dB) as compared with previous studies (55–60 dB). Nozza (1987) has reported that infants' discrimination performance for speech stimuli decreases from a proportion correct of 0.79–0.60 when the stimulus level is reduced from 60 dB to 50 dB. Likewise, infants' discrimination performance for tonal complexes decreased from a proportion correct of 0.80 when sounds were presented at 55–60 dB (Clarkson and Clifton, 1995; Clarkson and Rogers, 1995) to 0.63 with a 50-dB sound level.

Even for those infants who passed discrimination, perception of the pitch of the missing fundamental from tonal complexes presented at 50 dB appeared difficult in this experiment. Although performance approached significance ( $p=0.105$ ), as a group infants failed to reliably categorize the tonal complexes according to the missing fundamental. In a previous study (Clarkson and Rogers, 1995), where infants heard the same tonal complexes presented here except at 55–60 dB, infants achieved a proportion correct of 0.73. With the 50-dB stimuli in the present study, the proportion correct was 0.63. Thus just as performance in a simple discrimination task deteriorates as the sound level decreases, the more complex task of hearing the pitch of the missing fundamental is also influenced by stimulus level. The comparable performance by infants in both of these tasks (proportion correct=0.63) as well in Nozza's (1987) discrimination task with 50-dB speech stimuli (proportion correct=0.60) suggests that infants do, in fact, hear the pitch of the missing fundamental but that low stimulus levels interfere with that perception.

Although the lowered stimulus level, in and of itself, probably contributed to the infants' difficulty hearing the pitch of the missing fundamental, the lowered level may also have reduced the salience of that pitch. As stimulus level decreases, so does the level of combination tones resulting from nonlinearities in the auditory system (Goldstein, 1967) with the simple difference tone becoming inaudible below 50 dB for two-component tonal complexes (Plomp, 1965). To the extent that combination tones increase the strength of perceived pitch for adults (Houtsma and Goldstein, 1972), the 50-dB stimuli presented herein should have evoked a weaker pitch percept than the 55–60 dB stimuli presented in previous research. Under other conditions, infants' performance has been particularly poor when they were tested with sounds that evoke a weak pitch percept for adults. That is, infants' performance deteriorated when tonal complexes were rendered increasingly inharmonic (Clarkson and Clifton, 1995), when the number of harmonics in tonal complexes was decreased (Clarkson *et al.*, 1996), and when tonal complexes contained only high-frequency, unresolvable en-

ergy (Clarkson and Rogers, 1995). If combination tones do increase the salience of pitch for infants, then the relatively weak pitch associated with the lowered stimulus level in the current study is likely to have adversely affected infants' pitch perception. That infants' performance is more strongly impaired than is adults' performance for sounds having a weak pitch suggests that their central pitch processor may be immature.

If infants have somewhat immature pitch processors at 7 months of age, their poor group performance in the missing fundamental stage might also reflect individual differences in the maturity of the pitch processor. In which case, only infants with the most mature pitch processors would discriminate changes in the pitch of the missing fundamental when low stimulus levels are employed. Those same infants respond like adults when a masking noise is added to the stimuli. Other infants having less mature pitch processors might not hear the pitch of the missing fundamental under less than ideal conditions, including when the stimulus level is low. Despite the difficulties posed by the sound pressure level here, the masking data for the 7-month-old infants who showed clear evidence of hearing the pitch of the missing fundamental are consistent with those reported for adults (Patterson, 1969; Experiment 1) and suggest that infants do not rely on combination tones to hear the pitch of the missing fundamental.

According to the present experiment and previous research, infants' pitch perception shows striking parallels to that of adults (Clarkson and Clifton, 1995; Clarkson and Rogers, 1995). Nonetheless, infants' relatively poorer performance compared to adults with high-frequency energy, inharmonic complexes, small numbers of harmonics, and low stimulus level suggest that infants' central pitch processor may be immature. Although infants do not rely on combination tones to hear the missing fundamental, it remains to be seen whether combination tones contribute to the internal spectrum and therefore pitch strength in infants as in adults. The relative difficulty infants experienced in hearing the pitch of the missing fundamental for low intensity stimuli would suggest that distortion products may contribute to the strength of pitch for infants.

## ACKNOWLEDGMENTS

This research was presented as a master's thesis in partial fulfillment of the requirements for a Master of Arts degree for the first author. We thank Robin Morris and Mary Morris for their comments and assistance as members of the thesis committee.

This research was supported by Grants Nos. HD-16480 from the National Institute of Child Health and Human Development, and DC-00074 from the National Institute of Deafness and Other Communication Disorders to MGC. Experiment 1 was presented at the Annual Meeting of the Association for Research in Otolaryngology, St. Petersburg Beach, Florida, February 1996. Experiment 2 was presented at the Biennial Meeting of the International Society for Infant Studies, Providence, Rhode Island, April 1996. We thank Angela Fox, Sherry Godfrey, Billy Meyers, Rhonda Martin, and Sheridan Miciek for their assistance in data col-

lection and reduction. We thank Sheridan Miciek for her comments on the manuscript. Finally, we thank all the infants and parents who participated in this research.

<sup>1</sup>The experimenter could vary the reinforcer to maintain the subject's interest. Audiovisual reinforcers for adults included *Beyond the Mind's Eye* and *Fantasia*. An informal survey of undergraduate students indicated that these video were engaging to the population of interest. Audiovisual reinforcers for infants included *Barney and Friends*, *Disney Sing-a-long Songs*, and a customized video of women speaking infant-directed speech, and children singing, dancing, and playing.

<sup>2</sup>Eighteen infants were tested with only one shaping stage wherein stimuli had a sound level of 50 dB. Five out of 18 (27.8%) infants successfully met criterion in the shaping and discrimination stages. In previous studies using the same stimuli but with a sound level of 55–60 dB, 55 of 66 (83.3%) 7-month-old infants passed the shaping and discrimination stages (Clarkson and Clifton, 1995; Clarkson and Rogers, 1995).

Bakeman, R. (1992). *Understanding Social Science Statistics: A Spreadsheet Approach* (Erlbaum, Hillsdale, NJ).

Carlyon, R. P., and Shackleton, T. M. (1994). "Comparing the fundamental frequencies of resolved and unresolved harmonics: Evidence for two pitch mechanisms?," *J. Acoust. Soc. Am.* **95**, 3541–3554.

Clarkson, M. G., and Clifton, R. K. (1985). "Infant pitch perception: Evidence for responding to pitch categories and the missing fundamental," *J. Acoust. Soc. Am.* **77**, 1521–1528.

Clarkson, M. G., and Clifton, R. K. (1995). "Infants' pitch perception: Inharmonic tonal complexes," *J. Acoust. Soc. Am.* **98**, 1372–1379.

Clarkson, M. G., and Rogers, E. C. (1995). "Infants require low-frequency energy to hear the pitch of the missing fundamental," *J. Acoust. Soc. Am.* **98**, 148–154.

Clarkson, M. G., Martin, R. L., and Miciek, S. G. (1996). "Infants' perception of pitch: Number of harmonics," *Inf. Behav. Dev.* **19**, 191–197.

deBoer, E. (1976). "On the "residue" and auditory pitch perception," in *Handbook of Sensory Physiology*, edited by W. D. Keidel and W. D. Neff (Springer-Verlag, Berlin), pp. 479–583.

Goldstein, J. L. (1967). "Auditory nonlinearity," *J. Acoust. Soc. Am.* **41**, 676–689.

Goldstein, J. L., Gerson, A., Srulovicz, P., and Furst, M. (1978). "Verification of the optimal probabilistic basis of aural processing in pitch of complex tones," *J. Acoust. Soc. Am.* **63**, 486–497.

Hall, J. L. (1972). "Auditory distortion products,  $f_1 - f_2$  and  $2f_1 - f_2$ ," *J. Acoust. Soc. Am.* **51**, 1863–1871.

Houtsma, A. J. M., and Goldstein, J. L. (1972). "The central origin of the pitch of complex tones: Evidence from musical interval recognition," *J. Acoust. Soc. Am.* **51**, 520–529.

Houtsma, A. J. M., and Smurzynski, J. (1990). "Pitch perception and discrimination for complex tones with many harmonics," *J. Acoust. Soc. Am.* **87**, 304–310.

Licklider, J. C. R. (1954). "Periodicity pitch and place pitch," *J. Acoust. Soc. Am.* **26**, 945(A).

Nozza, R. J. (1987). "Infant speech-sound discrimination testing: Effect of stimulus intensity and procedural model on measures of performance," *J. Acoust. Soc. Am.* **81**, 1928–1939.

Patterson, R. D. (1969). "Noise masking of a change in residue pitch," *J. Acoust. Soc. Am.* **45**, 1520–1524.

Plomp, R. (1965). "Detectability threshold for combination tones," *J. Acoust. Soc. Am.* **37**, 1110–1123.

Ritsma, R. J. (1962). "Existence region of the tonal residue I," *J. Acoust. Soc. Am.* **34**, 1224–1229.

Ritsma, R. J., and Hoekstra, A. (1974). "Frequency selectivity and the tonal residue," in *Facts and Models in Hearing*, edited by E. Zwicker and E. Terhardt (Springer-Verlag, Berlin), pp. 156–163.

Schouten, J. F., Ritsma, R. J., and Cardoza, B. L. (1962). "Pitch of the residue," *J. Acoust. Soc. Am.* **34**, 1418–1424.

Smoorenburg, G. F. (1970). "Pitch perception of two-frequency stimuli," *J. Acoust. Soc. Am.* **48**, 924–941.

Spetner, N. B., and Olsho, L. W. (1990). "Auditory frequency resolution in human infancy," *Child Dev.* **61**, 632–652.

Wightman, F. L. (1973). "The pattern transformation model of pitch," *J. Acoust. Soc. Am.* **54**, 407–416.

# Electrode discrimination and speech recognition in postlingually deafened adult cochlear implant subjects

Terry A. Zwolan

*Department of Otolaryngology, University of Michigan, Ann Arbor, Michigan 48109-0312*

Leslie M. Collins

*Department of Electrical and Computer Engineering, Box 90291, Duke University, Durham, North Carolina 27708-0291 and Department of Electrical Engineering and Computer Science, University of Michigan, Ann Arbor, Michigan 48109-2122*

Gregory H. Wakefield

*Department of Electrical Engineering and Computer Science, University of Michigan, Ann Arbor, Michigan 48109-2122*

(Received 8 March 1996; accepted for publication 28 August 1997)

This study investigated the relationship between electrode discrimination and speech recognition in 11 postlingually deafened adult cochlear implant subjects who were implanted with the Nucleus/Cochlear Corporation multichannel device. The discriminability of each electrode included in a subject's clinical map was measured using adaptive and fixed-level discrimination tasks. Considerable variability in electrode discriminability was observed across subjects. Two subjects could discriminate all electrodes, and discrimination performance by the remaining nine subjects varied from near perfect to very poor. In these nine subjects, the results obtained from the discrimination tasks were used to create a map that contained only discriminable electrodes, and subjects' performance on speech recognition tasks using this experimental map was measured. Four different speech recognition tests were administered: a nine-choice closed-set medial vowel recognition task, a 14-choice closed-set medial consonant recognition task, the NU6 Monosyllabic Words Test [T. W. Tillman and T. Carhart, Tech. Rep. No. SAM-TR-66-55, USAF School of Aerospace Medicine, Brooks Air Force Base, Texas (1966)] scored for both words and phonemes correct, and the Central Institute for the Deaf (CID) Everyday Sentences test [H. Davis and S. R. Silverman, *Hearing and Deafness* (Holt, Rinehart, and Winston, New York, 1978)]. Seven of the nine subjects tested with the experimental map showed significant improvement on at least one speech recognition measure, even though the experimental map contained fewer electrodes than the original map. Three subjects' scores improved significantly on the CID Everyday Sentences test, three subjects' scores improved significantly on the NU6 Monosyllabic Words test, and five subjects' scores improved significantly on the NU6 Monosyllabic Words test scored for phonemes correct. None of the subjects' scores improved significantly on either the vowel or consonant tests. No significant correlation was observed between electrode discrimination ability and speech recognition scores or between electrode discrimination ability and improvement in speech recognition scores when programmed with the experimental map. The results of this study suggest that electrode discrimination tasks may be used to improve speech recognition of some cochlear implant subjects, and that each electrode site does not necessarily provide perceptually distinct information. © 1997 Acoustical Society of America. [S0001-4966(97)05212-0]

PACS numbers: 43.66.Ts, 43.66.Fe, 43.66.Ba, 43.64.Me [JWH]

## INTRODUCTION

Speech processing strategies for multichannel cochlear implants assume that different electrodes will activate neurons in tonotopically disparate regions of the cochlea and that stimulation of each electrode provides perceptually distinct information. Thus it is assumed that a unique place pitch percept is associated with each electrode. The MPEAK processing algorithm of the Nucleus/Cochlear Corporation device, which was used by all subjects in this study, uses electrode position to encode acoustic formant frequency [see Skinner (1991) for a detailed description of the MPEAK encoding strategy that was used in this study]. Under this encoding strategy, some speech cues may be lost if some elec-

trodes are indiscriminable. Multichannel performance by subjects implanted with this device may be optimized when the subject's map is limited to only include discriminable electrodes. However, the discriminability of electrodes is rarely assessed by clinicians when programming subjects' speech processors as it is routinely assumed that all of the electrodes in a subjects' array are discriminable. Thus speech encoding strategies must be robust to variations in electrode discrimination abilities across subjects.

Several investigators have used pitch scaling, labeling, or ranking techniques to measure the pitch associated with stimulation of each electrode, and have in some cases used this data to infer electrode discriminability in cochlear im-

plant subjects (Eddington *et al.*, 1978; Tong *et al.*, 1980; Tong *et al.*, 1982; Shannon, 1983; Tong and Clark, 1985; Clark *et al.*, 1988; Townshend *et al.*, 1987; Busby *et al.*, 1994; Nelson *et al.*, 1995). In general, these studies have found that the pitch percepts elicited by electrical stimulation vary in an orderly fashion along the electrode array for most subjects, and that the perceived order matches the presumed tonotopic organization of an unimpaired cochlea. Very few studies have investigated the effect that deviations from the expected structure of the pitch percept have on speech recognition. Additionally, the effect of indiscriminable electrodes on speech recognition has not been determined. Since a relationship between nerve survival and electrode discrimination was observed by Pflingst *et al.* (1985) in monkeys, and nerve survival may be related to speech recognition, electrode discrimination and speech recognition may be related in human subjects.

Although no studies have thoroughly investigated the relationship between speech recognition and electrode discrimination, three investigators have examined the relationship between place- or pitch-based psychophysical measures and speech recognition. Nelson *et al.* (1995) used an electrode ranking procedure to examine the relationship between subjects' ability to discriminate electrodes on the basis of pitch or sharpness and their ability to recognize consonants. They reported that ability to rank order electrodes according to pitch varied considerably across subjects, that electrode ranking performance improved linearly with increases in the spatial separation between electrodes, and that relatively good perception of consonant phoneme information did not necessarily require excellent place-pitch sensitivity. They concluded that the disparity between place-pitch sensitivity and consonant recognition may have been an indication that the spectrally coded speech information provided by the Nucleus speech processor failed to take advantage of the excellent place-pitch sensitivity shown by some of their subjects.

Busby *et al.* (1993) measured the ability of subjects implanted with the Nucleus/Cochlear Corporation device to discriminate electrode trajectories (stimuli in which electrode position was varied over time in an orderly fashion). Improvement in speech recognition performance between a single-electrode speech coding strategy and a multiple-electrode speech coding strategy was observed in subjects with good electrode trajectory discrimination, however, this observation was not statistically evaluated. Dorman *et al.* (1990) examined the relationship between pitch scaling and speech recognition in eight subjects implanted with the Ineraid device. Pitch magnitude was rated for 100–3000-Hz sinusoids processed through the Ineraid processor. They concluded that subjects who demonstrated above-average speech recognition also demonstrated pitch increases over a wider range of frequencies than subjects with poorer speech recognition. Although no statistical analyses were performed, the authors suggested that differences in speech recognition among Ineraid users may be affected by the range of pitch available through the implant. However, in their study, it is possible that the lower-frequency stimuli elicited different rate pitch cues, while the higher-frequency stimuli that could

not be discriminated on the basis of rate were coded onto different electrodes. Thus rate-pitch and place-pitch cues may have been confounded.

The studies described above have evaluated various aspects of the percepts elicited with electrical stimulation that are presumably spatially differentiated, primarily with respect to the relatively coarse measures of pitch. These studies have not measured the complete set of discriminable electrodes in the implanted electrode array. Additionally, it has not been determined whether results from such studies can be used clinically to improve subjects' ability to understand speech with a cochlear implant.

In the present study, electrode discrimination was evaluated in a group of 11 implanted subjects, and the relationship between speech recognition and electrode discrimination was investigated. An experiment was performed to determine if utilization of a speech processor that only stimulated discriminable electrodes would result in improved speech recognition. Thus this study investigated whether the removal of electrodes that were indiscriminable from other electrodes in the array would result in an improved ability to understand speech. The relationship between electrode discrimination and speech recognition was also investigated.

## I. METHODS

### A. Subjects and equipment

Eleven postlingually deafened adults served as subjects for this study. All subjects were implanted with the Nucleus/Cochlear Corporation Mini 22 multichannel device. Demographic information regarding the subjects is listed in Table I. All subjects had used their device a minimum of six months.

Only electrodes used in the subjects' clinically programmed map were stimulated in the electrode discrimination task; this number ranged from 10 to 20. (A map is the set of data that is used to translate acoustic signal features to stimulus parameters for subjects implanted with the Nucleus/Cochlear Corporation device. Among other things, a map contains the list of electrodes that are available for stimulation for a particular subject). All possible electrodes were not used in subjects' clinically programmed maps for a variety of reasons, including unpleasant sound associated with stimulation, partial insertion of the electrode array, and facial nerve stimulation. The electrodes were numbered from 1 to 22 in a basal to apical direction. Electrode pairs were identified by the active electrode of the pair, which in all cases was the basal member of the pair. The electrode spacing used to test each subject was the same as the one used in their clinically programmed map: Stimuli were presented in a bipolar plus one (BP+1) mode of stimulation (1.5-mm separation between active and indifferent electrodes) for nine of the 11 subjects and in a BP+2 mode (2.25-mm separation) for two subjects. Subjects participated in eight to ten test sessions lasting 2–4 h each.

Stimuli were presented to subjects through a Cochlear Corporation Mini Speech Processor (MSP) connected to a Cochlear Corporation Dual Processor Interface (DPI). A Compaq 386 computer controlled the psychophysical proce-

TABLE I. Biographical information for the implanted subjects. Dynamic range was averaged across all active electrodes for each subject and is presented in dB.

Subject	Sex	Age (years)	Age at onset of profound deafness (years)	Age at implantation (years)	Mean/standard deviation of dynamic range across all active electrodes (in dB)	Mode of stimulation
S1	M	49	33	45	8.9/7	BP+1
S2	F	75	40	71	2.2/4	BP+1
S3	F	70	51	66	4.7/1.8	BP+1
S4	M	33	7	31	7.5/2.0	BP+1
S5	M	67	16	62	6.6/1.1	BP+1
S6	M	66	25	62	6.9/1.4	BP+1
S7	F	51	42	47	3.2/9	BP+1
S8	F	40	8	39	5.4/2.5	BP+1
S9	M	60	20	57	11.6/2.9	BP+2
S10	M	61	12	57	10.6/1.6	BP+2
S11	F	73	70	72	6.3/1.0	BP+1

ture and the interface system. A color CRT was used to display stimulus cueing and to display response feedback to the subjects.

## B. Stimuli

### 1. Electrode discrimination

The stimuli for the two electrode discrimination tasks were 200-ms pulse trains consisting of biphasic rectangular pulses presented at a rate of 250 pps. Cochlear Corporation “current level” stimuli were used for testing with the pulse width held constant at 204  $\mu$ s per phase. When “current level” stimuli are used, the pulse width for a given electrode pair is fixed and only the current amplitude is variable. Such current units are arbitrary and vary from 1 to 239 (vary from approximately 20 to 1750  $\mu$ A). Each unit represents an approximately equal fixed percentage increase or decrease (approximately 2%) in the amount of charge delivered to the active electrode and is dependent upon each individual subject’s implant (Cochlear Corporation Technical Reference Manual, 1996).

### 2. Speech recognition

Four different speech recognition tests were administered: a nine-choice closed-set medial vowel recognition task in which stimuli were randomly presented five times each (heed, had, heard, hud, who’d, hawed, hid, head, and hood), a 14-choice closed-set medial consonant recognition task in which stimuli were randomly presented five times each (apa, aba, ama, ana, ata, ada, ava, afa, aga, aka, asa, aza, asha, and aja), the NU6 Monosyllabic Words Test consisting of 50 possible words and 175 possible phonemes correct (Tillman and Carhart, 1966), and the CID Everyday Sentences test (Davis and Silverman, 1978), which was comprised of 20 sentences containing 100 key words.

## C. Tasks

This study consisted of loudness balancing, electrode discrimination, and speech recognition tasks. Loudness balancing was performed prior to electrode discrimination to

reduce the confounding effect that differences in loudness may have had upon measures of electrode discrimination. Electrode discrimination was measured using two different procedures: an adaptive procedure to estimate the discrimination limen and a fixed-level procedure for finer estimates of the limen. The speech recognition task consisted of four different tests that examined closed-set vowel and consonant recognition and open set recognition of phonemes, words, and sentences. Loudness balancing was performed during the first one or two sessions, and once an acceptable balance was achieved, the procedure was not repeated. The electrode discrimination tasks were performed during sessions 2–9, and speech recognition testing was performed during the final test session.

### 1. Determination of “soft” and “most acceptable loudness” levels

A method of adjustment was used to determine subjects’ “soft” and “most acceptable loudness” levels. During this procedure, subjects used a control knob to increase or decrease the level of stimulation until it reached a level that was “soft.” This level was noted and the subject then increased the level of stimulation until a level that was “the loudest they could listen to comfortably for long periods of time,” their “maximum acceptable loudness level,” was obtained. Stimulus parameters used to determine the “soft” and “most acceptable loudness” levels were the same as those used in the other tasks and included 200-ms pulse trains consisting of biphasic rectangular pulses presented at a rate of 250 pps. Pulse width was held constant at 204  $\mu$ s per phase.

### 2. Loudness balance design

An adjacent-reference loudness balance design was used in this study where each electrode was balanced to its neighbor in ascending electrode order. In this design, the loudness of the second electrode was adjusted to match that of the first. This value became the reference loudness against which the level of the third electrode was adjusted to match the second, and so on until the loudness of the last electrode was

adjusted. The primary advantage of this method is that the loudness balance is most accurate between adjacent electrodes, although the accuracy decreases systematically as the separation between electrodes increases. An additional advantage of this procedure is that the entire procedure can be accomplished in a single 2-h experimental session while still maintaining a reliable psychophysical method.

### **3. Loudness balancing task**

The procedure used to balance loudness utilized a subjective version of Levitt's 2-down, 1-up procedure for matching the loudness of a comparison stimulus to that of a standard stimulus (Jesteadt, 1980). For each pair of observation intervals, subjects were asked to select the interval containing the "louder" stimulus. Two tracks were defined in this task according to their update rules and initialization point, and the tracks were selected at random from trial to trial. In the case of the "louder" track, the amplitude of the comparison stimulus was initialized at a level well above the expected point of subjective equality. The amplitude, or current level, of the comparison stimulus was decremented by one Cochlear device amplitude step when the subject indicated that the comparison stimulus was louder than the standard on two consecutive trials from the "louder" track. Once the comparison stimulus was judged to be softer than the standard, the amplitude, or current level, of the comparison stimulus was incremented by one Cochlear device amplitude step. In the "softer" track, the amplitude was initialized at a level well below the estimated point of subjective equality. In this track, two "softer" judgments for the comparison stimulus were required to increase the amplitude, and one "louder" judgment was required to decrease the amplitude. The block of trials proceeded with the stimuli drawn either from the louder or softer track on each trial, and the subject's response was used to update the appropriate track.

In the loudness balancing task, a 1-down, 1-up update rule was used for the first six reversals of each track to speed convergence to the region of the discrimination threshold. After six reversals, the update rule was switched to the standard 2-down, 1-up rule and threshold for loudness discrimination in each track was determined by averaging the stimulation amplitudes at each of the final eight reversals. The estimates of the threshold obtained from each of the two tracks were averaged to estimate the point of subjective equality. The loudness of each pair of adjacent electrodes was balanced once using this procedure. The balanced values obtained for each electrode were used for both of the electrode discrimination tasks.

The level of the first reference electrode was determined by calculating the midpoint between the level where the subject indicated the sound was "soft" and the level that was their "maximum acceptable loudness level" (measured in Cochlear device amplitude steps) for the most basal (lowest numbered) electrode. Each subject verified that the loudness level of this stimulus was comfortable.

Subjects were asked to report any problems or concerns with the loudness balancing task at any point during the procedure. Three of the 11 subjects reported a drift in the perceived loudness across a block of trials, and in these cases

the procedure was repeated. None of the three subjects reported a drift when the procedure was repeated. In addition, if the values that were obtained did not appear to be consistent with the approximate midpoint of the dynamic range, subjects were queried as to whether the sounds appeared to have approximately equal loudness. This pattern of data was observed in two subjects, however, both subjects reported an accurate loudness balance (see the Results section for additional details).

### **4. Adaptive electrode discrimination task**

The discrimination limen for a reference electrode was measured adaptively using a two interval forced-choice procedure. Testing was performed with the adaptation proceeding in both basal and apical directions, and every electrode in the array served as the reference electrode for a block of trials. Each trial consisted of four observation intervals. The first and fourth intervals served as flanking cues and always contained the reference stimulus. Flanking cues were used to provide subjects with additional information on which to base their response. The comparison stimulus occurred with equal probability in either the second or third interval. A 500-ms interval separated each of the four observation intervals. Subjects were asked to indicate the interval in which the "different" stimulus was presented, and feedback was provided.

For the first six reversals, following one correct response the difference in the position of the comparison electrode relative to that of the reference electrode was decremented by 1. Following one incorrect response, this difference was incremented by 1. For the final eight reversals, two correct responses were required to decrement the difference in electrode positions, resulting in an estimate of the 70.7% discrimination limen. This adaptive evaluation procedure determined the closest electrode that was consistently discriminated from the reference electrode in either an apical or basal direction.

During each test set, the closest discriminable electrode to each electrode was determined for a single direction (basal or apical). Testing was performed first in a basal direction, followed by testing in an apical direction. Testing was alternated between the two directions until data collection was completed. Discrimination limens for all electrodes programmed into subjects' clinical maps were measured. One block of trials was performed in each test set for each electrode. A minimum of three sets of data were obtained in each direction for each electrode. The values of the discrimination limen obtained for each electrode during the final three test sets in each direction were averaged to assign final values of the discrimination limen to each electrode.

### **5. Electrode discrimination verification task**

A fixed-level procedure was used to verify the results of the adaptive electrode discrimination task and to more precisely determine which electrodes would be included in the experimental MAPs. Most electrodes determined to be indistinguishable from a reference electrode, as well as the closest electrode that was consistently discriminated from the refer-



ence electrode, were included in the verification task. For example, if the results of the adaptive electrode discrimination task indicated that electrodes No. 6 and No. 7 were indiscriminable and that electrodes No. 6 and No. 8 were discriminable, electrodes No. 6 and No. 7 and No. 6 and No. 8 were compared in the verification task.

The verification task consisted of a 2IFC fixed-level procedure. Discrimination was measured in 60 trial blocks for each pair of electrodes tested. During each trial, subjects were presented with two stimuli and were asked to indicate if the two stimuli were the “same” or “different.” Same and different trials were equally likely and feedback was provided after each response.  $d'$  values were calculated for each pair of electrodes tested. Stimuli used in the verification task were identical to those used in the adaptive task: 200-ms pulse trains consisting of biphasic rectangular pulses presented at a rate of 250 pps. Pulse width was held constant at 204  $\mu$ s per phase.

### 6. Speech recognition task

Four different speech recognition tests were used in this study: a nine-choice closed-set medial vowel recognition task in which all stimuli were randomly presented five times each for a total of 45 stimuli, a 14-choice closed-set medial consonant recognition task in which stimuli were randomly presented five times each for a total of 70 stimuli, the NU6 Monosyllabic Words Test which contained 50 monosyllabic words and 150 phonemes, and the CID Everyday Sentences test which contained 100 key words presented in 20 different sentences. Different randomizations of these tests were administered to subjects under two test conditions: (1) while they utilized a map containing all functioning electrodes (clinical map), and (2) while they utilized a map containing only discriminable electrodes as determined by the electrode discrimination experiments (experimental map). For example, the most basal electrode (No. 1) was included in the map. Then, its closest discriminable electrode was determined (e.g., No. 3) and was also included in the map. The closest discriminable electrode for electrode No. 3 was then determined and was also included in the map. This process was repeated until the results for the entire electrode array were considered. The order in which the speech recognition tests were administered was random, as was the order in which the various maps were tested (clinical map versus experimental map). Subjects had no previous experience using the experimental map prior to speech recognition testing.

All maps were created using the default linear-logarithmic frequency spacing available with the Diagnostic Programming Software (Cochlear Corporation Audiologist's Handbook, 1993). Additional map parameters, such as percentage of threshold and comfort level reduction, base level,  $Q$  value, and noise cut out level, were identical for the two maps. All maps employed the MPEAK encoding strategy (Skinner, 1991) programmed to deliver stimuli in Cochlear Corporation “Stimulus level” units, the implications of which will be discussed later. The sensitivity control setting used by subjects during speech testing was identical for the two maps. The order in which the two maps were tested was random.

Subjects were tested in an IAC sound-treated booth. Taped stimuli were presented to a soundfield at a level of 70 dB SPL. Subjects were instructed to listen to the stimuli and to write down the word or sentence following its presentation. A single presentation of each speech token was allowed per trial.

## II. RESULTS

### A. Loudness balancing task

Standard deviations of the estimates of the discrimination limens were calculated to evaluate the consistency of the loudness balancing procedure. In addition, the number of times that the limen from the “louder” track was lower than the limen from the “softer” track was also determined. For each subject, the standard deviation of the reversal amplitudes was calculated in both tracks for all electrodes. The average standard deviation across all subjects in the “louder” track was 1.97 Cochlear device amplitude steps, and the average standard deviation in the “softer” track was 1.98 amplitude steps. The maximum standard deviations (3.56 and 3.02 in the “louder” and “softer” tracks, respectively) were observed in subject S9. The discrimination limen for the “louder” track was greater than the discrimination limen for the “softer” track in all but seven of the 162 blocks performed by the subjects. The magnitude of the difference between the two tracks in these seven cases were 0.2, 0.1, 0.2, 0.1, 0.8, 0.9, and 3.7 Cochlear device amplitude steps. In all of these cases, the midpoint of the two limens was reported by the subjects to provide an equivalent loudness to the reference stimulus.

The quality of the data obtained from the loudness balancing task was also analyzed by examining the relationship between the discrimination limens obtained from the two tracks for each electrode and the “soft” and “maximum acceptable loudness” values that had been measured for each electrode at the onset of the experiment. An example of the data obtained from two of the subjects is shown in Fig. 1, which illustrates the loudness balance data (circles), measured “soft” and “loud” levels (dashed lines with triangular symbols), and “soft” and “loud” levels obtained from the subjects' map (solid lines with triangular symbols). In nine of the 11 subjects, no apparent biases in the data were observed. The top portion of Fig. 1 contains a representative sample of the data obtained from one of these subjects (S1). In two of the 11 subjects (S2 and S3), the analysis indicated that loudness was potentially decreasing in a basal to apical direction when evaluated against the measured “soft” and “loud” levels, although both subjects indicated that the stimuli presented across the electrodes were in fact loudness balanced. The data for subject S2 is plotted in the lower portion of Fig. 1. However, when the data is evaluated against the “soft” and “loud” levels obtained from the subjects' map, it appears that the “soft” and “loud” levels obtained experimentally are not a valid indicator of the true dynamic range of the electrodes, and that the loudness balance results are in fact valid (as reported by the subjects).

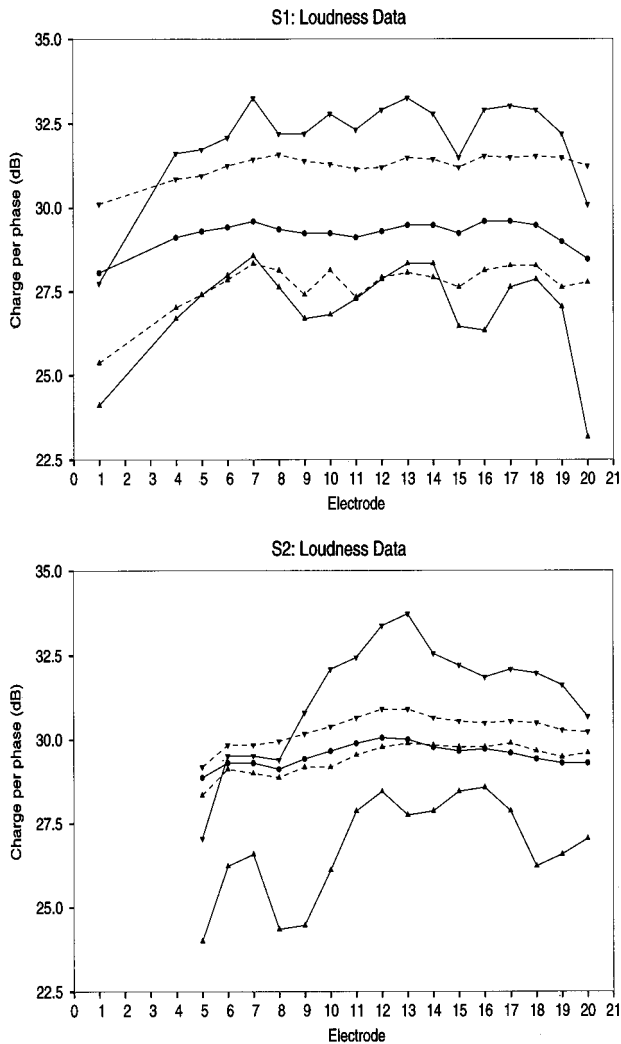


FIG. 1. Loudness balancing task results for two subjects. The ordinate plots the electrode number, and the abscissa lists amplitude in charge per phase (dB). The measured threshold and maximum acceptable loudness levels are plotted with dashed lines and upward and downward pointing triangles, respectively. The threshold and maximum acceptable loudness levels obtained from the subjects' map are plotted with solid lines and upward and downward pointing triangles, respectively. The average results from the loudness balance task are plotted with a solid line and filled circles.

## B. Electrode discrimination tasks

### 1. Adaptive electrode discrimination task

The results obtained from the 11 subjects on the electrode discrimination task are displayed in Fig. 2. This figure displays electrode discrimination data for each subject and indicates the discriminability of a reference electrode (abscissa) as a function of the closest discriminable electrode (ordinate) as measured with a minimal step of one electrode. Electrodes are numbered from 1 to 20 in a basal to apical direction. Data are provided for responses obtained in both basal and apical directions. The ideal discrimination values are indicated in the figures by dotted lines and lie at  $x - 0.5$  for testing performed in an apical direction, and by dashed lines at  $x + 0.5$  for testing performed in a basal direction, where  $x$  indicates the reference electrode number. The 0.5 limit was determined by the output of the adaptive algorithm and was based on the average of the final eight reversal

points. For example, perfect discrimination of electrode No. 7 was represented by a score of 6.5 when tested in an apical direction and by a score of 7.5 when tested in a basal direction. Such scores indicated that a subject was able to perfectly discriminate electrodes No. 6 and No. 7 as well as electrodes No. 7 and No. 8.

Two subjects (S10 and S11) demonstrated perfect discrimination of all electrodes when tested in both apical and basal directions. Six subjects (S1, S2, S3, S5, S6, and S9) demonstrated only a few indiscriminable electrodes, while the other three subjects (S4, S7, and S8) demonstrated poor discrimination of several electrodes. Across the group of subjects, discrimination limens appeared to be fairly independent of the directionality of the discrimination task. In general, symmetry was observed between the discrimination limens obtained in the basal and apical directions, except for subjects S4, S7, and S8. It was hypothesized that, for these three subjects, higher variance of the estimates in the discrimination limens produced by the adaptive task may have been one cause of the asymmetry observed in the data. (The statistical behavior of the adaptive procedure is discussed further in the next section.) Additionally, the number of electrodes in use by subjects was divided in half and responses obtained for electrodes located in the apical half of subjects' arrays were compared to responses obtained for electrodes located in the basal half of subjects' arrays. This analysis revealed no significant difference between the mean number of indiscriminable electrodes in the apical and basal halves of subjects' arrays when the data from all subjects was considered ( $p < 0.05$ ). However, inspection of individual subject data revealed that the subjects who demonstrated the poorest electrode discrimination skills (S4, S7, and S8) had more difficulty in the basal half of the array than in the apical half of the array.

### 2. Electrode discrimination verification task

Greater variance in the estimates of the discrimination limen occurred when there was a large separation between a reference electrode and its closest discriminable electrode (see discussion below). Therefore the fixed-level procedure was used to verify the results of the adaptive electrode discrimination task and to help determine which electrodes should be included in subjects' experimental maps for the speech recognition tests.

Electrodes were included in the fixed-level verification task under several conditions. The best (closest to perfect) discrimination score obtained for each electrode when tested in a basal and in an apical direction was determined for each subject. This value was compared to the perfect discrimination value for that electrode. If the difference between the two scores was greater than 0.125 (the number obtained if discrimination between two adjacent electrodes was perfect with allowance made for one attention error) when the electrode was tested in both an apical and a basal direction, the electrode was included in the fixed-level procedure. If no electrodes were selected for the fixed-level task using this bound and best performance, the same analysis was performed using the average performance found for each electrode. In some cases, more electrodes were selected for in-

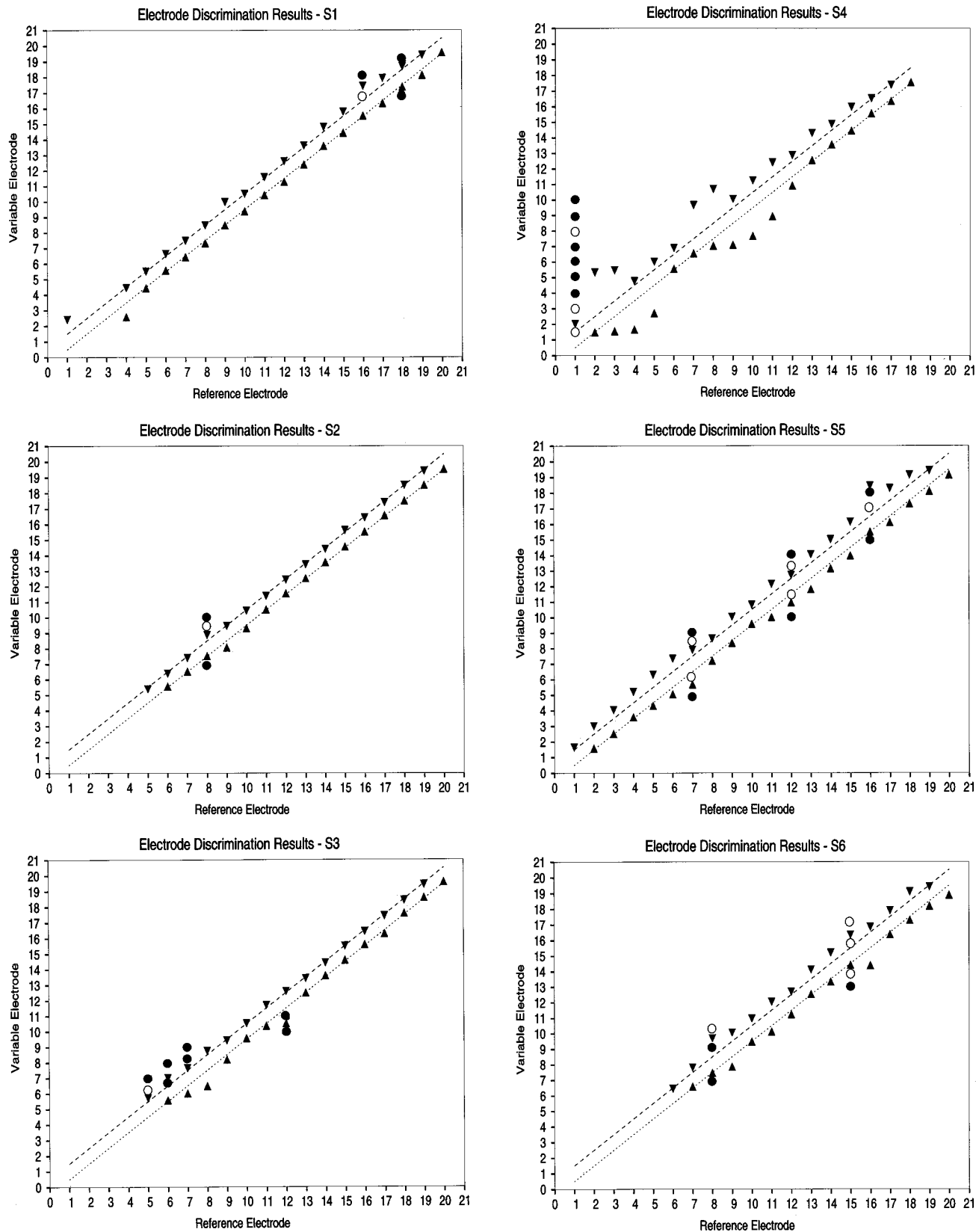


FIG. 2. Electrode discrimination and verification task results for the 11 subjects. This figure indicates the discriminability of a reference electrode (ordinate) as a function of the closest discriminable electrode (abscissa). Data obtained from the adaptive task in an apical direction are indicated by a ▲ while data obtained in a basal direction are indicated by a ▼. Perfect discrimination values are indicated by a dashed line for testing performed in a basal direction, and a dotted line for testing in an apical direction. Solid circles indicate the verification task was performed and that performance exceeded 70.7% correct. Open circles indicate performance less than 70.7% correct on the verification task.

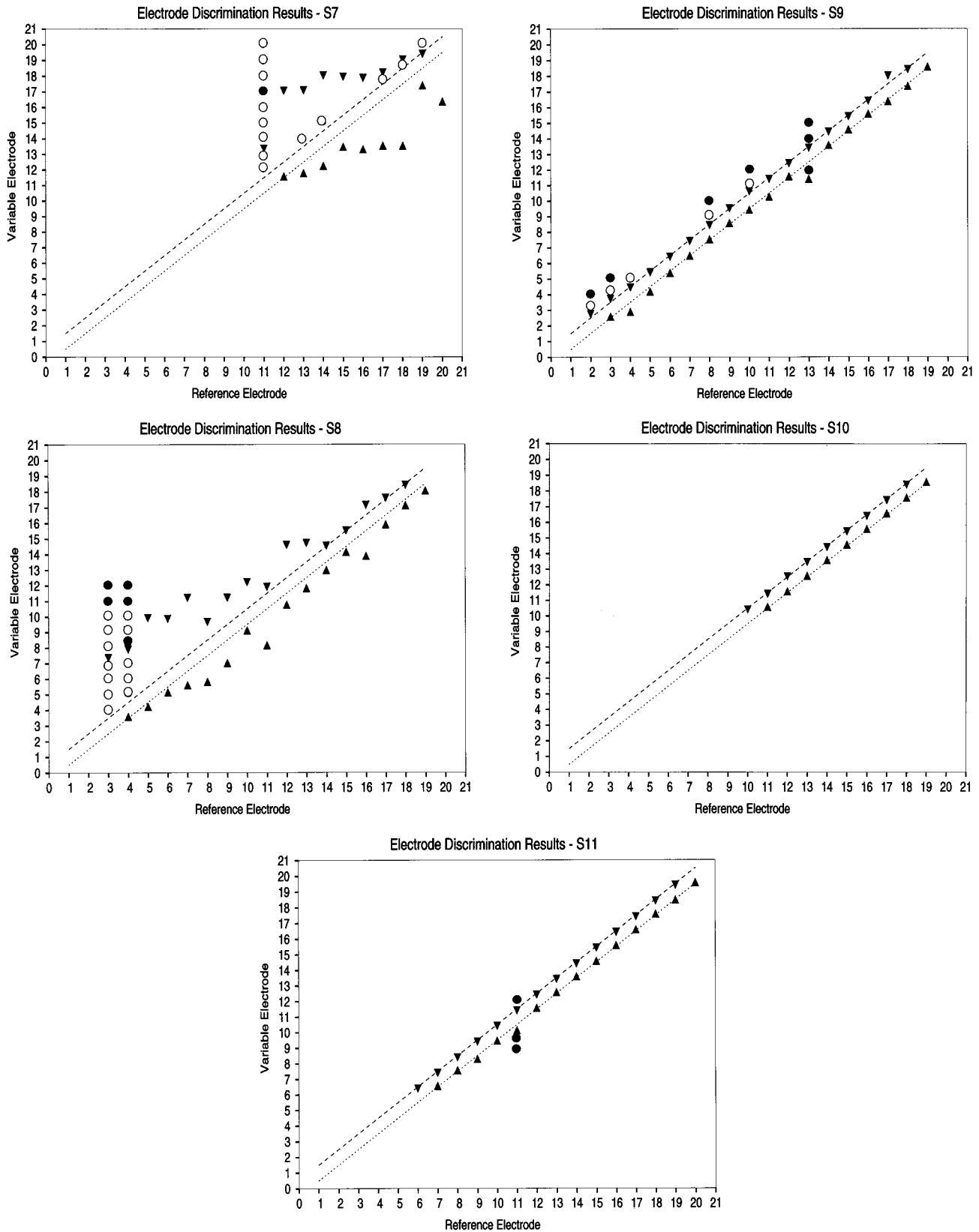


FIG. 2. (Continued.)

clusion in the verification task than could be tested within a reasonable period of time. In such cases, all electrode conditions were treated as equivalent and were tested at random as time would allow.

If an electrode was selected for inclusion in the fixed-

level task, it was compared to its adjacent electrode in both apical and basal directions. If the two electrodes were found to be indiscriminable, the reference electrode was compared to increasingly distant electrodes in the same direction using the fixed-level procedure until either a discriminable elec-

TABLE II. Summary of results from speech recognition and electrode discrimination experiments for each subject. Electrodes are numbered from 1 to 20 in a basal to apical direction.

Subject	Mean-square error between subject performance and ideal performance	Change in speech scores between clinical and experimental map	Number of changes in speech scores that are significant	Number of electrodes in clinical and experimental maps (clinical listed first)	Electrodes removed for experimental map
S1	0.27	Improve (4/5)	0	18/17	16
S2	0.04	Improve (5/5)	3	16/15	9
S3	0.23	Improve (5/5)	1	18/17	6
S4	2.57	(Improve (5/5)	3	18/11	2,3,5,8,9,11,14
S5	0.76	Improve (5/5)	1	20/17	7,12,16
S6	0.60	Decline (4/5)	1	15/11	10,14,15,16
S7	10.74	Decline (5/5)	3	10/3	12,13,14,15,16,18,19
S8	6.35	Improve (3/5)	3	17/8	4,5,6,7,8,9,10,13,14
S9	0.16	Improve (3/5)	0	18/14	3,5,9,11
S10	0.00	...	...	10	...
S11	0.00	...	...	15	...

trode was determined or until all electrodes were tested.

The results of the verification experiment are displayed in Fig. 2 along with the results of the adaptive task. The electrode number listed along the abscissa indicates the reference electrode; the electrode number shown on the ordinate indicates the comparison electrode. Results are presented as filled circles at the intersection of the two electrodes tested if the subject achieved an average score greater than or equal to 70.7% correct, or as empty circles if the performance was less than 70.7% correct.

The adaptive and fixed level experiments revealed similar results for most subjects but revealed variable results for three subjects (S4, S7, and S8). These three subjects were the poorest performers in terms of their electrode discrimination skills. The adaptive algorithm resulted in smaller discrimination limens than the fixed algorithm when a large separation existed between the reference electrode and the closest discriminable electrode, which is an inherent result of greater statistical variability in the adaptive tasks of this type. How-

ever, for the most part, the closest discriminable electrode measured for each electrode was the same for both tasks, particularly for the better performers.

### C. Speech recognition task

Four different speech recognition measures were administered to subjects in two different conditions: (1) while they utilized a map that employed all functioning electrodes (clinical map), and (2) while they used a map that employed only discriminable electrodes (experimental map). The number of electrodes programmed into subjects' clinical maps varied from 10 to 20. The number of electrodes programmed into subjects' experimental maps ranged from 3 to 17 (see Table II). Scores obtained by the 11 subjects on the speech recognition tests are displayed in Figs. 3–7. Two of the 11 subjects (S10 and S11) demonstrated perfect electrode discrimination skills and were not tested using an experimental

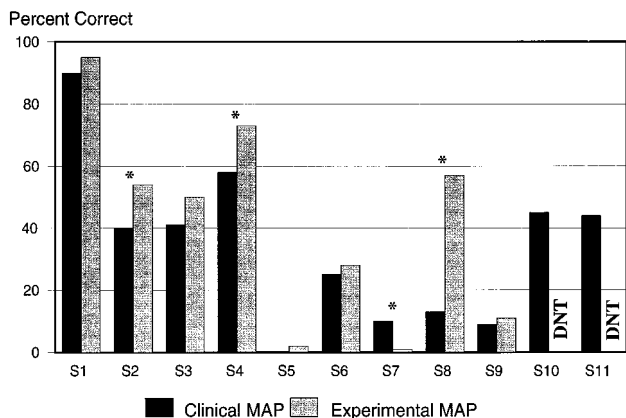


FIG. 3. Percent correct scores obtained by subjects on the CID Everyday Sentences test when using their clinical map and when using an experimental map that employed only discriminable electrodes. Significant differences between the two scores obtained by each subject are indicated by an asterisk ( $p < 0.05$ ).

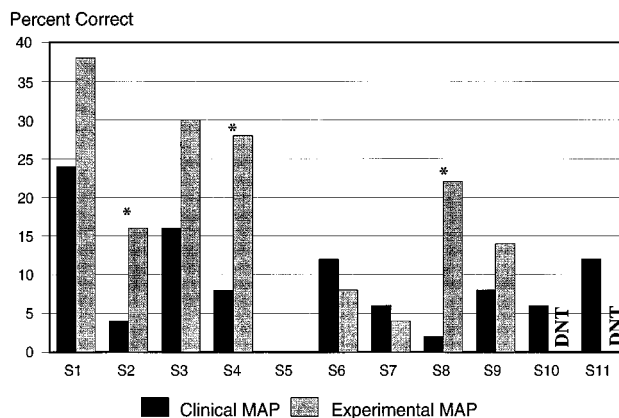


FIG. 4. Percent correct scores obtained by subjects on the NU6 Monosyllabic Words test (scored for words correct) when using their clinical map and when using an experimental map that employed only discriminable electrodes. Significant differences between the two scores obtained by each subject are indicated by an asterisk ( $p < 0.05$ ).

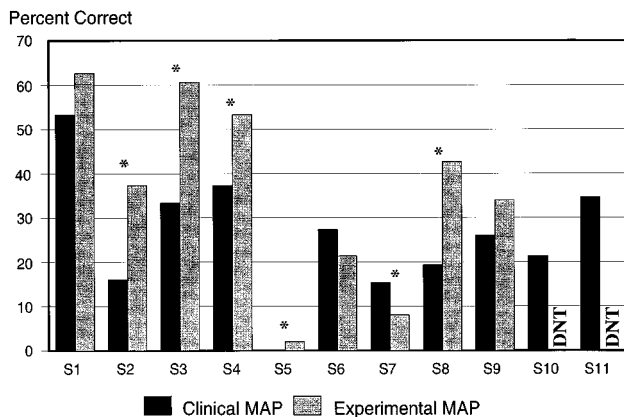


FIG. 5. Percent correct scores obtained by subjects on the NU6 Monosyllabic Words test (scored for phonemes correct) when using their clinical map and when using an experimental map that employed only discriminable electrodes. Significant differences between the two scores obtained by each subject are indicated by an asterisk ( $p < 0.05$ ).

map. This is denoted by the symbol DNT, or “did not test” where the experimental map score would normally be plotted.

The Binomial Test developed by Thornton and Raffin (1978) was used to determine if the individual speech recognition scores obtained while subjects used the different maps differed significantly for the nine subjects tested. The results of these analyses are presented in Figs. 3–7, where significance ( $p < 0.05$ ) is indicated by an asterisk (\*). This analysis revealed that three subjects’ scores improved on the CID Everyday Sentences test (S2, S4, and S8) while one subject’s score declined (S7). Three subjects’ scores improved on the NU6 Monosyllabic Words test for words correct (S2, S4, and S8), five subjects’ scores improved on the NU6 Monosyllabic Words test for phonemes correct (S2, S3, S4, S5, and S8) and one subject’s score declined (S7). One subject’s score declined on the Vowel test (S7), and one subject’s score declined on the Consonant test (S6).

There are two factors that may have contributed to these individual results. First, it is possible that remapping had a cumulative effect on phoneme perception that only revealed itself when contextual cues were present to aid in the recog-

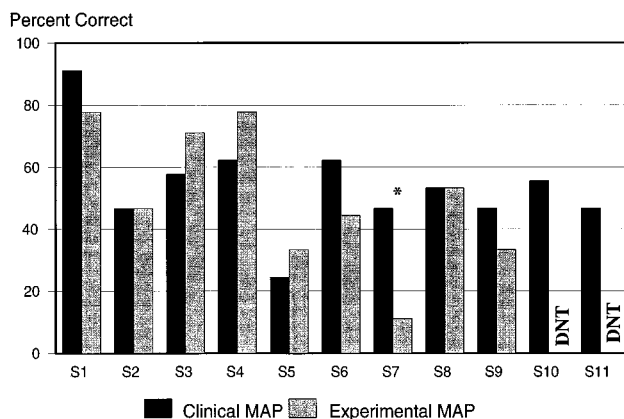


FIG. 6. Percent correct scores obtained by subjects on the Vowel test when using their clinical map and when using an experimental map that employed only discriminable electrodes. Significant differences between the two scores obtained by each subject are indicated by an asterisk ( $p < 0.05$ ).

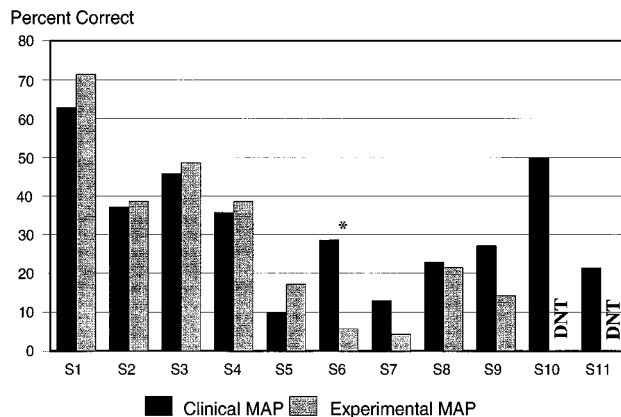


FIG. 7. Percent correct scores obtained by subjects on the Consonant test when using their clinical map and when using an experimental map that employed only discriminable electrodes. Significant differences between the two scores obtained by each subject are indicated by an asterisk ( $p < 0.05$ ).

niton, such as in the word and sentence tasks. Second, some subjects’ scores were likely affected by the number of electrodes programmed into their experimental maps. For example, S7’s poor performance with the experimental map (scores significantly declined on three of the five measures) was likely affected by the reduced number of electrodes (3) programmed into this map. The MPEAK coding strategy does not work optimally with so few electrodes. Although the results for this subject were not unexpected, she was tested under these conditions to maintain consistency of the experimental method. Last, there was no relationship noted between the order in which the speech tests were administered and the amount of improvement noted on the tests.

In order to further evaluate the effect that reprogramming had on speech recognition, subjects were divided into two groups: those whose performance improved with the experimental map (S1, S2, S3, S4, S5, S8, and S9) and those whose performance declined with the experimental map (S6 and S7). A Wilcoxon Signed Ranks test was used to test the significance of the differences in the mean scores obtained for the group whose scores improved when using the two different maps. The results of this analysis indicated that as a group, their scores significantly improved on three of the five test measures: CID Everyday Sentences ( $p = 0.008$ ), NU6 Monosyllabic Words scored for words correct ( $p = 0.016$ ), and NU6 Monosyllabic Words scored for phonemes correct ( $p = 0.008$ ). The group whose scores declined was too small to utilize this analysis method.

Electrode discrimination and speech recognition results are briefly summarized for each subject in Table II. The electrode discrimination performance is a mean-square error score calculated between the electrode discrimination results and the ideal discrimination results for each subject. Also listed are the number of speech recognition tests where the performance changed between the two mapping conditions for each subject, the number of changes that were statistically significant, the number of electrodes programmed in the clinical and experimental maps, and a list of the electrodes removed for the experimental maps. Although an information transmission analysis of the results were per-

TABLE III. Results of Spearman Rank Order Correlation Coefficient calculations. Error=mean-square deviation of electrode discrimination data from perfect discrimination data. Original speech score=score on each of five speech recognition measures obtained when subjects used their clinical map. Percent change in speech score=percent change in speech scores obtained when subjects used their experimental map and when subjects used their clinical map. Percent of electrodes removed=percent of electrodes removed to create the experimental map based on the number of active electrodes in the clinical map. Average dynamic range=dynamic range measured in Cochlear device amplitude steps averaged across all active electrodes in the clinical map.

Measure	CID	NU6		Consonants	Vowels
		Words	Phonemes		
Error versus original speech score	0.35	0.26	0.23	0.17	0.13
Error versus percent change in speech score	0.07	0.04	0.18	0.20	-0.13
Percent of electrodes removed versus percent change in speech score	0.02	0.13	0.28	0.60	0.10
Original speech score versus percent change in speech score	-0.33	-0.67	-0.42	0.12	-0.40
Average dynamic range versus original speech score	0.09	0.13	0.23	-0.08	0.10
Number of active electrodes in clinical map versus original speech score	-0.08	0.07	0.19	0.04	-0.02

formed on these data, no consistent results were observed between the speech results obtained under the two map conditions (Collins *et al.*, 1994).

Correlation analyses were performed to statistically examine the relationship between electrode discrimination and speech recognition, and the results are listed in Table III. First, the relationship between the mean-square error scores listed in Table II and the scores obtained on each of the speech recognition measures obtained in the clinical map condition was evaluated based on the Spearman Rank Order Correlation Coefficient. None of the speech recognition measures were significantly correlated with the error score. Additionally, the relationships between (1) the error and the percent change in speech recognition scores; (2) the percent of the electrodes in the array that were removed for the experimental map and the percent change in speech recognition scores; (3) the speech score obtained in the clinical map condition and the percent change in speech recognition scores; (4) the speech score obtained in the clinical map condition and the average dynamic range across all electrodes; and (5) the speech score obtained in the clinical map condition and the number of active electrodes programmed clinically were evaluated. These calculations were performed to determine whether poorer electrode discrimination would result in a larger improvement in speech recognition once subjects were remapped, whether baseline speech recognition abilities were correlated with improvement in speech recognition, and whether more traditional measures were correlated with improvement in speech recognition. However, none of the correlations from these analyses (or from those using a Pearson correlation coefficient) were statistically significant ( $p > 0.05$ ).

### III. DISCUSSION

It is difficult to directly compare the results of this study with previous experiments that have measured the pitch perception skills of cochlear implant subjects as such studies have employed ranking, scaling, labeling, or trajectory discrimination procedures rather than the electrode discrimination tasks used in the present experiments. The results of this

study indicate that the ability to discriminate electrode position along the scala tympani varied greatly across subjects. Some subjects demonstrated perfect discrimination of all electrodes while others demonstrated extremely poor discrimination. Such variability was also noted in subjects' abilities to recognize speech stimuli, both when tested with a clinically programmed map and when tested with a map based only on discriminable electrodes. The variability in speech recognition did not appear to be strongly related to electrode discrimination performance, since correlation analyses failed to reveal a significant relationship between electrode discrimination and speech recognition. Nelson *et al.* (1995) reported that place-pitch sensitivity measured using a pitch ranking technique was correlated with consonant recognition in a population of subjects implanted with the Nucleus device. Dorman *et al.* (1990) found that "excellent" and "above average" Ineraid users perceived a wider range of pitch than subjects who were classified as "poor" Ineraid users. Similarly, Busby *et al.* (1993) found that improvement in speech recognition performance from a single electrode strategy to a multiple electrode strategy was consistent with good electrode discrimination skills. Unlike these investigators, no significant relationship between subjects' speech recognition and their ability to discriminate electrode-based percepts was observed in this study.

Of the nine subjects evaluated, five subjects showed significant improvement on at least one speech recognition measure with an experimental map. When analyzed as a group, the seven subjects who demonstrated improved speech recognition scores with the experimental map showed a significant improvement in performance on CID Sentences, NU6 Words, and NU6 Phonemes. Two subjects showed a significant decline in performance on at least one speech recognition measure when using the experimental map. It is likely that the performance of one subject (S7) declined because her experimental map contained only three electrodes. It is possible that the speech information received by the other subject (S6) is so limited that no type of reprogramming will result in improved performance. Under such circumstances, it would be optimal to have a clinical screening

procedure to identify such subjects, thereby avoiding unproductive and time-consuming psychophysical testing.

Although not statistically significant, some differences were noted in subjects' abilities to discriminate electrodes based on their location in the cochlea; mean discrimination values obtained for more basally located electrodes were larger than the values obtained for more apically located electrodes. This discrepancy may be due to ambiguous place-pitch percepts caused by unusual current flow geometries of basal electrodes lying near or outside the round window. Busby *et al.* (1994) and Nelson *et al.* (1990) also reported differences between apical and basal perception. However, like these findings, no significant trends were noted.

The results of this experiment also indicate that, in some cases, discrimination limens could be substantially larger than a single electrode. Although the loudness balancing procedure appeared to be effective across the entire array, it is not the optimal procedure when the discrimination limens are greater than one electrode.<sup>1</sup> For this reason, future applications of this methodology should consider utilization of a different loudness balancing procedure when an initial screening procedure indicates large spatial separations between discriminable electrodes. Because loudness is subjective, it was not possible to check the accuracy of subjects' responses on the loudness balance task. If a subject failed to appropriately balance the loudness of the electrodes in his/her array, the procedures used in this study would have reported better electrode discrimination than would have occurred if all of the electrodes were appropriately loudness balanced. If this occurred, indiscriminable electrodes may have been included in the experimental map, although discriminable electrodes would not have been excluded from the experimental map. Thus the potential improvements in speech may not have been realized for some subjects. This may be an alternate explanation for the lack of improvement, or minimal amounts of improvement observed in some subjects. These observations, along with the findings of this study, suggest that an experiment comparing several exhaustive and partial loudness balancing designs, along with various balancing procedures and methods of manipulating loudness would be of great utility.

The MPEAK coding strategy of the Nucleus device codes acoustic formant frequency information by varying the spatial location of stimulation along the electrode array. This approach is based on the place-pitch theory of frequency coding in the normal cochlea. The variations in spectral peaks for different phonemes and phoneme transitions are thus directly coded as variations in the spatial location of stimulation. For these differences to be discriminable the spatial locations must be discriminable. Thus remapping to improve spatial discriminability was expected to have discrimination ramifications at the phoneme recognition level. This would imply that scores for all five of the speech recognition measures, including the Vowel and Consonant tests, would improve when subjects used maps that contained only discriminable electrodes. The data obtained in this study does not support this conclusion, since speech recognition scores tended to improve most on the word and sentence

tests, as opposed to the phonemic materials. This may indicate that a reduction of electrodes resulted in an improved perception of envelope cues. Or, it is possible that the slight improvements seen in the phonemic recognition task facilitated improvements made on the more natural speech materials, such as NU6 Words and CID Everyday sentences; however, this hypothesis has not yet been validated.

Last, the results of this study may have been influenced by the fact that Cochlear Corporation "current level" stimuli were used in the electrode discrimination experiments while "stimulus level" stimuli were used to program subjects' speech processors. Thus pulse width was held constant for the electrode discrimination tasks but was not held constant in the subjects' maps. "Stimulus level" units, like "current level" units, are arbitrary and vary from 1 to 239. Each unit represents an approximately equal fixed percentage increase or decrease in the amount of charge delivered to the active electrode. However, unlike "current level" stimuli, the actual charge delivered to the electrode is a combination of current and pulse width with "stimulus level" stimuli. For both types of stimuli, the actual current level delivered to the electrode (in  $\mu\text{A}$ ) is dependent upon each subject's individual implant (Cochlear Corporation Technical Reference Manual, 1996).

The results of this experiment suggest the feasibility of testing electrode discrimination in a clinical setting as an aid to optimal device fitting. The results also suggest the counterintuitive result that, at a time when many investigators, clinicians, and manufacturers are striving to introduce more electrodes, fewer electrodes may actually be better for a subset of the population. It is likely that improvements in speech recognition performance can be achieved using this approach since the processor will theoretically be better matched to the perceptual skills of the individual listener. However, the clinical applicability of the electrode discrimination task used in this study is currently limited by its data-intensive demands. In its current form, the task requires an excessive amount of time for completion. Alternative procedures are being explored that will quickly and effectively evaluate electrode discrimination. Only then will such a procedure hold promise as a clinically useful tool for improving the speech recognition of some cochlear implant subjects.

## ACKNOWLEDGMENTS

The authors would like to thank the subjects who participated in this study for their time, effort, and feedback. We would also like to acknowledge J. O'Neill for his assistance in the electrode discrimination experiment. In addition, we would like to thank Dr. R. Shannon and two anonymous reviewers for their constructive reviews of a previous version of this paper. This research was supported by NIH Grant No. NIDCD NS21440.

<sup>1</sup>An alternate procedure for balancing loudness that does not suffer from additive error and that requires the same number of measurements as the adjacent-reference design is the common-reference design. In this design, one electrode pair is selected as the reference and the stimulus levels of all other electrode pairs are adjusted to match this reference loudness. This procedure has been commonly used to control loudness in a variety of psychophysical studies and does a better job of eliminating systematic error



from the balanced loudness. However, it can be shown that the common-reference design suffers from the problem that adjacent electrodes will not be balanced as accurately as is possible using the adjacent-reference design (for adjacent electrodes, both designs generate equal loudness estimates that have the same expected error, or bias, but the estimate obtained from the common-reference design has a higher variance). The adjacent reference design was selected since, for this particular experiment, we were primarily interested in minimizing the loudness cues between adjacent electrodes and their nearest neighbors.

- Busby, P. A., Whitford, L. A., Blamey, P. J., Richardson, L. M., and Clark, G. M. (1994). "Pitch perception for different modes of stimulation using the Cochlear multiple-electrode prosthesis," *J. Acoust. Soc. Am.* **95**, 2658–2669.
- Busby, P. A., Tong, Y. C., and Clark, G. M. (1993). "Electrode position, repetition rate, and speech perception by early- and late-deafened cochlear implant patients," *J. Acoust. Soc. Am.* **93**, 1058–1067.
- Clark, G. M., Shepherd, R. K., Franz, B. K., Dowell, R. C., Tong, Y. C., Blamey, P. J., Webb, R. L., Pyman, B. C., McNaughton, J., and Bloom, D. M. (1988). "The histopathology of the human temporal bone and auditory central nervous system following cochlear implantation in a patient. Correlation with psychophysics and speech perception results," *Acta Oto-Laryngol. Suppl.* **448**, 1–65.
- Cochlear Corporation, "Audiologist's Handbook," April 1993, Englewood, Colorado.
- Cochlear Corporation, "Technical Reference Manual," 1996, Englewood, Colorado.
- Collins, L. M., Zwolan, T. A., and Wakefield, G. H. (1994). "Electrode discrimination measures: relationship with speech perception and clinical applicability of results," *J. Acoust. Soc. Am.* **95**, 2905–2906 (A).
- Davis, H., and Silverman, S. R. (1978). *Hearing and Deafness* (Holt, Rinehart and Winston, New York).
- Dorman, M. F., Smith, L., McCandless, G., Dunnivant, G., Parkin, J., and Dankowski, K. (1990). "Pitch scaling and speech understanding by patients who use the Ineraid cochlear implant," *Ear Hear.* **11**, 310–315.
- Eddington, D. K., Dobelle, W. H., Brackman, D. E., Mladejovsky, M. G., and Parkin, J. (1978). "Place and periodicity pitch by stimulation of multiple scala tympani electrodes in deaf volunteers," *Trans. Am. Soc. Artif. Intern. Organs* **XXIV**, 1–5.
- Jesteadt, W. (1980). "An adaptive procedure for subjective judgments," *Percept. Psychophys.* **28**, 85–88.
- Nelson, D. A., Van Tasell, D. J., Schroder, A. C., Soli, S., and Levine, S. (1995). "Electrode ranking of place pitch: and speech recognition in electrical hearing," *J. Acoust. Soc. Am.* **98**, 1987–1999.
- Pfingst, B. E., Glass, I., Spelman, F. A., and Sutton, D. (1985). "Psychophysical studies of cochlear implants in monkeys: clinical implications," in *Cochlear Implants*, edited by R. A. Schindler and M. M. Merzenich (Raven, New York), pp. 305–321.
- Shannon, R. V. (1983). "Multichannel electrical stimulation of the auditory nerve in man: Basic psychophysics," *Hearing Res.* **11**, 157–189.
- Skinner, M. (1991). "Performance of postlinguistically deafened adults with the wearable speech processor (WSP-III) and the mini speech processor (MSP) of the Nucleus multi-electrode cochlear implant," *Ear. Hearing* **12**, 3–22.
- Thornton, A. R., and Raffin, M. J. (1978). "Speech discrimination scores modeled as a binomial variable," *J. Sci. Food. Agric.* **21**, 507–518.
- Tillman, T. W., and Carhart, T. (1966). An expanded test for speech discrimination utilizing CNC monosyllabic words: Northwestern University Auditory Test No. 6. Technical Report No. SAM-TR-66-55, USAF School of Aerospace Medicine, Brooks Air Force Base, Texas.
- Tong, Y. C., and Clark, G. M. (1985). "Absolute identification of electric pulse rates and electrode positions by cochlear implant patients," *J. Acoust. Soc. Am.* **77**, 1881–2429.
- Tong, Y. C., Clark, G. M., Blamey, P. J., Busby, P. A., and Dowell, R. C. (1982). "Psychophysical studies for two multiple-channel cochlear implant patients," *J. Acoust. Soc. Am.* **71**, 153–160.
- Tong, Y. C., Millar, J. B., Clark, G. M., Martin, L. F., Busby, P. A., and Patrick, J. F. (1980). "Psychophysical and speech perception studies on two multiple channel cochlear implant patients," *J. Laryngol. Otol.* **94**, 11241–1256.
- Townshend, B., Cotter, N., Van Compernelle, D., and White, R. L. (1987). "Pitch perception by cochlear implant subjects," *J. Acoust. Soc. Am.* **82**, 106–115.

# Information from time-varying vibrotactile stimuli

Ian R. Summers, Philip G. Cooper, and Paul Wright

*Medical Physics Group, Department of Physics, University of Exeter, Exeter EX4 4QL, United Kingdom*

Denise A. Gratton, Peter Milnes, and Brian H. Brown

*Department of Medical Physics and Clinical Engineering, University of Sheffield, Royal Hallamshire Hospital, Sheffield S10 2JF, United Kingdom*

(Received 27 March 1997; revised 23 June 1997; accepted 16 July 1997)

Experiments have been carried out to investigate the information transfer available via a single vibrator on the fingertip. In a first experiment, for stimuli with durations 80 to 320 ms, discrimination of a one-octave step change in frequency at the halfway point was investigated. Results were similar for three stimulus types—sinewave, monophasic pulse and tetraphasic pulse—suggesting temporal cues are more important than spectral cues in this task. In a second experiment, subjects were required to perceive changes in a sequence of stimulus elements. A presentation rate of 6.25 elements  $s^{-1}$  was found to give better results than a rate of 12.5 elements  $s^{-1}$ . In the former case, the potential information transfer per element was estimated to be approximately 1.0 bits, corresponding to an information transfer rate of around 6 bits  $s^{-1}$ . Implications for the design of a tactile aid to lipreading are discussed. © 1997 Acoustical Society of America.

[S0001-4966(97)04111-8]

PACS numbers: 43.66.Wv, 43.66.Ts, 43.71.Ky, 43.71.Ma [WJ]

## INTRODUCTION

This paper describes an extension of our previous work (Summers *et al.*, 1994) on the perception of time-varying tactile stimuli. The principal aim of these studies is to establish the optimum strategy for transmitting information through the skin via a single stimulation site.

There is a substantial literature on the perception of vibratory stimuli by the skin (for a review, see Verrillo and Gescheider, 1992), but only a small proportion of this (e.g., Rothenberg *et al.*, 1977; Weisenberger, 1986; Summers and Farr, 1989; Formby *et al.*, 1992) relates to the perception of time-variations in such stimuli—as encountered, for example, with sensory-substitution devices with a tactile output. There exists no reliable estimate of the maximum information transfer rate which might be available. Kokjer (1987) suggests 100 bits  $s^{-1}$  as an order-of-magnitude upper limit, but this figure must significantly overestimate the rate as it derives from measurements of the timescale on which stimulus elements can be individually detected, as opposed to identified. Lechelt (1975, 1980) has investigated identification of the number of pulses in trains presented to the fingertip at rates of 3–15  $s^{-1}$ , and found that performance falls at the faster rates in this range, indicating that the limit for effective presentation of tactile stimulus elements may be around 10  $s^{-1}$ .

Recent developments in the area of haptic interfaces for computers, e.g., for virtual-reality applications (Srinivasan, 1995), have opened up new areas of interest in relation to the perception of time-varying vibrotactile signals. However, our results are particularly intended for application in the area of tactile aids for the hearing impaired (Bernstein, 1992; Summers, 1992; Weisenberger, 1992). Because of their limited information-carrying capacity, these devices, whether single-channel or multi-channel, are generally considered as a support for lipreading, rather than as a means of conveying all

the information necessary to perceive speech.

Electrotactile perception of “speechlike” signals has been investigated by Blamey and Clark (1987) and Blamey *et al.* (1990) in studies related to the “Tickle Talker,” an electrotactile aid which stimulates the digital nerve bundles (Blamey and Clark, 1985). Information transfer of around 1.5 bits was measured with variation of stimulus intensity, and around 1 bit with variation of stimulus repetition rate. Rabinowitz *et al.* (1987), using stimuli on the middle fingertip which differed in terms of frequency, intensity and/or contactor area, measured an information transfer of 1–2 bits for each dimension and 4–5 bits for all three dimensions. Tan *et al.* (1996) have measured an information transfer rate of 12 bits  $s^{-1}$  for three-channel tactile and kinaesthetic stimulation on the thumb and two fingers, corresponding to a rate per channel in the range 7–9 bits  $s^{-1}$  (Tan, 1997). The thesis by Tan (1996) contains much valuable background material.

In our previous study (Summers *et al.*, 1994), measurements were made on the perception of a frequency- and/or amplitude-modulated pulse train, with a comparison of the electrotactile and vibrotactile modalities. In one experiment, vibrotactile perception of two-octave step changes in stimulus frequency (50 to 200 Hz, or *vice versa*) was found to be significantly better than electrotactile for overall stimulus durations of 200, 300, 400, and 800 ms. On the same timescale, perception of step changes in stimulus amplitude was similar in the two modalities when changes in amplitude were tailored to match the different dynamic ranges available. In a second experiment, vibrotactile perception of voice fundamental frequency with various codings was investigated. Both experiments showed information transfer for vibrotactile stimuli to be greater when frequency and amplitude modulation were used together rather than with one or other in isolation. It was concluded that frequency- and amplitude-modulated vibratory stimulation is a good choice in a prac-

tical tactile device for the profoundly hearing impaired.

The results of Weisenberger and Russell (1989), using the Minifonator device (Siemens Hearing Instruments) whose tactile output is derived from a microphone signal with minimal signal processing, suggest that frequency information is not readily available from tactile stimuli with a complex waveform. Hence a pulse-train stimulus, which can offer both frequency and amplitude information, appears to be a better choice for optimisation of information transfer.

There are two experiments in the present study, which uses vibrotactile stimulation at the fingertip throughout. The first investigates perception of one-octave step changes of stimulus frequency (i.e., repetition rate), with comparison of transitions at lower frequencies (50–100 Hz) and higher frequencies (200–400 Hz). The second investigates perception of stimulus elements within a frequency- and amplitude-modulated sequence. Both experiments feature a comparison of different stimulus waveforms—the effect of stimulus waveform is an important consideration for a practical wearable device in which, because of the constraints of a limited-bandwidth output transducer, the output waveform may differ from the “ideal” sinewaves or pulses used in most laboratory experiments.

## I. STIMULUS DELIVERY SYSTEM

Vibrotactile stimuli were delivered to the distal pad of the right index finger via a Bruel & Kjaer type 4810 vibrator, driving a 2-cm<sup>2</sup> circular contactor with no surround. Subjects were instructed to rest the finger lightly on the contactor, whose surface was horizontal. The vibratory output was monitored by a Knowles type BU1771 miniature accelerometer, used in a motional-feedback loop. With this system, it proved possible to produce well-specified displacement outputs in the range 0–100  $\mu\text{m}$  over a frequency range of 20–500 Hz. Stimulus waveforms were generated in software and delivered as required to the motional-feedback drive system via a Cambridge Electronic Design type 1401 intelligent interface. Two identical systems were produced: one for each of the laboratories involved in this investigation—at Exeter and at Sheffield. In the two experiments described below, subject testing was at both sites in experiment 1 and at the Sheffield site only in experiment 2. Noise masking via headphones was used to eliminate acoustic cues from the vibrator.

## II. EXPERIMENT 1: PERCEPTION OF STEP CHANGES IN STIMULUS FREQUENCY

### A. Stimuli

In this experiment the basic stimulus format was a periodic signal of specified duration, containing at its halfway point a one-octave step change of frequency: 50 to 100 Hz or *vice versa* in one variant of the experiment, 200 to 400 Hz or *vice versa* in a second variant. There were also contrasting stimuli with no step change, i.e., whose frequency remained constant throughout the specified duration at one or other of the two specified frequencies. Overall stimulus duration was either 80, 160, 240, or 320 ms.

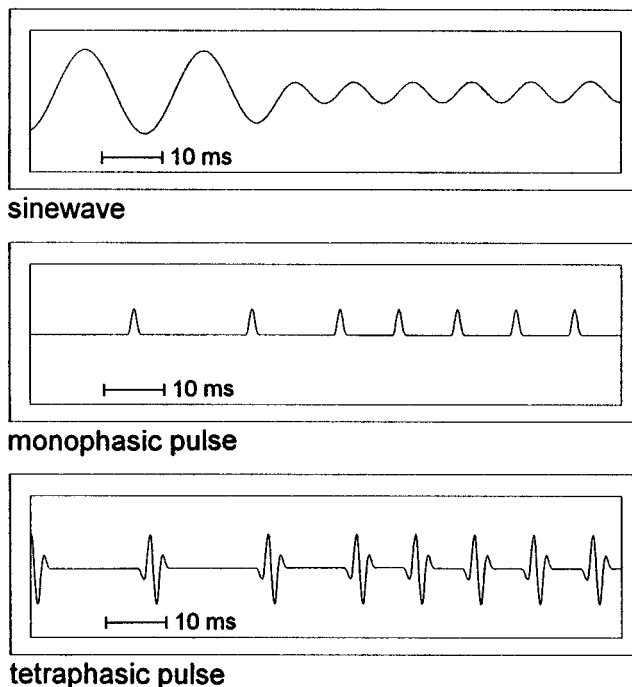


FIG. 1. Stimulus displacement waveforms (details) for 50- to 100-Hz transitions with the three different types of stimuli: sinewave, monophasic pulse and tetraphasic pulse. Each panel shows a transition from quasi-steady stimulation at 50 Hz to quasi-steady stimulation at 100 Hz via a single cycle of intermediate frequency. In the sinewave case the 100-Hz amplitude is 12 dB less than the 50-Hz amplitude in order to compensate for the variation of tactile sensitivity with frequency. These waveforms are illustrative of those at the input of the vibrator drive system—the response of this system rolls off below 10 Hz, producing some overshoot in the vibratory output for monophasic pulses; the roll-off has little or no effect on the sinewave or tetraphasic-pulse waveforms.

Three different waveform types were used: sinewave, monophasic pulse and tetraphasic pulse. Examples of stimulus displacement waveforms for the 50/100 Hz transitions are shown in Fig. 1; the 200/400 Hz case is an obvious extension. Each monophasic pulse corresponds to the signal obtained by passing a 1-ms rectangular pulse through a fourth-order low-pass Bessel filter at 500 Hz. Each tetraphasic pulse corresponds to the signal obtained by similarly filtering a sequence of four consecutive 1-ms rectangular pulses with amplitudes in the ratio  $-1.0337:3:-3:1.0337$ , these amplitudes being chosen to produce desired spectral characteristics (see below). The tetraphasic pulses are effectively brief tonebursts and are intended to be representative of the type of pulses which can most conveniently be delivered when using a limited-bandwidth vibratory transducer, as is typically the case in wearable tactile devices. Note that the overall duration of the tetraphasic pulse, at around 5 ms, is too long to allow a 400-Hz repetition rate, and so only two waveform conditions—sinewave and monophasic pulse—were used for measurements on 200/400 Hz transitions.

Sinewave amplitude was varied (see below for details) to compensate for the variation of tactile sensitivity with frequency (Verrillo *et al.*, 1969). This was in order to avoid cues to frequency changes from an associated change in subjective intensity. No such compensation was used for either

of the two pulse waveform types—in these cases subjective intensity is expected to be relatively independent of stimulus frequency for frequencies below 500 Hz (Rothenberg *et al.*, 1977; Bernstein *et al.*, 1986). For sinewave stimuli, continuity of displacement and velocity at a transition between two frequencies was achieved by including a single cycle of intermediate frequency and intermediate amplitude (see Fig. 1); similarly, continuity of displacement and velocity at the start and end of sinewave stimuli was achieved with a half cycle of reduced amplitude. The monophasic-pulse and tetrphasic-pulse stimuli also included a single cycle of intermediate frequency at a transition between two frequencies.

Measurements were made at two different sensation levels: 24 dB SL and 36 dB SL. With monophasic pulses, 24 dB SL was achieved by setting the baseline-to-peak pulse amplitude at 24 dB above a nominal threshold of  $0.5 \mu\text{m}$ . Similarly, with tetrphasic pulses, 24 dB SL was achieved by setting the peak-to-peak pulse amplitude at 24 dB above a nominal threshold of  $0.5 \mu\text{m}$ . With sinewaves, 24 dB SL was achieved at 100 Hz by setting the peak-to-peak amplitude at 24 dB above a nominal 100 Hz threshold of  $0.8 \mu\text{m}$ ; at the other stimulation frequencies of 50, 200, and 400 Hz, respectively, the amplitude was set at +12, -10, and -10 dB *re*: the amplitude at 100 Hz, in order to compensate for the variation of tactile sensitivity with frequency. Amplitudes for the 36 dB SL conditions were in all cases set 12 dB higher than the corresponding amplitudes in the 24 dB SL conditions. [The nominal thresholds of  $0.5 \mu\text{m}$ ,  $0.5 \mu\text{m}$ , and  $0.8 \mu\text{m}$  were set slightly above estimates of  $0.3 \mu\text{m}$ ,  $0.3 \mu\text{m}$ , and  $0.5 \mu\text{m}$ , respectively, obtained from preliminary threshold measurements. The variation of sinewave amplitude required to achieve constant sensation was estimated from preliminary measurements and on the basis of equal-sensation contours from Verrillo *et al.* (1969).]

It is clear that this procedure for setting stimulus amplitudes will not exactly achieve, for any of the waveform types, equal sensation across the four frequencies within the 24 dB SL or 36 dB SL sets (because, for the particular group of subjects used for these tests, the variation of average tactile sensitivity with frequency will not be exactly as has been assumed, and because there will in any case be inter-subject differences which are not allowed for.) Hence there is a danger that a change in stimulus frequency at a particular stimulation level might be detectable as a change in subjective intensity. No systematic effects of this nature were reported by the test subjects, however.

Figure 2 shows spectra for each waveform type at 50 and 100 Hz; the 200- and 400-Hz cases (two waveform types only) are an obvious extension—the monophasic-pulse spectra have the same envelope as in the 50- and 100-Hz cases but with increased spectral-line spacing. The spectral envelope of the tetrphasic pulses is tailored to have a zero at 50 Hz (see insets to Fig. 2) by choosing amplitudes for the four phases in the ratio  $-1.0337:3:-3:1.0337$ , i.e., slightly different to the “binomial” ratio of  $-1:3:-3:1$ . Thus, for tetrphasic pulses at repetition rates of both 50 and 100 Hz the lowest-frequency spectral component is at 100 Hz.

Temporal cues to stimulus frequency (i.e., to stimulus repetition rate) are available from the repetition period, irre-

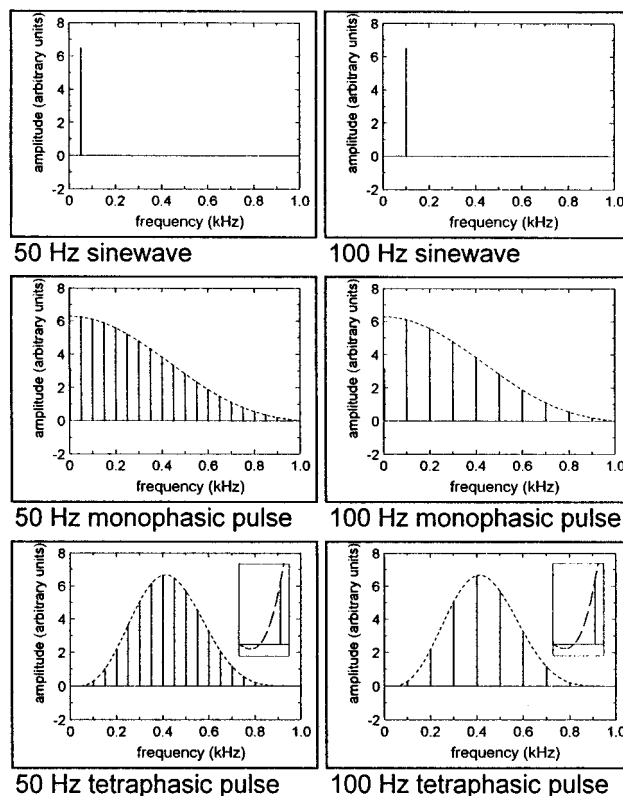


FIG. 2. Amplitude spectra for the three different types of stimuli—sinewave, monophasic pulse and tetrphasic pulse—at repetition rates of 50 and 100 Hz. The dotted line in each of the four lower panels indicates the spectral envelope, i.e., the curve which determines the magnitudes of the spectral lines. The spectra are calculated from the same parameters as those used in the waveform-generation software. The amplitude scales are arbitrary: In the case of sinewaves at a given sensation level the 50-Hz and 100-Hz amplitudes differ in practice because of compensation for the variation of tactile sensitivity with stimulus frequency; in the case of monophasic or tetrphasic pulses at a given sensation level the spectral envelope in practice scales proportionally with repetition rate. The inset panels in the case of tetrphasic pulses are enlargements of the low-frequency region, showing the zero in the spectral envelope at 50 Hz. These spectra are illustrative of those at the input of the vibrator drive system—the response of this system rolls off below 10 Hz, producing zero d.c. component in the spectrum of the monophasic-pulse vibratory output; the roll-off has little or no effect on the sinewave or tetrphasic-pulse spectra.

spective of the waveform type. However, there are also cues from changes in the distribution of energy across the spectrum. Since vibrotactile perception is mediated by several distinct populations of mechanoreceptors, each with its own particular frequency response (Bolanowski *et al.*, 1988; Lamoré and Keemink, 1988), it might be expected that such spectral cues could be perceived as a change in the pattern of relative excitation between the various populations. Examination of the spectra in Fig. 2 indicates that spectral cues for the 50/100 Hz transition (deriving principally in this case from components at the fundamental frequencies) are somewhat reduced with monophasic pulses, in comparison to sinewaves, and very much reduced with tetrphasic pulses. In the case of the 200/400 Hz transition, spectral cues are expected to be similar for the two waveform conditions: sinewave and monophasic pulse. This is because the monophasic-pulse spectra are dominated by their fundamental-frequency components (since, at these higher

repetition rates, the monophasic-pulse waveform approximates quite well to a sinewave).

## B. Subjects

These were 20 normally hearing adults (age range 21 to 54 years), 15 male and 5 female. They were not paid for their participation in the experiment. Because the experimental design required each subject to participate in a lengthy series of 20 test sessions, subject recruitment was difficult and it proved necessary to include in the subject group all six authors and four of their immediate colleagues, all of whom had previous experience of tactile experiments. The remaining ten subjects had little or no previous experience. Interestingly, no obvious correlation was subsequently observed between subjects' previous experience and their test performance, although there were initial concerns that such an effect might be apparent in view of the wide variation of experience across the subject group. Ten subjects (5 at each site — Exeter and Sheffield) participated in the experiment at a stimulation level of 24 dB SL and the remaining ten (again 5 at each site) participated in the experiment at a stimulation level of 36 dB SL. No significant differences were observed between the performance of subjects at the two testing sites: The results quoted below are from data pooled across the sites.

## C. Procedure

Separate measurements were made for each of the five possible frequency/waveform combinations: 50/100 Hz sine, 200/400 Hz sine, 50/100 Hz monophasic, 200/400 Hz monophasic, 50/100 Hz tetraphasic. Each subject participated in 20 test sessions, with each group of four consecutive sessions testing the same frequency/waveform condition and stimulus durations of 320 ms (for the first session of the four), 240 ms (for the second), 160 ms (for the third), and 80 ms (for the fourth). The order of the five frequency/waveform conditions was permuted across the subjects to give a balanced series of tests.

Each session followed a similar procedure to that developed during our previous study (Summers *et al.*, 1994): four consecutive runs of a demonstration/test block consisting of 12 demonstration items followed by 12 test items. All demonstration and test items were delivered 0.5 s after a 12.5-Hz tactile cue. The test sequence was preceded by a short training sequence lasting approximately 10 min. Subjects were able to request a repetition of this training sequence, or of any of the demonstration sequences within the demonstration/test blocks, but rarely chose to take advantage of this. The overall duration of each test session was around 30 min.

Subjects were introduced to a labelling system in which stimulus frequencies of 25 Hz (not used here), 50 Hz, 100 Hz, 200 Hz, and 400 Hz are described as "very low," "low," "medium," "high," and "very high," respectively. Hence they were required to identify each stimulus as "rising," "falling," "constant low," or "constant medium" (for the 50/100 Hz stimuli) and as "rising," "falling," "constant high," or "constant very high" (for the 200/400

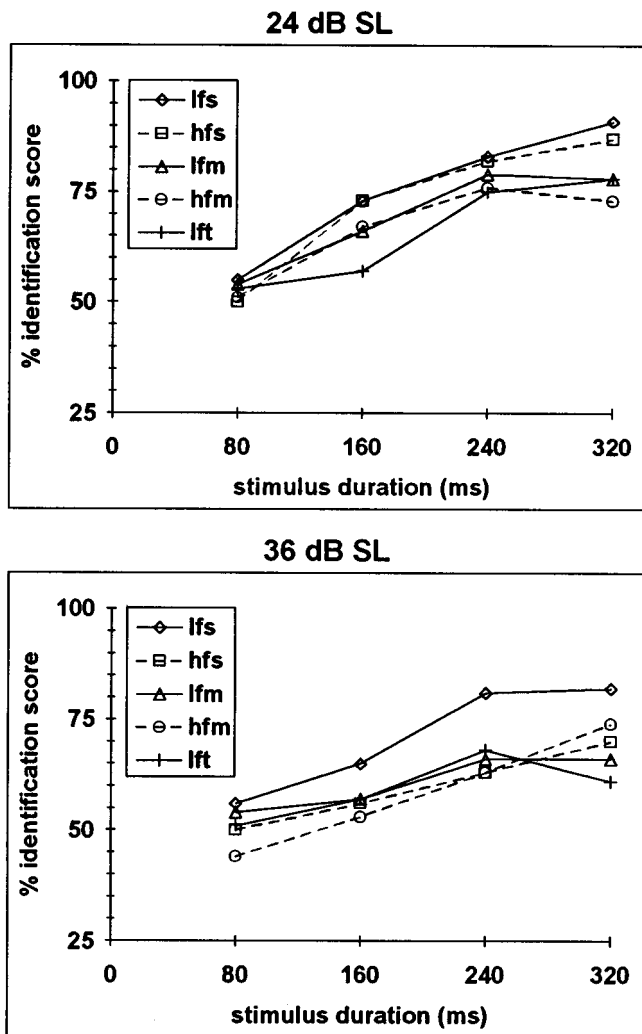


FIG. 3. Mean scores plotted as function of stimulus duration for the five frequency/waveform combinations in experiment 1: data from 10 subjects at 24 dB SL and 10 subjects at 36 dB SL. Key: lfs=50/100 Hz sine; hfs=200/400 Hz sine; lfm=50/100 Hz monophasic; hfm=200/400 Hz monophasic; lft=50/100 Hz tetraphasic. The standard error in each score is typically 5 percentage points. The chance score is 25%.

Hz stimuli). Each test block of 12 items contained four "rising" items, four "falling," and four "constant" (two of each type). Response (forced choice) was by keyboard entry. Subjects were informed of their overall score for each set of 12 test items at the end of that set, via a monitor display which also presented the corresponding confusion matrix.

Overall comparison of scores across the four blocks within each test session showed that asymptotic performance was reached by the second block. Hence the result of each test was calculated from the subject's combined scores for the second, third and fourth blocks. In total, 14 400 test items were scored, distributed over 400 test sessions and 20 subjects.

## D. Results

Mean scores for stimuli at the various durations are shown in Fig. 3. Corresponding values of information transfer IT, calculated from confusion matrices of subjects'

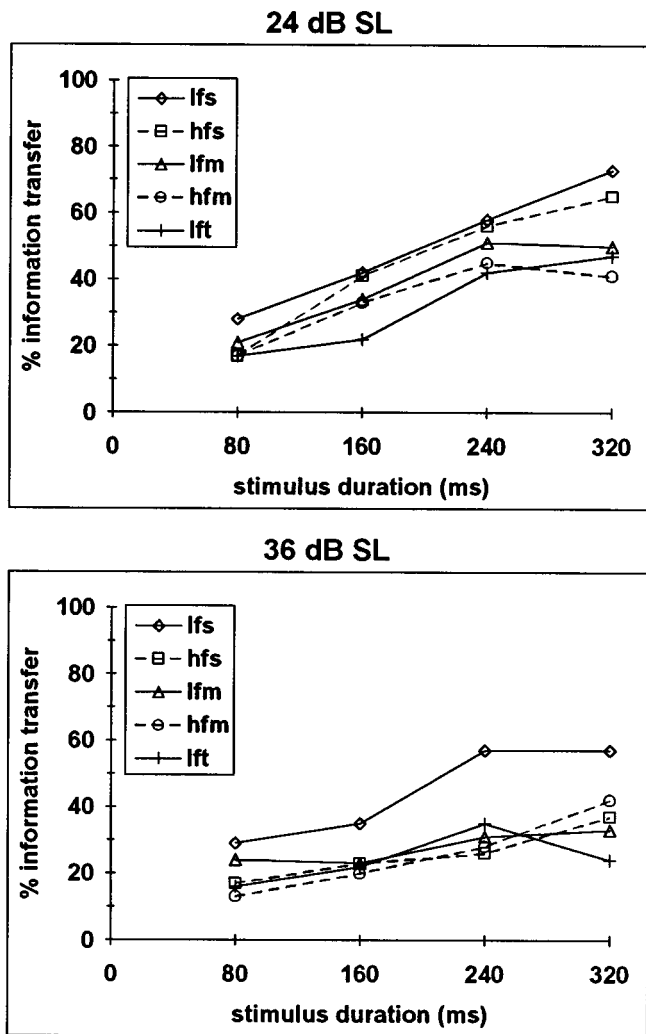


FIG. 4. Information transfer IT plotted as a function of stimulus duration for the five frequency/waveform combinations in experiment 1: data from 10 subjects at 24 dB SL and 10 subjects at 36 dB SL. Key: lfs=50/100 Hz sine; hfs=200/400 Hz sine; lfm=50/100 Hz monophasic; hfm=200/400 Hz monophasic; lft=50/100 Hz tetrphasic. The maximum possible IT (ordinate of 100%) corresponds to 1.92 bits, representing 4 alternatives with an imbalanced distribution. Estimated errors in these IT values are typically 6 percentage points.

pooled responses (Miller and Nicely, 1955), are shown in Fig. 4. Overall scores, for data pooled over stimulus durations, are shown in Fig. 5.

The data in Figs. 3 and 4 show, unsurprisingly, that performance falls as the stimulus duration is reduced. However, even at 80 ms duration (i.e., with each half of the stimulus only 40 ms) scores are well above chance. Examination of subjects' error patterns shows that scores for the various "constant" stimuli are better overall than scores for "rising" or "falling" stimuli. The proportion of "constant" stimuli that elicit one of the "constant" responses is similar to the proportion of "rising or falling" stimuli that elicit a response of either "rising" or "falling." However, a correct determination of "constant" is almost always associated with a successful identification of the type of "constant" stimulus, whereas a correct determination of "rising or falling" is often associated with an unsuccessful identification

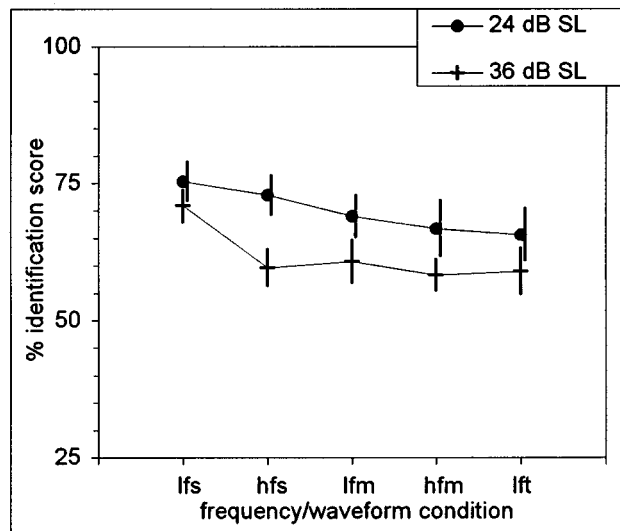


FIG. 5. Overall scores from experiment 1: data pooled over stimulus durations. Key: lfs=50/100 Hz sine; hfs=200/400 Hz sine; lfm=50/100 Hz monophasic; hfm=200/400 Hz monophasic; lft=50/100 Hz tetrphasic. The error bars indicate the standard error in each score, typically 4 percentage points. The chance score is 25%.

of the type, i.e., whether it is "rising" or "falling." (For example, pooled responses for all 160 ms stimuli at 24 dB SL show that 83% of "constant" items elicit one of the "constant" responses, with 99% of these correctly classified, giving a mean identification score of 82%. However, although 77% of "rising or falling" items are identified as either "rising" or "falling," only 78% of these are correctly classified, giving a mean identification score of 60%.) Blamey and Clark (1987) report a similar confusion between "rising" and "falling" in the perception of electro tactile stimuli.

The data in Fig 5 show that performance is better at 24 dB SL than at 36 dB SL. Analysis of variance on these data (1 between-subject factor: presentation level; 1 within-subject factor: frequency/waveform), after arcsine transformation, shows that this effect of stimulus level is just significant at the  $p=0.05$  level [ $F(1,18)=4.67$ ].

As described above, each subject participated in 20 test sessions: four with one frequency/waveform condition, followed by four with a second frequency-waveform condition, and so on. Although asymptotic performance was apparently achieved within each test session (see above), an analysis of the timecourse of subjects' scores suggests that learning effects on a longer timescale were present. Average scores for sessions 1-4, 5-8, 9-12, 13-16, and 17-20 were, respectively, 60%, 63%, 68%, 69%, and 68%. The additional variance contributed by this order effect does not affect the statistical significance of the between-subject effect of presentation level, but the same is not true for within-subject effects. Hence, before consideration of the within-subject effect of frequency/waveform in the data of Fig. 5, the order effect was compensated for by raising scores from sessions 1-4 and 5-8 so as to bring them into line with scores from sessions 9-20 (note: the mean scores in the figure are taken from uncompensated data; since the experimental design is

fully blocked, the differences between the means are unaffected by the compensation procedure). Analysis of variance on order-compensated, arcsine-transformed data for the 24 dB SL subject group shows that the effect of frequency/waveform is not significant at the  $p=0.05$  level [ $F(4,36) = 2.20$ ], and this is confirmed by a multiple comparison procedure (Tukey test,  $p=0.05$ ) which indicates that none of the score differences is significant. However, analysis of variance on order-compensated, arcsine-transformed data for the 36 dB SL subject group shows that the effect of frequency/waveform is highly significant [ $F(4,36) = 5.19$ ,  $p = 0.002$ ]. A multiple comparison procedure on the 36 dB SL data (Tukey test,  $p=0.05$ ) indicates that the 50/100 Hz sinewave score is significantly different from the four other scores, but that no other score differences are significant.

## E. Discussion

The data allow a number of interesting observations. First, the fact that scores for 24 dB SL are better than those for 36 dB SL (see Fig. 5) casts doubt on anecdotal sources which suggest that perception is better at higher levels—there is very little in the literature concerning the effect of level. A brief, informal experiment at 12 dB SL and 24 dB SL produced better scores at the higher of these two levels, perhaps indicating that perception is optimum in the region of 24 dB SL, i.e., around the center of the available dynamic range of approximately 55 dB (Verrillo and Gescheider, 1992).

Second, although 50/100 Hz results are better than corresponding 200/400 Hz results in the majority of the 16 individual comparisons available in the data of Fig. 3 or Fig. 4, the differences are generally not very great (and, in any case, these differences might partly derive from the presence of intensity cues, resulting from failure to achieve constant subjective intensity within the stimuli, which might be expected to vary across the frequency range and between the waveform types). Only one of the four equivalent comparisons in the pooled data of Fig. 5 shows a statistically significant difference, and that is at 36 dB SL where optimum performance is not attained. Larger differences might be expected in view of the results of other studies (e.g., Sherrick, 1985) which suggest frequency changes are less apparent when they occur in the upper part of the vibrotactile frequency range.

Third, the effect of waveform type is not very marked (and, in this case also, any effect might partly derive from the presence of intensity cues). This can be seen in the 32 individual comparisons available in the data of Fig. 3 or Fig. 4, and in the pooled data of Fig. 5, in which only two of the eight comparisons show a statistically significant effect of waveform type (and these are at 36 dB SL where optimum performance is not attained). For the 200/400 Hz transitions, a significant effect of waveform type is not expected because differences between the spectral cues offered by sinewaves and monophasic pulses are not great (see above). However, for the 50/100 Hz transitions, where there are significant differences in the spectral cues offered by the three waveform types (see above), it is perhaps surprising that the effect of waveform type is not greater. This absence of any marked

waveform effect suggests that perception of changes in frequency, at least in this experiment, is largely in terms of temporal information, rather than spectral.

This third observation has practical consequences for the design of sensory-substitution devices such as tactile aids for the hearing impaired, since it suggests that waveform details for a periodic stimulus produced by such a device are not critical. Thus it may be relatively unimportant if, because of the constraints of a limited-bandwidth output transducer, the output waveform from a practical wearable device differs from the “ideal” sinewaves or Gaussian-like pulses used in most laboratory-based studies. (If a frequency- and amplitude-modulated stimulus is required, the most convenient output from a wearable practical transducer is generally in the form of pulses whose waveform cannot be closely controlled.)

The IT values in Fig. 4 for perception of one-octave steps compare well to those measured in our previous study (Summers *et al.*, 1994) for perception of two-octave steps. (Two-octave steps were from 50 to 200 Hz or *vice versa*, in a train of monophasic pulses at 24 dB SL. Note that, in the previous study, subjects were presented with only a three-way choice: “rising,” “falling” or “constant.” However, results from the present study indicate that categorisation of “constant” stimuli into two types presents no additional difficulties, and so it is possible to estimate IT values which would have been obtained in the previous study if a four-way choice had been presented. Estimated figures for a four-way choice are around 0.3 bits higher than those originally measured with a three-way choice.) For two-octave steps of duration 200 and 300 ms, estimated IT values are 1.34 and 1.57 bits, respectively. For one-octave steps at 160, 240 and 320 ms, IT values are 0.65, 0.98 and 0.96 bits, respectively (50/100 Hz monophasic pulses at 24 dB SL) and 0.63, 0.86 and 0.79 bits, respectively (200/400 Hz monophasic pulses at 24 dB SL). Hence, on these timescales, two octave-steps give an IT of approximately 0.6 bits greater than the corresponding IT from one-octave steps, reflecting the greater discriminability of the two-octave transitions.

In the present study, scores for the 80 ms and 160 ms stimuli are in all cases well above chance. However, it is unclear how performance measured here for identification of isolated stimuli will carry over to recognition of the continuous sequences of stimuli, on a timescale of around 100 ms, which are of practical interest in a tactile speech aid. Direct measures of performance for sequences are clearly required, and experiment 2 (below) is intended to provide such a measure.

## III. EXPERIMENT 2: PERCEPTION OF STIMULUS ELEMENTS WITHIN A FREQUENCY- AND AMPLITUDE-MODULATED SEQUENCE

### A. Introduction

In our previous study (Summers *et al.*, 1994) it was established that information can be effectively conveyed by redundantly varying the stimulus amplitude and frequency. The second experiment in the present study is intended to produce a realistic estimate of the IT rate available from such

stimuli, by investigating the perception of a frequency- and amplitude-modulated sequence of stimulus elements.

For a given rate of information presentation, there is a trade-off between the rate at which stimulus elements are presented and the number of categories which a subject is required to discriminate within each stimulus element. (For example, 15 elements per second with 2 categories gives a potential IT rate of  $15 \times \log_2 2$ , i.e., 15 bits  $s^{-1}$ ; 5 elements per second with 8 categories gives a potential IT rate of  $5 \times \log_2 8$ , which is also 15 bits  $s^{-1}$ .) It is not clear what strategy will achieve best results, i.e., whether, when presenting information at a certain rate, subjects should be required to perceive gross features in a rapid sequence of elements or fine detail in a slow sequence of elements. In addition to providing an estimate of IT rate, experiment 2 is also intended to address this question of optimal coding for the stimulus.

## B. Stimuli

To avoid the need for extensive subject training, it was decided that subjects would not be asked to perform a recognition task on an extended sequence of elements. Rather, they were presented with short sequences in an “odd-one-out” task (see below). Each short sequence of quasi-steady elements was presented as a frequency- and amplitude-modulated stimulus with total duration 480 ms and with frequency and amplitude dynamic ranges of 25–400 Hz and 14–34 dB SL, respectively. Frequency and amplitude were covaried redundantly in the same sense, with a 5-dB amplitude change for each 1-oct change of frequency. Stimuli were of two types:

- (1) a sequence of six elements, each with 80-ms duration and in three possible categories (at steps of 10 dB and 2.0 oct across the available dynamic ranges);
- (2) a sequence of three elements, each with 160-ms duration and in nine possible categories (at steps of 2.5 dB and 0.5 oct across the available dynamic ranges).

The potential IT rate for an extended sequence of either type (1) or type (2) elements is 19.8 bits  $s^{-1}$  in each case.

The experiment was carried out in two variants—one with monophasic pulses as the periodic stimuli and one with sinewaves. Details of the stimulus waveforms, e.g., as regards monophasic-pulse shape and details of transitions between the elements, are very similar to those in experiment 1. Sensation levels were determined in the same way as in experiment 1—in the case of sinewaves the compensation for the variation of tactile sensitivity with stimulus frequency was extended to cover the larger number of frequencies used in this experiment.

## C. Subjects

These were 12 normally hearing adults (age range 20 to 54 years), 4 male and 8 female, including authors DAG, PM, and BHB. They were not paid for their participation in the experiment. All but two had previous experience of tactile tests and five had participated in experiment 1.

## D. Procedure

Subjects were presented with a series of three stimuli (each of 480 ms duration and separated by gaps of 1520 ms) and required to identify the “odd one out” which differed in respect of the middle third of the stimulus (the middle element in the case of three-element stimuli and either or both of the middle two elements in the case of six-element stimuli). Response (forced choice) was by keyboard entry. A typical sequence to test a single discrimination for three-element stimuli might be:

7 1 5                      7 4 5                      7 1 5

(where the 9 categories are labelled by integers 0–8). A typical sequence to test a single discrimination for six-element stimuli might be:

010121                      012021                      012021

(where the 3 categories are labelled by integers 0–2). This 3AFC “odd-one-out” procedure was repeated to give a test sequence of 25 such discriminations in each run, the last 20 of which were scored.

For both six-element and three-element stimuli, the middle third of the stimulus has nine possible variants, allowing 36 possible discriminations to be tested. The 20 discriminations scored in each test sequence were selected as a representative subset of the complete set of 36. The elements forming the first third and last third of each stimulus (which remain unchanged across a set of three stimuli forming the “odd-one-out” task) are “context” elements, included so that the elements to be discriminated occur in a similar context to elements in an extended sequence. These context elements were chosen to give, as far as possible, a representative variety of contexts for the test discriminations. However, in order to ensure that the middle-third “target” in each stimulus was delineated from the context elements, sequences of elements were chosen to exclude those sequences which, because of repeated elements, have no change in frequency/amplitude at the one-third or two-thirds points. Hence, the chosen stimuli are not entirely representative of all possible six-element or three-element sequences.

There was no specific training for the test, as the test protocol was designed to avoid the necessity for this. However, at the start of the experiment there was a short explanation and demonstration session lasting approximately 5 min. The two subjects with no previous experience of tactile experiments were given additional time for demonstrations and familiarisation.

Three-element pulse stimuli, three-element sinewave stimuli, six-element pulse stimuli and six-element sinewave stimuli were investigated in four experimental runs (split between two 15-min test sessions) whose order was permuted across the test subjects to balance any learning effects. A second set of four runs was subsequently carried out with the same group of test subjects, identical to the first except that stimulus frequency and amplitude were covaried redundantly *in the opposite sense* (frequency patterns were identical but amplitude patterns were inverted). The stimuli in this second set of four sessions will be referred to as “anticorrelated,” and those in the first set will be described as “correlated.”



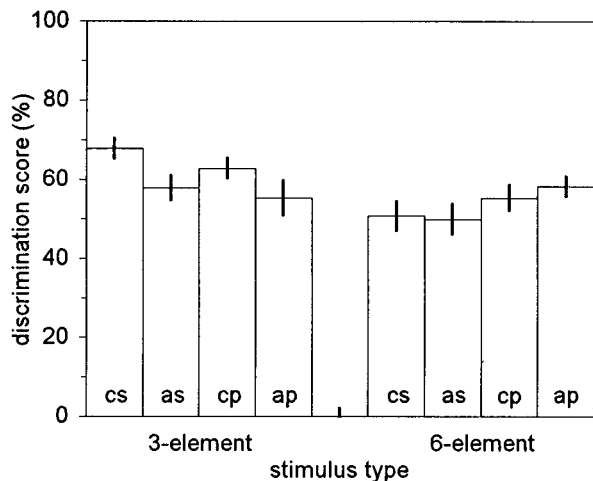


FIG. 6. Mean discrimination scores for each of the eight test conditions in experiment 2. Key: cs=correlated sine; as=anticorrelated sine; cp=correlated pulse; ap=anticorrelated pulse. The error bars indicate the standard error in each score, typically 3.5 percentage points. The chance score is 33%.

### E. Results

Mean scores for experiment 2 are shown in Fig. 6. As described above, the “anticorrelated” conditions were tested after the “correlated” conditions, but it seems unlikely that the correlated/anticorrelated comparison is affected significantly by a learning effect, since no evidence of learning was found through the timecourse of subjects’ first four tests (correlated conditions) or through the timecourse of subjects’ second four tests (anticorrelated conditions). Scores for three-element stimuli are in general somewhat higher than corresponding scores for six-element stimuli. Analysis of variance (three within-subject factors) on the individual subject scores corresponding to the Fig. 6 data shows the effect of coding (three-element or six-element) to be highly significant [ $F(1,11) = 24.2, p < 0.001$ ]; the effect of waveform type (sine or pulse) and the effect of modulation sense (correlated or anticorrelated) are not significant at the  $p = 0.05$  level [ $F(1,11) = 0.32$  and  $F(1,11) = 2.32$ , respectively].

The fact that there is no significant difference between the correlated and anticorrelated conditions, together with the fact that both frequency and amplitude contribute to the perceived sensation from this type of stimulus (Summers *et al.*, 1994), indicates that the stimulus dimensions of frequency and amplitude are in some sense orthogonal.

The similarity between scores for monophasic pulses and sinewaves reinforces the conclusion of experiment 1: When transmitting information via a frequency- and amplitude-modulated periodic stimulus, waveform details are relatively unimportant.

Examination of error patterns shows that, for the six-element stimuli, subjects have great difficulty assessing single elements of 80-ms duration—the only discriminations that can be made with any facility in the six-element stimuli are those which involve a stimulus whose two middle elements are identical and thus produce constant stimulation over 160 ms, e.g.,

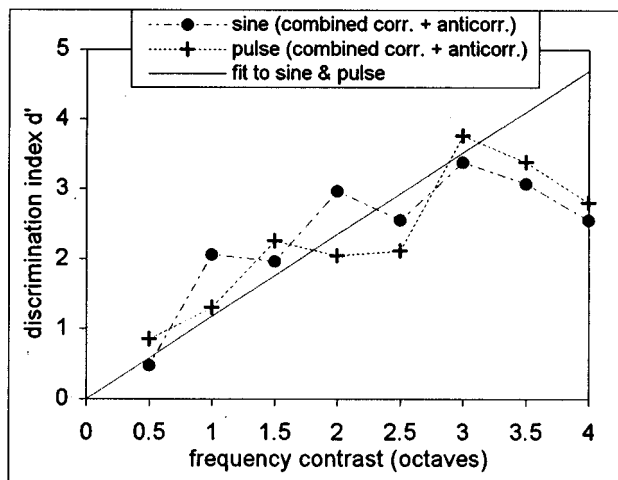


FIG. 7. Discrimination index  $d'$  for the three-element stimuli in experiment 2, plotted as a function of the contrast in frequency between the stimuli. Note that the stimuli are distinguished by a contrast in amplitude as well as a contrast in frequency (5 dB amplitude change per octave of frequency change). The data are derived from combined scores for the correlated and anticorrelated conditions. The full line is fitted to both sets of points (excluding the data at 3.5 and 4.0 octaves—see main text).

020011      020211      020211.

The easiest discriminations in the six-element stimuli are those in which all stimuli in the set of three contain “targets” which remain constant over 160 ms (i.e., the discrimination task becomes approximately equivalent to the three-element case). The most difficult discriminations in the six-element stimuli are those in which no stimuli in the set of three contain “targets” which remain constant over 160 ms.

Error patterns for the more easily perceived, three-element stimuli can be analyzed by classifying the required discriminations according to the magnitude of the frequency/amplitude contrast between the stimuli. Figure 7 shows values of discrimination index  $d'$ , derived from the mean scores for each class using the conversion table given by Craven (1992), plotted as a function of the frequency contrast between the stimuli. (These frequency contrasts are accompanied by corresponding amplitude contrasts.) It can be seen that the smaller contrasts (0.5 oct with 2.5 dB, 1 oct with 5 dB) are not well discriminated. The best-fit line to both sets of data (sine and pulse) corresponds to  $d' = 1.17 \times$  (frequency contrast in octaves). The discrimination index  $d'$  across the full range of stimuli (4 octaves and 20 dB) can thus be calculated as  $4 \times 1.17 \approx 4.7$ . Individual fits to the sine and pulse data give  $d' \approx 4.9$  and  $d' \approx 4.5$ , respectively. In the data of Fig. 7 there is some suggestion that the relation between  $d'$  and frequency/amplitude contrast is non-linear, with  $d'$  increasing less rapidly (or not at all) with contrast towards the top of the range. However, the data at the top of the range may be unreliable because the test sequences contain relatively few of the larger contrasts and because the small number of these items means that a representative set of contexts for them cannot be provided within the test sequences. (The data for contrasts of 3.5 and 4.0 octaves are not included in the line fits.)

## F. Discussion

The intention of experiment 2 was to compare the perception of gross features in a rapid sequence of elements (six-element stimuli) with perception of greater detail in a slower sequence of elements (three-element stimuli). However, results show that subjects could perceive very little on the 80-ms timescale of the six-element stimuli, and only gross features on the 160-ms timescale of the three-element stimuli [see Fig. 7—the discrimination index  $d'$  across the full range of three-element stimuli, at 4.7, corresponds to an IT of approximately 1 bit (see below) and hence to only two effective categories across the dynamic range of frequency/amplitude]. In other words, both types of stimulus were too difficult to allow the intended comparison.

In order to look at the effect of coding within easier stimuli, a subsidiary experiment was performed. This was identical to experiment 2, except that the stimulus timescale was increased by a factor of 2: stimuli had overall duration of 960 ms and were composed either of six 160-ms elements or of three 320-ms elements. (The inter-stimulus interval was reduced to 1040 ms to maintain the two-second intervals between the onsets of successive stimuli in each set of three.) Only the monophasic-pulse waveform was used, with both correlated and anticorrelated stimulus types.

For this “slowed-down” experiment there were 12 subjects, 10 of whom had participated in experiment 2. Scores (mean  $\pm$  s.e.) averaged over both correlated and anticorrelated stimuli were, for three-element stimuli:  $(64 \pm 3)\%$ , compared to  $(59 \pm 3)\%$  from the corresponding monophasic-pulse tests in experiment 2; for six-element stimuli:  $(64 \pm 3)\%$ , compared to  $(57 \pm 2)\%$  from experiment 2. Hence slowing down the stimuli by a factor of 2 does not produce much higher scores. Similarly, an analysis equivalent to that in Fig. 7 gives a discrimination index  $d'$  of 4.9 across the full dynamic range of the slowed-down three-element stimuli—only slightly higher than the value of 4.5 from the three-element monophasic-pulse data in experiment 2. It is surprising that slowing down the stimuli does not produce a larger effect, particularly in view of the marked effect of stimulus duration observed in experiment 1 (see below for further discussion).

## IV. OVERALL DISCUSSION

### A. Estimates of information transfer rate

A measure of some sort of IT rate for the one octave steps in experiment 1 can be obtained by calculating the slopes of lines from the origin to each data point in Fig. 4 (i.e., dividing IT values by the corresponding stimulus durations). This gives maximum IT rates for the various frequency/waveform combinations of around  $5 \text{ bits s}^{-1}$ . Using the same procedure, the two-octave steps in our previous study (Summers *et al.*, 1994) give a maximum IT rate of around  $7 \text{ bits s}^{-1}$ . If calculated on a similar basis, the available IT rate for the single vibrotactile channel at full capacity (with an available frequency range of, say, 4 octaves and an available intensity range of, say, 20 dB) is expected to be considerably higher, perhaps around  $15 \text{ bits s}^{-1}$ .

In experiment 2, for the more easily perceived three-element stimuli, the discrimination index  $d'$  across the full range of stimulation is approximately 4.7. Reference to the conversion graph given by Braida and Durlach (1972) suggests a corresponding figure of 0.9 bits for the available IT from each 160-ms stimulus element, giving an estimate for the IT rate of around  $6 \text{ bits s}^{-1}$ . This is considerably less than the estimate of  $15 \text{ bits s}^{-1}$  in the previous paragraph, as is to be expected—it is unlikely that performance measured for identification of isolated stimuli will carry over to recognition of continuous sequences of similar stimuli.

As mentioned above, an IT rate of  $12 \text{ bits s}^{-1}$  was obtained in the three-channel study by Tan *et al.* (1996), from which a rate per channel in the range  $7\text{--}9 \text{ bits s}^{-1}$  can be estimated. The estimate of  $6 \text{ bits s}^{-1}$  from the present study compares well with this, bearing in mind that the present experiment involves tactile stimulation only, as opposed to the tactile and kinaesthetic stimulation used by Tan. The IT rate for Tadoma, a “natural” method of tactile speech transmission which involves the entire hand, has been estimated at around  $12 \text{ bits s}^{-1}$  (Reed *et al.*, 1992a).

For three-element stimuli in the subsidiary “slowed-down” experiment, the dynamic range of the 320-ms “target” element corresponds to a  $d'$  of 4.9 (see above). This converts to a potential IT for each element of approximately 0.95 bits and hence a potential IT rate from extended sequences of such elements of around  $3 \text{ bits s}^{-1}$ . In the same experiment, the six-element stimuli produce an identical overall score, and hence we can estimate a potential IT rate of around  $3 \text{ bits s}^{-1}$  in that case also, i.e., an IT of approximately 0.5 bits for each 160-ms element. This figure contrasts with the figure of 0.85 bits for each 160-ms element which can be derived from the three-element monophasic-pulse data in experiment 2 (corresponding to  $d' = 4.5$ ). The discrepancy may relate to a problem in the format of these experiments: The six-element task involves perception of the order in which the two “target” elements are presented, but there is no equivalent ordering aspect to the three-element task. The error patterns observed for the six-element stimuli in experiment 2 (see above) suggest that this ordering aspect may present difficulties to subjects. Thus, in both experiment 2 and in the subsidiary experiment, it may be that three-element scores are unduly enhanced compared to six-element scores. Similarly, the estimated IT rate from the three-element data in experiment 2 may be an overestimate of the IT rate for extended sequences of this type, since performance with sequences will be affected by any difficulties in perception of element order.

In this regard it is interesting to note that, among the various types of six-element contrasts in experiment 2, the **02/20** contrast which might be expected to be one of the easiest discriminations—with a 4-oct and 20-dB change of each element in the “target”—but which cannot be discriminated without a perception of the order of the two elements, produces one of the lowest scores. (See also the discussion, above, concerning confusion of “rising” and “falling” stimuli in experiment 1.)

## B. Implications for the design of an aid to lipreading

The estimated IT rate of 6 bits  $s^{-1}$  from experiment 2 is disappointingly low, and suggests that the use of such vibrotactile stimuli to code segmental speech information [at a phoneme rate of, say, 10 per second (Crystal and House, 1988)] has little prospect of success. [It might be argued that this analysis is unduly pessimistic because it does not allow for the redundancy in speech. The 12 bits  $s^{-1}$  offered by Tadoma (see above) allows good reception of the entire speech signal at speaking rates 60%–75% of normal (Reed *et al.*, 1992b), suggesting that an IT rate of  $\sim 20$  bits  $s^{-1}$  would allow good reception of the entire speech signal at normal rates. Hence the IT rate required from an effective aid to lipreading might be expected to be considerably less than 20 bits  $s^{-1}$ .] It is possible that better results could be achieved with extensive subject training, but it seems unlikely that very much higher IT rates would be obtained. Frequency- and amplitude-modulated stimuli may be more suitable for transmitting suprasegmental speech-derived information, on a timescale of around 500 ms, say, rather than segmental information. Support for this conjecture is provided by measurements in our laboratories and elsewhere on transmission of suprasegmental information (Bernstein *et al.*, 1989; Summers *et al.*, 1994) and by measurements in our laboratories on transmission of segmental information (Summers *et al.*, 1996). Some success in the transmission of segmental information (consonants in nonsense syllables) was observed in the latter study, and at first sight it is difficult to reconcile this with the low estimate of IT rate from the present investigation. However, re-examination of the consonant-discrimination data showed that subjects did indeed derive little from modulations of frequency and amplitude in the tactile signal—they obtained most of their information from the temporal pattern of gaps (“silences”) in the speech-derived stimuli. This type of information is unavailable in experiment 2, from which our 6 bits  $s^{-1}$  estimate of IT rate is obtained, since all stimulus elements are suprathreshold.

The limited capacity of the tactile channel suggests that the visual channel may be a better choice for transmitting information to supplement lipreading. With such a strategy, it is necessary to avoid disruption of the visual information available directly from the speaker. However, the example of cued speech (Cornett, 1967), in which the speaker gives manual signals to augment the “natural” visual information, suggests that such disruption can be avoided. Uchanski *et al.* (1994) discuss aspects of the design of a system based around speech-recognition hardware, and a visual display in the peripheral vision has been investigated by Upton (1968) and Ebrahim and Kunov (1991). As a *coda* to the present study, a brief experiment was carried out in which the three-element stimuli of experiment 2 were presented visually, the nine levels within the stimuli displayed via a linear array of nine light-emitting diodes. Scores (mean  $\pm$  s.e.) from six subjects in this 3AFC procedure were (85 $\pm$ 2)% for a “moving dot” display and (78 $\pm$ 4)% for a display in terms of length of array illuminated. These figures are significantly higher than those obtained in the tactile case (Fig. 6), where the best of the three-element scores is (68 $\pm$ 3)%. Visual aids

for the deaf have received much less investigation than tactile aids: Further investigation is clearly warranted.

## V. CONCLUSION

It is clear that meaningful information can be transmitted via time-varying vibrotactile stimuli from a single transducer. The results of this investigation indicate the type of features which can be perceived in such patterns, with implications for the design of sensory-substitution systems and in the area of virtual environments, where a suitable interface can allow exploration of virtual surfaces to produce time-varying tactile patterns for the user.

The absence of a marked effect of waveform in experiment 1 suggests that vibrotactile frequency is perceived largely in terms of temporal cues, rather than spectral. In practice, this means that details of the output waveform are not a critical aspect of the design of tactile devices which transmit information as modulation of a periodic signal.

The results of experiment 2 suggest that the IT rate available from a single vibrotactile channel is relatively modest. Thus a tactile aid to lipreading may be better suited to transmitting suprasegmental information on a timescale of a few hundred milliseconds rather than segmental information on a timescale of several tens of milliseconds. An important consideration is the effect of stimulation site—the wrist is a common choice for tactile aids, rather than the fingertip used in the present study. We are currently investigating perception on the wrist: Early results suggest that, if stimulation level is increased to compensate for the reduced sensitivity at the wrist, perception of sequences via the glabrous skin on the underside of the wrist is similar to that on the fingertip.

## ACKNOWLEDGMENTS

This research was supported by the Engineering and Physical Sciences Research Council. Our co-workers John Stevens, Ruth Gray and Marjan Oloomi made valuable contributions. Hong Tan provided stimulating discussion. Bill Rabinowitz and an anonymous reviewer are thanked for their helpful comments and suggestions.

- Bernstein, L. E. (1992). “The evaluation of tactile aids,” in *Tactile Aids for the Hearing Impaired*, edited by I. R. Summers (Whurr, London), pp. 167–186.
- Bernstein, L. E., Schechter, M. B., and Goldstein, M. H. (1986). “Child and adult vibrotactile thresholds for sinusoidal and pulsatile stimuli,” *J. Acoust. Soc. Am.* **80**, 118–123.
- Bernstein, L. E., Eberhardt, S. P., and Demorest, M. E. (1989). “Single-channel vibrotactile supplements to visual perception of intonation and stress,” *J. Acoust. Soc. Am.* **85**, 397–405.
- Blamey, P. J., and Clark, G. M. (1985). “A wearable multiple-electrode electro-tactile speech processor for the profoundly deaf,” *J. Acoust. Soc. Am.* **77**, 1619–1620.
- Blamey, P. J., and Clark, G. M. (1987). “Psychophysical studies relevant to the design of a digital electro-tactile speech processor,” *J. Acoust. Soc. Am.* **82**, 116–125.
- Blamey, P. J., Alcantara, J. I., Cowan, R. S. C., Galvin, K. L., Sarant, J. Z., and Clark, G. M. (1990). “Perception of amplitude variations of pulsatile electro-tactile stimuli,” *J. Acoust. Soc. Am.* **88**, 1765–1772.
- Bolanowski, Jr., S. J., Gescheider, G. A., Verrillo, R. T., and Checkowsky, C. M. (1988). “Four channels mediate the mechanical aspects of touch,” *J. Acoust. Soc. Am.* **84**, 1680–1694.

- Braida, L. D., and Durlach, N. I. (1972). "Intensity perception. II. Resolution in one-interval paradigms," *J. Acoust. Soc. Am.* **51**, 483–502.
- Cornett, R. O. (1967). "Cued speech," *Am. Ann. Deaf* **112**, 3–13.
- Craven, B. J. (1992). "A table of  $d'$  for  $M$ -alternative odd-man-out forced-choice procedures," *Percept. Psychophys.* **51**, 379–385.
- Crystal, T. H., and House, A. S. (1988). "Segmental durations in connected-speech signals—Current results," *J. Acoust. Soc. Am.* **83**, 1553–1573.
- Ebrahimi, D., and Kunov, H. (1991). "Peripheral vision lipreading aid," *IEEE Trans. Biomed. Eng.* **38**, 944–952.
- Formby, C., Morgan, L. N., Forrest, T. G., and Raney, J. J. (1992). "The role of frequency selectivity in measures of auditory and vibrotactile temporal resolution," *J. Acoust. Soc. Am.* **91**, 293–305.
- Kokjer, K. J. (1987). "The information capacity of the human fingertip," *IEEE Trans. Syst. Man Cybern.* **17**, 100–102.
- Lamoré, P. J. J., and Keemink, C. J. (1988). "Evidence for different types of mechanoreceptors from measurements of the psychophysical threshold for vibrations under different stimulation conditions," *J. Acoust. Soc. Am.* **83**, 2339–2351.
- Lechelt, E. C. (1975). "Temporal numerosity discrimination: Intermodal comparisons revisited," *Br. J. Psychol.* **66**, 101–108.
- Lechelt, E. C. (1980). "Lateral differences and shifts as a function of tactile temporal pattern complexity: Implications for differential processing strategies of the cerebral hemispheres," *Psychol. Res.* **41**, 319–333.
- Miller, G. A., and Nicely, P. E. (1955). "An analysis of perceptual confusions among English consonants," *J. Acoust. Soc. Am.* **27**, 338–352.
- Rabinowitz, W. M., Houtsma, A. J. M., Durlach, N. I., and Delhorne, L. A. (1987). "Multidimensional tactile displays: Identification of vibratory intensity, frequency and contactor area," *J. Acoust. Soc. Am.* **82**, 1243–1252.
- Reed, C. M., Durlach, N. I., and Delhorne, L. A. (1992a). "The tactual reception of speech, fingerspelling and sign language by the deaf-blind," *SID-92 Digest*, 102–105.
- Reed, C. M., Durlach, N. I., and Delhorne, L. A. (1992b). "Natural methods of tactual communication," in *Tactile Aids for the Hearing Impaired*, edited by I. R. Summers (Whurr, London), pp. 218–230.
- Rothenberg, M., Verrillo, R. T., Zahorian, S. A., Brachman, M. L., and Bolanowski, Jr., S. J. (1977). "Vibrotactile frequency for encoding a speech parameter," *J. Acoust. Soc. Am.* **62**, 1003–1012.
- Sherrick, C. E. (1985). "A scale rate for tactual vibration," *J. Acoust. Soc. Am.* **78**, 78–83.
- Srinivasan, M. A. (1995). "Haptic interfaces," in *Virtual Reality, Scientific and Technical Challenges*, edited by N. I. Durlach and A. S. Mavor (National Academy Press, Washington, DC), pp. 161–187.
- Summers, I. R. (1992). "Signal processing strategies for single-channel systems," in *Tactile Aids for the Hearing Impaired*, edited by I. R. Summers (Whurr, London), pp. 110–127.
- Summers, I. R., and Farr, J. (1989). "Development of a single-channel tactile aid for the profoundly deaf," *Proc. Eurospeech '89, Paris, 2*, 706–709.
- Summers, I. R., Dixon, P. R., Cooper, P. G., Gratton, D. A., Brown, B. H., and Stevens, J. C. (1994). "Vibrotactile and electrotactile perception of time-varying pulse trains," *J. Acoust. Soc. Am.* **95**, 1548–1558.
- Summers, I. R., Milnes, P., Stevens, J. C., and Cooper, P. G. (1996). "Coding of acoustic features for a single-channel tactile aid," *Br. J. Audiol.* **30**, 238–248.
- Tan, H. Z. (1996). "Information transmission with a multi-finger tactual display," unpublished Ph.D. thesis, Massachusetts Institute of Technology.
- Tan, H. Z. (1997). Personal communication.
- Tan, H. Z., Durlach, N. I., Rabinowitz, W. M., and Reed, C. M. (1996). "Information transmission with a multi-finger tactual display," *Proc. ISAC-96, Sint-Michielsgestel*, 37–40.
- Uchanski, R. M., Delhorne, L. A., Dix, A. K., Braida, L. D., Reed, C. M., and Durlach, N. I. (1994). "Automatic speech recognition to aid the hearing impaired: Prospects for the automatic generation of cued speech," *J. Rehab. Res. Dev.* **31**, 20–41.
- Upton, H. W. (1968). "Wearable eyeglass speechreading aid," *Am. Ann. Deaf* **113**, 222–229.
- Verrillo, R. T., and Gescheider, G. A. (1992). "Perception via the sense of touch," in *Tactile Aids for the Hearing Impaired*, edited by I. R. Summers (Whurr, London), pp. 1–36.
- Verrillo, R. T., Fraioli, A. J., and Smith, R. L. (1969). "Sensation magnitude of vibrotactile stimuli," *Percept. Psychophys.* **6**, 366–372.
- Weisenberger, J. M. (1986). "Sensitivity to amplitude-modulated vibrotactile signals," *J. Acoust. Soc. Am.* **80**, 1707–1715.
- Weisenberger, J. M. (1992). "Communication of the acoustic environment via tactile stimuli," in *Tactile Aids for the Hearing Impaired*, edited by I. R. Summers (Whurr, London), pp. 83–109.
- Weisenberger, J. M., and Russell, A. F. (1989). "Comparison of two single-channel vibrotactile aids for the hearing-impaired," *J. Speech Hear. Res.* **32**, 83–92.

# Estimating parameters for psychometric functions using the four-point sampling method

Chan F. Lam

*Department of Biometry and Epidemiology, Medical University of South Carolina, Charleston, South Carolina 29425*

Judy R. Dubno, Jayne B. Ahlstrom, Ning-Ji He, and John H. Mills

*Department of Otolaryngology and Communicative Sciences, Medical University of South Carolina, Charleston, South Carolina 29425*

(Received 2 April 1996; accepted for publication 20 August 1997)

Although a psychometric function describing a subject's responses to some physical stimuli is of considerable value, characterizing such functions is time consuming and, hence, is not carried out routinely in psychophysical experiments. A principal reason for the lack of efficiency in characterizing a psychometric function is the use of sampling methods that either converge on a single point on the psychometric function, such as the PEST method, or which distribute observations uniformly over a wide range, such as the constant stimuli method. As an alternative, a multimodal four-point sampling method has been proposed [C. F. Lam, J. H. Mills, and J. R. Dubno, *J. Acoust. Soc. Am.* **99**, 3689–3693 (1996)]. A psychometric function is then fitted to the four points (each with several trials) to estimate the threshold and slope parameters of the psychometric function. Adaptive methods, such as the up–down methods [H. Levitt, *J. Acoust. Soc. Am.* **49**, 467–477 (1971)], can be used to provide good initial estimates of the threshold and spread parameters of a psychometric function described by a logistic function. In ongoing studies of age-related changes in auditory masking and discrimination, this new four-point sampling method has been applied to determine psychometric functions for absolute thresholds as a function of duration, thresholds in simultaneous and forward masking, frequency discrimination, and intensity discrimination in both young and aged human subjects. Results indicate that a reduction in data collection time of about 50% with no increase in variance can be achieved. This increase in efficiency applies to simple detection tasks by normal hearing subjects as well as to complex discrimination tasks by older subjects with hearing loss. © 1997 Acoustical Society of America. [S0001-4966(97)02512-5]

PACS numbers: 43.66.Yw [JWH]

## INTRODUCTION

Psychometric functions describe the relationship between physical stimuli and subjects' responses in a variety of psychophysical tasks. Because of the amount of data-collection time required to characterize most psychometric functions, typically, only the "threshold" or a particular performance level of the function is measured.

In experiments in which the entire psychometric function is required, the method of constant stimuli is the procedure of choice. However, the method of constant stimuli is inefficient because many trials are conducted at values where there are very low or very high probabilities of a positive response.

Hall (1981) proposed a hybrid adaptive procedure for estimating psychometric functions in which the parameter estimation by sequential testing (PEST) rules (Taylor and Creelman, 1967) were used to obtain responses and then a psychometric function was fitted to the responses to estimate the threshold (or central tendency) parameter and the slope parameter. As a result, the hybrid procedure requires much smaller numbers of trials than the method of constant stimuli. However, the PEST rules used by Hall concentrate data points near the threshold, the point of interest. If the

value of the threshold as well as the slope parameters are to be estimated, it is not necessary to place many data points in the neighborhood of the threshold. Recently, a four-point sampling method for psychometric function estimation has been proposed to reduce the number of data points needed (Lam *et al.*, 1996). In theory, 50% or better reduction in data collection time can be achieved. This paper presents the results of applying the new four-point sampling method to determine psychometric functions for a variety of psychometric tasks. Absolute thresholds as a function of duration, thresholds in simultaneous and forward masking, frequency discrimination, and intensity discrimination were measured in both young and aged human subjects.

To use the four-point sampling method to determine psychometric functions, one needs rough initial estimates of the threshold ( $M$ ) and spread ( $S$ ) parameters. This paper proposes two methods for determining such initial estimates.

## I. METHODS

A detailed description of the development of the four-point sampling method for psychometric function determination can be found in Lam *et al.* (1996). A summary of the procedure and the rationale is presented here. Assuming that

a psychometric function is expressed as a cumulative Gaussian function, with mean  $\mu$  and variance  $\sigma^2$ , Levitt (1971) stated that “a good compromise for estimating both  $\mu$  and  $\sigma$  with relative precision is to place observations at a distance  $\sigma$  on both sides of  $\mu$ , i.e., at the  $X_{15.9}$  and  $X_{84.1}$  levels,” where  $X_p$  is a stimulus level with  $p\%$  correct response. Unfortunately, the values of the threshold and spread parameters are unknown; in fact, they are to be estimated. Rather than sampling around  $\mu + \sigma$  and  $\mu - \sigma$  in a uniform manner (i.e., the constant stimuli method), four specifically placed stimuli locations are used.

For ease of discussion and for parameter estimation purposes, instead of a cumulative Gaussian function, a logistic function in the form of Eq. (1), is used:

$$P(X) = \alpha + (1 - \alpha) \frac{1}{1 + e^{-(X-M)/S}}, \quad (1)$$

where  $M$  and  $S$  are the threshold and spread parameters, and  $\alpha$  is the false alarm (Taylor and Creelman, 1967; Hall, 1981). The four sampling points for estimating parameters in the form of Eq. (1) are (Lam *et al.*, 1997):

$$\begin{aligned} X_{12} &= M - 2S, & X_{27} &= M - S, \\ X_{73} &= M + S, & X_{88} &= M + 2S. \end{aligned} \quad (2)$$

The responses from these four sets of stimuli are then used in nonlinear regression to estimate the parameters of the psychometric function of Eq. (1).

In order to use the four-point sampling method, some initial estimates of  $M$  and  $S$  are needed. The following sections discuss two methods for obtaining such initial estimates of  $M$  and  $S$ . The first one assumes that the investigators have some rough idea of the values of  $M$  and  $S$  for the psychometric task of interest, whereas the second one does not require any prior knowledge of the ranges of  $M$  and  $S$ .

## II. METHOD FOR ADJUSTING THE INITIAL ESTIMATES OF THRESHOLD AND SPREAD PARAMETERS

Most investigators generally have some rough estimates of the parameter values for threshold, denoted as  $M^*$ , and spread, denoted as  $S^*$ , for a particular psychophysical task. According to Eq. (2), the locations on the  $x$  axis of the four points are

$$\begin{aligned} X_{12} &= M^* - 2S^*, & X_{27} &= M^* - S^*, \\ X_{73} &= M^* + S^*, & X_{88} &= M^* + 2S^*. \end{aligned} \quad (3)$$

Ideally, the initial estimates ( $M^*$  and  $S^*$ ) should be reasonable, and, if not, they should be easily adjustable. To this end, responses to the above four stimuli can be obtained using a small number of trials (say, ten per point). Because the four data points will be used in a nonlinear regression process to estimate the threshold and spread parameters using Eq. (1), the data points should be roughly evenly distributed over the entire sigmoidal curve of the psychometric function, with two points above and two points below the 50% level (i.e., the threshold point), as shown in Fig. 1. The solid line in Fig. 1 is the calculated psychometric function of 11 data points obtained from the constant stimuli method; the

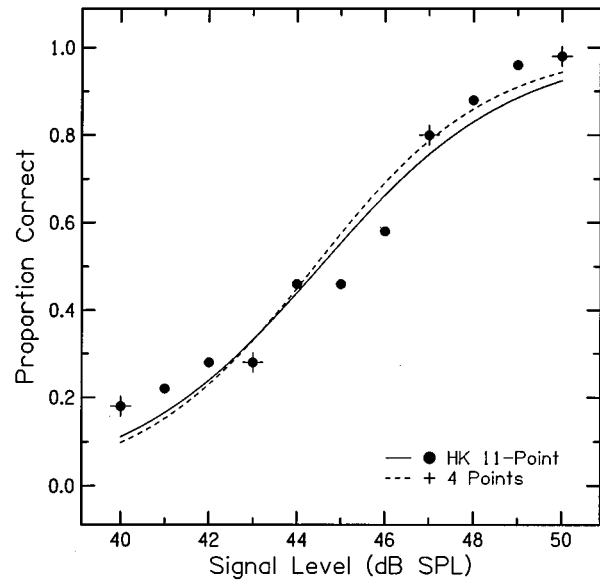


FIG. 1. Percent correct detection of a pure tone in a broadband noise for subject HK. Filled circles are data obtained using the method of constant stimuli (50 trials per point). The “+” indicates the four appropriately placed points of the four-point sampling method. The solid curve is the calculated proportion correct using Eq. (1) and 11 data points. The dashed line is the calculated proportion correct using Eq. (1) and four data points.

dotted line is the calculated psychometric function using four (of the 11) points. When the initial estimate of  $M$  (i.e.,  $M^*$ ) is too small [Fig. 2(A) and (B)] or too large [Fig. 2(C) and (D)], three or all of the four points will be below or above the 50% level. As a result, the calculated psychometric functions (dotted lines in Fig. 2) are different from the one using all 11 data points (solid line). Furthermore, the resulting psycho-

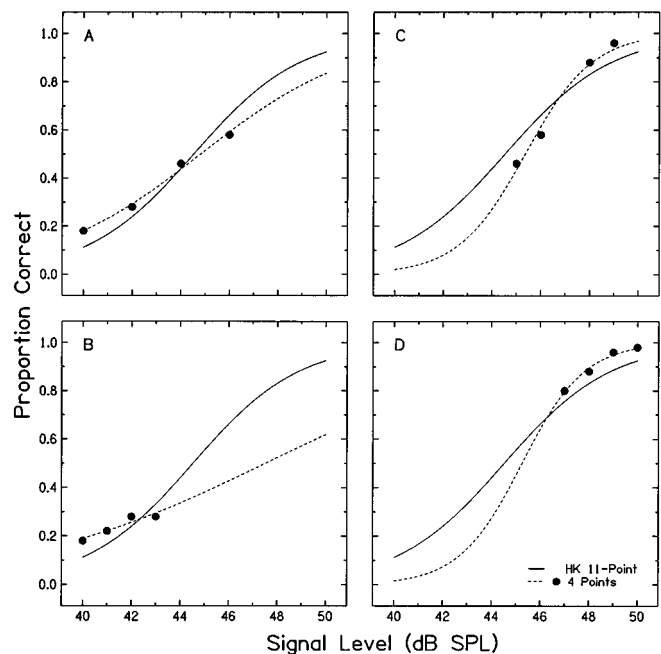


FIG. 2. The various placements of four points (filled circles) with incorrect initial threshold estimate  $M^*$  and the corresponding estimated psychometric functions (dashed lines). Panels (A) and (B) indicate  $M^*$  is too small, whereas panels (C) and (D) indicate  $M^*$  is too large.

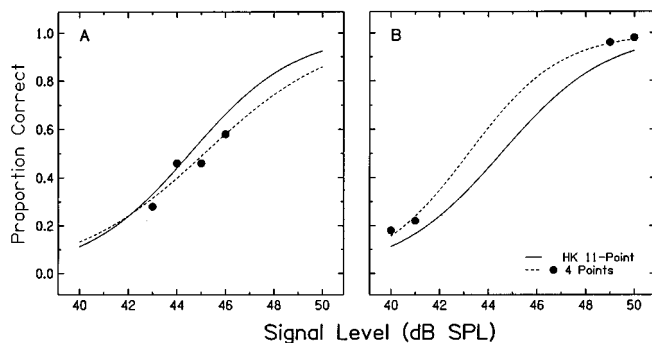


FIG. 3. The various placements of four points with incorrect initial spread estimate  $S^*$  and the corresponding estimated psychometric functions (dashed lines). Panel (A) indicates  $S^*$  is too small, whereas panel (B) indicates  $S^*$  is too large.

metric functions from different sets of four points are different from each other.

When the initial estimate of  $S$  (i.e.,  $S^*$ ) is too small, then the four points will center around the middle of the sigmoidal curve (which is approximately linear), as shown in Fig. 3(A). On the other hand, if two points are at the right most part of the sigmoidal curve (i.e.,  $p > 0.80$ ) and the other two points are at the left most part of the curve (i.e.,  $p < 0.20$ ), as shown in Fig. 3(B), the value of  $S^*$  is too large. The psychometric function estimated from either of the incorrectly placed four points varies considerably from the function estimated using all 11 points.

When both estimates ( $M^*$  and  $S^*$ ) need adjusting, the patterns shown in Fig. 2(B) and (D) would result. In Fig. 2(B), both  $M^*$  and  $S^*$  are too small. On the other hand, Fig. 2(D) indicates that  $M^*$  is too large and  $S^*$  is too small.

It is obvious that one would not be able to select  $M^*$  and  $S^*$  so that the proportions of positive responses are exactly 0.12, 0.27, 0.73, and 0.88 [see Eq. (2)]. As long as the four points distribute evenly and cover approximately the entire sigmoidal curve so that proportions of positive responses are between 0.10 and 0.90, the nonlinear regression process should be able to provide good estimates of  $M$  and  $S$ . In adjusting the value of  $S^*$ , one should keep in mind that  $X_{88} - X_{12} \approx 4S$ . It should be emphasized that it is better to have a wider range of responses, (i.e., 0.10–0.90) than a smaller range of responses (i.e., 0.30–0.70) for the obvious reason that the range of the stimulus values should be as wide as possible for regression analysis. Another reason to include stimulus values where the probability of a positive response is very high or very low is that such responses are more reliable. Note that the variance of an estimate  $p$  of a binomial distribution, for which the yes–no responses of any psychophysical tasks follow, is  $p(1-p)$ . With more reliable data points, better estimates of parameters would result.

### III. ADAPTIVE METHOD FOR DETERMINING INITIAL ESTIMATES OF THRESHOLD AND SPREAD PARAMETERS

Another, and probably better and more systematic, method for obtaining good initial estimates of  $M$  and  $S$  is to use the two-down–one-up and two-up–one-down adaptive

method of Levitt (1971) to estimate the stimulus values of  $X_{70.7}$  and  $X_{29.3}$ , which are close to  $X_{73}$  and  $X_{27}$  of Eq. (2), respectively. The values of  $M$  and  $S$  are approximately equal to

$$M \approx (X_{70.7} + X_{29.3})/2, \quad (4)$$

$$S \approx (X_{70.7} - X_{29.3})/2.$$

With the interleaved adaptive methods,<sup>1</sup> no prior information on either the location or spread of the response curve is needed. Using the obtained values of  $M$  and  $S$ , Eq. (2) is then used to determine the four stimulus levels for the four-point method.

## IV. EXPERIMENTAL METHODS

The four-point sampling method was tested against an 11-point constant stimuli method for young and aged subjects for different psychophysical tasks. For the constant stimuli method, 11 equally spaced increments were used, and each was presented 50 times in random order. For the four-point sampling method, the values at  $M \pm S$  and  $M \pm 2S$  were each presented in random order in five blocks of 10 trials each, resulting in 10, 20, 30, 40, and 50 trials/point. Five different psychophysical tasks were used in the comparison, including absolute threshold, forward masking, simultaneous masking, intensity discrimination, and frequency discrimination.

For all measurements, the frequency tested was 2000 Hz. A “yes/no” paradigm was used for both absolute and masked thresholds. Absolute thresholds were measured for 20- and 200-ms pure tones (5-ms rise–fall times). For simultaneous masking, a 350-ms signal was presented in a broadband masker (25 dB/Hz). For forward masking, a 20-ms signal followed a 350-ms broadband masker (50 dB/Hz). For intensity and frequency discrimination, signal level was 60 dB SPL. Subjects’ response paradigm was also yes–no (i.e., “Yes, the variable stimulus is higher than the standard stimulus,” versus “No, not higher.”) All measures were obtained monaurally under earphones.

All subjects had normal hearing through 2000 Hz (ANSI, 1989). Young subjects participated in all psychophysical tasks. The number of young subjects for each task ranged from 4 to 11. For aged subjects (age range 68–75), tasks included absolute threshold, simultaneous masking, and intensity discrimination. The number of aged subjects for each task ranged from 1 to 3.

## V. RESULTS

Figures 4 and 5, respectively, show the responses of a young and an aged subject for the simultaneous masking task using the four-point sampling method and the 11-point constant stimuli method. Generally, after 30–40 trials per point, psychometric functions determined from the four-point sampling method converge to that from the 11-point constant stimuli method of 50 trials per point. Figure 6 shows the mean estimated threshold and spread parameters as a function of the number of trials per datum point for 14 subjects. Error bars indicate  $\pm 1$  standard error. Results of  $t$  tests indicate that only the estimated  $M$  with ten trials/point is sig-

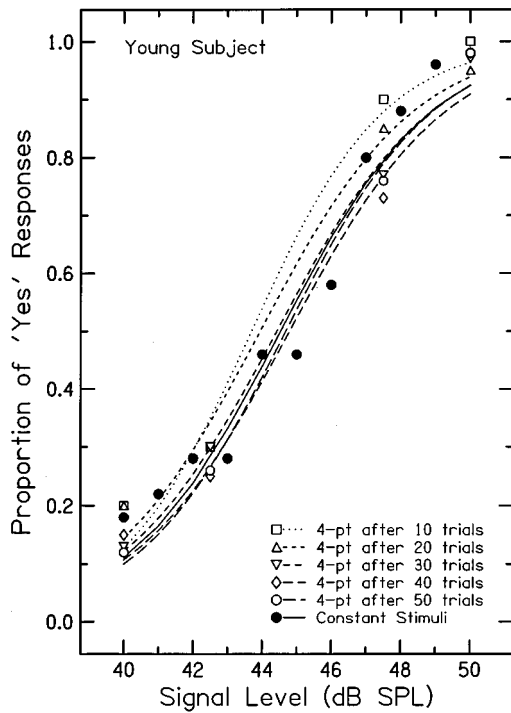


FIG. 4. Percent correct detection of a pure tone in a broadband noise (simultaneous masking) for a young subject. Filled circles are data obtained using the method of constant stimuli (50 trials per point). Open symbols are data collected using the four-point sampling method with 10, 20, 30, 40, or 50 trials per point. The solid curve is the calculated proportion correct using Eq. (1) and 11 data points. Each dashed line is the calculated proportion correct using Eq. (1) and four data points with various trials per point.

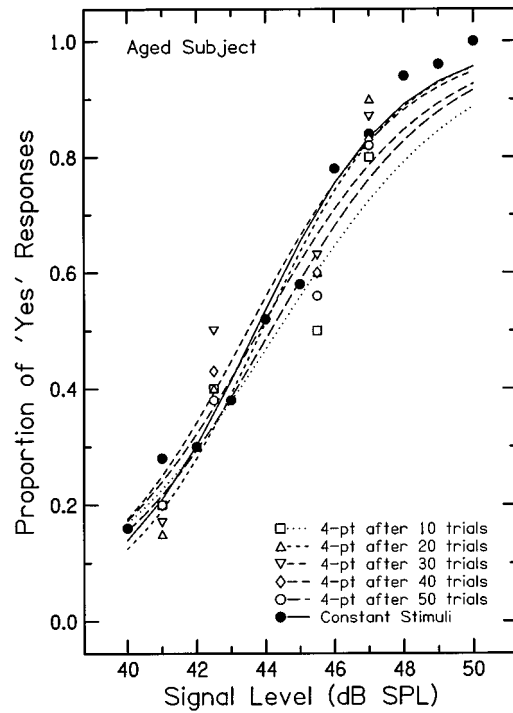


FIG. 5. Percent correct detection of a pure tone in a broadband noise (simultaneous masking) for an aged subject. Filled circles are data obtained using the method of constant stimuli (50 trials per point). Open symbols are data collected using the four-point sampling method with 10, 20, 30, 40, or 50 trials per point. The solid curve is the calculated proportion correct using Eq. (1) and 11 data points. Each dashed line is the calculated proportion correct using Eq. (1) and four data points with various trials per point.

nificantly different from that of the constant stimuli method ( $p < 0.05$ ). Changes in threshold and spread estimates as a function of the number of trials were similar for other psychophysical tasks. Based on these results, it appears that 30–40 trials per point for the four-point sampling method should be sufficient. Note also that the  $\pm 1$  standard error bars for the 11-point results (for a total of 550 trials) were slightly larger than those from the four-point method (from a total of 200 trials).

The mean estimated threshold ( $M$ ) and spread ( $S$ ) parameter values of the psychometric function using the four-point sampling method and 11-point constant stimuli method for forward masking, simultaneous masking, quiet threshold (20- and 200-ms signals), intensity discrimination, and frequency discrimination are shown in Figs. 7 and 8. The false alarm parameter (i.e.,  $\alpha$ ) was assumed to be zero in the non-linear regression processes for simultaneous masking, forward masking, and absolute thresholds; for intensity and frequency discrimination, the false alarm parameter was also estimated using Eq. (1).

From Fig. 7, the estimated threshold and spread parameter values for simultaneous masking, forward masking, and absolute thresholds were similar between the four-point sampling method and the constant stimuli method. This was the case for both young and aged subjects. Consequently, the calculated psychometric functions from the two methods were similar (Figs. 4 and 5). Results of  $t$  tests performed on the 14 estimated values of  $M$  and  $S$  for the simultaneous masking paradigm from 11 young and three aged subjects

revealed no statistical difference ( $p > 0.05$ ) between the four-point sampling method and the constant stimuli method. The sample sizes for the other paradigms were too small (between 4 and 6) for meaningful statistical analysis.

It should be pointed out that the total number of trials for the four-point sampling method was 200, whereas that of the 11-point method was 550, assuming 50 trials/point. It is of interest to compare the estimated parameters from a total of 200 trials for both the four-point sampling method and the 11-point constant stimuli method. A psychometric function of the form of Eq. (1), with known  $M = 40$  and  $S = 1.5$ , was

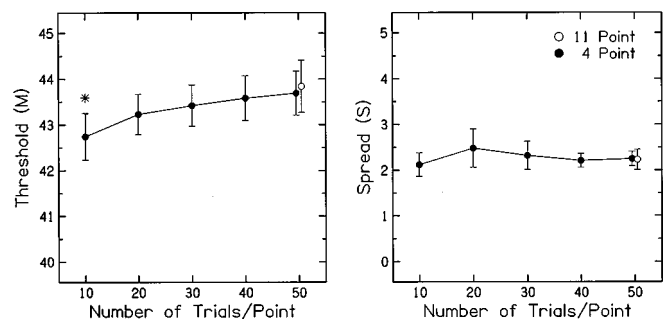


FIG. 6. Mean (and  $\pm 1$  standard error) estimates of threshold and spread parameters for the four-point sampling method as a function of the number of trials per point in comparison to the estimated values from the 11-point constant stimuli method (50 trials per point) for simultaneous masking. The asterisk indicates that the estimated threshold with ten trials/point was significantly different from the estimated threshold using the 11-point constant stimuli method.



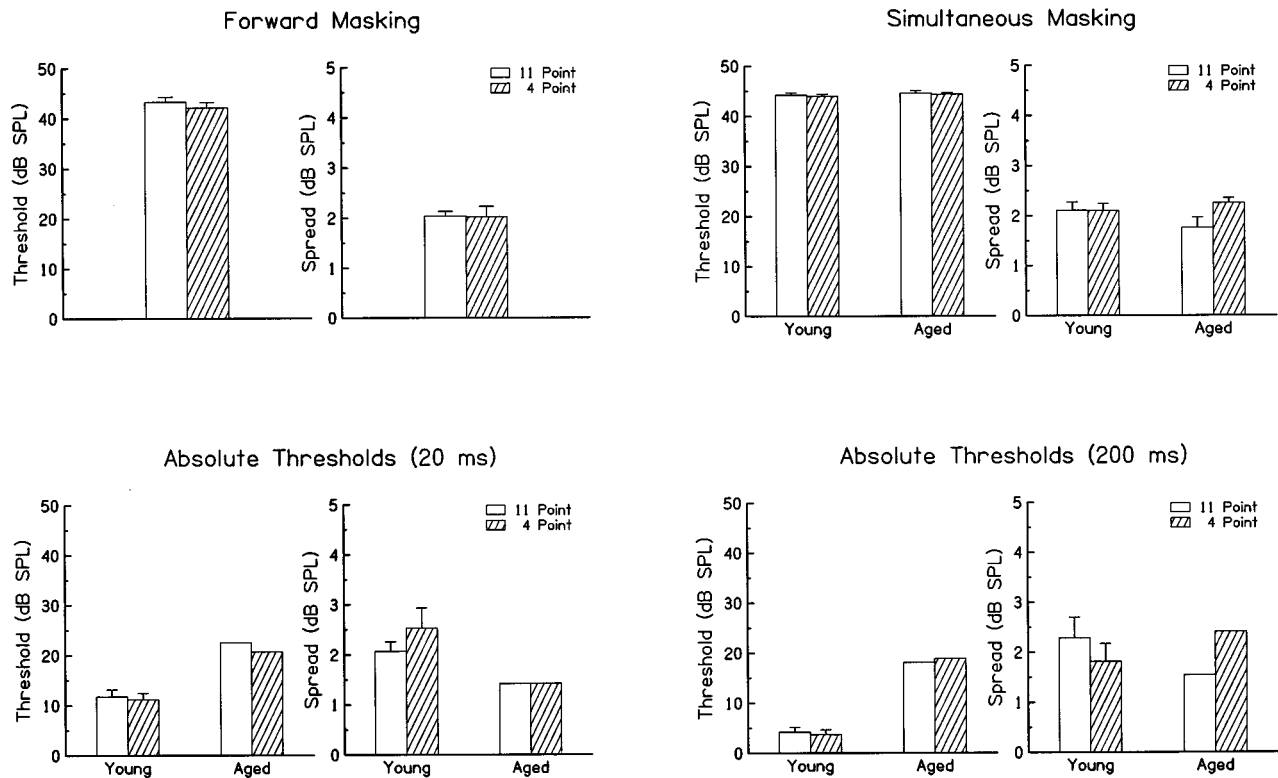


FIG. 7. Mean (and +1 standard error) estimates of threshold and spread parameters for the four-point sampling method and the 11-point constant stimuli method for simultaneous masking, absolute thresholds (20-ms signals), and absolute thresholds (200-ms signals) for young and aged subjects, and forward masking for young subjects.

used to generate data in a computer Monte Carlo simulation. Either 50 trials/point for the four-point sampling method or 18 trials/point for the 11-point constant stimuli method (resulting in a total of 198 trials) was generated by sampling a uniform random number generator. If the random number was smaller than the known psychometric function value (with  $M=40$ ,  $S=1.5$ ), it was counted as a yes response. After the appropriate number of trials/point for all four or 11 data points were generated, a nonlinear regression procedure was used to estimate the  $M$  and  $S$  parameters. This process was repeated 1000 times. It is not surprising that there was more randomness in the 18 trials/point data for the 11-point constant stimuli method than in the 50 trials/point data for the four-point sampling method. As a result of the randomness in the data, the estimated  $S$  for the 10–90 percentile of the 1000 simulations was between 1.18 and 1.88 for the 11-point constant stimuli method versus 1.47 and 1.69 for the four-point sampling method, with known  $S=1.50$ . The values of the estimated  $M$  were quite similar between the 11-point constant stimuli method (39.65–40.38) and the four-point sampling method (39.80–40.21).

## VI. DISCUSSION AND CONCLUSIONS

In most psychometric estimation methods, including constant stimuli, PEST, and adaptive procedures, some preliminary determination of the parameter values (e.g., starting value and step size in the up–down method) is needed. Similarly, the four-point method also needs initial estimates. By obtaining responses for a small number of trials per point,

say ten, the investigator may simply adjust the initial estimates of the threshold,  $M$ , and spread,  $S$ , parameters so that appropriately located data may be collected and good estimates of the parameters may be obtained by a nonlinear regression process. Another method of obtaining initial estimates of  $M$  and  $S$  is by the use of interleaving two-down–one-up and two-up–one-down adaptive procedures that determine the  $X_{71}$  and  $X_{29}$  stimulus levels [see Eq. (4)]. This probably is a more efficient method than the previous one of using a small number of trials to estimate  $M$  and  $S$ . Since the estimated  $M$  and  $S$  from the up–down method are to be used to determine the four stimulus levels [Eq. (2)] (from which the  $M$  and  $S$  of the psychometric function are estimated by means of nonlinear regression), it is not necessary to interleave the two up–down adaptive procedures.

One could argue that it is more efficient to use the two points already obtained from the up–down adaptive procedure as two of the four points for the four-point sampling method. Rather than obtaining four different points using Eq. (2), two more points ( $X_{12}$  and  $X_{88}$ ) may suffice. However, we found that the resulting estimate of  $S$  obtained from two up–down procedures and a two-point sampling procedure were statistically different from those obtained from the 11-point constant stimuli method and the four-point sampling method. One explanation for such a discrepancy is that the up–down method varies the stimulus level ( $X$ ) for a fixed response level (i.e., 88%), whereas the variation in the four-point sampling method and the 11-point constant stimuli

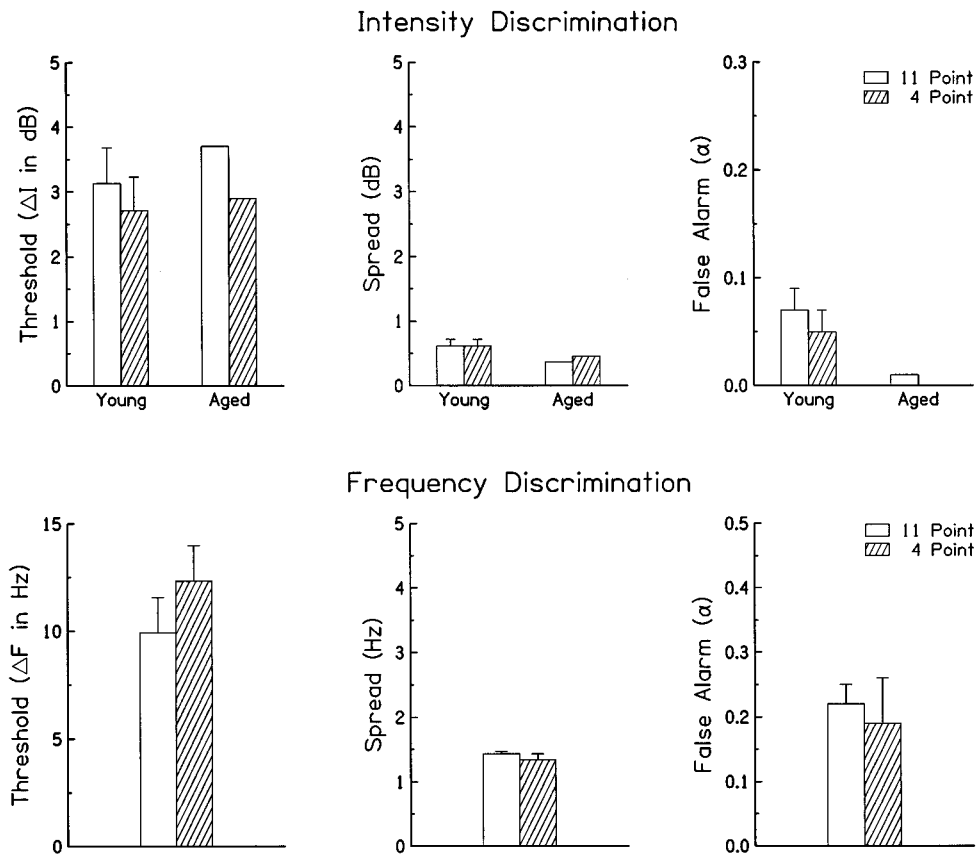


FIG. 8. Mean (and +1 standard error) estimates of threshold and spread parameters for the four-point sampling method and the 11-point constant stimuli method for intensity discrimination for young and aged subjects, and frequency discrimination for young subjects.

method is in the response level, while the stimulus values are fixed (i.e.,  $X_{88}$ ,  $X_{73}$ , etc.).

The four data points of the four-point sampling method can also be obtained entirely by the up-down adaptive method [i.e., four-up-one-down (16%), two-up-one-down (29%), two-down-one-up (71%), and four-down-one-up (84%)]. In order to minimize bias in the data, it is necessary to interleave the four up-down procedures (Jesteadt, 1980). However, implementation of the interleaving process is not straightforward. Furthermore, it is rather time consuming to obtain the four-up-one-down and four-down-one-up data points because of the number of reversals needed in such procedures. It is even more time consuming to obtain the two data points at  $X_{12}$  and  $X_{88}$  [Eq. (2)] because it would require five-up-one-down and five-down-one-up adaptive procedures. We have found that using two-up-one-down and two-down-one-up adaptive procedures to obtain initial estimates of  $M$  and  $S$  [according to Eq. (4)], and then obtaining four data points at stimulus levels calculated from Eq. (2) is efficient. It also has resulted in good estimates of the slope and threshold parameters of the psychometric function of interest.

Another advantage of the four-point sampling method, as is with any other methods that use nonlinear regression to estimate parameter values, is that the false alarm value can be estimated also without prior knowledge of its existence.

From our computer simulation study, we have found that

it is better to spread evenly (and randomly) a smaller number of trials (i.e., 200) between four points (of 50 trials each) according to Eq. (2) than between 11 points of 18 trials each. In other words, accurate data (e.g., 50 trials/point) with four points appropriately coated are better than 11 nonaccurate data points (with fewer trials/point) spread evenly over a wider range of stimuli.

In summary, the four-point sampling method has been used to determine psychometric functions for absolute threshold, forward masking, simultaneous masking, intensity discrimination, and frequency discrimination for young and aged subjects. The estimated values for threshold ( $M$ ) and spread ( $S$ ) parameters are similar between the four-point sampling and constant stimuli methods. Generally, after 30–40 trials per point, the four-point sampling method provides psychometric functions similar to those from the constant stimuli method using 11 points with 50 trials each. In conclusion, the four-point sampling placement of stimuli provides an efficient method for data collection for the determination of psychometric functions for various psychophysical tasks for young and aged subjects.

#### ACKNOWLEDGMENTS

This work is supported (in part) by research Grants Nos. P01 DC 00422 and R01 DC 00184 from the National Institute on Deafness and Other Communication Disorders, Na-

tional Institutes of Health. The critical comments and suggestions made by J. L. Hall and H. Levitt have resulted in a much better manuscript and are much appreciated.

<sup>1</sup>The authors express their thanks to J. L. Hall of Lucent Bell Laboratories for pointing out the interleaving adaptive procedures with different targets by Jesteadt (1980).

ANSI (1989). ANSI S3.6-1989, "Specifications for audiometers" (American National Standards Institute, New York).

Hall, J. L. (1981). "Hybrid adaptive procedure for estimation of psychometric functions," *J. Acoust. Soc. Am.* **69**, 1763–1769.

Jesteadt, W. (1980). "An adaptive procedure for subjective judgments," *Percept. Psychophys.* **28**, 85–89.

Lam, C. F., Mills, J. H., and Dubno, J. R. (1996). "Placement of observations for the efficient estimation of a psychometric function," *J. Acoust. Soc. Am.* **99**, 3689–3693.

Lam, C. F., Mills, J. H., and Dubno, J. R. (1997). "A change of subscripts of the stimulus placements for a four-point sampling method," *J. Acoust. Soc. Am.* **101**, 1742.

Levitt, H. (1971). "Transformed up-down methods in psychoacoustics," *J. Acoust. Soc. Am.* **49**, 467–477.

Taylor, M. M., and Creelman, C. D. (1967). "PEST: Efficient estimates on probability functions," *J. Acoust. Soc. Am.* **4**, 782–787.

# Speechreading and the structure of the lexicon: Computationally modeling the effects of reduced phonetic distinctiveness on lexical uniqueness

Edward T. Auer, Jr. and Lynne E. Bernstein

*Spoken Language Processes Laboratory, House Ear Institute, 2100 West Third Street, Los Angeles, California 90057*

(Received 10 October 1996; revised 19 August 1997; accepted 31 August 1997)

A lexical modeling methodology was employed to examine how the distribution of phonemic patterns in the lexicon constrains lexical equivalence under conditions of reduced phonetic distinctiveness experienced by speechreaders. The technique involved (1) selection of a phonemically transcribed machine-readable lexical database, (2) definition of transcription rules based on measures of phonetic similarity, (3) application of the transcription rules to a lexical database and formation of lexical equivalence classes, and (4) computation of three metrics to examine the transcribed lexicon. The metric percent words unique demonstrated that the distribution of words in the language substantially preserves lexical uniqueness across a wide range in the number of potentially available phonemic distinctions. Expected class size demonstrated that if at least 12 phonemic equivalence classes were available, any given word would be highly similar to only a few other words. Percent information extracted (PIE) [D. Carter, *Comput. Speech Lang.* **2**, 1–11 (1987)] provided evidence that high-frequency words tend not to reside in the same lexical equivalence classes as other high-frequency words. The steepness of the functions obtained for each metric shows that small increments in the number of visually perceptible phonemic distinctions can result in substantial changes in lexical uniqueness. © 1997 Acoustical Society of America. [S0001-4966(97)05112-6]

PACS numbers: 43.71.An, 43.71.Es, 43.71.Ma [WS]

## INTRODUCTION

Spoken word recognition depends on the process of selecting a word candidate from a set of word patterns stored in memory. Current models of auditory spoken word recognition agree that the speed and ease of this selection process is partially a function of the lexical properties of the target word (Lahiri and Marslen-Wilson, 1991; Luce *et al.*, 1990; McClelland and Elman, 1986; Norris, 1994). Spoken word recognition is facilitated for frequently used words and for words perceptually similar to few other words (i.e., words with few neighbors). The effects of these lexical properties are particularly important when the phonetic information in the speech signal is degraded (Luce *et al.*, 1990). In speechreading (lipreading), where spoken word recognition occurs on the basis of viewing rather than listening to the talker, the optical speech signal typically affords less phonetic distinctiveness<sup>1</sup> than the acoustic speech signal. The target word's frequency and perceptual similarity to other words will likely be a substantial contributor to the speed and ease of word recognition for the speechreader. In the current study, we modeled visual perceptual similarity among words as a function of the number of perceptually available phonemic distinctions.

Even under optimal perceptual conditions (e.g., adequate lighting, moderate speaking rate, highly visible articulatory gestures), phonetic information is inadequate to specify all the phonemes in the speechreader's language. For example, speechreaders may not perceive any distinctions among productions of the consonants /b/, /p/, and /m/ (Scheinberg,

1988). The degree to which phonemic distinctions are unavailable is to a certain extent due to the articulatory characteristics of the talker (Kricos and Lesner, 1982; Lesner, 1988), the conditions (lighting, viewing angle, distance), the place of articulation, and the perceptual abilities of the speechreader (Jeffers and Barley, 1971). Current spoken word recognition models (Lahiri and Marslen-Wilson, 1991; Luce *et al.*, 1990; McClelland and Elman, 1986; Norris, 1994) imply that loss of phonemic distinctions by itself does not predict word intelligibility: because words are hypothesized to be recognized within the lexical context of perceptually similar words, the distribution of phoneme patterns for words in the language is also determinative of intelligibility.

For example, the English word "bought" remains lexically distinct from all other words after the loss of the distinctions between /b/, /p/, and /m/. "Pought" and "mought" are not words; therefore, a misperception of "bought" as either of these nonwords could nevertheless result in an accurate identification of the only existing word "bought." Alternatively, under the same conditions, "bat" would not have a similar advantage versus "pat" and "mat."

Nitchie (1916) and Berger (1972) attempted to estimate the loss of perceptual uniqueness (i.e., homophony) of English words experienced by speechreaders. According to Nitchie, approximately 50% of words in colloquial English speech are perceptually unique for the average speechreader. Berger estimated that, taking frequency of use into account, between 51% and 55% of the common words in English remain unique. Although the authors never fully specified their methods, it is clear that they used a fixed estimate of the

number of available phonemic distinctions, which did not take into account the occurrence of variation in visual phonetic distinctiveness due to a range of factors (some of which were mentioned earlier). Furthermore, their analyses focused solely on percentage of unique words in the lexicon. Because the number of words perceptually similar to the target word influences its speed and ease of auditory spoken word recognition (Luce *et al.*, 1990), the number of words a speechreader must discriminate among during recognition must be taken into account in order to obtain informative estimates. A computational modeling study of lexical uniqueness in English was undertaken in which the number of available phoneme distinctions was systematically varied to model a range of visual-phonetic information. Several different quantitative measures were also examined in order to understand better how the distribution of word phoneme patterns in English is affected by the number of available phonemic distinctions.

## I. LEXICAL MODELING

### A. Methods

The methods employed for the current study were originally developed in automatic speech recognition to assess the feasibility of using broad phonetic transcription to select a small subset of lexical candidates from a large lexical database (Huttenlocher and Zue, 1984; Carter, 1987) and have also been applied to the study of human spoken word recognition (see Altmann, 1990; Altmann and Carter, 1989; Pisoni *et al.*, 1985).

The methodology was applied as follows: First, a phonemically transcribed machine-readable lexical database was selected to serve as a representative sample of the words in the language. Along with a phonemic transcription, each word in the database had an estimate of its frequency of occurrence in the language. Second, transcription rules were defined on the basis of measures of phonetic similarity. The transcription rules were in the form of single-symbol substitutions for all phonemes in phonemic equivalence classes. A *phonemic equivalence class* comprised the set of phonemes rendered equivalent by the loss of phonetic distinctiveness. (For example, if /b/, /p/, and /m/ belong to a single phonemic equivalence class, then a rule was defined to transcribe each occurrence of /b/, /p/, and /m/ into a symbol representing the equivalence class.) Third, the lexical database was then transcribed according to the rules. *Lexical equivalence classes* were formed by collapsing across identically transcribed words. (For example, under the phoneme equivalence class definition given above, “pat” and “bat” would both belong to the same lexical equivalence class.) Lastly, metrics were computed to compare the distribution of patterns in the newly transcribed lexicon with the distribution of patterns in the original lexicon.

### 1. Lexical database

The method described above was applied to the PhLex database (Seitz *et al.*, 1995). PhLex’s entries include the

19 052 most frequent words in the Brown corpus (Kucera and Francis, 1967), the 19 750 words listed in the Hoosier Mental Lexicon (Nusbaum *et al.*, 1984), and 1173 words extracted from stimulus and response sets from our laboratory. In total, after accounting for overlapping entries in the source lists, the PhLex database contains 32 377 unique orthographic entries. In addition to orthographic transcriptions, all of PhLex’s entries have baseform phonemic transcriptions<sup>2</sup> that include stress and syllabification symbols, estimates of frequency of usage (Kucera and Francis, 1967), and subjective familiarity ratings (Nusbaum *et al.*, 1984). When an estimate of a word’s frequency of occurrence was not available, it was assumed to be equal to 1. All frequencies were log-transformed to the base 10.

### 2. Transcription rules

Sets of transcription rules were developed using previously published perceptual data on speechreading (Eberhardt *et al.*, 1990; Montgomery and Jackson, 1983). Consonant transcription rules were based on visual consonant identification data collected in a Consonant-/a/ environment (Eberhardt *et al.*, 1990), with overall percent correct of approximately 34.6%. Vowel transcription rules were based on visual vowel identification data collected in the environment /h/-Vowel-/g/ (Montgomery and Jackson, 1983), with overall percent correct of 54.2%. Estimates of visual phonetic similarity were obtained from multidimensional scaling solutions of the obtained consonant and vowel confusion matrices (Bernstein *et al.*, 1994). The analyses employed 40 phonemes, 17 vowels and 23 consonants. The similarity estimates were submitted to separate hierarchical cluster analyses using the average linkage between groups method (Aldenderfer and Blashfield, 1984; SPSS, 1990). Hierarchical cluster analysis was used to algorithmically generate nested sets of phonemic equivalence classes by incrementally joining phonemes based on their estimated similarity.

Sets of transcription rules (see Table I) were generated to model a range of visual phonetic distinctiveness due to a range of viewing conditions, talker characteristics, and speechreaders’ abilities. Transcription rule sets were generated by hierarchically varying the total number of phonemic equivalence classes between 1 and 40. Thus, when there was only one equivalence class, all the consonants and vowels were transcribed as a single symbol. When there were 40 equivalence classes, each one contained a unique phoneme of English. Because perceptual data were not available for /ə j ŋ/, /ə/ was assumed to be most similar to /ʌ/, /j/ was assumed most similar to /a/, and /ŋ/ was assumed most similar to /g/. Vowels and consonants were assumed to be maximally dissimilar, except for the consonant /j/ which was included in the vowel confusion matrix. Thus, except for the one equivalence class that contained all the phonemes and the ones that contained /j/, no phonemic equivalence class contained both consonants and vowels.

Table I lists the sets of phonemic equivalence classes employed in the current study. The table shows that the number of vowel and consonant equivalence classes was allowed to increase at the same rate. One heuristic for determining the appropriate number of clusters to represent a perceptual

TABLE I. Phonemic equivalence classes employed in the development of transcription rule sets. All phonemes within a set of brackets were considered perceptually equivalent.

Number of phonemic equivalence classes	Phonemic equivalence classes
28	{u} {ʊ} {ɔr} {o} {au} {i,i} {e,ε} {æ} {ɔi} {ɔ} {ai} {ə,ɑ,ʌ,j} {b,p,m} {f,v} {l} {n} {k} {ŋ,g} {h} {d} {t} {s,z} {w,r} {ð,θ} {ʃ} {tʃ} {ʒ} {dʒ}
19	{u,ʊ,ər} {o,au} {i,i} {e,ε} {æ} {ɔi} {ɔ} {ai,ə,ɑ,ʌ,j} {b,p,m} {f,v} {l} {n,k} {ŋ,g} {h} {d} {t,s,z} {w,r} {ð,θ} {ʃ,tʃ,ʒ,dʒ}
12	{u,ʊ,ər} {o,au} {i,i,e,ε,æ} {ɔi} {ɔ,ai,ə,ɑ,ʌ,j} {b,p,m} {f,v} {l,n,k,ŋ,g,h} {d,t,s,z} {w,r} {ð,θ} {ʃ,tʃ,ʒ,dʒ}
10	{u,ʊ,ər} {o,au} {i,i,e,ε,æ} {ɔi,ɔ,ai,ə,ɑ,ʌ,j} {b,p,m} {f,v} {l,n,k,ŋ,g,h,d,t,s,z} {w,r} {ð,θ} {ʃ,tʃ,ʒ,dʒ}
2	{u,ʊ,ər,o,au,i,i,e,ε,æ,ɔi,ɔ,ai,ə,ɑ,ʌ,j} {b,p,m,f,v,l,n,k,ŋ,g,h,d,t,s,z,w,r,ð,θ,ʃ,tʃ,ʒ,dʒ}
1	{u,ʊ,ər,o,au,i,i,e,ε,æ,ɔi,ɔ,ai,ə,ɑ,ʌ,j,b,p,m,f,v,l,n,k,ŋ,g,h,d,t,s, z,w,r,ð,θ,ʃ,tʃ,ʒ,dʒ}

data set is to look for large increases in the distance coefficients over which clusters are being formed at each stage of the analysis. The logic behind this strategy is that a large increase in the distance coefficient reflects the joining of two relatively dissimilar clusters, and therefore the appropriate cluster solution includes all the clusters formed up to, but not including, that stage (Aldenderfer and Blashfield, 1984). Examination of the distance coefficients obtained in the current cluster analyses suggested that 12 phonemic equivalence classes best approximated the phonemic distinctions perceived by the speechreaders whose data generated the confusion matrices. Furthermore, these 12 phonemic equivalence classes correspond to previous estimates of visually available phonemic distinctions (see Jackson, 1988). In addition, 28, 19, and 10 phonemic equivalence classes were selected to represent  $\frac{3}{4}$ ,  $\frac{1}{2}$ , and  $\frac{1}{4}$  of total number of vowels and consonants.

### 3. Application of transcription rules

Following transcription, lexical equivalence classes were formed by collapsing across identically transcribed words. Table II displays examples of the application of rules to the words “tan” and “cat.” The first column in Table II gives the number of equivalence classes in the transcription set from which each set of relevant rules for the example is taken. (The complete sets are in Table I.) The third and fourth columns list the transcriptions of “tan” and “cat,” after the application of the transcription rules. The two words enter into the same lexical equivalence class for all rule sets with ten or fewer phonemic equivalence classes.

The distribution of perceptually similar word patterns could be influenced by lexicon size or method of subsampling the lexicon. Specifically, common and rare words differ in phonemic composition, and common words tend to be

TABLE II. Transcription examples for “tan” and “cat.” All phonemes within a set of brackets were rewritten into a single symbol represented here by upper-case letters.

Number of phonemic equivalence classes in transcription rule set	Relevant transcription rules	Transcriptions of	
		“tan”	“cat”
19	{æ} ⇒ A {t,s,z} ⇒ T {n,k} ⇒ N	TAN	NAT
12	{i,i,e,ε,æ} ⇒ A {d,t,s,z} ⇒ D {l,n,k,ŋ,g,h} ⇒ N	DAN	NAD
10	{i,i,e,ε,æ} ⇒ A {l,n,k,ŋ,g,h,d,t,s,z} ⇒ D	DAD	DAD
2	{u,ʊ,ər,o,au,i,i,e,ε,æ,ɔi,ɔ,ai,ə,ɑ,ʌ,j} ⇒ V {b,p,m,f,v,l,n,k,ŋ,g,h,d,t,s,z,w,r,ð,θ,ʃ,tʃ,ʒ,dʒ} ⇒ C	CVC	CVC
1	{u,ʊ,ər,o,au,i,i,e,ε,æ,ɔi,ɔ,ai,ə,ɑ,ʌ,j,b,p,m,f,v,l,n, k,ŋ,g,h,d,t,s,z,w,r,ð,θ,ʃ,tʃ,ʒ,dʒ} ⇒ P	PPP	PPP

more like other common words (Landauer and Streeter, 1973). Thus, transcriptions and metrics were applied to three partitionings of the lexical database. One corresponded to the 1052 most frequent words in the Brown Corpus (Kucera and Francis, 1967), henceforth, “1K;” the second to the 4995 most frequent words, “5K;” and the third to the entire 31 081 word lexicon, “30K.”<sup>3</sup> Several words at the 1000-word and 5000-word cutoff points had identical frequencies of occurrence.

The presence or absence of stress and syllabification in the transcriptions was manipulated to explore effects of suprasegmental information. The PhLex database contains two levels of marked stress and a third unmarked level. When stress and syllabification were taken into account, two words were considered equivalent only when their phonemic, stress, and syllabification patterns were identical. For example, the noun “convert” and the verb “convert” were not equivalent when stress was taken into account in the analysis.

#### 4. Quantitative analyses

Following transcription, three commonly employed metrics were computed on the results (see Altmann, 1990). Each metric examined a different aspect of lexical equivalence. The first metric, *frequency-weighted percent words unique*, estimated the proportion of unique words in the transcribed partition of the lexicon. The second metric, *frequency-weighted expected class size*, estimated the average number of words in lexical equivalence classes in the transcribed partition of the lexicon. The third metric, *percent information extracted*, or *PIE* (Carter, 1987), estimated information remaining in the lexicon. The PIE values are a function of the size of resulting lexical equivalence classes and the distribution of frequencies for words within lexical equivalence classes.

Frequency-weighted percent words unique was computed as

$$\% \text{WU} = \frac{\sum_{a=1}^{n_U} F_U}{\sum_{i=1}^{n_L} F_i} \times 100, \quad (1)$$

where  $n_U$  was the total number of unique entries after transcription,  $F_U$  was the frequency of occurrence for unique words in the transcribed lexical partition,  $n_L$  was the number of words in the lexicon, and  $F_i$  was the frequency of occurrence of words in the original lexical partition. The frequency-weighted metric was intended as an estimate of the extent to which unique words would be encountered in everyday language by a deaf speechreader.

Frequency-weighted expected class size was computed as

$$\text{ECS} = \frac{1}{F_L} \sum_{a=1}^{n_E} I_a F_a, \quad (2)$$

where  $F_L$  was the sum of frequencies of occurrence of all words in the lexical partition,  $n_E$  was the total number of lexical equivalence classes,  $I_a$  was the number of words in equivalence class  $a$ , and  $F_a$  was the sum of frequencies of occurrence of the words in equivalence class  $a$ . This metric

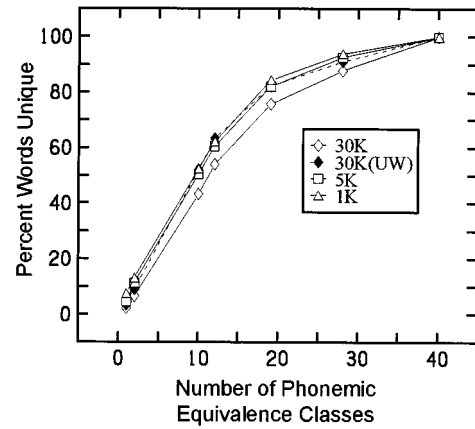


FIG. 1. The log-frequency-weighted percentage of words unique for 1–40 phonemic equivalence classes is plotted for 30 K-, 5 K-, and 1 K-word partitions of the lexicon. The unweighted percentage of words unique for 1–40 phonemic equivalence classes is plotted for the 30 K partition of the lexicon.

was intended as an estimate of the average size of the frequency-weighted equivalence classes that would typically be encountered in everyday language.

The PIE (Carter, 1987) was computed as

$$\text{PIE} = \frac{\sum_{a=1}^{n_E} p_a \log p_a}{\sum_{i=1}^{n_L} p_i \log p_i} \times 100, \quad (3)$$

where  $n_E$  was the total number of equivalence classes after transcription,  $p_a$  was the sum of the probabilities of occurrence for words in equivalence class  $a$ ,  $n_L$  was the number of words in the lexicon,  $p_i$  was the probability of occurrence of word  $i$ , and  $\log$  was taken to the base 2. The probability of a word’s occurrence was computed by dividing its raw frequency of occurrence by the total number of occurrences in the Brown corpus (Kucera and Francis, 1967).

The PIE is an information theoretic metric, developed by Carter (1987), of the amount of *information* extracted from the lexicon when the number of available phonemic distinctions is reduced. In essence, PIE is the number of binary units (bits) required to code the lexicon **after transcription** divided by the number of bits required to code the **original lexicon** multiplied by 100. For example, an original lexicon, containing four equally frequent words, could be coded by two bits. One bit dividing the entire lexicon in half and a second bit dividing each half of the lexicon in half again. A transcription of that lexicon resulting in two equally frequent lexical equivalence classes could be coded by a single bit. The resulting PIE would be equal to 50%. In contrast to expected class size, PIE is sensitive to the distribution of frequencies within lexical equivalence classes. Specifically, PIE is high when all the equivalence classes are roughly equal in frequency which is better approximated when frequent words are in different equivalence classes (see Carter, 1987, for a detailed discussion of PIE).

#### B. Results and discussion

The results of the analyses for each log-frequency-weighted metric are plotted in Figs. 1–3 as a function of the

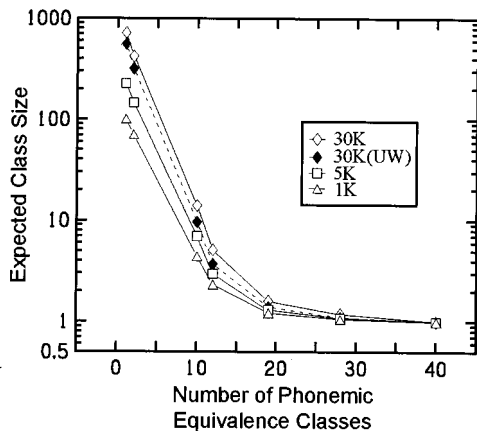


FIG. 2. The log-frequency-weighted expected class size for 1–40 phonemic equivalence classes is plotted for 30 K-, 5 K-, and 1 K-word partitions of the lexicon. The unweighted expected class size for 1–40 phonemic equivalence classes is plotted for the 30 K partition of the lexicon.

number of phonemic equivalence classes in a transcription rule set. Because results were unaffected by the presence versus absence of stress and syllabification, in Figs. 1–3 only the results for analyses with stress and syllabification were plotted. In addition, the unweighted statistics are also plotted in Figs. 1 and 2 for the 30K partition of the lexicon. Only small differences were observed between the unweighted and the log-frequency-weighted data for the 5K and 1K partitions, thus the unweighted 5K and 1K data were not plotted in Figs. 1 and 2. Examination of raw frequency-scaled analyses (i.e., frequencies were not log-transformed), in which all lexical partitions were influenced equivalently by the scaling, suggested that the small effect of log-frequency scaling on the 5K and 1K partitions was related to a trivial interaction of the log scaling and the distribution of frequencies in these lexical partitions.

In Figs. 1–3, 12 phonemic equivalence classes represented the best fit by the cluster analyses for both the consonant and vowel data. Beyond 12 equivalence classes, the distance coefficients in the cluster analyses were very small. This means that additional equivalence classes that were formed as a result of hierarchically separating larger ones

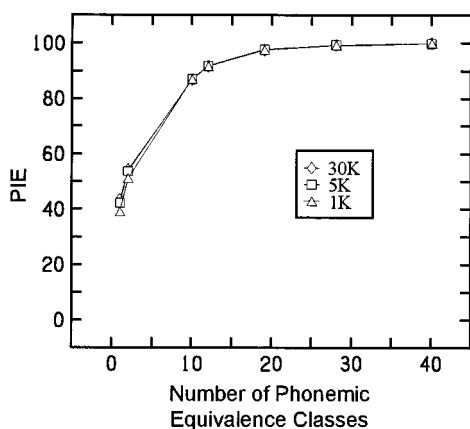


FIG. 3. The percent information extracted for 1–40 phonemic equivalence classes is plotted for 30 K-, 5 K-, and 1 K-word partitions of the lexicon.

into smaller ones represented perceptual distinctions not reliably made by the subjects who viewed the syllables. Thus, if the abscissas of the figures were translated into perceptual distance, they would be highly compressed as the number of equivalence classes increases beyond 12.

Frequency-weighted percent words unique (Fig. 1) increased as the number of visible phonemic equivalence classes increased. Only a small effect of lexical partition size was obtained. These results demonstrate that the distribution of phoneme patterns constituting words in English substantially preserves visual lexical uniqueness, even when the transcription employs only 12 phonemic equivalence classes (i.e., far fewer than half the number of phonemes in the language). This number of equivalence classes corresponds to 54%–63% words unique across partitions. Berger's (1972) frequency-weighted lexical uniqueness estimate of 51% falls below our estimates.

Frequency-weighted expected class size (Fig. 2) decreased as the number of phonemic equivalence classes increased. Expected class size increased slightly as the size of the lexical partition increased. For 12 phonemic equivalence classes, frequency-weighted expected class size was 5.1 words for the 30K lexicon. On average, any given word is predicted to be equivalent with only a few other words, when at least 12 equivalence classes are available.

The PIE (Fig. 3) increased as the number of phonemic equivalence classes increased. However, the largest change in PIE was between 0 and 12 equivalence classes: above 12 equivalence classes, most of the information has been extracted from the lexicon. For 12 phonemic equivalence classes, 92% of the information was extracted. The PIE values were essentially identical, independent of lexical partition size.

The high PIE values obtained even with few equivalence classes provide evidence that high-frequency words tend to reside in equivalence classes with lower frequency words. An implication of this finding is that a speechreader could optimize word recognition accuracy by selecting the most frequent word in a lexical equivalence class. The current results are somewhat surprising given the results Landauer and Streeter (1973) (Pisoni *et al.*, 1985; but see Bard and Shillcock, 1993) have reported indicating that common words tend to be more like other common words. However, the present study differed from previous investigations not only in terms of the nature of similarity among words (visual versus auditory), but also in terms of the operational definition of similarity among words, the lexical entries employed in the analyses, and the metrics employed to assess the similarity of words. Therefore, further analyses are required to assess whether the current results are idiosyncratic to speechreading or have general implications for spoken word recognition.

## II. GENERAL DISCUSSION

### A. Subject characteristics

The present results demonstrate that lexical uniqueness varies substantially with the number of available phonemic distinctions. Thus, the level of performance in the nonsense



syllable confusion matrices used to estimate phonemic equivalence must be considered in interpreting results of the type presented here.

Berger's (1972) previous estimate of 51% words unique for the average speechreader is below our estimate of 54%–63% for 12 phonemic equivalence classes obtained on the basis of data from relatively inaccurate hearing speechreaders. The consonant confusion data employed here were obtained from matrices with 34.6% correct responses. These subjects also speechread CID Everyday Sentences (Davis and Silverman, 1970) and had mean scores of 24.9% keywords correct at pretest and 35.3% at posttest. Although these scores are typical in the speechreading literature for hearing adult subjects, this performance level is low in comparison with that observed for expert deaf speechreaders. Bernstein *et al.* (1996) reported that expert deaf speechreaders (in the upper quartile of subjects) scored between 61% and 79% words correct on the same sentence materials. These expert deaf speechreaders have achieved 41% correct (with a range from 37%–47% correct) with the same CV materials (Eberhardt *et al.*, 1990; Bernstein *et al.*, 1996). The consonant confusion data employed in the current study is comparable to that used by Berger (1972). However, the current study may represent a conservative estimate of phonemic/lexical uniqueness in the skilled speechreader. We are currently collecting consonant and vowel confusion data from skilled deaf speechreaders to investigate this hypothesis.

## B. Lexical characteristics

The high obtained PIE values provide evidence that high-frequency words do not reside in the same lexical equivalence classes as other high-frequency words (Carter, 1987). As suggested earlier, a speechreader might optimize word recognition accuracy by selecting the most frequent word in a lexical equivalence class. Current models of spoken word recognition predict a bias toward selection of high-frequency words in the absence of other discriminating information. We predict that word recognition in speechreaders employs the same biasing processes as those for auditory spoken word recognition, a hypothesis that awaits empirical testing.

## C. Modeling assumptions

Two simplifying assumptions employed in our analyses are relevant when considering the relationship of our modeling results to human performance. First, vowels and consonants were operationally defined to be equally distinct and to change their distinctiveness at equal rates. The decision to increase the number of vowel equivalence classes at the same rate as the consonant equivalence classes was a pragmatic one. In the literature, phoneme identification studies have not been conducted in such a way as to provide information on how visibility of vowels and consonants covaries for individual speechreaders. Such data are needed for accurately modeling changes in visibility across the entire phonemic inventory of a language.

Second, phonetic similarity was estimated based on identification of phonemes in monosyllabic nonsense syllables. Coarticulation effects arising from variation in surrounding phonetic contexts have been demonstrated to alter phoneme identification by speechreaders (Bengueirel and Pichora-Fuller, 1982; Jackson, 1988). The use of phoneme identifications with monosyllabic nonsense syllables could lead to either an under- or overestimation of the phonetic information available to the speechreader. Although coarticulation is frequently thought to reduce phonetic information, Church (1987) has argued (for acoustic speech) that it is informative for identifying words. We are currently collecting consonant and vowel identification data within a wide variety of disyllabic nonsense word contexts to further refine our estimates of the visually available perceptual information. Preliminary analyses suggest that the distribution of words in the language substantially preserves uniqueness even when variability due to phonetic context is taken into account (Auer *et al.*, 1997).

## ACKNOWLEDGMENTS

This work was supported by a grant from the National Institutes of Health (DC02107). The authors thank Paul Iversen, Jennifer A. Johnson, Margaret MacEachern, Helena M. Saldana, Paula E. Tucker, and Robin S. Waldstein for their comments on earlier versions of this manuscript, and Paul A. Luce and Dominic W. Massaro for their reviewer's comments.

<sup>1</sup>We use *phonetic* or *visual phonetic distinctiveness* to refer to the discriminability of visual speech stimuli and *phonemic distinctions* to refer to the phonological differences that distinguish words from each other.

<sup>2</sup>Baseform transcriptions are basic phonemic representations that may involve the undoing of phonological rules. For example, the baseform transcription of the word "writer" would be /'raɪtər/, which would involve the undoing of an alveolar tapping rule from the pronunciation /'raɪrər/.

<sup>3</sup>Due to homophony, the total number of entries in the analysis, 31 081, was reduced from the total number of orthographic entries in the lexicon, 32 377.

Aldenderfer, M. S., and Blashfield, R. K. (1984). *Cluster Analysis* (Sage, Beverly Hills, CA).

Altmann, G. T. M. (Ed.) (1990). *Cognitive Models of Speech Processing* (MIT, Cambridge, MA).

Altmann, G., and Carter, D. (1989). "Lexical stress and lexical discriminability: Stress syllables are more informative, but why?" *Comput. Speech Lang.* 3, 265–275.

Auer, Jr., E. T., Bernstein, L. E., Waldstein, R. S., and Tucker, P. E. (1997). "Effects of phonetic variation and the structure of the lexicon on the uniqueness of words," in proceedings of the AVSP'97 workshop, (Rhodes, Greece), ESCA ISSN #1018 4554.

Bard, E. G., and Shillcock, R. C. (1993). "Competitor effects during lexical access: Chasing Zipf's tail," in *Cognitive Models of Speech Processing: The Second Sperlonga Meeting*, edited by G. Altmann and R. Shillcock (Earlbaum, Hove, UK), pp. 163–185.

Bengueirel, A. P., and Pichora-Fuller, M. K. (1982). "Coarticulation effects in lipreading," *J. Speech Hear. Res.* 25, 600–607.

Berger, K. W. (1972). "Visemes and homophenous words," *Teacher Deaf.* 70, 396–399.

Bernstein, L. E., and Auer, E. T., Jr. (1996). "Word recognition in speechreading," in *Speechreading by Humans and Machines: NATO ASI Series F*, edited by D. G. Stork and M. E. Hennecke (Springer-Verlag, Berlin).

- Bernstein, L. E., Demorest, M. E., and Eberhardt, S. P. (1994). "A computational approach to analyzing sentential speech perception: Phoneme-to-phoneme stimulus-response alignment," *J. Acoust. Soc. Am.* **95**, 3617–3622.
- Bernstein, L. E., Demorest, M. E., and Tucker, P. E. (1996). "Speech perception without hearing," manuscript submitted for publication.
- Carter, D. (1987). "An information theoretic analysis of phonetic dictionary analysis," *Comput. Speech Lang.* **2**, 1–11.
- Church, K. W. (1987). *Phonological Parsing in Speech Recognition* (Kluwer Academic, Boston, MA).
- Davis, H., and Silverman, S. R. (1970). *Hearing and Deafness* (Holt, Rinehart, & Winston, Winston, NY).
- Eberhardt, S. P., Bernstein, L. E., Demorest, M. E., and Goldstein, M. H. (1990). "Speechreading sentences with single-channel vibrotactile presentations of voice fundamental frequency," *J. Acoust. Soc. Am.* **88**, 1274–1285.
- Huttenlocher, D. P., and Zue, V. W. (1984). "A model of lexical access from partial phonetic information," in *Proceedings of ICASSP* (San Diego, CA).
- Jackson, P. L. (1988). "The theoretical minimal unit for visual speech perception: Visemes and coarticulation," in *New Reflections on Speechreading*, edited by C. DeFillipo and D. Sims (A. G. Bell Association for the Deaf, Washington, DC), pp. 99–115.
- Jeffers, J., and Barley, M. (1971). *Speechreading (Lipreading)* (Thomas, Springfield, IL).
- Kricos, P. B., and Lesner, S. A. (1982). "Differences in visual intelligibility across talkers," *Volta Rev.* **84**, 219–225.
- Kucera, H., and Francis, W. (1967). *Computational Analysis of Present-Day American English* (Brown U. P., Providence, RI).
- Lahiri, A., and Marslen-Wilson, W. (1991). "The mental representation of lexical form: A phonological approach to the recognition lexicon," *Cognition* **38**, 245–294.
- Landauer, T. K., and Streeter, L. A. (1973). "The structural differences between common and rare words: Failure of equivalence assumption for theories of word recognition," *J. Verbal Learn. Verbal Behav.* **12**, 119–131.
- Lesner, S. A. (1988). "The talker," in *New Reflections on Speechreading*, edited by C. DeFillipo and D. Sims (A. G. Bell Association for the Deaf, Washington, DC), pp. 89–98.
- Luce, P. A., Pisoni, D. B., and Goldinger, S. D. (1990). "Similarity neighborhoods of spoken words," in *Cognitive Models of Speech Processing*, edited by G. T. M. Altmann (MIT, Cambridge, MA), pp. 122–147.
- McClelland, J. L., and Elman, J. L. (1986). "The TRACE model of speech perception," *Cogn. Psychol.* **18**, 1–86.
- Mongomery, A. A., and Jackson, P. L. (1983). "The physical characteristics of lips underlying vowel lipreading performance," *J. Acoust. Soc. Am.* **73**, 2134–2144.
- Nitche, E. B. (1916) "The use of homophenous words," *Volta Rev.* **18**, 85–83.
- Norris, D. G. (1994). "Shortlist: A connectionist model of continuous speech recognition," *Cognition* **52**, 189–234.
- Nusbaum, H. C., Pisoni, D. B., and Davis, C. K. (1984). "Sizing up the Hoosier Mental Lexicon: Measuring the familiarity of 20,000 words." *Research on Spoken Language Processing PR-10* (Indiana University, Bloomington, IN).
- Pisoni, D. B., Nusbaum, H. C., Luce, P. A., and Slowiaczeck, L. M. (1985). "Speech perception, word recognition, and the structure of the lexicon," *Speech Commun.* **4**, 75–95.
- Scheinberg, J. C. S. (1988). "An analysis of /p/, /b/, and /m/ in the speechreading signal," unpublished doctoral dissertation, City University of New York, New York, NY.
- Seitz, P. F., Bernstein, L. E., and Auer, E. T., Jr. (1995). *PhLex (Phonologically Transformable Lexicon), A 35,000-word pronouncing American English lexicon on structural principles, with accompanying phonological rules and word frequencies* (Gallaudet Research Institute, Washington, DC).
- SPSS (1990). *SPSS Reference Guide* (SPSS Inc., Chicago, IL).

# Stop-consonant and vowel perception in 3- and 4-year-old children

Ralph N. Ohde and Katarina L. Haley<sup>a)</sup>

*Department of Hearing and Speech Sciences, Vanderbilt Bill Wilkerson Center for Otolaryngology and Communication Sciences, Vanderbilt University Medical Center, Nashville, Tennessee 37232*

(Received 28 August 1996; revised 22 July 1997; accepted 20 August 1997)

Recent research on 5- to 11-year-old children's perception of stop consonants and vowels indicates that they can generally identify these sounds with relatively high accuracy from short duration stimulus onsets [Ohde *et al.*, *J. Acoust. Soc. Am.* **97**, 3800–3812 (1995); Ohde *et al.*, *J. Acoust. Soc. Am.* **100**, 3813–3824 (1996)]. The purpose of the current experiments was to determine if younger children, aged 3–4 years, can also recover consonant and vowel features from stimulus onsets. Ten adults, ten 3-year olds, and ten 4-year-olds listened to synthesized syllables composed of combinations of [b d g] and [i u a]. The synthesis parameters included manipulations of the following stimulus variables: formant transition (moving or straight), noise burst (present or absent), and voicing duration (10, 30, or 46 ms). Developmental effects were found for the perception of both stop consonants and vowels. In general, adults identified these sounds at a significantly higher level than children, and perception by 4-year-olds was significantly better than 3-year-olds. A developmental effect of dynamic formant motion was obtained, but it was limited to only the [g] stop consonant. Stimulus duration affected the children's perception of vowels indicating that they may utilize additional auditory information to a much greater extent than adults. The results support the importance of information in stimulus onsets for syllable identification, and developmental changes in sensitivity to these cues for consonant and vowel perception. © 1997 Acoustical Society of America. [S0001-4966(97)02212-1]

PACS numbers: 43.71.An, 43.71.Es, 43.71.Ft [WS]

## INTRODUCTION

A conceptualization of speech is its lack of a one-to-one correspondence between attributes of the acoustic signal and the phonetic percept. Thus perception is presumably based on an active perceptual system which interprets the acoustic signal at a higher level in terms of some abstract features perhaps based on speech production (Liberman *et al.*, 1967). This view assumes that, for stop consonants, noise bursts and transitions provide independent cues at some level. However, others have speculated that formant transitions as well as noise bursts are secondary cues which are learned in the perceptual development of speech sounds (Blumstein and Stevens, 1980). According to Blumstein and Stevens, perceptual integration of bursts and the initial portion of formant transitions form a single integrated stimulus onset property. This stimulus onset property is characterized by an invariant gross shape for place of articulation independent of the vowel context.

It has been hypothesized that young children integrate acoustic cues in phonetic perception, but that they apply different perceptual weights to these properties than do adults (Morrongiello *et al.*, 1984). In the perception of stop-consonant place of articulation, Walley and Carrell (1983) found that young children's responses were influenced by the presence of formant transitions. They concluded that the di-

rection and extent (duration) of formant transitions were probably important in the perceptual development of place of articulation. Thus young children may place greater perceptual weight on dynamic cues such as formant transition motion than on potentially invariant stimulus onset cues composed of the burst and the initial part of the formant transition (Blumstein and Stevens, 1980).

Perceptual studies of the salience of formant transitions in adult stop-consonant perception show that these properties form trading relations with other acoustic correlates of sounds. Specifically, formant transitions appear to play a secondary role to the burst in the context of [i] and [u], whereas they play a primary role relative to the burst in the context of [a] (Dorman *et al.*, 1977). Children, on the other hand, appear to have difficulty processing stimulus onset cues such as noise bursts in the perception of stop-consonant place of articulation (Parnell and Amerman, 1978). Thus it may be that young children weight formant transition cues to a greater extent than adults, because of a basic difficulty in perceiving noise cues. If children weight formant transition cues to a greater extent than noise cues, it would be predicted that their stop-consonant perception would be poorer in the context of high vowels than low vowels, because formant cues play a secondary role to noise cues in these environments.

Previous research on children 5 years and older found that they were no more sensitive to the direction and extent of formant transitions than adults (Ohde *et al.*, 1995). In the Ohde *et al.* study, the general pattern of results for children and adults was similar for stimuli without formant motion as

<sup>a)</sup>Current address: Division of Speech and Hearing Sciences, Department of Medical Allied Health Professions, The School of Medicine, CB# 7190 Wing D Medical School, The University of North Carolina at Chapel Hill, Chapel Hill, NC 27599-7190.

for stimuli with formant motion. Furthermore, the presence of the burst improved identification for the alveolar and velar places of articulation for all age groups, although in the [g] context was particularly important for the 11-year-olds and adults. Other developmental studies that examined the effects of the presence and absence of noise bursts have found limited effects for this property (Williams and Bush, 1978; Elliot *et al.*, 1981).

According to Blumstein and Stevens (1980), stimulus onsets contain properties that facilitate the processing of the entire syllable, which then enables the listener to recover the consonants and vowels composing the syllable. In their view, place of articulation of consonants is cued by the gross shape of the short-time spectrum sampled at the onset of the stimulus, whereas vowel information is carried by the final values of formant transition trajectories in the first several tens of ms of the syllable onset. Vowels and consonants are processed in parallel and lead to the identity of the syllable. Blumstein and Stevens argue further that the identification of the stimulus does not consist of two perceptual operations involving the above properties, but rather the stimulus as a whole signals the identity of the syllable composed of consonant and vowel features. Thus acoustic properties at stimulus onset also appear to be important for the identification of vowels. Blumstein and Stevens found that adult listeners were generally able to identify vowels from brief initial segments as short as 10–20 ms. For most stimuli, vowel identification was only slightly better for moving than straight transitions. These perceptual findings are consistent with acoustic data showing the salience of vowel onsets in production (Sussman, 1990).

If the terminal values of formant transitions are important in vowel perception, then these dynamic cues may play a critical role in children's vowel identification. Moreover, if young children are more sensitive than adults to dynamic cues, then they may place more weight on formant motion cues than either static vowel targets or formant onset frequencies. Several studies examining children and adults support the importance of dynamic formant information in vowel perception (Parnell and Amerman, 1978; Jenkins *et al.*, 1983; Strange *et al.*, 1983; Parker and Diehl, 1984; Murphy *et al.*, 1989; Nearey, 1989; Fox *et al.*, 1992; Ohde *et al.*, 1996). Two developmental studies employed the "silent center" paradigm in which only the initial and final formant transitions were retained and the rest of the vowel was replaced by silence (Murphy *et al.*, 1989; Fox *et al.*, 1992). Both children and elderly adults were poorer than normal young adult controls at vowel identification from these silent center stimuli. In both of these studies, the formant transitions always contained motion so it is unclear if this dynamic cue accounts for the poorer perception by these populations. In a recent study (Ohde *et al.*, 1996), 5- to 11-year-old children identified vowels from short duration stimulus onsets with or without formant motion. The findings revealed that children and a normal adult control group were similar in vowel identification from the formant motion cue.

Recent findings (Ohde *et al.*, 1995, 1996) show that children 5 years and older perceptually weight formant transitions similarly to adults in both consonant and vowel iden-

tification. This is consistent with a hypothesis that by 6 years children identify at least some speech features similarly to adults (Sussman, 1993). However, it is unclear if children younger than 5 years of age uniquely weight dynamic cues in the perceptual development of stop-consonants and vowels. The general purpose of the current research was to determine if 3- to 4-year-old children weight dynamic properties of stop consonants and vowels in a manner different from adults, and to determine if vowel context influences perception as observed in phonological development (Stoel-Gammon, 1983; Davis and MacNeilage, 1990).

## I. TRAINING STIMULI: EXPERIMENTS I AND II

The stimuli were generated using a cascade/parallel formant synthesizer (Klatt, 1980). The sampling rate was 10 kHz and the output was low-pass filtered with a cutoff frequency of 4 kHz. Nine different syllables, composed of the voiced stops [b d g] followed by the vowels [i u a] were synthesized with source and resonance parameters appropriate for an adult male vocal tract. The synthesis parameters were varied according to one training condition and several experimental conditions. This section describes the generation of the training stimuli. Modifications of the training stimuli into the various experimental stimuli are described later in the contexts of the two experiments.

The training stimuli consisted of a 5–10 ms noise burst, followed by 300-ms voicing. The voiced portions of the syllables were generated with a cascade configuration of the synthesizer. The onset of voicing was abrupt and the amplitude remained constant throughout the syllable. The fundamental frequency ( $f_0$ ) contour started at 103 Hz and rose in a piecewise linear manner to 125 Hz within 30 ms, after which it remained constant throughout the duration of the voicing. Formant frequency specifications were modeled after Blumstein and Stevens (1980). The onset frequencies for the first four formants were appropriate to the consonants [b d g], and the steady state frequencies for these formants were appropriate to the vowels [i u a]. The starting frequency for  $F_1$  in the [i] context was 180 Hz, and a target frequency of 330 Hz was reached after a 15–30 ms transition duration. In the [u] context, the  $F_1$  starting frequency was 180 Hz, and a target frequency of 370 Hz was reached after a 15-ms transition duration. The starting frequency for  $F_1$  in the [a] context was 200 Hz, and a target frequency of 720 Hz was reached after a 20–45 ms transition duration. The duration of the  $F_1$  transition varied across different vowel and consonant contexts. The  $F_1$  transition durations were 15, 25, and 30 ms for [bi], [di], and [gi], respectively; 20, 30, and 45 ms for [ba], [da], and [ga], respectively; and 15 ms for [u] syllables. Transition durations for all other formants ( $F_2$ ,  $F_3$ , and  $F_4$ ) were 40 ms. Starting frequencies and target frequencies for the manipulated formants in the experiments are listed in Table I. The frequencies of formants higher than  $F_4$  were not manipulated, because of their limited correspondence with articulatory positions. However, the default value of  $F_5$  was raised from 3750 Hz to 4500 Hz and its band-

TABLE I. Onset (OF) and target frequencies (TF) of the first four formants (in Hz), and their absolute differences (TF-OF) for stimuli in experiments I and II.

	Onset frequency			Target frequency	TF-OF		
	[bi]	[di]	[gi]	[i]	[bi]	[di]	[gi]
<i>F1</i>	180	180	180	330	150	150	150
<i>F2</i>	1800	2000	2400	2200	400	200	400
<i>F3</i>	2600	2800	3000	3000	400	200	0
<i>F4</i>	3200	3900	3400	3600	400	300	200
	[ba]	[da]	[ga]	[a]	[ba]	[da]	[ga]
<i>F1</i>	200	200	200	720	520	520	520
<i>F2</i>	900	1700	1640	1240	340	460	400
<i>F3</i>	2000	2800	2100	2500	500	300	400
<i>F4</i>	3500	3500	3500	3500	0	0	0
	[bu]	[du]	[gu]	[u]	[bu]	[du]	[gu]
<i>F1</i>	...	180	180	370	...	190	190
<i>F2</i>	...	1600	1400	1100	...	500	300
<i>F3</i>	...	2700	2000	2350	...	350	350
<i>F4</i>	...	3200	3200	3200	...	0	0

width changed from 200 to 400, in order to minimize undesirable influences of the fifth resonator on the amplitude of adjacent formant peaks (Klatt, 1980; Walley *et al.*, 1984).

Linear prediction analyses were obtained with high-frequency preemphasis and a 25.6-ms half-hamming window positioned at consonantal release (Kewley-Port, 1983). These analyses confirmed onset spectra and template specifications as outlined by Blumstein and Stevens (1979). Labials had a diffuse-falling spectrum, alveolars a diffuse-rising spectrum, and velars a midfrequency spectral peak (Ohde *et al.*, 1995).

A 5–10 ms burst was appended to the stimuli 5–15 ms prior to the onset of voicing. The burst duration was 5 ms for stops in the [a] context and 10 ms for the [i] context. Like *F1* transition durations, the voice onset time was shortest for the labial (5 ms), intermediate for the alveolar (10 ms), and longest for the velar (15 ms) context. The bursts were generated by modifying the spectrum of a burst of white noise to a shape appropriate for each place of articulation. This was done by manipulating frequency specific amplitude controls within a parallel configuration of the synthesizer. The same noise burst was used to generate all stimuli, and the amplitude and frequency parameters were modeled after those out-

lined by Klatt (1980). Some modifications were employed in order to enhance the onset spectra (Blumstein and Stevens, 1979), and to obtain adequate burst amplitudes relative to the following vowel (Bush, 1977; Blumstein and Stevens, 1980). Table II outlines all burst parameters that were manipulated for the training stimuli in the experiments. Linear prediction analyses revealed that the bursts appropriately enhanced the integrated onset properties for each place of articulation, as theoretically and empirically predicted (Blumstein and Stevens, 1979, 1980).

In labial stops, noise energy is distributed throughout the spectrum. In order to obtain this effect, the AB (bypass path amplitude) parameter was used. The labial burst amplitude was adjusted to a value approximately 20 dB less than the vowel in the 3500-Hz region (Stevens and Blumstein, 1978). The frequency contents for the alveolar and velar stops were adjusted by manipulating amplitude controls for different formant frequencies. The primary excitation frequency was in the formant that corresponded with the spectral peaks of the following vowel. This resulted in an excitation of *F2* for [gu] and [ga], *F3* for [gi], and *F4* for [di], [du], and [da]. Although a single formant corresponded to the primary excitation for the alveolar and velar syllables, weaker energy

TABLE II. Amplitude (*A*; in dB) control levels and bandwidths (*B*; in Hz) for the burst synthesis in experiment I and Experiment II (*B3*, *B5*, and *B6* were 110, 400, and 1000 Hz, respectively, across stimuli).

	Amplitude controls						Bandwidth	
	<i>A2</i>	<i>A3</i>	<i>A4</i>	<i>A5</i>	<i>A6</i>	<i>AB</i>	<i>B2</i>	<i>B4</i>
[ba]	52	0	0	0	0	58	50	250
[da]	0	48	58	59	55	0	70	170
[ga]	52	43	46	46	36	0	70	250
[bi]	55	0	0	0	0	58	50	250
[di]	0	47	60	62	60	0	70	170
[gi]	0	53	43	45	45	0	70	250
[du]	0	53	60	48	36	0	70	170
[gu]	54	30	43	48	0	0	70	250

was distributed throughout the spectrum. This established continuity between burst release and vowel formants, similar to that seen in normally produced syllables. The amplitudes of the primary excitation for the alveolar and velar consonants were adjusted to be 0–5 dB less than the amplitude of the adjacent formant in the following vowels (Bush, 1977; Blumstein and Stevens, 1980).

## II. EXPERIMENT I: STOP CONSONANT PERCEPTION

The purpose of experiment I was to answer the following questions on the development of stop-consonant perception in 3- to 4-year-old children: (1) Do dynamic formant transitions enhance perception of place of articulation in young children? (2) What is the role of release bursts in children's perception of place of articulation? and (3) Is there evidence of consonant and vowel interdependencies in the perceptual development of place of articulation?

### A. Method

#### 1. Test stimuli

Six different syllables composed of the voiced stops [b d g] followed by the vowels [i a] were used in this experiment. The preparation of training stimuli is described in Sec. I. The experimental stimuli had a duration of either 10 or 46 ms, and formant transitions and bursts were either present or absent in accordance with four experimental conditions:

- (1) burst+moving transition, (2) burst+straight transition, (3) no burst+moving transition, and (4) no burst+straight transition.

The experimental stimuli were derived from the training stimuli (see Sec. I) by shortening the duration of voicing and by varying the conditions of the burst and formant transitions. As noted, parameters were manipulated according to four experimental conditions. One 10-ms stimulus corresponding to one glottal pulse, and one 46-ms stimulus consisting of five glottal pulses were generated within each condition. For the first condition, the experimental stimuli were generated directly from each training stimulus by reducing the duration of voicing. Thus these stimuli contained bursts as well as moving formant transitions, and had the same synthesis parameters as the training stimuli. However, the short duration of the 10-ms stimuli prevented the fundamental frequency and formant frequencies from reaching their target values. Instead, they reached values that were interpolated in a piecewise linear manner from the training stimuli. The second stimulus condition contained the burst, but not formant transitions. The generation of the bursts was identical to the moving transition conditions. The stimuli had the same onset frequencies as the corresponding stimuli with formant transitions. However, the frequencies of the second, third, and fourth formants remained constant, i.e., straight, at the onset value throughout the syllable. Only the first formant movement was retained in order to sustain the stoplike quality of the stimuli (Blumstein and Stevens, 1980). The third stimulus condition contained stimuli without bursts and with moving transitions. The stimuli for the fourth condition were equivalent to the third, except for the absence of a formant transition. The burst and formant transition condi-

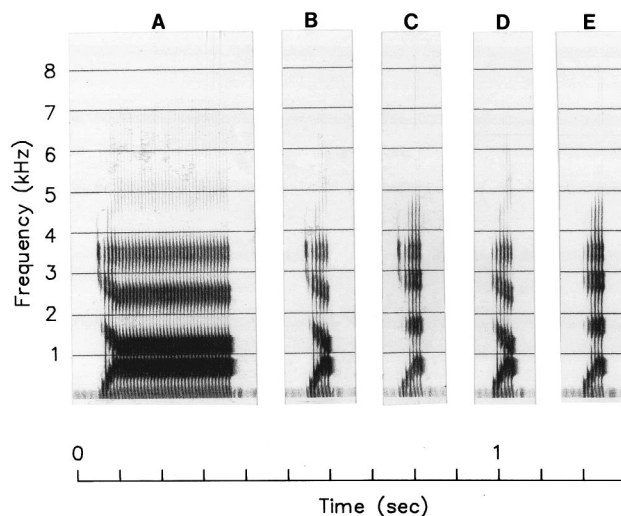


FIG. 1. Spectrograms of the training (A), burst+five glottal pulses moving transition (B), burst+five glottal pulses straight transition (C), no burst+five glottal pulses moving transition (D), and no burst+five glottal pulses straight transition (E) for the syllable [da].

tions for one 46-ms syllable are shown in Fig. 1. In all, 48 experimental stimuli were produced (2 vowels $\times$ 3 consonants $\times$ 4 conditions $\times$ 2 durations).

### 2. Subjects

The subjects were ten adults, ten 3-year-olds, and ten 4-year-olds. The 3-year-olds ranged in age from 3:5 (years: months) to 3:10 with a mean age of 3:9. The 4-year-olds ranged from 4:1 to 4:6, with a mean age of 4:3. The mean age for the adults was 26:1. All subjects were native speakers of English. The children exhibited normal articulation, defined as performance within normal limits on the *Arizona Articulation Proficiency Scale-Revised* (Fudala, 1970), and age appropriate language abilities based on performance within normal limits on the *Test of Early Language Development—2nd Edition* (Hresko *et al.*, 1991). The adults used a standard American dialect and showed no evidence of speech or language impairment on the basis of informal assessment. Finally, a hearing screening at 20 dB for the octave frequencies between 500 and 4000 Hz was performed on both children and adults prior to each testing session. All subjects were paid for their participation and the children selected a toy that was given as a prize at the completion of all testing. Three 4-year-olds did not pass the speech–language–hearing screening, and eight 3-year-olds and one 4-year-old were unable or unwilling to complete the perceptual testing. These children were replaced by new subjects.<sup>1</sup>

### 3. Procedure

The training and testing were conducted in an IAC booth over earphones at a comfortable listening level (80 dB SPL). The stimulus presentation and data collection were controlled by a PDP 11/73 computer. A 2AFC rather than a 3AFC testing paradigm was used, because previous pilot

testing suggested that children in these young age groups had difficulties learning and remembering three categories. Six experimental runs were presented, each preceded by a training sequence. The two vowel contexts were tested separately. Within each vowel context, stimuli were grouped in sets corresponding to the three possible pairwise combinations of consonants. The order of the vowel context as well as the syllable combinations were counterbalanced across subjects. The adults responded by pushing one of two buttons on a response box. The buttons were labelled either “b” and “d,” “b” and “g,” or “d” and “g,” depending on the presented contrast. The children responded by pointing to, and saying the name of one of two depicted puppets. The puppets were named according to the stimulus syllables. In the [i] context, the three puppet pairs were [bi]–[di], [bi]–[gi], and [di]–[gi]. Similarly, the pairs in the [a] context were [ba]–[da], [ba]–[ga], and [da]–[ga]. One experimenter was always in the booth with the child, monitoring the level of attention and recording the responses by pressing the corresponding buttons on the response box. The child and the experimenter sat facing each other on opposite sides of a small table. For all subjects, one experimenter outside the booth monitored the accuracy of the responses and controlled the presentation of the different conditions.

*a. Training.* A sequence of training procedures was used to obtain reliable performance. The children participated in an initial period of structured play in order to help them associate the names with the puppets. The experimenter interacted with the child in a play situation, using the two puppets that were to be used in the following perception test. During this interaction, an attempt was always made to follow the child’s lead of attention and in other ways prompt the child to participate actively. The names of the puppets were repeatedly modeled by the experimenter during the play, and the child was occasionally prompted to produce the names. When the child was able to name both puppets correctly, the real puppets were put aside and replaced by their photographs.

Next, the child was required to repeat the name produced in a live voice by the experimenter and point to the photograph of the named puppet. After two correct identifications of both puppets presented consecutively, the training proceeded to stimulus presentation through headphones. The experimenter that was in the booth was able to hear the stimuli through headphones as well, and was thereby able to give corrective feedback if needed. Three training runs were presented to the children as well as the adults. First, five digitized productions of each syllable by a male adult were presented. Next, five repetitions of each of the synthesized training syllables were presented. Subjects were required to identify at least eight of ten syllables in each of these conditions before proceeding to the experimental conditions. Occasionally, subjects did not demonstrate reliable identification of synthesized training stimuli. In these cases, additional training was provided by presenting several exemplars of the stimuli with concurrent feedback as to the correct response. Finally, one example of a five-glottal-pulse stimulus for each of the consonants was presented to familiarize the subjects

with the shorter stimuli that were to be presented in the experimental condition.

*b. Testing.* Within each experimental run, the stimuli were blocked according to the conditions of the burst and formant transitions. The sequence of presentation for a given run was burst+moving transitions, burst+straight transition, no burst+moving transition, and no burst+straight transition.<sup>2</sup> The four stimuli (2 consonants×2 durations) in each of these conditions were repeated two times and presented in a random order. Because each stimulus was tested in two runs (contrasting with each of the other consonants), this resulted in a total of four repetitions of each stimulus. For the adults, the stimuli were presented with a 3-s interstimulus interval. For the children, the stimulus presentation was adjusted to the child’s response rate, so that no stimulus was presented until the child had responded to the previous one. During the testing of the children, the experimenter did not wear earphones and was therefore unaware of the nature of the stimulus. However, the time of presentation for each stimulus was observed through the activation of a LED light on the response box. The children were prompted to respond to all presentations. If a discrepancy occurred between the child’s manual and verbal response, the experimenter asked for a clarification. This almost always resulted in a matching response. In the few cases where this did not occur, the manual response was noted. The children were reinforced verbally and with stickers at the end of each run.

Reliable performance throughout the testing was ensured by monitoring the subjects’ responses to synthesized training stimuli inserted among the experimental stimuli. Eight training stimuli were inserted within each of the six blocks of 32 stimuli for each consonant combination, and subjects were required to correctly identify an average of at least 75% of these across the six testing blocks. The mean level of performance was 85% for the 3-year-olds, 93% for the 4-year-olds, and 100% for the adults. The adults completed the testing within a single session. The mean number of sessions required for screening, training, and testing for the children were 4.1 for both the 3-year-old and 4-year-old groups.

#### 4. Statistical analyses

Three repeated measures analyses of variance on the arcsine transformed percents of each place of articulation ([b], [d], and [g]) were used to analyze the data. These analyses included the between factor of age, and the within factors of burst (burst and no burst), vowel ([i] and [a]), transition type (straight and moving), and voicing duration (10 and 46 ms). Followup analytical comparisons including tests of simple main effects and appropriate Newman Keuls’ *post hoc* tests were used to examine relevant significant interactions (Keppel, 1991). Significant results at the  $p < 0.05$  or  $p < 0.01$  levels are reported.

## B. Results and discussion

As Figs. 2, 3, and 4 illustrate, identification of stop-consonant place of articulation from the burst+moving transition stimuli was high for all listeners in the [a] context.

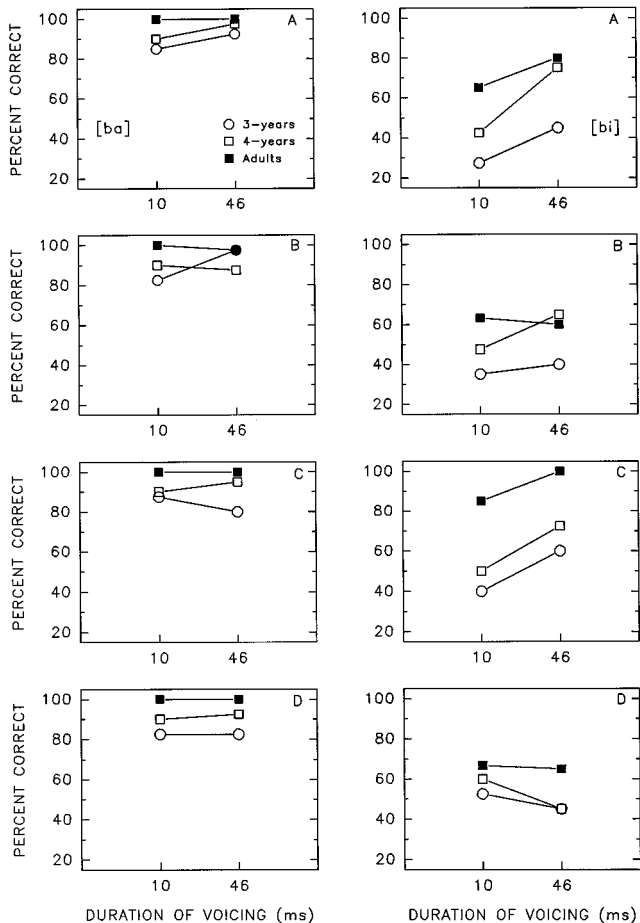


FIG. 2. Percent correct identification of [b] in stimuli with burst and moving transitions (A), with bursts and straight transitions (B), with no bursts and moving transitions (C), and with no bursts and straight transitions (D) as a function of duration and listener age.

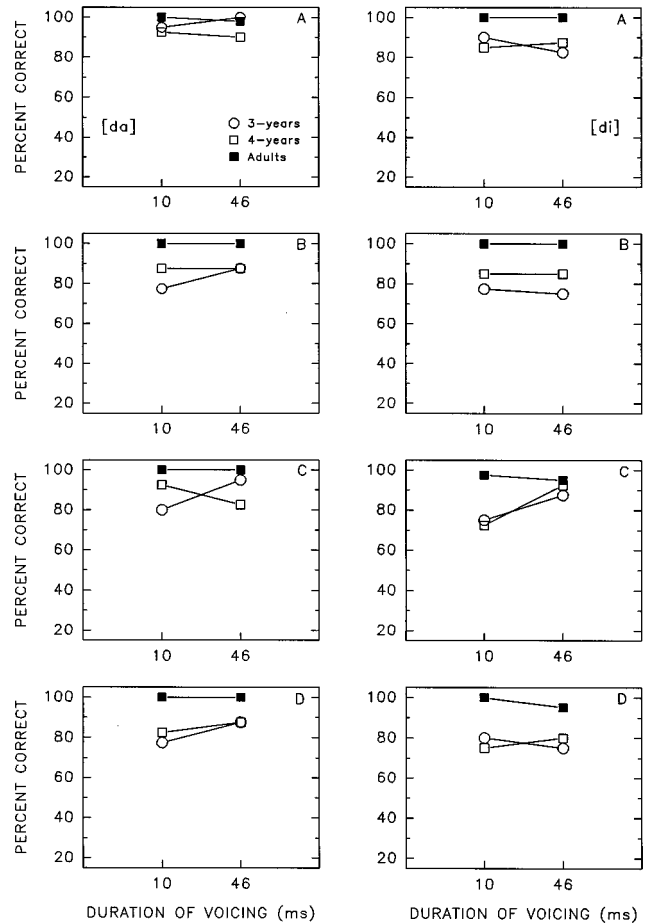


FIG. 3. Percent correct identification of [d] in stimuli with bursts and moving transitions (A), with bursts and straight transitions (B), with no bursts and moving transitions (C), and with no bursts and straight transitions (D) as a function of duration and listener age.

However, the 3-year-olds in particular had difficulty identifying [b] and [g] in the [i] context. Moreover, both 3- and 4-year-olds had more difficulty processing stop consonants than adults in both vowel contexts for burst+vowel onset stimuli without formant motions. On the other hand, formant motion contributed little to stop-consonant identification in adults. In general, listeners across age levels had more difficulty identifying the no burst+moving transition stimuli than stops with bursts, indicating the importance of the burst in the perception of place of articulation. The deletion of the burst influenced the short duration stimuli more than the longer duration stimuli. With the 46-ms stimuli, stop identification was near 100% across place of articulation for adult listeners. In contrast, 3- and 4-year-old children experienced difficulty in identifying place of articulation of stops for short and long duration stimuli in both vowel contexts. The general pattern of results obtained for the no burst+vowel onset stimuli without formant motions is similar to that for the no burst+vowel onset stimuli with formant motions. However, children were poorer at identifying stops, especially [g], for straight transition than moving transition stimuli.

A repeated measures analysis of variance of the [b] stimuli revealed significant main effects of age [ $F(2,27)$

$= 13.27$ ;  $p < 0.01$ ], vowel [ $F(1,27) = 84.68$ ;  $p < 0.01$ ], transition [ $F(1,27) = 5.96$ ;  $p < 0.05$ ], and voicing duration [ $F(1,27) = 12.96$ ;  $p < 0.01$ ].<sup>3</sup> None of the age interactions were significant. *Post hoc* comparisons revealed higher labial stop identification for adults than either the 3- and 4-year-olds. Also, the 4-year-olds identified [b] at a significantly higher rate than the 3-year-olds. Transition type, vowel context, and transition duration significantly influenced [b] perception with higher stop identification for the moving than straight transition, for the [a] than [i] environment, and for the 46 ms than 10-ms duration condition. Variability, as reflected in the average standard error collapsed across vowel, stimulus duration, and burst for each group, was not consistently greater for straight transitions (ST) than moving transitions (MT) (3-year-old: MT=7.52, ST=7.16; 4-year-old: MT=6.19, ST=6.52; Adult: MT=3.19, ST=5.32).

Results for the [d] stimuli showed significant main effects of age [ $F(2,27) = 6.74$ ;  $p < 0.01$ ], burst [ $F(1,27) = 9.37$ ;  $p < 0.01$ ], and transition type [ $F(1,27) = 4.18$ ;  $p < 0.05$ ], and significant interactions of voicing duration  $\times$  age [ $F(2,27) = 3.62$ ;  $p < 0.05$ ], and vowel  $\times$  voicing duration  $\times$  age [ $F(2,27) = 5.98$ ;  $p < 0.01$ ]. *Post hoc* tests revealed developmental effects of the [d] stimulus. First, identification of [d] was significantly higher for adults than 3- and 4-year-



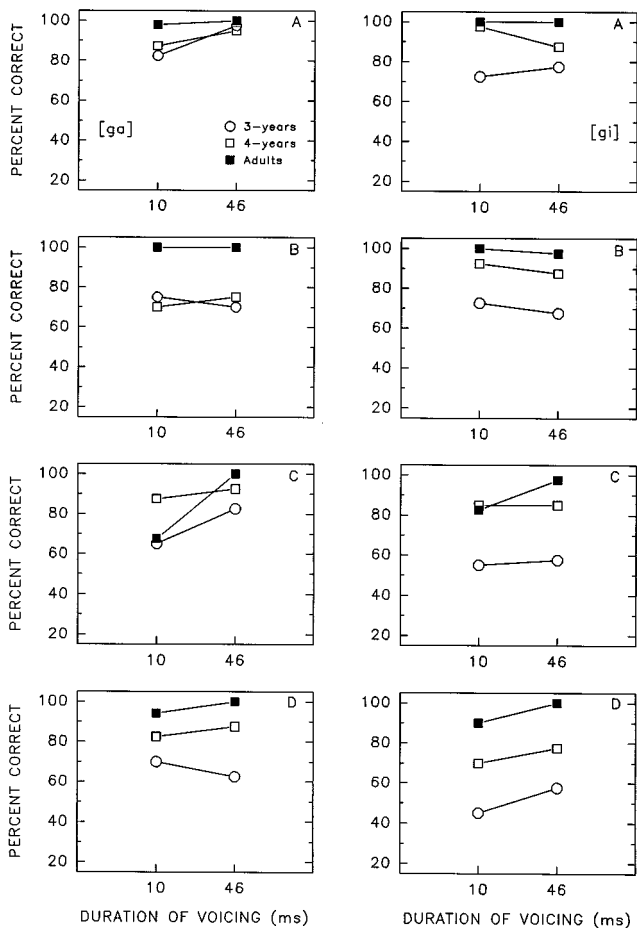


FIG. 4. Percent correct identification of [g] in stimuli with bursts and moving transitions (A), with bursts and straight transitions (B), with no bursts and moving transitions (C), and with no bursts and straight transitions (D) as a function of duration and listener age.

olds for the 10- and 46-ms conditions. Second, the 46-ms duration condition was perceived significantly better than the 10-ms duration condition for only the 3-year-olds. In addition, higher stop identification for all age groups was obtained for the moving than for the straight transition, and for the burst than for the no burst stimuli. Variability was greater for straight transitions (ST) than moving transitions (MT) for child groups only (3-year-old: MT=5.43, ST=8.03; 4-year-old: MT=6.02, ST=7.44; Adult: MT=1.04, ST=0.42).

For the [g] stimuli, an analysis of variance exhibited significant main effects of age [ $F(2,27)=18.07$ ;  $p<0.01$ ], burst [ $F(1,27)=17.68$ ;  $p<0.01$ ], transition type [ $F(1,27)=15.87$ ;  $p<0.01$ ], and voicing duration [ $F(1,27)=6.76$ ;  $p<0.05$ ], and a significant transition type $\times$ age interaction [ $F(2,27)=14.51$ ;  $p<0.01$ ]. As with [d], the results revealed that higher identification was obtained for the burst than for the no burst stimuli. The results of *post hoc* analyses showed differences among listener groups in the influence of transition type. In particular, 3- and 4-year-olds identified velar stops at a significantly higher level from moving transitions than straight transitions. Adults, on the other hand, identified velar stops at a higher level from straight than moving transitions. This finding appears due to their relatively low velar identification of the 10-ms no burst and moving transition

condition. Thus perceptual development of stops appears to be linked to place of articulation and dynamic cues. For example, formant transition motion may enhance the perception of the velar feature in young children but not adults. When compared across groups, adults and 4-year-olds identified [g] from moving transitions at a significantly higher level than 3-year-olds. On the other hand, when transitions were not moving (straight), [g] identification was significantly higher for adults than both 3- and 4-year-olds. In addition, 4-year-olds identified [g] from straight transitions at a significantly higher level than 3-year-olds. Variability was generally greater for moving transitions (MT) than straight transitions (ST) (3-year-old: MT=8.76, ST=8.25; 4-year-old: MT=5.42, ST=7.31; Adult: MT=2.49, ST=1.31).

In summary, these results reveal developmental trends in processing place of articulation of stop consonants. Although dynamic properties appear important in the perceptual development of stop consonants, the weighting of these cues is linked to specific places of articulation. It appears that 3- to 4-year-old children derive perceptual benefit above and beyond that for adults from dynamic transition motion, but that this advantage may be limited to the velar place of articulation.

### III. EXPERIMENT II: VOWEL PERCEPTION

The purpose of experiment II was to answer the following questions on the development of vowel perception in 3- to 4-year-old children: (1) Can young children identify vowels from short duration stimulus onsets? (2) Is dynamic formant motion important in the development of vowel perception? and (3) Is there evidence of consonant and vowel interdependencies in the development of vowel perception?

#### A. Method

##### 1. Test stimuli

The stimuli consisted of six syllables, composed of the voiced stops [d g] followed by the vowels [i u a]. Alveolar and velar stimuli described in Secs. I and II were used. The consonant contexts were chosen to represent the range of environments, which produced the highest and lowest vowel identifications by older children in a previous study (Ohde *et al.*, 1996). The vowel context [u] and a 30-ms duration condition were added, and only stimuli that contained a burst were used. Thus the experimental stimuli had durations of 10, 30, or 46 ms, appropriate bursts, and either moving or straight transitions. In all, six training stimuli (3 vowels $\times$ 2 consonants) and 36 experimental stimuli (3 vowels $\times$ 2 consonants $\times$ 3 durations $\times$ 2 formant conditions) were used.

##### 2. Subjects

Ten adults, ten 3-year-olds, and ten 4-year-olds served as listeners. The 3-year-olds ranged in age from 3:8 (years: months) to 3:10 with a mean age of 3:8. The 4-year-olds ranged in age from 4:0 to 4:6, with a mean age of 4:3. The mean age for the adults was 26:6. The criteria for speech, language, and hearing were the same as in experiment I. Three of the adults but none of the children had previously

participated in the consonant perception experiment. One 3-year-old and one 4-year-old did not pass the hearing screening. One 3-year-old and one 4-year-old were unable or unwilling to complete testing. These were replaced by new subjects.

### 3. Procedure

The training and testing procedures were similar to those in experiment I. Six experimental runs were presented, each preceded by a training sequence. The two consonant contexts were tested separately. Within each consonant context, stimuli were grouped in sets corresponding to the three possible pairwise combinations of vowels. The order of both consonant context and the contrast pairs were counterbalanced across subjects. The adults responded by pressing one of two buttons on a response box placed in front of them. The buttons were labelled either “i” and “u,” “i” and “a,” or “u” and “a,” depending on the tested contrast. The children responded by pointing to, and saying the name of one of two depicted puppets, named according to the tested syllables.

The two experimental conditions were presented separately within each consonant context. The stimuli with moving transitions were presented first, followed by the straight transition stimuli (see footnote 1). The six stimuli (2 vowels×3 durations) in each of these conditions were repeated two times and presented in a random order. Eight training stimuli were inserted within each stimulus set of 24 experimental stimuli, and subjects were required to correctly identify an average of at least 75% of these across the six testing blocks. The mean level of performance was 95% for the 3-year-olds, 99% for the 4-year-olds, and 100% for the adults. The adults completed all training and testing within a single session. The mean number of sessions required to complete all screening, training, and testing procedures for the children was 4.0 for the 3-year-olds, and 3.8 for the 4-year-olds.

### 4. Statistical analyses

Two repeated measures analyses of variance on the arcsine transformed percents of each place of articulation ([d] and [g]) were used to analyze the data. These analyses included the between factor of age and the within factors of vowel ([i], [u], and [a]), transition type (straight and moving), and voicing duration (10, 30, and 46 ms). Followup analytical comparisons including tests of simple main effects and appropriate Newman Keuls’ *post hoc* tests were used to examine relevant significant interactions (Keppel, 1991). Significant results at the  $p < 0.05$  or  $p < 0.01$  levels are reported.

### B. Results and discussion

In general, vowel identification for the 4-year-olds and adults was above 80% across most stimulus types. For the adult group, performance was generally at ceiling. Some important developmental and contextual effects were found. The findings for the [d] context revealed an influence of transition type on vowel perception. As shown in Fig. 5, vowel

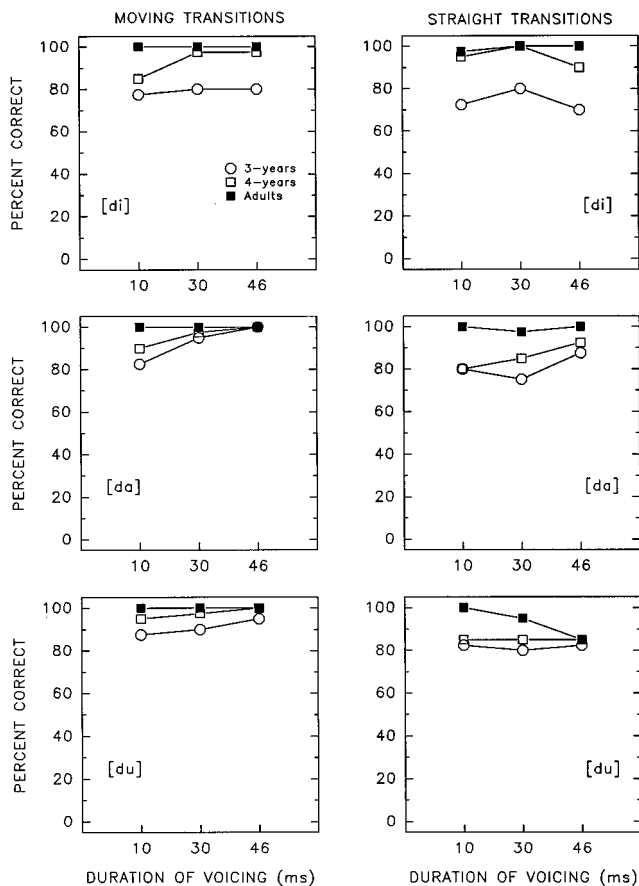


FIG. 5. Percent correct identification for vowels in the context of [d] as a function of duration, transition type, and listener age.

identification from moving transitions was generally higher than vowel perception from straight transitions. These effects occurred across all vowel contexts, and were found to be statistically significant. Variability was greater for straight transitions (ST) than moving transitions (MT) (3-year-old: MT=5.85, ST=7.15; 4-year-old: MT=2.68, ST=5.48; Adult: MT=0.00, ST=1.77).

The analysis of variance for the [d] stimuli showed significant main effects of age [ $F(2,27) = 23.94$ ;  $p < 0.01$ ] and transition type [ $F(1,27) = 24.61$ ;  $p < 0.01$ ], and a significant first order interaction of transition type×voicing duration [ $F(2,54) = 3.99$ ;  $p < 0.05$ ].<sup>4</sup> Thus vowel identification in the environment of [d] was not only influenced by transition trajectory but also by stimulus duration. As moving transitions increased in duration, correct vowel identification increased, but this same effect was not observed for straight transitions. Also, vowel identification was significantly higher for moving than straight transitions at the 30- and 46-ms stimulus durations. A developmental effect was observed for the [d] context. Vowel identification by adults was significantly higher than vowel identification by 3- and 4-year-olds. The 4-year-olds identified vowels at a significantly higher rate than 3-year-olds.

Contrary to the findings for [d], in the [g] environment transition trajectory had little effect on the identification of [i] and [u] compared to [a]. For this place of articulation, there were substantial differences in vowel perception as a function of listener age. As illustrated in Fig. 6, 3-year-olds

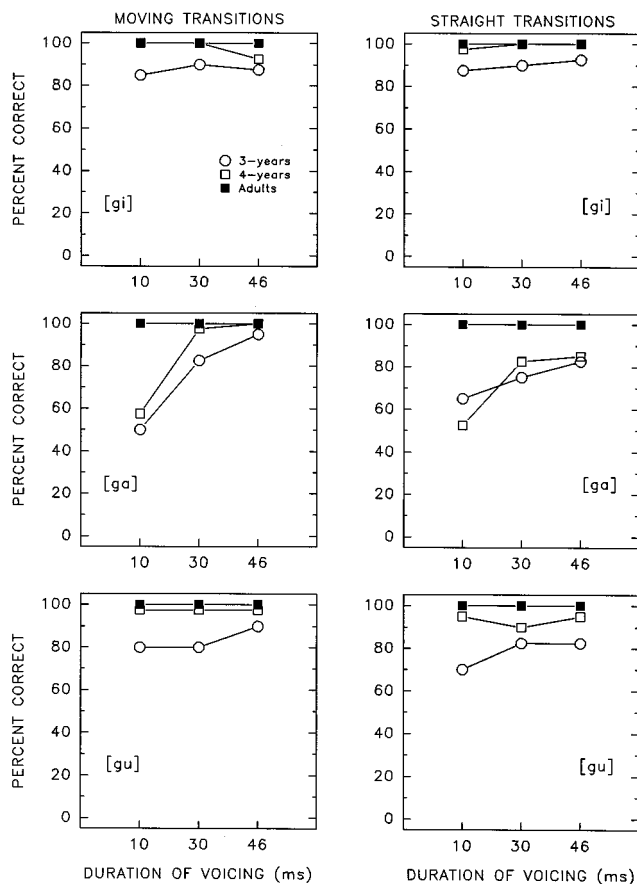


FIG. 6. Percent correct identification for vowels in the context of [g] as a function of duration, transition type, and listener age.

generally had more difficulty in identifying vowels in the velar context than adults or 4-year-olds.

Similar to the [d] place of articulation, variability (standard error) in vowel identification in the [g] context was generally greater for straight than moving transitions (3-year-old: MT=5.59, ST=6.42; 4-year-old: MT=2.71, ST=4.10; Adult: MT=0.00, ST=0.00). An analysis of variance exhibited significant main effects of age [ $F(2,27) = 40.97$ ;  $p < 0.01$ ], vowel [ $F(2,54) = 13.86$ ;  $p < 0.01$ ], and voicing duration [ $F(2,54) = 22.70$ ;  $p < 0.01$ ], significant first-order interactions of vowel $\times$ age [ $F(4,54) = 5.00$ ;  $p < 0.01$ ], voicing duration $\times$ age [ $F(4,54) = 6.39$ ;  $p < 0.01$ ], and vowel $\times$ transition type [ $F(2,54) = 4.47$ ;  $p < 0.05$ ], and a second-order interaction of vowel $\times$ voicing duration $\times$ age [ $F(8,108) = 3.46$ ;  $p < 0.01$ ].

Tests of simple effects revealed that adults identified vowels at a significantly higher level than 3- and 4-year-olds across voicing duration except for the 30-ms condition where adults were not different from 4-year-old children. Also, 4-year-old children identified vowels at a significantly higher level than 3-year-old children at each voicing duration. Thus this pattern of vowel identification reveals a dependency on voicing duration as a function of age.

The observed duration effects reveal differences not only between children and adults, but also between 3- and 4-year-old children. Only 3- and 4-year-olds were influenced by this parameter. Vowel identification was significantly higher at each level of duration for the 3-year-olds. For the

4-year-olds the two longer duration stimuli were significantly different from the shorter stimulus, but these long stimuli were not different from each other. Thus with increases in voicing duration, there was a concomitant increase in the extent of formant onset frequency or formant transition energy which benefitted the child listeners.

Tests of simple effects also showed that place of articulation of the vowel influenced perception of only the 3- and 4-year-old children. The 4-year-olds identified high vowels, [i u], at a significantly higher level than the low vowel, [a]. For the 3-year-olds, [i] was identified at a significantly higher level than both [u] and [a]. Thus in the context of a velar stop consonant, children's vowel identification appears to be most salient for high front followed by high back and then low back places of articulation. This pattern of place of articulation effects is also reflected in the differences among adults and children in vowel identification. For [i] and [u], adults and 4-year-olds identified these vowels at a significantly higher level than the 3-year-olds. On the other hand, adults identified [a] at a significantly higher level than both 3- and 4-year-old children.

Tests of simple effects revealed that vowel identification was significantly higher from moving transitions than from straight transitions for [a], but not for [i] and [u]. Thus the only syllable for which vowel identification was influenced by formant motion was [ga]. Within the velar feature, strong vowel place of articulation effects were found for both moving and straight transitions. For example, high vowels, [i u], were identified at a significantly higher rate than the low vowel, [a], from moving transitions. For straight transitions, vowel identification was significantly higher for [i] than for [u] and [a], and significantly higher for [u] than for [a].

In summary, the results show that vowel identification from brief synthetic CV syllables was consistently high for adult listeners. Dynamic formant motion improved vowel identification across all age groups and consonant contexts, with the exception of the [gi] and [gu] syllables. Strong developmental effects were observed for both alveolar and velar places of consonant articulation. For children, the accuracy of vowel identification increased as a function of place of articulation of vowels and consonants, and increases in stimulus duration.

#### IV. GENERAL DISCUSSION

##### A. The perceptual development of stop consonants and vowels

The current findings for children between 3- and 4-years of age indicate high levels of consonant and vowel identification from short duration stimulus onsets. For the consonant identification task, children and adults identified place of articulation for the burst+moving transition in the [a] context at levels above 80% for even the short 10-ms stimulus. For the vowel identification task, perceptual levels were generally 80% or above across duration for the [d]+moving transition syllables. These findings clearly show that children understood the tasks and could identify the place of articulation of consonants and vowels at high levels from short duration stimulus onsets.

However, clear developmental effects were observed for both consonant and vowel identification conditions. Across all places of stop-consonant articulation, adults performed significantly better than children. Moreover, adults identified vowels at much higher levels than children in both consonant contexts. In addition, 4-year-old children generally identified both consonants and vowels at higher levels than 3-year-old children. These trends are consistent with results from a developmental study using segmented natural speech (Parnell and Amerman, 1978). In the Parnell and Amerman research, 4- to 5-year-old children performed more poorly on both consonant and vowel identification tasks than 11-year-old children and adults. Thus based on these studies there is clear evidence of maturational changes in the processes and strategies involved in the perception of stop consonants and vowels.

In two previous studies (Ohde *et al.*, 1995, 1996), we examined stop-consonant and vowel perception in 5- to 11-year-old children. Identical stimuli were used in these studies and the current research. Thus a general developmental pattern of consonant and vowel perception can be provided for children ranging from 3- to 11-years-old. The findings of our research show that in about a six month period between 3- and 4-years of age rapid changes occur in the identification of stop consonants and vowels. Reliable differences in stop-consonant and vowel identification were observed for 3- and 4-year-olds. Furthermore, in comparing 3- and 4-year-old children to those 5 years and older, the younger children were more influenced by stimulus duration and syllable context than the older children. Although duration influenced vowel perception for children 5 years and older, it was a more salient cue for 3- and 4-year-olds. In the [g] context, both 3- and 4-year-old children's vowel identification substantially improved with increases in duration. Previous research has found little evidence supporting developmental differences in stop-consonant identification as a function of stimulus duration (Sussman and Carney, 1989). However, in the current research, [d] identification improved with increases in duration for the 3-year-olds.

One process that may account for the duration findings in the current study is potential differences in auditory processing abilities in children and adults. The findings for vowel identification support this view. Since vowels appear to be processed in an auditory (continuous) mode (Keating and Blumstein, 1978), changes in identification based on greater acoustic input support the importance of this variable in development. Several studies have shown that changes in duration can influence the discrimination of vowels in adults (Stevens, 1968; Fujisaki and Kawashima, 1969; Sachs, 1969; Pisoni, 1973). However, in the current study, duration had no influence on vowel identification in adults, whereas children's perception of vowels improved with increases in duration. These findings suggest an important developmental role of the auditory system in vowel identification, which continues to influence vowel perception even in children 11-years-old. Developmental differences in auditory sensitivity have been reported in previous psychophysical and speech perception experiments (Elliott *et al.*, 1981; Allen *et al.*,

1989; Wightman *et al.*, 1989; Allen and Wightman, 1992; Sussman, 1993).

In our previous developmental study (Ohde *et al.*, 1996) of vowel perception, age effects were observed for labial and velar syllable contexts, but not for the alveolar environment. We proposed that the developmental saliency of this syllable context was based on the distinctive acoustic correlates of vowels in this environment. For [a] and [u],  $F_2$  transition motion is substantially greater in the [d] context than either [b] or [g] environments (see Table I). Moreover, the [d] context appears to enhance the high-frequency prominent peak in [i] providing salient secondary cues for vowel fronting (Stevens and Keyser, 1989). In the current study, both 3- and 4-year-olds identified vowels in the [d] context at lower levels than adults. If our acoustic hypothesis discussed above is correct, then an auditory explanation may account for these differences observed for vowels, as well as those discussed for stop consonants.

### **B. Dynamic, static, and integrated cues in the perceptual development of stop consonants and vowels**

In the perception of stop consonants and vowels, several acoustic properties contribute cues to place of articulation. Two of these properties are formant transitions and stop-consonant bursts. While formant transition motion is a dynamic property, formant onset frequencies and bursts are static cues. The distinction between dynamic and static cues is presumably the extent of spectral change over time, with the former varying more than the latter. However, both of these cues are context dependent, influenced primarily by the following vowel. Because of the context dependency of these cues, it has been proposed that they are secondary properties in perception (Blumstein and Stevens, 1980). Alternatively, a primary cue may be the spectrum at stimulus onset. Since presumably the burst and formant transitions both contribute to this onset spectrum, they form a single integrated acoustic property. The onset spectrum shapes of labial, alveolar, and velar places of articulation are characterized by diffuse-falling, diffuse-rising, and mid-frequency spectral energy, respectively.

Although primary properties may be salient in the acoustic correlates of place of articulation, Blumstein *et al.* (1982) found that stop-consonant identification performance was determined by onset frequencies rather than the gross shape of the spectrum. Walley and Carrell (1983) found that the secondary formant transition was the dominant cue in identification of stop consonants for adults and 5-year-old children. Walley and Carrell suggested that formant transition motion was a potentially important cue in the perceptual development of stop consonants. However, research by Ohde *et al.* (1995) found no support for the influence of dynamic formant motion in the perceptual development of stop-consonant place of articulation for 5- to 11-year-old children. If dynamic formant motion is an important cue in perceptual development, then it must operate prior to 5 years of age. In the current research, dynamic formant motion was a developmental cue to stop-consonant perception for 3- and 4-year-old children, but only in the velar context. Nevertheless,

these findings suggest that young children perceptually weight dynamic cues more than adults. Thus for children between 3 and 11 years of age, dynamic formant motion appears to be a developmental cue for a limited number of sound features.

For [g], the magnitude of the difference in identification between adults and 3- and 4-year-old children was substantially greater than for the other places of articulation. This general effect may relate to a basic difficulty in children's processing a prominent midfrequency spectral peak which is characteristic of velars (Blumstein and Stevens, 1980; Kewley-Port, 1983; Stevens, 1985). Although the time interval over which this narrow prominence exists is longer than the more rapid changes observed for labials and alveolars, children have problems in perceiving this acoustic correlate of place of articulation. Moreover, when the mid-frequency spectral peak shifts from the lower to the higher-frequency range such as in the [i] context, children's perception of the velar feature is further compromised.

Another potentially important secondary cue to the perception of place of articulation for stop consonants is the static burst. Several studies have examined the developmental role of the burst in the perception of stop consonants (Parnell and Amerman, 1978; Williams and Bush, 1978; Elliott *et al.*, 1981; Ohde *et al.*, 1995). Williams and Bush examined infants' discrimination of a [da]–[ga] contrast, with and without release bursts. They found some evidence indicating that the presence of a burst facilitates place of articulation discrimination. These findings are consistent with Ohde *et al.* who found that the burst generally enhanced place of articulation identification in 5- to 11-year-old children and adults. However, Elliott *et al.* found only minimal differences in the identification of stimuli with and without bursts for 6- and 10-year-olds and adults. On the other hand, Parnell and Amerman found 4-year-old children poorer than 11-year-olds and adults in the identification of place of articulation of stops from noise bursts. Thus the developmental findings for perception of stop consonants from noise cues are controversial.

Most studies of stop-consonant perception have treated bursts and formant transitions as separate cues to place of articulation. If onset spectra are primary cues to stop-consonant perception, then identification of place of articulation should be relatively high independent of the status of secondary cues. The results for adults support this view. Very high levels of stop-consonant identification were obtained for even the noburst + straight transition stimuli. In fact, identification levels were above 90% for all stimulus conditions except [bi]. Thus adults appeared to base their identification on either spectral shape or formant onset cues or a combination of these properties (Blumstein *et al.*, 1982). Onset spectra also appear to be very important cues for young children. A comparison of the children's findings for the burst + moving to the noburst + straight (Figs. 2, 3, and 4) transition stimuli reveals that 10 of the 12 shortest (10-ms) conditions were at or above 70% in the former and 9 in the latter. Thus even the extreme stimulus conditions produced relatively similar results that were well above chance identification for young children.

For vowel perception, there was no evidence that formant motion enhanced identification in children. In the velar stop-consonant context, children's vowel identification was higher for longer than shorter duration stimuli. Since this duration effect occurred for both moving and straight transitions, children appeared to rely equally on additional auditory cues provided by the static formant onset and/or formant transition-target frequencies. Adults, on the other hand, identified vowels primarily from short duration stimulus onset frequencies.

## V. CONCLUSIONS

The purpose of this research was to determine the role of acoustic correlates of short duration stimulus onsets in 3- and 4-year-old children's stop consonant and vowel identification. It has been hypothesized that these abrupt onsets provide markers to indicate points in time where acoustic information appropriate for place of articulation is sampled by both adults and children (Blumstein and Stevens, 1980). The findings of this study provide clear evidence of the saliency of abrupt stimulus onsets in children's perception of stop consonants and vowels. Identification of stop consonants and vowels by adults and children was well above chance for stimuli containing no bursts and without formant transition motion. Evidence was found supporting the importance of dynamic cues in perceptual development, but it was limited to stop consonants and to a single place of articulation. The results support the following conclusions:

- (1) Dynamic formant transitions are developmentally salient cues in 3- and 4-year-old children, but only for the stop-consonant velar place of articulation.
- (2) Dynamic formant transitions and static noise bursts generally improve stop identification for subjects ranging in age from 3-years-old to adulthood.
- (3) For 3- to 4-year-old children, contextual interdependencies influenced stop-consonant and vowel perception, which were both poorer for syllables containing mid-frequency spectral prominences.
- (4) For 3- to 4-year old children, the most salient cues to consonant perception appear to be some integrated spectral property sampled at stimulus onset and/or formant onset frequencies. For these children, the most salient cues to vowel perception are formant frequencies and/or formant transition-target frequencies.

## ACKNOWLEDGMENTS

This work was supported by a NIH Grant No. DC00464, and a Vanderbilt University Research Council grant. The authors thank Winifred Strange, and two anonymous reviewers for comments on this paper. We express our sincere gratitude to the children who participated in this study, and to their parents. Special thanks are also extended to Betty Abernathy, Betty Beardslee, Carolyn Black Billings, Joanne Chase, Anne Colley, Carolyn Dangoor, Debbie Estes, Erika Gerth, Joyce Golden, Hilda Kohl, Nancy Ledbetter, Diane Neighbors, Cynthia Nichting, Anne Parker, Kelly Shikoh, Karen Stump, and Jean Voorhes for their help with subject recruitment, to Anne Bachmann, Maggie Barker, and Chris McMahon for assistance in data collection, and to Dan Ashmead for help on statistics.

<sup>1</sup>The mean age of the eight 3-year-old subjects who were dropped from the study was 3:8. Of these subjects, three were below this mean age and 5 were at or above the mean age. In the beginning stages of this research, we started testing children between 3:0 and 3:5. Because of the difficulty these children manifested with the experimental task, subjects older than 3:5 were deemed most appropriate for perceptual testing. It should be noted that this 3-year-old group is substantially younger than the 4- to 5-year-old children tested in related research (Parnell and Amerman, 1978; Walley and Carrell, 1983).

<sup>2</sup>This sequence of presentation was employed because it progressed from synthetic sounds that were most natural to least natural. Thus, it provided subjects some opportunity to listen to synthetic speech that was most similar to natural productions, which was deemed important for children. Others have used similar blocking procedures in adult and child perception experiments (Repp, 1986; Ohde, 1994; Ohde *et al.*, 1995).

<sup>3</sup>Because adult performance for many conditions was near ceiling, analyses of variance were also conducted on only the child groups. The results for main effects were identical in direction to the analyses that included the adult group, reported in experiment I. Most importantly, 4-year-olds were significantly better than 3-year-olds in the identification of labial [ $F(1,18)=5.35; p<0.05$ ] and velar [ $F(1,18)=8.23; p<0.05$ ] stops.

<sup>4</sup>As in experiment I (see footnote 3), analyses of variance were conducted on only the child groups. The results for main effects were identical in direction to the analyses that included the adult group reported in experiment II. Four-year-olds were significantly better than 3-year-olds in vowel identification for both alveolar [ $F(1,18)=10.72; p<0.01$ ] and velar [ $F(1,18)=15.27; p<0.01$ ] contexts.

Allen, P., and Wightman, F. (1992). "Spectral pattern discrimination by children," *J. Speech Hear. Res.* **35**, 222–233.

Allen, P., Wightman, F., Kistler, D., and Dolan, T. (1989). "Frequency resolution in children," *J. Speech Hear. Res.* **32**, 317–322.

Blumstein, S. E., and Stevens, K. N. (1979). "Acoustic invariance in speech production: Evidence from measurements of the spectral characteristics of stop consonants," *J. Acoust. Soc. Am.* **66**, 1001–1017.

Blumstein, S. E., and Stevens, K. N. (1980). "Perceptual invariance and onset spectra for stop consonants in different vowel environments," *J. Acoust. Soc. Am.* **67**, 648–662.

Blumstein, S. E., Isaacs, E., and Mertus, J. (1982). "The role of the gross spectral shape as a perceptual cue to place of articulation in initial stop consonants," *J. Acoust. Soc. Am.* **72**, 43–50.

Bush, M. A. (1997). "Integration of cues in the perception of stop consonants," SM thesis, M.I.T.

Davis, B. L., and MacNeilage, P. (1990). "Acquisition of correct vowel production: A quantitative case study," *J. Speech Hear. Res.* **33**, 16–27.

Dorman, M. F., Studdert-Kennedy, M., and Raphael, L. J. (1977). "Stop consonant recognition: Release bursts and formant transitions as functionally equivalent, context-dependent cues," *Percept. Psychophys.* **22**, 109–122.

Elliott, L., Longinotti, C., Meyer, D., Raz, I., and Zucker, K. (1981). "Developmental differences in identifying and discriminating CV syllables," *J. Acoust. Soc. Am.* **78**, 669–677.

Fox, R. A., Wall, L. G., and Gokcen, J. (1992). "Age-related differences in processing dynamic information to identify vowel quality," *J. Speech Hear. Res.* **35**, 892–902.

Fudala, J. B. (1970). *Arizona Articulation Proficiency Scale-Revised* (Western Psychological Services, Los Angeles, CA).

Fujisaki, H., and Kawashima, T. (1969). "On the modes and mechanisms of speech perception," *Ann. Rep. Eng. Res. Inst.* **28**, Fac. Eng., Univ. Tokyo, 67–73.

Hresko, W. P., Reid, D. K., and Hammill, D. D. (1991). *Test of Early Language Development* (Pro-Ed, Austin, TX), 2nd ed.

Jenkins, J. J., Strange, W., and Edman, T. R. (1983). "Identification of vowels in 'vowelless' syllables," *Percept. Psychophys.* **34**, 441–450.

Keating, P., and Blumstein, S. E. (1978). "Effects of transition length on the perception of stop consonants," *J. Acoust. Soc. Am.* **64**, 57–64.

Keppel, G. (1991). *Design and Analysis: A Researcher's Handbook* (Prentice-Hall, Englewood Cliffs, NJ), 3rd ed.

Kewley-Port, D. (1983). "Time-varying features as correlates of place of articulation in stop consonants," *J. Acoust. Soc. Am.* **73**, 322–335.

Klatt, D. (1980). "Software for a cascade/parallel formant synthesizer," *J. Acoust. Soc. Am.* **67**, 971–995.

Lieberman, A. M., Cooper, F. S., Shankweiler, D. P., and Studdert-Kennedy, M. (1967). "Perception of the speech code," *Psychol. Rev.* **74**, 431–461.

Morrongiello, B. A., Robson, R. C., Best, C. T., and Clifton, R. K. (1984). "Trading relations in the perception of speech by 5-year-old children," *J. Exp. Child Psych.* **37**, 231–250.

Murphy, W. D., Shea, S. L., and Aslin, R. N. (1989). "Identification of vowels in 'vowelless' syllables by 3-year-olds," *Percept. Psychophys.* **46**, 375–383.

Nearey, T. M. (1989). "Static, dynamic, and relational properties in vowel perception," *J. Acoust. Soc. Am.* **85**, 2088–2113.

Ohde, R. N. (1994). "The development of the perception of cues to the [m]–[n] distinction in CV syllables," *J. Acoust. Soc. Am.* **96**, 675–686.

Ohde, R. N., Haley, K. L., and McMahon, C. W. (1996). "A developmental study of vowel perception from brief synthetic consonant–vowel syllables," *J. Acoust. Soc. Am.* **100**, 3813–3824.

Ohde, R. N., Haley, K. L., Vorperian, H. K., and McMahon, C. W. (1995). "A developmental study of the perception of onset spectra for stop consonants in different vowel environments," *J. Acoust. Soc. Am.* **97**, 3800–3812.

Parker, E. M., and Diehl, R. L. (1984). "Identifying vowels in CVC syllables: Effects of inserting silence and noise," *Percept. Psychophys.* **36**, 369–380.

Parnell, M. M., and Amerman, J. D. (1978). "Maturational influences on perception of coarticulatory effects," *J. Speech Hear. Res.* **21**, 682–701.

Pisoni, D. B. (1973). "Auditory and phonetic memory codes in the discrimination of consonants and vowels," *Percept. Psychophys.* **13**, 253–260.

Repp, B. H. (1986). "Perception of the [m]–[n] distinction in CV syllables," *J. Acoust. Soc. Am.* **79**, 1987–1997.

Sachs, R. M. (1969). "Vowel identification and discrimination in isolation vs word context," *Q. Progr. Rep. Res. Lab. Electron., MIT 93*, 220–229.

Stevens, K. N. (1968). "On the relations between speech movements and speech perception," *Z. Phon., Sprachwiss., U. Komm. Fschg.* **21**, 102–106.

Stevens, K. N. (1985). "Spectral prominences and phonetic distinctions in language," *Speech Commun.* **4**, 137–144.

Stevens, K. N., and Blumstein, S. E. (1978). "Invariant cues for place of articulation in stop consonants," *J. Acoust. Soc. Am.* **64**, 1358–1368.

Stevens, K. N., and Keyser, S. J. (1989). "Primary features and their enhancement in consonants," *Language* **65**, 81–106.

Stoel-Gammon, C. (1983). "Constraints on consonant–vowel sequences in early words," *J. Child Lang.* **10**, 455–457.

Strange, W., Jenkins, J. J., and Johnson, T. L. (1983). "Dynamic specification of coarticulated vowels," *J. Acoust. Soc. Am.* **74**, 695–705.

Sussman, H. M. (1990). "Acoustic correlates of the front/back vowel distinction: A comparison of transition onset versus 'steady state,'" *J. Acoust. Soc. Am.* **88**, 87–96.

Sussman, J. E. (1993). "Auditory processing in children's speech perception: Results of selective adaptation and discrimination tasks," *J. Speech Hear. Res.* **36**, 380–395.

Sussman, J. E., and Carney, A. E. (1989). "Effects of transition length on the perception of stop consonants by children and adults," *J. Speech Hear. Res.* **32**, 151–160.

Walley, A. C., and Carrell, T. D. (1983). "Onset spectra and formant transitions in the adult's and child's perception of place of articulation in stop consonants," *J. Acoust. Soc. Am.* **73**, 1011–1022.

Walley, A. C., Pisoni, D. B., and Aslin, R. N. (1984). "Infant discrimination of two- and five-formant voiced stop consonants differing in place of articulation," *J. Acoust. Soc. Am.* **75**, 581–589.

Wightman, F., Allen, P., Dolan, T., Kistler, D., and Jamieson, D. (1989). "Temporal resolution in preschool children," *Child Dev.* **60**, 611–624.

Williams, L., and Bush, M. (1978). "Discrimination by young infants of voiced stop consonants with and without release bursts," *J. Acoust. Soc. Am.* **63**, 1223–1226.

# Perceptual differences in infant cries revealed by modifications of acoustic features

Athanassios Protopapas<sup>a)</sup> and Peter D. Eimas

*Department of Cognitive & Linguistic Sciences, Brown University, Providence, Rhode Island 02912*

(Received 22 July 1996; revised 12 June 1997; accepted 30 June 1997)

Previous studies of infant cry acoustics and their perceptual significance have remained inconclusive as to the graded nature of cry production and perception and to the exact role and importance of particular acoustic features. In this study, a set of infant cries were digitally analyzed and resynthesized to form natural-sounding cries with varying fundamental frequency ( $F_0$ ), degrees of jitter (period to period variations in  $F_0$ ), and rise time (time for  $F_0$  to reach its maximum value). In a perceptual rating task, higher- $F_0$  cries as well as cries with larger amounts of jitter tended to be given more negative ratings than were lower- $F_0$  cries and cries with less jitter, respectively. The perceptual ratings of the rise time manipulations were inconclusive. This study demonstrated a perceptual effect of  $F_0$  and jitter independently of other parameters, consistent with current notions of infant cry gradedness. It was also shown that digital signal processing techniques can be fruitfully applied to infant cry research. © 1997 Acoustical Society of America. [S0001-4966(97)05311-3]

PACS numbers: 43.71.Bp, 43.66.Lj, 43.71.Ft, 43.72.Ja [WS]

## INTRODUCTION

The infant cry is a signal of considerable communicative and adaptive value. It is an effective means of conveying information about the infant's state even in the absence of visual contact: Differences in the sound alone can lead to differences in listeners' perception of the needs or state of the crying infant. It has been a subject of debate for a long time whether the perceptually salient acoustic differences affect caretakers' responses in a graded or discrete nature, or perhaps a combination of the two. In other words, do graded differences in infant cry signals along acoustic continua convey to caretakers graded information about an infant's state and needs, or do cries fall into functional categories with distinct constellations of acoustic features? This study was undertaken to determine the extent to which a few actually graded acoustic features function in a perceptually graded manner.

Many acoustic features have been examined as candidates for conveying information about the infant's state, including fundamental frequency of phonation ( $F_0$ ), duration, and spectral characteristics of the cry. Cries with higher mean or maximum  $F_0$  have been found to sound more aversive on a number of different perceptual scales (e.g., Zeskind and Marshall, 1988) and to "elicit less optimal responses" (Frodi and Senchak, 1990). The formant structure of the cries (Johnston and O'Shaughnessy, 1988), the segmental duration or "tempo" (Tsukamoto and Tohkura, 1992), and the duration of pauses and expiratory sounds (Zeskind *et al.*, 1992; Bryan and Newman, 1988) have also been found to affect perceptual ratings. Boukydis (1985) has provided a review of earlier findings.

Consistent with current notions of infant crying as a graded signal (Zeskind *et al.*, 1985; Zeskind *et al.*, 1993;

Gustafson and Harris, 1990), Porter *et al.* (1986) found that durational as well as  $F_0$ -related characteristics are correlated with the severity of the procedure that the infant was undergoing at the time and that adult listeners were able to correctly assess the urgency of a cry. In addition, acoustic features have been found to correlate with situationally defined cry "types," which presumably reflect the infant's state. For example, Fuller and Horii (1986, 1988) found that the  $F_0$  and the energy distribution (tenseness) of cries differs between "pain-induced" and "fussy" or "hungry" cries.

The notion of gradedness is not incompatible with the use of situationally defined cry types. Cries within a category (type) may vary acoustically and perceptually along continuous scales. Furthermore, sets of cries with similar acoustic or perceptual characteristics may be taken to constitute a cry "type," if, for example, they occur in similar eliciting conditions. Thus "cry types" may refer to clusters of cries around particular points on graded acoustic or perceptual continua. Wolff (1969), for example, defined the "mad" cry as a variation of the basic pattern of "hunger" cry and also noted that "pain" cries settle down to the same basic rhythmic pattern. The notion of gradedness clearly underlies Wolff's observations even though situationally defined cry types are named.

Listeners can identify the cause of a cry, although not as accurately as they can assess its urgency (e.g., Gustafson and Harris, 1990; Papoušek, 1989). It is not clear, however, how each acoustic feature affects listeners' perception of the cry, and which features, singly or in combination, are the more salient components for perception. The  $F_0$ , for example, is generally considered to be a perceptually salient feature of infant crying. However, its precise role and significance remain to be determined. The correlations between  $F_0$  and perceptual ratings found by Zeskind and Marshall (1988), Zeskind and Collins (1987), and others cannot be interpreted with confidence because the acoustic context (i.e., the overall "quality" of the cries) may covary with  $F_0$ .

<sup>a)</sup>Present address: Scientific Learning Corp., 1995 University Ave., Ste. 400, Berkeley, CA 94704-1074; Electronic mail: protopap@scilearn.com

Gustafson and Green (1989) did not find any significant correlations between  $F_0$  measures and perceptual ratings but noted that “some of the correlations...[were] of a magnitude that would yield statistical significance with a larger sample” (p. 778). Based on strong correlations found between the perceptual ratings and other acoustic measures, such as cry duration, amount of dysphonation, and energy in low and high frequencies, they suggested that variations in  $F_0$  may not be very important to cry ratings when the range of variation in  $F_0$  is small. It is thus necessary to investigate small systematic variations in  $F_0$  in a controlled acoustic context, as was done in the present study.

Studies that are based on acoustic analyses of natural cries and the correlation of their acoustic features with either perceptual ratings or physiological measures suffer from lack of controlled acoustic conditions, because the effects of single acoustic parameters (and of two or more parameters together) cannot be isolated and identified in natural cries. Given the nature of the infants' cry production system, it is certain that many closely coupled parts are interacting when a cry is produced, and that the resulting sound is affected in many ways by single events. For example, increased tension of the laryngeal muscles stiffens the vocal folds, thus resulting in more energy in higher frequencies (affecting timbre) and in higher  $F_0$  (affecting pitch). It is therefore impossible in principle to completely separate acoustic features and their consequent perceptual effects in natural cries.

Studying the effects of specific features, individually and together, is the only way to identify the acoustic characteristics and their combinations that have perceptual effects as well as to determine whether and under which circumstances cries may be perceived as acoustic gestalts, i.e., with perceptual properties not directly attributable to their individual acoustic components. One way to accomplish this goal is to perform experiments with cries that are identical to one another in all respects but the single acoustic feature of interest. In order to create a set of stimuli that meet this condition, signal processing techniques must be used to alter a particular acoustic feature in a controlled way, while holding other features constant as much as possible. This was not feasible until recently, because of the technical demands of such a process.

Recognizing the merit of such an approach, Okada *et al.* (1987) used partially altered stimuli to investigate the perceptual effects of the ratio of voiced phonation to unvoiced phonation. More recently, Bisping *et al.* (1990) created resynthesized cries to control the  $F_0$  and the melodic structure of the cry using an interpolation technique that scaled the  $F_0$  and formant frequencies without affecting duration. (Some important methodological concerns regarding the latter study are discussed in the introduction to experiment 1 below.) Along the same lines, Zeskind *et al.* (1992) investigated the perceptual effects of variations in the temporal structure of cry bouts by digitally altering the duration of pauses and expiratory sounds.

It is becoming obvious that we need to retest the important findings from earlier studies using acoustically controlled procedures. In this study we used the linear predictive coding (LPC) method to decompose infant cries into sets of

parameters, which could be independently manipulated and then used to resynthesize artificial cries with precisely controlled acoustic differences in  $F_0$ -related parameters. LPC is a well-tested and widely applied method in speech research whose behavior and requirements are well understood. Although far from perfect, for reasons discussed in the final section, LPC can be fruitfully applied to infant cry research if care is taken in the selection of processing parameters and in the kinds and ranges of acoustic modifications that are applied.

Besides average pitch, the amount of short-time fluctuation of  $F_0$ , referred to as “jitter,” is an important acoustic characteristic of infant crying. Jitter is always present in adult speech (Lieberman, 1961) and has been found to be linked to “stressor-provoked anxiety” (Fuller *et al.*, 1992) and to the emotional condition of the speaker (Lieberman and Michaels, 1962). It is perceptible in artificial signals, even in small amounts (Pollack, 1968; Rosenberg, 1966), and it is of potential diagnostic value in cases of laryngeal pathologies in adults (Lieberman, 1963; Perkins, 1985; Jacobson, 1994) and in infants (Hirschberg, 1990), as well as in cases of central nervous system disorders in infants (Mende *et al.*, 1990; Lüdge and Rothgänger, 1990). Fuller and Horii (1986) did not find any differences in amount of jitter between “different types of infant vocalizations” and considered jitter an “inaudible variable.” Fitch *et al.* (1992), however, found a correlation between the intensity of the cry-eliciting stimulus and jitter, perhaps due to a more appropriate analysis and higher temporal resolution [see Titze *et al.* (1987) for a discussion of temporal accuracy requirements in jitter measurements]. If jitter is indeed reliably correlated with the infant's level of stress, it is reasonable to assume that adult listeners might make use of it in their judgments about infant cries.

We were also interested in the perceptual significance of the time from the onset of phonation until the pitch reaches its maximal value, known with regard to infant cries as rise time, in that it appears to be strongly correlated with the infants' level of distress. For example, Wasz-Höckert *et al.* (1968) reported that a falling-melody form was characteristic of pain cries, and a rising-falling melody form was characteristic of hunger cries, which are presumably less aversive, at least at the beginning of the cry episode (Zeskind *et al.*, 1985; Rothgänger *et al.*, 1990). Given that a cry rarely starts off at its maximum pitch, usually taking some time to reach it, a “falling melody” should be interpreted as rapidly rising at first (i.e., having a short rise time) and then gradually falling. Therefore, it seems reasonable to expect that cries with faster rise times correspond to higher levels of arousal. Porter *et al.* (1986) provided strong support for this association in their study of cries from infants undergoing circumcision. Specifically, they found that moderately invasive procedures evoked rising-falling pitch pattern cries, whereas invasive surgical steps elicited cries “with pitch rapidly rising to high frequencies at the onset of voicing.” Rise time is thus in a similar state as  $F_0$  in that its perceptual correlates, as identified in past studies, need to be rigorously investigated in controlled acoustic contexts.

A major contribution of the study of Porter *et al.* (1986)



TABLE I. Summary of cry characteristics of the eight natural cries that were analyzed and resynthesized.

Cry	Mean $F_0$ (Hz)	Max $F_0$ (Hz)	Duration (ms)	Risetime (ms)	Risetime (%)
1	435	500	907	505	56
2	425	476	1061	337	32
3	517	541	560	171	31
4	429	488	1983	558	28
5	455	500	2278	202	9
6	473	540	1673	232	14
7	579	625	996	272	27
8	596	667	1842	242	13

was that it provided clear evidence for the gradedness of infant crying, in both production and perceptual terms. They showed that the physical discomfort caused by the surgical procedures gradually affected acoustic characteristics and that these graded acoustic differences gave rise to graded perceptual differences. The issue of gradedness is a complex one, and many different lines of evidence are necessary before an appropriate definition of the term ‘‘graded’’ can be given. For the purposes of the present study the notion of gradedness is understood as follows: There is at least one continuum of discomfort that underlies the continua of acoustic features that can be perceived and ranked in a continuous manner along a number of perceptual scales. This study was designed to investigate whether this notion of gradedness applies to infant cry perception, addressing the perceptual role of gradations in individual acoustic features. The features that were investigated included fundamental frequency ( $F_0$ ), whose precise role has remained controversial after much studying, jitter, whose role has yet to be explored but is potentially very significant, and rise time, which is so hard to ignore in a cry and yet remains relatively unresearched.

## I. CONSTRUCTION OF STIMULI

Because of time constraints on the duration of experimental sessions, we could not use a large number of natural cries. As a consequence, in order to assess the generality of our method and perceptual findings, it was necessary to select a small but diverse set of cries for manipulation. We thus selected eight cries (individual cry expirations) from a set of 81 for their perceptual diversity, as indicated by a previous pilot experiment, and for their recorded quality and typicality of basic acoustic parameters. All cries were recorded with a cassette recorder from healthy, full-term infants at a hospital when they were between three and four weeks old. Cries 1 through 4 were spontaneous vocalizations of the infants prior to a medical examination. Cries 5 through 8 were elicited by the removal of a cardiac electrode, a moderately painful stimulus. Each cry that we used was produced by a different infant. Some acoustical characteristics of the eight cries are listed in Table I.

To create the resynthesized cry stimuli, each natural cry was low-pass filtered at 9.8 kHz, digitized at 12 bits with 20-kHz sampling rate,<sup>1</sup> upsampled to 80 kHz with quadratic interpolation for increased temporal resolution, and pro-

cessed by means of a fortieth-order linear predictive coding (LPC) analysis using the autocorrelation method with Durbin’s recursive algorithm for solving the LPC equations (Rabiner and Schafer, 1978, p. 411) on 10-ms frames with 50% overlap. A pitch tracking program estimated the pitch<sup>2</sup> at 20-ms intervals using an autocorrelation-based algorithm after low-pass filtering at 800 Hz using an odd-length zero-phase FIR filter. The pitch estimates were visually inspected against the plotted waveform and any erroneous values were manually adjusted. The LPC reflection (PARCOR) coefficients and pitch values were stored to be independently manipulated and then used by the synthesis program. Synthesis was done by direct implementation of the recursive LPC filter, driven by impulses scaled by the LPC residual energy. The PARCOR coefficients and the pitch and gain parameters were updated at the beginning of each pitch period by logarithmically interpolating their stored values. The final resynthesized cries were passed through a 89-tap low-pass FIR filter with a cutoff frequency of 9.5 kHz and were down-sampled to 20 kHz before being presented to the subjects.

There were four types of acoustic manipulation, henceforth termed ‘‘manipulation conditions.’’ In the first, termed simply ‘‘pitch’’, each cry was resynthesized with each pitch period scaled by a constant factor throughout the cry. There were five levels of pitch manipulation, with pitch periods equal to 90%, 95%, 100%, 105%, and 110% relative to those of the original cry.<sup>3</sup> The resynthesized cry with pitch periods equal to those of the original cry (scale value 100%) and the minimum amount of jitter is termed the ‘‘neutral’’ cry.

In the second manipulation condition, termed ‘‘jitter,’’ cries were resynthesized with pitch periods initially equal to those of the original cry (i.e., no scaling), but with increasing amounts of jitter across cries. Jitter was added by introducing random perturbations to the pitch estimates. There were three levels of jitter manipulation, with perturbation ranges  $\pm 45 \mu s$ ,  $\pm 70 \mu s$ , and  $\pm 90 \mu s$ . The neutral cry was treated as a fourth (baseline) level of jitter manipulation in the analysis.

The remaining two manipulation conditions involved shifting the point when the cry reached its maximum pitch. One can define that time either relative to the length of the entire cry (as a percentage) or as an absolute amount of time (in ms). We implemented both in order to investigate which would provide a better predictor of the perceptual differences. They were termed ‘‘risetime-P’’ and ‘‘risetime-T,’’ respectively. There were three levels of rise time manipulation in each of the two conditions: In risetime-P the peak was set at the point of 10%, 25%, and 50% of the length of the cry. In risetime-T the peak was set at 100, 250, and 500 ms from the onset of phonation. In order to shift the max- $F_0$  point, the LPC, pitch, and energy parameters were interpolated differentially around the original  $F_0$  peak, thus ‘‘stretching’’ time on one side and ‘‘squeezing’’ it on the other.

The range of manipulation was always well within the normal range for all the parameters we altered. In this manner the acoustic changes could be treated as gradual and not as changing the quality of the cry. In particular,  $F_0$  variations were kept small, so that the claim of Gustafson and Green

(1989) could be directly addressed and evaluated. Moreover, jitter variation was not so large as to create cries that would sound “dysphoned.” Our belief is that testing with more extreme parameter values might have produced results difficult to interpret if the perceived cries were qualitatively removed from the ends of their graded nature.

## II. EXPERIMENT 1

Before conducting the main experiment, it was necessary to test the resynthesized stimuli for naturalness. In a sense, this is more of a pretest for experiment 2 than an independent experiment. However, there are two reasons to present it independently. First, it is of interest with respect to the methodology whether our method of creating resynthesized stimuli results in tokens natural enough to be useful for perceptual experiments. A thorough investigation of the perceptual properties of our stimuli will be of use to researchers in search for a good method with which to acoustically modify infant cries. Second, we deemed appropriate to emphasize the issue of stimulus naturalness because it has been overlooked in previous research, leading to perceptual findings whose interpretation is unclear.

Previous studies using acoustically altered cries have not directly addressed the question of the “naturalness” of the stimuli. Certainly, the experimenters have found the resynthesized cries to sound natural, but it is not clear whether naive listeners could have detected aspects of the stimuli that did not quite sound natural. The study of Bisping *et al.* (1990), where the spectral envelope, and thus the formants, was scaled along with  $F_0$ , illustrates the point. It is well known that  $F_0$  may vary considerably, because it is mainly the result of the interactions of subglottal pressure and laryngeal muscular tension. In contrast, the range of formant frequencies is determined by the size and flexibility of the vocal tract and it is quite restricted for very young infants, whose larynges have not yet descended to their mature positions (Lieberman, 1980, 1985). Halving or doubling the formant frequencies of an infant cry is effectively similar acoustically to doubling or halving, respectively, the length of the infant’s vocal tract and the resulting cries may sound unnatural. Moreover, such dramatic alterations of  $F_0$  may cause different interpretations of the cries if, for example, they sound as if produced by abnormal infants or if they change the perceived mode of phonation (e.g., from phonated to hyperphonated). Unfortunately, Bisping *et al.* (1990) did not discuss these issues.

In our view, caution must be used in interpreting results where naturalness was not directly measured. To counter possible concerns of this kind regarding our experiment 2, we conducted the present experiment to justify the use of our computer-generated cries. Subjects were asked to decide whether each stimulus was natural or synthetic. Given an adequate procedure for cry generation, we expected to find a lack of discriminability between natural and synthetic cries.

### A. Method

#### 1. Subjects

The subjects were 11 graduate students (6 women and 5 men) at Brown University, ranging in age from 23 to 38

TABLE II. Frequencies and percentages of responses for natural and synthetic stimuli in experiment 1.

Stimulus	Response			
	Natural		Synthetic	
	<i>N</i>	%	<i>N</i>	%
Natural	282	55	232	45
Synthetic	448	43	602	57

years, who volunteered their participation. Five of the women reported having experience in childcare. One man was the father of a 2-year-old.

#### 2. Stimuli

There were two sets of stimuli in this experiment, a set of natural cries and a set of resynthesized cries. We used all 8 natural cries that had been analyzed and 6 resynthesized variants of each natural cry (for a total of 48 different resynthesized cries). Each natural cry was presented 3 times (in random positions) in each session, making for a total of 24 natural cry trials, in order to bring the number of natural cries closer to that of the synthetic cries ( $n=48$ ).

Besides time constraints, the number of resynthesized cries used in this experiment had to be kept small because we did not want to bias our subjects by using a large number of resynthesized cries and only eight natural cries. The same six variants were chosen from each of the eight series: The neutral (baseline jitter and 100% pitch), the maximum jitter ( $\pm 90 \mu\text{s}$ ), the minimum and maximum pitch (90% and 110%), and the slowest and fastest rise time (50% and 100 ms). These covered the entire range of manipulations and by testing with the most extreme levels we believed we were more likely to include sounds that might be judged to sound artificial. If these cries were found to sound natural, we could safely conclude that the remaining cries, being the products of less extreme acoustic manipulations, would also sound natural.

#### 3. Procedure

Subjects listened to one cry at a time and were asked to decide whether it was a natural or synthetic cry (forced choice task). The cries were played over a loudspeaker and the subjects responded by pressing a button on a response box. The entire set of stimuli was presented twice in different random orders, making for a total of 144 trials administered in each session, including 48 natural and 96 synthetic. Subjects had 3 s to respond and the next stimulus occurred 3 s after the response.

### B. Results and discussion

The total number of responses in each condition is shown in Table II. Twenty responses (1.3%, including 14 in natural trials and 6 in synthetic trials) were not recorded because of response times greater than 3 s. From the percentages of hits and false alarms we computed for each cry a  $d'$  score, which is a  $z$ -score discrimination index not affected by response biases (Macmillan and Creelman, 1991). When the

distributions underlying the subjects' responses are normal and their variances equal, the  $d'$  score is the distance between the distribution means of the two stimulus categories, expressed in standard deviation units. For each resynthesized cry only the responses to the corresponding natural cry were used in the calculation of the  $d'$  score.

The individual  $d'$  scores for each cry ranged between  $-0.47$  and  $1.20$ . There were four cries with an individual  $d'$  greater than  $1.00$ , and seven with  $d'$  between  $0.75$  and  $1.00$ . Of these 11 cries 5 were in one cry series, that of cry 6. Consequently, all stimuli from the cry 6 series were excluded from further experiments. Although there remained one cry with a  $d' = 1.03$ , we chose to include it in experiment 2, because the amount by which its  $d'$  score exceeded a commonly accepted cutoff point of discriminability ( $1.0$ ) was not large enough to justify rejection of this whole series of cries in our view. It was not feasible to discard only that particular stimulus, because the design of experiment 2 required that cries and levels be completely crossed. The 42 remaining synthetic cries were not nearly discriminable from the natural ones ( $d'$  well below  $0.75$ , with six exceptions between  $0.76$  and  $1.03$ ).

The individual  $d'$  scores for each subject (including each subject's responses to all cries) ranged from  $-0.22$  to  $1.02$ , indicating that large differences exist between individuals in what is taken to sound like a "natural" infant cry. Interestingly, it was the two males with the least experience with infants that discriminated best between the natural and resynthesized cries ( $d'$  scores of  $1.02$  and  $0.94$ ), whereas the two females who reported a lot of experience in babysitting and the one subject who was a father showed very poor discrimination ( $d'$  scores between  $0.23$  and  $0.30$ ). This experiment was not designed to investigate differences related to experience with natural infant cries and interpretation of *post hoc* observations is of questionable validity. This individual variation notwithstanding, we conclude that our stimuli retained the most important acoustic properties of baby cries, since they sounded natural to the experienced subjects.

In summary, the results indicated that subjects were unable to discriminate reliably between the natural and the synthetic cries. All subjects reported that they found the task extremely difficult and none were confident about their responses. They said that almost all cries sounded more or less natural. On the basis of these results, we concluded that it is possible to synthesize artificial infant cries that sound natural using the LPC method. Although some cries might present problems, perhaps due to undesirable interactions between formant frequencies and the fundamental and to spectral properties that LPC cannot always handle appropriately (e.g., nasality), our results justify the use of synthetic cries in cry perception experiments and allow experimental conclusions to be extended to natural cry perception.

### III. EXPERIMENT 2

The purpose of this experiment was to assess the perceptual effects of small variations in fundamental frequency, jitter, and rise time. In accord with earlier findings, we expected that higher fundamental frequencies would lead to

higher "negative" ratings of the cries. We also expected higher negative ratings for cries with more jitter and for cries with shorter rise times.

The subjects were asked to rate the cries on four seven-point perceptual scales, called "urgency," "distress," "health," and "feeling." In the past, some researchers have used as many as fifty scales (e.g., Brennan and Kirkland, 1982); however, Zeskind and Marshall (1988) and Gustafson and Green (1989) showed that almost all those scales are highly interrelated. Zeskind and Lester (1978) suggested that there is a basic dimension of "aversiveness," along which most cries differentiate, and an extra dimension of "sickness" or "abnormality," which has an effect only with special cases of cries. We thus selected the four scales that we believed cover the spectrum of salient perceptual features, namely, severity or urgency, the inferred emotional state of the infant (distress), the possible abnormal aspect of the cry (health), and the aversive character of the cry (feeling).

## A. Method

### 1. Subjects

The subjects were 20 undergraduate students at Brown University, including 8 men and 12 women ranging in age from 19 to 23, and were paid for their participation. None of the subjects were parents, but three of the men and eight of the women reported some experience in childcare (babysitting).

### 2. Stimuli

The total number of stimuli in this experiment was 105, 98 of which were resynthesized and 7 were natural cries. All 14 synthetic versions of each of the 7 remaining natural cries were used, i.e., there was a neutral version, 4 with altered pitch and baseline jitter, 3 with increased amounts of jitter, and 6 with altered rise time (3 by absolute time and 3 by proportion). The seven natural cries that had been originally analyzed were used in order for their ratings to be compared with those of the corresponding resynthesized cries. The ratings of the natural cries were excluded from the analyses for acoustic manipulation effects and were only used to measure the level of perceptual overlap between them and the resynthesized cries.

### 3. Procedure

Subjects heard one cry per trial and responded by pressing one of seven buttons arranged along an arc on a specially designed response box. The responses were automatically recorded in an IBM AT computer. Each stimulus was presented twice during each rating session and the mean of the two responses was used for the analysis. The order of the stimuli was randomized before each rating session. Subjects had 3 s to respond and the next stimulus occurred 2 s after the response.

The instructions given to the subjects were to rate the cries on a scale from one to seven according to how urgent they sounded, how distressing they sounded, how sick the infant sounded, and how angry or sad the cry made them feel; the endpoints of the scales were anchored by the words

TABLE III. Correlation of ratings of natural cries with ratings of corresponding neutral resynthesized cries and slope of linear regression. All correlations are significant to  $p < 0.0001$ .

Rating scale	Correlation coefficient	Linear regression slope
Urgency	0.994	0.890
Distress	0.981	0.887
Health	0.992	0.951
Feeling	0.991	0.879

“most” and “least” before the words “urgent,” “distressing,” “sick,” and “feeling angry or sad,” respectively, and were indicated next to the endpoint buttons throughout each rating session.

The stimuli were presented over a single loudspeaker positioned to face the subject directly. The sound level was adjusted to a comfortable level and remained unchanged throughout the experiment. Each subject rated all cries on one scale before proceeding to the next scale. This way interference between rating scales was minimized and, importantly, subjects did not have to remember the cry for a long time while indicating their responses to several rating scales. The presentation order of the four scales and the direction (polarity) of the rating scale were balanced across subjects using a latin square design. The experiment was divided into two parts, each lasting about one half hour.

## B. Results

In order to compare the ratings of the natural cries to those of the resynthesized ones across the 20 listeners, we calculated for each of the 4 rating scales the correlation coefficient between the mean ratings of the neutral resynthesized cries and the mean ratings of the corresponding natural cries, which were included for just this purpose. Table III shows the resulting correlation coefficients and linear regression slopes. Although the neutral cries may not always be the closest to the natural ones,<sup>4</sup> either acoustically or perceptually, and the analysis–synthesis procedure tended to decrease the perceptual range slightly, across subjects the order of the neutral cries, as given by the perceptual ratings, was always the same as the order of the natural cries and there was in fact a very close correspondence between the ratings of the natural and the neutral stimuli in all conditions.

The effects of the four manipulation conditions in the four rating scales are shown in Fig. 1. In brief, scale ratings tend to increase, i.e., become more negative, as  $F_0$  increases and as the amount of jitter increases, in agreement with initial expectations. Effects of the two rise time manipulations were very small, although risetime-P followed the expected pattern, i.e., toward lower (less negative) ratings for longer rise times. Risetime-T only followed the pattern for the two shorter rising times, and that was not the case for the health ratings.

Two-way, within-subjects analyses of variance were performed, separately for each of the four rating scales and for each of the four manipulation conditions. The two factors, treated as fixed-effects variables, were cry item (the seven natural cries on which the resynthesized cries were

based, henceforth termed plainly “cry”) and manipulation level of the acoustic variable (five levels for pitch, four for jitter, and three for each of the risetime conditions). Thus for each of the four rating scales we performed four ANOVAs: Cry(7)×Pitch(5), Cry(7)×Jitter(4), Cry(7)×Risetime-P(3), and Cry(7)×Risetime-T(3).<sup>5</sup>

The effect of pitch was significant for each rating scale at the 0.005 level or less, and the effect of jitter was significant for all rating scales except urgency at the 0.04 level or less. The exact  $F$  and  $p$  values are shown in Table IV, as calculated with the Huynh–Feldt method for adjusting the degrees of freedom according to the  $\tilde{\epsilon}$  estimate of the population treatment-difference variances (Maxwell and Delaney, 1990, p. 477). The adjusted degrees of freedom are fractional because there is no need to round them to the closest integer, given the use of computer programs to calculate the exact probability of occurrence for any  $F$  value with any possible adjusted degrees of freedom. Risetime-P never had a significant effect, whereas risetime-T produced significant effects, but only for the ratings of distress [ $F(2.0,38.0) = 3.33$ ,  $p = 0.047$ ] and feeling [ $F(2.0,38.0) = 6.73$ ,  $p = 0.003$ ]. There was always a significant effect of cry at the 0.0001 level for all manipulation conditions and rating scales, which shows that our selection of cries was diverse, as intended.

There was also, in three cases, a significant interaction of cry with pitch [urgency:  $F(17.0,323.7) = 2.27$ ,  $p = 0.003$ ; distress:  $F(17.0,323.8) = 2.10$ ,  $p = 0.007$ ; feeling:  $F(16.8,318.2) = 2.37$ ,  $p = 0.002$ ], and, in two cases, of cry with rise time [risetime-P, health:  $F(11.9,225.5) = 2.14$ ,  $p = 0.016$ ; risetime-T, urgency:  $F(11.4,216.2) = 1.89$ ,  $p = 0.040$ ]. These findings indicate that the effects of the pitch and rise time manipulations depended on the original characteristics of each cry and thus were not uniform across all cries. The interaction of cry with pitch is illustrated in Fig. 2, which shows the effects of pitch on each cry in the distress condition. It is clear that the effect of changing  $F_0$  is not the same for all cries but, except for cry 2, it is more pronounced and more in line with expectations for cries that received the highest overall ratings, i.e., the “pain cries.” Note also the rating consistency between subjects, evidenced by the small standard errors, and the use of the entire rating scale, indicating that our stimuli covered an extensive perceptual range.

In order to further investigate the effect of the pitch manipulation and its interaction with cry we performed a trend analysis on the ratings for each rating scale. In all four rating scales there was a significant linear trend in the ratings with higher, i.e., more negative, ratings with higher pitch levels [urgency:  $F(1,19) = 42.76$ ,  $p < 0.0001$ ; distress:  $F(1,19) = 67.10$ ,  $p < 0.0001$ ; health:  $F(1,19) = 11.84$ ,  $p = 0.0027$ ; feeling:  $F(1,19) = 55.00$ ,  $p < 0.0001$ ]. This linear trend interacted significantly with cry in all but the health ratings [urgency:  $F(6,114) = 6.72$ ,  $p < 0.0001$ ; distress:  $F(6,114) = 4.65$ ,  $p = 0.0003$ ; feeling:  $F(4.85,92.15) = 5.41$ ,  $p = 0.0002$ ], indicating that the slopes of the rating curves were different for different cries. Linear analyses were performed for each cry separately, whereby the effects of pitch were found to be significantly linear (after the Bonferonni adjustment for *post hoc* contrasts) for the urgency ratings of

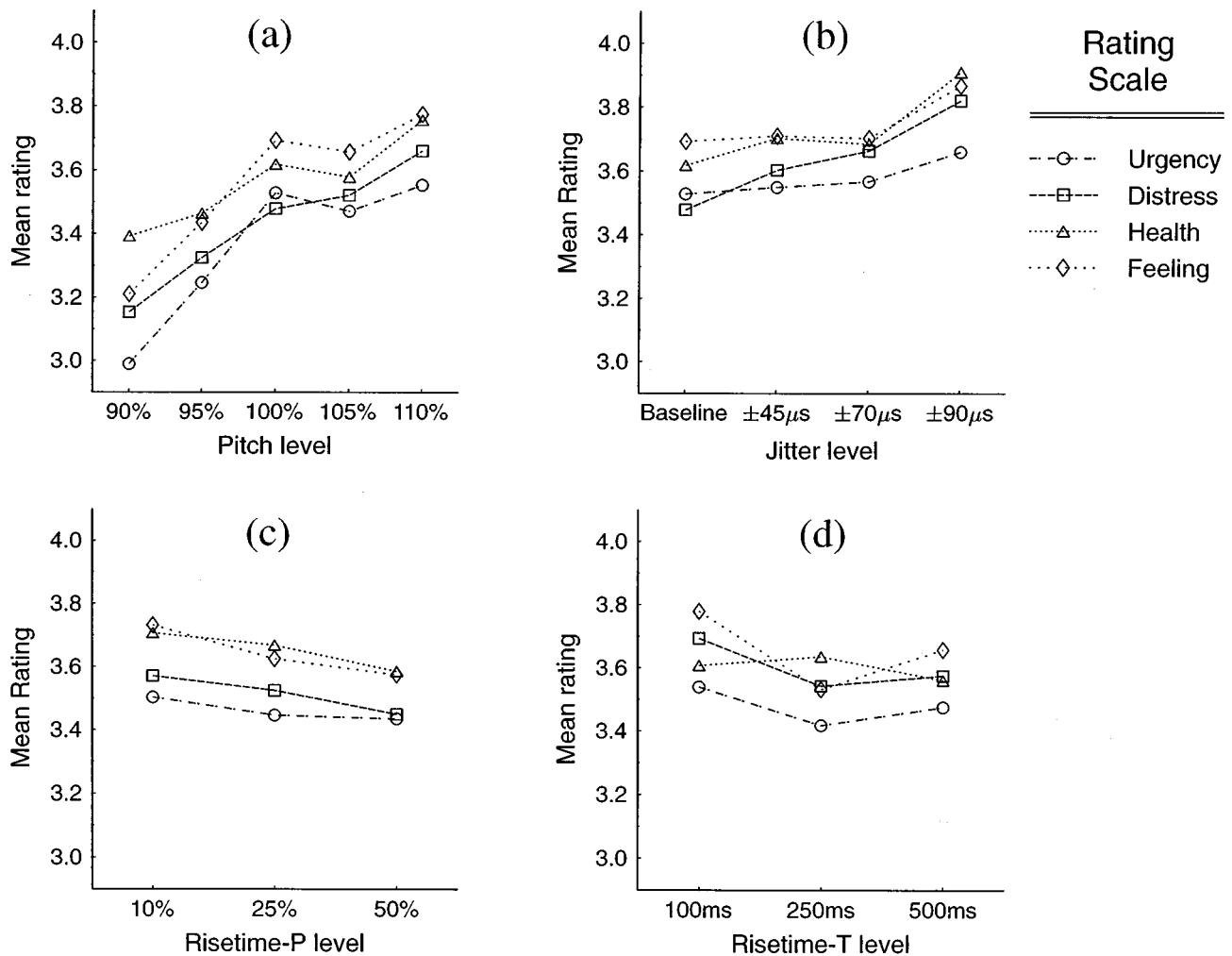


FIG. 1. Variation of ratings (averaged across cries) with level of acoustic manipulation in experiment 2 in all four rating scales. (a) Pitch (relative to original pitch of natural cry); (b) jitter (pitch period perturbation range); (c) risetime-P (cry portion before maximum pitch); and (d) risetime-T (time length before maximum pitch). The rating scale was always from 1 to 7, with 7 corresponding to the “negative,” i.e., most aversive, end of each scale.

cries 2, 5, 7, and 8, the distress ratings of cries 2, 5, and 8, and the feeling ratings of cries 4, 5, 7, and 8. Analysis of the health ratings was not performed for each cry separately since we found no significant interaction of the linear trend of health ratings with cry [ $F(6,114) = 1.14, p = 0.3410$ ]. In other words, the effects of the pitch manipulation vary with

cry and with rating scale. It appears that the cries that received the highest overall ratings, in particular the pain cries, tended to be more affected, but not without exceptions.

It is not surprising that the ratings to the pain cries (cries 5, 7, and 8) were higher than the ratings to the spontaneous cries (cries 1 through 4). Examination of Fig. 2 and Table I reveals that three of the four cries that received the highest overall ratings were the ones with the longest absolute duration (cries 5, 4, and 8, in order of decreasing duration). Two of these were also the cries for which the pitch manipulation always resulted in significant perceptual differences (cries 5 and 8). Since the duration factor was not explicitly manipulated or controlled for in the design of this experiment, it is not possible to draw any conclusions regarding possible perceptual effects of duration or of an interaction between duration and  $F_0$ . It is plausible that pitch differences in longer cries are perceptually more salient than comparable pitch differences in shorter cries (cf. Tsukamoto and Tohkura, 1990, on increased category identification rates with longer cries). Because there are many covarying factors in natural infant cries it is impossible to control simultaneously for more than

TABLE IV. Results of the significance tests for the main effects of acoustic manipulations of pitch and jitter in experiment 2 (with Huynh-Feldt adjustment).

Acoustic manipulation	Rating scale	Fixed-effects analysis		
		<i>F</i>	adj. <i>df</i>	<i>p</i>
Pitch	Urgency	19.67	3.7,69.7	<0.0001
	Distress	15.94	4.0,76.0	<0.0001
	Health	4.87	3.5,66.6	0.0026
	Feeling	18.30	4.0,76.0	<0.0001
Jitter	Urgency	1.21	2.5,46.7	0.3134
	Distress	7.88	2.6,50.2	0.0004
	Health	4.14	2.5,47.6	0.0152
	Feeling	3.14	2.9,55.2	0.0337

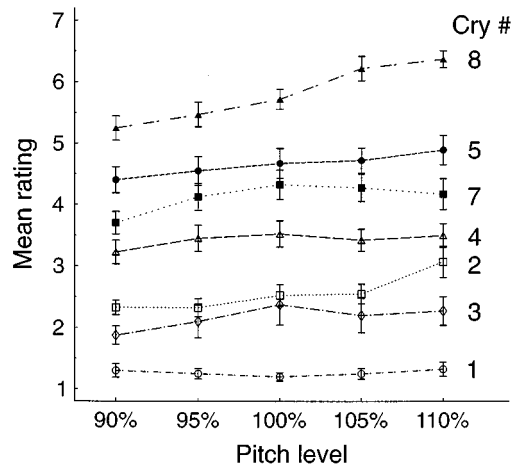


FIG. 2. Variation of ratings of individual cries with level of acoustic manipulation of pitch (relative to original pitch of natural cry) in experiment 2 in the distress rating scale. The errors bars show standard errors.

one or two of them. Another study is needed to investigate the effects of duration manipulations.

There was no significant interaction of cry with jitter in any of the rating scales, indicating that the perceptual effects of jitter were uniform across cries. A trend analysis indicated that the significant effect of the jitter manipulation on the distress, health, and feeling ratings was due to the statistically significant linear trend towards higher ratings for cries with more jitter [distress:  $F(1,19)=18.87$ ,  $p=0.0003$ ; health:  $F(1,19)=5.93$ ,  $p=0.0249$ ; feeling:  $F(1,19)=6.31$ ,  $p=0.0212$ ]. Although the main effect of jitter did not interact with cry in any rating scale, in the linear analysis the linear trend interacted with cry for the distress ratings only [ $F(5.52,104.97)=3.16$ ,  $p=0.0084$ ], indicating that the linear effect was not uniform across cries for this rating scale. Separate linear analyses of the distress ratings for each cry (with the Bonferonni adjustment) showed a significant linear trend for the ratings of cries 2, 7, and 8.

Surprisingly, the effects of risetime-P and risetime-T were very small. In addition, the effects of risetime-P were never statistically significant and the effects of risetime-T failed to show the expected trend. No clear global effect was seen in the risetime-P ratings, but several cries showed a small trend one way or the other. For some cries shorter rise time led to higher ratings, whereas for others longer rise times led to higher ratings. Similarly, the effects of risetime-T failed to show a uniform pattern. The fact that the effect of risetime-T was statistically significant in the feeling and distress conditions does not lend itself to a meaningful interpretation, in that the rating function for risetime-T is nonmonotonic. No significant linear trends were found for the ratings in the rise time manipulations.

Given these main effects and interactions of the various manipulations, it is reasonable to assess the extent to which any conclusions might be generalizable to infant cry perception in general. Treatment of the cry factor as a fixed-effects factor in the ANOVA only permits an inference of significance of reliable effects for the particular items (the natural original cries) that were used. Because the cries were chosen

TABLE V. Results of the significance tests for the main effects of acoustic manipulations of pitch and jitter in experiment 2 with cry treated as a random factor.

Acoustic manipulation	Rating scale	Mixed-model analysis		
		Quasi- $F$	adj. $df$	$p$
Pitch	Urgency	9.48	4,26	<0.001
	Distress	7.59	4,22	<0.001
	Health	4.70	4,23	<0.01
	Feeling	7.42	4,21	<0.001
Jitter	Urgency	0.93	3,16	>0.25
	Distress	7.19	3,20	<0.005
	Health	4.15	3,21	<0.025
	Feeling	2.53	3,9	>0.10

so as to cover a wide perceptual range, and because their acoustic characteristics are typical of clearly phonated yet quite diverse cries within that class, we can assume that they constitute a representative sample of all or at least of the most clearly phonated cries of comparable duration. We can then test the significance of the effects of the acoustic manipulations with cry considered a random factor. To do this, we used the method of Quasi- $F$  (Myers, 1979, pp. 188–192) to calculate the appropriate denominator terms and degrees of freedom. The results are shown in Table V. Note that the effect of the pitch manipulation is significant in all conditions, and that of the jitter manipulation is significant in two of the four conditions, namely distress and health. It would then seem that the effects of  $F_0$  are generalizable across cries for all rating scales, but only for ratings of distress and health in the case of jitter. Inasmuch as the results of the fixed-effects analyses for rise time were inconclusive, there was little point in performing this analysis for the risetime-P and risetime-T conditions.

#### IV. DISCUSSION

Fundamental frequency has long been hypothesized to affect perception of infant cries, both in a graded manner (as defined in the introduction) and in a discontinuous manner (as defined by the modes of infant cry phonation). Here we confirmed the graded effect with a manipulation in a constant context, the causal nature of which constitutes an improvement in methodology over that found in correlational studies. In addition, we have shown that jitter has similar (if smaller) perceptual effects that have not been emphasized in the literature and need to be further investigated. Finally, we have been unable to provide evidence for perceptual effects of rise time, although descriptions of cries in the literature might have led one to expect such effects. In the following we elaborate on the details of these findings and on their significance, in the context of the methodology we have used.

##### A. Gradedness

The main issue motivating this study was whether graded differences in particular acoustic features in a constant acoustic context would give rise to graded perceptual responses. The linear relation found between cry ratings differing only to a small degree in mean  $F_0$  or jitter unequivocally

cally supports the notion of gradedness in infant cry perception, inasmuch as a range of acoustic variability was shown to map onto a range of perceptual variability. This notion of gradedness has also been extended to temporal features by Zeskind *et al.* (1992, 1993), who found that cry bouts with shorter expirations and with shorter pauses between expirations were given higher negative ratings.

However, nongraded aspects of infant cry perception have also been reported and must temper our conclusions on the pervasiveness of graded infant cry perception. For example, Wiedenmann and Todt (1990) asked listeners to respond to recorded infants' cries when they felt "emphasis being expressed in the vocalizations" or when they would "get up to soothe the infant in a real life situation" (p. 181). They found that their subjects' responses, indicating high cry aversiveness, were clustered at particular points in the cries and were not uniformly distributed. It would be hard to ascribe that finding to graded perception; a more likely explanation is that a more or less discrete acoustic parameter, e.g., onset of dysphonation or "biphonation," was causing the abrupt changes in behavioral response (cf. Gustafson and Green, 1989, regarding separate treatment of phonation modes). Furthermore, the issue of gradedness cannot be examined independently of physiological and social factors that are active in the determination of the cry signal (Lester and Boukydis, 1992).

## B. Fundamental frequency

The present findings on the perceptual effects of  $F_0$  are in general agreement with those in the literature, showing a shift to more negative ratings as the mean  $F_0$  increases. The effect is highly significant, and although it may seem small, it should be borne in mind that pitch periods were altered by at most plus or minus 10%. The fact that the effect of the pitch manipulation was not uniform across all cries indicates that there are other acoustic attributes, as yet unknown, that take precedence in determining the overall quality of the cry, or that counter or neutralize the  $F_0$  manipulation. Also, in our manipulation, although the highest-pitched version of one cry was often higher pitched than the lowest-pitched version of another cry, their perceptual ratings rarely crossed, i.e., the effect of changes in  $F_0$  was relative to the particular cry and not to the absolute value of  $F_0$ . As illustrated in Fig. 2, the ratings of different cries were well separated, each cry series occupying a small region within the available rating space.

One reason that the ratings of each series of cries tended to cluster together might be that subjects tried to be consistent by remembering the cries. Some subjects reported that they thought they heard only a few cries, and were trying to give the same rating to the "same" cry. Admittedly, cries that only differ in  $F_0$  by 5% sound very similar. In fact, unless heard in succession, they might well sound identical and, consequently, if subjects were trying to be consistent, the effect would be a flattening of the rating curves. Therefore, the criticism of Zeskind and Huntington (1984) that within-subject designs may accentuate unreliable perceptual differences would not apply to our study because of the perceptual similarity between the items and the tendency of lis-

teners to be consistent. The fact that the effect of pitch is nonetheless clear for a number of cries and highly significant demonstrates that it is indeed robust.

As noted, this finding corroborates the findings from correlational studies that higher-pitched cries are perceived as being more aversive. Furthermore, by using small  $F_0$  ranges, we can address the point brought up by Gustafson and Green (1989) about the perceptual importance of  $F_0$  being small when  $F_0$  does not vary much. The overall subjective quality of each cry series did not change between versions with different mean pitch because the alterations were very small, so it cannot be the case that the perceptual differences we found were due to perception of resynthesized cries differing only in pitch as belonging to distinct cry types (i.e., cries that distinctly differ in their perceived quality). Furthermore, acoustic variables that may, in natural cries, be intrinsically coupled with  $F_0$  (such as spectral energy distribution) were kept constant, to the extent possible. Thus the observed effect shows clearly that  $F_0$  can have a direct gradual perceptual effect, independently of other parameters, albeit not for every cry.

Although it has long been accepted that  $F_0$  is perceptually salient, it was not previously possible to distinguish between the possibility that other parameters, related to  $F_0$ , were responsible for the observed correlations, and the possibility that  $F_0$  was directly perceived as a cue to cry aversiveness. Our study shows that small changes in  $F_0$  alone can give rise to significant perceptual differences, although there are probably other acoustic parameters that are as important or perhaps even more important in defining the overall aversive quality of a cry. We are therefore providing direct support both for Gustafson and Green's contention that  $F_0$  is not the most important acoustic determinant of perceived cry aversiveness and for their suggestion that the perceptual effects of  $F_0$  might be statistically significant in a larger (or, as in our case, better controlled) cry sample.

## C. Jitter

Similar conclusions with regard to gradedness may be drawn regarding the effect of jitter. Cries only differing by a small amount of jitter are difficult to discriminate, and thus subjects' striving for consistency would again have worked against our hypothesis and may have been the cause of the reduction in reliable effects when cries were taken to be a random variable. The trend for higher (more negative) ratings to cries with more jitter serves to strengthen a point of evolutionary adaptation of the mother-infant communication system. If jitter is indeed correlated with particular disorders of the nervous system or other indices of need for special treatment, our auditory system may have naturally evolved to incorporate jitter into the set of perceptually salient acoustic features of infant crying. Given recent findings on the potential value of jitter analysis for diagnostic purposes (Hirschberg, 1990; Mende *et al.*, 1990) and on the correlation of  $F_0$  variability with the short-term affective state and with the long-term dispositions of infants (Fitch *et al.*, 1992), there are many issues related to jitter that are worth investigating. It remains to investigate, for example, what kinds of jitter are

present in natural cries and how each kind correlates with production physiology and with perceptual judgements using our current methodology.

Notably, we discovered during pilot experiments that jitter failed to show a perceptual effect when the stimuli were presented through headphones. In fact, subjects were unable to discriminate cries with different amounts of jitter when they heard them through headphones, but could perform the task relatively easily when the same stimuli were presented over a loudspeaker. This finding is not surprising in the light of similar findings by Wilde *et al.* (1986) on the perception of jitter in synthesized speech. On the basis of those results, it is now becoming common practice by researchers who use synthetic voice stimuli to prefer loudspeaker presentation to headphone presentation (e.g., Hillenbrand, 1988; Milenkovic, 1993). Wilde *et al.* (1986) attributed this perceptual effect to reverberation, which is present in free-field presentation (i.e., speakers) but not through headphones. Little is known about other possible differences between the two modes of presentation, but this study shows that jitter plays a role in cry perception and appears to be affected by presentation mode. We thus suggest that cry perception experiments involving synthetic stimuli should be performed using loudspeakers rather than headphones, particularly if jitter perception is of interest.

#### D. Rise time

As for the effects of rise time, we were surprised to find that they were small and in most cases not statistically significant. Although informal listening showed that cries differing in rise time sounded quite distinct, it appears that this kind of difference carries little or inconsistent information about the infant's state. We suggest that rise time might only be correlated with the indicators of cry aversiveness and not a determinant of aversiveness by itself. Certainly, further research is necessary to resolve the issue.

#### E. Stimulus naturalness and LPC

Finally, we briefly discuss the merits of our resynthesis method for perceptual investigations. The correlation of the ratings of the original natural cries with the ratings of the resynthesized cries, in conjunction with the results of experiment 1, shows that resynthesized cries retain the acoustic properties of the natural cries of infants. They capture well the aversive character of the cry in that the ordering of cries by human listeners in all four rating scales is preserved in the resynthesized cries. Consequently, an acoustic feature that affects perception of resynthesized cries toward higher or lower ratings can be reasonably assumed to affect perception of natural cries in a similar manner and we feel confident in concluding that the trends in rating differences caused by our acoustic manipulations would be nearly the same with natural cries (were it possible to obtain cries with comparable acoustic properties). The fact that our synthetic stimuli were nearly indiscriminable from natural cries (experiment 1) serves to strengthen this conclusion.

The naturalness of synthetic stimuli is an important aspect of perceptual studies, often overlooked in previous re-

search. The use of synthesized cries is not a panacea for investigations involving acoustic features; a host of complications may interfere with the experimental manipulations. As already discussed, major problems can arise from allowing the formant frequencies to be scaled along with  $F_0$ . Nevertheless, within the range of parameters we have studied, LPC has proved to be an adequate signal processing method for constructing artificial cry stimuli (although, because of the noisy character of the infants' glottal excitation of the vocal tract and of the nasality of most infant vocalizations, the physical meaning of the LPC parameters is not as clear as it sometimes is in speech modeling). The ability to separate the quasi-periodic excitation component from the spectral shaping component according to the source-filter theory of speech (Fant, 1960; Lieberman and Blumstein, 1988) and cry production (Golub and Corwin, 1985) is important in that it allows almost independent control of many acoustic features, and our study shows that the applications of LPC can be fruitfully extended into infant cry processing as it already has in speech as well as in animal vocalization research.

However, it must be pointed out that LPC is probably not the optimal method for studies like this. The dependency of LPC spectra on  $F_0$  and the inherent inability of LPC to model correctly the nasality often present in infant cries make selection of cry stimuli and estimation of processing parameters an involved trial-and-error process. Keeping the extent of the acoustical modifications small is critical to retain the naturalness of the resulting stimuli. In light of more recent advances in digital signal processing for speech, it may be fruitful to explore the potential of time-domain pitch-synchronous overlap/add (PSOLA) methods (Moulines and Laroche, 1995; Veldhuis and He, 1996) for  $F_0$  modification of infant cries. As with LPC and any other speech processing methods, one must experimentally establish whether successful application to infant cry signals is possible, because of the many acoustic differences between cries and speech. In particular, the high  $F_0$  of infant cries may present problems for PSOLA methods since, in a recent psychoacoustical evaluation of PSOLA with single-formant synthetic stimuli, Kortekaas and Kohlrausch (1997) concluded that "distortions introduced to signals with higher fundamental frequencies are expected to be more easily detectable" (p. 2211).

#### V. CONCLUSION

In summary, we have found significant perceptual effects of the fundamental frequency of the cries, or pitch, and of its short-time perturbations, known as jitter. These findings support the notion of infant crying being a graded signal in the sense that gradual acoustic variation gives rise to gradually differing perceptual ratings. Our findings on the role of rise time were inconclusive. With respect to our methodology, we have showed that a digital signal processing technique can be successfully applied to infant cry perception research by providing acoustically controlled artificial cry stimuli that sound natural. By using this method it is possible to investigate the role not only of individual acoustic features but also of their various combinations, and to examine the relationships between the mechanisms of perception and production. Further research of this nature



should improve our understanding of the communicative function of infant crying, with important implications for developmental research and parenting.

## ACKNOWLEDGMENTS

This study was supported in part by Grant No. HD 05331 from the National Institute of Child Health and Human Development to PDE. Treatment of human subjects in the experiments described herein was in accordance with the ethical standards of the APA. The authors thank C. F. Zachariah Boukydis and three anonymous reviewers for comments on the manuscript. The infant cries that were used were originally recorded for research projects by Barry M. Lester, Brown University, E. P. Bradley Hospital, and Women and Infants Hospital, Providence, RI.

<sup>1</sup>The maximum amplitude of each cry was individually adjusted during digital sampling to cover the available dynamic range.

<sup>2</sup>The terms "pitch" and "fundamental frequency" are used interchangeably.

<sup>3</sup>A small amount of jitter was added to each period after scaling because some synthetic stimuli do not sound natural without jitter. The minimum amount necessary for each cry to sound natural was found by trial and error, and ranged between  $\pm 15 \mu\text{s}$  and  $\pm 30 \mu\text{s}$ . The same amount was added in all variants of each cry in the pitch and risetime manipulations.

<sup>4</sup>The neutral cries are not always the closest to the natural ones because the natural cries often contained more jitter than that in the neutral synthetic ones, whose pitch contour was smoothed to minimize the jitter content. Therefore it was expected that neutral cries would be given on average lower ratings than the corresponding natural cries if jitter had the expected perceptual effect. An additional reason concerns the fact that the spectral flattening of the most aversive sounding cries that is caused by noise excitation produced at the infant's glottis cannot be perfectly accommodated in the LPC model with periodic excitation.

<sup>5</sup>Separate analyses for the between-subjects factors of sex and childcare experience (with cry and level being within-subjects factors) showed no effect of experience [ $F(2,17) < 2, p > 0.17$ ], but a significant effect of sex [ $F(1,18) > 4.41, p < 0.05$ ], with men giving higher ratings than women in all conditions.

Bisping, R., Steingrüber, H. J., Oltman, M., and Wenk, C. (1990). "Adults' tolerance of cries: An experimental investigation of acoustic features," *Child Dev.* **61**, 1218–1229.

Boukydis, C. F. Z. (1985). "Perception of infant crying as an interpersonal event," in *Infant Crying*, edited by B. M. Lester and C. F. Z. Boukydis (Plenum, New York), pp. 187–215.

Brennan, M., and Kirkland, J. (1982). "Classification of infant cries using descriptive scales," *Inf. Behav. Dev.* **5**, 341–346.

Bryan, Y. E., and Newman, J. D. (1988). "Influence of infant cry structure on the heart rate of the listener," in *The Physiological Control of Mammalian Vocalizations*, edited by J. D. Newman (Plenum, New York).

Fant, G. (1960). *Acoustic Theory of Speech Production* (Mouton, The Hague).

Fitch, T., Bryan, Y., Huffman, L., Lester, B. M., and Newman, J. (1992). "Pitch perturbation in human infant cries," Paper presented at the IVth International Workshop on Infant Cry Research (Munich).

Frodi, A. M., and Senchak, M. (1990). "Verbal and behavioral responsiveness to the cries of atypical infants," *Child Dev.* **61**, 76–84.

Fuller, B. F., and Horii, Y. (1986). "Differences in fundamental frequency, jitter, and shimmer among four types of infant vocalizations," *J. Comm. Disord.* **19**, 441–447.

Fuller, B. F., and Horii, Y. (1988). "Spectral energy distribution in four types of infant vocalizations," *J. Comm. Disord.* **21**, 251–261.

Fuller, B. F., Horii, Y., and Conner, D. A. (1992). "Validity and reliability of nonverbal voice measures as indicators of stressor-provoked anxiety," *Res. Nursing Health* **15**, 379–389.

Golub, H. L., and Corwin, M. J. (1985). "A physioacoustic model of the infant cry," in *Infant Crying*, edited by B. M. Lester and C. F. Z. Boukydis (Plenum, New York), pp. 59–81.

Gustafson, G. E., and Green, J. A. (1989). "On the importance of fundamental frequency and other acoustic features in cry perception and infant development," *Child Dev.* **60**, 772–780.

Gustafson, G. E., and Harris, K. L. (1990). "Women's responses to young infants' cries," *Dev. Psychol.* **26**, 144–152.

Hillenbrand, J. (1988). "Perception of aperiodicities in synthetically generated voices," *J. Acoust. Soc. Am.* **83**, 2361–2371.

Hirschberg, J. (1990). "The value of the acoustic analysis of pathological infant cry and breathing noise in everyday practice," *Early Child Dev. Care* **65**, 57–69.

Jacobson, B. H. (1994). "Objective voice analysis: the clinical voice laboratory," in *Vocal Arts Medicine: The Care and Prevention of Professional Voice Disorders*, edited by M. S. Benninger, B. H. Jacobson, and A. F. Johnson (Thieme Medical, New York), pp. 135–152.

Johnston, C. C., and O'Shaughnessy, D. (1988). "Acoustical attributes of infant pain cries: Discriminating features," in *Proceedings of the Vth World Congress on Pain*, edited by R. Dubner, G. F. Gebhart, and M. R. Bond (Elsevier, Amsterdam).

Kortekaas, R. W. L., and Kohlrausch, A. (1997). "Psychoacoustical evaluation of the pitch-synchronous overlap-add speech-waveform manipulation technique using single-formant stimuli," *J. Acoust. Soc. Am.* **101**, 2202–2213.

Lester, B. M., and Boukydis, C. F. Z. (1992). "No language but a cry," in *Nonverbal Vocal Communication, Comparative and Developmental Approaches*, edited by H. Papoušek, U. Jürgens, and M. Papoušek (Cambridge U.P., Cambridge, UK).

Lieberman, P. (1961). "Perturbations in vocal pitch," *J. Acoust. Soc. Am.* **33**, 597–603.

Lieberman, P. (1963). "Some acoustic measures of the fundamental periodicity of normal and pathologic larynges," *J. Acoust. Soc. Am.* **35**, 344–353.

Lieberman, P. (1980). "On the development of vowel production in young children," in *Child Phonology: Perception and Production*, edited by G. Yeni-Komshian and J. Kavanaugh (Academic, New York).

Lieberman, P. (1985). "The physiology of cry and speech in relation to linguistic behavior," in *Infant Crying*, edited by B. M. Lester and C. F. Z. Boukydis (Plenum, New York), pp. 29–57.

Lieberman, P., and Blumstein, S. E. (1988). *Speech Physiology, Speech Perception, and Acoustic Phonetics* (Cambridge U.P., Cambridge, UK).

Lieberman, P., and Michaels, S. B. (1962). "Some aspects of fundamental frequency and envelope amplitude as related to the emotional content of speech," *J. Acoust. Soc. Am.* **32**, 922–927.

Lüdge, W., and Rothgänger, H. (1990). "Early diagnosis of CNS disturbance from computer analysis of infant cries: A new method of fundamental frequency jitter computation with high resolution in frequency and time," *Early Child Dev. Care* **65**, 83–90.

Macmillan, N. A., and Creelman, D. C. (1991). *Detection Theory: A User's Guide* (Cambridge U.P., Cambridge, UK).

Maxwell, S. E., and Delaney, H. D. (1990). *Designing Experiments and Analyzing Data: A Model Comparison Perspective* (Wadsworth, Belmont, CA).

Mende, W. E., Wermke, K., Schindler, S., Wilzopolski, K., and Höck, S. (1990). "Variability of the cry melody and the melody spectrum as indicators for certain CNS disorders," *Early Child Dev. Care* **65**, 95–107.

Milenkovic, P. H. (1993). "Voice source model for continuous control of pitch period," *J. Acoust. Soc. Am.* **93**, 1087–1096.

Moulines, E., and Laroche, J. (1995). "Non-parametric techniques for pitch-scale and time-scale modification of speech," *Speech Commun.* **16**, 175–205.

Myers, J. L. (1979). *Fundamentals of Experimental Design* (Allyn and Bacon, Boston, MA), 3rd ed.

Okada, H., Murai, N., and Adachi, T. (1987). "VP ratio of the infant cry sounds and its influences on their perception," *Tohoku Psychologica Folia* **46**, 36–42.

Papoušek, M. (1989). "Determinants of responsiveness to infant vocal expression of emotional state," *Inf. Behav. Dev.* **12**, 507–524.

Perkins, W. H. (1985). "Assessment and treatment of voice disorders: State of the art," in *Speech Disorders in Adults*, edited by J. Costello (College-Hill, San Diego, CA), pp. 79–111.

Pollack, I. (1968). "Detection and relative discrimination of auditory 'jitter'," *J. Acoust. Soc. Am.* **43**, 308–315.

Porter, F. L., Miller, R. H., and Marshall, R. E. (1986). "Neonatal pain cries: Effect of circumcision on acoustic features and perceived urgency," *Child Dev.* **57**, 790–802.

- Rabiner, L. R., and Schafer, R. W. (1978). *Digital Processing of Speech Signals* (Prentice-Hall, Englewood Cliffs, NJ).
- Rosenberg, A. E. (1966). "Pitch discrimination of jittered pulse trains," *J. Acoust. Soc. Am.* **39**, 920–928.
- Rothgänger, H., Lüdge, W., and Grauel, E. L. (1990). "Jitter-index of the fundamental frequency infant cry as a possible diagnostic tool to predict future development problems," *Early Child Dev. Care* **65**, 145–152.
- Titze, I. R., Horii, Y., and Scherer, R. C. (1987). "Some technical considerations in voice perturbation measurements," *J. Speech Hear. Res.* **30**, 252–260.
- Tsukamoto, T., and Tohkura, Y. (1990). "Perceptual units of the infant cry," *Early Child Dev. Care* **65**, 167–178.
- Tsukamoto, T., and Tohkura, Y. (1992). "Tempo as a perceptual cue for judgement of infant cries," *Percept. Motor Skills* **74**, 258.
- Veldhuis, R., and He, H. (1996). "Time-scale and pitch modifications of speech signals and resynthesis from the discrete short-time Fourier transform," *Speech Commun.* **18**, 257–279.
- Wasz-Höckert, O., Lind, J., Vuorenkoski, V., Partanen, T., and Valanne, E. (1968). "The infant cry: A spectrographic and auditory analysis," Vol. 29 of *Clinics in Developmental Medicine* (Spastics International Medical).
- Wiedenmann, G., and Todt, D. (1990). "Discrete responses of adult subjects during exposure to infant cry sequences," *Early Child Dev. Care* **65**, 179–188.
- Wilde, M. D., Martens, W. L., Hillenbrand, J. M., and Jones, D. R. (1986). "Externalization mediates changes in the perceived roughness of sound signals with jittered fundamental frequency," in *International Computer Music Conference* (Computer Music Association, San Francisco, CA).
- Wolff, P. H. (1969). "The natural history of crying and other vocalizations in early infancy," in *Determinants of Infant Behavior IV*, edited by M. Foss (Methuen, London).
- Zeskind, P. S., and Huntington, L. (1984). "The effects of within-group and between-group methodologies in the study of perception of infant crying," *Child Dev.* **55**, 1658–1665.
- Zeskind, P. S., and Lester, B. M. (1978). "Acoustic features and auditory perceptions of the cries of newborns with prenatal and perinatal complications," *Child Dev.* **49**, 580–589.
- Zeskind, P. S., and Marshall, T. R. (1988). "The relation between variations in pitch and maternal perceptions of infant crying," *Child Dev.* **59**, 193–196.
- Zeskind, P. S., and Collins, V. (1987). "Pitch of infant crying and caregiver responses in a natural setting," *Inf. Behav. Dev.* **10**, 501–504.
- Zeskind, P. S., Klein, L., and Marshall, T. R. (1992). "Adults' perceptions of experimental modifications of durations of pauses and expiratory sounds in infant crying," *Develop. Psychol.* **28**, 1153–1162.
- Zeskind, P. S., Wilhite, A., and Marshall, T. R. (1993). "Infant cry as a graded signal: Experimental modifications of durations of pauses and expiratory sounds alter mothers' perceptions," *Early Dev. Parenting* **2**, 99–105.
- Zeskind, P. S., Sale, J., Maio, M. L., Huntington, L., and Weiseman, J. R. (1985). "Adult perceptions of pain and hunger cries: A synchrony of arousal," *Child Dev.* **56**, 549–554.

# Do weak syllables count for newborns?

Brit van Ooijen<sup>a)</sup> and Josiane Bertoncini

*Laboratoire de Sciences Cognitives et Psycholinguistique, 54 Boulevard Raspail, 75006 Paris, France*

Alessandra Sansavini

*Department of Psychology, University of Bologna, Viale Berti Pichat 5, 40127, Bologna, Italy*

Jacques Mehler

*Laboratoire de Sciences Cognitives et Psycholinguistique, 54 Boulevard Raspail, 75006 Paris, France*

(Received 29 October 1996; revised 17 July 1997; accepted 20 August 1997)

Does the newborn's well-known sensitivity to human speech include awareness of the distinction between strong and weak syllables, as has been shown for older infants and adults? The non-nutritive high-amplitude sucking paradigm was used to investigate whether weak syllables play a role in neonate perceptual representation. Two-day-old French infants were tested on their capacity to discriminate phonetically highly varied words containing syllables with various strong vowels versus the weak, reduced vowel schwa in natural, isolated English words. Twenty infants heard lists of weak–strong and lists of strong words (e.g., *belief, control*, etc. versus *nose, dream*, etc.) and 20 heard lists of weak–strong and strong–strong words (e.g., *belief, control*, etc. versus *volume, rhubarb*, etc.). The results show that weak–strong words were reliably distinguished from strong words, but not from strong–strong words. Taken together, the findings indicate that a weak, reduced vowel is equivalent to a strong, full vowel to the extent that both count as syllabic nuclei. Moreover, this global equivalence in terms of number of syllabic constituents apparently overrules the more local acoustic difference between strong and weak vowels. The role of syllabic/vocalic information in neonate representation is discussed. © 1997 Acoustical Society of America.

[S0001-4966(97)02312-6]

PACS numbers: 43.71.Es, 43.71.Ft [WS]

## INTRODUCTION

All children begin to speak by producing utterances that simplify, in a systematic way, the items they hear adults pronounce. For example, it has long been observed that early words typically consist of stressed syllables, as in “RAFF” for “giRAFFE.” On the basis of these production data, it was first proposed that there is a perceptual advantage of stressed syllables over unstressed ones (e.g., Gleitman and Wanner, 1982), where weak syllables would be ignored by or even inaudible to young children. A strong syllable is defined by psycholinguists as one that contains a full vowel with primary or secondary stress, whereas a weak syllable contains an unstressed, reduced vowel, usually schwa (e.g., Bolinger, 1981; Fear *et al.*, 1995).<sup>1</sup>

Subsequent observations showed that early productions tend to include both stressed syllables and word-final syllables, as in “E-phant” for “Elephant” (Echols and Newport, 1992). So weak syllables do appear in early words, but only in certain restricted contexts. Gerken (e.g., 1991, 1994) recognized an organization based on strong–weak bisyllabic feet in these data. According to this, children apply to their intended utterances a metrical template for a strong syllable followed by an optional weak one. Since the restricted production of weak syllables not only applies to English but appears in linguistically highly dissimilar languages, it has been proposed that early speech obeys a so-called minimal word constraint for which the default universal setting is a

binary foot (e.g., Demuth, 1996). Taken together, these findings indicate that, at least by the time they start to talk, young children are by no means deaf to syllables with weak vowels. Yet it remains true that weak vowels are shorter and acoustically considerably less salient than strong vowels. It also remains true that, before they start to talk, children spend many months listening; indeed, research findings indicate that they start doing so before birth (DeCasper and Spence, 1986; DeCasper *et al.*, 1994).

By 9 months of age, English infants have acquired language-specific knowledge about the distribution of strong and weak syllables in their native language (Jusczyk *et al.*, 1993) and recent experiments suggest that infants use this information to locate likely word boundaries (Jusczyk, 1996). This is in line with studies on lexical segmentation in adults, which have shown that the strategies listeners use to segment speech are determined by the specific rhythmic properties of their native language (Cutler *et al.*, 1986; Cutler and Norris, 1988; Mehler *et al.*, 1981; Otake *et al.*, 1993). For example, in stress-timed languages such as English and Dutch, listeners are more likely to take the occurrence of a strong syllable in the speech stream to signal the presence of a word boundary than the occurrence of a weak syllable (Cutler and Butterfield, 1992; Cutler and Norris, 1988; McQueen *et al.*, 1994; Norris *et al.*, 1995; Vroomen and de Gelder, 1995; Vroomen *et al.*, 1997). Thus the distinction between strong and weak syllables is an important, language-specific parameter for speech processing.

Since the strong–weak syllable distinction is represented by English 9-month-olds and used in daily speech processing

<sup>a)</sup>Electronic mail: brit@lscp.ehess.fr

by English adults, this raises the question of when sensitivity to strong versus weak syllables appears. In particular, given the acoustically less salient nature of weak syllables, one may ask whether full awareness of these syllables form part of any newborn's universal "start-up kit," or whether this develops as a result of language-specific experience. Let us examine three logical possibilities for the neonate's initial state.

(1) Newborns do not initially attend to syllables with weak vowels, or in any case not the weak vowel nucleus. Consequently, those babies that grow up hearing a language which employs a strong-weak distinction gradually start to form perceptual representations of these vowels some time during the first year of life. On the basis of Jusczyk *et al.*'s (1993) work, we know that this must happen before 9 months, possibly around the same time detailed phonemic awareness starts to take shape, that is, from about 6 months onwards for vowels (Kuhl, 1991). If this is true, then a weak-strong word such as *belief* is not *a priori* classifiable as a bisyllable; rather, the initial percept to an infant will be more like the nonword *bleef*. Hence infants should ignore the distinction between a strong, monosyllabic word and a bisyllabic word that contains one strong and one weak vowel.

(2) Newborns initially attend to all syllables regardless of the relative acoustic prominence of their vocalic nucleus and do not treat them as being qualitatively different. Subsequent exposure to their native language induces them to split strong and weak into two categories, presumably on the basis of emerging awareness of rhythmic properties of those languages that make a systematic use of the strong-weak distinction (Mehler *et al.*, 1996). Again, this must happen some time before 9 months. If this is true, then the word *belief* is initially simply an indiscriminate bisyllable. Consequently, weak-strong words like *belief* will be effectively equivalent to strong-strong words like *banjo*.

(3) Newborns initially attend to all syllables and also respond to the full versus reduced syllable quality of the vowel nucleus. In this case, those babies that hear a language in which the contrast is not relevant may gradually lose the ability to discriminate strong from weak, whereas others learn the regularities associated with this distinction, such as the fact that strong-weak is the predominant stress pattern for multisyllabic words in English (Cutler and Carter, 1987). On this view, the newborn can classify the word *belief* as a weak-strong bisyllable. Therefore words like *belief* should be discriminated from strong-strong words like *banjo*.

The aim of this paper is to test which of the above possibilities most adequately describes early sensitivity to syllables containing strong versus weak vowels and thus to gain insight into the initial state of infant representation of vocalic information. Before doing so, let us briefly review some relevant work on vowel perception in infants.

One may expect infants to be especially sensitive to vocalic information, since vowels are the longest, loudest and most periodic portions of the speech stream (e.g., Crystal and House, 1988a, 1988b; Fry, 1979; Umeda, 1975, 1977). Indeed, evidence in favor of vowel sensitivity over consonant sensitivity emerged from a study by Bertoncini *et al.* (1988), using a variety of strong vowel types. Using the non-

nutritive high-amplitude sucking procedure, the authors repeatedly presented newborns with sets of four syllables that differed either in vowel quality, as in [ba] [bae] [bi] [bo], or in consonant quality, as in [bi] [si] [mi] [li]. After a familiarization phase, infants heard the old set plus one new syllable. It was shown in both contexts that newborns noticed the change from the old set to the new one when the new syllable had a new vowel but not when it had a new consonant. Accordingly, Cutler and Mehler (1993) proposed that infants are particularly sensitive to periodic portions of the speech signal. From this, one may suppose that even a weak vowel is sufficient to be noticed. After all, even reduced vowels are periodic sounds, produced with an unobstructed airflow from the lungs, and with comparatively high amplitude in relation to, for instance, voiceless plosives. On the other hand, assuming that the relative inferiority of consonantal information as found by Bertoncini *et al.* (1988) stemmed from relative acoustic nonprominence, this does not bode well for the reduced vowel schwa, which typically has very low acoustic salience. For example, durational measurements of schwa tokens have shown a range of about 20–50 ms, which is well below that typically found for full vowels, and even below that of certain consonants (van Santen, 1992; Van Ooijen, 1994). As a rough indication, a range more typical for full vowels would be 100–350 ms, for fricatives 75–250 ms, and for nasals 60–160 ms (van Ooijen, 1994).

Given this evidence for an advantage of at least full vowel information over consonantal information, the next question is whether differences in acoustics prominence within the category of vowels are perceived by the young infant. In a study on phonetic feature discrimination, Jusczyk and Thompson (1978) demonstrated amongst other things that 2-month-old English infants discriminated between the strings [ɪdaba] and [daɪba], indicating a sensitivity to the position of stress, and hence to the order of acoustic prominence. However, this study was limited to two contrasting stimuli at a time, with only one vowel type, namely [a], which is by definition unreduced.

Sansavini *et al.* (1997) tested sensitivity to stress patterns in Italian newborns. Their results showed that babies discriminated between the members of the phonetically unvaried word-pair [ɪmama]–[maɪma], the consonant-varied word-pair [ɪtacala]–[taɪcala], and lists of consonant-varied word pairs [ɪdaga], [ɪnata], etc. versus [daɪga], [naɪta], etc. Thus this study demonstrated once more a sensitivity to stress, this time with newborns, and using more varied stimuli at least in terms of the consonants. The limitation of this study, however, is that in two of the three experiments, again only two contrasting stimuli were used at a time, and again the vowel was always full, primary, or secondary stressed [a].

To conclude, we know that full vowel information is especially salient to newborns (Bertoncini *et al.*, 1998), that 2 to 3-month-olds are sensitive to differences in acoustic prominence with the same vowel type [a] (Jusczyk and Thompson, 1978), and that stress patterns are represented by newborns at least in consonant-varied items (Sansavini *et al.*, 1997). However, the strong-weak distinction crucially depends on strong versus *reduced* vowels. This, then, has mo-

tivated the present investigation of the initial state for this relatively nonprominent but at the same time important type of vowel. Given that the initial state of speech perception is commonly believed to be universal, we decided that the most stringent test of the distinction between strong and weak vowels would be one with infants whose intrauterine and early postnatal experience did not include reduced vowels. The French language does not have reduced vowels; therefore we tested French newborns on English words.

The three alternatives that were outlined earlier were tested in a straightforward manner by two basic comparisons. In the first condition, we contrasted monosyllabic words containing one strong vowel (henceforth: S words) with bisyllabic words with a weak–strong stress pattern (henceforth: WS words). Second, we used WS words versus words with a strong–strong stress pattern (henceforth: SS words). We reasoned that the outcome of the first condition would inform us on the validity of alternative 1, which states that weak vowels are not attended to initially: if no discrimination were found between S words and WS words, then alternative 1 would be correct. Moreover, this would predict discrimination in the second condition, which contrasted WS words with SS words: if W vowels are not attended to, then WS versus SS would be effectively equivalent to S versus SS. On the other hand, if discrimination did appear in condition 1, then this would indicate that WS words are perceived as being different from S words, and because of the large sets of stimuli we would be justified in saying that this difference lies in the successful extraction and subsequent representation of weak vowel information. However, in order to establish *why* discrimination was obtained, and to choose between alternatives 2 and 3, we needed to contrast WS words with SS words: If no further discrimination were found, then this would indicate that weak vowels are effectively equivalent to strong ones for the purpose of constructing an abstract representation (alternative 2). If, on the other hand, further discrimination were obtained, then this would be evidence that differences in acoustic prominence as present in full versus reduced vowel quality are sufficiently salient to the infant not only to represent weak vowels but also to have a separate representation for weak versus strong vowels (alternative 3).

## I. METHOD

### A. Stimuli

In addition to a specific comparison of full versus reduced vowel quality, we decided to use more than two stimuli at a time, with as wide a variety of syllabic structure, consonant, and full vowel types as possible. The reason for this is that discrimination between two single items may be due to the accurate memorization of those particular stimuli, and therefore the only justified conclusion is that infants perceived a difference. In contrast, if discrimination is found for lists of items, then one can infer that the infants must have succeeded in extracting the common property of an entire set of stimuli. Thus discrimination would ensue from the abstract representation infants had formed of the parameter of W versus S vowels, rather than just on the low-level perceptual difference between two items. The weak–strong stress

pattern was preferred over a strong–weak one for reasons of word-final lengthening; having weak vowels occur in the typically longer final position would have minimized, at least in terms of duration, the difference between the word types.

In order to ensure an accurate classification of stimulus words into the categories of WS and SS, we presented lists of selected disyllables to two native speakers of British English, one of whom is phonetically trained, and asked them to classify the words. This resulted in 100% agreement on the WS versus SS classification. Following this, a total of 108 words were selected as stimuli: 36 S words, (e.g., *blast*), 36 WS words (e.g., *belief*), and 36 SS words (e.g., *banjo*); all SS words had primary stress on their first syllable (see the Appendix). As a further check on these stimuli, the 108 words were presented to three phonetically untrained native speakers of British English, who were asked to indicate the stress pattern of the various words. Once more, we obtained 100% consensus. Thus with four adult speaker's intuitions perfectly matching our own, we were confident of the WS versus SS word classification. The materials were recorded by a 24-year-old female native speaker of standard southern British English who was naive as to the purpose of the experiment. In order to ensure similarity of production, each word was embedded in the carrier sentence "He said the word [ . . . ] to himself." The stimuli were digitized and measured using a waveform editor. The mean duration of the S words was 633 ms (s.d.=76), that of the WS words 665 ms (s.d.=78), and that of the SS words 710 ms (s.d.=103). The mean duration of the vowels within the words was 242 ms (s.d.=107) for the S words, 59 (s.d.=21) and 226 (s.d.=82) for the WS words (reduced vowels and full vowels, respectively), and 134 (s.d.=57) and 221 (s.d.=74) for the SS words.

### B. Apparatus

Infants' sucking responses were measured by means of a sterile pacifier (Babisol) which was mounted on an adjustable mechanical arm and connected to a pressure transducer (GOULD P23). This was in turn connected to a computer (IBM-PC 386) via an analog-to-digital board (Data Translation 2814). The computer registered each sucking response and selected high-amplitude (HA) sucks according to a fixed criterion, corresponding to an average of about 80% of all sucks. Detection of an HA suck resulted in a stimulus word being delivered by an OROS AU22 board, through a stereo amplifier (ROTEL RA820B\*3) and two loudspeakers (MARTIN Control Monitor DB92), at a comfortable level of intensity.

### C. Design

The materials were divided into two conditions: the S-WS condition and the WS-SS condition, in a between-subjects design. The testing paradigm was the non-nutritive high-amplitude sucking procedure (see Jusczyk, 1985 for a detailed description). Briefly, all infants in this paradigm start with one minute of silence, during which their baseline sucking rate is registered. Following this, they hear one type of stimulus during a so-called familiarization phase. After

this phase, “experimental” babies are switched to a new type of stimulus (e.g., from S words to WS words or from WS words to SS words) whereas “control” babies are switched to hearing new tokens of the same stimulus type (S to S, WS to Ws, or SS to SS). In this study, we assessed infants’ sensitivity to the variable of interest through statistical comparisons of the difference in mean sucking rates per minute between just before and just after the switch in auditory stimulation, for experimental versus control subjects.

#### D. Procedure

Infants were tested individually in a sound-attenuated chamber at the Maternité Baudelocque Port-Royal in Paris, about 2 h after feeding. Once a quiet, alert state was obtained, the infant was placed in a semireclining position in a special “baby bath seat” that reduces head movements. The criterion for familiarization to the first set of stimuli was a decrement in sucking rate of at least 25% over two consecutive minutes compared to the rate in the immediately preceding minute. At this point, the auditory stimulation changed. The postshift period lasted 4 min. To prevent control infants from hearing the same set of stimuli throughout, each set of stimuli was split in two subsets of 18 tokens each, resulting in 6 subsets of stimuli (S1, S2, WS1, WS2, SS1, and SS2). Within each subset, presentation was randomly ordered, and there was an interval of 1300 ms between two stimulus onsets. Since the longest word was 861 ms and the shortest one 495 ms, the silent interval between two stimuli was at least 439 and at most 805 ms. Order of presentation of the stimuli was counterbalanced such that, within each condition, half of the subjects started with, for example, S words before being switched to WS words, and half heard WS words before S words.

#### E. Subjects

108 healthy, full-term newborns were recruited at the Maternité Baudelocque Port-Royal in Paris and tested within the first 5 days after delivery. None had suffered complications during pregnancy and delivery, all weighed more than 2750 g at birth and had 1-min Apgar scores of at least 8, and 5-min Apgar scores of 10. Forty babies completed the experiment; their mean birth weight was 3419 g (s.d.=370), their mean age was 2.8 days (s.d.=1) and their mean gestational age was 39.7 weeks (s.d.=1). Data from the remaining babies were discarded for the following reasons: ceasing to suck or refusing to start sucking (26), insufficient or irregular sucking (13), falling asleep (11), crying (11), failing to reach the switch criterion (5), experimenter error (1), and parental interference (1). All the babies’ parents were native speakers of European French.

## II. RESULTS

Three analyses of variance (ANOVA) with subjects as the random factor were carried out. The first concerned the main dependent variable, namely, the difference between the mean sucking rate per minute before and after the switch (that is, the mean of the 2 min immediately preceding the switch versus the mean of the 2 min immediately following

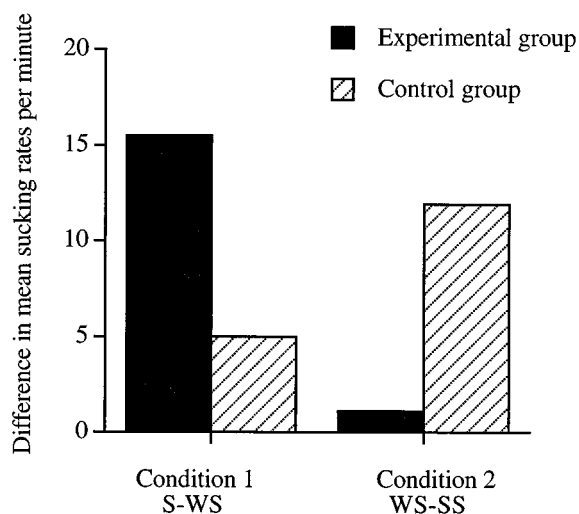


FIG. 1. The difference, in mean sucking rates per minute, is shown between before and after the switch in auditory stimulation, as a function of condition (S-WS or WS-SS). Separate bars are shown for experimental (word type change after switch) and control (no type change) subjects.

the switch). The second and the third analyses concerned the mean sucking rates during the baseline and the last two pre-shift minutes, respectively. The two relevant between-subject factors were Condition (S-WS versus WS-SS) and Group (experimental versus control). In addition, we included a counterbalancing between-subjects factor for order of presentation of the stimuli within each condition (for example, S words before the switch and WS words after, or vice versa). For the mean sucking rates during the baseline and the last two pre-shift minutes, no significant main effect or interactions were found, indicating that performance before the switch was comparable across conditions and groups.

For the main dependent variable, there was neither a main effect of Group, nor of Condition. However, the interaction between these factors was significant [ $F(1,32) = 7.72, p < 0.01$ ], reflecting the fact that, in Condition 1 (S-WS), experimental babies increased their sucking rates significantly more than control babies [ $F(1,16) = 4.53, p < 0.05$ ], while there was a nonsignificant tendency in the reverse direction for Condition 2 (WS-SS) [ $F(1,16) = 3.39, p > 0.08$ ]. There were no main effects of the counterbalancing factor, nor did this interact with any of the other variables. Figure 1 shows the difference, in mean sucking rates per minute, between before and after the switch, as a function of condition, for experimental versus control subjects.

## III. DISCUSSION

The present study was designed to provide insight into the pertinence of reduced vowels and, by implication, of the distinction between strong and weak syllables for newborns. The results from Condition 1 clearly showed that newborns distinguished strong from weak–strong words, even though one of the syllables in the bisyllabic words contained the reduced vowel schwa, and even though a wide variety of CV structures as well as of consonants and full vowels were

used. Thus the presence of the weak vowels was sufficient to have weak–strong words being represented as bisyllables. We can therefore say that, at birth, sensitivity to vocalic information is such that even reduced vowels are perceived as a syllabic nucleus, even by infants whose maternal language does not make a systematic use of reduced vowels.

At the same time, the results of Condition 2 yielded no evidence to suggest that newborns distinguished between lists of weak–strong versus strong–strong words. This finding qualifies the one from Condition 1: although the presence of weak vowels in the WS words did serve to signal a difference in relation to S words, this difference was not sufficiently salient to lead to a separate representation and hence to discrimination. This absence of discrimination indicates that, rather than striking the infants as being different, the predominant impression of the stimuli was their similarity in terms of number of syllabic components: weak vowels counted as syllabic nuclei, hence the WS words in this study were represented as bisyllables just like the SS words, and apparently this global representation of bisyllabicity overruled the difference in acoustic prominence between the two types of bisyllables. Since we know, however, that infants can pick up subtle auditory distinctions, this absence of discrimination should not be taken to imply that infants simply do not hear the difference between strong and weak vowels. Instead, we believe that, in this particular case, the common property of the number of syllabic components was more salient than the difference in acoustic prominence as captured by full versus reduced vowel quality.

Previous work has provided evidence that the number of syllabic components is a parameter that is readily represented by infants. Bijeljac-Babic *et al.* (1993) demonstrated that newborns discriminated lists of bisyllabic CV sequences such as [baku], [rifo], etc., from trisyllabic ones such as [mazopu], [rekivu], etc. Discrimination performance was not due to the durational difference between the sets of stimuli, nor to the difference in number of consonants. However, Bijeljac *et al.*'s (1993) study, as all the others to date, was limited to full (strong) vowels, as well as to relatively simple and uniform CV sequences. The contribution of this study, then, is that the capacity to extract an organizational property from sets of stimuli holds even when the stimuli are complex and highly variable, that is, when a great variety of CV structures together with a great variety of vowels and consonants is used. Moreover, the extraction of organizational information is apparently not hindered by having a relatively weak, short, nonprominent vowel function as a syllabic nucleus.

In contrast to strong indications that infants are sensitive to the number of syllabic components, no evidence has thus far emerged in favor of other perceptual units. For example, a study carried out by Bertencini *et al.* (1995) demonstrated that infants are not similarly sensitive to the number of morae. From the present study, it would appear that the SW distinction can join ranks with the mora, in that both serve to signal rhythmic regularities that are used in adult but not in infant speech processing. For the time being, then, evidence seems to be accumulating that the overall notion of syllabic unit is what counts predominantly for newborns.

A few caveats are in place, however. The first concerns

the notion of variability in the stimulus lists, which in the present study was deliberately maximized. Hence syllabic structure varied greatly with forms like CCV (tree), CCVCC (trunk), CVCV (halo), VCVC (appeal), VCCV (empire), VCVCC (ascent), CVCCVCC (suspense), and CVCCVCV (dandruff). Furthermore, phonetic variation was maximized with as many different consonants and full vowels as possible being used. Also, vowel quality was varied in that both strong primary stressed, strong secondary stressed, and weak reduced vowels occurred in the lists. It may well be the case that this considerable diversity has served to drown out the difference between strong and weak vowels while emphasizing the only property that was constant in the face of so much variety, namely the number of rhythmic beats.

A second point worth noting is that the weak–strong distinction may be more readily apparent when the weak syllable occurs in a SW disyllable rather than in a WS disyllable, since in the SW context the weak syllable would be more acoustically prominent by virtue of being longer and possibly louder. Our choice of WS rather than SW words was motivated by the desire to maximize the contrast with SS words. SS words in English typically have primary stress on their first syllable (e.g., *coffee*), whereas SS words with primary stress on the second syllable (e.g., *trustee*) are relatively rare, making the latter unsuitable as stimulus type. This being the case, the WS stress pattern was the best counterpart in terms of accent location. In addition, we reasoned that having weak vowels occur in SW words, because of word-final lengthening, would reduce the durational difference between these weak vowels and the second vowels within the SS words. Nevertheless, one could argue in favor of a SS (*coffee*) versus SW (*fever*) comparison with accent falling on the first syllable in both types: it is possible that more homogeneity allows for better representation and hence discrimination. Of course, this concern could be addressed empirically.

Finally, it may be that there is a methodological bias in the sense that presentation of isolated stimuli benefits the overall impression of the number of syllabic components. That is, when bounded by silence, a very salient feature of any one stimulus will be its number of rhythmic beats, so that the parameter of the overall number of components may interfere with that of rhythm as conveyed by variations in acoustic prominence. Perhaps the rhythmic alteration of strong and weak syllables only becomes salient at the suprasegmental level of speech prosody, namely in the characterization of overall rhythmic structure of connected speech. Hence it may be the case that infants are perfectly capable of distinguishing connected speech which is characterized by an alternation of strong and weak syllables from connected speech (drawn from the same language) in which this is not the case. This, too, remains an empirical question.

So, is it the syllable or the vowel that counts for infants? This question has been raised before (e.g., Bijeljac-Babic *et al.*, 1993), and remains difficult to answer, since it is virtually impossible to dissociate syllables and vowels, the former being by definition built around the latter.<sup>2</sup> We know that vowels play a crucial role in that only stimuli that contain a vocalic nucleus are discriminated (e.g., [pat] from [tap]

but not [pst] from [tsp], Bertoncini and Mehler, 1981). Thus it would seem that, as long as there is a vowel-like sound within a stimulus, infants can in principle use it as a perceptual unit; when there is no such sounds, discrimination is not found. Of course, to the extent that connected speech does not typically consist of sequences of vowels on their own, it seems unfruitful to argue over whether it is the syllable or the vowel that counts. Indeed, it could very well be that, though the vowel acts as a perceptual anchor, it does need to be bounded by something else, i.e., by consonants, in order to stand out. Given that all languages consists of alternations between vowels and consonants, the notion of a syllable defined as a vocalic nucleus optionally surrounded by consonants would seem a good candidate as an initial, universal unit of perception.

We can conclude that, at least in the form in which we tested it, infants can attend to weak vowel information, but the difference between weak and strong vowel information is not attended to, or at the very least not sufficiently so to affect discrimination performance. This in turn favors the second of the three alternatives that were outlined in the introduction as a way of characterizing the initial state of speech processing: newborns initially attend to all syllables regardless of the relative acoustic prominence of their vocalic nucleus, and only subsequent exposure to their native language induces them to start forming separate categories. If this is true, then sensitivity to strong versus weak syllables must develop sometime during the first year of life. Evidence to support this idea comes from the earlier mentioned study by Jusczyk *et al.* (1993) who showed that by 9 months (but not yet by 6 months), young children prefer to listen to stimuli that have the SW patterns characteristic of English words. Note, however, that there is a difference between sensitivity to and preference for a particular parameter. The former simply requires discrimination, whereas the latter requires recognition of a more familiar pattern. One obvious possibility for a follow-up study would therefore be to assess preference in English infants under 9 months in order to determine the critical age at which the ability to recognize these syllabic structures is acquired.

Thus this study has extended the existing knowledge about infants' representations of vocalic sounds with respect to reduced vowels. It has provided information about the structure of vocalic representations, in that weak vowels were found to be effectively equivalent to strong ones as far as the nature of their abstract representation is concerned. This indicates that, for the purpose of forming a syllable, one vowel is as good as any other for the newborn, and this in turn ties in with previous work that has demonstrated the importance of syllables containing a vocalic nucleus for neonate speech processing.

#### ACKNOWLEDGMENTS

This research was made possible through a grant from the Fyssen Foundation, Paris, to the first author. We wish to thank Anne Christophe, Emmanuel Dupoux, Thierry Nazzi, Linda Polka, and Janet Werker for valuable comments on an earlier draft of this paper. Correspondence should be addressed to Brit van Ooijen at the Laboratoire de Sciences

#### APPENDIX: WORD STIMULI

Strong words		Weak-strong words		Strong-strong words	
drink	string	lament	patrol	halo	metro
blast	gist	advice	veneer	endive	archive
wound	mould	belief	degree	banjo	hygiene
creed	hunch	device	ravine	turmoil	gargoyle
grape	surge	gavotte	police	methane	cyclone
train	felt	marine	delight	elbow	empire
toast	coast	raccoon	balloon	survey	sultan
nose	worm	control	consent	jockey	robot
tree	plea	career	canoe	vortex	volume
gloom	moon	cigar	manure	tepee	coffee
spring	fringe	grenade	guitar	curfew	rhubarb
stench	feast	charade	cassette	torso	cohort
help	dread	ascent	appeal	mushroom	cocktail
break	trunk	abode	award	bonfire	sapphire
jolt	scar	salute	facade	ozone	essay
sleigh	sky	fatigue	suspense	spondee	window
box	mind	gazelle	contempt	access	syntax
straw	crow	receipt	resort	upshot	dandruff

<sup>1</sup>In prosodic phonology, a slightly different definition is used: strong syllables are defined as stressed syllables, while weak syllables are defined as unstressed (whether full or reduced) syllables (e.g., Halle and Keyser, 1971).

<sup>2</sup>We are of course aware of the existence of so-called syllabic consonants such as /l/ in a word like *bottle*. However, at present no data exist to indicate whether the vowel-like nature of such consonants is sufficient to signal an entire syllable to prelinguistic listeners.

Bertoncini, J., and Mehler, J. (1981). "Syllables as units in infant speech perception," *Inf. Behav. Devel.* **4**, 247–260.

Bertoncini, J., Bijeljac-Babic, R., Jusczyk, P. W., Kennedy, L. J., and Mehler, J. (1988). "An investigation of young infants' perceptual representations of speech sounds," *J. Exp. Psychol.: General* **117**, 21–33.

Bertoncini, J., Floccia, C., Nazzi, T., and Mehler, J. (1995). "Morae and syllables: Rhythmical basis of speech representation in neonates," *Lang. Speech* **38**, 311–329.

Bijeljac-Babic, R., Bertoncini, J., and Mehler, J. (1993). "How do 4-day-old infants categorize multisyllabic utterances?," *Devel. Psych.* **29**, 711–721.

Bolinger, D. L. (1981). *Two Kinds of Vowels, Two Kinds of Rhythm* (Indiana University Linguistics Club, Bloomington).

Crystal, T. H., and House, A. S. (1988a). "Segmental durations in connected-speech signals: Current results," *J. Acoust. Soc. Am.* **83**, 1553–1573.

Crystal, T. H., and House, A. S. (1988b). *J. Acoust. Soc. Am.* **83**, 1574–1573.

Cutler, A., and Butterfield, S. (1992). "Rhythmic cues to speech segmentation: Evidence from juncture misperception," *J. Mem. Lang.* **31**, 218–236.

Cutler, A., and Carter, D. (1987). "The predominance of strong initial syllables in the English vocabulary," *Comput. Speech Lang.* **2**, 133–142.

Cutler, A., and Mehler, J. (1993). "The periodicity bias," *J. Phon.* **21**, 103–108.

Cutler, A., and Norris, D. (1988). "The role of strong syllables in segmentation for lexical access," *J. Exp. Psychol.: Hum. Percept. Perf.* **14**, 113–121.

Cutler, A., Mehler, J., Norris, D., and Segui, J. (1986). "The syllable's differing role in the segmentation of French and English," *J. Mem. Lang.* **25**, 385–400.

DeCasper, A. J., Lecanuet, J. P., Busnel, M. C., Granier-Deferre, C., and Maugeais, R. (1994). "Fetal reactions to recurrent maternal speech," *Infant Behav. Devel.* **17**, 159–164.



- DeCasper, A. J., and Spence, M. J. (1986). "Prenatal maternal speech influences newborn's perception of speech sounds," *Infant Behav. Devel.* **9**, 133–150.
- Demuth, K. (1996). "The prosodic structure of early words," in *From Signal to Syntax: Bootstrapping from Speech to Grammar in Early Acquisition*, edited by J. L. Morgan and K. Demuth (Erlbaum, Hillsdale, NJ), pp. 171–184.
- Echols, C., and Newport, E. (1992). "The role of stress and position in determining first words," *Lang. Acquisit.* **2**, 189–220.
- Fear, B. D., Cutler, A., and Butterfield, S. (1995). "The strong/weak syllable distinction in English," *J. Acoust. Soc. Am.* **97**, 1893–1904.
- Fry, D. B. (1979). *The Physics of Speech* (Cambridge U.P., Cambridge, England).
- Gerken, L. (1991). "The metrical basis for children's subjectless sentences," *J. Mem. Lang.* **30**, 431–451.
- Gerken, L. (1994). "Young children's representation of prosodic phonology: evidence from English-speakers' weak syllable productions," *J. Mem. Lang.* **33**, 19–38.
- Gleitman, L., and Wanner, E. (1982). "The state of the state of the art," in *Language Acquisition: The State of the Art*, edited by E. Wanner and L. Gleitman (Cambridge U.P., Cambridge, England), pp. 3–48.
- Halle, M., and Keyser, S. J. (1971). *English Stress: Its Form, Its Growth, and Its Role in Verse* (Harper and Row, New York).
- Jusczyk, P. W. (1985). "The high-amplitude procedure as a methodological tool in speech perception research," in *Infant Methodology*, edited by G. Gottlieb and N. A. Krasnegor (Ablex, Norwood, NJ), pp. 195–222.
- Jusczyk, P. W. (1996). "Investigations of the word segmentation abilities of infants," *Proc. ICSLP 1996* **3**, 1561–1564.
- Jusczyk, P. W., and Thompson, E. (1978). "Perception of a phonetic contrast in multisyllabic utterances by 2-month-old infants," *Percept. Psychophys.* **23**, 105–109.
- Jusczyk, P. W., Cutler, A., and Redanz, N. (1993). "Preference for the predominant stress patterns of English words," *Child Dev.* **64**, 675–687.
- Kuhl, P. (1991). "Human adults and human infants show a 'perceptual magnet effect' for the prototypes of speech categories, monkeys do not," *Percept. Psychophys.* **50**, 93–107.
- McQueen, J. M., Norris, D. N., and Cutler, A. (1994). "Competition in spoken word recognition: Spotting words in other words," *J. Exp. Psychol.: Learn. Mem. Cog.* **20**, 621–638.
- Mehler, J., Dommergues, J.-Y., Frauenfelder, U., and Segui, J. (1981). "The syllable's role in speech segmentation," *J. Verb. Learn. Verb. Behav.* **20**, 298–305.
- Mehler, J., Dupoux, E., Nazzi, T., and Dehaene-Lambertz, G. (1996). "Coping with linguistic diversity: The infant's viewpoint," in *From Signal to Syntax: Bootstrapping from Speech to Grammar in Early Acquisition*, edited by J. L. Morgan and K. Demuth (Erlbaum, Hillsdale, NJ), pp. 101–116.
- Norris, D. G., McQueen, J. M., and Cutler, A. (1995). "Competition and segmentation in spoken word recognition," *J. Exp. Psychol.: Learn. Mem. Cog.* **21**, 1209–1228.
- Otake, T., Hatano, G., Cutler, A., and Mehler, J. (1993). "Mora or syllable: Speech segmentation in Japanese," *J. Mem. Lang.* **32**, 258–278.
- Sansavini, A., Bertocini, J., and Giovanelli, G. (1997). "Newborns discriminate the rhythm of multisyllabic stressed words," *Devel. Psych.* **33**, 3–11.
- Umeda, N. (1975). "Vowel duration in American English," *J. Acoust. Soc. Am.* **58**, 434–445.
- Umeda, N. (1977). "Consonant duration in American English," *J. Acoust. Soc. Am.* **61**, 846–858.
- van Ooijen, B. (1994). "The processing of vowels and consonants," Doctoral dissertation, University of Leiden, The Netherlands.
- van Santen, J. P. H. (1992). "Contextual effects on vowel duration," *Speech Commun.* **11**, 513–546.
- Vroomen, J., and de Gelder, B. (1995). "Metrical segmentation and lexical inhibition in spoken word recognition," *J. Exp. Psychol.: Hum. Percept. Perf.* **21**, 98–108.
- Vroomen, J., van Zon, M., and de Gelder, B. (1997). "Cues to speech segmentation: Evidence from juncture misperceptions and word spotting," *Mem. Cog.* **24**, 744–755.

# Adult and infant perception of two English phones

Judith E. Pegg

*B.C. Research Institute for Child and Family Health, Centre for Community Child Health Research,  
Room L408, 4480 Oak Street, Vancouver, British Columbia V6H 3V4, Canada*

Janet F. Werker

*University of British Columbia, Department of Psychology, 2136 West Mall, Vancouver, British Columbia  
V6T 1Z4, Canada*

(Received 31 November 1996; revised 30 August 1997; accepted 30 August 1997)

Previous research has shown that young infants easily discriminate both native and non-native consonant contrasts, but by 10–12 months of age infants perform like adults and easily discriminate only native consonant contrasts. The present study was designed to determine what kind of experience is required to maintain discrimination of native consonants. To address this question, English listeners of three ages (6–8 months, 10–12 months, and adults) were presented with the phonetic difference, [d̥a] vs [t̥a]. This distinction occurs in English but is not phonemic: [t̥a] occurs when it follows an [s] (as in /sta/). If passive exposure is sufficient to maintain discrimination, all age groups should discriminate [d̥a] vs [t̥a]. However, if phonological status plays a role, then older infants and adults should fail. In experiment 1, English adults judged [d̥a] and [t̥a] to be equally good instances of the same phonemic category /da/. In an AX procedure in experiment 2, English adults discriminated [d̥a] vs [t̥a] better than chance but worse than native phonemic levels. In the Conditioned Head Turn procedure in experiment 3, adults and 6- to 8-month-old infants discriminated [d̥a] vs [t̥a], but 10- to 12-month-old infants did not. Taken together, these results are most consistent with the hypothesis that phonological status plays a role in maintaining discrimination of phonetic information. © 1997 Acoustical Society of America. [S0001-4966(97)05712-3]

PACS numbers: 43.71.Ft [WS]

## INTRODUCTION

In the process of becoming a speaker of a language, one must acquire a tacit understanding of the phonological principles inherent in the native language. Phonological principles specify both phonetic variations that signal differences in meaning (phonemic distinctions) as well as systematic differences in production that occur within a language but do not signal differences in meaning. It is now well established that infants begin the process of acquiring the phonology of the native language during the first year of life (Jusczyk, 1997; Werker and Pegg, 1992). Of particular interest to our work, numerous studies show that in the early months of life, infants discriminate both native and non-native contrasts with equal ease, but 10- to 12-month-old infants perform like adults and only easily discriminate those contrasts that are used to differentiate meaning in their native language (Best *et al.*, 1995, 1988; Kuhl *et al.*, 1992; Polka and Werker, 1994; Trehub, 1976; Werker, 1989; Werker and Lalonde, 1988; Werker and Tees, 1984a).

The changes that occur in perception of non-native contrasts do not constitute an ‘absolute loss’ of discriminative capacity. In tasks that mimic the processing demands of language comprehension, adults show an overwhelming bias to discriminate only that phonetic variation that carries phonemic status. However, when tested under other conditions, it is clear that the human auditory system retains the ability to discriminate non-native phonetic differences (for reviews see Strange, 1995; Werker, 1994). Thus the age-related decline in the ability to discriminate non-native contrasts is referred

to as a functional (linguistic) reorganization rather than an absolute loss (Werker, 1995). The assumption has been that the functional reorganization involves a mapping of phonetic variation on to potentially meaningful differences.

The conclusion that the functional reorganization reflects sensitivity to potential phonemic contrasts rather than just sensitivity to language-specific phonetic variation is premature, however. The major problem is that much of the above work comparing discrimination of native and non-native contrasts has confounded linguistic exposure and phonological status (see MacKain and Stern, 1982, for a discussion). Thus we did not know whether infants, during the first year of life, maintain sensitivity to native contrasts simply because they have *heard* that phonetic variation occurring systematically in the language input, or whether they maintain sensitivity to only that phonetic variation that corresponds to meaningful distinctions in the native language.

In most previous work, a non-native contrast has typically been defined as a pair of syllables differing in only a single consonant (or vowel) that would signal a contrast in meaning in an unfamiliar language but not in the native language. In these experiments, however, researchers have failed to systematically control whether variants of one or both members of the non-native contrast also occur in the native language (but see Best *et al.*, 1988; Polka, 1991). For example, in Werker’s research, one could argue that the initial position Hindi dental consonant does occur in English, but the initial position Hindi retroflex consonant does not (except in some speaker’s consonant clusters) in comparison

to the glottalized uvular and velar consonants from Nthlkampx, neither of which occurs in English (Werker and Tees, 1984b). Without proper control of these factors, it is impossible to confirm whether or not the functional reorganization really does involve a mapping onto meaning.

There are two ways to test whether the simple exposure hypothesis is sufficient to explain the developmental reorganization in phonetic perception. The first way to test this hypothesis is to ascertain whether complete lack of exposure necessarily leads to a decline in discrimination. The second way to test this hypothesis involves examining whether presence of exposure in the absence of phonemic status necessarily leads to maintenance of discrimination.

It has been shown that simple lack of exposure does not necessarily lead to a decline in discrimination performance on non-native contrasts. Best and colleagues (Best *et al.*, 1988, 1995) tested English adults and English-learning infants of 8 to 14 months of age on a Zulu apical/lateral click contrast. This non-native contrast is comprised of phones which do not occur in English, and are not similar in any respects to the phonology of English. All subjects easily discriminated this contrast. Best and colleagues concluded that discrimination was maintained because the non-native phones were not assimilable to English phonology, and thus were spared the reorganization process.

Although Best *et al.*'s research (1988) reveals that lack of linguistic exposure may not always lead to a reduced ability to discriminate, we did not yet know if presence of linguistic exposure independent of phonological status is sufficient to maintain an ability to discriminate consonant contrasts. To conduct such a study, it is necessary to present listeners with a pair of phones to which they are routinely and regularly exposed (i.e., native) but that do not constitute a phonemic contrast in their native language.

English allows two alveolar stops in initial position—the voiced unaspirated stop, and the voiceless aspirated alveolar stop, [t<sup>h</sup>]. A third variant occurs following /s/—the voiceless unaspirated alveolar stop [t<sup>̥</sup>]. Linguistically speaking, [t<sup>h</sup>] and [t<sup>̥</sup>] are allophonic variants of the phoneme /t/ while [d̥] and [t<sup>̥</sup>] are not allophonic variants of a single phoneme but rather come from two different underlying phonemic categories, /d/ and /t/. Thus, phonologically, [t<sup>h</sup>] and [t<sup>̥</sup>] are more similar to one another than either is to [d̥]. However, [t<sup>̥</sup>] and [d̥] are acoustically and perceptually more similar to one another than either is to [t<sup>h</sup>] (Lisker and Abramson, 1970; Lotz *et al.*, 1960). Furthermore, although there are many languages in the world with a voiced unaspirated [d̥] and a voiceless unaspirated [t<sup>̥</sup>] phonemic contrast, it is not known whether there are any languages that contrast [d̥]s and [t<sup>̥</sup>]s with the precise acoustic characteristics of the stimuli used in this study (see first Method section for description of the acoustic values).

To assess discrimination of a language specific phonetic difference using this set of phones, it was necessary to remove one of the context-dependent variants from its standard context and to present it in the context of the other. In previous work, Repp and Lin (1989) presented subjects with the [ba]–[pa] phonemic distinction but with both syllables preceded by an [s]. Adult English listeners were unable to per-

form the discrimination. This raises the possibility that the presence of [s] interferes with detection of phonetic information possibly due to masking. Thus, we decided to test English adults on the [t<sup>̥</sup>]–[d̥] phonetic difference and, to do this, we removed [t<sup>̥</sup>] from its standard [st<sup>̥</sup>] context (in English), and presented both [t<sup>̥</sup>] and [d̥] in syllable initial position.

The phones [t<sup>̥</sup>] and [d̥] are both components of English phonology and all English speakers are exposed to both [t<sup>̥</sup>] and [d̥]. However, although [t<sup>̥</sup>] and [d̥] are described formally as derived from two different underlying phonemes, the precise acoustic-phonetic difference between [t<sup>̥</sup>] and [d̥] in syllable initial position is never used to contrast meaning in English. Thus, by assessing discrimination of [t<sup>̥</sup>] vs [d̥], we can address the question of whether linguistic exposure lacking in phonemic status is sufficient to allow maintenance of discrimination.

To address this main question, adults and both 6- to 8- and 10- to 12-month-old infants were tested in the conditioned head turn procedure. It is in this category change procedure that much of the evidence of a developmental reorganization in phonetic perception has previously been revealed. If exposure is the main factor in the developmental reorganization, then listeners in all age groups should easily discriminate [t<sup>̥</sup>a] from [d̥a] because they are regularly and routinely exposed to this phonetic variation, albeit not both in initial position. If, on the other hand, phonological status plays a major role, then both adults and 10- to 12-month-old infants should have difficulty discriminating this nonmeaningful but native phonetic variation.

Before addressing the main question, it was necessary to examine English adults' perception of these stimuli in detail. In experiment 1, adults were tested in a procedure designed to determine if both [t<sup>̥</sup>a] and [d̥a] are perceived as members of the same English phoneme or as members of two different phonemes. To do this, adults were tested in a variation of a category goodness task (Miller, 1995). Next, to determine if these segments are discriminable under sensitive testing conditions, adults in experiment 2 were tested in a same/different (AX) task with a 500-ms ISI. The AX procedure with a short ISI is thought to be sensitive because adults tested in this procedure discriminate some difficult non-native contrasts (Werker and Logan, 1985) and also discriminate difficult within consonant phonetic variation (Carney *et al.*, 1977). Thus adults tested in an AX procedure may discriminate these consonants even if both segments are judged to be members of the same phonemic category.

## I. EXPERIMENT 1

### A. Introduction

The purpose of the first experiment was to determine if English adults judge the English syllable [t<sup>̥</sup>a] as linguistically equivalent to the syllable [d̥a], or, alternatively, detect subtle differences between them. Because of the overwhelming acoustic similarity of [t<sup>̥</sup>a] and [d̥a], it was predicted that English listeners would identify all exemplars as members of an English /d/. It was possible, however, that adults would identify differences in quality between [t<sup>̥</sup>a] and [d̥a]. Con-

TABLE I. The results of acoustical analyses of the exemplars.

Item	VOT (ms)	Burst duration (ms)	Syllable duration (ms)	F0 onset (Hz)	F1 onset (Hz)	F2 onset (Hz)
t <sup>h</sup> a1	17.45	23.60	336	106	675	1479
t <sup>h</sup> a2	41.00	22.90	397	105	726	1366
t <sup>h</sup> a3	35.75	20.45	389	103	726	1400
t <sup>h</sup> a4	46.50	34.50	407	102	718	1298
t <sup>h</sup> a5	36.10	33.75	415	105	675	1358
da1	6.30	15.20	350	96	449	1600
da2	5.30	12.95	374	101	476	1600
da3	3.50	14.60	353	98	458	1643
da4	3.35	14.05	403	98	432	1617
da5	6.20	13.05	369	100	458	1505
t <sup>̄</sup> a1	7.55	14.85	347	101	441	<b>1410</b>
t <sup>̄</sup> a2	2.95	15.60	338	100	458	<b>1418</b>
t <sup>̄</sup> a3	1.70	15.25	353	100	459	<b>1410</b>
t <sup>̄</sup> a4	6.35	17.45	339	100	484	<b>1436</b>
t <sup>̄</sup> a5	3.75	15.55	362	101	484	<b>1401</b>

sistent acoustic differences between these phones do exist, albeit not cues to a phonemic contrast (see Table I). This detail could allow at least some listeners to detect differences in quality between [t<sup>̄</sup>a] and [ɔ̄a]. Specifically, because [t<sup>̄</sup>a] never occurs in initial position and yet it is being presented in initial position, adults could have judged [ɔ̄a] to be a better example of the category of initial position alveolar stops than [t<sup>̄</sup>a].

One recent study investigated adult English speakers' discrimination of two English allophones presented in their natural context and an unnatural context (Whalen *et al.*, in press). In English, syllable initial "L" differs from syllable final "L." Initial position "L" is transcribed phonetically as light [l], and final position "L" is dark [ɫ]. Whalen *et al.* hypothesized that adults would judge an allophone presented in the appropriate position as a better example of the category "L" than the allophone presented in the inappropriate position. Accordingly, they presented adults with dark and light "L"s in both initial position and final position, [le, ɫe, el, eɫ], and care was taken to equate the vowels. When tested in a category goodness task, adults did not judge allophones occurring in their appropriate position, [le] and [eɫ], as better examples of the category than those allophones occurring in the inappropriate position, [el] and [ɫe]. All exemplars were considered good examples of the category. In addition, when tested in an AXB procedure, adults did not exceed chance levels of discrimination. Thus in their study, English adults were not able to detect differences between the English allophonic variates of dark and light "L" in either an identification or a discrimination task.

The stimuli used in our studies differ from the Whalen *et al.* (in press) stimuli. Whereas light [l] and dark [ɫ] are allophones of the same underlying consonant, the syllables [t<sup>̄</sup>a] and [ɔ̄a] arise from different underlying consonants. Thus, even though adults do not detect differences between [l] and [ɫ] it is possible that adults will detect differences in category goodness between [t<sup>̄</sup>a] and [ɔ̄a].

A variation of a procedure designed by Miller (1995)

was used to try to elicit differential ratings of quality among the phonetic exemplars. Adults were given a sheet with one syllable printed at the top (either **DA**, **STA**, or **SDA**). **SDA** was included because it was thought that subjects might attend to phonetic differences among the stimuli when comparing them to a phonologically and orthographically impossible syllable. They were asked to rate the quality of match of individually presented exemplars of [t<sup>̄</sup>a] and [ɔ̄a] to the letter printed in bold. If all exemplars are assimilated to the meaningful /d/ category, ratings from subjects with **DA** page headings should be better than ratings for those with **STA** and those with **SDA** should fall in the middle. Differences in quality will be evident if adults rate [ɔ̄a] exemplars as better examples of **DA** than [t<sup>̄</sup>a] and conversely, rate [t<sup>̄</sup>a] as better examples of **STA** than [ɔ̄a].

## B. Method

### 1. Subjects

Thirty university students between the ages of 18 and 30 years participated in this study. All subjects were monolingual speakers of English and had no knowledge of any other language before the age of 8 years.<sup>1</sup> Subjects initially indicated interest in participating in research by adding their name to a subject pool. They were then contacted by phone, given details of the procedure, and if they were interested, an appointment was made. Following the procedure, they were given a verbal description of the study and a two-page summary explaining the theoretical basis of the research project. Subjects were also given 1 credit for an undergraduate psychology course.

### 2. Stimuli

The speech samples used in this study were produced by a male, native English speaker. Several exemplars of [ɔ̄a] and [st<sup>̄</sup>a] were digitized directly into a Macintosh II FX computer using the Signalize speech analysis program via a GW Instruments analog-to-digital board (model GWI-AMP). In addition, several exemplars of [t<sup>h</sup>a] were recorded. The [t<sup>h</sup>a] exemplars were not used in experiments 1 and 2, but were used in experiment 3. All signals with perceived differences in cues such as pitch, loudness, intonation contour, and duration were eliminated.<sup>2</sup> Fifteen exemplars were selected—five for each category. Finally, the selected [st<sup>̄</sup>a] exemplars were modified by deleting the initial [s], taking care not to remove any of the characteristics of the burst release of the alveolar stop consonant.

The five exemplars selected for each [ɔ̄a], [t<sup>̄</sup>a], and [t<sup>h</sup>a] category were analyzed to identify criterial phonetic characteristics. As can be seen in Table I, the phonemes [ɔ̄a] and [t<sup>h</sup>a] differ in VOT, burst duration, fundamental frequency (*F0*) at vowel onset, *F1* at vowel onset (the first formant), and *F2* at vowel onset. In contrast, the syllables [ɔ̄a] and [t<sup>̄</sup>a] differ only in *F2* onset (possibly due to coarticulation of the preceding /s/) and have overlapping values in each of the other measures (see also Repp and Lin, 1987). The main acoustic cue for differentiating [t<sup>̄</sup>a] from [ɔ̄a] is, therefore, a higher *F2* onset for [ɔ̄a] than [t<sup>̄</sup>a]. It should be noted that it has been reported in the literature that the mean

$F_0$  onset of [t̄a] and [ɔ̄a] differ. Indeed, lower mean  $F_0$  onset for [ɔ̄a] is reported to be one of the consistent acoustic cues differentiating these allophonic variants (e.g., Hombert *et al.*, 1979). Although there is a mean difference in values of  $F_0$  at vowel onset for our stimuli ([ɔ̄a]=98.6 vs [t̄a]=100.4),  $F_0$  onset is not a distinguishing cue since there is overlap in  $F_0$  onset between the two categories.

The ten digitized stimuli used in the stimulus set (five [t̄a]s and five [ɔ̄a]s) were imported into the Bliss Experimental Control System. This program controlled the presentation of the stimuli.

### 3. Apparatus and procedure

Subjects were given a response sheet with either **DA**, **STA** or **SDA** printed at the top (ten subjects in each condition). Subjects were presented with the ten individual exemplars and their task was to rate the goodness of each of the exemplars in relation to the referent, the one printed in bold at the top of their page.<sup>3</sup> Each individual exemplar was followed by a 5-s response interval during which subjects wrote a number between 1 (poor) and 7 (excellent) on the response sheet.

Subjects were seated in a sound-attenuated chamber in groups of no more than three. They were seated with their backs to each other to ensure that no subject saw the other's response sheet. Before being given the response sheet, subjects were told not to utter the syllable on the top of the page and were given instructions to rate the quality of each presented signal relative to the referent shown in bold print at the top of their page. They were also told that although the task was very difficult for most people, they should nevertheless try to listen carefully for differences between the sounds. It was hoped that such explicit instructions would facilitate detection of subtle quality differences. Exemplars were presented free field by a Compaq 286 computer using the Bliss Program and were presented at a comfortable listening level of 65 dB over a Bose speaker.

Subjects were tested in two sessions with a 3–5-min break between sessions. Each of the ten individual exemplars was presented six times per session. Thus, in total there were 60 presentations of exemplars from the category [ɔ̄a] and 60 from the category of [t̄a] for a total of 120 responses, 12 judgments for each individual exemplar. The order of presentation was randomized for each group of subjects and for each session.

### C. Results and discussion

To determine if judgments of category goodness differed as a function of the category of the phone, a mixed-model analysis of variance (ANOVA) was conducted in which the group variable was page heading (**STA**, **SDA**, or **DA**) and the two repeated measures were session (session 1 versus session 2) and phone category ([ɔ̄a] vs [t̄a]). The dependent variable was the rating value.

There was a main effect for page heading [ $F(2,27) = 5.47, p < 0.01$ ] and an interaction between session and page heading [ $F(2,27) = 3.24, p < 0.05$ ]. No other main effects or interactions were significant. The main effect for page heading was analyzed by comparing mean rating values

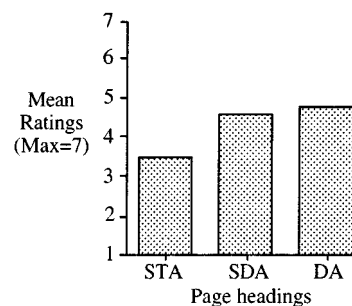


FIG. 1. Mean ratings for [t̄a] and [ɔ̄a] on a scale of 1 to 7 as a function of page heading “SDA,” “DA,” or “STA.”

using Fisher's Protected LSD. The results indicated that adults judged all exemplars as less good when **STA** was the page heading than when either **DA** ( $p < 0.005$ ) or **SDA** ( $p < 0.02$ ) were the headings (see Fig. 1). Ratings were not significantly different when **SDA** versus **DA** were page headings.

The interaction between session and page heading was analyzed by comparing session for each page heading. When **STA** was the page heading, session was not significant. Likewise, when **DA** was the page heading, session was not significant although the means were slightly higher during the second session (first session  $M = 4.71, s.d. = 0.92$ ; second session  $M = 4.85, s.d. = 1.00$ ). In contrast, when **SDA** was the page heading, there was a trend for higher goodness ratings during the first session [ $F(1,9) = 3.87, p < 0.08$ ] (first session  $M = 4.74, s.d. = 0.42$ ; second session  $M = 4.35, s.d. = 0.77$ ). Still, during the second session, signals were not necessarily considered poor examples of the category, simply less good.

This study also provided important information as to whether any of the ten individual exemplars in the stimulus set were perceived as consistently different in quality. A mixed model ANOVA was conducted using page heading as a group variable and exemplar as a repeated measure. This analysis of mean rating scores revealed that although page heading was significant [ $F(2,27) = 5.80, p < 0.008$ ], and there was an interaction between page heading and exemplar [ $F(18,243) = 2.75, p < 0.02$ ] (Greenhouse-Geiser adjustment), there was no main effect for exemplar. This suggests that all exemplars fell within an acceptable range and, therefore, all exemplars were used in subsequent experiments.

Taken together, these results support the prediction that adults judge all exemplars as better examples of “D” than “T.” Interestingly, even though English spelling rules do not allow “SD,” listeners also rated the signals as good examples of the **SDA** referent. They did not, however, rate the exemplars as good examples of the **STA** referent even though English spelling rules allow “ST.” Indeed, inspection of the means for ratings of the individual exemplars shows that even the highest rated exemplar for “ST” was rated as less good than the lowest rated exemplar for either **DA** or **SDA**. Thus, the most important fact arising from these results was that both [t̄] and [ɔ̄] were assimilated to the English phoneme “D.”

There was no indication that adults judged the phone in its appropriate context, [ɔ̄], as a better example of the category than the phone in its inappropriate context, [t̄]. This

replicates the results from Whalen *et al.* (in press) suggesting that native speakers do not detect allophonic variation. The present study goes one step further, however, in that even when the phonetic variation arises from two different underlying meaningful categories specified by English phonology, adults do not detect differences among phones.

## II. EXPERIMENT 2

### A. Introduction

The second step in assessing adult perception of a language-specific phonetic difference was to determine if adults can discriminate [ɔ̄a] from [t̄a] under relatively sensitive testing conditions. Even though adults did not detect quality differences in the signals in the first study, it was still possible that adults would discriminate [ɔ̄a] from [t̄a] if tested in a more sensitive procedure. The AX (same-different) procedure has been shown to facilitate discrimination of phonetic variation that is not meaningful in the native language (Carney *et al.*, 1977). In this procedure, adults are presented with a pair of speech sounds and are asked to say whether the two speech sounds are the same or different. As mentioned previously, ease of discrimination can differ as a function of the ISI between the pair of stimuli (Werker and Logan, 1985). Thus, to facilitate discrimination of the phonetic difference, adults were tested in the AX procedure using a 500-ms ISI.

Order was controlled in this study to allow for the possibility that adults would show better discrimination in one order than in another. Previous research in vowel perception has shown that order can affect discriminability. In particular, when infants are tested in the conditioned head turn procedure (Kuhl *et al.*, 1992; Polka and Werker, 1994) and adults are tested in an AXB procedure (Sussman and Lauckner-Morano, 1995) discrimination is worse in one order than the other. Kuhl *et al.* (1992, 1993) proposes a perceptual magnet effect to explain this phenomenon. According to the magnet effect, discrimination will be worse if the more prototypical vowel is presented as the referent than if the nonprototype is the referent because the more prototypical vowel acts as a "magnet," pulling the others toward it. In Kuhl's work, subjects were always presented with good and poor instances of a single phonetic category (i.e., good and poor /i/s). In an extension of this work, Polka and Werker (1994) presented subjects with two different German vowels, both of which were perceived by English listeners as instances of a single English vowel category (see also Polka and Bohn, 1996). Similarly, as revealed in experiment 1, both [ɔ̄a] and [t̄a] are perceived as instances of the single English phoneme category /da/ even though they are different phonetically and arise from two different underlying phonemes. Thus, to allow for an analysis of a possible magnet effect with our stimuli, order was controlled.

### B. Method

#### 1. Subjects

Eighteen adults between 18 and 25 years of age participated in this study. They were recruited as described in experiment 1 and the selection criteria were identical. Two

adults' data were excluded (one due to a self-reported hearing loss in one ear and one due to equipment error), resulting in a sample size of 16.

### 2. Stimuli

The ten stimuli used in this study were the five [t̄a]s and the five [ɔ̄a]s described in experiment 1. The set of pairings included each individual exemplar paired with every other exemplar. This resulted in five different (DIFF) pairs and four same (SAME) pairs for each exemplar (e.g., DIFF = [ɔ̄a]1 with [t̄a]1, [t̄a]2, [t̄a]3, [t̄a]4, and [t̄a]5). SAME = [ɔ̄a]1 with [ɔ̄a]2, [ɔ̄a]3, [ɔ̄a]4, and [ɔ̄a]5). Because physically identical pairings may alter the response bias of a subject (Werker, 1993; Whalen *et al.*, in press) no exemplar was paired with itself. Thus, one additional SAME contrast was randomly selected for each exemplar to equalize the numbers of SAME and DIFF pairs.

### 3. Apparatus and procedure

Presentation of contrasts was controlled by a 286 Compaq computer using the Bliss Program. Pairs were presented free field in an IAC sound attenuated chamber over a Bose speaker with a 500-ms ISI and a 2000-ms response interval. During the response interval, subjects pressed buttons marked SAME or DIFF on a mouse connected to the computer. The computer recorded all responses.

Adults were tested individually in three stages: a familiarization stage, and two testing stages. To familiarize adults with the procedure, they were presented with 16 pairings alternating between two SAME trials and then two DIFF trials (in the same order for all subjects). Each adult was given a list of the correct responses and was told to respond on each trial by pressing the appropriate button. After this brief familiarization, testing began.

Two rounds of testing were conducted with 100 trials in each set. Within each set, 50 pairs began with a [t̄a] and 50 began with a [ɔ̄a]. Of those 50, 25 were SAME pairs and 25 were DIFF. Each exemplar occurred ten times in the "A" position. To ensure that no adult heard the pairs in the same order twice or in the same order as another adult, the order of presentation of the 100 pairings was randomized for each round and for each adult.

A' scores were calculated for each adult. A' scores control for the response bias of a subject by taking into consideration the frequency of false alarms relative to the number of hits.<sup>4</sup> This is a nonparametric statistic similar to *d'* but, unlike *d'*, can be used with a smaller number of trials. In addition A' values are constrained to vary between 1 (perfect performance) and 0.5 (chance performance). A value below 0.5 is mathematically possible but suggests that the subject is systematically using some cue or strategy different than that required for the task.

### C. Results

To determine whether English listeners could discriminate the syllables, a repeated measures ANOVA was conducted. The repeated measures were session of testing (first versus second) and order of pairings ([ɔ̄a] first versus [t̄a]

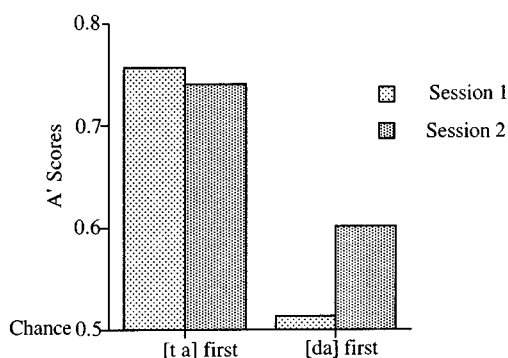


FIG. 2. A' scores for English adults tested in the AX procedure.

first). There was a main effect for order [ $F(1,15) = 36.87$ ,  $p < 0.001$ ] and an interaction between order and session [ $F(1,15) = 7.24$ ,  $p < 0.02$ ]. The main effect for order indicated that listeners had higher A' scores when [t̥a] was in first position ( $M = 0.75$ ,  $s.d. = 0.12$ ) than when [ɖa] was in first position ( $M = 0.56$ ,  $s.d. = 0.15$ ).

Follow-up analyses of the interaction between order and session revealed a significant difference between the first and the second session only when [ɖa] was in first position [ $F(1,15) = 8.68$ ,  $p < 0.01$ ] (see Fig. 2), but the magnitude of the order effect was still apparent even when taking into account the interaction. That is, although discrimination for [ɖa] first pairings improved from the first to the second session, discrimination for [ɖa] first pairings during the second session did not reach the levels of accuracy seen when [t̥a] was in first position.

A' scores in each of the conditions were compared to chance and then to levels of discrimination expected for a native contrast (A' native discrimination is 0.95; see Polka, 1991). Importantly, when [t̥a] was in first position, the A' scores were well above chance [session 1,  $t(15) = 10.44$ ,  $p < 0.0001$ ; session 2,  $t(15) = 7.01$ ,  $p < 0.0001$ ], and yet below native levels [session 1,  $t(15) = 7.39$ ,  $p < 0.0001$ ; session 2,  $t(15) = 6.02$ ,  $p < 0.0001$ ]. The results differ dramatically when [ɖa] was in initial position. In this condition, the A' scores were greater than chance only during the second session [ $t(15) = 3.078$ ,  $p < 0.008$ ] ( $M = 0.60$ ). As well, mean A' were still well below native levels of discrimination in both sessions [session 1,  $t(15) = 11.73$ ,  $p < 0.0001$ ; session 2,  $t(15) = 10.35$ ,  $p < 0.0001$ ]. Thus it appears that when [ɖa] was in first position, discrimination was attenuated.

The direction of the order effect is consistent with predictions from the perceptual magnet hypothesis (Kuhl *et al.*, 1992). Discrimination is attenuated when the (putatively) better exemplar is presented as the referent. Further investigation revealed, however, that the magnet effect cannot explain our results. In her original work, Kuhl (1991, 1993) suggested that when a "good" exemplar from within a category is the referent, discrimination is attenuated because perceptual distance is reduced between the good example and less good examples. Thus by extension, we can deduce that stimuli compared to the good exemplar should be judged the SAME more often than stimuli compared to the less good exemplar. In the present case, since [ɖa] first pairings showed reduced discriminability (appeared to act as the per-

ceptual magnet), adults should be responding SAME more often to pairs with [ɖa] first than with [t̥a] first. However, they were not. In a repeated measures ANOVA comparing percent of SAME responses as a function order of pairings ([ɖa] first versus [t̥a] first), subjects were significantly more likely to respond SAME to [t̥a] first pairings ( $M = 53.19$ ,  $s.d. = 22.61$ ) than to [ɖa] first pairings ( $M = 42.81$ ,  $s.d. = 15.54$ ), an effect opposite to predictions from the perceptual magnet effect.

## D. Discussion

The results from this experiment show that English adults can discriminate [t̥a] from [ɖa] when tested in a sensitive procedure with a 500-ms ISI. When [t̥a] was in first position, adults correctly discriminated well above chance levels. That this was not an easy or straightforward task was evidenced by the fact that when [ɖa] was in first position, performance was severely attenuated particularly during the first block of 100 trials and by the fact that performance in all cases was still worse than would be expected on a native language phonemic contrast. Accuracy improved during the second session for those pairings with [ɖa] first and reached greater than chance levels of accuracy. Thus, discrimination was better than chance in three of four conditions. These results provide evidence that adults tested in a sensitive procedure can discriminate (nonmeaningful) native language phones, and can do so even when one of the phones is presented in a nonstandard context but that their discrimination levels are lower than would be expected for a native phonemic contrast.

These results differ somewhat from the results in Whalen *et al.* (in press). Two main differences between this study and theirs may help us to understand this difference. First, the phonetic difference in the present study is drawn from two different meaningful categories while the Whalen *et al.* stimuli are drawn from a single underlying phonemic category. As such, the present stimuli might be more easily discriminated, although underlying phonological status does not necessarily predict phonetic dissimilarity. Second, a more adequate explanation may be that the AX procedure used herein may be more sensitive to within category distinctions than the AXB procedure used by Whalen *et al.* (see Carney *et al.*, 1977, for evidence). This difference in sensitivity between the two procedures may account for the different results.

There was strong evidence of an order effect. When [ɖa] was in initial position, performance was attenuated and even though there was improvement during the second session, accuracy did not reach the levels of accuracy seen when [t̥a] was in first position. The direction of the order effect was, at first blush, consistent with predictions from the perceptual magnet effect (Kuhl *et al.*, 1992). In contrast to predictions from the perceptual magnet hypothesis, however, adults were *less* likely to respond SAME to [ɖa] first pairings. The lack of support for a magnet effect was perhaps not surprising given the lack of differences in judgments of category goodness for [t̥a] vs [ɖa] in experiment 1. According to Kuhl's work (Kuhl, 1991, 1993) a magnet effect would only be predicted if there were differences in goodness be-

tween the two sets of stimuli. Thus if the order effect found here is interpretable, some mechanism other than the magnet effect must be responsible. It may be that a more differentiated explanation that includes both contrast and anchor effects is required (see Warren, 1985).

### III. EXPERIMENT 3

#### A. Introduction

The final and critical experiment was designed to assess discrimination of the English syllables [t<sup>̄</sup>a] and [ɔ̄a] by adults and by infants of both 6 to 8 and 10 to 12 months of age. The results from experiment 2 reveal that under sensitive testing conditions, English adults can discriminate [t<sup>̄</sup>a] from [ɔ̄a]. However, it was unclear if adults would discriminate this distinction when tested in a category change procedure. Previous research has shown that adults tested in a category change procedure easily discriminate only those consonant contrasts that are meaningful in the native language (Werker *et al.*, 1981; Werker and Tees, 1984b). Thus it was not known whether the conditioned head turn procedure, as an instance of a category change procedure, would be sufficiently sensitive to reveal discrimination of nonmeaningful, native language phonetic variation.

As mentioned in the Introduction, most previous research has confounded exposure and phonological status. The stimuli used in the present research were selected specifically to unconfound these two factors. If the phonological status of a contrast is important in adult speech perception and the category change procedure elicits discrimination of only meaningful contrasts, adults will not discriminate [t<sup>̄</sup>a] from [ɔ̄a] in this procedure. On the other hand, if simple exposure is sufficient to maintain (or reestablish) discriminability, adults should discriminate these syllables even when tested in the category change task.

There were also two possible outcomes for the younger infants. On the one hand, previous evidence suggests that 6- to 8-month-old infants can discriminate almost every consonant contrast with which they have been tested (Best *et al.*, 1995, 1988; Kuhl *et al.*, 1992; Polka and Werker, 1994; Trehub, 1976; Werker, 1989; Werker and Lalonde, 1988; Werker and Tees, 1984a). On the other hand, the broad-based sensitivities shown by 6- to 8-month-old infants could reflect a sensitivity to only those phonetic differences that are used as meaningful contrasts in the world's languages. As mentioned in the General Introduction, there are many languages that use voiced, unaspirated [d] versus voiceless unaspirated [t<sup>̄</sup>] as a phonemic contrast but our particular stimuli include no systematic differences in VOT. Thus the particular combination of phonetic cues used in our English [t<sup>̄</sup>] and [d] stimuli may not correspond to the phonetic cues in a meaningful contrast in any of the world's languages.

Finally, there were two possible outcomes for the older infants. As mentioned previously, absence of exposure to a speech contrast does not always lead to decreased ability in 10- to 12-month-old infants because English-learning infants this age and older discriminate the non-English Zulu apical/lateral click contrast (Best *et al.*, 1988). What we did not yet know was whether 10- to 12-month-old infants would dis-

criminate speech segments to which they are exposed but which do not signal meaningful differences in the native language. The variants [ɔ̄a] and [t<sup>̄</sup>a] allowed us to test this possibility since these syllables are part of the native language and yet do not contrast meaning.

#### B. Method

##### 1. Subjects

Twelve English monolingual adults between 18 and 22 years of age participated in the study. Recruitment was identical to experiment 1 and selection criteria were identical. Two additional subjects were also tested in this procedure but their data are reported separately because they had both received extensive phonetics training prior to participating in the study.

English-learning infants were recruited in several ways. Most parents whose babies participated were initially contacted by a research assistant from our laboratory who visited post-partum mothers in the hospital. The research assistant described the type of studies done in our laboratory in general terms and asked mothers if they were interested in participating in our studies. If the mother indicated interest, she provided her address and phone number and gave permission to be contacted at a later date. When the baby was the appropriate age, parents were contacted by phone and given detailed information about this study. If they were still interested, an appointment was made. Other infants were enrolled when their parents contacted the laboratory after seeing our posters or after hearing advertisements we had broadcast on local radio stations. Finally, some mothers and infants were recruited by parents who had participated in our research. These mothers called us to make appointments. All infants were healthy, born within 2 weeks of due date, were from English-speaking homes, and had not been exposed to any other language more than an estimated 10%. They were given a T-shirt and a certificate after participating.

Data from 32 infants were used: 20 English-learning infants aged 6 to 8 months (6 females, 14 males, mean age = 6 months and 28 days) and 12 English-learning infants aged 10 to 12 months (6 females, 6 males, mean age = 10 months 15 days). An additional 30 infants aged 6 to 8 months were excluded from the study due to failure to condition to the native meaningful contrast<sup>5</sup> on the first visit (15), failure to recondition to the phonemic contrast on the second visit (4), crying or ill (6), equipment error (2), and failure to return for the second visit (3). Seventeen additional older infants were excluded due to failure to condition to the native meaningful contrast on the first visit (9), failure to recondition to the meaningful contrast on the second visit (2), cried or ill (5), and equipment error (1).

##### 2. Stimuli

The stimuli were the ten exemplars described previously, the five [t<sup>̄</sup>a]s and five [ɔ̄a]s. The stimuli were presented on-line using a Data Translation 2801 A board. Syllables were presented free field over a Bose speaker at 65 dB with a 1500-ms ISI. The category change procedure was controlled by a 286 Compaq computer using custom software.



Since it was necessary to ensure that infants can and will perform in this task, infants were initially tested using an English phonemic contrast. We selected the phonemic distinction [t<sup>h</sup>a] vs [ɔ̣a] as a control so that all discriminations would involve alveolar stops. This would ensure at least some measure of comparability between the control and experimental sessions. Thus, in addition to the five [t<sup>h</sup>a] and the five [ɔ̣a] exemplars used in the adult studies, the five exemplars of the phoneme [t<sup>h</sup>a] described in experiment 1 were included in the set of stimuli.

### 3. Apparatus and procedure

The testing was conducted in an IAC sound-attenuated chamber. Subjects were presented with a repeating background signal with a 1500-ms ISI. At random intervals, the signal changed for at least three presentations and then returned to the background signal. Thus subjects heard either [ɔ̣a] as background and [t<sup>h</sup>a] as change or the reverse. The procedure for infants involves conditioning infants to turn their head when they detect a sound change (for more details see Polka *et al.*, 1995; Werker *et al.*, in press).

Infants were tested in three stages: familiarization, conditioning, and testing. During the first two stages, infants were presented with only one exemplar from each of the two categories of speech sounds. During the testing stage, infants were presented with several exemplars and thus must attend to categorical differences among the speech signals. During the first stage, every trial was a change trial. When the infant was judged to be in a state of readiness, syllables from the other category were presented and the reinforcer was activated immediately. This stage comprised five trials. During the second stage, the delay between the change in stimuli and activation of the reinforcer was lengthened, giving the infant the opportunity to make an anticipatory head turn and learn the contingency between a change in the speech signal and the activation of the visual reinforcers. Once an infant correctly performed three consecutive head-turns or the number of trials reached a maximum of 15, the third stage began. The third stage was the testing stage. The computer randomly selected control (no-change) or experimental (change) trials. During this stage, the randomization program was set such that change trials occurred on approximately 60% of the trials with the further restriction that no more than three consecutive control or three consecutive change trials could occur. The testing stage included 25 trials unless an infant was within two trials of reaching criterion (seven out of eight consecutive correct responses) at which time an additional five trials were presented. If an infant failed to respond on three successive change trials, retraining occurred in which the infant was presented with only single exemplars. During these retraining trials, if no head-turn occurred the reinforcer was automatically activated on the third change stimulus and two more presentations of the change stimulus were presented. After the three retraining trials, the program automatically returned to testing. Each infant was limited to a maximum of two retraining sets and these trials were not included in the analyses.

Infants were tested on two days: the first day they were presented with the English contrast [t<sup>h</sup>a] vs [ɔ̣a] to ensure

that they would perform in the task. Infants who failed to show evidence of discriminating [t<sup>h</sup>a] from [ɔ̣a] were not tested on a second day. Those infants who successfully discriminated the syllables [t<sup>h</sup>a] and [ɔ̣a] on the first day were presented with the syllables [t<sup>h</sup>a] and [ɔ̣a] on the second day. If they failed to discriminate between these syllables they were retested with the [t<sup>h</sup>a] vs [ɔ̣a] phonemic contrast to ensure that their failure was not due to forgetting the task. If infants failed to recondition on the phonemic contrast, their data were not included in the analyses.

The procedure for adults is very similar to that used for infants except adults are asked to raise their hand rather than turn their head when they detect a change from the referent to a different category (see Polka, 1995 for details). In our procedure, adults were only tested on the [t<sup>h</sup>a] and [ɔ̣a] phones, unlike the infants who were also tested on the [t<sup>h</sup>a] vs [ɔ̣a] phonemic contrast. As such, there were only two phases to the adult testing procedure, training and testing. During the training phase, subjects were presented with ten change trials to familiarize them with the procedure. If subjects raised their hand during a change trial, the reinforcer (a light) was activated. If a subject failed to respond to a change trial (a miss), the reinforcer was turned on automatically after the third presentation of the exemplar from the change category and two more presentations of the different exemplar occurred while the light remained on. Then the background exemplar was presented again. At the end of ten trials, the subjects were told that testing was about to begin. The test phase was otherwise identical for infants and adults.

Indicators of performance included number of subjects reaching criterion and A' scores (see experiment 2).

### C. Results

To allow comparison of 6- to 8- and 10- to 12-month-old infants, an analysis of proportions (ANPRO, Marascuilo, 1966) was conducted comparing the number of subjects in each group reaching the criterion of seven out of eight consecutive correct responses. The ANPRO is an analog of chi-square that allows comparison of unequal *n*'s and does not require a minimum number in each cell. The analysis revealed that a significantly greater proportion of 6- to 8-month-old infants reached criterion than did the proportion of 10- to 12-month-old infants ( $\chi^2 = 11.62, p < 0.003$ ). There was no effect of order of presentation. Whereas 11 of the 20 younger infants reached criterion (6 when [ɔ̣a] was the referent and 5 when [t<sup>h</sup>a] was the referent), only 1 of the 12 older infants did so (and this was when [ɔ̣a] was the referent).

To compare the infant to the adult data, a second ANPRO was conducted including adults, as well as 6- to 8- and 10- to 12-month-old infants. This analysis revealed a significant difference between the proportion of adults and the proportion of 10- to 12-month-old infants reaching criterion ( $\chi^2 = 13.67, p < 0.001$ ), indicating that discrimination of the syllables was attenuated in 10- to 12-month-old infants (see Fig. 3). The difference between the proportion of adults and the proportion of 6- to 8-month-old infants reaching criterion was not significant.

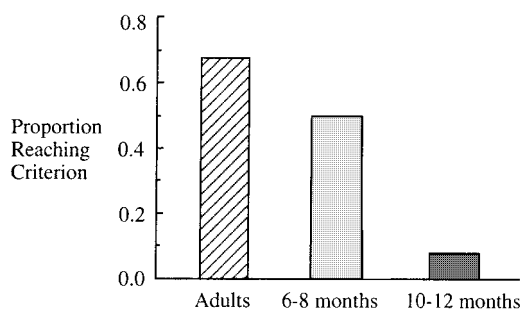


FIG. 3. The proportion of adults and infants reaching criterion in the Conditioned Head Turn procedure on the [t̄a]-[ɔ̄a] comparison.

Before conducting an analysis using  $A'$ , we inspected the subjects'  $A'$  values to ensure that no  $A'$  values were extremely low. As mentioned previously, very low  $A'$  scores indicate the use of a strategy different from that required for the task. Three infants had a low  $A'$ ; one older infant ( $A' = 0.09$ ) and two younger infants, one when [t̄a] was the referent ( $A' = 0.26$ ) and one when [ɔ̄a] was the referent ( $A' = 0.15$ ). All other  $A'$  scores were over 0.30. Data from the three infants with very low  $A'$  scores were dropped from subsequent analyses.<sup>6</sup>

We conducted a 3 (age) × 2 (order) ANOVA using  $A'$  as the dependent variable excluding the three aforementioned infants. There was a significant main effect for age [ $F(2,35) = 6.89, p < 0.003$ ]. Order was not significant and there was no significant interaction. The follow-up comparison of the main effect revealed that older infant  $A'$  scores were significantly lower than younger infant  $A'$  scores [ $F(1) = 7.29, p < 0.01$ ] and than adult  $A'$  scores [ $F(1) = 19.34, p < 0.0003$ ], but there was no significant difference between younger infants and adults (see Fig. 4). This result parallels the results from the ANPRO and provides further support for the assertion that both younger infants and adults can discriminate [t̄a] from [ɔ̄a].

A final analysis was conducted comparing each age group's  $A'$  scores to both chance (0.50) and native levels (0.95) of discrimination.  $A'$  scores were significantly greater than chance for both younger infants' ( $t = 3.62, p < 0.002$ ) and adults' ( $t = 6.10, p < 0.0001$ ), but not for older infants and  $A'$  scores were significantly less than native levels for all three age groups (younger infants,  $t = 8.51, p < 0.0001$ ; older infants,  $t = 9.91, p < 0.0001$ ; and adults  $t = 6.19, p < 0.0001$ ).

Two additional adults, who had received extensive train-

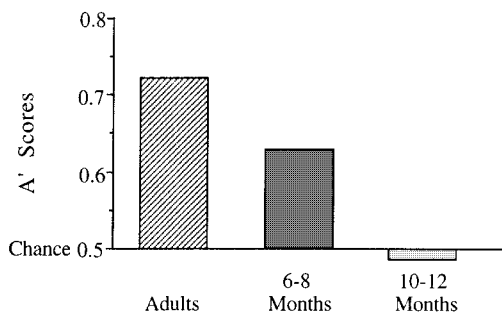


FIG. 4.  $A'$  scores of adults and infants tested in the Conditioned Head Turn procedure.

ing in phonetics, performed extremely well in this task. One was correct on 22 out of the 25 trials and the other was correct on all of the trials. Such evidence suggests that there is a systematic and detectable phonetic difference between [ɔ̄a] and [t̄a].

#### D. Discussion

The results from this study reveal that English infants aged 6 to 8 months perform better on the native [t̄a] [ɔ̄a] difference than do English infants aged 10 to 12 months. This finding was revealed on both an analysis of the proportion of subjects reaching criterion and in an analysis of  $A'$  scores. Furthermore, the  $A'$  scores were significantly better than chance for younger but not older infants. This evidence is consistent with previous cross-language research showing a developmental change in phonetic perception during the first year of life, but also increases our understanding of the mechanisms explaining age-related changes in speech perception. First, the present results show that the sensitivities of 6- to 8-month-old infants are indeed broad based. Second, older infants' failure to discriminate [t̄a] vs [ɔ̄a] shows that the developmental reorganization in speech perception occurring at 10 to 12 months is not a function of simple linguistic exposure *per se*. Instead, the results are consistent with the notion that the shift is based on the phonemic status of the contrast.

This experiment also revealed that adults show moderate discrimination of the native language phonetic difference [t̄a] vs [ɔ̄a]. Adults did not perform as well as would be expected if tested with a native phonemic contrast. Nevertheless, adults discriminated better than chance on the present distinction unlike their typical chance level performance in this procedure with non-native contrasts. These results indicate that passive experience goes some way toward facilitating adult discrimination but is not sufficient to allow discrimination at the levels shown for meaningful contrasts.

#### IV. GENERAL DISCUSSION

The purpose of these studies was to further elucidate our understanding of the developmental reorganization in speech perception by investigating adult and infant discrimination of a phonetic difference that occurs in the native language but is not used to contrast meaning. Three experiments were designed to test two alternative hypotheses for explaining the functional reorganization. According to the first hypothesis, this reorganization occurs as a result of simply being exposed to phonetic variation in the language. If this hypothesis is correct, all age groups should have discriminated the difference between [ɔ̄a] and [t̄a] because this phonetic difference occurs in the linguistic input. According to the second hypothesis, the reorganization occurs as a function of the phonemic status of the phones in question. If this hypothesis is correct, only the younger infants, who as yet have no knowledge of the system of phonological contrasts in their native language, should have discriminated [t̄a] and [ɔ̄a], and both older infants and adults should have failed to discriminate this pairing.

In experiment 3, a significant number of English-learning infants aged 6 to 8 months discriminated [t̄a] from [ɔ̄a] whereas English-learning infants aged 10 to 12 months did not. This pattern was evident in both the analysis of the proportion of subject at each age reaching criterion on the distinction as well as in the analysis of A' scores. Although discrimination by younger infants does not allow us to differentiate between the two hypotheses, it does provide additional understanding of younger infants' speech perception abilities. Discrimination by the infants aged 6 to 8 months shows that initial sensitivity to phonetic differences is very broad based, and possibly extends beyond sensitivity to just those phonetic differences that are used by one of the world's languages to contrast meaning.

In contrast to younger infants, older infants, who discriminated a meaningful English contrast ([t<sup>h</sup>a] vs [ɔ̄a]), failed to discriminate [t̄a] from [ɔ̄a]. Ten- to 12-month-old infants' failure to discriminate [t̄a] from [ɔ̄a] shows that simple exposure alone is not sufficient to maintain discriminability at the end of the first year of life. These results are consistent with the second hypothesis that was posed: it is the match between the input and the phonological status of the distinction in question that governs infant speech perception by the end of the first year of life.

Data regarding adults did not provide clear support for either hypothesis. Experiment 1 showed that adult English speakers judge all exemplars of both [t̄a] and [ɔ̄a] categories to be better examples of a written "D" than an "I." Also, English adults considered exemplars of the syllable in the inappropriate context, [t̄a], to be equally good members of the "D" category as exemplars of the syllable in the appropriate context, [ɔ̄a]. Thus, the evidence from the adults in experiment 1, like that from older infants in experiment 3, appears to be consistent with the phonemic status hypothesis because there was no evidence that English adults can judge quality differences between [t̄a] and [ɔ̄a] syllables. Nevertheless, when English adults were tested in an AX task with 500-ms ISI (experiment 2), they discriminated [t̄a] vs [ɔ̄a] better than chance in three of four conditions. Even when tested in a category change procedure (experiment 3), adults discriminated this English phonetic difference at levels better than chance. This evidence appears to contradict the phonemic status hypothesis: English adults are able to detect the acoustic/phonetic differences between [t̄a] and [ɔ̄a]. Importantly, however, adult levels of performance were consistently below those shown for discrimination of native phonemic contrasts. These findings suggest that it is not essential for two phones to be used to contrast meaning for adults to be able to discriminate them, but that phonological status does influence the level of discriminability obtained.

Taken together, the results from this series of studies are most consistent with the hypothesis that perception of phonetic information by older infants and adults is best explained by the phonological status of the distinction in question. Together with previous work (Best, 1994; Best *et al.*, 1995, 1988; Polka, 1995; Werker, 1989, 1994; Werker and Pegg, 1992; Werker and Tees, 1984a) these results provide strong support for the notion that it is the map between the phonetic input and the phonological system that best ex-

plains age-related shifts in perception of fine phonetic detail. In this particular set of experiments, support is gained for the notion that it is the set of phonological contrasts that provides the strongest influence on age-related changes in phonetic perception.

Two caveats need to be kept in mind when considering this conclusion. First, although adults were unable to distinguish [ɔ̄a] and [t̄a] in experiment 1, and performed more poorly on this distinction than is typically shown for native contrasts in experiments 2 and 3, their level of performance was still significantly better than chance in three of four conditions in experiment 2 and in both orders in experiment 3. As well, the performance of the adults in experiment 3 was significantly better than that of 10- to 12-month-old infants. Thus it is incorrect to conclude that phonological status entirely accounts for sensitivity to fine phonetic detail in adults, and it is essential to offer some account of how performance improves again between late infancy and adulthood. We think the best explanation for these results is that although a phonemic (meaning based) listening strategy is the most robust listening style shown by adults, the ability to redirect attention to other acoustic/phonetic differences is also present. This view is consistent with evidence provided by numerous studies on the adaptability of adults' listening strategies and acquisition of second languages (e.g., Pisoni and Tash, 1974; Werker, 1994; Werker and Logan, 1985; see Strange, 1995 for a review). Strategic processing may account for the superior performance of adults in comparison to 10- to 12-month-old infants: older infants are unable to deploy selective listening strategies and are more constrained to listen to speech for that information that is most meaningful for them.

The second caveat concerns the nature of "meaning" in infants of 10 to 12 months of age. By meaning, we intend the notion of functionally useful. Although infants of 10 to 12 months undoubtedly comprehend some words (Fenson *et al.*, 1994), they are speaking few words at this age. Furthermore, there is little evidence that they are, at this age, able to distinguish between phonetically similar words (Stager and Werker, 1995, 1997; Werker and Pegg, 1992). Thus it may be that what infants are listening for at this time is "possible words" rather than actual words that map sound on to meaning. This is the functional aspect of infants' listening strategies.

There is considerable evidence that by 10 months of age, but not before, infants have sensitivity to the stress patterns (Jusczyk *et al.*, 1993a), acceptable (Jusczyk *et al.*, 1993b) and common (Jusczyk *et al.*, 1994) phonotactic sequences, and other distributional properties of the native language (Aslin *et al.*, 1996). They have also the ability to coordinate two sources of information (Lalonde and Werker, 1995) allowing simultaneous consideration of stress pattern and position-specific phonetic information (Morgan and Saffran, 1995). With the emergence of these abilities, infants are able to extract even unfamiliar word forms (Meyers *et al.*, 1996) and recognize words in fluent speech (Jusczyk and Aslin, 1995; Jusczyk *et al.*, 1995). Listening for possible words without actually mapping those words on to specific objects and events would yield the same outcome for the older in-

fants. It would bias them to treat the syllables [t<sup>-</sup>a] and [ɔ̄a] as equivalent. Since unaspirated [t<sup>-</sup>] does not occur in syllable initial position in English, both [t<sup>-</sup>a] and [ɔ̄a] could be equivalent English word forms.

In summary, this series of experiments has provided convincing support for the hypothesis that it is the phonological status of phonetic detail that best explains the age-related changes in speech perception across the first year of life. Although adult speech perception is also influenced by phonological status, adults seem to be able to apply flexible listening strategies when required. With these results in hand, future research can focus directly on the question of what "phonological status" entails to the infant of 10 to 12 months, on the conditions under which adults can be resensitized to nonphonemic phonetic variation, and on the age at which adultlike flexible strategies emerge.

## ACKNOWLEDGMENTS

This work was supported in part by a Post Graduate Scholarship from the Natural Sciences and Engineering Council of Canada (NSERC) and a Studentship from the Medical Research Council of Canada (MRC), awarded to the first author as well as a research grant from NSERC awarded to the second author (OGP0001103). We would like to thank the adults, parents, and infants who participated in this research. Finally, we would like to acknowledge the efforts of several individuals who participated in booking appointments, assisted in testing infants and adults, and/or generally kept the laboratory running smoothly: Diane Hobday, Gary MacIsaac, Brian Moorehead, Tracey Smiley, and Carmen Swanson.

<sup>1</sup>One person had been briefly exposed to Greek at 4 years of age.

<sup>2</sup>Prevoicing is common in spoken English. We sampled several speakers before finding one male who did not prevoice or devoice /d/.

<sup>3</sup>We did not include a condition with "TA" page heading because the set of stimuli did not include [t<sup>h</sup>a] and our pilot observation indicated that English subjects simply do not perceive any of these stimuli as 't.'

<sup>4</sup>The formula for A' is  $0.5 + (H - FA) / (1 + H - FA) / [4H(1 - FA)]$  where H = proportion of hits and FA = proportion of false alarms (from Grier, 1971).

<sup>5</sup>It is not unusual in this procedure to have high attrition rates, but it is possible that [t<sup>h</sup>a] vs [ɔ̄a] may be somewhat more difficult for infants than other phonemic contrasts on which they have been tested.

<sup>6</sup>Even though very low A' scores are invalid, all the analyses reported below were repeated including the three low A' scores and every significant result reported remained significant.

Aslin, R. N., Woodward, J. Z., La Mendola, N. P., and Bever, T. G. (1996). "Models of word segmentation in fluent maternal speech to infants," in *Signal to Syntax: Bootstrapping from Speech to Grammar in Early Acquisition*, edited by J. L. Morgan and K. Demuth (Earlbaum, Mahwah, NJ).

Best, C. T. (1994). "Learning to perceive the sound pattern of English," in *Advances in Infancy Research*, edited by C. Rovee-Collier and L. Lipsitt (Ablex, Norwood, NJ).

Best, C. T., McRoberts, G. W., and Sithole, N. N. (1988). "The phonological basis of perceptual loss for non-native contrasts: Maintenance of discrimination among Zulu clicks by English-speaking adults and infants," *J. Exp. Psychol.* **14**, 345–360.

Best, C. T., McRoberts, G., LaFleur, R., and Silver-Isenstadt, J. (1995). "Divergent developmental patterns for infants' perception of two non-native consonant contrasts," *Infant Behav. Dev.* **18**, 339–350.

Carney, A. E., Widin, G. P., and Viemeister, N. F. (1977). "Non-categorical perception of stop consonants differing in VOT," *J. Acoust. Soc. Am.* **62**, 961–970.

Fenson, L., Dale, P. S., Reznick, J. S., Bates, E., Thal, D. J., and Pethick, S. J. (1994). "Variability in early communicative development," *Monogr. Soc. Res. Child Dev.* **59**(5).

Grier, J. B. (1971). "Nonparametric indexes for sensitivity and bias: Computing formulas," *Psychol. Bull.* **75**, 424–429.

Hombert, J. M., Ohala, J. J., and Ewan, W. G. (1979). "Phonetic explanation for the development of tones," *Language* **55**, 37–58.

Jusczyk, P. W. (1997). *The Discovery of Spoken Language* (MIT, Cambridge, MA).

Jusczyk, P. W., and Aslin, R. N. (1995). "Preference for the predominant stress pattern of English words," *Child Dev.* **64**, 675–687.

Jusczyk, P. W., Culter, A., and Redanz, N. J. (1993a). "Infants' preference for the predominant stress pattern of English words," *Child Dev.* **64**, 675–687.

Jusczyk, P. W., Friederici, A. D., Wessels, J., Svenkerud, V. Y., and Jusczyk, A. M. (1993b). "Infants' sensitivity to the sound patterns of native language words," *J. Memory Lang.* **32**(3), 402–420.

Jusczyk, P. W., Hohne, E. A., and Mandel, D. R. (1995). "Picking up regularities in the sound structure of the native language," in *Speech Perception and Linguistic Experience: Theoretical and Methodological Issues in Cross-Language Speech Research*, edited by W. Strange (York, Baltimore, MD).

Jusczyk, P. W., Luce, P. A., and Charles-Luce, J. (1994). "Infants' sensitivity to high frequency versus low frequency phonetic sequences in the native language," *J. Memory Lang.* **33**, 630–645.

Kuhl, P. K. (1991). "Human adults and human infants exhibit a prototype effect for phoneme categories; monkeys do not," *Percept. Psychophys.* **50**(2), 93–107.

Kuhl, P. K. (1993). "Innate predispositions and the effects of experience in speech perception: The native language magnet theory," in *Developmental Neurocognition: Speech And Face Processing in the First Year of Life*, edited by B. D. Boysson-Bardies, S. D. Schonen, P. Jusczyk, P. McNeilage, and J. Morton (Kluwer, London).

Kuhl, P. K., Williams, K. A., Lacerda, F., Stevens, K. N., and Lindblom, B. (1992). "Linguistic experience alters phonetic perception in infants by 6 months of age," *Science* **255**(5044), 606–608.

Lalonde, C. E., and Werker, J. F. (1995). "Cognitive influences on cross-language speech perception in infancy," *Infant Behav. Dev.* **18**, 459–475.

Lisker, L., and Abramson, A. S. (1970). "The voicing dimension: Some experiments in comparative phonetics," in *The 6th International Congress of Phonetic Sciences*, edited by B. Hala, M. Romportl, and P. Janota (Academia, Prague), pp. 563–567.

Lotz, J., Abramson, A. S., Gerstman, L. J., Ingemann, R., and Nemeser, W. J. (1960). "The perception of English stops by speakers of English, Spanish, Hungarian, and Thai: A tape cutting experiment," *Lang. Speech* **3**, 71–77.

MacKain, K. S., and Stern, D. N. (1982). "The concept of experience in speech development," in *Children's Language*, edited by K. E. Nelson (Gardner, New York).

Marascuilo, L. A. (1966). "Large scale multiple comparisons," *Psychol. Bull.* **69**, 280–290.

Meyers, J., Jusczyk, P. W., Kemler Nelson, D. G., Charles-Luce, J., Woodward, A. L., and Hirsh-Pasek, K. (1996). "Infants' sensitivity to work boundaries in fluent speech," *J. Child Lang.* **23**, 1–30.

Miller, J. L. (1995). "On the internal structure of phonetic categories: A progress report," in *Cognition on Cognition*, edited by J. Mehler and S. Granck (Elsevier, Amsterdam, The Netherlands), pp. 333–348.

Morgan, J. L., and Saffran, J. R. (1995). "Emerging integration of segmental and supra-segmental information in prelingual speech segmentation," *Child Dev.* **66**(4), 911–936.

Pisoni, D. B., and Tash, J. (1974). "Reaction times to comparisons within and across phonetic categories," *Percept. Psychophys.* **15**, 258–290.

Polka, L. (1991). "Cross-language speech perception in adults: Phonemic phonetic, and acoustic contributions," *J. Acoust. Soc. Am.* **89**(6), 2961–2977.

Polka, L. (1995). "Linguistic influences in adult perception of non-native vowel contrasts," *J. Acoust. Soc. Am.* **97**, 1286–1296.

Polka, L., and Bohn, O. (1996). "A cross-language comparison of vowel perception in English-learning and German-learning infants," *J. Acoust. Soc. Am.* **100**, 577–592.

Polka, L., and Werker, J. F. (1994). "Developmental changes in perception

- of nonnative vowel contrasts," *J. Exp. Psychol.* **20**(2), 421–435.
- Polka, L., Jusczyk, P. W., and Rvachew, S. (1995). "Methods for studying speech perception in infants and children," in *Speech Perception and Linguistic Experience: Issues in Cross-Language Research*, edited by W. Strange (York, Baltimore, MD).
- Repp, B. H., and Lin, H. (1987). "Difference in second-format transitions between aspirated and unaspirated stop consonants preceding [a]," *Lang. Speech* **30**(2), 115–129.
- Repp, B. H., and Lin, H. (1989). "Effects of preceding context on discrimination of voice onset times," *Percept. Psychophys.* **45**(4), 323–332.
- Stager, C. L., and Werker, J. F. (1995). "Phonetic similarity influences learning word-object associations in 14-month-old infants," in *The Annual Conference of the American Psychological Society* (Am. Psych. Soc., New York).
- Stager, C. L., and Werker, J. F. (1997). "Listening for sounds versus listening for meaning in infancy," *Nature* **388**, 381–382.
- Strange, W. (1995). "Cross-language studies of speech perception: A historical review," in *Speech Perception and Linguistic Experience: Issues in Cross-Language Research*, edited by W. Strange (York, Baltimore, MD).
- Sussman, J. E., and Lauckner-Morano, V. J. (1995). "Further tests of the 'perceptual magnet effect' in the perception of [i]: Identification and change/no change discrimination," *J. Acoust. Soc. Am.* **97**(1), 539–552.
- Trehub, S. E. (1976). "The discrimination of foreign speech contrasts by infants and adults," *Child Dev.* **47**, 466–472.
- Warren, R. M. (1985). "Criterion shift rule and perceptual homeostasis," *Psychol. Rev.* **94**(4), 574–584.
- Werker, J. F. (1989). "Becoming a native listener," *Am. Sci.* **77**, 349–353.
- Werker, J. F. (1993). "Developmental changes in cross-language speech perception: Implications for cognitive models of speech processing," in *Cognitive Models of Speech Processing: The Second Sperlonga Workshop*, edited by G. T. Altmann and R. Shillcock (Erlbaum, Essex, England).
- Werker, J. F. (1994). "Cross-language speech perception: Developmental change does not involve loss," in *Speech Perception and Word Recognition*, edited by J. Goodman and H. Nusbaum (MIT, Cambridge).
- Werker, J. F. (1995). "Exploring developmental changes in cross-language speech perception," in *Invitation to Cognitive Science, Volume I: Language*, volume edited by L. Gleitman and M. Liberman (MIT, Cambridge, MA).
- Werker, J. F., and Lalonde, C. E. (1988). "Cross-language speech perception: Initial capabilities and developmental change," *Dev. Psychol.* **24**, 672–683.
- Werker, J. F., and Logan, J. S. (1985). "Cross-language evidence for three factors in speech perception," *Percept. Psychophys.* **37**, 35–44.
- Werker, J. F., and Pegg, J. E. (1992). "Infant speech perception and phonological acquisition," in *Phonological Development: Models, Research, and Implications*, edited by L. M. C. Ferguson and C. Stoel-Gammon (York, Parkton, MD).
- Werker, J. F., Polka, L., and Pegg, J. E. (in press). "The conditioned head-turn procedure as a method for assessing infant speech perception," *Early Development and Parenting*.
- Werker, J. F., and Tees, R. C. (1984a). "Cross language speech perception: Evidence for perceptual reorganization during the first year of life," *Infant Behav. Dev.* **7**, 49–63.
- Werker, J. F., and Tees, R. C. (1984b). "Phonemic and phonetic factors in adult cross-language speech perception," *J. Acoust. Soc. Am.* **75**, 1865–1878.
- Werker, J. F., Gilbert, J. H. V., Humphrey, K., and Tees, R. C. (1981). "Developmental aspects of cross-language speech perception," *Child Dev.* **52**, 349–353.
- Whalen, D. H., Best, C. T., and Irwin, J. (in press). "Perception of American English /l/ allophones," *Haskins Laboratories Status Report on Speech Research*.

# Estimating articulation scores

Christine M. Rankovic and Robin M. Levy

Northeastern University, Department of Speech-Language Pathology and Audiology, 133 Forsyth Building, 360 Huntington Avenue, Boston, Massachusetts 02115

(Received 3 February 1997; revised 30 May 1997; accepted 18 August 1997)

The ability of listeners to estimate articulation scores for lists of nonsense syllables was evaluated. Normal-hearing subjects were presented with lists of from 50 to 60 nonsense syllables that were degraded with various amounts of noise or filtering and were instructed to estimate consonant-correct scores for each condition. To provide a reference for estimating, subjects were shown the accurate orthographic representation of the syllable on a computer monitor to compare with the auditory presentation. The printed version was displayed either simultaneously with the auditory presentation or 500 ms after the offset of the syllable. Estimates were collected on two occasions to examine test–retest reliability, and actual percent-correct scores were obtained to check the accuracy of the estimates. Most subjects overestimated actual scores when the printed representation was provided simultaneously, but estimates were strikingly similar to actual scores when the printed representation was delayed. The delay appeared to prevent the printed representation from favorably biasing the reception of the syllable. The average of two or three estimates gave highly repeatable results for both visual displays. Crossover frequencies derived from the filtered-speech conditions were within the range reported in the literature. This supports the conclusion that subjects based their estimates on the recognition of speech sounds rather than other percepts associated with the speech-in-noise conditions such as loudness of the noise. The estimation procedure permits the collection of articulation scores in much less time than required by traditional test procedures. © 1997 Acoustical Society of America. [S0001-4966(97)03712-0]

PACS numbers: 43.71.Gv, 43.71.Es [WJ]

## INTRODUCTION

A speedy and sensitive speech recognition test is needed to expedite laboratory assessment of speech processing algorithms proposed for hearing aids and for the clinical tasks of hearing aid selection and adjustment. Although digital signal processing allows fine control over acoustical parameters both in laboratories and in many newer hearing aids, traditional word or sentence identification test procedures are too time consuming to evaluate all manipulations of interest because they require collecting written, typed, or spoken responses to each item. Another shortcoming of speech testing is that ceiling and floor effects are encountered frequently and these can obscure meaningful differences between conditions. To avoid these problems, some researchers have adopted procedures in which the intensity level of test items is increased or decreased—depending on the accuracy of the listener's response to the previous item—to track the speech level or speech-to-noise ratio required for 50% recognition (Nilsson *et al.*, 1994; Plomp and Mimpen, 1979). The result is referred to as the speech reception threshold (SRT). Although SRT tests are very quick, they require altering the listening condition and therefore are not applicable when speech recognition in particular fixed conditions is of interest.

This study describes a new speech recognition test procedure that requires the listener to *estimate* the consonant percent-correct score after hearing a list of *nonsense syllables*. Collecting estimates is much quicker than requiring listeners to identify each test item. Nonsense syllable materials were chosen because they have important advantages

over meaningful test materials. They are sensitive over a broader range of conditions than are contextually loaded materials such as sentences (Fletcher and Steinberg, 1929; Miller *et al.*, 1951) or narrative passages (e.g., Speaks *et al.*, 1972) so ceiling and floor effects are encountered less often. Another advantage of nonsense syllables is their relative immunity to learning effects. Test items can be reused because they are not remembered. Nonsense materials are preferable when evaluating communication channels because they are free of the linguistic context that facilitates identification of speech sounds in words or sentences even when the channel fails to transmit the sounds (Fletcher and Steinberg, 1929).

For meaningful speech, intelligibility ratings depend on message comprehension (e.g., Cox and McDaniel, 1989; Speaks *et al.*, 1972), but this reference does not exist for nonsense syllables because they are meaningless. Therefore an alternative reference must be provided to listeners. Here, the auditory presentation of each syllable was supplemented with a visual display that provided the correct orthographic representation either at the same time as the auditory presentation or 500 ms after the offset of the syllable. The delayed condition was included because it seemed likely that the simultaneous presentation of the printed syllable would bias the recognition of syllables toward the printed syllable whereas a delay would allow listeners to perceive the syllable separately from the display.

Subjects were instructed to estimate consonant percent-correct scores for lists of nonsense syllables that were masked by various amounts of broadband noise or were high- or low-pass filtered. The experiment was repeated in

separate sessions to examine the reliability of estimates. Estimated scores were compared with actual consonant percent-correct scores collected from the same subjects to check validity. The filtered-speech experiment was included to further confirm that estimates were based on speech recognition rather than other perceptual attributes that may have been associated with the speech-in-noise conditions, such as the loudness of the noise. Crossover frequencies were derived from the filtered-speech data and compared to those used to derive the band importance weights that are part of articulation theory (Fletcher and Galt, 1950; French and Steinberg, 1947).

## I. METHODS

### A. Subjects

Of the eight female subjects who participated in the experiment, seven were ages 20–24 and one was age 48. Two other subjects did not complete the experiment; their partial data (not reported here) do not contradict the conclusions of this report. All subjects had audiometric thresholds (ANSI, 1969) of 15 dB HL or less at test frequencies 0.25, 0.5, 1, 2, 4, and 8 kHz. Subjects were assigned randomly either to the condition in which the orthographic representation of the nonsense syllable appeared simultaneously with the auditory presentation or to the condition in which it was delayed by 500 ms. These conditions are referred to as “SIMULTANEOUS” and “DELAYED,” respectively. All subjects were students at Northeastern University and were paid for their participation.

Two of the eight subjects had participated with six other subjects in a pilot experiment that evaluated a subset of the speech-in-noise conditions. These two subjects took part in both experiments because they expressed interest and were available. Although they had exposure to the estimation procedures prior to participation in the main experiment, they had never received specific feedback regarding their previous estimates so were not considered to be practiced listeners. Results of the pilot experiment were the same as those of the main experiment and the pilot data are included in the figures whenever applicable.

### B. Equipment and calibration

Subjects were tested individually in a single-walled sound-treated chamber (IAC) situated in a quiet laboratory. Speech was presented to the left earphone of a set of Sennheiser HDA 200 audiometric earphones that are mounted in snug-fitting circumaural cushions.<sup>1</sup> The subject faced a high-resolution, 15-in. computer monitor that was located along with a two-button “mouse” pointing device on a desktop attached to the subject’s chair. Outside the test booth was a 486 66-MHz computer that controlled the subject interface and the equipment for signal generation and presentation (Tucker-Davis Technologies). This included a D/A converter (PD1) and antialiasing filter (FT5) for presentation of speech, a waveform generator that was the source of a broadband masking noise (WG1), a programmable filter used to spectrally shape the noise and to filter the speech (PF1), and two programmable attenuators to control presentation levels

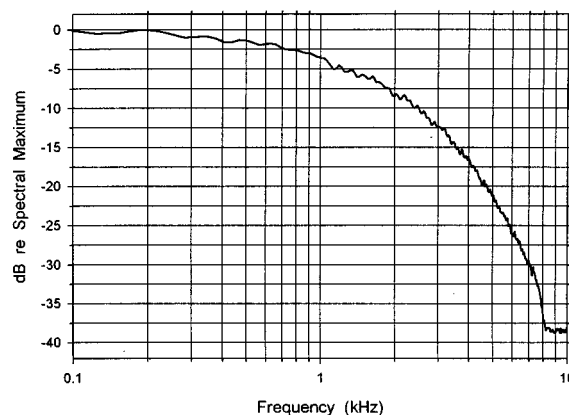


FIG. 1. Spectrum of the noise used in the speech-in-noise experiment.

(PA4). Speech and noise levels and filter characteristics were measured with a Stanford Research Systems 770 Network Analyzer and were checked before and after the experiment.

### C. Speech materials

Speech materials were those described by Rankovic (1989, 1991). Briefly, two female and two male talkers each recited a different list of 57 consonant-vowel-consonant nonsense syllables constructed from the 19 consonants /b, d, f, g, d<sub>3</sub>, k, l, m, n, p, r, s, t, v, z, θ, ð, ʃ, ʒ/ combined with each of the three vowels /a, i, u/. In each talker’s list, each consonant appeared in the initial and final positions with each vowel. The total speech corpus comprised 228 nonsense syllables (4 talkers×57 syllables). Syllables were recorded digitally with 12-bit resolution at a sampling rate of 18.181 kHz and were low-pass filtered at 7.8 kHz prior to presentation to prevent aliasing. Syllables were selected at random with replacement from the entire corpus to construct lists and a new list was assembled for each trial. Lists were never reused, even when identical experimental conditions were repeated to examine the reliability of the estimates. The speech level was fixed at an average overall intensity of 60 dB SPL in the noise condition, and was also 60 dB SPL prior to high- or low-pass filtering.

### D. Noise and filters

A white noise was filtered to approximate a long-term average spectrum of connected speech and is displayed in Fig. 1. The spectrally shaped noise was relatively flat through 1 kHz, decreased at a rate of about 6 dB/oct through 4 kHz, and decreased 20 dB more between 4 and 8 kHz. The noise was attenuated by various amounts and then summed with the speech to achieve 13 speech-to-noise ratios (overall rms-to-rms) (S/Ns) that ranged from –15 dB to +15 dB in 2.5-dB steps.

Low-pass filter cutoff frequencies were 0.25, 0.5, 1, 1.5, 2, and 3 kHz and high-pass filter cutoff frequencies were 1, 1.5, 2, 3, 4, and 5 kHz. These Butterworth IIR filters were provided with the programmable filter. Low-pass filters with cutoff frequencies of 0.25 and 0.5 and the high-pass 1.0-kHz filter had skirts that rolled off at a rate of about 30 dB/oct.

All other filters had rejection rates that were between 50 and 60 dB/oct. A pilot listening test indicated that these filters were adequate for the purposes of the present experiment even though the slopes of their skirts are relatively shallow. Low- and high-pass filtered conditions were randomized together.

### E. Estimation test

Messages on the computer monitor directed the task and subjects used the mouse pointer to initiate trials and enter estimates. Brief printed instructions were read to each subject. The instructions were:

“A list of consonant-vowel-consonant nonsense words will be listed on the screen. Follow these words and estimate what percentage of the consonants you have understood after all words have been presented. Each word contains two consonants highlighted in black. Consider each consonant separately. For example, if you’ve understood all initial consonants and none of the final, your score would be 50 percent.”

The task was then demonstrated by the experimenter. Subjects were given a sheet of paper that listed the alphabetic characters used in the experiment with an example of the sound denoted by each character in a simple word. Subjects made two or three estimates in a demonstration test after which the experimenter answered any additional questions about the task. All subjects were told not to attempt to count up correct or incorrect responses. Rather, they were advised to assign estimates corresponding to their overall impression of their performance based on comparing what was heard over the earphone with the correct orthographic representation displayed on the monitor.

A message on the subject’s monitor instructed the subject to initiate a trial by pressing a button on the mouse pointer. Figure 2 illustrates the SIMULTANEOUS and DELAYED displays. Five light gray columns containing from 10 to 12 stacked rectangles that were approximately 1.8 cm high by 2.8 cm wide appeared on a blue background. The total number of rectangles reflected the total number of syllables comprising a list. Previous experience with the same speech materials indicated that articulation scores collected for lists of 57 items are sensitive to noise-masked and filtered conditions similar to those used here (Rankovic, 1989). For the estimation procedure, the list length was varied randomly from 50 to 60 items to deter subjects from attempting to calculate actual articulation scores and this accounts for the variation in column length in the display.

For the SIMULTANEOUS display (Fig. 2, top), the rectangles contained the orthographic representation of each nonsense syllable. The alphabetic characters were about 0.6 cm high and consonants and vowels were depicted in black and light blue, respectively, thereby highlighting the consonants. Syllables were played out in the order they appeared on the screen beginning at the top of the left-most column and continuing down each column until all syllables were presented. A bright green arrow pointed to each syllable as it

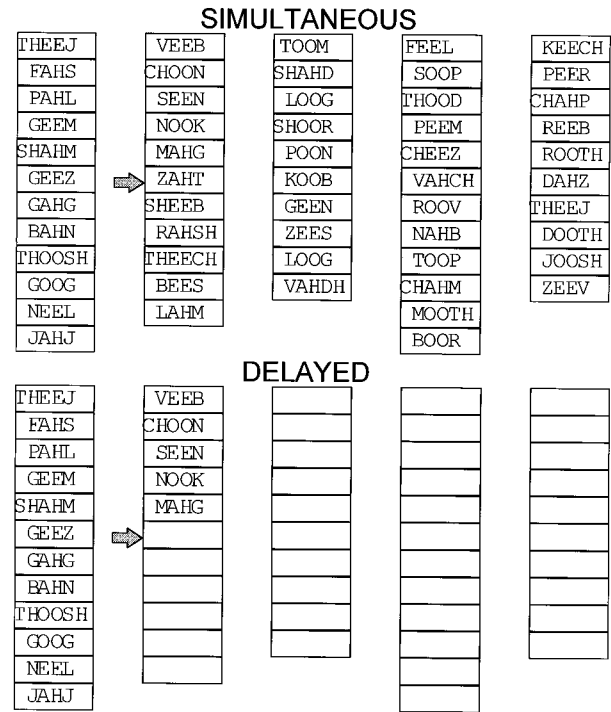


FIG. 2. Subjects’ visual display for SIMULTANEOUS (top) and DELAYED (bottom) conditions. The syllable [zat] is being delivered over the earphone at the moment captured here. See text for details.

was played over the earphone. Syllables were presented one immediately following another, and so were effectively concatenated.

The display for the DELAYED condition was identical except that columns of rectangles did not contain orthographic representations of the syllables initially: they were empty (Fig. 2, bottom). The green arrow pointed to a blank rectangle beginning at the top of the left-most column, a syllable was played over the earphone, and, after a 500-ms delay, the printed representation of the syllable appeared in the blank rectangle. After another 500-ms delay, the green arrow moved to the next empty rectangle and the task repeated until all rectangles were filled with printed representations of the syllables that had been played out.

After a list of syllables was presented, the screen was cleared and a percentage scale appeared on a light gray background. The scale was a magenta horizontal bar that was 3-cm high with equally spaced yellow tick marks at each percentage point and numeric labels every ten percentage points (e.g., 0,10,20,...,100). The tick marks located at multiples of 5% and 10% were longer than those at intermediate percentages for visual ease. As the mouse pointer was moved, the position of a blue screen cursor moved along the scale. A number corresponding to the highlighted tick mark appeared in a box directly above the percentage scale. Pressing the left mouse button locked the cursor onto the selected percentage. Changing the selected percentage required the subject to hold down the left mouse button while sliding the mouse to position the cursor over the new selection. The screen contained only a portion of the scale at any time so



that the scale was large enough to assure easy selection of percentages with the mouse pointer. The portion of the scale shown was either the range from 0% to 70% or from 30% to 100%. When necessary, the subject changed the range by moving the cursor to the appropriate end of the scale. Pressing the right mouse button recorded the estimate and cleared the screen except for a message instructing the subject to initiate another trial by pressing the right mouse button. No time limits were imposed and no feedback was provided to subjects. For the SIMULTANEOUS condition, the presentation of a list and collection of the estimate took approximately 1 min. Each estimate in the DELAYED condition was collected in approximately 2 min.

Each subject made a total of 78 estimates for the speech in noise experiment (3 estimates  $\times$  13 speech-to-noise ratios  $\times$  2 sessions) and 72 estimates for the filtered-speech experiment (3 estimates  $\times$  12 filter settings  $\times$  2 sessions). Three estimates for each of the speech-in-noise conditions were collected first, then three estimates for each of the filtered-speech conditions, then each set of conditions was repeated to check reliability. Each subject was presented with a different random order of the trials except that the first two trials in the speech-in-noise condition were always the highest speech-to-noise ratio (+15 dB); this was an effort to ease subjects into the task. No more than two consecutive trials consisted of identical conditions.

## F. Articulation test

Actual consonant percent-correct scores were collected for all conditions after all estimates were collected. Procedures were identical to those reported by Rankovic (1989, 1991). Briefly, subjects responded to each nonsense syllable by marking an initial consonant, a vowel, and a final consonant displayed on the computer monitor by manipulating the mouse pointer. No feedback was provided. Articulation scores presented here represent scoring the consonants in one list of 57 nonsense syllables (114 consonants), approximately the same number of syllables presented for each estimate. It took 6–8 min to collect each articulation score.

Altogether, subjects participated in from two to four sessions that were from 0.45–2.5 h for the estimation test and two additional 2-h sessions for the articulation tests. Some subjects preferred to separate the four parts of the estimation experiment into four separate sessions due to scheduling conflicts or to prevent boredom. Other subjects finished the estimation experiment in two sessions by completing both a speech-in-noise and a filtered-speech condition during each visit. Subjects took frequent breaks as needed.

## II. RESULTS AND DISCUSSION

Subjects expressed that the estimation procedures were very easy to follow. Those who were asked confirmed that they were not scoring correct/incorrect recognition to arrive at estimates. Examination of individual estimates indicated that all subjects took advantage of the 1% increments available on the percentage scale although there was a strong tendency to select percentages that were multiples of 5%.

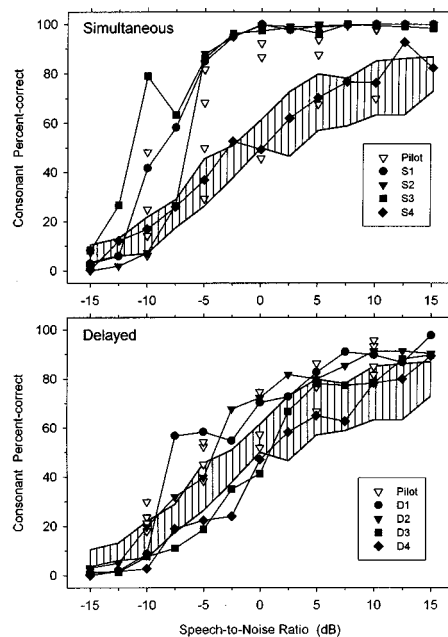


FIG. 3. Estimated consonant-correct scores (symbols) and actual scores (shaded range) for speech-in-noise conditions. Filled symbols are estimates of subjects participating in the main experiment. Open inverted triangles represent data from four subjects who participated in the pilot experiment.

## A. Speech in noise

### 1. Accuracy of estimates

Figure 3 shows estimated consonant percent-correct scores (symbols) and actual scores (shaded range) for the noise-masked conditions. The top and bottom panels are for the SIMULTANEOUS and DELAYED display conditions, respectively. Each data point represents the average of the first three estimates made by each subject at each S/N. Filled symbols represent estimates obtained in the main experiment and open inverted triangles represent data from the pilot experiment. The pilot experiment included the S/Ns  $-15$ ,  $-10$ ,  $-5$ ,  $0$ ,  $5$ , and  $10$  dB only. Shaded regions show the range of actual percent-correct scores collected from all eight subjects participating in the main experiment. The shaded range is identical in the two panels.

In the SIMULTANEOUS condition (Fig. 3, top panel), some subjects overestimated scores particularly for S/Ns higher than  $-7.5$  dB where estimated scores reached a ceiling at 100% that did not exist for actual scores. Two subjects (S4 and a subject who participated in the pilot experiment) did not overestimate; their data fall within the shaded range at almost all S/Ns. Their performance suggests that it is possible to discriminate conditions in the region of the ceiling. However, this appears to require a different listening strategy than that adopted by most of the subjects.

In the DELAYED condition (Fig. 3, bottom panel), the range for estimated scores is surprisingly similar to the range for actual scores. Except at the lowest and highest S/Ns ( $-15$ ,  $-12.5$ , and  $+15$  dB), the range of estimated scores overlaps with the range of actual scores. There is some tendency to overestimate scores for S/Ns greater than  $2.5$  dB. The underestimates at S/Ns of  $-15$  and  $-12.5$  dB in both SIMULTANEOUS and DELAYED conditions are elimi-

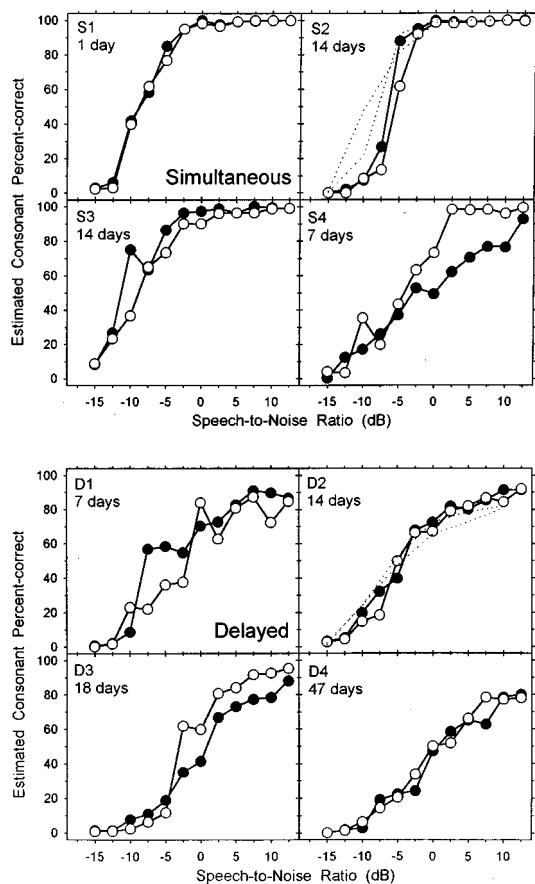


FIG. 4. Estimated consonant-correct scores for speech-in-noise conditions collected on two separate occasions. Filled and open symbols indicate the first and second sessions, respectively. Dotted lines are from data collected in a pilot experiment and appear in the panels of the two subjects who participated in the pilot experiment (S2 and D2). Duration between sessions is indicated in each panel.

nated if the actual scores are corrected for chance performance (Clarke, 1960) which is 5% for this test. The dramatic difference in performance found among the four subjects exposed to the SIMULTANEOUS condition was not observed for the four subjects exposed to the DELAYED condition.

The type of visual display had a strong influence on estimates. The DELAYED display is clearly superior because estimates reflect actual scores. When presented with the SIMULTANEOUS display, three of the four subjects were inclined to overestimate scores at mid and high S/Ns, but not at low S/Ns. Therefore the influence of the SIMULTANEOUS display on estimated scores varied with S/N. Scores were underestimated infrequently and only by very small amounts.

## 2. Reliability of estimates

Figure 4 contains estimated scores collected during two separate sessions for individual subjects. The top and bottom groupings of panels provide the results for the SIMULTANEOUS and DELAYED display subject groups, respectively. Filled and open circles represent the average of estimates collected during the first and second sessions (three estimates per session), respectively. Dashed lines are estimates from the pilot experiment and appear in the panels of

the two subjects who participated in both experiments. The time between sessions is indicated in each panel and ranged from 1 to 47 days.

Three aspects of the data are of interest: (1) the test-retest reliability of estimates; (2) the slopes of the functions; and (3) the monotonicity of the functions. Estimates are highly repeatable over time irrespective of which display was supplied. This was demonstrated by all subjects in the pilot experiment as well. Excellent reliability was demonstrated by subjects S1, S2, S3 (except at S/N = -10 dB), D2, and D4. Subject S4 shows the poorest reliability. Both functions for S4 exhibit more gradual slopes than those of other subjects in the SIMULTANEOUS group. S4 assigned scores near 100% for S/Ns higher than 0 dB during the second session, suggesting a change in the criteria for estimating.

When measured on the steep part of these functions, estimated articulation scores rise at a rate of approximately 12% per dB for the SIMULTANEOUS condition (excluding S4), similar to the slope found for sentences materials (Speaks *et al.*, 1967). Functions were less steep for the DELAYED condition, approximately 4% per dB. The shallower slopes are consistent with the slope of the function for actual scores and demonstrate that the DELAYED test is sensitive to a broader range of S/Ns than the SIMULTANEOUS test.<sup>2</sup>

Monotonic growth of estimates with S/N was expected because it was observed for the actual articulation scores. We defined "nonmonotonicity" conservatively, as a decrease in estimated score of 2.5% or more when the estimate should have remained the same or increased. Considered over all subjects, there were 4 nonmonotonicities out of a possible 96 in the first session (subject S3 at S/N = -7.5 dB; S4 at S/N = 0 dB; and D1 at S/N = -2.5, 12.5 dB) and 4 occurrences in the second session (subject S4 at S/N = -7.5 dB; and D1 at S/N = 2.5, 10, 12.5 dB). For comparison, there were five occurrences in the actual articulation scores (subject S1 at S/N = 5, 12.5 dB; S3 at S/N = 7.5 dB; S4 at S/N = 10 dB; and S2 at S/N = 2.5 dB). Overall, then, monotonicity is a strong feature of the individual subject data and there were no more nonmonotonicities in functions derived from the average of three estimates than from functions derived from actual scores. Monotonicity is so strong in the estimated-score functions that it is likely that differences in S/N smaller than 2.5 dB could be resolved easily.

## B. Filtered speech

When articulation scores are plotted as a function of filter cutoff frequency, the location of the crossover of high- and low-pass functions provides an indication of the contribution of different frequency regions to speech recognition (Fletcher and Galt, 1950; French and Steinberg, 1947). The crossover frequency for nonsense syllable materials is known to lie roughly between 1.5 and 2 kHz (Fletcher and Galt, 1950; French and Steinberg, 1947). If the crossover frequency for estimated scores lies within this range, it would support the contention that estimates reflect speech sound recognition rather than, say, loudness or other perceptual attributes that may have served as the basis for assigning estimates in the speech-in-noise conditions.

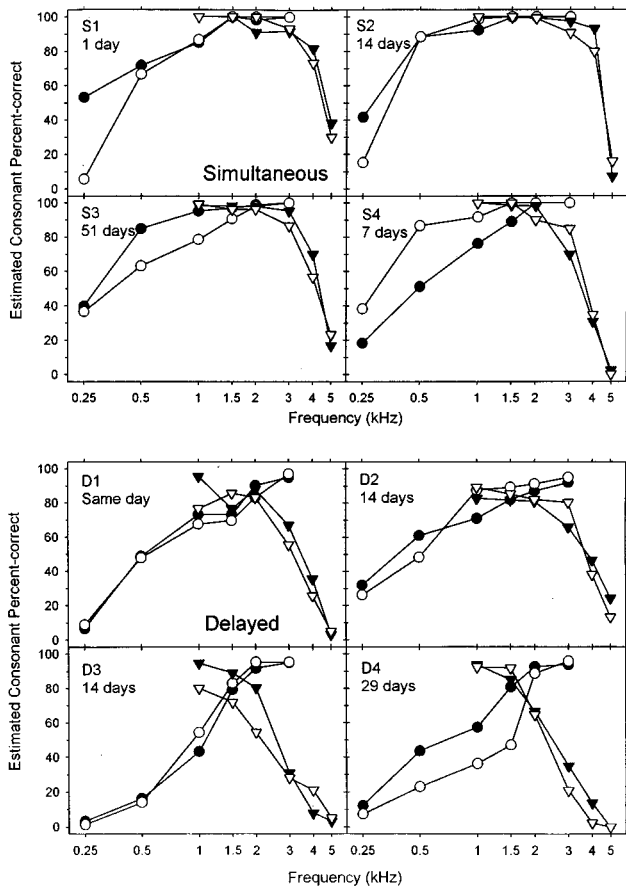


FIG. 5. Estimated consonant-correct scores for filtered-speech conditions collected on two separate occasions (except for subject D1 for whom the filtered-speech experiment was repeated on the same day). Filled and open symbols indicate the first and second sessions, respectively. Scores for low-pass conditions are indicated by circles and scores for high-pass conditions are indicated by inverted triangles.

### 1. Reliability of estimates

Estimated consonant-correct scores for filtered speech conditions are plotted in Fig. 5. The format of Fig. 5 is comparable to that of Fig. 4. Filled and open symbols represent the average of three estimates obtained from the first second repetitions of the filtered-speech conditions, respectively. Subject D1 repeated the filtered-speech experiment on the same day, separated in time by the second speech-in-noise session. Low-pass functions are indicated by circles and high-pass functions are indicated by inverted triangles. The repeatability of estimated scores was surprisingly good and similar to that observed for the speech-in-noise experiment. The exceptions were subjects S1 (low-pass 0.25 kHz), S3 (low-pass 0.5 and 1 kHz), S4 (low-pass 0.25, 0.5, and 1 kHz), D3 (high-pass 1, 1.5, and 2 kHz), and D4 (low-pass 0.5, 1, and 1.5 kHz). The exceptions tended to occur for low-pass conditions.

### 2. Crossover frequency

The SIMULTANEOUS and DELAYED estimated scores and actual consonant-correct scores are plotted together in Fig. 6 so that crossover frequencies can be compared. The heavy and thin lines represent estimates assigned

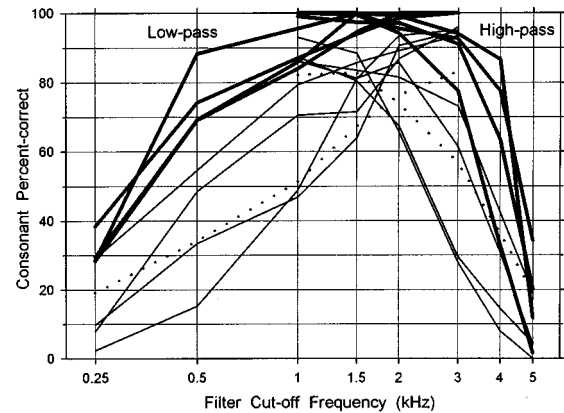


FIG. 6. Estimated consonant-correct scores (solid lines) and actual scores (dotted lines) for filtered-speech conditions. Heavy and light solid lines are results from individual subjects presented with the SIMULTANEOUS and DELAYED displays, respectively. Vertical grid lines mark filter cutoff frequencies used in the experiment.

by individual subjects in the SIMULTANEOUS and DELAYED groups, respectively. These lines were constructed from averages of all six estimates collected in each condition so that the crossover frequency is reflected as accurately as possible. The dotted lines represent the average of the actual articulation scores collected from all eight subjects.

The range of actual articulation scores obtained for each filtered-speech condition is provided separately in Table I. The range is comparable in size to the range observed for the noise-masked conditions (cf. Fig. 3). It overlaps with the range of estimates obtained with the DELAYED display except for the low-pass 2- and 3-kHz conditions in which subjects overestimated scores. Subjects presented with the SIMULTANEOUS display assigned estimates that were substantially higher than subjects presented with the DELAYED display for all filtered speech conditions. The relationships between SIMULTANEOUS, DELAYED, and actual articulation scores are consistent with the results for noise-masked speech reported above.

The average crossover frequency for both display conditions is the same, approximately 1.7 kHz with average estimated scores of 98% for the SIMULTANEOUS group and 80% for the DELAYED group. The crossover frequency for actual articulation scores is higher than for estimated scores, about 1.9 kHz at a score of 75%. The crossover frequencies for estimates are within the range expected for nonsense syl-

TABLE I. Lowest and highest actual articulation scores (percent-correct) for filtered-speech conditions.

Cutoff (kHz)	Low pass		High pass		
	Low	High	Cutoff (kHz)	Low	High
0.25	14	28	1	75	90
0.5	25	39	1.5	73	90
1	41	60	2	68	82
1.5	61	81	3	43	67
2	69	87	4	15	55
3	77	90	5	7	25

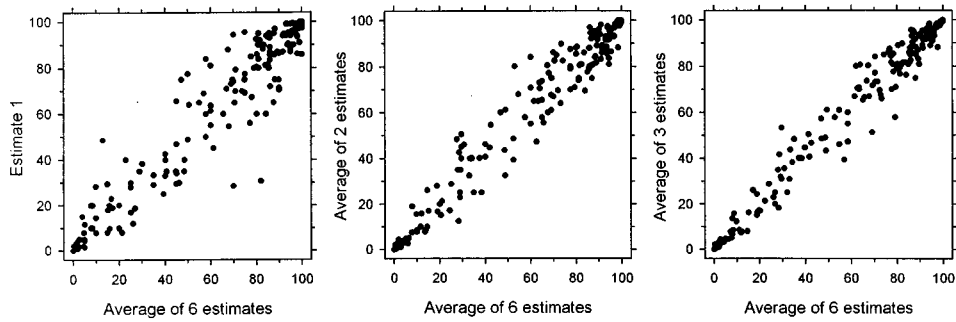


FIG. 7. Relationship between the average of six estimates and (from left to right) the first estimate, the average of the first two estimates, and the average of the first three estimates. Estimates from all test conditions (SIMULTANEOUS and DELAYED, speech-in-noise, and filtering) are included.

lables. The similarity between crossover frequencies reported here and those reported in the literature provides evidence that speech sound reception is the basis for estimating. The filtered-speech results also demonstrate that the estimation procedure is sensitive to a form of distortion other than additive noise.

### C. Minimum number of estimates

The most representative estimated score from individual subjects in each condition is the average of all six estimates made in that condition. However, the results depicted in Figs. 3–5 suggest that as few as three estimates can yield scores that are repeatable and sensitive to differences in the test conditions in this report. A correlation analysis was conducted in an effort to determine whether fewer than three estimates would yield similarly stable estimated scores. The average of all six estimates was correlated with: (1) the first estimate, (2) the average of the first two estimates, and (3) the average of first three estimates. Although correlating parts with wholes is unusual, it is appropriate within the context of the present experiment under the assumption that the experimenter will average together all estimates that are collected.

Figure 7 displays these comparisons for all data collected in the main experiment. The reduction in scatter of the data in the three panels when viewed from left to right suggests that averaging more estimates is better, and this is an inevitable outcome of this type of comparison. The interesting finding in Fig. 7 is that the relationships depicted in each panel appear to be all quite strong. Before calculating correlation coefficients, data points near 0% and 100% were excluded because there was an excessive number of estimates in these regions (attributable to estimates assigned in the SIMULTANEOUS conditions) and this yielded correlation coefficients very near 1.0 for all comparisons. Data points were excluded if either abscissa or ordinate values were less than 10% or greater than 90%. This rule eliminated approximately half of the data points shown in Fig. 7.

Correlation coefficients for the remaining data are presented in Table II. Results indicate that both the averages of two and of three estimates are highly correlated with the average of six estimates. The higher correlation for three estimates indicates that there is an advantage to collecting the additional estimate. However, the conclusions drawn ear-

lier about the data shown in Figs. 3–5 would not be different had they been based on two rather than three estimates. That is, estimated scores based on the average of two or even on a single estimate are very repeatable and functions are strongly monotonic according to the definition stated earlier. For the speech-in-noise data (both SIMULTANEOUS and DELAYED displays), there were only eight instances of non-monotonicity in individual-subject functions constructed from the first estimate alone and seven in functions constructed from the average of the first two estimates. As stated earlier, there were four instances for functions defined by the average of three estimates. Based on inspection of the data, the main advantage of averaging three estimates appears to be to reduce the impact of the occasional very poor estimate. Experimenters who use the test procedures similar to those described here can determine for themselves whether the time it takes to collect the additional estimates is worthwhile for their applications.

### D. Further remarks on estimation procedures

Two features of the procedures may explain the surprising stability of the estimated scores. The percentage scale used here is fine grained and familiar to subjects. Other rating tests use coarser scales such as integers in the range from 0–10 (Cox and McDaniel, 1989), thereby fixing the precision of estimates *a priori*.

More significant is the contribution of the visual display. The correct orthographic representation of the syllable served as a precise external reference on which to base estimates. Other rating procedures rely on internal references consisting of sensory evidence as well as a host of other

TABLE II. Pearson product moment correlations ( $r$ ) of the average of six estimates with (1) the first estimate, (2) the average of the first two estimates, and (3) the average of the first three estimates. Consonant-correct estimates less than 10% or greater than 90% were excluded from the analysis because there was an excessive number of these estimates. Estimates were arcsine transformed before submission to the correlation. Pairs of scores were treated as if they were independent.

Number of estimates averaged	$N$	$r$
1 versus 6	89	0.834
2 versus 6	96	0.916
3 versus 6	98	0.940

factors including contextual evidence, knowledge of the language and of the world (Boothroyd, 1993), and other cognitive and psychological factors that influence how individual listeners consider and combine the information available in the test situation. Although these factors are integral to speech understanding in typical listening situations, the internal reference is inherently less stable than an external reference due to uncertainty regarding the intended message. The procedures presented here were designed to minimize the contribution of linguistic, cognitive, and psychological factors by using meaningless speech materials and by removing doubt about the identity of the test items.

### III. CONCLUSIONS

There are three categories of speech recognition tests that yield percent-correct scores. Traditional procedures involve presenting a list of speech items to the listener for identification and this yields a percent-correct score (Fletcher and Steinberg, 1929). In SRT tests, the listener or the experimenter adapts the speech or noise intensity levels to find the S/N that yields a predetermined percent-correct score. This report introduces a third type of test procedure that requires listeners to estimate the percent-correct score for consonants in lists of nonsense syllables based on comparing the auditory presentation to the correct orthographic representation of the syllable. The results demonstrate for nonsense syllables a phenomenon that Speaks *et al.* (1972) observed for sentence materials (with no visual display): that untrained listeners have a remarkable ability to accurately estimate speech recognition on a percentage scale. Furthermore, results demonstrate that speech tests that incorporate this ability can be quick, reliable, and sensitive if nonsense syllables are used. Additional evaluations of the test procedures using a larger, less homogeneous population are necessary to verify the findings reported here. The most efficient test parameters for laboratory or clinical assessment of hearing aid benefit have yet to be determined.

### ACKNOWLEDGMENTS

The authors wish to thank all of the subjects for their cooperation and Gregory L. Lof for helpful suggestions regarding the design and functioning of the visual display. This work was supported by Grant No. R29 DC02127 from the National Institute on Deafness and Other Communication Disorders (National Institutes of Health).

<sup>1</sup>Sound pressure levels produced by the Sennheiser HDA 200 earphone were deduced from the manufacturer's specification sheet provided with the earphones. To verify specification sheet values, the HDA 200 earphones were

calibrated against TDH-50P earphones by collecting pure-tone audiometric thresholds from 20 subjects with each set of earphones and examining the threshold differences. Thresholds were measured with a Grason-Stadler GS10 audiometer in an IAC double-walled sound-treated chamber. Average threshold differences were in agreement with differences expected based on the specification sheets. It is noteworthy that average thresholds with the HDA 200 earphones were 12 and 4 dB lower at 0.25 and 0.5 kHz, respectively, than thresholds obtained with the TDH-50P earphones. This presumably reflects the difference between the HDA 200's circumaural cushion (Peltor brand ear protectors) and the TDH-50P's supra-aural cushion (MX-41/AR).

<sup>2</sup>The SIMULTANEOUS display condition is intriguing not only for its speed, but also because concatenated syllables are a form of connected speech that may be useful for evaluating temporal distortions such as reverberation or compression. As mentioned earlier, two subjects demonstrated that it was possible to estimate accurately in the SIMULTANEOUS condition. Therefore, we attempted to increase the accuracy of the estimated scores for one of these "less-discriminating" subjects through training. After completing the main experiment, S2 returned for an additional session in which we "calibrated" her in the speech-in-noise conditions by printing a 10 percentage-point-wide range of actual scores on the screen after she entered each estimate. After 30 min of training, new estimates were collected in the filtered-speech conditions *without feedback*. S2's new estimates were much more in line with actual scores. In particular, conditions that were assigned 100% prior to training were now assigned much lower scores and were differentiated and ordered like the actual scores. The behavior persisted in a second test session conducted two weeks later in which S2 was asked to recall her performance after training. This type of "calibration" of listeners may be appropriate in certain test situations.

- ANSI (1969). ANSI S3.6-1969, "American National Standards Specifications for Audiometers (American National Standards Institute, New York).
- Boothroyd, A. (1993). "Speech perception, sensorineural hearing loss, and hearing aids," in *Acoustical Factors Affecting Hearing Aid Performance*, 2nd ed., edited by G. A. Studebaker and I. Hochberg (Allyn and Bacon, Boston).
- Clark, F. R. (1960). "Confidence ratings, second-choice responses, and confusion matrices in intelligibility tests," *J. Acoust. Soc. Am.* **32**, 35–46.
- Cox, R. M., and McDaniel, M. (1989). "Development of the Speech Intelligibility Rating (SIR) test for hearing aid comparisons," *J. Speech Hear. Res.* **32**, 347–352.
- Fletcher, H., and Galt, R. H. (1950). "The perception of speech and its relation to telephony," *J. Acoust. Soc. Am.* **22**, 89–151.
- Fletcher, H., and Steinberg, J. C. (1929). "Articulation testing methods," *Bell Syst. Tech. J.* **8**, 806–854.
- French, N. R., and Steinberg, J. C. (1947). "Factors governing the intelligibility of speech sounds," *J. Acoust. Soc. Am.* **19**, 90–119.
- Miller, G. A., Heise, G. A., and Lichten, W. (1951). "The intelligibility of speech as a function of the context of the test materials," *J. Exp. Psychol.* **41**, 329–335.
- Nilsson, M., Soli, S. D., and Sullivan, J. A. (1994). "Development of the Hearing In Noise Test for the measurement of speech reception thresholds in quiet and in noise," *J. Acoust. Soc. Am.* **95**, 1085–1099.
- Plomp, R., and Mimpen, A. M. (1979). "Improving the reliability of testing the speech reception threshold for sentences," *Audiology* **18**, 43–52.
- Rankovic, C. M. (1989). "An application of the articulation index to hearing aid fitting," Doctoral dissertation, University of Minnesota, Minneapolis.
- Rankovic, C. M. (1991). "An application of the articulation index to hearing aid fitting," *J. Speech Hear. Res.* **34**, 391–402.
- Speaks, C., Parker, B., Harris, C., and Kuhl, P. (1972). "Intelligibility of connected discourse," *J. Speech Hear. Res.* **15**, 590–602.

# Central auditory system plasticity: Generalization to novel stimuli following listening training

Kelly Tremblay<sup>a)</sup>

Department of Communication Sciences and Disorders, Auditory Neuroscience Laboratory,  
Northwestern University, 2299 N. Campus Drive, Evanston, Illinois 60208-3540

Nina Kraus

Department of Communication Sciences and Disorders, Auditory Neuroscience Laboratory, Northwestern  
University, 2299 N. Campus Drive, Evanston, Illinois 60208-3540 and Departments of Neurobiology  
and Physiology, and Otolaryngology, Northwestern University, Chicago, Illinois 60208-3540

Thomas D. Carrell

Department of Communication Disorders, University of Nebraska, Lincoln, Nebraska 68588

Therese McGee

Department of Communication Sciences and Disorders, Auditory Neuroscience Laboratory,  
Northwestern University, 2299 N. Campus Drive, Evanston, Illinois 60208-3540

(Received 3 June 1996; revised 17 June 1997; accepted 5 August 1997)

Behavioral perceptual abilities and neurophysiologic changes observed after listening training can generalize to other stimuli not used in the training paradigm, thereby demonstrating behavioral “transfer of learning” and plasticity in underlying physiologic processes. Nine normal-hearing monolingual English-speaking adults were trained to identify a prevoiced labial stop sound (one that is not used phonemically in the English language). After training, the subjects were asked to discriminate and identify a prevoiced alveolar stop. Mismatch negativity cortical evoked responses (MMN) were recorded to both labial and alveolar stimuli before and after training. Behavioral performance and MMNs also were evaluated in an age-matched control group that did not receive training. Listening training improved the experimental group’s ability to discriminate and identify an unfamiliar VOT contrast. That enhanced ability transferred from one place of articulation (labial) to another (alveolar). The behavioral training effects were reflected in the MMN, which showed an increase in duration and area when elicited by the training stimuli as well as a decrease in onset latency when elicited by the transfer stimuli. Interestingly, changes in the MMN were largest over the left hemisphere. The results demonstrate that training can generalize to listening situations beyond those used in training sessions, and that the preattentive central neurophysiology underlying perceptual learning are altered through auditory training. © 1997 Acoustical Society of America. [S0001-4966(97)00912-0]

PACS numbers: 43.71.Pc [WS]

## INTRODUCTION

The auditory cortex is plastic, that is, it is capable of reorganization as a function of experience. This fact has been well documented by animal experiments, and by human behavioral and electrophysiologic studies. For example, single- and multiple-unit recordings from mammalian cortical neurons show learning-induced changes in the auditory cortex (Buchwald *et al.*, 1966; Olds *et al.*, 1972; Kraus and Disterhoft, 1982; Diamond and Weinberger, 1984, 1986, 1989; Bakin and Weinberger, 1990; Recanzone *et al.*, 1993; Edeleine *et al.*, 1993; Weinberger, 1993). In humans, Näätänen *et al.* (1993) have reported learning-related neurophysiologic changes reflected in a far-field electrophysiologic response called the mismatch negativity (MMN). They showed that the MMN changed following discrimination training using

tonal stimuli. Similarly, Kraus *et al.* (1995a) demonstrated learning-related changes in the MMN when elicited by synthetic speech stimuli.

The MMN is an auditory-evoked response that reflects preattentive discrimination of acoustic signals (Näätänen *et al.*, 1978; Sams *et al.*, 1985; Näätänen and Picton, 1987; Scherg and Picton, 1990; Giard *et al.*, 1990; Csépe *et al.*, 1987). The MMN is elicited by a rarely occurring stimulus when it is presented within a series of homogeneous stimuli (Näätänen *et al.*, 1978). Animal and human studies indicate that the encoding of different acoustic cues important for speech perception involve distinct neuroanatomic and neurophysiologic processes (Blackburn and Sachs, 1990; Delgutte and Kiang, 1984; Steinschneider *et al.*, 1982, 1990) and that the MMN can be used to probe the neurophysiologic encoding of essential speech features (McGee *et al.*, 1996; Micco *et al.*, 1995; Csépe, 1995; Sharma *et al.*, 1995; Kraus *et al.*, 1993, 1994a, 1994b, 1995b, 1996).

The Näätänen *et al.* (1993) and Kraus *et al.* (1995a) findings suggest that changes in the MMN reflect experience-related changes in central auditory processing of

<sup>a)</sup>Present address: House Ear Inst., Electrophysiology Lab., 2100 West Third St., Los Angeles, CA 90069.

complex signals such as speech. However, in those studies, subjects were trained and tested using the same stimuli. What is of great interest is if changes in stimulus representation are limited to the stimuli used in training, or whether the changes in acoustic representation at a preattentive level will generalize to novel stimuli with acoustic properties similar to the trained stimuli. This “transfer of learning” is important from a clinical perspective because it is important to know if efforts at (re)habilitation using auditory training will generalize beyond the training sessions to other listening events.

Behavioral evidence of “transfer of learning” already has been established in the speech-learning literature. For example, McClaskey *et al.* (1983) found that adult listeners generalized their newly acquired ability to perceive prevoiced labial syllables to prevoiced alveolar phonemes. However, little is known about the neurophysiologic changes associated with such learning and transfer of learning.

Consequently, this study combined the behavioral approaches of Pisoni *et al.* (1982) and McClaskey *et al.* (1983) with the neurophysiological approach used by Näätänen *et al.* (1993) and Kraus *et al.* (1995a) to explore whether behavioral training modified the neurophysiologic representation of speech, and to test the hypothesis that neurophysiologic modification is not limited to the stimuli used to establish the change. Specifically, this study was designed to determine if surface-recorded mismatch negativity responses in humans reflect behavioral changes in perception following training, and whether “transfer of learning” is evident behaviorally and neurophysiologically in response to novel speech contrasts having an equivalent voice-onset-time distinction but a different place of articulation.

## I. METHODS

### A. Subjects

The subjects were 18 normal hearing, right-handed monolingual speakers of English. Normal hearing was defined as pure tone sensitivity better than or equal to 20 dB HL bilaterally for octave frequencies between 250 Hz and 8 kHz. All subjects were born into monolingual English-speaking households and had less than five years of exposure to a foreign language(s) in school. Each subject was randomly assigned to either an experimental or control group. The mean age for the control group was 21 years with an age range of 18–28 years. The mean age for the experimental group was 22 years with an age range of 18–26 years.

### B. Stimuli

The stimuli were synthesized tokens modeled after those used by McClaskey *et al.* (1983). Labial (/ba/–/pa/) and alveolar (/da/–/ta/) continua were created in which voice-onset-time (VOT) varied from –50 ms to +50 ms in 10-ms steps. Therefore, each continuum consisted of eleven items. The VOT is defined as the interval between the release from stop closure and the onset of laryngeal pulsing. A negative VOT indicates laryngeal pulsing during the stop closure period before the release. The stimuli were generated using a Klatt digital speech synthesizer (Klatt, 1980).

The steady-state portion of the stimuli consisted of the vowel /a/, which varied in duration relative to the VOT so that the overall duration for each stimulus remained constant at 180 ms. The formant values for this vowel were:  $F1 = 700$  Hz,  $BW1 = 90$  Hz;  $F2 = 1200$  Hz,  $BW2 = 90$  Hz;  $F3 = 2600$  Hz,  $BW3 = 130$  Hz,  $F4 = 3300$  Hz,  $BW4 = 400$  Hz;  $F5 = 3700$  Hz,  $BW5 = 500$  Hz. The fundamental frequency of the stimuli began at 120 Hz and then fell to 100 Hz during the steady-state portion of the vowel. The labial formant transitions were 40 ms in duration. The alveolar formant transitions were 50 ms in duration. To simulate a burst, a turbulent noise source (AF) 10 ms in duration and 60 dB in amplitude was added to both bilabial and alveolar stimuli. The spectrum of the burst was centered around 2500–4000 Hz.

Because the MMN is elicited by any acoustic change, we chose to use synthetic rather than natural speech in order to precisely control the acoustic parameters and to determine systematically which acoustic dimension was reflected in the MMN. The use of natural speech would have complicated the interpretation because natural speech contains many simultaneously changing parameters that might be reflected in the MMN.

### C. Procedure

The entire testing procedure took nine days for each individual. The experimental and control group participated in exactly the same testing on days 1, 2, 8, and 9. The only difference was that the experimental group participated in training sessions on days 3–7 whereas the control group did not receive any training.

#### 1. Day 1

*a. Electrophysiology baseline.* Baseline MMN responses were obtained on the first day for both the experimental and control groups in response to the two stimulus pairs; the training stimuli (labial) and the transfer stimuli (alveolar). The –10-ms VOT stimulus (either labial or alveolar) was the standard stimulus (frequency of occurrence = 85%) and the –20-ms VOT stimulus (either labial or alveolar) was the deviant stimulus (frequency of occurrence = 15%). The stimuli were presented in a pseudorandom sequence with at least three standard stimuli separating presentations of deviant stimuli (oddball paradigm). Although 3500 standard stimuli were presented, the responses to the standard stimuli following each deviant were not included in the averaged response. In an “alone” condition, 1000 presentations of the deviant stimulus were presented alone for comparison with the response to that same stimulus when it was the deviant stimulus in the oddball paradigm. The rationale for using a deviant-stimulus-alone control condition is reviewed by Kraus *et al.* (1995b). The order of labial and alveolar presentation was counterbalanced across subjects to prevent any potential order effects. For each individual, the order of stimulus presentation was the same before and after training.

All subjects were tested in a sound-treated booth. The stimuli were presented monaurally to the right ear using Etymotic Research (ER3) insert earphones. Subjects were instructed to ignore the stimuli. To ensure that the subject was

not attending to the stimuli, each subject watched a videotape of his or her choice. The test stimuli were presented at 74 dB SPL while the background videotape sound, presented in free field, was 40 dB SPL.

Previous studies by Näätänen *et al.* (1993) and Kraus *et al.* (1995a) recorded over the midline of the scalp only and therefore did not report topographical distributions of MMN change. This study included nine active electrode locations. Active electrodes were placed at Fz, Cz, Pz, over the frontal lobes (*F3* and *F4*), temporal lobes (TL and TR), and mastoids (A1 and A2). Electrode TR was situated halfway between T4 and T6. Electrode TL was situated half way between T3 and T5 according to the International 10/20 recording system (Jasper, 1958). A nose electrode served as the reference and a forehead electrode served as ground. Eyeblink activity was monitored using electrodes located on the superior and outer canthus of one eye. Artifacts measuring in excess of 100  $\mu\text{V}$  on the EOG channel were rejected off-line during data processing.

Each individual's grand-averaged "difference" wave was calculated by subtracting the average response to the deviant stimulus when presented alone from the response to the same stimulus when it was presented in the oddball paradigm. The MMN onset latency, duration, and area were measured from the individual subject grand-averaged difference wave. Latency was measured between 120 and 500 ms. Duration was defined as the offset minus the onset latency. The MMN area was calculated by drawing a line between the onset and offset of the MMN in the difference wave, and determining the number of  $\text{ms} \times \mu\text{V}$ .

Individual grand averages were averaged together for each group. Group MMN onset latency, duration, and area measurements were calculated using the same methods. The present study intentionally focused on group effects. To date, methods for statistically defining the MMN in individuals are evolving (McGee, 1997a, 1997b). Extracting the MMN signal from noise in individual responses has been a longstanding methodological issue.

## 2. Day 2

*a. Behavioral baseline: Discrimination testing.* During behavioral tests, subjects were seated in a sound-treated booth in front of a computer monitor which provided visual instructions to the subjects. Subjects in both the experimental and control groups were instructed to listen to two stimuli and to indicate whether the stimuli were the same or different. This AX discrimination task served as a practice task and included ten trials without feedback using two-step stimulus pairs from the labial series. Once the subjects demonstrated proficiency with this task, they performed the same discrimination test using all of the labial stimuli in the VOT continuum. That is, each subject was presented with 264 trials consisting of both one- and two-step pairs of the labial stimuli with no feedback. The two-step pairs were included to provide reinforcement since these were "easier" contrasts.

The discrimination task was an AX paradigm with an interstimulus interval of 750 ms. The interpair interval varied since the test was self-paced. Once the subject provided a

response, the next stimulus pair was delivered 1 s later. The discrimination test was repeated using stimuli from the alveolar continuum. The number of correct and incorrect responses for the  $-20/-10$  ms VOT contrast were calculated for each individual. These results served as a baseline discrimination measure. The order of labial and alveolar presentation was counterbalanced across subjects to prevent influences of order effects. For each individual, the order of stimulus presentation was the same before and after training.

*b. Identification testing.* Following discrimination testing, each subject was asked to identify, from three choices displayed as text on the computer screen, what sound they heard. This paradigm was a three-alternative forced-choice identification task. When a single labial stimulus from the labial continuum was presented, the choices were /mba/, /ba/, and /pa/. When the stimulus was from the alveolar continuum, the choices were /nda/, /da/, and /ta/. Each test consisted of 210 trials and included all 11 items from the continuum. No feedback was provided to the subject. However, in order to score identification data, labels were arbitrarily assigned such that the  $-50-$ ,  $-40-$ ,  $-30-$ , and  $-20-$ ms VOT stimuli were assigned the label /mba/, the  $-10-$ ,  $0-$ ,  $+10-$ , and  $+20-$ ms VOT were assigned the label /ba/, and the  $+30-$ ,  $+40-$ , and  $+50-$ ms VOT stimuli were assigned the label /pa/. Percent correct was calculated for the number of times the  $-20-$ ms VOT stimulus was identified as /mba/. These results served as a baseline identification measure.

## 3. Day 3

*a. Behavioral training (experimental group only).* The experimental subjects were asked to listen to single presentations of the labial stimuli in order from  $-50-$ ms through  $+50-$ ms VOT. This served as a familiarization session. Using a fading technique described by Jamieson and Morosan (1986, 1989), subjects were presented with either a  $-10-$ ms or  $-30-$ ms VOT stimulus from the labial continuum. Subjects were asked to identify the sound as either /mba/ or /ba/. Both choices were presented as text on the computer monitor. Feedback in the form of a green reinforcement light appeared when the subject correctly identified the  $-30-$ ms VOT stimuli as /mba/ and the  $-10-$ ms VOT stimuli as /ba/. This task was repeated 50 times to train the listener to label the acoustic prevoiced component as /mba/.

The  $-10-$ ms and  $-30-$ ms stimuli were chosen based on a pilot study in which listeners were able to identify these stimuli well above chance without training. Therefore, this initial session allowed the subjects to listen to the prevoiced stimuli and orient themselves to the prevoiced cue using an easy stimulus pair. Following this fading session, each subject began their first training session using a more difficult stimulus ( $-20-$ ms VOT). This stimulus was now assigned the label /mba/. The training session consisted of four blocks of 50 trials where either a  $-10-$ ms or  $-20-$ ms VOT labial stimulus was presented. Feedback in the form of a green reinforcement light appeared when the  $-20-$ ms VOT stimuli was labeled as /mba/ and the  $-10-$ ms VOT was labeled as /ba/. Each stimulus was presented randomly with equal probability of occurrence. Percent correct was calculated based



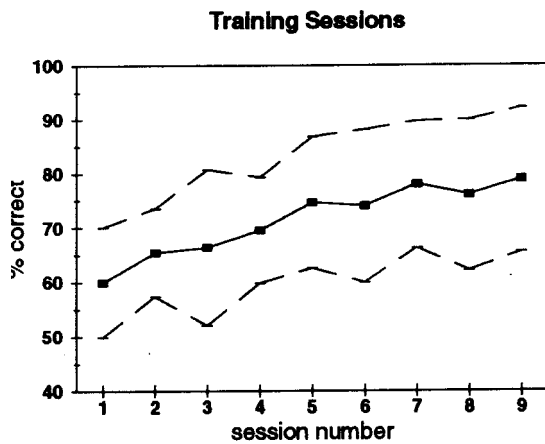


FIG. 1. Average correct identification scores (■---■) and one standard deviation (---) are shown as a function of training session for the experimental group. Identification scores improved significantly from the first to final training session ( $n=9$ ).

on the number of correct responses for each block of 50 trials. Performance on all four blocks of 50 trials was averaged to obtain a final training session score.

#### 4. Days 4–7

*a. Behavioral training continued (experimental group only).* Each subject in the experimental group continued the training sessions, listening, and identifying the  $-20$ - and  $-10$ -ms VOT labial stimuli. Nine sessions were conducted over 5 days. Each training session (200 trials) lasted approximately 20 min.

#### 5. Day 8

*a. Electrophysiology posttraining test.* Electrophysiologic responses were measured for both groups in response to the  $-20$ - and  $-10$ -ms VOT contrasts (labial and alveolar) using the same procedure described for day 1.

#### 6. Day 9

*a. Behavioral posttraining test.* Discrimination and identification measures were obtained for both the labial and alveolar stimuli for both the experimental and control groups as described under day 2.

## II. RESULTS

The results are presented in two sections: (A) Behavioral data and (B) Electrophysiological data.

### A. Behavioral results

#### 1. Identification training

Through training, all subjects in the experimental group learned to identify the  $-20$ -ms VOT stimulus as /mba/ and the  $-10$ -ms VOT stimulus as /ba/. Grouped data show a significant improvement from the first to the last training session ( $t=3.43$ ,  $df=8$ ,  $p<0.01$ ). Group averaged data across sessions are shown in Fig. 1.

### 2. Pre- and postdiscrimination and identification testing

*a. Trained stimuli /mba/.* Training resulted in improved posttraining discrimination and identification scores for the experimental group but not the control group (Fig. 2). Planned comparisons revealed a significant improvement in the experimental group's ability to identify the  $-20$ -ms VOT stimuli as /mba/ when comparing pre- versus posttraining identification scores ( $t=2.11$ ,  $df=8$ ,  $p<0.05$ ). The control group did not show any significant change in performance from pre- to posttesting ( $t=0.85$ ,  $df=8$ ,  $p>0.05$ ). Similarly, the experimental group demonstrated a significant improvement in their ability to discriminate the  $-20$ -ms VOT /mba/ contrast ( $t=2.39$ ,  $df=8$ ,  $p<0.05$ ) whereas the control group did not ( $t=1.51$ ,  $df=8$ ,  $p>0.05$ ).

*b. Transfer stimuli.* The effects of training transferred to the /nda/ stimuli with posttraining discrimination scores improving significantly for the experimental group ( $t=2.60$ ,  $df=8$ ,  $p>0.05$ ) but not the control group ( $t=1.71$ ,  $df=8$ ,  $p>0.05$ ). Improvement in the identification of the  $-20$ -ms VOT /nda/ stimulus narrowly missed reaching significance for the experimental group ( $t=1.71$ ,  $df=8$ ,  $p=0.06$ ). The control group did not show any significant changes in the ability to correctly identify the  $-20$ -ms VOT /nda/ stimulus ( $t=0.09$ ,  $df=8$ ,  $p>0.05$ ).

### 3. Summary

In summary, listening training improved the experimental group's ability to discriminate and identify the unfamiliar prevoiced labial stimulus /mba/. That enhanced ability transferred from one place of articulation (labial) to another (alveolar). No significant changes in performance were seen for the control group since they did not receive the training.

## B. Electrophysiology results

#### 1. MMN onset latency, duration, and area

Planned comparisons revealed a significant decrease in MMN onset latency for the experimental group but not the control group for the training stimuli /mba/ ( $t=2.31$ ,  $df=8$ ,  $p>0.05$ ;  $t=0.99$ ,  $df=8$ ,  $p>0.05$ ). No significant changes were seen in onset latency for either the experimental or control groups when tested using the transfer stimuli ( $t=1.48$ ,  $df=8$ ,  $p>0.05$ ;  $t=0.22$ ,  $df=8$ ,  $p>0.05$ ).

Planned comparisons comparing pre- versus posttraining scores revealed significant increases in MMN duration for the experimental group for both the trained and transfer stimuli ( $t=4.97$ ,  $df=8$ ,  $p>0.01$ ;  $t=2.91$ ,  $df=8$ ,  $p<0.05$ ). The control group did not show significant changes for either stimulus condition ( $t=0.90$ ,  $df=8$ ,  $p>0.05$ ;  $t=0.25$ ,  $df=8$ ,  $p>0.05$ ).

Planned comparisons comparing pre- versus posttraining revealed significant increases in MMN area for the experimental group for both the trained and transfer stimuli ( $t=2.77$ ,  $df=8$ ,  $p>0.05$ ;  $t=2.94$ ,  $df=8$ ,  $p>0.05$ ). The control group did not show significant changes for either stimulus condition ( $t=1.13$ ,  $df=8$ ,  $p<0.05$ ;  $t=0.91$ ,  $df=8$ ,  $p>0.05$ ).

## Identification of -20 msec VOT

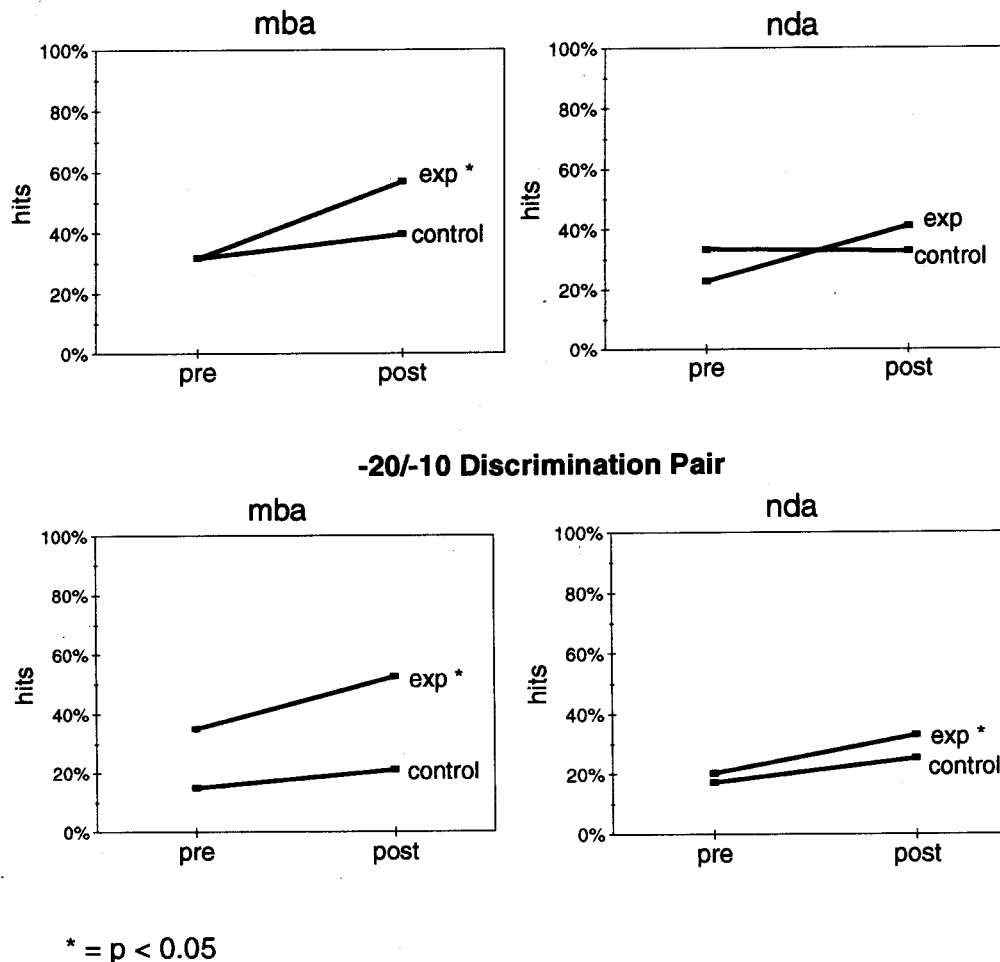


FIG. 2. Pre- versus posttraining identification and discrimination performance for the training and transfer stimuli for the experimental and control groups. Asterixes denote a significant change in performance with  $p$  values  $< 0.05$ .

In summary, an increase in MMN duration and area were seen for the experimental group when elicited by either the training or transfer stimuli following training (Fig. 3). No significant pre- versus posttraining changes were seen for the control group.

### 2. Laterality differences

Changes in MMN were largest over the left hemisphere. Figure 4 provides right versus left hemisphere MMN data pre- and posttraining for the experimental group in response to the training stimuli. Enhancement of the MMN was evident visually at all electrode sites in response to the training stimuli. For the transfer stimuli, changes were evident at Fz and FL only. Because there appeared to be a greater amount of change over the left hemisphere in the experimental group, MMN onset latency, duration, and area measures were analyzed using a  $2 \times (2 \times 2)$  repeated measures ANOVA (experimental versus control group, left versus right hemisphere, and frontal versus temporal lobe), using post- minus pretraining values as the dependent variable.

For the training stimuli (mba), there were significant group effects for onset latency ( $F=4.135$ ,  $p=0.05$ ). A

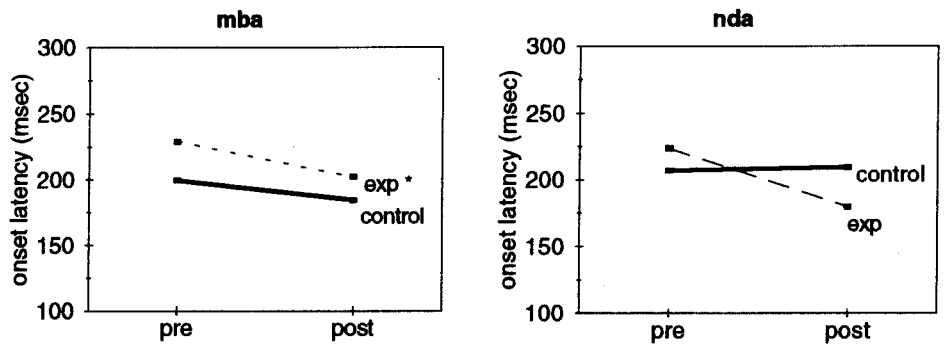
group  $\times$  hemisphere interaction was seen for MMN onset latency ( $F=5.62$ ,  $p<0.05$ ). *Post hoc t* tests revealed that the significant difference between right and left onset latency was seen over the frontal lobes. The decrease in onset latency following training was greater at electrode site FL when compared to FR ( $t=3.10$ ,  $df=8$ ,  $p<0.01$ ).

For the training stimuli (mba), there were significant group effects for MMN duration and area ( $F=4.41$ ,  $p<0.05$ ;  $F=5.63$ ,  $p<0.05$ ). A group  $\times$  hemisphere  $\times$  lobe interaction was seen for MMN duration ( $F=4.6$ ,  $p<0.05$ ). *Post hoc t* tests revealed that the degree of duration change was greater at electrode site FL compared to FR in the experimental group ( $t=3.74$ ,  $df=8$ ,  $p<0.01$ ). No significant onset latency, duration, or area differences were seen across hemispheres for the control group. For the transfer stimuli (nda), there were no significant hemispheric differences.

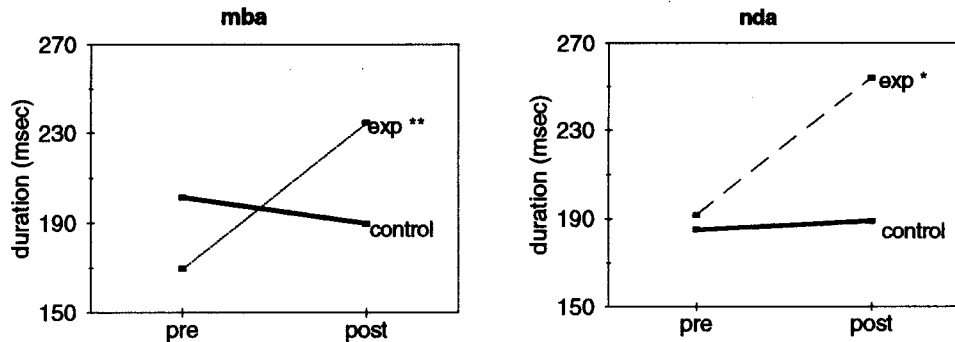
### C. Summary of results

Listening training improved the ability to discriminate and identify an unfamiliar VOT contrast. That enhanced ability transferred from one place of articulation (labial) to another (alveolar). The behavioral training effects were re-

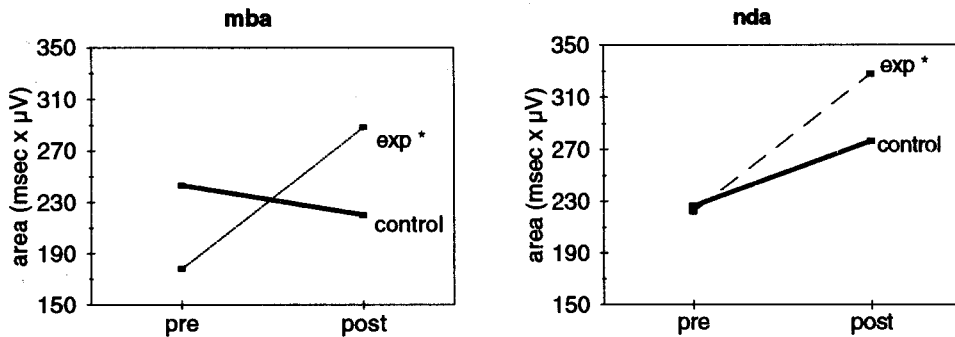
## ONSET LATENCY



## DURATION



## AREA



\* =  $p < 0.05$   
 \*\* =  $p < 0.01$

FIG. 3. Increases in MMN duration and area and a decrease in onset latency (recorded from Fz) were seen in the experimental group and not in the control group for both training and transfer stimuli. Single asterixes denote a significant change with  $p$  values  $< 0.05$ . Double asterixes denote a significant change with  $p$  values  $< 0.01$ .

flected in the MMN, which showed an increase in duration and area when elicited by the training or transfer stimuli for the experimental group but not the control group. This finding is illustrated in Figs. 5 and 6, which show grand-averaged MMN waveforms for each group. Figure 7 illustrates that the grand-averaged MMN measures reflect the individual trends in the data and are not simply a result of one or two outliers. Figure 4 shows that changes in the MMN were largest over the left hemisphere.

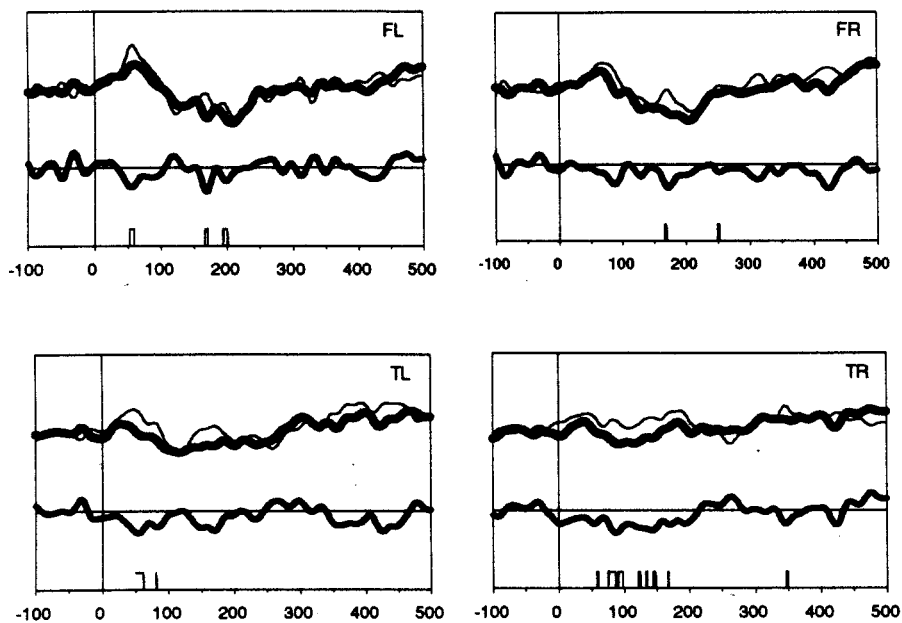
### III. DISCUSSION

#### A. Main findings

Auditory training alters the perception of novel stimuli. Behavioral learning was shown by the improved identifica-

tion scores during training sessions as well as the improved pre- versus posttraining discrimination and identification scores. Concurrently, neurophysiological plasticity was shown by the changes in the mismatch response. Specifically, this study showed that (1) through training, the experimental group learned to identify speech contrasts (differing in VOT) that are not phonemically different in the English language, (2) improvement of voice-onset-time discrimination generalized to spectrally different stimuli that also varied in VOT, (3) electrophysiological responses to the training and transfer stimuli reflected this improved perception as an increase in MMN duration and area, as well as a decrease in the onset of the mismatch response for the experimental group but not the control group, and (4) electrophysiological

### Pre-Training Condition



### Post-Training Condition

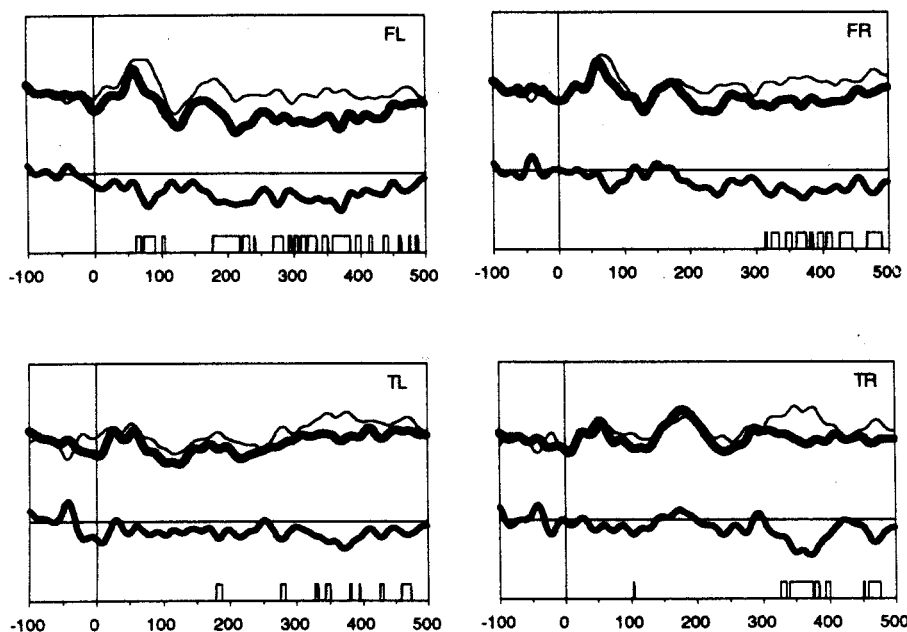


FIG. 4. Pre- and posttraining group-averaged electrophysiologic responses at four electrode sites (FL, TL, FR, and TR) are shown for the experimental group to the training stimuli ( $-20/-10$ -ms VOT) when the deviant was presented alone (thin line) and when it was presented in the mismatch condition (thick line). The MMN is seen in the subtraction wave below. The area of significance ( $p < 0.05$ ) is depicted by the blocked area on the x axis ( $n = 9$ ).

duration changes were greater over the left hemisphere than the right hemisphere.

The behavioral data are consistent with those of McClaskey *et al.* (1983) who reported that the perception of a new linguistic contrast can be acquired by adult listeners and that this trained ability generalizes to novel stimuli not used during training. The electrophysiologic data reinforce the

findings of Näätänen *et al.* (1993) and Kraus *et al.* (1995a) that neurophysiologic changes can be demonstrated in humans following listening training, thereby reflecting auditory system plasticity. Most importantly, this study showed that both behavioral and electrophysiologic changes are generalizable to other auditory stimuli that were not used during the training sessions.

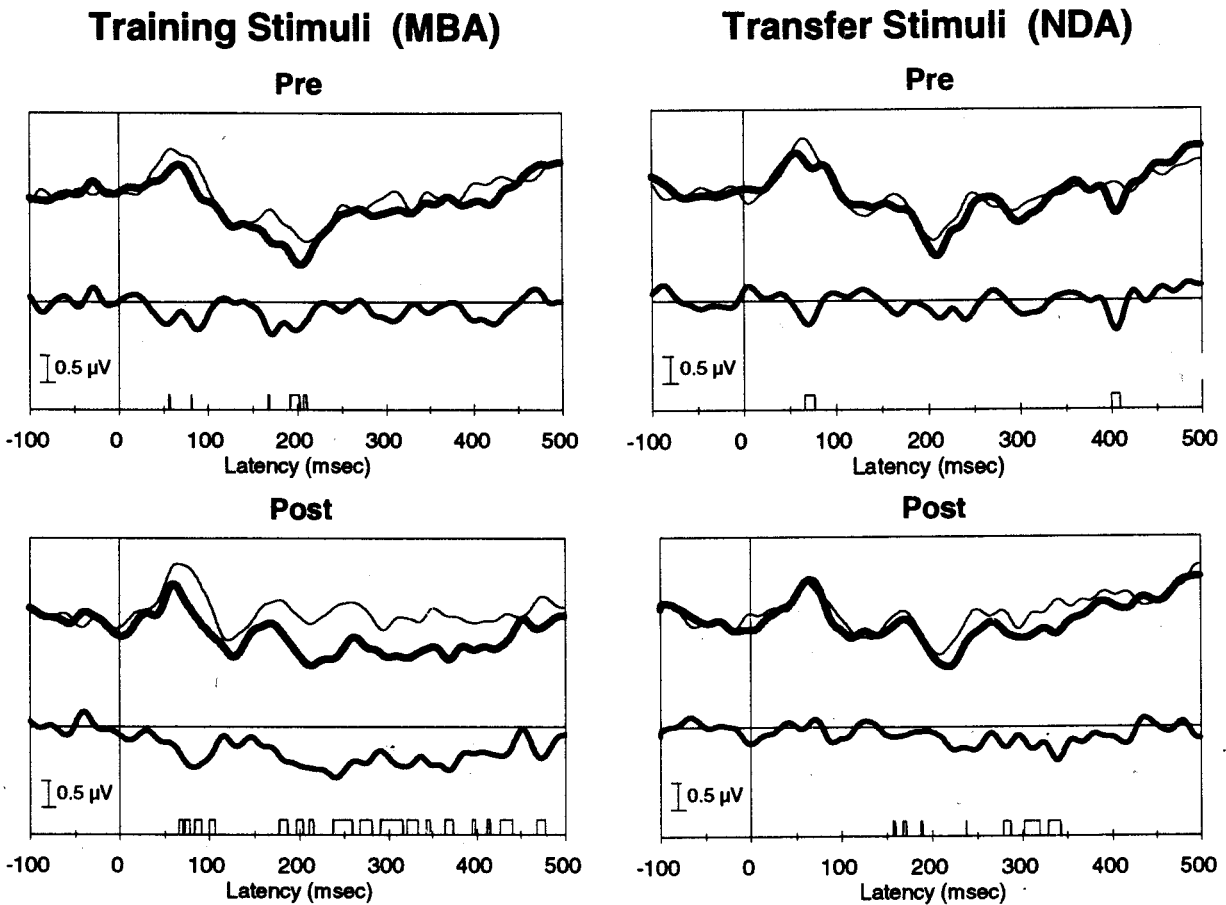


FIG. 5. A significant increase in duration and area of the mismatch response was seen following training for the experimental group. Group-averaged electrophysiologic responses (electrode Fz) are shown for the experimental group to the training and transfer stimuli ( $-20/-10$ -ms VOT) when the deviant stimulus was presented alone (thin line) and when it was in the mismatch paradigm (thick line). The MMN is seen in the subtraction wave below. The area of significance ( $p < 0.05$ ) is depicted by the blocked area on the x axis ( $n = 9$ ).

## B. Implications of experimental results to other areas of research

### 1. Plasticity of the adult system

In the past, there was debate concerning the flexibility of the mature perceptual system to accommodate new phonetic categories. Both successful as well as unsuccessful training and generalization attempts subsequently have led to the conclusion that the adult system does not lose the ability to acquire new linguistic contrasts, provided specific experimental procedures are used to train the listeners (Carney *et al.*, 1977; Aslin and Pisoni, 1980; Strange and Dittmann, 1984; Jamieson and Morosan, 1989; Pisoni *et al.*, 1982; Werker and Tees, 1984a; Lively *et al.*, 1993, 1994; Logan *et al.*, 1991). Until now, this line of research has been limited to behavioral studies. The present study establishes that the adult perceptual system is indeed plastic and that transfer of training can be shown through both behavioral and neurophysiologic measures.

### 2. Locus of neurophysiologic change

Neurophysiological evidence of learning-induced plasticity as well as representation of VOT have both cortical and subcortical origins (Disterhoft and Stuart, 1976, 1977; Ryugo

and Weinberger, 1978; Kraus and Disterhoft, 1982; Weinberger *et al.*, 1984; Edeline *et al.*, 1990; Sinex and McDonald, 1988; Steinschneider *et al.*, 1982, 1990, 1995; Eggemont, 1995; McGee *et al.*, 1996). Furthermore, there is evidence for cortical and subcortical mismatch generators (Näätänen *et al.*, 1978, 1980; Hari *et al.*, 1984; Csépe *et al.*, 1987; Näätänen and Picton, 1987; Giard *et al.*, 1990; Scherg and Picton, 1990; Sams and Näätänen, 1991; Alho *et al.*, 1992; Javitt *et al.*, 1992; Kraus *et al.*, 1994a, 1994b). Training-induced neurophysiologic changes as well as their generalizability may be the result of (1) a greater number of neurons responding in the sensory field, (2) increased synchrony of neuronal responses, or (3) an expansion of receptive fields (Berger *et al.*, 1976; Merzinech *et al.*, 1983, 1984; Kaas *et al.*, 1983; Merzinech and Jenkins, 1983).

Although this study does not specifically address whether changes occurred cortically or subcortically, it does provide insight into where neural changes might have occurred and how neuroanatomy may relate to perceptual learning. Specifically, changes in MMN were greater over the left compared to the right hemisphere following training, thereby suggesting that preattentive aspects of speech processing may also be lateralized. This laterality finding is new and may have implications regarding the role of each hemi-

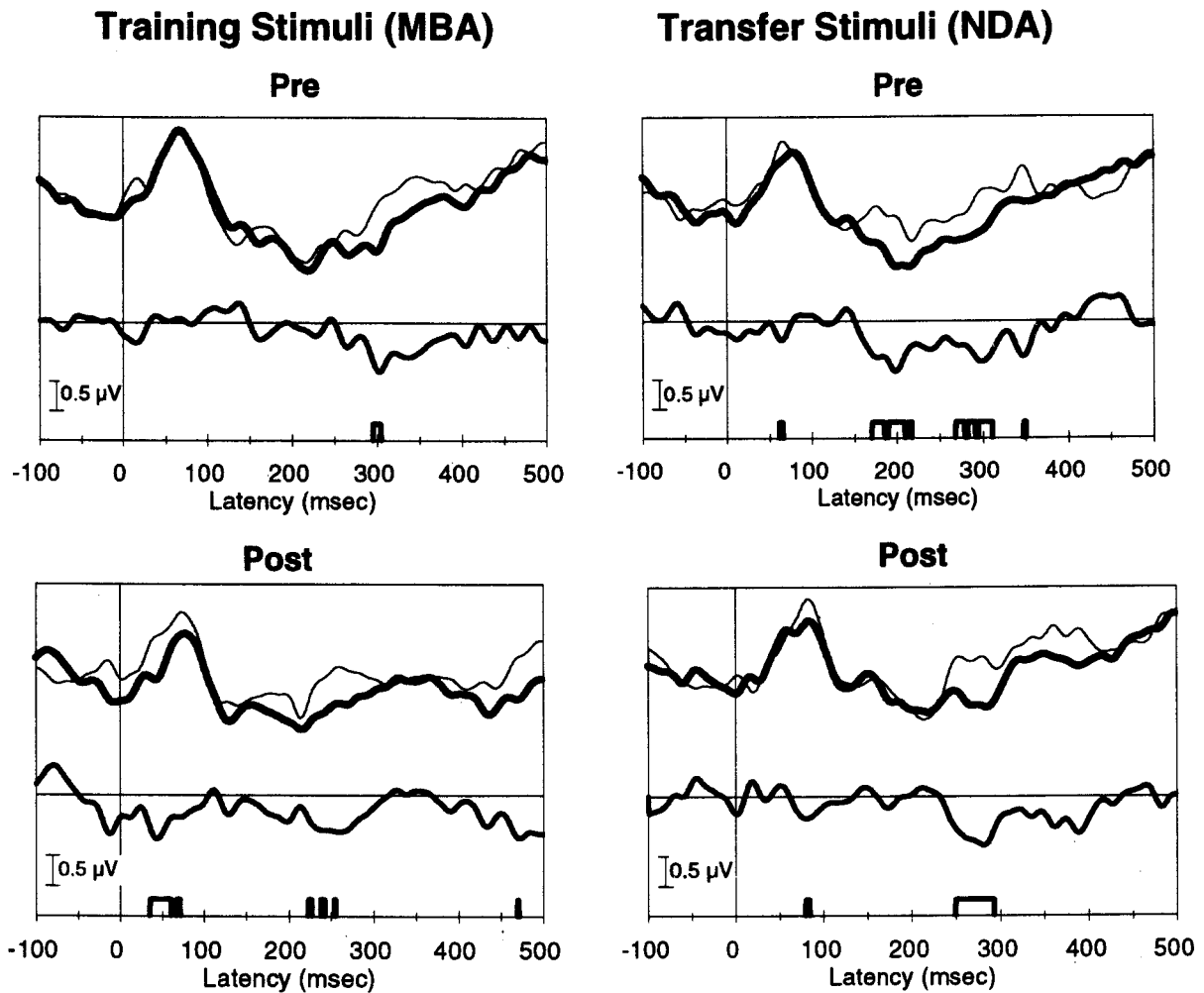


FIG. 6. No significant changes in onset latency, duration, and area of the mismatch response was seen for the control group. Group-averaged electrophysiologic responses (electrode Fz) are shown for the control group to the training and transfer stimuli ( $-20/-10$ -ms VOT) when the deviant stimulus was presented alone (thin line) and when it was in the mismatch paradigm (thick line). The MMN is seen in the subtraction wave below. The area of significance ( $p < 0.05$ ) is depicted by the blocked area on the x axis ( $n = 9$ ).

sphere in processing learning-associated stimulus change.

Mapping studies using current source density analysis have reported both bilateral cortex involvement and predominantly right-hemispheric frontal involvement in MMN generation (Giard *et al.*, 1990; Paavilainen *et al.*, 1991). In the present study, the pretraining MMN was seen bilaterally and was not significantly larger over one hemisphere. The absence of laterality may result in part from the nature of the stimuli. Prior to training, subjects did not perceive the /mba/ and /nda/ stimuli to be phonetically distinct from /ba/ and /da/. Identification training may have resulted in these stimuli being recognized linguistically rather than as simple acoustic variants of /ba/ and /da/, thereby leading to greater activity in the left hemisphere. For example, when Giard *et al.* (1990) and Paavilainen *et al.* (1991) observed right-hemispheric dominance when recording the MMN, they used tonal stimuli. Because tones do not convey linguistic or phonetic information, the left hemisphere may not have played a dominant role in encoding those stimuli. Sharma and Kraus (1995) showed that the MMN lateralizes to the left if the change in a stimulus sequence signals a phonetic rather than a tonal pitch contrast. Thus, these studies in combination

with the findings from the present study suggest that the linguistic/phonetic nature of the stimuli may relate to which hemisphere is most active in detecting the stimulus change and that preattentive aspects of speech processing are modifiable and may also be lateralized.

### 3. The role of attention and perceptual learning

Regardless of where and how these neurophysiological changes take place, the data suggest that some degree of speech learning occurs at a preattentive level that can be measured in the absence of an overt response. Until now, the role of attention in comparable training and generalization experiments has been explored primarily in the visual modality. Visual experiments suggest that high-level attentional mechanisms are necessary for demonstrating "transfer" of visual learning (Ahissar and Hochstein, 1993). Even though the behavioral tasks in this study required attention and cognitive processing of the stimuli during training, changes in the MMN elicited by the training as well as the transfer stimuli indicate that speech-sound learning is evident at an automatic, preattentive level. Future studies examining the role of attention and other high-level cognitive processes

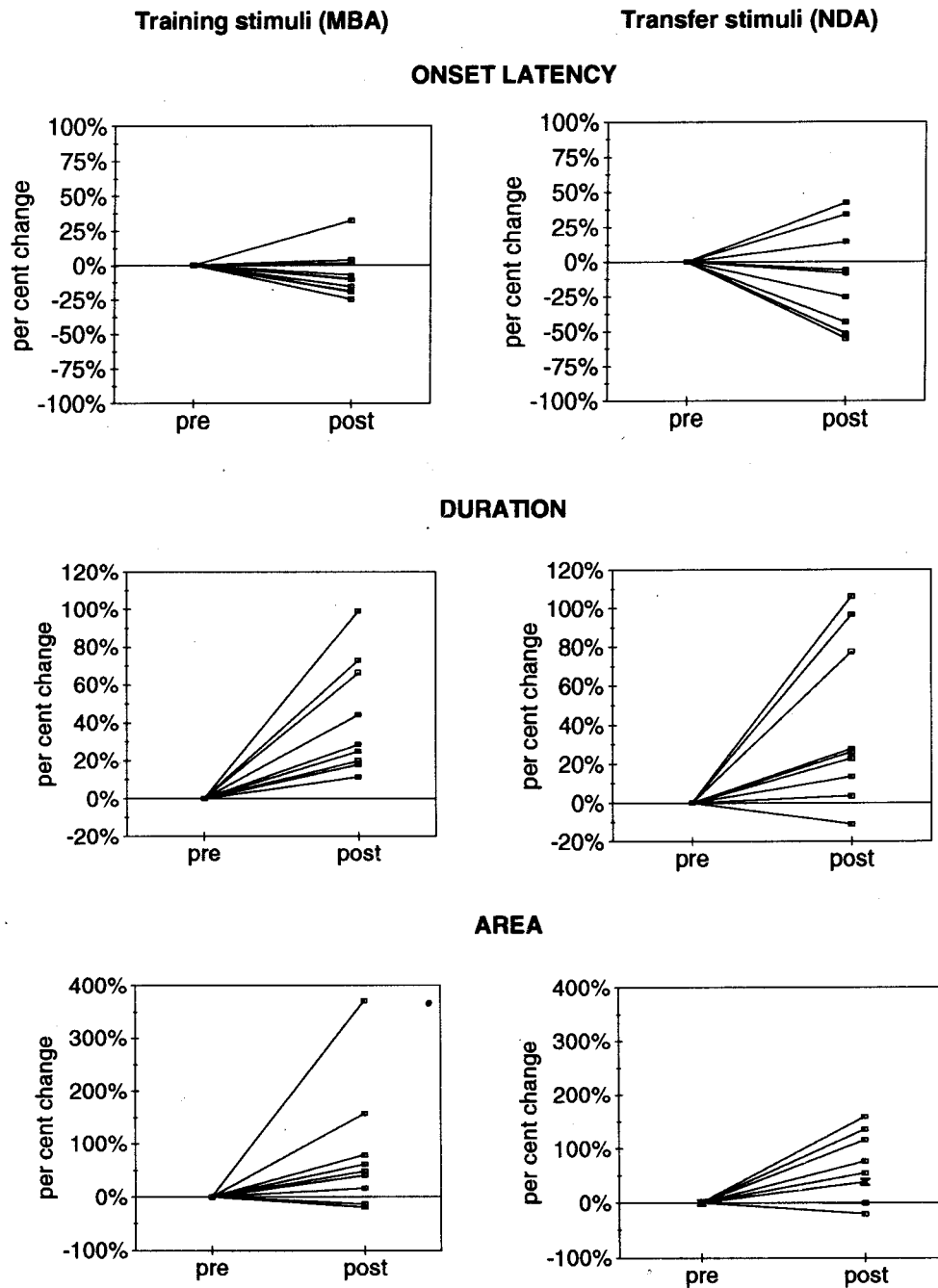


FIG. 7. Individual subject changes in MMN onset latency, duration, and area after training are shown for the experimental group. Posttraining changes are plotted relative to normalized pretraining values and show a significant increase in both duration and area as well as a significant decrease in onset latency. Note that overlapping individual scores are indicated by the X symbol.

may yield information pertaining to the site(s) of perceptual learning, and how learning manifests itself as behavior.

#### IV. CONCLUSIONS

Ultimately, the goal of successful (re)habilitative training is to have listeners transfer learned behaviors to new listening situations. The behavioral results of this study have confirmed that controlled laboratory-based training procedures can be effective in modifying listeners' preattentive phonetic perception in a short period of time and that the learned behavior transfers to new acoustic conditions. The

corresponding neurophysiologic findings are significant from a clinical perspective because they provide an objective approach for examining the neurophysiologic change that may occur following (re)habilitation efforts in populations such as hearing-impaired individuals and children with auditory-based learning problems, who may not be able to participate in behavioral testing. From a more theoretical standpoint, these findings establish an avenue for examining the human capacity for change, and for understanding neurophysiologic processes associated with foreign language training, musician ear training, and other forms of auditory learning.

## ACKNOWLEDGMENTS

The authors thank Dawn Burton and Koch, Ph.D., Steve Zecker, Ph.D., Ann Bradlow, Ph.D., and Trent Nicol, the two JASA reviewers as well as the associate editor for their helpful comments. This work was supported by the National Institutes of Health R01 DC 01510.

- Ahissar, M., and Hochstein, S. (1993). "attentional control of early perceptual learning," *Proc. Natl. Acad. Sci. USA* **90**, 5718–5722.
- Alho, K., Woods, D. L., Algazi, A., and Näätänen, R. (1992). "Intermodal selective attention. II. Effects of attentional load on processing of auditory and visual stimuli in central space," *Electroencephalogr. Clin. Neurophysiol.* **85**, 356–368.
- Aslin, R. L., and Pisoni, D. B. (1980). "Some development processes in speech perception," in *Child Phonology: Perception and Production*, edited by G. Yeni-Komshian, J. F. Kavanagh, and C. A. Ferguson (Academic, New York), pp. 67–96.
- Bakin, J. S., and Weinberger, N. M. (1990). "Classical conditioning induces CS specific receptive field plasticity in the auditory cortex of the guinea pig," *Brain Res.* **536**, 271–286.
- Berger, T. W., Alger, B., and Thompson, R. F. (1976). "Neuronal substrate of classical conditioning in the hippocampus," *Science* **192**, 483–485.
- Blackburn, C. C., and Sachs, M. B. (1990). "The representations of the steady-state vowel sound /e/ in the discharge patterns of cat anteroventral cochlear nucleus neurons," *J. Neurophysiol.* **63**, 1191–1212.
- Buchwald, J. S., Halas, E. S., and Schramm, S. (1966). "Changes in cortical and subcortical unit activity during behavioral conditioning," *Physiol. Behav.* **1**, 11–22.
- Carney, A. E., Widin, G. P., and Viemeister, N. F. (1977). "Noncategorical perception of stop consonants differing in VOT," *J. Acoust. Soc. Am.* **62**, 961–970.
- Csèpe, V. (1995). "On the origin and development of the mismatch negativity," *Ear Hear.* **16**, 91–104.
- Csèpe, V., Karmos, G., and Molnar, M. (1987). "Evoked potential correlates of stimulus deviance during wakefulness and sleep in the cat-animal model of mismatched negativity," *Electroencephalogr. Clin. Neurophysiol.* **66**, 571–578.
- Delgutte, B., and Kiang, N. Y. S. (1984). "Speech coding in the auditory nerve. I. Vowel-like sounds," *J. Acoust. Soc. Am.* **75**, 866–878.
- Diamond, D. M., and Weinberger, N. M. (1984). "Physiologic plasticity of single neurons in auditory cortex of the cat during acquisition of the pupillary conditioned response. I: Secondary field (AII)," *Behav. Neurol.* **98**, 189–210.
- Diamond, D. M., and Weinberger, N. M. (1986). "Classical conditioning rapidly induced changes in frequency receptive fields of single neurons in secondary and ventral ectosylvian auditory cortical fields," *Brain Res.* **372**, 357–360.
- Diamond, N. M., and Weinberger, N. M. (1989). "Role of context in the expression of learning-induced plasticity of single neurons in auditory cortex," *Behav. Neurol.* **103**, 471–494.
- Disterhoft, J. F., and Stuart, D. K. (1976). "Trial sequence of changed unit activity in the auditory system of alert rat during conditioned response acquisition and extinction," *J. Neurophysiol.* **39**, 266–281.
- Disterhoft, J. F., and Stuart, D. K. (1977). "Differentiated short latency response increases after conditioning in inferior colliculus of alert rat," *Brain Res.* **130**, 315–334.
- Edeline, J. M., Neuenschwander-El Massioui, N., and Dutrieux, G. (1990). "Frequency-specific cellular changes in the auditory system during acquisition and reversal of discriminative conditioning," *Psychobiology* **18**, 382–393.
- Edeline, J. M., Pham, P., and Weinberger, N. M. (1993). "Rapid development of learning-induced receptive field plasticity in the auditory cortex," *Behav. Neurol.* **107**, 539–551.
- Eggmont, J. J. (1995). "Representation of a voice onset continuum in primary auditory cortex of the cat," *J. Acoust. Soc. Am.* **98**, 911–920.
- Giard, M., Perrin, F., Pernier, J., and Bouchet, P. (1990). "Brain generators implicated in the processing of auditory stimulus deviance: a topographic event-related potential study," *Psychophysiology* **27**, 627–640.
- Hari, R., Hamalainen, J., Ilmoniemi, R., Kaukoranta, E., Reinikainen, K., Salminen, J., Alho, K., Näätänen, R., and Sams, M. (1984). "Responses of the primary auditory cortex to pitch changes in a sequence of tone pips: neuromagnetic recordings in man," *Neurosci. Lett.* **50**, 127–132.
- Jamieson, D., and Morosan, D. (1986). "Training nonnative speech contrasts in adults: Acquisition of the English / /-θ/ contrast by francophones," *Percept. Psychophys.* **40**, 205–215.
- Jamieson, D., and Morosan, D. (1989). "Training new, nonnative speech contrasts in adults: A comparison of the prototype and perceptual fading techniques," *Can. J. Psychol.* **43**, 88–96.
- Jasper, H. H. (1958). "The ten-twenty system of the international federation," *Electroencephalogr. Clin. Neurophysiol.* **10**, 371–375.
- Javitt, D., Schroeder, C., Steinschneider, M., Arezzo, J., and Vaughan, Jr., H. (1992). "Demonstration of mismatch negativity in monkey," *Electroencephalogr. Clin. Neurophysiol.* **83**, 87–90.
- Kaas, J. H., Merzinech, M. M., and Killackey, H. P. (1983). "The reorganization of somatosensory cortex following peripheral nerve damage in adults and developing mammals," *Annu. Rev. Neurosci.* **6**, 325–356.
- Klatt, D. (1980). "Software for cascade/parallel formant synthesizer," *J. Acoust. Soc. Am.* **67**, 971–995.
- Kraus, N., and Disterhoft, J. F. (1982). "Response plasticity of single neurons in rabbit association cortex during tone-signalled learning," *Brain Res.* **246**, 205–215.
- Kraus, N., Micco, A., Koch, D., McGee, T., Carrell, T., Sharma, A., and Nicol, T. (1993). "Mismatch negativity in the neurophysiologic/behavioral evaluation of auditory processing deficits: A case study," *Ear Hear.* **14**, 223–234.
- Kraus, N., McGee, T., Littman, T., Nicol, T., and King, C. (1994a). "Encoding of acoustic change involves the non-primary auditory thalamus," *J. Neurophysiol.* **72**, 1270–1277.
- Kraus, N., McGee, T., Carrell, T., King, C., Littman, T., and Nicol, T. (1994b). "Discrimination of speech-like signals in auditory thalamus and cortex," *J. Acoust. Soc. Am.* **96**, 2758–2768.
- Kraus, N., McGee, T., Carrell, T., King, C., Tremblay, K., and Nicol, T. (1995a). "Central auditory system plasticity with speech discrimination training," *J. Cog. Neurosci.* **7**, 25–32.
- Kraus, N., McGee, T., Carrell, T., and Sharma, T. (1995b). "Neurophysiologic bases of speech discrimination," *Ear Hear.* **16**, 19–37.
- Kraus, N., McGee, T., Carrell, T., Zecker, S. G., Nicol, T., and Koch, D. (1996). "Neurophysiologic response reflect behavioral discrimination deficits in children with learning problems," *Science* **273**, 971–972.
- Lively, S., Logan, J., and Pisoni, D. (1993). "Training Japanese listeners to identify English /r/ and /l/: II. The role of phonetic environment and talker variability in learning new perceptual categories," *J. Acoust. Soc. Am.* **94**, 1242–1255.
- Lively, S., Pisoni, D., Yamada, R. A., Yoh'ichi, T., and Yamada, T. (1994). "Training Japanese listeners to identify English /r/ and /l/. III. Long-term retention of new phonetic categories," *J. Acoust. Soc. Am.* **96**, 2076–2087.
- Logan, J. S., Lively, S. E., and Pisoni, D. B. (1991). "Training Japanese listeners to identify English /r/ and /l/: A first report," *J. Acoust. Soc. Am.* **89**, 874–886.
- McClaskey, C., Pisoni, D., and Carrell, T. (1983). "Transfer of training of a new linguistic contrast in voicing," *Percept. Psychophys.* **34**, 323–330.
- McGee, T., Kraus, N., King, C., Nicol, T., and Carrell, T. (1996). "Acoustic elements of speech-like stimuli are reflected in surface recorded responses over the guinea pig temporal lobe," *J. Acoust. Soc. Am.* **99**, 3606–3614.
- McGee, T., Kraus, N., and Nicol, T. (1997a). "Is it really a mismatch negativity? an assessment of methods for determining response validity in individual subjects," *Electroenceph. Clin. Neurophysiol.* **104**, 359–368.
- McGee, T., Nicol, T., and Kraus, N. (1997b). "Improving the MMN signal-to-noise ratio." XV International Evoked Response Audiometry Study Group (IERASG) Abstract, p. 49.
- Merzinech, M. M., and Jenkins, W. M. (1983). "Dynamic maintenance and alterability of cortical maps in adults; some implications," in *Hearing—Physiological Bases and Psychophysics*, edited by R. Klinke and R. Hartmann (Oxford U.P., New York), pp. 162–167.
- Merzinech, M. M., Kaas, J. H., Wall, J. T., Sur, M., and Nelson, R. J. (1983). "Progression of change following median nerve section in the cortical representation of the hand in areas 3b and 1 in adult owl and squirrel monkey," *Neuroscience (NY)* **10**, 639–665.
- Merzinech, M. M., Nelson, R. J., Stryker, M. P., Cynader, M. S., Schoppmann, A., and Zook, J. M. (1984). "Somatosensory cortical map changes following digit amputation in adult monkeys," *J. Comp. Neurol.* **224**, 591–605.
- Micco, A., Kraus, N., Koch, D., McGee, T., Carrell, T., Sharma, A., Nicol, T., and Wiet, R. (1995). "Speech-evoked cognitive potentials in cochlear implant recipients," *Am. J. Otolaryngol.* **16**, 514–520.



- Näätänen, R., and Picton, T. (1987). "The N1 wave of the human electric and magnetic response to sound: a review and an analysis of the component structure," *Psychophysiology* **24**, 375–425.
- Näätänen, R., Gaillard, A., and Mantysalo, S. (1978). "Early selective attention effect on evoked potential reinterpreted," *Acta Psychol.* **42**, 313–329.
- Näätänen, R., Gaillard, A., and Mantysalo, S. (1980). "Brain potential correlated in voluntary and involuntary attention," *Prog. Brain Res.* **54**, 343–348.
- Näätänen, R., Schroger, E., Karakas, S., Tervaniemi, M., and Paavilainen, P. (1993). "Development of neural representations for complex sound patterns in the human brain," *NeuroReport* **4**, 503–506.
- Olds, J., Disterhoft, J. T., Segal, M., Kornblith, C. L., and Hirsh, R. (1972). "Learning centers of rat brain mapped by measuring the latencies of conditioned unit responses," *J. Neurophysiol.* **35**, 202–219.
- Paavilainen, P., Alho, K., Reinikainen, K., Sams, M., and Näätänen, R. (1972). "Right hemisphere dominance of different mismatch negativities," *Electroencephalogr. Clin. Neurophysiol.* **78**, 466–479.
- Pisoni, D. B., Aslin, R. N., Perey, A. J., and Hennessy, B. L. (1982). "Some effects of laboratory training on identification and discrimination of voicing contrasts in stop consonants," *J. Exp. Psychol.* **8**, 297–314.
- Recanzone, G., Schreiner, C., and Merzenich, M. (1993). "Plasticity in the frequency representation of primary auditory cortex following discrimination training in adult owl monkeys," *J. Neurosci.* **13**, 87–104.
- Ryugo, D. K., and Weinberger, N. M. (1978). "Differential plasticity of morphologically distinct neuron populations in the medial geniculate body of the cat during classical conditioning," *Behav. Biol.* **22**, 275–301.
- Sams, M., and Näätänen, R. (1991). "Neuromagnetic responses of the human auditory cortex to short frequency glides," *Neurosci. Lett.* **121**, 43–46.
- Sams, M., Paavilainen, P., Alho, K., and Näätänen, R. (1985). "Auditory frequency discrimination and event-related potentials," *Electroencephalogr. Clin. Neurophysiol.* **62**, 437–448.
- Scherg, M., and Picton, T. (1990). "Brain electric source analysis of mismatch negativity," in *Psychophysiological Brain Research*, edited by C. Brunia, A. Gaillard, and A. Kok (Tilberg U. P., Tilberg), pp. 94–98.
- Sharma, A., and Kraus, N. (1995). "Effect of contextual variations in pitch and phonetic processing: Neurophysiologic correlates." *Assoc. for Research in Otolaryngology. Eighteenth Midwinter Research Meeting, Abstract #729.*
- Sinex, D. G., and McDonald, L. P. (1988). "Average discharge rate representation of voice onset time in the chinchilla auditory nerve," *J. Acoust. Soc. Am.* **83**, 1817–1827.
- Steinschneider, M., Arezzo, J., and Vaughan, Jr., H. (1982). "Speech-evoked activity in the auditory radiations and cortex of the awake monkey," *Brain Res.* **252**, 353–365.
- Steinschneider, M., Arezzo, J., and Vaughan, Jr., H. (1990). "Tonotopic features of speech-evoked activity in primate auditory cortex," *Brain Res.* **519**, 158–168.
- Steinschneider, M., Schroeder, C., Arezzo, J., and Vaughan, Jr., H. (1995). "Physiological correlates of the voice onset time boundary in primary auditory cortex (AI) of the awake monkey: temporal response patterns," *Brain Lang.* **48**, 326–340.
- Strange, W., and Dittmann, S. (1984). "Effects of discrimination training on the perception of /r-l/ by Japanese adults learning English," *Percept. Psychophys.* **36**, 131–145.
- Weinberger, N. M. (1993). "Learning-induced changes of auditory receptive fields [Review]," *Curr. Opin. Neurobiol.* **3**(4), 570–577.
- Weinberger, N. M., Hopkins, W., and Diamond, D. M. (1984). "Physiologic plasticity of single neurons in auditory cortex of the cat during acquisition of the pupillary conditioned response. I: Primary field (AI)," *Behav. Neurosci.* **98**, 171–188.
- Werker, J., and Tees, R. (1984). "Phonemic and phonetic factors in adult cross-language speech perception," *J. Acoust. Soc. Am.* **75**, 1866–1878.

# Acoustic properties of egg yolk and albumen in the frequency range 20–400 MHz

N. Akashi and J. Kushibiki

*Department of Electrical Engineering, Faculty of Engineering, Tohoku University, Sendai 980-77, Japan*

F. Dunn

*Bioacoustics Research Laboratory, University of Illinois, Urbana, Illinois 61801*

(Received 1 April 1997; accepted for publication 22 August 1997)

The acoustic propagation properties of egg yolk and albumen are characterized in the frequency range 20–400 MHz by the bioultrasonic spectroscopy system using an ultrasonic transmission comparison method. Significant differences in the attenuation, velocity, impedance, and density among yolk and thick and outer thin albumen are observed. The acoustic properties of 10% aqueous solutions of ovalbumin and bovine hemoglobin are also measured in order to investigate the contribution of proteins to the acoustic properties of albumen. The differences obtained between thick and outer thin albumen may be mainly due to their macromolecular level structural differences, as their constituents are nearly the same. © 1997 Acoustical Society of America. [S0001-4966(97)04212-4]

PACS numbers: 43.80.Cs, 43.80.Jz, 43.80.Ev, 43.35.Bf [FD]

## INTRODUCTION

Studies on biological tissue characterization using ultrasound have been conducted extensively. In general, quantitative analysis of the acoustic properties of biological tissues is difficult because of their complicated structures and various constituents, including several kinds of proteins and lipids. Poultry egg provides readily accessible biomacromolecular specimens for which the acoustic attenuation coefficient and velocity have been studied.<sup>1–3</sup> Choi *et al.* measured the ultrasonic absorption of albumen in the frequency range 0.2–10 MHz over the temperature range of 10 °C–50 °C.<sup>1</sup> Javanaud *et al.* reported the velocities of egg yolk and albumen in the frequency range 2–7 MHz and the absorption coefficients in the frequency range 2–124 MHz.<sup>2</sup> However, in both studies differences of the acoustic properties between thick and thin albumen were not observed. Povey and Wilkinson measured the velocities and attenuations at 1.25 MHz and reported that the attenuation of thick albumen is greater than that of thin albumen.<sup>3</sup> However, they did not detect differences in velocity between thick and thin albumen.

The reported data from the previous studies did not have sufficient measurement accuracy and resolution to distinguish the difference in viscoelasticity between thick and thin albumen, recognized easily by human sensibility. For a better understanding of the acoustic properties of egg yolk, and thick and thin albumen, more reliable data over a much broader frequency range are necessary.

The bioultrasonic spectroscopy system has been developed for biological tissue characterization in the VHF and UHF ranges<sup>4</sup> and applied to fundamental studies of bovine tissues in the frequency range 20–200 MHz.<sup>5</sup> The acoustic properties, viz., attenuation coefficient, velocity, impedance, and density, can be determined with high accuracy by an ultrasonic transmission comparison method using distilled water as the reference.

In this paper, egg yolk and albumen as biological macromolecular liquids are characterized in the frequency range 20–400 MHz. The acoustic properties of aqueous solutions of ovalbumin and bovine hemoglobin are also measured to provide details of the ultrasonic behavior of some biological macromolecules to help in understanding the behavior of the acoustic properties of thick and thin albumen.

## I. MEASUREMENT METHOD

The measurement method and system is described in detail elsewhere.<sup>4</sup> The experimental configuration for characterization is shown in Fig. 1, in which a specimen is inserted between the parallel surfaces of synthetic silica (SiO<sub>2</sub>) buffer rods having ZnO piezoelectric film transducers on their outer ends. A rf burst signal is supplied to the transmitting transducer TR(1) in order to generate ultrasonic longitudinal plane waves, which then propagate in the buffer rod. The ultrasonic attenuation coefficient, velocity, impedance, and density are determined by measuring the transducer outputs  $V_i$  ( $i=1-3$ ) in the ultrasonic transmission line model, as shown in Fig. 1. In the measurement method, measurement errors due to diffraction losses in the acoustic media, and to mode conversion at the buffer-rod/sample interfaces, can be corrected experimentally by performing measurements for both sample and distilled water as medium 2. The gap length between the two buffer rods is determined by measuring frequency characteristics of the interference output of  $V_1$  and  $V_2$  for distilled water of which the velocity is used as the reference.<sup>4</sup> The attenuation coefficient and velocity of the sample were measured in the transmission mode using the output  $V_3$  of the transducer TR(2).

The velocity is obtained by the  $z$ -interference method,<sup>4</sup> in which the interference output of  $V_3$  and the reference electrical signal derived from the signal generator of the measurement system is measured as a function of gap length. The acoustic impedance is obtained with the pulse echo

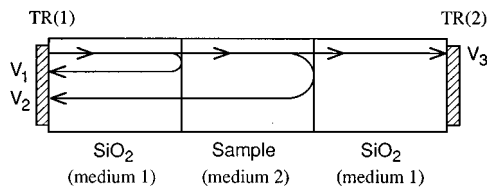


FIG. 1. Definition of transducer outputs  $V_i$  for measuring acoustic properties of liquid samples.

method by measuring  $V_1$  for sample and for air as medium 2, in order to determine the reflection coefficient at the buffer-rod/sample interface, and by using the acoustic impedance of  $\text{SiO}_2$  as the reference. The attenuation coefficient is obtained by measuring  $V_3$  and by using the reflection coefficient determined in the impedance measurement with the known attenuation coefficient of distilled water. The density  $\rho$  is calculated by using the equation that  $\rho = Z(f)/v(f)$ , where  $Z(f)$  is the acoustic impedance and  $v(f)$  is the velocity. The acoustic impedance and velocity in acoustically lossy media have a frequency dependence, whereas the density is independent of frequency. The velocity and attenuation coefficient of water reported in the literature,<sup>6,7</sup> and the acoustic impedance of  $\text{SiO}_2$  measured to be  $13.11 \times 10^6 \text{ N s/m}^3$  were employed as the reference data.

## II. EXPERIMENTS AND RESULTS

Measurements were conducted on yolk and albumen of white leghorn eggs. They were purchased at a wholesale store within less than 12 h of being laid and stored in a 5 °C temperature refrigerator until the measurement preparation procedure began. The specimens were thus measured within less than 36 h of being laid. The albumen is divided into three concentric layers, viz., outer thin albumen, thick albumen, and inner thin albumen. The yolk is composed of alternate yellow and white yolk layers. For measurements, outer thin albumen, thick albumen, and mixture of yellow and white yolk were used. After the egg shell was carefully broken on a glass plate, the thick albumen surrounding the yolk was spread and the outer thin albumen was spread beyond the thick albumen. The sample was taken from the spread material by a syringe having an inner diameter of 1 mm, and no needle attached. Yellow and white yolk became mixed during the procedure. The volume of sample required for measurements was about 1 ml, which was much less than the content of one egg.

The parameters of the ultrasonic devices used for measurements are listed in Table I.

The measurement accuracy in the present study is estimated to be better than  $\pm 0.1\%$  for velocity and  $\pm 1\%$  for attenuation coefficient, impedance, and density. The reproducibility is estimated to be better than  $\pm 0.02\%$  for velocity and  $\pm 0.5\%$  for attenuation coefficient, impedance, and density.

The measured attenuation coefficients of thick and outer thin albumen in the frequency range 30–400 MHz at 23.1 °C–23.4 °C are shown in Fig. 2. Two pairs of devices (see Table I), with the center frequencies of 150 and 400 MHz, were employed with the gap lengths 1200  $\mu\text{m}$  for

TABLE I. Parameters of the acoustic devices used for measuring acoustic properties of specimens (T: transmitter; R: receiver).

Device No.	No. 1 (T)	No. 1 (R)	No. 2 (T)	No. 2 (R)
Center frequency	150 MHz	150 MHz	400 MHz	400 MHz
Transducer material	ZnO	ZnO	ZnO	ZnO
Diameter of transducer	2.5 mm	2.5 mm	1.3 mm	1.3 mm
Diameter of buffer rod	8 mm	20 mm	8 mm	20 mm
Length of buffer rod	8 mm	8 mm	8 mm	8 mm

30–150 MHz and 600  $\mu\text{m}$  for 150–400 MHz, respectively. The samples for the measurements in the two frequency ranges were taken from different egg samples. The attenuation coefficients of thick albumen are greater than those of outer thin albumen in this frequency range, for example, 9.3% greater at 100 MHz. Povey and Wilkinson reported that the attenuation for thick albumen is greater than that for thin albumen at the frequency of 1.25 MHz.<sup>3</sup> The attenuations for both thick and outer thin albumen are proportional to the 1.4 power of frequency around 30 MHz, the 1.4–1.5 power around 100 MHz, and gradually increase with frequency up to the 1.7–1.8 power around 400 MHz.

The measured attenuation coefficients of egg yolk in the frequency range 25–400 MHz at 23.9 °C using a pair of ultrasonic devices with a 400-MHz center frequency (see Table I) are shown in Fig. 2. The gap lengths of the two ultrasonic devices were 1500, 300, and 100  $\mu\text{m}$ , in the frequency ranges 25–70, 70–250, and 250–400 MHz, respec-

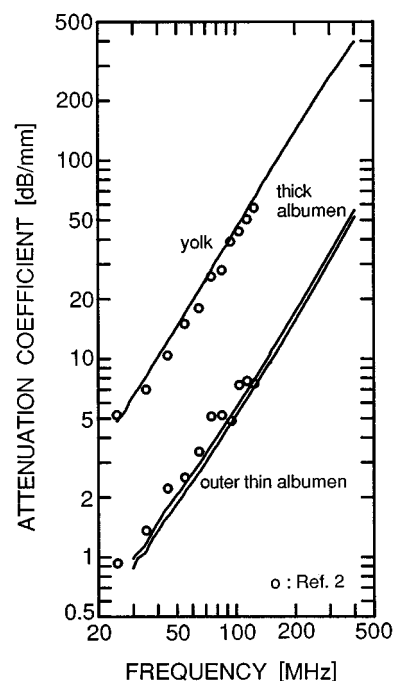


FIG. 2. Frequency dependence of attenuation coefficients of thick albumen and outer thin albumen at 23.1 °C–23.4 °C, and of yolk at 23.9 °C.

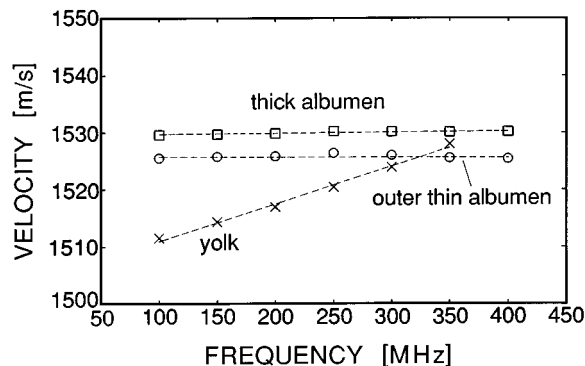


FIG. 3. Velocity dispersion of yolk, and thick and outer thin albumen at 23.4 °C–23.7 °C. Broken lines fitted by the method of least squares.

tively. The attenuation coefficients of yolk are about ten times greater (in decibels) than those of albumen. The attenuation for yolk exhibits different frequency dependences than those for albumen. The attenuation for yolk is proportional to the 1.65 power of frequency in the range 25–300 MHz and dropping to the 1.5 power of frequency around 400 MHz.

The open circles in Fig. 2 show the published data measured by Javanaud *et al.* for a mixture of thin and thick albumen in the temperature range 21.5 °C–23.5 °C and yolk in the range 20 °C–25 °C, respectively.<sup>2</sup> The measured attenuations of yolk and albumen compare well with the data reported by Javanaud *et al.*<sup>2</sup>

Figure 3 shows the measured velocities for yolk in the frequency range 100–350 MHz and for thick and outer thin albumen in the frequency range 100–400 MHz at the temperatures of 23.4 °C–23.7 °C. Yolk exhibits clear velocity dispersion characteristics and thick albumen shows slight dispersion. The velocity dispersion values of 0.065 (m/s)/MHz for yolk and of 0.0019 (m/s)/MHz for thick albumen were obtained by linear approximation, as shown in Fig. 3. On the other hand, the velocity dispersion for outer thin albumen was not seen in the frequency range measured. The values of velocities for thick albumen were greater than those for outer thin albumen and the differences for the three samples ranged from 4–15 m/s.

Figure 4 shows the acoustic impedances for yolk and thick and outer thin albumen determined by measuring the reflection coefficients at the buffer-rod/sample boundary in the frequency range 150–300 MHz at the temperatures of 23.4 °C–23.7 °C. Yolk exhibits a small frequency dependence of impedance, with a rate of increase of 88 (Ns/m<sup>3</sup>)/MHz.

Table II shows the values of the attenuation coefficient,

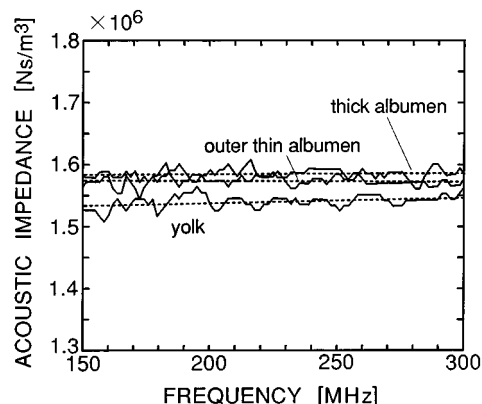


FIG. 4. Frequency dependence of acoustic impedance of yolk, and thick and outer thin albumen at 23.4 °C–23.7 °C. Broken lines fitted by the method of least squares.

velocity, and acoustic impedance for yolk and thick and outer thin albumen from three different eggs at 200 MHz, along with the densities calculated by dividing the measured acoustic impedances by the measured velocities. Significant differences in each acoustic parameter among yolk and thick and outer thin albumen are obtained.

The densities were also measured with a pycnometer in order to compare them with the data obtained by our ultrasonic method. The pycnometer has a volume of 10 ml and needed three eggs for each measurement. The measured results, which are average values of two different sample groups, are shown in Table II. The differences between the measured values obtained with the ultrasonic method and those with the pycnometer are 0.19%, 0.19%, and 1.8% for thick and outer thin albumen, and yolk, respectively. The measured results by the two methods agree well with each other.

### III. DISCUSSION

Table III shows the percentages of water, protein, lipid, carbohydrate, and mineral contents of egg yolk and albumen.<sup>8</sup> As seen, egg yolk has a rich lipid content averaging 33% and a water content of 49%, and albumen is rich in water and protein with a total percentage of 99%. Thus it is tempting to ascribe the differences in the measured acoustic properties of yolk and albumen to the differences in their constituents. As the protein content of albumen is about 10% and its water content is about 88%, a 10% aqueous solution of protein may be considered a simple model of albumen. The acoustic parameters of aqueous solutions of proteins [Ovalbumin (Sigma Chemical Co., A-5503) and bovine he-

TABLE II. Measured attenuation coefficients, velocities, impedances, and densities of egg yolk and albumen at 23.4 °C–23.7 °C.

	$\alpha$ (dB/mm) (200 MHz)	$v$ (m/s) (200 MHz)	$Z$ ( $\times 10^6$ Ns/m <sup>3</sup> ) (200 MHz)	$\rho$ (kg/m <sup>3</sup> ) Ultrasonic method	$\rho$ (kg/m <sup>3</sup> ) Pycnometer
Outer thin albumen	13.6 (13.3–14.2) <sup>a</sup>	1527 (1525–1529)	1.576 (1.566–1.588)	1032 (1027–1039)	1034
Thick albumen	15.7 (14.6–16.9)	1535 (1530–1540)	1.585 (1.553–1.616)	1033 (1015–1049)	1035
Yolk	129 (116–139)	1522 (1517–1526)	1.531 (1.520–1.537)	1006 (996–1013)	1024

<sup>a</sup>Example, mean value 13.6 dB/mm, total range of values 13.3–14.2 dB/mm.

TABLE III. Average percentages of the major groups of chemical compounds in yolk and albumen of chicken egg.<sup>8</sup>

Component	Average percentage	
	Yolk	Albumen
Water	48.7%	87.9%
Proteins	16.6%	10.6%
Lipids	32.6%	trace
Carbohydrates	1.0%	0.9%
Minerals	1.1%	0.6%

moglobin (Hb) (Sigma Chemical Co., H-2625)] were measured and the contribution of protein and water to the acoustic properties of albumen is assessed. Solutions, prepared with protein and distilled water, were stirred at room temperature and degassed under vacuum. Ten percent weight-fractional aqueous solutions of the two proteins were studied.

Figure 5 shows the measured frequency characteristics of attenuation coefficients for 10% aqueous solutions of ovalbumin and bovine hemoglobin at 23.7 °C and 23.8 °C, respectively. The attenuation coefficients of thick and outer thin albumen were also measured at 23.2 °C for comparison. The ultrasonic devices with the center frequency of 400 MHz were used for the measurements. Clearly the attenuation coefficients for all four specimens have very nearly the same frequency dependence in the frequency range 100–400 MHz, being proportional to the 1.4–1.5 power around 100 MHz and to the 1.7–1.8 power around 400 MHz. It is noted that the bovine hemoglobin and ovalbumin solutions show similar frequency characteristics of the attenuation while their molecular components and structure are different. At 200 MHz, attenuation coefficients for the 10% ovalbumin solution, the outer thin albumen, the 10% hemoglobin solution, and the thick albumen are 13.8, 14.6, 15.6, and 17.4 dB/mm, respectively.

Previously, we reported the frequency characteristics of

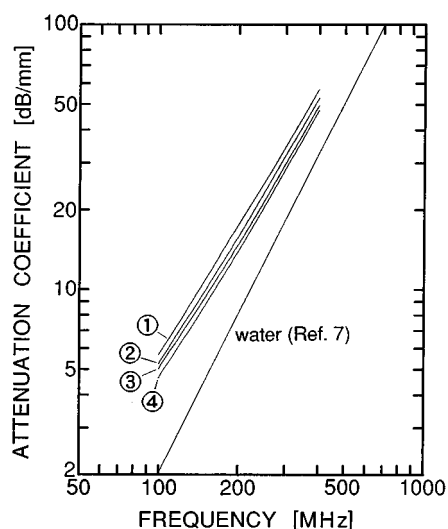


FIG. 5. Frequency dependence of attenuation coefficients of albumen and aqueous solutions of proteins. ① thick albumen (23.2 °C), ② 10% aqueous solution of bovine hemoglobin (23.8 °C), ③ outer thin albumen (23.2 °C), and ④ 10% aqueous solution of ovalbumin (23.7 °C).

TABLE IV. Proteins in albumen.<sup>9</sup>

Protein	Molecular weight (Dalton)	Relative abundance in albumen
Ovalbumin	45 000	60%–69%
Conalbumin	76 000	9%–17%
Ovomucoid	27 000	9%–14%
Lysozyme	14 500	2%–4%

the attenuation coefficients of bovine hemoglobin aqueous solutions in the frequency range 70–200 MHz as a function of hemoglobin concentration.<sup>5</sup> It was observed that as hemoglobin concentration increases, attenuation increases and the exponent on frequency decreases monotonically; around 150 MHz the exponent decreases from 1.70 to 1.52 as the concentration increases from 5% to 25%. The curves of Fig. 5 may be used to support the view that the similarity of the magnitude and frequency dependences of the attenuation coefficients of the four specimens are determined to a great extent by their protein concentrations.

Velocity dispersion was essentially not observed for the ovalbumin and bovine hemoglobin solutions in the frequency range 100–400 MHz, having values less than 0.001 (m/s)/MHz. The average values of velocities for 10% aqueous solutions of ovalbumin and hemoglobin in the frequency range were found to be 1522.2 m/s (23.7 °C) and 1520.9 m/s (23.6 °C), respectively; very close, though they represent different protein structures.

The molecular weights of ovalbumin and hemoglobin are 45 000 Dalton<sup>9</sup> and 64 000 Dalton,<sup>10</sup> respectively, while their attenuation coefficients of 10% aqueous solutions at 200 MHz are 13.8 and 15.6 dB/mm. Albumen consists largely of the proteins, ovalbumin, conalbumin, ovomucoid, and lysozyme; their molecular weights and relative abundance are shown in Table IV.<sup>9</sup> If it is assumed that the relative abundances of ovalbumin, conalbumin, ovomucoid, and lysozyme are 68%, 16%, 13%, and 3%, respectively, a calculated molecular weight of 46 700 Dalton for albumen can be obtained by the simple mixture law of summing each protein constituent's molecular weight multiplied by its relative abundance, yielding the value of 46 700 Dalton within 4% of the ovalbumin value of 45 000 Dalton. Table V shows the experimental results of the attenuation coefficients and velocities at 200 MHz for thick and outer thin albumen, and 10% aqueous solutions of hemoglobin and ovalbumin where it is seen that the magnitudes of both properties are greater in order of thick albumen, outer thin albumen, and 10% aqueous solution of ovalbumin. Lang and Rha<sup>11</sup> considered that the differences of the viscoelastic properties of thick and thin albumen are associated with their content of ovomucin which is four times greater in the thick albumen. A portion of ovomucin aggregates into filamentous super-aggregates with molecular weights of the order of 10<sup>7</sup> Dalton, which give the gellike character to the thick albumen. It would seem, from the measurements reported herein, that the attenuation and velocity value increases may be related to the super aggregations.

TABLE V. Measured attenuation coefficients and velocities in albumen and 10% aqueous solutions of ovalbumin and bovine hemoglobin.

	Attenuation (dB/mm) (200 MHz)	Velocity (m/s) (200 MHz)	Molecular weight (Dalton)
Thick albumen	17.4 (23.2 °C)	1535 (23.4 °C–23.7 °C)	
Outer thin albumen	14.6 (23.2 °C)	1527 (23.4 °C–23.7 °C)	
10% ovalbumin	13.8 (23.7 °C)	1522.2 (23.7 °C)	45 000 <sup>9</sup>
10% hemoglobin	15.6 (23.8 °C)	1520.9 (23.6 °C)	64 000 <sup>10</sup>

#### IV. CONCLUDING REMARKS

The acoustic properties of velocity, attenuation, impedance, and density for egg yolk and thick and outer thin albumen have been measured in the frequency range 20–400 MHz using the bioultrasonic spectroscopy system. In order to investigate the contribution of proteins to the acoustic properties of albumen, the acoustic properties of 10% aqueous solutions of albumin and bovine hemoglobin were also measured. The acoustic properties of albumen appear to be roughly dominated by their constituents of water and proteins. The differences of the acoustic properties between thick and outer thin albumen are considered to be mainly due to their structural differences at the macromolecular level as their constituents are nearly the same.

#### ACKNOWLEDGMENT

The authors would like to thank N. Chubachi for his helpful discussions and encouragement throughout this work.

<sup>1</sup>P.-K. Choi, J.-R. Bae, and K. Takagi, “Frequency dependence of ultrasonic absorption in egg white,” *J. Acoust. Soc. Am.* **80**, 1844–1846 (1986).

<sup>2</sup>C. Javanaud, R. R. Rahalkar, and P. Richmond, “Measurement of speed and attenuation of ultrasound in egg white and egg yolk,” *J. Acoust. Soc. Am.* **76**, 670–675 (1984).

<sup>3</sup>M. J. W. Povey and J. M. Wilkinson, “Application of ultrasonic pulse-echo techniques to egg albumen quality testing: A preliminary report,” *Br. Poult. Sci.* **21**, 489–495 (1980).

<sup>4</sup>J. Kushibiki, N. Akashi, T. Sannomiya, N. Chubachi, and F. Dunn, “VHF/UHF range bioultrasonic spectroscopy system and method,” *IEEE Trans. Ultrason. Ferroelectr. Freq. Control* **42**, 1028–1039 (1995).

<sup>5</sup>N. Akashi, J. Kushibiki, N. Chubachi, and F. Dunn, “Acoustic properties of selected bovine tissues in the frequency range 20 to 200 MHz,” *J. Acoust. Soc. Am.* **98**, 3035–3039 (1995).

<sup>6</sup>W. Kroebel and K.-H. Mahr, “Recent results of absolute sound velocity measurements in pure water and sea water at atmospheric pressure,” *Acustica* **35**, 154–164 (1976).

<sup>7</sup>J. M. M. Pinkerton, “The absorption of ultrasonic waves in liquids and its relation to molecular constitution,” *Proc. Phys. Soc. London, Sect. B* **20**, 129–141 (1949).

<sup>8</sup>A. L. Romanoff and A. J. Romanoff, *The Avian Egg* (Wiley, New York, 1949), Chap. 6, p. 316.

<sup>9</sup>R. D. Palmiter, “Regulation of protein synthesis in chick oviduct,” *J. Biol. Chem.* **247**(20), 6450–6461 (1972).

<sup>10</sup>G. R. Tristram, *The Proteins*, edited by N. Neurath and K. Bailey (Academic, New York, 1954), Vol. I, p. 197.

<sup>11</sup>E. R. Lang and C. Rha, “Apparent shear viscosity of native egg white,” *J. Food Technol.* **17**, 595–606 (1982).

# Ultrasonic relaxation associated with proton transfer reaction in aqueous solutions of heterocyclic amines

Sadakatsu Nishikawa and Masumi Satoh

Department of Chemistry, Faculty of Science and Engineering, Saga University, Saga, 840 Japan

(Received 11 April 1997; accepted for publication 12 August 1997)

Ultrasonic absorption coefficients were measured in aqueous solutions of imidazole and pyrazole by pulse and resonance methods in the frequency range from 3 to 220 MHz at 25 °C. Excess absorption was observed in both solutions. From the concentration dependence of the ultrasonic relaxation parameters associated with a single relaxational process in the solution of imidazole, the cause of the relaxation was proven to be due to a proton transfer reaction and the rate and equilibrium constants were determined for the process. The association rate constant for the ions was reasonable as a diffusion controlled reaction, although it is considerably greater than those in other amine solutions. A standard volume change of the reaction was also determined from the reactant concentration dependence of a maximum absorption per wavelength. The diffusion controlled rate constant for imidazole was considered in relation to the unique molecular structure of imidazole and the effect of the solute on water structure. In the solution of pyrazole, it was not possible to determine the relaxational parameters because the relaxation frequency was located quite below the measurement frequency range. © 1997 Acoustical Society of America. [S0001-4966(97)00512-2]

PACS numbers: 43.80.Cs, 43.80.Ev [FD]

## INTRODUCTION

Dynamic characteristics concerning solute and solvent interactions in aqueous media are very important for understanding the specificity of solutions in biological systems. Hydrolysis of amines which is associated with a very fast proton transfer reaction is one of the reactions between the solute and solvent<sup>1</sup> and it is widely investigated by ultrasonic method. The reaction mechanism is, nowadays, examined theoretically.<sup>2,3</sup> Especially, Tukerman *et al.*<sup>4</sup> have published an interesting and attractive report that the proton transfer reaction due to hydroxide ion is only observed when the complex accompanying plural hydrogen-bonded water molecules transforms into another complex. The present authors<sup>5,6</sup> have been paying attention to the structural effects of solvent water on the reaction, and it has been considered that the proton transfer reaction may be used as a probe monitoring the solvent water structure using the ultrasonic relaxation method. When water structure is promoted or disrupted by other additives which do not participate in the reaction directly, it is expected that the rate of the proton transfer reaction is facilitated or diminished. However, the additives may also block the movement of the reactants, which is a diminishing effect on the diffusion controlled reaction. If the reactant molecules affect the solvent structure by themselves, then the solvent structural effect on the reaction would be directly observed through the proton transfer reaction. However, some complex reactions are also proceeding in solutions of some amines.<sup>7</sup> It has been clarified that these arise from the balance of the hydrophobicity and hydrophilicity of amine molecules.

An introduction of a suitable hydrophilicity moiety into an amine molecule may give us an adequate system to examine the effect of solute on water structure. For this purpose, imidazole and pyrazole have been chosen as solutes and the examination of these aqueous solutions by the ultra-

sonic absorption method has been performed in a wide frequency range, along with sound velocity and density, in this study. The clarification of the solution properties for these solutes is also desired because they are the functional groups for biologically important compounds. Although the proton transfer reaction in the aqueous solution of imidazole was examined by the dissociation field effect, the detail of the relaxation parameters was not reported.<sup>8</sup> Slutsky *et al.*<sup>9</sup> studied the kinetics of the proton transfer between imidazole and hydrogen phosphate, and Rogez *et al.*<sup>10</sup> reexamined similar systems, using the ultrasonic absorption. Recently, Holmes and Challis<sup>11</sup> reported the ultrasonic absorption result in an aqueous solution of histidine in which imidazole plays an important role. We have considered that clarification of the ultrasonic absorption mechanism in aqueous solutions of these heterocyclic amines is particularly desirable for understanding more complex biological reactions and solute and solvent interactions.

## I. EXPERIMENTS

Imidazole and pyrazole were purchased from Wako Pure Chemicals Co. Ltd. and Tokyo Kasei Kogyo Co. Ltd. They were the purest grade and were guaranteed to be more than 98%. Therefore, we used them without further purification. Sample solutions were prepared by weight using distilled and filtered water through the MilliQ SP-TOC system from Japan Millipore Ltd. They were kept in an N<sub>2</sub> gas atmosphere and were left at least one day before measurements.

Ultrasonic absorption coefficients,  $\alpha$ 's, were measured by a pulse method in the frequency range from 15 to 220 MHz using 5- and 20-MHz fundamental x-cut quartz crystals, where the absolute values of the coefficient were obtainable.<sup>12</sup> A resonance method was used to obtain the absorption coefficient in the range from 2.8 to 7.5 MHz; in general, the relative values were obtained because of the me-

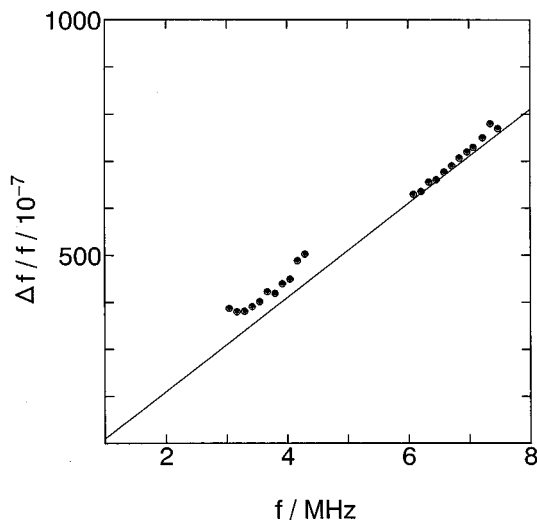


FIG. 1. Frequency dependence of half-bandwidth divided by frequency for water at 25 °C. The solid line is the calculated one using the value of  $\alpha/f^2 = 21 \times 10^{-15} \text{ s}^2 \text{ m}^{-1}$  for water.

chanical loss of the resonator,  $Q^{-1}$ . The absorption coefficient and the half-bandwidth,  $\Delta f$ , are related by  $\Delta f/f = \alpha f/\pi c + Q^{-1}$ , where  $f$  is the frequency and  $c$  is the sound velocity. The reference solution with a similar acoustical impedance was measured to check the mechanical loss. Figure 1 shows the representative result of the plots of  $\Delta f/f$  vs  $f$ , and it is found that the mechanical loss of the resonator used is so small. This means that the almost absolute values of the absorption coefficient are obtainable in our frequency range employed here. However, the symmetry of the resonance curve is lost when the absorption coefficient is large. This is because of overlapping the resonance peak with a satellite one. In this case, the absorption data were not accepted. Details of our resonator are described elsewhere.<sup>6</sup>

Sound velocity was obtained by a sing-around meter at 1.92 MHz<sup>13</sup> and by the resonator at around 3 MHz. The agreement between the two methods was within  $\pm 1 \text{ m s}^{-1}$ . Density was measured by a vibrating density meter (SS-D-200 Shibayama) of which accuracy is less than  $\pm 0.0001 \text{ kg dm}^{-3}$ . Solution  $p\text{H}$  was measured by a glass electrode (HM-60S Toa Denpa) which was inserted in the ultrasonic absorption cell. This gave an accurate  $p\text{H}$  value of the solution because the absorption was very sensitive to  $p\text{H}$ . Water bath and circulating water maintained at a constant temperature within less than  $\pm 0.004 \text{ }^\circ\text{C}$  were used to keep all the measurement cells at 25 °C.

## II. RESULTS AND DISCUSSION

Figure 2 shows the representative ultrasonic absorption spectra in aqueous solutions of imidazole and pyrazole. Figure 3 shows the spectra for imidazole solutions at some conditions. For both solutions, it is seen that the frequency dependence of the absorption coefficient divided by square of the frequency,  $\alpha/f^2$ , is surely observed. It is also seen that the  $\alpha/f^2$  values are almost independent of the frequency in the range over 35 MHz. The frequency dependence is commonly tested through a Debye-type relaxational equation as

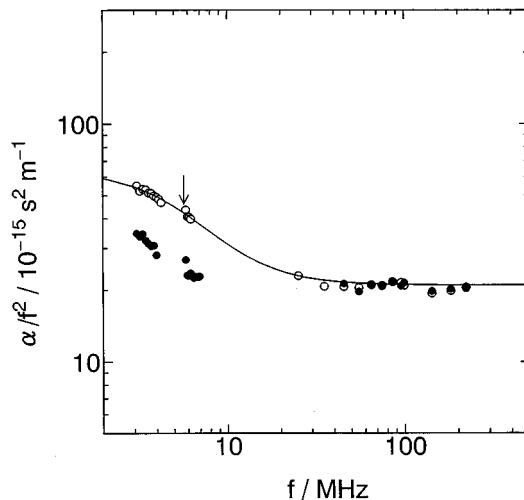


FIG. 2. Representative ultrasonic absorption spectra in aqueous solution of 1.000 mol dm<sup>-3</sup> imidazole (○) and 1.000 mol dm<sup>-3</sup> pyrazole (●) at 25 °C.

$$\alpha/f^2 = A/[1 + (f/f_r)^2] + B, \quad (1)$$

where  $f_r$  is the relaxation frequency,  $A$  is the amplitude of the ultrasonic relaxation, and  $B$  is the background absorption. The ultrasonic parameters have been usually determined by a nonlinear least-mean-square method.<sup>12</sup> This has been carried out as  $\alpha/f$  vs  $(A/[1 + (f/f_r)^2] + B)f$ , because Eq. (1) is a monotonous decreasing function of the frequency. Although such a calculation procedure was applied to the solutions investigated in this study, large errors or unphysical parameters (e.g., negative ultrasonic parameters) were obtained. This is because the relaxation frequency locates in the frequency range less than 7 MHz. Equation (1) is rearranged to the next equation,

$$(\alpha/f^2 - B)^{-1} = 1/A + \{1/(Af_r^2)\}f^2. \quad (2)$$

The background absorption,  $B$ , which is close to solvent value, is roughly estimated in the pulse frequency range

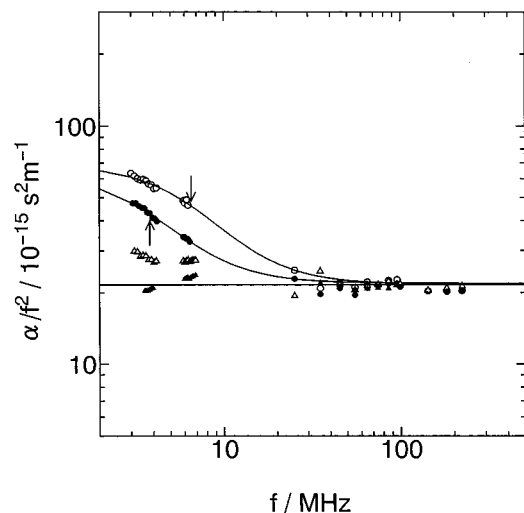


FIG. 3. Ultrasonic absorption spectra in aqueous solution of imidazole. ●: 0.5005 mol dm<sup>-3</sup>, ○: 2.001 mol dm<sup>-3</sup> ( $p\text{H}=10.348$ ), △: 2.000 mol dm<sup>-3</sup> ( $p\text{H}=9.500$ ), ▲: 0.250 mol dm<sup>-3</sup> ( $p\text{H}=7.53$ ).



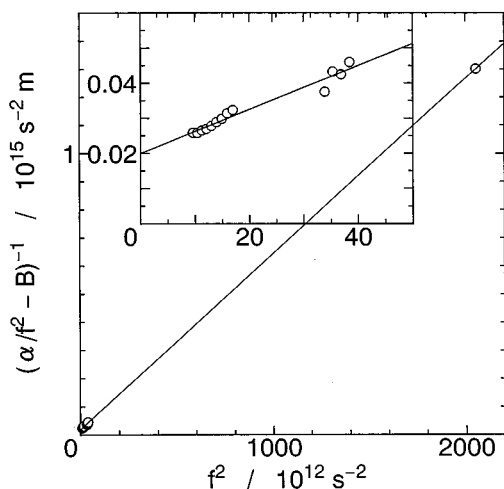


FIG. 4. The plots of  $(\alpha/f^2 - B)^{-1}$  vs  $f^2$  for aqueous solution of imidazole at  $1.000 \text{ mol dm}^{-3}$  imidazole.

more than 35 MHz by trial and error. Once the background absorption is determined, it is easy to determine the other two parameters,  $A$  and  $f_r$ , from the plots of the left term of Eq. (2) vs the square of the measurement frequency. Then, the plots according to Eq. (2) were tested, and the parameters and the standard deviations were calculated. The  $B$  value was changed slightly and the same plots were repeated until the smallest standard deviation was obtained. One of the plots following Eq. (2) is shown in Fig. 4. Good linear relations were obtained in the absorption data for the solution of imidazole. The solid curves in Figs. 2 and 3 are the calculated values using the determined ultrasonic parameters and it is seen that they have given good agreements with the experimental data. Thus determined parameters are listed in Table I. The measurements in the more dilute solutions were carried out, but unreasonable or unplausible relaxation parameters were obtained because of the small amplitude and the low relaxation frequency. On the other hand, although the above analytical procedure was applied to the solution of pyrazole, the results gave large errors. This is because the relaxation frequency is considered to locate in the range less than that of the present experiment. Therefore, we have concentrated on the detailed analysis for solution of imidazole.

TABLE I. Ultrasonic parameters for aqueous solutions of imidazole at  $25^\circ\text{C}$ .

Co mol dm <sup>-3</sup>	pH	$f_r$ MHz	A		c m s <sup>-1</sup>	$\rho$ kg dm <sup>-3</sup>
			$10^{-15} \text{ s}^2 \text{ m}^{-1}$			
0.2004	9.811	4.00±0.10	20.8±0.6	21.6	1499	1.0010
0.3008	9.914	3.28±0.08	30.6±0.8	21.8	1502	1.0012
0.4009	9.985	4.11±0.09	37.8±0.8	21.4	1504	1.0021
0.5005	10.044	4.42±0.03	42.6±0.3	20.7	1508	1.0029
0.6029	10.090	4.75±0.06	42.5±0.5	20.5	1511	1.0040
0.7510	10.145	4.80±0.10	47.0±1.0	20.8	1515	1.0050
1.000	10.203	5.68±0.08	49.7±0.7	20.6	1519	1.0068
1.215	10.248	5.87±0.03	50.3±0.2	21.4	1525	1.0090
1.500	10.284	5.79±0.04	47.6±0.3	21.8	1530	1.0113
1.700	10.310	6.41±0.04	44.9±0.3	22.3	1534	1.0128
2.001	10.348	6.76±0.06	47.3±0.4	21.8	1539	1.0151

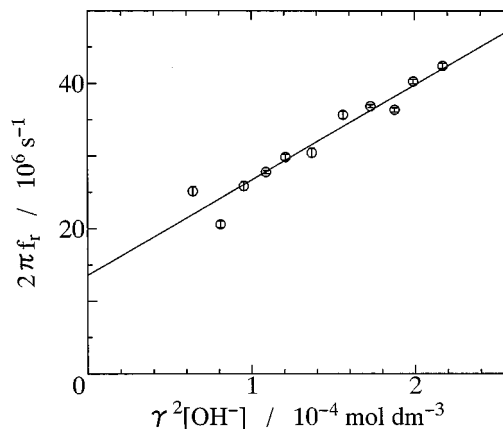
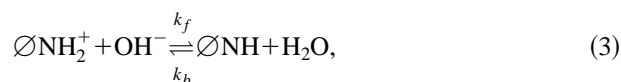


FIG. 5. The plots of  $2\pi f_r$  vs  $\gamma^2[\text{OH}^-]$  for aqueous solution of imidazole.

As seen in Table I, the relaxation frequency increases with the analytical concentration,  $C_0$ , and the amplitude of the ultrasonic relaxation increases and then reaches a plateau with increase of  $C_0$ . These profiles are very similar to those observed for the case of the proton transfer reaction in other amine solutions.<sup>5-7</sup> Also, the absorption measurements were carried out in imidazole solution at different pH's, as seen in Fig. 3. With decreasing pH by an addition of concentrated HCl solution, the relaxational absorption decreases steeply, the result of which is also characteristic to the proton transfer reaction. At pH=7.53, no relaxational absorption was observed, the result of which is important for the ultrasonic absorption in the solutions of related compounds such as histidine.<sup>11</sup>

The reaction between  $\text{NH}_2^+$  group in imidazole and solvent hydroxyl ion is expressed as



where  $\text{O} \text{NH}$  stands for imidazole molecule. The relation between the relaxation frequency and the reactant concentrations is derived as Eq. (4) and it is simplified to Eq. (4') when only imidazole is dissolved in water where the concentration of water is assumed to be much larger than other reactants:

$$2\pi f_r = k_f \gamma^2 ([\text{OH}^-] + [\text{O} \text{NH}_2^+]) + k_b, \quad (4)$$

$$= 2k_f \gamma^2 [\text{OH}^-] + k_b, \quad (4')$$

where  $\gamma$  is the activity coefficient calculated by Davis' equation.<sup>14</sup> Figure 5 shows the plots of  $2\pi f_r$  vs  $\gamma^2[\text{OH}^-]$ . A good straight line is obtained, which means that the observed ultrasonic relaxation is surely associated with the proton transfer reaction. Using a linear least-mean-square method, the slope gives the forward rate constant,  $k_f$ , and the intercept gives the backward rate constant,  $k_b$ . Then, the ratio,  $k_b/k_f$ , should be close to the base dissociation constant,  $K_b = \gamma^2[\text{OH}^-][\text{O} \text{NH}_2^+]/[\text{O} \text{NH}]$ . However, it is far apart from the literature value,<sup>15</sup> as is clearly seen in Table II.

The proton transfer reaction mechanism proposed by Eigen<sup>1</sup> is that coupled with intermediate reactants and is expressed as

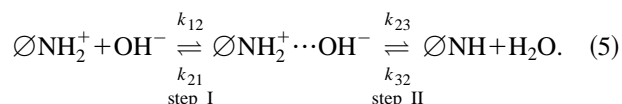
TABLE II. The rate and thermodynamic constants for proton transfer reaction in aqueous solutions of heterocyclic amines.

Solute	$k_{12}^a$	$k_{21}'$	$K_{32}$	$K_b^b$	$K_b^c$
	$10^{10} \text{ mol}^{-1} \text{ dm}^3 \text{ s}^{-1}$	$10^7 \text{ s}^{-1}$		$\text{mol dm}^{-3}$	
Pyrrolidine	$2.6 \pm 0.1$	$18 \pm 1$	$5.7 \times 10^{-1}$	$(2.5 \pm 0.5) \times 10^{-3}$	$1.3 \times 10^{-3}$
Morpholine	$2.9 \pm 0.3$	$3.7 \pm 0.2$	$9.0 \times 10^{-4}$	$(1.2 \pm 0.6) \times 10^{-6}$	$3.1 \times 10^{-6}$
Piperidine	$2.3 \pm 0.2$	$15 \pm 3$	$2.0 \times 10^{-1}$	$(1.3 \pm 0.2) \times 10^{-3}$	$1.3 \times 10^{-3}$
Imidazole	$6.6 \pm 0.4$	$1.4 \pm 0.1$	$1.2 \times 10^{-4}$	$(2.4 \pm 0.5) \times 10^{-8}$	$1.2 \times 10^{-7}$

<sup>a</sup>The value of  $k_{12}$  for morpholine solution appearing in Ref. 21 is mistyped.

<sup>b</sup>From the relation,  $K_b = \gamma^2[\text{OH}^-]^2/(\text{Co}-[\text{OH}^-])$ .

<sup>c</sup>From Ref. 14.



The intermediate may include several steps.<sup>1</sup> It is quite natural that step II is proceeding much faster than step I because step II is almost an intramolecular process. Ordinarily, the faster process affects the slower one and the obtained rate constants  $k_f$  and  $k_b$  correspond to  $k_{12}$  and  $k_{21}/(1+K_{32}^{-1})$ , respectively, where  $K_{32}$  is defined as  $K_{32} = k_{32}/k_{23}$ . The contribution from the faster process appears in  $k_{21}/(1+K_{32}^{-1})$  term. Still then, the  $k_b/k_f$  value should be close to the base dissociation constant because  $K_b = \gamma^2[\text{OH}^-]^2/([\text{O} \text{NH}_2^+ \cdots \text{OH}^-] + [\text{O} \text{NH}^-])$  in this case. Even if other equilibria are taken into account in addition to the second process in Eq. (5),<sup>1</sup> which might be probable [such as  $(\text{O} \text{NH}_2^+(\text{OH}_2)_2\text{OH}^-)$ ,  $(\text{O} \text{NH}_2^+(\text{OH}_2)\text{OH}^-)$ ,  $(\text{O} \text{NH}(\text{OH}_2))$  and so on], the ratio of  $k_b/k_f$  should still have been close to the dissociation constant if the second step influences the first one. These kinds of results have been obtained in other aqueous solutions of amines.<sup>7,16,17</sup> The contribution term of the faster process to the slower one on the relaxation frequency, in general, arises from the relation between the small concentration changes in the reactants which are produced by the external perturbation (the alternating pressure change in this study) as  $\delta[\text{O} \text{NH}_2^+] + \delta[\text{O} \text{NH}_2^+ \cdots \text{OH}^-] + \delta[\text{O} \text{NH}] = 0$  for Eq. (5). For the discrepancy of the base dissociation constant,  $K_b$ , obtained by a static method and by the dynamic one in this study, the simplest interpretation may follow from an assumption that the perturbed concentration,  $\delta[\text{O} \text{NH}]$ , is too small compared with others, and then,  $k_f$  and  $k_b$  are corresponding to  $k_{12}$  and  $k_{21}$ , respectively. Thus postulated rate constants are tabulated in Table II along with those for aqueous solutions of other heterocyclic amines for comparison. It is possible to estimate the dissociation constant using the determined rate constants and the experimental relaxation frequency on the assumption that the perturbation of only first equilibrium in Eq. (5) is the cause of the observed relaxation.<sup>16</sup> It is  $K_b = (2.5 \pm 0.7) \times 10^{-8} \text{ mol dm}^{-3}$  and is very close to the value in Table II.

It is seen that the forward rate constant is reasonable for a diffusion controlled reaction, although the value for imidazole solution is considerably greater than others. Eigen *et al.*<sup>8</sup> have reported the rate constant using the dissociation field method to be  $k_{12} = 2.3 \times 10^{10} \text{ mol}^{-1} \text{ dm}^3 \text{ s}^{-1}$ .<sup>1</sup> However, details of the measured concentration range and the relaxation

times were not shown. It is said that the fastest proton transfer reaction in aqueous solutions of amines is found in solution of ammonia as  $3 \times 10^{10} \text{ mol}^{-1} \text{ dm}^3 \text{ s}^{-1}$ .<sup>1</sup> The result for imidazole is still larger than this value. Imidazole consists of two virtually identical nitrogen atoms, and therefore the number of the reaction site is twice when compared with other amines listed in Table II. Then, the steric factor for the reaction may be greater than those for others.

It should be noticed that only the relaxational absorption due to the proton transfer reaction is observed in the concentration up to  $2.00 \text{ mol dm}^{-3}$  for imidazole. Ordinarily, the proton transfer reaction in an aqueous solution by the ultrasonic method is examined in relatively dilute solutions in order to avoid the system with complex reactions. When the concentration of solute is relatively high, it is naturally expected that the solute may disturb the solvent structures, which has been also found in aqueous solutions of various alcohols.<sup>18</sup> As is shown in Table II, imidazole has a quite low base dissociation constant,  $K_b$ , which provides the high concentration of the nonionized molecules. However, imidazole is considered to still have a high hydrophobic character from its molecular structure and it may affect the solvent water molecules. If the proposed reaction model by Tuckerman *et al.*<sup>4</sup> is taken into account, the diffusion controlled reaction of hydroxide ion is closely related to hydrogen-bonded complex of water molecules. The hydrophobic group of imidazole promotes the hydrogen-bonded network of solvent water molecules. Then, the greater rate constant,  $k_{12}$ , is reasonably understood because the diffusion rate of hydroxide ion is facilitated through the hydrogen-bonded network. This aspect has been noticed also in other systems by Grimshaw and Wyn-Jones.<sup>19</sup>

The base dissociation constant,  $K_b$ , is obtainable from the relation as  $K_b = \gamma^2[\text{OH}^-]^2/(\text{Co}-[\text{OH}^-])$ , which is listed in Table II. The obtained value is slightly larger than that in the literature,<sup>15</sup> which may be due to its determination in the relatively concentrated solutions of imidazole in this study. The equilibrium constant,  $K_{32}$ , for the second step in Eq. (3) is considered to be a representative one with further plural equilibria, and it is possible to calculate the value using the relation as  $K_b = K_{21}/(1+K_{32}^{-1})$  under the assumption of equilibria of Eq. (5).  $K_{21}$  value is obtained by  $k_{21}/k_{12}$ , and  $K_{32}$ , which is listed in Table II, is calculated with the above relation. It is seen from these results that the concentrations of the ions and the intermediate which participate in the reaction are quite low.

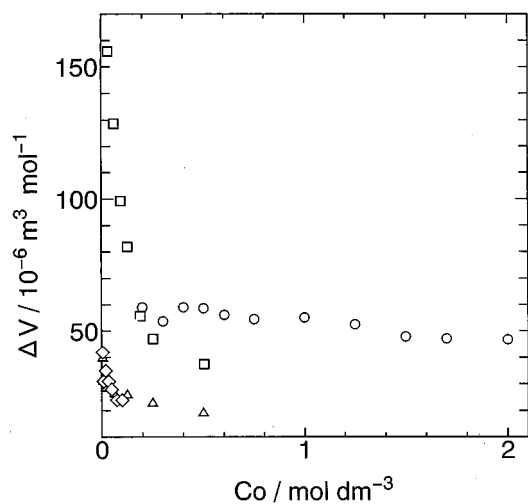


FIG. 6. Analytical concentration dependence of the standard volume change of the reaction. ○: imidazole; □: morpholine; △: piperidine; ◇: pyrrolidine.

From the ultrasonic absorption measurements, a standard volume change of the reaction,  $\Delta V$ , is also determined with the help of the sound velocity,  $c$ , and the solution density,  $\rho$ , data. The maximum absorption per wavelength,  $\mu_{\max} = 0.5A f_r c$ , is given as<sup>7</sup>

$$\mu_{\max} = \pi \rho c^2 (2[\text{OH}^-] + 1/[\text{ONH}_2^+ \cdots \text{OH}^-])^{-1} (\Delta V)^2 / (2RT). \quad (6)$$

In this analysis, a contribution of the enthalpy term to the maximum absorption per wavelength is ignored, which is a good approximation for aqueous solutions.<sup>16,17</sup> Also, the contribution of the activity coefficient to  $\mu_{\max}$  is negligibly small because the term,  $\delta \ln \gamma / \delta [\text{OH}^-]$ , is much smaller than  $1/[\text{OH}^-]$  (less than 0.8%). Further, the contribution of the faster processes to the observed one was neglected because of the same reasons mentioned above. The standard volume change of the reaction has been found to be dependent on the analytical concentration, as is shown in Fig. 6, in which the results for other heterocyclic amine solutions are also indicated for comparison. This kind of evidence was pointed out by Atkinson *et al.*<sup>17</sup> for the aqueous solution of t-butylamine. The present authors have also noticed that it is dependent on the concentration for various amine solutions.<sup>5,6,21,22</sup> However, such dependence has not been well interpreted quantitatively yet. Qualitatively, it is explained as follows: The intermediate may still include the plural water molecules and the large volume change of the reaction is caused by these molecules which are also influenced by the hydrophobic moiety of imidazole. When the analytical concentration of the amines decreases, the number of water molecules participating in the intermediate increases, and then the concentration dependent volume change of the reaction is considered to appear. It has been shown in our previous report<sup>21</sup> that the volume change reflects the effect of water structural change. When water structure is promoted, the volume change tends to increase. As is seen in Fig. 6, the volume change for imidazole is larger than others in the concentration range of more than  $0.200 \text{ mol dm}^{-3}$ . This is another indication that

imidazole works as the water structure promoter, the result of which is consistent with the interpretation for the diffusion controlled rate constant,  $k_{12}$ , as mentioned above. The concentration dependence of the volume change seems to indicate no systematic trend for different heterocyclic amines. The proton transfer reaction is only observed in restricted concentration ranges (i) because another relaxational absorption appears in the concentrated solutions of morpholine and piperidine, and (ii) because the position of the relaxation frequency is in the higher frequency range (more than 200 MHz) for that of pyrrolidine; therefore, that the analysis for the absorption associated with the proton transfer reaction could not be able to carry out.

In conclusion, imidazole molecules are considered to exist mostly as monomers in the concentration up to  $2.00 \text{ mol dm}^{-3}$  and these molecules promote the hydrogen bond network of solvent water. Then, the diffusion controlled rate for the ion association is facilitated.

- <sup>1</sup>J. E. Crooks, "Fast and slow proton-transfer reactions in solution," in *Proton Transfer Reaction*, edited by E. Caldin and V. Gold (Chapman and Hall, London, 1975), p. 153.
- <sup>2</sup>H. Bueker and E. Uggerced, "Energies and dynamics of intermolecular proton-transfer processes," *J. Phys. Chem.* **99**, 5945 (1995).
- <sup>3</sup>A. L. Sobolewski and L. Adamowicz, "Theoretical investigations of the proton transfer reaction in the hydrogen-bonded complex of 2-pyrimidione with water," *J. Phys. Chem.* **99**, 14 277 (1995).
- <sup>4</sup>M. Tuckerman, K. Laasonen, M. Sprik, and M. Parrinello, "Ab initio molecular dynamics simulation of the solvation and transport of  $\text{H}_3\text{O}^+$  and  $\text{OH}^-$  ions in water," *J. Phys. Chem.* **99**, 5749 (1995).
- <sup>5</sup>N. Kuramoto and S. Nishikawa, "Proton transfer reaction affected by water structure breaker, urea, by the ultrasonic relaxation method," *J. Phys. Chem.* **99**, 14 372 (1995).
- <sup>6</sup>N. Kuramoto, M. Ueda, and S. Nishikawa, "Solvent effect on proton transfer reaction rate by ultrasonic absorption method," *Bull. Chem. Soc. Jpn.* **67**, 1560 (1994).
- <sup>7</sup>S. Nishikawa and R. Gouhara, "Ultrasonic relaxations in aqueous solutions of piperidine and pyrrolidine," *Bull. Chem. Soc. Jpn.* **69**, 1855 (1996).
- <sup>8</sup>M. Eigen, G. G. Hammes, and K. Kustin, "Fast reactions of imidazole studied with relaxation spectroscopy," *J. Am. Chem. Soc.* **82**, 3482 (1960).
- <sup>9</sup>L. J. Slutsky, M. Madsen, R. D. White, and J. Harkness, "Kinetics of the exchange of protons between hydrogen phosphate ions and a histidyl residue," *J. Phys. Chem.* **84**, 1325 (1980).
- <sup>10</sup>D. Rogez, R. Andreanara, and C. H. Choi, "Kinetic studies of proton-exchange reactions between imidazole groups of small molecules and hydrogen phosphate ions in aqueous solution using ultrasonic relaxation," *J. Phys. Chem.* **95**, 4015 (1991).
- <sup>11</sup>A. K. Holmes and R. E. Challis, "Acoustic absorption due to proton transfer in solutions of proteins, peptides, and amino-acids at neutral pH," *J. Acoust. Soc. Am.* **100**, 1865 (1996).
- <sup>12</sup>S. Nishikawa and K. Kotegawa, "Structure and kinetics in aqueous solution of butyl cellosolve from the temperature dependence of ultrasonic properties," *J. Phys. Chem.* **89**, 2896 (1985).
- <sup>13</sup>T. Yasunaga, N. Tatsumoto, and M. Miura, "Studies of chemical kinetics by means of the velocity of sound," *Bull. Chem. Soc. Jpn.* **37**, 1655 (1964).
- <sup>14</sup>R. A. Robinson and R. H. Stokes, in *Electrolyte Solutions* (Butterworths, London, 1959), p. 232.
- <sup>15</sup>J. J. Christensen, R. M. Izatt, D. P. Wrathall, and L. D. Hansen, "Thermodynamics of proton ionization in dilute aqueous solution," *J. Chem. Soc. (A)* **1969**, 1212.
- <sup>16</sup>Y. Yoshida and S. Nishikawa, "Analysis of proton-transfer reaction in aqueous solutions of butylamines by ultrasonic methods," *Bull. Chem. Soc. Jpn.* **59**, 1941 (1986).
- <sup>17</sup>G. Atkinson, M. Emara, H. Endo, and B. L. Atkinson, "Ultrasonic absorption in aqueous binary mixtures. 1. Tert-butylamine-water at 25 °C," *J. Phys. Chem.* **84**, 259 (1980).

- <sup>18</sup>S. Nishikawa and M. Ueda, "Ultrasonic relaxations in aqueous solutions of alcohols and the balance between hydrophobicity and hydrophilicity of the solutes," *J. Phys. Chem.* **97**, 3539 (1993).
- <sup>19</sup>D. Grimshaw and E. Wyn-Jones, "Proton transfer in some Dodel equilibria studied by the ultrasonic method," *J. Chem. Soc. Faraday Trans. II* **69**, 168 (1973).
- <sup>20</sup>S. Nishikawa and Y. Harano, "Reinvestigation of ultrasonic absorption mechanisms in tert-butylamine aqueous solution," *J. Phys. Chem.* **93**, 7152 (1989).
- <sup>21</sup>S. Nishikawa, N. Arakane, and N. Kuramoto, "Ultrasonic absorption and velocity of aqueous solutions of heterocyclic amines," *J. Phys. Chem.* **99**, 369 (1995).
- <sup>22</sup>N. Kuramoto and S. Nishikawa, "Effect of 2-propanol on proton transfer reaction by ultrasonic absorption method," *J. Phys. Chem.* **100**, 10 629 (1996).

# Decorrelation of intravascular echo signals: Potentials for blood velocity estimation

Wenguang Li<sup>a)</sup>

Thoraxcentre, Erasmus University Rotterdam, 3000 DR Rotterdam, The Netherlands and Interuniversity Cardiology Institute Netherlands (ICIN), 3501 DG Utrecht, The Netherlands

Charles T. Lancée

Thoraxcentre, Erasmus University Rotterdam, 3000 DR Rotterdam, The Netherlands

E. Ignacio Céspedes

Thoraxcentre, Erasmus University Rotterdam, 3000 DR Rotterdam, The Netherlands and Endosonics Corporation, Rancho Cordova, California 95670

Antonius F. W. van der Steen and Nicolaas Bom

Thoraxcentre, Erasmus University Rotterdam, 3000 DR Rotterdam, The Netherlands and Interuniversity Cardiology Institute Netherlands (ICIN), 3501 DG Utrecht, The Netherlands

(Received 25 March 1997; revised 24 June 1997; accepted 16 August 1997)

When blood particles travel through an intravascular ultrasound imaging plane, the received echo signals decorrelate at a rate that is related to the flow velocity. In this paper, the feasibility of extracting blood velocity from the decorrelation function of radio frequency signals was investigated through theoretical analysis and computer simulation. A computer model based on the impulse response method was developed to generate the ultrasound field of a 30-MHz intravascular transducer. The decorrelation due to the scatterer displacement as well as other nonmotion related decorrelation sources were studied. The computer simulations show that the decorrelation function is linearly related to the lateral displacement. The monotonic relationship between correlation and displacement provides possibilities to estimate flow velocity with decorrelation measurements. Because of the complexity of the beam profile in the near field, assessment of local velocities requires detailed knowledge of the decorrelation at each axial beam position. Sources of signal decorrelation other than the lateral displacement may cause a bias in the decorrelation based velocity measurements. For localized decorrelation estimation, measurement variations in small range windows present a major challenge. An approach based on multiple decorrelation measurements should be adopted in order to reduce the variations. In conclusion, results of this study suggest that it is feasible to measure flow velocity by quantifying the decorrelation of intravascular ultrasound signals from blood. © 1997 Acoustical Society of America. [S0001-4966(97)00612-7]

PACS numbers: 43.80.Ev, 43.80.Cs, 43.80.Qf [FD]

## INTRODUCTION

The displacement of an ultrasound-scattering material such as blood moving through the beam of an ultrasound transducer results in concomitant changes (decorrelation) in the received echo signal. This phenomenon is clearly exhibited by a catheter-based intraluminal imaging technique, intravascular ultrasound (IVUS), in which the ultrasound beam is transmitted almost perpendicularly to the arterial tissue and blood flow. With real-time IVUS imaging, it can be seen that the scattering pattern of flowing blood varies rapidly over time. This is caused by the fact that the flow stream drives randomly distributed blood particles through the imaging volume, resulting in decorrelation of the received echo signals as a function of time.

Two important characteristics of the decorrelation of intravascular echo signals should be addressed. First, because the flow usually has a higher velocity than wall motion, blood echo signals decorrelate significantly faster than those

of tissues. Several groups have demonstrated that methods based on either video or radio frequency (rf) processing can take advantages of the time-varying feature of blood echoes to improve the IVUS image.<sup>1-5</sup> Li *et al.* have documented a significant difference in the correlation time between blood and tissue through rf analysis of *in vivo* echo data.<sup>6</sup> Therefore, the contrast in the decorrelation of blood and tissue may be used to enhance the luminal boundary. Second, it is a reasonable hypothesis that the speed of such a decorrelation procedure should be a function of the flow velocity.<sup>7-10</sup> In other words, the faster blood particles move across the ultrasound beam, the higher the decorrelation rate of the received signals. The velocity-decorrelation relation may be used to estimate flow velocity by means of quantifying the decorrelation rate from blood scattering signals. For both applications, the decorrelation as a function of scatterer displacements is the most important basis. Several applications of echo signal decorrelation for the assessment of tissue dynamics have been reported. The decorrelation due to lateral beam translation has been studied in detail for texture analysis and compound scanning.<sup>11-13</sup> Decorrelation factors such as trans-

<sup>a)</sup>Electronic mail: li@tch.fgg.eur.nl

verse velocities and velocity variances/gradients have been addressed as error sources in time-domain velocity measurement techniques.<sup>14–16</sup> Decorrelation measurements have been proposed for detection of tissue motion and the transverse blood velocity. Dickinson *et al.* reported a decorrelation based method for tissue motion estimation.<sup>17</sup> Zhang *et al.* and Dotti *et al.* applied the decorrelation measurement to estimate the angle between the ultrasound beam and blood flow in order to retrieve the true blood velocity vector.<sup>18,19</sup>

In all the previous work, however, decorrelation assessment was concentrated on the far field or the focus of a transducer. Conversely, most intravascular imaging is performed within the near field of the transducer. A typical IVUS system employs a circular unfocused transducer with a diameter of approximately 1 mm; the scanning depth starts at the extreme near field ( $\approx 0.1$  mm) and extends up to the far field ( $> 5$  mm) of the ultrasound beam. Another characteristic in IVUS imaging as compared to most of conventional medical ultrasound applications is the use of high ultrasonic frequencies (20–40 MHz) and a wide system bandwidth ( $\approx 20$  MHz). The present study was therefore designed to investigate the decorrelation properties of the near field of a high-frequency broadband transducer. The investigation was conducted using theoretical analysis and a computer simulation of an IVUS transducer. The ultimate goal was to study the feasibility of extracting blood velocity from the decorrelation function of rf intravascular echo signals.

## I. THEORETICAL ANALYSIS

The ultrasound beam considered in this study is generated from a circular transducer, which is symmetric on the cross-sectional plane ( $x$ - $y$  plane). Thus a two-dimensional ( $x$ - $z$ ) coordinate system can be used to represent an IVUS imaging configuration (Fig. 1). The  $x$  axis is the typical direction of blood flow and the  $z$  axis is defined by the center of the ultrasound beam. With reference to this coordinate system, the movement of blood particles across and along the ultrasound beam is termed the *lateral* and *axial* displacement, respectively.

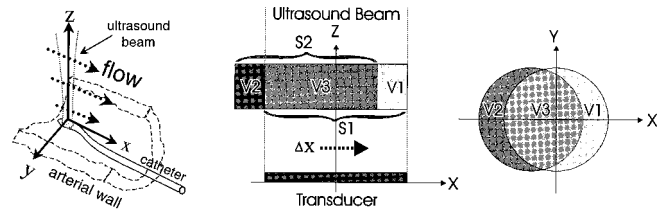


FIG. 1. Left panel: Three-dimensional geometry of intravascular imaging with the  $z$  axis representing central axis of the ultrasound beam. Blood scatterers move laterally through the beam along the  $x$  axis. Middle panel: Scatterer volumes represented by  $\mathbf{V1} + \mathbf{V3}$  at  $T1$  and  $\mathbf{V2} + \mathbf{V3}$  at  $T2$ . Right panel: Corresponding view on the  $X$ - $Y$  plane.

The following decorrelation factors are investigated:

- (1) lateral displacement
- (2) axial displacement
- (3) signal to noise ratio
- (4) velocity gradient
- (5) correlation variance.

### A. Lateral decorrelation

Figure 1 illustrates a volume of blood scatterers moving across the ultrasound beam. At time  $T_1$  and  $T_2 = T_1 + \Delta T$ , the scatterer volume that generates rf signals  $S_1$  and  $S_2$  can be divided into three parts:

**V1:** scatterers inside the beam at  $T_1$  move outside the beam at  $T_2$ ;

**V2:** new scatterers move inside the beam at  $T_2$ ;

**V3:** scatterers remain inside the beam at  $T_1$  and  $T_2$ .

Denote  $S_{v1}$  and  $S_{v2}$  are signals from volume **V1** and **V2**, respectively;  $S_{v3}$  and  $S'_{v3}$  represent the signals of before and after the lateral displacement of **V3**. The rf trace  $S_1$  and  $S_2$  can be written as

$$S_1 = S_{v1} + S_{v3}, \quad S_2 = S_{v2} + S'_{v3}. \quad (1)$$

The correlation coefficient between  $S_1$  and  $S_2$  with zeros mean is calculated by

$$\begin{aligned} \rho_{12} &= \frac{\int S_1 S_2 dt}{\sqrt{\int [S_1]^2 dt} \sqrt{\int [S_2]^2 dt}} = \frac{\int (S_{v1} + S_{v3})(S_{v2} + S'_{v3}) dt}{\sqrt{\int [(S_{v1} + S_{v3})]^2 dt} \sqrt{\int [(S_{v2} + S'_{v3})]^2 dt}} \\ &= \frac{\int (S_{v1} S_{v2} + S_{v1} S'_{v3} + S_{v3} S_{v2} + S_{v3} S'_{v3}) dt}{\sqrt{\int [(S_{v1})^2 + 2S_{v1} S_{v3} + (S_{v3})^2] dt} \sqrt{\int [(S_{v2})^2 + 2S_{v2} S'_{v3} + (S'_{v3})^2] dt}}, \end{aligned} \quad (2)$$

where  $\int S_{v1} S_{v2} dt$ ,  $\int S_{v1} S'_{v3} dt$ ,  $\int S_{v3} S_{v2} dt$ ,  $\int S_{v1} S_{v3} dt$ , and  $\int S_{v2} S'_{v3} dt$  are the cross-correlation values of echo signals of **V1**, **V2**, and **V3**. Since scatterers are assumed to be randomly distributed, the cross-correlation terms of different volumes in (2) are close to zero when integrated over a sufficiently long period. Removing the cross-correlation terms, expression (2) is written as

$$\rho_{12} = \frac{\int S_{v3} S'_{v3} dt}{\sqrt{\int [(S_{v1})^2 + (S_{v3})^2] dt} \sqrt{\int [(S_{v2})^2 + (S'_{v3})^2] dt}}. \quad (3)$$

Assuming a homogenous scatterer density, the number of scatterers that enters the beam is identical to the number of scatterers that leaves the beam. Let  $\kappa$  be the signal power

ratio between the scatterers moving in or out and those staying inside the beam

$$\kappa \approx \frac{\int [S_{v2}]^2 dt}{\int [S'_{v3}]^2 dt} \approx \frac{\int [S_{v1}]^2 dt}{\int [S_{v3}]^2 dt}. \quad (4)$$

The correlation coefficient for the scatterers remaining in the beam after a lateral displacement is

$$\rho'_{12} = \frac{\int S_{v3} S'_{v3} dt}{\sqrt{\int [S_{v3}]^2 dt \int [S'_{v3}]^2 dt}}. \quad (5)$$

Combining (4) and (5),  $\rho_{12}$  can be rewritten as

$$\rho_{12} = \frac{\rho'_{12}}{\sqrt{1 + 2\kappa + \kappa^2}} = \frac{\rho'_{12}}{1 + \kappa}. \quad (6)$$

Equation (6) indicates that there are two contributing factors for the lateral decorrelation: (1) due to the scatterers moving laterally inside the beam; (2) due to scatterers entering and leaving the beam. The relative weight of these factors is determined by the beam profile of a transducer.

## B. Axial displacement

The correlation coefficient of the received rf signals decreases quickly when the phase is shifted as a result of the axial displacements of blood scatterers. The decorrelation due to a phase shift is determined by the autocorrelation function of rf signals, mainly by the central frequency and bandwidth. For example, at a central frequency of 30 MHz, an axial displacement of 12  $\mu\text{m}$  will cause a 180-deg phase shift and produce a negative correlation value. Although the axial velocity in the IVUS setup is typically very small due to the near 90° angle between the beam and flow, the phase decorrelation is still much higher than the decorrelation of a lateral displacement. Thus differences in the signal phase must be removed by a phase matching procedure. For an ideal beam profile of uniform intensity distribution, the signal generated by a scatterer moving axially is a time delayed replica of its initial position. The two signals will be perfectly correlated after the phase matching procedure. In reality, the beam profile is inhomogeneous along the axial direction, particularly in the extreme near field. Therefore, the correlation output may be modulated by the axial beam pattern.

## C. Decorrelation due to noise

Electronic noise and quantization are well-known sources for a decrease of signal correlation. Similar to the earlier development,<sup>20,21</sup> considering that  $S_1$  and  $S_2$  are the partially correlated rf signals at time  $T_1$  and  $T_2$ , and  $n_1$  and  $n_2$  are additive bandpass white noises, the received signals  $S_{n1}$  and  $S_{n2}$  can be written as

$$S_{n1} = S_1 + n_1, \quad S_{n2} = S_2 + n_2. \quad (7)$$

The correlation coefficient of  $S_{n1}$  and  $S_{n2}$  is defined by

$$\begin{aligned} \rho_{n12} &= \frac{\int S_{n1} S_{n2} dt}{\sqrt{\int [S_{n1}]^2 dt} \sqrt{\int [S_{n2}]^2 dt}} \\ &= \frac{\int (S_1 + n_1)(S_2 + n_2) dt}{\sqrt{\int [(S_1 + n_1)]^2 dt} \sqrt{\int [(S_2 + n_2)]^2 dt}}. \end{aligned} \quad (8)$$

The noise signals  $n_1$  and  $n_2$  are assumed to have random amplitudes and phases with zero means and are uncorrelated with each other as well as with the true signals  $S_1$  and  $S_2$  at any given  $T_1$  and  $T_2$ . In this case, expression (8) has the same cross-correlation components with a mean value of zero as discussed in (2). Thus a similar analysis of (6) can be applied to (8). Let the signal-to-noise ratio (SNR) be the power ratio between signal and noise:

$$\text{SNR} \approx \frac{\int [S_1]^2 dt}{\int [n_1]^2 dt} \approx \frac{\int [S_2]^2 dt}{\int [n_2]^2 dt}, \quad (9)$$

and the correlation coefficient of the signals  $S_1$  and  $S_2$  be

$$\rho_{12} = \frac{\int S_1 S_2 dt}{\sqrt{\int [S_1]^2 dt} \sqrt{\int [S_2]^2 dt}}. \quad (10)$$

Expression (8) can be rewritten as

$$\rho_{n12} = \frac{\rho_{12}}{\sqrt{1 + 2/\text{SNR} + [1/\text{SNR}]^2}} = \frac{\rho_{12}}{\left(1 + \frac{1}{\text{SNR}}\right)}. \quad (11)$$

The ratio of  $\rho_{n12}/\rho_{12}$  representing the reduction in correlation due to noise is

$$\frac{\rho_{n12}}{\rho_{12}} = \frac{\text{SNR}}{1 + \text{SNR}}. \quad (12)$$

Equation (12) indicates that correlation in the received signals decreases as the SNR decreases. At a given SNR level, the correlation output is reduced by a constant weighting factor, which can be compensated if the SNR level is known or ignored if it is sufficiently small.

## D. Decorrelation associated with velocity gradient

Scatterers may move at different velocities within a range cell due to a nonuniform velocity profile along the ultrasound beam. For example, in vascular applications the commonly observed parabolic velocity profile has a maximum velocity gradient at the region close to the arterial wall. A velocity gradient causes a range of lateral or axial scatterer displacements within the correlation window.

The axial velocity gradient may increase the signal decorrelation dramatically since it produces different phase shifts along an rf signal time trace. Thus phase can be matched within the correlation window only in small parts of the trace; mismatching parts will reduce the correlation output rapidly. Bonnefous *et al.* established that correlation reduced by variances in time shifts follows<sup>14</sup>

$$\rho = \rho_0 (1 - 2\pi^2 f_0^2 \sigma^2 [\delta T]), \quad (13)$$

where  $f_0$  is the central frequency and  $\sigma^2 [\delta T]$  is the variance in the axial time shift. The term  $\sigma^2 [\delta T]$  can be derived from the gradient value of the velocity distribution. Since the term

$\sigma^2[\delta T]$ , caused by an axial velocity gradient, is proportional to the time interval between two rf traces, its contribution soon may become a dominant factor. The lateral decorrelation can be considered as an averaged effect of the lateral beam modulation in combination with the exchange of many scatterers in a sample volume, which is less dependent on the displacement of each individual scatterer. Hence, the lateral velocity gradient is expected to have a smaller influence on the decorrelation procedure as compared to the axial velocity gradient.

### E. Variance of correlation estimate

The ideal correlation estimator needs to integrate the rf signals over infinite time. In practice, the correlation value is usually estimated with a limited time window to achieve spatial resolution and may deviate from the true value. For the measurement of local velocities, the size of a correlation window determines the resolution of the measured velocity profile. To obtain a good resolution, a small correlation window is preferred. Furthermore, as discussed above, the presence of an axial velocity gradient limits the use of a large time window. Thus the accuracy of a decorrelation based technique for local velocity measurements depends to a large extent on the variance of correlation estimate in a small window.

Variation in the correlation estimate at a given window length is closely related to the system bandwidth. When an rf signal is modeled as bandwidth limited Gaussian white noise with zero mean,<sup>22</sup> it can be shown that the error in the estimate of the cross-correlation function is given by

$$\epsilon \approx \frac{1}{\sqrt{2BT}} [1 + \rho_{12}^{-2}]^{1/2}, \quad (14)$$

where  $B$  is the bandwidth of Gaussian noise,  $T$  is the length of a time window, and  $\rho_{12}$  is the correlation coefficient. The product of  $B$  and  $T$  represents the number of available independent measurements in a given window length. To reduce the variation in correlation estimate, one should either increase the system bandwidth or use a longer time window. Equation (14) also indicates that a low correlation value results in a high degree of measurement variations. Thus low correlation values should be excluded in the velocity estimation.

## II. COMPUTER SIMULATION

### A. Computer model

Blood scattering was modeled as point scattering in the computer simulations. At 30 MHz, the ratio between the radius of red blood cell (RBC, radius:  $\alpha \approx 4 \mu\text{m}$ ) and the wavelength ( $\lambda = 50 \mu\text{m}$ ) is approximately 0.08. This ratio is higher than but close to the requirement of Rayleigh scattering:  $\alpha = 0.05\lambda$ .<sup>23</sup> At normal shear rates without significant cell aggregation, Foster *et al.*<sup>24</sup> and van der Heiden *et al.*<sup>25</sup> have observed the frequency dependence of blood scattering signals is close to Rayleigh. At low shear rates, the scatterer size increases due to aggregation of RBCs. Nevertheless, our experience shows the scattering structure of blood remains

too fine to be resolved even in the low flow condition. Thus the point scattering model could still be used as a reasonable approximation; a more precise scattering model for varying shear flow conditions is a subject for further investigation.

To study the correlation properties of blood scattering, a model using the impulse response method was developed to describe the beam profile of a circular transducer from the extreme near field to far field.<sup>26</sup> Details of the impulse response modeling are presented in the Appendix. Briefly, each scatterer is considered as a point source retransmitting a spherical sound field towards the transducer. At the surface of the transducer the pressure distribution can be described as a Rayleigh integral. In the frequency domain this integral can be expressed in discrete form with a desired precession irrespective of near- or far-field scatterer positions. Thus there is no theoretical constraints for the geometry of the transducer as well as the position of scatterers in this modeling approach.

### B. Transmission pulse

The pulse was defined as a 30-MHz central frequency wave with a Gaussian envelope:

$$p(t) = e^{-t^2/2\sigma^2} \sin(2\pi f_c t)$$

with  $f_c = 30$  MHz, the central frequency, and  $\sigma = 20$  ns, the pulse length factor. The signal bandwidth was expressed as the equivalent noise bandwidth, which is the width of a rectangular spectrum having the same power and peak amplitude as the Gaussian.<sup>27</sup> The bandwidth of the transmission pulse was determined by

$$B = \frac{1}{2\sqrt{\pi}\sigma}, \quad (15)$$

which was approximately 14 MHz for  $\sigma = 20$  ns. The rf signals simulated with the impulse response model were sampled at 1 GHz.

### C. Blood scattering signal

#### 1. Insonified volume

Blood scattering signals were generated from five distinct scatterer sets over the depth of 0.5–4 mm, which was within the near field of a 1-mm disk transducer (natural focus point:  $Z_0 = 5$  mm). This scan depth was the target range in all simulations except for simulation V, in which the target range changed accordingly with the window length over the depth of 1–3.5 mm. Each set contains 5000 scatterers randomly distributed in a volume of  $X = 2$  mm,  $Y = 1$  mm, and  $Z = 3.5$  mm at the range of 0.5–4 mm. The scatterer concentration was 700 scatterer per  $\text{mm}^3$ . The number of scatterers within the resolution cell was 60. Each rf trace was generated from approximately half of the total scatterer number inside the cylindrical insonified volume. Simulations I–V in the next section were performed using exactly the same data sets.



## 2. Scatterer displacement

Axial and lateral displacements were simulated by moving the whole scattering volume along the corresponding directions. The lateral position of the scatterer volume was shifted from left to right at a displacement of 50  $\mu\text{m}$  per step. A total of 20 rf traces with a maximum lateral displacement of 1 mm was generated per simulation.

## D. Correlation procedure

The correlation curve in each simulated rf sequence ( $S_1 \cdots S_{20}$ ) was calculated in two steps. First, a phase matching procedure was performed to remove the phase difference induced by the axial displacement. The time shift between two consecutive rf traces was determined by the maximum value of a cross-correlation function. The rf traces ( $S_2 \cdots S_{20}$ ) were shifted in time to line up with the first trace  $S_1$ . The second step was to calculate the correlation coefficient  $\rho_{n,m}$  between two traces  $S_n$  and  $S_m$ ,  $n=1, \dots, 19$ ,  $m=2, \dots, 20$ . The correlation curve was obtained by an ensemble averaging of the available correlation values:

$$\rho(n) = \frac{\sum_{k=1}^{N-n} \rho_{k,k+n}}{N-n}, \quad n=1, \dots, 19, \quad N=20. \quad (16)$$

## E. Simulation methods

The correlation curve as a function of a lateral displacement was first established through computer simulation I, where only lateral movements were introduced. The result of simulation I was then used as a reference to evaluate the combined effect of other decorrelation factors with respect to the lateral decorrelation. Mean and standard deviations were obtained for each simulation from the calculations in the five scatterer volumes. The correlation calculation was performed with a range window of 3.5 mm (depth=0.5–4 mm) for simulations I–IV except for simulation V, in which the window length was changed accordingly.

### 1. Simulation I: Lateral displacement

In order to observe the independent effect of  $\kappa$  and  $\rho'_{12}$  in Eq. (6), the responses of (a) the scatterers staying inside the beam, (b) the scatterers entering and leaving the beam, and (c) the whole scatterer volume were simulated separately. With the separate responses of (a) and (b), the values of  $\kappa$ ,  $\rho'_{12}$ , and  $\rho_{12}$  were computed using (4)–(6) in the range window of 3.5 mm and plotted as a function of the lateral displacement for comparison with the complete response (c).

In the subsequent investigations, the correlation function simulated from the whole scatterer volume was used as a reference curve.

### 2. Simulation II: Axial displacement

An axial displacement of 5  $\mu\text{m}$  per step (10% of the lateral motion corresponding to a beam-to-flow angle of 84°) was included in this simulation. The maximum axial displacement was 100  $\mu\text{m}$ . The resulting rf traces were aligned in time by the phase matching procedure before the correlation calculation. The phase matching and correlation were performed in the range window of 3.5 mm.

### 3. Simulation III: Signal-to-noise ratio

Band limited white noises with zero mean were added to the rf data in simulation I. The SNR level was changed from 0 to 40 dB at a step of 5 dB. The decorrelation curve was recalculated in the range window of 3.5 mm at each noise level and compared to the reference curve with zero noise level.

### 4. Simulation IV: Velocity gradients

The velocity gradient was defined as the difference between the maximum and minimum velocities (or displacements at a given time delay) within the correlation window. To study the effect of velocity gradients in the lateral and axial displacement, a linear velocity profile was added in this simulation. The velocity distribution along the beam axis was defined by

$$v(z) = \alpha z + \beta.$$

Velocity gradients ranging from 25% to 200% of the mean velocity were introduced by changing  $\alpha$ ,  $\beta$  while keeping the mean velocities constant. The mean lateral and axial velocities were the same as in simulations I and II (lateral: 50  $\mu\text{m}$ ; axial: 5  $\mu\text{m}$ ). Two separate simulations were performed in the complete range window of 3.5 mm. In the first simulation, pure lateral displacements with velocity gradients of 100% and 200% were studied (analogous to simulation I). In the second simulation, lateral and axial displacements with 25%–200% velocity gradients were combined (analogous to simulation II). Variance terms in Eq. (13) for the linear velocity distribution were derived to compare results obtained with Bonnefous's formula.

### 5. Simulation V: Variance of correlation estimate

Narrow-band signals were generated by reducing the bandwidth of the transmission pulse with  $\sigma=40$  ns. The equivalent noise bandwidth was 7 MHz. In the first simulation, the correlation curve of the narrow-band signals calculated in the complete range window of 3.5 mm was compared to that obtained in simulation I. In the second simulation, correlation outputs were computed with different window lengths ranging from 20  $\mu\text{m}$  to 2.5 mm at a step of 20  $\mu\text{m}$ . The windows started at the depth of 1 mm. The standard deviation of the correlation values was measured at the displacement of 0.2 mm ( $\rho \approx 0.6$ ). The degree of variation in correlation estimate was expressed as the ratio between the standard deviation and the mean correlation value.

## III. RESULTS

### A. Beam profile

The beam profile obtained with the model is displayed in Fig. 2. The roundtrip response (maximum received amplitude) of the transducer as a function of the scatterer position in the first few millimeters shows a high variation; this is the typical near-field situation. Correlation of echo signals within this area is influenced by the complex field distribution in a way that is difficult to express with an analytical method.

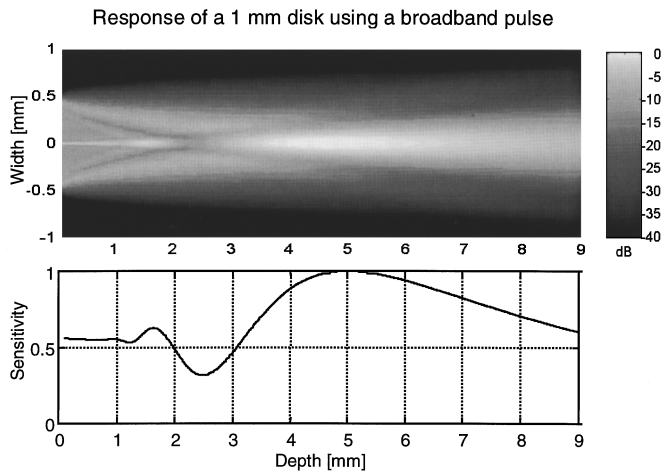


FIG. 2. The roundtrip response of a 30 MHz transducer calculated with the computer model in both the near and far field (top) and the response at the central axis of the transducer (bottom). The complexity of the near-field profile can be appreciated in the range of 0–3 mm. The beam becomes homogenous at the depth  $\geq 5$  mm, which is the theoretical start point of the far field.

## B. Simulation results

### 1. Simulation I

Figure 3 shows the correlation curve as a function of the lateral displacement. The decorrelation curve simulated from the complete response shows a good agreement with the theoretical output predicted by Eq. (6). For a small displacement ( $< 0.4$  mm), the decorrelation is mainly caused by the lateral beam modulation in both amplitude and phase. When a scatterer moves across the near field, rapid modulation of signal amplitudes may occur due to its complex intensity pattern. Phase modulation may be easier to interpret using a far-field model, wherein the phase of a scattered signal is simply determined by the distance between the center of the transducer and the scatterer position:  $r = \sqrt{x^2 + y^2 + z^2}$ . Thus displacement in  $x$  or  $y$  directions will alter the phase response of

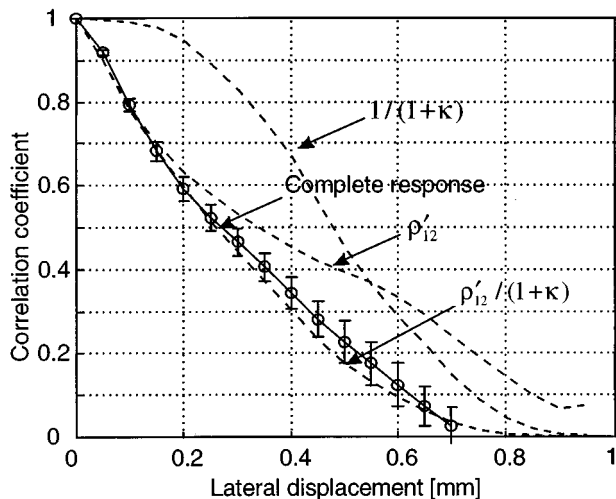


FIG. 3. Correlation curves (dotted line) from three separate responses of **V11**, **V2**, and **V3** showing the decorrelation effects of the lateral beam modulation ( $\rho'_{12}$ ) and scatterers moving in/out the beam ( $1/(1+k)$ ). The complete response (solid line) simulated from the whole scatterer volume follows the curve calculated with  $\rho'_{12}/(1+k)$ .

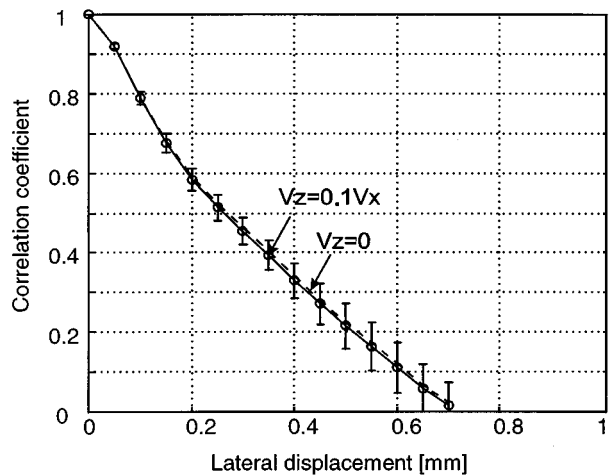


FIG. 4. Comparison of simulation with 10% of axial displacements to the decorrelation curve with pure lateral displacement (dotted line). After the phase matching procedure, the curve with axial displacement shows no noticeable differences as compared to the reference curve.

each scatterer. This effect could be ignored when  $z \gg x, y$ . For IVUS applications, it may become an important factor because of the combination of the near-field nature and high ultrasonic frequencies. At the stage of a small displacement, the contribution of new scatterers entering the beam is minimal since they are located at the edge of the beam profile where the ultrasonic intensity is usually much lower than at the center. As the scatterers move closer to the beam axis and their number increases, decorrelation due to the exchange of scatterers overtakes the effect of the lateral beam decorrelation. The combined effect of these two decorrelation factors causes the decorrelation curve decreases approximately linearly with an increase of the lateral displacement.

The decorrelation effect as a function of lateral beam translation has been studied by Wagner *et al.* under the far-field and narrow-band assumptions.<sup>11,13</sup> They have demonstrated the lateral autocovariance function can be derived from the convolution of the point spread function (PSF), which is independent of scattering media and usually nonlinear for Bessel or Sinc PSF. Although their theory can not be directly applied, one may speculate the linear decorrelation curve shown in this study is partly due to a rectangular-like PSF in the near field; the convolution of such a rectangular PSF results in a linear autocovariance function.

### 2. Simulation II

After the phase matching procedure, the decorrelation curve with axial displacements is almost identical to that obtained in simulation I (Fig. 4). The axial beam modulation in IVUS imaging is negligible because of the large beam-to-flow angle. The axial displacement is expected to be in the order of a few micrometers, which will not result in a significant intensity change due to the beam modulation.

### 3. Simulation III

Figure 5(a) plots the results of Eq. (12) as a function of SNR. To keep the errors in the correlation estimate less than 10%, the SNR in the measurement system needs to be better

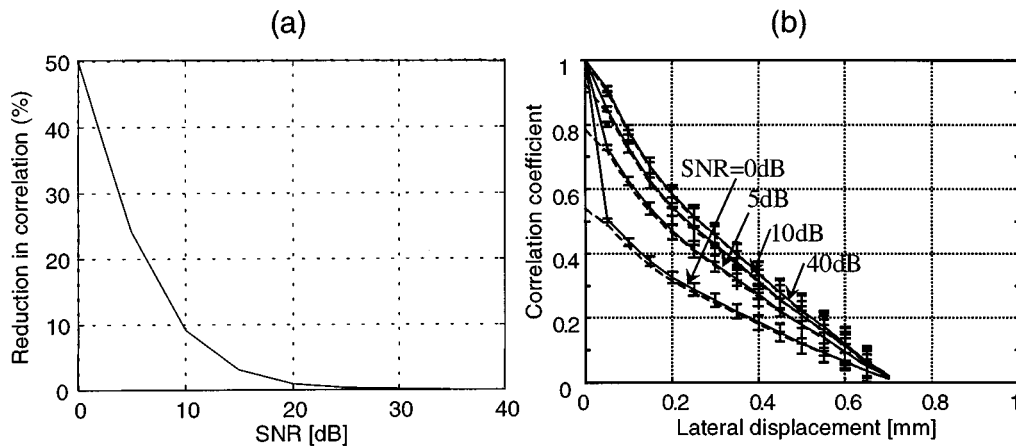


FIG. 5. (a) Percent decrease of the signal correlation as a function of SNR. (b) Correlation curves obtained after adding different noise levels. The dotted lines plot the results calculated by  $\rho_{12}/(1 + 1/\text{SNR})$ . A high noise level can be recognized from a large offset in decorrelation curve.

than 10 dB. In practice, the expected SNR is usually over 20 dB when an optimal gain setting is used for blood scattering signals. At this noise level, the correlation will be reduced by less than 1%, which will not affect the flow measurement significantly.

The correlation curves calculated from the signals with different SNR levels were plotted in Fig. 5(b). The simulated curves follow the trend predicted by Eq. (13). The main effect of noise signals is an additional offset added to the beginning of the decorrelation curves. Thus a high noise level could be identified from the discontinuity at the beginning of the correlation output.

#### 4. Simulation IV

Results show that the correlation curves simulated with lateral gradients only were identical to the curve obtained with a uniform displacement (Fig. 6). This confirms the expectation that a lateral velocity gradient may have a minimal effect on the decorrelation procedure. As shown in Fig. 6, the

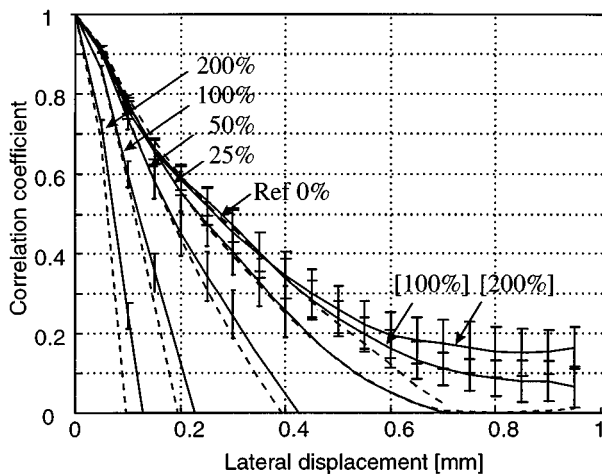


FIG. 6. The curves (indicated by [200%] and [100%]) simulated with only transverse velocity gradients showing little difference with the reference curve (0% velocity gradient). The correlation curves obtained with axial velocity gradients decrease rapidly as the gradient increases from 25% to 200%. The results predicted by the theoretical model in Eq. (13) are plotted in dotted lines.

slope of the correlation curve is progressively modified as the axial velocity gradients increase from 25% to 200%; a larger axial velocity gradient results in a faster decrease in the correlation output. This may introduce an overestimate in the velocity measurement using a decorrelation based method. The simulations show that the axial velocity gradient should be limited to 25% of the mean velocity (a difference of  $1.25 \mu\text{m}$  between the maximum and minimum axial displacements in two consecutive rf traces). Since the beam-to-flow angle is close to  $90^\circ$  in intravascular imaging, the magnitude of axial velocity gradients is usually very small. When the flow measurement is performed with a sufficiently small range window in a short time period, the decorrelation effect of a velocity gradient can be neglected.

#### 5. Simulation V

The result of the first simulation shows that no difference was observed between the narrow-band and broadband signals for the correlation curves of the complete insonified volume [Fig. 7(a)]. Figure 7(b) shows variances of correlation in the narrow-band signals were consistently higher than those obtained with broadband signals. Both simulations indicate that variances decrease as the window length increases. The trend of decrease in correlation variances follows the function of  $1/\sqrt{BT}$  with  $B$  defined as the equivalent noise bandwidth. To obtain a reproducible correlation output of  $<20\%$  variations, the window length should be longer than 0.5 mm for the broadband signal.

### IV. DISCUSSION

Using the computer model, we have analyzed the decorrelation properties of the ultrasound beam from a circular transducer used for IVUS imaging. As main results, correlation of the rf signals from a moving cloud of randomly distributed scatterers decreases monotonically with lateral displacement. The decrease in a correlation range of 1–0.5 is approximately linearly related to the lateral displacement. The decorrelation-displacement relationship provides the basis for extraction of the flow velocity based on decorrelation estimate. Once the decorrelation function of a specific trans-

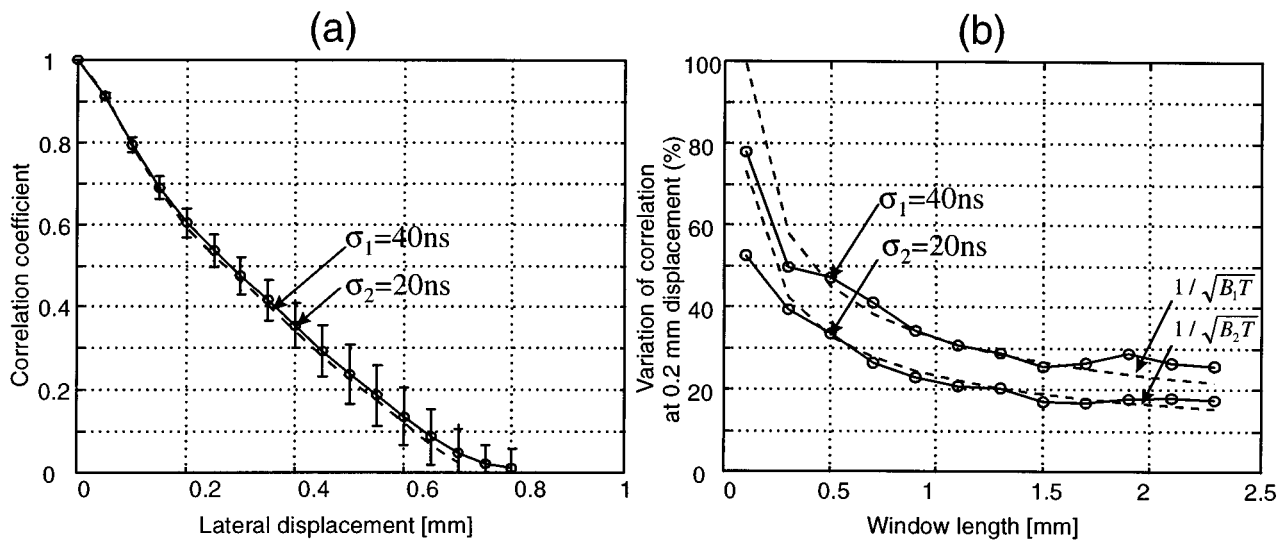


FIG. 7. (a) Correlation curve obtained with a narrow band signal ( $\sigma_1=40$  ns) showing no significant differences to the reference curve ( $\sigma_2=20$  ns). (b) Variations in correlation estimate as a function of the window length for both narrow-band ( $\sigma_1=40$  ns) and broadband ( $\sigma_2=20$  ns) simulations. The narrow-band signals show a higher degree of variations than the broad band signals. Both curves follow the theoretical reference of  $1/\sqrt{BT}$  plotted with  $B_2=14$  MHz and  $B_1=7$  MHz in the dotted lines.

ducer has been assessed, measured decorrelation values in blood signals can be converted to displacements; when the decorrelation measurement is performed at a controlled time interval, flow velocities can be derived from the ratio of displacement and time.

The beam profile calculated with the computer model exhibits rapid changes of the sound intensity in the near field. Since the lateral decorrelation is mainly determined by the beam characteristics, the decorrelation rate will be range dependent. Thus in order to measure local velocity, the lateral decorrelation rate needs to be assessed as a function of axial beam positions for the complete scan depth. It should be noticed that most of the computer simulation results were obtained over the large range of the near field (0.5–4 mm). Assessment of the local beam decorrelation properties was not within the scope of this study.

The effect of the axial beam modulation is negligible in IVUS imaging due to an almost  $90^\circ$  angle between the ultrasound beam and the flow direction. Noise signals may bias decorrelation estimates. Since the lateral decorrelation function is reduced by a constant factor, a high noise level could be detected from the offset at the beginning of the correlation curve. Another solution to the noise problem is using the decorrelation measured in a stationary arterial tissue as a reference noise level; the noise decorrelation can be then deducted from the total decorrelation measured in moving blood. The change in the system bandwidth does not alter the lateral decorrelation function significantly, but increases measurement variations in decorrelation estimate. For the purpose of local velocity assessment, the decorrelation needs to be measured in a small range-gated window.

A velocity gradient exists because flow velocities are nonuniformly distributed over the vessel cross section, e.g., a parabolic velocity profile, and the ultrasound sampling volume has a certain dimension. For intravascular imaging, the blood velocity changes significantly along the scan depth,

which usually has a high velocity gradient at positions near the wall and catheter. Thus the size of a correlation window should also be sufficiently small to reduce velocity differences within the correlation window in order to limit the error caused by the axial velocity gradient. The use of a small window with a limited number of data points, however, may induce high variations in correlation measurements. Thus there is a trade-off in the window length between variations in decorrelation estimate and the resolution of velocity measurement or the error caused by velocity gradients. Alternatively, several decorrelation values should be obtained for one window position to reduce the variation of the measurement.

For a time-delay estimator, echo decorrelation usually results in variation/jitter errors, which has an indirect effect as long as the corresponding peak value is still detectable. Decorrelation sources that are not related to the lateral displacement, however, will directly produce an overestimate in the velocity measurement using a decorrelation method. Thus all the undesired decorrelation sources must be identified and excluded from the decorrelation-displacement calculation.

So far we have discussed the decorrelation properties of the IVUS beam assuming that the blood is a cloud of randomly distributed point scatterers. However, normally RBCs tend to form clusters, a process called aggregation, and arrange themselves in “strings” called rouleaux. In the flowing blood, rouleaux are positioned along the direction of flow. The presence of RBC aggregation and rouleaux is a function of the cyclic variation of the local shear: Regions of high shear (near static structures) have low aggregation and areas of low shear (near the center of the free lumen) have high aggregation.<sup>28</sup> The dependence of blood scattering power upon shear rates has been well established over a wide range of ultrasonic frequencies.<sup>23,24,29</sup> A correlation-based technique, however, is usually amplitude independent; the

change in the scattering level may have little effect as long as the blood echo signals are uncorrelated. Thus the effect of the shape and size of the backscattering particles at low shear rates on the decorrelation phenomenon needs to be investigated.

The computer model based on the impulse response method is able to delineate the complicated intensity distribution of the near field. The efficiency of the model in terms of computation time was improved by implementing the calculation of each scatterer response in the frequency domain. In principle, this modeling method can be used to study different types of IVUS transducers such as a phase array transducer from the extreme near field up to the far field. Knowledge of the lateral beam modulation obtained with the computer model will also provide important information for optimization of the rf lumen enhancement techniques.

## V. CONCLUSION

Results of this study demonstrate that it is feasible to derive blood velocity from the original rf intravascular echo signals by means of decorrelation analysis. Using an optimized measurement setup, decorrelation due to the SNR and axial velocity gradients is expected to be negligible for clinical applications. Localized velocity measurements require detailed assessment of the lateral decorrelation rate at different axial positions along the beam. To overcome the problem of the high variation in a small window, an approach for velocity estimation should be based on multiple assessments of the decorrelation of echo signals.

## ACKNOWLEDGMENTS

This project was supported by the Dutch Technology Foundation (RGN44.3462).

## APPENDIX

The geometry of the computer model used in the simulation is illustrated in Fig. A1. Let  $u$  be the response of the element surface  $S$  is the sound field of a point scatterer located at the end of pointing vector  $\mathbf{R}$ .

If the soundfield contains only a single frequency component with wave number  $\mathbf{k}$ , then the pressure response can be expressed as

$$u(k) = C \oint_S \frac{1}{R} \exp(-jk\mathbf{R}) dS, \quad (\text{A1})$$

where the wave number  $k = 2\pi/\lambda$  and  $C$  is a conversion constant. The relation between  $\mathbf{R}$  and  $r$  is  $r^2 + h^2 = \mathbf{R}^2$ . Differentiation of left- and right-hand terms yields  $r \cdot dr = \mathbf{R} \cdot d\mathbf{R}$ . The elementary surface  $dS = r \cdot dr \cdot d\theta$  can now be expressed as a function of  $\mathbf{R}$ :  $dS = \mathbf{R} \cdot d\mathbf{R} \cdot d\theta$ .

Equation (A1) can be simplified to:

$$u(k) = C \int_{R_{\min}}^{R_{\max}} \int_{\theta_{\min}}^{\theta_{\max}} \exp(-jk\mathbf{R}) d\mathbf{R} \cdot d\theta. \quad (\text{A2})$$

In order to use Eq. (A2) in a discrete computer model the equation can be approximated by

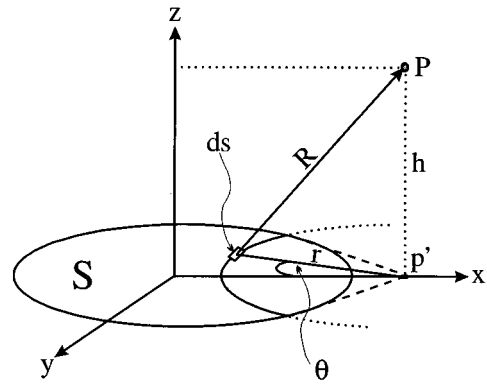


FIG. A1. Geometry of the ultrasound model.

$$u(k) = CdR \sum_{i=1}^N \left( \exp(-jk\mathbf{R}_i) \int_{\theta_{\min}}^{\theta_{\max}(i)} d\theta \right), \quad (\text{A3})$$

where  $N$  is the discrete number of increments  $d\mathbf{R}$  that is used to sample the range of  $\mathbf{R}$ . Equation (A3) can be simplified into

$$u(k) = CdR \sum_{i=1}^N [\theta_{\max}(i) - \theta_{\min}(i)] \exp(-jk\mathbf{R}_i). \quad (\text{A4})$$

Use of Eq. (A4) for the computation of the response involves the following steps:

- define a number  $N$  for the range of  $\mathbf{R}$ .
- determine the minimum and maximum value of  $\mathbf{R}$ , and using  $N$ , the value of  $d\mathbf{R}$ .
- at each value of  $\mathbf{R}_i$  evaluate the phase term  $\exp(-jk\mathbf{R}_i)$ .
- at each value of  $\mathbf{R}_i$  evaluate the angles  $\theta$ , where the wavefront intersects the element boundary.

Because of the reciprocity of the propagation of sound, Eq. (A4) also expresses the pressure at the location of the scatterer when the transducer is acting as the sound source. The roundtrip response  $U$  of the element acting as transmitter and receiver with a single scatterer in the sound field can be expressed in the frequency domain as:

$$U(k) = u(k) \cdot u(k). \quad (\text{A5})$$

When instead of a single frequency a spectrum of frequencies is transmitted, the broadband response of the transducer is obtained by weighting the individual  $u(k)$  components with the amplitude and phase terms of the spectrum.

<sup>1</sup>G. Pasterkamp, M. S. van der Heiden, M. J. Post, B. Ter Haar Romeny, W. P. T. M. Mali, and C. Borst, "Discrimination of intravascular lumen and dissections in a single 30 MHz ultrasound image: use of 'confounding' blood backscatter to advantage," *Radiology* **187**, 871–872 (1993).

<sup>2</sup>W. Li, E. J. Gussenhoven, Y. Zhong, S. H. K. The, H. Pieterman, H. van Urk, and N. Bom, "Temporal averaging for quantification of lumen dimensions in intravascular ultrasound images," *Ultrasound Med. Biol.* **20**, 117–122 (1994).

<sup>3</sup>W. Li, A. F. W. van der Steen, C. T. Lancée, E. J. Gussenhoven, and N. Bom, "Lumen enhancement and flow estimation by temporal correlation of radio frequency intravascular ultrasound," in *Proc. 18th IEEE EMBS*, pp. 839 (1996).

<sup>4</sup>A. Gronningsaeter, B. A. J. Angelsen, A. Gresli, and H. Torp, "Blood noise reduction in intravascular ultrasound imaging," *IEEE Trans. Ultrason. Ferroelectr. Freq. Control* **42**, 200–208 (1995).

- <sup>5</sup>A. Gronningsaeter, B. A. J. Angelsen, A. Heimdal, and H. Torp, "Vessel wall detection and blood noise reduction in intravascular ultrasound imaging," *IEEE Trans. Ultrason. Ferroelectr. Freq. Control* **43**, 359–369 (1996).
- <sup>6</sup>W. Li, A. F. W. van der Steen, C. T. Lancée, E. J. Gussenhoven, and N. Bom, "Temporal correlation of blood scattering signals in vivo from radiofrequency intravascular ultrasound," *Ultrasound Med. Biol.* **22**, 583–590 (1996).
- <sup>7</sup>K. W. Ferrara and V. R. Algazi, "A statistical analysis of the received signal from blood during laminar flow," *IEEE Trans. Ultrason. Ferroelectr. Freq. Control* **41**, 185–198 (1990).
- <sup>8</sup>K. W. Ferrara, "Effect of the beam-vessel angle on the received acoustic signal from blood," *IEEE Trans. Ultrason. Ferroelectr. Freq. Control* **42**, 416–428 (1990).
- <sup>9</sup>J. F. Chen, J. B. Fowlkes, P. L. Carson, J. M. Rubin, and R. S. Adler, "Autocorrelation of integrated power Doppler signals and its application," *Ultrasound Med. Biol.* **22**, 1053–1057 (1996).
- <sup>10</sup>R. S. Adler, J. M. Rubin, J. R. Fowlkes, P. L. Carson, and J. E. Pallister, "Ultrasonic estimation of tissue perfusion: A stochastic approach," *Ultrasound Med. Biol.* **21**, 493–500 (1995).
- <sup>11</sup>R. F. Wagner, S. W. Smith, J. M. Sandrik, and H. Lopez, "Statistics of speckle in ultrasound B-scan. Images," *IEEE Trans. Ultrason. Ferroelectr. Freq. Control* **40**, 156–163 (1983).
- <sup>12</sup>G. E. Trahey, S. W. Smith, and O. T. Von Ramm, "Speckle pattern correlation with lateral aperture translation: Experimental results and implications for spatial compounding," *IEEE Trans. Ultrason. Ferroelectr. Freq. Control* **33**, 257–264 (1986).
- <sup>13</sup>R. F. Wagner, M. F. Insana, and S. W. Smith, "Fundamental correlation lengths of coherent speckle in medical ultrasonic images," *IEEE Trans. Ultrason. Ferroelectr. Freq. Control* **35**, 34–44 (1988).
- <sup>14</sup>O. Bonnefous, "Statistical analysis and time correlation processes applied to velocity measurement," *IEEE Ultrasonics Symp.*, pp. 887–892 (1989).
- <sup>15</sup>S. G. Foster, P. M. Embree, and W. D. O'Brien, "Flow velocity profile via time-domain correlation: Error analysis and computer simulation," *IEEE Trans. Ultrason. Ferroelectr. Freq. Control* **37**, 164–175 (1990).
- <sup>16</sup>A. Hein and W. D. O'Brien, "Current time-domain methods for assessing tissue motion by analysis from reflected ultrasound echoes—A review," *IEEE Trans. Ultrason. Ferroelectr. Freq. Control* **37**, 84–102 (1993).
- <sup>17</sup>R. J. Dickinson and C. R. Hill, "Measurement of soft tissue motion using correlation between A-scans," *Ultrasound Med. Biol.* **18**, 263–271 (1982).
- <sup>18</sup>X. Zhang, M. Shikutani, and K. Yamamoto, "Measurement of displacement and flow vectors with a single ultrasound beam using a correlation technique (II)—Computer simulation and basic experiments," *Tech. Report IEICE* **35**, 23–30 (1995).
- <sup>19</sup>D. Dotti and R. Lombardi, "Estimation of the angle between ultrasound beam and blood velocity through correlation functions," *IEEE Trans. Ultrason. Ferroelectr. Freq. Control* **43**, 864–869 (1996).
- <sup>20</sup>B. H. Friemel, "Real-time ultrasonic two-dimensional vector velocity estimation utilizing speckle-tracking algorithm: implementation and limitations," Ph.D. dissertation, Duke University, Raleigh, NC, 1994.
- <sup>21</sup>I. Céspedes, J. Ophir, and S. K. Alam, "The combined effect of signal decorrelation and random noise on the variance of time delay estimation," *IEEE Trans. Ultrason. Ferroelectr. Freq. Control* **44**, 220–225 (1997).
- <sup>22</sup>J. S. Bendat and A. G. Piersol, *Random Data: Analysis and Measurement Procedures* (Wiley-Interscience, New York, 1983), pp. 272–274.
- <sup>23</sup>Y. W. Yuan and K. K. Shung, "Ultrasonic backscatter from flowing whole blood. II: Dependence on frequency and fibrinogen concentration," *J. Acoust. Soc. Am.* **84**, 1195–1200 (1988).
- <sup>24</sup>F. S. Foster, H. Obara, T. Bloomfield, L. K. Ryan, and G. R. Lockwood, "Ultrasound backscatter from blood in the 30 to 70 MHz frequency range," *IEEE Ultrasonics Symp.*, pp. 1599–1602 (1994).
- <sup>25</sup>M. S. van der Heiden, M. G. M. de Kroon, N. Bom, and C. Borst, "Ultrasound backscatter at 30 MHz from human blood: Influence of rouleau size affected by blood modification and shear rate," *Ultrasound Med. Biol.* **21**, 817–826 (1995).
- <sup>26</sup>P. R. Stepanishen, "Transient radiation from pistons in an infinite planar baffle," *J. Acoust. Soc. Am.* **49**, 1627–1638 (1971).
- <sup>27</sup>I. Céspedes, Y. Huang, J. Ophir, and S. Spratt, "Methods for estimation of subsample time delays of digitized echo signals," *Ultrason. Imaging* **17**, 142–171 (1995).
- <sup>28</sup>M. G. M. De Kroon, C. J. Slager, W. J. Gussenhoven, P. W. Serruys, J. R. T. C. Roelandt, and N. Bom, "Cyclic changes of blood echogenicity in high-frequency ultrasound," *Ultrasound Med. Biol.* **17**, 723–728 (1991).
- <sup>29</sup>Y. W. Yuan and K. K. Shung, "Ultrasonic backscatter from flowing whole blood. I: Dependence on shear rate and hematocrit," *J. Acoust. Soc. Am.* **84**, 52–58 (1988).

# Frequency tuning of the dolphin's hearing as revealed by auditory brain-stem response with notch-noise masking

Vladimir V. Popov, Alexander Ya. Supin, and Vladimir O. Klishin

*Institute of Ecology and Evolution, Russian Academy of Sciences, 33 Leninsky Prosp., 117071 Moscow, Russia*

(Received 8 January 1997; accepted for publication 11 August 1997)

Notch-noise masking was used to measure frequency tuning in a dolphin (*Tursiops truncatus*) in a simultaneous-masking paradigm in conjunction with auditory brain-stem evoked potential recording. Measurements were made at probe frequencies of 64, 76, 90, and 108 kHz. The data were analyzed by fitting the rounded-exponent model of the auditory filters to the experimental data. The fitting parameter values corresponded to the filter tuning as follows:  $Q_{ER}$  (center frequency divided by equivalent rectangular bandwidths) of 35 to 36.5 and  $Q_{10\text{ dB}}$  of 18 to 19 at all tested frequencies. © 1997 Acoustical Society of America. [S0001-4966(97)00412-8]

PACS numbers: 43.80.Nd, 43.66.Dc, 43.66.Fe, 43.66.Gf [FD]

## INTRODUCTION

The auditory system of dolphins demonstrates a number of unique abilities, such as capability of underwater hearing and echolocation, extremely wide frequency range, high sensitivity, acute frequency tuning, precise spatial selectivity, and high temporal resolution (rev. Au, 1993). However, many properties of the dolphin's auditory system remain uncertain.

In particular, data on frequency tuning are to be measured to higher accuracy. Several attempts were made to estimate the frequency tuning in dolphins. There were behavioral experiments using the critical ratio and critical band paradigms (Johnson, 1968; Johnson *et al.*, 1989; Au and Moore, 1990) and tone masking (Johnson, 1971). However, the results were variable enough, perhaps since the complexity of the behavioral method limited available data.

Later, the frequency tuning in dolphins was measured using the evoked-potential method and tone masking (tuning curves) paradigm. Several types of evoked potentials, particularly the auditory brain-stem responses (ABR) can be recorded in dolphins noninvasively without any surgical procedure and anesthesia. They were used to assess a number of the dolphin's hearing characteristics (Popov and Supin, 1985a,b, 1987, 1990a,b), in particular, to obtain frequency tuning curves (Supin *et al.*, 1993; Popov *et al.*, 1995). These studies have provided tuning curves for the dolphin's hearing in a wide frequency range. The data revealed very acute tuning:  $Q_{10\text{ dB}}$  index was as high as 16 to 20, although in many other mammals and in humans this index, in similar experimental conditions, was several times less.

Tone masking is a useful method to measure frequency tuning; however, it has some disadvantages. Tuning curves obtained in such a way may overestimate the frequency tuning because of the off-frequency listening effect. This effect arises because of responses of filters which are not centered at the probe frequency. These side filters can have better signal-to-noise ratio than the probe-centered filters. As a result, the tuning curve gets sharpened around its tip and does not reproduce precisely the shape of the probe-centered filter.

To avoid this effect, other masking paradigms are used.

In particular, the off-frequency listening is little with the two-tone masker. This masker consists of two tones on either side of the probe frequency (Green, 1965; Patterson and Henning, 1977; Nelson, 1979; Johnson-Davis and Patterson, 1979; O'Loughlin and Moore, 1981; Glasberg *et al.*, 1984). The method was used to study frequency tuning in dolphins (Klishin and Popov, 1996). However, it was found that masking efficiency was markedly influenced by masker envelope fluctuation arising because of beats between two tones. This effect caused no serious complications for studies in humans since the beats were not perceived at two tone separation exceeding 50–100 Hz. However, evoked potentials in dolphins are capable of following fluctuation rates as high as 2 kHz (Dolphin, 1995; Supin and Popov, 1995a). These responses to two-tone masker beats interfered with the probe response and influenced the probe detection efficiency.

A popular method to study frequency tuning is the notch-noise masking (Patterson, 1976; Patterson and Nimmo-Smith, 1980; Glasberg and Moore, 1990). In this method, the masker is a noise with a spectral notch (narrow stop band) around the probe frequency. The variation of masking threshold as a function of notch width can be used to estimate the frequency tuning. Advantages of this method are that (i) it effectively prevents the off-frequency listening and (ii) the broadband masker has less prominent envelope fluctuations than the two-tone one. In humans the notch-noise masking was used in conjunction with ABR recording (Abdala and Folsom, 1995), although very low amplitude of masked ABR in humans is not favorable for precise measurements. In dolphins, ABR amplitude is an order of magnitude higher than it is in humans, so using the notch-masking technique in conjunction with ABR recording seems reasonable.

In the present study, we estimated the frequency tuning in a dolphin using the evoked-potentials method and the notch-noise masking paradigm. Only simultaneous masking was used because it was shown in dolphins that suppression of a probe ABR lasts not longer than a few ms after the preceding stimulus (Popov and Supin, 1985b, 1990a,b; Supin

and Popov, 1995b). This makes it difficult to obtain deep forward masking.

## I. MATERIAL AND METHODS

### A. Subject

The experimental subject was a young bottlenosed dolphin, *Tursiops truncatus*, female, 180-cm body length. The animal was caught 2 months before the study and was adapted to the holding and experimental conditions. The care and use of the animal were made under regulation of guidelines established by the Russian Ministry of Higher Education on the use of animals in biomedical research.

### B. Experimental conditions

Experiments were carried out during the 1996 summer season at the Utrish Marine Station of the Russian Academy of Sciences (Black Sea coast).

During the experiments, the dolphin was placed in a bath (4×0.6×0.6 m) filled with sea water. The animal was supported by a stretcher so that the dorsal part of its body was above the water surface. No surgical procedure, anesthesia, or miorelaxants were used. Each experiment lasted 3–4 h, after which the animal was returned into the home pool.

### C. Stimuli

Probe stimuli were 64-, 76-, 90-, and 108-kHz tone pips with a cosine-wave envelope; i.e., the envelope was one cycle of a function  $1 - \cos(2\pi t/\tau)$ . Duration of the pip (cosine cycle) was 1 ms. This pip has a spectrum with the equivalent rectangular bandwidth of around 1.5 kHz and the -10-dB bandwidth of around 2.5 kHz. Although probe spectrum as narrow as possible is desirable for frequency-tuning studies, pips with longer rise-fall times are little effective to produce ABR (Supin *et al.*, 1993; Supin and Popov, 1995a). Probe intensity is indicated below as the effective sound pressure.

Notch noise was digitally generated at a 500-kHz sampling rate. The generation procedure involved steps as follow (Fig. 1). A desirable filter form was inversely Fourier transformed to obtain the filter transfer function in the temporal domain. Inverse Fourier transform of a power spectrum results in an infinite variety of transfer functions which have different phase spectra. However, our pilot studies showed that results did not depend on the phase spectra; therefore, among all possible transfer functions, that composed of cosine components was always arbitrary chosen. The function of such type is symmetrical relative to the central point (Fig. 1, trace 1). This transfer function was used to filter a wide-band signal which was a random digital sequence with the sampling rate (Fig. 1, trace 2). For filtering, the wide-band signal was convoluted with the transfer function:

$$N(t) = \int_{r=-T/2}^{r=T/2} R(t+\tau)F(\tau)d\tau, \quad (1)$$

where  $N(t)$  is the obtained noise signal (Fig. 1, trace 3),  $R(t)$  is the random sequence, and  $F(\tau)$  is the filter transfer function,  $T$  is the integration range which was taken as large as

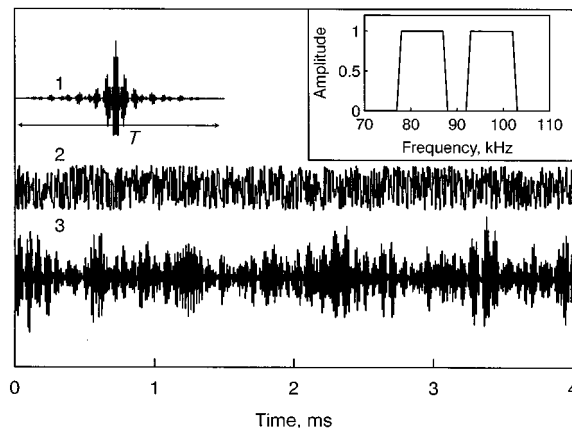


FIG. 1. Notch noise generation procedure. 1—filtering transfer function; 2—wide-band signal (random digital sequence); 3—filtered noise obtained by convolution of signals 1 and 2.  $T$ —integration limit. All the curves are digitally computed signals; arbitrary ordinate scale. Inset shows the filter form used for computation (90-kHz center frequency, 5-kHz notch width).

was necessary to reach  $F(\tau)$  values not exceeding a level of -60 dB *re*: maximum.

As to the used filter forms, they had a flat level in passbands and zero level in stopbands. The outer cutoffs were at 12.5 kHz below and 12.5 kHz above the center frequency, with 1-kHz ramps [Fig. 1, inset; Fig. 2(a)]. The notch of 1–12 kHz width was always centered at the probe frequency and had 1-kHz ramps. The notch width is specified at the -6-dB level. Filters with no notch (zero notch width) were used as well.

Of course, only long-term spectra of generated noise reproduced precisely a given filter shape. The spectra of short noise samples deviated from the filter shape because of ran-

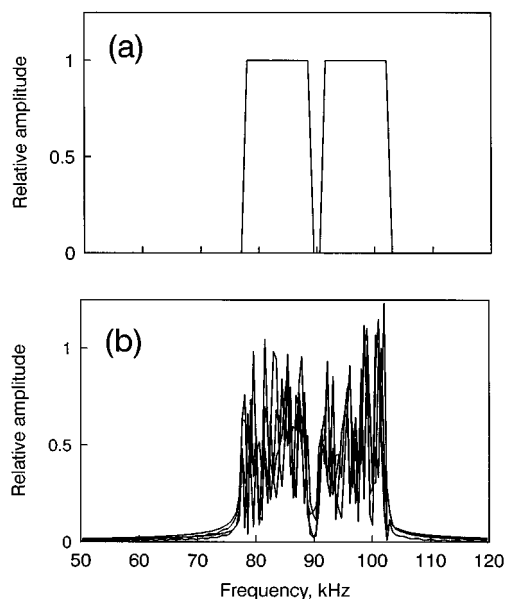


FIG. 2. Notch-noise spectral characteristics. (a) An example of digital notch filter shape. The filter is centered at 90 kHz, notch width is 2 kHz. (b) Fourier transforms (superimposed) of four randomly chosen digital samples, each 2 ms long, of the notch noise obtained with using the filter shown in (a).



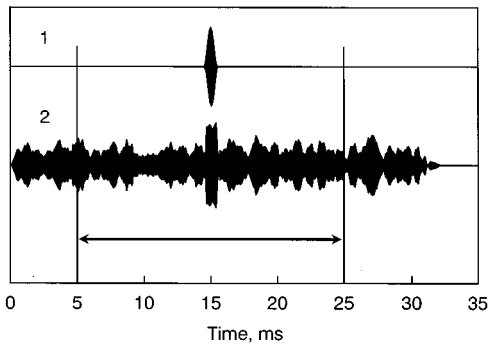


FIG. 3. Temporal diagram of probe and notch-noise presentation. 1 and 2—envelopes of the probe pip and a noise burst, respectively. Double-headed arrow shows the time range where the probe pip could appear.

dom fluctuations inherent in noise [Fig. 2(b)]. Nevertheless, even in short samples, narrow notches were noticeable: in 2-ms samples, notch depths were about  $-20$  dB at a 2-kHz notch width and much deeper (down to  $-60$  dB) at wider notches. Noise bursts of 30-ms duration were generated with their rise and fall functions being dictated by the filter transfer function (Fig. 3).

During the experiment, the pregenerated digital noise bursts were played using a 14-bit D/A converter. Probe and masker were independently attenuated, mixed and emitted through a piezoceramic transducer of 3 cm in diameter. The transducer was placed in the bath at a depth of 30 cm, 1 m in front of the animal's head. The transducer frequency response varied by 16 dB within the frequency range of 50–120 Hz, however this variation did not exceed  $\pm 3$  dB within  $\pm 12.5$ -kHz bands (this is the noise bandwidth) and did not exceed  $\pm 1.5$  dB within  $\pm 6$ -kHz bands (this is a maximal notch width) around any of the tested center frequencies.

Intensity and frequency spectra of signals were monitored through a hydrophone with a band pass of 150 kHz, located near the animal's head.

#### D. ABR recording

ABR recording was performed using plate electrodes 1 cm in diameter. They were attached to the body surface by adhesive electrode jelly only. The active electrode was placed in the dorsal part of the head, 6–8 cm behind the

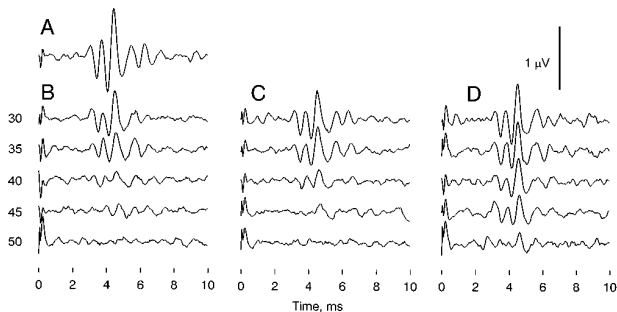


FIG. 4. ABR suppression by masker. (a) Unmasked ABR evoked by a probe stimulus of 90-kHz frequency, 80 dB re:  $1 \mu\text{Pa}^2/\text{Hz}$  level. (b) Response to the same probe in the background of the no-notch masker. (c) The same with 1-kHz notch in the masker. (d) The same with 5-kHz notch. Masker levels (dB re:  $1 \mu\text{Pa}^2/\text{Hz}$ ) are shown on the left.

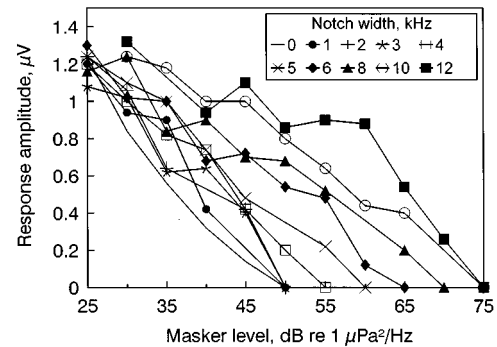


FIG. 5. Response amplitude as a function of masker level with notch width as the parameter (the same experiment as in Fig. 3).

blowhole, the reference one in the back near the dorsal fin, both electrodes above the water surface. The recorded signals were amplified by  $5 \times 10^4$  within a passband of 200–5000 Hz, digitized (sampling rate 20 kHz), averaged and stored in computer memory for subsequent analysis. Each record was obtained by averaging one thousand sweeps.

During ABR collection, the masker and probe stimuli were presented at a rate of 10/s. Since one and the same noise sample was played repeatedly during the collection procedure, special precautions were necessary to make masking effect independent of the particular noise fragment coinciding with the probe. For this purpose, the probe was presented with varied delay relative to the noise onset, so the probe coincided randomly with various parts of the noise burst. The delay varied within the range of 5–25 ms with the noise burst lasting 30 ms (Fig. 3). ABR collection was coherent with probe presentations.

## II. RESULTS

### A. Experimental data

Successive stages of data collection and processing are shown in Figs. 4–7. Figure 4 exemplifies ABR evoked by a probe without a masker (a) and in the presence of various maskers (b–d). In the exemplified experiment, probe frequency was 90 kHz and noise notch was centered at the same

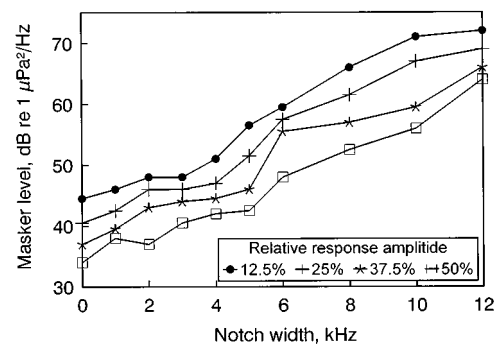


FIG. 6. Masker level required to a certain reduction of ABR amplitude as a function of notch width (the same experiment as in Figs. 2–3). The legend shows ABR amplitude as a percentage of the unmasked response.

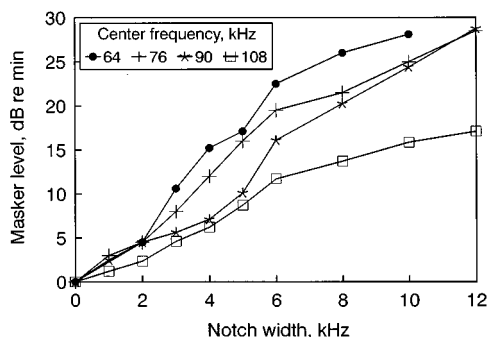


FIG. 7. Averaged data on masker level as a function of notch width for four center frequencies, 64–108 kHz.

frequency. As reported earlier (Popov and Supin, 1990a,b), ABR in dolphins are of very high amplitude as compared with other mammals and humans: at optimal stimulus parameters, they may exceed 20  $\mu\text{V}$ . However, for frequency selectivity measurements, we used probe stimuli of rather long rise time (cosine envelope duration of 1 ms) and of low intensity. In the presented case, the probe level was 80 dB re: 1  $\mu\text{Pa}$  which was 20 dB above the threshold. Therefore, ABR amplitude was rather low even without masking—about 1  $\mu\text{V}$  peak-to-peak [Fig. 4(a)].

The same stimulus in a masker background evoked a smaller response [Fig. 4(b)–(d)]. As the masker level increased, the ABR amplitude diminished until the response disappeared in the EEG background noise. The masking degree depended on the notch width. Even at a notch as narrow as 1 kHz (c), ABR amplitudes were slightly but noticeably higher than with no notch (b); i.e., the masking effect decreased. Further notch widening led to a further increase of the ABR amplitude, i.e., to the decrease of the masking effect (d).

Near the masking threshold, ABR amplitude was comparable with the background EEG noise. This made it difficult to extract a characteristic ABR waveform for measuring ABR amplitude with a satisfactory precision. In view of this, the following measurement procedure was developed. A cross-correlation function was calculated between the measured record and the standard record containing unmasked ABR of higher amplitude. Since ABR of lower amplitude had longer latency, this function peaked at a delay from 0 to 0.25 ms. This peak value was taken as a measure of ABR waveform weight in the analyzed record. The auto-correlation function of the standard ABR was also calculated; it gave the ratio between the correlation function peak value and peak-to-peak response amplitude. Using this ratio, the obtained values of cross-correlation functions were converted to response amplitudes.

Figure 5 shows the results of ABR amplitude measurements carried out as described above. It presents the ABR amplitude as a function of masker level taking notch width as a parameter. Unfortunately, we failed to avoid significant data scatter. Nevertheless, the general tendency is obvious: the wider the notch, the higher the masker level required to reduce ABR amplitude to a certain value. Therefore, the next step in the data processing was to present the masker level

required for a certain degree of ABR reduction as a function of notch width. These functions are presented in Fig. 6 for several degrees of ABR reduction, namely, for response amplitudes of 12.5%, 25%, 37.5%, and 50% of the unmasked response. Since all the plots run mostly in parallel, we found it possible to average them in order to reduce data scatter. In the resulting plot, the noise level was expressed in dB relative to the level obtained at the zero notch. The result is presented in Fig. 7.

Similar measurements and data processing were performed for four center frequencies separated by quarter-octave steps, namely 64, 76, 90, and 108 kHz. Frequencies below 64 kHz were not tested since it was shown (Supin *et al.*, 1993) that irrespective of the stimulus rise–fall time, ABR in dolphins is evoked by a short stimulus part with a rather wide spectrum; therefore ABR is unsuitable for frequency tuning measurements at frequencies below 64 kHz where filter bandwidths may be narrower than the probe spectrum. Frequencies above 108 kHz were not tested since the next quarter-octave value (128 kHz) is near the upper frequency limit of the bottlenose dolphin’s hearing; therefore, there is not enough room on the frequency scale for the noise band. At all the center frequencies tested, the used probe level was 20 dB above the ABR threshold corresponding to 80–90 dB re: 1  $\mu\text{Pa}$ .

The data obtained for all the tested frequencies are summarized in Fig. 7. The data pattern was regular enough: noise level required for a certain degree of masking increased as the notch in the noise widened. The increasing rate depended on center frequency. All the plots have the same basic shape: in the region of up to 6 kHz the data formed an essentially straight line when plotted on these dB power versus linear frequency coordinates; some of the plots tend to flatten in the region below 2 kHz; at frequencies above 6 kHz all the plots tend to flatten as well.

## B. Data analysis

The plots shown in Fig. 7 have a shape typical for threshold curves obtained in notch-noise masking experiments in humans (Patterson, 1976; Patterson and Nimmo-Smith, 1980; Moore and Glasberg, 1981; Patterson *et al.*, 1982). Thus it is reasonable to apply the models elaborated in human psychophysics to the data described herein.

To describe auditory filter shapes in humans, a few models were suggested such as cubic rounded exponential (Patterson and Nimmo-Smith, 1980) and rounded exponential (roex, Patterson *et al.*, 1982). The latter gives a rather simple expression to describe the auditory filter shape. According to this model, the filter shape  $W(g)$  has the form

$$W(g, r) = (1 - r)(1 + pg)e^{-pg} + r, \quad (2)$$

where  $g$  is the normalized frequency deviation from the center of the filter. The term  $p$  determines the filter tuning in the passband, and the term  $r$  approximates the shallow tail section of the filter shape. Thus the power of notched masker transmitted by each side of the filter when the notch is centered on the filter, that is the power transmitted beyond a given  $g = N/2f$  ( $N$  is the notch width and  $f$  is the center frequency) is

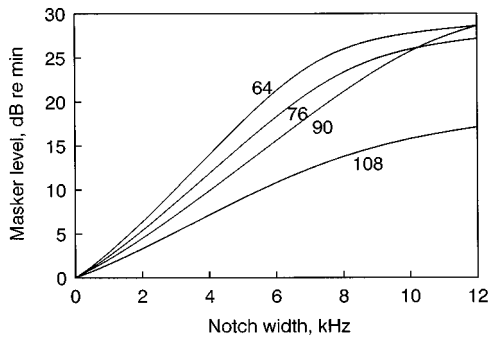


FIG. 8. Predicted masker levels required to a certain masking degree as a function of notch width, according to Eq. (4), for four center frequencies, 64–108 kHz, as indicated.

$$P_m(g) = \int_g^L W(g,r)dg$$

$$= (1-r)[2/p+g]e^{-pg} - (2/p+L)e^{-pL} + r(L-g), \quad (3)$$

where  $P_m$  is the transmitted masker power and  $L$  is the integration limit which is necessary to keep the integral bounded at  $r \neq 0$ . When  $L \gg 1/p$  (i.e.,  $e^{-pL} \rightarrow 0$ ) and  $r \ll 1$  (i.e.,  $1-r \rightarrow 1$ ), the expression may be reduced to

$$P_m = (2/p+g)e^{-pg} + r(L-g). \quad (4)$$

The dB ratio  $R$  between no-notch noise power ( $g=0$ ) and notch-noise power transmitted by the filter is

$$R = 10 \log(2/p+rL) - 10 \log[(2/p+g)e^{-pg} + r(L-g)]. \quad (5)$$

The last expression predicts how the masker level required for a certain masking degree depends on notch width. To estimate frequency tuning on the basis of this model, the lines drawn according to Eq. (5) were fitted to the data presented above. For each curve, the values of the parameters  $p$  and  $r$  were found which minimized the mean-square deviation of the predicted values from the data; the integration limit  $L$  was chosen to keep  $fL = 12.5$  kHz (this is the half-width of the noise). The obtained lines are shown in Fig. 8 as functions of notch width. The found  $p$  and  $r$  values fitting the experimental data are presented in Table I. Noteworthy are high values of the parameter  $p$  which determines the filter tuning. For all the filters, these values were from 140 to 146.

TABLE I. Values of the best fitting parameters  $p$  and  $r$ .

Center frequency, kHz	$p$	$r$
64	142.1	0.0002
76	145.9	0.0003
90	145.8	0.0002
108	140.4	0.0043

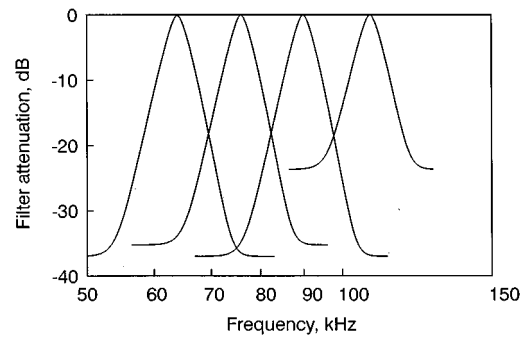


FIG. 9. Auditory filter shapes (roex functions) derived from the data for four center frequencies, from left to right: 64, 76, 90, and 108 kHz.

The underlying auditory filters are derived by substitution of the found  $p$  and  $r$  values into Eq. (2). The results are shown in Fig. 9 which presents filter attenuation in dB as a function of frequency. Being presented at the logarithmic frequency scale, all the filters seem very similar, except shorter dynamic range of the filter centered at 108 kHz (higher  $r$  value). Note that the filter shapes are symmetric by definition because we restricted ourselves to conditions in which the masker spectrum was symmetric about the center frequency. This reduced the possibility of off-frequency listening and simplified the data analysis but did not allow us to obtain any information on possible asymmetries in the auditory filters.

An adopted metric of auditory filter tuning is the equivalent rectangular bandwidth (ERB). For the roex filter, neglecting the parameter  $r$ , ERB is

$$W_{ER} = 4f/p, \quad (6)$$

where  $W_{ER}$  is ERB and  $f$  is the center frequency for the filter. Thus filter tuning is defined as the center frequency divided by ERB is

$$Q_{ER} = f/W_{ER} = p/4. \quad (7)$$

Another convenient measure of tuning is a  $Q_{10 \text{ dB}}$  value, that is, the center frequency divided by the bandwidth at a level of  $-10$  dB. For the roex filter,  $Q_{10} \approx p/7.78$ . Thus the found values of the parameter  $p$  correspond to  $Q_{ER}$  of 35–36.5 and  $Q_{10 \text{ dB}}$  of 18–19 (Fig. 10).

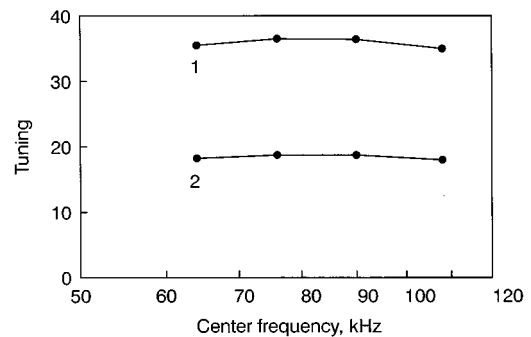


FIG. 10. Filter tuning expressed as  $Q_{ER}$  (1) and  $Q_{10 \text{ dB}}$  (2) as functions of center frequency.

### III. DISCUSSION

#### A. Data representativity

The data volume in this study was restricted since only one animal was available. Thus the representativity of the data is limited. Nevertheless, we consider these data as worthwhile to be analyzed because a large number of dolphins was rarely available for a particular study. However, taken together, the results of such limited studies provide important information.

#### B. Influence of probe bandwidth on frequency-tuning measurements

The main difficulty associated with using the evoked potentials in frequency tuning measurements arises from the fact that these responses are evoked by transient acoustic stimuli which feature broader frequency spectra than long duration, slowly rising and falling stimuli. The probes used in this study had rather narrow spectra (ERB of 1.5 kHz,  $-10$ -dB bandwidth of 2.5 kHz). However, the problem is that we do not know exactly which part of a stimulus is actually effective in eliciting the evoked response. It may be only a part of the stimulus which is shorter than the whole stimulus and has a wider spectrum.

It was shown in our preceding study (Supin *et al.*, 1993) that even with a slowly rising and falling stimulus, only a part of it was effective to produce ABR. The bandwidth of this effective part was about 3.5 kHz at the  $-10$ -dB level. This was a reason why we tested frequency tuning only at frequencies of 64 kHz and higher: according to the previous study, at these frequencies, filter bandwidths are broader than the effective probe spectrum. The results obtained herein confirm this suggestion: the found  $Q_{10\text{ dB}}$  values of 18–19 correspond to bandwidths from 3.5 to 6 kHz at center frequencies from 64 to 108 kHz, respectively. It is noteworthy that all the found filters were of constant  $Q$ , i.e., the bandwidth was proportional to the center frequency, whereas probe spectra were of constant bandwidth at all frequencies. Hence, we consider the found filter shapes as reflecting the real frequency tuning of the auditory system.

#### C. Data relation to previous results

The presented estimations of frequency tuning are in close agreement with previous estimations obtained in tone-masking experiments (Supin *et al.*, 1993; Popov *et al.*, 1995). In those studies, the  $Q_{10\text{ dB}}$  values were estimated to be 16–20 in the high-frequency range (64–110 kHz). In the present study, the  $Q_{10\text{ dB}}$  values were found to be 18–19. Taking into account a possible data scatter, the coincidence is very strict.

This coincidence was somewhat surprising since tone masking data could be affected by off-frequency listening whereas notch-noise masking data must not be noticeably affected. Apparently, the off-frequency listening almost was not manifested in the tone-masking experiments. It does not seem impossible. First, the off-frequency listening could influence the very tip of the tuning curves whereas their tuning sharpness was estimated at the 10-dB level. Second, contrary

to psychophysical threshold measurements, evoked responses are recorded at a certain level above their threshold. At a suprathreshold level, the filter tuned to the probe frequency gives higher response than side filters; this may make evoked responses less sensitive to the off-frequency listening.

#### D. Comparison of frequency tuning in dolphins with that in other mammals and humans

Thus both the previous and the present data indicate very acute frequency tuning in dolphins, at least in the high-frequency range. In the majority of studies in terrestrial mammals and humans, the maximal  $Q_{10\text{ dB}}$  values of evoked-potential tuning curves were 4–6 (Dallos and Cheatham, 1976; Mitchel and Fowler, 1980; Harrison *et al.*, 1981); in rare cases the values greater than 10 were reported (Brown and Abbas, 1987), contrary to 16–20 in dolphins.

In humans, a number of data were obtained by use of the notch-noise method, these data can be directly compared with the data presented herein. Normally, the parameter  $p$  of roex filters in humans was 20–50 depending on the listener's age, probe values, etc. (Patterson *et al.*, 1982; Glasberg and Moore, 1984, 1990; Moore and Glasberg, 1995), contrary to about 140 in the dolphin.

Apart from these data, there is a large amount of psychophysical data on frequency tuning of human hearing, obtained in various experimental paradigms. To summarize these data, several analytical expressions have been proposed which describe ERB of the auditory filters as a function of frequency. For example, a simple equation given by Glasberg and Moore (1990) may be used:

$$W_{\text{ER}} = 24.7(4.37f + 1), \quad (8)$$

where  $W_{\text{ER}}$  is ERB in Hz, and  $f$  is the center frequency in kHz. At high frequencies ( $f \gg 24.7$  Hz) it may be reduced to:  $W_{\text{ER}} = 0.108f$ , thus  $Q_{\text{ER}} = f/W_{\text{ER}} = 9.3$ . This is almost four times less than the corresponding values in dolphins.

Thus the data presented herein confirm the very acute frequency tuning of the dolphin's hearing. Supposedly, it may be associated with the frequency range of their hearing which is wider than 100 kHz. Indeed, both frequency tuning and temporal resolution in the auditory system are limited by passbands of peripheral filters. Acute frequency tuning requires narrow passbands whereas temporal resolution requires wide passbands. This contradiction becomes less important at high frequencies because the filter center frequency  $f$ , passband  $B$  and tuning  $Q$  are related as:  $Q = f/B$ . At high frequency  $f$ , auditory filters can combine high tuning  $Q$  with wide passband  $B$  which renders transfer of rapid sound modulations. Thus at high frequencies, acute frequency tuning can be combined with high temporal resolution. This possibility is realized in the dolphin's auditory system.

#### ACKNOWLEDGMENT

This study was supported by Russian Foundation for Basic Research, Grants Nos. 94-04-11844 and 97-04-49024.

- Abdala, C., and Folsom, R. C. (1995). "The development of frequency resolution in humans as revealed by auditory brain-stem response with notched-noise masking," *J. Acoust. Soc. Am.* **98**, 921–930.
- Au, W. W. L. (1993). *The Sonar of Dolphins* (Springer-Verlag, New York).
- Au, W. W. L., and Moore, P. W. B. (1990). "Critical ratio and critical band width for the Atlantic bottlenose dolphin," *J. Acoust. Soc. Am.* **88**, 1635–1638.
- Brown, C. J., and Abbas, P. J. (1987). "Comparison of AP and ABR tuning curves in guinea pig," *Hearing Res.* **25**, 193–204.
- Dallos, P., and Cheatham, M. A. (1976). "Compound action potential (AP) tuning curves," *J. Acoust. Soc. Am.* **59**, 591–597.
- Dolphin, W. F. (1995). "Steady-state auditory-evoked potentials in three cetacean species elicited using amplitude-modulated stimuli," in *Sensory Systems of Aquatic Mammals*, edited by R. A. Kastelein, J. A. Thomas, and P. E. Nachtigall (De Spill, Woerden, The Netherlands), pp. 25–47.
- Glasberg, B. R., and Moore, B. C. J. (1984). "Comparison of auditory filter shapes derived with three different maskers," *J. Acoust. Soc. Am.* **75**, 536–544.
- Glasberg, B. R., and Moore, B. C. J. (1990). "Derivation of auditory filter shapes from notch-noise data," *Hearing Res.* **47**, 103–138.
- Glasberg, B. R., Moore, B. C. J., and Nimmo-Smith, I. (1984). "Comparison of auditory filter shapes derived with three different maskers," *J. Acoust. Soc. Am.* **75**, 536–544.
- Green, D. M. (1965). "Masking with two tones," *J. Acoust. Soc. Am.* **37**, 802–813.
- Harrison, R. V., Aran, J.-M., and Erre, J.-P. (1981). "AP tuning curves from normal and pathological human and guinea pig cochleas," *J. Acoust. Soc. Am.* **69**, 1374–1385.
- Houtgast, T. (1977). "Auditory-filter characteristics derived from direct-masking data and pulsation-threshold data with a rippled-noise masker," *J. Acoust. Soc. Am.* **62**, 409–415.
- Johnson, C. S. (1968). "Masked tonal thresholds in the bottlenosed porpoise," *J. Acoust. Soc. Am.* **44**, 965–967.
- Johnson, C. S. (1971). "Auditory masking of one pure tone by another in the bottlenosed porpoise," *J. Acoust. Soc. Am.* **49**, 1317–1318.
- Johnson, C. S., McManus, M. W., and Skaar, D. (1989). "Masked tonal hearing thresholds in the beluga whale," *J. Acoust. Soc. Am.* **85**, 2651–2654.
- Johnson-Davis, D., and Patterson, R. D. (1979). "Psychophysical tuning curves: Restricting the listening band to the signal region," *J. Acoust. Soc. Am.* **65**, 765–770.
- Klishin, V. O., and Popov, V. V. (1996). "Two-tone tuning curves in the bottlenosed dolphin *Tursiops truncatus*" (in Russ.) *Sensornyie Systemy (Sensory Systems)* **10**, 30–37.
- Mitchell, C., and Fowler, C. (1980). "Tuning curves of cochlear and brain-stem responses in the guinea pig," *J. Acoust. Soc. Am.* **68**, 896–900.
- Moore, B. C. J., and Glasberg, B. R. (1981). "Auditory filter shapes derived in simultaneous and forward masking," *J. Acoust. Soc. Am.* **70**, 1003–1014.
- Moore, B. C. J., and Glasberg, B. R. (1995). "Comparison of auditory filter shapes obtained with notched-noise and noise-tone maskers," *J. Acoust. Soc. Am.* **97**, 1175–1182.
- Nelson, D. A. (1979). "Two-tone masking and auditory critical bandwidths," *Audiology* **18**, 279–306.
- O'Loughlin, B. J., and Moore, B. C. J. (1981). "Off-frequency listening: Effects of psychophysical tuning curves obtained in simultaneous and forward masking," *J. Acoust. Soc. Am.* **69**, 1119–1125.
- Patterson, R. D. (1976). "Auditory filter shapes derived with noise stimuli," *J. Acoust. Soc. Am.* **59**, 640–654.
- Patterson, R. D., and Henning, G. B. (1977). "Stimulus variability and auditory filter shape," *J. Acoust. Soc. Am.* **62**, 649–664.
- Patterson, R. D., and Nimmo-Smith, I. (1980). "Off-frequency listening and auditory filter asymmetry," *J. Acoust. Soc. Am.* **67**, 229–245.
- Patterson, R. D., Nimmo-Smith, I., Weber, D. L., and Milroy, R. (1982). "The deterioration of hearing with age: Frequency selectivity, the critical ratio, the audiogram, and speech threshold," *J. Acoust. Soc. Am.* **72**, 1788–1803.
- Popov, V. V., and Supin, A. Ya. (1985a). "Determination of characteristics of the dolphin hearing with the brain stem evoked potentials," *Dokl. Akad. Nauk SSSR* **283**, 496–499.
- Popov, V. V., and Supin, A. Ya. (1985b). "Recovery cycles of brain stem evoked potentials to paired acoustic stimuli in dolphins," *Dokl. Akad. Nauk SSSR* **283**, 740–743.
- Popov, V. V., and Supin, A. Ya. (1987). "Hearing characteristics of the white whale, *Delphinapterus leucas*," *Dokl. Akad. Nauk SSSR* **294**, 1255–1258.
- Popov, V. V., and Supin, A. Ya. (1990a). "Auditory brain stem responses in characterization of dolphin hearing," *J. Comp. Physiol. A* **166**, 385–393.
- Popov, V. V., and Supin, A. Ya. (1990b). "Electrophysiological studies of hearing in some cetaceans and a manatee," in *Sensory Abilities of Cetaceans: Laboratory and Field Evidence*, edited by J. A. Thomas and R. A. Kastelein (Plenum, New York), pp. 405–415.
- Popov, V. V., Supin, A. Ya., and Klishin, V. O. (1995). "Frequency tuning curves of the dolphin's hearing: Envelope-following response study," *J. Comp. Physiol. A* **178**, 571–578.
- Supin, A. Ya., and Popov, V. V. (1995a). "Envelope-following response and modulation transfer function in the dolphin's auditory system," *Hearing Res.* **92**, 38–46.
- Supin, A. Ya., and Popov, V. V. (1995b). "Temporal resolution in the dolphin's auditory system revealed by double-click evoked potential study," *J. Acoust. Soc. Am.* **97**, 2586–2593.
- Supin, A. Ya., Popov, V. V., and Klishin, V. O. (1993). "ABR frequency tuning curves in dolphins," *J. Comp. Physiol. A* **173**, 649–656.

# LETTERS TO THE EDITOR

This Letters section is for publishing (a) brief acoustical research or applied acoustical reports, (b) comments on articles or letters previously published in this Journal, and (c) a reply by the article author to criticism by the Letter author in (b). Extensive reports should be submitted as articles, not in a letter series. Letters are peer-reviewed on the same basis as articles, but usually require less review time before acceptance. Letters cannot exceed four printed pages (approximately 3000–4000 words) including figures, tables, references, and a required abstract of about 100 words.

## Surface-controlled drop oscillations in space

R. Glynn Holt

Department of Aerospace and Mechanical Engineering, Boston University, Boston, Massachusetts 02215

Yuren Tian, Joseph Jankovsky, and Robert E. Apfel

Department of Mechanical Engineering, Yale University, New Haven, Connecticut 06520-8286

(Received 15 July 1996; accepted for publication 12 August 1997)

Large liquid drops were deformed by an acoustic standing wave in a resonant air chamber called the Drop Physics Module, which was carried on Space Shuttle Columbia as part of the second United States Microgravity Laboratory mission. When this deforming force was suddenly reduced, the drops executed free oscillations about a perfect spherical equilibrium. The complex frequency of these oscillations was measured. The first results from a series of experiments are presented here. Results for pure water compare favorably with fundamental theoretical predictions. Drops containing aqueous solutions of soluble surfactants exhibited remarkable differences in both frequency and damping, and these are explained phenomenologically by a discussion of the multiple time scales introduced by the addition of surfactants. © 1997 Acoustical Society of America. [S0001-4966(97)06611-3]

PACS numbers: 43.25.Uv, 43.25.Qp [MAB]

### INTRODUCTION

STS-73 (20 October–5 November 1995) was the seventeenth flight of the Space Shuttle Columbia. The primary payload was the second United States Microgravity Laboratory, a Spacelab module housing a series of fluids and materials science experiments designed to take advantage of the small ( $\sim 10^{-6}$  g, or “microgravity”) residual acceleration afforded by low earth orbit. In the relative absence of thermal and buoyant convection and their effects, surface tension becomes the dominant fluid force, and ideal experiments can be performed to provide absolute and rigorous tests of fluid dynamic theories, which would be impossible on the ground.

In this Letter, we report the first results of liquid surface characterization experiments using the acoustic environment of a resonant chamber called the Drop Physics Module. The Module facilitated positioning and manipulation of centimeter-radius liquid drops in air. The aim was to study the rheological properties of liquid drop surfaces on which are adsorbed surface-active (*surfactant*) molecules, and to infer surface properties, such as Gibb’s elasticity, and surface dilatational viscosity, by using a theory which relies on spherical symmetry to solve the momentum and mass transport equations.<sup>1</sup> The technique involves the acoustic squeezing and release of the liquid drop, and the measurement of the complex frequency  $\omega_n = 2\pi f_n + i\alpha_n$  of shape modal oscillations, which becomes a function of surfactant type and concentration. The Spacelab environment allows us to avoid

undesirable nonlinear effects (acoustic streaming, drop deformation, and strong acoustic field coupling) present in 1-g experiments.<sup>2</sup> These ground experiment effects cause changes in  $\omega_n$  which can dominate those due to surfactant effects, and render impossible a strict comparison with theory.

### I. THEORY

For a fixed liquid volume, a spherical shape minimizes surface area and hence surface energy. An initially non-spherical liquid drop will, when the deforming external force is removed, execute free-decaying modal oscillations about this stable spherical equilibrium. Classic theoretical studies of the pure liquid problem are found in Ref. 3, the fundamental results being a family of eigenmodal frequencies  $\omega_n$  for axisymmetric ( $m=0$ ) oscillations of drop shape described by an expansion of the shape in spherical harmonics  $Y_{nm}(\theta, \phi)$ . The primary contribution to the damping is the presence of vorticity in the convective boundary layer near the surface.

Recently, mass transport and interfacial rheology have been studied using liquid drops and soluble surfactants.<sup>1,4</sup> A spherical liquid drop possessing a time-varying free surface is an ideal laboratory in which to conduct sensitive studies of surface-controlled flows. Any perturbation to the spherical equilibrium shape increases its surface area in deformation-dependent local regions of the surface. If a surfactant species

(which produces a lower static equilibrium surface tension than the pure liquid case) is present on the deformed surface, a nonuniform surface concentration of that species develops. Surface flows driven by the surface concentration gradients will develop as the surfactant redistributes to achieve equilibrium. Vortical flow in the surface boundary layer and hence total dissipation is enhanced. The finite time scale defined by the surfactant molecules' surface diffusivity will impart a net elasticity to the surface.

The effect of allowing surfactant mass transport between the bulk and surface is to mitigate this otherwise (material dependent of course) more dominant viscoelasticity present in the case of an insoluble species on the surface. The exchange of dissolved surfactant material from the bulk to the surface is a two-step, rate-limited process. For some surfactants, the exchange is rapid: that is, both diffusion and sorption occur on a time scale short compared with surface disturbances. For others, especially long-chain molecules, the diffusive transfer rate can be the slowest step (*diffusion-controlled*), while for some protein molecules the adsorption/desorption step can be the limiting factor (*sorption-controlled*). Thus both frequency and damping of the drops eigenmodal shape oscillations will be altered by the mere presence of a surfactant, and will be sensitive to the rate-dependent mass transport effects to and from the surface.

In Ref. 1 relations are derived between the complex frequency of the  $(n,m)=(2,0)$  (*quadrupole*) oscillation mode and the surface properties of an aqueous surfactant-bearing drop. For a wide range of conditions, a limiting form is obtained for  $\omega_2^2 \approx i\omega_2^{*2}(1 + \epsilon^1)$ , where  $\omega_2^*$  is the Lamb frequency for the quadrupole mode, and  $\epsilon^1$  is the complex first-order correction term containing the surface viscoelastic parameters and implicitly containing the diffusion/adsorption mass transport relations. The model accounts for convection/diffusion of a soluble surfactant, allowing for isothermal sorption to occur between the diffusion boundary layer and the surface. The major mechanical assumptions of the theory are the requirement of a spherical equilibrium, axisymmetric oscillation and negligible external field stress. While it is possible to simultaneously satisfy only the first two on the ground (a combination of acoustic and electric fields of high strength can yield a spherical equilibrium for small drops), the present space experiments satisfy all three conditions. Equally important is the fact that in ground-based experiments the oscillation time scale is much shorter than the diffusive time scale, and almost always much shorter than the sorptive time scale. For the large drops described in the present experiments, the frequencies of oscillation are low enough that, by changing the type and concentration of surfactant, we can obtain either diffusion, sorption or mixed time-scale control of the dynamics. Thus we can test parameter ranges of the theory which are inaccessible on the ground.

## II. DESCRIPTION OF THE MEASUREMENTS AND TECHNIQUES

The module contains a rectangular resonant chamber at one atmosphere pressure with inner dimensions ( $X$ ,  $Y$ , and  $Z$ ) of 12.4 cm, 12.4 cm, and 15.2 cm, respectively. Custom

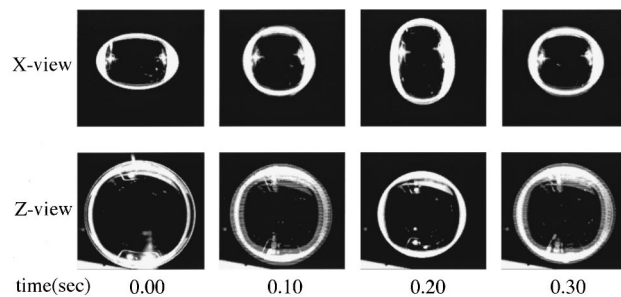


FIG. 1. Simultaneous side (above) and top view (below) of a single cycle of a quadrupole (2,0) free oscillation of a pure water drop. Time is increasing left to right. The equilibrium diameter is 2.5 cm, and the ambient sound pressure level is 142 dB (*re*: 20  $\mu$ Pa) on all axes.

high-amplitude, titanium-dome acoustic loudspeakers were used to drive a superposition of the three fundamental [(100)  $X$  mode, (010) degenerate  $Y$  mode, and (001)  $Z$  mode] plane-wave modes at approximately 1350, 1350, and 1130 Hz, respectively. The intersection of the pressure nodal planes of each mode is a point at the geometrical center of the chamber, toward which a drop will be forced by the acoustic radiation pressure.<sup>5</sup> Two video cameras positioned along the  $Z$  and  $X$  axes were employed for simultaneous orthogonal views. For zero or very low ( $<142$  dB *re*: 20  $\mu$ Pa) acoustic pressure amplitudes, the drop shape remains spherical. Our ambient conditions ranged from 139 to 142 dB, with the measured pressure balanced on all axes. The relative phase of the degenerate  $X$  and  $Y$  signals was switched from 90 degrees to 270 at approximately 15 Hz to null unwanted rotation in the ambient state.

In a typical experiment run, the spherical drop is squeezed by increasing the amplitude of the  $Z$  axis mode. Then the ambient rotation, which might be about any axis, is converted into rotation about the  $Z$  axis by appropriate duty cycle control of the phase modulation of the  $X$ - $Y$  speakers.<sup>6</sup> This is a delicate procedure which is followed by a reduction of the  $Z$  rotation to a minimal level. At this crucial stability point, the amplitude of the  $Z$  axis mode is lowered to its original value in a single step. This sudden relaxation of the acoustic field to the conditions for a surface-tension-dominated spherical shape produced “ringing” oscillations of the drop about the spherical shape.

Spatio-temporal information was obtained from video. Normal speed (30 fps) video was digitally analyzed frame-by-frame to obtain the drop shape. Shape modal distributions, and the complex frequency of each participating mode were obtained from the free decay data.

## III. RESULTS

Figure 1 shows a single cycle of a free oscillation of a 2.5-cm-diam water drop in the Drop Physics Module. The drop equilibrium shape was spherical to within less than 1%, as was the axisymmetry. We were not always so fortunate—oscillations for liquids with low surface viscosity were often unstable to nonaxisymmetric oscillations, and a precession of the axis of symmetry of the drop was also possible. Nevertheless, many drops exhibited nearly perfect, low amplitude (2,0) mode oscillations. Figure 2 shows the change in radius

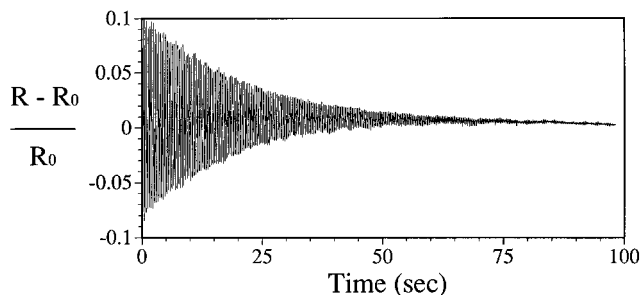


FIG. 2. The decay of the normalized azimuthal radius of the drop in Fig. 1 as a function of time. The data is sampled at 1/30 s. The results of fitting the data to a decay functional  $Ae^{-\alpha t} \cos(2\pi ft)$  (where  $A$  is the amplitude,  $\alpha$  the damping constant, and  $f$  the frequency) are  $\alpha = 0.053 \pm 0.001 \text{ s}^{-1}$ , and  $f = 2.78 \pm 0.01 \text{ Hz}$ .

along an azimuthal vector versus time for the drop in Fig. 1. A slow 0.5-Hz rotation rate was imposed on the drop to gyro-stabilize the symmetry axis. Table I compares the results for frequency and damping with the theoretical results for pure water. Although the effect of the rotation on the frequency is negligible (less than 0.1%, Ref. 7), there may be an additional damping due to enhanced vorticity induced by the Coriolis effect.

Figure 3 shows three decay curves for 2.5-cm-diam drops released from the same initial deformation. Drop (a) is pure water. Drop (b) is water with  $1.4 \times 10^{-4} \text{ g/ml}$  of the nonionic surfactant Triton-X-100 dissolved in the bulk, yielding an equilibrium surface tension of  $31 \text{ dyn/cm}^2$ . Drop (c) is water containing  $1.0 \times 10^{-5} \text{ g/ml}$  of Bovine Serum Albumin dissolved in the bulk, yielding an equilibrium surface tension of  $54 \text{ dyn/cm}^2$ . Both concentrations reported represent the "Critical Micelle Concentration" for each surfactant.<sup>8</sup> The amount of surfactant in both (b) and (c) is too small to affect bulk properties, yet both the frequency and damping of the quadrupole oscillation are very different from pure water.

#### IV. DISCUSSION

The phenomena shown in Fig. 3 can be explained by an analysis of the time scales in the problem. During a quarter cycle of the oscillation, the deviation from spherical equilibrium creates fresh surface locally. Since this will cause a surface gradient in surfactant concentration, there will be a retarding Marangoni stress or surface tension gradient opposing the motion. Excess vorticity in the convective boundary layer is thus generated, and the resultant measurable damping of the normal mode will be increased. Surfactant mass transfer from the sublayer to the surface can mitigate this

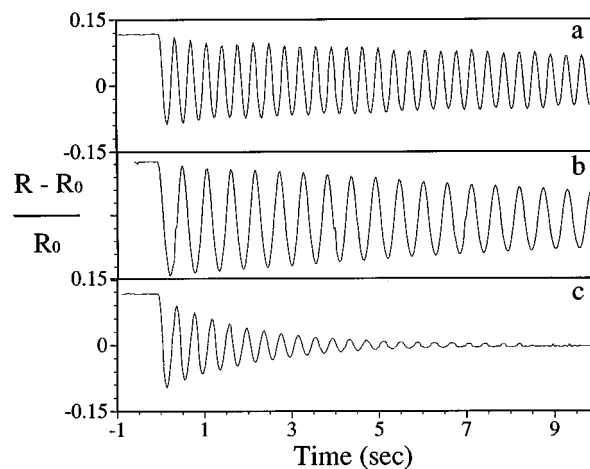


FIG. 3. Decay of the azimuthal radius for 2.5-cm-diam aqueous drops with an initial deformation of approximately 20%: (a) pure water; (b) water with  $1.4 \times 10^{-4} \text{ g/ml}$  Triton-X-100 dissolved in the bulk; (c) water with  $1.0 \times 10^{-5} \text{ g/ml}$  Bovine Serum Albumin dissolved in the bulk.

damping if (a) both diffusion and sorption occur more rapidly than the convection, and (b) if there is a high enough concentration of surfactant present in the sublayer (and the bulk) to replenish the surface.<sup>9</sup> This can be compared with the case of an insoluble surfactant, where measurements of normal mode damping on bubbles with adsorbed stearic acid have exhibited a factor of 10 greater damping.<sup>10</sup>

For Bovine Serum Albumin, surface tension relaxation measurements<sup>11</sup> yield a (concentration dependent) relaxation time  $t_{1/2}$  of about 100 s for a drop solution at the Critical Micelle Concentration, much longer than the period of shape oscillations. Thus for these drop sizes and oscillation frequencies, we expect the interface to exhibit a higher damping rate. For the drop in Fig. 3(c), the damping was 15 times that of pure water. We see qualitatively different behavior for Triton-X-100, which possesses short relaxation times ( $t_{1/2}$  is on the order of a second, compared with  $t_{\text{osc}} \sim 0.5 \text{ s}$ ). Even though the surface tension is much less than that for the Albumin protein (as evidenced by the lower frequency), the damping is not much different than water (about 1.7 times that of water). This is because Triton-X-100 at the Critical Micelle Concentration is not only a rapid diffuser, but suffers no sorption barrier such as Bovine Serum Albumin. At these frequencies, the surface concentration remains nearly uniform, able to be replenished rapidly by molecules in the diffusion boundary layer.

#### V. CONCLUSION

We have presented some selected results of over 100 h of experimentation conducted during the flight of STS-73.

TABLE I. Comparison of the measured frequency and damping for two different pure water drops (the 2.5-cm drop is the same as that depicted in Figs. 1 and 2) to the theoretical values for water at 20 °C. The theoretical values are the classic results.<sup>3</sup>

Water drop diameter (cm)	Rotation Hz	$f_{\text{measured}}$ (Hz)	$f_{\text{theoretical}}$ (Hz)	$\alpha_{\text{measured}}$ $\text{s}^{-1}$	$\alpha_{\text{theoretical}}$ $\text{s}^{-1}$
$2.07 \pm 0.01$	$< 0.1 \hat{x}$	$3.64 \pm 0.01$	3.63	$0.051 \pm 0.001$	0.047
$2.50 \pm 0.01$	$0.5 \hat{z}$	$2.78 \pm 0.01$	2.73	$0.053 \pm 0.001$	0.032



We continue to analyze video and microphone data for drop sizes from 3 cc up to 14 cc in volume, and surfactant concentrations spanning two orders of magnitude in the context of a theory<sup>1</sup> which can incorporate the effects of mass transport of surfactant. One of the goals of this research is to validate the modelling approach for the ideal case, in order to be able to extend the modelling to include the effects of a constant high-amplitude acoustic field. This will allow us to conduct research in earth-based levitators, where the acoustic field necessary to hold the drop is of the order of 150 dB and higher, resulting in both a static deformation and a nonlinear, amplitude-dependent restoring force for oscillations which can mask surfactant effects on the oscillations. Ultimately, the acoustic technique described here will yield information on surface diffusivity and frequency-dependent sorption rate constants. Such information, incorporated into the theoretical model, will allow the prediction of macroscopic rheological effects in a practical situation from the specification of fundamental structural and transport properties of a given surfactant species.

### ACKNOWLEDGMENTS

The research described in this paper was carried out under contract with the National Aeronautics and Space Administration. The Drop Physics Module was designed and built by a team of scientists and engineers at the Jet Propulsion Laboratory and Loral Electro-Optical Systems in Pasadena, CA. The authors gratefully acknowledge the efforts of the crew of STS-73 and the entire team at Marshall Space Flight Center. We also acknowledge invaluable discussions with A. Croonquist, P. Marston, J. Reimer, K. Stebe and E. Trinh, and D. Thiessen for setting up a pendant drop apparatus.

<sup>1</sup>Y. Tian, R. G. Holt, and R. E. Apfel, *Phys. Fluids* **7**, 2938–2949 (1995).

- <sup>2</sup>E. H. Trinh, P. L. Marston, and J. Robey, *J. Colloid Interface Sci.* **124**, 95–103 (1988); H. L. Lu and R. E. Apfel, *J. Colloid Interface Sci.* **134**, 245–255 (1990); Y. Tian, R. G. Holt, and R. E. Apfel, *Rev. Sci. Instrum.* **66**, 3349–3354 (1995).
- <sup>3</sup>H. Lamb, *Hydrodynamics* (Dover, New York, 1945), and reference to Rayleigh therein; W. H. Reid, *Q. Appl. Math.* **18**, 86–89 (1960); C. A. Miller and L. E. Scriven, *J. Fluid Mech.* **32**, 417–435 (1968), and reference to Kelvin therein. Results which correct and extend Miller and Scriven's analysis can be found in P. L. Marston, *J. Acoust. Soc. Am.* **67**, 15–26 (1980) and in A. Prosperetti, *J. Mech.* **19**, 149–182 (1980) and *J. Fluid Mech.* **100**, 333–347 (1980).
- <sup>4</sup>C. J. Hsu and R. E. Apfel, *J. Acoust. Soc. Am.* **82**, 2135–2144 (1987); H. L. Lu and R. E. Apfel, *J. Fluid Mech.* **222**, 351–368 (1991).
- <sup>5</sup>K. Yosioka and Y. Kawasima, *Acustica* **5**, 167–173 (1955); P. L. Marston and R. E. Apfel, *J. Colloid Interface Sci.* **68**, 280–286 (1979); P. L. Marston, *J. Acoust. Soc. Am.* **67**, 15–26 (1980); A. A. Doinikov, *J. Fluid Mech.* **267**, 1–21 (1994).
- <sup>6</sup>F. H. Busse and T. G. Wang, *J. Acoust. Soc. Am.* **69**, 1634–1638 (1981).
- <sup>7</sup>F. H. Busse, *J. Fluid Mech.* **142**, 1–8 (1984).
- <sup>8</sup>The relaxation time  $t_{1/2}$  for a surface is the time it takes for a freshly created surface (at  $t=0$ ) to achieve a value of the surface tension one-half the asymptotic value ( $t=\infty$ ). Thus it depends on diffusion, sorption, and bulk concentration. The "Critical Micelle Concentration" refers to that bulk concentration of soluble surfactant above which the equilibrium surface tension remains a constant. It loosely represents a saturation of the surface concentration, and surfactant molecules in the bulk at concentrations in excess of this concentration form energetically favorable clusters called micelles. Thus the Critical Micelle Concentration can be interpreted as a surface and bulk phase transition. For a general introduction to this and related ideas, see D. A. Edwards, H. Brenner and D. T. Wasan, *Interfacial Transport Processes and Rheology* (Butterworth-Heinemann, Boston, 1991).
- <sup>9</sup>S. Y. Lin, K. McKeigue, and C. Maldarelli, *AIChE J.* **36**, 1785–1795 (1990); K. Stebe, S. Y. Lin, and C. Maldarelli, *Phys. Fluids A* **3**, 3–20 (1991).
- <sup>10</sup>T. J. Asaki, D. B. Thiessen, and P. L. Marston, *Phys. Rev. Lett.* **75**, 2686–2689 (1995).
- <sup>11</sup>Unpublished results using a pendant drop method; see also F. MacRitchie and A. E. Alexander, *J. Colloid Interface Sci.* **18**, 453–457 (1962); D. E. Graham and M. C. Phillips, *J. Colloid Interface Sci.* **70**, 403–414 (1979); *J. Colloid Interface Sci.* **76**, 227–239 (1980). It is important to note that Bovine Serum Albumin, due to a reversible denaturation upon adsorption, exhibits a resistance to desorption, and this will induce a nonlinear element into the dynamics.

# Collective and localized modes of mono-coupled multi-span beams with large deterministic disorders

A. S. Bansal

*Department of Mechanical Engineering, Punjab Agricultural University, Ludhiana-141 004, India*

(Received 26 March 1997; revised 21 June 1997; accepted 2 August 1997)

Natural frequencies of two-span beams have been studied in the presence of different amounts of deterministic disorder (mistuning) arising from displacement of the intermediate simple support (prop) to different locations away from its tuned (periodic) position. The two beam-segments are assumed to be fully (strongly) coupled in the absence of any torsional constraint offered by the prop. Conditions under which the beam systems with different end conditions and support locations have the same natural frequencies have been identified and explained. Unlike the tuned multi-span beams, the natural frequencies of disordered beams with extreme ends simply supported and clamped have been found to coincide even when they do not belong to the same group(s) of natural frequencies. The deflection mode shapes and the phenomenon of normal mode localization have been presented and discussed for some specific prop locations. Conditions have been identified under which the disordered beams can behave as ordered (tuned, periodic) beams and their normal modes become perfectly collective with peak deflections exactly the same in both spans. Normal modes of fully coupled multi-span beams can become and appear to be strongly localized only if they are strongly disordered. Just as in the case of periodic beams, study of natural modes of two-span disordered beams is also helpful in understanding the natural modes of disordered beams having more than two spans. © 1997 Acoustical Society of America. [S0001-4966(97)05511-2]

PACS numbers: 43.40.Cw [CBB]

## INTRODUCTION

In an earlier paper,<sup>1</sup> natural frequencies and deflection mode shapes were discussed for four-span uniform beams on unequally spaced (disordered) simple supports. In the absence of any torsional constraint offered by the simple supports, the ends of beam elements resting on intermediate supports were fully (strongly) coupled through a single coordinate as the beam elements had only rotational degree of freedom at their ends. The disordered beams considered had arbitrarily chosen relative span lengths, 0.95–1.05–1.05–0.95 (symmetric) and 0.925–0.975–1.025–1.075 (unsymmetric). The first groups of natural modes of these beams, with the extreme ends simply supported (SS ends) and clamped (CC ends), were compared with those of equivalent periodic beams resting on equally spaced simple supports. The responses (moments and slopes) at the ends of the unsymmetric beam executing free vibration are unequal, unlike those for symmetric (and periodic) beams. The symmetric beams always behave like periodic ones, as far as their end responses are concerned. The peak deflection ratios (minimum/maximum) for the normal modes of the beam disordered unsymmetrically have been found to be quite low (upto 0.15), a value only slightly more than 0.1 below which the systems are considered to be strongly localized.<sup>2</sup>

Deviation from perfect periodicity due to the irregularities can localize the modes of free vibration and inhibit the free-wave propagation along the structure. During the last decade, much work has been reported by Pierre *et al.*,<sup>2</sup> Cai and Lin,<sup>3</sup> and Lust *et al.*<sup>4</sup> (to name only a few) on normal mode localization in weakly coupled, weakly disordered multi-span beams. It is well known that the systems that are weakly coupled (beam resting on simple supports having

large torsional stiffness) are most susceptible to localization even if they are slightly disordered. It is also well established that the degree of localization depends on the disorder (beam length deviation, as considered here) to coupling ratio. In almost all the studies on normal mode localization in beam-type systems conducted so far, only random irregularities arising from manufacturing processes and material being inhomogeneous have been considered. Large deliberate disorders have to be introduced sometimes as an unavoidable necessity for mounting a machine and for passive vibration control as mechanical filters.<sup>5</sup> There is thus a need to study the phenomenon of normal mode localization in strongly coupled systems when disordered strongly. One of the aims of this Letter is to discuss localization in such systems.

In the present study, which stems from the work reported earlier,<sup>1</sup> a model of a two-span continuous uniform beam has been considered. Unlike Pierre *et al.*<sup>2</sup> and Lust *et al.*,<sup>4</sup> the two spans are considered to be fully (strongly) coupled in the absence of a torsional spring at the prop, and a full range of deterministic disorder arising from the prop moved to various locations between the extreme ends has been covered. The variation of natural frequencies of the beams having SS and CC ends has also been studied for all locations of the prop when moved from mid-span to an extreme end. The mode shapes and hence the normal mode localization have been studied for some specific prop location.

The present study is helpful in identifying the conditions under which unsymmetrically mistuned (disordered) beams can behave like a perfectly tuned (ordered) one, such that its normal modes become perfectly collective. Although the normal modes of strongly coupled and weakly disordered

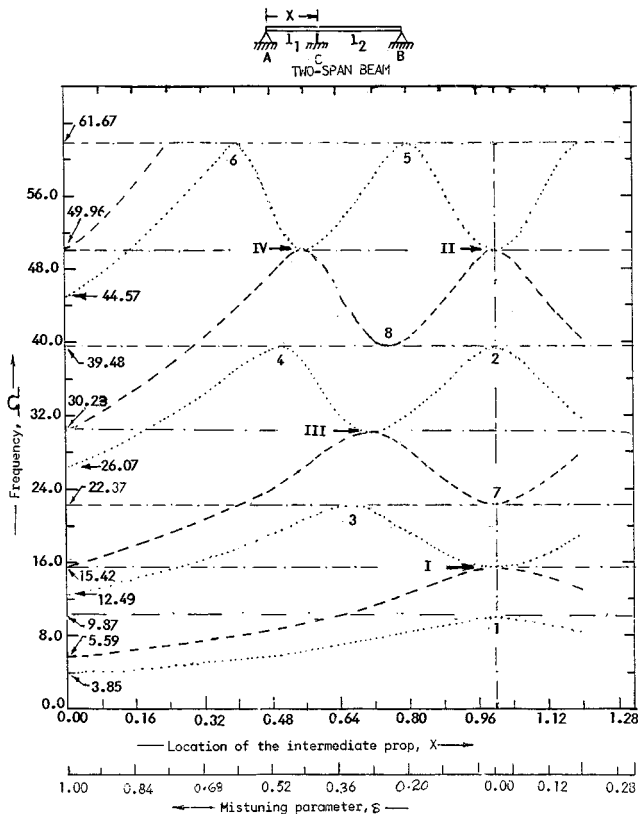


FIG. 1. Natural frequencies of the beams for different locations ( $X$ ) of the intermediate support and the mistuning ( $\delta$ ). 1,2,...,8, S. No. corresponding to Fig. 2(a); I, II, III, IV, S No. corresponding to Fig. 2(b); ..... SS ends natural frequencies, ---- CC ends natural frequencies.

systems cannot be localized, it has been shown that the fully coupled beam with very large deterministic disorder due to length deviation can become strongly localized. When the two-span beams vibrate in second and higher modes, it can be visualised how they represent the modes of multi-span beams of more than two spans that can be unsymmetric, symmetric, and even periodic.

### I. STRUCTURAL MODEL AND THE PARAMETERS CONSIDERED

Consider a finite beam with an intermediate simple prop at C and terminating at the ends A and B, where they may be simply supported (as shown in Fig. 1) or clamped. The prop is considered to be located at distance  $x$  from the left end A, such that the beam of length  $l$  is divided into beam elements of lengths  $l_1$  and  $l_2$ . The beam may be considered to be uniform and of homogeneous material, such that its elements can be treated as symmetric and linear. Natural frequencies and the moments induced at all the supports of the two-span ( $N=2$ ) beams may be computed as done earlier.<sup>1</sup> The deflection mode shapes that are governed by the moments at the ends of individual beam elements have been computed by using the basic beam theory.<sup>6</sup> The results are presented in terms of nondimensional parameters. The beam length  $l$  and that of its elements  $l_1$  and  $l_2$  and the distance  $x$  of the location of intermediate prop can be written as  $L(=2)$ ,  $L_1$ ,  $L_2$ , and  $X$ , respectively, when normalized in terms of average element length  $l_a(=l/2)$  of the elements. Thus  $X$  varies from

0 to 2 as the prop is moved from end A to end B of the beam. Obviously,  $L_1=X$ ,  $L_2=(2-X)$ ,  $l_1/l_2=L_1/L_2=X/(2-X)$ , and  $X=2(l_1/l_2)/(1+l_1/l_2)$ .

The deviation of length from the periodic value, known as the mistuning (or disorder) parameter, may be defined as  $\delta=|1-X|$ , which is zero when the prop is at mid-span ( $X=1$ ) and equal to 1 when the prop is moved to an extreme end of the beam. It may be noted that the various parameters have been normalized here with respect to the tuned-span length  $l_a$ , which is half the total length of the beam,  $l$ . The degree of localization  $A$  of a mode may be defined in terms of the response ratio as  $A=|a/b|$ , where  $a$  and  $b$  are the maximum displacements in the spans having smaller and larger response, respectively. Modes are said to be strongly localized if  $A<0.1$ . The radian frequency  $\omega$  can be nondimensionalized in terms of  $l_a$ ,  $m_b$ , and  $EI$  such that  $\Omega=\omega l_a^2(m_b/EI)^{1/2}$ , where  $m_b$  is the mass per unit length of the beam having flexural rigidity  $EI$ .

### II. NATURAL FREQUENCIES AND DEFLECTION MODE SHAPES

The variation of SS and CC ends natural frequencies with location of intermediate prop of two-span beams are presented in Fig. 1 over the frequency range  $\Omega=0-61.67$  which covers up to the second flexural mode of the beam elements of average length,  $l_a$ . The values of  $(X,\Omega)$ ,  $\delta$  at which the frequency curves do not coincide and coincide are given in Fig. 1 and labeled as 1,2,...,8 and I, II, III, IV. Deflection mode shapes of the actually tuned ( $\delta=0$ ), and when the mistuned beams ( $\delta\neq 0$ ) behave like the tuned beams for certain prop locations, are presented in Fig. 2. Mode shapes of beams corresponding to noncoinciding and coinciding peaks/troughs of natural frequencies are presented in Fig. 2(a) and (b), and labeled as S. No. 1,2,3,...,8 and S. No. I, II, III, IV, respectively, as in Fig. 1. The values of  $(X,\Omega)$ ,  $\delta$  and  $l_1/l_2$  for particular modes are also given in the figures. From the symmetry of the frequency curves, as the prop is moved from  $x=0$  to 2, it may be noted that the range  $X=0-1$  (or  $\delta=0-1$ ) is sufficient, although it extends up to  $X=1.2$ .

#### A. Variation of natural frequencies with prop location/mistuning

When the beam has SS ends and the prop is moved very close to an end support, as in the present study, the beam will behave like those having one end clamped and the other simply supported (CS ends). This will not be the case if the prop is altogether removed or when it coincides/merges with the end support. The natural frequencies of the beams with the prop moved very close to an end are  $\frac{1}{4}$  times those of the tuned beam elements ( $X=1$ ,  $\delta=0$ ) with similar end conditions. For instance,  $\Omega=3.85$  and  $5.95$  corresponds to  $\Omega=15.42$  and  $22.34$  of the beam with CS and CC ends, respectively (Fig. 1). With slight displacement of the prop toward mid-span, constraint offered by the prop increases and so does all the SS and CC natural frequencies. Depending on the mode of vibration, the SS and CC curves attain some maximum values (peaks) and minimum values (troughs) as the prop is moved to the mid-span,  $\delta=0$ . To further elabo-

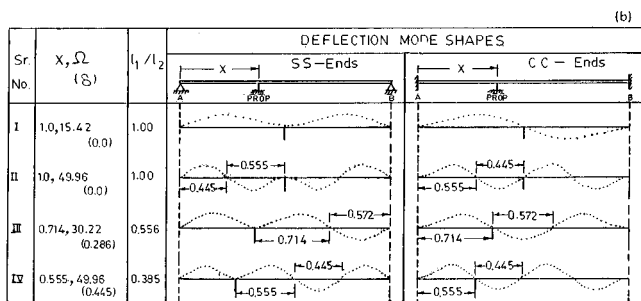
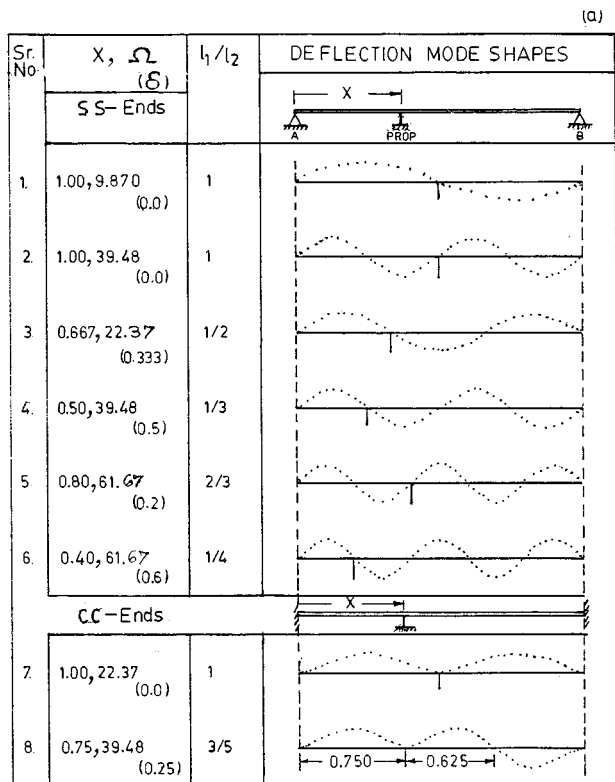


FIG. 2. Deflection mode shapes of beams vibrating in flexure corresponding to natural frequencies of beams with SS and CC ends (a) noncoinciding, (b) coinciding.  $(X, \Omega)$ , denotes the support location, frequency;  $\delta$ , the mistuning;  $l_1/l_2$ , the span ratio.

rate and have insight into the variation of normal modes with prop location, SS natural frequencies of the second mode of the first group may be considered, as follows.

For small values of  $X$  (hence large  $\delta$ ) the beam segments of span  $l_1$  and  $l_2$  vibrate in the first and the second modes, respectively, such that the maximum deflection  $b$  of  $l_2$  is considerably higher as compared to  $a$  of  $l_1$ . (For large values of  $\delta$ , the ratio of  $a$  to  $b$  can be less than 0.1 and the modes can thus be strongly localized,<sup>2</sup> as discussed later.) As the prop is moved further toward mid-span, the constraint and the natural frequency attain maximum value at  $X=0.667$  ( $=\frac{1}{3}$  of the total beam length) and  $b$  and  $a$  become equal and  $l_2=2l_1$ . The beam AB vibrates in its third mode with the prop located at its left nodal point; Fig. 2(a). Although the beam is mistuned due to the prop displaced from mid-span, it behaves like a tuned one and has its modes collective. Further displacement of the prop toward mid-span renders the beam mistuned once again, until it reaches the mid-span ( $\delta=0$ ) and is tuned. Variation of the rest of the frequency

curves can be understood in a similar way. All the peaks and troughs of the frequency curves clearly correspond to the natural frequencies of the beam with SS or CC ends and with or without the prop at mid-span. Even the mistuned beam behaves like a tuned one at these frequencies.

It is interesting to note that all the CC peaks and SS troughs coincide, whereas the SS peaks and CC troughs do not. It is easy to understand based on the knowledge of mode shapes of the beams corresponding to the coinciding frequencies; Fig. 2(b). At the coinciding frequencies, the beam with SS ends will always vibrate in a mode immediately higher than that when it has CC ends. It may further be pointed out that the coinciding SS and CC frequencies of the disordered beam may or may not belong to the same group of natural frequencies (S. No. III and IV, Fig. 1), whereas those frequencies of a tuned beam always belong to the same group of natural frequencies (S. No. I and II, Fig. 1).

### B. Collective normal modes of disordered beams

The deflection mode shapes of the disordered (mistuned) beams corresponding to the noncoinciding and coinciding peaks/troughs of SS and CC frequencies that are presented in Fig. 2(a) and (b) are collective, just like those for the periodic (tuned) beams. Mode shapes of beams vibrating at noncoinciding natural frequencies [Fig. 2(a)] are such that the end conditions of the beam elements coupled at the prop are similar to those at the extreme ends. Thus at the noncoinciding frequencies, both the elements vibrating in identical or different modes will have either both the ends simply supported or clamped; Fig. 2(a). However, when the modes correspond to the coinciding natural frequencies [Fig. 2(b)], the conditions at the coupled ends of the beam elements are different from those at the extreme ends of the beam. Thus at the coinciding frequencies, both the beam elements vibrating in identical or different modes will always have one end clamped and the other simply supported, irrespective of the extreme end conditions of the beams; Fig. 2(b).

All the mode shapes for the specific prop locations considered are such that the slopes at the ends of the beams (or moments for CC ends) are equal in magnitude but they are either in phase or in anti-phase, depending on the modes being anti-symmetric or symmetric, respectively. It implies that the beams, which are unsymmetric due to the prop being displaced to some specific locations away from the mid-span, can behave like symmetric/periodic beams. This becomes possible either (i) when the prop locations coincide with any of the "pinned nodal points" (points of zero moment) of simply supported beams [Fig. 2(a)] and clamped beams [Fig. 2(b)] vibrating at noncoinciding and coinciding frequencies, respectively, or (ii) when the prop is located at such a point that it provides "clamped nodal points" (point of zero slope) to the simply supported beams [Fig. 2(b)] and clamped beams [Fig. 2(a)] vibrating at coinciding and noncoinciding frequencies, respectively.

The mode shapes corresponding to SS and CC coinciding frequencies for periodic ( $X=1$ ) and unsymmetrically disordered ( $X=0.714$  and  $X=0.556$ ) beams are presented in Fig. 2(b). Just like the periodic beams (S. No. I and II) the nonperiodic beams (S. No. III and IV) have SS and CC natu-

ral frequencies coinciding. Also, like the periodic beams of symmetric elements, the ends of the disordered beams vibrating at coinciding frequencies always have their end responses equal in magnitude but they can be either in phase or in counterphase. Therefore, it follows that the unsymmetric beams can behave like symmetric and periodic beams when the intermediate prop(s) have some specific locations. This study is also helpful in understanding the phenomenon of confinement of free waves and vibrations in periodically disordered systems, studied separately.<sup>5</sup>

The natural modes of beams may not be affected due to the transfer of prop from one point to another one, provided they are the pinned nodal points [see mode shapes at 2, ( $\Omega = 39.48$ ) 5, 6, ( $\Omega = 61.67$ ) and II, IV ( $\Omega = 49.96$ , CC ends)]. It may also be understood that the presence of props at all these nodal points will not interfere with the natural modes. Except for the beams vibrating in the fundamental mode (modes 1 and 7 and I, Fig. 2), the rest of the beams, when assumed to have simple supports at all the nodal points in addition to the existing prop, can be considered to be multi-span beams having upto five spans. Some of these are periodic, others are disordered. The mode shapes studied here also apply to these multi-span beams.

### C. Localized normal modes of beams with large deliberate disorders

Collective modes in two-span beams having specific deterministic beam length disorders have been discussed above, and it has been shown that the disordered beams with specific prop location can behave like ideally periodic (tuned) beams. Except for the specific prop locations for particular modes, the beams will always behave as disordered ones. The beam elements being fully (strongly but finitely) coupled at the prop, the effect of small and very large disorder (or mistuning), which cannot and can strongly localize the normal modes, respectively, are discussed next.

For mistuned prop locations other than the nodal points, the modes will not remain collective but will be very weakly localized in the presence of strong coupling, except when the disorder is very large. As the prop is moved away from the mid-span, the first and the second normal mode SS and CC frequencies of various groups are lowered and raised, respectively, and the coinciding SS and CC curves (see I and II and  $\delta=0$ ,  $X=1$  in Fig. 1) for the tuned beam veer away, as pointed out earlier by Pierre *et al.*<sup>2</sup> Depending on the specific prop location and mode of vibration, conditions similar to these can occur due to further mistuning when the prop locations correspond to collective modes (3–5 and III and IV, Fig. 1) of the mistuned beam. Further displacement of the prop toward the end support continuously increases the disorder, with the result that span  $l_1$  becomes considerably smaller than  $l_2$ . Situations like this that result in a large amount of disorder can give rise to the normal modes that appear to be strongly localized. Figure 3 shows the strongly localized ( $A=0.08$ ) fundamental deflection mode shape of strongly disordered beam with  $\delta=0.56$ . Further increase in  $\delta$  will lower the value of  $A$  and hence the modes will be more strongly localized. Just like the harmful effects of normal mode localization in weakly coupled and weakly disordered

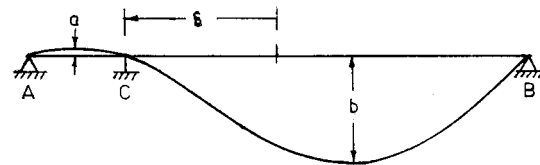


FIG. 3. Deflection mode shape of fully coupled and strongly disordered beam ( $\delta=0.56$ ,  $A=|a/b|=0.08$ , and  $\Omega=6.0$ ).

systems, high local response due to large deliberate (deterministic) disorders will also be associated with high local stresses, besides being useful for vibration isolation. Emphasis may be made to study the effect of deterministic disorders without and in the presence of small random disorders/imperfections. The effect of small random disorders on the response of deterministically disordered structures in the presence of different amounts of coupling and damping will be of special interest and should be a topic of future research.

### III. CONCLUSIONS

Natural frequencies and mode shapes of two-span finite beams, simply supported and clamped at their ends, have been studied for different locations of the intermediate simple support. Just as in the case of periodic beams, the study of natural modes of two-span disordered beams is also helpful in understanding the natural modes of disordered beams having more than two spans. When the intermediate supports of disordered beams are located at certain nodal points of the beam vibrating in flexure, it can behave like a periodic beam. The normal mode frequencies of periodic (tuned) beams with extreme ends simply supported and clamped can occur in pairs and coincide only if they belong to the same group, whereas the coinciding frequencies of the disordered beams need not necessarily belong to the same group.

The phenomenon of normal mode localization has been studied in fully (strongly) coupled beam-type systems with deterministic span length disorder. For small amounts of disorders, the normal modes of strongly coupled systems can become only very weakly localized (which has no significance in engineering structures). The mistuned beam in the presence of some particular amounts of disorders can behave like a tuned system and its modes become delocalized (collective). Normal modes of fully coupled multi-span beams can become and appear to be strongly localized only if they are strongly disordered.

<sup>1</sup>A. S. Bansal, "Flexural waves and deflection mode shapes of periodic and disordered beams," *J. Acoust. Soc. Am.* **72**, 476–481 (1982).

<sup>2</sup>C. Pierre, D. M. Tang, and E. H. Dowell, "Localized vibrations of disordered multi-span beams: Theory and experiment," *Am. Inst. Aero. Astro. J.* **25**, 1249–1257 (1987).

<sup>3</sup>C. Q. Cai and Y. K. Lin, "Statistical distribution of frequency response in disordered periodic structures," *Am. Inst. Aero. Astro. J.* **30**, 1400–1407 (1992).

<sup>4</sup>S. D. Lust, P. P. Friedmann, and O. O. Bendiksen, "Mode localization in multi-span beams," *Am. Inst. Aero. Astro. J.* **31**, 348–355 (1993).

<sup>5</sup>A. S. Bansal, "Free waves in periodically disordered systems: Natural and bounding frequencies of unsymmetric systems and normal mode localization. *J. Sound Vib.* (accepted).

<sup>6</sup>R. E. D. Bishop and D. C. Johnson, *The Mechanics of Vibration* (Cambridge U.P., Cambridge, U.K., 1966).

# Cochlear models and minimum phase<sup>a)</sup>

Egbert de Boer<sup>b)</sup>

Room D2-226, Academic Medical Center, Meibergdreef 9, 1105 AZ, Amsterdam, The Netherlands

(Received 11 April 1997; revised 11 July 1997; accepted 12 July 1997)

In this paper the extent to which the response of a linear cochlear model has the “minimum-phase” property is discussed, along with the topic of what it should mean when experiments confirm or deny the validity of minimum-phase in the response of the actual cochlea. This paper shows that short-wave, long-wave and three-dimensional cochlear models of the “classical” type, in which the operation of the cochlear partition is described by a *local* function (namely, a driving-point impedance) that produces a cochlear map (from frequency to place), have a response that is minimum-phase, or very close to minimum-phase. Conversely, when the response is found to be non-minimum-phase, the best-fitting model cannot be a classical one. © 1997 Acoustical Society of America. [S0001-4966(97)03012-9]

PACS numbers: 43.64.Kc, 43.64.Bt [RDF]

## INTRODUCTION

Understanding the operation of the cochlea can be approached from (at least) two directions. In one strategy the emphasis is on experimenting, and a very large variety of stimulus signals are employed in order to separate and unravel parts of the mechanism involved. In the other approach a mathematical model of the cochlea is formulated, and the computed response of the model is compared with results of appropriately chosen experiments. An intermediate way is possible, in which general properties of models are studied and predictions are made as to what to look for in experiments. The present paper attempts to follow this strategy. It is discussed to which extent the response of a cochlear model has the “minimum-phase” property, and what it should mean when experiments demonstrate the validity or the absence of minimum-phase in the response of the actual cochlea.

Consider a model of the cochlea in which the fluid in the channels interacts mechanically with the cochlear partition, and assume that the model is *linear* and *stable*. Many models treated in the literature can be defined as “classical” models; they have the property that the mechanical reaction of the cochlear partition at the longitudinal location  $x$  depends only on the movements of the basilar membrane (BM) at the *same* location  $x$  (de Boer, 1991, 1996, 1997a). For a linear model this means that the mechanics of the partition is completely described by the *driving-point impedance* of the partition. Because the mechanical properties of the BM dominate over those of other elements, it is usual to speak of the *BM impedance*, and we will call it  $Z_{BM}(x, \omega)$ , where  $x$  is the longitudinal coordinate and  $\omega$  the radian frequency. We assume that  $Z_{BM}(x, \omega)$  shows resonance for the radian frequency  $\omega$  at the location  $x_\omega$  which depends on  $\omega$  so that the model is capable of transforming (mapping) “frequency” into “place.”

In a classical model the BM impedance must be a real-

izable driving-point impedance, that is, the *BM impedance*  $Z_{BM}(x, \omega)$  and its inverse, the *BM admittance*  $Y_{BM}(x, \omega)$ , must both be physically realizable (the associated impulse responses must not start before zero time). This implies that neither  $Z_{BM}(x, \omega)$  nor  $Y_{BM}(x, \omega)$  can have *poles* in the right half of the complex  $s$  plane.<sup>1</sup> This implies, too, that  $Z_{BM}(x, \omega)$  does not have zeros in the right-half  $s$  plane.

Recently, “non-classical” models have appeared in the literature (Hubbard, 1993; Steele *et al.*, 1993; Geisler and Sang, 1995). In these models the mechanical reaction of the cochlear partition (or of the BM) at one location is additionally controlled by BM movements elsewhere, at other locations  $x$ . In such non-classical models the concept of BM impedance  $Z_{BM}(x, \omega)$  can formally be retained, by defining it in terms of the quotient of the pressure (just above the BM)  $p(x, \omega)$  and the BM velocity  $v_{BM}(x, \omega)$ . We will call this impedance the *effective BM impedance* and denote it by  $Z_{BM}^{(eff)}(x, \omega)$ . The effective impedance can, of course, only be found *after* the model solution has been computed. Because this impedance is no longer determined by *local* mechanical properties, it is no longer restrained to be a driving-point impedance. And the effective BM impedance may not even be a realizable transfer impedance, that is, this function or its inverse, or both, may have poles in the right-half of the complex  $s$  plane. Apart from this aspect of realizability, classical and non-classical models are equivalent as has recently been shown by the author (de Boer, 1997a).

A concept that, in linear-filter theory, is related to realizability is that of “minimum-phase.” By definition, a minimum-phase filter function has no *zeros* in the right-half of the  $s$  plane. When a filter response is minimum-phase, *the phase delay produced by the filter is smaller than that of any other filter that has the same amplitude-versus-frequency response*. A condensed proof of this property is given in the Appendix. In a minimum-phase filter there is a unique relation between *amplitude response* and *phase response* (both considered as functions of frequency), each of these is fully determined by the other one, namely, via the Hilbert transform. From the response of a filter that is *not* minimum-phase, a part can be isolated that has the characteristics of a pure delay. That delay may depend on frequency, but is *not*

<sup>a)</sup>Note: The proof of Section I formed part of a poster presentation at the 1996 ARO Midwinter meeting (de Boer and Nuttall, 1996).

<sup>b)</sup>Electronic mail: e.deboer@amc.uva.nl

associated with variations of the amplitude with frequency.

In the case of the cochlea we have the situation where a traveling wave is present which also shows a pronounced frequency selectivity, and it is attractive to try to separate the two aspects, wave propagation and frequency selectivity. Is one fully determined by the other, and vice versa, or is there some freedom? Such questions may be answered from a deeper study of minimum-phase in cochlear models. In the present paper the question is addressed: *Does a model of the cochlea have a minimum-phase response?* It is found that the property of minimum-phase is intricately connected with realizability of the impedance  $Z_{BM}(x, \omega)$  of the model as a driving-point impedance. We will first consider a *classical* model. When, as is the case in a classical model,  $Z_{BM}(x, \omega)$  is a realizable driving-point impedance, the response of a *short-wave* classical model of the cochlea is minimum-phase (Section I). In good approximation, the response of a *long-wave* classical model is also minimum-phase, and the same is true for a *three-dimensional* classical model (Section II). In the case of a *non-classical* model the effective BM impedance  $Z_{BM}^{(eff)}(x, \omega)$  is not necessarily a driving-point impedance. For this class of models the following is proven. When the effective BM impedance does not have zeros in the right-half of the  $s$  plane, the response is minimum-phase, or very close to it, otherwise, it is not minimum-phase.

The theory described in this paper is based on *linear* models. Application of the results to experimental data is only justified in those cases where the response of the cochlea can be considered as linear or where nonlinear effects can be neglected. This is the case for stimulation of the normal cochlea with extremely weak signals (say, below 30 dB SPL), or for the cochlea in a dead animal. For higher levels of stimulation nonlinear effects do appear. In those cases one can resort to the use of noise bands as stimulus signals and computing input–output *cross-correlation functions* (ccfs). The present author has shown that the ccf for wide-band noise, determined for a *nonlinear* model, is equal to that of a *linear* model of the same structure with different parameters (de Boer, 1997b). The latter model is called the ‘‘comparison model’’ and the cited paper describes how it has to be constructed. From experimentally determined ccfs one can then derive the properties of the comparison model (de Boer and Nuttall, 1997). The results derived in the present paper apply equally well to the comparison model because it is linear. We repeat that one of the requirements that the model has to meet is that it maps frequency to place.

## I. THEORY: SHORT-WAVE CLASSICAL MODEL

Consider a classical linear model of the cochlea as described in the Introduction. Two elongated fluid-filled channels are separated by a movable partition that is completely described by its local mechanical impedance  $Z_{BM}(x, \omega)$ . That impedance has to be realizable as a driving-point impedance (see the Introduction). Choose a long rectangular box for the shape of the model. Assume that the height of the channels (in the  $z$  direction) is ‘‘infinite,’’ i.e., so large that fluid movements near the movable partition do not reach the upper (or lower) wall of the channels; this is the *short-wave* case

(cf. de Boer, 1991, Section 2.3; de Boer, 1996, Section 5.2). Assume also that there are only waves going in one direction, from stapes toward helicotrema, i.e., in the direction of increasing  $x$ . For this case the fluid pressure  $p(x, \omega)$  just above the basilar membrane for a wave with radian frequency  $\omega$  obeys the following differential equation (de Boer, 1991, Eq. 2.3.n; de Boer, 1996, Eq. 5.2.3):

$$\frac{dp(x, \omega)}{dx} + \frac{2\omega\rho}{Z_{BM}(x, \omega)}p(x, \omega) = 0. \quad (1)$$

Here,  $\rho$  is the density of the fluid. The solution to this equation is of the form

$$p(x, \omega) = p_0 \exp\left(-i \int_0^x k(x', \omega) dx'\right), \quad (2)$$

where the *local wave number*  $k(x, \omega)$  is given by

$$k(x, \omega) = \frac{-2i\omega\rho}{Z_{BM}(x, \omega)}, \quad (3)$$

and  $p_0$  is a constant. To investigate the properties of  $p(x, \omega)$  as a function of  $\omega$  at a fixed location  $x$  is not simple because  $p(x, \omega)$  is a function of both  $x$  and  $\omega$  and Eq. (2) involves an integration over  $x$ . Therefore, we have to assume some form of relation between these two variables. Take the case where  $Z_{BM}(x, \omega)$  depends on  $x$  and  $\omega$  in such a way that a variation of  $x$  can be offset by a variation of  $\omega$ . In particular, assume that *place is logarithmically related to frequency*. This means that, when  $x$  and  $\omega$  are varied in such a way that

$$u = \frac{\exp(-\alpha x/2)}{\omega} \quad (4)$$

does *not* vary (where  $\alpha$  is a constant parameter), the impedance changes only by a factor, namely, the factor  $\omega$ , and the wave equation [Eq. (1)] remains exactly the same. The response pattern,  $p(x, \omega)$  as a function of  $x$ , then retains the same form, it is only shifted over  $x$  (apart from a small influence of the boundary condition at  $x=0$  upon the level). We assume that this property holds true for all values of  $\omega$ , even for complex ones, but for the moment we only consider real values of  $\omega$ . Applying the property to the value of  $u$  where  $Z_{BM}(x, \omega)$  shows resonance, we find that  $u = \text{constant}$  reduces to the following expression:

$$\omega_{\text{res}}(x) = \omega_0 \exp(-\alpha x/2), \quad (5)$$

where  $\omega_{\text{res}}(x)$  is the radian resonance frequency corresponding to location  $x$  and  $\omega_0$  the radian resonance frequency corresponding to  $x=0$ . Under conditions of constant  $u$ , variations  $dx$  and  $d\omega$  of  $x$  and  $\omega$  are linked by

$$(\alpha/2)dx = -d\omega/\omega. \quad (6)$$

Combine this with Eq. (3) and substitute in Eq. (2):

$$\begin{aligned} p(x, \omega) &= p_0 \exp\left(-\int_0^x \frac{2\omega\rho}{Z_{BM}(x', \omega)} dx'\right) \\ &= p_0 \exp\left(\frac{4}{\alpha} \int_{\omega_0}^{\omega} \frac{\omega\rho}{\omega' Z_{BM}(x, \omega')} d\omega'\right). \end{aligned} \quad (7)$$

This relation can be interpreted in more than one way. If we think in terms of resonance frequencies, the integration is to be carried out from  $\omega_0$  to  $\omega$ , i.e., over the range of radian

resonance frequencies that corresponds to going from 0 to  $x$ . Note, however, that the result is now solely a function of  $\omega$  at location  $x$ , therefore, complex values of  $\omega$  (and  $\omega_0$ ) can be considered too, and the full mechanism of complex-function theory can be applied.

A filter transfer function  $F(\omega)$  is defined as minimum-phase when it has no zeros in the right-half of the complex  $s$  plane. Equivalently, this is the case when its logarithm has no poles in that half-plane. A realizable driving-point impedance or admittance, like the BM impedance function  $Z_{\text{BM}}(x, \omega)$  or its inverse, has zeros nor poles in the right-half of the  $s$  plane. The same is true for the end values of the integration in Eq. (7). Hence the logarithm of the function  $[p(x, \omega)/p_0]$  for the short-wave model has no singularities in the right-half of the  $s$  plane, and the function  $[p(x, \omega)/p_0]$  itself is a minimum-phase function. The same applies to the BM velocity  $v_{\text{BM}}(x, \omega)$ . Note that this holds true only when  $Z_{\text{BM}}(x, \omega)$  is a realizable driving-point impedance. In more general terms, *the response of a classical short-wave model is minimum-phase when  $Z_{\text{BM}}(x, \omega)$  has no zeros in the right-half  $s$  plane.* The only proviso is that there should be only uni-directional waves in the model.

## II. THEORY: LONG-WAVE CLASSICAL MODEL

Next consider the case in which it is assumed that the height of the model is so small that the sound pressure at the upper wall is only slightly smaller in magnitude than the pressure just above the BM. This assumption leads to what is called the *long-wave* approximation (de Boer, 1991, Section 2.2; de Boer, 1996, Section 4.2). We will show that the response of the classical long-wave model is also very close to being minimum-phase. The equation for the long-wave model reads (de Boer, 1991, Eq. 2.1.b; de Boer, 1996, Eq. 4.2.4):

$$\frac{d^2 p(x, \omega)}{dx^2} - \frac{2i\omega\rho}{h_{\text{eff}}Z_{\text{BM}}(x, \omega)} p(x, \omega) = 0. \quad (8)$$

The parameter  $h_{\text{eff}}$  is the effective height of the model's cochlear channels. Take the Liouville–Green (or WKB) expression for an approximate solution (de Boer, 1996, Section 4.3):

$$p(x, \omega) = p_0(x, \omega) \exp\left(-i \int_0^x k(x', \omega) dx'\right), \quad (9)$$

where the local wave number  $k(x, \omega)$  is given by

$$k^2(x, \omega) = \frac{-2i\omega\rho}{h_{\text{eff}}Z_{\text{BM}}(x, \omega)}, \quad (10)$$

and  $p_0(x, \omega)$  is a slowly varying function of  $x$  and  $\omega$ . Equation (10) implies that singularities of  $k(x, \omega)$  can only occur in the quadrant where  $[1/Z_{\text{BM}}(x, \omega)]$  has singularities. In a classical model  $[1/Z_{\text{BM}}(x, \omega)]$  has no singularities in the right-half of the  $s$  plane because  $Z_{\text{BM}}(x, \omega)$  is a driving-point impedance. The factor  $p_0(x, \omega)$  is proportional to  $[k^{-1/2}(x, \omega)]$  (de Boer, 1996, Eq. 4.3.4), and will have no zeros in the right-half of the  $s$  plane either. Therefore, in the Liouville–Green (or WKB) approximation, the pressure

$p(x, \omega)$  is minimum-phase, and the BM velocity  $v_{\text{BM}}(x, \omega)$  will be minimum-phase too.

However, the *actual* response of a long-wave model may deviate somewhat from the Liouville–Green (LG) solution, and may show a small extra delay component. It is unlikely that such a component can be detected in computed model responses because the LG approximation is such a “good” one (de Boer and Viergever, 1982).

For the more general case of a *three-dimensional* model we can again start from the LG approximation (cf. Steele and Taber, 1979; de Boer and Viergever, 1982). Equation (10) is replaced by a similar one (Eq. 6 in de Boer and Viergever, 1982), in which  $k^2(x, \omega)$  is replaced by a function that goes to infinity as  $k(x, \omega)$  [compare the short-wave case of Eq. (3)]. The same argumentation can then be used to show that, in the LG approximation, the response of a three-dimensional classical model is minimum-phase. Again, we have to keep in mind that there should only be uni-directional waves in the model.

## III. IMPLICATIONS

The first theorem derived (Sec. I) implies that in the short-wave classical model of the cochlea, when the cochlear partition exhibits any particular form of resonance or filtering involving a cochlear mapping from frequency to place, *the traveling time of the cochlear wave is entirely determined by the type of resonance or filtering* and has no component that is specifically attributable to wave propagation without resonance or filtering.<sup>2</sup> Conversely, the type of resonance exhibited by the model is so intimately interwoven with wave propagation that it cannot be separated from it. The same is true, within the Liouville–Green approximation, for both the classical long-wave model and the classical three-dimensional model (Sec. II). In general terms this result can be expressed by saying that it is not possible to *separate* the parts played by wave propagation and frequency-specific filtering from an analysis of the model response; one part cannot be modified without affecting the other, and all details of the response are due to the two processes involved. It is repeated that all this holds true only for classical models.

For a *non-classical* model the effective BM impedance  $Z_{\text{BM}}^{\text{(eff)}}(x, \omega)$  is not a “given” parameter which controls the response. The effective impedance can only be computed *after* the model solution has been obtained. This impedance may turn out to have zeros (or poles) in the right-half of the  $s$  plane. If that is the case, the response of the model may or may not be not minimum-phase.<sup>3</sup> In the converse sense, if we would find the response of a cochlear model to be non-minimum-phase, the BM impedance  $Z_{\text{BM}}^{\text{(eff)}}(x, \omega)$  must have at least one zero pair in the right-half of the  $s$  plane; that impedance then cannot be realized as a driving-point impedance, and the model must have been a non-classical one.

In the derivation it has been assumed that the cochlear map is logarithmic [Eq. (5)] over the whole range of  $x$ . For a model that is closer to reality, the mapping should be different in the basal and apical parts. It should be clear, however, that the major point of the derivation remains valid when a



slowly varying function of  $x$  is included in the transformation Eq. (5).

#### IV. DISCUSSION OF EXPERIMENTAL ASPECTS

From the foregoing discussion, one can understand that the question of whether the response of the actual cochlea is minimum-phase or not, relates to the problem whether the operation of the cochlea is to be described by a classical or a non-classical model. In experimental terms there is conflicting evidence on this issue. De Boer and Nuttall (1996) reported that input–output cross-correlation functions of the cochlea (measured from the basal turn of the guinea-pig cochlea) can be matched very well by artificial response functions from *minimum-phase* filters. This would mean that, for this match to be obtained, it was not necessary to include an extra (traveling-wave) delay. In different terms: the response showed, within the accuracy of this analysis, minimum-phase character. On the other hand, Recio *et al.* (1997) reported that their “first-order Wiener kernels,” which they measured in the basal turn of the chinchilla cochlea, and which are equivalent to input–output cross-correlation functions, are non-minimum-phase. It may be that the matching technique employed by de Boer and Nuttall (1996) has been too crude, or that the analysis by Recio *et al.* (1997) is in error. At any rate, in digital signal processing minimum-phase analysis is a difficult and tricky procedure.<sup>4</sup> To confound the issue more, de Boer and Nuttall (1997) reported that the effective BM impedance, which they derived by “inverse analysis” from their experimental data, shows clear signs of containing a non-realizable component. This property would entail that the cochlear response is non-minimum-phase. And in its turn this property would imply that the cochlea functions according to a non-classical model. Further study in this field is clearly indicated.

#### ACKNOWLEDGMENTS

The author is grateful to Luc-Johan Kanis (Amsterdam, Neth.), Fred Nuttall (Portland, OR), Alberto Recio (Evanston, IL), and Christopher Shera (Cambridge, MA) for their contributions in lively and fruitful discussions on the theme of this paper. In addition, Christopher Shera refined the author’s understanding of the long-wave case (Section II) and the handling of non-minimum-phase responses. Two anonymous reviewers are gratefully acknowledged for their suggestions to improve the clarity of the text. This study was carried out as a sequel to Project No. SLW 01.011 of NWO (The Netherlands).

#### APPENDIX: THE MEANING OF “MINIMUM-PHASE”

Consider a given response function  $F(\omega)$ , and consider all realizable response functions  $G_i(\omega)$  ( $i=0,1,2,3,\dots$ ) that have the same magnitude as  $F(\omega)$ . Take one such function  $G_i(\omega)$ . It is characterized by a specific pole-zero pattern in the complex  $s$  plane in which all poles and zeros occur in conjugate complex pairs, and the pole pairs are in the left-

half of the  $s$  plane. Assume that one pair of conjugate complex zeros is added in the *right*-half of the  $s$  plane. Then, this pair must be offset by a pole pair in the *left*-half of the  $s$  plane, *symmetrically* located with respect to the imaginary axis, in order to ensure that  $|G_i(\omega)|$  remains the same. The added zero- and pole pairs together represent an all-pass filter that implies a (possibly frequency-dependent) delay. Hence by the addition of such a combination of a pole and a zero pair the phase lag of  $G_i(\omega)$  will always *increase*.

Therefore, the function  $G_0(\omega)$  that has *no* zeros in the right-half of the  $s$  plane is the one that has the *smallest* phase lag among all functions  $G_i(\omega)$  with  $|G_i(\omega)|=|F(\omega)|$ . The function  $G_0(\omega)$  is, by definition, a minimum-phase function. The logarithm of a minimum-phase function has no singularities in the right-half of the  $s$  plane, and that is the property used in the proof in the main text.

<sup>1</sup>The complex  $s$  plane is defined so that for real  $\omega$ ,  $s$  equals  $i\omega$ .

<sup>2</sup>In the case where the cochlear partition does not show resonance, our derivation does not apply, and we have the trivial case of “pure” wave propagation.

<sup>3</sup>This depends on the sign of the integral in Eq. (7).

<sup>4</sup>Minimum-phase analysis is only useful when *all* signals involved are narrow-band signals. For a minimum-phase response the phase function corresponding to a given amplitude function is the Hilbert transform of the logarithm of the amplitude. First, this logarithm is not guaranteed to be a narrow-band (or even a low-pass) function, and second, the kernel of the Hilbert transform does not have a finite energy. Both factors can easily lead to divergence problems in digital computations, and one should always be aware of these pitfalls.

de Boer, E. (1991). “Auditory physics. Physical principles in hearing theory. III,” *Phys. Rep.* **203**, 127–229.

de Boer, E. (1996). “Mechanics of the cochlea: modeling efforts,” in *The Cochlea*, edited by P. Dallos, A. N. Popper, and R. R. Fay (Springer-Verlag, New York), pp. 258–317.

de Boer, E. (1997a). “Classical and non-classical models of the cochlea,” *J. Acoust. Soc. Am.* **101**, 2148–2150.

de Boer, E. (1997b). “Connecting frequency selectivity and nonlinearity for models of the cochlea,” *Aud. Neurosci.* **3**, 377–388.

de Boer, E., and Viergever, M. A. (1982). “Validity of the Liouville-Green (or WKB) method for cochlear mechanics,” *Hearing Res.* **8**, 131–155.

de Boer, E., and Nuttall, A. L. (1996). “Cochlear travel time and minimum phase,” *ARO Mid-Winter Meeting Abstracts* **19**, 57 (no. 228).

de Boer, E., and Nuttall, A. L. (1997). “On cochlear cross-correlation functions: connecting nonlinearity and ‘activity’,” in *Diversity in Auditory Mechanisms*, edited by E. R. Lewis, G. R. Long, R. F. Lyon, P. M. Narins, C. R. Steele, and E. Hecht-Poinar (World Scientific, Singapore), pp. 291–297.

Geisler, C. D., and Sang, C. (1995). “A cochlear model using feed-forward outer-hair-cell forces,” *Hearing Res.* **86**, 132–146.

Hubbard, A. E. (1993). “A traveling wave-amplifier model of the cochlea,” *Science* **259**, 68–71.

Recio, A., Narayan, S. S., and Ruggero, M. A. (1997). “Wiener-kernel analysis of basilar-membrane responses to white noise,” in *Diversity in Auditory Mechanisms*, edited by E. R. Lewis, G. R. Long, R. F. Lyon, P. M. Narins, C. R. Steele, and E. Hecht-Poinar (World Scientific, Singapore), pp. 325–331.

Steele, C. R., and Taber, L. A. (1979). “Comparison of WKB and finite difference calculations for a two-dimensional cochlear model,” *J. Acoust. Soc. Am.* **65**, 1001–1006.

Steele, C. R., Baker, G., Tolomeo, J., and Zetes, D. (1993). “Electromechanical models of the outer hair cell,” in *Biophysics of Hair-Cell Sensory Systems*, edited by H. Duifhuis, J. W. Horst, P. van Dijk, and S. M. van Netten (World Scientific, Singapore), pp. 207–214.

## Erratum: “Elasto-acoustics of a two-dimensional strip by a hybrid method” [J. Acoust. Soc. Am. 102, 955–967 (1997)]

Michael El-Raheb

*The Dow Chemical Company, Midland, Michigan 48674*

(Received 18 August 1997; accepted for publication 21 August 1997)

PACS numbers: 43.40.Dx, 43.40.Rj, 43.10.Vx [CBB]

[S0001-4966(97)06712-X]

The caption of Fig. 7 should read:

FIG. 7. Center point impedance of flat rectangular plate with  $n=0$ , (3-D) analysis,  $l_x=1$  m,  $l_z=2$  m,  $(x_b, z_b)=(0.5$  m,  $-1$  m),  $(x_f, y_f, z_f)=(0.5$  m,  $1$  m,  $-1$  m).

The purpose of Fig. 7 is an attempt to reproduce the (1-D) acoustic impedance in Fig. 5 by computing the (3-D) impedance of a rectangular plate oscillating with finite wave number along  $x$  and translating along  $z$ . To approach the (1-D) asymptotic values in Fig. 5,  $l_z$  was increased from 1 m for the square plate in Fig. 6 to 2 m for the rectangular plate in Fig. 7.

# TECHNICAL NOTES AND RESEARCH BRIEFS

Paul B. Ostergaard

10 Glenwood Way, West Caldwell, New Jersey 07006

**Editor's Note:** Original contributions to the Technical Notes and Research Briefs section are always welcome. Manuscripts should be double-spaced, and ordinarily not longer than about 1500 words. There are no publication charges, and consequently, no free reprints; however, reprints may be purchased at the usual prices.

## Tuning process of xylophone and marimba bars analyzed by finite element modeling and experimental measurements [43.75.Kk, 43.40.Cw]

J. Bretos and C. Santamaría

Departamento de Física Aplicada II, Universidad del País Vasco, Apdo. 644-48080 Bilbao, Spain

J. Alonso Moral

Conservatorio Superior de Música de Bilbao "Juan Crisóstomo de Arriaga," Bilbao, Spain

The natural frequencies of a constant section bar and two types of undercut bars (with parabolic and rectangular outlines) have been calculated by finite element modeling (FEM) and compared with experimental measurements. With these undercuts, two different tunings were achieved for the two first partials, the 1:4 relationship between them (marimba bars) and the 1:3 case (xylophone bar). The agreement between the calculated and measured data is good. Thus, finite element analysis can be considered as a good tool to study the tuning of this kind of musical instrument. © 1997 Acoustical Society of America. [S0001-4966(97)06912-9]

Finite element modeling (FEM) can be useful to study certain musical problems. An example is the tuning of xylophone-like instrument bars. This work offers a brief report on FEM calculations of three cases of bars with different shapes using the ABAQUS software (Hibbit, Karlsson & Sorensen). Figure 1 plots the meshes corresponding to the three types of bar analyzed. The length ( $L$ ), width ( $b$ ), and height ( $h$ ) of the three bars studied were  $L=330$  mm,  $b=34$  mm, and  $h=18$  mm, respectively, which are the typical geometrical parameters of bars used by xylophone makers. Cases (b) and (c) show nonconstant section bars with a parabolic undercut (case b) and a rectangular undercut (case c). Thus, the undercut must be characterized by its length ( $L_u$ ) and its height ( $h_u$ ).

Regarding the mechanical parameters required by FEM (density and elastic constants) the bars were modeled as made of a special kind of wood, the *lophera alata azobe*.<sup>1</sup> This variety of wood is similar to those used for xylophone and marimba bars (palissandre, rosewood,...) and all of them are characterized by their high density and stiffness.<sup>2</sup> The specific values for the density and elastic constants of this wood are as follows:  $\rho=1020$  kg/m<sup>3</sup>; Young moduli:  $E_1=19.2$  GPa,  $E_2=4.7$  GPa, and  $E_3=2.9$  GPa; Poisson moduli:  $\nu_{12}, \nu_{13}=0.03$ ;  $\nu_{23}=0.3$ ; shear moduli:  $G_{12}=2$  GPa;  $G_{13}=1.4$  GPa, and  $G_{23}=0.96$  GPa. The sub-indices 1, 2, 3 are related to the direction—parallel, radial, and tangential—to the grain, respectively.

The meshes defined for these types of bars contain 668 nodes belonging to 150 elements. The elements are solid elements with second order of integration. Analysis consisted of the extraction of the natural eigenmodes of the bars, calculating their corresponding frequencies. Table I shows the values of the frequencies calculated for the constant section case and the two different undercuts and a set of labels corresponding to the type of natural eigenmode associated with each frequency. These labels are  $FY_i$  for flexural or bending modes in the  $OY$  direction;  $FZ_i$  for flexural or bending modes in the  $OZ$  direction; and  $T_i$  for torsional modes. The most important eigenmodes for musical purposes will obviously be  $FY_i$ , because in xylophone bars they are the most easily excited by the beat of the mallets. Moreover, their natural frequencies are tuned into harmonic relationships to achieve a dominant periodicity.<sup>3</sup>

In this sense, it can be observed directly that these undercuts were designed to achieve two different tunings. On the one hand, in the case of the parabolic outline the first and second natural frequencies (of  $FY_i$  eigen-

modes) have a double-octave relationship ( $\approx 1:4$ ), like the case of a marimba bar.<sup>3</sup> On the other hand, the rectangular-undercut bar features a relationship of an octave and a fifth between the two first frequencies ( $\approx 1:3$ ), like the case of a xylophone bar.<sup>3</sup> The main aim of this work was therefore to achieve, by means of finite element analysis, the two most important types of tunings in the xylophone family using two different types of geometrical outline.

Table I also offers a comparison of the calculated frequencies with experimental values obtained from wooden bars with the same mechanical and geometrical parameters as those used in the FEM. The latter measurements were accomplished using an experimental setup described in an earlier publication.<sup>4</sup> The tight agreement between them can be easily checked. Thus, for the constant section bars, the differences between the experimental and numerical results ( $\delta f_i$ ) are less than 3% for all types of natural eigenmodes. In the special case of  $FY$  eigenmodes the differences are less than 0.1%.

In the case of the parabolic undercut, the geometrical outline chosen was that afforded by finite element analysis to tune this bar in the  $E_4$  tone (330 Hz) with the 1:4 harmonic relationship between the first overtone and the fundamental. The length and height of the undercut were  $0.5L$  and  $0.55h$ , respectively (Fig. 1). The experimental value for the fundamental frequency was 326.2 Hz, 1.2% lower than the frequency associated with  $E_4$ . The agreement between experimental and numerical results for frequencies holds for all types of natural eigenmode (the highest deviation is  $-2.76\%$  and is observed for the first  $FZ$  eigenmode). Thus, the agreement for the  $FY$  eigenmodes is specially good, because only deviations of less than 1.2% were encountered.

Finally, the rectangular undercut is characterized by a length  $L_u=0.50L$  and a height  $h_u=0.53h$ . These parameters define the geometrical design given by the finite element modeling to tune the initial constant

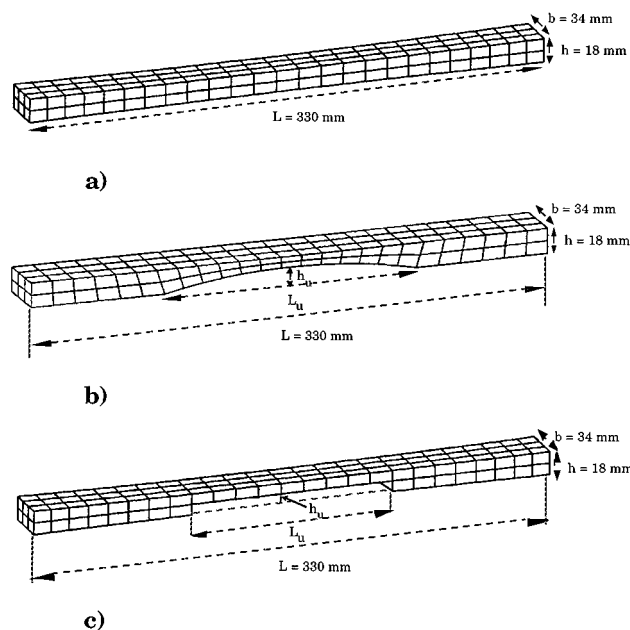


FIG. 1. Meshes defined for the finite element modeling: (a) constant section bar; (b) parabolic undercut bar; (c) rectangular undercut bar.

TABLE I. Values for the natural frequencies of a constant section bar, a parabolic undercut bar, and a rectangular undercut bar calculated by finite element modeling and experimental measurements.

	$f_i$ (Hz) exp	$f_i$ (Hz) FEM	$\delta f_i$ (%)	Mode type	$f_i:f_1$ exp.	$f_i:f_1$ FEM
Constant section bar	720	719.1	-0.13	$FY_1$		
	1560	1559.2	-0.05	$T_1$		
	1880	1880.1	0.01	$FY_2$	2.61	2.61
	3011	3045.7	-1.15	$FZ_1$		
	3240	3142.8	-3.00	$T_2$		
	3440	3436.1	-0.11	$FY_3$	4.78	4.78
	4856	4770.5	-1.76	$T_3$		
	5232	5239.4	0.14	$FY_4$	7.27	7.29
Parabolic undercut bar	326.2	330.0	1.16	$FY_1$		
	809.4	816.2	0.84	$T_1$		
	1153	1121.2	-2.76	$FZ_1$		
	1291	1306.7	1.22	$FY_2$	3.96	3.96
	2875	2825.3	-1.73	$FZ_2$		
	2878	2882.0	-0.14	$FY_3$	8.82	8.73
	3233	3205.5	-0.84	$T_2$		
	4368	4356.1	-0.27	$T_3$		
4488	4502.6	0.33	$FY_4$	13.8	13.6	
Rectangular undercut bar	290.5	293.6	1.07	$FY_1$		
	712.0	705.8	-0.87	$T_1$		
	893.8	890.0	-0.43	$FY_2$	3.08	3.03
	...	1059.3	...	$FZ_1$		
	2000	1993.5	-0.32	$FY_3$	6.89	6.79
	2312	2239.5	3.14	$T_2$		
	3632	3654.8	0.63	$FY_4$	12.5	12.5
	4224	4182.4	-0.98	$T_3$		
4620	4495.0	2.78	$FZ_3$			
4848	4822.2	-0.53	$FY_5$	16.7	16.4	

section bar into the  $C_4$  musical tone with a 1:3 harmonical ratio between its first two partials (or  $FY$ -eigenmode frequencies). Comparison of the numerical and experimental data leads to successful results similar to those found for the parabolic-undercut bar. Thus, the deviations are less than 1.1% for  $FY$  eigenmodes.

The good results of this type of FEM calculations can also be seen from Fig. 2. The figure compares the values calculated in the present work for the  $f_2:f_1$  relationship of gradually undercut bars with a rectangular outline and the values reported by Summers *et al.*<sup>5</sup> for the same cases: rectangular-undercut with a constant length  $L_u=0.25L$  and an increasing height  $h_u$  from 0 to  $0.6h$ . In this figure the good agreement between the numerical and experimental data can be observed, except for the values relating to the highest undercut length fraction (or height of undercut).

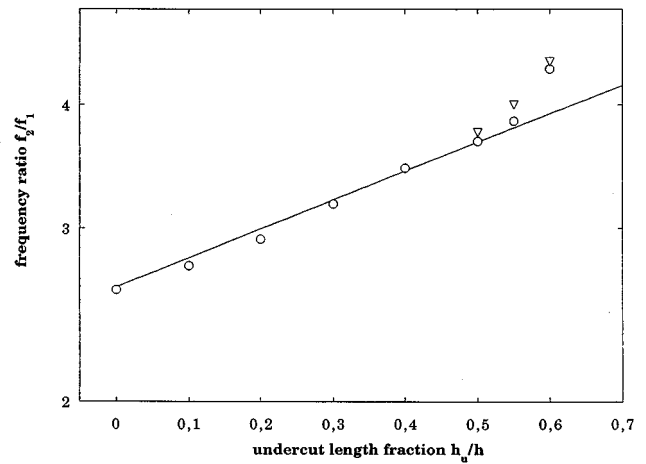


FIG. 2. Calculated values for the ratio between the frequencies corresponding to the two first natural  $FY$  eigenmodes of rectangular undercut wooden bars performed versus the length and height of the carving (—: fitting of numerical results obtained in this work by FEM; O, ∇: first and second set of experimental measurements of Summers *et al.*<sup>5</sup>).

In the light of the above, finite element modeling can be said to be a good tool to describe the carving process used to tune bars used in xylophones and similar musical instruments. This numerical method may thus offer an alternative method to the mathematical algorithms successfully used by other authors for the same purposes.<sup>5,6</sup>

<sup>1</sup>D. Guitard, *Mecanique du materiau bois et composites* (Collection Nabra, Cepadue-Editions, Toulouse, France, 1987).

<sup>2</sup>D. Holz, "Investigations on Acoustically Important Qualities of Xylophone-Bar Materials: Can We Substitute Any Tropical Woods by European Species?," Communication to the International Symposium on Musical Acoustics, Dourdan, France (VIII-95).

<sup>3</sup>N. H. Fletcher and T. D. Rossing, *The Physics of Musical Instruments* (Springer-Verlag, New York, 1991), Chaps. II and XIX.

<sup>4</sup>J. Bretos, C. Santamaria, and J. Alonso-Moral, "Frequencies, input admittances and bandwidths of the natural bending eigenmodes in xylophone bars," *J. Sound Vib.* **203**(1), 1-9 (1997).

<sup>5</sup>I. R. Summers, S. Elsworth, and R. Knight, "Transverse vibrational modes of a simple undercut beam; an investigation of overtone tuning for keyed percussion instruments," *Acoust. Lett.* **17**(4), 66-70 (1993).

<sup>6</sup>F. Orduña-Bustamante, "Nonuniform beams with harmonically related overtones for use in percussion instruments," *J. Acoust. Soc. Am.* **90**, 2935-2941 (1991).

## Advanced-degree dissertations in acoustics

*Editor's note:* Abstracts of Doctoral and Master's theses will be welcomed at all times. Please note that they must be double spaced, limited to 200 words, must include the appropriate PACS classification numbers, and formatted as shown below (don't make the editor retype them, please!). The address for obtaining a copy of the thesis is helpful. Please submit two copies.

**Vibrational modes of two violins** [43.75.Ef, 43.40.Dx, 43.75.Yy]—Mark A. Roberts, *Physics Department, Northern Illinois University, DeKalb, IL 60115, August 1997 (MS)*. Using electronic TV holography, the vibrational motion of two violins has been studied and the normal modes of vibration determined. These normal modes are determined by the coupled motion of the top plate, back plate, enclosed air, ribs, neck, fingerboard, etc. In this investigation, the normal modes were excited in three ways: with an oscillating force applied to the violin bridge; with an oscillating internal pressure; and with the sound field of a loudspeaker. As a help in understanding the normal modes of vibration, the air cavity modes were determined with the top and back plates held stationary with sand bags. The most strongly radiating mode in the frequency range below 1000 Hz in both violins was the  $C_3$  mode around 530 Hz. Some modes appeared as doublets. In one violin, for example, longitudinal (0,1)-type air motion within the violin body was the basis of a pair of modes at 473 and 825 Hz.

Thesis advisor: Thomas D. Rossing.

**Linear and nonlinear properties of cochlear transduction—Application of a nonlinear system identification technique** [43.64.Bt, 43.64.Jb, 43.64.Ri]—Geetha Krishnan, *University of Kansas Medical Center, Department of Hearing and Speech, Kansas City, KS, June 1995 (Ph.D.)*. Contact address: 1517 Ridgeview Dr., Louisville, CO 80027. E-mail: geetha@cs.cmu.edu. A new system identification procedure is used to characterize linear and nonlinear cochlear processes using transient evoked otoacoustic emissions (TEOAE) data. In this technique, a computational model of the system is first developed. From the measured input and output data, spectral density functions and multiple coherence functions are calculated. The coherence functions allow the characterization of linear/nonlinear processes as a function of frequency. Summation of linear and nonlinear coherences provide a goodness-of-fit of the chosen model. TEOAE were recorded from 11 adults with normal hearing using FIR pulse as stimulus. Third- and fifth-order polynomial models were used to model

the data and the results indicate that the fifth-order model is a better fit to the TEOAE data. Two-tone simulation experiments were performed using the identified systems from the third- and the fifth-order models to obtain predictions of  $2f_1 - f_2$  distortion products for a variety of stimulus parameters. Some behaviors of the predicted distortion product ( $ADP_m$ ) from the fifth-order model were consistent with ADP behaviors in the literature. This finding suggests a common generator for TEOAEs and ADPs. It is concluded from this study that this system identification procedure is a viable approach to the study of cochlear transduction.

Thesis advisor: Mark E. Chertoff.

**Acoustics of long enclosures** [43.55.Br, 43.55.Fw, 43.55.Hy, 43.38.Tj]—Jian Kang, *The Martin Centre, University of Cambridge, 6 Chaucer Road, Cambridge CB2 2EB, United Kingdom, November 1996 (Ph.D.)*. The aim of this research is to develop theories for a better understanding of the behavior of sound in long enclosures and to provide guidelines and prediction models for practical design. The thesis is in four parts, namely theory, scale modeling, speech intelligibility, and prediction. In Part 1, the usefulness of existing formulae for calculating the sound attenuation along the length is examined; formulae for calculating the reverberation time in rectangular long enclosures are derived; and a theoretical/computer model considering multiple sources is developed. It is demonstrated that the reverberation time varies systematically along the length, and at a receiver the reverberation time can be significantly increased by adding sources beyond a single source. In Part 2, the effectiveness of architectural acoustic treatments in long enclosures is analyzed based on a series of scale model measurements. The effectiveness of diffusers for increasing the sound attenuation along the length is proved. In Part 3, a series of articulation tests is described based on English, Mandarin, and Cantonese languages using loudspeaker sources. For a constant speech transmission index, it is found that the speech intelligibility in long enclosures is typically higher than that in regularly-shaped (i.e., quasi-cubic) rooms. The results also show some differences in speech intelligibility among the languages. In Part 4, a computer model is developed for predicting acoustic indices in long enclosures. As a subprogram, a model for predicting the temporal and spatial distribution of train noise in underground stations is also produced. The models have been validated in actual underground stations. [Work supported by ORS, COT, and MTRC.]

Thesis advisor: Rafal J. Orłowski.